IAHR 2017

37th IAHR WORLD CONGRESS
13-18 August, 2017
Kuala Lumpur, Malaysia

# RIVER SEDIMENT MANAGEMENT AND MORPHODYNAMICS

# EQUILIBRIUM SCOUR MORPHOLOGIES DOWNSTREAM OF BLOCK RAMPS LOCATED IN BOTH STRAIGHT AND CURVED CHANNELS

STEFANO PAGLIARA[(1)] & MICHELE PALERMO[(2)]

[(1, 2)]DESTEC-Department of Energy, Systems, Territory and Construction Engineering, University of Pisa, Pisa, Italy,
s.pagliara@ing.unipi.it; michele.palermo@ing.unipi.it

## ABSTRACT

The local scour occurring downstream of block ramps is carefully analyzed and studied in correspondence with straight river branches. But no studies are performed in order to analyze the scour mechanism in correspondence with river bends. In the present study, a dedicated model is built in order to analyze the scour process under several hydraulic conditions and ramp configurations. Namely, a succession of block ramps is tested in a laboratory flume, characterized by three different curvatures. Four ramps are located in the mentioned branches, whose slope is fixed at 0.083. Tests are conducted adopting one uniform bed material. Block ramps are located in the flume in such a way that both the effect of the upstream and downstream curvature on the scour process could be highlighted. The resulting equilibrium morphology downstream of the block ramp mainly depends on the channel geometric configuration and hydraulic conditions. Namely, the scour morphology results to be either three-dimensional or bi-dimensional are based on the river geometric configuration. In addition, the presence of the upstream curvature further amplifies the scour three-dimensionality, as the flow velocity distribution in the channel cross-section depends on the river curvature, i.e., its asymmetry is strictly related to the channel curvature. In the present paper, the resulting equilibrium morphologies are carefully surveyed and analyzed, highlighting both the effect of hydraulic conditions and channel bed curvatures. The analysis is conducted to identify those combinations of both hydraulic and geometric parameters which determine an increase of the scour depth with respect to the reference configuration, i.e., that in the straight branch of the channel. The results of the present paper can be useful to optimize the stilling basin design in the perspective of a harmonization of both hydraulic functioning of the analyzed river restoration structure and reduction of their impact on the natural contest.

**Keywords:** Block ramps; curved rivers; river morphology; sediment transport.

## 1 INTRODUCTION

Block ramps are river restoration structures which receive a considerable attention, because they are suitable both to control sediment transport and, at the same time, to minimize their impact on the river eco-system. Therefore, especially in the recent years, they have been widely adopted, thus leading the scientists to improve and define design criteria which can optimize both their hydraulic functioning and minimize the erosion occurring downstream of them. Nevertheless, a correct assessment of their characteristics, such as a detailed identification of proper design criteria is strictly necessary in order to avoid both structural problems and excessive erosion. This last aspect assumes a particular relevance, especially for low-head structures, therefore modeling in situ conditions is generally required. In fact, hydraulic models can help in understanding structural behavior and avoid design errors, which can eventually be also due to scale effects, as also shown, among others, by Bormann and Julien (1991), Chinnarasri et al. (2008), Pegram et al. (2009) and Heller (2011).

Nevertheless, the physical phenomena related to the presence of low-head structures are generally very complex and are not strictly connected to their hydraulic functioning. In fact, in the last decades, this structure typology has been widely used also because they contribute to improve the water quality characteristics (Whitaker and Potts, 2007; Phillips, 2010; Lisle, 1982). Namely, it is found that especially rock structures can substantially influence the water quality, because of their capacity to increase water flow oxygenation, resulting in a more suitable environment for biological species. However, the conjugation of this last aspect with their proper hydraulic functioning (e.g., sediment transport control) stimulate further researches on the topic, based on a more organic and extensive approach to the problems. In particular, several studies are conducted in order to understand the evolution of the river bed morphology in the presence of such structures. These studies suggested that the influence of the structure on the river bed evolution is strictly connected to its location. In general, they are not isolated structures but they can be built in series along the river. Therefore, it appears fundamental to understand the mutual interaction between the river bed evolution and structure positions, as shown by Lenzi et al., (2003), Marion et al. (2004), Martín-Vide and Andreatta (2006) and Pagliara et al. (2016a-b).

 

In other words, low-head structures cannot be considered as isolated elements but they are part of a more complex system. The scientific literature is rich of contributions focusing on the localized erosive process occurring either downstream or in correspondence with control structures (e.g., Veronese, 1937; Hassan and Narayanan, 1985; Mason and Arumugam, 1985; D'Agostino and Ferro, 2004; Dey and Raikar, 2005; Dey and Sarkar, 2006; Whitakerand Potts, 2007; Pagliara and Mahmoudi Kurdistani, 2015; Pagliara et al., 2015). Nevertheless, these studies mainly focus on the scour phenomena related to the consequences of excessive shear stresses originating from localized erosive processes. Although these last phenomena should be carefully controlled, their analysis and interpretation cannot be considered exhaustive in the perspective of an organic and complete understanding of the complexity of phenomena which can occur in a water body. Therefore, the analysis of these phenomena should also be taken into consideration. In particular, the energy dissipation due to the structure presence assumes a relevant and fundamental importance, as also shown by Bathurst et al. (1981), Oertel and Schlenkhoff (2012) and Pagliara and Palermo (2013).

In particular, at the University of Pisa, a significant effort in understanding the complexity of the phenomena occurring in correspondence with block ramps has been conducted (Pagliara and Palermo, 2008; Pagliara and Palermo, 2010; Pagliara and Palermo, 2011; Pagliara et al., 2012, Pagliara and Palermo, 2015). These studies are limited to straight channels and analyzed the scour process downstream of the block ramp both in clear water and live-bed conditions. The analysis is conducted in order to understand the main geometric characteristics of the scour hole and equilibrium morphology both in the presence and in the absence of protection rock sills located downstream of a block ramp. It is observed that the scour phenomenon is very complex and mainly depends on the following parameters: block ramp geometry, flow discharge, channel bed granulometric characteristics and channel geometry.

Nevertheless, only very recently that another fundamental aspect is taken into consideration. Pagliara et al. (2016c) analyzed the effect of the river geometry on the erosive process, i.e., the effect of river curvature on the maximum scour depth downstream of a block ramp. They found that the maximum scour depth mainly depends on the same parameters mentioned above, but it is also strongly influenced by the river curvature. The scour depth decreases with the river curvature, i.e., the maximum scour depth is generally less in straight channels if compared with that occurring in river bends under the same ramp geometry and hydraulic conditions.

This paper aims to furnish preliminary insights on the erosive process occurring in river bends downstream of succession of block ramps, characterized by a mild slope. In particular, this study will analyze the resulting equilibrium morphology under different hydraulic conditions and will highlight the effect of river curvature on it. The equilibrium scour morphology is the result of combined and multiple effects due to both hydraulic characteristics and geometric parameters. Although this paper merely demonstrates the results of a preliminary analysis of such complex phenomena, it represents the first systematic attempt to investigate the complexity of the scour process in correspondence with such structures by adopting an organic and exhaustive approach. Further studies are still ongoing to better understand the effect of ramp geometries and mutual locations in curved channels on the erosive phenomenon.

## 2 EXPERIMENTAL SETUP

The flume adopted to conduct the experimental tests was characterized by a first curved branch (whose curvature radius is $R_1$=11 m), followed by a straight branch (whose curvature radius $R_2$ is equal to infinity) and by a second curved branch (whose curvature radius is equal to $R_3$=6 m). The width of the flume was B=0.5 m. The channel bed material was characterized by the following granulometric characteristics: mean material diameter $d_{50}$=1.75 mm, geometric standard deviation $\sigma = (d_{84}/d_{16})^{0.5}$=1.2 and density $\rho_s$=2214 kg/m$^3$. A succession of four block ramps was located in the channel. Ramp 1 was located at the beginning of the first curved river branch, ramp 2 at the beginning of the straight channel, ramp 3 at the beginning of the second curved river branch and ramp 4 in the middle of this last curved branch. The ramp slope, S was fixed and equal to 0.083 (see Figure 1)

All the ramps were built by using rounded gravel material, where $D_{50}$ was 22.7 mm. In addition, two rows of the same rounded gravel material constituting the ramps were located on the channel bed immediately upstream and downstream of ramps (see Figure 2). Ramps were located in the channel in such a way that, for the tested hydraulic conditions, the equilibrium scour morphology did not reach the successive ramp, i.e., there was a negligible influence of the downstream ramp on the upstream scour process. In addition, all tests were conducted in clear water conditions.

Five different discharges were tested: Q=2.5, 3.5, 4.5, 5.9 and 12 l/s. The tail water (downstream of ramp 4 was regulated by using a sluice gate, whereas for the intermediate ramps there was no regulation. Two tanks were used in the model and they were connected by a pressurized pipe which allowed for water re-circulation. Prior to starting each experimental test, the stilling basin between two consecutive ramps was carefully leveled and made horizontal. Both channel bed morphology and water levels were measured during the tests using a 0.1 mm precise point gauge. The duration of each test was preliminarily fixed, i.e., preliminary tests were conducted in order to understand the minimum duration at which the equilibrium

 

morphology configuration could be reached. For the tested stilling basin material, the test duration was approximately 3 hours. When the equilibrium scour condition was reached, the water flow was stopped and the bed morphology was carefully surveyed. It was observed that no stilling basin material was trapped on the block ramp surface, thus confirming that all tests were conducted in clear water conditions and that the influence of a downstream ramp on the upstream scour is negligible. Figure 1 shows a schematic diagram of the experimental apparatus along with its components and Figure 2 shows pictures of the succession of block ramps simulated in the channel.

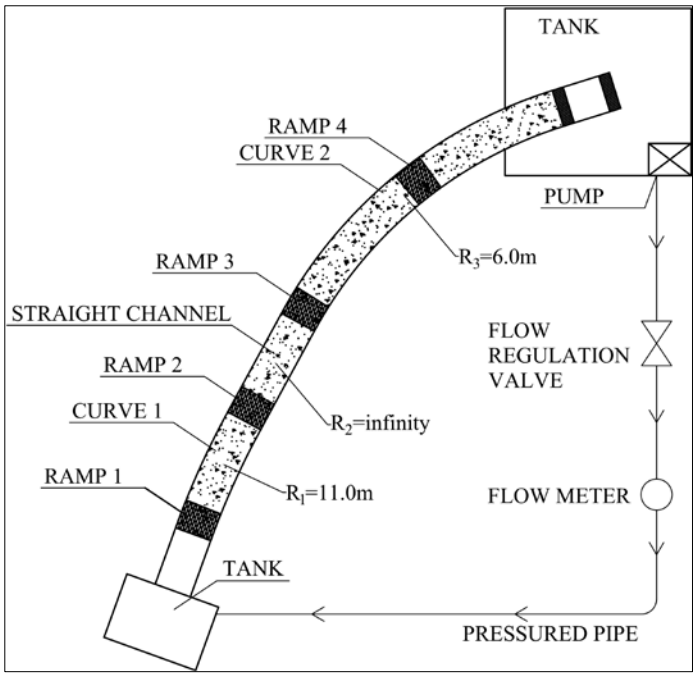


**Figure 1.** Diagram sketch of the experimental apparatus along with the indication of the location of the tested block ramps and channel bend succession.

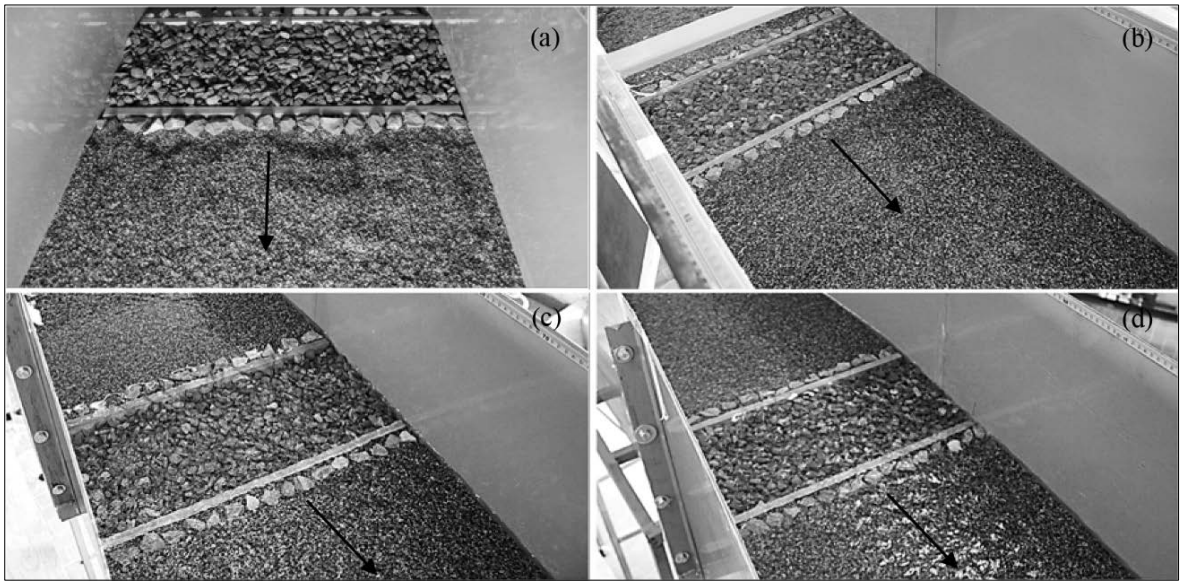


**Figure 2.** Succession of block ramps: (a) ramp 1, (b) ramp 2, (c) ramp 3, and (d) ramp 4, with the indication of flow direction (black arrow).

## 3 RESULTS AND DISCUSSION

### 3.1 Scour morphology in straight channels

The scour morphology in straight channels in clear water conditions was extensively studied by Pagliara and Palermo (2008) and Pagliara and Palermo (2010). They analyzed the equilibrium morphology furnishing predicting equations to evaluate the main scour hole lengths both in the presence and absence of rock protection sills located in the stilling basin. Pagliara and Palermo (2008) proposed the following equations to

 

predict the maximum non-dimensional scour depths $Z_m=z_m/h_1$ and $Z_{ms}$, where $z_m$and $z_{ms}$ are the maximum scour depths in the absence and presence of a protection sill downstream of the block ramp, respectively, and $h_1$ is the water depth at the ramp toe. Note that S is the ramp slope, $F_{d90}=V/[g\cdot(\rho_s/\rho-1)\cdot d_{90}]^{0.5}$ is the densimetric Froude number, where g is the acceleration due to gravity, $\rho$ is the water density, $d_{xx}$ is the stilling basin material diameter for which xx% is finer, and V is the approaching flow velocity at the ramp toe. a, b, c, d, e, f are coefficients which takes into account the effect of the downstream rock sill on the scour process, and $\lambda$ and $Z_{op}$ are the non-dimensional longitudinal and vertical positions of the protection sill, respectively. For the modeled configuration, $\lambda=0$ and $Z_{op}=0$, i.e., $Z_{ms}=0.912Z_m$ (see Pagliara and Palermo, 2008).

$$Z_m = 0.58 \cdot S^{0.75} \cdot F_{d90}^{1.8} \quad [1]$$

$$Z_{ms} = Z_m \cdot \left(a\lambda^2 + b\lambda + c\right) \cdot \left(dZ_{op}^2 + eZ_{op} + f\right) \quad [2]$$

Previous equations show that both in the presence and absence of a protection sill, the scour morphology depends on hydraulic conditions, ramp geometry, granulometric characteristics of the stilling basin and sill spatial position. In addition, it is also evident that the presence of the sill located immediately downstream of the stilling basin contributes to reducing the scour depth. Figure 3 shows the equilibrium morphology obtained from two experimental tests. Figure 3a-b shows the plan and 3D view of the equilibrium morphology for Q=2.5 l/s whereas Figure 3c-d shows the same for Q=5.9 l/s.

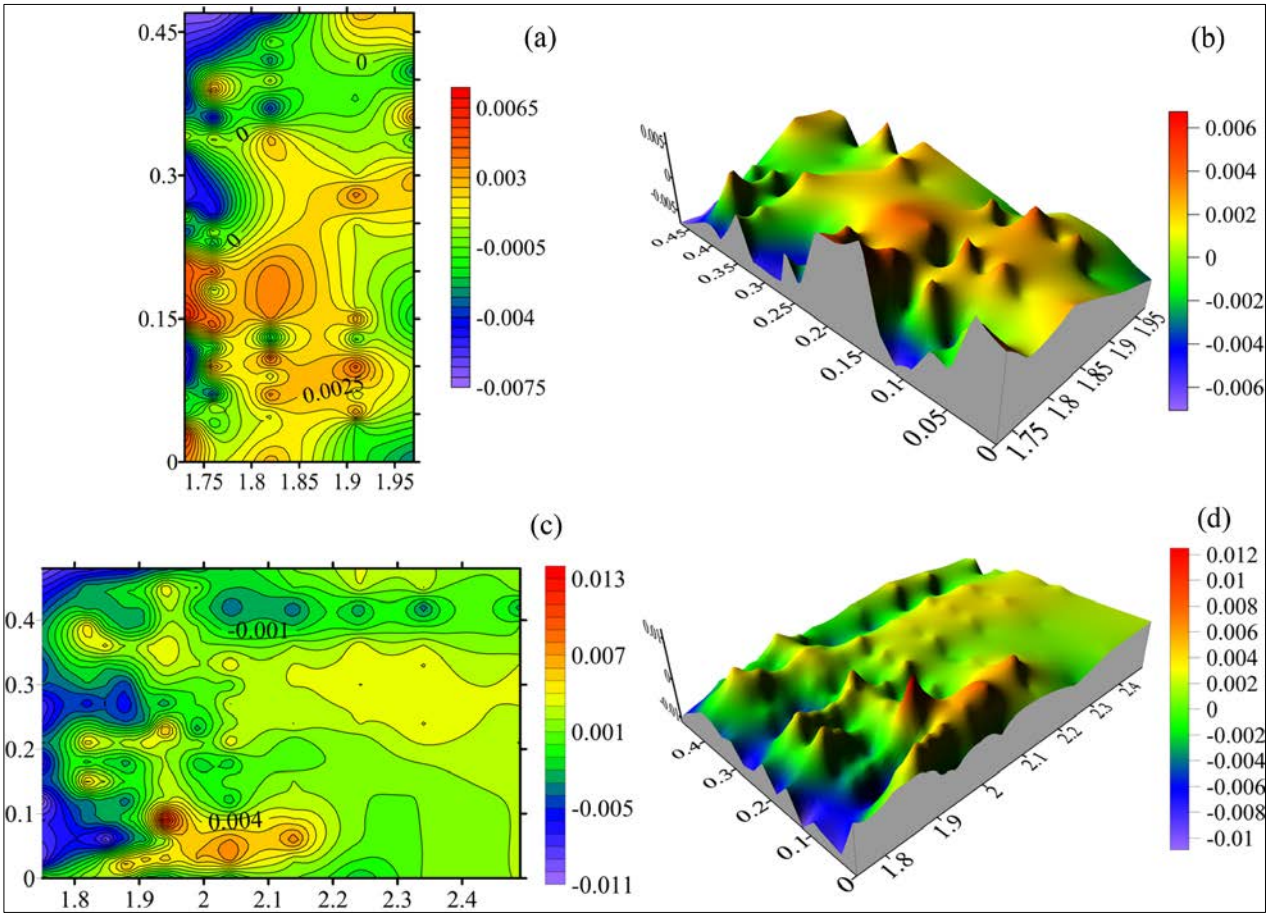


**Figure 3.** Ramp 2: (a) Plan view and (b) 3D view of equilibrium morphology for Q=3.5 l/s;(c) Plan view and (d) 3D view of equilibrium morphology for Q=12 l/s (flow from left to right).

It appears evident that the scour morphology is essentially 2D, independent of the discharge. In addition, by increasing the discharge, the two-dimensionality of the scour morphology is also more obvious. This is mostly due to the fact that for low discharges there are secondary effects which contribute to the scour process. Rocks protrusion has an effect on the localized scour hole immediately downstream of the protection sill which tends to vanish by increasing the discharge. Further, wall effects are also more relevant for lower discharges. Therefore, as shown by Pagliara and Palermo (2008), the ratio between the maximum scour

 

depth and the average scour depth in the section in which $Z_m$ occurs tends to 1 by increasing the flow discharge.

Furthermore, hydraulic jump characteristics also influence the equilibrium morphology. Namely, two different hydraulic jump types can occur downstream of block ramp: $F_{MB}$ and $S_{MB}$, respectively (see also Pagliara and Palermo, 2010). $F_{MB}$ hydraulic jump is characterized by a clock-wise roller and by a sediment transport directed both upstream and downstream. It occurs for selected ramp geometry and hydraulic conditions. Experimental tests performed in this study are all characterized by a $F_{MB}$ hydraulic jump formation.

3.2 Scour morphology in curved channels

Tests conducted in the curved branches of the channel allow understanding of the effect of curvature on the equilibrium morphology. In general, the maximum scour depth increases with river curvature as it is also observed by Pagliara et al. (2016c), who proposed the following equation to estimate $Z_{msc}=z_{msc}/h_1$, with $z_{msc}$ as the maximum scour depth in a curved branch in the presence of a downstream protection sill:

$$Z_{msc} = 0.912 Z_m \cdot \left(1+\frac{B}{R}\right)^{2.82} \qquad [3]$$

The river curvature modifies the transversal velocity distribution, thus varies the approaching flow condition at the ramp toe. In other words, the transversal velocity distribution is strongly influenced by the river curvature. A decrease of the parameter R contributes to an increase of the velocity transversal asymmetry, resulting in a transversal asymmetric shear stresses distribution acting on the mobile bed. This is the main reason for which the scour morphology tends to be more 3D than in the corresponding straight case.

The modification of flow conditions downstream of a block ramp strongly contributes to varying equilibrium morphology. Figures 4 and 5 show equilibrium morphologies occurring downstream of two block ramps (ramp 1 and ramp 3, respectively), characterized by similar upstream flow conditions. In fact, the upstream flow for both the ramps is symmetrically distributed, as for both the ramps the upstream channels are straight. Therefore, the difference in scour morphology is essentially due to the downstream geometry of the channel and the resulting asymmetric flow velocity distribution.

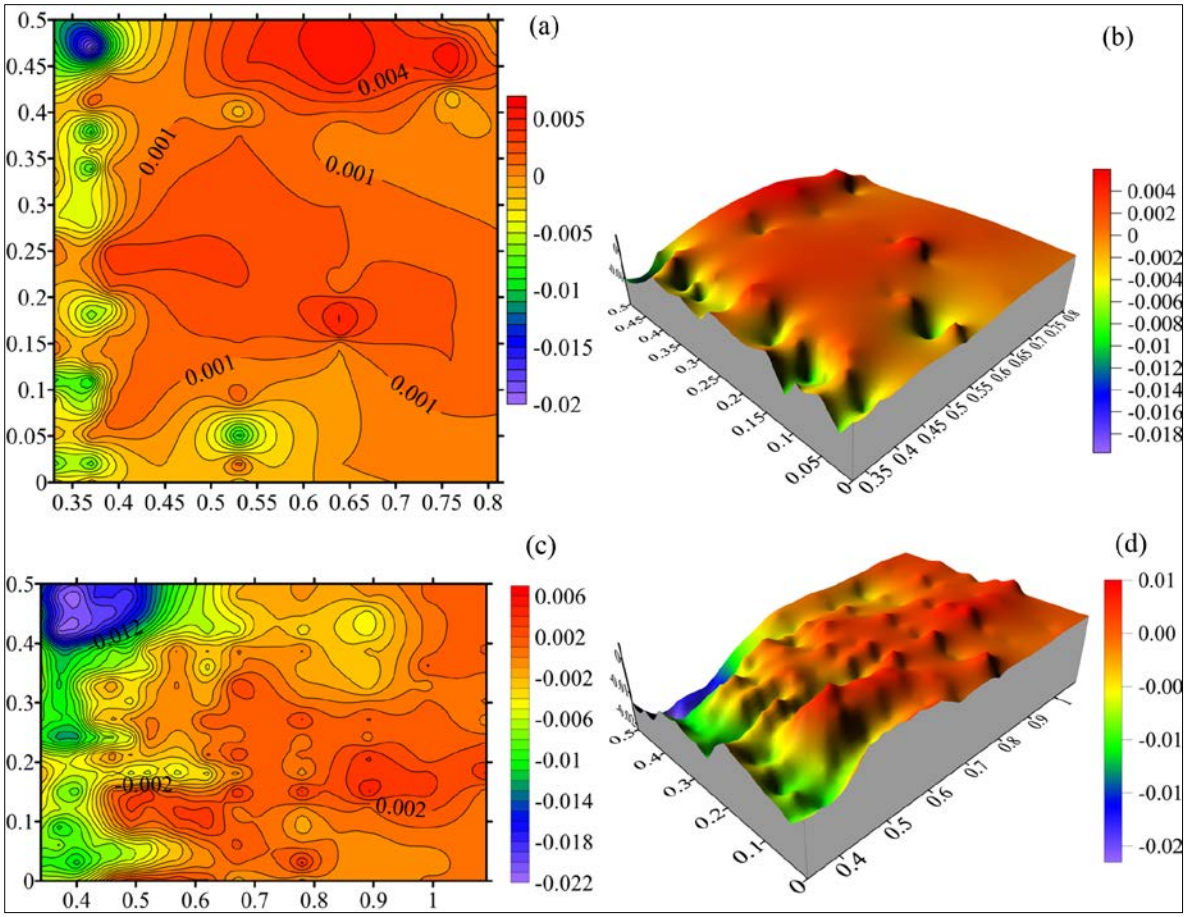


**Figure 4.** Ramp 1: (a) Plan view and (b) 3D view of equilibrium morphology for Q=3.5 l/s; (c) Plan view and (d) 3D view of equilibrium morphology for Q=12 l/s (flow from left to right).

 

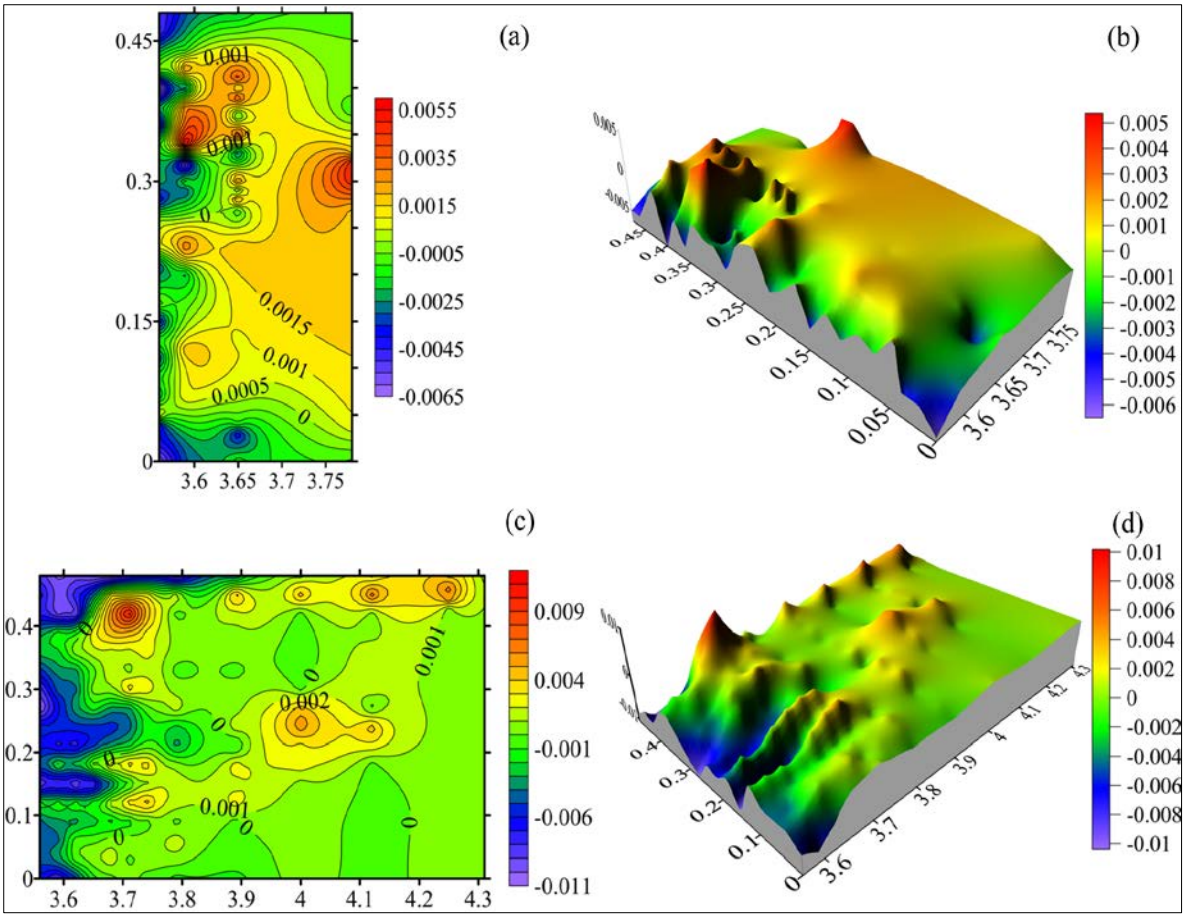


**Figure 5.** Ramp 3: (a) Plan view and (b) 3D view of equilibrium morphology for Q=3.5 l/s; (c) Plan view and (d) 3D view of equilibrium morphology for Q=12 l/s (flow from left to right).

By comparing Figure 4a-b with Figure 5a-b and Figure 4c-d with Figure 5c-d, relative to ramps 1 and 3, located at the beginning of two different curved branches ($R_1$=11m and $R_3$=6m, respectively), it can be easily observed that both the scour hole morphologies and deposit areas distribution in the stilling basin are quite different. Namely, for low discharges (Figures 4a-b and Figures 5a-b), the scour morphology still appears quite 2D. This is mainly due to the fact that low discharges result in low shear stresses acting on the stilling basin, thus contributing to transport a relatively low quantity of sediment downstream. Furthermore, in this case, the maximum local scour peaks can eventually be due to the random distribution of rocks constituting the ramp and their protrusion with respect to the average level of rock tops. Nevertheless, in the second case (Figures 5a-b), it is already evident that the increase of the channel curvature results in a more 3D equilibrium morphology, which is characterized by more prominent erosion areas located close to the outer part of the channel. Similarly, sediment bars (deposit areas) also appear quite short and mostly located close to the central part of the channel. Therefore, for a low discharge, a sort of channelization process of the stilling basin starts to occur. The flow downstream of the ramp starts forming a sort of preferential flow path mostly located in the outer part of the channel, thus increasing both the local scour peak and the three-dimensionality of the phenomenon.

The increase of the flow discharge further amplifies the mentioned sediment transport dynamics (Figure 4c-d and Figure 5c-d). The discharge increase models the stilling basin by amplifying the channelization of the flow pattern. In other words, the scour hole mainly occurs close to the outer part of the channel whereas the sediment deposits are located either in central part of the channel (lower curvature) or closer to the inner part of the channel (higher curvature). In addition, the longitudinal extension of deposit areas also increases and it tends to occur further away from the ramp toe.

The three-dimensionality of the scour morphology is more evident, such as the increase of the maximum local scour depth. In particular, by increasing the river curvature, the increase of the scour depth can be significant, up to 50% more than the corresponding scour depth occurring in straight channels. This evidence is fundamental in terms of a correct design of the structure and of the downstream stilling basin. It appears fundamental to take into consideration the scour depth increase in order to avoid structural problems for both the hydraulic structure and river banks.

 

In fact, it can lead to two main problems: 1) blocks constituting the ramp can become locally unstable due to the modified transversal flow velocity distribution; 2) the localized increase of the scour depth, mainly located close to the outer part of the river bend, can lead to river banks collapse. Therefore, it is essential to adopt several countermeasures, i.e., rocks constituting the block ramp should be bigger than in the case of straight channel and the foundations or the river banks should be deeper or properly protected in order to avoid their failure.

Nevertheless, there is also other element which increases the complexity of the phenomenon. In previous cases, block ramps were located at the beginning of curved river branches preceded by straight channels. It means that the flow velocity asymmetry is mainly due to the downstream geometry of the river branch. But in the case in which the ramp is both preceded and followed by a curved river branch, the flow velocity asymmetry occurs both upstream and downstream of the structures. This is the case of ramp 4, whose equilibrium morphologies are shown in Figure 6.

By comparing Figure 5a-b with Figure 6a-b and Figure 5c-d with Figure 6c-d, relative to ramps located in river branches characterized by the same curvature but by different upstream velocity distribution, the differences between the two configurations can be easily pointed out.

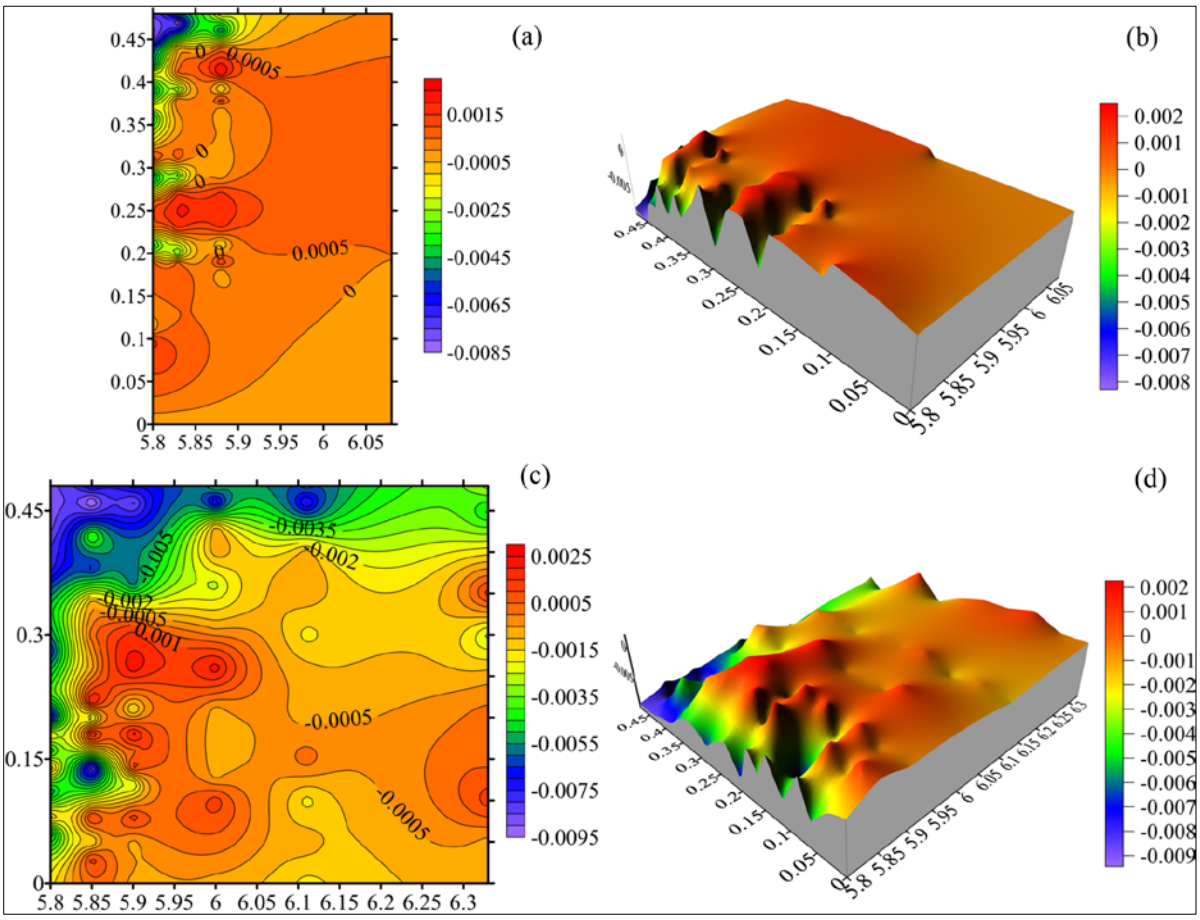


**Figure** 6. Ramp 4: (a) Plan view and (b) 3D view of equilibrium morphology for Q=3.5 l/s; (c) Plan view and (d) 3D view of equilibrium morphology for Q=12 l/s (flow from left to right).

The presence of an upstream flow velocity distribution asymmetry modifies the downstream flow distribution. In correspondence with a structure located inside a curved river branch, the physical phenomena described for block ramp 3 are further amplified and some differences in bar formation take place. In other words, the process of channelization of the stilling basin is more prominent and, at the same time, the bar formation occurs further downstream and mostly located in the central/inner part of the curved river branch. It should be noted that the flow velocity asymmetry is more prominent in the case in which a curved river branch is present upstream of the structure. Therefore, the flow distribution on the ramp toe is already affected by a significant asymmetry, resulting in shear stresses at the toe of the ramp which are more prominent in the outer part of the downstream river branch with respect to the case of ramp 3. It implies that the erosive action of the flow immediately downstream of the ramp toe is more significant in correspondence with the outer part of the downstream stilling basin, shifting sediment deposits further downstream.

Nevertheless, the analysis of experimental data shows that in the tested range of parameters and configurations, the maximum scour depth is slightly influenced by the upstream asymmetry of the flow

 

velocities. Therefore, for practical applications and relatively mild river curvatures, the effect of the upstream flow velocity distribution on the maximum scour depth can be considered negligible. Thus, the equation proposed by Pagliara et al. (2016c) can be applied for both the cases.

## 4 CONCLUSIONS

This paper focuses on the effect of river curvature on equilibrium scour morphology characteristics downstream of a block ramp. The analysis is conducted based on experimental evidences. A dedicated model is built in which four ramps are located. Ramps are located in a straight channel and in two curved branches. In addition, another ramp is located inside a river branch in order to test the effect of both upstream and downstream flow velocity asymmetry on the scour characteristics. Although the results of the present study are preliminary, they can be considered useful in the perspective of a correct design of such structure typologies. It is shown that the effect of the river curvature increases the maximum scour depth and the three-dimensionality of the erosive phenomenon. In other words, it is shown that the maximum scour depth increases with curvature. In addition, sediment deposit formation is also strongly influenced by the river curvature. Namely, deposit areas shift towards the inner part of the curved river branch by increasing the curvature and a significant process of stilling basin channelization takes place. The effect of an upstream river curvature does not have significant effects in terms of maximum scour depth increase if compared with the case in which only the downstream river branch is curved. Nevertheless, it influences the sediment deposit area distribution. The sediment deposit formation occurs further downstream and closer to the inner part of the downstream river branch.

This study shows that a proper design of such structures in curved river branches requires a detailed analysis and comprehension of the erosive process, as the maximum scour depth can increase up to 50% with respect to the corresponding case in which the structure is located in a straight channel. Therefore, further experimental tests are still ongoing to better understand the effect of block ramp geometries on equilibrium morphologies and furnish relationships to allow for a generalization of these preliminary results which could be very useful in terms of practical applications.

## REFERENCES

Bathurst, J.C., Li, R.M. & Simons, D.B. (1981). Resistance Equation for Large Scale Roughness. *Journal of Hydraulic Engineering Division*, 107(12), 1593–1613.

Bormann, E. & Julien, P.Y. (1991). Scour Downstream of Grade Control Structures. *Journal of Hydraulic Engineering*, 117(5), 579-594.

Chinnarasri, C., Donjadee, S. & Israngkura, U. (2008). Hydraulic Characteristics of Gabion-Stepped Weirs. *Journal of Hydraulic Engineering*, 134(8), 1147-1152.

D'Agostino, V. & Ferro, V. (2004). Scour on Alluvial Bed Downstream of Grade-Control Structures. *Journal of Hydraulic Engineering*, 130(1), 1-14.

Dey, S. & Raikar, R.V. (2005). Scour in Long Contractions. *Journal of Hydraulic Engineering*, 131(12), 1036-1049.

Dey, S. & Sarkar, A. (2006). Scour Downstream of an Apron Due to Submerged Horizontal Jets. *Journal of Hydraulic Engineering*, 132(3), 246-257.

Hassan, N.M.K.N. & Narayanan, R. (1985). Local Scour Downstream of an Apron. *Journal of Hydraulic Engineering*, 111(11), 1371-1385.

Heller, V. (2011). Scale Effects in Physical Hydraulic Engineering Models. *Journal of Hydraulic Research*, 49(3), 293-306.

Lenzi, M.A., Marion, A. & Comiti, F. (2003). Interference Processes on Scouring at Bed Sills. *Earth Surface Processes and Landforms*, 28(1), 99-110.

Lisle, T.E. (1982). Effects of Aggradation and Degradation on Riffle-Pool Morphology in Natural Gravel Channels, Northwestern California. *Water Resources Research*, 18(6), 1643-1651.

Marion, A., Lenzi, M.A. & Comiti, F. (2004). Effect of Sill Spacing and Sediment Size Grading On Scouring At Grade-Control Structures. *Earth Surface Processes and Landforms*, 29(8), 983-993.

Martin-Vide, J.P. & Andreatta, A. (2006). Disturbance Caused By Bed Sills on the Slopes of Steep Streams. *Journal of Hydraulic Engineering*, 132(11), 1186-1194.

Mason, P.J. & Arumugam, K. (1985). Free Jet Scour below Dams and Flip Buckets. *Journal of Hydraulic Engineering*, 111(2), 220-235.

Oertel, M. & Schlenkhoff, A. (2012). Crossbar Block Ramps: Flow Regimes Energy Dissipation, Friction Factors, and Drag Forces. *Journal of Hydraulic Engineering*, 138(5), 440-448.

Pagliara, S. & Mahmoudi Kurdistani, S. (2015). Clear Water Scour at J-Hook Vanes in Channel Bends for Stream Restorations. *Ecological Engineering*, 83, 386-393.

Pagliara, S. & Palermo, M. (2008). Scour Control Downstream of Block Ramps. *Journal of Hydraulic Engineering*, 134(9), 1376-1382.

Pagliara, S., Hassanabadi, L. & Mahmoudi Kurdistani, S. (2015). Clear Water Scour Downstream of Log Deflectors in Horizontal Channels. *Journal of Irrigation and Drainage Engineering*, 141(9), 04015007.

 

Pagliara, S., Mahmoudi Kurdistani, S., Palermo, M. & Simoni, D. (2016a). Scour due to Rock Sills in Straight and Curved Horizontal Channels. *Journal of Hydro-Environment Research*, 10, 12-20.
Pagliara, S. & Palermo, M. (2010). Influence of Tailwater Depth and Pile Position on Scour Downstream of Block Ramps. *Journal of Irrigation and Drainage Engineering*, 136(2), 120-130.
Pagliara, S. & Palermo, M. (2011). Effect of Stilling Basin Geometry on Clear Water Scour Morphology Downstream of a Block Ramp. *Journal of Irrigation and Drainage Engineering*, 137(9), 593-601.
Pagliara, S. & Palermo, M. (2015). Hydraulic Jumps on Rough and Smooth Beds: Aggregate Approach for Horizontal and Adverse-Sloped Beds. *Journal of Hydraulic Research*, 53(2), 243-252.
Pagliara, S., Palermo, M. & Carnacina, I. (2012). Live-Bed Scour Downstream of Block Ramps for Low Densimetric Froude Numbers. *International Journal of Sediment Research*, 27(3), 337-350.
Pagliara, S. & Palermo, M. (2013). Rock Grade Control Structures and Stepped Gabion Weirs: Scour Analysis and Flow Features. *Acta Geophysica*, 61(1), 126-150.
Pagliara, S., Palermo, M. & Das, R. (2016b). Eco-Friendly Countermeasures for Enlarged Basins Erosion. *River Research and Applications*, 32(3), 441- 451.
Pagliara, S., Radecki-Pawlik, A., Palermo, M. & Plesiński, K. (2016c). Block Ramps in Curved Rivers: Morphology Analysis and Prototype Data Supported Design Criteria for Mild Bed Slopes. *River Research and Applications,* 33(3), 427- 437.
Pegram, G.G.S., Officer, A.K. & Mottram, S. (1999). Hydraulics of Skimming Flow on Modeled Stepped Spillways. *Journal of Hydraulic Engineering*, 125(5), 500-510.
Phillips, J.D. (2010). The Job of the River. *Earth Surface Processes and Landforms*, 35(3), 305-313.
Veronese, A. (1937). Erosioni di Fondo a Valle di uno Scarico. *Annali Lavori Pubblici*, 75, 717-726 [In Italian].
Whitaker, A.C. & Potts, D.F. (2007). Analysis of Flow Competence in an Alluvial Gravel Bed Stream, Dupuyer Creek, Montana. *Water Resources Research*, 43(7), 1-16.

 

Proceedings of the 37th IAHR World Congress
August 13 – 18, 2017, Kuala Lumpur, Malaysia

# EFFECT OF RIVER CURVATURE ON SCOUR PROCESS IN CORRESPONDENCE WITH ARCHED SILLS

MICHELE PALERMO[1] & STEFANO PAGLIARA[2]

[1,2] DESTEC-Department of Energy, Systems, Territory and Construction Engineering, University of Pisa, Pisa, Italy,
michele.palermo@ing.unipi.it; s.pagliara@ing.unipi.it

## ABSTRACT

Hydraulic structures functioning and erosive processes occurring in curved rivers are still under-investigated. In the present paper, an experimental analysis is conducted focusing on a particular structure typology: rock arched sills. This type of structure is similar to linear rock sills, but they are shaped in such a way that they can more properly orientate the flow. The analysis of this structure typology is conducted in a dedicated flume. The laboratory flume is characterized by four different curved branches. One uniform channel bed material is used to simulate the mobile bed and experimental tests are carried out up to when the equilibrium scour configuration is reached. Experiments are conducted for different flow discharges and tail water levels. Furthermore, different sills are tested, i.e., the height of the sill from the original bed level is varied. In addition, the transversal location of sills is also varied. Namely, sills are located in different spatial positions and in succession in the same curve, in order to test the mutual interference on the scour process. When the equilibrium scour condition is achieved, the channel bed morphology is carefully surveyed. The analysis of the experimental evidences allow to establish that different scour typologies take place. In addition, it is experimentally proven that the maximum scour depth, such as the scour hole length, are significantly affected by the channel curvature. Experimental results are elaborated and empirical relationships are furnished in order to estimate the maximum scour lengths. This paper could be useful for a correct design of this structure typology. Nevertheless, further experimental tests are required in order to optimize the location of such structures and to better understand the physics of the scour mechanism in a larger range of both hydraulic parameters and geometric configurations.

**Keywords:** Arched sills; curved rivers; river morphology; scour process.

## 1 INTRODUCTION

Small river structures are often used in practical applications in order to create optimal conditions for fish species. In particular, the adoption of relatively small rock structures in order to control sediment erosion and minimize their impact on the natural contests becomes very frequent in the last decades. Therefore, several studies analyzed different structure typologies in order to derive relationships for a correct design. In the last decades, the use of submerged vanes, cross vanes, W-weirs, rock sill, etc. has become very popular (e.g., Pagliara and Kurdistani, 2015; Pagliara et al, 2015; Pagliara et al., 2016a). These structures are characterized by a limited environmental impact and, at the same time, they are very flexible. Nevertheless, the actual design criteria are mainly related to structures located in straight rivers, whereas, in usual applications, it is not rare to find them in correspondence with river bends. This last configuration is still under-investigated and requires further efforts from scientific community.

However, the analysis of the erosive processes in correspondence with hydraulic structures is a fundamental topic, whose importance is also highlighted by the amount of the studies which have been conducted in the last decades. Namely, hydraulic structures are widely adopted for multiple uses, e.g., sediment transport control, erosion protection, energy dissipators, etc. In particular, the analysis of the erosive processes occurring in their correspondence assumes a significant importance (e.g., Bathurst et al., 1981; Dey and Raikar, 2005; Dey and Sarkar, 2006; Hassan and Narayanan, 1985; Veronese, 1937) due to the consequences of a potential failure of a hydraulic structure because of the excessive scour at the toe (Bormann and Julien, 1991; Chinnarasri et al., 2008; D'Agostino and Ferro, 2004). In particular, the conjugation of the hydraulic functioning, including the erosive process at the toe of the structures, and the environmental sustainability led hydraulic engineers to develop and analyze further structure typologies in order to control the sediment transport. Namely, low-environmental impact structures (e.g., rock sills, rock grade control structures, block ramps, etc.) receive a great attention. Several studies were conducted in order to analyze both the hydraulics of these structure typologies and the equilibrium morphology at their toe. Lenzi et al. (2003), Marion et al. (2004), and Martin-Vide and Andreatta (2006) analyzed the scour process due to rock sill successions located both in laboratory model and in rivers, also focusing on the potential scale effects (Heller, 2011). They concluded that the scour process is mostly due to the geometric configuration of the

 

structure, to the hydraulic conditions and to the spatial location, i.e., to the longitudinal distance of a rock sill from the succeeding one.

Other studies analyzed different rock structures (e.g., block ramps and stepped gabion weirs), focusing on their capacity to dissipate flow energy. Stepped gabion weir hydraulics was analyzed by Pagliara and Palermo (2013) and Pegram et al. (1999). They concluded that the dissipative mechanism strongly depends on the upstream hydraulic conditions and on the structure geometry, resulting in the possibility of three different flow regimes occurring on the structure itself (i.e., skimming, transition and nappe flow).

A similar approach is also developed for other rock structures which have become particularly important, as they are widely adopted recently. Namely, both the hydraulics and the erosive process occurring in the presence of a block ramp were deeply analyzed by Oertel and Schlenkhoff (2012) and Pagliara and Palermo (2010), under clear water conditions and prismatic stilling basin. Further investigations are also conducted to understand the erosive mechanism under live-bed conditions and for both protected and non-prismatic stilling basins (Pagliara and Palermo, 2008; Pagliara and Palermo, 2011; Pagliara et al., 2012; Pagliara et al., 2016b). It is observed that the dissipative mechanism is strongly affected by the downstream hydraulic jump which can be either located in the stilling basin or, partially, on the structure itself (Pagliara and Palermo, 2015). Nevertheless, as noted by Lisle (1982) and Phillips (2010), rivers are dynamic systems, characterized by a continuous evolution and by morphologies which can be significantly different from those generally modelled in laboratories. In particular, they highlighted the complexity of the erosive processes in correspondence with river bends. This complexity is further amplified in the presence of a hydraulic structure. Nevertheless, this last aspect is still not well-known. Namely, there are almost no studies in literature dealing with the river morphology evolution in the presence of low-environmental impact structures.

Only recently, Pagliara et al. (2016c) analyzed the scour morphology downstream of block ramp located in river bends. They showed that the scour mechanism is significantly affected by the river curvature, such as the geometric characteristics of the scour hole. It is shown that the maximum scour depth increases with river curvature and shifts towards the river banks. Therefore, the understanding of the river dynamics in the presence of a grade-control structure assumes a fundamental importance.

The aim of the present manuscript is to test innovative low-environmental impact structures (arched rock sills), by which it is possible to both create suitable local conditions for fish species and, at the same time, to protect river banks in bends (if opportunely located). The analysis is conducted by modelling such structure typology in a dedicated laboratory channel. The scour morphology is analyzed and useful relationships are derived to estimate the maximum scour depth.

## 2 EXPERIMENTAL SET UP

A dedicated model was built at the hydraulic laboratory of the University of Pisa. The channel was characterized by three different curved branches. Namely, the first curved branch was characterized by a curvature radius $R_1$=2 m, followed by a straight branch (whose curvature $R_2$ is equal to infinity). Furthermore, two other curved branches were present in the channel, characterized by curvature radii equal to $R_3$=1 m and $R_4$=4 m, respectively. Grids were located at the beginning of each channel sector in order to regulate the entering flow characteristics. Rock arched sills were located at different spatial positions (i.e., 1/3 and 2/3 of the channel transversal width) and in succession in the same curve (sills A and B), in order to test the effect of their longitudinal position for constant curvature. In the present study, tests were performed in two of the three channel bends, i.e., for $R_1$=2 m, $R_3$=1 m.

Further tests were also conducted in the straight part of the channel in order to understand the effect of river curvature on the scour mechanism. Figure 1 shows the diagram sketch of the experimental apparatus, along with the indication of the transversal sections in which the arched sills were located. Namely, sills A and B were located in the first channel bend ($R_1$=2 m): sill A was located at the beginning of the branch, whereas sill B was located at the middle of the same channel branch. Sill C was located at the middle of the straight branch. Finally, sill D was located at the beginning of the second curved branch ($R_3$=1 m). Two tanks and a pump system allowed for water re-circulation.

Different sills types were built and tested. They were built with different rocks, arranged in such a way that the height $h_{st}$ of the rock tops from the original channel bed level was equal to 6, 3 and 1 cm, respectively. The average diameter $D_{50}$ of rocks constituting the sills varied from 3 to 7 cm. They were located at selected transversal sections in such a way that y/B=1/3 or 2/3, respectively, where y is the distance of the arched rock sill symmetry axis from the inner channel wall and B is the channel width. Figure 2a shows a diagram sketch of a rock sill, along with the main scour hole lengths and hydraulic parameters, i.e., maximum scour depths upstream and downstream of the structure ($z_{mu}$ and $z_{md}$, respectively), upstream and downstream water depths (h and $h_0$, respectively), water discharge Q and water depth difference between upstream and downstream of the structure ($\Delta$y). Figure 2b-d show pictures of sills located at different transversal sections, i.e., sills A, B and D, respectively.

 

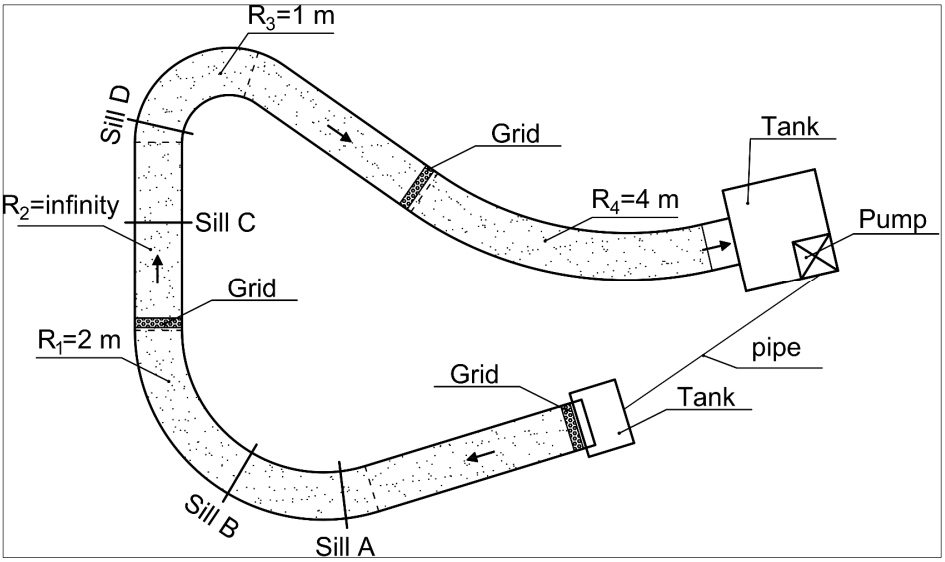


**Figure 1.** Diagram sketch of the experimental apparatus along with the indication of the location of tested sills.

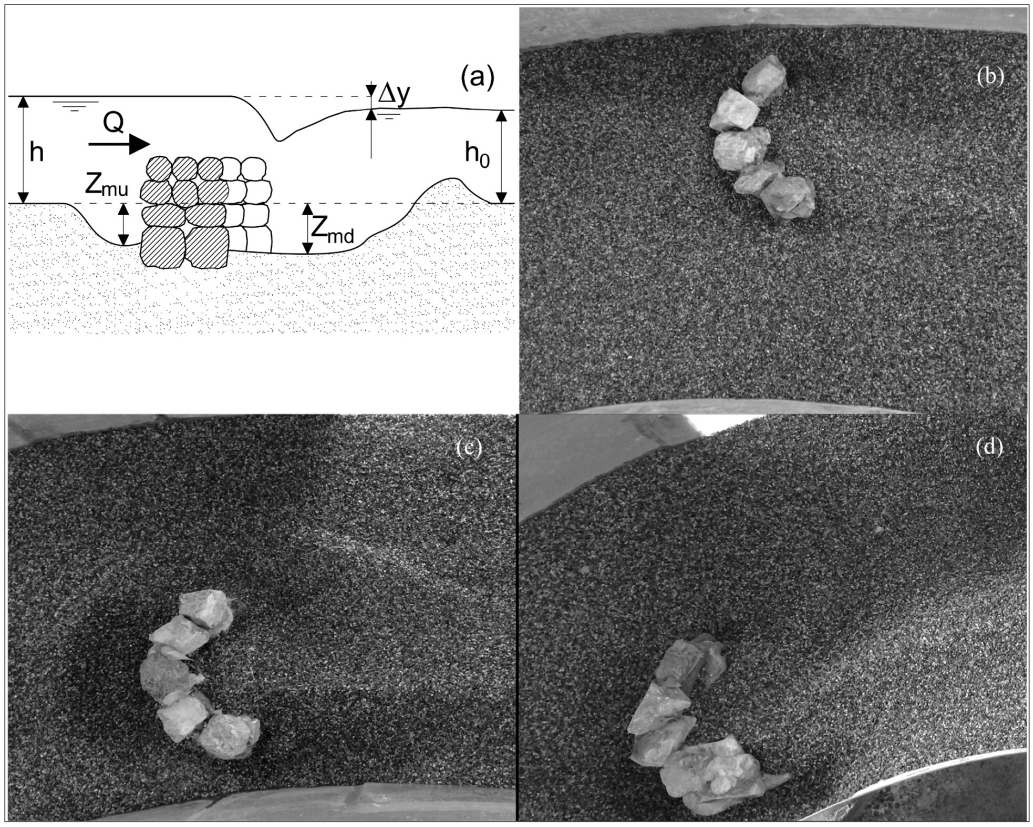


**Figure 2.** (a) Diagram sketch of the longitudinal section of the equilibrium morphology along with the indication of the main scour characteristics; picture of (b) sill A located at 2/3 of the channel width, (c) sill B located at 1/3 of the channel width and (d) sill D located at 2/3 of the channel width (flow from left to right).

The channel bed was made of a uniform granular material whose average diameter $d_{50}$=0.00175 m and density $\rho_s$=2214 kg/m$^3$. Before starting each experimental test, channel bed was carefully levelled. Tests were conducted under different hydraulic conditions, i.e., both water discharge and water depths were varied. Once the equilibrium scour configuration had been reached (approximately after 3 hours from the tests beginning), the channel bed was carefully surveyed by using a 0.1 mm precise point gauge. For the present study, the non-dimensional parameter $\eta=A_{50}^2\cdot(\Delta y/h_{st})$, introduced by Pagliara et al. (2016a) for linear rock sills in curved rivers, varied between 0.2 and 95, where $A_{50}=Q/\{l_{st}\cdot h_{st}\cdot[g\cdot(\rho_s/\rho-1)\cdot d_{50}]^{0.5}\}$, in which $l_{st}$ is the structure length, g is the acceleration due to gravity and $\rho$ the water density.

 

## 3 RESULTS AND DISCUSSION

### 3.1 Equilibrium morphologies

The analysis of the equilibrium morphologies is conducted for all tested configurations and sills. Namely, the scour is carefully surveyed and contour maps are developed for each test. Therefore, it is possible to understand the qualitative behavior of the erosive process. When a sill is located at the beginning of a river bend (e.g., sills A and D), the equilibrium scour morphology becomes asymmetric. The scour asymmetry is a consequence of the velocity field asymmetry. Namely, the channel curvature causes a variation of the kinematic field, resulting in an increase of shear stresses close to the inner channel wall. Sediment dynamics is subjected to an asymmetric shear stress distribution. Namely, in the case of sill A (located at the channel bend whose $R_1$=2 m), the resulting equilibrium morphology exhibits a clear asymmetry, resulting in a prominent longitudinal extension of both the inner part of the scour hole and ridge (Figure 3). This effect is further amplified by two parameters: the transversal location of the sill (y/B) and the height of the structure ($h_{st}$). Namely, when the structure is located close to the inner part of the channel, both the scour hole and ridge result to be more longitudinally extended with respect to the case in which y/B=2/3. This is mostly due to shear stress distribution, which decreases with R+y, where y is the radial distance from the inner wall of the bend. In addition, the presence of a higher sill contributes to increase the difference between upstream and downstream water depths, resulting in a deeper and more longitudinally extended scour formation. The described mechanism applies for both sills A and sill B. Nevertheless, in correspondence with sill B, experimental evidences show a slight increase of both scour and ridge lengths. But no significant differences can be noted in terms of maximum scour depth. Therefore, for practical applications, the inflow conditions play a negligible role in the tested range of parameters. In other words, for sill B, the flow upstream of the structure is already characterized by an asymmetric kinematic field, whereas for sill A, located at the beginning of the bend the upstream kinematic field is essentially symmetric. This slight difference results in a slight increase of the planar extension of both scour hole and ridge but does not cause a significant increase of the maximum scour depth. Furthermore, there is also a difference between linear rock sills and arched rock sills. In this last case, the scour process involves both the upstream and downstream channel bed. This is mainly due to the structure shape, allowing for a flow circulation around the structure itself. Whereas, for linear sills, the relevant increase of the water depth upstream of the structure does not allow for upstream scour formation.

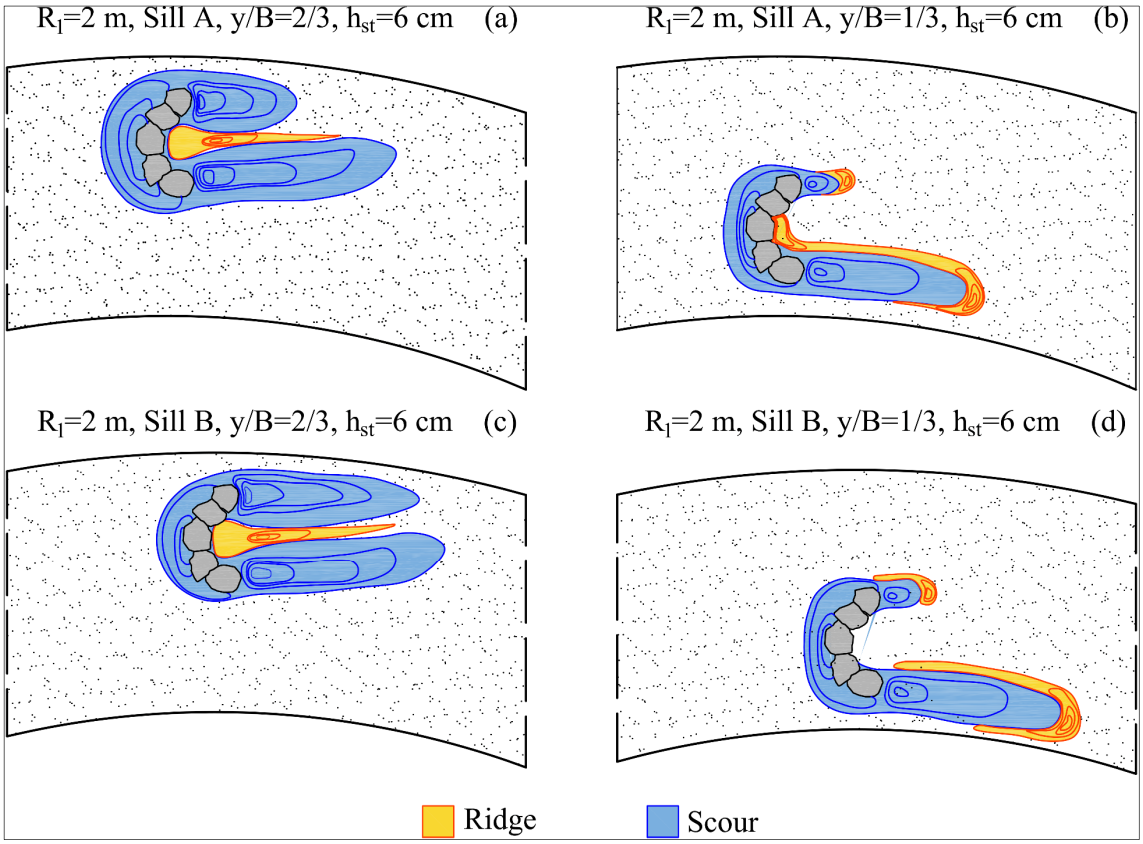


**Figure 3.** Diagram sketch of the equilibrium morphologies for $R_1$=2 m, $h_{st}$=6 cm and (a) sill A located at y/B=2/3; (b) sill A located at y/B=1/3; (c) sill B located at y/B=2/3; and (d) sill B located at y/B=1/3 (flow from left to right).

 

The increase of channel curvature further amplifies the described mechanism (Figure 4). Namely, if the curvature of the channel becomes more prominent, the asymmetry of both shear stresses distribution and kinematic field appears more significant, resulting in more longitudinally extended scour hole and axial ridge formation. Also in this case, the effect of the parameter y/B on the maximum scour depth appears negligible. The effect of the difference between upstream and downstream flow depths does not seem to play the same fundamental role pointed out by Pagliara et al. (2016a) for linear rock sills. In conclusion, it can be noted that the maximum scour depth mainly depends on the structure geometry, hydraulic conditions and channel curvature.

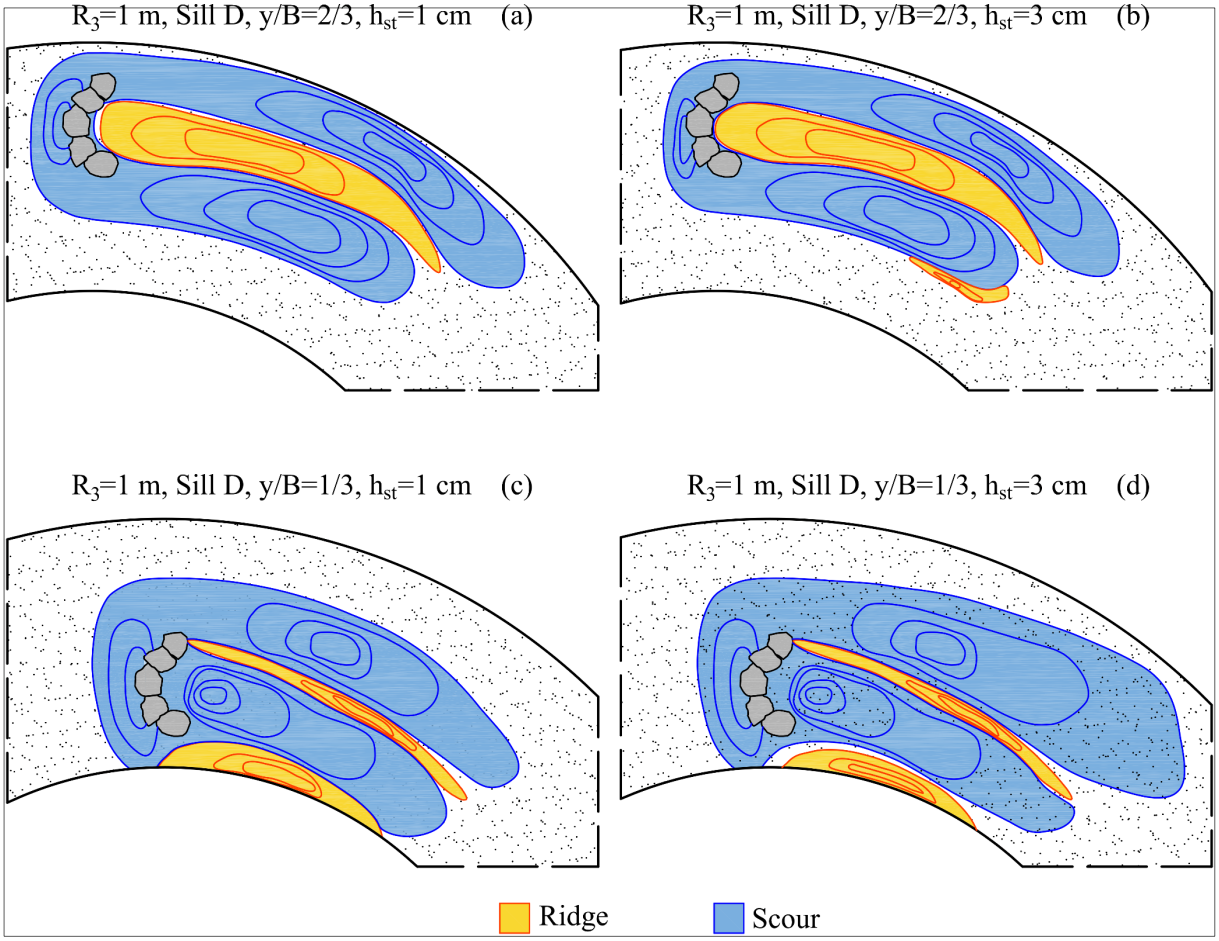


**Figure 4.** Diagram sketch of the equilibrium morphologies for $R_3$=1 m and sill D (a) located at y/B=2/3 and $h_{st}$= 1 cm; (b) located at y/B=2/3 and $h_{st}$=3 cm; (c) located at y/B=1/3 and $h_{st}$=1 cm; (d) located at y/B=1/3 and $h_{st}$=3 cm (flow from left to right).

The same analysis is also conducted for arched sills located in the straight part of the channel. Figure 5 shows the observed qualitative equilibrium morphologies. In this last case, it can be easily noted that differences with respect to the previous two described channel geometries are very relevant. In fact, the absence of a kinematic field asymmetry results in a much more symmetric distribution of the shear stresses both upstream and downstream of the structure. This occurrence appears evident by observing that both the scour hole and the ridge downstream of the structure are essentially symmetric. In addition, Figure 5 shows the effect of the structure height on the upstream scour formation, i.e., the upstream scour hole is significantly affected by the structure height. Therefore, the maximum scour depth upstream of the structures increases with $h_{st}$. This is mainly due to the fact that the upstream flow conditions are significantly locally modified by structure geometry. Under the same hydraulic conditions, the effect of the structure height is to increase the upstream flow re-circulation around the structure, resulting in a local increase of the shear stresses due to the creation of preferential flow paths.

 

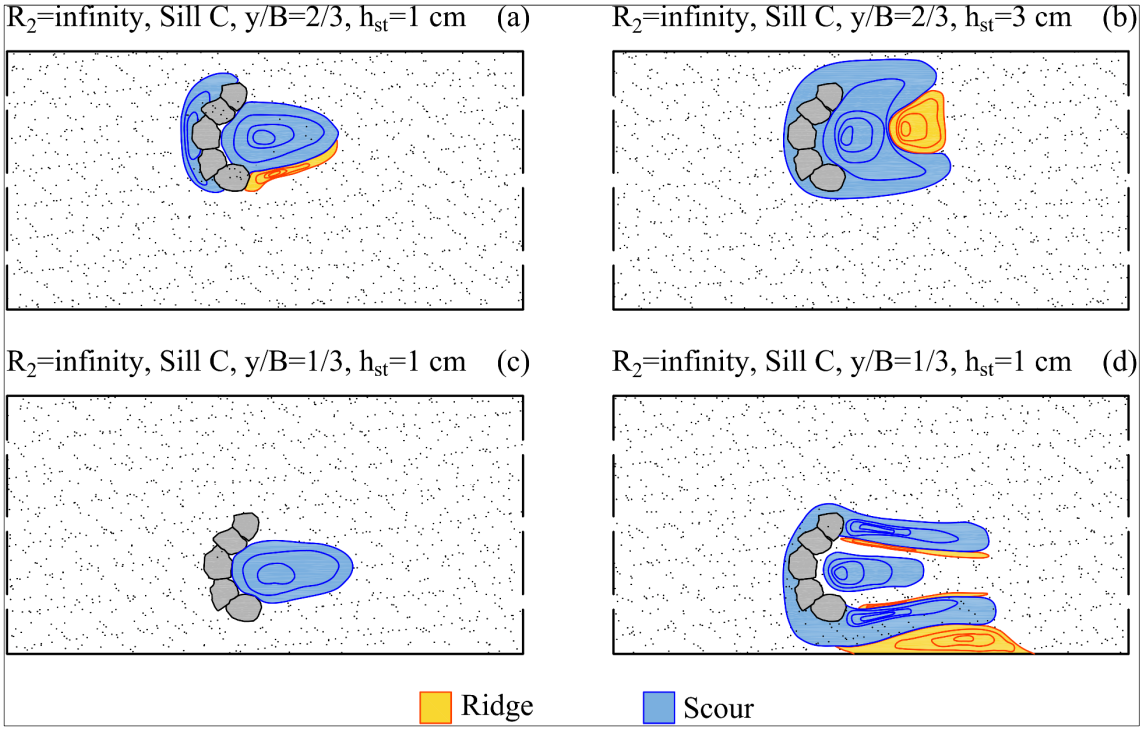


**Figure 5.** Diagram sketch of the equilibrium morphologies for $R_2$=infinity and sill C (a) located at y/B=2/3 and $h_{st}$= 1 cm; (b) located at y/B=2/3 and $h_{st}$=3 cm; (c) located at y/B=1/3 and $h_{st}$=1 cm; (d) located at y/B=1/3 and $h_{st}$=3 cm (flow from left to right).

3.2 Effect of channel curvature on maximum scour depth

In general, the maximum scour depth increases with curvature. Nevertheless, a prominent role is also played by the tail water. In fact, it is observed that, due to the increase of the diffusion length, the maximum scour depth generally decreases with tail water. Furthermore, previous studies showed that the maximum scour depth depends on a non-dimensional parameter$\eta$, which was introduced by Pagliara et al. (2016a) for linear rock sills in both straight and curved channels. Pagliara et al. (2016a) analysed the scour morphology due to rock sills whose width was the same of the channel. In the present manuscript, an attempt to optimize the rock sill geometry is conducted. In fact, testing different rock sills geometries aims to find solutions for several problems, by conjugating different aspects. Namely, these structures minimize their impact on the surrounding environment, but at the same time, they can be located at different spatial positions in order both to assure suitable conditions for fish species resting and to avoid excessive erosion close to the channel banks, i.e., limiting channel bank failure risk.

Nevertheless, some similarities in terms of hydraulic functioning with linear sills can be observed. In particular, the equilibrium morphologies downstream of arched rock sills appear similar to those described by Pagliara et al. (2016a). In addition, also in this case, the effect of river curvature on the erosive process is found significant. It is observed that the maximum scour depth increases with the river curvature. The structure geometry also influences the scour depth, as the maximum scour depth increases with the rock sill height ($h_{st}$). This last occurrence is mainly due to the fact that the scour process for higher structures and lower downstream tail waters appears similar to that characterizing plunging jets (see also Mason and Arumugam, 1985; and Bormann and Julien, 1991). Therefore, the scour mechanism strongly depends on the downstream tail water and on the head of the structure. The river curvature further amplifies the scour mechanism complexity, because of the secondary flows. Namely, the shear stress distribution in correspondence with river bends are strongly asymmetric, reaching their maximum close to the inner channel bend. This asymmetry is particularly evident by observing the scour hole and ridge shape.

As mentioned in previous sections, the resulting equilibrium morphology is a consequence of the shear stress distribution but, at the same time, contributes to vary the kinematic field. Therefore, the scour dynamics appears much more complex in the presence of a structure with respect to the case in which the structure is absent. Such complexity is extremely evident considering the slight differences in the equilibrium configuration, i.e., maximum scour depths for structures located at the same channel bend can be considered negligible, independently of both transversal and longitudinal positions of the sill. This is the case of sills A and B, for which a clear different trend in terms of maximum scour depths between sills located at y/B=1/3 and 2/3 cannot be detected. Furthermore, maximum scour depths in correspondence with sill A are essentially similar to those measured in correspondence with sill B under same geometric configurations and hydraulic conditions. This last occurrence allows to group scour data relative to these sill configurations. Furthermore,

 

the same occurrence is registered for sills C and D, i.e., the effect of y/B on $z_{md}$ can be considered negligible. It should be noted that although negligible, some differences can be detected, resulting in different equilibrium morphologies as stated in previous sections. Nevertheless, for practical applications, they are not relevant therefore, for the maximum scour depth can be expressed as only function of $\eta$ and R, as shown in Figure 6. In this last figure, experimental data of the variable $z_{md}/h_{st}$ were plotted as function of $\eta$ for different channel curvatures. Namely, Eq. (1) is relative to R=1 m, Eq. (2) to R=infinity and Eq. (3) to R=2 m. The maximum scour depth does not seem to be significantly influenced by the transversal location of the structure. By observing both the experimental data and the relative curves plotted in Figure 6, it appears evident that the non-dimensional maximum scour depth increases with $\eta$ and decreases with R, thus confirming the findings of Pagliara et al. (2016a) relative to linear rock sills, whose width is the same of the channel.

Nevertheless, a significant difference between linear rock sills and arched rock sills can be detected, i.e., the role of tail water. Tail water plays a role in the scour process, because of the variation of the downstream diffusion length. But, the effect of this last parameter on the scour dynamics is less significant than for linear sills. This occurrence is mainly due to the fact that, in the presence of an arched sill, the flow can be deflected by the structure and pass laterally, forming preferential flow paths, i.e., the structure width is less than that of the channel, thus it does not cause a significant increase of the water depth upstream of the structure itself. In other words, the difference between upstream and downstream water depths is less prominent under identical hydraulic conditions. This last occurrence strongly influences the scour morphology as the non-dimensional parameter $\eta$ depends on $\Delta y$. It means that such structures contribute to locally modify the equilibrium morphology and hydraulic conditions, but they slightly interfere with the global sediment transport dynamics.

$$z_{md} / h_{st} = 1.41 \cdot \exp[0.04 \cdot \eta] \quad [1]$$

$$z_{md} / h_{st} = 0.1 \cdot \exp[0.06 \cdot \eta] \quad [2]$$

$$z_{md} / h_{st} = 0.4 \cdot \exp[0.05 \cdot \eta] \quad [3]$$

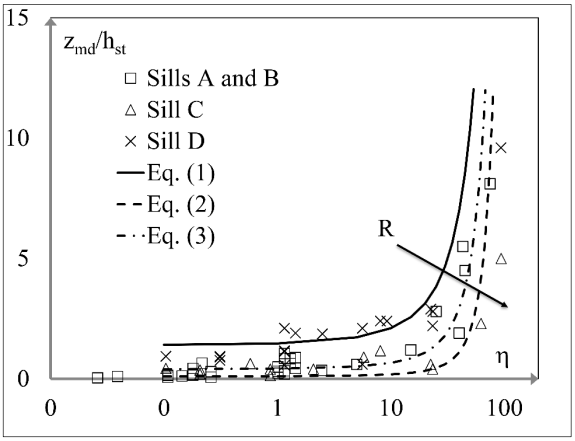


**Figure 6.** $z_m/h_{st}$ versus $\eta$ for all tested structures and sills locations.

## 4 CONCLUSIONS

In this manuscript a preliminary analysis of the scour mechanism occurring in correspondence with arched-shaped rock sills is conducted. Namely, a dedicated model is built and different sills are tested. They are located in different longitudinal and transversal positions inside a channel characterized by both curved branches and straight sectors. Experimental tests are performed under different hydraulic conditions, involving different tailwater levels, discharges and structure geometries. The equilibrium morphologies are carefully surveyed and analyzed. The experimental evidences allow to establish the effect of different parameters on the maximum scour depth and qualitative scour morphology. Namely, the effect of structure height results to be prominent, i.e., the increase of the structure height causes an increase of the maximum scour depth.

A similar effect is observed in correspondence with higher curved channel branches, i.e., the maximum scour depth increase with river curvature. In addition, the curvature of the channel has a prominent effect on the equilibrium morphology, resulting in an asymmetry in both scour hole and ridge formation downstream of the structure. The mentioned asymmetry is both a consequences and a cause of the kinematic field asymmetry downstream of the structure, resulting in a non-uniform transversal distribution of the shear stresses. Nevertheless, three parameters are found more significant in terms of maximum scour depth, i.e., the structure height, the discharge and the channel curvature. Therefore, three empirical equations are

 

proposed in order to estimate the maximum scour depth, depending only on the non-dimensional parameter $\eta$ and on the channel curvature R. Further investigations are going on, involving also other structure typologies and another channel curvature. These ongoing investigations will furnish further elements for the understanding of such complex phenomenon and, at the same time, will allow for a generalization of the proposed empirical equation.

**REFERENCES**

Bathurst, J.C., Li, R.M. & Simons, D.B. (1981). Resistance Equation for Large Scale Roughness. *Journal of Hydraulic Engineering Division*, 107(12), 1593–1613.

Bormann, E. & Julien, P.Y. (1991). Scour Downstream of Grade Control Structures. *Journal of Hydraulic Engineering*, 117(5), 579-594.

Chinnarasri, C., Donjadee, S. & Israngkura, U. (2008). Hydraulic Characteristics of Gabion-Stepped Weirs. *Journal of Hydraulic Engineering*, 134(8), 1147-1152.

D'Agostino, V. & Ferro, V. (2004). Scour on Alluvial Bed Downstream of Grade-Control Structures. *Journal of Hydraulic Engineering*, 130(1), 1-14.

Dey, S. & Raikar, R.V. (2005). Scour in Long Contractions. *Journal of Hydraulic Engineering*, 131(12), 1036-1049.

Dey, S. & Sarkar, A. (2006). Scour Downstream of an Apron Due to Submerged Horizontal Jets. *Journal of Hydraulic Engineering*, 132(3), 246-257.

Hassan, N.M.K.N. & Narayanan, R. (1985). Local Scour Downstream of an Apron. *Journal of Hydraulic Engineering*, 111(11), 1371-1385.

Heller, V. (2011). Scale Effects in Physical Hydraulic Engineering Models. *Journal of Hydraulic Research*, 49(3), 293-306.

Lenzi, M.A., Marion, A. & Comiti, F. (2003). Interference Processes on Scouring at Bed Sills. *Earth Surface Processes and Landforms*, 28(1), 99-110.

Lisle, T.E. (1982). Effects of Aggradation and Degradation on Riffle-Pool Morphology in Natural Gravel Channels, Northwestern California. *Water Resources Research*, 18(6), 1643-1651.

Marion, A., Lenzi, M.A. & Comiti, F. (2004). Effect of Sill Spacing and Sediment Size Grading on Scouring at Grade-Control Structures. *Earth Surface Processes and Landforms*, 29(8), 983-993.

Martin-Vide, J.P. & Andreatta, A. (2006). Disturbance Caused by Bed Sills on the Slopes of Steep Streams. *Journal of Hydraulic Engineering*, 132(11), 1186-1194.

Mason, P.J. & Arumugam, K. (1985). Free Jet Scour Below Dams and Flip Buckets. *Journal of Hydraulic Engineering*, 111(2), 220-235.

Oertel, M. & Schlenkhoff, A. (2012). Crossbar Block Ramps: Flow Regimes Energy Dissipation, Friction Factors, and Drag Forces. *Journal of Hydraulic Engineering*, 138(5), 440-448.

Pagliara, S. & Mahmoudi Kurdistani, S. (2015). Clear Water Scour at J-Hook Vanes in Channel Bends for Stream Restorations. *Ecological Engineering*, 83, 386-393.

Pagliara, S. & Palermo, M. (2008). Scour Control Downstream of Block Ramps. *Journal of Hydraulic Engineering*, 134(9), 1376-1382.

Pagliara, S., Hassanabadi, L. & Mahmoudi Kurdistani, S. (2015). Clear Water Scour Downstream of Log Deflectors in Horizontal Channels. *Journal of Irrigation and Drainage Engineering*, 141(9), 1-8.

Pagliara, S., Mahmoudi Kurdistani, S., Palermo, M. & Simoni, D. (2016a). Scour Due to Rock Sills in Straight and Curved Horizontal Channels. *Journal of Hydro-Environment Research*, 10, 12-20.

Pagliara, S. & Palermo, M. (2010). Influence of Tailwater Depth and Pile Position on Scour Downstream of Block Ramps. *Journal of Irrigation and Drainage Engineering*, 136(2), 120-130.

Pagliara, S. & Palermo, M. (2011). Effect of Stilling Basin Geometry on Clear Water Scour Morphology Downstream of a Block Ramp. *Journal of Irrigation and Drainage Engineering*, 137(9), 593-601.

Pagliara, S. & Palermo, M. (2015). Hydraulic Jumps on Rough and Smooth Beds: Aggregate Approach for Horizontal and Adverse-Sloped Beds. *Journal of Hydraulic Research*, 53(2), 243-252.

Pagliara, S., Palermo, M. & Carnacina, I. (2012). Live-Bed Scour Downstream of Block Ramps for Low Densimetric Froude Numbers. *International Journal of Sediment Research*, 27(3), 337-350.

Pagliara, S. & Palermo, M. (2013). Rock Grade Control Structures and Stepped Gabion Weirs: Scour Analysis and Flow Features. *Acta Geophysica*, 61(1), 126-150.

Pagliara, S., Palermo, M. & Das, R. (2016b). Eco-Friendly Countermeasures for Enlarged Basins Erosion. *River Research and Applications*, 32(3), 441-451.

Pagliara, S., Radecki-Pawlik, A., Palermo, M. & Plesiński, K. (2016c). Block Ramps in Curved Rivers: Morphology Analysis and Prototype Data Supported Design Criteria for Mild Bed Slopes. *River Research and Applications*, 33(3), 427- 437.

Pegram, G.G.S., Officer, A.K. & Mottram, S. (1999). Hydraulics of Skimming Flow on Modeled Stepped Spillways. *Journal of Hydraulic Engineering*, 125(5), 500-510.

Phillips, J.D. (2010). The Job of the River. *Earth Surface Processes and Landforms*, 35(3), 305-313.

Veronese, A. (1937). Erosioni Di Fondo A Valle Di Uno Scarico. *Annali Lavori Pubblici*, 75, 717-726 [In Italian].

 

Proceedings of the 37th IAHR World Congress
August 13 – 18, 2017, Kuala Lumpur, Malaysia

# TURBULENT CHARACTERISCTICS OF FLOW OVER NON UNIFORM SAND BED CHANNEL

ANURAG SHARMA[(1)] & BIMLESH KUMAR[(2)]

[(1,2)]Indian Institute of Technology, Guwahati, India
gokarna29@gmail.com; bimk@iitg.ac.in

## ABSTRACT

The present study focuses on the influence of downward seepage flow on the turbulent flow characteristics over non uniform sand bed channel. Experiments are conducted for free-surface flows subjected to downward seepage from the boundary. The experimental result will deliver important information related to the turbulence characteristics, such as velocity, Reynolds shear stress, turbulent intensity and conditional Reynolds shear stresses. Reynolds shear stress increases along the channel bed are associated with the provided momentum from the flow to maintain sediment transport overcoming the bed resistance and then again decrease towards the boundary because of the presence of a roughness sub layer in the near bed region. The profiles of Reynolds shear stress is slightly scattered in general and increase with seepage which signifies the greater momentum transfer towards the boundary. The variations of stream wise velocity with vertical distance in flows with downward seepage in the near bed region are greater than no seepage flow. The thickness of roughness sub layer and shear velocities increase with seepage. The reduced value of von Karman's constant corresponds to increase in the bed load transport with seepage. In the presence of seepage, stream wise and vertical turbulence intensities increase compared to turbulence intensities in no-seepage. The anisotropy of turbulence is strong being seepage independent and varying approximately linear with flow depth. In quadrant analysis, the contribution of sweep events towards Reynolds shear stress production near the boundary increases with increased zone of sweep dominance. The mean time of occurrence of ejections and that of sweeps in seepage are longer than those in no-seepage.

**Keywords:** Reynolds shear stress; seepage**;** sediment transport; velocity.

## 1 INTRODUCTION

Flow over sand bed occurs frequently in nature. Riverbeds usually consist of non-uniform sediment mixtures and the respective particle size distribution of sediment in transport is generally finer than the distribution of bed material because of selective transport. Most of the early experiments on sediment transportation and deposition were confined to the homogeneous sediment mixture (Wilcock 1993; Zyserman and Fredsøe, 1994). Recent years experimental studies have attempted to understand the basic grain-sorting process during sediment transportation and deposition in heterogeneous sediment mixtures (Kleinhans, 2005; Curran, 2007). Most of the studies on the non- uniform sediment transport are based on introducing correction factors to understand this hiding and exposure effect and use these factors to modify the existing formula for uniform sediment transport (Parker et al., 1982; Andrews, 1983). Fractional sediment transport was calculated for non-uniform sediment based on correction factors related to bed material sizes (Fang and Yu, 1998; Karim, 1998). On transport of sediments mixture, the effect of sand and gravel contents on overall transport rate was studied in the laboratory flume (Wilcock and Crowe, 2003; Curran and Wilcock, 2005). Previous researchers (Mittal et al., 1990; Patel and Range Raju, 1996) assumed that the motion of fine particles was led by the lift force while the motion of coarse particles was by the drag force, and introduced a semi-theoretical hiding-exposure correction factor. Flume experiments were conducted for non-uniform sediment to find the sediment transport rate of individual fraction of sediment mixture (Misri et al., 1984; Samaga et al., 1986). Ghoshal et al. (2010) investigated the bed layer concentration of each size fraction that was transported as bedload over a mixture of sand/sand–gravel beds; and estimated the patterns of grain size distribution at the active layer resulting from variations in flow discharge and bed roughness.

The important hydraulic nature of sand bed in natural channel is that it provokes lateral flow as seepage. Depending on the difference in water level in the channel and the surrounding groundwater table, seepage can occur either flow from the channel (suction) or flow into the channel (injection). The important features are that the seepage influences the main stream flow characteristics in the wall shear layer as well as the outer-flow layer (Devi et al., 2016). Devi et al. (2016) observed that downward seepage increased stream wise velocity near the bed resulting in the formation of a more uniform velocity distribution. Increment of bed shear stress with downward seepage causes increased sediment transport (Sreenivasulu et al., 2011).

Although many studies have investigated flow hydrodynamics or turbulent characteristics with seepage in case of uniform sand, the flow characteristics over non-uniform sand bed channel with downward seepage

 

remain unexplored. Since riverbeds are usually composed of non-uniform sediment mixture, the present study therefore focuses on the influence of downward seepage flow on the turbulent flow characteristics over a mobile rough boundary (made of non-uniform sand of size 0.5mm). The experimental result will deliver important information related to the turbulence characteristics, such as velocity, Reynolds shear stress, anisotropy, von Kármán constant and conditional Reynolds shear stresses.

## 2 EXPERIMENTAL SETUP AND MEASUREMENT

In the present work, experiment was conducted in a large tilting flume with dimensions of 17.24 m in length, 1m in width, and 0.72m in deep. A tank of dimensions 2.8 m long, 1.5 m wide and 1.5 m deep was provided at the upstream of the flume which straightened the flow before its introduction into the flume. A control valve was located at the overhead tank and was used to regulate the flow in the main channel. A couple of wooden baffle was installed at the upstream tank to prevent turbulences in the water coming from the overhead tank to enter the main channel. A tail gate was provided at the downstream end of the main channel to control the flow depth. A tank was provided at the downstream end of the flume to collect the water coming from channel and discharge it to the underground trench that delivered it to an underground tank from where the water was pumped into the overhead tank. This way the water was recirculating in the experiment. The flume was having seepage chamber of 15.2 m long, 1m wide and 0.22 m deep located at 2 m from the upstream end of the flume that collected water and allowed free passage of water through the sand bed. Non-Uniform river sand of particle sizes $d_{50}$ = 0.5 mm was used as bed material in the experiments that was kept on the fine mesh in order to prevent entrance into the bottom chamber. A bottom pressure chamber was formed between the bottom of the mesh and the channel. The bottom pressure chamber was used to absorb water from the channel through the sand bed in a perpendicular direction in the form of downward seepage. The seepage flow rate that was measured by an electromagnetic flow meter (accuracy of ±0.5%) could be controlled by a valve which was installed at the downstream end of the flume. The flow depth in the channel was measured with digital point gauge attached to a moving trolley. Main Flow discharge in the channel was measured using the flow depth over the rectangular notch at the downstream collection tank.

Non-uniformity in the particle size distribution for the sand was confirmed with the value of geometric standard deviation greater than 1.4 (Marsh et al., 2004). The characteristics of sediment mixture and flow parameters used in this study are shown in Table 1. In the no seepage (NS) run, water was introduced to the channel by gradually opening a valve located at the overhead tank till required discharge Q and corresponding flow depth y were registered. Consequently after conducting the experiment with no seepage, downward seepage discharge of 10% of the main flow discharge were applied by controlling the electromagnetic flow meters installed at the downstream section of the flume.

Instantaneous velocity measurements were captured with the help of acoustic Doppler probe manufactured by Nortek. Data was collected at the center line of the channel cross section at a distance of 8m from the downstream end of the flume. In all the experiments, signal to noise ratio was kept at 15 or above and the signal correlation between received and transmitted signals of 70% was recommended as cut-off value. The data measured from the vectrino contained spikes so spike removal algorithm based on the acceleration threshold method was used to filter the data (Goring and Nikora 2002). The threshold value was maintained in between 1 to 1.5 based on trial and error basis so that velocity power spectra should reasonably fit with Kolmogorov "-5/3 scaling law" in the inertial sub range (Lacey and Roy, 2008).

**Table1.** Summary of flow measurement.

| Median grain size, $d_{50}$ (mm) | Discharge, Q ($m^3$/sec) | Depth of flow, y (m) | Kramers coefficient, M | Bed Slope, $S_0$ |
|---|---|---|---|---|
| 0.50 | 0.0402 | 0.112 | 0.16 | 0.0001 |

## 3 RESULTS AND DISCUSSIONS

### 3.1 Reynolds shear stress (RSS)

Reynolds shear stress was calculated as

$$\left.\begin{aligned} \tau_{uw} &= -\rho_w \overline{u'w'} \\ \overline{u'w'} &= \frac{1}{n}\sum_{i=1}^{n}\left(U_i - u\right)\left(W_i - w\right) \end{aligned}\right\} \quad [1]$$

Where, $\rho_w$ is the density of water, $u'$ and $w'$ are the fluctuating components of velocities in the stream wise and vertical directions, respectively and n is the number of samples. Time averaged stream wise ($u$) and vertical ($w$) velocities were calculated as:

 

$$u = \frac{1}{n}\sum_{i=1}^{n} U_i \qquad w = \frac{1}{n}\sum_{i=1}^{n} W_i \qquad [2]$$

Figure 1 shows the vertical variations of Reynolds shear stress (RSS) in flows subjected to no seepage and seepage runs with the vertical ordinate ($z$). It can be seen from Figure 1 that RSS increases along the channel bed are associated with the provided momentum from the main flow to maintain sediment particle motion overcoming the bed resistance and then again decreases towards the boundary because of the presence of a roughness sub layer in the near bed region. In the present experiments, the profiles of Reynolds shear stress distribution were found to be similar for both no seepage and seepage runs but the magnitude was higher in both inner and outer layer with the application of seepage.

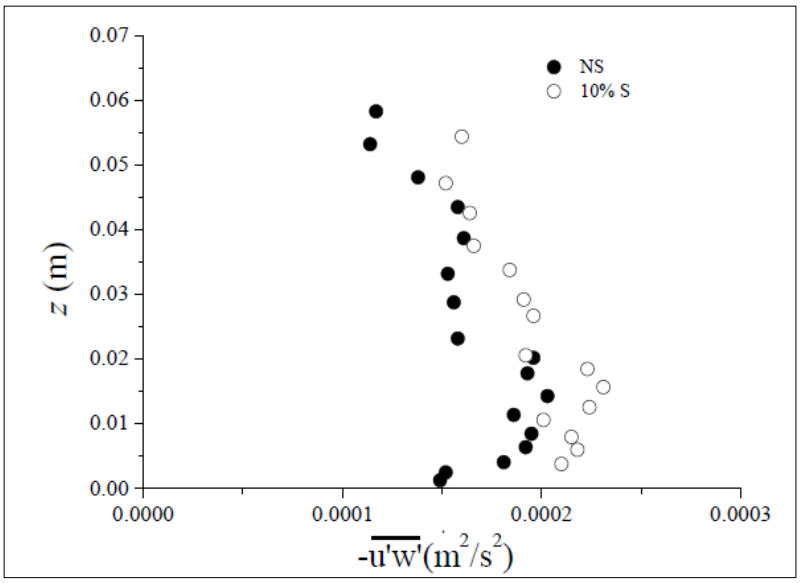


**Figure 1.** Vertical distributions of RSS.

3.2 Time averaged velocity

Figure 2 shows the variations of time averaged stream wise velocity $u$ with vertical distance (=$z$) in flows subjected to no seepage and seepage for 10%. It is interesting to note in Figure 2 that the velocity increased with the application of downward seepage as compared to no seepage for a particular discharge. Experimental data has been fitted to the Deshpande and Kumar (2016) log law as expressed in the following non-dimensional form.

$$\frac{u}{u_*} = \frac{1}{k}\ln\left(z^+ + \Delta z^+\right) - \frac{1}{k}\ln\left(\varepsilon^+\right) \qquad [3]$$

Where, $u_*$ is shear velocity which is obtained by extending RSS profile at $z$=0,$z^+$=$z/d_{50}$, $\Delta z^+$= $\Delta z/d_{50}$, $\Delta z$ is depth of virtual bed level from the bed surface, $\varepsilon^+$= $z_0/d_{50}$, $z_0$ is zero velocity level, $k$ is von Karman constant. Average values of the shear velocity, von Karman's constant, depth of the virtual bed level and the zero velocity level are tabulated in Table 2. Value of the $k$ for no seepage condition has been observed to be slightly higher than the universal value (0.41). The downward seepage influence upon the bed particles starts to move rapidly and value of $k$ drastically decreases .Further, from the regression equation shown in Figure 3, it is observed that with the application of seepage, the depth of virtual bed level and the zero velocity level from the bed surface increase, suggesting an exposure of increased velocity component in the stream wise direction to the particles on the bed surface.

**Table 2.** Coefficient value observed from log law equation.

| Flow Condition | $u_*$(mm/s) | $k$ | $\Delta z$ (mm) | $z_0$ (mm) |
|---|---|---|---|---|
| NS | 15.25 | 0.418 | 3.03 | $8.258\times10^{-3}$ |
| 10% S | 16.14 | 0.355 | 4.25 | $31.58\times10^{-3}$ |

 

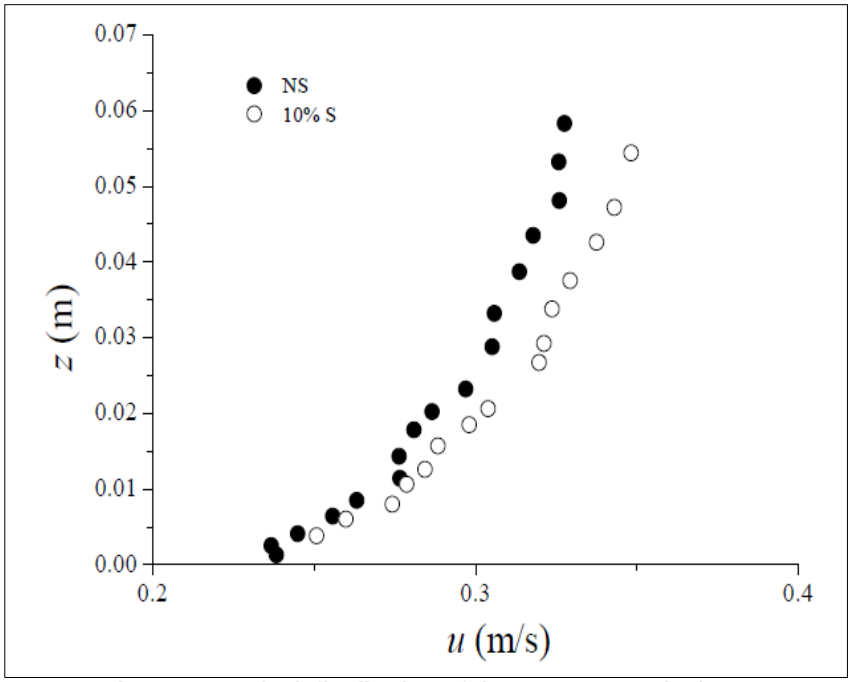


**Figure 2.**Vertical distribution of time average velocity.

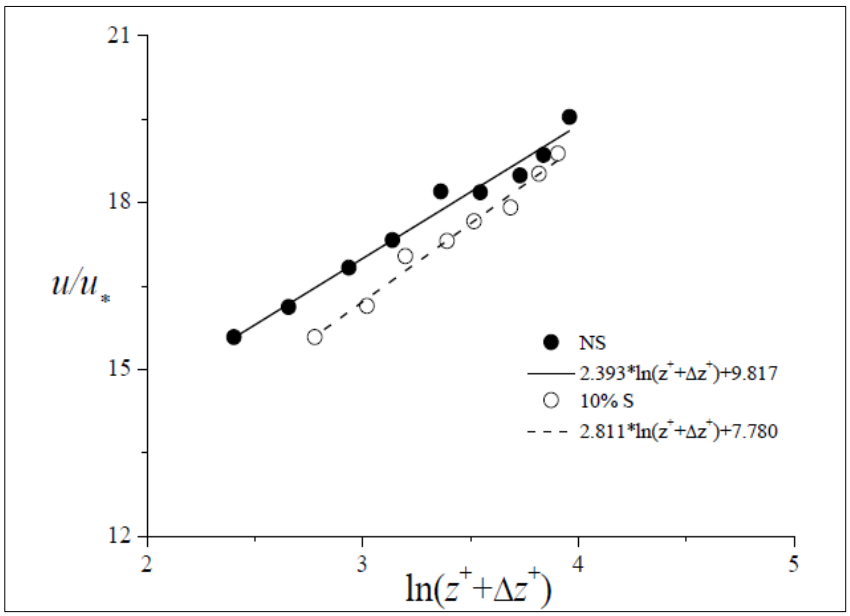


**Figure 3**. Velocity log law.

3.3 Turbulent Intensities

Turbulence intensities are defined as:

$$\sigma_u = \sqrt{\frac{\sum_{i=1}^{n}(u_i - u)}{n}} \quad [4]$$

$$\sigma_w = \sqrt{\frac{\sum_{i=1}^{n}(w_i - w)}{n}} \quad [5]$$

Where $\sigma_u$ and $\sigma_w$ are the longitudinal and vertical turbulent intensities.The vertical profiles of stream wise turbulence intensity $\sigma_u$ and vertical turbulence intensity $\sigma_w$ are shown in Figure 4. It is observed that the profiles of $\sigma_u$ and $\sigma_w$ with downward seepage are greater than the profiles of $\sigma_u$ and $\sigma_w$ with no seepage.

 

Vertical profiles of turbulence intensities are evident within the near bed flow zone. As compared to no seepage, the degree of damping increases by an average value of 10 % for $\sigma_u$ and 9.8 % for $\sigma_w$ with 10% S.

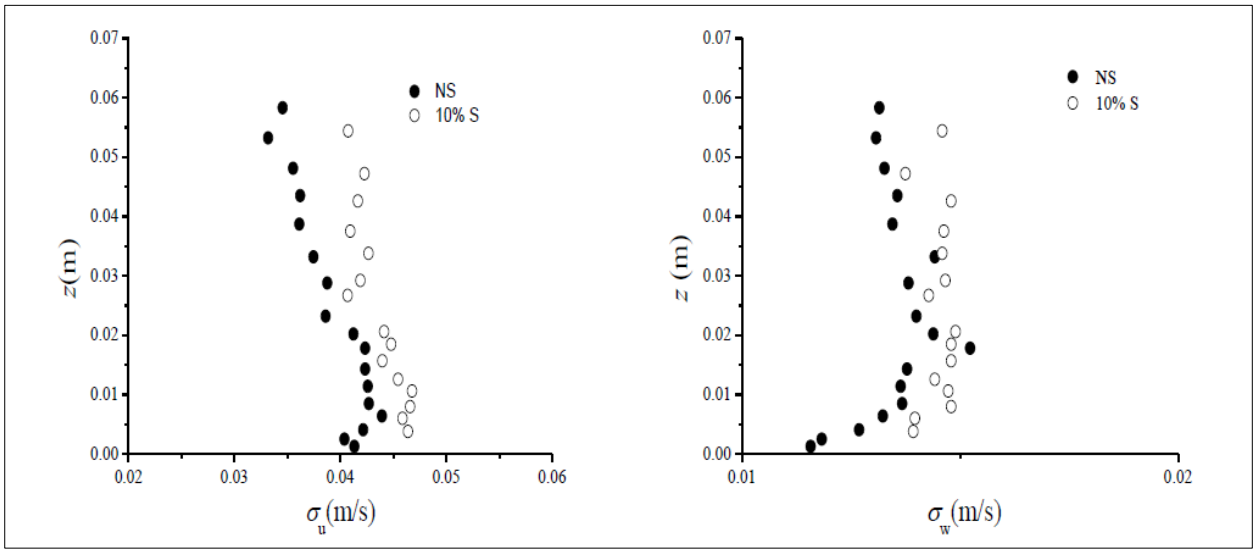


**Figure 4.** Turbulent intensities in stream wise and vertical direction.

The degree of flow anisotropy is measured by the ratio $\sigma_w/\sigma_u$ . Figure 5 shows the vertical distribution of $\sigma_w/\sigma_u$ plotted against $z$, from which it is observed that theflow is highly anisotropic as $\sigma_w/\sigma_u$ <1. The $\sigma_w/\sigma_u$ ratio is approximately 0.28 near the boundary irrespective of the flow condition, i.e. for both no seepage and seepage runs, varying almost linearly with flow depth. However, the influence of seepage on the profiles of $\sigma_w/\sigma_u$ is not apparent.

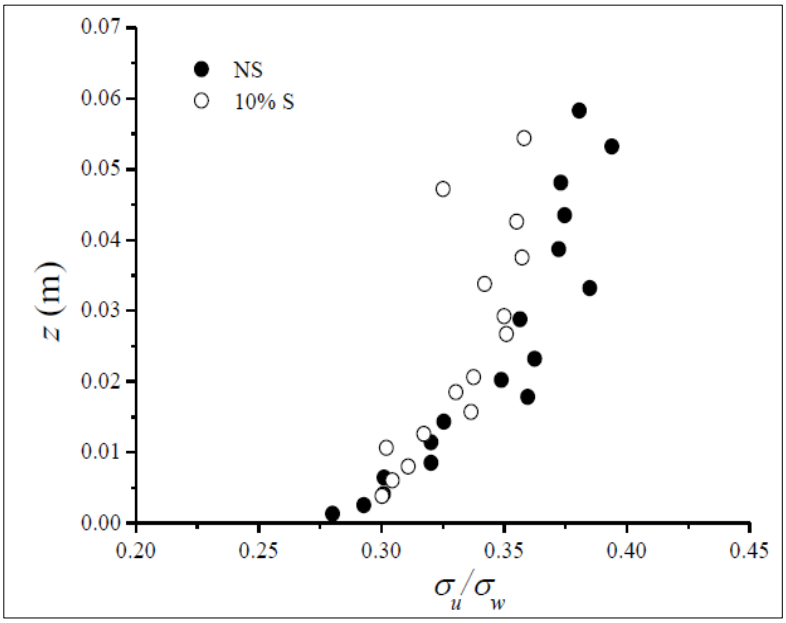


**Figure 5**. Flow anisotropy.

3.4 Conditional Reynolds shear stress

The Reynolds shear stress at any given point is the summation of different types of bursting events. To quantify the bursting events, it is necessary to plot velocity fluctuation $u'$ and $w'$ on $u'w'$ plane (Lu and Willmarth 1973). The hyperbolic hole region $H$ is introduced to differentiate the larger contributions to - $\overline{u'w'}$ from each quadrant leaving the smaller u' and w' corresponding to more quiescent periods.

The hole region $H$ also represents the threshold level which is determined by the curve $|u'w'|=H\ (\overline{u'2})^{0.5}$ $(\overline{w'2})^{0.5}$ (Nezu and Nakagawa 1993). Hence, depending upon the relative sign of velocity fluctuations $u'$ and $w'$ ,the bursting events are defined by four quadrants such as outward interactions ($i$=1, $u'$>0, $w'$>0 ), ejections

 

(*i*=2, *u*'<0, *w*'>0 ), inward interactions (*i*=3, *u*'<0, *w*'<0) and sweeps (*i*=4, *u*'>0, *w*'<0). At any point, the contribution to the total Reynolds stress through the different forms of momentum transfer can be calculated as:

$$\left\langle u'w' \right\rangle_{i,H} = \lim_{T\to\infty} \frac{1}{T} \int_0^T u'(t)w'(t) I_{i,H}[u'(t)w'(t)]\,\mathrm{d}t \qquad [6]$$

Where *t* is time, *T* is sampling duration, $I_{i.H}$ is the indicator function defined as

$$\mathrm{I}_{i,H}[u'(t)w'(t)] = \begin{cases} 1, if \ \ (u', w') \ is \ in \ quadranti \ and \ if \ |u'w'| \geq H\left(\overline{u'^2}\right)^{0.5}\left(\overline{w'^2}\right)^{0.5} \\ 0, otherwise \end{cases} \qquad [7]$$

The quadrant analysis provides the estimation of stress fraction transported by the contribution as

$$S_{i,H} = \frac{\left\langle u'w' \right\rangle_{i.H}}{\overline{u'w'}} \qquad [8]$$

Here, $S_{i,H}$ is positive for *i*=2 and 4 (Q2 and Q4) and $S_{i,H}$ is negative for *i*=1 and 3 (Q1 and Q3). Hence, sum of contributions from bursting events is unity that is: $\sum_{i=0}^{i=4}\left[S_{i,H}\right]_{H=0} = 1$

The vertical distributions of $S_{i,H}$ in flows subjected to no seepage and seepage are examined. The most frequent events *H*=0 is considered to be associated with the use of $u'$ and $w'$ in flows subjected to no seepage and seepage cases (Figure 6).

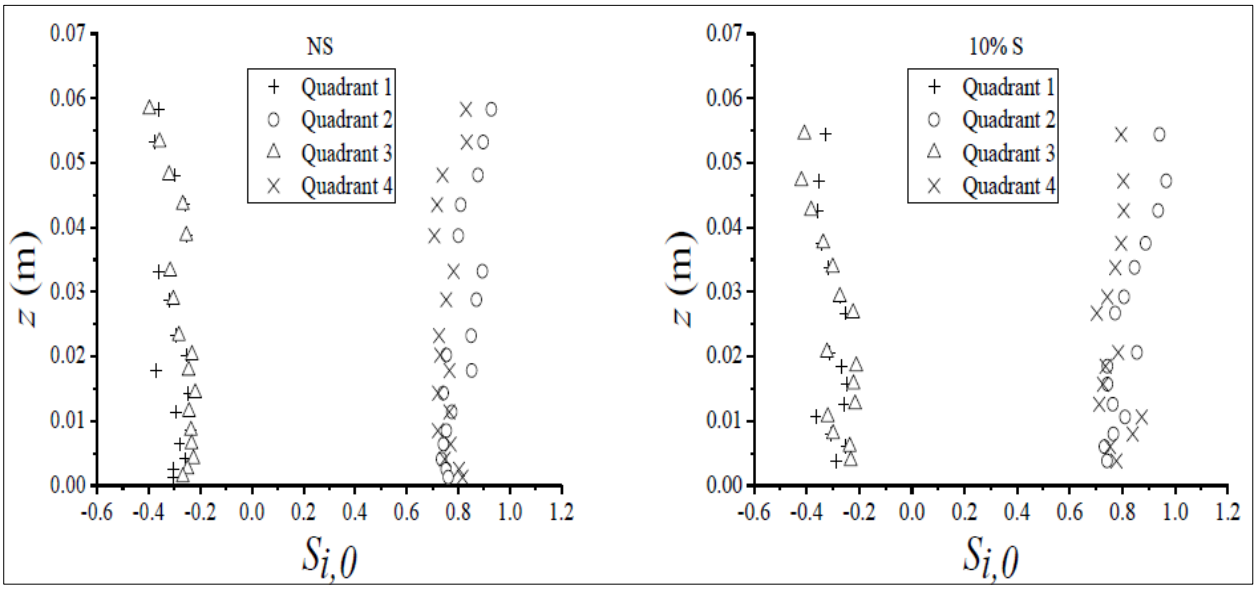


**Figure 6.** Variations of conditional Reynolds shear stresses $S_{i,0}$ for *H=0*

In Figure 6, the contributions from Q2 and Q4 events are positive while those from Q1 and Q3 events are negative. For H=0, primary contribution is from Q2 and Q4 events and feebly contribution from Q1 and Q3 towards the RSS production. The divergence in between Q2 and Q4 events is accomplished with the large scale of eddies. In Figure 6 (NS case) with H=0, Q2 and Q4 events in near bed contribute about 73.5% and 74.7%, respectively towards the production of RSS while, Q1 and Q3 events contribute minimally as 25.6% and 22.6%, respectively. While away from the bed, ejection events dominate in contributing to the Reynolds shear stress production.

For 10% S, within the near bed surface, Q2 and Q4 events contribute about 74.2% and 77.7%, respectively while, Q1 and Q3 events contribute minimally as 28.7% and 23.2%, respectively. The result predicts that the contribution from all bursting events to RSS production in the near bed flow zone increases with the seepage as compared to that with no seepage run. Further, the present result suggests that

 

dominance of sweep events over the ejection events at near the bed increases progressively with the seepage. The thickness of the zone of sweep dominance increases from z~0.0063m with no seepage to z ~ 0.01m in the seepage run of 10% S. These increased contributions from sweep events and thickening of the zone of sweep dominance in the seepage run increase momentum exchange from the flow to bed particles due to which sediment transport is increased with the application of downward seepage as compared to no seepage. Hence, for downward seepage, sweep is the major event in the near bed flow zone. With the application of downward seepage, the high speed fluid parcel becomes more persistently preserving near to the bed as compared to that with no seepage.

In order to study the time scales of Q2 and Q4 events, the occurrences of bursting events Q2 and Q4 in a sample were counted by keeping a hole size *H=0* and calculating the number of changeover of the series of ( $u'$ , $w'$ ) in the applicable quadrant. The mean time of occurrence of Q2 and Q4 events $t_E$ and $t_S$, respectively were thus obtained. Figure 7 shows the vertical profiles of normalised time scales $T_E$ ($=t_E u_*/y$) and $T_S$ ($=t_s u_*/y$) in flows subjected to no seepage and seepage for $H$=0. Generally for $H$=0, $T_E$ increases with $z$ while $T_S$ decreases with $z$. It suggests that the time of occurrence of stronger Q4 events is less than that of stronger Q2 events. It is evident from Figure 7 that both $T_E$ and $T_S$ in seepage are more persistent than those in no seepage.

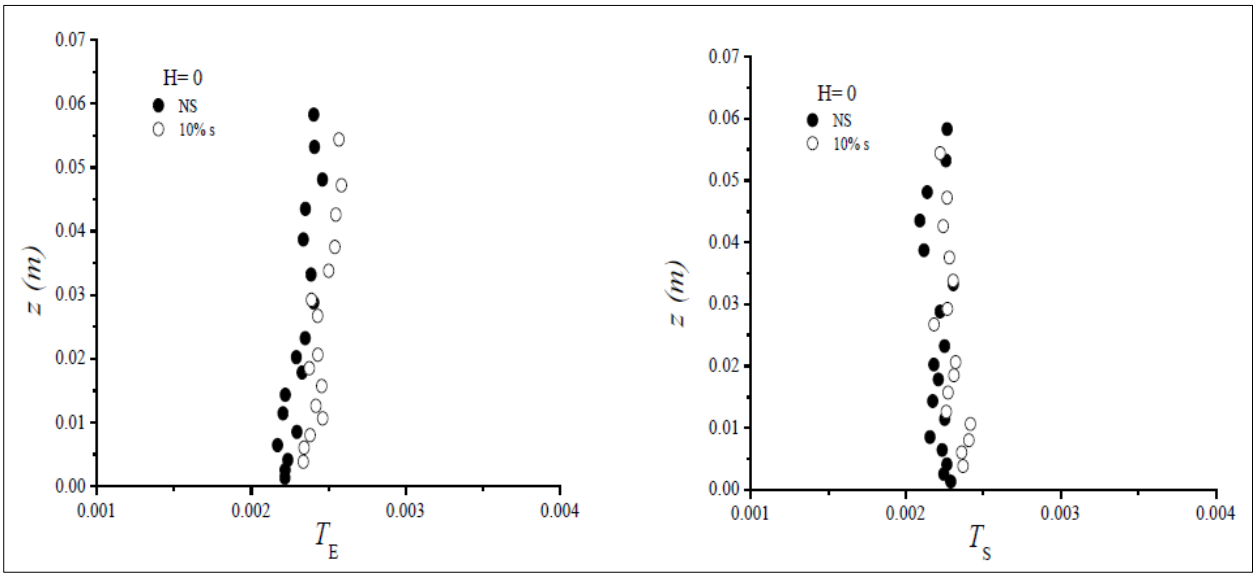


**Figure 7.**. Vertical profile of $T_E$ and $T_S$ for H=0

## 4 CONCLUSIONS

An experimental study has been carried out to observe changes in the turbulent characteristics of flow when downward seepage is applied to an alluvial channel composing of non-uniform sediment mixture. The present study addresses on the flow zone in the vicinity of the bed surface. The variations of stream wise velocity with vertical distance in flows with downward seepage in the near bed region are greater than no seepage flow. This increase in stream wise velocities is sufficient for increased rate of sediment transport with seepage. The profiles of Reynolds shear stress are slightly scattered in general and increase with seepage which signifies the greater momentum transfer towards the boundary. The distribution of Reynolds shear stress undergoes a damping due to a decreasing level of turbulence fluctuation within the wall shear layer. The thickness of roughness sub layer and shear velocities increase with the application of downward seepage. The reduced value of von Karman's constant corresponds to increase in the bed load transport with seepage.In the presence of seepage, increases in stream wise and vertical turbulence intensities are observed than turbulence intensities in no-seepage. The turbulence is strongly anisotropic being seepage independent and varying approximately linear with flow depth. In quadrant analysis, the contribution of sweep events towards Reynolds shear stress production near the boundary increases with increased zone of sweep dominance. This increase in high speed fluid parcel towards the boundary in seepage runs is responsible for higher rate of sediment transport. The mean time of occurrence of ejections and that of sweeps in seepage are longer than those in no-seepage.

## REFERENCES

Andrews, E.D. (1983). Entrainment of Gravel from Naturally Sorted Riverbed Material. *Geological Society of America Bulletin*, 94(1), 1225-1231.

Curran, J. C. (2007). The Decrease in Shear Stress and Increase in Transport Rates Subsequent to an Increase in Sand Supply to a Gravel-Bed Channel. *Sedimentary Geology,* 202, 572–580.

 

Curran, J. C. & Wilcock, P. R. (2005). Effect of Sand Supply on Transport Rates in a Gravel-Bed Channel. *Journal of Hydraulic Engineering,* 131(11), 961–967.

Deshpande, V. & Kumar, B. (2016). Turbulent Flow Structures in Alluvial Channels with Curved Cross-Sections under Conditions of Downward Seepage. *Earth Surface Processes and Landforms*, 41(8), 1073-1087.

Devi, T. B., Sharma, A. & Kumar, B. (2016). Turbulence Characteristics of Vegetated Channel with Downward Seepage. *Journal of Fluids Engineering,* 138(12),121102.

Fang, D. & Yu, G.L. (1998). Bedload Transport in Cobble-Bed Rivers. *Proceeding Of International Water Resources Engineering Conference*, Memphis, USA.

Ghoshal, K., Mazumder, B. S. & Purkait, B. (2010). Grain-Size Distributions of Bed Load: Inferences from Flume Experiments Using Heterogeneous Sediment Beds. *Sedimentary Geology,* 223(1-2), 1-14.

Goring, D. G. & Nikora, V. I. (2002). Despiking Acoustic Doppler Velocimeter Data. *Journal of Hydraulic Engineering,* 128(1), 117-126.

Karim, F. (1998). Bed Material Discharge Prediction for Nonuniform Bed Sediments. *Journal of Hydraulic Engineering,* 124(6), 597-604.

Kleinhans, M. G. (2005). Autogenic Cyclicity of Foreset Sorting in Experimental Gilbert-type Deltas. *Sedimentary Geology,* 181(3), 215-224.

Lacey, R. W. & Roy, A. G. (2008). Fine-Scale Characterization of the Turbulent Shear Layer of an Instream Pebble Cluster. *Sedimentary Geology,* 134(7), 925-936.

Lu, S. S. & Willmarth, W. W. (1973). Measurements of the Structure of the Reynolds Stress in a Turbulent Boundary Layer. *Journal of Fluid Mechanics,* 60(3), 481-511.

Marsh, N. A., Western, A. W. & Grayson, R. B. (2004). Comparison of Methods for Predicting Incipient Motion for Sand Beds. *Journal of Hydraulic Engineering,* 130(7), 616-621.

Misri, R. L., Garde, R. J. & Ranga Raju, K. G. (1984). Bed Load Transport of Coarse Nonuniform Sediment.*Journal of Hydraulic Engineering,* 110(3), 312-328.

Mittal, M.K., Porey, P.D. & Raju, K.G.R. (1990). Bed Load Transport of Nonuniform Sediments. *Proceeding of the Euromech 262-Colloquium on Sand Transport in Rivers*, Estuaries and the Sea, Wallingford, U.K.

Nezu, I. & Nakagawa, H. (1993). *Turbulence in Open Channels*, *IAHR/AIRH Monograph*. Balkema, Rotterdam, The Netherlands.

Parker, G., Kilingeman, P.C. & Mclean, D.G. (1982). Bed Load and Size Distribution in Paved Gravel-Bed Streams. *Journal of the Hydraulics Division*, 108(4), 544-571.

Patel, P. L. & Ranga Raju, K. G. (1996). Fraction Wise Calculation of Bed Load Transport. *Journal of Hydraulic Research,* 34(3), 363-379.

Samaga, B. R., Raju, K. G. R. & Garde, R. J. (1986). Bed Load Transport of Sediment Mixtures. *Journal of Hydraulic Engineering,* 112(11), 1003-1017.

Sreenivasulu, G., Kumar, B. & Ramakrishna Rao, A. (2011). Variation of Stream Power with Seepage in Sand Bed Channels. *Water SA*, 37(1), 115-119.

Wilcock, P. R. (1993). Critical Shear Stress of Natural Sediments. *Journal of Hydraulic Engineering,* 119(4), 491-505.

Wilcock, P. R. & Crowe, J.C. (2003). Surface-Based Transport Model for Mixed-Size Sediment. *Journal of Hydraulic Engineering,* 129(2), 120-128.

Zyserman, J. A. & Fredsøe, J. (1994). Data Analysis of Bed Concentration of Suspended Sediment. *Journal of Hydraulic Engineering,* 120(9), 1021-1042.

 

Proceedings of the 37th IAHR World Congress
August 13 – 18, 2017, Kuala Lumpur, Malaysia

# EFFECT OF POSITIVE STEP LOCATION ON SCOUR DOWNSTREAM THE BASIN OF MULTTI-VENTS REGULATOR

YASSER ABDALLAH MOUSSA[(1)] & MOHAMED AHMED AWAD[(2)]

[(1)]Jazan University, College of Engineering, Ksa (Leave on Zagazig University, Egypt)
Yasser_Eng1997@Zu.Edu.Eg
[(2)] Zagazig University, College Of Engineering, Egypt.
Eng_Awad2004@Yahoo.Com

## ABSTRACT

Scour downstream of multi-vents regulator represents a great harmful effect to the stability of such hydraulic structures. In this paper, the scour formed downstream of stilling basin is investigated experimentally for different positions of positive step. The experimental work is carried out in a 0.4m wide and 44.1m long rectangular channel. The experimental measurements include contours of scour depth, location of maximum scour depth and velocity vectors along rigid and mobile bed. The location of positive step close to vertical gates ($L_o$= 44%) decreases the scour depth and length by 72% and 65%, respectively. In addition, as the positive step moves away the vertical gates, asymmetric flow is formed and large dimensions of scour holes are generated downstream of stilling basin. Multiple linear regressions are used to have empirical correlations to predict maximum local scour depth and length downstream multi-vents regulator with correlation coefficients of 82% and 86%, respectively. The simulated results agree well with the measured data.

**Keywords:** Positive step; local scour; hydraulic structures; hydraulic jump.

## 1 INTRODUCTION

The hydraulic jump is a rapid transitional event from supercritical to subcritical flow. If the downstream water depth is less than the sequent water, the jump will sweep downstream. Hence, the supercritical flow will continue downstream to a large distance from the control structure. This leads to design a long stilling basin, which is considered uneconomical. For these cases, baffle blocks, sills, or positive step could be used to control length of hydraulic jump. Valentin (1967) studied the scour characteristics downstream of a sluice gate under free discharge conditions. Rajaratnam and Beltaos (1977) studied the erosion that caused by impinging circular turbulent jets. It was found that the maximum depth of erosion varied linearly with the logarithm of time. Rajaratnam (1982) investigated the erosion by submerged circular jets. It was found that, the erosion was a function of Froude number relative to height of jet. Rajaratnam and Macdougall (1983) studied the erosion formed by plane turbulent wall jets downstream of a rigid apron. It was observed that the relative scour depth becomes less than the corresponding value for the case of a deep tailwater. Hassan and Narayanan (1986) investigated the local scour downstream of a solid apron. Uyumaz (1989) investigated the scour phenomenon in non-cohesive soils downstream of the vertical gate in the different cases of flow passing over, under the gate and the combination between them. It was found that the scour depth is of a smaller value for the case of a simultaneous flow over and under the gate. Kalifa et al. (1989) studied the effect of different arrangement of rectangular stilling basins on local scour downstream of a regulator. The maximum scour depth was correlated to other independent variables. It was found that, the end sill case produces larger values of local scour depth downstream of stilling basin compared to the smooth case. Hoffmans and Pilarczyk (1995) investigated the functional design of the bed protection downstream of stilling basin. The undermining at the end of the bed protection was estimated. Abouel-Atta (1995) investigated the scour phenomena due to a radial free hydraulic jump flowing over a rigid diverging apron to an erodible bed. Floor jets are used as appurtenance to reduce erosion. Lenzi et al. (2003) studied the effect of bed sill to avoid erosion in high gradient slope channels. Equations were proposed to estimate scour depth and length. Adduce and La Rocca (2006) studied different scour developments of a trapezoidal drop followed by a rigid apron under submerged flow conditions. Pagliara (2007) proposed empirical equations to estimate the maximum local scour depth that formed downstream of block ramps. Oliveto and Comuniello (2009) studied the local scour downstream of positive-step stilling basins, mainly referring to the quasi-equilibrium stage. An experimental study was carried out to investigate the impact of a rectangular baffle inside a square channel by Gajusingh et al. (2010). It was concluded that the flow characteristics are significantly modified due to the insertion of a baffle inside the channel. Pagliara and Palermo (2011) investigated the effect of width and length of the downstream stilling basin on scour characteristics and flow pattern in clear water conditions. Melville and Lim (2014) introduced the analysis of laboratory data for local scour depth developed by two-dimensional horizontal jets, which leads to create of a new comprehensive prediction equation. The effect of end sill on scour formed downstream regulator was investigated by Mohmed et al. (2016). Eghbalzadeh et al.

 

(2016) predicted the equilibrium scour depth in uniform non-cohesive sediments downstream of stilling basin using artificial intelligence. Oertel and Bung (2016) studied the scour forming downstream of block ramps. In the present paper, the effect of different positive step positions on scour formed downstream of multi-vents regulator is investigated.

## 2 EXPERIMENTAL WORK

A rectangular flume of re–circulating system was used. Its overall length was 44.1m and the working section of it had 39.1m length, 0.5m width and 0.6m depth. The distance from the main gate to the end of apron was 125cm ($L_b$). Two piers made from Base-form were fastened at the contraction part with 50cm length. There were vertical gates which were made from perspex, and slided through vertical grooves, as shown in Figure 1. The false bed height was 12cm and the model height over it equaled 48cm. The positive step with constant height of 2.5cm was placed over stilling basin at distances ($L_e$ =) 55, 60, 70, 85 and 107 cm from the vertical gate. The ultrasonic flow-meter was used to measure the passing discharge into the flume. It was installed on the feeding pipe to the flume. The ultrasonic flow-meter measures the flow rate with accuracy of about ± 1%. Flow velocity in the model was measured using the Electromagnetic Current-meter. The Electromagnetic Current-meter type E.M.S. was manufactured by Delft Hydraulics, Holland. This Current-meter is a well-known pipe Flow-meter employing Faraday's Induction Law for velocity measurements of a conductive liquid moving through a magnetic field. The flow velocity was measured at six cross-sections by a distance 1.5 cm away from the bed of stilling basin. The distance between the first three cross-sections which located on the apron area was 25cm and 10cm for the remaining cross-sections over mobile bed. In addition, the vertical velocity profile at the end of rigid bed was measured, see Figure 2. Movable sand bed of length 9m and 0.12m thickness was placed downstream rigid bed. Uniform sample of sand had median size of 0.5 mm and geometric standard deviation of 1.28.

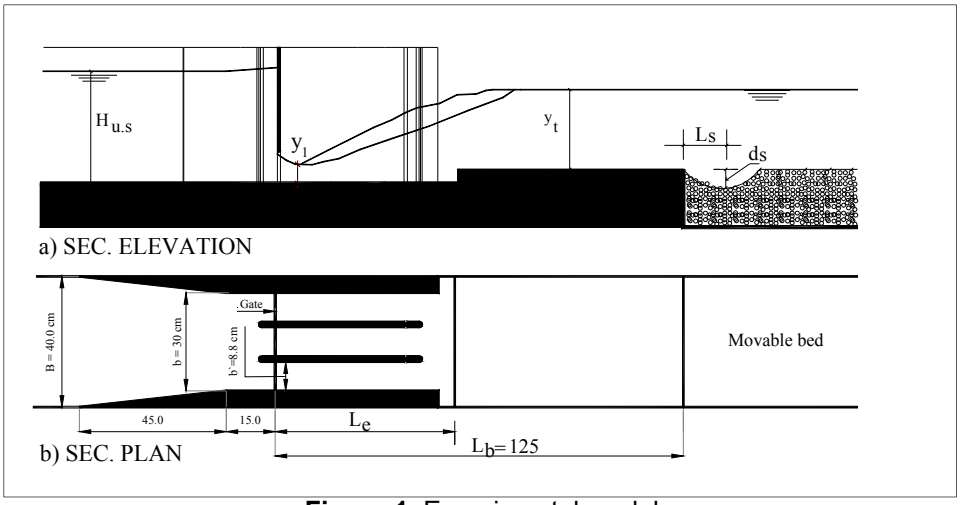


**Figure 1.** Experimental model.

The experiments were carried out under the condition of clear water scour with flow rates ranging between 3.8 and 16 l/s. The ranges of Froude number ($F_r$ =($v_1$/($gy_1$)^0.5; $v_1$ is the velocity at supercritical flow depth $y_1$), and Reynolds number are (1.8 to 3.8) and (9000 to 19000), respectively. For each experimental run, the mobile bed was leveled. The water level was controlled after reaching the desired discharge, in such a way that free hydraulic jump formed in stilling basin. Point gauge with 0.1mm accuracy was used to survey the bed topography. The time for each run was taken 8 hrs at which more than 85% of equilibrium scour was achieved. Palgiara et al. (2009) clarified that when varying flume dimension, up to reasonably dimensions, the non-dimensional scour parameters were not significantly affected by the scale and walls.

## 3 RESULTS AND DISCUSSION

### 3.1 Scour morphology and velocity vectors

Velocity vectors that generated over stilling basin and mobile bed depends on the location of positive step and also the nature of flow. The movable bed is significantly affected with the existence of positive step. A T-jump was created at which the toe position was located in the approaching multi-vents of a regulator. According to the step position, the flow pattern over stilling basin and mobile bed and bed morphology varied. The asymmetric velocity vectors especially at the end of stilling basin were created to form unsymmetrical scour holes downstream rigid bed. Contour maps of bed morphology downstream rigid bed at $F_r$= 3.7 were created for all different positions of positive step. Moreover, the velocity vectors over rigid and mobile bed

 

were traced to show and explain the formation of scour characteristics downstream stilling basin. Bed shapes for the different positive step positions could be shown as follow:

- Positive step at $L_o$, ($L_e/L_b$)= 44%,
  In this case, the velocity vectors downstream positive step had slightly high values, Figure 2a. As these vectors moved away positive step location, the velocity values decreased. In addition, the directions of velocity vectors along the right side of channel were different than those formed at the left side of channel. So, the asymmetric flow downstream positive step caused to generate unsymmetrical scour profile at the end of rigid bed. Scour was formed along the channel width downstream of the stilling basin. The scour depth at the right side of channel was deeper than that formed at the left side. The vertical velocity profiles at the end of stilling basin assessed the last results, at which asymmetric velocity distribution was around the centerline of channel, Figure 2b. In this case, the existence of step close to the sluice gates compared to the other positions of positive steps, led to smaller scour depth and more control to the flow patterns over rigid and mobile beds.

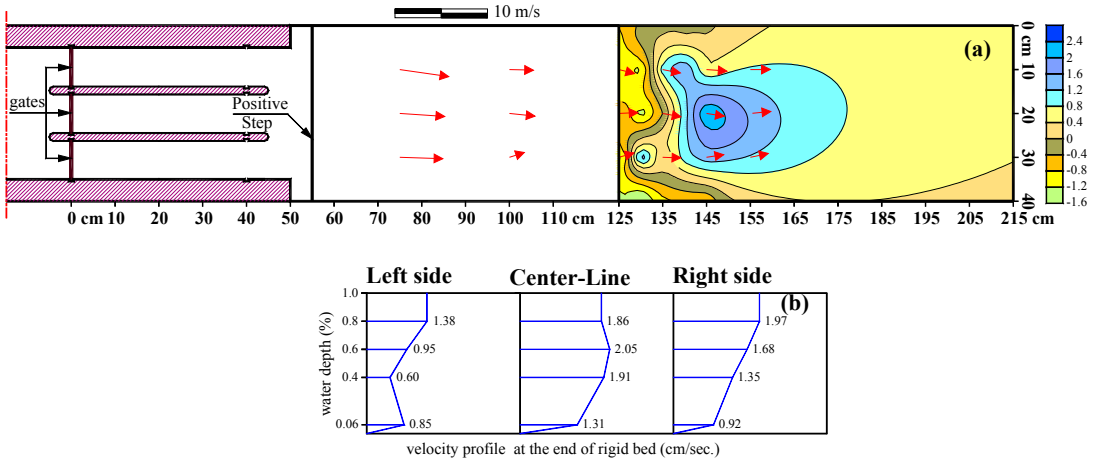


**Figure 2.** Scour contour map for bed morphology and velocity vectors for $L_o$= 44%, and Froude number equals 3.7.

- Positive step at $L_o$= 48%,
  The flow released the sudden expanding part of channel to impinge the channel sides (flow pattern with blue lines). Part of flow returned towards the channel centerline and the other part moved towards the end of stilling basin. The traced velocity vectors beside the channel sides in the first half of stilling basin were directed to canal center line as shown in Figure 3a. In the last half of the rigid bed, the velocity vectors were directed to the mobile bed with nearly unequal values. Two scour holes were formed at the channel sides, the maximum scour depth was created at the left side of channel. Figure 3b showed an increase in the velocities in the vertical profile at the left of channel side to confirm the result of maximum scour depth at this location. The values of scour depths for this case were larger than those formed for positive step at $L_o$=44%. At which, bundle of the flow concentrated at the channel sides.

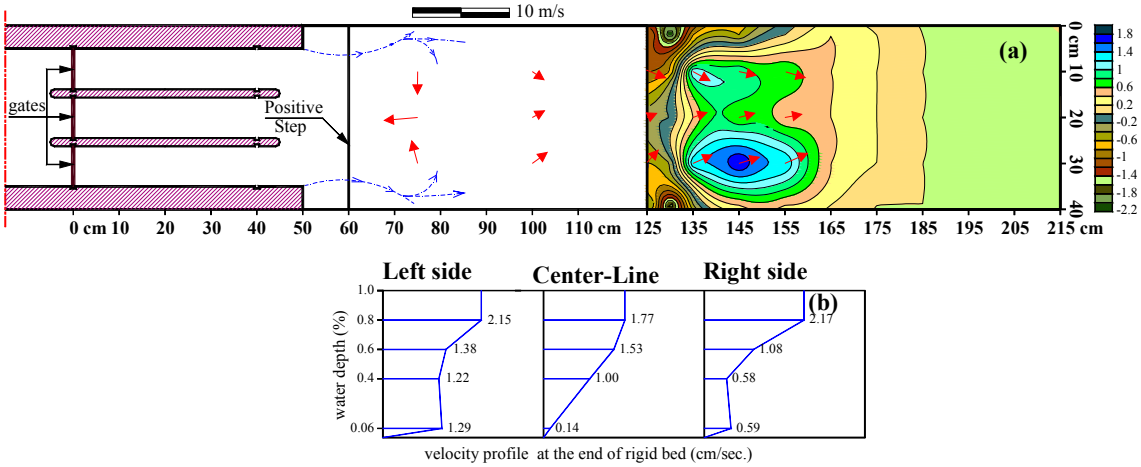


**Figure 3.** Scour contour map for bed morphology and velocity vectors for $L_o$= 48%, and Froude number equals 3.7.

 

- Positive step at $L_o$= 56%,
  The velocity vectors over rigid and mobile beds showed that an asymmetric reverse flow was generated. This reverse flow generated over mobile bed towards the position of positive step, Figure 4a. At this position of positive step, the harmful effect of reverse flow caused to produce larger dimensions of scour holes compared to the other position of positive step. Velocities at the right side did not match those formed at the left side of channel, so, asymmetric flow was generated. It caused to form unequal two scour holes at the channel sides and deposited sediment along the middle of channel. The deposition extended over the rigid bed. The lines of flow patterns beside the channel walls showed that the reverse flow at the right side of channel started early before the reverse flow at left side. Figure 4b showed a significant decline in the values of velocities in the centerline of waterway at the end of stilling basin compared to those formed at the channel sides. The velocity profiles at the end of stilling basin demonstrated the formation of the asymmetric erosion at both sides of the channel.

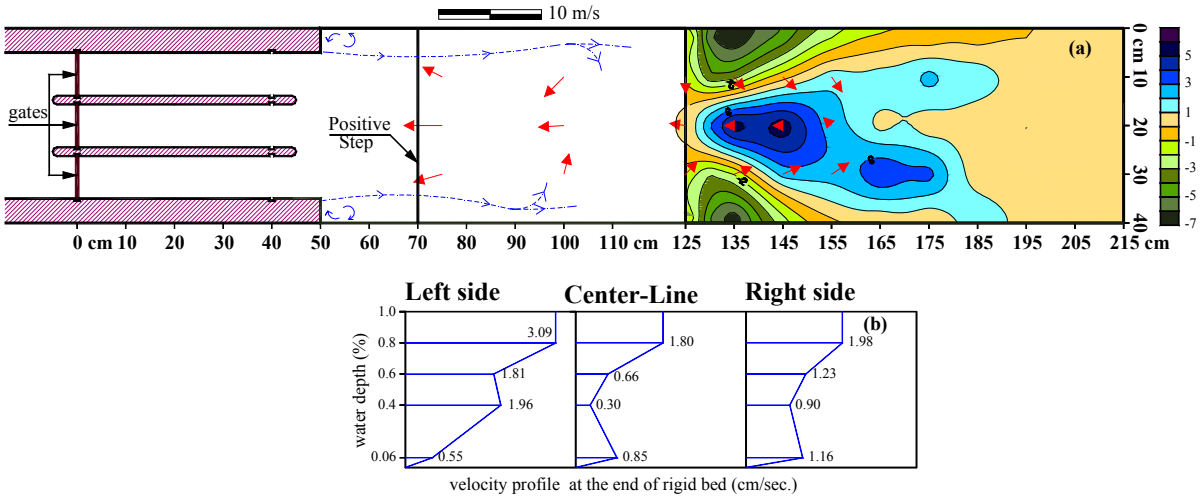


**Figure 4.** Scour contour map for bed morphology and velocity vectors for $L_o$= 56%, and Froude number equals 3.7.

- Positive step at $L_o$= 68%,
  As the positive step moved slightly away from the sudden expanding, high values of velocity vectors were generated before the position of positive step compared to the other values of velocities beyond this step, Figure 5a. The incoming velocities impinging the sides of channel showed reverse velocities between the end of rigid bed and the position of positive step. The lines of flow patterns beside the walls of channels indicated asymmetric flow, at which the velocity vectors near channel sides were not the same, (i.e., direction and magnitude were not the same). The asymmetric flow caused the formation of unequal scour holes at flume sides, Figure 5b.

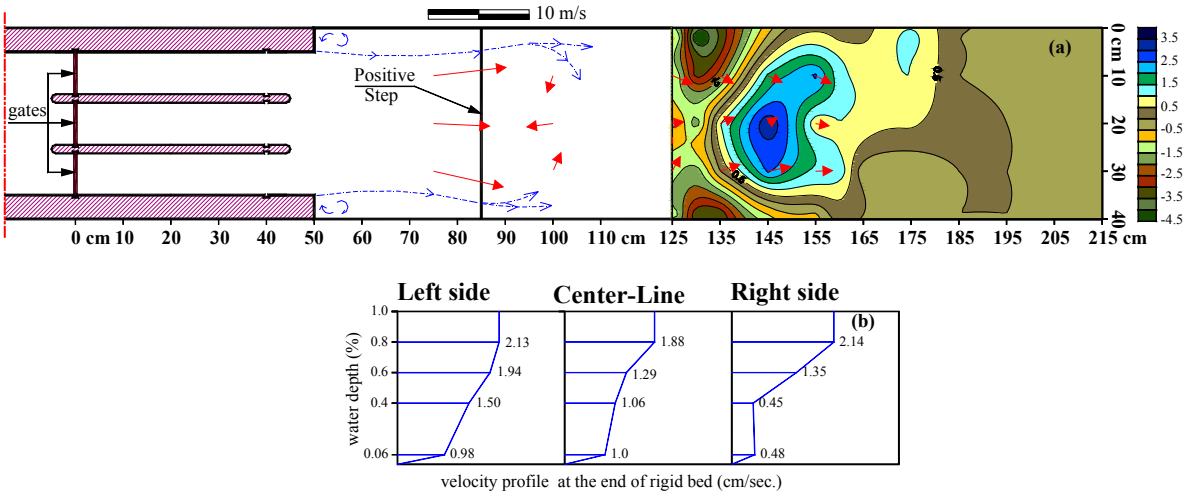


**Figure 5.** Scour contour map for bed morphology and velocity vectors for $L_o$= 68%, and Froude number equals 3.7.

 

- Positive step at $L_o$= 84%,
  The impact of flow with the positive step at this location led to significant decrease in the values of velocity vectors downstream stilling basin. The velocity vectors had nearly uniform distribution along the total width of the open channel. In addition, the scour formed downstream rigid bed was proportional to the velocity vectors over rigid bed, see Figure 6. A slightly asymmetric flow can be observed through the vertical velocity distribution at the end of apron, as shown in Figure 6.

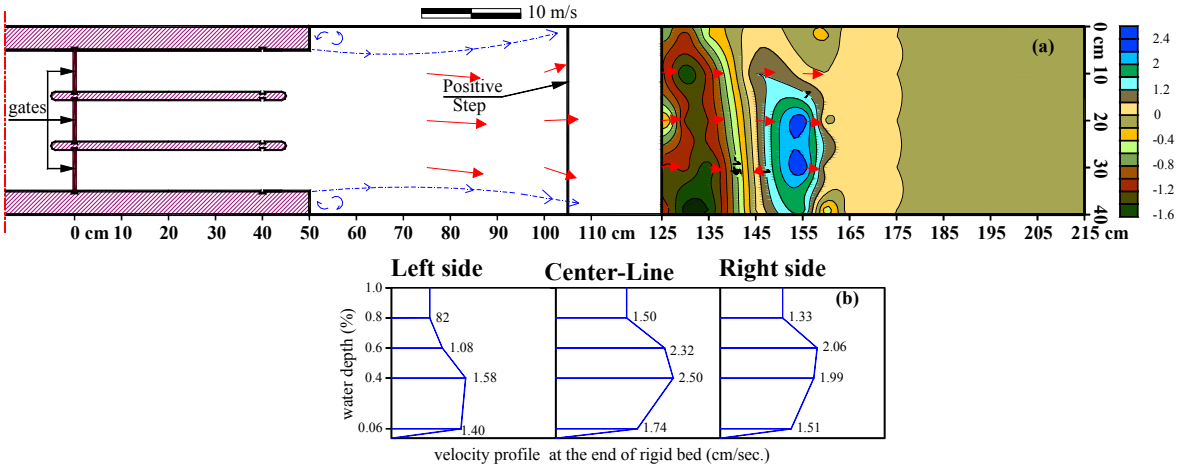


**Figure 6.** Scour contour map for bed morphology and velocity vectors for $L_o$= 84%, and Froude number equals 3.7.

3.2 Scour characteristics and velocity gradient

The relationship between the relative scour depth $d_s/y_1$ and Froude number $F_r$ for different relative positions of positive step ($L_o$= $L_e/L_b$) was presented in Figure 7. It was found that, $d_s/y_1$ increased as $F_r$ increased for different ratios of $L_o$. In addition, the local scour depth downstream stilling basin was smaller as the positive step was close to the sudden expansion of multi-vents regulator, i.e. $L_o$= 44%. The impinging of the incoming velocity jet with positive step damps significantly the velocities downstream this obstruction to have small scour depth downstream rigid bed. As the positive step movesaway from the sluice gates, it is found that, the major factor affecting scour is the formation of asymmetric and a reverse flow. The asymmetric flow generates high velocities at one side of the channel compared to the other one. In addition, the reverse flow in cases of $L_o$= 48%, 56% and 68% contributes to re-distribution of velocities over aprons which leads to generate more dimensions of scour holes downstream stilling basin. The relative scour depth decreased by 72%, 60%, 30%, and 47% for $L_o$= 44%, 48%, 68% and 84%, respectively compared with the relative position of positive step at $L_o$= 56%. From these results, it is obvious that the optimum position of positive step to have minimum scour depth and avoid asymmetric flow is at $L_o$= 44% (i.e. the closest position of positive step to piers of multi-vents regulator)

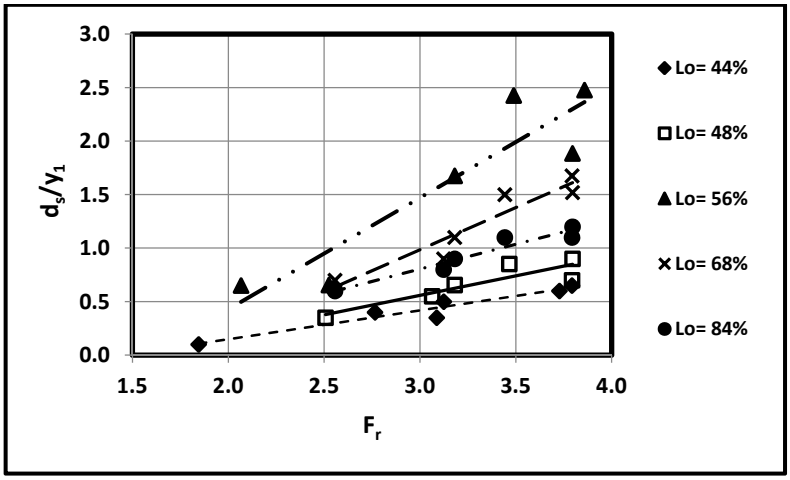


**Figure 7.**The relationship between Froude number and relative scour depth and different relative positions of positive step.

The velocity gradients for different ratios of $L_o$ and $F_r$ were shown in Figure 8. This figure shows the values of scour depth downstream stilling basins. The velocity gradients over bed at the end of stilling basin at $L_o$=44%

 

was smaller compared to the other ratios of $L_o$, and hence, the smallest values of local scour depth was obtained at this position. Figure 9 presents the relationship between $F_r$ and relative length of scour $L_s/y_1$ at different ratios of $L_o$. The minimum $L_s/y_1$ was obtained at $L_o$= 44%, (positive step is close to piers), and it increased for the other ratios of $L_o$ to have maximum $L_s/y_1$ at $L_o$= 56%. The relative length of scour decreased by 65%, 45%, 17% and 36% for $L_o$= 44%, 48%, 68% and 84%, respectively compared with $L_o$= 56%.

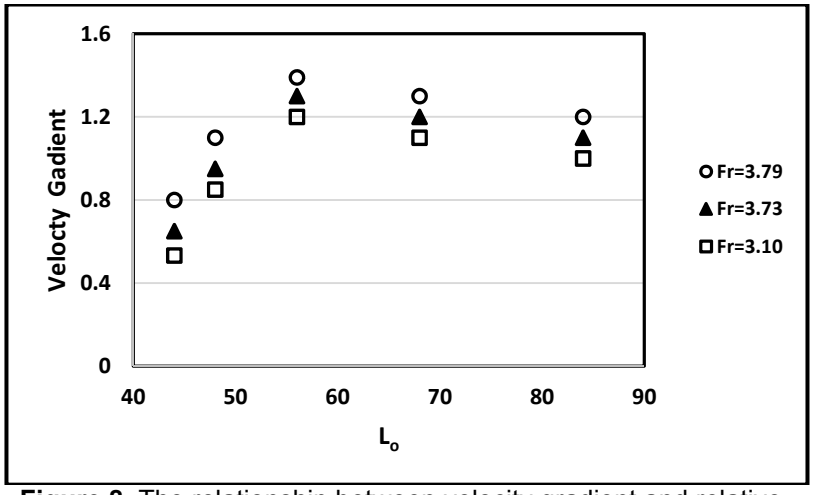


**Figure 8.** The relationship between velocity gradient and relative position of positive step.

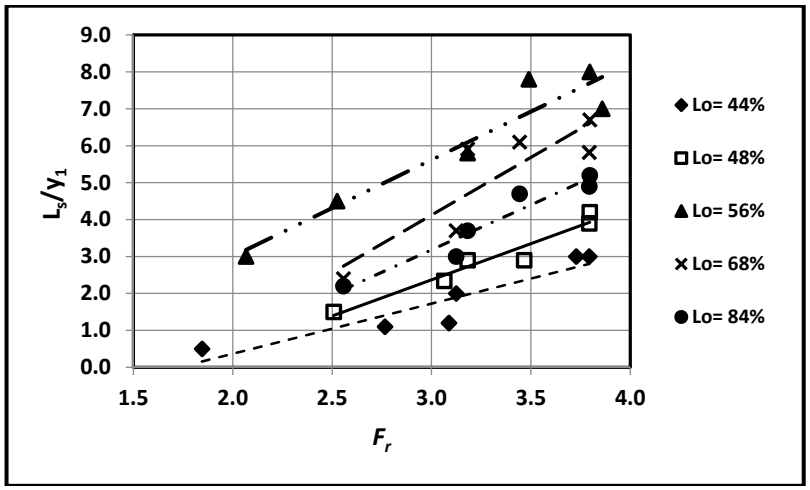


**Figure 9.** The relationship between Froude number and relative scour length and different relative positions of positive step.

3.3 Predicted equations of scour depth and length

In the present paper, the multi-vents regulator provided with positive step with constant height of 2.5cm was located at different positions over stilling basin. The maximum relative scour depth and length can be expressed as a function of the following in non-dimensional groups;

$$[d_s/y_1\,, L_s/y_1] = f(F_r, L_o, v_b/v_1) \qquad [1]$$

where $d_s$ and $L_s$ are the maximum scour depth and length, respectively, $F_r$ is the Froude number at supercritical flow depth. $L_o$ is ratio of distance from gate to positive step and length of stilling basin, i.e. $L_e/L_b$, $v_b$ is the velocity at the end of stilling basin over rigid bed, and $v_1$ is the velocity at super critical flow depth $y_1$. The following relationships were proposed to predict the relative scour depth and length;

$$d_s/y_1 = -1.9 + 0.80F_r + 0.60L_o + 6.60(v_b/v_1) \qquad [2]$$
$$L_s/y_1 = -7.6 + 2.2F_r + 3.90L_o + 28(v_b/v_1) \qquad [3]$$

The coefficients of determination ($R^2$), equalled 0.82 and 0.86 between the measured and predicted values of $d_s/y_1$ and $L_s/y_1$, respectively. Figure 10 shows the comparison of experimental and predicted data of Eqs. [2] and [3]. The standard error and mean relative error were (0.18 and 0.15) and (0.61 and 0.13) for Eqs. [2] and

 

[3], respectively. This figure clarified that the data points were reasonably distributed around the perfect agreement line, and the proposed equations expressed well the measured data for both $d_s/y_1$ and $L_s/y_1$.

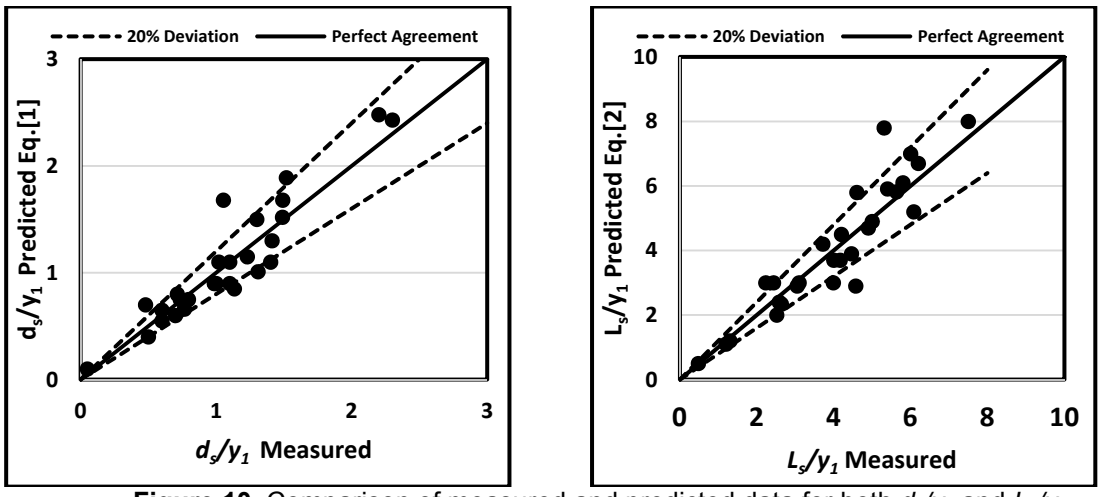


**Figure 10.** Comparison of measured and predicted data for both $d_s/y_1$ and $L_s/y_1$.

## 4 CONCLUSIONS

This paper analyzes the effect of different positions of positive step ($L_o$) on the scour featured downstream stilling basin of multi-vents regulator. The experimental work is carried out under a clear water scour conditions. Uniform sand bed is used with median size of 0.5mm. From the present study, it is found that the scour depth and length increase as Froude number increases for different experimental models. The presence of positive step close to the piers of multi-vents regulator minimizes the scour hole dimensions formed downstream rigid bed. The relative scour depth and length are reduced by 72% and 65% at $L_o$= 44%, respectively. In addition, as the positive step moves away from the piers, an asymmetric flow is generated leading to production of more scour depth and length downstream stilling basin. The proposed equations for predicting relative scour depth and length agree well with the measured data.

## ACKNOWLEDGEMENTS

The authors would like to thank Prof. Dr. Abdel Azim Mohamed Ali, for his support and the possibility to perform experimental investigation program at the hydraulic research institute, Egypt.

## REFERENCES

Abouel-Atta, N. (1995). Scour Prevention Using a Floor Jets Mechanism. *Civil Eng. Research Magazine, Faculty of Engineering, Al-Azhar University,* Egypt, 17(2), 256-268.

Adduce, C., & La Rocca, M., (2006). Local Scouring Due to Turbulent Water Jets Downstream of a Trapezoidal Drop: Laboratory Experiments and Stability Analysis. *Water Resources Research*, 42(2), 1–12.

Eghbalzadeh, A., Hayati, M., Rezaei, A. & Javan, M. (2016). Prediction of Equilibrium Scour Depth in Uniform Non-Cohesive Sediments Downstream of an Apron Using Computational Intelligence. *European Journal of Environmental and Civil Engineering*, 10, 1-14.

Gajusingh, S.T., Shaikh, N. & Siddiqui K. (2010). Influence of a Rectangular Baffle on the Downstream Flow Structure. *Experimental Thermal and Fluid Science*, 34, 590–602.

Hassan, N.M.K. & Narayanan, R. (1986). Local Scour Downstream of an Apron. *Journal of Hydraulic Engineering*, 111(11), 1371-1385.

Hoffmans, G.C.M. & Pilarczyk, K.W. (1995). Local Scour Downstream of Hydraulic Structures. *Journal of Hydraulic Engineering,* 121(4), 326-339.

Kalifa, A.M., Abdellateef, M. & Abdel-Hafiz, E. (1989). *Characteristics of Scour Accompanied by Supercritical Flow,* Submitted Bulletin, Faculty of Engineering, Ain Shams University, 23, 135-149.

Lenzi, A.A., Maion, A., Comiti, F. & Gaudio, R. (2003). Local Scouring in Low and High Gradient Streams at Bed Sills. *Journal of Hydraulic Research,* 40(6), 731-739.

Melville, B.W. & Lim, S. (2014). Scour Caused by 2D Horizontal Jets. *Journal of Hydraulic Engineering,* 140(2), 49-155.

Mohamed, Y.A., Saleh, Y.K. & Ali, A.M. (2016). Performance of Sills over Aprons under the Effect of Submerged Hydraulic Jump, (Case study: NagaHammadi Barrage). *Ain Shams Engineering Journal (ASEJ)*. (Available online 6 October 2016).

Oertel, M. & Bung D.B. (2016). Scouring Processes Downstream a Crossbar Block Ramp. 6th *International Symposium on Hydraulic Structures Portland*, Oregon, USA.

 

Oliveto, G. & Comuniello, V. (2009). Local Scour Downstream of Positive-Step Stilling Basins. *Journal of Hydraulic Engineering,* 135(10), 846–851.

Pagliara, S. (2007). Influence of Sediment Gradation on Scour Downstream of Block Ramps. *Journal of Hydraulic Engineering,* 133(11), 1241–1248.

Pagliara, S. & Palermo, M. (2011). Effect of Stilling Basin Geometry on Clear Water Scour Morphology Downstream of a Block Ramp. *Journal of Irrigation and Drain Engineering,* 137(9), 593-601.

Pagliara, S., Palermo, M. & Carnacina, I. (2009). Scour and Hydraulic Jump Downstream of Block Ramps in Expanding Stilling Basins. *Journal of Hydraulic Research,* 47(4), 503-511.

Rajaratnam, N. (1982). Erosion by Submerged Circular Jets. *Journal of the Hydraulic Division*, 108(2), 262-267.

Rajaratnam, N. & Beltaos, S. (1977). Erosion by Impinging Circular Turbulent Jets. *Journal of the Hydraulic Division*, 103(10), 1191-1205.

Rajaratnam, N. & Macdougall, R.K. (1983). Erosion by Plane Wall Jets with Minimum Tailwater. *Journal of Hydraulic Engineering,* 109(7), 1061-1064.

Uyumaz, A. (1988). Scour Downstream of Vertical Gate. *Journal of Hydraulic Engineering,* 114(7), 811-816.

Valentin, F. (1967). Considerations Concerning Scour in The Case of Flow under Gates. *Proceeding of 12th Congress IAHR, International Association of Hydraulic Research* (IAHR), Madrid, Spain, 3, 92–96.

 

Proceedings of the 37th IAHR World Congress
August 13 – 18, 2017, Kuala Lumpur, Malaysia

# EFFECT OF PILE ARRANGEMENT ON LOCAL SCOUR DEPTH

YASSER A. MOUSSA[(1)] & MAHMOUD ATTA[(2)]

[(1)]Jazan University, Ksa (Leave onZagazig University, Egypt)
yasser_eng1997@zu.edu.eg
[(2)]Jazan University, Ksa (Leave onzagazig University, Egypt)
matta767@gmail.com

## ABSTRACT

In this study, analysis of local scour at pile groups is conducted. These piles are widely used to support bridge foundations on deep alluvial riverbeds. The supporting area of such piles can be arranged in the form of one or more piles. The effect of different arrangements of such piles on the stability of hydraulic structures is investigated experimentally and numerically. Eight models of piles are investigated under different flow conditions. The caps of these piles are above the water surface. A numerical model, that is, Sediment Simulation in Water Intakes with Multiblock Option program, is developed to simulate scour around bridge pile groups. This model solves the three-dimensional Navier–Stokes equations and the bed load conservation equation. The $k$–$\varepsilon$ turbulence model is used to solve the Reynolds stress term. Notably, the tandem pile arrangement reduces the local scour depth by 42% compared to the one-pile case. Results of simulation models show a distinct correlation with experimental data.

**Keywords:** Hydraulic structure; local scour; pile groups; bridge; local scour.

## 1 INTRODUCTION

Piles are used to support hydraulic structures in coastal and ocean engineering, where many hydraulic structures are located on erodible bottoms. Scour formed around piers and pile-supported hydraulic structures can result in structural collapse and loss of life and property (Bayran and Larson, 2000). In New Zealand, at least one serious bridge failure each year is related to scour at the foundations (Melville and Coleman, 2000). The mechanism of scouring around bridge foundations is complex (Hjorth, 1975; Dargahi, 1990). Generally, three types of scour affect the performance and safety of bridges, namely, local scour, contraction scour, and degradation scour (Parker et al., 1997). In the simplest case, pile groups are capped above the water surface and only the piles obstruct the flow field (Zounemat-Kermani et al., 2009). Scour characteristics around typical solid piers have been presented extensively by numerous researchers (Melville and Sutherland, 1988; Dey et al., 1995; Abdel-Aal and Mohamed, 2010; Mohamed et al., 2016). However, the literature on scouring at pile groups is limited (Hannah, 1987; Salim and Jones, 1996; Ataie-Ashtiani and Beheshti, 2006). Experiments were conducted to measure local scour around exposed pile groups for a variety of conditions, including different spacing, skew angles, and exposures of a pile cap in the flow field (Fayun et al., 2016). Local scour at pile groups in meandering channels was investigated by placing a group of four piles consisting of two lines in parallel at different locations in the meandering section of the channel (Nouh, 1986). The turbulence intensity outside the pile group was greater than that inside the pile group. The maximum scour depths at the upstream piles were larger than that at the downstream piles. In addition, local scour depth increases as the transversal pile spacing decreases. The effect of flow skew angle on sediment scour near pile groups was investigated experimentally (Zhao and Sheppard, 1998). The experiments were conducted for the flow skew angle ranging from 0° to 90°. When the flow skew angle is less than 20°, the maximum scour depth occurs near the front of the pile group. Meanwhile, when the flow skew angle is greater than 20°, the maximum scour depth occurs at the upstream edge of the pile group. Sumer et al. (2005) conducted experiments on seven different configurations of pile groups in a flume with 23 m length, 0.2 m width, and 0.5 m depth. When a pile group was exposed to the flow, two kinds of scour patterns emerge. The first pattern was the scour in the vicinity of individual piles, which is local scour. The second pattern was the scour around the pile groups in the form of a saucer-shaped depression, which is global scour. An estimation of current-induced scour depth around pile groups was conducted using the neural network and adaptive neuro-fuzzy inference system developed by Zounemat-Kermani et al. (2009). It was found that, the pile diameter and the ratio of pile spacing to pile diameter are the most significant parameters of local scour depth. Amini et al. (2012) presented the results of experimental work on scour at arrays of pile groups under steady flows. A new method was used to estimate the local scour depth at pile groups and was developed for shallow-water conditions. A comprehensive review of local scour depth estimation methods around pile groups was presented (Rashed and Amini, 2015). Numerical models were used to simulate the scour depth around bridge foundations (Morales and Ettema, 2011; Mohamed et al., 2015; Nasr-Allah et al., 2016) using the Sediment Simulation in Water Intakes with Multiblock Option (SSIIM) program. In the present study, the effect of different

 

arrangements of pile groups on scour formation is investigated experimentally and numerically. The simulated models are created using the SSIIM program (Olsen, 2007).

## 2 EXPERIMENTAL WORK

The experimental work was conducted in a recirculating channel with 5.7m length, 20cm depth, and 40 cm width. The flume entrance and outlet lengths were 0.3 and 1.4m, respectively. The discharge was measured using a precalibrated orifice meter. Stones with different sizes were used at the entrance to dampen disturbances carefully. The flume was filled with uniform bed sediment with a thickness of 0.10m and geometric standard deviation ($\sigma_g$) of 1.28. The median sand size ($D_{50}$) was 1.4mm. The experimental work was conducted under clear-water conditions. For each test of the experimental program, the sand was levelled along the entire length of the flume using a wooden screed with the same width as the flume. The flume was filled gradually with water to the required depth. Then, the pump was turned on and its speed was increased gradually until the desired flow rate was achieved. Thereafter, the tailgate was adjusted to obtain the required water depth. At the end of the test, the pump was turned off and the flume was drained gradually without disturbing the scour topography. The bed topography was measured with a point gauge with 0.10 mm accuracy. The grid pattern was dense and exhibited an accurate bed topography at the end of each experiment. The flow rate was 3.3 L/s. Tail water depth was changed to obtain the range of Froude numbers ($F_t$= 0.20–0.52). The total cross-sectional area for each pile group is the same and is equal to the area of a reference case (one pile arrangement). The area of pile in each group arrangement equals to area of reference case (i.e., d^2) divided by the number of piles in group arrangement. Figure 1 presents the different arrangements of pile groups and contains the following arrangements: one pile, two piles (side by side and tandem), three piles (triangular 2 × 1 and 1 × 2), four piles (2 × 2), and five piles (pentagonal 1 × 4 and 4 × 1). The maximum model width was less than 12% of the channel width to avoid contraction effects (Melville and Sutherland, 1988). The time duration for each experiment was taken as 6 h; at this time, the scour depth reached more than 85% of the equilibrium scour depth based on preliminary experiments. Studies conducted by other researchers have shown that most of the scour occurs during the first 3 or 4h of a test (Mia et al., 2003; Yanmaz and Altinbilek, 1991).

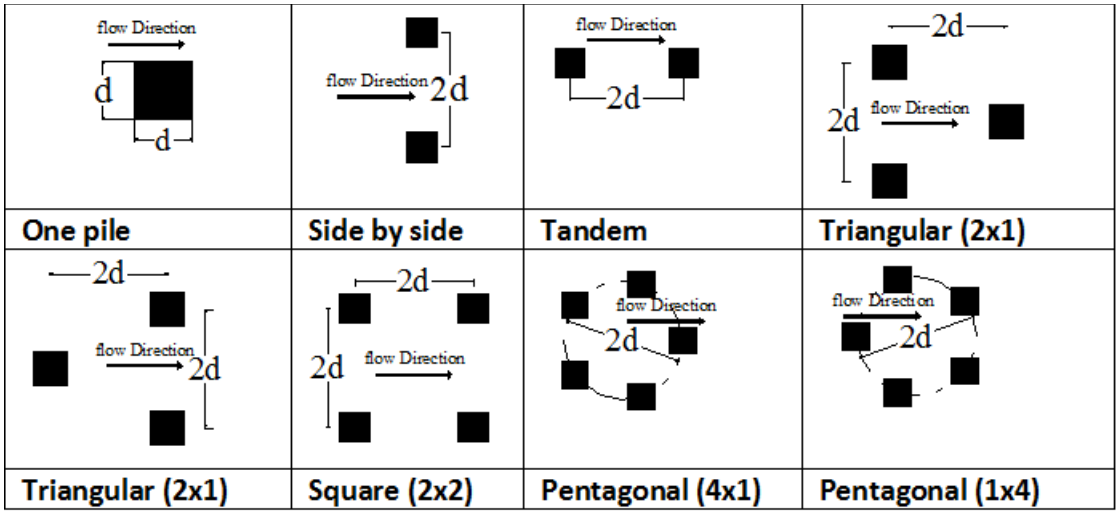


**Figure 1.** Different configurations of pile groups.

## 3 NUMERICAL MODEL

The SSIIM program solves the Navier–Stokes equations with the $k-\varepsilon$ on three-dimensional (3D) and general non-orthogonal coordinates. These equations are discretized with a control volume approach. An implicit solver is used, producing the velocity field in geometry. The velocities are used when solving the convection–diffusion equations. The Navier–Stokes equations for noncompressible and constant density flow can be modeled as

$$\frac{\partial u_i}{\partial t} + U_j \frac{\partial u_i}{\partial x_j} = \frac{1}{\rho}\frac{\partial}{\partial x_j}\left[-p\delta_{ij} - \rho\overline{u_i u_j}\right] \quad [1]$$

The first term on the left-hand side of Eq. [1] indicates the time variations. The second term denotes the convective term. The first term on the right-hand side of Eq. [1] indicates the pressure term. The second term denotes the Reynolds stress. The Reynolds stress is evaluated using the turbulence model $k-\varepsilon$. The free surface is calculated using the fixed-lid approach, with zero gradients for all variables. The locations of the

 

fixed lid and its movement as functions of time and water flow field are computed using different algorithms. The 1D backwater computation is the default algorithm and is invoked automatically. The formula developed by Van Rijin(1987) was used to calculate the equilibrium sediment concentration close to the bed. This equation has the following form:

$$C_{bed} = 0.015 \frac{d^{0.3}[(\tau-\tau_c)/\tau_c]^{1.5}}{a\left[((\rho_s-\rho_w)g)/(\rho_w v^2)\right]^{0.1}} \quad [2]$$

where $C_{bed}$ is the sediment concentration, $d$ is the sediment particle diameter, $a$ is the reference level set equal to the roughness height, $\tau$ is the bed shear stress, $\tau_c$ is the critical bed shear stress for the movement of sediment particles according to Shield's curve, $\rho_w$ and $\rho_s$ are the densities of water and sediment, respectively, $v$ is the kinematic viscosity of water, and $g$ is the gravitational acceleration. The bed load discharge ($q_b$) can be calculated using the following equation (Van Rijin 1987):

$$\frac{q_b}{D_{50}^{1.5}\sqrt{((\rho_s-\rho_w)g)/\rho_w}} = 0.053 \frac{d^{0.3}[(\tau-\tau_c)/\tau_c]^{1.5}}{D_{50}^{0.3}\left[((\rho_s-\rho_w)g)/(\rho_w v^2)\right]^{0.1}} \quad [3]$$

where $D_{50}$ is the mean size of sediment.
The influence of rough boundaries on the fluid dynamics is modeled through the inclusion of the wall law:

$$\frac{U}{U_*} = \frac{1}{K}\ln(30z/K_s) \quad [4]$$

where $k_s$ is equal to the roughness height, $K$ is the von Karmen constant, $U$ is the mean velocity, $U_*$ is the shear velocity, and $z$ is the height above the bed.

A structured grid mesh on the $x$–$y$–$z$ plane was generated. The 3D grid mesh had 273 elements in the $x$-direction, 120 elements in the $y$-direction, and 22 elements in the $z$-direction. An uneven distribution of grid lines in the horizontal and vertical directions was chosen to keep the total number of cells in an acceptable range and to obtain valuable results in the area. The following grid line distributions were chosen: In the $x$-direction, 3 cells with 0.25 m, 10 cells with 0.05 m, 25 cells with 0.02 m, 200 cells with 0.002 m, 19 cells with 0.02 m, 10 cells with 0.05 m, and 5 cells with 0.11 m. In the $y$-direction, 10 cells with 0.01 m, 100 cells with 0.002 m, and 9 cells with 0.01 m. In the $z$-direction, 10 cells with 1% height of the water depth, 4 cells with 5% height of the water depth, and 7 cells with 10% height of the water depth. The piles were generated by blocking their area.

## 4 RESULTS AND DISCUSSION

The effect of different arrangements of unsubmerged pile groups on scour was investigated experimentally and numerically. Figure 2 shows the relationship between the relative scour depth ($D_s/D_{50}$) and Froude number ($F_r = u/(gy_t)$^0.5, where $u$ is the mean flow velocity, $y_t$ is the tail water depth, and $g$ is the gravitational acceleration). All of the different arrangements of piles produced lower values of scour depth than the one-pile case. When using more than one pile, the impinging flow velocity at the upstream piles depresses for the downstream piles. The scoured bed material in front of the upstream piles deposits upstream of the downstream piles. Thus, reduction in the horse shoe vortex power, which is due to the upward pushing flow in front of the downstream piles, is obtained. The reduction in the horseshoe vortex power and velocity downstream of the bridge piles causes a reduction in the scour depth. The arrangement of tandem piles reduced the relative scour depth by 42% compared with the reference case (one-pile case). Reduction percentages of the local scour depth for other arrangements of pile groups are presented in Figure 3. Scour depth contours for one pile and tandem pile arrangements are plotted in Figure 4. The scour depth at the upstream of the one-pile case was higher than that of the back of the one-pile pile because of the mechanism of sediment transport at the upstream. The approaching flow scoured the bed sediment and transported it to the downstream. For the tandem arrangement of piles, the maximum scour depth was generated between piles. Part of the incoming horizontal velocity vectors was directed toward the inside zone between these piles. The overlap between the velocity vectors behind the first pile and the reverse velocities upstream of the second pile leads to the creation of the maximum scour depth midway between these pillars (Figure 8a). The scour depth contours for side-by-side arrangements are presented in Figure 5a. The maximum scour depth was generated upstream of these piles, at which velocity vectors concentrated in front of these piles (Figure 8b). Three scour holes were formed downstream of each pile for the 1 × 2 and 2 × 1 pile arrangements, as shown in Figs. 5b and 6a, respectively. Two scour holes with large scour depths were created behind the upstream piles compared with the small scour depth that was created behind the downstream pile for the case

 

of the 2 × 1 pile arrangement, at which a part of the velocity vectors upstream of the first two piles is transported downstream and shocked with the reverse velocities formed upstream of the last pile (Figure 8c). For the 1 × 2 pile arrangement, the deepest scour hole was created behind the upstream pile and two scour holes were created behind the downstream piles. For either the 2 × 1 or 1 × 2 pile arrangement, the horizontal velocity vectors explain the existence of scour holes downstream of the pillars of the bridge (Figs. 8c and 8d). Scour holes were formed between the supported piles for the case of the 2 × 2 pile arrangement (Figure 6b). The 1 × 4 and 4 × 1 pile arrangements produce large values of local scour depth inside the area of the surrounding piles (Figure 7). The distribution of the horizontal velocity vectors around the pillars of the bridge for different pile arrangements (i.e., 2 × 2, 1 × 4, and 4 × 1) are presented in Figure 9. Figure 9 also shows the accumulation and concentration of the velocity vectors toward the mid-area surrounding the pile arrangements. The simulated values of scour depth using the computational fluid dynamics (CFD) model of SSIIM versus the measured data are presented in Figure 10. Moreover, the bed surface profiles of the experimental and simulated models are similar for different bridge pile arrangements (Figure 11). Notably, the simulation model expressed the experimental models well, with the correlation coefficient of 0.91. Finally, more studies are needed to clarify the effect of varying the distances between piles on the scour hole characteristics.

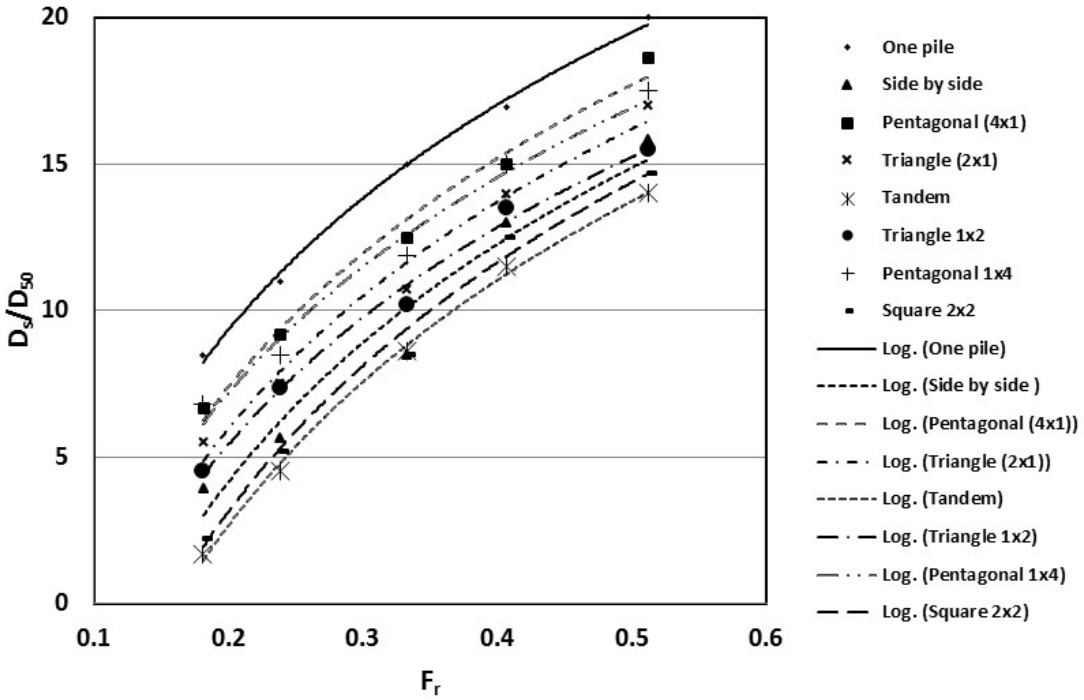


**Figure 2.** Relative scour depth ($D_s/D_{50}$) versus Froude number ($F_r$) for different arrangements of pile groups.

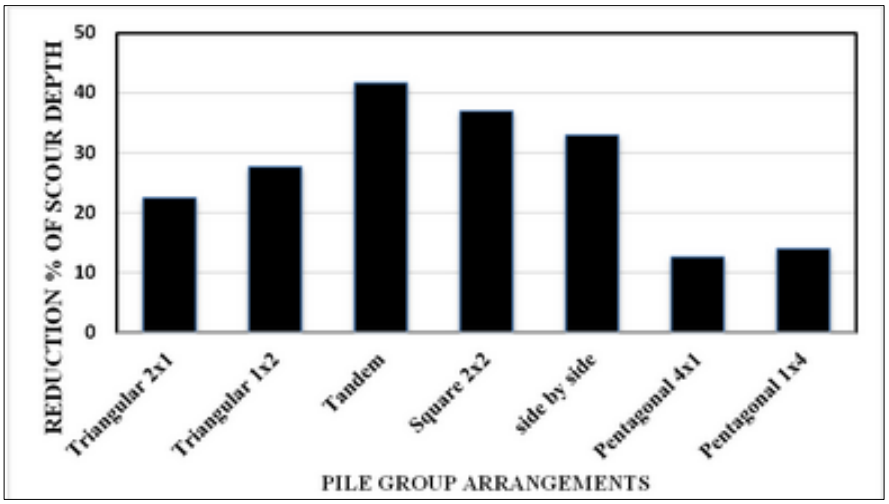


**Figure 3.** Reduction percentage of scour for different arrangements of pile groups.

 

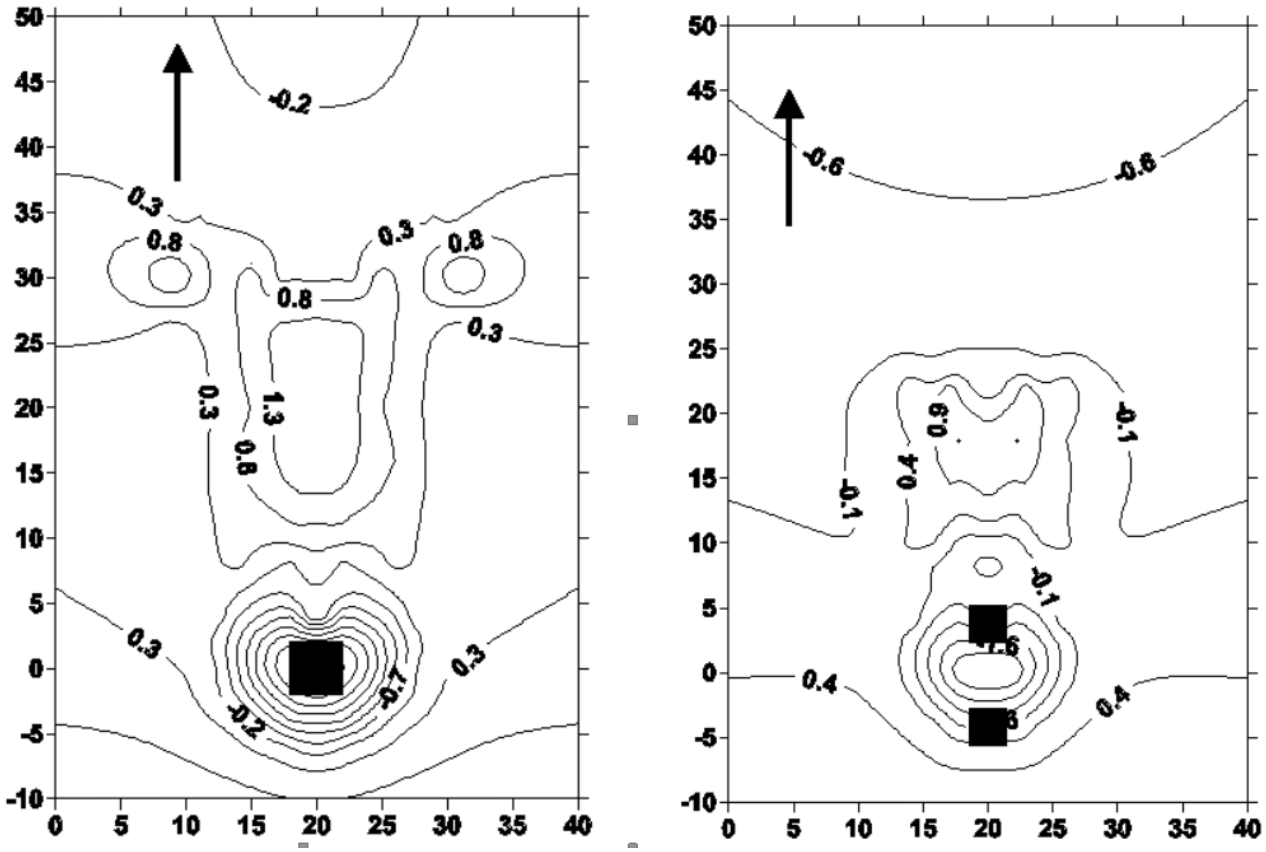

**Figure 4.** Scour contour maps of bed morphology for one pile and tandem pile arrangements at $F_r$=0.52.

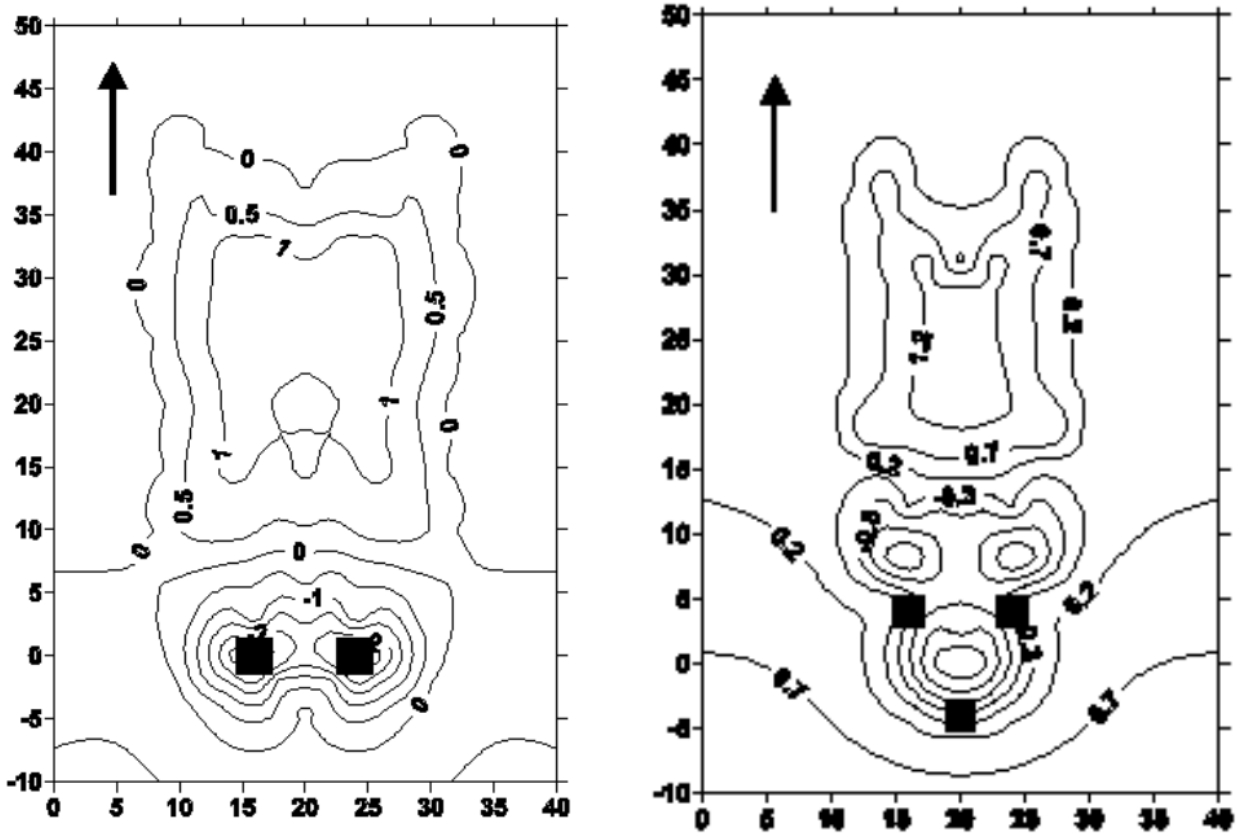

**Figure 5.** Scour contour maps of bed morphology for side-by-side and 1 × 2 triangular pile arrangements at $F_r$=0.52.

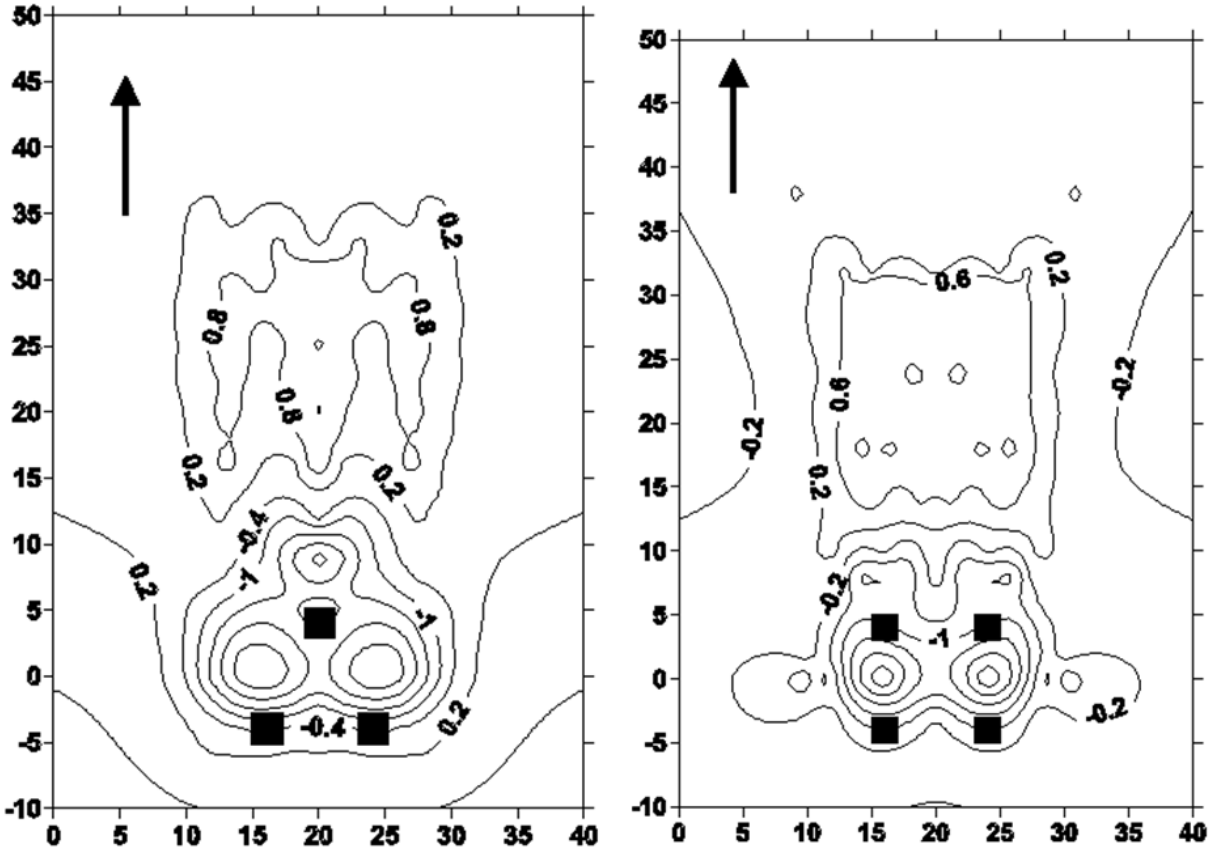


**Figure 6.** Scour contour maps of bed morphology for 2 × 1 and 2 × 2 pile arrangements $F_r$=0.52.

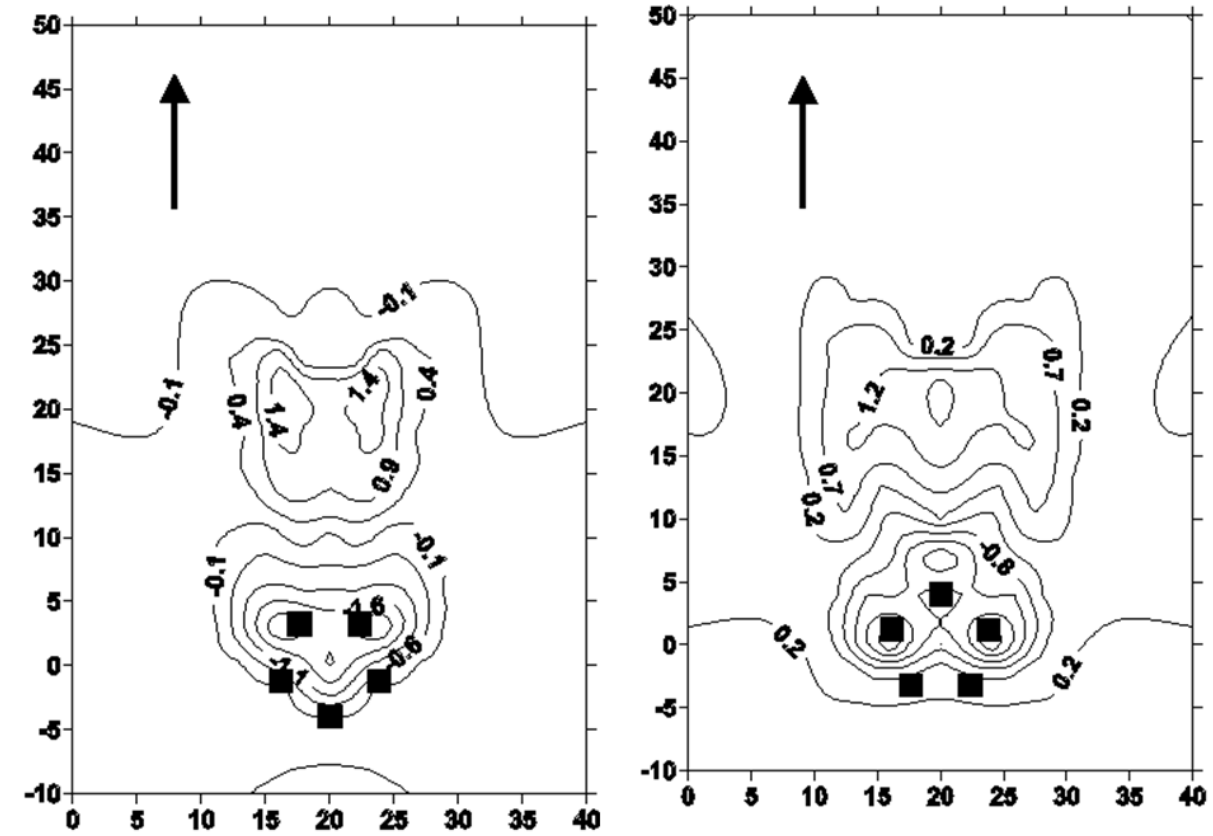


**Figure 7.** Scour contour maps of bed morphology for 1 × 4 and 4 × 1 pentagonal pile arrangements at $F_r$=0.52.

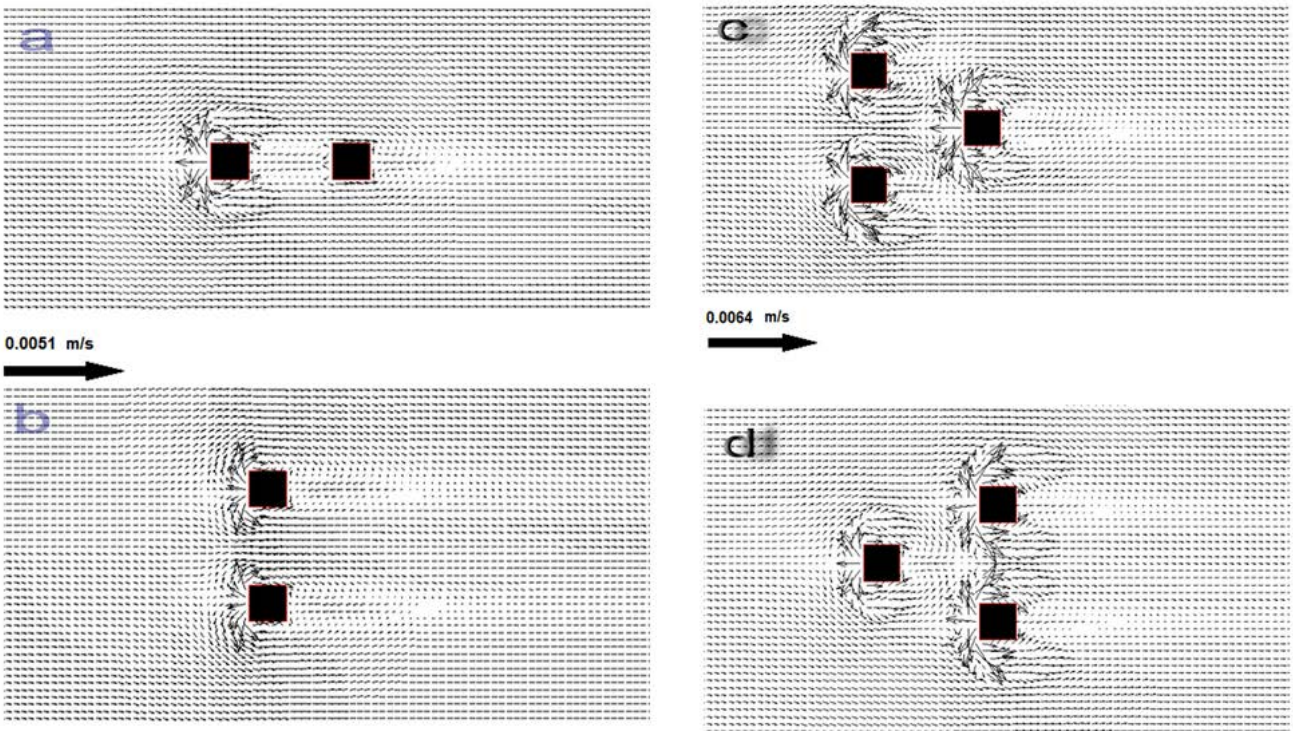


**Figure 8.** Horizontal velocity vectors over mobile bed by $0.01y_t$ for two and three pile arrangements.

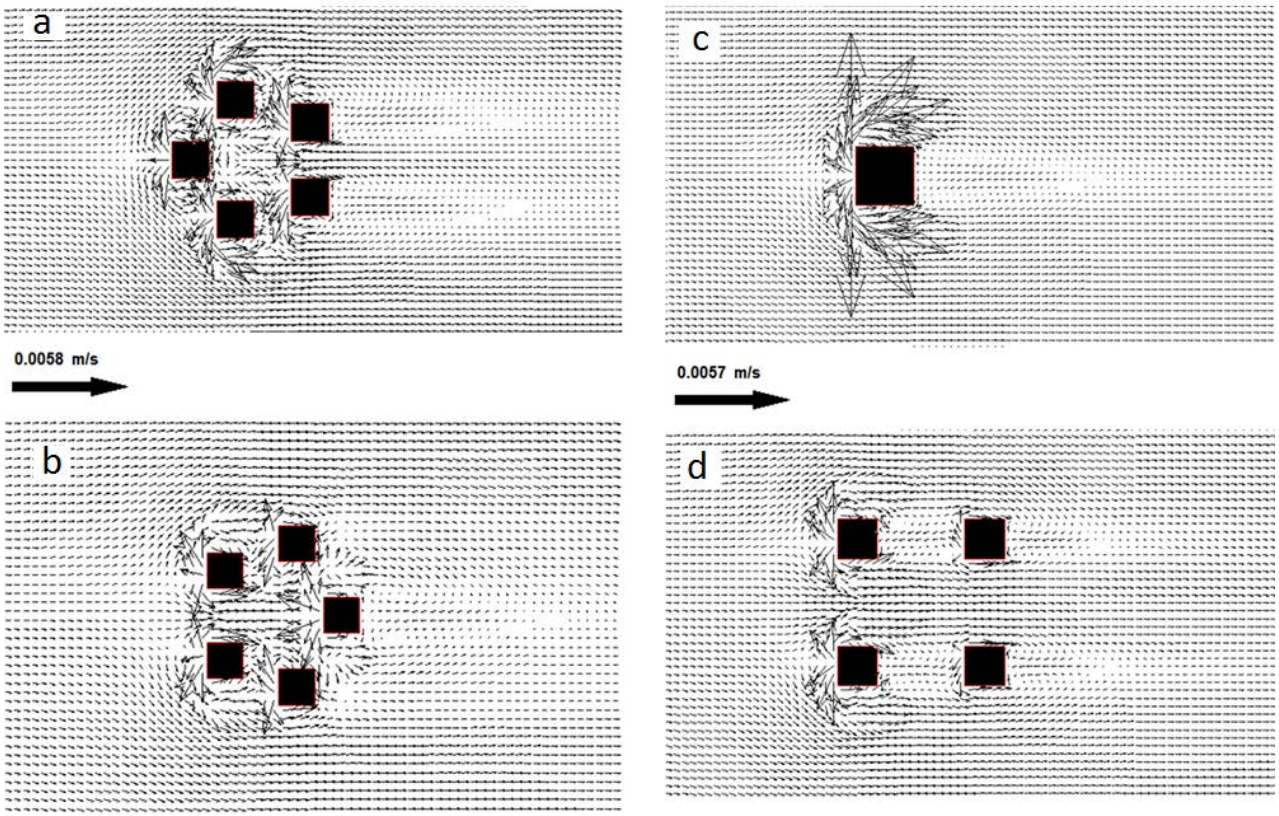


**Figure 9.** Horizontal velocity vectors over mobile bed by $0.01y_t$ for one, four, and five pile arrangements.

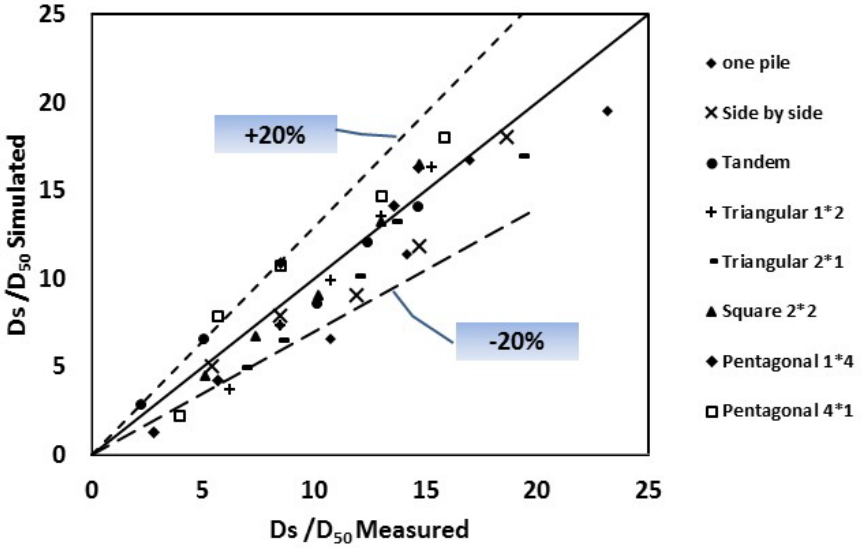


**Figure 10.** Simulated versus measured data for relative scour depth and different configurations of pile groups.

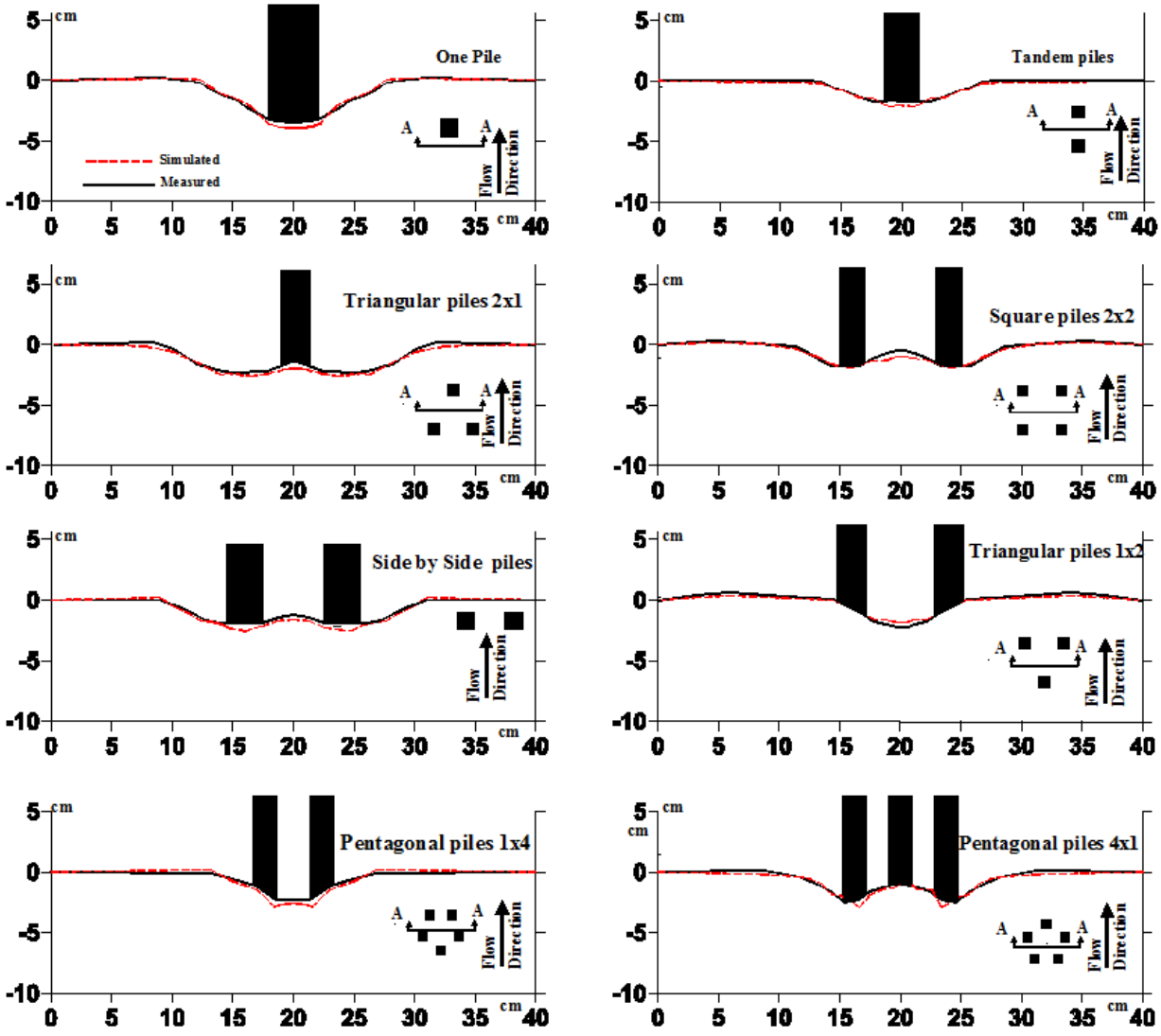


**Figure 11.** Simulated and measured bed level for different cases of pile group arrangements at $F_r$=0.52.

## 5 CONCLUSIONS

In the present study, experimental and numerical investigations on different pile arrangements are conducted to simulate scour around these supports. 3-D CFD models, which are based on the finite volume method used to solve the Navier–Stokes equations, are created using the SSIIM program. From the results of this investigation, the following conclusions can be drawn:

1. For all cases of pile arrangements, the local scour depth increases as the Froude number increases.
2. The pile arrangements control the location and size of the scour holes.
3. The local scour depth decreases by 42%, 33%, 28%, 23%, 14%, and 12% for tandem, square (2 × 2), side-by-side, triangular (1 × 2), triangular (2 × 1), pentagonal (1 × 4), and pentagonal (4 × 1) pile arrangements, respectively, compared to the one-pile case.
4. The results of the numerical models obtained using the SSIIM program are observed to be consistent with the measured data for different experimental models.

## ACKNOWLEDGMENTS

The authors wish to acknowledge the financial support from the Deanship of Scientific Research, Jazan University through research project 0013/7/37.

## REFERENCES

Abdel-Aal, G.M. & Mohamed, A. (2010). The Effect of Collar Size and Shape on Scour Depth around Bridge Piers. *Scientific Bulletin, Faculty of Engineering, Ain Shames University*, Faculty of Engineering, Cairo, Egypt.

Amini, A., Melville, B.W., Ali, T.M. & Ghazali, A.H. (2012). Clear-Water Local Scour around Pile Groups in Shallow-Water Flow. *Journal of Hydraulics Engineering,* 138(2), 177-185.

Ataie-Ashtiani, B. & Beheshti, A. (2006). Experimental Investigation of Clear-Water Local Scour at Pile Groups. J*ournal of Hydraulics Engineering,* 132(10), 1100–1104.

Bayran, A. & Larson, M. (2000). Analysis of Scour around a Group of Vertical Piles in the Field. *Journal of Waterway, Port, Coastal*, *Ocean Engineering,* 126, 215-220.

Dargahi, B. (1990). Controlling Mechanism of Local Scouring. *Journal of Hydraulics Engineering,* ASCE, 116(10), 1197-1214.

Dey, S., Bose, S.K. & Sastry, G.N. (1995). Clear-Water Scour at Circular Piers: A Model. *Journal of Hydraulics Engineering,* 121(12), 869–876.

Liang, F. Wang, C., Huang M. & Yu, W. (2016). Experimental Observations and Evaluations of Formulae for Local Scour at Pile Groups in Steady Currents. *Marine Georesources and Geotechnology*, 35(2), 245-255.

Hannah, C.R. (1978). *Scour at Pile Groups,* Research Report No. 28-3, Civil Engineering Department, University of Canterbury, Christchurch, New Zealand.

Hjorth, P. (1975). *Studies on the Nature of Local Scour,* Department of *Water Resources Engineering, Lund Institute of Technology*, Bulletin Series A, No. 46.

Melville, B.W. & Sutherland, A.J. (1988). Design Method for Local Scour at Bridge Piers. *Journal of Hydraulics Engineering,* 114(10), 1210–1226.

Melville, B.W. & Coleman, S.E. (2000). *Bridge Scour.* Colorado: Water Resources Publications, 6-31.

Mia, Md., F. & Nago, H. (2003). Design Method of Time-Dependent Local Scour at a Circular Bridge Pier. *Journal of Hydraulics Engineering,* 129(6), 420-427.

Mohamed, Y.A., Nasr-Allah, T.H., Abdel-Aal, G.M. & Awad, A.S. (2015). Investigating the Effect of Curved Shape of Bridge Abutment Provided with Collar on Local scour, Experimentally and Numerically. *Ain Shams Engineering Journal,* 6 (2), 403-411.

Mohamed, Y.A., Abdel-Aal, G.M., Nasr-Allah, T.H.& Awad, A.S. (2016). Experimental and Theoretical Investigations of Scour at Bridge Abutment. *Journal of King Saud University - Engineering Sciences*, 28(1), 32–40

Mohamed, Y.A., Saleh, Y.K. & Ali, A.M. (2015). Experimental Investigation of Local Scour around Multi-vents Bridge Piers. *Alexandria Engineering Journal*, 54(2), 197–203

Morales, R. & Ettema, R. (2011). Insights from Depth-Averaged Numerical Simulation of Flow at Bridge Abutments in Compound Channels. Department of Civil and Architectural Engineering, University of Wyoming Laramie, WY 82071, 701, 231-7708.

Nasr-Allah, T.H., Mohamed, Y.A, Abdel-Aal, G.M. & Awad, A.S. (2016). Experimental and Numerical Simulation of Scour at Bridge Abutment Provided with Different Arrangements of Collars. *Alexandria Engineering Journal,* 55(2), 1455-1463.

Nouh, M. (1986). Local Scour at Pile Groups in Meandering Channels. *IAHR, Symposium on Scale Effects in Modelling Sediment Transport Phenomena,* Toronto, Canada, 164-179.

Olsen, N.R. (2007). *A Three Dimensional Numerical Model for Simulation of Sediment Movements in Water Intakes with Multiblock Option,* User's manual [Online], Available: http://www.ntnu.no.

Parker, G.W., Bratton, L. & Armstrong, D.S. (1997). *Stream Stability and Scour Assessments at Bridges in*

 

*Massachusetts. U.S,* Geological Survey Open File Report No. 97-588 (CD-ROM), Massachusetts Highway Dept. Bridge Section, Marlborough, Massachusetts, Report, 53.

Rashed-Hosseini & Amini, A. (2015). Scour Depth Estimation Methods around Pile Groups. *KSCE*, *Journal of Civil Engineering,* 19(7), 2144-2156.

Salim, M. & Jones, J.S. (1996). Scour around Exposed Pile Foundations. Compilation of Conference Scour Papers (1991–1998), ASCE, Reston, VA.

Sumer, B.M., Bundgaard, K. & Fredsøe, J. (2005). Global and Local Scour at Pile Groups. *Proceedings of the Fifteenth International Offshore and Polar Engineering Conference*, Seoul, Korea, 577-583.

Van Rijn, L.C. (1987). Mathematical Modeling of Morphological Processes in The Case Of Suspended Sediment Transport, *Ph.D. Thesis.* Delft University.

Yanmaz, A. M. & Altinbilek, H.D. (1991). Study of Time-Dependent Local Scour around Bridge Piers. *Journal of Hydraulics Engineering,* 117(10), 1247–1268.

Zhao, G. & Sheppard, D.M. (1998). The Effect of Flow Skew Angle on Sediment Scour near Pile Groups. Stream Stability and Scour at Highway Bridges. *Compendium of papers ASCE Water Resource Engineering conferences,* 1991-1998, Reston, Virginia, 377-391.

Zounemat-Kermani, M., Beheshti, A., Ataie-Ashtiani, B. & Sabbagh-Yazdi, S. (2009). Estimation of Current-Induced Scour Depth around Pile Groups Using Neural Network and Adaptive Neuro-Fuzzy Inference System. *Applied Soft Computing*, 9(2), 746-755.

 

Proceedings of the 37th IAHR World Congress
August 13 – 18, 2017, Kuala Lumpur, Malaysia

# REAL-TIME MONITORING OF THE SCOURING DEPTH LOCATED INSIDE A GRAVEL-BED RIVER

MARKO SHAOHUA HSU [(1)], YU-HUAN CHANG [(2)], CHONG-YU SUN [(3)] & PI-FANG HUNG [(4)]

[(1,2,3)]Dept. of Water Resource Engineering and Conservation, Fung Chia University, Taichung 402, Taiwan
shhsu@fcu.edu.tw
[(4)]Associate Professor, Department of Finance, Overseas Chinese University, Taiwan

## ABSTRACT

Under the influence of climate change, the intensity and frequency of rainfall events are increasing significantly. During typhoon seasons, warning announcement of the safety of a bridge cannot rely on numerical simulation in advance; the authority counts on the real-time monitoring of bridge scouring to making decision for bridge closure. In recent years, in order to secure the safety of a bridge across the river, the units in-charge will usually arrange energy-dissipating blocks around bridge piers or structures to form a simple groundsill protection. The characteristics of aggradation and degradation of Taiwan rivers are, however, more dramatic than continental rivers with mild slopes. These features increase the local scouring behind the protection works and cause structures damage starting from exposure of their foundations. Because the protection works fail, it will lead to the breakage of river dikes, bridge piers, and embankments, hence endangering people's lives and properties. Real-time monitoring on a river-bed fluctuation during a flood event is still difficult. One approach is by scour blocks, which can only obtain the maximum scour depth after the events; but in reality, the scour depth varies real-time with the discharge hydrograph still not available. In this study, a real-time monitoring has been conducted successfully during year 2015 to 2016, by employing the wireless tracer with scour blocks, and collecting the scouring data of gravel bed river during flood events. By real-time transfer of the data, we can monitor the progress of scouring hole with flow hydrograph behind the protection works. Furthermore, by receiving the signal in real-time can help the authorities in making decision on bridge closure more accurately.

**Keywords:** Gravel-bed river; scouring processes; field monitoring; wireless tracer; scour block pile.

## 1 INTRODUCTION

Taiwan is an island with precipitous mountains and steep slopes. Located at the junction of the Eurasian Plate and the Philippine Sea Plate, it also features constant earthquake activity. The mountain ranges are mostly composed of sedimentary and metamorphic rocks, which entail fragile geological formations that can easily be fractured and weathered. Taiwan was originally characterized by a clear distinction between dry and rainy seasons, but in recent years, the trend of rainfall concentration has become increasingly noticeable because of climate change. According to the Taipei Weather Station's records for the past 103 years, the overall average annual rainfall has increased by 268 mm, but with 28 fewer annual days of rainfall. Multiple extreme rainfall events, such as the typhoons Nari, Mindulle, Haitang, Sinlaku, and Morakot, have exceeded the upper limit of previous flood-control designs.

The concentrated high-intensity rainfall during typhoons and floods can cause drastic scouring–depositing fluctuations in rivers, severely damaging the stability of hydraulic structures such as bridge piers, embankments, grade-control structures, and dykes. In addition, scouring prevention and control in numerous bridges crossing major rivers in western Taiwan depends heavily on downstream grade-control structures. Therefore, identifying the characteristics and processes of river scouring behind the grade-control structures facilitates applying disaster prevention technologies to improve engineering protection proposes. Moreover, accurate observational data aid authorities in quickly determining when to close bridges and effective evacuation behind embankments to protect civilian lives and property.

In Taiwan, the high-intensity rainfall during typhoons and floods causes considerable scouring–depositing fluctuations in riverbed cross sections, bringing substantial sediment that can hinder observation. In addition, the conventional manual observation method is time-consuming, strenuous, and dangerous, and the accuracy of the results remains to be improved. Scouring and depositing in riverbed cross sections is closely associated with the stability of nearby structures, which must be maintained to ensure civilian lives and property. This study evaluates the safety of currently implemented designs of grade-control structures by comparing the results of a laboratory investigation on these structures and real-time on-site scouring processes during a rainfall event. In addition, wireless tracking devices and scouring bricks are adopted to measure the dynamic changes in the scour holes downstream from grade-control structures in an attempt to obtain a temporal relationship between the dynamic records of the flooding and scouring processes.

 

Grade-control structures are a responsive measure taken to prevent local erosion in a river course. Through stabilizing the thalweg of a river, lowering the steepness of the river course, and regulating the speed of water flow, grade-control structures can stabilize the riverbed at specific locations. However, severe scouring of the riverbed surface is often observed downstream from the grade-control structures, threatening the stability of the riverbed and nearby structures. Research has shown that riverbed gradient and tailwater depth are the main development factors of scour holes. Early grade-control structures in Taiwan were built mainly with a reference to the design manuals of the United States Bureau of Reclamation or Japanese sources. However, the experimental conditions of those countries are different from those of Taiwan. Specifically, because the tested inflow conditions were mostly steady flows, the results cannot be easily applied to estimating the scouring depth of immediate on-site discharge.

Numerous laboratory studies have been conducted on the scouring downstream from the grade-control structures; nevertheless, data on the actual on-site scouring process remain lacking. This study aims to obtain such data. Observations are made with a combination of scouring bricks and wireless tracking devices and these are compared with laboratory investigation results of the scouring process. The obtained scouring processes at scour holes downstream from the grade-control structures can be used to improve disaster-prevention technologies and applications to protect civilian lives and property.

## 2 FACTORS INFLUENCING THE SCOURING DOWNSTREAM OF GRADE-CONTROL STRUCTURES

### 2.1 Factors influencing the scouring downstream of grade-control structures

The hydraulic characteristics affecting the scour holes downstream from grade-control structures include maximum scouring depth, scour hole length, and scour hole shape. Chen, Guo, and Chung (1993) conducted a hydraulic model experiment on a large pebble channel bed, proposing that the dimensionless maximal scouring depth D_max/H is related to the number of free overfalls and particle diameter d_s/H. Mason and Arumugam (1985) adopted a hydraulic model to reveal through experimentation that the maximal scouring depth in scour holes y_(s,me) is related to specific discharge q, embankment height H, gravitational acceleration g, and the median grain diameter of sediment D_50. Yu (1991) analyzed the scours upstream and downstream of a detention dam under a sediment-laden flow and determined the maximal scouring depth of the scour holes downstream from the dam. Chen (2000) performed a scour test in a steadily flowing channel at various inclinations to investigate the effect of riverbed girdle arrangement on free overfall, finding that the relationships among maximum scouring depth y_(s, me), the number of free overfalls N_d, the slope So, the length of the riverbed girdle structures L, and the impacting position of the flow L_P can be expressed in functions. Su and Lian (1993) adopted the free jet theory to investigate the depth of local scours in a riverbed downstream from a sand-trap dam affected by crest overflows, finding that the depth was influenced by relative velocity and the Froude number of scour.

Bed characteristics, flow characteristics, and the specific value between scouring time (t) and the time needed for a scouring process to reach balance (te) are the factors influencing scour downstream from grade-control structures.

a. Bed characteristics

The factors influencing bed characteristics included the median grain diameter ($\mathrm{D}_{50}$), geometric standard deviation ($\sigma_g$), and density ($\rho_s$) of the bed material. The Shields threshold curve (1936) shows that when temperature and particle density do not vary considerably, the threshold shear velocity ($u_{*_c}$) can be estimated from $\mathrm{D}_{50}$. Melville-Coleman (2000) performed another regression calculation on threshold experiment data to obtain

$$u_{*_c} = 0.0115 + 0.125\mathrm{D}_{50}{}^{1.4},\ 0.1\text{mm} < \mathrm{D}_{50} < 1\text{mm}$$

$$u_{*_c} = 0.0305\mathrm{D}_{50}{}^{0.5} - 0.0065\mathrm{D}_{50}{}^{-1},\ 1\text{mm} < \mathrm{D}_{50} < 100\text{mm}$$

The threshold velocity of bed material can be obtained from a known value of water depth (y)

$$\frac{V_n}{u_{*_c}} = 5.75\log\left(5.53\frac{y}{\mathrm{D}_{50}}\right)$$

where $\mathrm{V_c}$= the threshold velocity of bed material (m/s), and $u_{*_c}$= corresponding threshold shear velocity (m/s).

b. Flow characteristics

The flow characteristics consist of average velocity (V), water depth (y), water density (ρ), tailwater depth ($H_d$), gravitational acceleration (g), and the Froude number of specific gravity ($F_d$). Farhoudi-Smith (1985) and Oliveto et al. (2008) have indicated in laboratory investigations of spillway scour that tailwater depth affects both the position where hydraulic jumps occur and the maximal scouring depth downstream from structures.

 

Pagliara (2007) found in a test on the scour holes downstream from rock ramps that the maximal average scouring depth is related to the Froude number of specific gravity of the ramps $F_d = U_1/\sqrt{[(\rho_S - \rho)/\rho]gD_{50}}$ and the ramps' gradients. Based on the known data on scouring depth and existing research, dimensionless scouring depth is found to be proportional to the Froude number of specific gravity.

c. Time ratio between the scouring time (t) and the time needed for a scouring process to reach balance (te).

This specific value reflects local scouring percentage in grade-control structures. In clear water flow, the depth of local scour increases slowly over time, whereas in sediment-laden flow, the scour reaches balance and is maintained at a fixed depth much faster.

d. Formulas of scouring downstream from grade-control structures

Table 1 presents the empirical formulas commonly applied to estimate local scours downstream from free overfall structures in pebble and gravel-bed rivers in Taiwan and other countries, as well as research results on the length arrangement of protection works. The depth and size of scour holes are related to the energy difference before and after free overflow and jet, as well as to the size of the riverbed where the grade-control structures are located.

**Table 1.** Empirical formulas commonly applied to estimate local scours downstream from free overfall structures in pebble- and gravel-bed rivers and research results on length arrangement of protection works.

| Scour behind grade-control structures | | |
|---|---|---|
| Water Resources Planning Institute, Water Resources Agency, Ministry of Economic Affairs, Taiwan (WRPI) (2005) | 1. Position of the maximum scour hole occurrence<br>$\frac{X_s}{H_W}=14.255\left(\frac{gH_W^3}{q^2}\right)^{0.049}\left(\frac{H_W}{D_{50}}\right)^{0.005}\left(\frac{H_d}{H_W}\right)^{0.583}$<br>2. Maximum scour hole depth<br>$\frac{y_{s,me}}{H_W}=0.271\left(\frac{q^2}{gH_W^3}\right)^{1.014}\left(\frac{H_W}{D_{50}}\right)^{0.528}\left(\frac{H_d}{H_W}\right)^{2.08}$ | $X_s$= distance between the maximum scouring depth and grade-control structures<br>$H_w$= upstream–downstream water level difference<br>q = specific discharge<br>$D_{50}$= median grain diameter of riverbed material<br>$H_d$ = water depth downstream |
| Pagliara (2007) | $\frac{Z_m}{h_1}=0.58\sigma_g^{-.055}i^{-0.5}(F_d^{1.8})$<br>$\frac{y_{s,me}}{Z_m}=1+1.75F_d^{-1.75}$<br>$\frac{l_s}{h_1}=3.75\sigma_g^{0.8}i^{-0.5}\left(\frac{Z_m}{h_1}\right)^{0.8}$<br>$\Delta E_r=\frac{\Delta E}{E_0}=A+(1-A)\exp[(B_1+C*i)\frac{y_c}{D_P}]$ | $Z_m$= average scouring level of the cross sections<br>$h_1$= water depth at the foot of the rubble slope<br>$\sigma_g$ = standard deviation of sediment particle diameter<br>i = gradient of the rubble slope<br>$F_d=\frac{V_d}{\sqrt{\left[\frac{\rho_S-\rho}{\rho}\right]gD_{50}}}$= Froude number of specific gravity<br>$V_d=\frac{q}{h_1}$<br>$D_{50}$ = median sediment grain diameter<br>H = height of the rubble slop |

## 3 SITE DESCRIPTIONS

### 3.1 Overview of the catchment area and river section

The riverbed downstream from the Shigang Dam in Dajia River, Taiwan has undergone significant changes in scouring and depositing due to typhoons and floods over the years. Furthermore, climate change in recent years has brought extreme rainfall, and the propagation of floods can easily lead to scour. This study focused on observing the riverbed downstream from the highway bridge of the Dajia River, Provincial Highway 1. Simple grade-control structures comprising clipping blocks were installed under the bridge. This bridge is a main traffic route connecting the Qingshui and Dajia Districts of Taichung City.

The major weir built upstream of the observed river section is the Shigang Dam (Dajia River Cross-section 36, which is 23.356 km from the river mouth). Several bridges in this section were equipped with automatic radar water-level meters, which are the Dajia River Bridge on Provincial Highway No. 1 (by the third River Management Office), the Dajia River Bridge on National Highway No. 3, the High Speed Railway Bridge, the Dajia River Bridge on National Highway No. 1, and the Houfeng Bridge on Provincial Highway No. 13.

 

Records of flood peak runoffs in the river basin are key references for river course management planning and on-site observations.

Shigang Dam began regulating the river flow since 1977. Table 2 presents the records of the maximum flood peak runoffs at the Shigang Dam during typhoons and floods over the years (including records before the operation by the Shigang Dam). Table 3 shows the flow at the flood peaks at recurrence intervals at various control points and includes corresponding specific discharges.

Dajia River Bridge on Provincial Highway No. 1 (Fig. 1) is approximately 18 km away from the Shigang Dam. When the surface velocity of peak typhoon-induced floods us = 6 m/s, the peak flood discharge at the Shigang Dam was approximately 1 hour earlier than that at the Dajia River Bridge on Provincial Highway No. 1, which was identified by the automatic radar water-level meter installed at the Dajia River Bridge on Provincial Highway No. 1. The measuring station where the observation was conducted in this study was located in a gravel-bed river section with steep slopes (S0 = 1/90).

No major tributary flows into the Dajia River downstream from Shigang Dam. Therefore, the discharge data of Shigang Dam were adopted and assumed as the flow data for all cross-sections of the typhoon-induced flood at the study site for observation of dynamic scouring. Fig. 2 shows a satellite photo of the investigated river section.

**Table 2.** Flood peak discharge records of the Shigang dam on Dajia River.

| Year | Maximal flow at flood peak(m3/s) (m3/s) | Year | Maximal flow at flood peak(m3/s) (m3/s) | Year | Maximal flow at flood peak(m3/s) (m3/s) |
|---|---|---|---|---|---|
| 1963 | 7,840 | 1980 | 3,119 | 1997 | 2,106 |
| 1964 | 358 | 1981 | 3,149 | 1998 | 933 |
| 1965 | 1,570 | 1982 | 1,527 | 1999 | 484 |
| 1966 | 2,990 | 1983 | 3,361 | 2000 | 790 |
| 1967 | 1,440 | 1984 | 896 | 2001 | 3,954 |
| 1968 | 1,110 | 1985 | 2,411 | 2002 | 709 |
| 1969 | 2,710 | 1986 | 983 | 2003 | 594 |
| 1970 | 3,940 | 1987 | 978 | 2004 | 6,195 |
| 1971 | 2,030 | 1988 | 315 | 2005 | 3,541 |
| 1972 | 4,540 | 1989 | 3,062 | 2006 | 1,227 |
| 1973 | 1,120 | 1990 | 2,788 | 2007 | 2,589 |
| 1974 | 2,040 | 1991 | 835 | 2008 | 4,225 |
| 1975 | 927 | 1992 | 1,419 | 2009 | 5,410 |
| 1976 | 2,940 | 1993 | 1,542 | 2010 | 720 |
| 1977 | 2,290 | 1994 | 4,140 | *2011 | 184 |
| 1978 | 635 | 1995 | 663 | *2012 | 4,077 |
| 1979 | 1,647 | 1996 | 3,668 | *2013 | 6,692 |

Sources: WRPI (2008–2011), * Shigang Dam Control Center

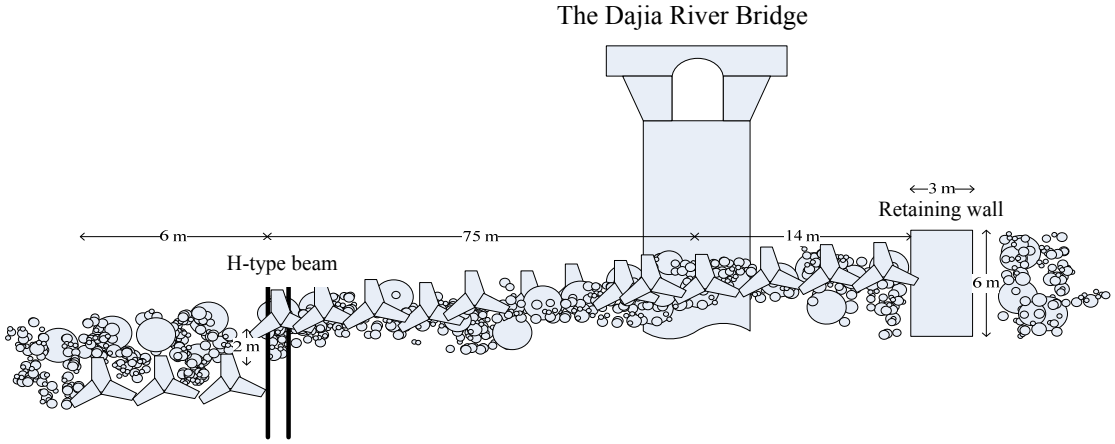


**Figure 1.** Illustration of the grade-control structures in the submerged weir under the Dajia River Bridge on Provincial Highway No. 1.

 

**Table 3.** Peak flood flow at various recurrence intervals of the Dajia River Basin.

| Recurrence interval (year) | Control point: river mouth 1244.1 km2 | Shigang Dam 1095.4 km2 | Tianleng 955.5 km2 | confluence of Hengliou River 907.4 km2 | confluence of Dongmou River 877.6 km2 | confluence of Lileng River 848.4 km2 | confluence of Shiwen River 784.8 km2 |
|---|---|---|---|---|---|---|---|
| 200 | 11,500 (9.24) | 9,800 (8.95) | 8,840 (9.25) | 8,490 (9.36) | 7,850 (8.95) | 7,590 (8.95) | 7,560 (9.63) |
| 100 | 10,300 (8.28) | 8,800 (8.03) | 8,000 (8.37) | 7,630 (8.41) | 7,050 (8.03) | 6,820 (8.03) | 6,790 (8.65) |
| 50 | 8,900 (7.15) | 7,600 (6.94) | 6,900 (7.22) | 6,590 (7.26) | 6,090 (6.94) | 5,890 (6.94) | 5,870 (7.48) |
| 25 | 7,570 (6.08) | 6,430 (5.87) | 5,820 (6.09) | 5,570 (6.14) | 5,160 (5.88) | 4,980 (5.87) | 4,960 (6.32) |
| 20 | 7,300 (5.87) | 6,200 (5.66) | 5,600 (5.86) | 5,370 (5.92) | 4,970 (5.66) | 4,800 (5.66) | 4,780 (6.09) |
| 10 | 5,900 (4.74) | 5,000 (4.56) | 4,500 (4.71) | 4,330 (4.77) | 4,010 (4.56) | 3,870 (4.56) | 3,850 (4.91) |
| 5 | 4,500 (3.62) | 3,800 (3.47) | 3,400 (3.56) | 3,290 (3.63) | 3,040 (3.47) | 2,940 (3.47) | 2,930 (3.73) |
| 2 | 2,600 (2.09) | 2,200 (2.01) | 1,980 (2.07) | 1,910 (2.10) | 1,760 (2.01) | 1,710 (2.01) | 1,700 (2.17) |

Note: the unit is $m^3/s$; values within parentheses are corresponding specific discharge ($m^3/s/km^2$).
Source: Report on the Results of Comprehensive Management and Planning of the Dajia River Basin, WRPI, 2005.

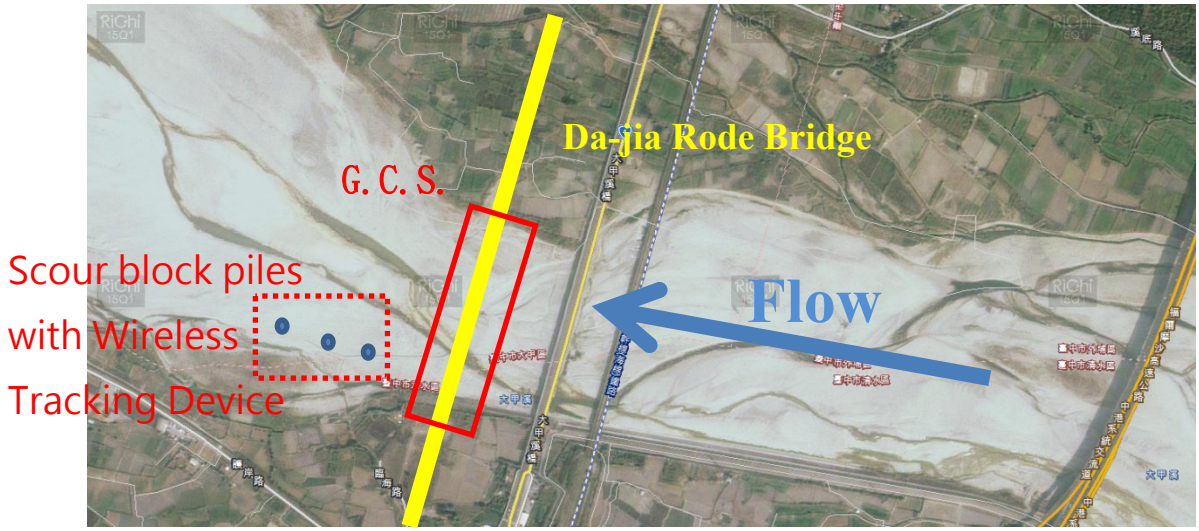


**Figure 2.** Satellite view of the investigated river section.

3.2 Riverbed material

Sampling on riverbed material was conducted upstream of the study site where the scouring brick columns were buried. Fig. 3 presents the results of sieve analysis. The median grain diameter (D50) is 63 mm, and the grain diameter corresponding to 90% of the cumulative percentage of sieved weight (D90) is 375 mm. Fig. 4 presents the grain diameter composition of the riverbed material collected at the River Cross-section 7.01 of the Dajia River Bridge on Provincial Highway No. 1, indicating a median grain diameter (D50) of 96 mm.

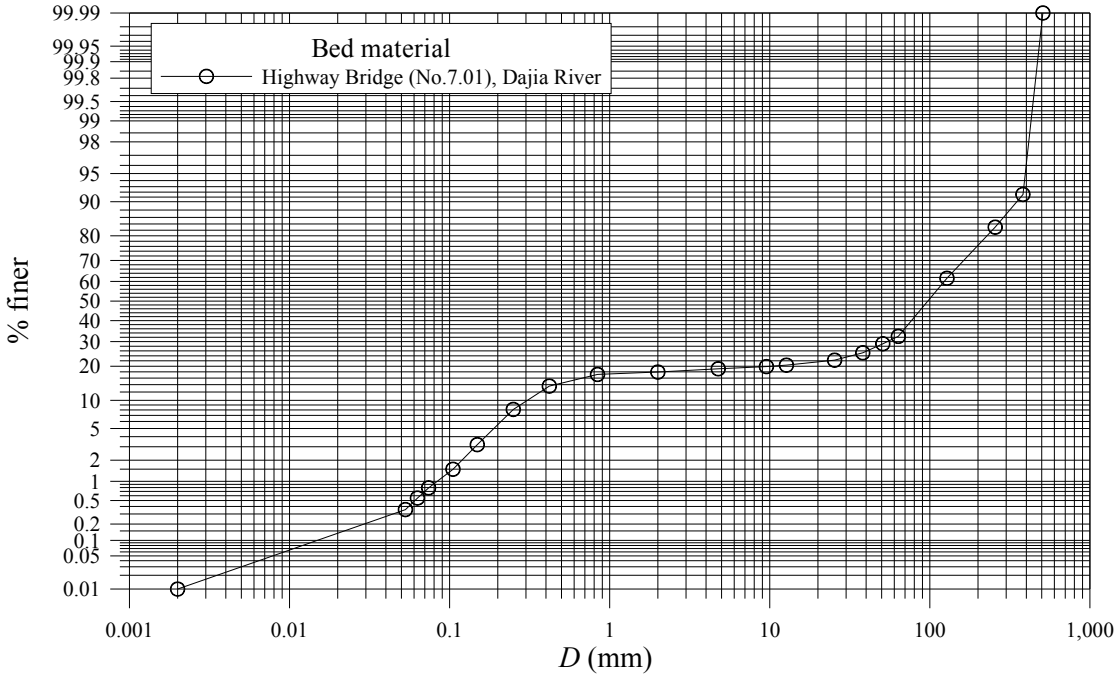


**Figure 3.** Distribution curve of riverbed material grain diameter.
(The sample was collected in the river channel upstream of Dajia River Cross-section 7.01 of the Dajia River Bridge on Provincial Highway No. 1)(Sampled, sieved, and analyzed on September 3, 2008).

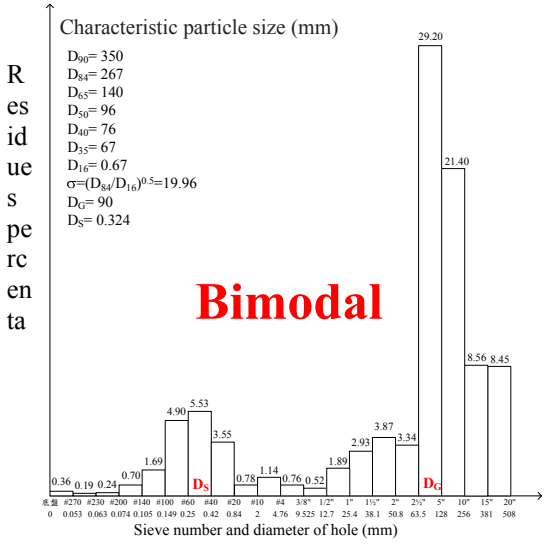


**Figure 4.** Composition of riverbed material grain diameter.
(The sample was collected in the river channel upstream of Dajia River Cross-section 7.01 of the Dajia River Bridge on Provincial Highway No. 1)(Sampled, sieved, and analyzed on September 3, 2008)

## 4 METHODOLOGY

Yang and Su (2015) successfully adopted wireless tracking devices to observe the maximum general scour caused by Typhoon Soulik in the central section of the Zhuoshui River. Similarly, the present study employed conventional scouring brick columns combined with newly modified wireless tracking devices, buried under the investigated river section during a dry season using proper machinery.

### 4.1 Observation equipment

Scouring brick columns are a relatively affordable and easily installed on-site observation method. All bricks were coded in advance and buried under the riverbed under a dry-bed condition. Subsequently, accurate location was determined using a total station theodolite. After the flood retreats, the riverbed was excavated. By examining the number of bricks washed away by the flood, the maximum scouring depth of the riverbed can be determined. A scouring brick is approximately 5.5 cm high, 10 cm wide and 20 cm long.

 

In this study, wireless tracking devices (Fig. 5) were added between the scouring brick columns. The devices send signals using a long-distance wireless transceiver. When the riverbed scouring reaches the depth of the device, the device floats to the surface or moves, turning on the transceiver to send signals. The scouring depth at that moment can then be determined.


(a) Long-distance wireless transceiver (RD232-H); (b) wireless tracking device

**Figure 5.** Dynamic scouring observation technologies.

4.2 Deploying the Observation Equipment

The scouring brick columns and wireless tracking devices were buried downstream from the Dajia River Highway Bridge, mainly at 40 m, 80 m, and 100 m behind the grade-control structure of the weir (Fig. 6). The bricks and devices were buried approximately 5 m deep. Five wireless tracking devices were distributed evenly between the brick columns. Fig. 7 illustrates the installation locations of the devices.

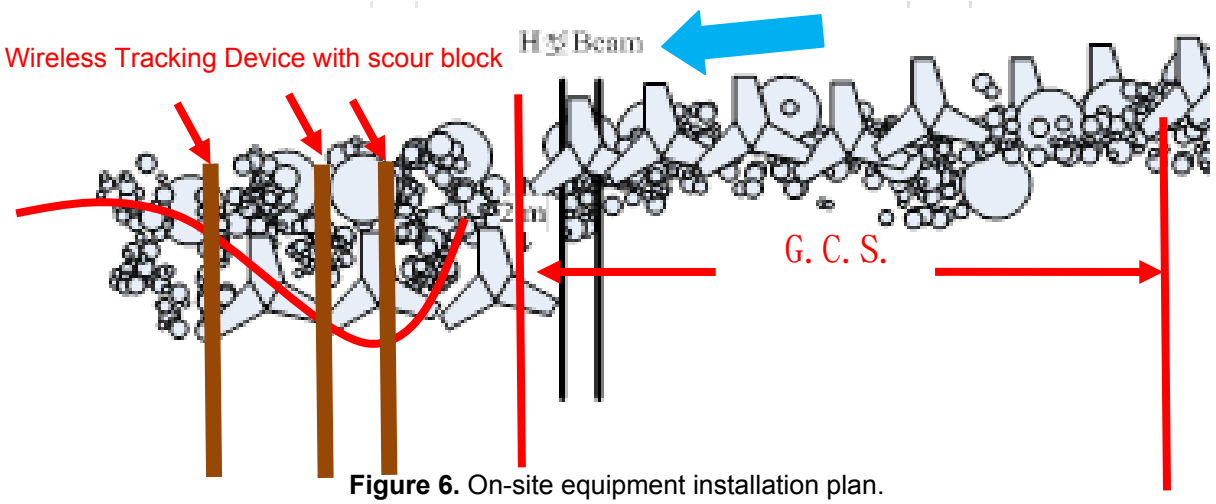


**Figure 6.** On-site equipment installation plan.

| Tracking device number | Vertical elevation (m) | Scour depth (m) | Tracking device number | Vertical elevation (m) | Scour depth (m) | Tracking device number | Vertical elevation (m) | Scour depth (m) |
|---|---|---|---|---|---|---|---|---|

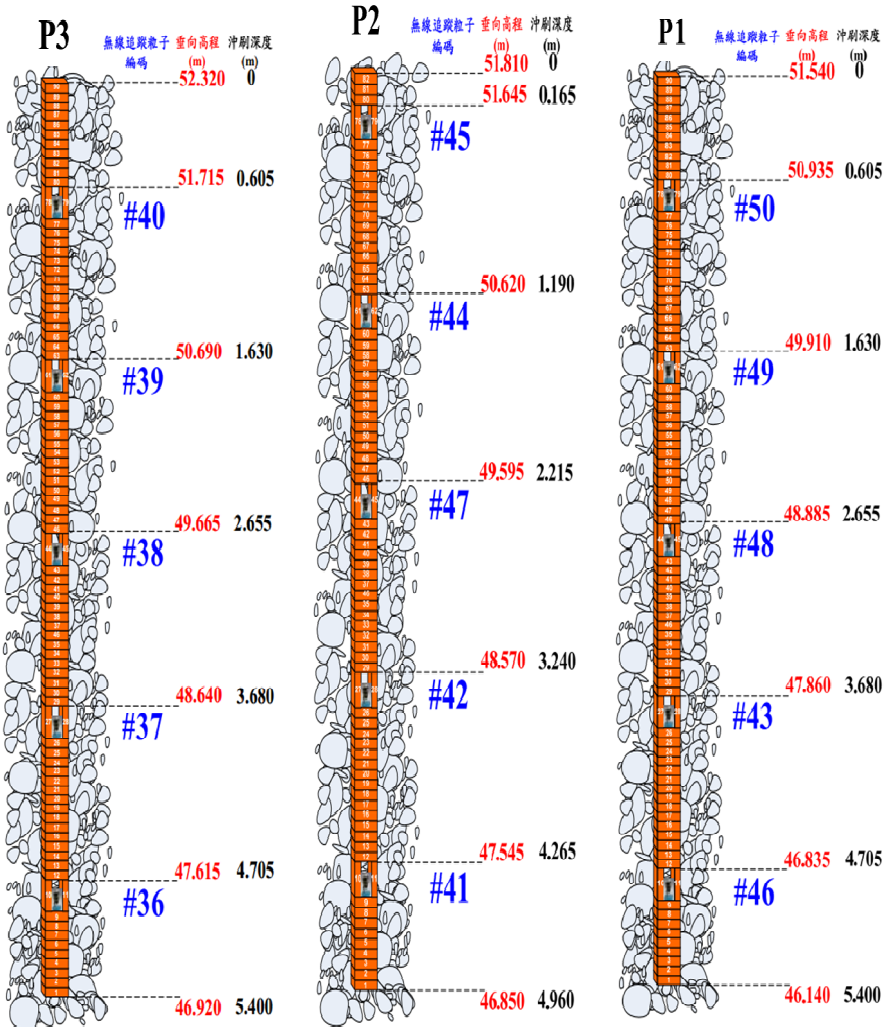


**Figure 7.** Illustration of the on-site dynamic scouring observation equipment installation.

4.3 Observation process of dynamic scouring

Fig. 8 shows the scouring observation process. During a typhoon-induced flood, runoff collected in the upstream catchment area was discharged by the Shigang Dam. The discharge would arrive at the observation site of the experiment approximately 1 hour after it left Shigang Dam. The water level of the Dajia River Bridge upon the arrival of the discharge could be determined using the radar level meter operated by the third River Management Office. The discharge then scoured the rear part of the grade-control structures of the weir of the Dajia River Bridge.

When the scouring reached the depth of the devices, the devices would float to the surface because of their own buoyancy and turn on power to send signals. Ground base stations received the signals and sent them to laboratory server, so that the initiating time of the coded devices could be recorded to identify the scouring position at that specific time point. If an adequate number of devices were initiated, the dynamic scouring process could be estimated.

 

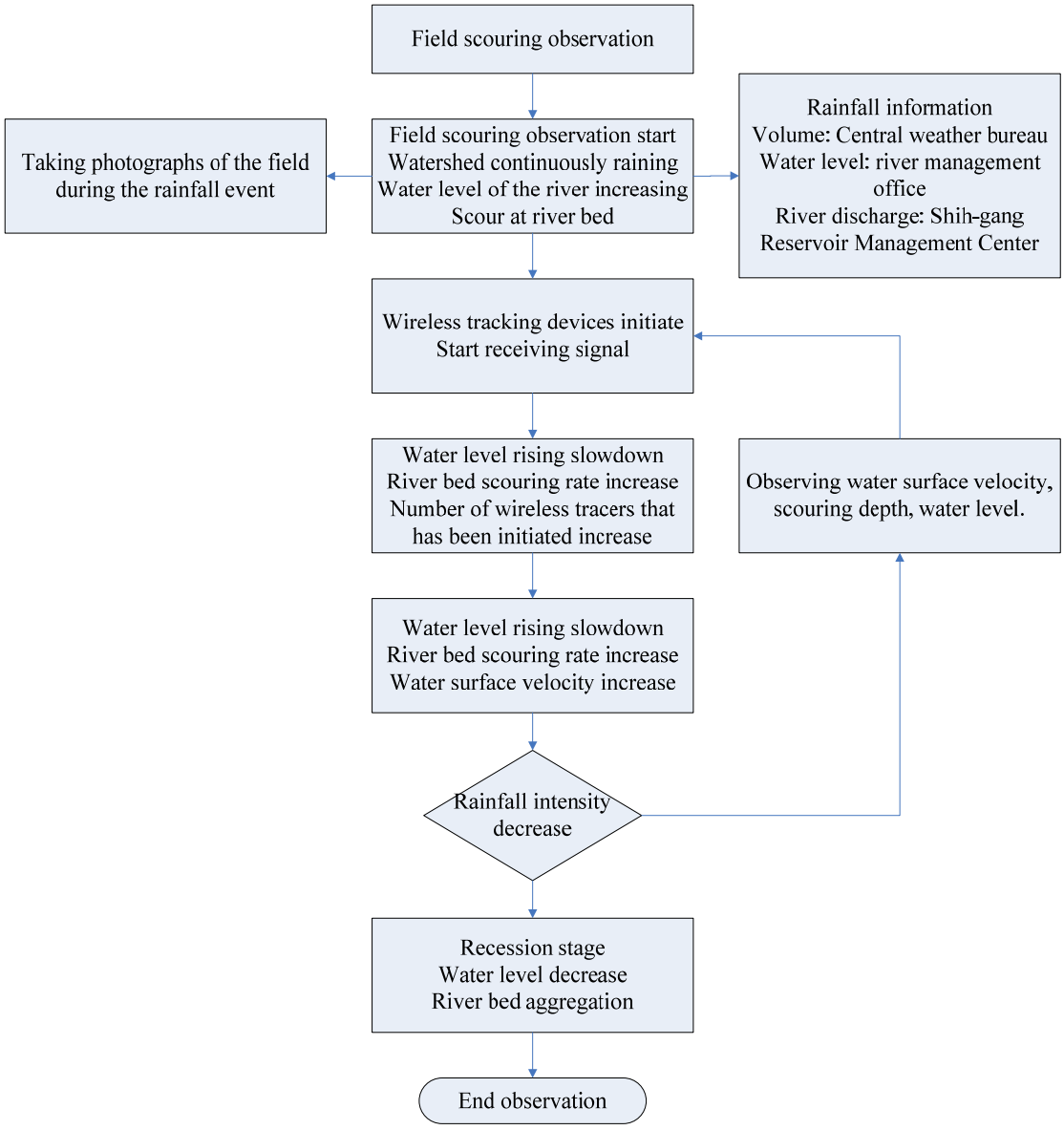


**Figure 8.** Flowchart for dynamic scouring observation during typhoon-induced floods.

## 5 RESULTS AND DISCUSSIONS

### 5.1 Observation results of the scouring process of flood events

In this study, the discharge from Shigang Dam during the typhoon-induced floods was considered as the upstream inflow to the grade-control structures. Table 4 presents the observation results of the flood event induced by Typhoon Dujuan, and Fig. 9 presents the discharge hydrograph of Shigang Dam (on Dajia River) during the typhoon, the water level hydrograph of the Dajia River Bridge, and the data of an automatic water level-meter installed downstream at the observation site. The maximum peak discharge was 1858 cms, the duration of flood peak discharge was 9 hours, and the duration of typhoon-induced flooding was approximately 30 hours. The discharge varied from 300 cms to 1858 cms, and the extent of water-level fluctuation at the observed section was approximately 2.5 m.

The highest water level upstream of the grade-control structures was 56.4 m, with a depth of 1.97 m; the highest water level downstream from the grade-control structures was 53.66 m, with a depth of 2.12 m. The distance between the upstream and downstream water levels was approximately 120 m. The water surface gradient was also calculated. The water level first rose at 02:00 am on September 29th, and the water surface gradient then was approximately 0.024. The highest water level was achieved at 06:00 am, when the water surface gradient reached approximately 0.025, which was approximately twice that of the riverbed gradient (1/90). At 00:00, September 30th, the flood retreated, and the water surface gradient was approximately 0.014, which was close to the original riverbed gradient.

During Typhoon Dujuan, a signal was received from Wireless Tracking Device 44 at 06:27 am on September 29th. Signal interpretation indicated that 76.7 m downstream from the grade-control structures of

 

the weir in the Dajia River under the Provincial Highway No. 1, the scouring depth was at least 1.19 m deep. Fig. 10 presents the on-site measurements of the riverbed depositing elevation after Typhoon Dujuan. The elevations at Poles P3 and P2 after scouring and depositing were respectively 1.26 m and 0.43 m lower than the bed before the flood; however, the elevation of Pole P1 after scouring and depositing was 0.59 m higher than that of the bed before the flood.

The maximum scouring depth was obtained by excavating the investigated area during a dry season, which was further long after Typhoon Dujuan. A dynamic scouring process at Pole P2 was plotted (Fig. 11). The three subfigures of Fig. 11 correspond, from top to bottom, with the water-level hydrograph, the water depth of Dajia River Bridge, and the scouring depth observed at Pole P2; the horizontal axis designates time. Excavation results revealed that the maximum scouring depths at the three scouring brick columns were 1.83 m, 2.44 m, and 1.72 m, respectively. The elevations after depositing were all lower than the original ones, indicating that the riverbed at this site remained in the process of scouring.

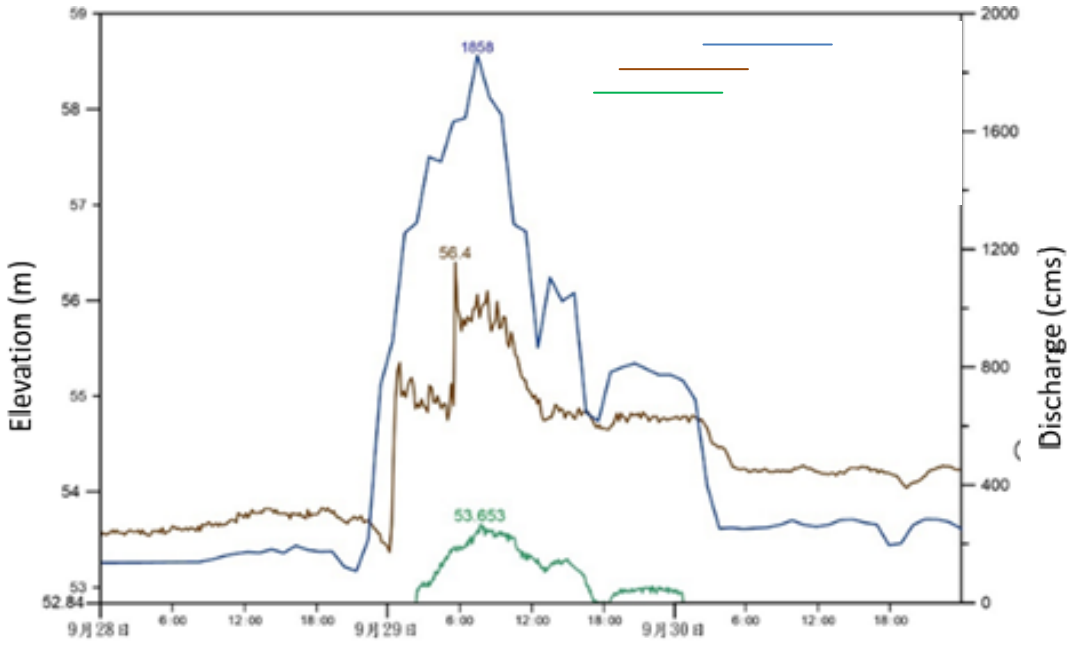


**Figure 9** Hydrographs of discharge and water level during Typhoon Dujuan.

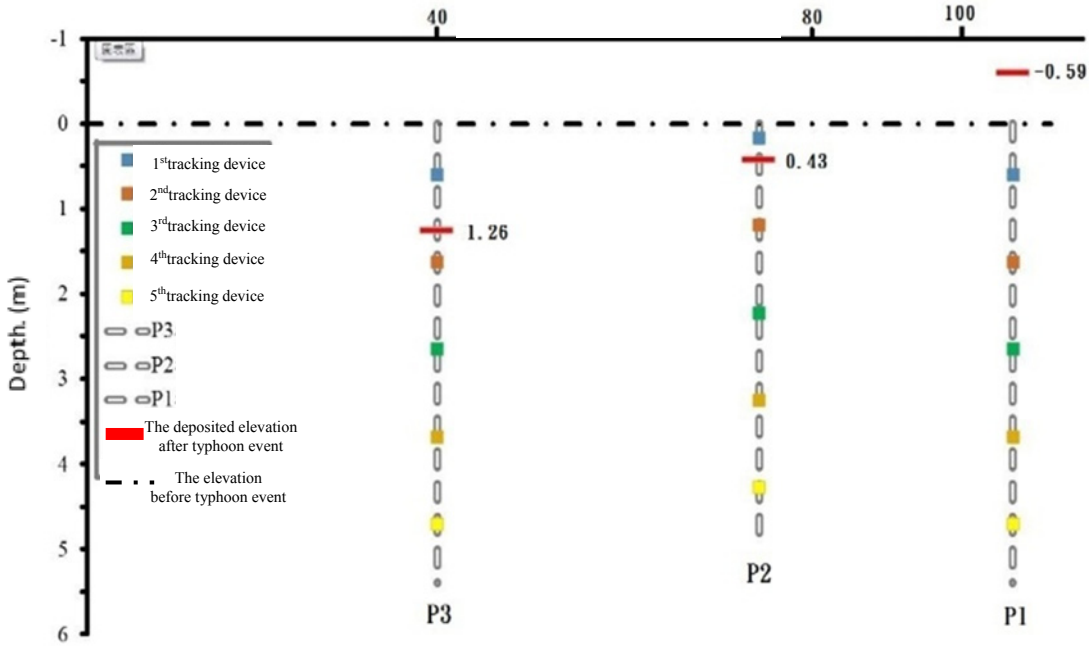


**Figure 10.** Relationship between the deposited elevations and devices after Typhoon Dujuan

 

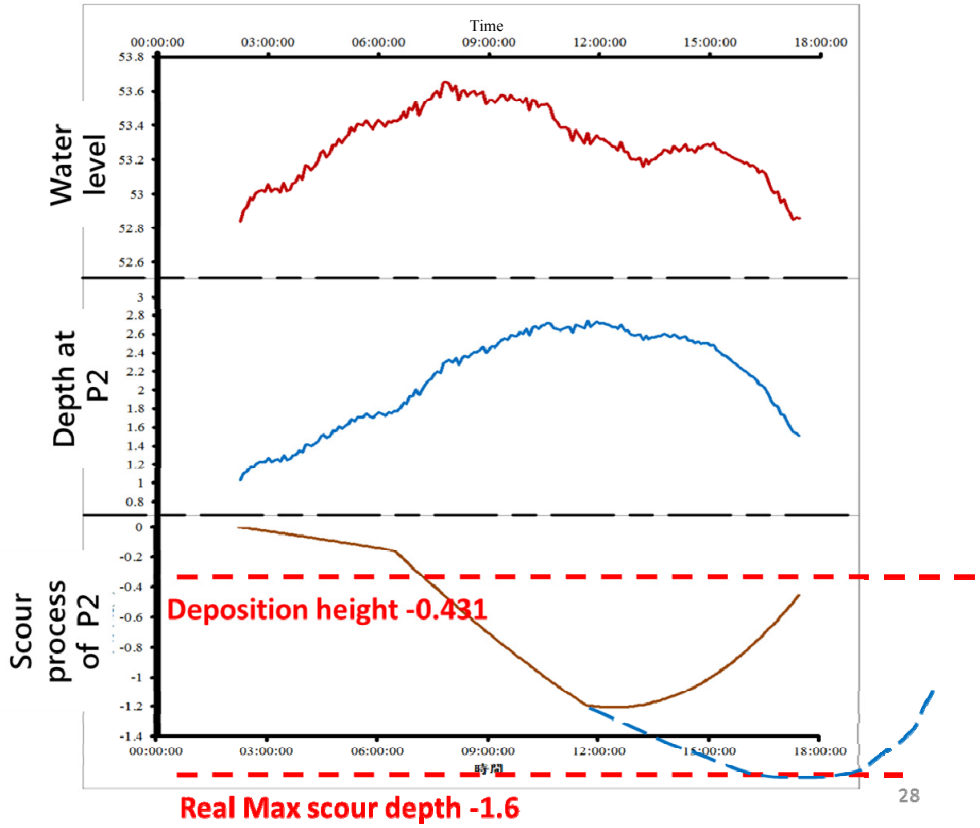


**Figure 11.** Schematic diagram of the dynamic scouring process occurred at Pole P2 during Typhoon Dujuan.

Fig. 12 shows that compared with the observation data obtained using wireless tracking devices, the estimation results from the scouring formula proposed by Pagliara (2007) deviated considerably in size and spatial distribution. By contrast, the formula proposed by WRPI (2005) yielded results more consistent with the observation data regarding the maximum scouring depths and their locations.

Given the observation data and estimation results generated from related formulas proposed by WRPI (2005) and Pagliara (2007), the maximum local scour that Typhoon Dujuan caused to the downstream grade-control structures was possibly located between the scouring brick columns P2 and P3.

Peak discharge was adopted as the calculated discharge in this study. Nevertheless, differences definitely exist between the influence level of on-site effective flood discharge and the long-term steady-flow condition assumed in most laboratory experiments. More on-site observation data should be collected to further examine the reliability of the equations.

 

**Table 4.** Compiled observation results of scouring and depositing during the Typhoon Du-Juan induced flood in 2015.

| Measurement position (scour type) | Location | | Flood event (time of $Q_p$) | Flood peak discharge $Q_p$ ($m^3$/s) Flood peak duration ($t_p$) | (1) | (2) | (3)= (2)-(1) | (4) | (5)= (1)-(4) | (6)=(2)-(5) | GPRS real-time scour monitoring | | |
|---|---|---|---|---|---|---|---|---|---|---|---|---|---|
| | N (m) | E (m) | | | Pre-flood riverbed level (top level of numbered-brick) (m) | Riverbed level after flood (m) | Difference of riverbed level before and after flood (m) | Riverbed level for maximum scour depth $H(d_{gs})$, $H(d_{bs})$ (m) | Maximum scour depth $d_{gs}$, $d_{bs}$ (m) | Deposited height during falling limb(m) | Monitored time | Coed wireless tracer (7)(level of its upper Brick m) | (8)=(1)-(7) Scouring depth (m) |
| P5 (Scour downstream GCS) | 2689970.013 | 209778.889 | Typhoon Dujuan (7:00 am, 2015/9/29) | 1,858 (9 h) | 52.63 | 51.11 | -1.52 | 50.80 (Brick No.64) | 1.83 | 0.31 | 6:17 am 11:38 am | #45(El.=51.645) #44(El.=50.620) | 0.555 1.580 |
| P6 (Scour downstream GCS) | 2689988.815 | 209747.419 | | | 52.20 | 51.2 | -1.00 | 49.76 (Brick No.48) | 2.44 | 1.44 | | | |
| P7 (Scour downstream GCS) | 2690003.181 | 209722.353 | | | 51.96 | 51.40 | -0.56 | 50.24 (Brick No.68) | 1.72 | 1.16 | | | |

5.2 Observation results of maximum scouring depths

Table 5 integrates the calculation results by both Water Resources Planning Institute [WRPI] (2005), and Pagliara formulas (2007) based on two riverbed materials. These results and the observation data furnished the figures in Fig. 7, where the coordinate (0, 0) indicates the starting point of the downstream side of the grade-control structures, the black solid dots mark the scouring depths that the employed wireless tracking devices detected during Typhoon Dujuan, and the dotted line shows the scour hole profile obtained using the scouring equation proposed by Pagliara (2007).

## 6 CONCLUSIONS

Through a test of on-site rainfall events, the wireless tracking device adopted in this study is confirmed capable of effectively providing real-time reports of riverbed scouring. Therefore, this device can be applied for future real-time alerts concerning the safety of river-crossing structures and embankment foundations.

Various representative grain diameters are employed in this study to yield calculation results of two distinct scouring formulas. Comparing the calculation results and the maximum scouring depths obtained through post-event excavation reveals that the estimation results from the formula developed by WRPI (2005) are relatively accurate regarding the maximum scouring depths and the positions where maximum scouring occurs. However, attention should be paid to the median grain diameter incorporated into the formulas.

The dynamic scouring process recorded in this study indicates that the scouring depth of this event occurs after the arrival of peak flooding. No further explanation can be proposed from the currently available observation data; however, this mechanism warrants further investigation.

**Table 5.** Comparison of the estimation results obtained using different formulas to calculate the scouring depth downstream of the grade-control structures during typhoon Dujuan

| Location: the grade-control structures of the Dajia River under the Provincial Highway No. 1<br>Event: Typhoon Dujuan, September 2015 | | | | |
|---|---|---|---|---|
| Formula developer | Median grain diameter $D_{50} = 0.063$m (sample data of riverbed material collected and analyzed before the typhoon-induced flood) | | Median grain diameter $D_{50} = 0.096m$ (Research report on the sediment transport characteristics of the Dajia River) | |
| | Maximum scouring depth $y_{s,me}$(m) | Position where the maximum scouring depth occurred $X_s$(m) | Maximum scouring depth $y_{s,me}$(m) | Position where the maximum scouring depth occurred $X_s$(m) |
| Pagliara | 0.86 | 39.2 | 0.59 | 28.9 |
| WRPI | 1.52 | 64.9 | 1.22 | 63.4 |

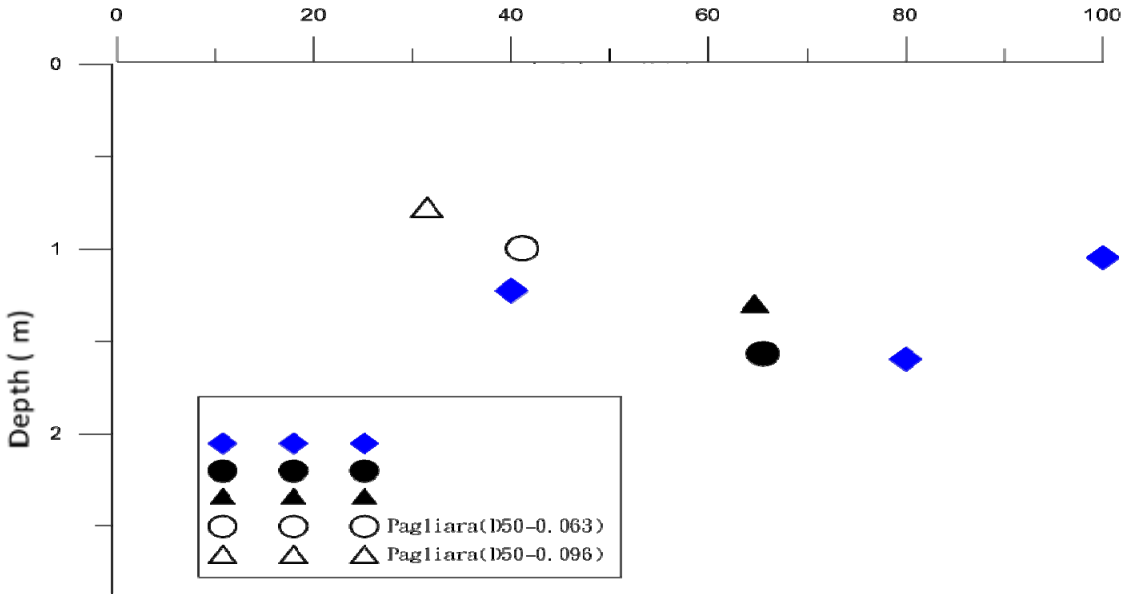


**Figure 12.** Comparison on scouring analysis in the investigated section during Typhoon Dujuan.

 

**REFERENCES**

Cheng, L. (1999). *Study on Technology and Tactics for Scour Prevention of Cross-River Structures-Part 1,* Evaluation of Using Rigid or Deformable Sabo-Weir as Protection Method for Bridge Foundation.

Pagliara, S. (2007). Influence of the Sediment Gradation on Scour Downstream of Block Ramps. *Journal of Hydraulic Engineering,* 133(11), 1241-1248.

Water Resource and Planning Institute, (2014). *Field Study of Short-term Riverbed General Scour for Typhoon-Induced Floods.*

Water Resource and Planning Institute, (2011). *Study on River Bed Stability for the Reach. Downstream of Shigang Dam in Dajia River.*

Water Resource and Planning Institute, (2010). *Field Study of Sediment Transport Characteristics for Dajia River.*

Water Resource and Planning Institute, (2009). *Investigation of Failure Mechanism and New Scour Counter Measures at Grade Control Structures.*

Water Resource and Planning Institute, (2005). *Physical Model Studies of Hydraulic Structure Protection Works in Streams.*

Yang, H.C. & Su, C.C. (2015). Real-Time River Bed Scour Monitoring and Synchronous Maximum Depth Data Collected during Typhoon Soulik in 2013. *Hydrological Processes,* 29, 1056–1068.

 

Proceedings of the 37th IAHR World Congress
August 13 – 18, 2017, Kuala Lumpur, Malaysia

# TURBULENT SHEAR FLOW OVER A SINUSOIDAL BED

SK ZEESHAN ALI[1] & SUBHASISH DEY[2]

[1, 2]Department of Civil Engineering, Indian Institute of Technology Kharagpur, West Bengal 721302, India
skzeeshanali@iitkgp.ac.in;
sdey@iitkgp.ac.in

## ABSTRACT

A steady turbulent shear flow over a sinusoidal bed is investigated by applying the Reynolds averaged Navier–Stokes equations. The vertical acceleration induced by the sinusoidal bed yields a pressure profile having a departure from the linear hydrostatic pressure profile. Assuming a one-seventh power law of streamwise velocity, including the effects of curvilinear streamlines through Boussinesq approximation and using the Reynolds stress closure relation, the mathematical equations of the free surface profile and the Reynolds shear stress profile are obtained. The streamwise profiles of free surface and bed shear stress, and the vertical profiles of Reynolds shear stress at different streamwise locations are presented. In subcritical flow regime, the free surface profile is out of phase with the bed undulations; while the bed shear stress is nearly in phase with the bed. However, the free surface and the bed shear stress profiles in supercritical flow regime are contrary to those in subcritical flow regime. On the downstream portion of the crest of the sinusoidal bed, the Reynolds shear stress is characterized by a convex profile due to a decelerated flow; while on upstream of the crest of the bed, it is characterized by a concave profile due to an accelerated flow. However, over the crest and the trough of the bed, the Reynolds shear stress profiles are nearly linear, as observed in a zero-pressure gradient flow. The outcome of this study is used to analyze the sinusoidal erodible bed. The continuity equation of sediment motion is used to determine the phase lag distance between the locations of the maximum sediment flux and the maximum bed shear stress. The effects of the Froude number and the resistance parameter on the phase lag are investigated. The dependency of the Froude number on the phase lag is more noticeable than the resistance parameter.

**Keywords:** Fluvial hydraulics; hydrodynamics; turbulent flow; boundary layer; sediment transport

## 1 INTRODUCTION

Turbulent shear flow over a sinusoidal bed is a problem of practical importance due to its relevance to the bed forms (dunes and antidunes) in fluvial systems (Dey, 2014). For a sinusoidal bed, the solutions of the flow parameters, such as flow depth, velocity and bed shear stress are periodic by nature with the periodicity equaling the wavelength of the sinusoidal bed. Another key feature is the existence of a phase shift between the flow and the bed profiles. Lamb (1932) was the pioneer to obtain the solution for the characteristics of an ideal fluid flow over a sinusoidal bed. Benjamin (1959) analyzed the shear flow over a wavy bed to obtain the normal and shear stresses exerted on the bed. Iwasa and Kennedy (1968) determined the flow profiles and their phase shift relative to the BED profiles for different flow conditions. Mizumura (1995) solved the flow profile over a wavy bed using the Laplace equation for both subcritical and supercritical flow conditions. Dey et al. (2012) used Reynolds averaged Navier-Stokes (RANS) equations to determine the flow profile over a sinusoidal bed.

When the local bed shear stress surpasses its threshold value at the beginning of sediment motion, the sediment is transported. The local sediment removal and deposition processes give rise to bed forms. The flow features predominantly control the formation of bed forms. However, the bed form configurations significantly influence the flow characteristics in general and the resistance to the flow in particular. From the viewpoint of the bed instability, several investigators studied the flow over bed forms representing the Froude number as a function of nondimensional wave number of the bed forms. The potential flow over a sinusoidal bed of varying amplitudes was studied by Kennedy (1963) to analyze the bed forms in the context of the instability at the fluid- bed interface. Instability of bed forms was further analyzed by Reynolds (1965) relating the bed resistance to flow with the average flow velocity and the local flow depth and extending the analysis of Kennedy (1963) in three dimensions. A real fluid flow over a sinusoidal bed was reported by Engelund and Hansen (1966) considering the streamline curvature to analyze the bed form instability. Hayashi (1970) presented an improved version of two-dimensional instability analysis adopting a similar boundary condition as that of Kennedy (1963). Fredsøe (1974) also analyzed the bed form instability by applying the vorticity transport equation and considering the internal fluid friction. Bose and Dey (2009) presented an analytical model stemming from the RANS equations and considering the effects of streamline curvature to analyze the sand wave instability.

 

Zilker et al. (1977) and Zilker and Hanratty (1979) conducted experimental investigations to determine the influence of amplitude of the wavy boundaries on the separated and unseparated turbulent flows. Using the particle image velocimetry (PIV), Buckles et al. (1984) investigated the time-averaged flow field and the extent of the separated flow zone over a sinusoidal bed with large amplitude. Using the laser Doppler velocimetry (LDV), Frederick and Hanratty (1988) obtained the bed shear stress for the unseparated flow over a wavy bed from the streamwise velocity profiles. Hudson et al. (1996) studied the profiles of velocity, turbulence intensities, Reynolds shear stress, and turbulent kinetic energy (TKE) production over a wavy bed for the separated flow. Also, the two-dimensional spatial structure of time-averaged flow and the variation of Reynolds stress over a wavy bed were investigated by Poggi et al. (2007).

Several numerical attempts were reported to analyze the flow over wavy boundaries (Zhaoshun and Zhan, 1989; Patel et al., 1991). An investigation of the instantaneous turbulent flow field over a wavy bed by Calhoun and Street (2001) revealed that the Görtler instability is the primary mechanism to relate the streamwise vortices with the wavy bed profile. The direct numerical simulation (DNS) of turbulent flow showed a significant variation in the flow and turbulence characteristics over a wavy bed (De Angelis et al., 1997; Cherukat et al., 1998). De Angelis et al. (1997) argued that near the bed, the streamwise turbulence intensity increases, but the transverse turbulence intensity decreases.

The above overview reveals that although there is a significant advancement in analyzing the flow over a wavy bed, little is known about the vertical profile of Reynolds shear stress at different streamwise locations. In this study, a theoretical analysis based on the RANS equations is presented to determine the Reynolds shear stress profile in flow over a sinusoidal bed. Importantly, the present theory is limited to the unseparated flow over a sinusoidal bed. The analysis also enables us to determine the profiles of free surface and bed shear stress from the mean turbulent diffusivity consideration. Further, it gives a quantitative estimation of the phase shift between the flow and the bed profiles. The analysis is then extended to the sinusoidal erodible bed to determine the phase lag distance between the locations of the maximum sediment flux and the maximum bed shear stress.

## 2 GOVERNING EQUATIONS

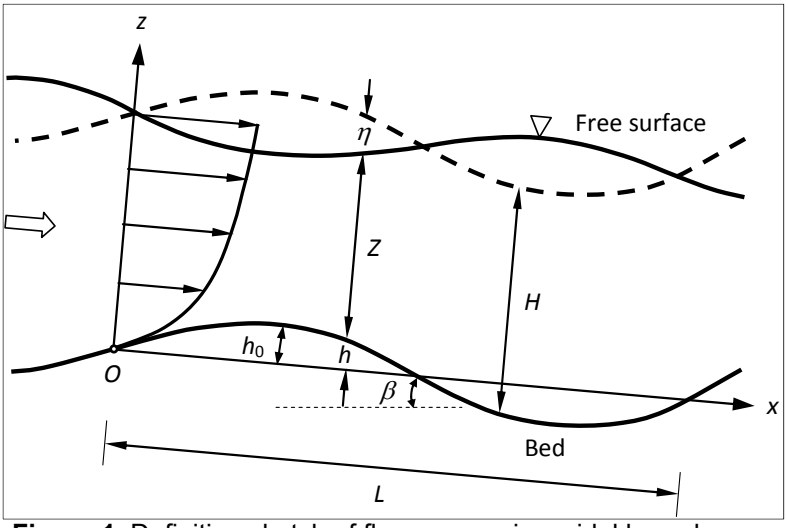


**Figure 1.** Definition sketch of flow over a sinusoidal boundary

A steady two-dimensional turbulent flow over a sinusoidal bed is considered. The origin *O* of the Cartesian coordinate system (*x*, *z*) is assumed at a convenient location on the bed (Figure 1). The angle $\beta$ is created by the *x*-axis with the horizontal. First, the flow over a rigid-bed is analyzed. The bed profile $h(x)$ is given by

$$h(x) = h_0 \sin kx \qquad [1]$$

where $h_0$ is the half amplitude; $k$ is the wave number (= $2\pi/L$); and $L$ is the wavelength. The local flow depth $Z(x)$ is $Z(x) = H + \eta(x)$, where $H$ is the uniform flow depth and $\eta(x)$ is the free surface perturbations. Since the bed undulations are small, $h_0$ is smaller than the streamwise length scale $L$ and $|dh/dx| \ll 1$. Similarly, $\eta$ is also small and $|dZ/dx| \ll 1$.

Applying the Reynolds decomposition, the two-dimensional instantaneous velocity components ($u$, $w$) in ($x$, $z$) and instantaneous pressure $p$ are decomposed as

$$u = \overline{u}(x,z) + u'(x,z,t)\,;\; w = \overline{w}(x,z) + w'(x,z,t)\,;\; p = \overline{p} + p' \qquad [2]$$

 

where an overbar denotes the time-averaged quantity and a prime denotes the fluctuations with respect to time-averaged quantity and *t* is the time.

The continuity equations of time-averaged and fluctuating velocity components are

$$\frac{\partial \overline{u}}{\partial x}+\frac{\partial \overline{w}}{\partial z}=0\,;\ \frac{\partial u'}{\partial x}+\frac{\partial w'}{\partial z}=0 \qquad [3]$$

and the RANS equations are

$$\overline{u}\frac{\partial \overline{u}}{\partial x}+\overline{w}\frac{\partial \overline{u}}{\partial z}=-\frac{1}{\rho}\cdot\frac{\partial \overline{p}}{\partial x}+\upsilon\frac{\partial^2 \overline{u}}{\partial z^2}-\frac{\partial \overline{u'^2}}{\partial x}+\frac{1}{\rho}\cdot\frac{\partial \tau}{\partial z}+g\sin\beta \qquad [4]$$

$$\overline{u}\frac{\partial \overline{w}}{\partial x}+\overline{w}\frac{\partial \overline{w}}{\partial z}=-\frac{1}{\rho}\cdot\frac{\partial \overline{p}}{\partial z}+\upsilon\frac{\partial^2 \overline{w}}{\partial x^2}-\frac{\partial \overline{w'^2}}{\partial z}+\frac{1}{\rho}\cdot\frac{\partial \tau}{\partial x}-g\cos\beta \qquad [5]$$

where $\rho$ is the mass density of fluid, $\upsilon$ is the coefficient of kinematic viscosity of fluid, $\tau(x, z)$ is the Reynolds shear stress (= $-\rho\overline{u'w'}$) and *g* is the gravitational acceleration.

For the $S_0$ (= tan$\beta$) to be small, we apply sin$\beta\approx$ tan$\beta$ and cos$\beta\approx$ 1 in Eqs. (4) and (5), respectively.

## 3 VELOCITY COMPONENTS

The streamwise velocity profile is expressed in the form of a one-seventh power law, which is a good substitution for the logarithmic law for a turbulent boundary layer flow. Thus, $\overline{u} = U_0\zeta^{1/7}$, where $U_0$ is the maximum velocity and $\zeta$ is $(z - h)/Z$. The $\overline{u}$ is also expressed as $\overline{u} = (8/7)U\zeta^{1/7}$, where *U* is the depth-averaged velocity. The time-averaged velocity components and the Reynolds shear stress are expressed in functional forms as $\overline{u} = U\psi(\zeta)$; $\overline{w} = U\phi(\zeta)$; and $\tau = \tau_0\xi(\zeta)$.

Substituting the expression for $\overline{u}$ into Eq. (3) and then integrating yield

$$\phi=\psi\left(\frac{dh}{dx}+\zeta\frac{dZ}{dx}\right)-\frac{1}{U}\cdot\left(Z\frac{dU}{dx}+U\frac{dZ}{dx}\right)\int_0^{\zeta}\psi\,d\zeta \qquad [6]$$

For a steady flow, the fluid flux per unit width *q* (*q* = *UZ*) is a constant. Thus, Eq. (6) reduces to

$$\phi=\psi\left(\frac{dh}{dx}+\zeta\frac{dZ}{dx}\right) \qquad [7]$$

## 4 PRESSURE PROFILE

In the turbulent shear-layer, $\partial\tau/\partial x \approx \rho\upsilon(\partial^2\overline{w}/\partial x^2)$ and $\partial\tau/\partial z \approx \rho\upsilon(\partial^2\overline{u}/\partial z^2)$ are prevalent. Moreover, the $\partial\overline{u'^2}/\partial x$ and $\partial\overline{w'^2}/\partial x$ are vanishingly small in case of a shear flow over a wavy bed with small amplitude relative to the wavelength (Bose and Dey, 2009).

The vertical acceleration induced by the sinusoidal bed results in a pressure profile having a departure from the linear hydrostatic pressure profile (Dey, 2014). As the streamwise variations of both the bed and the free surface are small, their curvatures are approximated as $\Re(h)\approx d^2h/dx^2$ and $\Re(Z)\approx d^2Z/dx^2$. Applying the Boussinesq approximation (Dey, 2014), the streamline curvature between the bed and the free surface is considered as $\Re = \Re(h) + \zeta\Re(Z)$.

With this assumption, Eq. (5) is integrated to obtain the expression for the pressure:

$$\overline{p}=\rho gZ(1-\zeta)-\left(\frac{8}{7}\right)^2\rho ZU^2\left[\frac{7}{9}\Re(h)(\zeta^{9/7}-1)+\frac{7}{16}\Re(Z)(\zeta^{16/7}-1)\right]-\rho\overline{w'^2} \qquad [8]$$

## 5 REYNOLDS SHEAR STRESS

It is pertinent to mention that the total fluid shear stress (Reynolds shear and viscous shear stresses) at the bed equals the local bed shear stress, that is $\xi(\zeta = 0) = 1$. Note that in the turbulent shear-layer, only the Reynolds shear stress composes the total fluid shear stress, in absence of viscous shear stress. Substituting

 

the expressions for $\overline{u}$, $\overline{w}$, and $\overline{p}$ in preceding sections into Eq. (4) and performing the integration using the boundary condition $\xi(\zeta = 0) = 1$ yield

$$\xi\big|_{\zeta} = 1 + \frac{\rho g Z}{\tau_0}\left(\frac{dh}{dx} + \frac{dZ}{dx}\right)\zeta - \frac{64}{49}\cdot\frac{\rho Z^2 U^2}{\tau_0}\left[\frac{7}{9}\left(\frac{7}{16}\zeta^{16/7} - \zeta\right)\frac{d^3h}{dx^3} - \frac{7}{9}\cdot\frac{1}{Z}\cdot\frac{dZ}{dx}\cdot\frac{d^2h}{dx^2}\cdot\zeta(\zeta^{9/7} - 1)\right.$$
$$\left. + \frac{7}{16}\left(\frac{7}{23}\zeta^{23/7} - \zeta\right)\frac{d^3Z}{dx^3} - \frac{7}{16}\cdot\frac{1}{Z}\cdot\frac{dZ}{dx}\cdot\frac{d^2Z}{dx^2}\zeta(\zeta^{16/7} - 1)\right] - \frac{\rho g Z S_0}{\tau_0}\zeta - \frac{64}{63}\cdot\frac{\rho U^2}{\tau_0}\cdot\frac{dZ}{dx}\zeta^{9/7} \qquad [9]$$

At the free surface, $\xi(\zeta = 1) = 0$. Therefore, from Eq. (9), the expression for the $\tau_0$ is obtained by substituting $\zeta = 1$. For the analysis of flow profile, it is a usual practice to linearize Eq. (9) considering the flow behaves as if it were a uniform flow with a flow depth $H$ and a velocity $U_m$ over the sinusoidal bed (Bose and Dey, 2009). Thus, using $Z(x) = H + \eta(x)$ and $\zeta = 1$, Eq. (9) takes the form

$$\frac{\tau_0}{\rho g Z} = -\left(\frac{dh}{dx} + \frac{d\eta}{dx}\right) - \frac{64}{7}F^2H^2\left(\frac{1}{16}\cdot\frac{d^3h}{dx^3} + \frac{1}{23}\cdot\frac{d^3\eta}{dx^3}\right) + S_0 + \frac{64}{63}F^2\frac{d\eta}{dx} \qquad [10]$$

where $F$ is the Froude number [$= U_m/(gH)^{0.5}$].

The uniform flow velocity $U_m$ is determined from the Manning equation

$$U_m = \frac{1}{n}H^{2/3}S_0^{1/2} \qquad [11]$$

where $n$ is the Manning roughness coefficient. If $u_{*m}$ denotes the shear velocity for the uniform flow [$= (gHS_0)^{0.5}$], then $U_m/u_{*m} = \Omega^{-0.5}$; where $\Omega$ is the resistance parameter ($= gn^2/H^{1/3}$). Also, the average slope of the bed is related to the Froude number and the resistance parameter as $S_0 = F^2\Omega$.

Combining Eqs. (9) and (10), the Reynolds shear stress is

$$\frac{\tau}{\rho g Z} = \frac{\tau_0}{\rho g Z} + \left(\frac{dh}{dx} + \frac{d\eta}{dx}\right)\zeta - \frac{64}{63}F^2\frac{d\eta}{dx}\zeta^{9/7} - \zeta S_0 - \frac{64}{7}F^2H^2\left[\frac{1}{9}\left(\frac{7}{16}\zeta^{16/7} - \zeta\right)\frac{d^3h}{dx^3} + \frac{1}{16}\left(\frac{7}{23}\zeta^{23/7} - \zeta\right)\frac{d^3\eta}{dx^3}\right] \qquad [12]$$

Eq. (12) clearly demonstrates the dependency of Reynolds shear stress on streamwise and vertical distances. Note that the Reynolds shear stress can only be determined when the streamwise gradient terms in Eq. (12) are known. For this reason, another expression for the bed shear stress, independent of Eq. (10), is derived with the aid of the turbulent diffusivity concept.

The Reynolds shear stress in a boundary layer flow is defined by the Boussinesq hypothesis (Dey,2014) as:

$$\tau = \rho\varepsilon_t\frac{d\overline{u}}{dz} \qquad [13]$$

where $\varepsilon_t$ is the turbulent diffusivity. The mean turbulent diffusivity $\varepsilon_t$ is

$$\varepsilon_t = \sigma\int_0^1 Z(U_0 - \overline{u})d\zeta \qquad [14]$$

where $\sigma = 1/28$ (Engelund and Hansen, 1966). It is approximated that the turbulent shear-layer is extended up to the bed neglecting the thin viscous sublayer. This results in a velocity profile that has a slip velocity $u_b$ on the bed (Engelund and Hansen, 1966). The expression for the slip velocity given by Engelund (1964) is

$$\frac{u_b}{u_*} = \Omega^{-0.5} - \frac{1}{3}\left(\frac{6}{\sigma}\right)^{0.5} \qquad [15]$$

 

Substituting Eq. (13) into Eq. (12) and then integrating yield

$$\frac{\varepsilon_t(\overline{u}-u_b)}{gZ^2}=\frac{\tau_0}{\rho gZ}\zeta+\frac{1}{2}\left(\frac{dh}{dx}+\frac{d\eta}{dx}\right)\zeta^2-\frac{4}{9}F^2\frac{d\eta}{dx}\zeta^{16/7}-\frac{1}{2}\zeta^2S_0-\frac{64}{7}F^2H^2\left\{\frac{1}{9}\left[\frac{49}{368}\zeta^{23/7}-\frac{\zeta^2}{2}\right]\frac{d^3h}{dx^3}+\frac{1}{16}\left[\frac{49}{690}\zeta^{30/7}-\frac{\zeta^2}{2}\right]\frac{d^3\eta}{dx^3}\right\} \quad [16]$$

At the free surface ($\zeta$= 1), Eq. (16) reduces to

$$\frac{\varepsilon_t(U_0-u_b)}{gZ^2}=\frac{\tau_0}{\rho gZ}+\frac{1}{2}\left(\frac{dh}{dx}+\frac{d\eta}{dx}\right)-\frac{4}{9}F^2\frac{d\eta}{dx}-\frac{1}{2}S_0+\frac{64}{7}F^2H^2\times\left\{\frac{15}{368}\frac{d^3h}{dx^3}+\frac{37}{1380}\frac{d^3\eta}{dx^3}\right\} \quad [17]$$

Subtracting Eq. (17) from Eq. (16), the resulting equation is integrated. Then, using Eqs. (10) and (14), the $\varepsilon_t$ is obtained as

$$\varepsilon_t=\left(\frac{\sigma}{6}\right)^{0.5}u_*Z\left[1+\frac{128}{1449}\cdot\frac{F^2}{S_0}\cdot\frac{d\eta}{dx}\right]+192\left(\frac{\sigma}{6}\right)^{0.5}u_*Z\frac{F^2H^2}{S_0}\left\{\frac{1}{1440}\cdot\frac{d^3h}{dx^3}+\frac{1}{2553}\cdot\frac{d^3\eta}{dx^3}\right\} \quad [18]$$

Furthermore, integrating Eq. (16) over the entire flow depth and rearranging yield

$$\frac{\tau_0}{\rho gZ}=\frac{2\varepsilon_t(U-u_b)}{gZ^2}-\frac{1}{3}\left(\frac{dh}{dx}+\frac{d\eta}{dx}\right)+\frac{56}{207}F^2\frac{dZ}{dx}+\frac{1}{3}S_0-\frac{128}{7}F^2H^2\left\{\frac{499}{33120}\cdot\frac{d^3h}{dx^3}+\frac{163}{17020}\cdot\frac{d^3\eta}{dx^3}\right\} \quad [19]$$

The first term on the right hand side of Eq. (19) is

$$\frac{2\varepsilon_t(U-u_b)}{gZ^2}=\frac{2\varepsilon_t}{gZ^2}u_*\left(\frac{U}{u_*}-\frac{u_b}{u_*}\right)=\frac{2\varepsilon_t}{gZ^2}u_*\left[\frac{q}{g^{0.5}Z^{1.5}}\left(\frac{\tau_0}{\rho gZ}\right)^{-0.5}-\frac{u_b}{u_*}\right] \quad [20]$$

Using Eqs. (16), (19) and (20), the expression for the bed shear stress, $\tau_0$ is obtained as

$$\frac{\tau_0}{\rho gZ}=\left[1-9\frac{\eta}{H}\Omega^{-0.5}\left(\frac{\sigma}{6}\right)^{0.5}\right]F^2\Omega-\left[1-3\Omega^{-0.5}\left(\frac{\sigma}{6}\right)^{0.5}\right]\left(\frac{dh}{dx}+\frac{d\eta}{dx}\right)+\left[\frac{1432}{1449}-\frac{64}{21}\Omega^{-0.5}\left(\frac{\sigma}{6}\right)^{0.5}\right]F^2\frac{d\eta}{dx}+\frac{384}{7}F^2H^2\left\{\left[-\frac{49}{6210}+\frac{1}{32}\Omega^{-0.5}\left(\frac{\sigma}{6}\right)^{0.5}\right]\frac{d^3h}{dx^3}+\left[-\frac{1651}{34040}+\frac{1}{46}\Omega^{-0.5}\left(\frac{\sigma}{6}\right)^{0.5}\right]\frac{d^3\eta}{dx^3}\right\} \quad [21]$$

## 6 FLOW PROFILE AND BED SHEAR STRESS

Eqs. (10) and (21) are the two independent expressions for the bed shear stress. Equating them, we obtain a third-order ordinary differential equation of $\eta$ which governs the flow profile.The solution is sought in the form of

$$\eta=\eta_c\cos kx+\eta_s\sin kx \quad [22]$$

where $\eta_c$ and $\eta_s$ are the coefficients. Eq. (22) is also expressed in the form of $\eta = \eta_m \sin(kx + \chi_\eta)$, where $\eta_m = (\eta_c^2 + \eta_s^2)^{0.5}$; and $\chi_\eta$ is the phase shift between the flow and the bed profiles [$= \tan^{-1}(\eta_c / \eta_s)$].

Now, Eq. (22) is inserted into Eq. (10) to obtain

$$\frac{\tau_0}{\tau_{0m}}=1+\varpi_1\sin kx+\varpi_2\cos kx \quad [23]$$

where $\tau_{0m}$ is the mean bed shear stress ($= \rho gHS_0$);and $\varpi_1$ and $\varpi_2$ are the coefficients.

 

In similar way, Eq. (23) is expressed as $\tau/\tau_{0m} = 1 + \varpi_m \sin(kx + \chi_\tau)$, where $\varpi_m = (\varpi_1^2 + \varpi_2^2)^{0.5}$; and $\chi_\tau$ is the phase shift between the locations of the maximum bed shear stress and the crest of the bed profile [ = $\tan^{-1}(\varpi_2/\varpi_1)$]. Eqs. (22) and (23) represent the flow profile and the bed shear stress profile, respectively. It is evident that the variations of the free surface and the bed shear stress with streamwise distance take sinusoidal form.

## 7 RESULTS

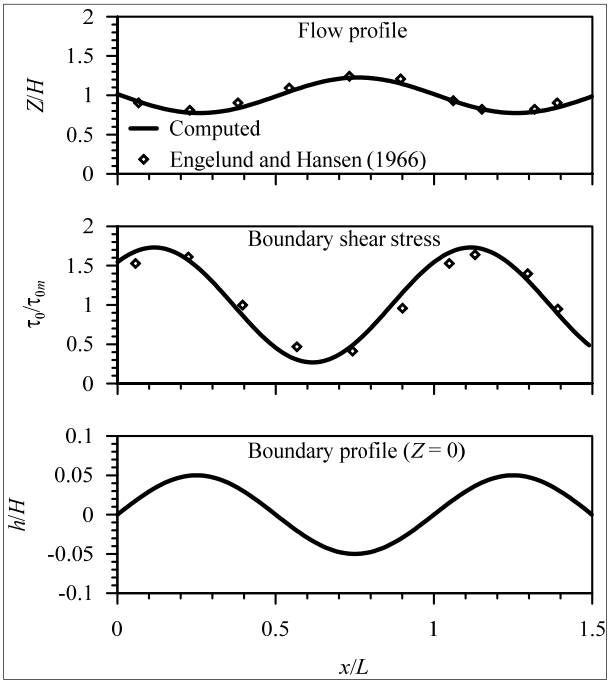


**Figure 2.** Computed flow profile and boundary shear stress profile for subcritical flow and comparison with the experimental data of Engelund and Hansen (1966).

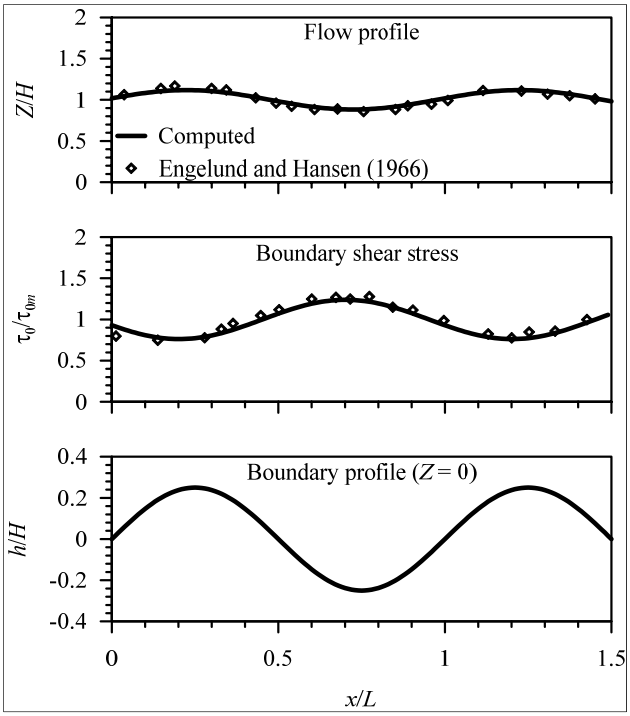


**Figure 3.** Computed flow profile and boundary shear stress profile for supercritical flow and comparison with the experimental data of Engelund and Hansen (1966).

 

For the computation of the flow profile and the bed shear stress profile, the values of the flow parameters are considered as $h_0/H$ = 0.05, $F$ = 0.79, $\Omega = 4.5\times10^{-3}$, and $kH$ = 0.9 for subcritical flow; and $h_0/H$ = 0.25, $F$ = 1.69, $\Omega = 6.94\times10^{-3}$,and $kH$ = 0.19 for supercritical flow. Using these parameters, the flow profile and the bed shear stress profile are computed from Eqs. (22) and (23), respectively. For subcritical flow, Figure 2 depicts the variations of nondimensional free surface ($Z/H$) and bed shear stress ($\tau_0/\tau_{0m}$) with nondimensional streamwise distance ($x/L$) corresponding to bed profile ($h/H$). On the other hand, for supercritical flow, Figure 3 shows the variations of $Z/H$ and $\tau_0/\tau_{0m}$ with $x/L$ corresponding to $h/H$. The phase shifts, $\chi_\eta$ of the flow profile from the bed profile in subcritical and supercritical flows are 3.082 and 0.157, respectively. On the other hand, the phase shifts, $\chi_\tau$ of the location of the maximum/minimum bed shear stress from the crest/trough of the bed in subcritical and supercritical flows are 0.842 and 2.841, respectively. Therefore, in subcritical flow, the flow profile is out of phase with the bed profile; while the bed shear stress profile is almost in phase with the bed profile (Figure 2). However, the flow profile and the bed shear stress profile in supercritical flow are opposite to those in subcritical flow (Figure 3). It is also evident that the amplitudes of the flow profile and the bed shear stress profile in subcritical flow are much larger than those in supercritical flow. In both Figures 2 and 3, the flow and the bed shear stress profiles correspond well to the experimental data of Engelund and Hansen (1966) in subcritical and supercritical flows.

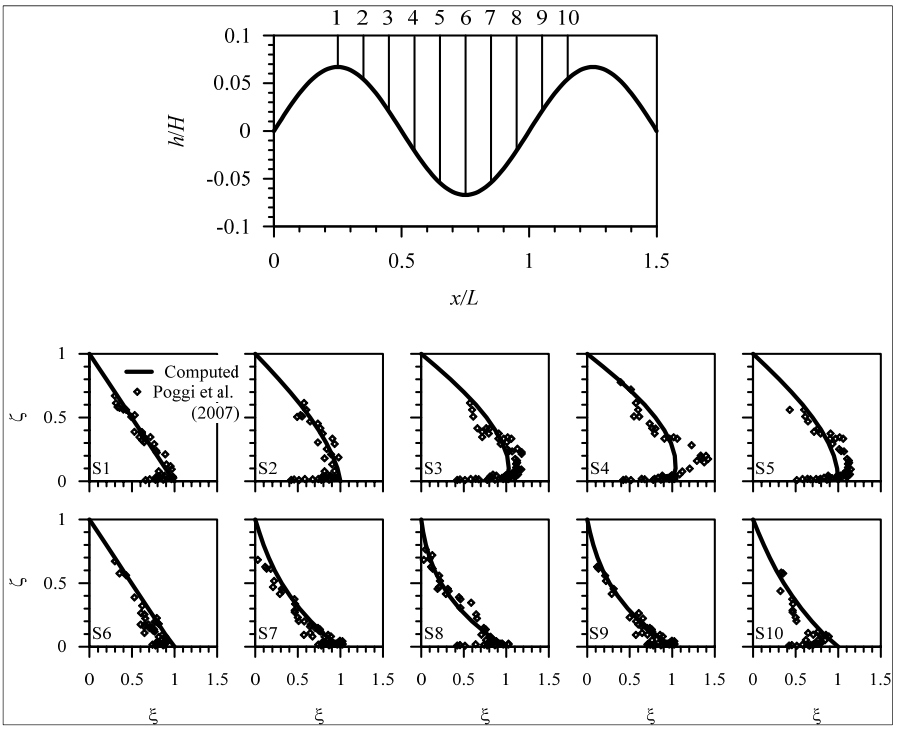


**Figure 4.** Reynolds stress profiles at different sections (S1 to S10) and experimental data of Poggi et al. (2007).

In another numerical experiment, the values of the flow parameters are considered as $h_0/H$ = 0.07, $F$ = 0.1, $\Omega = 5.5\times10^{-3}$, and $kH$ = 0.19. Using these parameters, the nondimensional Reynolds shear stress, $\xi$ as a function of nondimensional vertical distance $\zeta$ at different streamwise locations (S1 to S10, where S1 and S10 refer to sections 1 and 10, respectively, as shown in Figure 4) are computed from Eq. (12) and shown in Figure 4. The $\xi(\zeta)$- profiles are also compared with the corresponding experimental data of Poggi et al. (2007). The flow accelerates over the upslope of the sinusoidal bed and decelerates over the downslope. As a consequence, the $\xi(\zeta)$- profile takes a concave shape over the upslope (S7 to S10); while it is convex over the downslope (S2 to S5). However, the $\xi(\zeta)$- profiles are nearly linear over the crest and the trough (S1 and S6). At S3 and S4, it is evident that close to the bed, the values of $\xi$ exceed unity because of the curvilinear flow induced by the bed resulting in substantial accelerated and decelerated flows. Despite the computed Reynolds shear stress obtained from the present theory underestimates the corresponding experimental data of Poggi et al. (2007) in the vicinity of the bed for some sections, the computed results in general agree satisfactorily with the experimental data.

 

## 8 MOBILE BED FLOW

The analysis for the rigid sinusoidal bed flow in the preceding sections is now extended to the erodible bed. Due to the curvilinear streamlines over a sinusoidal bed, the maximum sediment flux and the maximum bed shear stress do not occur at the same location. There is always a phase lag between the locations of the maximum sediment flux and the maximum bed shear stress. The continuity equation of sediment flux is given by Exner equation (Dey,2014):$\partial q_t/\partial x + (1 - \rho_0)\partial h/\partial t = 0$, where $q_t$ is the total sediment flux and $\rho_0$ is the porosity of sediment. Applying $\Gamma = x - U_w t$, where $U_w$ is the bedform migration velocity, results in $\partial q_t/\partial \Gamma - (1 - \rho_0)U_w \partial h/\partial \Gamma = 0$, which after integration yields $q_t = \overline{q}_t + U_w(1 - \rho_0)h$, where $\overline{q}_t$ is the average total sediment flux ($= q_t|_{h=0}$). Introducing a phase lag distance $l$ between the locations of the maximum sediment flux and the maximum bed shear stress, the following functional relationship at any streamwise location is obtained:

$$\Phi_t(x+l) = f[\Theta(x)] \qquad [24]$$

where $\Phi_t$is the total sediment flux intensity [$= q_t/(\Delta g d^3)^{0.5}$]; $\Delta$ is the submerged relative density; $d$ is the representative sediment size; and $\Theta$ is the Shields parameter [$= u_*^2/(\Delta g d)$]. Thus, Eq. (24) reduces to

$$\Phi_t(x+l) = \overline{\Phi}_t + \frac{U_w(1-\rho_0)}{(\Delta g d^3)^{0.5}} h(x+l) \qquad [25]$$

Using the Taylor series, the local Shields parameter is decomposed as

$$f[\Theta(x)] = f(\overline{\Theta}) + (\Theta - \overline{\Theta}) f'(\overline{\Theta}) \qquad [26]$$

where $\overline{\Theta}$ is the average Shields parameter; and $f(\overline{\Theta}) = \overline{\Phi}_t$. Therefore, combining Eqs. (25) and (26) yields

$$\tau_0(x) = \tau_{0m} + \vartheta h(x+l) \qquad [27]$$

where $\vartheta = U_w(1 - \rho_0)[f'(\overline{\Theta})]^{-1}.(\Delta/gd)^{0.5}$. Using the decomposition $Z(x) = H + \eta(x)$, Eq. (27) is written as

$$\frac{\tau_0}{\rho g Z} = S_0 - \frac{\eta}{H} S_0 + \frac{\vartheta h(x+l)}{H} \qquad [28]$$

Equating Eqs. (28) and (10), the following relationship is obtained:

$$kl = \tan^{-1}\left(\frac{\Im_1 + \Im_2}{\Im_3}\right) \qquad [29]$$

where $\Im_1$, $\Im_2$, and $\Im_3$ are the coefficients.

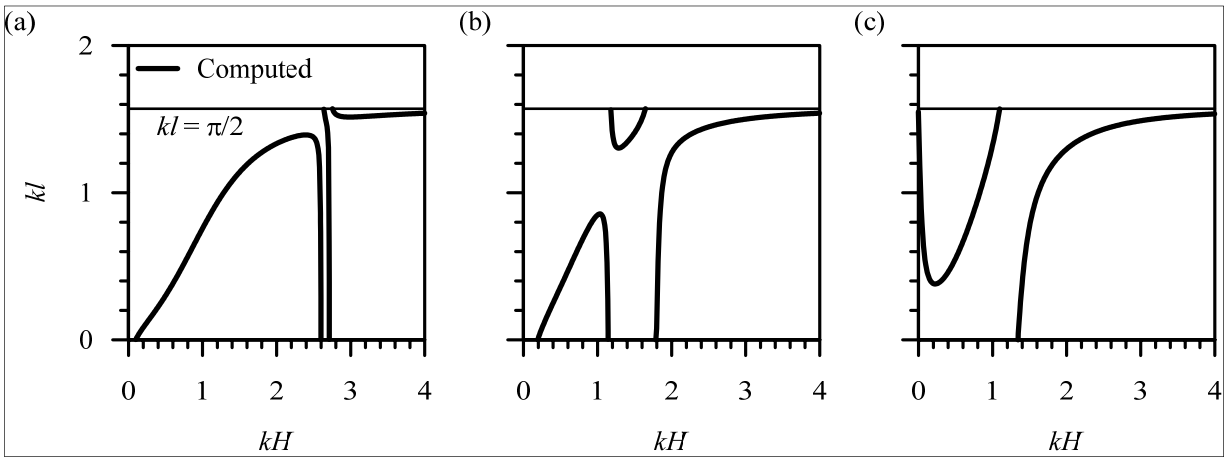


**Figure 5.** Variations of nondimensional phase lag distance, $kl$ with nondimensional uniform flow depth, $kH$ for $\Omega = 5.1\times10^{-3}$ and different values of (a) $F = 0.5$, (b) $F = 0.8$, and (c) $F = 1.2$

 

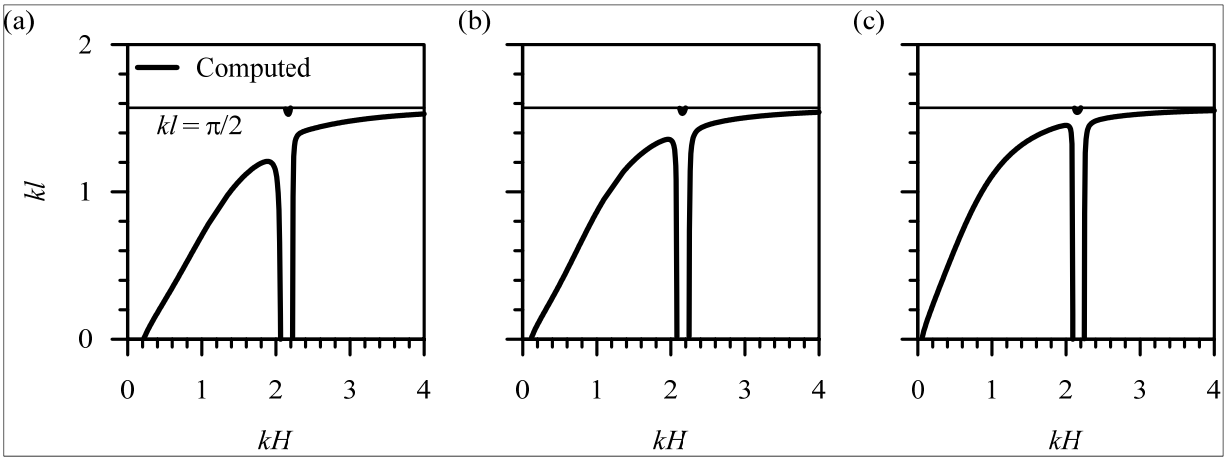


**Figure 6.** Variations of nondimensional phase lag distance, *kl* with nondimensional uniform flow depth, *kH* for $F$ = 0.6 and different values of (a) $\Omega = 1.563\times10^{-2}$, (b) $\Omega = 5.1\times10^{-3}$, and (c) $\Omega = 2.07\times10^{-3}$

In Figures 5(a–c), the variations of nondimensional phase lag distance, *kl* between the sediment flux and the bed shear stress with nondimensional uniform flow depth, *kH* obtained from Eq. (29) for resistance parameter $\Omega = 5.1\times10^{-3}$ and Froude number $F$ = 0.5, 0.8, and 1.2 are shown. Figures 5(a–c) suggest the solution of a feasible flow depth corresponding to a specific phase lag distance, Froude number, and resistance parameter. The feasible solution of *kl* is obtained in the domain of (0, $\pi$/2). Note that Eq. (29) is a cubic equation of *kH*. However, a single root for *kH* is also obtained for some specific values of *kl* as shown in Figures 5(a–c). For $F$ = 0.5 (lower flow regime to occur dunes), three curves appear in the *kl*–*kH* plane [Figure 5(a)]. The phenomenon is due to the periodic nature of the phase lag distance arising from the curvilinear streamlines. For the left curve in Figure 5(a), *kl* increases nonlinearly with an increase in *kH* reaching a peak value *kl* = 1.393 at *kH* = 2.39, and then sharply drops down to *kl* = 0 at *kH* = 2.6. After *kH*= 2.6, the middle curve starts from *kl* = $\pi$/2 and reaches *kl* = 0 at *kH* = 2.72. The right curve originating from *kl* = $\pi$/2, decreases with an increase in *kH*. Then, after reaching *kH* = 2.99, it increases with *kH* and asymptotically approaches to *kl* = $\pi$/2. For an increased value of $F$ ($F$ = 0.8, transitional flow regime to occur washed-out dunes and near-plane beds), three curves appear again in the *kl*–*kH* plane [Figure 5(b)], but the size of the left curve gets smaller than that in Figure 5(a). The left curve in Figure 5(b) reaches the peak (*kl* = 0.856) at *kH* = 1.03 and then sharply reaches *kl* = 0 at *kH* = 1.15. The trends of the middle and right curves shown in Figure 5(b) are fairly different from those shown in Figure 5(a). Starting from *kl* = $\pi$/2, the middle curve reduces with *kH* and after reaching *kl* = 1.303 at *kH*= 1.29, it increases with *kH* reaching *kl* = $\pi$/2 at *kH* = 1.65. The right curve starts from *kH* = 1.79 and increases with *kH* approaching *kl* = $\pi$/2 line asymptotically. With further increase in $F$ ($F$ = 1.2, upper flow regime to occur antidunes) [Figure 5(c)], the middle and right curves shift towards the origin and the left curve does not appear at all. Also, it is identified that the size of the middle curve in Figure 5(c) gets larger than that in Figure 5(b). Therefore, it is obvious from Figures 5(a–c) that the Froude number has substantial effects on the *kl*–*kH* relationship. The effects of the Froude number is attributed to the different characteristics of the flow profiles and the bed shear stress profiles in subcritical and supercritical flows.

Figures 6(a–c) show the variations of *kl* with *kH* obtained from Eq. (29) for $F$ = 0.6 and $\Omega = 1.563\times10^{-2}$, $5.1\times10^{-3}$, and $2.07\times10^{-3}$. It is apparent that the size of the left curve appearing in Figure 6(a) grows slowly with an increase in $\Omega$ [Figures 6(a–c)], indicating a weak effect of $\Omega$ on the *kl*–*kH* relationship. Also, the overall variation of *kl* with *kH* remains nearly similar for all the cases, as the flow belongs to a lower flow regime.

Therefore, from Figures 5 and 6, it is concluded that the influence of the Froude number on the phase lag distance is more predominant than the resistance parameter.

## 9 CONCLUSIONS

A steady turbulent flow over a sinusoidalbed is analyzed by applying the RANS equations and time-averaged continuity equation. A one-seventh law of velocity profile is assumed and the effects of curvilinear streamlines are included in the RANS equations. The flow profiles, bed shear stress and Reynolds shear stress profiles are computed. In subcritical flow, the flow profile is out of phase with the sinusoidal bed profile; while the bed shear stress profile is almost in phase with the sinusoidal bed profile. On the other hand, the flow profile and the bed shear stress profile in supercritical flow are opposite to those in subcritical flow. Upstream of the crest of sinusoidal bed, the Reynolds shear stress profile takes a concave shape, whereas downstream of the crest of sinusoidal bed the Reynolds stress profile takes a convex shape. However, a near-linear profile of the Reynolds shear stress is preserved over the crest and the trough of the sinusoidal bed. The analysis is then extended to the sinusoidal erodible bed by using the sediment continuity equation and

 

introducing the phase lag distance between the sediment flux and the bed shear stress. It is identified that the phase lag distance is primarily influenced by the Froude number.

**REFERENCES**

Benjamin, T.B. (1959). Shearing Flow over a Wavy Boundary. *Journal of Fluid Mechanics*, 6(2), 161-205.

Bose, S.K. & Dey, S. (2007). Curvilinear Flow Profiles Based on Reynolds Averaging. *Journal of Hydraulic Engineering*, 133(9), 1074-1079.

Bose, S.K. & Dey, S. (2009). Reynolds Averaged Theory of Turbulent Shear Flow over Undulating Beds and Formation of Sand Waves. *Physical Review E*, 80(3), 1- 9.

Buckles, J., Hanratty, T.J. & Adrian, R.J. (1984). Turbulent Flow over a Large-Amplitude Wavy Surfaces. *Journal of Fluid Mechanics*, 140, 27- 44.

Calhoun, R.J. & Street, R.L. (2001). Turbulent Flow over a Wavy Surface: Neutral Case. *Journal of Geophysical Research*, 106, 9277-9293.

Cherukat, P., Na, Y., Hanratty, T.J. & McLaughlin, J.B. (1998). *Direct Numerical Simulation of A Fully Developed Turbulent Flow Over A Wavy Wall.* Theoretical and Computational Fluid Dynamics, 11(2), 109-134.

De Angelis, V., Lombardi, P. & Banerjee, S. (1997). Direct Numerical Simulation of Turbulent Flow Over A Wavy Wall. *Physics of Fluids*, 9(8), 2429.

Dey, S. (2014). *Fluvial Hydrodynamics: Hydrodynamic and Sediment Transport Phenomena*. Book, Springer-Verlag, Berlin, Germany.

Dey, S., Bose, S.K. & Castro-Orgaz, O. (2012). *Hydrodynamicsof Undular Free Surface Flows, Experimental and Computational Solutions of Hydraulic Problems.* Springer-Verlag, Berlin, Germany, 53 - 70.

Engelund, F. (1964). *A Practical Approach to Self-Preserving Turbulent Flows*. Acta Polytechnica Scandinavica, Civil Engineering and Building Construction Series, 27.

Engelund, F. & Hansen, E. (1966). *Investigations of Flow in Alluvial Streams*. Acta Polytechnica Scandinavica, Civil Engineering and Building Construction Series, 35.

Frederick, K.A. & Hanratty, T.J. (1988). Velocity Measurements for a Turbulent Nonseparated Flow over Solid Waves. *Experiments in Fluids*, 6(7), 477-486.

Fredsøe, J. (1974). On The Development of Dunes in Erodible Channels. *Journal of Fluid Mechanics*, 64(1), 1-16.

Hayashi, T. (1970). Formation of Dunes and Antidunes in Open Channels. *Journal of the Hydraulic Division*, 96(2), 357-366.

Hudson, J.D., Dykhno, L. & Hanratty, T.J. (1996). *Turbulence Production in Flow over a Wavy Wall.* Experiments in Fluids, 20(4), 257-265.

Iwasa, Y. & Kennedy, J.F. (1968). Free Surface Shear Flow over a Wavy Bed. *Journal of the Hydraulic Division*, 94(2), 431-454.

Kennedy, J.F. (1963). The Mechanics of Dunes and Antidunes in Erodible-Bed Channels. *Journal of Fluid Mechanics*, 16(4), 521-544.

Lamb, H. (1932). *Hydrodynamics*. Book, Cambridge University Press, Cambridge, UK.

Mizumura, K. (1995). Free-Surface Profile of Open-Channel Flow with Wavy Boundary. *Journal of Hydraulic Engineering*, 121(7), 533-539.

Patel, V.C., Chon, J.T. & Yoon, J.Y. (1991). Turbulent Flow in a Channel with a Wavy Wall. *Journal of Fluids Engineering*, 113(4), 579-586.

Poggi, D., Katul, G.G., Albertson, J.D. & Ridolfi, L. (2007). An Experimental Investigation of Turbulent Flows over a Hilly Surface. *Physics of Fluids*, 19(3), 036601.

Reynolds, A.J. (1965). Waves on the Erodible Bed of an Open Channel. *Journal of Fluid Mechanics*, 22(1), 113-133.

Zhaoshun, Z. & Zhan, C. (1989). Numerical Study of Turbulent Flows over Wavy Boundaries. *Acta Mechanica Sinica*, 5(3), 197-204.

Zilker, D.P. & Hanratty, T.J. (1979). Influence of the Amplitude of a Solid Wavy Wall on a Turbulent Flow. Part 2. Separated Flows. *Journal of Fluid Mechanics*, 90(2), 257-271.

Zilker, D.P., Cook, G.W. & Hanratty, T.J. (1977). Influence of the Amplitude of a Solid Wavy Wall on a Turbulent Flow. Part 1. Non-Separated Flows. *Journal of Fluid Mechanics*, 82(1), 29-51.

 

Proceedings of the 37th IAHR World Congress
August 13 – 18, 2017, Kuala Lumpur, Malaysia

# SEDIMENT INCEPTION BY STREAM FLOW: A NOVEL MATHEMATICAL MODEL

SUBHASISH DEY[1] & SK ZEESHAN ALI[2]

[1,2] Department of Civil Engineering, Indian Institute of Technology Kharagpur, West Bengal 721302, India
sdey@iitkgp.ac.in;skzeeshanali@iitkgp.ac.in

## ABSTRACT

In this paper, the inception of non-cohesive sediment motion under a steady uniform free-surface flow over a plane sediment bed is studied by applying the deterministic concept of force analysis. The mathematical formulation starts with the consideration of the force system along with a proper three-dimensional configuration of bed sediment particles. The hydrodynamic force (drag and lift) on a target sediment particle resting over a compact bed formed by equal sized sediment particles is analyzed from the viewpoint of micro-mechanics. The drag force comprises the form drag due to pressure difference across the particle and the form induced drag due to streamwise pressure gradient arising from the convective streamwise acceleration. The hydrodynamic lift force is constituted by the Saffman lift, the Magnus lift, the centrifugal lift, and the lift due to velocity fluctuations. Special emphasis is rendered to determine the points of action of the force system from the basics of micro-mechanics. The primary mode of inception is considered as rolling mode, where the target particle has a tendency to roll either over the summit of a single bed particle or over the valley formed by the two adjacent bed particles. Thus, the turning moment of the force system on the target particle at the pivoting point forms the governing equation of motion. Three different velocity distributions are considered to analyze the sediment inception under hydraulically smooth, transitional, and rough flow regimes. The decay of the viscous sublayer with shear Reynolds number is incorporated into the mathematical analysis. The effects of turbulent fluctuations are addressed by applying the statistical theory of turbulence. This study reveals that for a hindrance coefficient of 0.3, the proposed theoretical sediment inception curve (critical Shields parameter versus shear Reynolds number) shows a satisfactory agreement with the experimental data of uniform sediments.

**Keywords**: Fluvial hydraulics; hydrodynamics; turbulent flow; sediment inception; sediment transport.

## 1 INTRODUCTION

When stream flow interacts with sediments forming the stream bed, hydrodynamic forces are exerted on the sediment particles at the bed surface. As the flow velocity increases, the sediment particles on the bed surface intermittently move at a random rate if the magnitude of the induced hydrodynamic forces acting on the sediment particles exceeds a certain critical value. The flow condition that is adequate to initiate sediment motion is termed *sediment inception* (Shields, 1936; Dey, 2014).

To determine the condition of sediment inception, the concept of critical bed shear stress was widely applied by several researchers (Dey, 2014). This concept is primarily based on the principle of force balance between the destabilizing and the stabilizing forces. However, the concept of moment balance of the force system about the pivoting point was also applied to determine the condition of sediment inception (Coleman, 1967; Dey, 1999; Lee and Balachandar, 2012). Importantly, White (1940) was the first to include the effects of turbulence in the force balance model by considering the instantaneous bed shear stress. The effects of turbulence on sediment inception were effectively addressed in several studies (Iwagaki, 1956; Jackson, 1976; Sechet and le Guennec, 1999; Papanicolaou et al., 2002; Zanke, 2003; Schmeeckle et al., 2007). Although the drag force is the motivating hydrodynamic force responsible for the sediment inception, the lift force also plays a vital role to initiate the sediment motion (Jeffreys, 1929; Wiberg and Smith, 1987; Dey, 1999). The effects of pivoting angle, sorting and hiding of sediment particles on sediment inception were reported by Fenton and Abbott (1977), Wiberg and Smith (1987), Kirchner et al. (1990), Komar and Carling (1991) and Johnston et al. (1998). Moreover, the effects of bed slope on the critical bed shear stress was investigated by Fernandez Luque and van Beek (1976), Ikeda (1982),Chiew and Parker (1994), Armanini and Gregoretti (2005) and Lamb et al. (2008). The trajectories and the different states of motion of sediment particles were evaluated by Francis (1973), Abbott and Francis (1977) and Ancey et al. (2006).

The shortcomings of the previous mathematical models are precisely given in Table 1. Besides, the main drawback of most of the existing force or moment balance models is that the point of action of the force system was not determined following the basics of the mechanics. In addition, the force acting on a target particle was analyzed assuming a two-dimensional approach. Although handful efforts were made to provide an analysis of sediment inception treating a three-dimensional configuration of the bed particles, the effects of turbulence and particle hindrance were overlooked. Therefore, as far as the mechanics of sediment inception

 

are concerned, this model not only overcomes these shortcomings, but also provides a significant advancement of understanding over the existing models.

**Table 1.** Shortcomings of previous studies on modeling the sediment inception.

| Previous models | Shortcomings |
|---|---|
| Iwagaki (1956) | Considered 2D geometry of sediment bed; and ignored lift force in hydraulically smooth flow regime, Saffman lift, Magnus lift, centrifugal lift, and lift due to velocity fluctuations appropriate points of action of force system. |
| Wiberg and Smith (1987) | Considered 2D geometry of sediment bed; and overlooked form induced drag, Magnus lift, centrifugal lift, lift due to velocity fluctuations, appropriate points of action of force system, and turbulence effects. |
| Ling (1999) | Considered 2D geometry of sediment bed; and overlooked form induced drag, lift due to velocity fluctuations, appropriate points of action of force system, turbulence effects and hindrance coefficient. |
| Zanke (2003) | Considered 2D geometry of sediment bed; and ignored form induced drag, Magnus lift, centrifugal lift, lift due to velocity fluctuations, and appropriate points of action of force system. |
| Vollmer and Kleinhans (2007) | Considered 2D lever arms and pivoting angle, a single velocity law for the hydraulically rough flow regime and constant turbulence intensity in the proximity of the bed; and overlooked form induced drag, Magnus lift, centrifugal lift, and hindrance coefficient. |

## 2 THEORETICAL ANALYSIS

### 2.1 Geometry of bed sediment particles

The geometry of bed sediment particles is considered as a spherical target sediment particle of diameter D rests over a compact bed formed by three similar spherical bed particles of diameter d (Figure 1(a)). A tetrahedron $CC_1C_2C_3$ is obtained by connecting the centers of the target and the bed particles (Figure 1(b)). Note that $C_1$, $C_2$ and $C_3$ lie on the plane parallel to xy-plane and $G_1$, $G_2$ and $G_3$ are the points of contact. The projections of point C on $G_1G_2G_3$ and $C_1C_2C_3$ planes are the points I and J, respectively; and the midpoints of $G_2G_3$ and $C_2C_3$ are the points H and P, respectively.

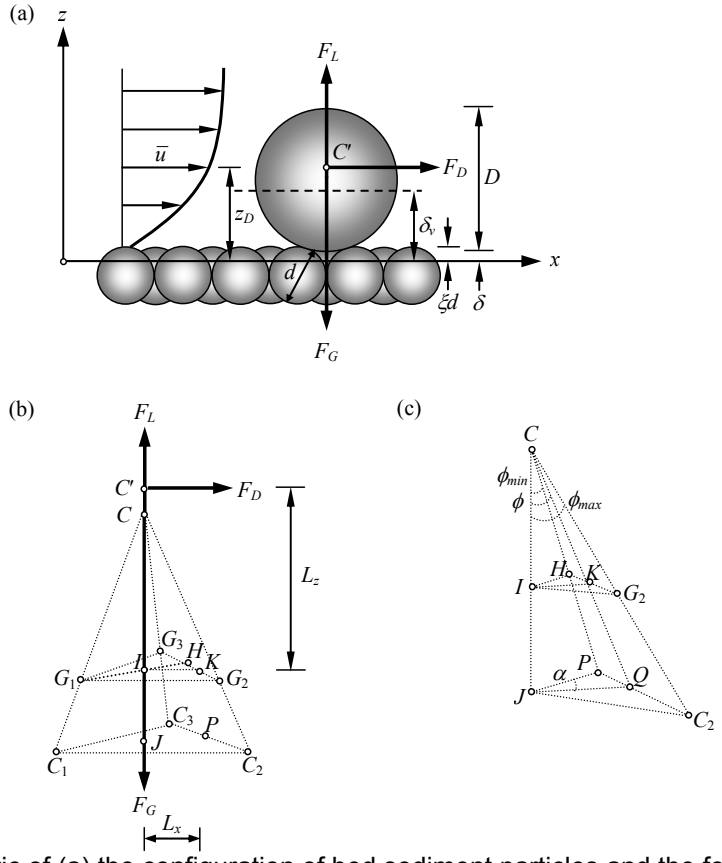


**Figure 1.** Schematic of (a) the configuration of bed sediment particles and the force system, (b) the tetrahedron $CC_1C_2C_3$ and (c) the tetrahedron $CJC_2P$.

 

The coordinate system is depicted in Figure 1(a). The x-axis is considered at a normal distance ξd below the summit of the bed particles. Here, ξ is a proper fraction (< 1). The lowermost point of the target particle is located at a distance δfrom z = 0. Thus, δ = ξd– 0.5(D + d) + CJ. From the geometry, the length CJ isCJ = $(3D^2 + 6Dd – d^2)^{1/2}/(2\sqrt{3})$. Therefore, the $\delta^+$(=δ/D) is given by:

$$\delta^+ = \xi d^+ - 0.5(1 + d^+) + \frac{1}{2\sqrt{3}}(3 + 6d^+ - d^{+2})^{1/2} \quad [1]$$

where $d^+$ is $d/D$.

In the rolling mode, the target particle can roll either over the summit of a single bed particle or through the valley formed by the two adjoining bed particles. In the former case, the target particle rolls the direction $JC_2$ (angle $C_2CJ = \phi_{max}$) (Figure 1(c)). On the other hand, in the latter case, the target particle rolls in the direction $JP$ (angle $PCJ = \phi_{min}$) (Figure 1(c)). We consider the most expected route followed by the target particle is in the direction $JQ$ (Figure 1(c)). The mean value of $JQ$ is obtained as:

$$\overline{JQ} = \frac{1}{\pi/3}\int_0^{\pi/3} JQ\,\mathrm{d}\alpha = \frac{3}{\pi} JP \ln(2 + \sqrt{3}) \quad [2]$$

Therefore, the mean value of pivoting angle $\phi_m$ is:

$$\phi_m = \tan^{-1}\frac{\overline{JQ}}{CJ} = \tan^{-1}\left[\frac{3}{\pi}\ln(2 + \sqrt{3})\frac{k_s^+}{(3 + 6d^+ - d^{+2})^{1/2}}\right] \quad [3]$$

2.2 Force system

The force system is shown in Figure 1(a). The drag force $F_D$ and the lift force $F_L$ act in the $x$- and $z$-direction, respectively. In addition, the submerged weight $F_G$ of the particle acts through its center of gravity vertically downward. The $F_G$ is given by:

$$F_G = \frac{\pi}{6} D^3 \Delta \rho_f g \quad [4]$$

where $\Delta$ is the submerged relative density [= $(\rho_s - \rho_f)/\rho_f$], $\rho_s$ is the sediment mass density, $\rho_f$ is the fluid mass density and $g$ is the gravitational acceleration.

The local instantaneous velocity components ($u$, $w$) in ($x$, $z$) are decomposed as $u = \overline{u} + u'$ and $w = \overline{w} + w'$, where over-bar denotes the time-averaged quantity and prime denotes the fluctuations with respect to time-averaged quantity. The frontal area $A_{z=z}$, representing the projected area bounded within $z = D + \delta$ and $z = z \in (\xi d, D + \delta)$, is obtained as:

$$A_{z=z} = 0.25D^2\{\pi - \cos^{-1}(D + 2\delta - 2z) + 2(D + 2\delta - 2z)[(D + \delta - z)(z - \delta)]^{0.5}\} \quad [5]$$

The drag force $F_D$ comprises the form drag $F_{D1}$ due to pressure difference across the particle and the form induced drag $F_{D2}$ due to streamwise pressure gradient arising from the convective streamwise acceleration. Thus, $F_D = F_{D1} + F_{D2}$. The form drag $F_{D1}$ is given by:

$$F_{D1} = 0.5C_D\rho_f \int_{\xi k_s}^{D+\delta} \overline{u}^2\,\mathrm{d}A \quad [6]$$

where $C_D$ is the drag coefficient. The point of action of $F_{D1}$ is at $z_{D1} = \xi d + r_p$. The $r_p$ can be obtained by equating the summation of the moment of the distributed form drag with the moment of the resulting form drag about the pivoting point. The lower and upper limits of the distributed form drag are considered as ($\xi d$, $D + \delta$).

The form induced drag $F_{D2}$ is given by:

$$F_{D2} = -\left(\frac{\partial \overline{p}}{\partial x}\right)_{z=z_{D2}} TA_{z=\delta_v} \quad [7]$$

 

where $\overline{p}$ is the time-averaged pressure, $z_{D2}$ is the point of action of $F_{D2}$, $T$ is the width of an elementary strip in the $yz$-plane across the target particle at $z = \delta_v$ and $\delta_v$ is the viscous sublayer thickness. The $T$ is expressed as:

$$T(0.5D+\delta \le \delta_v \le D+\delta) = 2[(\delta_v - \delta)(D+\delta-\delta_v)]^{0.5}, \quad [8]$$

$$T(0 < \delta_v < 0.5D+\delta) = D. \quad [9]$$

The point of action of $F_{D2}$ is at:

$$z_{D2}(\xi d \le \delta_v \le D+\delta) = 0.5(D+\delta+\delta_v), \quad [10]$$

$$z_{D2}(0 \le \delta_v \le \xi d) = 0.5(D+\delta+d), \quad [11]$$

Here, we assume that the time-averaged pressure gradients are free from the viscous effects in simplify the analysis. Thus, the Euler equations in $x$- and $z$-direction produce

$$-\left(\frac{\partial \overline{p}}{\partial x}, \frac{\partial \overline{p}}{\partial z}\right) = \rho_f \left(\frac{\overline{\mathrm{D}u}}{\mathrm{D}t}, \frac{\overline{\mathrm{D}w}}{\mathrm{D}t}\right) \quad [12]$$

where D$u$/D$t$ and D$w$/D$t$ refer to the total acceleration components in ($x$, $z$).

Thus, using Eqs. (6), (7) and (12), we obtain:

$$F_D = C_D \rho_f \int_{\xi d}^{D+\delta} \overline{u}^2 [(z-\delta)(D+\delta-z)]^{0.5} \mathrm{d}z + \rho_f \left(\frac{\overline{\mathrm{D}u}}{\mathrm{D}t}\right)_{z=z_{D2}} T A_{z=\delta_v} \quad [13]$$

Therefore, the $F_D^+$ [= $F_D/(\rho_f u_*^2 D^2)$] is:

$$F_D^+ \left(= \frac{F_D}{\rho_f u_*^2 D^2}\right) = C_D \int_{\xi d^+}^{1+\delta^+} \overline{u}^{+2} [(z_0^+ - \delta^+)(1+\delta^+ - z_0^+)]^{0.5} \mathrm{d}z_0^+ + \left(\frac{\overline{\mathrm{D}u^+}}{\mathrm{D}t^+}\right)_{z_0^+ = z_{D2}^+} T^+ A^+_{z_0^+ = \delta_v^+} \quad [14]$$

where $\overline{u}^+$ is $\overline{u}/u_*$, $z_0^+$ is $z/D$, $\delta_v^+$ is $\delta_v/D$, $u^+$ is $u/u_*$, $u_*$ is the shear velocity, $t^+$ is $tu_*/D$, $T^+$ is $T/D$ and $A^+$ is $A/D^2$.

The drag coefficient $C_D$ as a function of shear Reynolds number $R_*$ (= $u_* d/\upsilon$, where $\upsilon$ is the kinematic viscosity) given by Vollmer and Kleinhans (2007), is considered in this study. The $F_D$ acting at the point $C'$ (Figs. 1(a) and 1(b)) is at an elevation $z_D = (F_{D1} z_{D1} + F_{D2} z_{D2})/F_D$.

For a steady flow, the time-averaged forms of D$u$/D$t$ and D$w$/D$t$ are expressed as:

$$\frac{\overline{\mathrm{D}u}}{\mathrm{D}t} = \sqrt{\overline{u'^2}} \sqrt{\overline{\left(\frac{\partial u'}{\partial x}\right)^2}} + \sqrt{\overline{w'^2}} \sqrt{\overline{\left(\frac{\partial u'}{\partial z}\right)^2}} \quad [15]$$

$$\frac{\overline{\mathrm{D}w}}{\mathrm{D}t} = \sqrt{\overline{u'^2}} \sqrt{\overline{\left(\frac{\partial w'}{\partial x}\right)^2}} + \sqrt{\overline{w'^2}} \sqrt{\overline{\left(\frac{\partial w'}{\partial z}\right)^2}} \quad [16]$$

By applying the statistical theory of turbulence (Iwagaki, 1956), we obtain:

$$\overline{\left(\frac{\partial u'}{\partial x}\right)^2} = \frac{\overline{u'^2}}{\lambda^2}, \ \overline{\left(\frac{\partial u'}{\partial z}\right)^2} = \frac{2\overline{u'^2}}{\lambda^2} + \frac{1}{4\overline{u'^2}} \left(\frac{\partial \overline{u'^2}}{\partial z}\right)^2, \ \overline{\left(\frac{\partial w'}{\partial x}\right)^2} = \frac{2\overline{w'^2}}{\lambda^2} \quad [17]$$

where $\lambda$ is the Taylor micro-scale.

 

Substituting Eq. (17) into Eqs. (15) and (16) yields:

$$\overline{\frac{\mathrm{D}u^+}{\mathrm{D}t^+}} = \frac{1}{d^+}\left\{\frac{\sigma_u^{+2}}{\lambda^+} + \sigma_w^+\left[\frac{2\sigma_u^{+2}}{\lambda^{+2}} + \left(\frac{\partial\sigma_u^+}{\partial z^+}\right)^2\right]^{0.5}\right\} \quad [18]$$

$$\overline{\frac{\mathrm{D}w^+}{\mathrm{D}t^+}} = \frac{1}{d^+}\left[\frac{\sqrt{2}\sigma_u^+\sigma_w^+}{\lambda^+} + \sigma_w^+\frac{\partial\sigma_w^+}{\partial z^+}\right] \quad [19]$$

where $w^+$ is $w/u_*$, $\sigma_u^+$ is $\sigma_u/u_*$, $\sigma_u$ is the turbulence intensity in x-direction [= $(\overline{u'u'})^{0.5}$], $\sigma_w^+$ is $\sigma_w/u_*$, $\sigma_w$ is the turbulence intensity in z-direction [= $(\overline{w'w'})^{0.5}$], $z^+$ is z/d and $\lambda^+$ is $\lambda/d$.

The $\sigma_u$ in nondimensional form is expressed as follows (Zanke, 2003):

$$\sigma_u^+ = 0.31z^+R_*\exp(-0.1z^+R_*) + 1.8\exp(-0.88\varpi^{-1})[1-\exp(-0.1z^+R_*)] \quad [20]$$

where $\varpi$ is the relative submergence (= $h/d$) and $h$ is the flow depth. The $\sigma_u^+$ is practically independent of $\varpi$ for $\varpi \geq 100$.

The $\sigma_w$ in nondimensional form is expressed as follows (Grass, 1971):

$$\sigma_w^+ = 0.5\sigma_u^+ \quad [21]$$

To find $\lambda^+$, which appears in the right hand side of Eqs. (18) and (19), we proceed as follows. The turbulent kinetic energy (TKE) dissipation rate $\varepsilon$ is expressed as (Nezu and Nakagawa, 1993):

$$\varepsilon = \frac{0.691}{h^{0.5}}\frac{\sigma_u^3}{z^{0.5}} \quad [22]$$

The Taylor micro-scale $\lambda$ can be related to the TKE dissipation rate $\varepsilon$ as (Pope, 2000):

$$\lambda = \left(15\upsilon\frac{\sigma_u^2}{\varepsilon}\right)^{0.5} \quad [23]$$

Substituting Eq. (22) into Eq. (23) yields:

$$\lambda^+ = \lambda_0^+ + \left(\frac{21.71}{R_*\varpi^{1.5}\sigma_u^+}\right)^{0.5} z^{+0.25} \quad [24]$$

where $\lambda_0^+$ is $\lambda_0/d$ and $\lambda_0$ is the amount of increase in size of the eddies depending on the bed roughness (Iwagaki, 1956).

The hydrodynamic lift force $F_L$ is formed by the Saffman lift $F_{LS}$, the Magnus lift $F_{LM}$, the centrifugal lift $F_{LC}$ and the turbulent lift $F_{LT}$. Thus, $F_L = F_{LS} + F_{LM} + F_{LC} + F_{LT}$.

The Saffman lift $F_{LS}$ on a particle arises when the particle is placed in a shear flow, which has a gradient in velocity distribution. The $F_{LS}^+$ [= $F_{LS}/(\rho_f u_*^2 D^2)$] is expressed as (Saffman, 1965; 1968):

$$F_{LS}^+ = C_L V^+\left(\frac{d^+}{R_*}\frac{\partial\overline{u}^+}{\partial z_0^+}\right)^{0.5} \quad [25]$$

where $C_L$ is the Saffman lift coefficient, $V^+$ is $V/u_*$ and $V$ is the velocity of fluid at an elevation of the center of the target particle. In this study, we consider $C_L = 0.85C_D$. (Chepil, 1961).

The Magnus lift $F_{LM}$ arises due to the spinning motion of particle. The $F_{LM}^+$ [= $F_{LM}/(\rho_f u_*^2 D^2)$] is expressed as (Rubinow and Keller, 1961):

 

$$F_{LM}^{+} = 0.25\overline{u}_{m}^{+}\frac{\partial\overline{u}^{+}}{\partial z_{0}^{+}} \quad [26]$$

where $\overline{u}_{m}^{+}$ is $\overline{u}_m/u_*$, $\overline{u}_m$ is the mean velocity received by the target particle. Note that in the formulation of Eq. (26), we have considered the mean angular velocity $\Omega_m = 0.5\Omega_{max}$, where $\Omega_{max} = 0.5(\partial\overline{u}/\partial z)$.

The centrifugal lift $F_{LC}$ arises due to the rolling motion of solitary particle over the curvature of bed particles. The $F_{LC}^{+}$ [$= F_{LC}/(\rho_f u_*^2 D^2)$] is expressed as (Ling, 1995):

$$F_{LC}^{+} = \frac{\pi}{384\Re^{+}}(1+\alpha_m+\Delta)\left(\frac{\partial\overline{u}^{+}}{\partial z_{0}^{+}}\right)^2\cos\phi_m \quad [27]$$

where $\Re^{+}$ is $\Re/D$,$\Re$ is the radius of curvature of the locus of the moving target particle over the bed particles and $\alpha_m$ is the added mass coefficient (= 0.5). The $\Re$ is considered as the length *CQ* (Figure 1(c)). Thus, the $\Re^{+}$ is:

$$\Re^{+} = \frac{1}{2\sqrt{3}}\left[(3+6d^{+}-d^{+2})+\frac{9d^{+2}}{\pi^2}\ln^2(2+\sqrt{3})\right]^{1/2} \quad [28]$$

The lift due to velocity fluctuations $F_{LT}$ resulting from turbulence is developed due to the pressure gradient along the vertical. The $F_{LT}^{+}$ [$= F_{LT}/(\rho_f u_*^2 D^2)$] is expressed as (Iwagaki, 1956; Ikeda, 1982):

$$F_{LT}^{+}\left(=\frac{F_{LT}}{\rho_f u_*^2 D^2}\right) = \frac{\pi}{4}(1+\delta^{+}-\delta_v^{+})T^{+2}\left(\frac{\overline{\mathrm{D}w^{+}}}{\mathrm{D}t^{+}}\right)_{z_0^{+}=z_{D2}^{+}} \quad [29]$$

Thus, the total lift force $F_{LT}^{+}$ [$= F_{LT}/(\rho_f u_*^2 D^2)$] is $F_{LT}^{+} = F_{LS}^{+} + F_{LM}^{+} + F_{LC}^{+} + F_{LT}^{+}$. The point of action of the lift force passes through the center of the target particle.

### 2.3 Critical shields parameter

For the sediment inception, the moment balance of the force system about the pivoting point is $F_D L_z + F_L L_x = F_G L_x$, where $L_x$ and $L_z$ are the horizontal and the vertical lever arms, respectively (Figure 1). Substituting Eq. (4) into the above condition yields

$$\Theta_c\left(=\frac{u_*^2}{\Delta g D}\right) = \frac{\pi L_x^{+}}{6(F_L^{+}L_x^{+}+F_D^{+}L_z^{+})} \quad [30]$$

where $L_x^{+}$ is $L_x/D$ and $L_z^{+}$ is $L_z/D$.

### 2.4 Lever arms

The horizontal lever arm $L_x$ of the force system is *IK* (Figure 1). Using the geometrical configuration, the $L_x^{+}$ is expressed as

$$L_x^{+} = \frac{\sqrt{3}}{2\pi}\frac{d^{+}}{1+d^{+}}\ln(2+\sqrt{3}) \quad [31]$$

The vertical lever arm $L_z$ of the force system is *C′I* (Figure 1). Using the geometrical configuration, the $L_z^{+}$ is expressed as:

$$L_z^{+} = z_D^{+} - \delta^{+} + \frac{1}{2\sqrt{3}}\frac{(3+6d^{+}-d^{+2})^{1/2}}{1+d^{+}} - 0.5 \quad [32]$$

 

2.5 Mean velocity and velocity gradient

The mean velocity $\overline{u}_m^+$ received by the target particle is expressed as:

$$\overline{u}_m^+ = \frac{2S_c}{A^+_{z_0^+=\xi d^+}} \int_{\xi d^+}^{1+\delta^+} \overline{u}^+ [(z_0^+ - \delta^+)(1+\delta^+ - z_0^+)]^{1/2} \mathrm{d}z_0^+ \qquad [33]$$

where $S_c$ is the hindrance coefficient (< 1).The reason to introduce the hindrance coefficient $S_c$ in this study is that the presence of bed sediment particles upstream of the target particle results in a reduction of flow area received by the target particle. Further, the velocity field in the vicinity of the sediment bed is considerably affected by the surface of the bed particles. As a result, the mean velocity received by the target particle reduces to some extent.

The velocity gradient $\partial \overline{u}^+ / \partial z_0^+$ is then obtained as:

$$\frac{\partial \overline{u}^+}{\partial z_0^+} = \frac{\overline{u}^+_{z_0^+=1+\delta^+} - \overline{u}^+_{z_0^+=\xi d^+}}{1+\delta^+ - \xi d^+} \qquad [34]$$

To obtain the critical Shields parameter $\Theta_c$ for hydraulically smooth, transitional and rough flow regimes, the following cases are considered:

Case 1 ($\delta_v \geq D$): In this case, the target particle is submerged within the viscous sublayer. It, therefore, corresponds to the hydraulically smooth flow regime. The velocity law for this case is expressed as (Dey, 1999):

$$\overline{u}^+ = \frac{u_* z}{\upsilon} = \frac{R_*}{k_s^+} z_0^+ \qquad [35]$$

Case 2 ($0 < \delta_v < D$): In this case, the target particle is partially exposed to the turbulent flow. It, therefore, corresponds to the hydraulically transitional flow regime. The velocity law for this case is expressed as follows (Rotta, 1950):

$$\overline{u}^+ = \frac{1}{\kappa \zeta_{z_0^+=z_0^+}} (0.5 - \sqrt{\zeta^2_{z_0^+=z_0^+} + 0.25}) + \frac{1}{\kappa} \ln(2\zeta_{z_0^+=z_0^+} + 2\sqrt{\zeta^2_{z_0^+=z_0^+} + 0.25}) + R_v \qquad [36]$$

where $\kappa$ is the von Kármán constant, $\zeta = \kappa R_* (z_0^+ - \delta_v^+)/d^+$ and $R_v = u_* \delta_v / \upsilon$. The experimental observation of Nikuradse (1933) on pipe flow indicated that the $R_v$ decreases with $R_*$. Considering the experimental observation of Nikuradse (1933), the $R_v$ is expressed as follows:

$$R_v(R_* < 54.3) = a_0 + a_1 R_* + a_2 R_*^2 + a_3 R_*^3 + a_4 R_*^4 \text{ and}$$
$$R_v(R_* > 54.3) = 0 , \qquad [37]$$

where $a_0 = 7.084$, $a_1 = -14.95 \times 10^{-2}$, $a_2 = -4.46 \times 10^{-3}$, $a_3 = 1.72 \times 10^{-4}$ and $a_4 = -1.54 \times 10^{-6}$.

Case 3 ($\delta_v = 0$): In this case, the target particle is fully exposed to the turbulent flow. It, therefore, corresponds to the hydraulically rough flow regime. The velocity law for this case is expressed as follows (Rotta, 1950):

$$\overline{u}^+ = \frac{1}{\kappa \eta_{z_0^+=z_0^+}} (0.5 - \sqrt{\eta^2_{z_0^+=z_0^+} + 0.25}) - \frac{1}{\kappa R_l} (0.5 - \sqrt{R_l^2 + 0.25}) + \frac{1}{\kappa} \ln \left( \frac{\eta_{z_0^+=z_0^+} + \sqrt{\eta^2_{z_0^+=z_0^+} + 0.25}}{R_l + \sqrt{R_l^2 + 0.25}} \right) \qquad [38]$$

where $\eta$is $(R_l + \kappa R_* z_0^+)/k_s^+$, $R_l$ is $u_* l / \upsilon$ and $l$ is the intercept of the mixing length at $z = 0$. Using the experimental data of Nikuradse (1933), the $R_l$ can be expressed in the following form (Rotta, 1950):

$$R_l(R_* > 54.3) = 0.014 R_* - 0.76 \text{ and}$$
$$R_l(R_* < 54.3) = 0 \qquad [39]$$

 

The experimental investigations of Best et al. (1997) and Dey et al. (2011; 2012) revealed that the value of $\kappa$ decreases in flows over weakly mobile beds. Best et al. (1997) reported an average value of $\kappa$ = 0.385 which is considered here. Further, using the experimental observation of Dey et al. (2012), we consider $\xi$= 0.21.

## 3 RESULTS AND DISCUSSION

In this study, we considered the values of sediment mass density $\rho_s$, fluid mass density $\rho_f$ and kinematic viscosity $\upsilon$ as 2650 kg m$^{-3}$, 10$^3$ kg m$^{-3}$ (water) and 10$^{-6}$ m$^2$ s$^{-1}$, respectively.

Figure 2 shows the curve of critical Shields parameter $\Theta_c$ as a function of critical shear Reynolds number $R_{*c}$ obtained from the present study for $S_c$ = 0.3 along with the experimental data of uniform sediments (Gilbert, 1914; Casey, 1935; Kramer, 1935; Shields, 1936; USWES, 1936; White, 1940; Vanoni, 1946; Meyer-Peter and Müller, 1948; Iwagaki, 1956; Neill, 1967; Grass, 1970; White, 1970; Karahan, 1975; Mantz, 1977; Yalin and Karahan, 1979; Julien 1995; Soulsby and Whitehouse, 1997; Zanke, 2003). The $\Theta_c(R_{*c})$-curve for $S_c$ = 0.3 provided an excellent fitting with the thick band of experimental data over a wide range of $R_{*c}$. Figure 2 showed that for $S_c$ = 0.3, the $\Theta_c$ decreased with an increase in $R_{*c}$ becoming a minimum as $\Theta_c(R_{*c}$ = 16) = 0.025 at and then gradually increased to attain a constant value as $\Theta_c(R_{*c}\geq$ 100) = 0.044 for. According to Yalin and Karahan's (1979) $\Theta_c(R_{*c})$-curve, the critical Shields parameter $\Theta_c$ for hydraulically rough flow regime has a constant value of $\Theta_c$ = 0.046, which closely corresponds to the value of $\Theta_c$ = 0.044 obtained from this study.

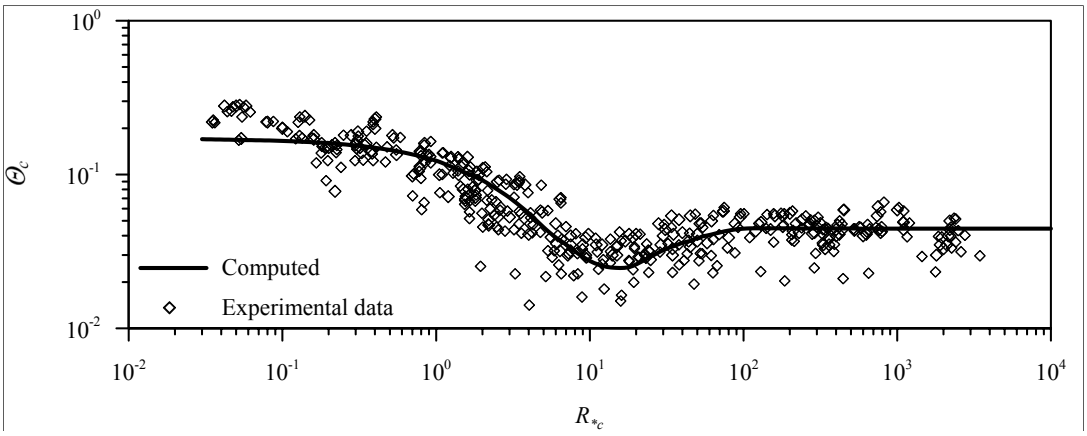


**Figure 2.** Comparison of the curve of critical Shields parameter $\Theta_c$ versus critical shear Reynolds number $R_{*c}$ obtained from the present study for $S_c$ = 0.3 with the experimental data of uniform sediments.

Thus, this study analyzed the inception of sediment particles in 3D configuration by applying the fundamental concepts of hydrodynamics and micro-mechanics. The hydrodynamic force was resolved into drag and lift taking part to the micro-mechanical force system that governed the sediment inception phenomenon. The development of force components depending on the shear Reynolds number was well focused and the decay of viscous sublayer with the shear Reynolds number was incorporated into the mathematical analysis. The points of action of the hydrodynamic forces were obtained from the basics of mechanics. The effects of velocity fluctuations were addressed in the analysis by applying the statistical theory of turbulence. In addition, the reduction in mean velocity received by the target particle due to the bed particles was incorporated by introducing the hindrance coefficient. Thus, the present study provides a more realistic treatment of sediment inception phenomenon than previous ones.

## 4 CONCLUSIONS

A novel analytical model is developed to obtain the critical bed shear stress to initiate non-cohesive sediment motion under a steady uniform free-surface flow. The principal mode of sediment inception is considered as rolling mode. The forces acting on a target sediment particle resting over three similar closely packed bed particles are analyzed from the basics of the hydrodynamics and micro-mechanics. The hydrodynamic drag force consists of form drag and form induced drag; while the hydrodynamic lift force includes Saffman lift, Magnus lift, centrifugal lift and lift due to velocity fluctuations. The effects of velocity fluctuations are addressed by applying the statistical theory of turbulence. Different velocity laws are used in the analysis to investigate the sediment inception under hydraulically smooth, transitional and rough flow regimes. The inception curve obtained from this study shows a reasonable agreement with the experimental data of uniform sediments.

 

**REFERENCES**

Abbott, J.E. & Francis, J.R.D. (1977). Saltation and Suspension Trajectories of Solid Grains in a Water Stream. *Philosophical Transactions of the Royal Society of London A*, 284, 225–254.

Ancey, C., Böhm, T., Jodeau, M. & Frey, P. (2006). Statistical Description of Sediment Transport Experiments. *Physical Review E*, 74(011302), 1–14.

Armanini, A. & Gregoretti, C. (2005). Incipient Sediment Motion at High Slopes in Uniform Flow Condition. *Water Resources Research*, 41(W12431), 1–8.

Best, J., Bennett, S., Bridge, J. & Leeder, M. (1997). Turbulence Modulation and Particle Velocities over Flat Sand Beds at Low Transport Rates. *Journal of Hydraulic Engineering*, 123, 1118–1129.

Casey, H.J. (1935). Über Geschiebebewegung. Mitteilungen der Preussischen Versuchsanstalt für Wasserbau und Schiffbau, Berlin, Germany.

Chepil, W.S. (1961). The Use of Spheres to Measure Lift and Drag on Wind-Eroded Soil Grains. *Proceedings of the Soil Science Society of America*, 25, 343–345.

Chiew, Y. & Parker, G. (1994). Incipient Sediment Motion on Non-Horizontal Slopes. *Journal of Hydraulic Research*, 32, 649– 660.

Coleman, N.L. (1967). A Theoretical and Experimental Study of Drag and Lift Forces Acting on a Sphere Resting on a Hypothetical Stream Bed. *Proceedings of the 12th congress of International Association for Hydraulic Research* (Fort Collins, Colorado), 3, 185–192.

Dey, S. (1999). *Sediment Threshold.* Applied Mathematical Modelling, 23, 399–417.

Dey, S. (2014). *Fluvial Hydrodynamics: Hydrodynamic and Sediment Transport Phenomena*, Book, Springer-Verlag, Berlin, Germany.

Dey, S., Das, R., Gaudio, R. & Bose, S.K. (2012). Turbulence in Mobile-Bed Streams. *Acta Geophysica*, 60, 1547–1588.

Dey, S., Sarkar, S. & Solari, L. (2011). Near-Bed Turbulence Characteristics at the Entrainment Threshold of Sediment Beds. *Journal of Hydraulic Engineering*, 137, 945–958.

Fenton, J.D. & Abbott, J. E. (1977). Initial Movement of Grains on a Stream Bed: The Effect of Relative Protrusion. *Proceedings of the Royal Society of London A*, 352, 523–537.

Fernandez Luque, R. & van Beek, R. (1976). Erosion and Transport of Bed-Load Sediment. *Journal of Hydraulic Research*, 14, 127– 144.

Francis, J.R.D. (1973). Experiments on the Motion of Solitary Grains along the Bed of a Water-Stream. *Proceedings of the Royal Society of London A*, 332, 443–471.

Gilbert, G.K. (1914). *The Transportation of Debris by Running Water,* Professional Paper Number 86, United States Geological Survey, Washington DC, USA.

Grass, A.J. (1970). Initial Instability of Fine Bed Sand. *Journal of the Hydraulic Division*, 96, 619–632.

Grass, A.J. (1971). Structural features of Turbulent Flow over Smooth and Rough Boundaries. *Journal of Fluid Mechanics*, 50, 233–255.

Ikeda, S. (1982). Incipient Motion of Sand Particles on Side Slopes. *Journal of the Hydraulic Division*, 108, 95–114.

Iwagaki, Y. (1956). Fundamental Study on Critical Tractive Force. *Transactions of the Japan Society of Civil Engineers*, 41, 1–21.

Jackson, R.G. (1976). Sedimentological and Fluid-Dynamic Implications of Turbulent Bursting Phenomenon in Geophysical Flows. *Journal of Fluid Mechanics*, 77, 531–560.

Jeffreys, H. (1929). On the Transport of Sediments by Streams. *Proceedings of the Cambridge Philosophical Society*, 25, 272–276.

Johnston, C.E., Andrews, E.D. & Pitlick, J. (1998). In Situ Determination of Particle Friction Angles of Fluvial Gravels. *Water Resources Research*, 34, 2017–2030.

Julien, P.Y. (1995). *Erosion and Sedimentation*. Cambridge University Press.

Karahan, E. (1975). Initiation of Motion for Uniform and Non-Uniform Materials, PhD Thesis. Technical University, Istanbul, Turkey.

Kirchner, J.W. Dietrich, W.E., Iseya, F. & Ikeda, H. (1990). The Variability of Critical Shear Stress, Friction Angle & Grain Protrusion in Water-Worked Sediments. *Sedimentology*, 37, 647–672.

Komar, P.D. & Carling, P.A. (1991). Grain Sorting in Gravel-Bed Streams and the Choice of Particle Sizes for Flow-Competence Evaluations. *Sedimentology*, 38, 489– 502.

Kramer, H. (1935). Sand Mixtures and Sand Movement in Fluvial Model. *Transactions of the ASCE*, 100, 798–838.

Lamb, M.P., Dietrich, W.E. & Venditti, J.G. (2008). Is the Critical Shields Stress for Incipient Sediment Motion Dependent on Channel-Bed Slope? *Journal of Geophysical Research*, 113(F02008), 1–20.

Lee, H. & Balachandar, S. (2012). Critical Shear Stress for Incipient of a Particle On A Rough Bed. *Journal of Geophysical Research*, 117(F01026), 1–19.

Ling, C.H. (1995). Criteria for Incipient Motion of Spherical Sediment Particles. *Journal of Hydraulic Engineering*, 121, 472–478.

 

Mantz, P.A. (1977). Incipient Transport of Fine Grains and Flakes by Fluids–Extended Shields Diagram. *Journal of the Hydraulic Division*, 103, 601–615.
Meyer-Peter, E. & Müller, R. (1948). Formulas for Bed-Load Transport. *Proceedings of the 2nd meeting of International Association for Hydraulic Research* (Stockholm, Sweden), 3, 39–64.
Neill, C.R. (1967). Mean Velocity Criterion for Scour of Course Uniform Bed Material. *Proceedings of the 12th Congress of International Association for Hydraulic Research* (Fort Collins, Colorado, USA), 3, 46–54.
Nezu, I. & Nakagawa, H. (1993). *Turbulence in Open-Channel Flows*. Book, Balkema, Rotterdam, The Netherlands.
Nikuradse, J. (1933). *Strömungsgesetze in Rauhen Rohren,* Research Bulletin, 361, Berlin, Germany.
Papanicolaou, A.N., Diplas, P., Evaggelopoulos, N. & Fotopoulos, S. (2002). Stochastic Incipient Motion Criterion for Spheres under Various Bed Packing Conditions. *Journal of Hydraulic Engineering*, 128, 369–380.
Pope, S.B. (2000). *Turbulent Flows*. Book, Cambridge University Press, Cambridge.
Rotta, J. (1950). *Das in Wandnähe Gültige Geschwindigkeitsgesetz Turbulenter Strömungen.* Archieve of Applied Mechanics, 18, 277–280.
Rubinow, S.I. & Keller, J.B. (1961). The Transverse Force on a Spinning Sphere Moving in a Viscous Fluid. *Journal of Fluid Mechanics*, 11, 447–459.
Saffman, P.G. (1965). The Lift on a Small Sphere in a Slow Shear Flow. *Journal of Fluid Mechanics*, 22, 385–400.
Saffman, P.G. (1968). Corrigendum, the Lift on a Small Sphere in a Slow Shear Flow. *Journal of Fluid Mechanics*, 31, 624.
Schmeeckle, M.W., Nelson, J.M. & Shreve, R.L. (2007). Forces on Stationary Particles in Near-Bed Turbulent Flows. *Journal of Geophysical Research*, 112(F02003), 1–21.
Sechet, P. & le Guennec, B. (1999). Bursting Phenomenon and Incipient Motion of Solid Particles in Bed-Load Transport. *Journal of Hydraulic Research*, 37, 683–696.
Shields, A.F. (1936). Application of Similarity Principles and Turbulence Research to Bed-Load Movement. *Mitteilungen der Preussischen Versuchsanstalt für Wasserbau und Schiffbau,* 26, 5–24, Berlin, Germany.
Soulsby, R.L. & Whitehouse, R.J.S. (1997). Threshold of Sediment Motion in Coastal Environments. *Proceedings of the Combined Australasian Coastal Engineering and Port Conference*, Christchurch, New Zealand, 149–154.
USWES. (1936). *Flume Tests Made to Develop a Synthetic Sand which will not Form Ripples when Used in Movable Bed Models,* Technical memorandum 99-1, United States Waterways Experiment Station, Vicksburg, Mississippi, USA.
Vanoni, V.A. (1946). Transportation of Suspended Sediment by Water. *Transactions of the ASCE*, 111, 67–102.
Vollmer, S. & Kleinhans, M.G. (2007). Predicting incipient motion, including the Effect of Turbulent Pressure Fluctuations in the Bed. *Water Resources Research*, 43(W05410), 1–16.
White, C.M. (1940). The Equilibrium of Grains on the Bed of a Stream. *Proceedings of the Royal Society of London A*, 174, 322–338.
White, S.J. (1970). Plane Bed Thresholds of Fine Grained Sediments. *Nature*, 228, 152–153.
Wiberg, P.L. & Smith, J.D. (1987). Calculations of the Critical Shear Stress for Motion of Uniform and Heterogeneous Sediments. *Water Resources Research*, 23, 1471–1480.
Yalin, M.S. & Karahan, E. (1979). Inception of Sediment Transport. *Journal of the Hydraulic Division*, 105, 1433–1443.
Zanke, U.C.E. (2003). On the Influence of Turbulence on the Initiation of Sediment Motion. *International Journal of Sediment Research*, 18, 17–31.

 

Proceedings of the 37th IAHR World Congress
August 13 – 18, 2017, Kuala Lumpur, Malaysia

# DAM BREAK FLOW OVER MOBILE BED: VELOCITY DISTRIBUTION

ILARIA FENT[(1)]

[(1)]Université Catholique De Louvain (Uclouvain), Louvain-La-Neuve, Belgium,
ilaria.fent@uclouvain.be

## ABSTRACT

Knowledge of the velocity distribution is a key for understanding and modelling any type of flow. The velocity profile can provide an image of turbulent exchanges inside the flow and constitutes one of the classical ways for evaluating the flow resistance. Moreover, most of depth-averaged 1D and 2D-H numerical models are based on assumptions about the velocity distribution, especially if bed load sediment transport is involved. The velocity distribution is extensively studied in the first half of the 20$^{th}$ century, mainly for steady uniform flows in smooth and rough pipes. Theoretical and experimental approaches apply a logarithmic law in the inner region, in the vicinity of the bed. With the development of non-intrusive measurement techniques, more and more complex situations are investigated: unsteady flows on fixed bed, steady and unsteady flows over mobile bed. Logarithmic velocity distribution is observed in all these cases. In particular, Sumer et al. (1996) experiments on steady flow over mobile bed show that the log-law also prevails in the upper part of the moving sediment layer. This paper presents results in an extreme transient case: a dam-break flow over mobile bed. The velocity distribution in the clear-water layer is observed as quasi uniform, while the sediment layer presents a velocity distribution very similar to the observations made in steady uniform flow cases.

**Keywords:** Dam-break flow; PIV; depth velocity profiles; mobile bed.

## 1 INTRODUCTION

Velocity distribution inside a free-surface flow is one of the most interesting and challenging problems in fluid mechanics. It is interesting because it allows for a better understanding of the flow structure and the flow resistance, and challenging because accurate measurements require non-intrusive techniques in order to prevent flow perturbation by the measurement itself.

In line with the development of these measurements, velocity distributions in closed pipes and in free-surface flow have been investigated in more and more complex and realistic situations.

Nikuradse (1933) carried out numerous experiments in steady flow condition in circular pipes covered on the inside with sand of a known grain size glued on the wall, the diameter of this sand grains being defined as the Nikuradse's sand roughness $k_s$. From his experiments and from Keulegan's (1938) experiments in a flume with steady uniform flow, a logarithmic velocity distribution was observed, in accordance with Prandtl's mixing-length theory. However, deviations from this logarithmic distribution were observed in the close vicinity of the wall, at least for smooth walls, and in the upper part (the outer region) of the flow where a wake effect affects the velocity. The zone where a log-law profile was observed is defined as the inner region.

With the progression of non-intrusive measurements based on imagery techniques, like PIV (Particle Image Velocimetry) based on autocorrelation between successive images (Keane and Adrian, 1992; Raffel et al., 2007; Adrian, 2011), and PTV (Particle Tracking Velocimetry) following the particles in their trajectories (Capart et al., 2002), it became possible to investigate the velocity distribution also in non-uniform and unsteady flows. For instance, Tu (1991) investigated the velocity field in a gravel-bed flume supplied by thirteen typical hydrographs as close as possible to natural ones. In his work, the velocity distribution revealed to be slightly different in the rising branch of the hydrograph compared to the falling branch, but the log-law distribution is still valid in the so-called inner region.

Sumer et al. (1996) carried out extensive investigation in a tilting flume (10 m in length, 0.3 m in depth, 0.3 m in width) with recirculation of water and sediment, under steady flow conditions. Using 4 types of sediment, 158 experiments were carried out with measurement of velocity not only in the clear water layer but also in the sheet-flow layer. It was observed that the log-law developed also in the upper part of the sediment layer, in line with the log-law in the water inner region.

For unsteady flows over mobile bed, velocity profiles over the water depth have been studied by some researchers, e.g. Nikora and Goring (2000), Qu (2003) and de Moraes Franklin et al. (2014). They confirmed the presence of a logarithmic velocity profile in the lower zone of the water column and they observed that the friction at the bottom is affected by the granular mobility. No significant differences were observed in the inner region between experiments conducted over fixed bed or mobile bed. Apparently, the velocity distribution inside the sediment layer was not considered in these approaches.

 

With regards to highly unsteady flows such as dam-break flows, numerous experimental data are available for fixed bed conditions, generally flatbed (Bellos et al., 1992; Lauber and Hager, 1998; Stansby et al., 1998; Aleixo et al. 2011), but there are fewer data sets of dam-break flow over mobile bed (Capart and Young, 1998; Khan et al., 2000; Fraccarollo and Capart, 2002; Leal et al. 2006; Soares-Frazão et al., 2007; Aleixo, 2013; Spinewine et Capart, 2013). Also, in these available experiments concerning either high concentration transport flow such as debris flow or bed load transport flow, the detailed velocity field is seldom measured.

The present paper aims at presenting such detailed dam-break flow experiments over mobile bed, composed by non-cohesive sand, and the velocity distributions measured as well in the water inner region as in the sheet-flow layer.

## 2 EXPERIMENTAL SET-UP

### 2.1 The dam-break channel

Experiments were performed in a dedicated flume designed at the Universitécatholique de Louvain, Civil Engineering Department. The dam-break channel had on overall length of 6 m, and a rectangular cross section defined by a width of 0.25 m and a height of 0.5 m. The channel was divided in two equal reaches by a downward moving gate used to simulate the instantaneous removal of a dam. Special attention was devoted to the design of this gate, with the ambition to reach initial test conditions that approach as much as possible the idealization of an instantaneous dam collapse, while minimizing perturbations to the sediments and water during gate removal (Spinewine and Zech, 2007). Indeed, upward moving gates in a sediment bed induced significant spurious flow circulations as shown in Shin et al. (2004). The walls of the channel were made of glass, allowing optical access to the flow. The bottom of the channel was made of impervious polished wood, yet it can be changed and modified to fit the research needs. Figure 1 shows an overview of the experimental apparatus during the tests.


**Figure 1.** Dam-break channel at the laboratory of Université Catholique de Louvain.

The bottom of the channel was filled with 0.1 m of non-cohesive sand with the following characteristics: the grain-size distribution was quasi-uniform with a mean diameter $d_{50}$ = 1.72 mm, a density $\rho$ = 2.682x10$^{-3}$ kgm$^{-3}$, a friction angle $\phi$ = 38° and the bed porosity $\varepsilon_0$ = 0.42. In order to ensure the repeatability of the experiments for each test, the sand on the bed was compacted and saturated. This aims at avoiding the creation of air bubbles within the dam-break wave and at bypassing the difficulty of drying the entire volume of sand after each experiment.

The upstream half of the channel (i.e. the first 3 meters) consisting of the reservoir was filled with a water depth of $h_0$ = 0.325 m over the sand bed.

### 2.2 Velocity field measurement by imagery technique

For measuring bed and water profiles and the velocity field for such a fast transient flow, Particle Image Velocimetry (PIV) technique was adopted. A continuous red laser sheet (power = 100 mW, wave length = 660 nm) illuminated a section of the flow previously seeded with pliolite particles and the high speed camera acquired images at regular short interval (500 frames per second).

The detection of velocity vectors was made with sub-pixel accuracy by fitting a Gaussian curve to the correlation intensity distribution (Raffel et al., 2007). Moreover, the possibility of deforming and decreasing the size of the interrogation window in which the velocity vector was detected allowed better survey flow gradients. This technique is called multi-pass. The PIV algorithm used was the one developed by the company LaVision: Davis 8.2.

Thanks to this non-intrusive technique, it is possible to measure not only the velocity profile but also the water and bottom surface contours that are also space and time dependent.

 

2.3 Bottom and water surface profile extraction

The accuracy and the high frequency of recorded images allow the measurement of the water and bottom profiles that are rapidly evolving in space and time. Each image was treated in an automated way (Soares-Frazão et al., 2007) in order to determine the two main limits (bottom and free water surface) of the fluids. The line corresponding to the water surface was directly defined. The bottom with moving sediments showed a thicker zone to be delineated, due to some laser light reflections on the sediment grains. In order to identify the real sediment bed, the image was blurred by a Gaussian function or similar and then a threshold color was applied. Thanks to this practice, the moving sediment layer was isolated and the two lines corresponding to its upper and lower limits were determined.

The final water surface ($z_w$) and upper ($z_{b,up}$) and lower ($z_{b,low}$) bottom profiles were successively compared to the velocity field. Superposing the velocity profiles with the fixed bottom profile, it was possible to check the correct position of $z_{b,low}$ (Figure 2).

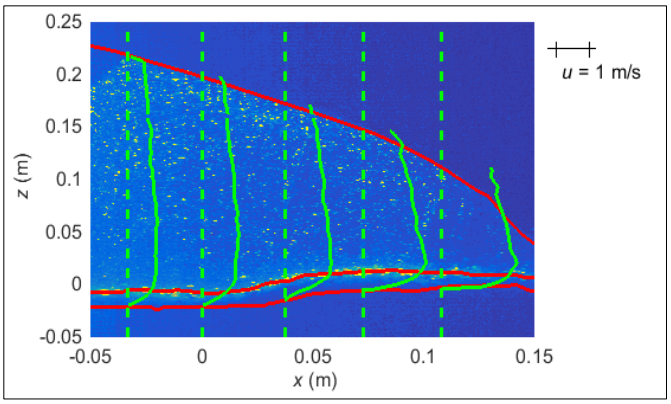


**Figure 2.** Velocity profiles (green lines) at time 0.3s, for different sections, superposed to the rough image and the extracted water profile and bed profiles (red lines).

## 3 VELOCITY DISTRIBUTION IN VARIOUS TYPES OF FLOW

3.1 Velocity distribution in steady uniform flow over fixed bed

The velocity profile for uniform flows in a channel has been extensively studied in the early years of the 20th century, but experimental results reported by Nikuradse (1933) for smooth and rough pipes are generally considered as decisive.

From these measurements, the vertical distribution of the longitudinal velocity component $u$ is described by a logarithmic function, at least along a part of the flow depth. For smooth walls, the flow profile is linear near the wall (Eq.[1a]), while it is logarithmic above a certain level (Eq.[1b]).

$$\frac{u}{u_*} = \frac{u_* z}{\nu} \qquad [1a]$$

$$\frac{u}{u_*} = \frac{1}{\kappa} \ln\left(\frac{u_* z}{\nu}\right) + B_s \qquad [1b]$$

where $u_*$ is the shear velocity, $z$ is the distance from the fixed bottom, $\nu$ is the kinematic viscosity of water, $\kappa = 0.4$ is the Von Karman constant and $B_s$ is the integral constant for smooth boundaries, equal to 5.50 from Nikuradse experiments (Figure 3).

 

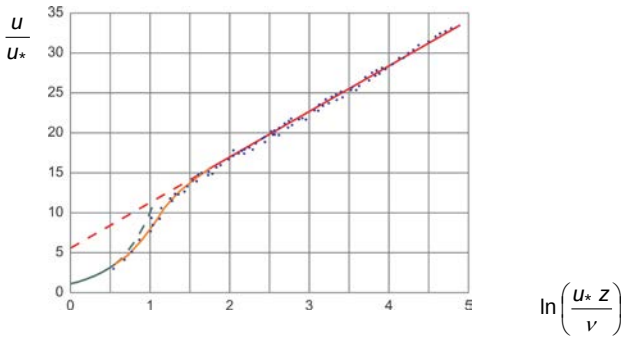


**Figure 3.** Velocity distribution for smooth pipes (Nikuradse, 1933).

Eq. [1a] prevails in the immediate neighboring of the wall in the laminar sub-layer where turbulent friction may be neglected compared to the laminar shear stress. This zone is defined by the condition

$$\frac{u_* z}{\nu} < 5 \qquad [2c]$$

Conversely, Eq. [1b] corresponds to a purely turbulent friction in a zone defined by the condition

$$\frac{u_* z}{\nu} > 70 \qquad [3d]$$

that defines the turbulent boundary layer. The logarithmic distribution [1b] could also be deduced from Prandtl's mixing-layer theory (Schlichting, 1968) where the mixing length is proportional to the distance from the wall, with the idea that turbulent friction is due to momentum exchanges between flow layers, and that this exchange is easier further away from the wall, where turbulent components of the vertical velocity may develop with less constraint.

For a boundary that is hydraulically rough, the wall irregularities break down the laminar layer and they determine directly the velocity profile. Eq. [4a] describes the logarithmic velocity profile that depends on $k_s$, which is the equivalent sand roughness, i.e the grain size of the glued sand used by Nikuradse onto the wall for representing the roughness:

$$\frac{u}{u_*} = \frac{1}{\kappa} \ln\left(\frac{z + z_0}{k_s}\right) + B_r \qquad [4a]$$

where $z_0$ is a reference level and $B_r$ is the integral constant for rough boundaries. If the wall is completely rough, it corresponds to the condition

$$\frac{u_* k_s}{\nu} > 70 \qquad [2b]$$

the constant $B_r$ = 8.5 for $z_0$ = 0, according to Nikuradse results (Figure 4). For experiments with flows over non-moving sediments of diameter $d_s$, Song and Graf (1996) defined the origin of $z$ as the top surface of the gravel bed but with a reference adjustment $z_0 = 0.25\ d_s$.

For free-surface flows, the logarithmic distribution is affected by a wake effect due to the influence of the water surface. So an additional term due to Coles (1956) is to be added in the so-called outer region. The inner region, where the log law is valid, is limited to a given value of the relative depth z/h, where h is the water depth. The value z/h = 0.20 is often considered for this limit (Graf and Altinakar, 1998). As only the inner region is affected by the moving sediments, the outer region was not considered in detail in this work.

 

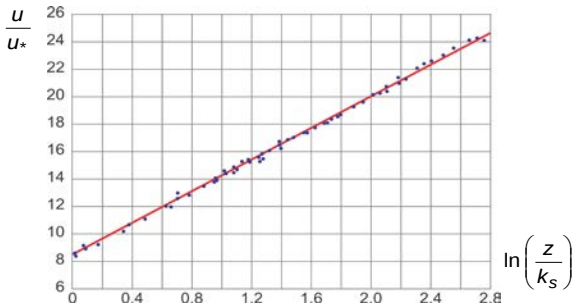


**Figure 4.** Velocity distribution for rough pipes (Nikuradse, 1933).

3.2 Velocity distribution in unsteady flow over fixed bed

Song and Graf (1996) proved that the log law [4a] is valid even for unsteady flows in open channels with gravel bed. The reference level $z_0$ is posed equal to 0.25 $k_s$ by Song and Graf (1996) and the constant Br = 8.5 ± 15% in the inner region, being almost independent of the flow unsteadiness. Following the authors, the dominant mechanisms for production of turbulence in these unsteady flow turbulent boundary layers cannot differ greatly from those in the steady flow boundary layer (Brereton et al., 1990). In particular they found that, similarly to steady flow cases, the logarithmic law is valid in the inner region near the bed, where $z/h \leq 0.2$, and Coles' wake law is valid in the outer region.

The flow unsteadiness induces a pressure gradient, where the influence is negligible in the inner region but effective in the outer region. If the flow is decelerated, the maximum velocity is found at the free surface and $u/u_*$ is larger than the log-law value in the outer region, while the maximum velocity is found below the free surface for accelerating flow and $u/u_*$ is smaller than the log-law value in the outer region (Kironoto and Graf, 1994).

3.3 Velocity distribution in steady flow over mobile bed

In a flume with recirculation of water and sediments, Sumer et al. (1996) reproduced a steady uniform flow over a mobile bed. They studied the sediment transport near the bed, which takes place in a layer with a thickness much larger than the grain size, called the sheet flow layer. Regarding the velocity profile, Sumer et al. (1996) discovered that the logarithmic velocity profile is present as well in the water inner region as in the upper part of the sediment layer (Figure). It must be noted that in their experiments the water surface was smoothened by a rigid lid that affects the outer zone.

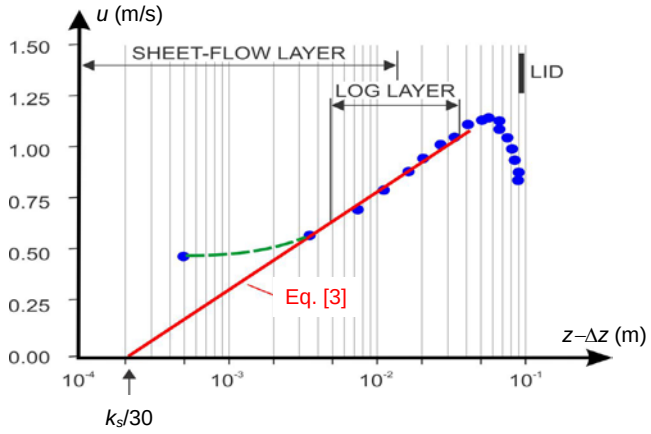


**Figure 5.** Typical velocity distribution with logarithmic law near bed in presence of a sheet-flow layer, after Sumer et al. (1996).

Following Sumer et al. (1996), the upper part of the sheet flow layer and the inner region of the water flow present a logarithmic velocity distribution similar to Eq. [2a] but with a modified definition of $z$:

$$\frac{u}{u_*} = \frac{1}{\kappa}\ln\left(\frac{30(z-\Delta z)}{k_s}\right) = \frac{1}{\kappa}\ln\left(\frac{z-\Delta z}{k_s}\right) + 8.50 \qquad [3]$$

where $z$ is now the distance to the bottom of the sheet-flow layer, i.e. the limit between immobile and mobile sediments, and $\Delta z$ is the "theoretical" bed level above the bottom of the sheet-flow layer. This level depends on the Shield's parameter defined as

 

$$\theta = \frac{\rho u_*^2}{g\left(\rho_s - \rho\right)d} \qquad [4]$$

where $\rho_s$ and $\rho$ are the density of grains and water, respectively, $g$ the acceleration of gravity, and $d$ the grain size. Figure 6 gives $\Delta z/d$ according to $\theta$.

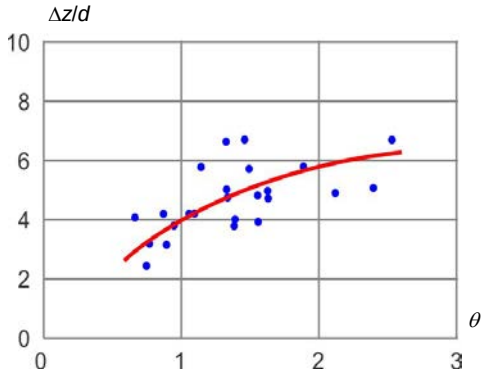


**Figure 6.** Level of the "theoretical" bed level $\Delta z$, after Sumer et al. (1996).

In the lowest part of the sheet-flow region, which constitutes the major part of the moving sediment layer, Sumer et al. (1996) proposed a Power Law for the velocity distribution:

$$\frac{u}{u_*} = \frac{2.50}{\theta^{3/4}}\left(\frac{z}{d}\right)^{3/4} \qquad [5]$$

3.4 Velocity distribution in unsteady flow over mobile bed

Some researchers studied the velocity profiles for unsteady flows with weak bed-load transport (Nikora and Goring, 2000, Qu, 2003, and de Moraes Franklin et al, 2014) and analyzed the effects of the granular mobility on $u_*$.

Once again, a logarithmic velocity profile was detected in the lower zone of the water flux with the friction at the bottom affected by the granular mobility. For instance, Qu (2003) carried out a series of experiments with various hydrographs in a flume with a mobile bed. For the same flow depth, the velocity was observed as higher during the rising limb than during the decreasing phase of the hydrograph, but no significant differences were observed in the inner region between experiments on fixed bed or mobile bed. The velocity distribution inside the sediment layer was not considered in this approach.

3.5 Velocity distribution in dam-break flow over mobile bed

Spinewine and Capart (2013) carried out dam-break flow experiments (Figure 7) in a flume with an upstream reservoir filled with a depth $h_0$ = 0.35 m of water above a sediment layer of thickness $h_s$ = 0.10 m consisting of PVC pellets with an equivalent diameter $d$ = 3.92 mm and a density $\rho_s$ = 1580 kg/m$^3$.

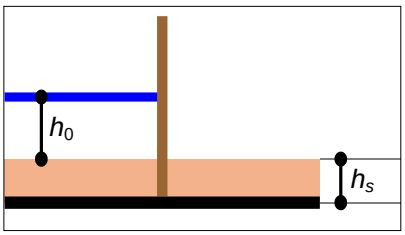


**Figure 7.** Dam-break experiment with PVC pellets (Spinewine and Capart, 2013).

Using PTV techniques, they obtained velocity distribution like those represented in Figure 8. Three layers are defined in the flow: an upper layer of pure water above a mixed layer of water and moving sediments and a lower layer of sediments at rest. From their measurements, they concluded that the velocity was uniform in the clear-water layer, while linearly distributed inside the mixed layer with a velocity equal to the water velocity at the interface with the clear water. However, as the main focus of their work was on the sediment concentration in the moving sediment layer, the velocity profile in the clear water layer was not measured with the same level of detail.

 

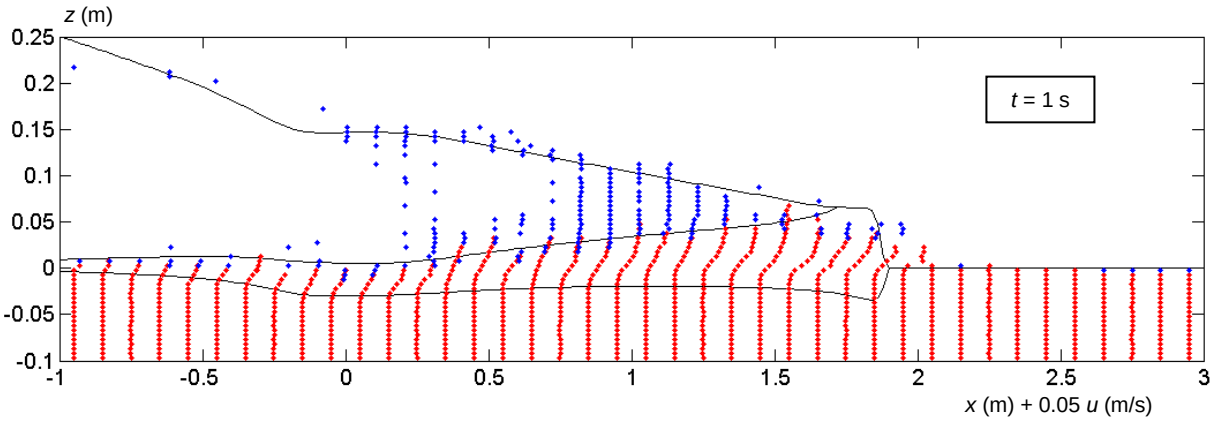


**Figure 8.** Typical velocity distribution at time $t$ = 1 s after the gate opening (Spinewine and Capart, 2013).

## 4 RESULTS

### 4.1 Early stage of dam-break flow

At the beginning of the phenomenon, just after the gate removal, the water falls down with a velocity in the upper part of the flow much larger than the velocity of the water below. The flow is highly unsteady and the velocity field is rather complex: the vertical components of the velocity vectors have the same order of magnitude as the horizontal ones (Figure 9). The velocity vectors present an angle between 0 and −30° with respect to the horizontal line. Figure 10 shows the vector field recorded at $t$ = 0.3 s after the gate opening. The background color shows the order of magnitude of the two components (horizontal and vertical) of these velocity vectors.

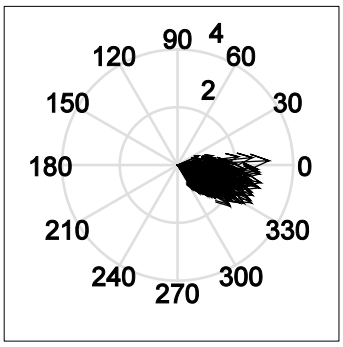

**Figure 9.** Polar plot of velocities (m/s) at time 0.3 s.

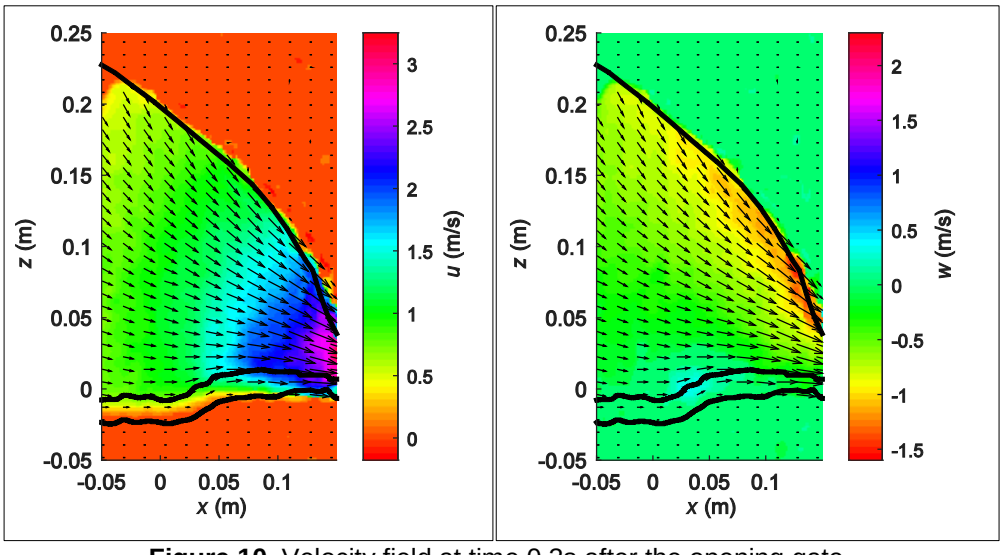


**Figure 10.** Velocity field at time 0.3s after the opening gate.
Background color: left: horizontal component $u$; right: vertical component $w$.

At this moment ($t$ = 0.3s), the assumptions of 1D shallow water flows are not applicable, as the vertical velocity components cannot be neglected. It is possible to represent the distribution of the horizontal component (Figure 11) but no clear velocity distribution law may be defined.

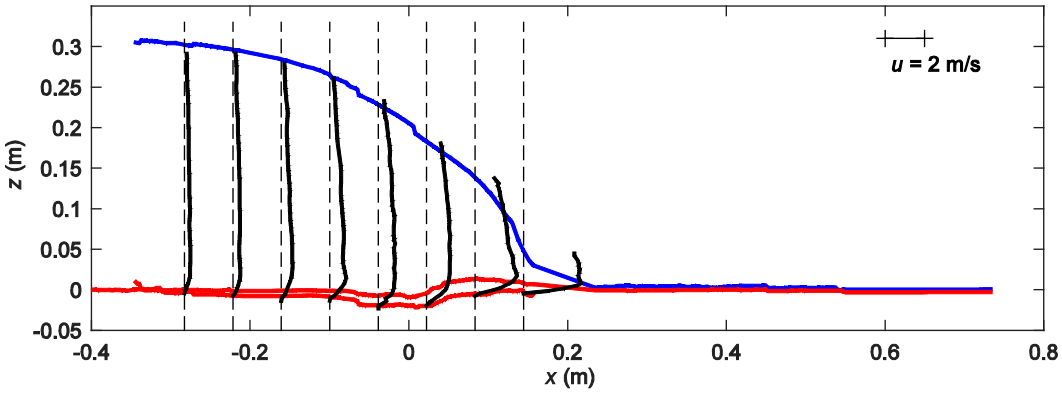


**Figure 11.** Velocity horizontal component profiles at time 0.3s after the gate opening. The origin of $x$ is fixed at the initial position of the gate.

4.2 Shallow-water stage of dam-break flow

After 0.7 s, the polar plot of velocity vectors (Figure 12) shows an average direction of the velocities that is horizontal, so the shallow water assumptions can be considered as valid from this moment forward. Figures 13 and 14 show the horizontal component of the velocity after 0.7 and 2 s, respectively, while Figure 15 gives the evolution in time of the velocity profile at $x$ = 0 m, corresponding to the initial location of the removed gate. Figure 16 shows the same profiles in semi-log plots.

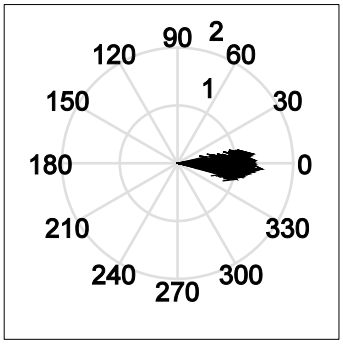


**Figure 12.** Polar plot of velocities (m/s) at time 0.7s after the opening gate.

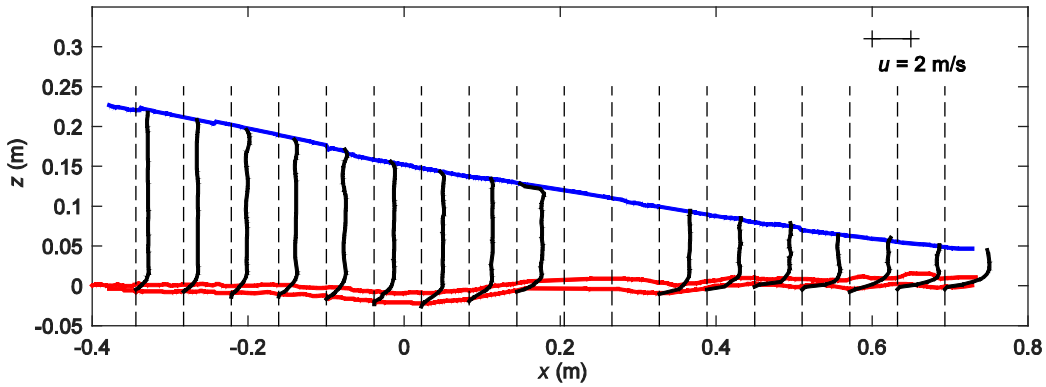


**Figure 13.** Distribution of the horizontal velocity component at time 0.7 s after the gate opening. The origin of $x$ is fixed at the initial position of the gate.

 

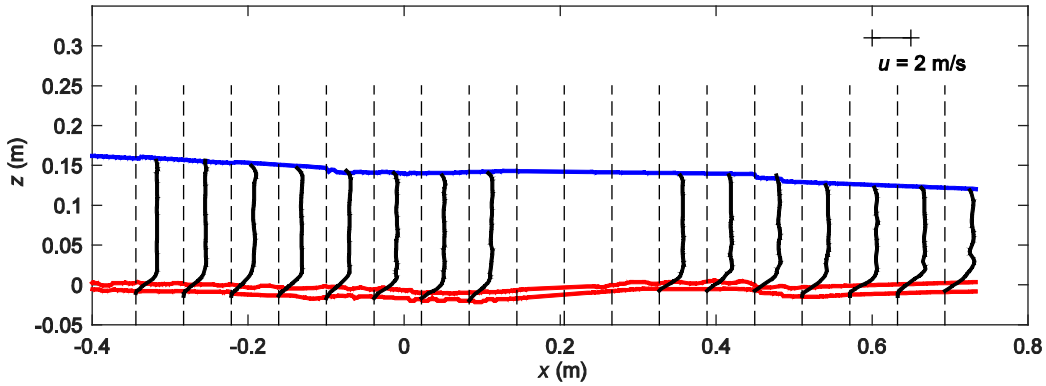


**Figure 14.** Distribution of the horizontal velocity component at time 2 s after the gate opening. The origin of *x* is fixed at the initial position of the gate.

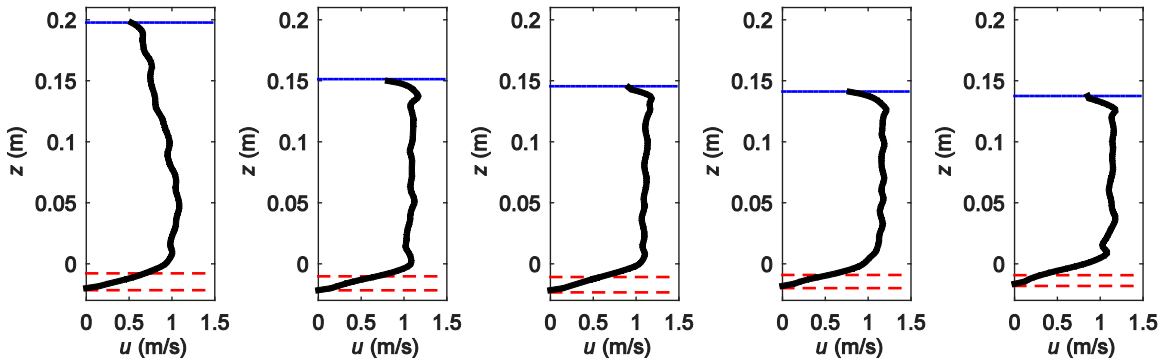


**Figure 15.** Horizontal velocity profiles at times 0.3 s, 0.7 s, 1.0 s, 2.0 s, and 3.0 s.

Referring to Figure 15, the velocity profile inside the clear water layer is practically uniform at least from 0.7 s, corresponding to the time where horizontal velocity component clearly predominates. This is in line with previous observations, among others by Spinewine and Capart (2013) and may be explained by the speed of the phenomenon that does not allow the development of turbulence from the bed and wake effects from the water surface. The magnitude of the velocity at this location is around 1.1 m/s, and remains almost constant during the main part of the event. As the reservoir is progressively emptying, the discharge and the water depth also progressively decrease.

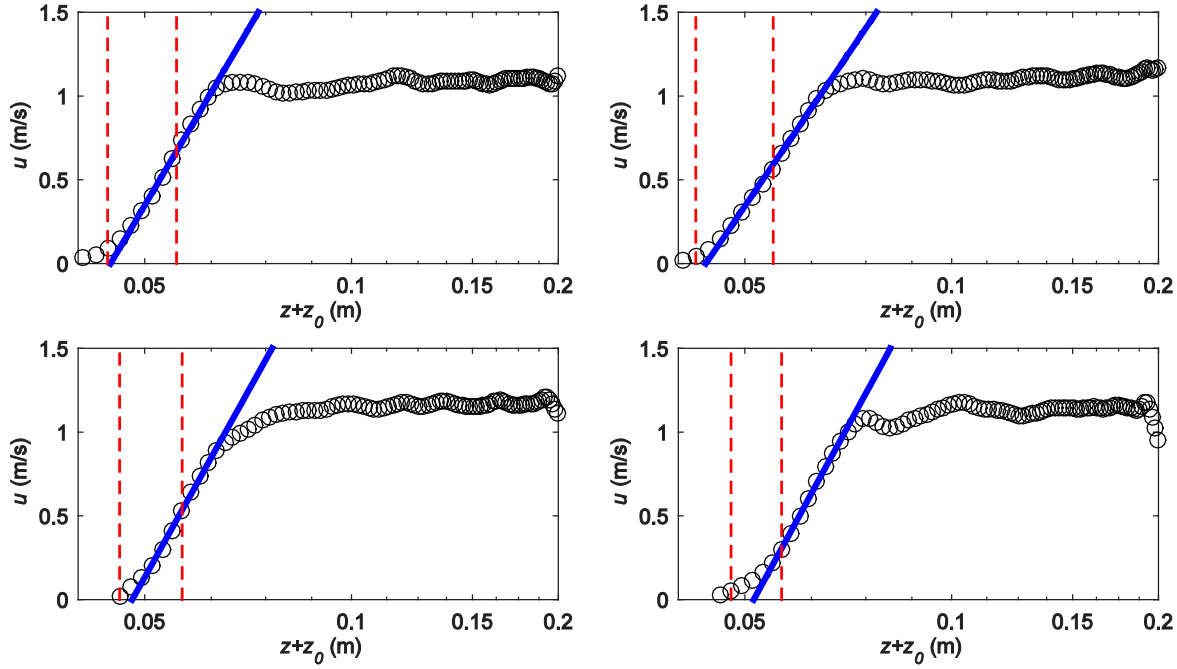


**Figure 16.** Semi-logarithmic plot of horizontal velocity for times 0.7 s, 1.0 s, 2.0 s and 3.0 s.

However, similarly to Sumer's observation in steady flow cases, a log-law is detected, but only on the lower part of the water column, partly in the sediment layer, partly in the water layer. Figure 16 shows the logarithmic profiles of the horizontal velocity components for times 0.7 s, 1.0 s, 2.0 s and 3.0 s. The abscissa does not correspond to the real *z* position, but is moved upwards by a quantity of 0.0659m, corresponding to the minimum quantity to be added in order to avoid the impossible calculation of logarithmic function of negative values. In the lower part of the sediment layer, the velocity distribution deviates from the log-law similar to the observations by Sumer et al. (1996) reproduced in Figure 5. It is possible that a power law prevails in this region but more points should be measured in order to deduce an accurate relationship. Moreover, in such a highly transient phenomenon, there is no guarantee that a general relationship really exists.

## 5 CONCLUSIONS

The velocity distribution in steady uniform flows on fixed bed presents three typical regions: a laminar sub-layer along the bed, an inner region until a certain level where the distribution is logarithmic according to the mixing-layer theory for turbulence convection from the bed, and an outer region where the velocity is slowed down by a wake effect.

Measurements by non-intrusive PIV techniques of dam-break flows over mobile bed show that in the clear-water layer, the velocity distribution is quasi uniform as turbulence conveyance is not developed in such a fast phenomenon, while the upper part of the sediment layer effectively presents a log-law velocity profile.

## ACKNOWLEDGEMENTS

This work is supported in part by the Multi-ITN EU-FP7 project SEDITRANS (Sediment transport in fluvial, estuarine and coastal environments).

## REFERENCES

Adrian, R.J. (2011). Bibliography of Particle Image Velocimetry Using Imaging Methods. *Symposium 25 Years of Particle Image Velocimetry in Aerodynamics*, Institute of Aerodynamics and Flow Technology, Göttingen.

Aleixo, R., Soares-Frazão, S. & Zech, Y. (2011). Velocity Field Measurements in a Dam Break Flow using a PTV Voronoï Imaging Technique. *Experiments in Fluids*, 50(6), 1633-1649.

Aleixo, R. (2013). Experimental Study of the Early Stages of a Dam Break Flow over Fixed and Mobile Beds, *PhD Thesis*. Université Catholique de Louvain, Louvain-la-Neuve, Belgium.

Bellos, C.V., Soulis, V. & Sakkas, J.G. (1992). Experimental Investigation of Two Dimensional Dam Break induced Flows. *Journal of Hydraulic Research*, 30(1), 47-63.

Brereton, G.J., Reynolds, W.C. & Jayaraman, R. (1990). Response of a Turbulent Boundary Layer to Sinusoidal Free Stream Unsteadiness. *Journal of Fluid Mechanics*, 221, 131-159.

Capart, H. & Young, D.L. (1998). Formation of a Jump by the Dam Break Wave over a Granular Bed. *Journal of Fluid Mechanics*, 372, 165-187.

Capart H., Young, D.L. & Zech, Y. (2002). Voronoï Imaging Methods for the Measurement of Granular Flows. *Experiments in Fluids*, 32, 121-135

Coles, D. (1956). The law of the Wake in the Turbulent Boundary Layer. *Journal of Fluid Mechanics*, 1(02), 191-226.

Fraccarollo, L. & Capart, H. (2002). Riemann Wave Description of Erosional Dam Break Flows. *Journal of Fluid Mechanics*, 461, 183-228.

Graf, W.H. & Altinakar, M.S. (1998). *Fluvial Hydraulics: Flow and Transport Processes in Channels of Simple Geometry*, Wiley

Keane, R.D. & Adrian, R.J. (1992). Theory of Cross Correlation Analysis of PIV images. *Applied Scientific Research*. 49, 191-215.

Keulegan, G.H. (1938). *Laws of Turbulent Flow in Open Channels*, 21, 707-741. US: National Bureau of Standards.

Khan, A.A., Steffler, P.M. & Gerard, R. (2000). Dam Break Surges with Floating Debris. *Journal of Hydraulic Engineering*, 126(5), 375-379.

Kironoto, B. & Graf, W.H. (1994). Turbulence Characteristics in Rough Uniform Open Channel Flow. Proceedings of the Institution of Civil Engineers, Water and Maritime Engineering, 106-4, 333-344

Lauber, G. & Hager, W.H. (1998).Experiments to Dam Break Wave: Horizontal Channel. *Journal of Hydraulic Research,* 36(3), 291-307

Leal, J.G., Ferreira, R.M. & Cardoso, A.H. (2006). Dam Break Wave Front Celerity. *Journal of Hydraulic Engineering*, 132(1), 69-76.

De Moraes, Franklin, E., de Figueiredo, F.T. & Rosa, E.S. (2014). The Feedback Effect caused by Bed Load on a Turbulent Liquid Flow. *Journal of the Brazilian Society of Mechanical Sciences and Engineering*, 36(4), 725-736.

 

Nikora, V. & Goring, D. (2000). Flow Turbulence over Fixed and Weakly Mobile Gravel Beds. *Journal of Hydraulic Engineering*, 126(9), 679-690.

Nikuradse, J. (1933). *Laws of Flow in Rough Pipes*. In VDI Forschungsheft.

Qu, Z. (2003). Unsteady Open Channel Flow over a Mobile Bed, *Doctoral dissertation*. No. 2688, Laboratoirede Recherches Hydrauliques, Ecole Polytechnique Fédérale, Lausanne, Switzerland.

Raffel, M., Willert, C., Werely, S. & Kompenhans, J. (2007). *Particel Image Velocimetry.* A practical guide 2nd Edition. *Springer*.

Schlichting, H. (1968). *Boundary Layer Theory*. New York: McGraw-Hill, 727-730.

Shin, J. O., Dalziel, S. B. & Linden, P. F. (2004). Gravity Currents Produced by Lock Exchange. *Journal of Fluid Mechanics*, 521, 1-34.

Soares-Frazão, S., Le Grelle, N., Spinewine, B. & Zech, Y. (2007). Dam-break induced Morphological changes in a Channel with Uniform Sediments: Measurements by a Laser Sheet Imaging Technique. *Journal of hydraulic Research*, 45(1), 87-95.

Song, T.C. & Graf, W.H. (1996). Velocity and Turbulence Distribution in Unsteady Open Channel Flows. *Journal of Hydraulic Engineering*, 122(3), 141-154.

Spinewine, B. & Zech, Y. (2007). Small Scale Laboratory Dam Break Waves on Movable Beds. *Journal of Hydraulic Research*, 45(1), 73-86.

Spinewine, B. & Capart, H. (2013). Intense Bed Load due to a Sudden Dam Break. *Journal of Fluid Mechanics*, 731, 579-614.

Stansby, P.K., Chegini, A. & Barnes, T.C.D. (1998). The Initial Stages of Dam Break Flow. *Journal of Fluid Mechanics*, 374, 407-424.

Sumer, B.M., Kozakiewicz, A., Fredsøe, J. & Deigaard, R. (1996). Velocity and Concentration Profiles in Sheet Flow Layer of Movable Bed. *Journal of Hydraulic Engineering*, 122(10), 549-558.

Tu, H. (1991). Velocity Distribution in Unsteady Flow over Gravel Beds, *Doctoral Dissertation,* No. 911, Laboratoire de Recherches Hydrauliques, Ecole Polytechnique Fédérale, Lausanne, Switzerland.

 

# EXPERIMENTAL STUDY ON MIGRATION PATTERN OF FLUIDS IN POROUS MEDIA UNDER VIBRATION EFFECT

KOK FOONG LOKE [1], NORHAN ABD RAHMAN[2], RAMLI NAZIR[3] & RADZUAN SA'ARI[4]

[1, 2, 3, 4]Faculty of Civil Engineering, Universiti Teknologi Malaysia, Johor, Malaysia
edwinloke84@yahoo.com; norhan@utm.my; ramlinazir@utm.my; radzuans@utm.my
[2, 3]Centre of Tropical Geoengineering, Faculty of Civil Engineering, Universiti Teknologi Malaysia, Johor, Malaysia

## ABSTRACT

The rapid growths of the country and evolution in manufacturing have contributed to climate change and natural disasters that give a negative impact on the environment and humans. The main issues are leaking and dumping of contaminants through the surface or subsurface that has experienced earthquake vibration and that probably cause groundwater pollution. Experiments on porous media such as deformable double-porosity soil still need to be understood and may provide more comprehensive understanding with respect to fluid migration under the phenomena of vibration. A physical experimental model is conducted to study the patterns of fluid migration in deformable double-porosity soil under the vibration effect by using image analysis. The double-porosity characteristic of the soil sample is created through kaolin soil aggregation with 25% moisture content and deformation by vibration at 0.98Hz vibration frequency. In the experiment, the specially assembled acrylic soil column with triangle base plate is placed on the vibratory table to vibrate and monitor the whole area of acrylic circular columns. A digital image acquisition system using Nikon D90 Digital Single Lens Reflex camera is chosen to observe and capture images of the fluid migration pattern in fractured double-porosity soil sample at designated time intervals. Digital image processing and analysis technique is accomplished by using Matlab routine and Surfersoftware. The results show that the digital image analysis technique is capable to provide additional information such as the fluid flow rates and migration patterns in understanding the fluid migration behaviour. Outcome of the experiments shows that the fractured double-porosity has high permeability due to faster fluid migration and contributes to dominant factors for fluid migration in the subsurface system when the soil structure has been rearranged and loosened after vibration in double-porosity soil. This study indicates that the fractured double-porosity soil under vibration effect has severe ramifications on groundwater sources.

**Keywords:** Porous media; vibration; fluid migration; vibratory table; digital image analysis.

## 1 INTRODUCTION

The influence of natural disasters and climate change such as flash flood, El-Nino and earthquake events were reported at Ranau and Tawau, Sabah, Malaysia (Muguntan et al., 2015; Stephanie, 2015). These incidents of earthquake phenomena had caused damage and leakage to underground drainage pipes and liquid tanks. Hence, vibration and leakage of liquids on the ground is a problem that requires attention and focus to ensure the sustainability of the geo-environment. Earthquake led to cracked soil, soil structure rearrangement, and fractured soil deformation. The fractured soil reduced the intact soil shear strength and increased the hydraulic conductivity (Fredlund et al., 2010).

The soil structure ultimately affects the speed and pattern of fluid migration. Existing research by Krisnanto et al. (2014) recognizes that the cracked soil played an influential role in the water flow through problematic soil. In the same way, Fredlund et al. (2010) determined the significant changes of mechanical properties and hydrological behavior in fractured porous media. As widely acknowledged, soil that displays two specific scales of porosity media are termed as double porosity media (Carminati et al., 2008). Double-porosity soil is used to characterize soils that consist of two specific sub-regions that display different characteristics of pore sizes and hydraulic properties. The double-porosity soils also display bimodal pore-size distribution due to the condition of intra-aggregate and inter-aggregate pores in aggregated soil, which can be found in compacted soil and also in agricultural top-soils (El-Zein et al., 2006; Li and Zhang, 2009).

According to Lakeland et al. (2014), double-porosity soil formed due to earthquake or vibration effect, where loosely packed water-saturated granular soils are subjected to earthquake shaking, may liquefy and cause large soil deformations. Furthermore, the researchers had proven via the first principles analysis that liquefaction is not a strictly undrained process, but in fact is the interplay between soil rearrangement, permeability changes, and fluid migration that has led to loss of strength observed in numerous earthquake events.

Lewandowska et al. (2005) found that the double-porosity characteristics in soil could be created in the laboratory, where most studies relating to double-porosity soil were carried out. Meanwhile, Bagherieh et al.

 

(2009) conducted a series of one-dimensional drying and consolidation experiments on laboratory-prepared aggregated kaolin sample. The experiment's results indicated that the aggregated soil response approached that of non-aggregated soil in terms of compressibility and fluid retention when applied above a certain vertical stress. Furthermore, Krisnanto et al. (2014) performed an experimental model to predict the flow rate through a cracked soil network. The researchers found that the soil matrix for seepage rate is small when compared to the flow rate through the cracked soil network.

The previous mentioned experiments on double-porosity media have contributed to the body of knowledge with significant view point on double-porosity soil behavior, but the experiments were limited to common intact aggregated method and never applied reaction such as vibration to the aggregated porous media. Moreover, Ngien et al. (2012) mentioned that there is still a gap in open literature with consideration to investigations via experiment on immiscible fluid movement in double-porosity soils. The researchers stated that widespread problem of difficulty gathering reliable data concerning immiscible fluid movement behavior and the physical experiments will go a long way in the effort to understand, observe, monitor and solve such problem. Additionally, the research of Krisnanto et al. (2014) show the significance of understanding lateral flow characteristics through a cracked soil, and the authors suggested for further investigation that a more complex crack network and a model are needed to predict the water flow rate.

The study in this article attempts to bridge the gap with the objectives (i) to determine the behavior of dye water migration in fractured double-porosity soil using digital camera image close range photogrammetry technique, (ii) to identify the dye water migration speed rate for specific soil column circumference zone in fractured double-porosity soil. This study covers the double-porosity aggregated soil medium vibrated by using a vibration table involving a specially assembled acrylic glass soil column. The migration of dye water is observed in a 100mm height fractured soil sample in acrylic glass circular column with 300mm high and 100mm outer diameter. The aggregated soil sample mixed with 25% water is added to dry kaolin S300 soil in the experiment. Distilled water is used as a liquid source. The distilled water is dyed red with red powder to enhance the migration observation. Dyed water with 70ml is poured instantaneously on top of the soil surface for each aggregated soil sample. The image analysis is accomplished by using Matlab routine and Surfer programme to analyze the dye water flow migration behaviour or pattern and migration speed rate.

## 2 EXPERIMENTAL CONCEPT

According to Black (1998), the manufacturing of petroleum that was initiated by drilling an early commercial oil well in 1859 in North America can be related to double-porosity concept. The overlapping continuum technique had been the basis for the double-porosity theory (Barenblatt et al., 1960). There are two types of porosity systems in petroleum reservoir engineering, primary porosity and secondary porosity. Fractured soil based on a continuum mechanics method is used for initiation of unsaturated water storage and conductivity functions. Using the dual-continuum method, the researchers found that the double-porosity model is capable to deal with fracture matrix interplay more efficiently compared to discrete-fracture model. Thus, this study used the model concept with the soil that overlaps the three continuums of fracture porosity, primary porosity and secondary porosity features developed by Loke et al. (2016a). The fracture porosity continuum developed through the vibration effect had caused the double-porosity soils to fracture. Meantime, the primary porosity and secondary porosity continuums concept represents the concept of double-porosity soils that contain inter-aggregate and intra-aggregate pores matrix blocks, respectively.

Earthworm activities and root holes can cause the occurrence of double-porosity in soils (Jongmans et al., 2003). According to Lakeland et al. (2014), the saturated and roughly filled granular soils for specimen of sand and soils exposed to earthquake vibration may lead to greater deformations and liquefy; which was the concept of double-porosity soil transformation due to earthquake or vibration. Fractured porosity formations were characterized by water-bearing formations where the flows of groundwater were along the fractured solid rock. Moreover, the change in either the total stress boundary conditions or fluid pressure applied to the system could be the result of deformation behavior in porous medium, where the important fluid interchange between fractures and matrix blocks occurs (Bai et al., 1993). According to Sa'ari et al. (2015), the double-porosity soil constitutes highly different hydraulic properties of two sub-region media due to the varying pore size characteristics.

Digital image analysis was used to analyze and understand the fluid migration in fractured double-porosity soil. Digital image analysis is a kind of analysis using computer to obtain information data from the digital image. The common ways to observe and monitor the fluid migration involve many measuring apparatus that may interfere with the sample original setup; however, using digital image close range photogrammetry technique will overcome the problem with non-destructive techniques. In this case, a number of researches (Ngien et al., 2016; Sa'ari et al., 2015; Kamarudin et al., 2011; Ngien et al., 2011; Bob et al., 2008; Kechavarzi et al., 2008; Oostrom et al., 2007; Bridge et al., 2006; McNeil et al., 2006; Darnault et al., 1998; Van Geel et al., 1994; Shincariol et al., 1993) have carried out the non-intrusive imaging techniques for experiment of liquid migration analysis. The previous mentioned researchers have used various techniques and methods such as image analysis method (IAM), light reflection method (LRM), saturation imaging analysis techniques (SIAT), time-lapse fluorescent imaging (TLFI), multispectral image analysis method (MIAM), digital

 

image processing technique (DIPT) and photographic technique (PT). The work in this study used the digital camera image close range photogrammetry method (DCIPM) as the technique to monitor and observe fluid migration in fractured double-porosity soil. According to Maas and Hampel (2006), image analysis in civil engineering field was frequently utilized to study the migration of very small properties specific to structure crack extension and object flow absorption in boundary layers. The porosity and cracked soils are very hard to monitor by naked eye, and for this reason, digital camera image analysis was suitable to be used to study the migration of dye water in fractured double-porosity soil. This has sparked the interest to look into the effect of vibration applied to the double-porosity soil on dyed water migration.

## 3 EXPERIMENTAL MATERIALS AND METHODS

In this study, details of the fractured double-porosity soil sample preparation, experimental procedure, and digital camera imaging process were discussed in the following subsections. The brief flow chart for experimental methodology as shown in Figure 1 has been developed in order to achieve the study objectives.

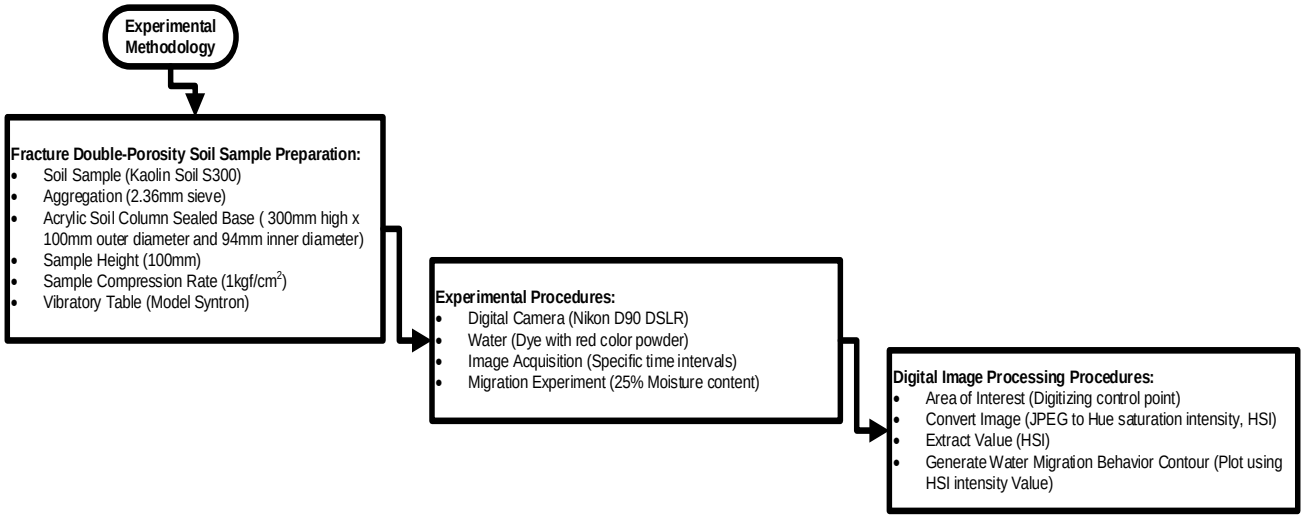


**Figure 1.** Flow chart of the experimental methodology.

### 3.1 Fractured double-porosity soil sample preparation

Commercially available kaolin soil S300 was used as the soil sample for this study to create double-porosity. The kaolin soil properties were tested based on British Standard BS1377-2:1990 and BS 1377-5:1990 for the purpose of obtaining the Atterberg limits, particle size distribution, solid particle density and saturated permeability of the kaolin soil. The kaolin soil S300 was classified under Unified Soil Classification System (USCS) based on the value of particle size distribution and Atterberg limits. The properties of kaolin soil S300 sample are shown in Table 1.

**Table 1.** Kaolin soil S300 properties

| Property | Value |
|---|---|
| Liquid Limit (%) | 40.50 |
| Plastic Limit (%) | 27.00 |
| Plasticity Index (%) | 13.50 |
| Particle Density ($Mg/m^3$) | 2.65 |
| USCS Classification | ML (Silt with low plasticity) |
| Saturated Permeability, $K_{average}$ (m/s) | $5.40 \times 10^{-9}$ |

The aggregated soil sample was prepared based on the method expressed by Loke et al. (2016a) and Bagherieh et al. (2009), where the dried kaolin powder was first mixed with 25% of moisture content for the experiment. Water was constantly poured when mixing dried kaolin powder with water to control moisture content within the mixture. The moisture content value in this study was chosen because the kaolin soil mixture was mouldable. At moisture content more than 35%, the kaolin granules started to disintegrate and were unable to form kaolin aggregates (Sa'ari et al., 2015). Meanwhile, at moisture content value less than 25%, the kaolin granules were too dry and too crumbly, hence unable to form kaolin aggregates (Ngien et al., 2016). After that, the mixture was kept at a cool condition for a minimum of 24 hours to cure both samples that were placed in a plastic bag for the purpose of maintaining the condition of moisture content. After curing, the mixture was broken by hand and passed through a 2.36mm sieve to obtain kaolin granules to create double-porosity structure. The kaolin granules soil sample was transposed in an acrylic soil column and then compressed kaolin granules to a height of 100mm using a compression machine at a compression rate of $1kgf/cm^2$. The sample height was kept at 100mm because of the uniformity throughout the soil sample depth.

 

The falling head permeability test was carried out to acquire aggregated soil sample average permeability value ($K_{average}$) as shown in Table 1.

The laboratory experiments were conducted in acrylic soil column sealed base with newly custom designed soil column with dimension of 300 mm high x 100 mm-outer diameter and 94 mm-inner diameter. The acrylic soil column with aggregated soil sample was perfectly fixed and bolted on the vibratory table in order to avert and prevent any movement of the circular column. Figure 2 shows a 3D diagram of vibratory table setup to vibrate the aggregated soil sample (Loke et al., 2016a). The vibration frequency for the vibratory table was set on the control panel with 0.98Hz and the vibration period of 60 seconds has been used based on the method and setup expressed by Loke et al. (2016a). The results of fractured soil pattern before and after vibration process are displayed in Figure 3.

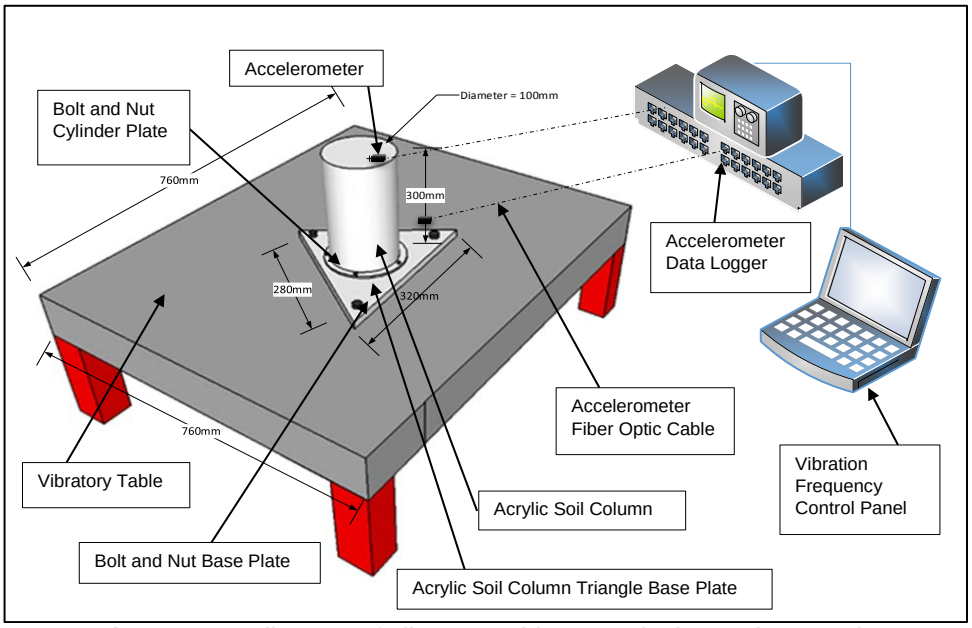


**Figure 2.** 3D diagram of vibratory table setup (Loke et al., 2016a).

(a) Soil sample before vibration process

(b) Soil sample after vibration process with fractured

**Figure 3.** The results of before and after vibration process for soil sample with 25% moisture content.

3.2 Experimental procedures

The fractured double-porosity characteristic in the soil sample was represented by the inter-aggregate and intra-aggregate pores created through aggregation and vibration as previously explained. The fractured double-porosity soil in acrylic soil column was used to measure and to detect the fluid migration that took place inside the whole circular column area with the aim of not interfering with the sample original setup. The experimental setup was arranged as shown in Figure 4 for fluid migration image acquisition setup.

 

A Nikon D90 DSLR digital camera was the main equipment for fluid migration image acquisition system and the V shape reflection mirror was used to reflect the whole area of soil column image. The Nikon D90 DSLR camera fixed with sensor size of 23.6mm x 15.8mm and used medium size image format of 3216 x 2136 pixels, resulted in each pixel having the size of 5.6 x 5.6 µm. The digital camera setup during the laboratory experiments was setup with minimum shutter speed of 1/640 second, aperture fixed at f/5.6 and ISO speed set at ISO-2500 that had been applied for all the experiments. All recorded digital images were saved in JPEG format. The V shape mirror was set and adjusted until a clear image and whole circular area of soil column as seen fit which allowed 100% soil column surface exposure in a single view of image acquisition throughout the experiment. The soil column with fractured aggregated soil sample was secured in position throughout the experiment in order to minimize error and prevent movement of the soil column. The light source for the experiment came from linear fluorescent lamp-40 watt with output luminous flux of 2600 lumens/watt that was placed above the soil column.

**Figure 4.** Image acquisition experiment setup.

In the experiment, a white paper with pre-drawn gridline (20mmx20mm) was first sheathed onto the soil column and used as a control point on the reference image. The pre-drawn gridline paper can be removed from the soil column when the reference image was taken. The experiment began by pouring the dyed water instantaneously onto the top center fractured aggregated soil sample in acrylic soil column. 70ml of dyed water was used in the experiment. After the dyed water was poured and the whole surface area of the soil sample was covered, the first digital image of dyed water migration was taken at a room temperature of 24$^{o}$C. The subsequent digital images were taken at a specific time interval to capture the dyed water migration pattern. In the experiment, 119 digital images were taken in 40 minutes.

3.3 Digital image processing procedures

The recorded images then were transferred from digital camera to computer for further image processing using Matlab routine and Surfer Software version 10. The Matlab routines were used to perform the following task; to extract area of interest from captured image and transform the area of interest from distorted image to a scale image via affine transformation method; to convert the JPEG scale images to Red Green Blue (RGB) and Hue Saturation Intensity (HSI) images; to extract HSI digital value from HSI image and save the HSI value in a text file format. Surfer software was then used to digitize the control point from reference image and to generate map or plot the migration pattern of dye fluid in porous media using HSI value. The first step was digitization of control points of area of interest on reference image to extract the image coordinates of control points. Area of interest refers to pre-determined migration boundary area (front image and V shape refection image) for the experiment that contained the dyed water as shown in Figure 5. The true grid coordinate on pre-drawn grid line and coordinates of the control points on reference image are required for image transformation.

After completing the image control point, Matlab routine was used to convert data from area of interest into red-green-blue (RGB) and HSI digital image format. The RGB and HSI intensity values from image were extracted and saved in text files using American Standard Code for Information Interchange (ASCII) format. The subsequent digital image will loop three times by using Matlab routine to extract and save the intensity values for all three section areas of interest (front image and V shape refection image) of the acrylic soil column. Lastly, Surfer software version 10 had been used to plot the contour pattern of dyed water migration based using the HSI intensity values. The HSI intensity contour plot of dyed water migration behavior can provide detailed information to facilitate researchers to understand the pattern of dyed water migration behavior or characteristic.

 

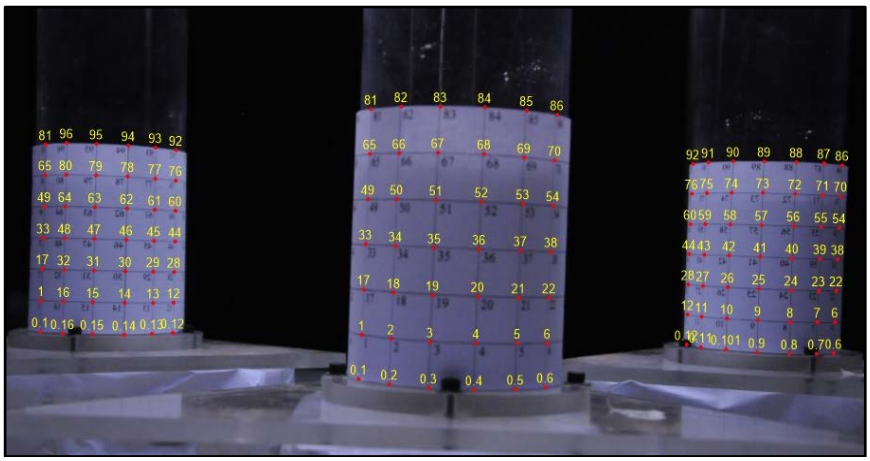

**Figure 5.** Position of control points on reference image covers the area of interest for front and V shape reflection image.

## 4 RESULTS AND DISCUSSION

The results after the migration process for the top soil surface with the divided measurement of actual size for column circumference zone to visualize the crack position are shown in Figure 6. The downward migration of dyed water in the fractured aggregate kaolin soil sample with 25% moisture content for the experiment is shown in Figure 7, using HSI value obtained via digital camera image close range photogrammetry technique. The HSI plots were clearly apparent in two-dimensional shape when the plot in curve joined the left and right boundary that formed a circular shape similar to soil column; however, the dyed water migration in the acrylic soil column was actually one-dimensional. In the experiment, the selected HSI plots of dyed water migration were recorded at intervals of minute such as 0.5, 6, 20 and 36 minutes, respectively. The 70ml dyed water was poured instantaneously on top of the soil sample surface by using glass funnel to ensure the dyed water penetrated in one-dimension. It was unavoidable that some of the dyed water would have penetrated into the test sample before the whole sample surface was covered. The flow of the dyed water migration was not uniformly downward at the front boundary horizontal line because of the non-homogeneity of the fractured double-porosity soil. In addition, the fast migration occurred at the cracked soil surface condition compared to other locations on the soil surface that were not cracked as shown in Figure 6. At 0.5 minute after the commencement of the experiment, the dyed water migration reached three quarters through the test sample at the location of fractured soil surface as shown in Figure 7. The dyed water migrated fastest between 90 to 150mm and 250 to 300mm along the soil column circumference zone.

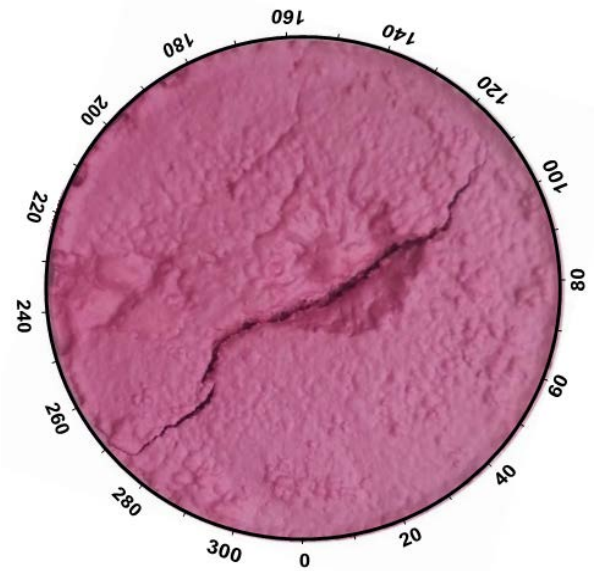


**Figure 6.** Fluid migrated soil surface with measurement of actual column circumference zone.

 

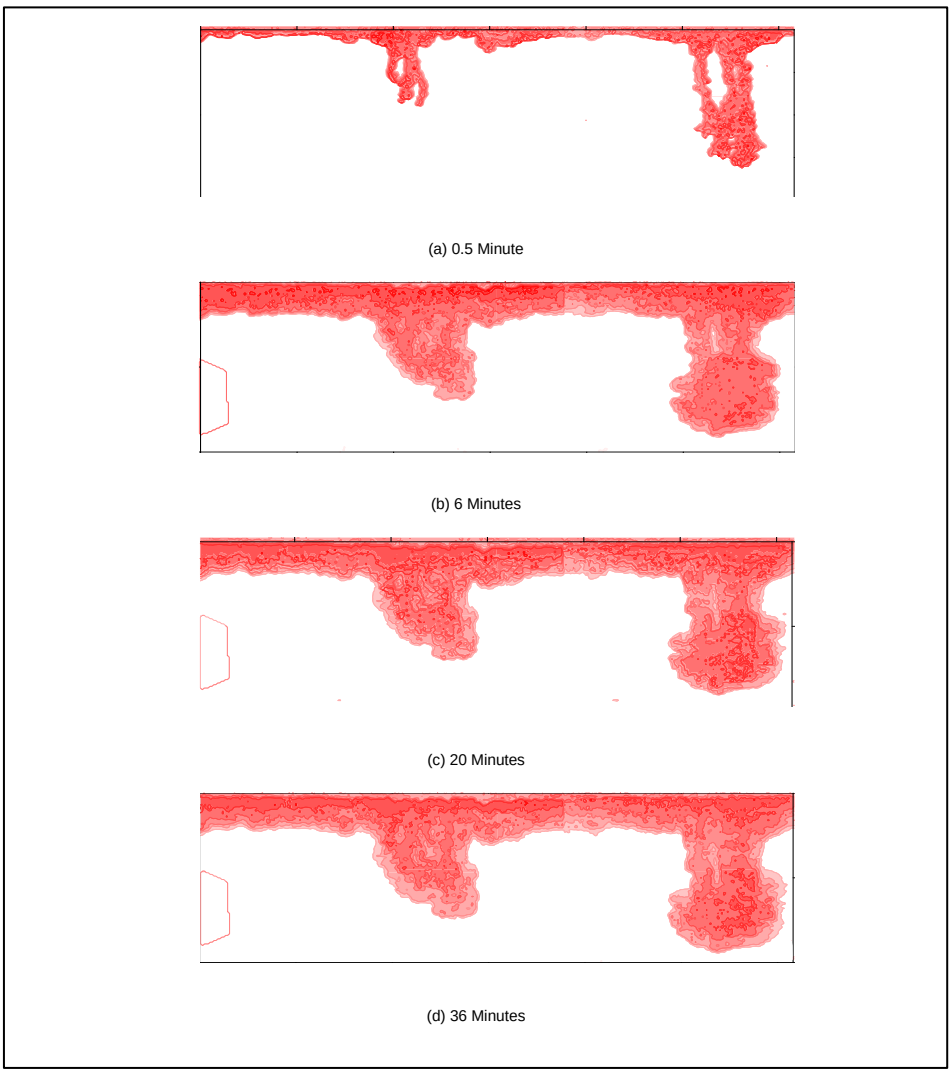


**Figure 7.** HSI plots of downward dyed water migration in fractured double-porosity soil for soil sample with 25% moisture content at (a), (b), (c), and (d) time interval.

It took about 6 minutes for the dyed water to completely migrate from the whole top soil surface area into the fractured soil sample of the test. Meanwhile, the duration for dyed water migration from the top surface to the stop point was 36 minutes and further observation at 60 minutes showed no changes in migration pattern where the dyed water migration between 250 to 300mm along the x-axis nearly reached the bottom of soil column. In a previous research, Sa'ari et al. (2015) performed an experiment on toluene migration in aggregated soil sample with 25% moisture content and the results have shown the toluene migration from top to bottom was 38 minutes, which differs from the migration duration to the bottom of soil column in this study. The dyed water migration was stopped at 36 minutes in this study since the water viscosity was 0.00089kg/(m.s), while toluene viscosity was 0.00055 kg/(m.s), with the viscosity difference of about 38% (Assael et al., 2001; Joseph et al., 1978). Water has higher viscosity compared to toluene. Thus, dyed water caused the high friction and resistance to gradual migration compared to toluene. According to Loke et al. (2016b), the fractured soil sample structure with 25% moisture content experienced worse and large surface fractures during the vibration process when compared to the aggregated kaolin soil with other moisture content. Therefore, this study strengthened the idea that the fractured double-porosity soil experienced faster migration compared to the condition with intact double-porosity soil. This study had proven that the faster migration in fractured soil with dyed water migration took 36 minutes compared to previous research that took 38 minutes to reach the bottom of soil column, even though this study used dyed water that had higher viscosity compared to toluene.

Figure 8 presents the measured values of dyed water saturation depth as a function of time for every 30mm column circumference zone. The measured column circumference zone is shown in Figure 6. From Figure 8, the cumulative saturation depth of dyed water migration at 270mm column circumference zone was the fastest critical penetration within 0.5 minute as the steepest gradient of the graph lines was within that duration and continued to incline horizontally gradual until the end of the experiment. The 120mm column circumference zone had the second fastest critical penetration within 1 minute as sharp gradient of the graph

 

lines was displayed within that duration and continued after 1 minute to incline horizontally gradual until the end of the experiment. The column circumference zone at 90mm was the third fastest critical penetration with gradual decline from start until the end of the experiment. The 150mm column circumference zone also went through critical penetration with slight gradual decline from start until the end of the experiment. The rest of the column circumference positions continued to slightly decrease proportionally with slow migration from start until the end of the experiment.

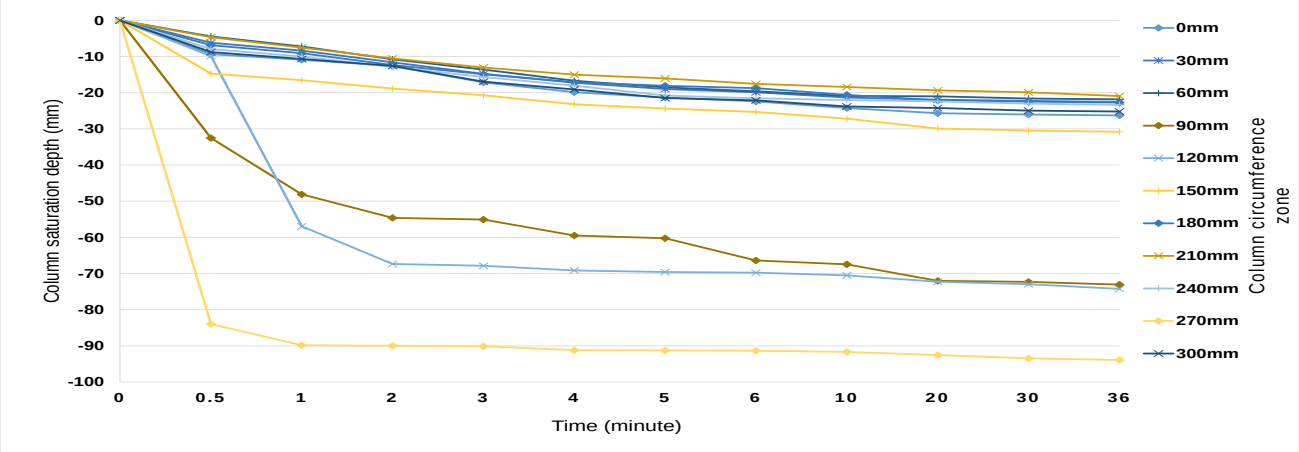


**Figure 8.** Measured values of dyed water saturation depth as a function of time for every 30mm column circumference zone.

Based on Figure 8, the migration speed rate can be calculated based on the migration depth in unit of millimeters (mm) divided by time in unit of seconds (s) for every 30mm column circumference zone. Table 2 presents the calculated migration speed for the higher and overall average speed for every 30mm column circumference zone. Referring to Table 2 and Figure 8, the higher migration speed rate which occurred between initial to 0.5 minute took place at 270mm column circumference zone with 2.799mm/s migration speed rate. Meanwhile, the column circumference zone at 150mm, 90mm and 120mm also had a high migration speed rate with the value of 0.491mm/s, 0.355 mm/s and 0.329 mm/s, respectively. The higher migration speed rate happened due to the fractured or cracked soil sample as shown in Figure 6. The lower migration speed rate occurred between 30 to 36 minutes for all column circumference zones with the speed range of about 0.001 mm/s to 0.002 mm/s because the migration had reached the stop point of downward penetration. The overall average dyed water migration speed rate for this experiment which was 0.087 mm/s was faster than 0.04 mm/s in the previous research by Sa'ari et al. (2015). Thus, the higher average migration speed rate occurred at 270mm column circumference zone with 0.275 mm/s and the deeper downward migration along the soil column depth with the value of 93mm. This could be caused by the capillary force exerted by the dyed water pressure on top surface of the soil sample that has not yet migrated into the soil sample. Observation showed that the position of 270mm soil column had undergone the worst fractured and cracked soil structure after the vibration process. From the results, it can be concluded that factors that significantly influenced the dyed water migration in the experiment were the fractured pattern of the soil sample, structure of the soil sample and the capillary pressure of the dyed water.

**Table 2.** Migration speed rate for every 30mm column circumference zone.

| Column Circumference Zone (mm) | Migration Speed Rate (mm/s) | |
|---|---|---|
| | Higher Speed Between Initial to 0.5 Minute | Average Speed for All the Time Interval |
| 0 | 0.311 | 0.052 |
| 30 | 0.206 | 0.044 |
| 60 | 0.149 | 0.041 |
| 90 | 0.355 | 0.101 |
| 120 | 0.329 | 0.193 |
| 150 | 0.491 | 0.065 |
| 180 | 0.229 | 0.043 |
| 210 | 0.156 | 0.039 |
| 240 | 0.265 | 0.048 |
| 270 | 2.799 | 0.275 |
| 300 | 0.292 | 0.051 |

## 5 CONCLUSION

A laboratory experiment on dyed water migration in a fractured double-porosity soil with 25% moisture content has been conducted. The present experiment study is deliberately designed to observe the dyed water migration behavior and pattern in the fractured double porosity soil placed in acrylic soil column model. The digital camera image close range photogrammetry technique is applied to capture the dyed water migration using DSLR camera. Digital image processing technique using Matlab routine and Surfer software version 10 is applied to extract and analyze HSI data obtained from digital image. The experiment is successful where the results of the migration speed rate for every 30mm column circumference zone are obtained. The observation shows the dyed water migrates faster at the initiation of the experiment and maintains slight downward migration until the end of the experiment. Comparison of results with related previous research to this experiment with moisture content of 25% shows that the migration time is shorter and migration speed rate faster in the current study due to the fractured soil sample. It is proven that the capillary pressure, fractured pattern and soil structure of the soil sample have influenced the migration behavior. Based on the study carried out, the hypothesis advanced by the authors that the fractured or cracked double-porosity soil will affect the migration speed rate compared to intact double-porosity soil is found to be valid. In conclusion, the HSI intensity value contour plot of water migration behavior could provide details and practical information to facilitate researcher to understand the pattern of water migration by using digital camera image close range photogrammetry technique.

## ACKNOWLEDGEMENTS

This study is supported by the Research Management Centre (RMC), Universiti Teknologi Malaysia under Research University Grant – Tier 1 (PY/2016/06547) from the Ministry of Higher Education Malaysia. The authors would also like to thank their University, Geotechnical Laboratory, Hydraulic and Hydrology Laboratory, Engineering Seismology and Earthquake Engineering Research Group (eSEER), and Survey Unit, Faculty of Civil Engineering, Universiti Teknologi Malaysia for kind assistance lent to this research. The first author is fully supported through the federal training award by the Public Service Department under Prime Minister's Department, Malaysia.

## REFERENCES

Assael, M.J., Avelino, H.M.T., Dalaouti, N.K., Fareleira, J.M.N.A. & Harris, K.R. (2001). Reference Correlation for the Viscosity of Liquid Toluene from 213 to 373k at Pressures to 250Mpa. *International Journal of Thermophysics*, 22(3), 789-799.

Bagherieh, A.R., Khalili, N., Habibagahi, G. & Ghahramani, A. (2009). Drying Response and Effective Stress in a Double Porosity Aggregated Soil. *Engineering Geology*, 105(1-2), 44–50.

Bai, M., Elsworth, D. & Roegiers, J.C. (1993). Multiporosity/Multipermeability approach to the Simulation of Naturally Fractured Reservoirs. *Water Resources Research*, 29(6), 1621–1633.

Barenblatt, G.I., Zheltov, P.I. & Kochina, I.N. (1960). Basic Concepts in the Theory of Seepage of Homogeneous Liquids in Fissured Rocks [strata]. *Journal of Applied Mathematics and Mechanics*, 24(5), 1286–1303.

Black, B. (1998). Oil Creek as Industrial Apparatus: Re-Creating the Industrial Process through the Landscape of Pennsylvania's Oil Boom. *Environmental History*, 3(2), 210–229.

Bob, M.M., Brooks, M.C., Mravik, S.C. & Wood, A.L. (2008). A Modified Light Transmission Visualization Method for DNAPL Saturation Measurements in 2-D Models. *Advances Water Resource*, 31, 727-742.

Bridge, J.W., Banwart, S.A. & Heathwaite, A.L. (2006). Non-Invasive Quantitative Measurement of Colloid Transport in Mesoscale Porous Media using Image Lapse Fluorescene Imaging. *Environment Science Technology*, 37, 1859-1868.

Carminati,A., Kaestner, A., Lehman, P. & Flühler, H. (2008). Unsaturated Water flow across Soil Aggregate Contacts. *Advances in Water Resources*, 31(9), 1221–1232.

Darnault, C.J.G., Throop, J.A., Dicarlo, D.A., Rimmer, A., Steenhuis, T.S. & Parianges, J.Y. (1998). Measurement of Fluid Contents by Light Transmission in Three-Phase-Oil-Water-Air Systems in Sand. *Water Resource Research*, 37, 1859-1868.

El-Zein, A., Carter, J.P. & Airey, D.W. (2006). Three-Dimensional Finite Elements for the Analysis of Soil Contamination using a Multiple-Porosity Approach. *International Journal for Numerical and Analytical Methods in Geomechanics*, 30(7), 577–597.

Fredlund, D.G., Houston, S.L., Nguyen, Q. & Fredlund, M.D. (2010). Moisture Movement through Cracked Clay Soil Profiles. *Geotechnical and Geological Engineering*, 28(6), 865–888.

Jongmans, A.G., Pulleman, M.M., Balabane, M., van Oort, F. & Marinissen, J.C.Y. (2003). Soil Structure and Characteristics of Organic Matter in Two Orchards Differing in Earthworm Activity. *Applied Soil Ecology*, 24(3), 219–232.

Joseph, K., Mordechai, S. & William, A.W. (1978). Viscosity of Liquid Water in the Range 8$^{o}$C to 150$^{o}$C. *Journal Physical and Chemical Reference Data*, 7(3), 941-948.

 

Kamaruddin, S.A., Sulaiman, W.N.A., Rahman, N.A., Zakaria, M.P., Mustaffar, M. & Sa'ari, R. (2011). A Review of Laboratory and Numerical Simulations of Hydrocarbons Migration in Subsurface Environments. *Journal of Environmental Science and Technology*, 4(3), 191-214.

Kechavarzi, C., Soga, K., Illangasekare, T.H. & Nikolopoulos, P. (2008). Laboratory Study of Immiscible Contaminant flow in Unsaturated Layered Sands. *Vadose Zone Journal*, 7(1), 1-9.

Krisnanto, S., Rahardjo, H., Fredlund, D.G. & Leong, E.C. (2014). Mapping of Cracked Soils and Lateral Water flow Characteristics through a Network of Cracks. *Engineering Geology*, 172, 12–25.

Lakeland, D.L., Rechenmacher, A. & Ghanem, R. (2014). Towards a Complete Model of Soil Liquefaction: The Importance of Fluid flow and Grain Motion. *Proceedings of the Royal Society A: Mathematical, Physical and Engineering Sciences,* London, A470:20130453.

Lewandowska, J., Szymkiewicz, A., Gorczewska, W. & Vauclin, M. (2005). Infiltration in a Double-Porosity Medium: Experiments and Comparison with a Theoretical Model. *Water Resources Research*, 41(2), 1-14.

Li, X. & Zhang, L.M. (2009). Characterization of Dual-Structure Pore-Size Distribution of Soil. *Canadian Geotechnical Journal*, 46, 129–141.

Loke, K.F., Rahman, N.A. & Ramli, M.Z. (2016a). A Laboratory Study of Vibration Effect for Deformable Double-Porosity Soil with Different Moisture Content. *Malaysian Journal of Civil Engineering*, 28(3), 207-222.

Loke, K.F., Rahman, N.A. & Nazir, R. (2016b). Laboratory Study for Deformable Double-Porosity Soil with Vibration Effect. *Proceedings of 6th International Graduate Conference on Engineering, Science and Humanitie*, Johor Bahru, Malaysia, 65-68.

Maas, H.G. & Hampel, U. (2006). Photogrammetric Techniques in Civil Engineering Material Testing and Structure Monitoring. *Photogrammetric Engineering & Remote Sensing*, 72(1), 39-45.

McNeil, J.D., Oldenborger, G.A. & Chincariol, R.A. (2006). Quantitative Imaging of Contaminant Distributions in Heterogeneous Porous Media Laboratory Experiments. *Journal of Contaminant Hydrology*, 84, 36-54.

Muguntan, V., Ruben, S. & Stephanie, L. (2015). *Strong Earthquake Strikes Sabah*. The Star Newspaper Online. June.

Ngien, S.K., Chin, P.Q., Hasan, M., Ali, M.I., Tadza, M.Y.M. & Rahman, N.A. (2016). Image Analysis of Non-Aqueous Phase Liquid Migration in Aggregated Kaolin. *ARPN Journal of Engineering and Applied Sciences*, 11(10), 6393-6398.

Ngien, S.K., Rahman, N.A., Ahmad, K. & Lewis, R.W. (2012). A Review of Experimental Studies on Double-Porosity Soils. *Scientific Research and Essays*, 7(38), 3243–3250.

Ngien, S.K., Rahman, N.A., Bob, M.M., Ahmad, K., Sa'ari, R. & Lewis, R.W. (2011). Observation of Light Non-Aqueous Phase Liquid Migration in Aggregated Soil using Image Analysis. *Transport in Porous Media*, 92(1), 83–100.

Oostrom, M., Dane, J.H. & Wietsma, T.W. (2007). A Review of Multidimentional, Multifluid, Intermediate-Scale Experiments: Flow Behaviour, Saturation Imaging and Tracer Detection and Quantification. *Vadose Zone Journal*, 6(3)570-598.

Sa`ari, R., Rahman, N.A., Latif Abdul, N.H., Yusof, Z.M., Ngien, S.K., Kamaruddin, S.A., Mustaffar, M. & Hezmi, M.A. (2015). Application of Digital Image Processing Technique in Monitoring LNAPL Migration in Double Porosity Soil Column. *Jurnal Teknologi*, 3(72), 23–29.

Shincariol, R.A., Herderick, E.E. & Schwartz, F.W. (1993). On the Application of Image Analysis to Determine Concentration Distribution in Laboratory Experiments. *Journal of Contaminant Hydrology*, 12, 197-215.

Stephanie, L. (2015). *Tawau Residents Shaken By Quake*. The Star Newspaper Online. December.

Van Geel, P.J. & Sykes, J.F. (1994). Laboratory and Model Simulations of a LNAPL Spill in a Variably-Saturated Sand. *Journal of Contaminant Hydrology*, 17, 1-25.

 

# CHANGE IN SEDIMENT CHARACTERISTICS AND SEDIMENT LOAD OF THE NAN RIVER DUE TO LARGE DAM CONSTRUCTION

BUTSAWAN BIDORN[(1)], STEPHEN A. KISH[(2)], JOSEPH F. DONOGHUE[(3)], KOMKRIT BIDORN[(4)] & RUETAITIP MAMA[(5)]

[(1)] Water Resources Engineering Department, Chulalongkorn University, Bangkok, Thailand,
butsawan.p@chula.ac.th
[(2)] Earth, Ocean and Atmospheric Science, Florida State University, Florida, USA
skish@fsu.edu
[(3)] Planetary Sciences Program, Department of Physics, University of Central Florida, Florida, USA
joseph.donoghue@ucf.edu
[(4)] Pothi Sirin Thai Consultant Co., Ltd., Bangkok, Thailand
b_komkrit@yahoo.com
[(5)] Royal Irrigation Department, Bangkok, Thailand
vmm@hotmail.com

## ABSTRACT

The sediment transport characteristics and long-term trends of total sediment loads of the Nan River, which is the major sediment supply source to the Chao Phraya River, have been studied to evaluate the effects of the construction of the Sirikit Dam on sediment reduction in the Nan and Chao Phraya River system. Survey data include river cross sections, flow velocities, suspended sediment concentration, and bed load transport. Additionally, historical data on river discharge and suspended sediment load at two hydrological stations (Stations N.1 and N.7) operated by the Royal Irrigation Department (RID) during the period 1923-2012 are utilized to estimate the suspended sediment loads transported at the upstream and downstream of the Sirikit Dam. Based on river surveys of the Nan River during the period 2011-2013 and on historical data observed by the Royal Irrigation Department over six decades, total sediment loads of the river can be calculated. Results of this study reveal that suspended sediment loads at upstream and downstream the Sirikit Dam have a strong correlation with river discharge, and the relationships can be represented by power equations with coefficients of determination more than 0.93. It also appears that the bed-to suspended load ratio of the Nan River varies in a narrow range between 0 and 0.14. Time series of total sediment load at the upstream and downstream the dam over the past six decades show slight increasing trends on the Nan River. Additionally, significant reduction in the total sediment yield of the Nan River occurs during the 1976-1993 related to a drought period. Then, total sediment loads on the Nan River significantly increase during 1995-2012 as a result of flood events, which occur more frequently during the past two decades. Therefore, existing of the Sirikit Dam may not be a direct cause of a 60-85% sediment reduction on the Chao Phraya River as suggested by previous studies.

**Keywords:** Sediment transport; dam; suspended load; bed load; human activities.

## 1 INTRODUCTION

Rivers play a major role in delivering sediment from the land to the oceans. However, sediment discharge of many of the world's rivers has been significantly modified as a result of human activities during the past few centuries. Land clearance, land use change, soil and water conservation, and mining activities may cause an increase in sediment load in rivers (Syvitski and Kettner, 2011; Walling, 2006). Meanwhile, dam construction may reduce sediment flux by partially trapping sediment behind dams (Syvitski and Saito, 2007; Walling 1999). In the Nan River, which is one of the most important rivers in Thailand, the Sirikit Dam was completed in 1972 as an additional component of the Chao Phraya Project, one of the largest irrigation projects in Asia. The dam mainly supplies water for the purpose of irrigation, flood control, hydroelectric power, and navigation. Earlier in 1964, the Bhumibol Dam was completed on the Ping River, another major tributary of the Chao Phraya (CPY) River. The normal storage capacity of the Sirikit Dam is about 9,510 million cubic meter (MCM), (Manee et al., 2015). Combining with the Bhumibol Dam (13,462 MCM), these two dams capture approximately 12,000 MCM (22%) of the Chao Phraya River's annual discharge (Mikhailov and Nikitina, 2009; Molle, 2007). After the completion of the Sirikit Dam, a backwater region was formed upstream of the dam, and the deposition of sediment was found in the upstream reaches of the Nan River (Electricity Generating Authority of Thailand (EGAT), 1993). The construction of the Bhumibol and Sirikit dams is believed to be a cause of 60-85% sediment load reduction at the Chao Phraya River, of which the Nan is a tributary (Gupta et al. 2012; Syvitski et al., 2009; Saito et al., 2007; Walling, 2006; Winterwerp et al., 2005; Japan International Cooperation Agency (JICA), 2001). However, it remains unclear that how these two dams, which control only about one fourth of the CPY River's flow have reduced a large amount of sediment of the CPY River.

 

Because existing data of the Nan River are limited for sediment transport analysis, the objectives of this study are 1) to examine sediment characteristics of the Nan River and 2) to qualitatively evaluate the effect of large dam construction on the sediment load reduction of the Nan River. Sediment characteristics of the Nan River are studied using data from river surveys. With sediment characteristics and historical river flow data at hydrological stations observed by RID, long-term total sediment load from 1923 to 2013 is estimated. The effect of the Sirikit Dam is assessed based on the variation of long-term sediment load at the lower reach of the Nan River and based on reservoir sediment surveys of the Sirikit Dam in 1980 and 1992 conducted by Electricity Generating Authority of Thailand (EGAT).

## 2 STUDY AREA

The Nan River originates in the mountainous region of the northern watershed of Thailand. The river basin extends from latitudes 15° 42′ N to 18° 37′ N and longitudes 99° 51′ E to 101° 21′ E (Figure 1) with a catchment area of 34,682 square kilometers ($km^2$) (Hydro and Agro Informatics Institute (HAII), 2012). The river basin is mainly characterized by terraced mountains and floodplain with elevations ranging from 10 to 300 m. above MSL (Amnatsan et al., 2009; JICA, 2001). The total length of the river is approximately 627 km with the river gradient varying from 1:3,500 to 1:13,600 (JICA, 2001; EGAT, 1993). The channel width ranges between 100 and 300 m with river depths of 10 to 15 m (JICA, 2001). Mean annual runoff of the Nan River is 12,015 MCM (Wuttichaikitcharoen and Babel, 2014), which is about 38% of the Chao Phraya River's annual discharge (31,400 MCM) (Hungspreug et al., 2000).

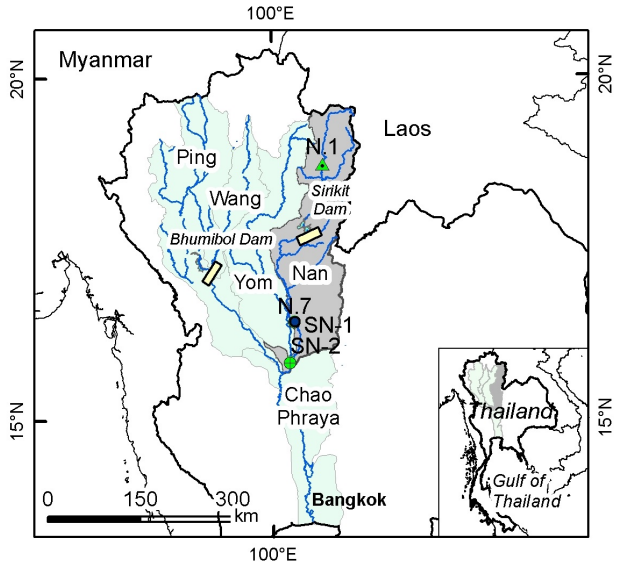


**Figure 1.** Location map of the Nan River basin, Thailand, and observation stations.

The climate of the Nan River basin is under the influence of the northeast and southwest monsoons. The southwest monsoon brings a warm moist air from the Indian Ocean toward Thailand from mid-May to mid-October causing wet season in this region. From November to mid-March, the northeast monsoon brings the cold and dry air from the anticyclone in China mainland over the major part of Thailand causing dry season of the country (https://www.tmd.go.th/en/downloads.php). Annual rainfall averages about 1,287 mm, and 90% of rainfall occurs between May and October (HAII, 2012). The Sirikit Dam is located at Tha Pla, Uttaradit province, (about 575 km from the Chao Phraya River mouth) with the drainage area of about 13,130 $km^3$ (EGAT, 1993). The dam construction began in March 1968 and completed in 1972 by the Royal Irrigation Department. To date, the dam is operated and managed by EGAT.

## 3 METHODS

To study sediment characteristic of the Nan River basin, river surveys were carried out on nine occasions during the period 2011-2013 at Stations SN-1 and SN-2 located at 233 km and 300 km downstream the Sirikit Dam, respectively (Figure 1). Station SN-1 is situated 3 km away from a RID's gauging station (Station N.7 in Figure 1). Meanwhile, the location of Station SN-2 is about 27 km upstream of the river basin outlet. Survey data included river cross-sections, flow velocities, suspended sediment concentrations, and bedload samples. River depth was gauged along the traverse distance to provide a cross-sectional profile of the river. The flow velocities were measured using an AEM1-D in-situ portable single-axis current meter with the measurement range of 0.01-5 m/s. The mean flow velocities were calculated from six separate measurement data at various depths. Suspended sediment was collected using an inverted and corked cylindrical bottle at the proportional depths of 0.2, 0.4, 0.6, and 0.8 between the river bed and water surface. Suspended sediment was filtered

 

from the samples using GIF filter paper, which retained particles larger than 0.5 μm. The filters were dried and weighed and the suspended sediment concentration was calculated by weight difference. A Helley-Smith sampler, which is a medium-weight sampler containing a polyester sampling bag was used to collect bed load in this study. The sampler operation is limited to flow velocity less than 2.5 m/s, and the sample bag allowed the collection of gravel and sand with a diameter greater than 0.25 mm. Each bedload sample was taken over 30 to 60 second. The bedload samples were analyzed using a standard test method of particle-size analysis of soil (ASTM D422).

In this study, historical river discharge and sediment data observed at the gauging stations N.1 and N.7 operated by the RID.) were collected to study sediment characteristics of the Nan River. Stations N.1 and N.7 are located 150 km upstream and 230 km downstream from Sirikit Dam, respectively (Figure 1). At Station N.1, the RID has recorded river runoff since 1923, and the measurement of suspended sediment data was started in 1982. Daily river discharge and suspended sediment data at Station N.7 have been gauged since 1944 and 2001, respectively. However, bed load data are not available at all RID's gauging stations. In general, the bed load is estimated as about 10-20% of total sediment load for non-mountainous rivers, and as much as 20-40% for mountainous rivers (Turowski et al. (2010). EGAT (1993) estimated annual bed load at the Sirikit Dam site as 60% of the suspended load. However, according to river sediment studies in several rivers in Thailand (Table 1), bed load of the Nan River ranges from 1 to 14 percent of the suspended sediment load.

Total sediment load consists of suspended sediment load and bed load. To evaluate the variation in total sediment load in the Nan River, long-term suspended load data, which covered pre- and post-dam periods were estimated from sediment rating curves. The bed load transported along the Nan River was calculated using bed-to suspended sediment ratio analyzed from river survey data. The variation of long-term sediment load can be used to indicate the influence of the Sirikit Dam on sediment load of the Nan River.

**Table 1.** Bed-to suspended sediment ratio in Thailand's rivers.

| **Authors** | **Bed-to suspended sediment ratio (%)** | | | | |
|---|---|---|---|---|---|
| | Ping | Wang | Yom | Nan | Kok |
| Kitisuntorn (1994) | | | | 1-2 | |
| Chanyotha and Thaka-udom (1995) | | | | | 38 |
| Bidorn et al. (2015) | 4-26 | 0-6 | 0-5 | 11-14 | |

## 4 RESULTS AND DISCUSSION

### 4.1 River flow and sediment characteristics during the period 2011-2013

The observation data of river flow and sediment load at Stations SN-1 and SN-2 during the period 2011-2013 are summarized in Table 2. Figure 2 presents the observed sediment discharge (suspended load and bed load) at Stations SN-1 and SN-2. The observation data of Station SN-1 covered the Thailand's Great Flood of 2011, which is ranked as the world's fourth costliest disaster as of 2011 (Wongsa, 2014). The flood caused high river discharge of 847 $m^3/s$ (almost double the average discharge of the Nan River) producing the transport of suspended sediment and bed load of 7,300 and 1,040 mt/d, respectively. Between 2012 and 2013, the observed river discharge ($Q_w$) at Station SN-01 during the wet season varied between 68 and 493 $m^3/s$ with a mean river flow of about 333 $m^3/s$. The measured flow velocities ranged from 0.37 to 1.0 m/s. The suspended sediment loads ($Q_s$) varied between 710 and 7,518 mt/d, whereas, bed load ($Q_b$) significantly dropped to 0-360 mt/d after the Flood of 2011. Based on the bed load samples, the Nan River bed material was medium sand with a median diameter ($d_{50}$) of 0.33-0.55 mm. For the dry season, the observed river discharge at Station SN-1 ranged between 154 and 256 $m^3/s$, which yielded suspended sediment load of 900-1,340 mt/d and bed load of 0-123 mt/d. According to the observation data, bed-to suspended sediment ratio of Station SN-1 varied between 0 and 0.14.

At Station SN-2, observed river data showed that the river discharge was generally greater than that observed at the Station SN-1 (about 2 times on average). The river discharges observed at the Station SN-2 during the wet season fluctuated between 134 and 461 $m^3/s$, which yielded 1,295-10,541 mt/d of the suspended sediment load and 0-424 mt/d of the bed load. During the dry season, the river discharge of the Station SN-2 varied between 94 and 289 $m^3/s$ producing suspended sediment load of 956-2,573 mt/d. However, bed load at Station SN-2 was under detectable during the dry season of 2012-2013.

According to the observation data, it revealed that the river runoff of the Nan River generally increased toward downstream of the Nan River, and the suspended sediment load seemingly rose in the direction of water flow. In contrast, the rate of bed load transport appeared to decrease away from the upstream, and the

 

movement of bed loads was generally under detectable when river current was less than 0.6 m/s. However, some bed load measurement during the high discharge events (11 May and 24 September, 2013 in Table 2) experienced a difficulty on controlling the sediment trap, so the bed load could not be collected.

4.2 Historical river flows at the upstream and downstream of the Sirikit Dam

In this study, daily river flow data at Stations N.1 and N.7 were obtained from the RID. Station N.1 is located at about 150 km upstream of the Sirikit Dam. The catchment area of this station is 4,609 km$^2$. The river discharge data at Station N.1 covered the period 1923-2012. Meanwhile, Station N.7 is situated on the floodplain area in the lower portion of Nan River basin (about 230 km downstream of the Sirikit Dam) with a drainage area of 29,153 km$^2$. The Station N.7's river discharge data are available from 1944 to 2013. Time series of daily river discharge at Stations N.1 and N.7 are shown in Figure 3. Based on statistical analysis of historical river flow data, it appeared that mean annual runoff at Station N.1 ranged between 1,293 and 6,078 MCM/y. At Station N.7, the annual runoff varied from 4,561 to 20,120 MCM/y, which was significantly higher than mean annual runoff at Station N.1. The maximum annual runoff at both stations occurred in 2011. Figure 3 revealed that the flow regime of the Station N.1 had not significantly changed during the past 90 years. In contrast, the dam has completely controlled and changed the river flow regime at Station N.7 since 1972. The water regulation by the Sirikit dam obviously increases minimum flows and stabilizes river flow downstream of the dam. With the smaller area than Station N.7's watershed, the river discharge per unit area at Station N.1 is relatively high compared to that at Station N.7 because an average annual rainfall of the watershed varies between 1,300-1,800 mm/y across the watershed. Meanwhile, annual rainfall over the watershed of Station N.7 ranges from 1,000 to 1,500 mm/y.

**Table 2.** Observation data from river surveys at Stations SN-1 and SN-2 during 2011-2013.

| Date | Flow area, A (m) | Mean flow velocity, V (m/s) | Discharge, $Q_w$ ($m^3$/s) | Suspended load, $Q_s$ (mt/d) | Bed load, $Q_b$ (mt/d) | $Q_b/Q_s$ |
|---|---|---|---|---|---|---|
| **SN-1 (wet season)** | | | | | | |
| 21-Oct-11 | 899 | 0.94 | 847 | 7,305 | 1,040 | 0.14 |
| 2-Jun-12 | 321 | 1.00 | 321 | 6,501 | 357 | 0.05 |
| 5-Aug-12 | 535 | 0.92 | 493 | 7,518 | 360 | 0.05 |
| 18-Oct-12 | 190 | 0.64 | 121 | 1,082 | 120 | 0.11 |
| 11-May-13 | 250 | 0.80 | 201 | 1,151 | 0 | 0.00 |
| 21-Jul-13 | 186 | 0.37 | 68 | 710 | 0 | 0.00 |
| 23-Sep-13 | 494 | 0.56 | 277 | 2,496 | 411 | 0.16 |
| **SN-1 (dry season)** | | | | | | |
| 27-Jan-13 | 306 | 0.87 | 265 | 1,340 | 123 | 0.09 |
| 9-Mar-13 | 234 | 0.66 | 154 | 901 | 0 | 0.00 |
| **SN-2 (wet season)** | | | | | | |
| 2-Jun-12 | 611 | 1.05 | 641 | 10,071 | 138 | 0.014 |
| 3-Aug-12 | 765 | 0.84 | 646 | 10,541 | 62 | 0.006 |
| 16-Oct-12 | 752 | 0.85 | 641 | 5,156 | 423 | 0.082 |
| 12-May-13 | 261 | 0.51 | 134 | 1,295 | 0 | 0.000 |
| 22-Jul-13 | 327 | 0.51 | 165 | 2,268 | 0 | 0.000 |
| 24-Sep-13 | 736 | 0.58 | 429 | 2,892 | 0 | 0.000 |
| **SN-2 (dry season)** | | | | | | |
| 26-Jan-13 | 474 | 0.61 | 289 | 2,573 | 0 | 0.000 |
| 8-Mar-13 | 206 | 0.46 | 94 | 956 | 0 | 0.000 |

4.3 Historical suspended sediment load at the upstream and downstream of the Sirikit Dam

Suspended sediment has been sampled at Stations N.1 and N.7 since 1982 and 2001, respectively. However, RID did not monitor suspended sediment data on a regular basis. Water samples were taken several times per year (but not every year) for analyzing suspended sediment concentration and calculating suspended sediment load. The relationship between $Q_s$ and $Q_w$ (sediment rating curve) were obtained from Linear Regression analysis. Daily suspended sediment load data were estimated by substituting daily water discharge data -- which have been routinely gauged -- into the regression equation. Figure 4 depicts daily suspended sediment load at Stations N.1 and N.7. It appears that the suspended sediment load at Station N.7 fluctuated with a narrower range than that at Station N.1 as a result of river flow regulation. Based on the plots of $Q_s$ versus $Q_w$ shown in Figure 5, the data showed a strong correlation between river discharge and suspended sediment load for Stations N.1 and N.7 with the coefficient of determination of 0.97 and 0.93, respectively. The regression equation for each station is given below.

Station N.1: $$Q_s = 0.085 Q_w^{2.01} \quad [1]$$

 

Station N.7: $$Q_s = 0.83Q_w^{1.40}$$ [2]

where $Q_s$ is the suspended sediment load (mt/s), and $Q_w$ is river discharge ($m^3/s$).

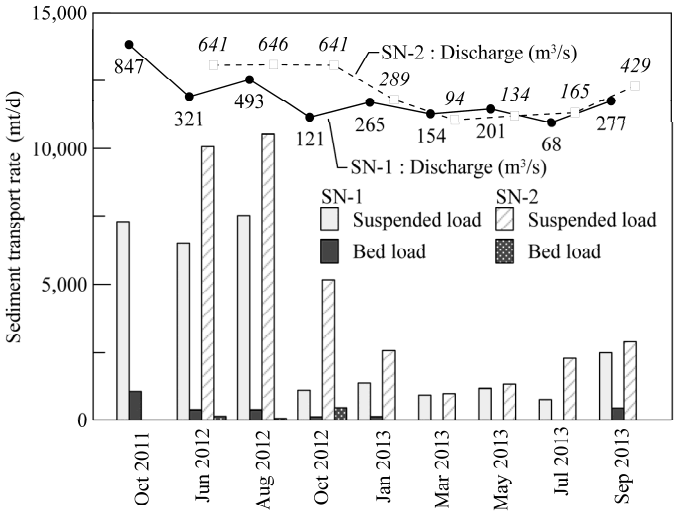


**Figure 2.** Sediment transport characteristics at Stations SN-1 and SN-2 during 2011-2013.

The sediment rating curves showed that Station N.1's sub-basin supplied higher sediment than Station N.7. This is expectable because Station N.1 watershed is situated in a mountainous area with the highest rate of soil erosion in the northern part of Thailand (>200 Mg/ha/y)(Plageon et al. 2013). Since the suspended load on the Nan River is directly related to the river discharge, the regression Eqs.[1] and [2] were used to estimate long-term sediment load at the upstream (Station N.1) and downstream (Station N.7) of the Sirikit Dam, respectively. Time series of the estimated suspended sediment load at Stations N.1 and N.7 are illustrated in Figure 6. The annual mean suspended sediment load transported through the Station N.1 during the period 1923-2013 was 1.17 million mt/y with the minimum and maximum of 0.18 and 4.7 million mt/y, respectively. Meanwhile, the suspended load at Station N.7 during 1944-2013 ranged between 0.36 to 3.47 mt/y with a mean suspended sediment load of 1.23 mt/y.

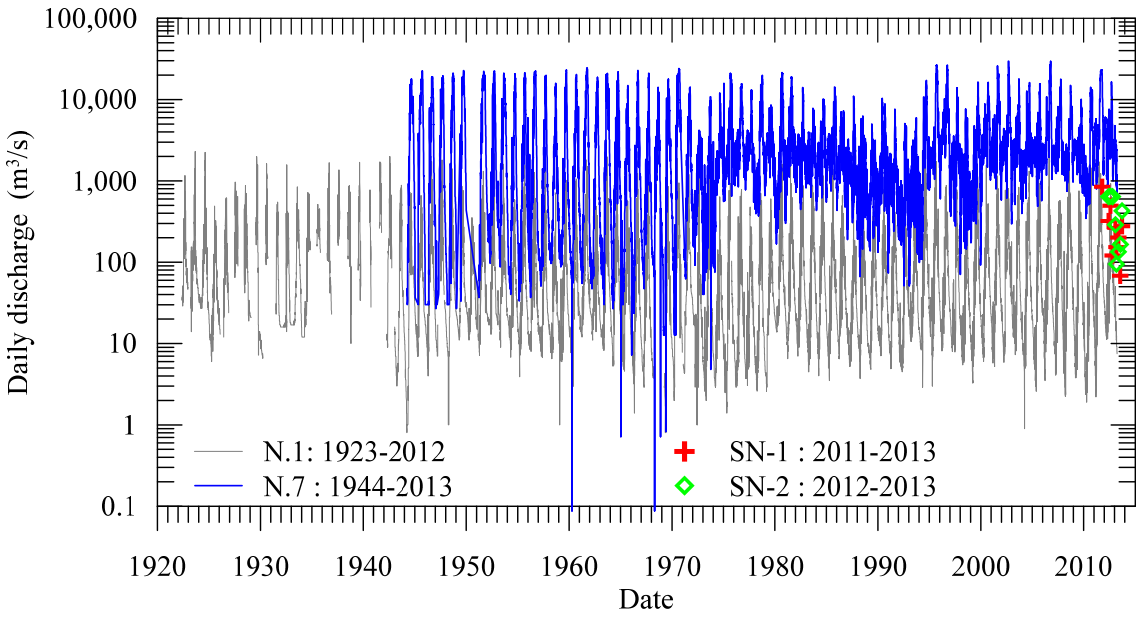


**Figure 3.** Daily river discharge variation at Stations N.1, N.7, SN-1, and SN-2 from 1923 to 2013.

 

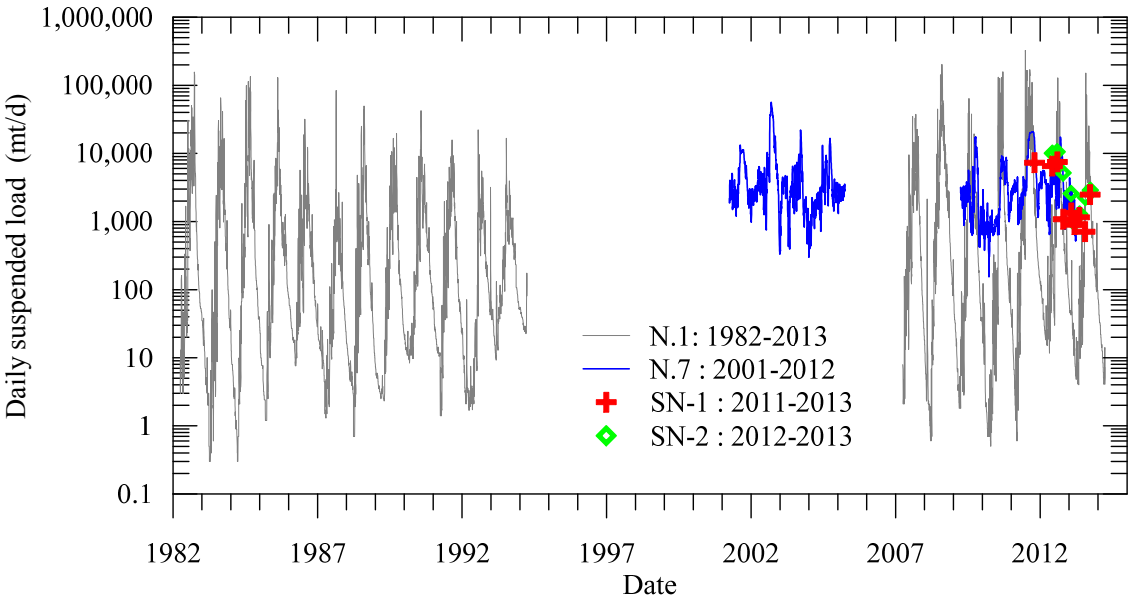


**Figure 4.** Daily suspended load variation at Stations N.1, N.7, SN-1, and SN-2 from 1982 to 2013.

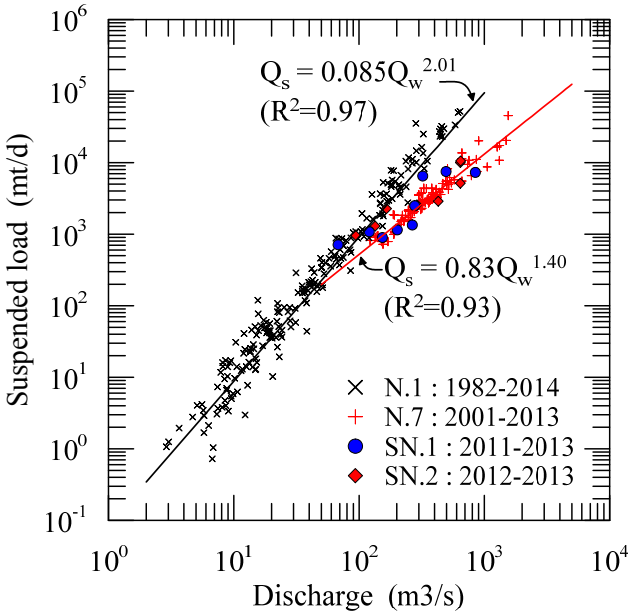


**Figure 5.** Relationship between suspended sediment load and river discharge at Stations N.1, N.7, SN-1, and SN-2.

4.4 Estimated total sediment load on the Nan River

Based on the results of sediment characteristic analysis, total sediment load on the Nan River is mainly transported as suspended load and minor bed load. The field data revealed that bed-to suspended sediment ratios observed on the Nan River varied between 0 and 14% of suspended sediment load with a mean value of 4%. By combining suspended sediment data estimated from Eqs. [1] and [2] to bedload data (4% of suspended sediment load), the long-term total sediment load at Stations N.1 and N.7 can be determined. The time series of estimated annual total sediment load of Stations N.1 (1923-2013) and N.7 (1944-2012) are shown in Figure 6. Based on the comparison of annual total sediment loads between Stations N.1 and N.7, the amount of total sediment load at each station was not obviously different during the pre-dam period and during the past twenty years. Long-term trends of total sediment load somewhat increased at both stations. For Station N.1, an average annual total sediment load was 1.18 mt/y with the minimum sediment load of 0.18 million mt/y occurring in 1993. The estimated maximum total sediment load at this station is 4.9 million my/t in 2011 when the Thailand's Great Flood took place. Even though the drainage area of Station N.7 is much higher than Station N.1, the mean annual total sediment load at Station N.7 was about 1.27 million mt/y, which was slightly higher than that at Station N.1. The lowest total sediment loads estimated at Station N.7 was 0.38 million mt/y, and the maximum total sediment load was 3.62 million mt/y occurring in 2002, which was one of the major flood events of the country.

 

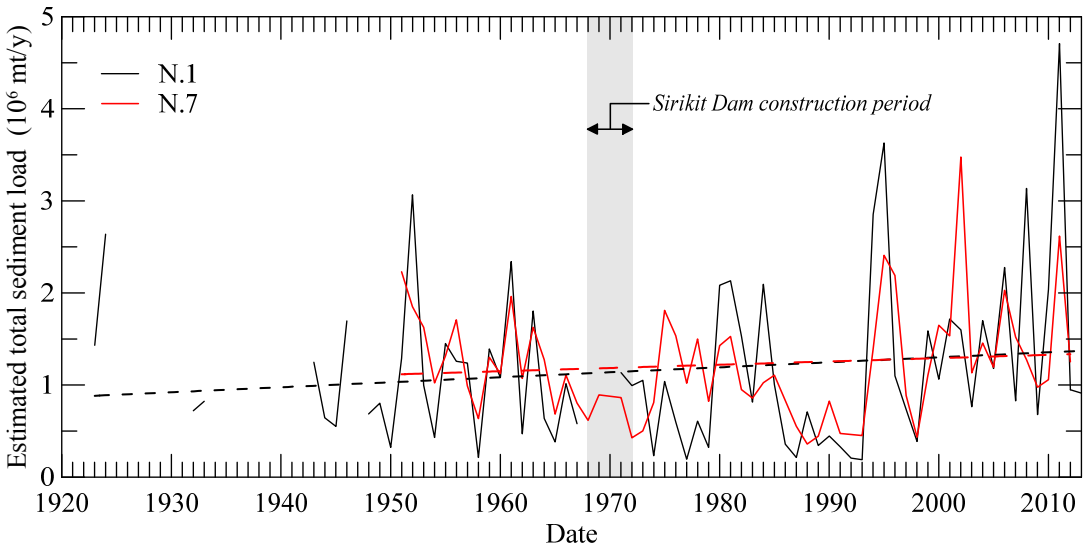


**Figure 6.** Time series for estimated total sediment load at Stations N.1 and N.7 during the period 1923-2013.

4.5 Effect of dam construction on sediment load of the Nan River

Theoretically, the effects of a dam must be evaluated by comparing sediment data between before and after dam construction without changes in other conditions. However, historical sediment data covered pre-dam period are usually not available, especially in developing countries. Moreover, because of randomness of hydrologic events and the time-dependent of river response, the possibility of measuring sediment data during post-dam period with the same conditions as pre-dam period is low. This study attempts to assess the effect of the Sirikit Dam on sediment reduction on the Nan River based on the variation of sediment loads at upstream and downstream of the Siritkit Dam. The time series of the annual total sediment load of the Stations N.1 and N.7 (Figure 6) revealed a slightly increasing trend in total sediment load during the period 1923-2013 at both stations. The significantly high total sediment load at Station N.1 compared to Station N.7 is possibly caused by the gauging location, which situates in the mountainous area with a very steep gradient of 1:1,000. Meanwhile, Station N.7 is situated in the large flood plain area of the Nan River basin (about 500 km downstream of Station N.1). The average river gradient between the Sirikit Dam and Station N.7 is approximately 1:12,500. The change of a river gradient from steep to mild slopes may cause a significant amount of sediment deposition along the reach between these two stations. Figure 7 depicts sediment deposition along the Nan River between Station N.1 and N.7 that may cause a low sediment load observed at Station N.7 compared to Station N.1.

Although the Sirikit Dam has trapped some suspended and bedload sediment behind it, the dam did not cause any abruptly decrease of the sediment load at Station N.7 after the completion of the dam in 1972. In contrast, total sediment load at Station N.7 was still high during the first decade of the Sirikit Dam operation. In general, dam completely impounds bed load and partially hold some suspended sediment load within the reservoir causing sediment reduction downstream the dam. However, released water from the dam normally contains little sediment. The downstream flow may have eroded the downstream channel to equilibrate with the new upstream gradient, resulting in an increase of suspended loads downstream. Moreover, downstream the dam can receive additional sediment load from sub-basin below the dam. The reduction of sediment as a result of the Sirikit Dam construction seems to be compensated by extra sediment loads from river channel adjustment combined with additional sediment from downstream sub-basin.

However, between 1982 and 1994, sediment loads in both upstream and downstream of the dam significantly declined as a result of a drought period. Based on sediment survey of the Sirikit Dam studied by EGAT (1993), cross-section data measured in 1980 and 1992 showed insignificant changes on the reservoir storage over 12 years. From 1995 to 2013, the trend of sediment load at the upstream and downstream of the dam was likely increasing. The significantly high amount of sediment loads downstream the dam appears to relate to flood events, which occurred more frequently during the last two decades.

Figure 8 illustrates the mean total sediment load of Stations N.1 and N.7 for each decade during 1941 to 2012. It appears that the mean sediment volumes at Station N.1 was slightly less than those at Station N.7 during the pre-dam period, even though the drainage area of the N.7 is 6.4 times larger than the N.1's drainage area. Generally, land use change may cause an increase in total sediment load in the river. Many natural vegetation areas in the lower Nan River basin (downstream the Sirikit Dam) have been converted to agricultural areas since the Sirikit Dam completed. However, the mean total sediment load at Station N.7 tends to be less than Station N.1's sediment loads since 1980s. Therefore, solely sediment sources or existing of the Sirikit Dam may not play a key role on sediment loads transported along the Nan River. The Nan River basin features or the river characteristics, which are complicated and are different from other river basins,

 

possibly are the important parameters controlling sedimentation processes and sediment loads on the Nan River. Moreover, land development including highways, roads, irrigation diversion system along the Nan River downstream of the Sirikit Dam (as shown in the left panels of Figure 7) can also create some sediment blockage to the main river. More sediment observation data along the Nan River including upstream and downstream of the Sirikit Dam and detailed sedimentation process analysis are recommended for assessing the actual effects of the Sirikit Dam on sediment loads of the Nan River.

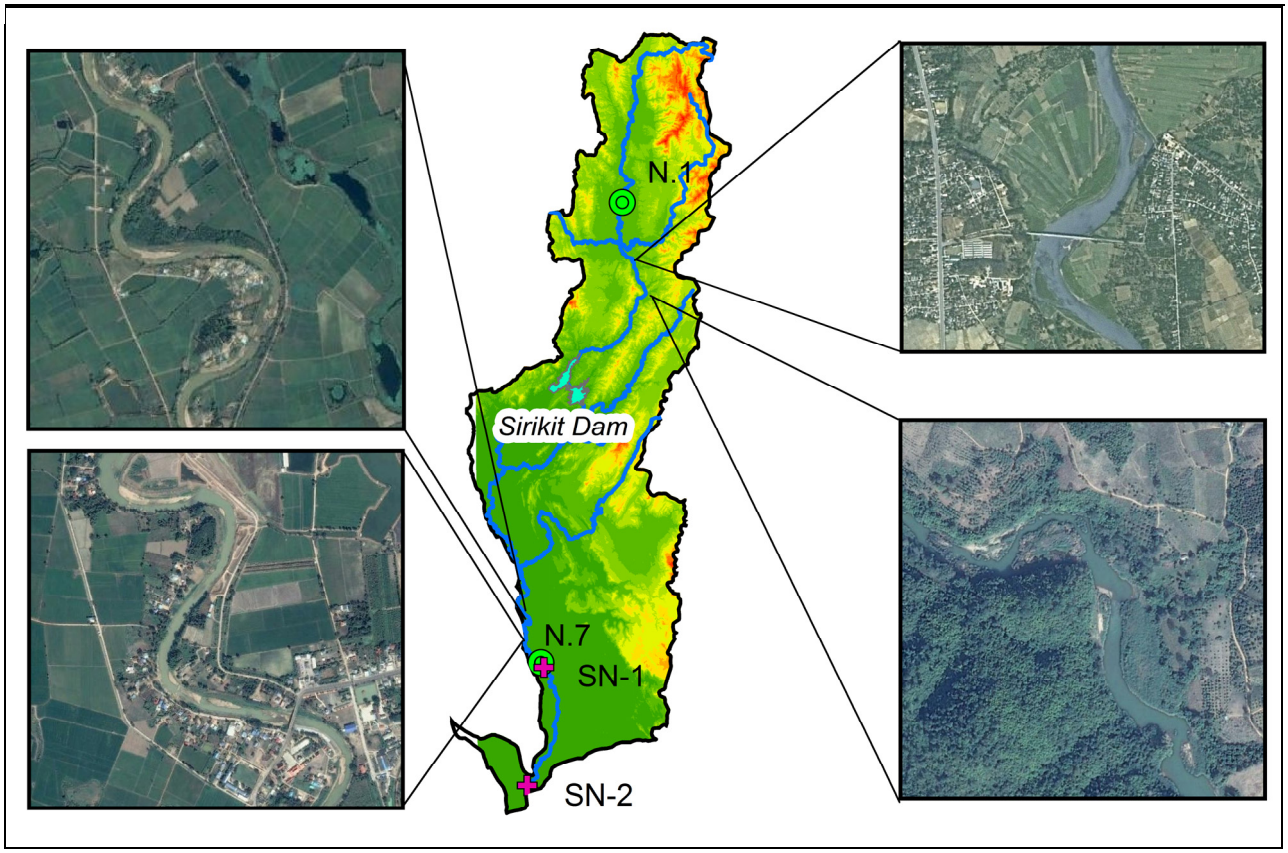


**Figure 7.** Sediment deposition found along the Nan River between Stations N.1 and N.7.

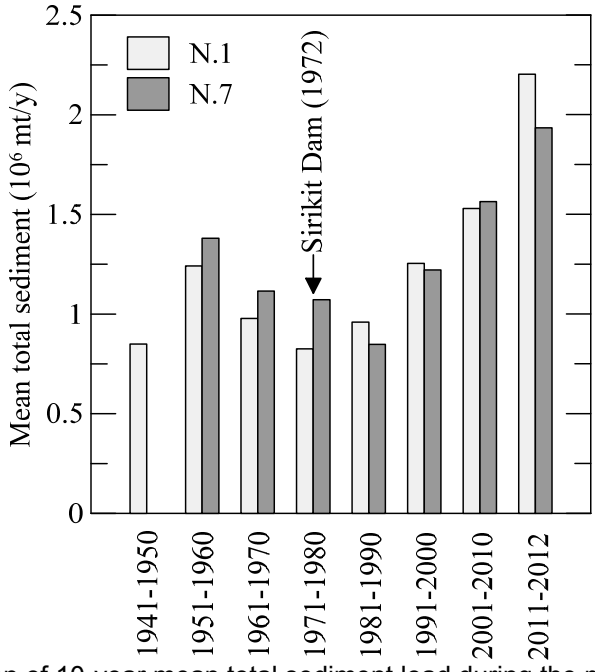


**Figure 8.** Variation of 10-year mean total sediment load during the period 1941-2012.

## 5 CONCLUSIONS

This study has demonstrated the characteristics of river flow and sediment load transported in the Nan River and evaluated effects of the construction of the Sirikit Dam on sediment loads reduction on the Nan River. Based on river survey data carried out over the period 2011-2013 at Station SN-1 and SN-2 (233 km and 310 km downstream the Sirikit Dam, respectively), it appears that sediment load of the Nan River mainly transports as suspended sediment and minor bed load. Bed material of the Nan River is mainly medium sand with $d_{50}$ of about 0.33-0.55 mm. The observed sediment data also reveal that the bed-to suspended load ratio at the Nan River fluctuates in the narrow range of 0-14%, while EGAT (1993) estimates bed load as a 60% of suspended sediment load.

The results from the analysis of historical river and sediment data at two gauging stations operated by the RID suggest that observed suspended sediment load at 150 km upstream (Station N.1), and 270 km downstream (Station N.7) the Sirikit Dam has a strong correlation with the river discharge. Power equations can represent these relationships with the goodness of fits ($R^2$) of 0.97 and 0.93, respectively. The sediment rating curves also reveal that the sub-basin situated in the upper reach provides a higher sediment transport rate than that located in the lower reach.

Hydrological records from 1923 to 2013 also show that river discharge at the Station N.1 varies between 1,300 and 6,000 MCM/y with an average discharge of 2,900 MCM. Meanwhile, maximum, minimum, and mean water discharges at the Station N.7 are approximately 3.5 times higher than those of the upstream reach. Based on sediment analysis, however, the estimated annual total sediment loads over the past nine decades range from 0.18 to 4.9 million mt/y at the upstream of the Sirikit dam. Meanwhile, estimated total sediment load at the downstream of the dam varies between 0.38 and 3.6 million mt/y during the past sixty years. Even though the Sirikit Dam has been operated since 1972, the time series of the annual total sediment loads over 60 years show a slightly increasing trend in sediment loads at both upstream and downstream of the dam over the past six decades. Moreover, the completion of the Sirikit Dam does not cause a significant reduction of total sediment load at Station N.7 during the first ten years after the dam completed. The reduction of sediment load occurs between 1976 and 1993 as a result of drought period. However, total sediment loads at the Station N.7 significantly increase during 1995-2012 corresponding to the flood events, which occur more frequently during the past two decades. The results of this study also indicate that the effect of a large dam construction possibly outweigh by additional sediment from channel erosion due to clear water released from the reservoir and/or from the lower sub-basin sediment load in the Nan River. Therefore, existing of the Sirikit Dam is not a major cause of a dramatic sediment reduction in the Chao Phraya River. However, further river sediment observation and detailed study on river sedimentation along the upstream and downstream the dam are recommended for assessing the actual effects of the Sirikit Dam on sediment load of the Nan River.

## ACKNOWLEDGMENTS

This study is partially supported by the Water Resources Engineering Department, Chulalongkorn University and the Science and Technology Re-search Partnership for Sustainable Development, JST-JICA, Japan.

## REFERENCES

Amnatsan, S., Fowze, J.S.M., Bormudoi, A., Hazarika, M.Z. & Samarakoon, L. (2009). Flood Hazard Mapping in Nan River, Thailand. *Proceedings of the 7th Annual Mekong Food Forum*, Bangkok, Thailand, 297–303.

Bidorn, B., Chanyotha, S., Kish, S.A., Donoghue, J.F., Bidorn, K. & Mama, R. (2015). The Effects of Thailand's Great Flood of 2011 on River Sediment Discharge in the Upper Chao Phraya River Basin, Thailand. *International Journal of Sediment Research*, 30(4), 328-337.

Chanyotha, S. & Taksa-udom, C. (1995). Changes of Stream Channel Configuration and Geometry of the Mae Kok River near Amphor Muang, Chiang Rai. *Proceedings of the 2nd National Convention on Civil Engineering,* Chiang Mai, Thailand, 246-260. (In Thai)

Electricity Generating Authority of Thailand (EGAT). (1993). *Sediment survey of Sirikit Dam*, Report No. 31303-3603. October 1993.

Gupta, H., Kao, S.J. & Dai, M. (2012). The Role of Mega Dams in reducing Sediment Fluxes: A Case Study of Large Asian Rivers. *Journal of Hydrology, 464*, 447-458.

Hungspreug, S., Khao-uppatum, W. & Thanopanuwat, S. (2000). Flood Management in Chao Phraya River Basin. *Proceedings of the International Conference: The Chao Phraya Delta: Historical Development, Dynamics and Challenges of Thailand's Rice Bowl.*

Hydro & Agro Informatics Institute (HAII). (2012). *Nan River Basin*, Report on Data Collection and Analysis: Database Development Project and Flood and Drought Modeling of 25 River Basins. Prepared by Asdecon Co-operation Co. Ltd. (In Thai)

 

Japan International Co-operation Agency (JICA). (2001). *The Feasibility Study on Mangrove Revival and Extension Project in the Kingdom of Thailand*, Final Report. Sanyu Consultants and Panya Consultants for the Ministry of Agriculture.

Kitisuntorn, P. (1994). Sediment Transport and Navigation Problem in Lower Nan River, *Doctoral Dissertation*. Chulalongkorn University. (In Thai)

Manee, D., Tachikawa, Y. & Yorozu, K. (2015). Analysis of Hydrologic Variable Changes related to Large Scale Reservoir Operation in Thailand. *Journal of Japan Society of Civil Engineers*, 59, I_61-66

Mikhailov, V.N. & Nikitina, O.I. (2009). Hydrological and Morphological Processes in the Chao Phraya Mouth Area (Thailand) and their Anthropogenic Changes. *Water Resources,* 36(6), 613-624.

Molle, F. (2007). Scales and Power in River Basin Management: The Chao Phraya River in Thailand. *The Geographical Journal*, 173(4), 358-373.

Plangoen, P., Babel, M.S., Clemente, R.S., Shrestha, S. & Tripathi, N.K. (2013). Simulating the Impact of Future Land Use and Climate Change on Soil Erosion and Deposition in the Mae Nam Nan Sub-Catchment, Thailand. *Sustainability, 5*(8), 3244-3274.

Saito, Y., Chaimanee, N., Jarupongsakul, T. & Syvitski, J.P. (2007). Shrinking Megadeltas in Asia: Sea-Level Rise and Sediment Reduction Impacts from Case Study of the Chao Phraya Delta. *Newsletter of the IGBP/IHDP Land Ocean Interaction in the Coastal Zone, 2*, 3-9.

Syvitski, J.P. & Kettner, A. (2011). Sediment Flux and the Anthropocene. Philosophical Transactions of the Royal Society of London A: *Mathematical, Physical and Engineering Sciences, 369*(1938), 957-975.

Syvitski, J.P., Kettner, A.J., Overeem, I., Hutton, E.W., Hannon, M.T., Brakenridge, G.R. & Nicholls, R.J. (2009). Sinking Deltas due to Human Activities. *Nature Geoscience,* 2(10), 681-686.

Syvitski, J.P.M. & Saito, Y. (2007). Morphodynamics of Deltas under the Influence of Humans. *Global and Planetary Change,* 57(3–4), 261-282.

Turowski, J.M., Rickenmann, D. & Dadson, S.J. (2010). The Partitioning of the Total Sediment Load of a River into Suspended Load and Bedload: A Review of Empirical Data. *Sedimentology*, 57(4), 1126-1146.

Walling, D.E. (1999). Linking Land Use, Erosion and Sediment Yields in River Basins. *Hydrobiologia, 410*, 223-240.

Walling, D. (2006). Human Impact on Land–Ocean Sediment Transfer by the World's Rivers. *Geomorphology,* 79(3), 192-216.

Winterwerp, J.C., Borst, W.G. & de Vries, M.B. (2005). Pilot Study on the Erosion and Rehabilitation of a Mangrove Mud Coast. *Journal of Coastal Research,* 21,223-230.

Wongsa, S. (2014). Simulation of Thailand flood 2011. *International Journal of Engineering and Technology,* 6(6), 452.

Wuttichaikitcharoen, P. & Babel, M. (2014). Principal Component and Multiple Regression Analyses for the Estimation of Suspended Sediment Yield in Ungauged Basins of Northern Thailand. *Water,* 6(8), 2412-2435.

 

# EFFECT OF SKEWNESS ON CLEAR-WATER LOCAL SCOUR AT COMPLEX BRIDGE PIERS

YIFAN YANG[(1)], BRUCE W. MELVILLE[(2)], ASAAD Y. SHAMSELDIN[(3)] & HEIDE FRIEDRICH[(4)]

[(1,2,3,4)] PhD Student, Department of Civil and Environmental Engineering, University of Auckland, Auckland, New Zealand, e-mail: yyan749@aucklanduni.ac.nz; b.melville@auckland.ac.nz; a.shamseldin@auckland.ac.nz; h.friedrich@auckland.ac.nz

## ABSTRACT

A laboratory study on clear-water local scour at a complex pier is performed to investigate effects of pier skewness and the pile-cap elevation on scour depth. The model has a 3:50 scale, and is representative of several bridge piers that failed in New Zealand in the past decades. The model pier consists of a wall-like rectangular column, a rectangular pile-cap and a 2×4 array of circular piles underneath. Tests are performed in a 45-m long, 1.54-m wide tilting recirculating flume and in a 16.5-m long, 2.4-m wide non-recirculating flume. Skewness varies from 0° to 45° in 15° increments, and the pile-cap elevation relative to bed level is also varied. All the tests are performed with 30 hours duration, and the measured scour depths are extrapolated to equilibrium using validated equations. Results show that, for complex piers aligned to the flow, the maximum equilibrium scour depth occurs when the top of the pile-cap is close to the undisturbed bed level; for skewed complex piers, the equilibrium scour depth increases significantly compared with aligned ones. The increase of scour depth is proportional to the skew angle $\alpha$, and becomes less sensitive to $\alpha$ when $\alpha > 30°$. For skewed complex piers, the column generates most of the scour depth, if it is inserted significantly into the flow. The sediment coarseness $D_e/d_{50}$ also varies with pier skewness, and is inversely proportional to the normalized scour depth when $D_e/d_{50}$ is larger than a specific value. This phenomenon is in accordance with the previous studies, and the equations of Lee and Sturm (2009) show the best agreement with the data of the present study. In addition, the location of the maximum scour depth varies with different configurations, implying a need to arrange countermeasures accordingly.

**Key Words:** Complex pier; local scour; skewness; pile-cap elevation; sediment coarseness.

## 1 INTRODUCTION

Scour is one of the most common causes of damage to bridge piers, leading to numerous bridge failure cases around the world every year. One aspect of bridge scour that is deserving of more research is the scour at piers with complex geometry (namely complex piers), especially where significant flow skewness is possible. Normally, a complex pier consists of a wall-like column supporting the bridge superstructure, a pile-cap underpinning the column, and an underlying array of piles, called the pile group. Previous studies on scour at non-uniform piers addressed the situations for simple uniform piers founded on caissons or footings, include Jones et al. (1992), Melville and Raudkivi (1996),Parola et al. (1996), Lu et al. (2010) and Kothyari et al. (2012). Jones and Sheppard (2000) completed one of the first studies of scour at complex bridge piers; subsequent studies of scour at complex piers include Coleman (2005), Sheppard and Glasser (2009), Ataie-Ashtiani et al. (2010), Grimaldi and Cardoso (2010), Moreno et al. (2012; 2014; 2015; 2016a; 2016b); Ferraro et al. (2013) and Amini et al. (2014). However, the effect of pier skewness was not addressed in any of the studies mentioned above, this being a major shortcoming.

An idealized approach to deal with the structural complexity of a complex pier is to use the equivalent pier width, whereby a complex pier can be regarded as a cylindrical pier with a diameter equals to the equivalent width. This approach is inherent in the methods proposed by Coleman (2005) and Sheppard and Renna (2010).

The HEC-18 method (Arneson et al., 2012) uses the so-called superposition approach; however, overestimation is often reported. In the present study, a series of tests are performed with various pier skew angles and the pile-cap elevations, to investigate the variation of scour depth and the characteristic of the scour pattern.

## 2 EXPERIMENTAL SETUP

### 2.1 Facilities

Tests were conducted in a 1.54-m wide flume and a 2.4-m wide flume in the Fluid Mechanics Laboratory of the University of Auckland. The 1.54-m wide flume was 45-m long, 1.2-m deep and was a glass-sided recirculating flume having a maximum tilt of 1%. It was supported on two castellated beams which were

 

centrally pivoted so that the slope of the flume can be adjusted by electrically driven screw-jack supports at either end of the flume. It had two pumps for recirculating the water and a pump for recirculating sediments, with a combined capacity of 1189-litre per second. The flume consisted of an inlet section, 35-m long channel, and an outlet section. A false floor 0.4-m in height was placed along the length of the channel section, with a 4-m long sediment recess box located 26-m downstream of the inlet section. Water entered the flume at the base of the inlet section and passed through a wave skimmer, which suppressed surface wave formation. The flume was filled from the laboratory reservoir via an inflow pipe located at the end of the outlet section of the flume and was drained by an outlet valve in the bottom of the outlet section. During experiments, the water levels in the flume were controlled by an overflow pipe in the outlet section of the flume.

The 2.4-m wide flume was 16.5-m long, 2.4-m wide, and 0.3-m deep. It was a non-recirculating flume supported by two universal-beams which pivoted about a central support. Screw jacks supported the beams at either end so that the flume slope was adjustable. The flume consisted of an inlet tank, flow straightener, 13-m long channel, sediment collection tank and an outlet tank. A 2.8-m long and 0.45-m deep sediment recess box was located 7-m downstream of the inlet tank. Water was supplied to the flume inlet from the laboratory constant head tank. Before entering the test section of the flume, the water passed through a baffle system at the bottom of the inlet tank, through a wire mesh screen to smooth the flow, and then through a flow straightener made of PVC pipes.The sediment recess boxes of both flumes were filled with uniform quartz sand with median particle diameter $d_{50}$=0.84-mm and geometrical standard deviation$\sigma_g$=1.35.

2.2 Pier model and configuration

A complex pier model was used to perform tests in the two flumes. The model was made of solid wood, and was painted to avoid being damaged by water. The model consisted of a wall-like column, a pile-cap and pile group supporting the pile-cap, representing the piers of several failed bridges in the past several decades in New Zealand. These bridges include the Bull Road Bridge, the Blackmount Road Bridge, the Oreti River Road Bridge, and the Whakatane River Road Bridge (Melville and Coleman, 2000). The dimensions of the model are shown in Table 1, with a 3:50 geometric scale to prototype. Figure 1 illustrates the plan view, the front view and the 3-D view of the model.

**Table 1.** Dimensions of complex pier model.

| Variable | $b_c$ (m) | $l_c$ (m) | $b_{pc}$ (m) | $l_{pc}$ (m) | $T$ (m) | $f_{cl}$ (m) | $f_{cb}$ (m) | $b_{pg}$ (m) | $S_m$ (m) | $S_n$ (m) |
|---|---|---|---|---|---|---|---|---|---|---|
| **Dimension** | 0.030 | 0.310 | 0.120 | 0.362 | 0.060 | 0.026 | 0.045 | 0.025 | 0.070 | 0.070 |

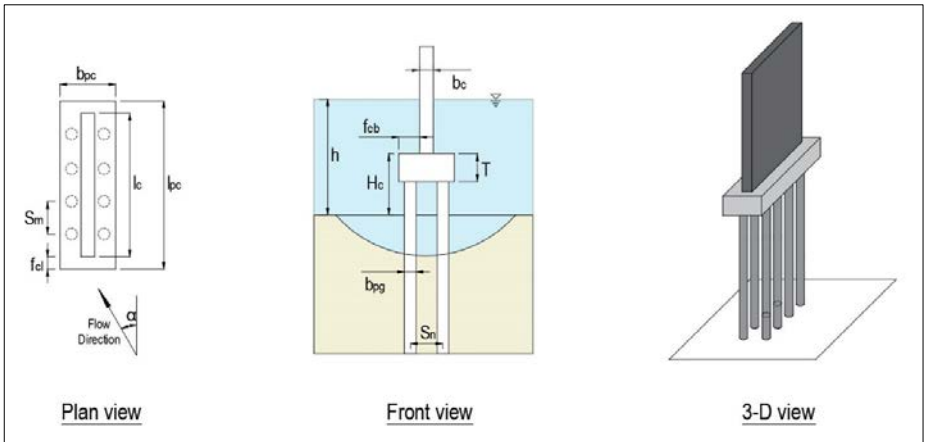


**Figure 1.** Scheme of the model used in the present study

To investigate the effects of pier skewness and the pile-cap elevation, tests with 4 skew angles (0°, 15°, 30°and 45°) and 9 pile-cap elevations were undertaken, as shown in Table 2.

Tests with skewness angles of 0°, 15° and 30° were conducted in the 1.54-m flume, but to avoid contraction effects, the tests for 45° skew angle were performed in the 2.4-m flume. According to Breusers and Raudkivi (1991) and Ballio et al. (2009), contraction scour is negligible for a pier diameter less than 1/8 of the flume width. Considering that bed degradation was not observed, it was appropriate to conclude that the contraction effect was absent. For both flumes, the wall effect was also negligible because $B/y_0$> 5 (Yalin, 1972), where B was the flume width. In previous studies, researchers tended to keep the relative flow depth $y_0/D_e$ not less than a specific value, e.g. 3, to diminish the effect of flow shallowness.

 

**Table 2.** Design of pile-cap elevations

| Position | $H_c$ (mm) | Description |
|---|---|---|
| **A** | 310 | Pile group only |
| **B** | 250 | The pile-cap is exposed to the flow |
| **C** | 120 | |
| **D** | 60 | The pile-cap is close to the bed |
| **E** | 30 | |
| **F** | 0 | |
| **G** | -60 | The pile-cap is fully buried |
| **H** | -110 | |
| **I** | -- | Column only |

However, in the present study, increasing skewness to flow was inevitably accompanied by a stronger shallowing effect, thereby complicating the mechanism of scour at complex piers. Thus, a strict control of flow shallowness was inappropriate in this study.The flow depth and flow velocity were controlled as 0.25-m and 0.354-m/s respectively, giving a flow intensity parameter, $U/U_c$≈0.9, while $U_c$=0.394-m/s. Here $U_c$ was the critical mean approach flow velocity for sediment incipient motion and was calculated using equations in Melville and Coleman (2000).

2.3 Data measurement

Flow velocity were measured using a 3-receiver Vectrino+ side-looking acoustic Doppler velocimeter (ADV) made by Nortek, which had a sampling rate of 200-Hz. The sampling volume was cylindrical, having 6-mm diameter and an adjustable height varying from 1-mm to 7-mm. The output data from the velocimeter were filtered using WinADV software. The filter was set to remove spikes and data with low correlation.

A SeaTek multiple transducer array (MTA) was used to monitor the temporal evolution of scour at specific locations. The instrument was an ultrasonic ranging system, which can detect the distances from the sensors to reflective objects. The measuring accuracy of the system was approximately ± 1-mm. A detailed description of this device was given in Friedrich et al. (2005). Transducers were fixed in small holes drilled in the pile-cap to measure the instantaneous scour depth in front of each pile during the entire time span of the test with a time interval of 1 second.

As a supplementary method for measurement and calibration of the transducers data, scales printed on paper were wrapped around the pier components (e.g. pile group) and fastened using transparent tape so that the scales were visible. The scour depth at each component was read off the scales at the end of the tests for verification of the MTA data.

2.4 Experimental procedures

After the model was installed in the recess box, the bed surface was compacted and leveled using a metal beam fixed on a carriage moving on rails on the top edge of the side of the flumes. The recess box was filled with water gradually to avoid disturbing the leveled sediments. In the 1.54-m flume, before the tests began, the inflow pipe was opened to let the flume fill slowly to the desired depth. In the 2.4-m flume, the filling process started from the sediment collection tank downstream to submerge the recess box before opening the upstream valves to avoid any sediment bed disturbance during filling. At the early stage of the tests, before a steady flow condition had been reached, the bed surface was protected from uncontrolled scour by plastic plates. Then the plates were removed and the tests began; the transducers started collecting data at the same time. The flow depth was examined periodically by a point gauge for the tests in the 2.4-m flume, with an accuracy of ±0.5-mm, and using a scale on the outside of the flume for the tests in the 1.54-m flume. At the end of each test, after draining the flume, the scour depth at each pile was read using the scale.

If the pile-cap was not exposed entirely, or maximum scour depth did not occur at one of the piles (rather than in front of the pile-cap, for example), the point gauge was also used to measure the scour depth at locations of interest.

Tests lasted for 30 hours. Although equilibrium cannot be reached within 30 hours, there was a consensus that the time to reach 90% of the equilibrium scour depth was less than 20% of the time for complete equilibrium (Sheppard et al., 2011). Thus, 30 hours was sufficient to acquire relationships between scour depth and experimental parameters. However, more study to determine the reliability of the relations is still necessary in the future.

 

## 3 RESULTS AND DISCUSSION

### 3.1 Data presentation

Table 3 shows the results of the36 tests undertaken with duration of 30 hours. A number of variables are included: the position of the complex pier model with respect to the pile-cap elevation (Position A~I), the pile-cap elevation $H_c$, the pier skew angle $\alpha$, the test duration $t_d$, the equivalent width of pier $D_e$, the sediment coarseness ratio $D_e/d_{50}$, the measured scour depth $d_{sm}$, and the equilibrium scour depth $d_{sme}$.

**Table 3.** Test results for varying pier skewness and the pile-cap elevation

| Position | $H_c$ (mm) | $\alpha$ (°) | $t_d$ (h) | $D_e$ (mm) | $D_e/d_{50}$ | $d_{sm}$ (mm) | $d_{sme}$ (mm) |
|---|---|---|---|---|---|---|---|
| **A** | 310 | 0 | 30 | 47 | 56 | 98 | 118 |
| | 310 | 15 | 30 | 68 | 81 | 114 | 142 |
| | 310 | 30 | 30 | 72 | 85 | 119 | 149 |
| | 310 | 45 | 30 | 56 | 67 | 110 | 134 |
| **B** | 250 | 0 | 30 | 47 | 56 | 110 | 132 |
| | 250 | 15 | 30 | 68 | 81 | 135 | 168 |
| | 250 | 30 | 30 | 72 | 85 | 137 | 172 |
| | 250 | 45 | 30 | 56 | 67 | 133 | 163 |
| **C** | 120 | 0 | 30 | 58 | 70 | 111 | 136 |
| | 120 | 15 | 30 | 78 | 93 | 137 | 173 |
| | 120 | 30 | 30 | 88 | 105 | 160 | 205 |
| | 120 | 45 | 30 | 84 | 100 | 184 | 234 |
| **D** | 60 | 0 | 30 | 68 | 81 | 117 | 146 |
| | 60 | 15 | 30 | 107 | 128 | 140 | 183 |
| | 60 | 30 | 30 | 132 | 157 | 177 | 237 |
| | 60 | 45 | 30 | 132 | 157 | 188 | 251 |
| **E** | 30 | 0 | 30 | 75 | 89 | 131 | 165 |
| | 30 | 15 | 30 | 126 | 150 | 154 | 205 |
| | 30 | 30 | 30 | 158 | 189 | 186 | 254 |
| | 30 | 45 | 30 | 163 | 194 | 213 | 292 |
| **F** | 0 | 0 | 30 | 82 | 98 | 84 | 107 |
| | 0 | 15 | 30 | 147 | 175 | 168 | 227 |
| | 0 | 30 | 30 | 187 | 222 | 209 | 291 |
| | 0 | 45 | 30 | 198 | 236 | 214 | 300 |
| **G** | -60 | 0 | 30 | 97 | 115 | 60 | 78 |
| | -60 | 15 | 30 | 191 | 227 | 169 | 236 |
| | -60 | 30 | 30 | 249 | 296 | 243 | 350 |
| | -60 | 45 | 30 | 276 | 328 | 272 | 397 |
| **H** | -110 | 0 | 30 | 104 | 124 | 70 | 91 |
| | -110 | 15 | 30 | 228 | 271 | 140 | 199 |
| | -110 | 30 | 30 | 302 | 360 | 223 | 329 |
| | -110 | 45 | 30 | 342 | 408 | 280 | 420 |
| **I** | -- | 0 | 30 | 37 | 44 | 70 | 82 |
| | -- | 15 | 30 | 102 | 121 | 190 | 247 |
| | -- | 30 | 30 | 156 | 186 | 286 | 390 |
| | -- | 45 | 30 | 207 | 246 | 287 | 404 |

Specifically, the equivalent width $D_e$ is calculated using the method proposed by Sheppard and Renna (2010), namely the Florida Department of Transport (FDOT) method; and$d_{sme}$is converted from $d_{sm}$using the temporal evolution equations proposed by Sheppard et al. (2011), to eliminate the effect of test duration. The equations are proposed by modifying the equations of Melville and Chiew (1999), and they are considered to be the most accurate method available currently for predicting temporal evolution at bridge piers.

### 3.2 Effect of pier skewness and the pile-cap elevation

The data presented in Table 3 are plotted in Figure 2, using the normalized scour depth $d_{sme}/y_0$ as a function of the normalized pile-cap elevation $H_c/y_0$, where $y_0$ is the flow depth. It can be seen that, for the

 

complex piers aligned to the flow ($\alpha$=0°), the scour depth increases with closer distance between the pile-cap and the undisturbed bed level, and reaches a maximum when the top of the pile-cap is close to the bed (which is $H_c/T$ =0.5 in the present study). After this situation, with the decreasing pile-cap elevation, the top of the pile-cap is at the undisturbed level, and eventually lower than the bed level. During this stage, the scour depth decreases sharply, which is attributed by many researchers to the protection effect of the pile-cap that disturbs the downflow in front of the pier. In general, the data for the pier aligned to the flow are in accordance with the results of other studies.

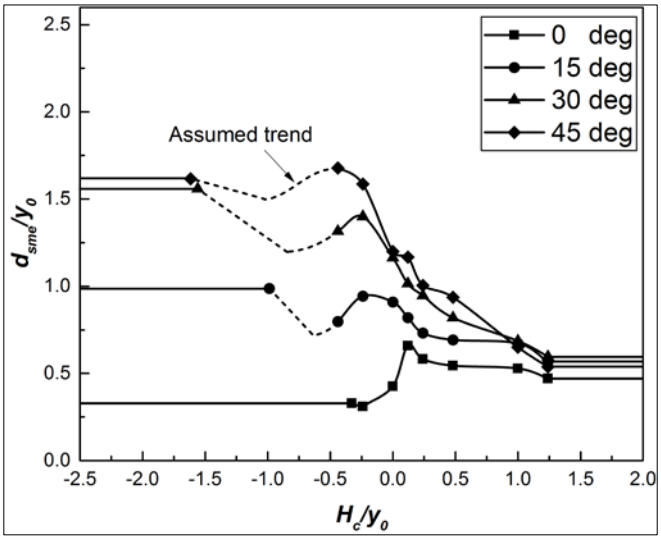


**Figure 2.** Effect of pier skewness and the pile-cap elevation on scour depth

For the complex piers with a skew angle to the flow, the variation of the scour depth with the varying pile-cap elevation is completely different. Once a comparatively small skew angle exists (e.g. $\alpha$=15°), the scour depth increases strikingly, especially in the situations where the top of the pile-cap is flushed with the bed level, or is fully buried. In addition, the increase of scour depth is proportional to the skew angle, as shown in Figure 2, and becomes less sensitive to skewness when $\alpha$>30°. As a consequence, situations that are considered to be safe for aligned piers (e.g. $H_c/T$≤0) can be extremely dangerous when the flow direction changes because of, for example, obstacles in the flow, flow contraction, or a particular flood event.

The dashed lines in Figure 2 are assumed based on existing data because of the limited test numbers, but the general trend of the lines are still reasonable. These lines start from the case where the equilibrium scour hole can just reach the top of the pile-cap. With increasing pile-cap elevation, the scour depth is assumed to be inversely proportional to the pile-cap elevation (where$d_{se} = |H_c|$), until the side of the pile-cap can be exposed after scouring. Thereafter, the equilibrium scour depth starts to increase again with increasing pile-cap elevation, until a maximum value is obtained when the pile-cap is close to the bed level.

Generally, for skewed complex piers, if the column is inserted significantly into the flow, it causes much more disruption to the flow and much stronger downflow than that due to the pile-cap and the pile group. Thus, the increased scour depth for skewed piers is mostly attributed to the presence of the wall-like column. A complex pier behaves more like a wide pier with increasing skewness to the flow. This phenomenon also causes the variation of flow shallowness and sediment coarseness with skew angle.

### 3.3 Effect of sediment coarseness on scour depth

Because of the structural complexity and wide-pier feature of skewed complex piers, the sediment coarseness ratio $D_e/d_{50}$ becomes variable with changing pier skewness and pile-cap elevation, rather than being a constant value as that for simple cylindrical piers. Melville (1997), Sheppard et al. (2004), Lee and Sturm (2009) and Lança et al. (2013) proposed different equations for the relation between $D_e/d_{50}$ and $d_{se}/D_e$.

Recent studies show a decreasing trend of the normalized equilibrium scour depth $d_{se}/D_e$ with increasing $D_e/d_{50}$, when $D_e/d_{50}$ exceeds a specific value. This feature is also apparent in the present study, as shown in Figure 5. To isolate the effect of sediment coarseness, all the scour depth data are corrected for factors related to flow intensity and flow depth. The equations proposed by Sheppard et al. (2011) are used for the correction, because this method has been proven to be the most accurate method currently available. The scour depths are corrected to those of circular piers in deep water, with threshold flow conditions.

 

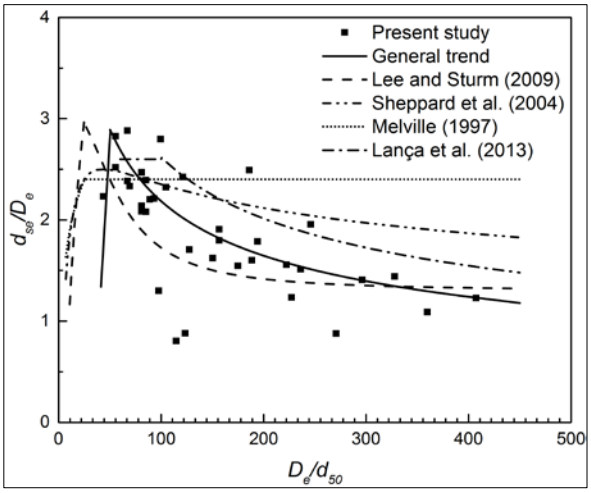


**Figure 3.** Effect of sediment coarseness on scour depth

In Figure 3, the solid line represents the general trend plotted based on the test data from the current study; the dashed lines are plotted according to equations proposed by the studies mentioned above. It can be seen that the trend in the data from the present study is in accordance with the trends shown in the more recent studies, with the equations of Lee and Sturm (2009) showing quite good agreement with the new data.

As reported by Sheppard (2004) inter alia, the pressure gradient around the pier is a significant factor that influences the scouring process. For complex piers, the vertical distribution of pressure gradient becomes uneven because of the structural complexity, especially when the pile group is exposed after scouring. The pressure gradient generated in front of the pile group is obviously smaller than that generated in front of a cylindrical pier with diameter equals to $D_e$. Thus, the existing equations may not be able to accurately describe the scouring mechanism around a complex pier.

For further study in the future, the flow field and turbulence structure around complex piers should be treated as an important research area, thereby facilitating a better understanding of the basic scouring mechanism with respect to flow complexity.

### 3.4 Scour pattern at complex piers

For the protection of complex bridge piers that can potentially be damaged during the scouring process, it is necessary to determine the location where the maximum scour depth is likely to occur, such that countermeasures or reinforcement can be appropriately designed. Conversely to that which occurs at simple cylindrical piers, the location of the maximum scour depth observed at complex piers varies with pier skewness and the pile-cap elevation. The presence of the lower structure (the pile-cap and the pile group) significantly increases the complexity of the scour pattern at complex piers with different configurations.

Figure 4 shows the locations of the maximum scour depth observed at aligned complex piers. When the scour hole can only reach the top of the pile-cap, the scour depth is equal to the distance between the undisturbed bed level to the top of the pile-cap (Figure 4(a)), corresponding to the linear stage mentioned in 3.1. When the pile group is exposed after scouring and the scour hole is fully developed, the maximum scour depth occurs at the two upstream piles (Figure 4(c)). Another situation exists between the two cases mentioned above when the bottom of the scour hole cannot reach the upstream piles. In this case, the maximum scour occurs under the front edge of the pile-cap (Figure 4(b)). Thus, it could be deduced that, with a specific pile-cap elevation between those of Figure 4(a) and Figure 4(c), the pile group cannot be exposed, and the maximum scour depth occurs in front of the pile-cap.

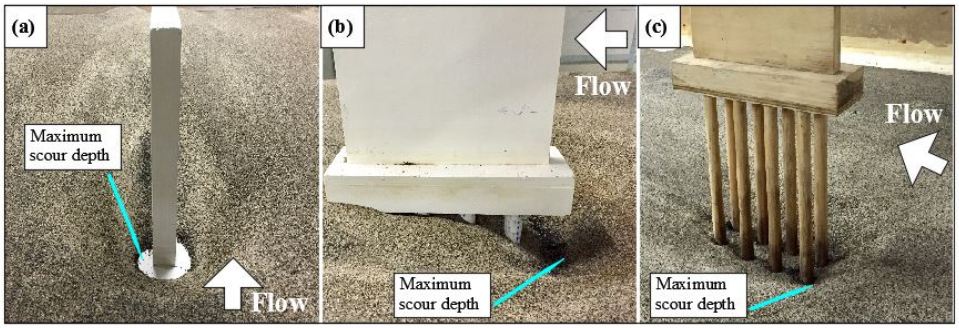


**Figure 4.** Location of the maximum scour depth for aligned complex piers:
(a) $H_c = -110\ mm, \alpha = 0\ °$; (b) $H_c = 30\ mm, \alpha = 0\ °$; (c) $H_c = 250\ mm, \alpha = 0\ °$.

Figure 5 shows the locations of the maximum scour depth observed at skewed complex piers. When the pier is skewed to the flow ($\alpha$=15°~75°) and the pile group can be fully exposed after scouring, the maximum scour depth occurs at the downstream end of the upstream row of piles (Figure 5(a) (b)). For the piers perpendicular to the flow ( $\alpha$=90° ) , the maximum scour depth occurs at the two middle piles of the upstream row (Figure 5(c)). This phenomenon is in accordance with the results of scour at a pile group reported by Zhao and Sheppard (1998), demonstrating that the exposed pile group becomes the dominant factor to determine the scour pattern at complex piers. When the scour hole cannot reach the top of the pile-cap (namely the column-only situation), the maximum scour depth occurs at one of the corners of the upstream flank (Figure 5(d)). In that case, the complex piers can be treated as a uniform simple pier, and the lower structure does not influence the scour depth.

In order to reduce scour depth at specific locations, countermeasures for complex piers can be optimized based on observed scour patterns in the present study. If a potential changing of flow direction in the future is predicted before construction, the riprap layer placed around the pier can be strengthened accordingly, e.g. larger layer depth or different stone size in the area where the maximum scour depth potentially occurs. The piles with high failure possibility can also be reinforced, for example, by using materials of higher standard or fixing the piles deeply upon bed rock.

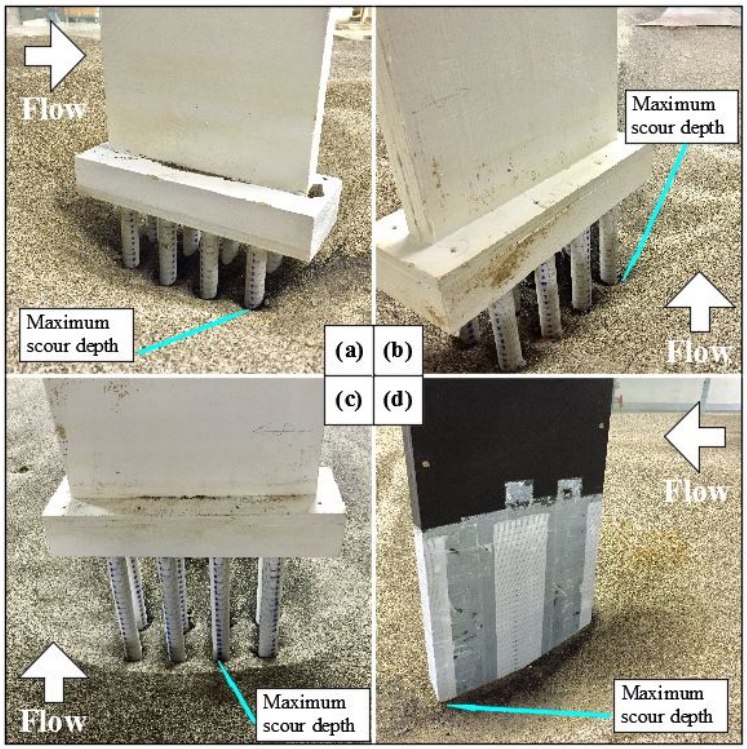


**Figure 5.** Location of the maximum scour depth for skewed complex piers:
(a) $H_c = -60\ mm, \alpha = 30$ °; (b) $H_c = 30\ mm, \alpha = 30$ °; (c) $H_c = 30\ mm, \alpha = 90$ °; column-only, $\alpha = 30$ °.

## 4 CONCLUSIONS

According to the data presented and analyzed in previous sections, the following conclusions can be drawn:

(1) When a complex pier is aligned to the flow, the maximum scour depth occurs for situations where the top of the pile-cap is close to the undisturbed bed level. This is in accordance with results reported by other studies. After the peak value occurs, with a lowering of the pile-cap position, the protection effect of the pile-cap decreases the scour depth significantly by disturbing the downflow in front of the pier.

(2) Once the flow becomes skewed, and even for a comparatively small skewness angle, e.g. 15°, the scour depth increases significantly, especially in situations where the pile-cap is fully buried. The increase is proportional to the skew angle $\alpha$, and becomes less sensitive to $\alpha$ when $\alpha$ >30°. This phenomenon shows that, for complex piers with a wall-like column part, the column makes the greatest contribution to scour depth, and the wide-pier feature of the column is significant when skewness exists. Thus, the column should be treated as the most contributive part of a complex pier that can potentially fail in flow with varying directions.

(3) The equivalent width of a complex pier becomes larger with increasing skew angle, making the sediment coarseness ratio $D_e/d_{50}$ variable, and bringing more uncertainty to existing predictors. Results show that the existing equations, including Melville (1997), Lee and Sturm (2009), Sheppard and Renna (2010) and

 

Lança et al. (2013) are incapable of accurately describing the effect of sediment coarseness. Comparatively, the equations of Lee and Sturm (2009) show better agreement with data from the present study. This feature is attributed to the structural complexity and corresponding flow complexity around complex pier. Thus, more study on the flow field is needed.

(4) For skewed complex piers where the pile group is exposed after scouring, the maximum scour depth usually occurs at the downstream end of the upstream row of piles; when the pier is aligned to flow, the maximum scour depth occurs at the two upstream piles, or under the front edge of the pile-cap, according to the degree of the pile-cap's exposure after scouring; when the pier is perpendicular to the flow, the maximum scour depth usually occurs at the middle two piles of the upstream row. For piers where the pile-cap is partially buried after scouring, the maximum scour depth normally occurs in front of the pile-cap (aligned pier) or at the side of the pile-cap (skewed pier). If the pile-cap is completely buried after scouring, namely the column-only situation, the maximum scour depth occurs at one of the corners of the upstream flank of the column. This case typically shows the deepest scour.

**ACKNOWLEDGEMENTS**

The leading author acknowledges the financial support from China Scholarship Council (CSC), the valuable suggestions for the manuscript from Dr Keith Adams, and the help from Mr. Chunguang Yuan in conducting the experiments.

**NOTATION**

$b_c$ = width of column;
$b_{pc}$ = width of pile-cap;
$b_{pg}$ = diameter of piles;
$B$ = flume width;
$d_s$ = scour depth;
$d_{se}$ = equilibrium scour depth;
$d_{sm}$ = measured scour depth at the end of test;
$d_{sme}$ = equilibrium scour depth calculated by S/M method using 30 hours data;
$d_{50}$ = median diameter of sediment particles;
$D$ = pier width;
$D_e$ = equivalent width of complex pier calculated by FDOT method;
$f_{cb}$ = pile-cap extension in lateral direction;
$f_{cl}$ = pile-cap extension in longitudinal direction;
$H_c$ = pile-cap elevation, e.g. the height of column base to the bed, positive when above the bed;
$l_c$ = length of column;
$l_{pc}$ = length of pile-cap;
$S_m$ = longitudinal pile row spacing ;
$S_n$ = lateral pile row spacing;
$t_d$ = test duration;
$T$ = thickness of pile-cap;
$U$ = depth-averaged mean approach flow velocity;
$U_c$ =mean critical velocity for incipient motion of bed sediment, depth-averaged;
$y_0$ = flow depth;
$\alpha$ = skew angle to flow of pier;
$\sigma_g$ = geometric standard deviation of sediment size distribution.

**REFERENCES**

Amini, A., Melville, B. W. & Ali, T. M. (2014). Local Scour at Piled Bridge Piers Including an Examination of the Superposition Method. *Canadian Journal of Civil Engineering*, 41(5), 461-471.

Arneson, L. A., Zevenbergen, L. W., Lagasse, P. F. & Clopper, P. E. (2012). *Evaluating Scour at Bridges (HEC-18)*. Technical Rep. No. HIF-12-003, Federal Highway Administration, Washington, DC.

Ataie-Ashtiani, B., Baratian-Ghorghi, Z. & Beheshti, A. A. (2010). Experimental Investigation of Clear-Water Local Scour of Compound Piers. *Journal of Hydraulic Engineering*, 136(6), 343-351.

Ballio, F., Teruzzi, A. & Radice, A. (2009). Constriction Effects in Clear-Water Scour at Abutments. *Journal of Hydraulic Engineering*, 135(2), 140-145.

Breusers, H. N. C. & Raudkivi, A. J. (1991). *Scouring*. Rotterdam: Balkema.

Coleman, S. E. (2005). Clearwater Local Scour at Complex Piers. *Journal of Hydraulic Engineering*, 131(4), 330-334.

Ferraro, D., Tafarojnoruz, A., Gaudio, R. & Cardoso, A. H. (2013). Effects of Pile Cap Thickness on the Maximum Scour Depth at a Complex Pier. *Journal of Hydraulic Engineering*, 139(5), 482-491.

 

Friedrich, H. (2010). Evaluation of Statistical Analysis Techniques for Developing Bedforms Recorded In 3D, *Doctoral Dissertation*. University of Auckland.

Grimaldi, C. & Cardoso, A. H. (2010). Methods for Local Scour Depth Estimation at Complex Bridge Piers. *In Procedings of 1st IAHR European Division Congress*.

Jones, J. S., Kilgore, R. T. & Mistichelli, M. P. (1992). Effects of Footing Location on Bridge Pier Scour. *Journal of Hydraulic Engineering*, 118(2), 280-290.

Jones, J. S. & Sheppard, D. M. (2000). Local Scour at Complex Pier Geometries. *In* P*proceedings of the ASCE 2000 Joint Conference on Water Resources Engineering and Water Resources Planning and Management*.

Kothyari, U. C. & Kumar, A. (2012). Temporal Variation of Scour around Circular Compound Piers. *Journal of Hydraulic Engineering*, 138(11), 945-957.

Lança, R. M., Fael, C. S., Maia, R. J., Pêgo, J. P. & Cardoso, A. H. (2013). Clear-Water Scour at Comparatively Large Cylindrical Piers. *Journal of Hydraulic Engineering*, 139(11), 1117-1125.

Laursen, E. M. & Toch, A. (1956). *Scour Around Bridge Piers and Abutments*, Bulletin No.4, Iowa Highways Research Board, Ames, IA.

Lee, S. O. & Sturm, T. W. (2009). Effect of Sediment Size Scaling on Physical Modeling of Bridge Pier Scour. *Journal of Hydraulic Engineering*, 135(10), 793-802.

Lu, J. Y., Shi, Z. Z., Hong, J. H., Lee, J. J. & Raikar, R. V. (2010). Temporal Variation of Scour Depth at Nonuniform Cylindrical Piers. *Journal of Hydraulic Engineering*, 137(1), 45-56.

Melville, B. W. (1997). Pier and Abutment Scour: Integrated Approach. *Journal of Hydraulic Engineering*, 123(2), 125-136.

Melville, B. W. & Chiew, Y. M. (1999). Time Scale for Local Scour at Bridge Piers. *Journal of Hydraulic Engineering*, 125(1), 59-65.

Melville, B. W., & Raudkivi, A. J. (1996). Effects of Foundation Geometry on Bridge Pier Scour. *Journal of Hydraulic Engineering*, 122(4), 203-209.

Moreno, M., Maia, R., & Couto, L. (2015). Effects of Relative Column Width and Pile-Cap Elevation on Local Scour Depth around Complex Piers. *Journal of Hydraulic Engineering*, 142(2), 1-9.

Moreno, M., Maia, R. & Couto, L. (2016a). Prediction of Equilibrium Local Scour Depth at Complex Bridge Piers. *Journal of Hydraulic Engineering*, 142(11), 1-13.

Moreno, M., Maia, R., Couto, L. & Cardoso, A. (2012). Evaluation of Local Scour Depth around Complex Bridge Piers. *Proceedings of River Flow 2012*, 2, 935-942.

Moreno, M., Maia, R., Couto, L. & Cardoso, A. (2014). Contribution of Complex Pier Components on Local Scour Depth. In *Proc. 3rd IAHR Europe Congress*.

Moreno, M., Maia, R., Couto, L. & Cardoso, A. H. (2016b). Subtraction Approach to Experimentally Assess the Contribution of the Complex Pier Components to the Local Scour Depth. *Journal of Hydraulic Engineering*, 06016030.

Parola, A. C., Mahavadi, S. K., Brown, B. M. & El Khoury, A. (1996). Effects of Rectangular Foundation Geometry on Local Pier Scour. *Journal of Hydraulic Engineering*, 122(1), 35-40.

Sheppard, D. M. & Glasser, T. (2009). Local Scour at Bridge Piers with Complex Geometries, In Contemporary Topics in In Situ Testing, Analysis, and Reliability of Foundations*. International Foundation Congress and Equipment Expo 2009,* ASCE, 506-513.

Sheppard, D. M., Odeh, M. & Glasser, T. (2003). Large Scale Clear-Water Local Pier Scour Experiments. *Journal of Hydraulic Engineering*, 130(10), 957-963.

Sheppard, D. M. & Renna, R. (2010). *Bridge scour manual*. Florida Department of Transportation, Florida.

Yalin, M. S. (1972). *Mechanics of Sediment Transport*. Pergamon Press.

Zhao, G. & Sheppard, D. M. (1998). The effect of flow skew angle on sediment scour near pile groups. *In Stream Stability and Scour at Highway Bridges: Compendium of Stream Stability and Scour Papers Conference, Sponsored by the Water Resources Engineering (Hydraulics) Division of the American Society of Civil Engineers* (pp. 377-391). ASCE.

 

Proceedings of the 37th IAHR World Congress
August 13 – 18, 2017, Kuala Lumpur, Malaysia

# MANAGEMENT PLAN FOR RIVER SAND MINING ACTIVITY IN SEGAMA RIVER, SABAH

KOK HOU KU[(1)], CLAUS PEDERSEN[(2)], HANS CHRISTIAN AMMENTORP[(3)], YABI YANGKAT[(4)] & VITALIS MODUYING[(5)]

[(1,2)] DHI Water and Environment (M) Sdn Bhd, Kota Kinabalu, Malaysia,
kkh@dhigroup.com; clp@dhigroup.com
[(3)]DHI Horsholm, Denmark,
hca@dhigroup.com
[(4, 5)]Environment Protection Department Sabah, Kota Kinabalu, Malaysia,
yabi.yangkat@sabah.gov.my; vitalis.moduying@sabah.gov.my

## ABSTRACT

The Segama River is located within the Districts of Lahad Datu and Kinabatangan, on the east coast of Sabah, Malaysia. This paper highlights an assessment to determine sustainable levels of sand mining in the river and describes the formulation of a resource management plan and guidelines for the mid-reaches of the Segama River. A river sediment transport model (MIKE 11 ST) is developed to assess the carrying capacity for river sand mining along the mid-reaches of Segama River. The sediment transport capacity is estimated to be approximately 70,000 $m^3$/year. This compares to an estimated sediment yield from the upper catchment estimated in the range of 250,000 to 500,000 $m^3$/year with natural erosion / deposition within the river estimated to be approximately 130,000 $m^3$/year. The current river sand extraction at the rate of 100,000 $m^3$/year is in the same order of magnitude as the transport capacity and the natural erosion/deposition, and is significantly lower than the total sediment yield to the river system. Based on these findings, it is considered that the sediment yield from the catchment combined with sediment from natural erosion/deposition can replenish the extracted volumes without significant risk of causing regional deficit erosion within the river. The development of a Resource Management Plan and Guidelines was undertaken to manage river sand mining activities and prevent over exploitation and consequent environmental damage along the mid-reaches of Segama River. Sensitive areas (eg. fisheries spawning area, area experiencing river bank erosion and etc.) are mapped and the river classified into zones (Permitted, Restricted, Prohibited and Prohibited (Subjected)) that regulate the river sand mining activities. The findings of the study have been implemented into a GIS database and decision support system that enables the regulatory authority to better manage the sand resource in the future.

**Keywords:** Carrying capacity assessment; river bank erosion; exclusion zone mapping; sediment extraction rate.

## 1 INTRODUCTION

River sand mining is an important industry contributing to socioeconomic development in the state of Sabah as it supplies raw materials for the construction industry, housing and roads. In addition to commercial mining activities, sand dredging is also carried out for the purposes of flood control, navigation or maintenance of water intake points.

However, as is often the case with the utilization of natural resources, unplanned and uncontrolled river sand mining activities can result in serious environmental degradation and loss of natural resources in the long term. Issues that may arise due to uncontrolled sand mining activities include:

- Significant sediment plumes in the river due to the release of the fines back into the river;
- Sand mining may starve the river for sediment on a local or regional scale, and lead to river bank erosion and destabilization of the river system down-drift of the mining activity. In turn, as the river is degraded, banks become higher and more prone to erosion with the collapse of bank vegetation;
- Excessive river sand mining may affect the coastal sediment budget and lead to coastal erosion.

The potential decrease in the supply of sediments to a shoreline, due to the regulation or modification of rivers, which previously supplied material to the shoreline, is a common cause of coastal erosion. The river regulation works can be the construction of dams for power production and irrigation purposes, or the deepening of navigation channels and sand mining, but all of them cause a reduction in supply of sediment to the shoreline.

## 2 STUDY LOCATION

The study area consisted of the mid-reaches of Segama River within the Segama catchment located in the Districts of Lahad Datu and Kinabatangan, Sabah. The Segama River with a total length in the order of 367 km and a catchment area of approximately 4,515 $km^2$ originates in the steeper Danum Valley

 

conservation area and flows towards a floodplain located at the downstream end of the catchment before discharging into the Sulu Sea, refer Figure 1. Approximately 85% of the floodplain area is flat alluvial with the remainder consisting of mangrove and nipah swamps.

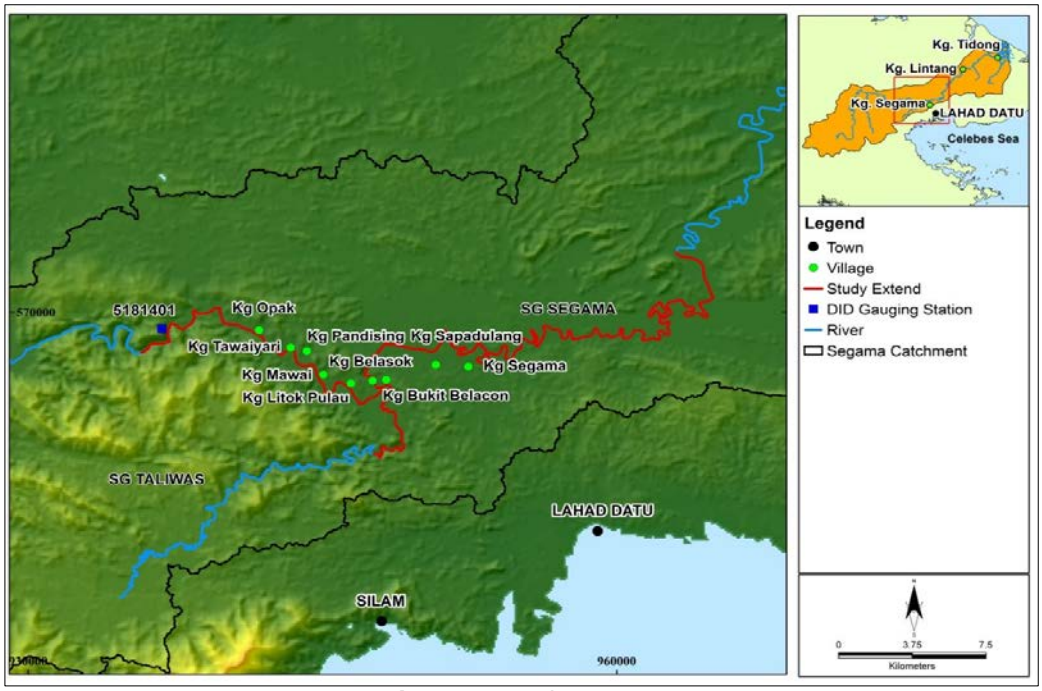


**Figure 1.** Study extent.

## 3 CATCHMENT SEDIMENT YIELD

The catchment sediment yield is an important component for the overall sediment balance in the river. The sediment yield was therefore estimated through a soil erosion and transport assessment. The sediment yield from the catchment to the river is complex and not easily quantified.

For a given terrain, it depends both on the magnitude and intensity of the rainfall and on the vegetation, soil properties and runoff characteristics of the catchment. The original rainforest has a high capacity for absorbing the rain without causing soil erosion and sediment runoff. This will drastically change when the forest is cleared for establishment of oil palm plantations. After the initial clearing and during the earthwork in preparation for planting, it will be completely exposed and the soil erosion and runoff will typically be very high.

To estimate the catchment sediment yield, modeling was carried out using a Soil Erosion Assessment Module (known also as SEAGIS). This module (part of the Mike Basin package) is a GIS based application that allows erosion risk assessment. The application comprises two different terms for describing soil erosion: source erosion and transported erosion:

- The source erosion is estimated using the Universal Soil Loss Equation (USLE) combined with the revised version of this model (RUSLE).
- The transported erosion is assessed by multiplying source erosion by the delivery ratio and describes the eroded soil reaching the outlet of the catchment.

### 3.1 SEAGIS model calibration and sensitivity analysis

The soil erosion process is a degree of magnitude more complex compared to the rainfall runoff process. Soil erosion processes include the detachment of soil particles by raindrops or overland flow and the transport of the detached material to the rivers. Physically-based soil erosion modeling at catchment and basin scale is not yet feasible, which is the reason that simpler and largely empirically based approaches are used. This implies that soil erosion modeling in time and space cannot attain the same degree of precision as hydrological modeling. This is important to bear in mind when considering model calibration and applying the results in a broader perspective.

Calibration of the soil erosion model involved adjustment of the following parameters:

- Cropping management factor
- Soil erodibility factor
- Erosion control practice factor

Calibration of the model was performed against limited data on Total Suspended Solids (TSS) at a water quality monitoring station within the study area maintained by Alam Sekitar Malaysia Sdn. Bhd. (ASMA), refer Figure 2. Whereas there were significant discrepancies for individual points, the overall range of the predicted

 

and measured concentrations were similar, and the calibration was considered reasonable within the level of uncertainty for this type of modeling.

The average concentration over the modeled period (1998 – 2009) derived from the SEAGIS model is slightly lower at about 132 mg/l compared to 140 mg/l from the measured ASMA data. The ASMA data spans many years but with limited frequency. With the ongoing development in the catchment, there is a risk that the long time span could lead to a bias in the data (i.e. sediment yield and concentrations could be increasing), while the low frequency obviously involves a risk that short-lasting, high runoff events are not fully captured.

The SEAGIS model was further run for estimated historical, current and potential future land-use maps, where the historical map had increased forest cover upstream, the current land-use map (year 2014, refer Figure 3) is a best estimate based on available data, and the future land-use map assumes further development of oil palm plantations in the part of the catchment not under forest reserves.

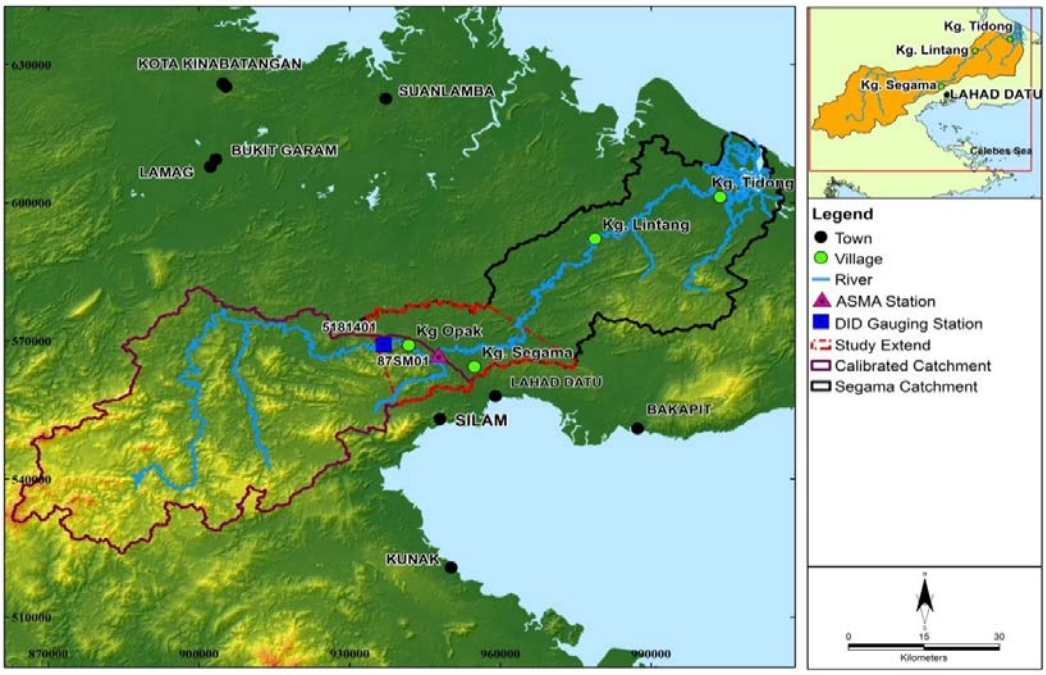


**Figure 2.** Location of ASMA Water Quality Station (87SM01) and DID Gauging Station (Segama River at Limkabong - 5181401) located within the study area.

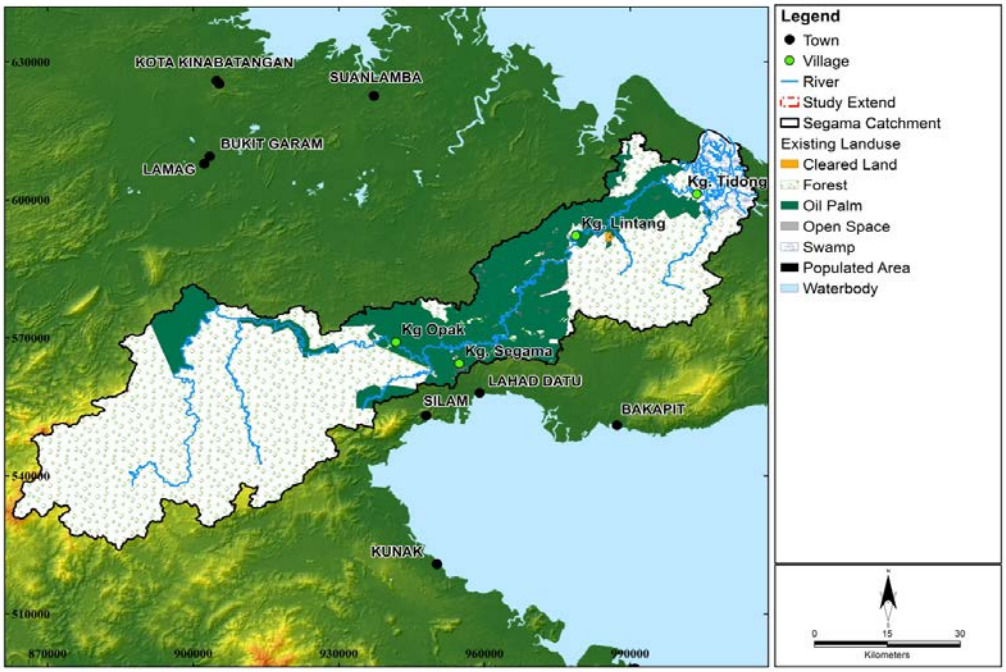


**Figure 3**. Land-use distribution in Segama catchment for year 2014 (Source: Google Earth satellite imagery, Department of Agriculture Sabahlanduse map and ground survey)

**Table 1.** Sensitivity analysis of simulated sediment yield for different land-use maps (simulations based on rainfall-runoff for 1998 to 2009).

| No | Simulation & Land-use Map applied | Average TSS at ASMA station (mg/l) | Sediment Yield (ton/year) |
|---|---|---|---|
| 1 | **Calibration:** Estimated land-use map representative for year 1998 to 2009 | 132 | 270,000 |
| 2 | **Current Conditions**: Best estimate land-use map for year 2014 | 275 | 650,000 |
| 3 | **Historical Conditions**: Increased forest cover in the upstream catchment | 82 | 190,000 |
| 4 | **Potential Future Conditions:** Increased oil palm outside forest reserves | 350 | 840,000 |

Results from the analysis for different land-use maps for different development stages are listed in Table 1. A test in SEAGIS using a higher crop management factors for oil palm led to the sediment yield for the potential future condition to increase to more than 1.1 million ton/year.

The sensitivity analysis demonstrates that the sediment yield changes radically with the land use pattern change. The sediment yield from the upper Segama catchment area is likely to further increase in the future if the present expansion of oil palm plantations continues, in particular as it moves into steeper parts of the catchment.

3.2 Assessment of catchment sediment yield based on rating curve data

The calculated upper catchment sediment yield obtained from the SEAGIS model was further compared to an assessment using a sediment-discharge rating curve obtained from the Department of Irrigation and Drainage (DID) covering the period 1979 – 2010 for Limkabong (see location in Figure 2). Using a time series of discharge data from the DID station at Limkabong and the rating curve, the average discharge for the upper catchment for the period 1979 – 2010 (excluding 1981 and 2009 which had no or too little data coverage) was estimated to approximate 380,000 ton/year. The results showed a very large variation between years with the estimated sediment discharge ranging from about 20,000 ton in 2010 to about 1.2 million ton in 2000.

For the period 1998 to 2008 (no data available for 2009), the average annual discharge was about 395,000 ton/year. This is significantly higher than the SEAGIS estimated sediment yield of 270,000 ton/year at the ASMA station for almost the same period. The DID station at Limkabong is upstream of the ASMA station where the model was calibrated, and the ASMA data and SEAGIS results should thus be higher than the sediment load in the river at Limkabong (assuming that the river is in a state of dynamic equilibrium between the catchment sediment yield and the transport).

This may indicate that the ASMA and SEAGIS estimates for the sediment yield could be on the low side, but mainly demonstrates the significant uncertainties in estimating both catchment sediment yield and sediment transport in the river. Both estimates can best be classified as order of magnitude estimates, and as such, they are of the same order of magnitude. Based on the combined assessments of ASMA data, DID rating curve and SEAGIS modeling, a best estimate of the sediment yield from the Upper Segama Catchment is currently in the order of 0.5 to 1 million tons/year.

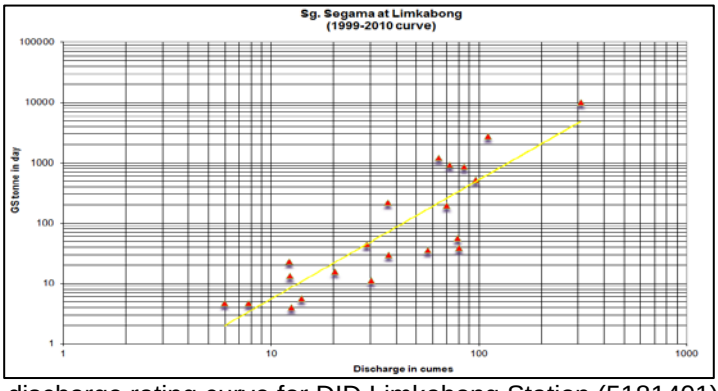


**Figure 4**. Sediment-discharge rating curve for DID Limkabong Station (5181401) for period 1999 – 2010.

 

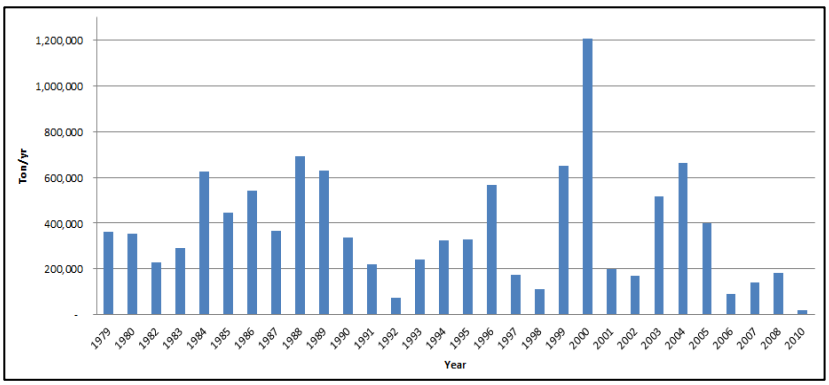


**Figure 5.** Variation of annual average sediment discharge derived based on DID Limkabong station (5181401) sediment-discharge rating curve.

## 4 RIVER SEDIMENT TRANSPORT

The sediment transport capacity at the mid-reaches of Segama River was estimated using river sediment model, MIKE 11 ST (DHI, 2013). This is a one-dimensional fully dynamic morphological model. It simulates the sediment transport capacity of (potentially) several grain size fractions simultaneously as function of the local flow velocity and depth as simulated with the hydrodynamic model (HD).

For the lower reaches of the river where the bottom is covered in loose sediment deposits, it can be assumed that the actual sediment transport is of same order of magnitude as the transport capacity, although for instance the presence of significant loads of fine sediment can reduce the transport capacity for coarser sediments.

Model simulations covered the period January 1998 – December 2009 as a basis to predict long-term effects. The sediment transport modeling is intended to provide best estimate transport rates for the coarser grain size fractions that are typically targeted by the river sand extraction, and is thus not representative of the total sediment transport which includes a potentially much larger transport of finer grain sizes.

The large difference between the different sediment theories emphasizes the necessity to have reliable long term measured data for calibration and validation of a sediment transport formula. This can be initiated by setting up water quality stations that measure discharges, suspended solids and river bed loads and aerial photography that documents sediment built up or erosion at river banks covering the area of interest.

Based on previous experience, the Engelund and Hansen sediment transport model was selected and the mean annual sediment transport estimated ranging from about 25,000 to 115,000 $m^3$ for mid-reaches of Segama River with grain sizes ranging from 0.6 mm to 0.2 mm, respectively.

**Table 2.** Simulated mean total annual sediment transport for a variety of sediment transport theories and mean grain size of bed material – values extracted in mid-reaches of Segama River, approximately 2.4 km upstream before the confluence between Segama River and Taliwas River.

| Sediment Transport Theory | Grain Sizes (mm) | | | | |
|---|---|---|---|---|---|
| | 0.2 | 0.3 | 0.4 | 0.5 | 0.6 |
| Ackers and White | 59,559 | 18,083 | 11,067 | 8,061 | 6,266 |
| Engelund and Hansen | 114,479 | 69,045 | 46,523 | 33,231 | 24,533 |
| Engelund and Fredsoe | 2,323,225 | 118,898 | 32,808 | 13,132 | 8,648 |

## 5 COASTAL SEDIMENT TRANSPORT AND MORPHOLOGY

The Segama River connects with other smaller channels as well as the larger Tabin River before discharging to the Sulu Sea through a series of mangrove and nipah lined channels spanning about 35 km of the Kinabatangan coastline, refer Figure 6. The main Kuala Segama expands to approximately 1.5 km wide channel/estuary over the last 8 km from the sea. This changes the transport characteristics of the river from being flood flow dominated to being tidally flushed.

The coastline is characterized by wide tidal flats of varying sandy/silty/muddy composition, and a significant alluvial fan extends out from the main outlet of the Segama River, refer Figure 7. The supply of fine sediments from the rivers is large along the Kinabatangan coastline with the largest contributors being Kinabatangan and Segama. The plumes from the rivers and from re-suspension of fine sediment along the coast generally make the coastal waters heavily sediment laden and murky.

The morphology of the sediment through the various channel with some areas building up and being colonized by casuarina trees, while other areas are subjected to significant erosion affecting mature trees. Erosion and sedimentation patterns along the coastline indicate that some of the presently minor channels would previously have carried larger volumes of sediments. The coastline is fairly exposed to waves from the Sulu Sea during the NE monsoon season and the overall sediment transport and morphology are wave

 

controlled. The large discharge of sediments has, however, led to a very shallow profile and wide tidal flats, which reduce the wave energy reaching the shoreline sufficient to allow mangroves to establish along part of the coastline.

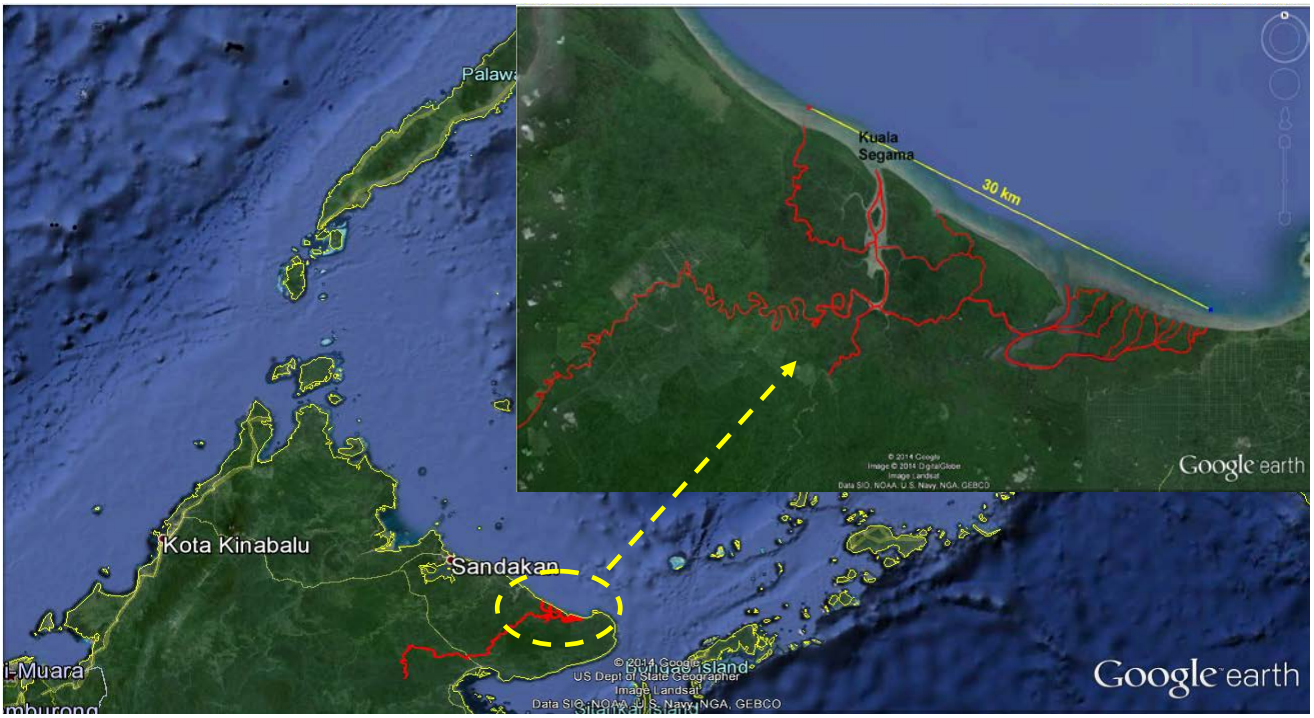


**Figure 6.** Google Earth image showing Segama River (marked in red) discharging into the Sulu Sea along the south-eastern Kinabatangan coastline (Background: Google Satellite Imageries).

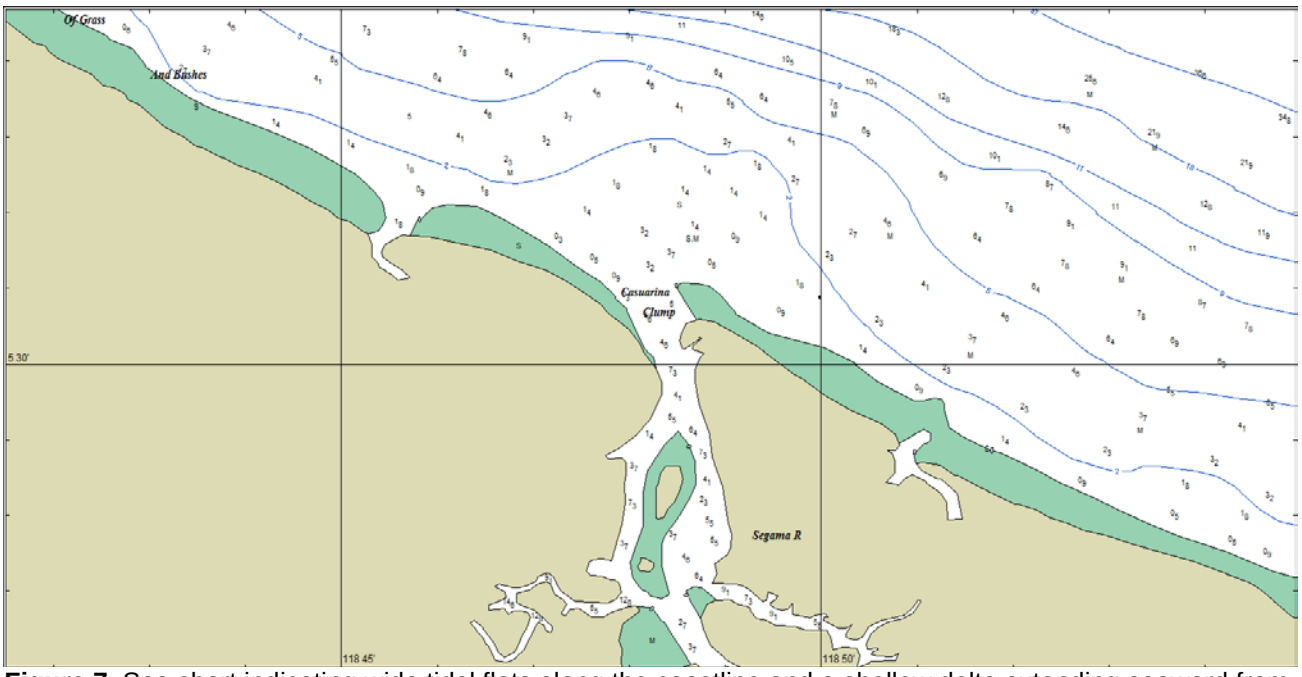


**Figure 7.** Sea chart indicating wide tidal flats along the coastline and a shallow delta extending seaward from Kuala Segama.

The large sediment discharges from the rivers along Kinabatangan coastline are overall causing the advancing tidal flats and expanding mangrove forest along the fringe. Development in the catchment, most notably the conversion of forest to oil palm plantations, is causing a significant increase in the sediment runoff which may not be fully captured in the catchment sediment discharge model. It is anticipated that the additional sediment runoff due to conversion from forest to oil palm more than out weights the sediment removed through sand mining. Overall, it is thus estimated that the discharge of sediment from the Segama River will remain higher than the natural (catchment fully forested) state.

 

The river sand mining targets the coarser fractions of sediments, while the fine sediment is flushed back into the river. The localized removal of the coarser sediments will locally change the composition of the bottom material and reduces the potential for transport of coarser material downriver. This may in the medium to longer term reduce the amount of coarser sediments discharged from the Segama River to the coastline, although this is not entirely clear. The Segama River is very active morphologically with constant reshaping through migrating meanders. This will tend to replenish the sediment extracted with sediments from natural erosion, and any effects from the sand mining on the sediment discharge and composition will be reduced at the river mouth.

## 6 RIVER SEDIMENT BUDGET – MID-REACHES OF SEGAMA RIVER

The current sediment yield to the river from the upstream catchment was estimated to be in the order of 500,000 to 1 million ton/year. Assuming an average density of the sediment in the order of 2000 kg/$m^3$ leads to a volume of 250,000 to 500,000 $m^3$/year. A rough estimate for the lower catchment was in the order of 50,000 to 100,000 $m^3$/year. The sediment yield comprises all fractions, and the information available does not give information on the fraction of coarser sediment. The present sediment yield from the catchment is estimated to be at least twice and up to 5 times the yield from an "undisturbed" catchment.

River meandering was very roughly estimated on average to "turn over" in the order of 2,000 $m^3$/year for each kilometer of river. Within the study reach of approximately 65 km of river, this corresponds to 130,000 $m^3$/year. This sediment will mainly consist of previously deposited sediment from the river and is anticipated to have a reasonably high content of coarser material (i.e. corresponding to the sediment typically deposited along the convex bank in the meandering process) although there will also be areas with higher fines content.

The transport capacity of the river for coarser sediment is estimated at 70,000 $m^3$/year for 0.3 mm sand, which is the approximate median grain size of the extracted material. The transport capacity for finer sediments increases rapidly, and is estimated to be in the order of 115,000 $m^3$/year for 0.2 mm sand. These volumes are highly variable with rainfall and runoff conditions.

River sand mining in mid-reaches of Segama River was estimated to extract in the order of 100,000 $m^3$/year. This is the similar order of magnitude as the transport capacity at a typical cross-section, and also similar order of magnitude as the estimated "sediment turnover" along this stretch caused by natural erosion/deposition due to the evolving meandering of the river.

With the river sand mining distributed at sites with smaller extraction volumes along the river, it is anticipated that a combination of the sediment yield from the catchment and the "sediment turnover" by the natural erosion/deposition will replace the extracted coarser fractions of sediment. The sand extraction at the present volume in the order of 100,000 $m^3$/year is not expected to lead to regional "deficit" erosion, i.e. erosion caused by an overall deficit of sediment in the river compared to the transport capacity, but is rather expected to be limited to localized effects.

## 7 RIVER SAND MINING RESOURCE MANAGEMENT PLAN

Based on the above analysis, a River Sand Mining Resource Management Plan was prepared for the Environment Protection Department Sabah (EPD). Broadly, the river sand mining strategy is tailored to the different environmental objectives for different river stretches. Exclusion zones around sensitive receptors were established based on the existing guidelines on the river sand mining (Department of Irrigation and Drainage, 1993; Department of Irrigation and Drainage, 2009; Environmental Conservation Department, 2001) and as set out below:

- Permitted - Permitted areas are generally those where sand mining may be allowed with standard conditions, such as EIA study, best practice mitigation measures and regular monitoring.
- Restricted – Reaches may be demarcated as restricted and permitted for sand mining. Restricted areas are those where sand mining may be permitted following more detailed studies or with the application of more stringent mitigation measures.
- Prohibited - River reaches where sand mining should be prohibited due to sensitive environmental factors, whether human, biological or physical.
- Prohibited (Subjected) – Reaches which are tentatively classified as prohibited based on the guidelines, but where exemption may be considered following detailed studies to see whether the "prohibited" conditions per the guideline are valid for these sites or whether special conditions apply that could form the grounds for an exemption.

The study reach within the mid-reaches of Segama River has been divided into nineteen (19) management units and an example of the detailed map of the upper-middle reaches of the study area is indicated in Figure 8.

 

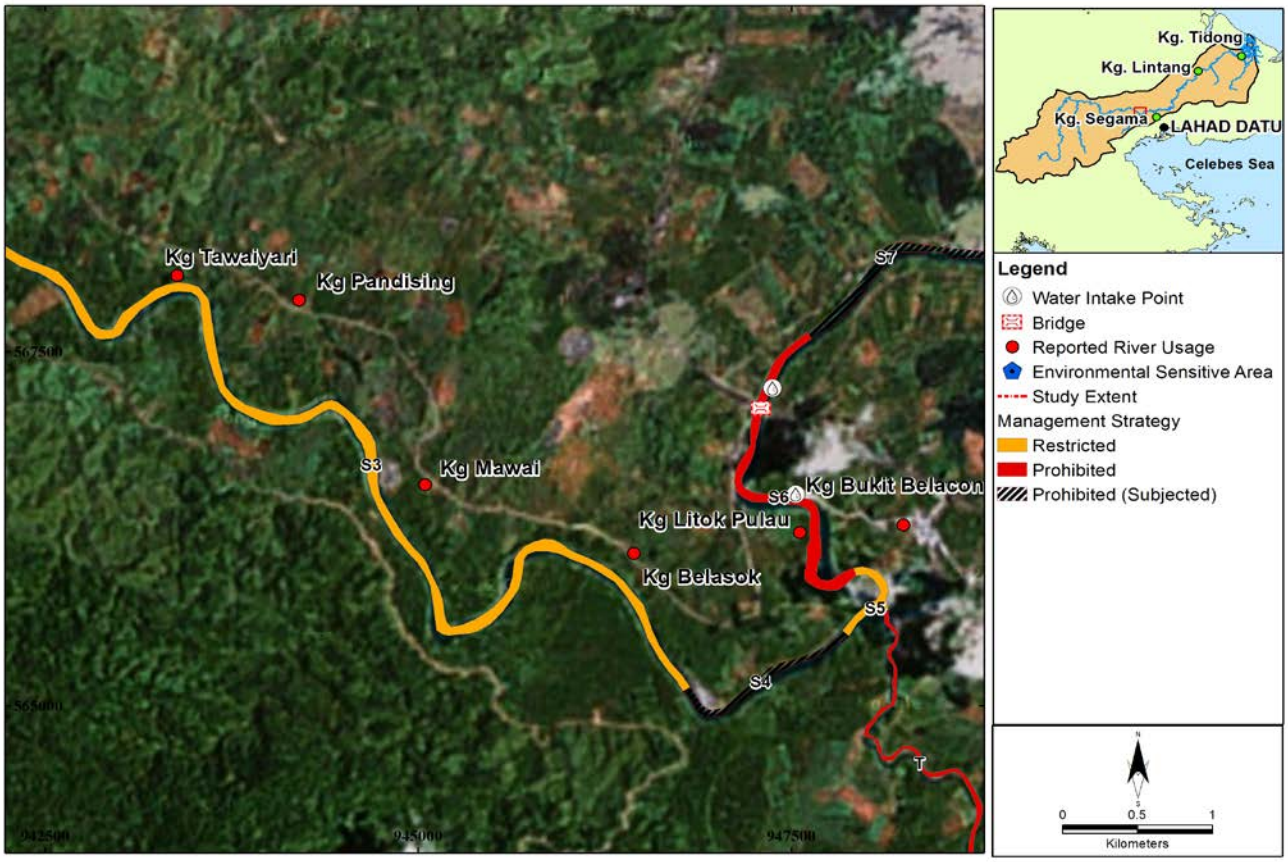


**Figure 8.** River sand mining management strategy based on sensitive receptor – upper mid-reaches of Segama River (Area 2).

## 8 CONCLUSION

A sediment budget for the river is complex to establish with highly variable flow and transport conditions and limited data. Due to the highly dynamic river morphology with constantly developing meanders, the natural erosion and deposition also need to be considered in an overall assessment of the potential impacts from river sand mining. The estimated volumes from the study are considered same order of magnitudes for average annual conditions, but these will be highly variable from year to year. Best estimate components are summarized as:

- Sediment yield from Upper Catchment: 250,000 to 500,000 $m^3$/year (all fractions)
- Sediment transport capacity for Mid-reaches:~70,000 $m^3$/year (0.3mm sand)
- Natural erosion/deposition in meanders:~130,000 $m^3$/year (study area)

The estimated current sand extraction of ~100,000 $m^3$/year is considered same order of magnitude as the transport capacity and the natural erosion/deposition, and significantly lower than the total sediment yield from upstream to the river system.

With the sand extraction distributed throughout the study area, it is considered that the sediment yield from the catchment combined with sediment from the natural erosion/deposition can replenish the extracted volumes without significant risk of causing regional deficit erosion.

The current river sand mining is considered to mainly have localized effects, which can be potentially severe if not managed appropriately. Existing guidelines from EPD and DID have been applied for mapping of zones where river sand mining should be prohibited or restricted.

A river sand mining management strategy for the mid-reaches of Segama River developed based on the existing guidelines identified 67.9% of river length covering within the study area located within “Restricted” zones, 15.8% of river length within the study area located within the “Prohibited (Subjected)” zones and 16.3% of river length located within the “Prohibited” zones. The findings of this study have been implemented into a GIS database and decision support system that enables the regulatory authority to further better manage the sand resource within the mid-reaches of Segama River in the future.

## ACKNOWLEDGEMENTS

The study which is the subject of this paper has been carried out by DHI Water & Environment (M) Sdn. Bhd. for the Environment Protection Department Sabah. The authors wish to acknowledge the support and assistance provided by the Environment Protection Department Sabah in the preparation of this paper.

 

**REFERENCES**

Department of Irrigation and Drainage Malaysia, (River Engineering Section). (1993). *Garis Panduan untuk Memproses Permohonan dan Menetapkan Syarat-Syarat Pengamiblan Pasir Sungai*, Department of Irrigation and Drainage Malaysia, Kuala Lumpur, Malaysia.

Department of Irrigation and Drainage Malaysia (2009). *River Sand Mining Management Guideline*, Ministry of Natural Resources and Environment, Kuala Lumpur, Malaysia.

DHI (2013), *A Modelling System for Rivers and Channels,* MIKE 11 Reference Manual.

Environmental Conservation Department (2001),*Environmental Impact Assessment (EIA) Guidelines for River Sand and Stone Mining, Sabah, Malaysia*, Environmental Conservation Department, Sabah, Malaysia.

Environment Protection Department (2011). *Guidelines for Minimising Impacts of Sand Mining on Quality of Specific Rivers in Sabah*, First Edition, Environment Protection Department, Ministry of Tourism, Culture and Environment, Kota Kinabalu, Sabah.

 

# A NEW METHODOLOGY FOR PRESENTING HYDRODYNAMICS DATA FROM A LARGE RIVER CONFLUENCE

FARHAD BAHMANPOURI[(1)], NAZIANO FILIZOLA[(2)], MARCO IANNIRUBERTO[(3)] & CARLO GUALTIERI[(4)]

[(1, 4)]Department of Civil, Construction and Environmental Engineering, University of Napoli Federico II, Napoli, Italy, farhad.bahmanpouri@unina.it, carlo.gualtieri@unina.it
[(2)]Universidade Federal do Amazonas, Manaus, AM, Brazil
[(3)]Instituto de Geociências - Universidade de Brasília, Campus Universitário Darcy Ribeiro - ICC Centro, 70910-900 Brasília / DF, Brazil iannirubertо@unb.br

## ABSTRACT

Confluences are very complex fluvial networks where the combination of matter (water and sediment) and energy (flow strength) from two different channels take place. The confluence of Rio Negro, with its black waters, and the Rio Solimões, with its suspended white sediments, is one of the biggest confluences on the earth and attracts thousands of tourists every year near by the city of Manaus, Amazonas – Brazil. This paper presents the application of a new method to analyze the ADCP data which is using an in-house FORTRAN code in combination with the Tecplot and Surfer Softwares. The method is applied to ADCP transects collected on this confluence within the EU-funded Clim-Amazon Project in two different periods of the hydrological cycle: low flow conditions on 30 and 31 October 2014, during the FS−CNS1 campaign, and relatively high flow conditions on 29 and 30 April 2015, during the FS−CNS2 campaign, both of them included 23 transects. These data are first extracted with WinRiver II software to produce ASCII files. The ASCII files are first processed using the code to derive input files containing the three velocity components, the average backscatter as well as the secondary currents from the Rozovskii method. These data are plotted in Tecplot to gain cross-sectional profiles. Furthermore, as past investigations are limited to the analysis of the depth-averaged quantities, the FORTRAN code is used even to extract the values of the velocity components as well as the backscatter along three layers in the channel: near the bed, at mid-depth and near the water surface. The data are then used to prepare Surfer maps, in a plane contour map format, of these quantities. The analysis of the data along these three layers can provide further findings into the complex three-dimensional structure of the flow at the Negro/Solimões confluence.

**Keywords:** Environmental hydraulics; Negro/Solimoes confluence; hydrodynamics; ADCP; data presentation.

## 1 INTRODUCTION

River channel confluences form important morphological elements of every river system, being points at which rapid changes in flow, sediment discharge and hydraulic geometry must be accommodated. River confluences with complex hydrodynamics and typical morphologies are basic nodes and key features of river systems; they are very important for the routing of water, sediments, and pollutants through a river system and are the focus for a range of fluvial processes (Biron and Lane, 2008). In the last four decades, a wide body of theoretical, numerical, experimental and field research has emerged on the fluvial dynamics of river confluences. Due to the difficulties associated with the extrapolation of laboratory results to real cases, field investigations are becoming an increasingly popular tool in the study of confluences (Parsons et al., 2007). To date, most experimental studies have focused either on laboratory confluences (Best, 1987) or on small natural confluences (Kenworthy and Rhoads, 1995), whereas an extremely limited number of investigations conducted on large river confluences, i.e. channel widths > 100 m (Lane et al., 2008; Konsoer and Rhoads, 2014). Further, thus far, numerical studies have generally only focused on simulating the flow structure observed in laboratory (Huang et al., 2002) and small natural confluences (Constantinescu et al., 2011). In terms of numerical simulation, Bradbrook et al. (1988) used the three-dimensional form of the Navier-Stokes equations to simulate the flow in a parallel confluence of unequal depth channels and to investigate the effect of different combinations of velocity and depth ratio between the two tributaries. Shakibainia et al. (2010) used SSIIM2.0, a 3-D numerical model, which was validated and applied to investigate secondary currents, velocity distribution, flow separation, and water surface elevation in different conditions of confluence angle, discharge, and width ratios. Zhong-chao et al. (2011) investigated on the confluence of Yangtze River and Jialing River based on the finite element model of two-dimensional depth-averaged surface-water flow which included the hydraulic behavior. Schindfesselet al. (2015) compared experimental results with OpenFOAM to investigate three-dimensional complex flow patterns for three different discharge ratios. Martin-vide et al (2015) studied the confluence of Toltén River and its tributary, the Allipén (south of Chile) to quantify total bedload and to understand the balance between tributary and main river and the bedload distribution in space and texture.

 

There has been an increasing interest in the use of Acoustic Doppler Current Profilers (ADCPs) to characterize the hydraulic conditions near river engineering structures such as dams, fish passes and groins, as part of ecological and hydromorphological assessment. In order to evaluating, analyzing, and displaying ADCP parameters, different methods and softwares have been developed. Some methods just for single process regarding moving-vessel deployments have been described and most involve collection of data along transects (Muste et al., 2004a; Dinehart and Burau, 2005a, 2005b; Szupiany et al., 2007, 2009). For example, Le Bot et al. (2011) presented a methodology, called CASCADE, for extracting ADCP data collected in marine environments along vessel transects and outline a routine to derive spatially-averaged velocities along such transects. Dinehart and Burau (2005a, 2005b) presented a method in which multiple transects can be projected and averaged onto a 2D planar grid to allow analysis of the 3D flow field, whereas Rennie and Church (2010) developed a procedure whereby spatially-distributed ADCP data can be interpolated onto a planar-horizontal 2D grid covering large areas up to entire channel reaches. Müller et al., (2001) developed a tool, LOG_aFlow W, for interpolation of ADCP-derived velocity onto 2D horizontal planes and 3D volumes using hydrodynamic interpolation in space and time. However, this tool is not specifically designed for mapping of cross-section data, which are often used for analysis of morphodynamics and geomorphological flow processes (Dinehart and Burau, 2005a, 2005b; Parsons et al., 2007; Szupiany et al., 2009). Kim et al. (2007) developed AdcpXP, a post-processing software package for ADCP data that includes spatial- and depth-averaging routines. A freely available software tool, called VMS, includes analytical capabilities for quality assurance of moving-vessel, multiple-transect ADCP data, with the general aim of improving processing and visualization of large, reach-scale ADCP data sets for comparison with results of numerical and physical models (Kim et al., 2009). While useful, none of these ADCP data-processing packages computes three-dimensional velocity components, including components used to identify secondary flow, using techniques employed by the geomorphological process community. Parson et al. (2012) developed a software, called VMT (Velocity Mapping Toolbox), which allows rapid processing (vector rotation, projection, averaging and smoothing), visualization (planform and cross-section vector and contouring), and analysis of a range of ADCP-derived dataset. The output formats for different parameters vorticity, shear velocity, bed shear stress, the longitudinal dispersion coefficient, and suspended sediment concentrations (with a sediment calibration option for acoustic backscatter) in 2D and 3D and in vertical and plan views could be possible. In this study, a new methodology for analyzing and presenting the ADCP data has been introduced.

The paper is structured as it follows: in Section 2 a detailed description of the field site and instrumentation is presented, including the geographic description of the confluence, hydrodynamic properties, devices, measured parameters, etc. Section 3 focuses on the data analyzing and post processing: it first describes the averaging data and extracting graphs, then presenting near surface, mid-depth and near bed data and finally calculation and presentation of secondary velocity.

## 2 FIELD SITE AND INSTRUMENTATION

The confluence of the Negro and Solimões rivers is located near Manaus in Northern Brazil, where these rivers merge to form the Amazon River, approximately 1600 km upstream from its mouth at the Atlantic Ocean. This confluence is famous for the meeting of the black and white waters of the two rivers which is shown in figure 1. As part of the CLIM-Amazon Project, which was a joint European and Brazilian Research Project funded by the EU about climate and sedimentary processes of the Amazon River Basin, two field studies were conducted about that confluence in both low (October 2014, FS−CNS1 campaign) and relatively high flow conditions (April/May 2015, FS−CNS2 campaign) (Trevethan et al., 2015a; 2015b; 2016). In these field trips, acoustic Doppler velocity profiling (ADCP) and high-resolution seismic methods, such as echo-sounding and sub-bottom profiling, were used as well as water sampling for the measurement of several water chemistry parameters (temperature, conductivity, pH, turbidity, dissolved oxygen, oxygen isotopes) and suspended sediments concentration. These data were collected to investigate key features about hydrodynamics, mixing, sediment transport and morphodynamics about this confluence. During both FS−CNS1 and FS−CNS2, a Teledyne RDI 600 kHz Rio Grande acoustic Doppler current profiler (ADCP) was used to collect cross-sectional measurements at key locations about the confluence, as indicated by lines in Figure 2.

During FS−CNS1, water samples at surface, 10 m, and 20 m depths at twelve locations about confluence were collected. These water samples were used to understand the characteristics of the two tributary rivers (temperature, pH, conductivity) and measure local suspended sediment concentration (SST) and oxygen isotope values. In FS−CNS2, vertical physico-chemistry profiles were collected with a YSI EVO2 multi-parameter probe. The locations are indicated by black point in Figure 2 (right). For each vertical profile, this probe collected the variation in temperature, pH, conductivity, turbidity, chlorophyll and dissolved oxygen concentrations with depth. Further water samples were collected at Sites S0 and N0 to measure the local SST concentration on the Solimões and Negro Rivers, respectively.

 

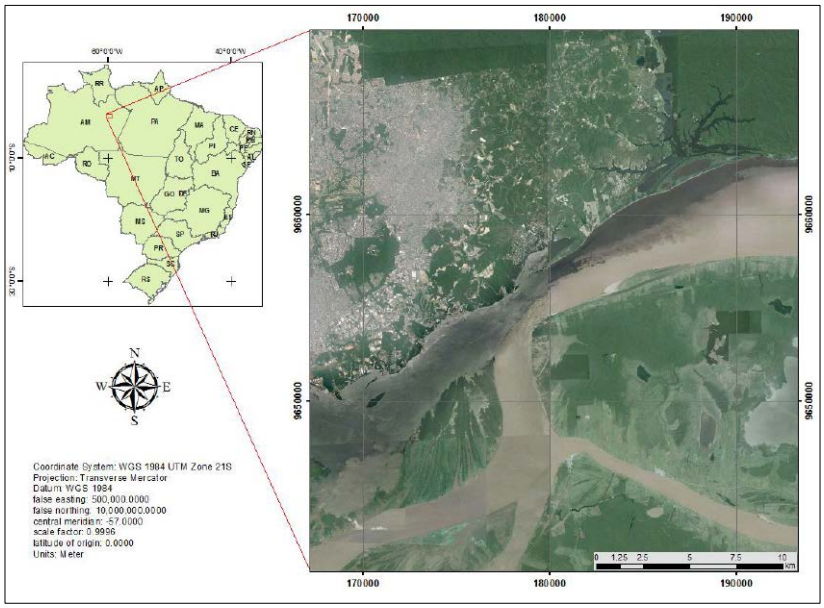


**Figure 1.** Confluence of the Negro and Solimões Rivers near Manaus.

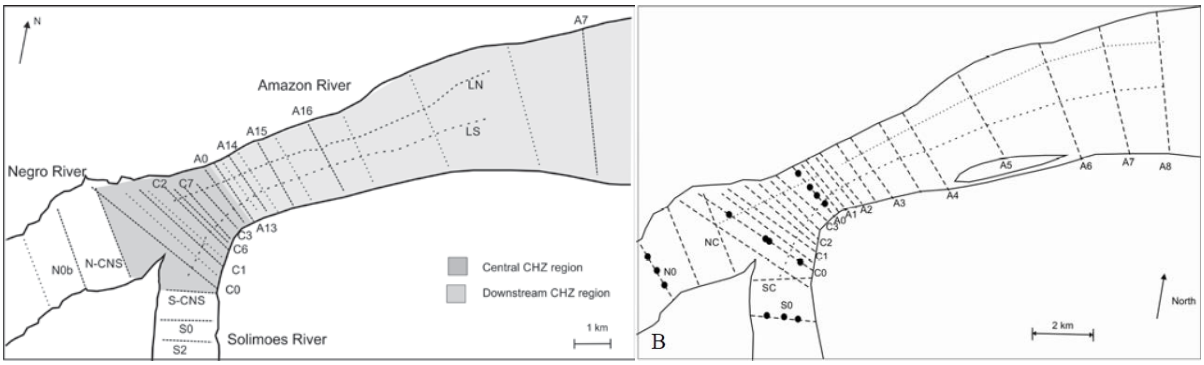


**Figure 2.** Map of confluence of Negro and Solimões rivers, with sampling positions during Field Study FS−CNS1 (left) and FS−CNS2 (right) are highlighted. Dots show the locations were vertical profiles and were collected in FS−CNS2 (Trevethan et al., 2015a; 2016).

Table 1 lists the measured median main flow properties of Negro and Solimõesrivers at the ADCP transects just upstream of the confluence (N-CNS and S-CNS, three for each river and each field study) on both the field trips. In Table 1, it can be seen that large differences in discharge and flow velocities are observed in the Solimões River between field studies FS−CNS1 and FS−CNS2, whereas on the Negro River these differences are smaller.

**Table 1.** Main flow properties of Negro and Solimões Rivers during FS−CNS1/FS−CNS2.

| | Field trip | Q ($m^3s$) | A ($m^2$) | W (m) | $h_{med}$ (m) | $W/h_{rect}$ (-) | $V_{avg}$ (m/s) | $V_{depth-avg}$ (m/s) | Dir (°) | $V_{max}$ (m/s) |
|---|---|---|---|---|---|---|---|---|---|---|
| **Negro** | FS−CNS1 | 24510 | 64784 | 2830 | 24.4 | 117 | 0.38 | 0.39 | 59 | 0.69 |
| | FS−CNS2 | 33501 | 86952 | 2875 | 31.2 | 95 | 0.38 | 0.40 | 58 | 0.67 |
| **Solimões** | FS−CNS1 | 63380 | 42789 | 1589 | 27.2 | 59 | 1.49 | 1.33 | 289 | 2.20 |
| | FS−CNS2 | 105205 | 61895 | 1925 | 28.6 | 60 | 1.70 | 1.52 | 255 | 2.59 |

**Legend:** Q = discharge; A = cross-sectional area; W = width; $h_{med}$ = median depth; $W/h_{rect}$ = median of the aspect ratio; $V_{avg}$ = median of the cross-section velocity (Q/A); $V_{depth-avg}$ = median of the depth-averaged velocity; Dir = median of flow direction degrees from North; $V_{max}$ = maximum depth-averaged velocity

Previous confluence studies have largely acknowledged that the momentum flux ($M_R = \rho_N Q_N V_{ave-N}/\rho_S Q_S V_{ave-S}$), discharge($Q_R = Q_N/Q_S$) and velocity ($V_R = V_{ave-N}/V_{ave-S}$) ratios can be related to the observed hydrodynamic and morphodynamic features about the confluence, where the subscripts N and S represent the Negro and Solimõesrivers, respectively. These ratios for field studies FS−CNS1 and FS−CNS2 are listed in Table 2.

 

**Table 2.** Discharge, velocity and momentum.

| Field trip | $Q_R$ | $V_R$ | $M_R$ |
|---|---|---|---|
| FS−CNS1 | 0.39 | 0.25 | 0.10 |
| FS−CNS2 | 0.32 | 0.22 | 0.07 |

The relatively high values of these ratios are indicative of the large difference in the flow properties of the two tributary rivers. As discussed in previous studies, high tributary over main river discharge ratio narrows the scour hole and pushes it toward the main river bed, hampering the entry of much of the bedload (Best, 1988; Rhoads et al., 2009).

## 3 DATA ANALYSIS AND POST-PROCESSING

In order to evaluate the data which had been collected with ADCP; in the first step, the initial raw data were extracted with WinRiver II. The output file of WinRiver II which was in text format contains a large volume of data including different parameters per ensemble with different depth. Since these data were completely unorganized, it required to convert the data to organized format and also an important issue was that the average of all parameters per ensemble was required for analyzing the data. In the second step, data were averaged per ensemble with FORTRAN code, and also primary and secondary velocities were calculated. Then in the third step, The Surfer13 software was used for plotting graphs based on geographical coordinates for the different type of parameters. Surfer is a full-function contouring and surface modeling package that runs under Microsoft Windows. Surfer is used extensively for terrain modeling, bathymetric modeling, landscape visualization, surface analysis, contour mapping, watershed and 3D surface mapping, gridding, view shed analysis, volumetric, and much more. In order to get an acceptable presentation of graphs for each parameter, based on the statistical criteria, a lot of trials were made for kriging the data especially radius and angle of searching points. In some areas because of transect's location, near or far distance, and river angle with longitudinal coordinate, the total area was divided into three or four parts with different kriging setting. And finally, in fourth step secondary velocity with other parameters were plotted using Tecplot. Figure 3 depicts the flowchart of this process.

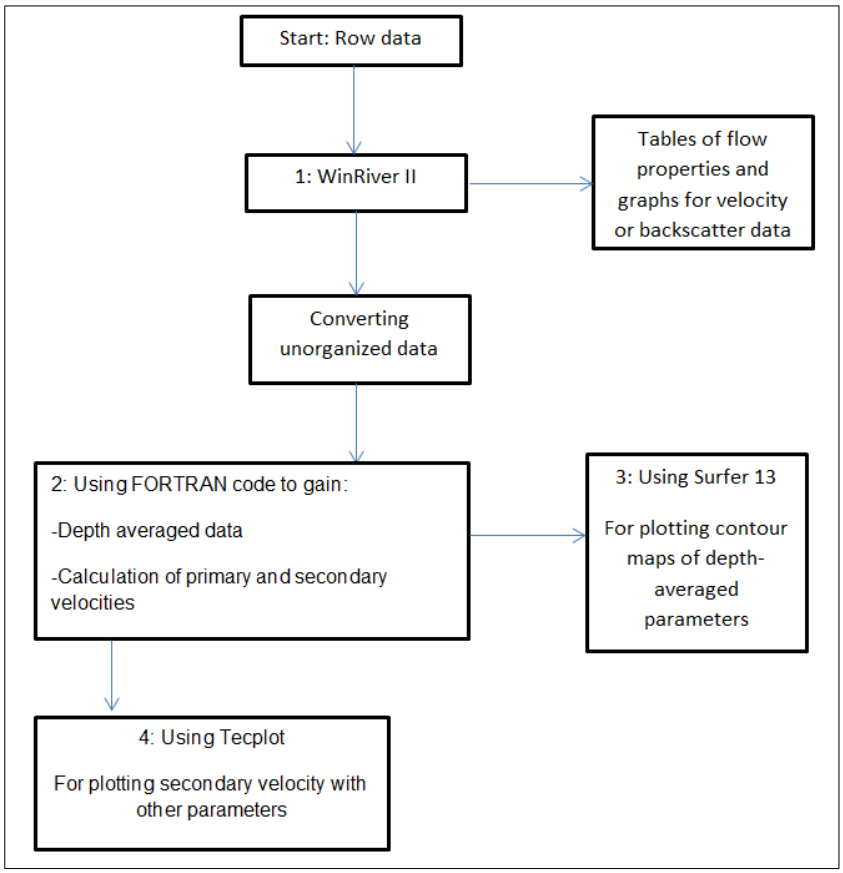


**Figure 3.** Flow-chart of post-processing of the ADCP data.

To compute depth-average velocities, the average value was computed by

 

$$V_{av} = \frac{1}{d_2 - d_1} \int_{d_1}^{d_2} v dz \qquad [1]$$

Where, $V_{av}$ is the depth-averaged velocity and *v* is the velocity magnitude, north or east component of velocity and $d_1$ and $d_2$ are the lower and upper limits of the depth range used in averaging, respectively. For all other parameters, this method is used for averaging the data.

Figures 4 and 5 show the depth-averaged velocity and bathymetry for two different days, 30/10/2014 (left) and on 29/04/2015 (right), in relatively low and relatively high flow conditions respectively. The graphs were extracted with Surfer 13 software. Maps of the channel bed topography (Figure 5) show that at the beginning of the confluence zone although the incoming channels are of a similar depth with no distinct discordance in bed level, for low flow conditions a deep scour is present within the confluence zone at downstream side and for high flow condition it happens in two areas; at Negro side and middle of confluence.

The contours in Figure 4 reveal how the tributary affects the main flow regime because of the difference of velocities and angle of confluence. It also shows that firstly, the maximum velocity region is in the mixing interface and secondly, the maximum velocity area for low flow conditions happens at the downside of the intersection but for relatively high flow conditions, it happens exactly at intersection area. Based on bathymetry, the area of maximum scouring, which equals to maximum depth, is exactly at the downside of the area of maximum velocity for low flow conditions but for relatively high flow conditions, the area of maximum velocity exactly coincides with maximum scouring area.

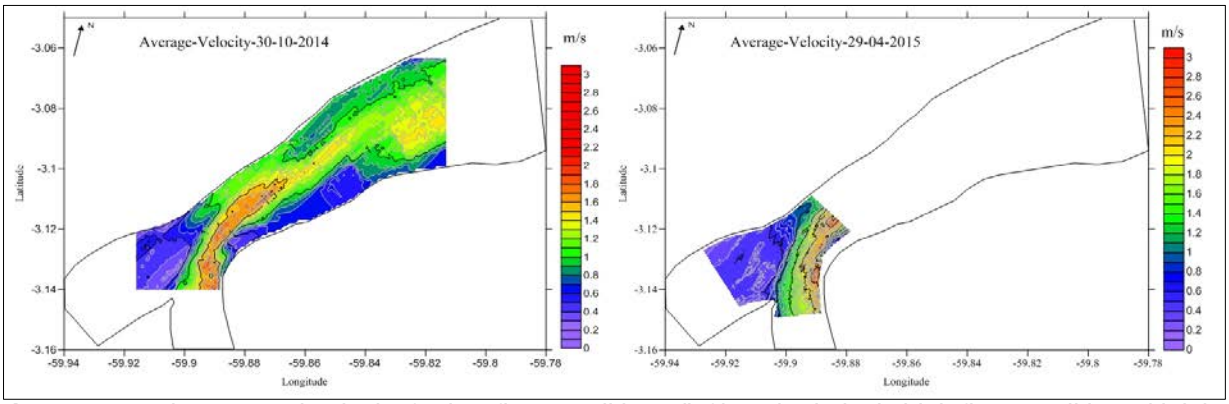


**Figure 4.** Depth-averaged velocity for low flow conditions (left) and relatively high flow conditions (right).

Based on Best model (1987) for key hydrodynamic features about a confluence, all morphological features could be seen about this confluence which include: separation zone, flow deflection zone, separation zones, maximum velocity and a scour hole normally orientated along the region of maximum velocity where both flows begin to converge and finally, flow recovery.

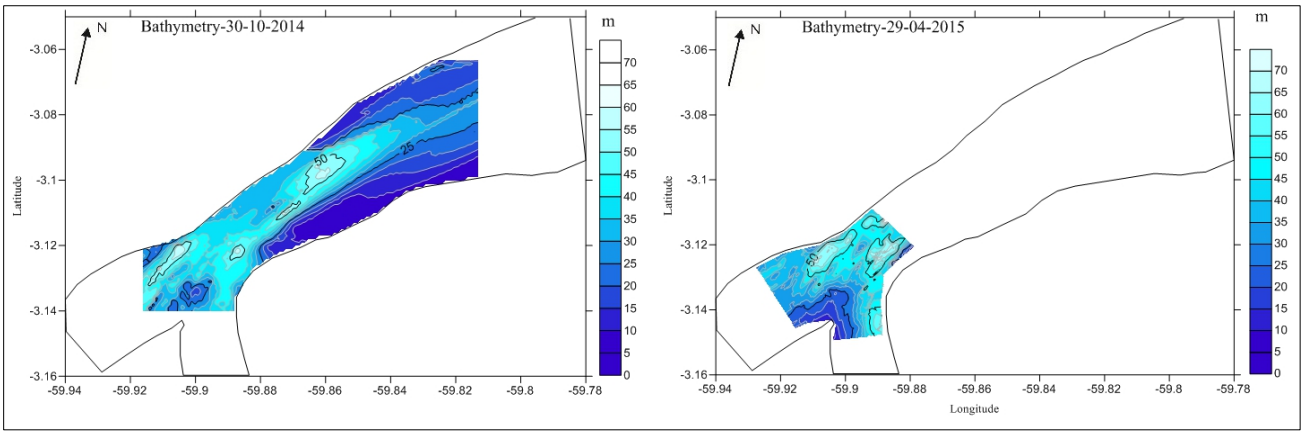


**Figure 5.** Bathymetry for low flow conditions (left) and relatively high flow conditions (right).

Figure 6 presents the velocity contours in three different layers; near surface, mid-depth and near-bed for two days in low and relatively high flow conditions. Velocity near surface is higher than mid-depth and near bed areas and in both days, maximum velocity for upper and lower layers, near surface and near bed, are higher than velocity in mid-depth layer.There are three possible reasons for this phenomenon: first the effect

of river bend, second the effect of variation in bed topography and third the effect of difference in rivers flow density.

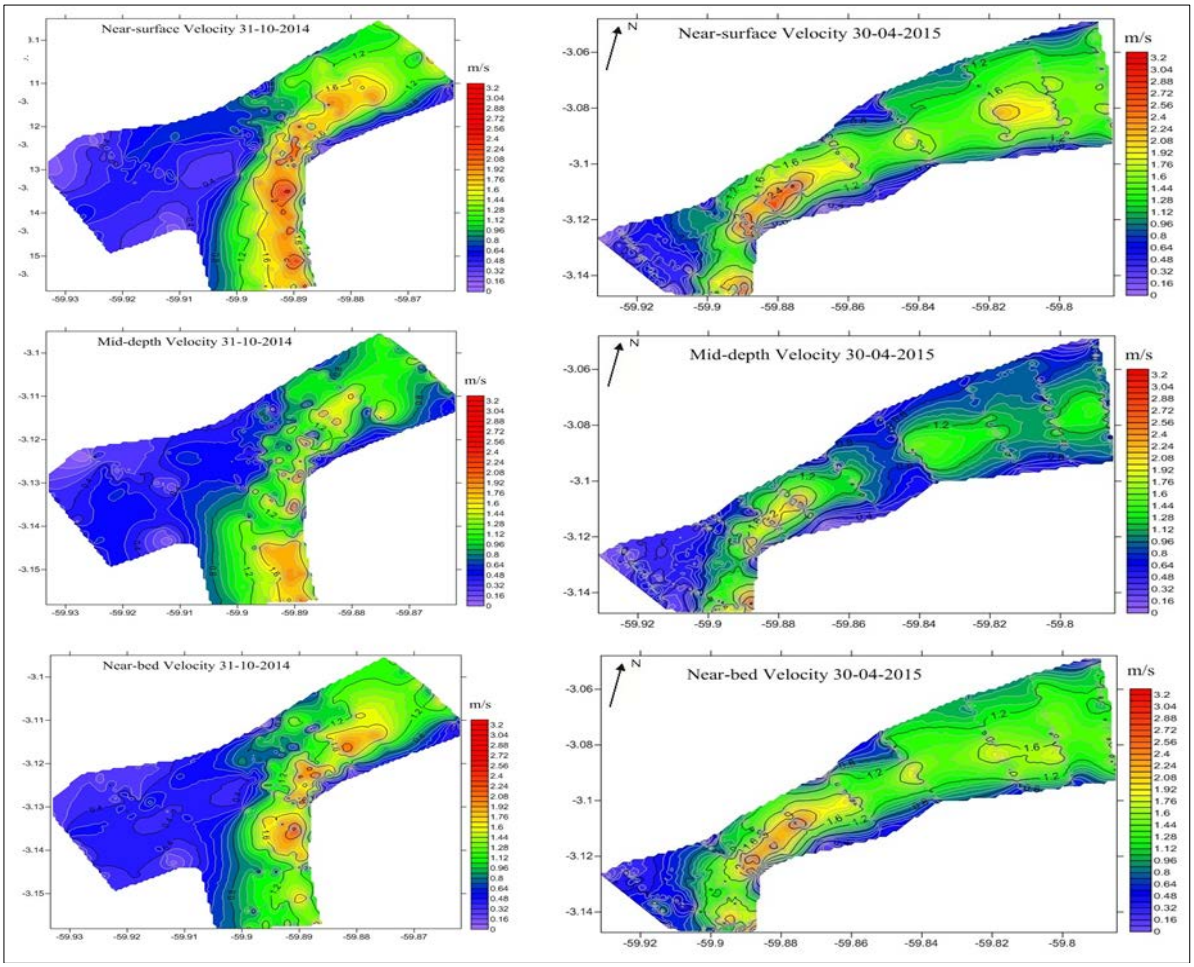


**Figure 6.** Velocity in three different regimes for low flow conditions (right) and relatively high flow conditions (left).

Since in the confluence zone the effect of river bend and difference in density is low, here the focus is on the bed level discrepancy. As previous studies, (Trevethan et al. (2015)) have investigated on the topography of this confluence, there is a large hole, length 1500m, width 700m, depth 20m in the middle part and a small hole like V-shaped valley, width 150m, height 5m, in Negro side of cross section. Therefore, these variations in bed topography could result in changing velocity profile and as Parson et al. (2007) based on studies on a large confluence in Rio Paraná Argentina stated, the discordance inbed height between the combining flows is known to produce a zone of negative dynamic pressure in the lee of the shallower channel, resulting in downstream advection and upwelling of fluid from the deeper channel into the waters of the shallower channel. Shugar et el. (2010) based on investigation on the Rio Paraná Argentina asserted that coherent flow structure is generated by dunes which result in the cyclic pattern of upwelling and down welling fluid over the dune crest. In other words, Phase coherence wavelet analysis shows that streamwise and vertical velocities are strongly and inversely correlated over the dune crest, where flow decelerations are linked to fluid upwelling and vice versa. Rhoads and Kenworthy (1995) elucidated two main features of helical motions: (1) the direction of the primary velocity vectors changes consistently, with maximum deviation angles near the water surface and near the bed and (2) this pattern is maintained across many verticals.

Finally, all variations in velocity profiles maybe also some evidence of flow acceleration into the confluence and deceleration downstream of the confluence, as reported by Roy et al. (1988) and Roy and Bergeron (1990).

One approach to exploring the existence of helical motion at confluences is to decompose the cross-stream velocity at each point in a vertical into components oriented parallel and orthogonal to the depth-averaged velocity vector at this vertical (Rhoads and Sukhodolov, 2001). Primary and secondary velocities were calculated based on Rozovskii method as used by Lane et al (2000). This method essentially identifies the primary velocity direction for each profile as the depth-integrated flow vector, and the secondary currents are then obtained by the differences from this average vector within the profile. This procedure effectively identifies individual secondary planes at each vertical profile across a given section, thus permitting

 

identification of variations in the primary flow direction within a section, without distorting the secondary flow results (Szupiany et al. 2009). Application of the Rozovskii method followed Rhoads and Kenworthy (1998). Primary $(v_p)$ and secondary components $(v_s)$ of each point velocity in each vertical, as shown in Figure 7, were determined from.

$$v_p = (v_x^2 + v_y^2)^{0.5} \cos(\theta - \phi) \quad [2]$$

$$v_s = (v_x^2 + v_y^2)^{0.5} \sin(\theta - \phi) \quad [3]$$

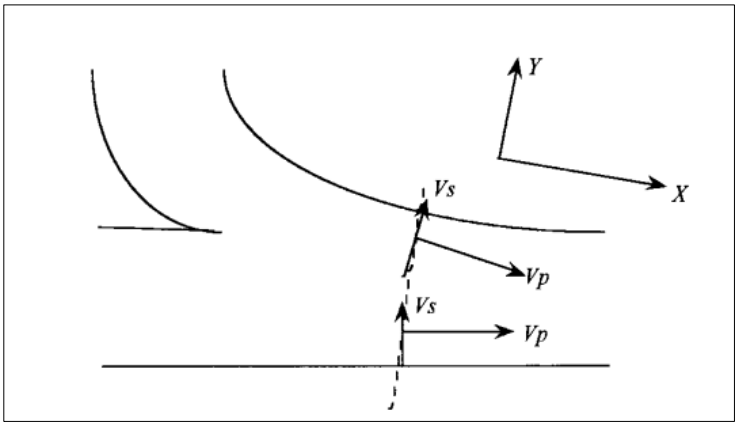


**Figure 7.** Definition of Rozovskii method (Lane et al. 2000).

Where θ is the orientation of the point velocity vector and ϕ is the orientation of the depth-averaged velocity vector, defined as zero when parallel to x, and becoming positive in an anti-clockwise direction from x. Following both Bathurst et al. (1977) and Rhoads and Kenworthy (1998), ϕ was determined from the direction of the depth-averaged velocity vector defined by integrating v_x and v_y separately over the flow depth for each vertical.

To illustrate the secondary velocity, one of transects in the confluence zone for low flow condition, transect CNS6 as shown in figure 2, was used. Figure 8 reveals the calculated secondary flow vectors superimposed on the depth-averaged backscatter contours for two cases, without and with smoothing. Two methods of smoothing were used, first smoothing in Fortran code and second smoothing with Tecplot. For both graphs, smoothing with the code was done, but one without Tecplot smoothing and the other with Tecplot smoothing. Smoothing in the code was done based on averaging three points per ensemble i.e. three points in the vertical direction.

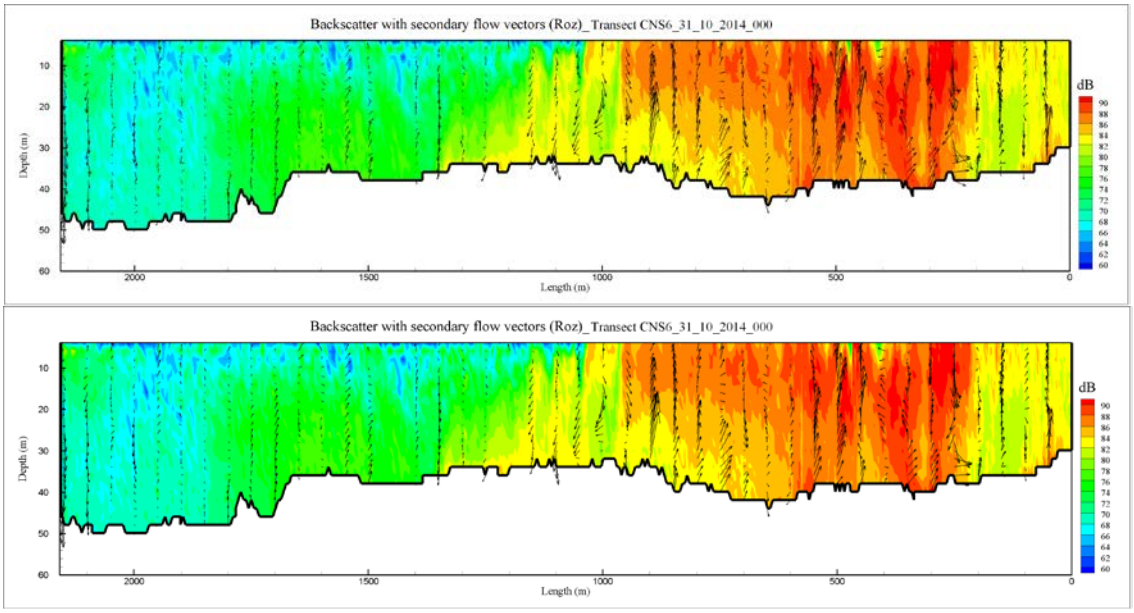


**Figure 8.** Backscatter with secondary velocity based on Rozovskii method, without smoothing (up) and with smoothing (down). Transect CNS6 on 31/10/2014.

 

For all figures of secondary velocity, sections are viewed looking downstream with the left bank on the left hand side. Backscatter intensity on the right side of the cross-section is higher than the left side with maximum 90 dB and 82 dB in the right and left sides, respectively. The interface line of confluence sharply divide the backscatter range for two rivers and this phenomenon reveals that the mixing process is quite complex.

In Figure 8, right side is in the mouth of Solimões River. Scattered and irregular secondary flow circulation are seen especially in right side of the cross-section. The first or main reason is the high turbulence in the mixing interface of confluence because of the angle of the tributary and the second reason is the difference in momentum flux. Rio Solimões meets the Rio Negro with the angle of 80 degree, therefore it results in creating intense circulation in flow and secondary flow. Changes in bed topography have even an effect. As it can be seen in figure 5 right, the scour hole is in the mixing area which has an important effect on the circulation.

Figure 9 shows the VMT output for the average backscatter data and secondary velocity based on Rozovskii method. The first point is that VMT interpolates available ensemble data with random distance on the length of transect line to the ensembles with fixed distant. So, it results in differences between our code output and VMT output. And the second point is that in order to calculate the secondary velocity, the resultant vector is based on vertical velocity and the velocity in direction y, so that the vertical velocity should be the same as original input vertical velocity. But, in VMT the vertical velocity has been changed in the process of calculations. In the FORTRAN code, there is no interpolation and secondary velocity is calculated exactly on the initial location of the ensembles.

Figure 10 illustrates the primary velocity with secondary velocity based on Rozovskii method with smoothing. As it is obvious in the right side, the primary velocity is higher. Therefore, it again shows that difference in discharge or velocity is the reason that in right side, the secondary velocity is stronger and it makes the flow more turbulent. In some areas, vertical velocity is stronger than transverse velocity which results in downward or upward of flow circulation and in some areas, transverse velocity is stronger and results in horizontal flow circulation. Generally, direction of secondary velocity depends on collision of two rivers, bed topography, primary velocity and channel width.

Depth-averaged primary and secondary velocities based on Rozovskii method are shown in figure 11. The primary velocity starts increasing from middle part toward right bank due to higher discharge rate in Solimões side. Since, depth-averaged secondary velocity is the summation of positive and negative velocity values per different layers; So, the average values are restricted between -0.5 to 0.5. The average secondary velocity in Solimões side is greater than on the Negro side.

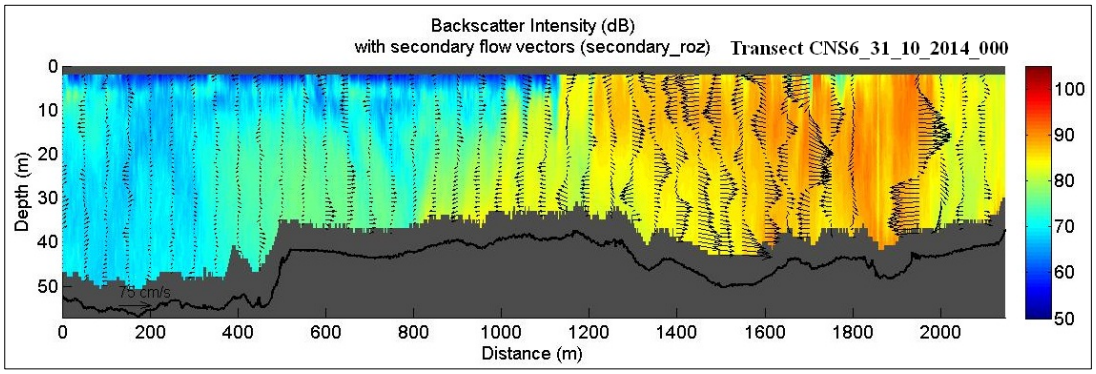


**Figure 9.** Backscatter with secondary velocity based on Rozovskii method, VMT output. Transect CNS6 on 31/10/2014.

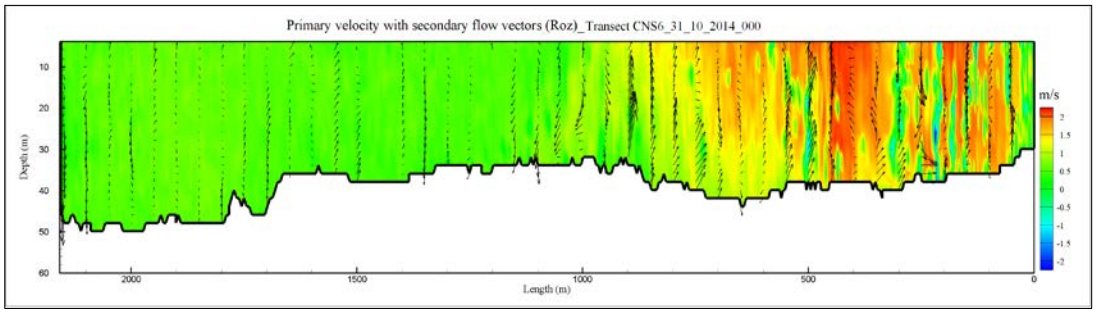


**Figure 10.** Primary velocity with secondary velocity based on Rozovskii method with smoothing. Transect CNS6 on 31/10/2014.

 

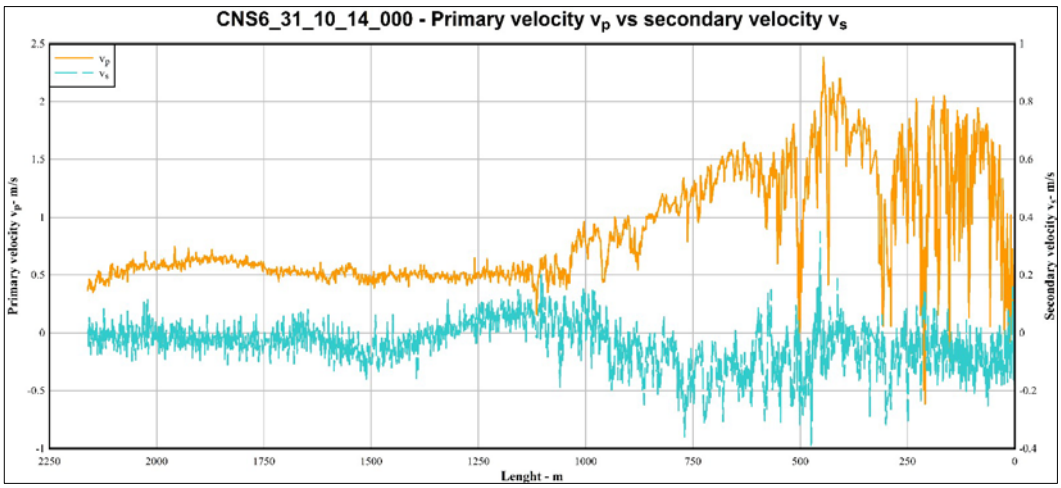


**Figure 11.** Depth-averaged primary and secondary velocities based on Rozovskii method for transect CNS6 on 31/10/2014.

## 4 CONCLUSIONS

This paper presents a method to analyze and present the ADCP data collected in a large field studies at the confluence of the Negro and Solimõesrivers, in Brazil. To illustrate this method, flow properties in this confluence are evaluated. Depth averaged data for different parameters using Surfer software are presented. Second, the complex three-dimensional features of the flow at the confluence requires the analysis of velocity at different depths. Hence, data at the water surface, at mid-depth and near the bed are extracted using Fortran code and then plotted with the Surfer software. Finally, secondary velocities based on Rozovskii method are calculated. The analysis of these velocities shows a complex circulation at the Rio Negro and Rio Solimões. The presented method could be applied to a wide range of applications where flow measurements are conducted along transects using ADCPs.

## ACKNOWLEDGEMENTS

This paper is part of a research for PhD degree in Civil System Engineering (31st cycle), at the University of Federico II Napoli, Italy. The authors acknowledge that this research is carried out within the Clim-Amazon European Laboratory in Brazil funded by grant agreement FP7 INCO-LAB n° 295091 from the European Commission and the partial support from the MIUR PRIN 2010-2011 Research Project HYDROCAR (CUP n. E61J12000210001). The authors also acknowledge Dr. Mark Trevethan for his collaboration on preparing data and some maps.

## References

Best, J. (1987). *Flow Dynamics at River Channel Confluences: Implications for Sediment Transport and Bed Morphology. 12 Recent Developments in Fluvial Sedimentology.* Special Publications 39, Society of Economic Paleontologists and Mineralogists, 27-35.

Best, J. (1988). Sediment Transport and Bed Morphology at River Channel Confluences. *Geomorphology* 35(3), 481-498.

Biron, P. & Lane, S. (2008). *Modelling Hydraulics and Sediment Transport at River Confluences. River Confluences, Tributaries and the Fluvial Network.* J. Wiley & Sons, 17-43.

Bradbrook, K. F., Biron, P. M., Lane, S. N., Richards, K. S. & Roy, A. G. (1998). Investigation of Controls on Secondary Circulation in a Simple Confluence Geometry using a Three-Dimensional Numerical Model. *Hydrological Processes*, 12, 1371-1396.

Constantinescu, G., Miyawaki, S., Rhoads, B., Sukhodolov, A. & Kirkil, G. (2011). Structure of Turbulent Flow at a River Confluence with a Momentum and Velocity Ratios Close to 1: Insight from an Eddy-Resolving Numerical Simulation. *Water Resources Research*, 47, 1-16.

Dinehart, R. L. & Burau, J. R. (2005a). Repeated Surveys by Acoustic Doppler Current Profiler for Flow and Sediment Dynamics in A Tidal River. *Journal of Hydrology* 314, 1-21.

Dinehart, R. L. & Burau, J. R. (2005b). Averaged Indicators of Secondary Flow in Repeated Acoustic Doppler Current Profiler Crossings of Bends. *Water Resources Research* 41, 1-18.

Kenworthy, S. & Rhoads, B. (1995). Hydrologic Control of Spatial Patterns of Suspended Sediment Concentration at a Stream Confluence. *Journal of Hydrology*, 168, 251-263.

Konsoer, K. & Rhoads, B. (2014). Spatial–Temporal Structure of Mixing Interface Turbulence at Two Large River Confluences. *Environmental Fluid Mechanics*, 14(5), 1043–1070.

Huang, J., Weber, L. & Lai, Y. (2002). Three-Dimensional Numerical Study of Flows in Open-Channel Junctions. *Journal of Hydraulic Engineering*, 128(3), 268-280.

 

Kim, D., Muste, M., Mueller, D.S. & Winkler, M. (2009). A Quick Tutorial for using VMS.*U.S. Army Corps of Engineers, 68.* (Online publication accessed October 15, 2012; http://chl.erdc.usace.army.mil/Media/1/1/2/0/VMS_quick_tutorial.pdf).

Lane, S., Parsons, D., Best, J., Orfeo, O., Kostaschunk, R. & Hardy, R. (2008). Causes of Rapid Mixing at a Junction of Two Large Rivers: Rio Parana and Rio Paraguay, Argentina. *Journal of Geophysical Research*, 113, 1-16.

Le Bot, P., Kermabon, C., Lherminier, P. & Gaillard, F. (2011). *CASCADE V6.1: Logiciel de Validation et de Visualisation des Mesures ADCP de Coque. Rapport TechniqueOPS/LPO 11–01.Ifremer*, Centre de Brest, France; 93.

Martín-Vide, J.P., Plana-Casado, A., Sambola, A. & Capapé, S. (2015). Bedload Transport in a River Confluence. Geomorphology, 250, 15-28.

Muste, M., Yu, K. & Spasojevic, M. (2004a). *Practical Aspects of ADCP Data use for Quantification of Mean River Flow Characteristics: Part I: Moving-Vessel Measurements*, Flow Measurement and Instrumentation 15, 1–16.

Müller, V., Eden, H. & Vorrath, D. (2001). Flow The Hydraulic Software for Hydraulic Engineering and Navigation. *Proceedings of the International Conference on Port and Maritime R&D and Technology*, National University of Singapore, 953–957.

Parsons, D., Best, J., Lane, S., Orfeo, O., Hardy, R. & Kostaschuk, R. (2007). Form Roughness and the Absence of Secondary Flow in a Large Confluence-Diffluence, Rio Parana, Argentina. *Earth Surface Processes and Landforms*, 32, 155-162.

Parsons, D., Jackson, P., Czuba, J., Engel, F., Rhoads, B., Oberg, K., Best, J., Mueller, D., Johnson, K. & Riley, J. (2013). Velocity Mapping Tool (VMT): A Processing and Visualization Suite for Moving-Vessel ADCP Measurements. *Earth Surface Processes and Landforms*, 38, 1244-1260.

Rennie, C. D. & Church, M. A. (2010). Mapping Spatial Distributions and Uncertainty of Water and Sediment Flux in a Large Gravel Bed River reach using an Acoustic Doppler current Profiler. *Journal of Geophysical Research* 115, 1-27.

Rhoads, B. L. & Sukhodolov, A. N. (2001). Field Investigation of Three-Dimensional Flow Structure at Stream Confluences: 1. Thermal Mixing and Time-Averaged Velocities. *Water Resources Research,* 37(9), 2393-2410.

Rhoads, B.L., Riley, J. D. & Mayer, D.R. (2009). Response of Bed Morphology and Bed Material Texture to Hydrological Conditions at an Asymmetrical Stream Confluence. *Geomorphology*, 109(3-4), 161-173.

Roy, A. G. & Bergeron, N. (1990). Flow and Particle Paths at a Natural River Confluence with Coarse Bed Material. *Geomorphology*, 3, 99 -1122.

Roy, A. G., Roy, R. & Bergeron, N. (1988). Hydraulic Geometry and Changes in Flow Velocity at a River Confluence with Coarse Bed Material. *Earth Surface Processes and Landforms*, 13, 583-598.

Schindfessel, L., Creëlle, S. & De Mulder, T. (2015). Flow Patterns in an Open Channel Confluence with Increasingly Dominant Tributary Inflow*. Water, 7, 4724-4751*.

Shakibainia, A., MajdzadehTabatabai, M. R. & Zarrati, A. R. (2010). Three-Dimensional Numerical Study of Flow Structure in Channel Confluences. *Canadian Journal of Civil Engineering*, 37(5), 772-781.

Shugar, D. H., Kostaschuk, R., Best, J. L., Parsons, D. R., Lane, S. N., Orfeo, O. & Hardy, R. J. (2010). On the Relationship between Flow and Suspended Sediment Transport over the Crest of a Sand Dune, Río Paraná, Argentina. *Sedimentology*, 57: 252–272.

Szupiany, R. N., Amsler, M. L., Best, J. L. & Parsons, D. R. (2007). Comparison of Fixed- and Moving Vessel Measurements with an aDp in a Large River. *Journal Hydraulics Engineering*, 133(12), 1299-1310.

Szupiany, R. N., Amsler, M. L., Parsons, D. R. & Best, J. L. (2009). Morphology, Flow Structure, and Suspended Bed Sediment Transport at Two Large Braid-Bar Confluences. *Water Resources Research,* 45, 1-19.

Trevethan, M., Martinelli, A., Oliveira, M. Ianniruberto, M. & Gualtieri, C. (2015a). Fluid Dynamics, Sediment Transport and Mixing about the Confluence of Negro and Solimões Rivers, Manaus, Brazil. *36th IAHR World Congress, The Hague, the Netherlands*.

Trevethan, M., Ventura Santos, R., Ianniruberto, M., Santos, A., De Oliveira, M. & Gualtieri, C. (2016). Influence of Tributary Water Chemistry on Hydrodynamics and Fish Biogeography about the Confluence of Negro and Solimões Rivers, Brazil. *11th International Symposium on Eco Hydraulics*, Melbourne, Australia.

Zhong-Chao, Y. & Ze-Yi, Y. (2011). Numerical Simulation Study on Hydraulic Behaviour at the Confluence of Yangtze River and Jialing River. *Procedia Engineering*, *Conference on Engineering Modelling and Simulation,* 12, 197-203.

 

# NUMERICAL SIMULATION OF SEDIMENT ENTRAINMENT BY LOCK-EXCHANGE GRAVITY CURRENTS

FOTEINI KYROUSI[(1)], ALESSANDRO LEONARDI[(2)], CARMELO JUEZ[(3)], JESSICA ZORDAN[(4)], FRANCESCA ZANELLO[(5)], FEDERICO ROMAN[(6)], VINCENZO ARMENIO[(7)] & MÁRIO J. FRANCA[(8)]

[(1,2,5)]Idrostudi Srl, Area di Ricerca, Trieste, Italy
foteini.kyrousi@phd.units.it
[(3,4,7,8)]Department of Engineering and Architecture, University of Trieste, Italy
[(6)]Laboratoire de Constructions Hydrauliques, École polytechnique fédérale de Lausanne, Switzerland
[(4)]Iefluids S.r.l., Trieste, Italy

## ABSTRACT

Gravity currents are flows driven by buoyancy differences between two contacting fluids caused by differences in temperature, salinity, or by the presence of suspended particles. Such flows can reach high velocities near the bed, especially on the area behind the front of the current. As a result, rapid morphological changes may take place in river and estuarine beds due to the passage of these flows. Essential to determine the erosion induced by the current, are the spatial and temporal distributions of the bed shear stress. However, these are troublesome to measure in laboratory or in the field. To bridge this difficulty, the eddy-solving numerical simulations may be used. This study presents here the three-dimensional numerical simulations of lock-exchange salinity currents flowing over a mobile bed. It is aimed at the characterization of the sediment entrainment capacity of the current. The large eddy simulation technique is employed for analyzing the evolution and the structure of the current. For the sediment simulation, an Euler-Euler methodology based on a single phase approach is used. The main features of the current are compared with experimental data obtained in the laboratory. Velocity fields and bed shear stress distributions for different initial current densities are analyzed and linked to entrainment scenarios. The influence of small variations in particle size of the mobile bed is also discussed.

**Keywords**: Gravity current; large Eddy simulations (LES); suspended sediment transport; sediment erosion.

## 1 INTRODUCTION

The propagation of gravity currents, triggered by the release of a heavier fluid in a less dense water body, can cause, among other phenomena, important environmental impacts such as rapid morphological changes in river and estuarine beds, reservoir sedimentation, damages in submarine emissaries and cables, and pollutant dispersion. All of this makes their understanding of prime interest in environmental sciences. Gravity currents can be formed in many different natural situations. They can be caused by natural events e.g., sea breeze fronts, oceanic overflow, avalanches and volcanic eruption; or by anthropogenic activities e.g. accidental release of a dense gas, oil spillages or pollutant discharge in water bodies (Simpson, 1997).

Due to the unpredictable nature of such flows and to technical difficulties, field studies are quite limited. Hence, our understanding on the dynamics of gravity currents is based mainly on laboratory experiments and high-resolution simulations. The numerical tools that have been mainly used over the last years to study the behavior of gravity currents are Direct Numerical Simulations (DNS), that resolves all the relevant scales in the flow down to the dissipative range, and Large Eddy Simulations (LES), where a subgrid-scale model is used instead of resolving the smaller scales. In particular, pioneering DNS for density-driven gravity currents in low Reynolds number were presented by Härtel et al. (2000a; 2000b) and Necker et al. (2002). However, DNS is restricted mainly to low Reynolds number flows and simple geometries due to its computational cost, whereas LES has proven useful on high Reynolds number flows over complex geometries. Gravity currents with high Reynolds number, its effects on the bed shear stress distribution, and its interaction with obstacles, were investigated using LES by Ooi et al. (2009), Gonzalez-Juez et al. (2009) and Tokyay et al. (2011).

Gravity currents have the capacity to erode a loose bed, if they are fast enough so that the bed shear stress exceeds the threshold of motion of the bed material (see Figure 1). The sedimentation induced by turbidity currents has been extensively investigated in literature (Akiyama et al., 1985; Eames et al. (2001); Necker et al., 2002; Blanchette et al., 2005). However, to the best of our knowledge, few studies (Garcia and Parker, 1991) focused on the lift-off mechanisms and the distribution of the entrained material in the body of the current. To study the particle entrainment induced by gravity currents requires detailed, spatial and temporal, measurements of velocities, bed shear stress distribution and sediment concentration. The purpose of the present work is to investigate numerically the capacity of salinity current to bring bed material into suspension. For this purpose, the LES of compositional gravity currents is performed in lock-exchange configuration, flowing over a channel reach where the bed is mobile. Different buoyancy Reynolds numbers of

 

the current and different grain size of the bed particles are tested. The change of particle diameters is modeled by changing the critical Shields number and the settling velocity. The density gradient is given by a salinity difference between the heavier and the ambient fluid, which is small enough for the Boussinesq approximation to be valid. The initial aspect ratio of the lock fluid, *R*, is large ($R = {}^{H}/_{x_0} \ll 1$, where H is the water depth and $x_0$ is the distance between the lock and the rear wall), and this study considers a full-depth release. The governing equations of the flow are numerically integrated using LES-COAST, an unsteady Navier-Stokes solver, written under the Boussinesq approximation and based on the work in Zang et al. (1994). The sub-grid scale (SGS) terms have been modeled using a Smagorinsky dynamic Lagrangian model (Meneveau et al., 1996). Both salinity and sediment concentration are considered as active scalars and an Euler-Euler approach has been employed, which considers the two phases as a mixture. The numerical results provide a detailed description of the salinity current, the comparison of its main features with experimental results provided by Zordan et al. (2017). LES supplies information on the velocity and density fields, the spatial and temporal distribution of the bed shear stress exactly before the erodible section of bed, and the evolution of the sediment concentration above the mobile bed.

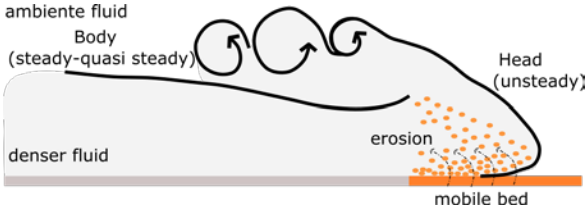


**Figure 1.** Sketch of a gravity current propagation and entraining and bed sediment.

The article is organized as follows: First the case that this paper is planning to study is described along with the illustration of the mathematical and numerical model. Sec. 4 presents the main characteristics of the current and their comparison with experimental data, while the results for the velocity field and the estimation of bed shear stress are discussed in Sec. 5. The contours of entrained sediment concentration are analyzed in Sec. 6 followed by a brief summary and the main conclusions.

## 2 DESCRIPTION OF THE STUDY CASE

The geometry used in this work was inspired by the experimental configuration described in Zordan et al. (2017). A sketch description of the experimental set-up is given in Figure 2. The flume used in the experiments was *7.48* m long, *0.275* m wide and was filled at both sides of the gate up to a depth of *H=0.2* m. Downstream of the horizontal flume the current dissipates in a large tank. The horizontal flume was separated by a movable lock-gate at a distance $x_0 = 2.5$m from the rear wall. At each side of the gate, volumes of fluid with different densities were contained. The fluid volume behind the lock had an initial salinity equal to $C^1_{sal}$ and density $\rho_{lock}$ (see Table 1), while the fluid volume beyond the lock had a zero-initial salinity $C^0_{sal}$*=0* kg/m$^3$ and the density of clear water $\rho_w$. Density is connected to salinity by the state equation shown hereafter (Eq. 1), where $\beta$ is the salinity contraction coefficient whose value can be found in UNESCO/IOC et al. 2010.

$$\rho = \rho_w[1 + \beta(C_{\mathrm{sal}} - C^0_{\mathrm{sal}}] \qquad [1]$$

The apparatus simulates the classical lock exchange gravity current (Nogueira et al. 2013; Theiler and Franca, 2016). When the gate is removed, the heavier fluid starts flowing towards the bottom of the flume creating a current that flows away from the gate, while the lighter fluid is displaced creating a counter current that protrudes on top of the heavier fluid. As a consequence, between the two fluids a shear layer forms, which provokes mixing due to Kevin-Hemholtz instabilities.

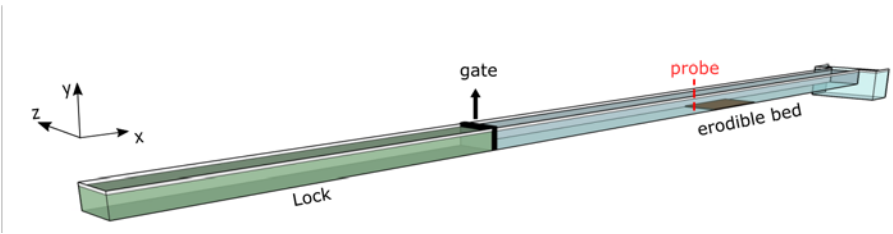


**Figure 2.** Lock-exchange configuration corresponding to the experiments by Zordan et al. (2017) which has inspired the numerical set-up. The volume indicated by green color represents the heavier fluid, while the volume with the blue color indicates the lighter fluid. The erodible section of the bed is shown by brown color. The red dashed line demonstrates the position of the probe where the numerical measurements are collected.

 

The fluid density on the two sides of the lock-gate is very similar (they do not exceed *O* (1%)), and the Boussinesq hypothesis is valid. Four different simulations are performed using two different values for the initial salinity $C^1_{sal}$ and changing the bed material characteristics, such as critical Shields parameter, $\theta_{cr}$ and settling velocity, $w_s$. The numerical parameters for the different runs are reported in Table1.

The buoyancy Reynolds number, $\mathrm{Re_b}$, and the Froude number, *Fr*, are defined as,

$$\mathrm{Re}_b = \frac{u_b H}{\nu}, \qquad [2]$$

$$\mathrm{Fr} = \frac{u_{front}}{u_b}, \qquad [3]$$

where $\nu$ is the molecular viscosity, $u_{front}$ is the velocity of the current front at the slumping phase and $u_b$ is defined as,

$$u_b = \sqrt{g' H}, \qquad [4]$$

where

$$g' = g\,\frac{\rho_{\mathrm{lock}} - \rho_w}{\rho_w}. \qquad [5]$$

**Table 1.** Parameters of lock-exchange numerical simulations.

| | $\rho_{lock}$ (kg/m$^3$) | $C^1_{sal}$ (psu) | g' (m/s$^2$) | $u_b$ (m/s) | $u_{front}$ (m/s) | $Re_b$ | Fr | $\theta_{cr}$ | $w_s$ |
|---|---|---|---|---|---|---|---|---|---|
| **A** | 1030 | 40 | 0.294 | 0.2426 | 0.109 | 48991 | 0.449 | 0.25 | 5.5x $10^{-4}$ |
| **B** | 1030 | 40 | 0.294 | 0.2426 | 0.109 | 48991 | 0.449 | 0.17 | 13.7 x$10^{-4}$ |
| **C** | 1040 | 53 | 0.392 | 0.2801 | 0.117 | 55961 | 0.417 | 0.25 | 5.5x $10^{-4}$ |
| **D** | 1040 | 53 | 0.392 | 0.2801 | 0.117 | 55961 | 0.417 | 0.17 | 13.7 x$10^{-4}$ |

## 3 MATHEMATICAL MODEL AND NUMERICAL SET-UP

### 3.1 Governing equations and numerical method

The dynamics of the gravity current obey the Navier-Stokes equations for incompressible flows, in the form given by the Boussinesq approximation for the buoyancy effects. The momentum and mass conservation equations are also coupled with two scalar transport equations: one for the salinity and one for the sediment concentration. In the Navier-Stokes equations, the influence of the density variations due to salinity and sediment concentration is taken into account through additional forcing terms in the vertical momentum conservation. The LES-filtered continuity equation, momentum equation, and the two scalar transport equations have been scaled using the buoyancy velocity of the current $u_b$ and the water depth $H$ as follows:

$$\frac{\partial \bar{u}_i}{\partial x_i} = 0, \qquad [6]$$

$$\frac{\partial \bar{u}_i}{\partial t} + \frac{\partial \bar{u}_j \partial \bar{u}_i}{\partial x_j} = -\frac{\partial \bar{p}}{\partial x_i} + \frac{1}{\mathrm{Re_b}} \frac{\partial^2 \bar{u}_i}{\partial x_j \partial x_j} - \frac{\Delta \hat{\rho}}{\rho_{\mathrm{lock}} - \rho_{\mathrm{w}}} \delta_{i,j=2} - \frac{\partial \tau_{ij}}{\partial x_j}, \qquad [7]$$

$$\frac{\partial \bar{C}_{\mathrm{sal}}}{\partial t} + \frac{\partial \bar{u}_j \bar{C}_{\mathrm{sal}}}{\partial x_j} = \frac{1}{\mathrm{Re_b Sc_{sal}}} \frac{\partial^2 \bar{C}_{\mathrm{sal}}}{\partial x_j \partial x_j} - \frac{\partial \lambda_j}{\partial x_j}, \qquad [8]$$

$$\frac{\partial \bar{C}_{\mathrm{sed}}}{\partial t} + \frac{\partial (\overline{u}_{j - w_s \delta_{i2}}) \bar{C}_{\mathrm{sed}}}{\partial x_j} = \frac{1}{\mathrm{Re_b Sc_{sed}}} \frac{\partial^2 \bar{C}_{\mathrm{sed}}}{\partial x_j \partial x_j} - \frac{\partial \eta_j}{\partial x_j}. \qquad [9]$$

In the equations above, $\bar{p}$ represents the filtered pressure and $\bar{u}_i$ the filtered velocity vector where $i$ represents the $x, y$ and $z$ directions of the computational domain. $\delta_{i,j=2}$ is a unit vertical vector against gravity, $w_s$ is the settling velocity of the particles, and $\mathrm{Sc_{sal}}$ and $\mathrm{Sc_{sed}}$ indicate the Schmidt number of salt and sediments concentration, equal to *600* and *1*, respectively. The effect of the small-scale diffusion in the momentum equations (Eq. 7) appears as additional SGS stresses $\tau_{ij}$, defined by:

$$\tau_{ij} = -2\nu_{\mathrm{t}} \bar{S}_{ij}, \qquad [10]$$

 

where $\nu_t$ denotes the SGS eddy viscosity. The additional salinity and concentration SGS fluxes $\lambda_i$ and$\eta_i$ appearing in the scalar transport equation are defined by:

$$\lambda_j = -\frac{\nu_\mathrm{t}}{\mathrm{Sc}^\mathrm{t}_\mathrm{sal}}\frac{\partial \bar{C}_\mathrm{sal}}{\partial x_j}, \quad [11]$$

$$\eta_j = -\frac{\nu_\mathrm{t}}{\mathrm{Sc}^\mathrm{t}_\mathrm{sed}}\frac{\partial \bar{C}_\mathrm{sed}}{\partial x_j}, \quad [12]$$

with $\mathrm{Sc}^\mathrm{t}_\mathrm{sal}$and $\mathrm{Sc}^\mathrm{t}_\mathrm{sed}$ denoting the SGS Schmidt numbers. The SGS quantities are calculated using the Lagrangian dynamic model introduced by Meneveau et al. (1996).
The density variation due to gradients in salinity and sediments is equal to:

$$\frac{\Delta\hat{\rho}}{\rho_\mathrm{lock}-\rho_\mathrm{w}} = \frac{\rho-\rho_\mathrm{w}}{\rho_\mathrm{lock}-\rho_\mathrm{w}} = \frac{\bar{C}_\mathrm{sal}}{\bar{C}^1_\mathrm{sal}} + \frac{s}{\beta\bar{C}^1_\mathrm{sal}}\bar{C}_\mathrm{sed}, \quad [13]$$

with $s$ the sediment buoyant density:

$$s = \frac{\rho_\mathrm{sed}-\rho_\mathrm{w}}{\rho_\mathrm{w}}. \quad [14]$$

3.2 Sediment parameters

When the gravity current passes over the mobile bed, particles can be eroded and brought into suspension. Following the typical approach, it is here assumed that the erosion of sediments begins only when the dimensionless bed shear stress, $\theta$ exceeds a critical value. This critical value$\theta_\mathrm{cr}$ has been determined using the model for suspended sediments of Vanoni (1975), in turn based on the seminal work by Shields (1936). The erosion rate is calculated using the pick-up function proposed by Luque et al. (1976) which yields to good results for small particle sizes (<*200*μm), (Van Rijn, 1984):

$$E = a\rho_\mathrm{sed}(sgd_\mathrm{sed})^{0.5}(\theta-\theta_\mathrm{cr})^{1.5}, \quad [15]$$

where $a = 0.02$ for spherical particles, $d_\mathrm{sed}$ is the sediment diameter and $\theta$ represents the Shields parameter equal to $\frac{\tau_\mathrm{w}}{sg\rho_\mathrm{w}d_\mathrm{sed}}$.

The settling velocity of the suspended sediments is one of the key parameters to characterize their behavior. In this work, the particles are cohesionless and have a mean diameter $d$ in the range from *75* to *150*μm. For this particle range size, there are many different formulations for calculating the settling velocity. Here, the approach proposed by Zanke (1977) was chosen, for its simplicity (Eq. 16).

$$w_\mathrm{s} = \frac{10\nu}{d_\mathrm{sed}}\left[\left(1+\frac{0.01sgd_\mathrm{sed}{}^3}{\nu^2}\right)^{0.5}-1\right]. \quad [16]$$

3.3 Numerical set up and boundary conditions

The 3D code LES-COAST developed at the University of Trieste was used to simulate the gravity current and the particle entrainment. A detailed discussion of the governing equations and their spatial and temporal discretization is provided in Armenio and Sarkar, (2002). The code has been widely tested in the past for similar cases (Dallali and Armenio, 2015). The spatial resolution of the domain is 1336x128x80 grid points in the streamwise (x), vertical (y) and spanwise (z) direction, respectively. Stretching has been applied in the vertical and spanwise directions, following Vinokur's algorithm (Vinokur, 1983), so that close to the bottom walls $\Delta y^+ = 1$ and close to the side walls $\Delta z^+ = 1$ at the first grid point. This discretization satisfies the requirements for wall-resolved LES, and no further wall model is required.
In the simulations, the bottom and side surfaces are modeled as no-slip smooth walls, while the top free-surface condition is approximated using a free-slip condition. The presence of the tank is simulating numerically by a downstream extension of the numerical domain. Zero salinity fluxes are imposed at all boundaries. Concerning the sediment concentration, on the top surface the mass exchange is assumed to be equal to zero:

$$\frac{1}{Re_\mathrm{b}Sc_\mathrm{sed}}\frac{\partial \bar{C}_\mathrm{sed}}{\partial y} + w_\mathrm{s}\bar{C}_\mathrm{sed} = 0. \quad [17]$$

At the bottom, the mass exchange is a function of the particle erosion $E$ and deposition $S$ rates, given by:

 

$$\left(\frac{1}{Re_{\mathrm{b}}Sc_{\mathrm{sed}}}\frac{\partial \bar{C}_{\mathrm{sed}}}{\partial y}+w_{\mathrm{s}}\bar{C}_{\mathrm{sed}}\right)\cdot \boldsymbol{n}=S(\boldsymbol{n}\cdot\delta_{i2})-\frac{E}{\rho_{\mathrm{sed}}}, \qquad [18]$$

where $\boldsymbol{n}$ is a unit vector normal to the sediment surface. Erosion rate, *E*, is imposed equal to zero everywhere except on the mobile section of the bed. The sedimentation rate of the particles is defined as:

$$S=w_{\mathrm{s}}c_{\mathrm{ref}}, \qquad [19]$$

in which $c_{\mathrm{ref}}$ refers to the sediment concentration at the vicinity of the wall, chosen to be equal to the concentration of the first grid point away from the wall.

## 4 DESCRIPTION OF THE CURRENT

The main focus of this section is to study the main features of the salinity current. In this regard, two density currents with different buoyancy Reynolds numbers are simulated (case A and C). The Reynolds numbers are chosen to be equal to those used by Zordan et al. (2017). Being the experiments analogous to simulations A and C, they will be referred to as $A_{exp}$ and $C_{exp}$ in the following.

The behavior of the current is comparable to similar results found in literature. Figure 3 shows the spanwise-averaged density field obtained from simulation A. These results are in accordance with those described in Constantinescu (2014) for high-buoyancy Reynolds numbers. More specifically, the flow is strongly turbulent behind the front, and the billows lose their coherence after a short time. A stable stratification over a slightly tilted layer can be observed at a distance from the front.

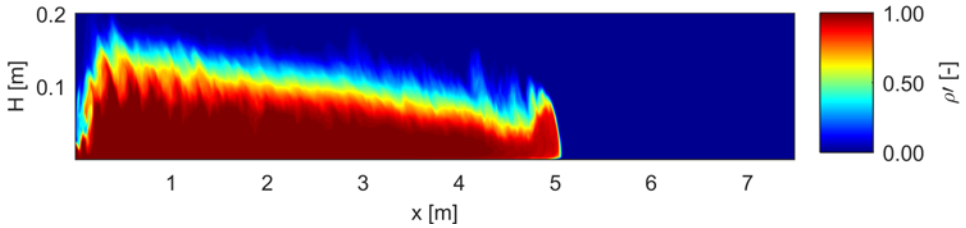


**Figure 3.** Simulations A: spanwise-averaged dimensionless density contour illustrating the propagation of the current for case A at time $t = 23t_0$. $\rho'$ represents the dimensionless density field equal to $\frac{\rho-\rho_w}{\rho_{lock}-\rho_w}$.

For case A, the evolution of the front position of the current with respect to the lock-gate is calculated numerically and compared with experimental data obtained by the experimental work of Zordan et al. (2017). It is worth noting that during the slumping phase, the velocity of the front is roughly constant, which allows the head of the front to be examined under quasi-steady conditions (Härtel et al, 2000a). The front velocity is measured indirectly by recording the time evolution of the front location, which is defined as the position of the nose of the current in the streamwise direction at a height of *2*mm from the bed. Simulations can provide the whole record of the front location. However, experimentally the position of the front is recorded only above the mobile section of the bed. The front location with respect to the gate position measured for A and $A_{exp}$ is shown in Figure 4. A very good agreement for the front velocity becomes evident comparing the slopes of the lines. Moreover, these results illustrate that in case A, the presence of suspended sediments does not alter the current dynamics. This subject is discussed in details in the next Section.

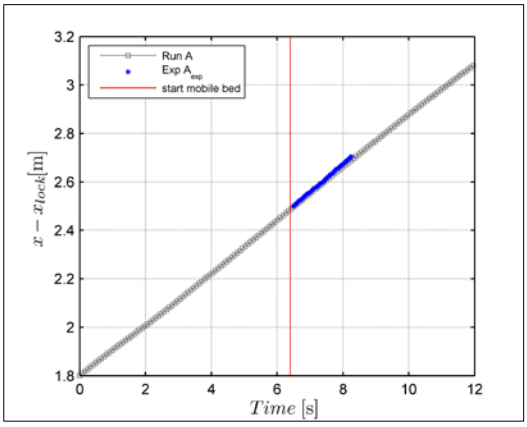


**Figure 4.** Time evolution of the front position, with respect to the lock gate, for numerical case A and experimental case $A_{exp}$. The red vertical line represents the time instant when the current reaches the mobile bed.

 

The shape of the current at a given location also serves as a good validation criterion (Constantinescu, 2014). Thus, an accurate depiction of the current shape must consider the interface between current and counter-current. This interface, however, cannot be obtained directly from $A_{exp}$ and $C_{exp}$ because density measurements are not available. Nevertheless, by evocating the following assumptions: (1) frozen turbulence hypothesis hold true (Parsons and Garcia, 1998), and (2) the interface of the gravity current is conserved along streamlines, it is considered that the current is advected by a constant velocity equal to the velocity of the front. In this regard, time series of velocities measurements can be used as means of retrieving the shape of the gravity current. It is believed that the inflection point of the velocity profile roughly coincides with the interface between the denser and the lighter fluids; that is where the velocity changes sign. Note however that this velocity is chosen to be very close to zero, as choosing zero is too general and not measurable in practice. The outcomes of the numerical simulations A and C are compared with the experimental results Aexp and Cexp. The velocity measurements used in the present work have been taken along the vertical axis at a probe located at the same distance from the lock as in Zordan et al. (2017). This is just before the mobile bed, and erosion has not started yet. A direct comparison between experimental and numerical data is given in Figure 5. The velocity measurements at the present work have been taken along the vertical at a probe located at the entrance of the mobile bed. From the plot, it is clear that during the first 7 seconds the head of the current, where most of the mixing and dynamics occurs, passes through the probe. After the head, the remaining part of the denser fluid, which is carried inertially, passes. Numerical and experimental results show very good agreement.

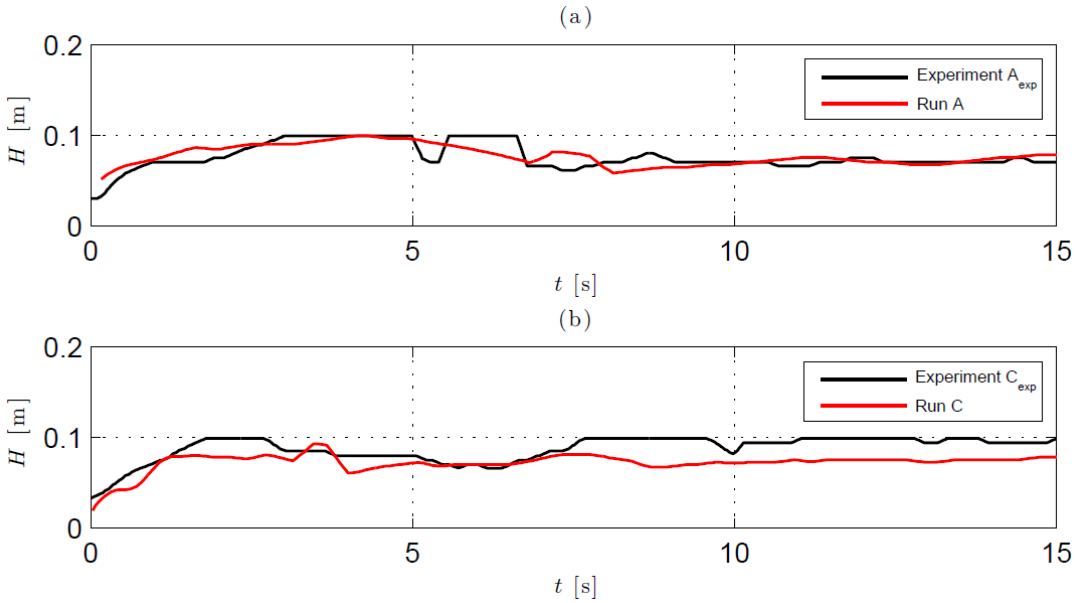


**Figure 5.** Current shape simulated in run A and C compared with the recorded in the laboratory experiments $A_{exp}$ and $C_{exp}$, respectively. Plot (a) represents simulation A and experiment $A_{exp}$, while plot (b) represents simulation C and experiment $C_{exp}$.

## 5 VELOCITY PROFILES AND BED SHEAR STRESS

The instantaneous streamwise velocity contours for runs A and C, measured at a probe located at the half width of the channel at the entrance of the mobile bed are shown in Figure 6. In the same figure, the solid line represents the time series of the bed shear stress measured in the same location. The results indicate that the portion with the highest erosive power is, as expected, located at the front of the current. This relates to the region of high shear in the interface of the billow with the ambient fluid where most instabilities of the cleft-lobe type occur. The high-shear region, however, does not present a homogeneous structure in the spanwise direction. In accordance to Ooi et al. (2009), the regions of high bed shear show the emergence of elongated streamwise streaks of high/low shear.

In the current, this happens below head and billow. These streaks are responsible of the saltation and suspension mechanisms found on loose bed hydraulics. In the billow behind the head, a sudden decrease in bed shear is seen instead. The time series of bed shear stress at different spanwise locations is shown in Figure 7. Section $z1$ corresponds to the mid-spanwise probe, while section $z_2$ is located at distance ¼ z from the lateral wall. The high variation of $\tau$ that is observed between sections $z_1$and $z_2$ may be also an indication of the presence of such streaks.

 

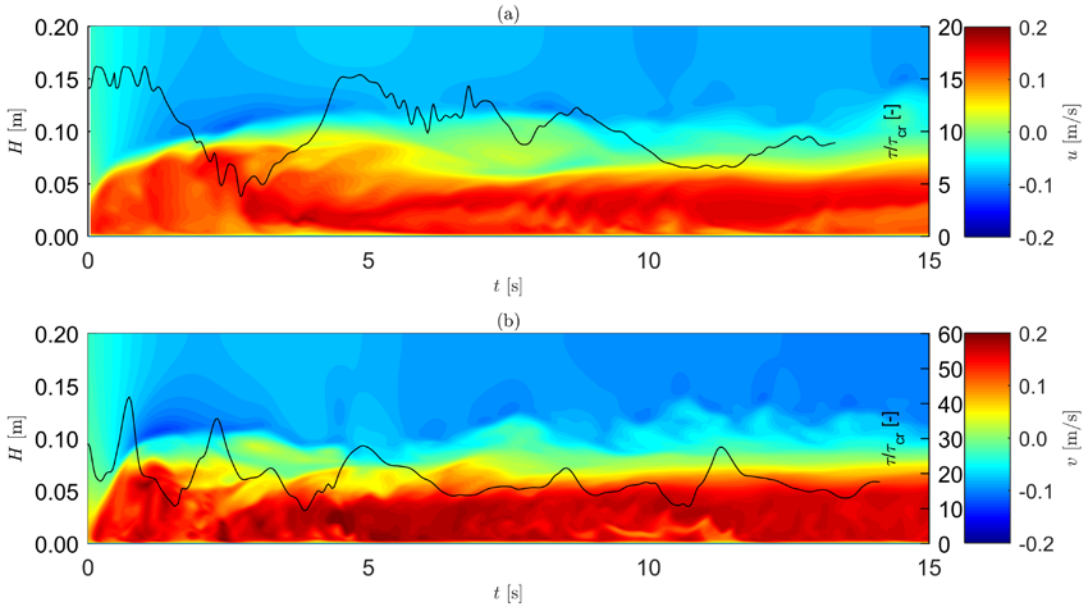


**Figure 6.** Streamwise velocity contours and bed shear stress evolution on a specific probe in the mid-spanwise section, (a) represents run A, (b) represents run C.

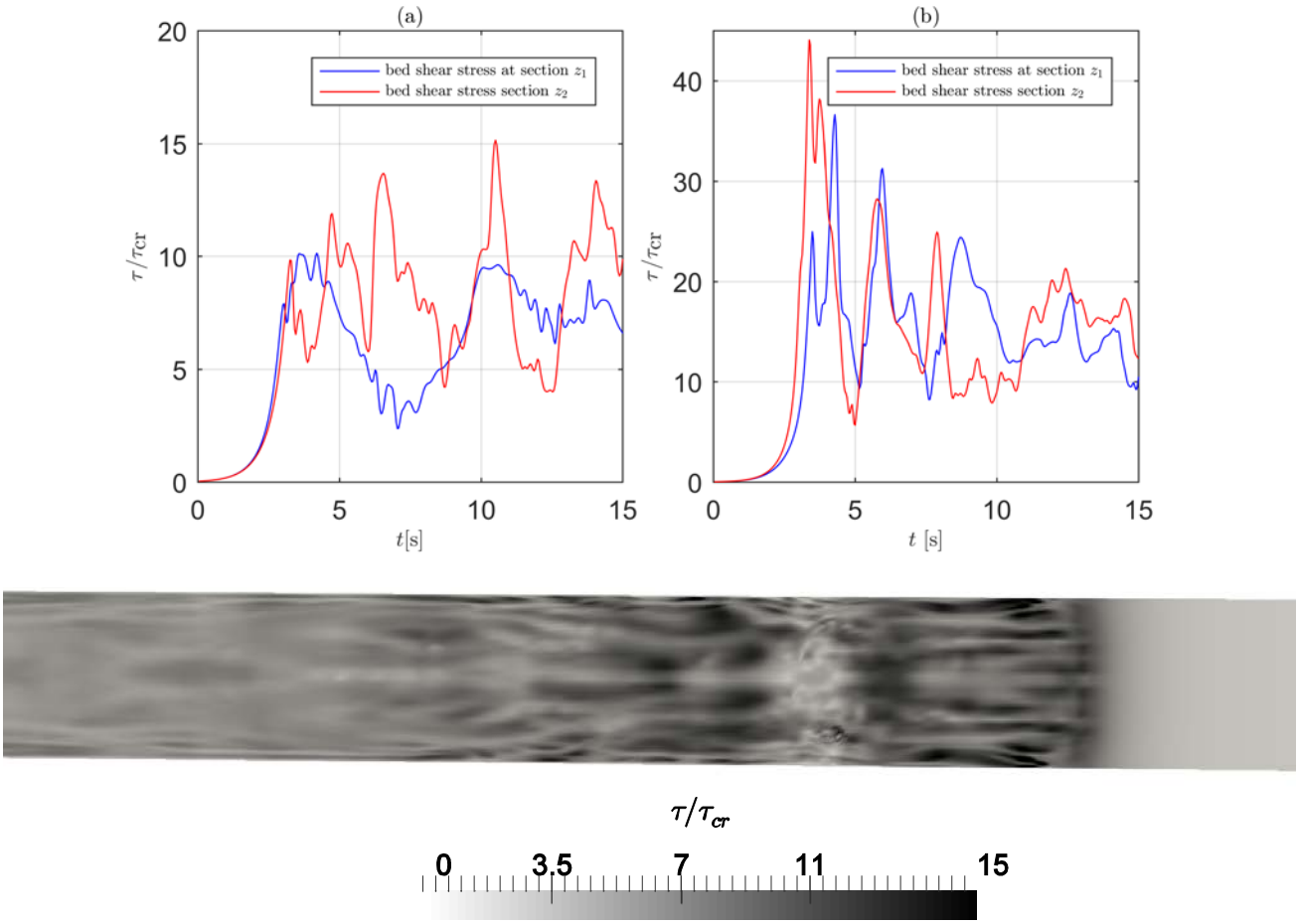


**Figure 7.** Time and space evolution of the dimensionless bed shear stress. Section $z_1$ corresponds to the mid-spanwise probe, while section $z_2$ is located at distance ¼ $z$ from the lateral wall. Plot (a) represents the time evolution for simulation A, plot (b) represents the time evolution for simulation C, and plot (c) represents the space evolution of bed shear stress for simulation A.

## 6 SEDIMENT ENTRAINMENT

The previous sections argued that most of the sediment entrainment originating from the mobile bed should come from the front of the current, which carries most of the erosive energy. Four different simulations are performed (see Table 1) in order to study the capacity to entrain particles. In Figure 8, the spanwise

 

averaged sediment concentration, $\langle c \rangle$, contours for the various entrainment scenarios are shown. In particular, Figure 8a and 8b represent simulations A and B respectively, where the buoyancy Reynolds number is constant ($Re_{\mathrm{b}} = 48991$), but different particle diameters are used for the erodible section of the bed. These diameters are chosen within the range of applicability of the pick-up function described with Eq. 15 and also different enough to study the forces causing entrainment and suspension. More specifically, changing the particle diameter influences the Shields parameter $\theta_{\mathrm{cr}}$ in Eq. 15 and the settling velocity $w_{\mathrm{s}}$ in Eq. 16. Decreasing the particle diameter, particle entrainment increases, as expected. However, the suspension is restricted behind the front and drops to almost zero in the body of the current. The total sediment concentration in the flow is quite low, *O* (0.001%). That means that, in cases A and B, the suspended sediments can be considered passive without visibly influencing the current dynamics. For this reason, as it has been observed in previous section, the front velocity of the current does not change significantly due to the presence of the mobile bed.

**(a). Simulation A**

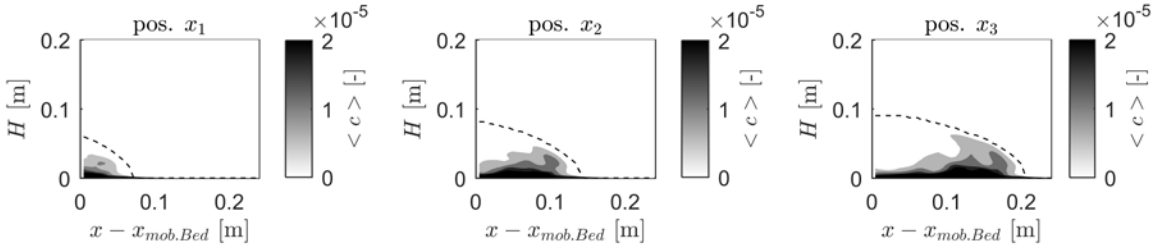


**(b). Simulation B**

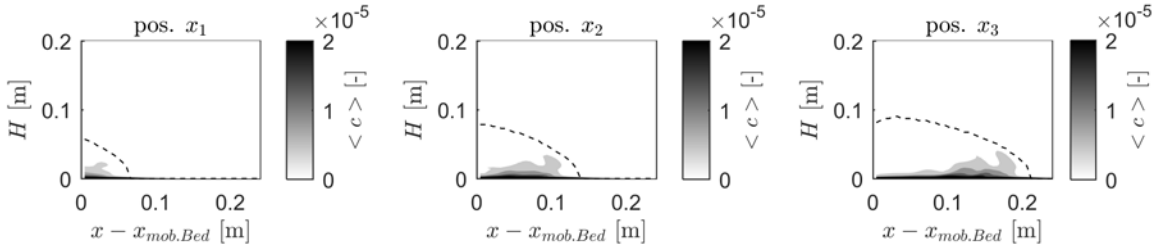


**(c). Simulation C**

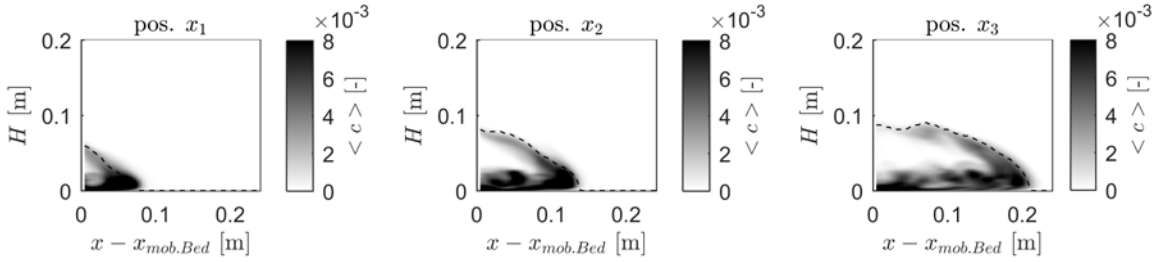


**(d). Simulation D**

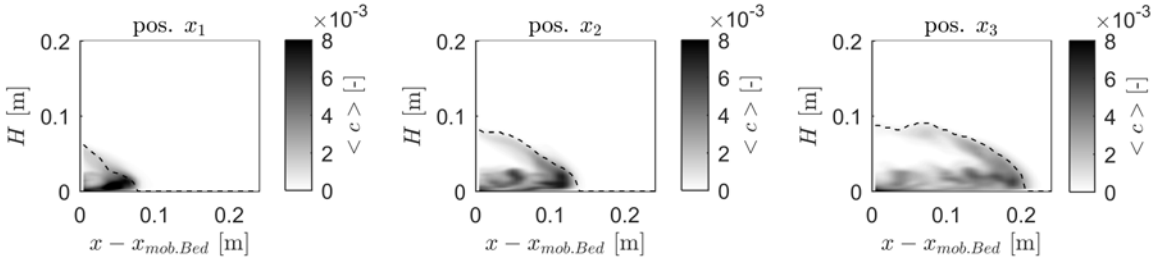


**Figure 8.** Visualization of the shape of the current (dashed line) and spanwise averaged sediment concentration $\langle c \rangle$ contours at different positions above the mobile bed. The shape of the current is identified by choosing the iso-density contour $\frac{\rho - \rho_w}{\rho_{lock} - \rho_w} = 0.02$ as a threshold between the current and the ambient fluid, as proposed by Ottolenghi et al., 2016. (a) represents run A, (b) represents run B, (c) represents run C, and (d) represents run D.

For simulations C and D, presented in Figure 8c and 8d, the buoyancy Reynolds number of the current has been changed to $Re_{\mathrm{b}} = 55961$, and the same particle diameters mentioned above are tested. In this manner, this study discerns the role of turbulence in the transport of the particles. It is clear that the increase of the initial density difference leads to a current with higher erosive energy. This is also in agreement with the

 

graphs in Figure 7, where a substantial increase of the bed shear stress is observed by increasing the density of the current. Additionally, by increasing the turbulence, the sediments are able to travel higher in the body of the current C.

A general observation is that the suspended material takes a shape similar to that of the head recirculation which might imply some type of scale similarity and coherence between the flows. This trend, apparent in Figure 8, is an inverse function of the particle diameter and directly proportional to the density of the gravity current.

## 7 CONCLUSIONS

In this work, LES has been used to study the sediment entrainment capacity of salinity currents with large release volumes and characterized by high Reynolds numbers. In the first part of the paper, the simulation results taking into account different Reynolds number have been compared with experimental data by Zordan et al. (2017). Very good agreement between numerical output and experimental measurements has been obtained for both front velocity and shape of the current. In the second part, the numerical results have been analyzed and the dynamics of the currents have been discussed for what concerns velocities and bed shear distribution. Finally, the sediment entrainment for different cases has been presented. Presented results indicate that the flow behind the front of the current is strongly turbulent, which leads to high peaks of bed shear stress. However, the spatial bed shear stress distribution is not uniform behind the front. When the current passes over the mobile bed, the stress peaks are the main contributor to sediment entrainment, which in turn concentrates just behind the front. Furthermore, as it is expected that by increasing the density of the current, its capacity to entrain particles is also increased.

It is worth mentioning that the numerical results, regarding the particle entrainment, may change depending on the mathematical models that are chosen to reproduce erosion and the deposition of the particles. Further studies are needed to define the implications behind the choice of a specific model. Comparisons with experimental data would also be important for the validation of the numerical model regarding the sediment entrainment.

Finally, the dynamics of the current in general are also dependent on the bed forms that create during its passage. These should follow the spatial distribution of the bed shear stress. However, since the bed forms influence the current itself, the results might deviate consistently from those reported in this work. Hence, further effort should be devoted into clarifying this mechanism as well as to study the feedback of the suspended sediments in the current dynamics, as for example their influence on the front velocity of the current.

## ACKNOWLEDGEMENTS

The research leading to these results has received funding from the People Programme (Marie Curie Actions) of the European Union's Seventh Framework Programme FP7/2007-2013/ under REA grant agreement n’ 607394-SEDITRANS. The authors are grateful to S. López Castaño for useful discussions. The experimental data can be made available upon request to J. Zordan and C. Juez.

## REFERENCES

Akiyama, J. & Stefan, H. (1985). Turbidity Current with Erosion and Deposition. *Journal of Hydraulic Engineering,* 111(12), 1473-1496.

Armenio, V. & Sarkar, S. (2002). An Investigation of Stably Stratified Turbulent Channel flow using Large-Eddy Simulation. *Journal of Fluid Mechanics,* 459, 1-42.

Blanchette, F., Strauss, M., Meiburg, E., Kneller, B. & Glinsky, M. E. (2005). High-Resolution Numerical Simulations of Resuspending Gravity Currents: Conditions for Self-Sustainment. *Journal of Geophysical Research: Oceans,* 110(C12).

Constantinescu, G. (2014). LES of Lock-Exchange Compositional Gravity Currents: A Brief Review of Some Recent Results. *Environmental Fluid Mechanics,* 14(2), 295-317.

Dallali, M. & Armenio, V. (2015). Large Eddy Simulation of Two-Way Coupling Sediment Transport. Advances in Water Resources, 81, 33-44.

Eames, I., Hogg, A.J., Gething, S. & Dalziel, S.B. (2001). Resuspension by Saline and Particle-Driven Gravity Currents. *Journal of Geophysical Research,* 106(C7), 14095-14111

Garcia, M. & Parker, G. (1991). Entrainment of Bed Sediment into Suspension. *Journal of Hydraulic Engineering,* 117(4), 414-435.

Gonzalez-Juez, E., Meiburg, E. & Constantinescu, G. (2009). The Interaction of a Gravity Current with a Circular Cylinder Mounted above a Wall: Effect of the Gap Size. *Journal of Fluids and Structures,* 25(4), 629-640.

Härtel, C., Carlsson, F. & Thunblom, M. (2000b*).* Analysis and Direct Numerical Simulation of the Flow of a Gravity Current Head. *Journal of Fluid Mechanics,* 418, 213-229

 

Härtel, C., Meiburg, E. & Necker, F. (2000a). Analysis and Direct Numerical Simulation of the Flow at a Gravity-Current Head. Part 1: Flow Topology and Front Speed for Slip and No-Slip Boundaries. *Journal of Fluid Mechanics,* 418, 189-212

IOC, SCOR and IAPSO, (2010). *The International Thermodynamic Equation of Seawater – 2010: Calculation and Use of Thermodynamic Properties*, Intergovernmental Oceanographic Commission, Manuals and Guides No. 56, UNESCO (English), 196.

Luque, F.R. & Van Beek, R. (1976). Erosion and Transport of Bed-Load Sediment. *Journal of Hydraulic Research,* 14(2), 127-144.

Meneveau, C., Lund, T.S. & Cabot, W.H. (1996). A Lagrangian Dynamic Subgrid-Scale Model of Turbulence. *Journal of Fluid Mechanics,* 319, 353-385.

Necker, F., Härtel, C., Kleiser, L. & Meiburg, E. (2002). High-Resolution Simulations of Particle-Driven Gravity Currents. *International Journal of Multiphase Flow,* 28, 279–300.

Nogueira, H.I., Adduce, C., Alves, E. & Franca, M.J. (2013). Analysis of Lock-Exchange Gravity Currents over Smooth and Rough Beds. *Journal of hydraulic Research,* 51(4), 417-431.

Ooi, S.K., Constantinescu, G. & Weber, L. (2009). Numerical Simulations of Lock-Exchange Compositional Gravity Current. *Journal of Fluid Mechanics,* 635.

Ottolenghi, L., Adduce, C., Inghilesi, R., Roman, F. & Armenio, V. (2016). Mixing in Lock-Release Gravity Currents Propagating Up a Slope. *Physics of Fluids,* 28(5), 056604.

Parsons, J.D., & García, M.H. (1998). Similarity of Gravity Current Fronts. *Physics of Fluids,* 10(12), 3209-3213.

Shields, A. (1936). *Anwendung der Ähnlichkeitsmechanik und der Turbulenzforschung auf die Geschiebebewegung*. Mitteilung der Preußischen Versuchsanstalt für Wasser und Schiffsbau, Berlin, 26.

Simpson, J.E. (1997). *Gravity Currents: In the Environment and the Laboratory.* Cambridge University Press.

Theiler, Q. & Franca, M.J. (2016). Contained Density Currents with High Volume of Release. *Sedimentology,* 63(6), 1820-1842.

Tokyay, T., Constantinescu, G. & Meiburg, E. (2011). Lock-Exchange Gravity Currents with a High Volume of Release Propagating over a Periodic Array of Obstacles. *Journal of Fluid Mechanics,* 672, 570-605.

Vanoni, V. A. (1975). *Sedimentation Engineering,* ASCE Task Committee for the Preparation of the Manual on Sedimentation of the Sedimentation Committee of the Hydraulics Division.

Vinokur, M. (1983). On One-Dimensional Stretching Functions for Finite-Difference Calculations. *Journal of Computational Physics,* 50, 215

Van Rijn, Leo C. (1984). Sediment Pick-Up Functions. *Journal of Hydraulic Engineering,* 110.10, 1494-1502.

Zang, Y., Street, R.L. & Koseff, J.R. (1994). A Non-Staggered Grid, Fractional Step Method for Time-Dependent Incompressible Navier-Stokes Equations in Curvilinear Coordinates. *Journal of Computational Physics,* 114(1), 18-33.

Zanke, U.C.E. (1977). *Berechnung der Sinkgeschwindigkeiten von Sedimenten*. Mitteilungen des Franzius-Instituts für Wasserbau, Technische Universität Hannover, 46, 243.

Zordan, J., Juez, C., Schleiss, A.J. & Franca, M.J. (2017). Experimental Results on Gravity Current's Dynamic initiating Sediments Entrainment. *In IAHR 2017.*

 

# EFFECT OF THE BED LOAD GRADATION ON THE MORPHODYNAMICS OF DISCORDANT CONFLUENCES

SEBASTIÁN GUILLÉN-LUDEÑA[(1)], MÁRIO J. FRANCA[(2)], ANTÓNIO H. CARDOSO[(3)] & ANTON J. SCHLEISS[(4)]

[(1,2,4)] Laboratoire de ConstructionsHydrauliques, ÉcolePolytechniqueFédérale de Lausanne, Switzerland
sebastian.ludena@epfl.ch; mario.franca@epfl.ch; anton.schleiss@epfl.ch
[(3)]CERIS, Instituto Superior Técnico, Universidade de Lisboa, Portugal
antonio.cardoso@tecnico.ulisboa.pt

## ABSTRACT

Within the fluvial network, river confluences are particular areas characterized by complex hydrodynamic, morphodynamic and sedimentary processes. These processes have been observed to be governed by parameters such as the discharge ratio, the junction angle, the sediment rates and the bed material. This study analyzes the influence of the sediment gradation on the hydro-morphodynamics of open channel confluences, characterized by a bed discordance between the tributary and main channel. For that purpose, experiments are conducted at two different laboratory confluences in which only the gradation of the supplied sediment mixtures is different. This paper presents the results of two of these experiments with a discharge ratio between the tributary and main channel of $Q_r = Q_t/Q_m = 0.15$. In one experiment, non-uniform sediment mixtures with a mean diameter of $d_{50} = 0.82$ mm are supplied to the main channel and tributary. These mixtures are representative of the sediments found in mountain river confluences such as those of the Upper-Rhone River. In the other experiment, a uniform sediment mixture with the same mean diameter ($d_{50} = 0.82$ mm) is supplied both to the tributary and main channel. The latter mixture is rather representative of the bed material found in low-land confluences. At equilibrium conditions, i.e. when the outgoing sediment rate is nearly equal to the incoming, bed and water surface topographies are recorded. These measurements show that with non-uniform sediments, the bed morphology at equilibrium presents a high topographic gradient, with a developed bar and scour hole in the main channel, a marked bed discordance and a steep bed-slope in the tributary. In contrast, with uniform sediments, the bed morphology presents attenuated features compared to those observed with non-uniform sediments. Also, with uniform sediments bedforms are observed throughout the flumes, whereas the non-uniform mixtures favor the bed armor.

**Keywords:** Confluences; sediment gradation; bed discordance; morphodynamics; armored bed.

## 1 INTRODUCTION

The hydrodynamic, morphodynamic and sedimentary processes involved in river confluences are controlled by a broad range of factors such as planform geometries, discharge ratios, bed material and sediment rates (Best, 1987; Best, 1988; Bristow et al., 1993; Best and Rhoads, 2008; Rhoads et al., 2009). Many studies focused on the influence of the confluent angles and discharge ratios on the confluence dynamics (Best, 1987; Best, 1988; Bristow et al., 1993; Rhoads et al., 2009; Leite Ribeiro et al., 2012; Guillén-Ludeña et al., 2015; Guillén-Ludeña et al., 2016; Schindfessel et al., 2015). However,few studies if any, analyzed the role of the gradation of the bed material on the flow dynamics and bed morphology of open-channel confluences. This study represents thus a novelty in the analysis of the dynamics of confluences, as it focuses on the influence of the sediment gradation on the hydrodynamics and morphodynamics of open-channel confluences. The gradation of a sediment mixture is defined in this study by means of the gradation coefficient $\sigma$ defined as:

$$\sigma = \frac{1}{2}\left(\frac{d_{84}}{d_{50}} + \frac{d_{50}}{d_{16}}\right) \quad [1]$$

where $d_{84}$, $d_{50}$, $d_{16}$ are the particle sizes coarser than the 84%, 50% and 16% by weight of the sediment mixture, respectively. A high value of σ indicates a non-uniform sediment mixture and, on the opposite, a low value of σ denotes a uniform sediment mixture.

This study presents the results of two laboratory experiments in which different sediment mixtures are continuously supplied to the tributary and main channel. These results show that with non-uniform mixtures, bed topography and flow dynamics evolve to high gradients in order to gain enough transport capacity to convey the large amount of sediment sizes that compose the non-uniform mixtures. In contrast, with uniform

 

mixtures, the flow dynamics and bed morphology present attenuated gradients, since the fine particles which form the uniform mixtures are more easily transported.

## 2 METHODOLOGY

### 2.1 Experimental facilities

The experiments were conducted in two experimental facilities, one located at EPFL in Switzerland and other located at IST in Portugal. The facility at EPFL consisted of an 8.0 m long and 0.5 m wide rectangular straight main channel, and a 4.9 m long and 0.15 m wide rectangular straight tributary that joined the main channel at an angle of 70º. The facility at IST consisted of a 12.0 m long and 0.5 m wide rectangular straight main channel, and a 5.9 long and 0.15 m wide rectangular straight tributary which joined the main channel at an angle of 70º. Figure 1 shows the schematic plan view of the two laboratory confluences. The results presented in this study are referred to the reference axis *X, Y* and *Z* indicated in Figure 1.

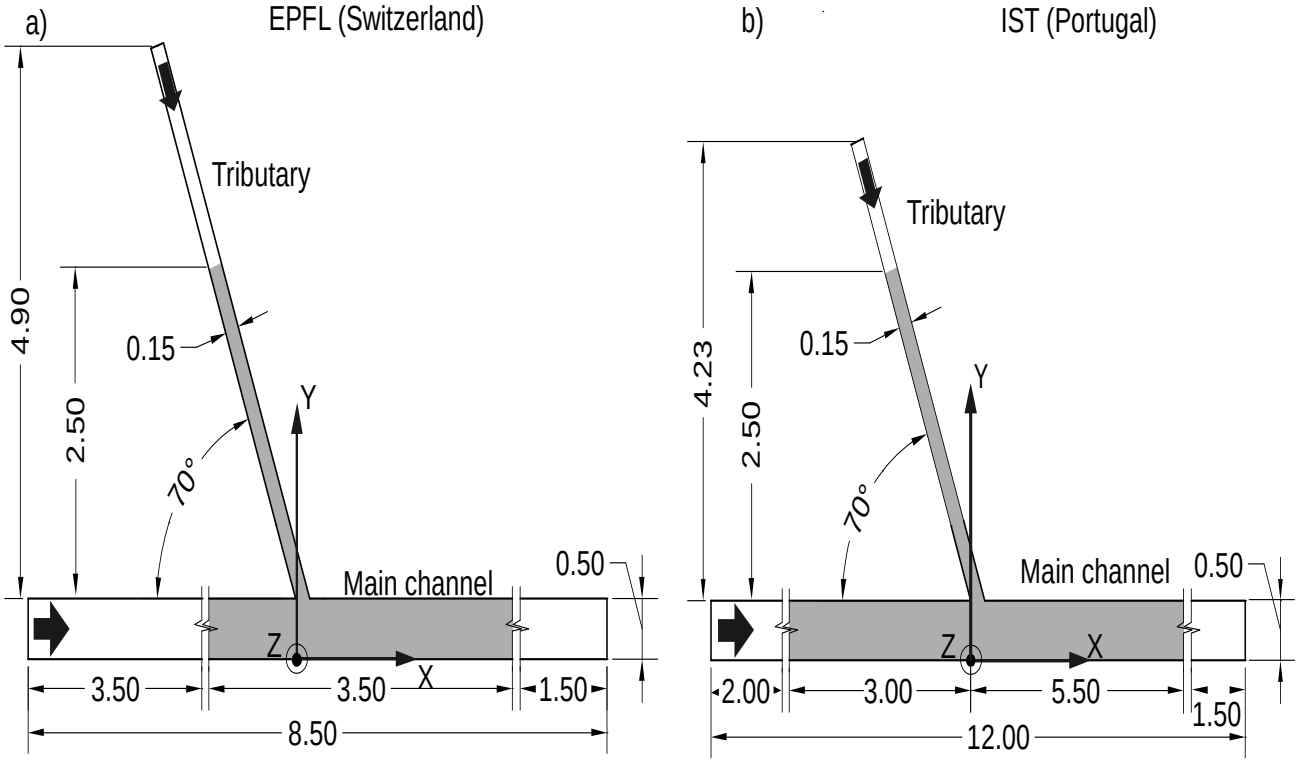


**Figure 1.** Sketch of the laboratory confluences. The shadow regions represent the measurement domain.

### 2.2 Experimental parameters

Both experiments were performed with a discharge ratio of $Q_r$ = 0.15, which is representative of confluences in which the main channel provides the dominant flow discharge, compared to that provided by the tributary. The discharge ratio is defined as:

$$Q_r = \frac{Q_t}{Q_m} \qquad [2]$$

where $Q_t$ is the flow discharge of the tributary upstream of the confluence and $Q_m$ denotes the flow discharge of the main channel upstream of the confluence.

The sediment mixtures were different for each experiment. For the experiment performed at EPFL, a poorly-sorted sand-gravel mixture with $d_{50}$ = 0.82 mm and $\sigma$ = 3.15 was supplied to the tributary; and another poorly-sorted sand-gravel mixture with $d_{50}$ = 0.82 mm and $\sigma$ = 4.50 was supplied to the main channel. For the experiment performed at IST, a uniform sand with $d_{50}$ = 0.80 mm and $\sigma$ = 1.35 was supplied to both, the tributary and main channel. Figure 2 shows the grain size distribution (GSD) of the supplied sediment mixtures.

 

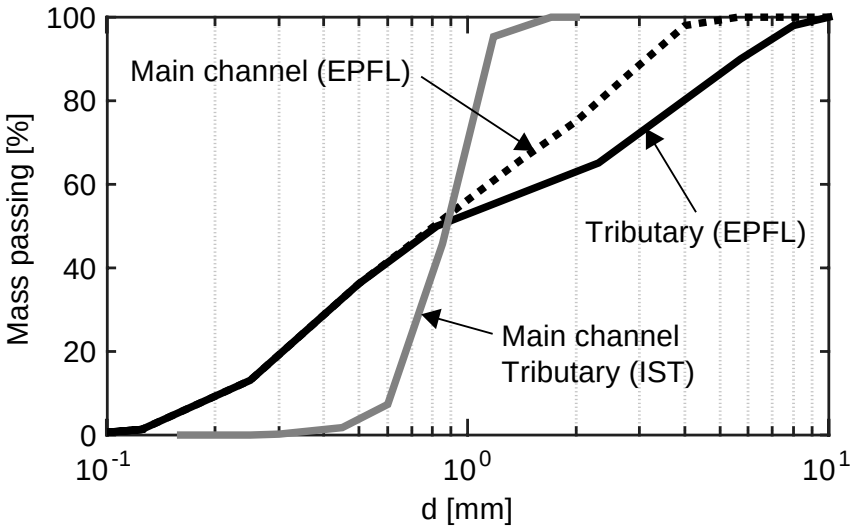


**Figure 2.** Grain size distribution of the supplied sediment mixtures

The sediment mixtures were continuously supplied during the experiment at rates of 0.5 kg/min for the tributary and 0.3 kg/min for the main channel. These rates were estimated by assuming that the bed slope and grain size distributions were in the range of those observed in the Upper-Rhone river confluences (Guillén-Ludeña, 2015), where the tributaries provide the dominant sediment load to the confluences. With these sediment rates and the adopted flow discharges, the downstream flow depth $h_d$ was calculated by assuming uniform flow at the downstream end of the main channel. The values of $h_d$, the associated flow velocity ($U_d$), and the width of the main channel ($B$) were used to normalize the different magnitudes.

### 2.3 Experimental procedure and measurements

At the beginning of each experiment, the bed of each flume was prepared with the same sediment mixture that was subsequently supplied to the flume. In the main channel, the initial bed was nearly horizontal. In the tributary, a small bed discordance of ~0.03 m at the tributary mouth, and a bed slope of ~ 0.5% were imposed in order to accelerate the bed evolution. The initial bed morphology was observed to not affect the final morphology, since the bed discordance and bed slope at equilibrium were higher than those imposed initially.

The experiments were run until reaching equilibrium, i.e. when the outgoing sediment rate was nearly equal to the incoming, and the bed topography reached a steady state. To assess whether equilibrium was reached, the outgoing sediments captured in a sediment trap at the downstream end of the main channel were weighed periodically. Additionally, the evolution of the bed topography was monitored by means of periodical topography surveys.

Once equilibrium was reached, water surface and bed topography were recorded in the tributary and main channel. The bed topography was measured with a Mini Echo Sounder with ± 1 mm accuracy. The water surface was measured with an ultrasonic limnimeter with ± 1 mm accuracy. For the experiment performed at EPFL, with non-uniform sediments, the measurements consisted in 9 longitudinal profiles laterally spaced by 0.05 m along the main channel, and in 1 profile along the axis of the tributary. For the experiment performed at IST, with uniform sediments, the measurements consisted in 22 longitudinal profiles laterally spaced by 0.02 m along the main channel, and in 1 profile along the axis of the tributary. The spatial resolution was of 0.01 m for all the measurements.

## 3 RESULTS

### 3.1 Hydro-morphodynamics of the main channel

With non-uniform sediments, the bed morphology in the main channel at equilibrium was characterized by: i) a bank-attached bar along the inner bank downstream of the confluence, ii) a scour hole that extended from the tributary mouth to the outer bank, iii) a bed raise at the inner bank, upstream of the confluence, and iv) penetration of the tributary-mouth bar into the main channel.

In this experiment, the water surface at equilibrium presented: i) a horizontal profile upstream of the confluence associated with a back-water curve, ii) a drop at the downstream junction corner indicating the presence of a low pressure zone, and iii) a steep slope downstream of the confluence associated with higher flow velocities. These features are depicted in Figure 3, which shows, for the experiment performed with non-uniform sediments, the bed topography at equilibrium as well as two longitudinal profiles of the bed and water surface elevations, along the inner and outer bank of the main channel.

 

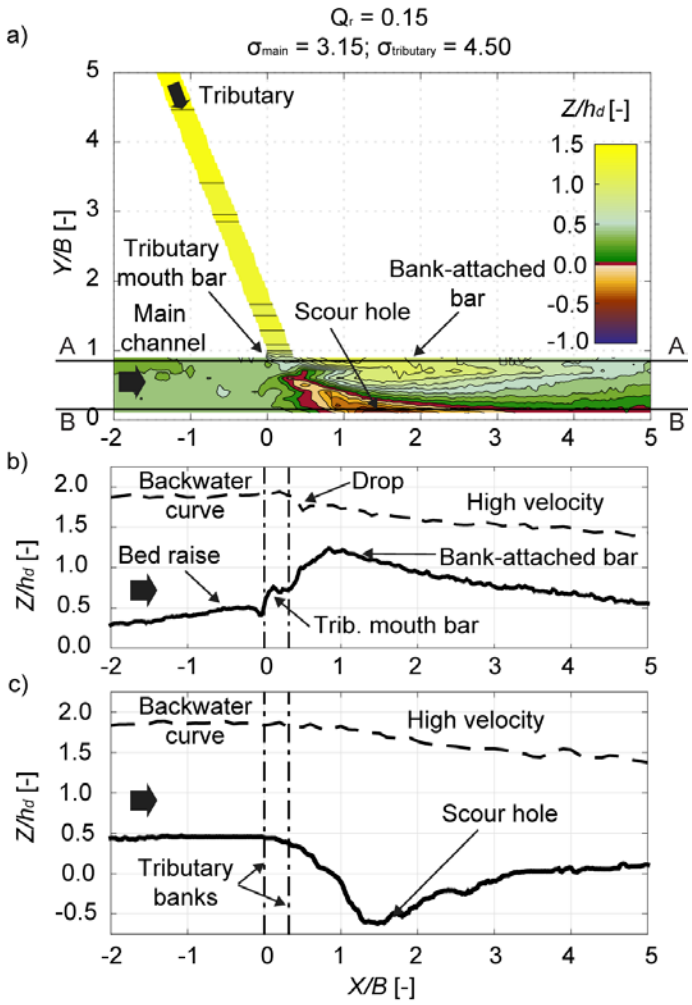


**Figure 3.** Bed topography and water surface at equilibrium with non-uniform sediments. a) Plan view of the bed topography at equilibrium for the tributary and main channel. b) Bed elevation and water surface elevation along the inner bank of the main channel (Section A-A indicated in Figure 3a). c) Bed elevation and water surface elevation along the outer bank of the main channel (Section B-B indicated in Figure 3a).

Figure 4 shows, for the experiment performed with uniform sediments, the bed topography at equilibrium and two longitudinal profiles of the bed and water surface elevations, along the inner and outer bank of the main channel. In this experiment, the bed morphology of the main channel at equilibrium presented similar features as those observed with non-uniform sediments, i.e. a bank-attached bar and a scour hole. Besides these features, the bed morphology obtained with uniform sediments included dune-like bedforms throughout the main channel.

The bedforms observed in the main channel upstream of the confluence presented an average wave length of $\lambda \sim 3\ h_d$ and a height of about $\Delta \sim 0.1\text{-}0.3\ h_d$. Downstream of the confluence, the length and height of the bedforms were $\lambda \sim 10\text{-}12.5\ h_d$ and $\Delta \sim 0.5\ h_d$, respectively. No tributary penetration into the main channel was observed with uniform sediments. The water surface at equilibrium presented attenuated features, compared to those observed with non-uniform sediments. These features are: i) a steeper slope of the water surface downstream of the confluence, indicating higher velocities; and ii) the water surface drop at the downstream junction corner associated with a low-pressure zone.

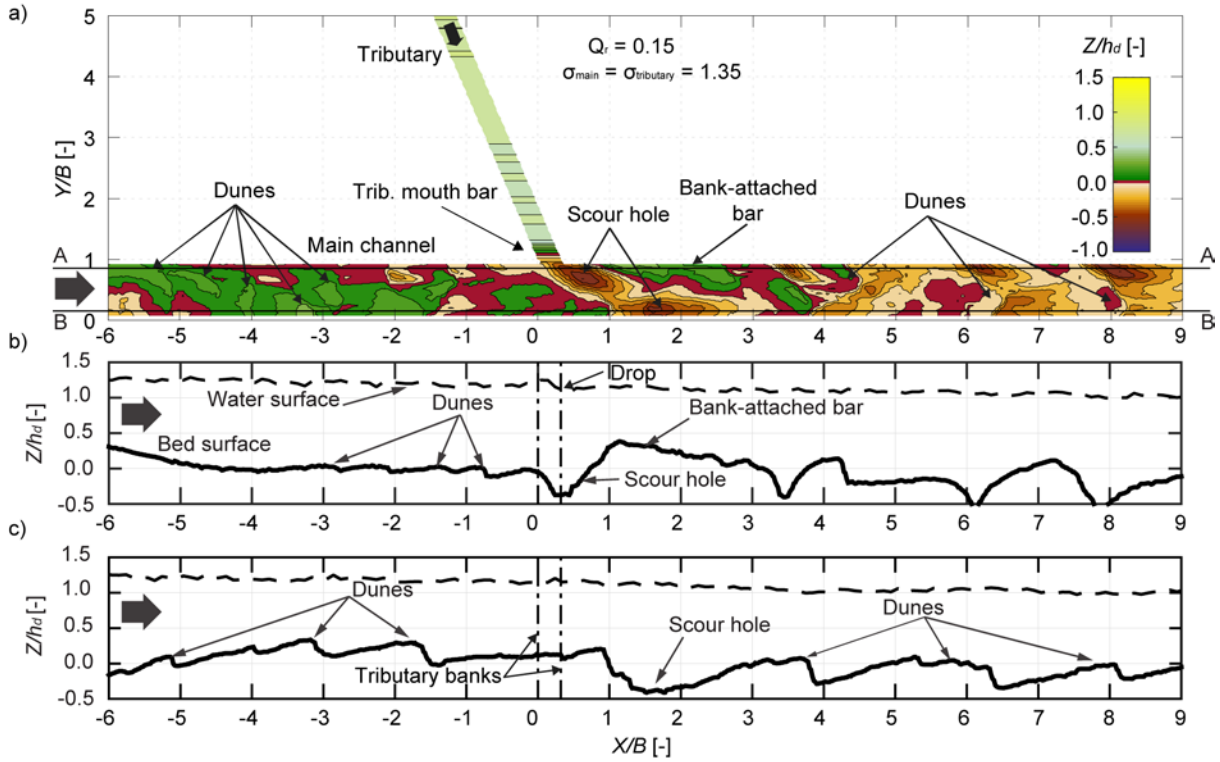


**Figure 4.** Bed topography and water surface at equilibrium with uniform sediments. a) Plan view of the bed topography at equilibrium for the tributary and main channel. b) Bed elevation and water surface elevation along the inner bank of the main channel (Section A-A indicated in Figure 4a). c) Bed elevation and water surface elevation along the outer bank of the main channel (Section B-B indicated in Figure 4a).

The flow regime of the main channel was classified based on the mean values of flow depth ($h$), mean velocity ($U$), and Froude number ($Fr$). In addition, the van Rijn's (1984b) method was used upstream and downstream of the confluence to classify the bedforms of the main channel. According to this method, the bed material and the sediment transport capacity are characterized by $D_*$ and $T$, respectively. Both are defined as:

$$D_* = d_{50}\left[\frac{(s-1)g}{v^2}\right]^{1/3} \quad [3]$$

$$T = \frac{(u_*)^2 - (u_{*,cr})^2}{(u_{*,cr})^2} \quad [4]$$

In this study, the mean diameter $d_m$ was adopted to characterize the bed material instead of the median diameter $d_{50}$. The reason of this modification is that the supplied sediment mixtures have the same $d_{50}$ values ($d_{50}$ = 0.82 mm, see Figure 2), which do not reflect the differences between them. Therefore, in equation [3], $d_{50}$ is substituted by the mean diameter $d_m$, $s$ denotes the specific density, $g$ is the gravity acceleration, and $v$ is the kinematic viscosity coefficient. In equation [4], $u_*$ denotes the bed-shear velocity, and $u_{*,cr}$ is the critical bed-shear velocity (Shields, 1936). $u_*$ and $u_{*,cr}$ were obtained as follows:

$$u_* = U\left(g^{0.5}/C'\right) \quad [5]$$

$$u_{*,cr} = \sqrt{\tau_{cr}(s-1)d_m} \quad [6]$$

where $C'$ is the Chézy roughness coefficient and $\tau_{cr}$ denotes the critical shear stress. These were obtained according to van Rijn (1984a):

$$C' = 18\ \log(12R_h/3d_{90}) \quad [7]$$

$$\tau_{cr} = 0.013\ (D_*)^{0.29} \text{for} \quad 20 \le D_* \le 150 \quad [8]$$

 

where $R_h$ denotes the hydraulic radius and $d_{90}$ is the particle size coarser than 90% by weight of the bed material.

For the experiment performed with non-uniform sediments, the bed material of the main channel upstream of the confluence was characterized by the GSD of the sediment mixture supplied to the main channel ($d_m$ = 1.4 mm and $d_{90}$ = 3.0 mm). The bed material of the tributary and that of the main channel downstream of the confluence were characterized by the GSD of the sediment mixture supplied to the tributary ($d_m$ = 2.3 mm and $d_{90}$ = 5.7 mm). In the case of the experiment performed with uniform sediments, the bed material of both flumes was approached by the GSD of the sediment mixture supplied to them ($d_m$ = 0.82 mm and $d_{90}$ = 1.40 mm)

Table 1 shows the normalized mean values of flow depth ($h/h_d$) and flow velocity ($U/U_d$) for the main channel upstream and downstream of the confluence. Also, the Froude number ($Fr$) and the dimensionless parameters of van Rijn(1984b) ($D_*$ and $T$) are shown in Table 1. Sub-indexes *up* and *dw* refer to upstream and downstream of the confluence, respectively.

**Table 1.** Non-dimensional mean values of the hydraulic variables of the main channel at equilibrium.

| Sediment mixture | $Q_r$ | Upstream (X/B < 0) | | | | | Downstream (X/B > 0) | | | | |
|---|---|---|---|---|---|---|---|---|---|---|---|
| | | $h_{up}/h_d$ | $U_{up}/U_d$ | $Fr_{up}$ | $D_{*up}$ | $T_{up}$ | $h_{dw}/h_d$ | $U_{dw}/U_d$ | $Fr_{dw}$ | $D_{*dw}$ | $T_{dw}$ |
| | [-] | [-] | [-] | [-] | [-] | [-] | [-] | [-] | [-] | [-] | [-] |
| Non-uniform | 0.15 | 1.45 | 0.60 | 0.42 | 35 | 0.82 | 1.04 | 0.96 | 0.80 | 58 | 2.71 |
| Uniform | | 1.05 | 0.83 | 0.55 | 22 | 2.19 | 1.04 | 0.97 | 0.57 | 22 | 3.33 |

Both experiments presented subcritical flow regime (Fr <1) upstream and downstream of the main channel at equilibrium. Also, for both experiments, the flow velocity increased from upstream to downstream of the confluence, which resulted in an increase of the sediment transport capacity ($T_{dw}$>$T_{up}$). The differences in flow depth, flow velocity, Froude number, and sediment transport capacity between upstream and downstream of the confluence were more pronounced for the experiment performed with non-uniform sediments (Table 1).

The dune-like bedforms observed in the main channel at equilibrium in the experiment performed with uniform sediments, as well as the absence of bedforms reported for the experiment performed with non-uniform sediments, are in agreement with the observations made by van Rijn(1984b) for the pairs of values {$D_*$,T}, corresponding to each experiment. In addition, the increase of the length and height of the bedforms of the main channel, observed from upstream to downstream of the confluence is consistent with the increase of the sediment transport capacity, reported above. This increase may be attributed to the augmented shear stress associated with the higher velocities registered downstream of the confluence, compared to those registered upstream.

### 3.2 Hydro-morphodynamics of the tributary

Figure 5 visualizes, for both experiments, the elevation of the bed and water surface of the tributary at equilibrium. Figure 6 depicts the tributary-mouth bar at equilibrium of each experiment. The bed morphology of the experiment performed with non-uniform sediment was characterized by a steep and nearly constant slope where $Y/B$> 1.5, a marked bed discordance with the main channel, a significant penetration of the tributary mouth bar into the main channel, and armored bed along the tributary (Figures 5a and 6a). In the case of the experiment performed with uniform sediments, the bed morphology presented a mild and nearly constant slope where $Y/B$> 1.5, a marked bed discordance with the main channel, a little penetration of the tributary-mouth bar into the main channel, and dune-like bedforms where 3 >$Y/B$> 1.5 (Figure 5b and 6b). The wave length of these bedforms was of $\lambda$~ 3.2-3.6$h$ and the height increased from $\Delta$ ~ 0.12$h$ to $\Delta$ ~ 0.20$h$ as approaching the confluence. $h$ is the mean flow depth of the tributary where $Y/B$> 1.5.

 

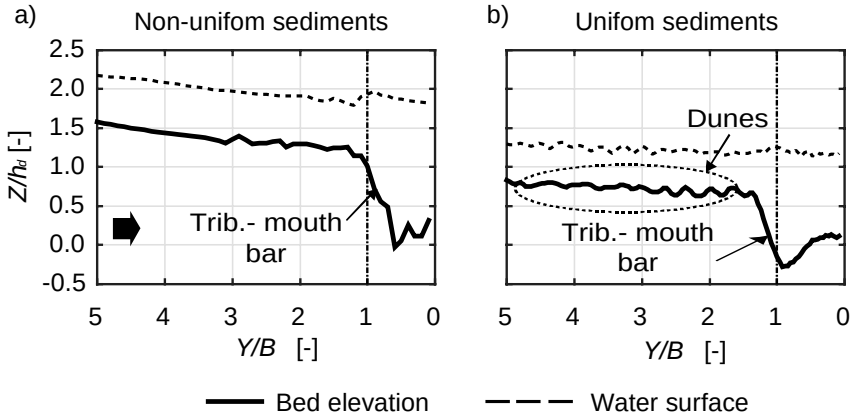


**Figure 5.** Longitudinal profiles of the bed elevation and water surface measured at equilibrium along the axis of the tributary. a) Non-uniform sediments, b) Uniform sediments.

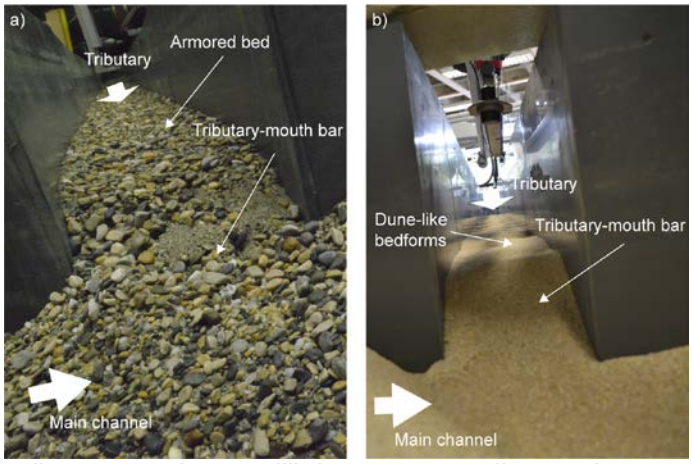


**Figure 6.** Views of the tributary mouth at equilibrium corresponding to: a) Non-uniform sediments, and b) uniform sediments.

Table 2 contains the values of the non-dimensional mean values of the flow depth ($h/h_d$), flow velocity ($U/U_d$), Froude number (Fr), and the particle and transport stage parameters of van Rijn(1984b) ($D_*$ and T), corresponding to the upstream reach of the tributary (Y/B >1.5) at equilibrium. These values revealed that the flow regime of the tributary at equlibrium was subcritial (Fr< 1) for both experiments. Also, the armored bed observed for non-uniform sediments, and the bedforms observed for uniform sediments are in agreement with the observations made by van Rijn(1984b) for the pair of values {$D_*$, T} obtained for each experiment.

**Table 2.** Non-dimensional values of the hydraulic variables of the tributary at equilibrium where Y/B> 1.5.

| Sediment mixture | $Q_r$ [-] | $h/h_d$ [-] | $U/U_d$ [-] | $Fr$ [-] | $D_*$ [-] | $T$ [-] |
|---|---|---|---|---|---|---|
| Non-uniform | 0.15 | 0.63 | 0.69 | 0.74 | 58 | 1.97 |
| Uniform | | 0.50 | 0.86 | 0.74 | 22 | 4.01 |

## 4 DISCUSSION

The bed morphology at equilibrium presented common features in both experiments. These features are typically observed in river confluences (Best, 1987; Best, 1988; Biron et al., 1993; Bristow et al., 1993; Best and Rhoads, 2008), and consist of: i) a bank-attached bar at the inner bank of the main channel, ii) a scour hole which extends from the tributary mouth to the outer bank, iii) and a marked bed discordance between the tributary and main channel. Such features are influenced by the gradation ($\sigma$) of the sediment mixtures supplied to the flumes during the experiments.

The bank-attached bar formed with non-uniform sediments (high $\sigma$) is considerably larger than that formed with uniform sand (low $\sigma$) (Figures 3 and 4). With non-uniform sediments, the coarser particles provided by the tributary to the confluence could not be conveyed downstream. They consequently tend to deposit at the downstream junction corner, building the bar. During the experiments, the size of the bar increases, which reduces the effective flow section and accelerates the flow until the necessary conditions to transport the bedload imposed from upstream are met. In contrast, the finer sediments supplied to the

 

confluence for the experiment performed with uniform sand, are conveyed more easily by the resultant flow, yielding smaller bars.

In the experiment performed with non-uniform sediments, the scour hole is mostly concentrated at the outer bank, whereas in the experiment performed with uniform sediments the scour hole extends from the tributary mouth to the outer bank (Figures 3 and 4). The comparatively deeper scour holes at the tributary mouth observed with uniform sediments (Figure 4) can be justified as the fine particles are transported more easily than the coarse ones, promoting more erosion. The deeper erosion observed at the outer bank of the main channel with non-uniform sediments (Figure 3), compared with the results obtained with uniform sediments (Figure 4), may be attributed to a stronger flow concentration and acceleration at that location. This major concentration and acceleration of the flow is caused by the larger bank-attached bar formed with non-uniform sediments. In contrast, the smaller bars formed with uniform sediments lead to less flow deflection, resulting in lesser erosion at the outer bank.

In the tributary and with non-uniform sediments, the bed morphology at equilibrium presented steeper bed slopes upstream of the confluence and further penetration of the tributary-mouth bar in the main channel, with respect to the results obtained with uniform sediments (Figure 5). To convey the wide range of particle sizes supplied to the tributary in the experiment performed with non-uniform sediments, the bed adopted a steep slope increasing the available shear stress. In contrast, the bed evolves toward comparatively flatter slopes in the experiment performed with uniform sand, since the sediment load is composed of finer particles. These fine particles are easily eroded by the turbulence associated with the flow junction and thus, the tributary bed does not penetrate into the main channel as far as it does with the coarser sediments of the non-uniform mixtures. The bed discordance is related to the different sediment rates transported by each flume (Leite Ribeiro et al., 2012; Guillén-Ludeña et al., 2015; Guillén-Ludeña et al., 2016). The similar bed discordance observed for the low and intermediate discharge ratios in both experiments may be attributed to the fact that the sediment rates are the same. In the case of uniform sediments, the turbulence associated to the flow junction erodes the fine bed increasing the discordance, whereas for the experiment performed with non-uniform sediments, the flow resulting from the junction is not able to erode the bed at the tributary mouth because it is composed of coarse particles.

The morphodynamics differences observed between both set of experiments may be qualitatively explained through the Lane's (1955) balance:

$$Q \times J \sim Q_s \times d \qquad [9]$$

where $Q$ and $J$ denote the flow discharge and bed slope, and $Q_s$ and $d$ denote the rate and characteristic grain size of the sediment supplied from upstream. Lane (1955) stated that the river regime requires a balance between the sediment supply and the transport capacity. The idea is based on that if any of the variables is altered, at least any one other will change to maintain the regime. In this study, the sediment rates ($Q_s$) and the flow discharges (Q) were fixed for the experiments run with the same discharge ratio, and the characteristic grain diameter of the supplied sediments (d) was coarser for the non-uniform sediments than for the uniform. This implies that the variable which must compensate the variation in $d$ is the bed slope ($J$). In this line, the coarser sediments supplied with the non-uniform mixtures lead to an increase of the bed slope, which in turn is reflected in a steeper slope of the water surface (Figure 3).

In the experiment performed with non-uniform sediments, the morphodynamics of the confluence seem to be governed by the imposed sediment loads. In this experiment, the bed morphology evolves as to enhance the sediment transport capacity of the flow and thus conveys the coarser sediments provided by the tributary. The development of the bank-attached bar, the scour hole, and the steep bed slope of the tributary are evidences of this morphological evolution. In the experiments performed with uniform sediments, the dunes observed in both flumes at equilibrium reveal a relative excess of transport capacity (Dey, 2014), which lead to attenuated morphological features that are masked by the bedforms. The differences in bed morphology are reflected in the water surface. With non-uniform sediments, the water surface exhibits an abrupt change of slope from upstream to downstream of the confluence (Figure 3), revealing a high velocity gradient. With uniform sediments, only minor changes are observed in the slope of the water surface (Figure 4), indicating a smoother flow acceleration.

In the experiment performed with non-uniform sediments, the high gradation coefficient of the mixture supplied to the tributary results in an armored bed which inhibits the formation of bedforms (Chiew, 1991). On the contrary, in the experiment performed with uniform sediments, the low gradation of the supplied sediment mixture leads to the formation of bedforms in the tributary and main channel. These bedforms are dunes, agreeing with the bedform predicted by van Rijn (1984) and Yalin (1992), though the length of these dunes differs from what is proposed by them.

## 5 CONCLUSIONS

The effects of the sediment gradation coefficient ($\sigma$) on the hydro-morphodynamics of open-channel confluences are analyzed and discussed in this study.

 

With non-uniform sediments (high $\sigma$), the confluence morphodynamics evolve until the sediment transport capacity, necessary to transport the wide range of particle sizes, is attained. This evolution results in a bed morphology characterized by a high topographic gradient with a large bank-attached bar, a deep scour hole at the outer bank of the main channel, and a steep and armored tributary bed that notably penetrates into the main channel. Also, the high value of $\sigma$ promotes bed armoring, which inhibits the formation of bedforms.

The lack of coarse particles in the uniform sediment mixture (low $\sigma$) facilitates the transport of the imposed sediment load. This results in a bed morphology with an attenuated bank-attached bar and scour hole, a flatter bed slope in the tributary and a slight penetration of the tributary-mouth bar into the main channel. Also, the migrating dunes observed in both channels mask the typical morphological features of the confluence.

## ACKNOWLEDGEMENTS

This study is supported by the Portuguese national Funding agency for Science, research and Technology (FCT) and the Laboratory of Hydraulic Construction (LCH) at EPFL in the framework of the Joint Doctoral Initiative IST-EPFL (SFRH/BD/51453/2011) and of the project PTDC/ECM/118775/2010. The presented data are available upon request to the authors.

## REFERENCES

Best, J.L. (1987). Flow Dynamics at River Channel Confluences: Implications for Sediment Transport and Bed Morphology. *Recent Developments in Fluvial Sedimentology,* 39, 27-35.

Best, J.L. (1988). Sediment Transport and Bed Morphology at River Channel Confluences. *Sedimentology*, 35(3), 481-498.

Best, J.L. & Rhoads, B.L. (2008). *Sediment Transport, Bed Morphology and the Sedimentology of River Channel Confluences, River Confluences, Tributaries and the Fluvial Network.* John Wiley & Sons, Ltd, 45–72.

Biron, P., Roy, A., Best, J.L. & Boyer, C.J. (1993). Bed morphology and Sedimentology at the Confluence of Unequal Depth Channels. *Geomorphology*, 8(2–3), 115–129.

Bristow, C.S., Best, J.L. & Roy, A.G. (1993). *Morphology and Facies Models of Channel Confluences.* Alluvial Sedimentation, Ltd, Oxford, United Kingdom, 91–100.

Chiew, Y.M. (1991). Bed Features in Nonuniform Sediments. *Journal of Hydraulic Engineering*, 117(1), 116–120.

Dey, S. (2014). *Bedforms, Fluvial Hydrodynamics. Hydrodynamic and Sediment Transport Phenomena* Berlin, Heidelberg, Springer, 453–528.

Guillén-Ludeña, S. (2015). Hydro Morphodynamics of Open Channel Confluences with Low Discharge Ratio and Dominant Tributary Sediment Supply, *PhD Thesis.* Ecole Polytechnique Fédérale de Lausanne, Lausanne, Switzerland.

Guillén-Ludeña, S., Franca, M.J., Cardoso, A. H. & Schleiss, A.J. (2015). Hydro Morphodynamic Evolution in a 90° Movable Bed Discordant Confluence with Low Discharge Ratio. *Earth Surface Processes and Landforms*, 40(14), 1927–1938.

Guillén-Ludeña, S., Franca, M.J., Cardoso, A.H. & Schleiss, A.J. (2016). Evolution of the Hydromorphodynamics of Mountain River Confluences for Varying Discharge Ratios and Junction Angles. *Geomorphology*, 255, 1–15.

Leite Ribeiro, M., Blanckaert, K., Roy, A.G. & Schleiss, A.J. (2012). Flow and Sediment Dynamics in Channel Confluences. *Journal of Geophysical Research: Earth Surface*, 117(F1), 1–19.

Rhoads, B.L., Riley, J.D. & Mayer, D.R. (2009). Response of Bed Morphology and Bed Material Texture to Hydrological Conditions at an Asymmetrical Stream Confluence. *Geomorphology*, 109(3–4), 161–173.

Schindfessel, L., Creëlle, S. & De Mulder, T. (2015). Flow Patterns in an Open Channel Confluence with Increasingly Dominant Tributary Inflow. *Water*, 7(9), 4724-4751.

Shields, A. (1936). *Application of Similarity Principles and Turbulence Research to Bed Load Movement, Hydrodynamics Laboratory, Published No. 167*. Berlin: U.S. Department of Agriculture, Soil Conservation Service Cooperative Laboratory, California Institute of Technology, Pasadena, California.

van Rijn, L.C. (1984). Sediment Transport, Part I: Bed Load Transport. *Journal of Hydraulic Engineering*, 110(10), 1431–1456.

van Rijn, L.C. (1984). Sediment Transport, Part III: Bed forms and Alluvial Roughness. *Journal of Hydraulic Engineering*, 110(12), 1733–1754.

Yalin, M.S. (1992). *River Mechanics*, Pergamon Press Ltd.

 

# HISTORICAL EVOLUTION OF CHANNEL SHIFTING AND ITS RESPONSE TO TRADITIONAL BANK PROTECTION WORK ALONG A REACH OF THE SAND BED BRAIDED AT JAMUNA/BRAHMAPUTRA

MD. MARUF DUSTEGIR[1], MD. RASHEDUL ISLAM[2], MD. MUNSUR RAHMAN[3], ANISUL HAQUE[4], REZAUL KARIM[5], GAZI RIASAT AMIN[6], LUTFOR RAHMAN[7], MOTAHAR HOSSAIN[8], HAJIME NAKAGAWA[9] & YUJI HASEGAWA[10]

[1,2,3,4,5,6] Bangladesh University of Engineering and Technology, Dhaka, Bangladesh
maruf.dustegir@gmail.com; rezaul.k1992@gmail.com; riasat.amin32@gmail.com; rakib_buet08@hotmail.com; munsurbuet1989@gmail.com; anisul.buet@gmail.com
[7] River Research Institute, Faridpur, Bangladesh
mdlutforrahman10@yahoo.com
[8] Bangladesh Water Development Board, Dhaka, Bangladesh
motaher.hossain@yahoo.com
[9,10] Kyoto University, Kyoto, Japan
nakagawa@uh31.dpri.kyoto-u.ac.jp; hasegawa.yuji.3e@kyoto-u.ac.jp

## ABSTRACT

Brahmaputra River has one of the most active and dynamic fluvial system in the world and shifts its bank line continuously which causes land loss to thousands of people. Due to this phenomenon, the social and economic life of the people residing along Brahmaputra is highly vulnerable and unstable and hinders the gross development of that region. For comprehensive development to happen for the people, the incorporation of the dynamic behaviours of Brahmaputra with its morphological changes is needed. The aim of this study is to assess the bankline shifting during last few decades, the rate of change of the bank retreat and morphological response of the river before and after the installation of the bank protection structure (RCC spurs) with the help of time series analysis using remote sensing. Analysis shows that erosion rate of the study reach is 89.9753 m/year which is between the year 1973 to 2016. Before the construction of protective structure the rate was 131.907 m/year and after the installation of the structure it dropped to a rate of 3.63667 m/year. This study also reveals the fact that the river is migrating westwards continuously during 1973 to 2016. Recently successful studies of bamboo bandalling for sediment management and land reclamation along the Jamuna River are executed. This explores the potential of such structures in protecting eroding bank of the current study site which will be used as a test case under the ongoing protect jointly funded by JST-JICA under SATREPS program.

Keywords: Erosion; brahmaputra river; sedimentation; RCC spur; bandallings.

## 1 INTRODUCTION

The Brahmaputra, a trans-boundary river, is the fifth largest river in terms of discharge and eleventh largest river in terms of drainage area in the world. It is at a length of some 3000 km originating from the great glacier mass of Chema-Yung-Dung in the Kailas range of southern Tibet and flowing through China, India and Bangladesh (Hovis, 1998; Tandon and Sinha, 2007; Elahi and Rogge, 1990). The average annual flood of the Brahmaputra River is about 60,000 m3/s, and the discharge during low flow lies between 4,000 to 12,000 m3/s. The water level slope gradually decreases from 10 cm/km at the Indian border to 6 cm/km near the confluence of the Ganges River with a mean of 7 cm/km. On the Tibetan plateau the river changes regularly between a braided platform and the channel is steep and narrow with gradients as high as 14.8 m/km and entrenched meanders. After leaving the Himalayas, in the plain land of Assam and Bangladesh the Brahmaputra flows as a braided river, marked by the presence of numerous mid-channel and lateral bars and islands (Jagers, 2003). The Brahmaputra basin is characterized by a unique physiographic setting in the eastern Himalayas that includes a powerful monsoon rainfall regime and a fragile geologic base and active seismicity (Goswami, 2008).

The Brahmaputra River is a classic example of a braided river which forms multiple meandering channels twining around lateral sandbars, locally known as chars (Thorne et. al., 1993). Huge discharge along with massive amount of sediment induces this river to be dynamic and unstable (Coleman, 1993). Every year, notable erosion occurs along the banks of this river and parts of the flood plain are reshaped significantly (Klaassen and Masselink, 1992). The Brahmaputra demonstrates radical changes in channel formation in erosion-prone areas representing the dynamic nature of river morphology and the intensity of erosion caused by it (Goswami, 1985). These changes have a substantial impact on the local settler as well as planning and design of infrastructural and bank protection works. Hundreds of metres of banks is eroded each year and the

 

locations of maximum erosion prone area changes rapidly over the years (Thorne et. al., 1993). Different bank protection works like embankments, dikes and groynes has been constructed along the river for the last five decades (Sarker et. al., 2011). However, the construction and maintenance costs of these hundreds of kilometers of protection works are very expensive for a developing country like Bangladesh. Moreover, there is a growing perception that there are limits to the extent to which large rivers can be controlled. Before intervening with the natural behavior of a river, the consequences in both the near future and the long run need to be identified.

However, the morphological activity of the river does not only affect the construction of bridges and training works, but it also directly influences the lives of the people living along the river and on its islands. Erosion causes loss of land at one location, while land is gained by sedimentation at other places. The Brahmaputra River, however, is much larger and more dynamic than those rivers, which makes a conventional approach much more expensive and less appropriate. Different soft river training measures i.e. Bandallings can be introduced to control the prodigious flow of the Brahmaputra. Bandallings divert the flow towards the main channel leading to stable channel formation. Thus, the reduced velocity accelerates sedimentation behind the bandal structures and lessen the severity of erosion. The objective of this study is to quantify the erosion and bank shifting process of Brahmaputra River at an eroding bend and to identify the possibilities of accelerated sedimentation along the erosion prone bank using bandalling.

## 2 STUDY AREA

The present study was conducted on the secondary channel having meandering platform in the braided Brahmaputra River at Shuvogacha which is situated under Kazipur upazila of Sirajgonj district in Bangladesh (Figure 1). This highly erodible bank shifted almost 4 km towards western right bank in the last 44 years. The prominent characteristics of the secondary channels are that they become inactive during dry season. But during flood season they become active and erosion occurs. Several consecutive spurs had been constructed by Bangladesh Water Development Board (BWDB) to protect the Shuvagacha region from erosion during 2000's. One spur washed away during 2001 flood and another spur is now standing into the Branch channel adjacent to Shuvagacha bank. Thus, in recent years erosion process is continuing laterally. Subsequently a meander channel had been developed. A sand bar had been developed in between the meander channel and the main river. After the failure of the spurs, erosion process has been continuing along this bend and it acts like a free eroding bend.

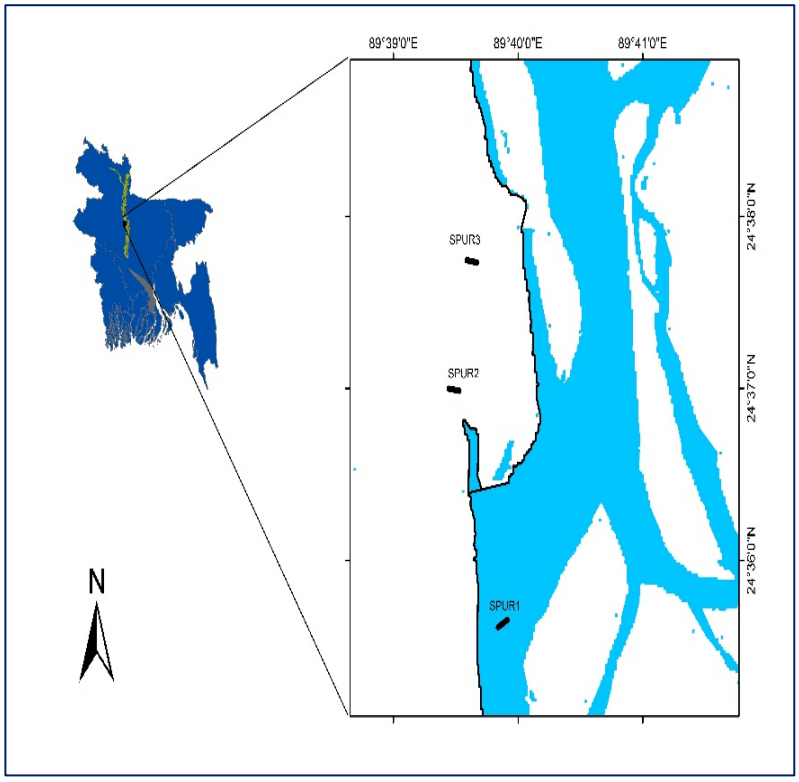


**Figure 1.** Shuvagacha bend along Jamuna river.

## 3 DATA COLLECTION PROGRAM

Remote Sensing Analysis, is an effective and reliable tool and is widely used in river morphology investigation and channel migration over a wide area (Thorne et. al., 1993; Yang et. al., 1999). Although remote sensing is normally used to investigate the channel migration, its application to the braided channel

 

dynamics is also often employed (Milton et. al., 1995; Gilvear et. al., 1995; Gupta, 1995; Ashworth et. al., 2000; Gupta et. al., 2002; Gilvear and Bryant, 2003; Ollero, 2010). The migration and bank shifting pattern near Shuvagacha bend of the Brahmaputra River have been analyzed for the past 43 years which is from 1973 to 2016. In this study, Landsat images were extracted from the United States Geological Survey (USGS) landsat archive with a spatial resolution of 30 m. A visual evaluation of the cloud cover in the available images was undertaken, and 44 images were selected based on minimal or absent cloud cover near or over the main channel. The water level on the acquisition date of each of the 44 images was obtained in the dry season to avoid the high water level implication to the planform changes, which allows a better detection of changes in fluvial dynamics.

The normalized difference water index (NDWI) threshold approach was used to delineate the land water boundary and to extract the bank line from the images (Gao, 1996). The NDWI water index algorithm was generated in the ERDAS Imagine environment by combining the green and mid-infrared bands. Due to the high sensitivity of sediment and green surfaces to the green band (0.52–0.6 µm), high degree of absorption by water, and high degree of reflectance by vegetation in the mid-infrared band (1.60–1.70 µm), the combination of green band and mid-infrared band in the NDWI is ideal for discriminating between land and water at their interface.

## 4 RESULTS AND DISCUSSIONS

### 4.1 Historical Planform Changes and Bank Erosion

Brahmaputra is also called Tsangpo-Brahmaputra, a trans-boundary river which is one of the most dynamic and active braided channel in the world. It frequently changes its course, forms large sand bars at the location where it might form one of the deep channels in the preceding years. The change of the course of Brahmaputra has been assessed through Landsat Image analysis.

Figure 2-a shows the change of river course between 1973 and 1978. Between these years the main channel flows besides the left bank which is located at eastern side of the Brahmaputra having approximately a 12km distance from the spur that was constructed in 1999. In 1978 in can be observed that, the main channel tends to shift rightward. On the contrary, a narrow small channel flows along the rightmost bank near Kazipur Sadar in 1973 as well as in 1978. Observations of 1988 is represented in Figure 2-b. It is clearly visible that the main channel shifted to the previous narrow course and that main channel conveys most of the discharge of that time. Also, an eroding scenario can be clearly observed in 1988. This eroding phenomenon was further intensified in the following years in Figure 2-c, which contains the river bank scenario of 1997 with respect to the year 1988. It has been observed that the eroded bank was almost adjacent to the spur constructed in 1999 and during those years the eroding trend was so drastic that it leads BWDB to take a strict decision to construct the bank protection structure. During 1999-2000 three RCC spurs were constructed and after the construction of the spurs, no further erosion had taken place except on spur1. In 2003, a sharp bend formed just downstream of the spur2 and prolonged alongside the spur1. As a consequence of this severe erosion, spur1 was outflanked which denotes westward movement of the bankline.

From the previous literature (Uddin and Rahman, 2012), it is seen that the spur1 was standing on the chars (sandbar). Within a few years (Figure 2-d) this branch channel dried up and the main channel was flowing at a substantial distance from the spurs which were already constructed. In the subsequent years (2010-2016),this branch channel was showing further migration towards the right bank and frequent analysis and observations of the subsequent years showed that, the spur1 has receded from the bank and the branch channel migrated toward right bank gradually (Figure 2-e, f, g, h).

 

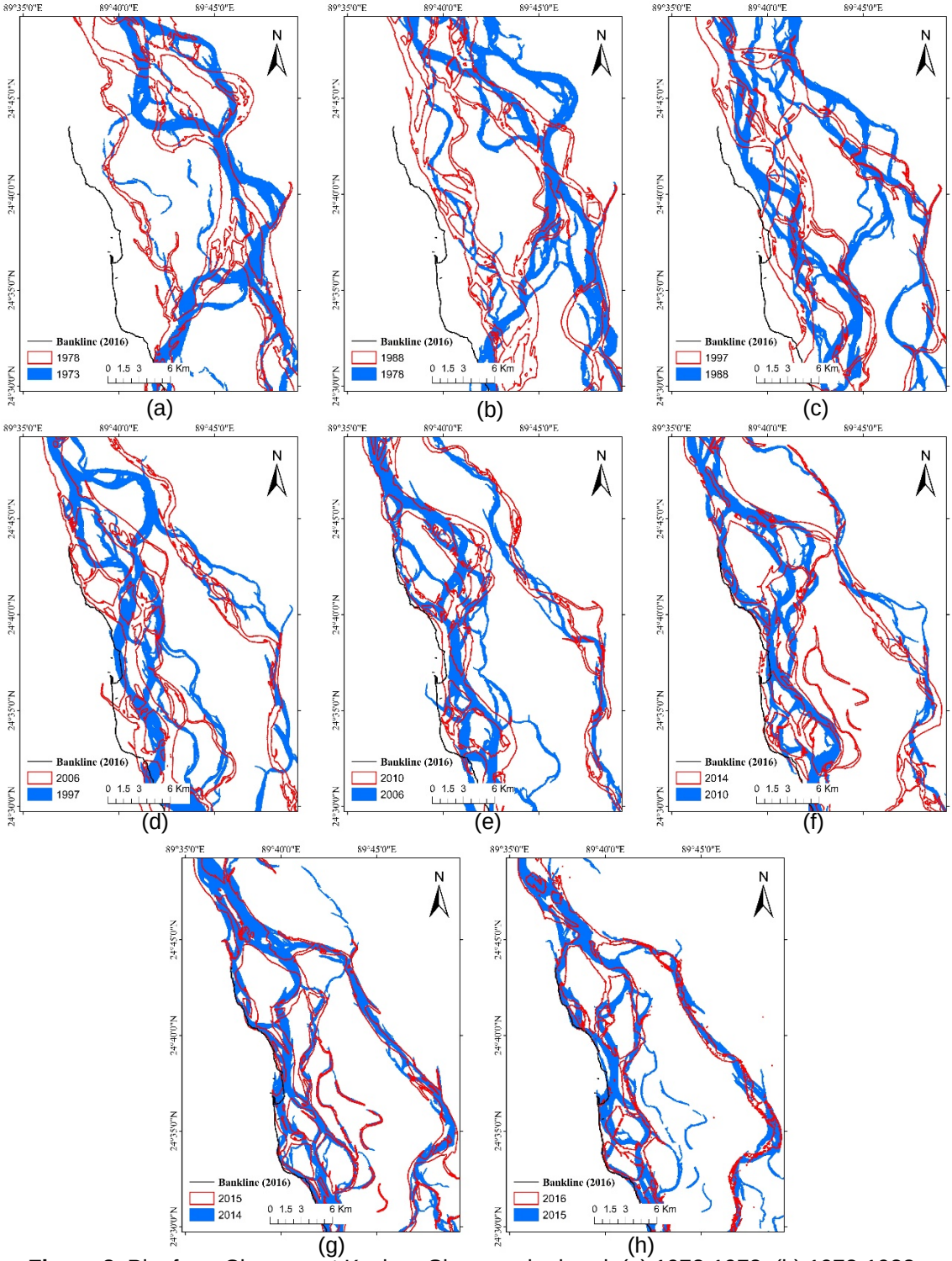


**Figure 2.** Planform Changes at Kazipur-Shuvagacha bend (a) 1973-1978, (b) 1978-1988, (c) 1988-1997, (d) 1997-2006, (e) 2006-2010, (f) 2010-2014, (g) 2014-2015, and (h) 2015-2016

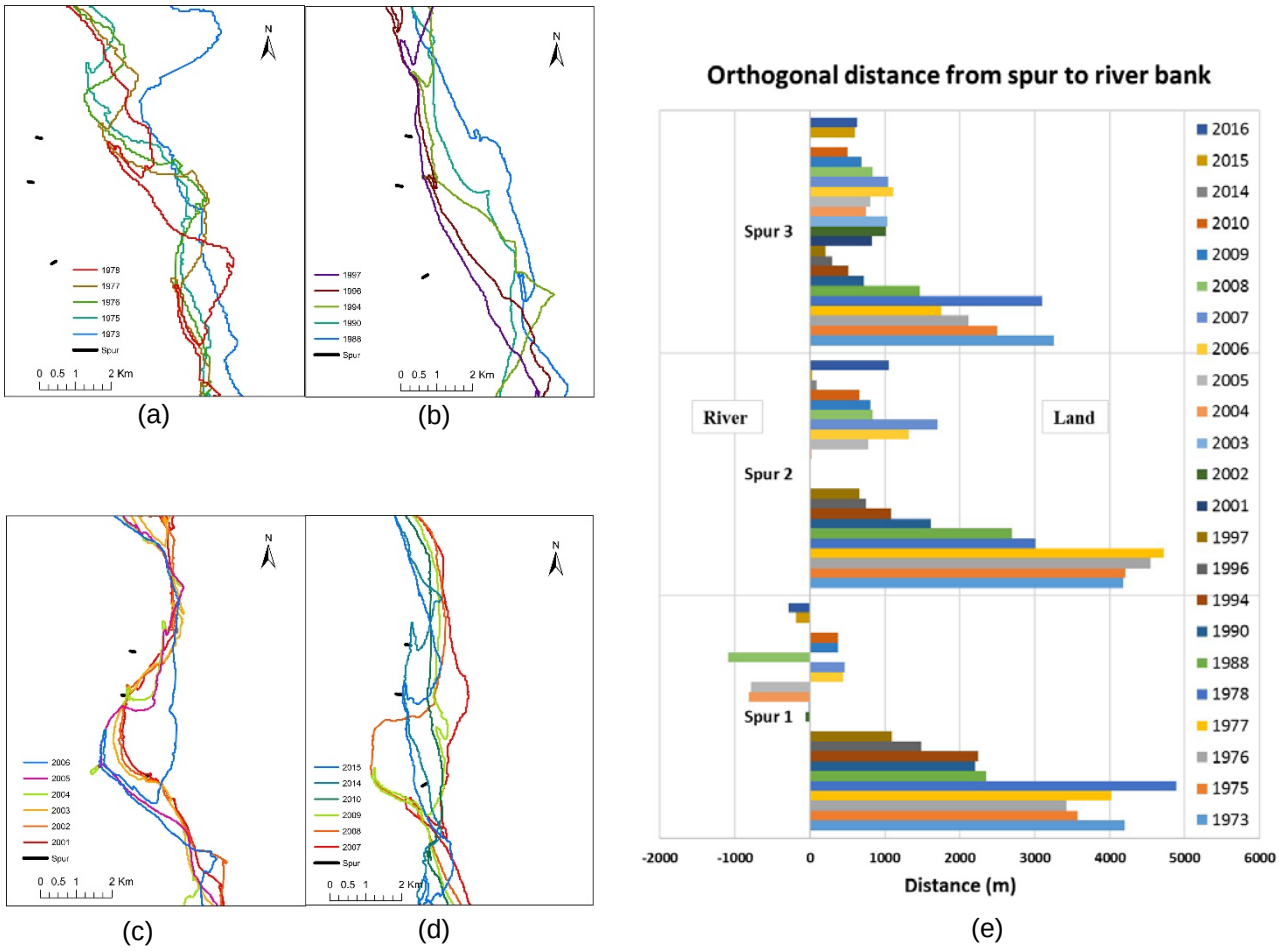


**Figure 3.** Bankline at Shuvagacha in different timescales (a, b, c, d) and (e) Orthogonal distance from spur location to the river

In Figure 3 it is clearly visible that the outer bank of Brahmaputra tends to migrate towards the right side in western direction. Before the construction of the spur in 1999 and 2000 (Figure 3-a, b), the location where the spurs were constructed shows an extreme eroding trend. After construction of the spurs this phenomenon changed (Figure 3-c, d). Detailed analysis has been demonstrated in the above graph (Figure 3-e). In Figure 4, it is demonstrated that before construction of the spurs the orthogonal distance of the bank from the location of the spur1 was being eroded at 120m/year and after the installation of the spur this phenomenon turns into reverse at a rate of 6.33m/year which has been noted by analyzing 15 years of Landsat images (2001-2016). But from frequent analysis of last few years' satellite images, it had been found that the bank was being rapidly eroded away towards western bank near spur1. The historical trend demonstrates a clear observation that Brahmaputra is shifting its course rightward in the western direction. To rehabilitate the spur1, huge sedimentation is needed to connect this hydraulic structure with the mainland. Thus, an ecofriendly and low cost bandalling can be considered for sedimentation in the Brahmpautra near Shuvagacha bankline at Kazipur.

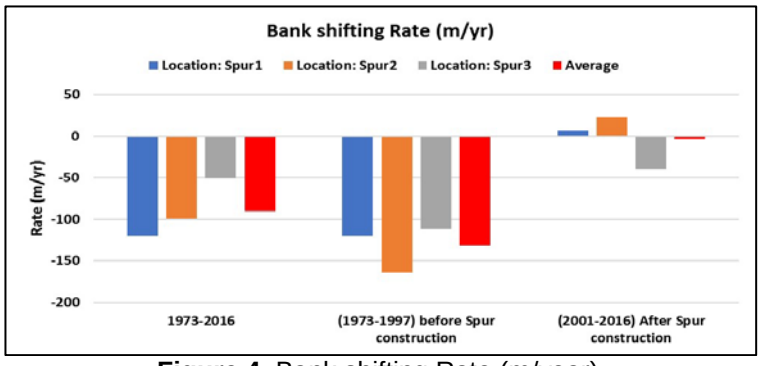


**Figure 4.** Bank shifting Rate (m/year)

4.2 Embayment Behaviour

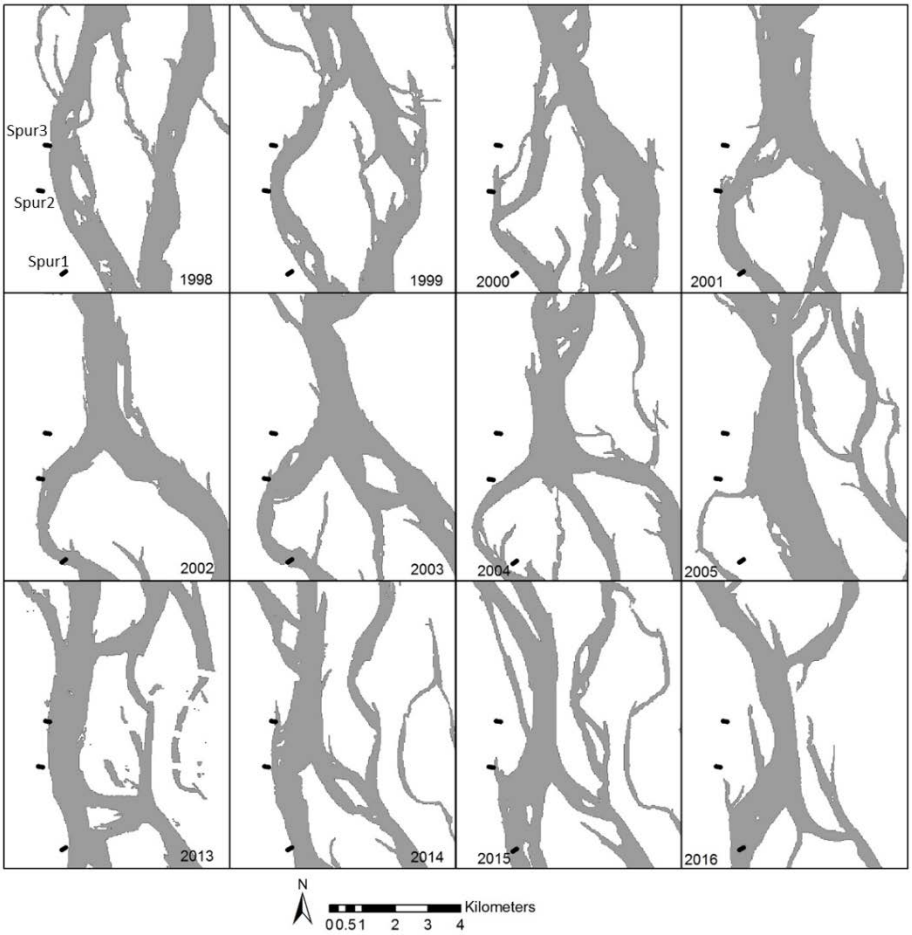


**Figure 5.** Local Planform Changes and Embayment development between Spurs

In previous years of spur construction, the increasing tendency of bank erosion at Kazipur bend leads to the responsible agency to construct spurs. After the construction of the spurs, the in between bank of the spur1 and spur2 demonstrates an embayment formation (Figure 5). In consecutive years of 2001 and 2002, this embayment was being sharpened. In 2003, the downstream spur mentioned as spur1 was outflanked and in the following year of 2004, the channel adjacent to the bank moved further inland. With the increasing ratio of the arc-cord at Kazipur bend, the discharge of the upstream main channel disintegrates/breaks the sandbar and the major discharge flows through the breaking channel. In the same year (2004), the channel adjacent to the bank further migrates to the bank leaving spur3 on the laterally widening sandbar. In the consecutive years the bar breaking channel further widened and embayment became inactive. In recent years (2013-2016), the main channel was flowing adjacent again to the spurs exerting huge hydrodynamic pressure on the Kazipur bank. A young and developing point bar since 2014-2016 along the Kazipur bend keeps spur2 and Spur3 functioning and stable plus oblique flow along Spur1 helps expediting erosion at the nearside bank of Spur1. In the recent years the embayment behavior was not as before because of the loose and young sediment deposition in 2005. That is why in recent years the embayment between spur1 and spur2 was not so evident as in 2000-2003.

A general schematic figure (Figure 6) is demonstrated to understand the basic process of embayment between two consecutive spurs. In Figure 6, the upstream flow was distributed into two bifurcated channels. The main stream, carrying large share of total discharge, exerts hydraulic force on the bank and develops embayment between two consecutive spurs. The embayment becomes more dilated in the preceding years. This scenario continues up to a certain threshold of arc-cord ratio. At Kazipur bend after exceeding this threshold of 1.6, the sand bar along the bend splits into two on the embayment causing the channel to turn into an inactive channel. The major flow flows through channel which splits the bar.

 

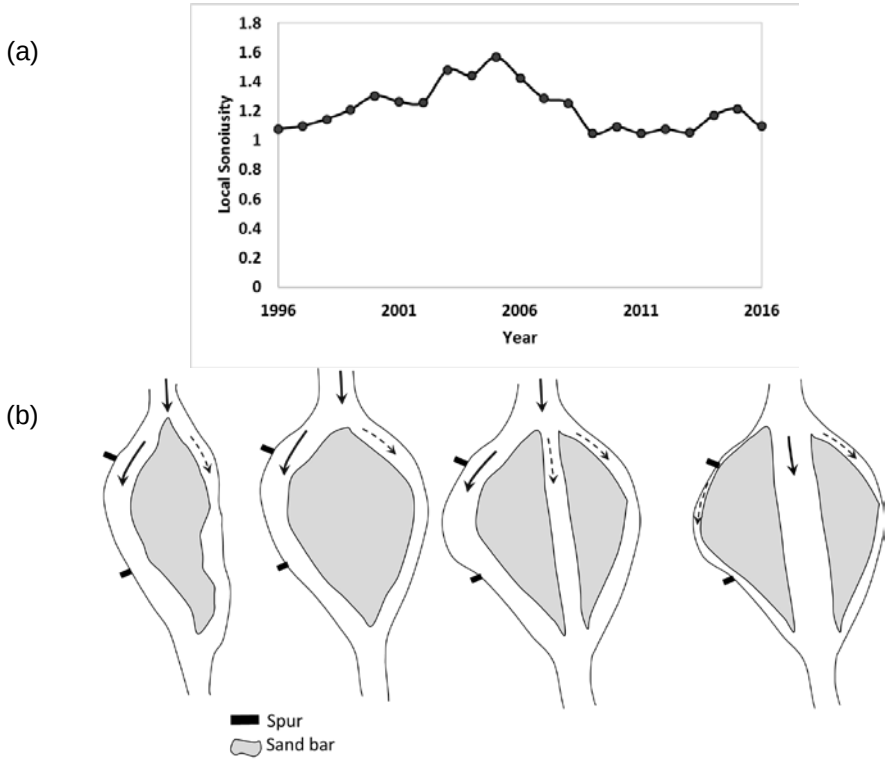


**Figure 6.** (a) Arc-cord ratio beside the sandbar along the Kazipur bend and (b) A general Schematic figure of embayment formation

4.3 Bandallings

Sedimentation is one of the major problems to maintain with least available depth along the navigational routes, especially, during the dry season. To maintain navigability of the River like Brahmaputra, dredging was introduced. But several studies and experience showed that dredging is an unsustainable measure as it is expensive and the bed formation of Brahmaputra is highly dynamic. These consequences lead Bangladesh Inland Water Transport Authority (BIWTA) to adopt low cost, environment friendly bandalling to maintain the navigation route to be active during the dry season.

Bandalling is one of the local structures developed in the Indian sub-continent that obstruct flow near the water surface and allow it to pass near the riverbed to maintain Least Available Depth (LAD) for maintaining navigation route. These were made of naturally available materials such as bamboo, wood and etc. It is regarded as inexpensive method over conventional structures, and mostly applied for the improvement of navigational channels during the low flow season. Therefore, the use of the bamboo bandalling structure for riverbank erosion protection is a new concept and application of bandalling for riverbank protection is extremely limited.

The working principles of bandals for the control of water and sediment flow are shown schematically in Figure. 7, where sediments were transported as bed load and suspended load. The bandals were installed at an angle with main current having an opening at the lower half while the upper portion was blocked. Within the lower half of the flow depth, major portion of the sediment flow was concentrated (Rahman et. al., 2003; IWFM, 2007). The surface current is being forced to divert away from the previous track to the outer face of the bandals. On the other hand, the sediment was transported through the opening was carried by the reduced flow. The reduced flow cannot transport all the sediment which resulted in sedimentation behind the bandals.

At laboratory scale, the preliminary idea on the possibility of the use of bandalling for erosion control was tested. Capability of bandalling for flow diversion towards the main channel in order to protect the bank from erosion was tested in the laboratory. Moreover, few field experiments were carried out in the Surma River. It was found that the velocity behind the bamboo bandalling structures was less than that of the upstream velocity away from this bamboo bandalling structure in both the field's case study and in the laboratory study. Due to the reduced velocity, the water borne sediment was deposited behind bandals in both the laboratory and field which had given an indication of river bank erosion protection and reclamation of eroded agricultural land. But large scale experiment is yet to be carried out. Thus to connect the Shuvagacha Spur1 with the

 

mainland in order to protect the Shuvagacha bank from continued erosion, bandalling is being considered in the next monsoon.

The Shuvogacha bend channel originated from the main channel and flows towards western direction. It gradually turns towards southward direction that flows as a straight channel about 2 km towards southward direction. After that it turns its course towards south-eastern direction and meets with the main channel. A velocity vector at one-meter depth is demonstrated in Figure 8-b from the velocity vector at one-meter depth of water surface. It is clearly visible that flow hits the western bank obliquely near and upstream of Spur1. The magnitude of velocity was relatively higher at the mid-channel of the starting point at the bend channel. It is observed that the bank along the straight channel was severely eroded when filed measurement was carried out. Gradually the bank moves towards the western direction and relatively higher depth was found near the bank line. Maximum depth was found adjacent to Spur1.

The purpose of the field experiment is to divert the flow towards the eastern direction so that the western bank is protected from erosion. Thus, brandlings are to be installed on the upstream sandbars obliquely to the downward direction of the flow.

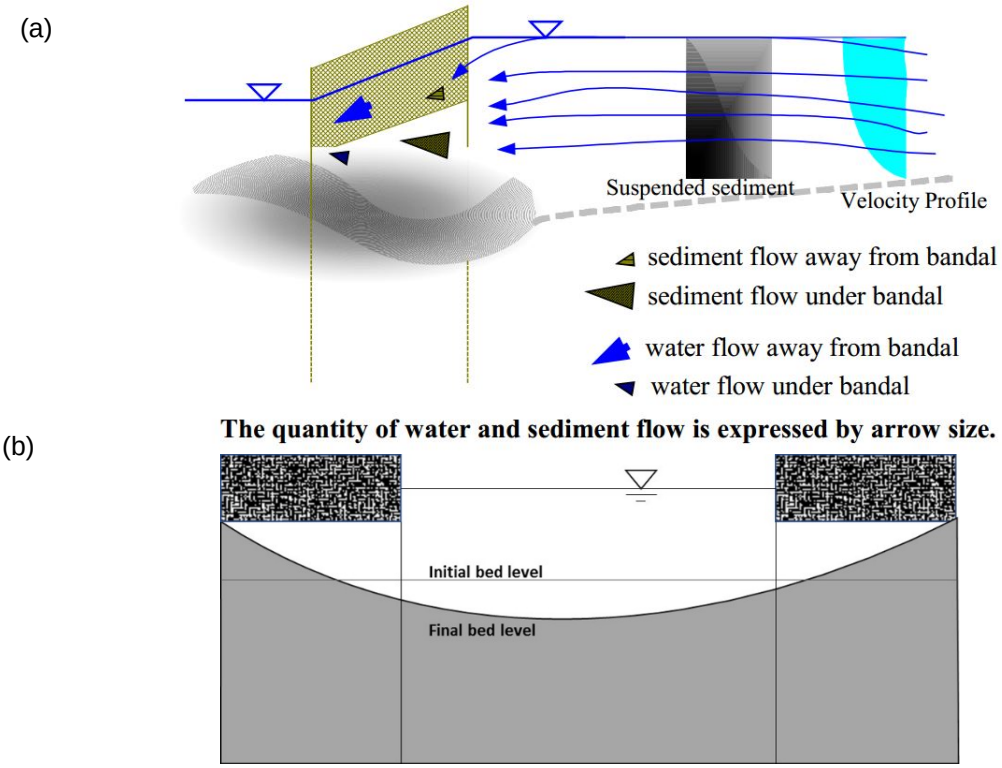


**Figure 7.** (a)Working principles of bandals. (Rahman et. al., 2003) and (b) Channel bed change due after bandal installation (IWFM, 2007)

 

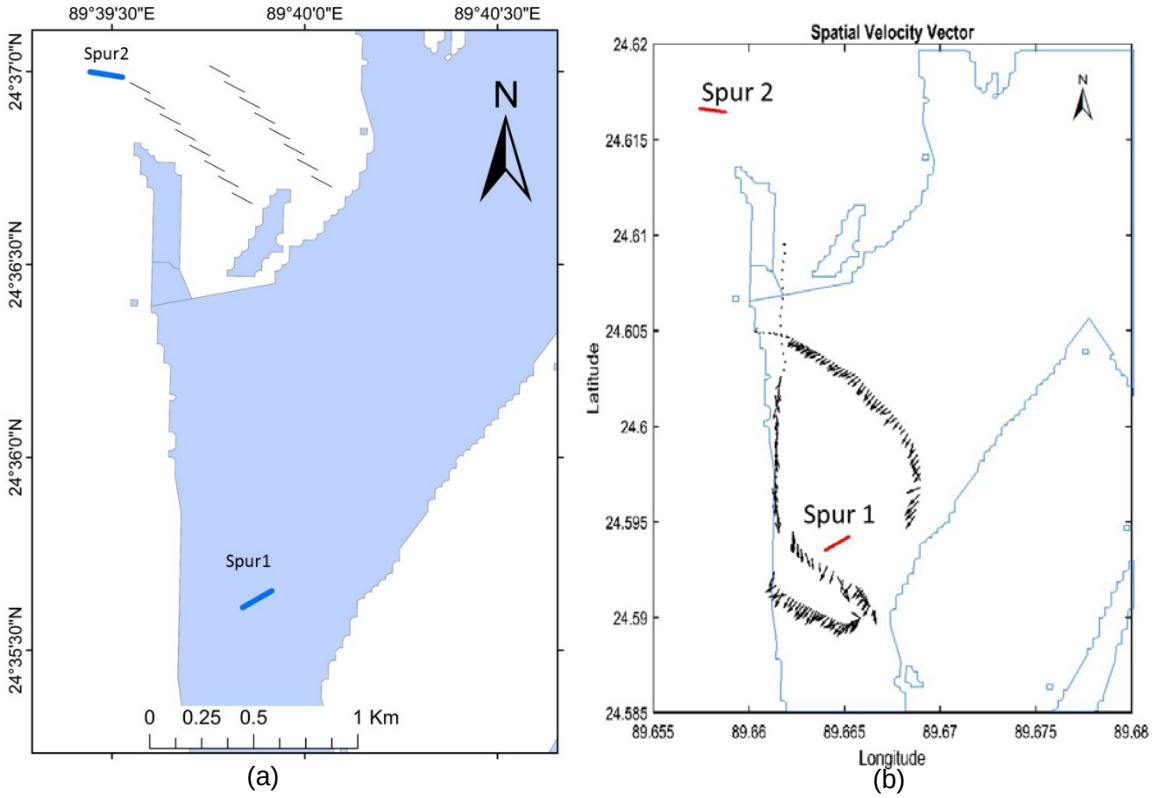


(c)

**Figure 8.** (a) Tentative layout of the proposed bandallings, (b) Near surface flow pattern along the horizontal plane (c) Paradigm of Bamboo bandallings in a river.

## 4 CONCLUSIONS

The erosion and bankline shifting process of Brahmaputra is a continuous process. Over the years. this morphological change sometimes might be very abrupt that the old course completely changes to a new course. The huge sediment flux of this river aggravates this phenomenon. The historical satellite image analysis reveals that this erosion and bankline shifting processes and rate of the study reach have been changed after the construction of the bank protection structures on the previous unprotected course. Whether there was occurring erosion at a rate of 131.907 m/year before the construction of the structures during 1973-1997, this scenario changed to 3.63667 m/year after the construction of the structure during 2001-2016. The most important revelation of this study is the migration of the Brahmaputra towards western direction at a rate of 89.9753 m/year for the study reach during 1973-2016. Due to highly dynamic behavior of this braided channel the bank protection work was isolated from the bank. Moreover, by analyzing the flow data measured by ADCP it is found that oblique flow in the eroding bank of the branch channel induces the bank erosion that might be intensified during the following monsoon flood. To restore this bank protection structure, to stop

 

erosion and to reclaim the land of the eroded bank, low cost environment friendly soft measures like bamboo bandallings are proposed to be installed for sedimentation catchment between the isolated structure and eroding bank.

**ACKNOWLEDGEMENTS**

The research reported herein is funded by JICA-JST under SATRES program. The authors would like to thank JICA-JST staff for their involvement in this project.

**REFERENCES**

Ashworth, P.J., Best, J.L., Roden, J.E., Bristow, C.S. & Klaassen, G.J. (2000). Morphological Evolution and Dynamics of a Large, Sand Braidedbar, Jamuna River, Bangladesh. *Sedimentology,* 47**,** 533–555

Coleman, J.M. (1969). Brahmaputra River: Channel Processes and Sedimentation. *Sediment. Geol.*, 3, 129-139.

Elahi, K.M. & Rogge, J. (1990). Riverbank Erosion, Flood, And Population Displacement in Bangladesh: A Report on The Riverbank Erosion Impact Study, Dhaka. *Riverbank Erosion Impact Study (REIS)*. Jahangirnagar University (JU).

Hovius, N. (2010). Controls on Sediment Supply by Large Rivers. *Relative Role of Eustasy, Climate, and Tectonism in Continental Rocks,* 1(1), p.2.

Gao, B.C. (1996). NDWI—A Normalized Difference Water Index for Remote Sensing of Vegetation Liquid Water from Space. *Remote sensing of environment,* 58(3), 257-266.

Gilvear, D.J., Waters, T.M. & Milner, A.M. (1995). Image Analysis of Aerial Photography to Quantify Changes in Channel Morphology and Instream Habitat Following Placer Mining in Interior Alaska. *Freshwater Biology,* 34, 389–398.

Gilvear, D.J. & Bryant, R. (2003). Aerial Photography and Other Remotely Sensed Data. In: *Tools in fluvial geomorphology* ed M Kondolf and H Piegey (Chichester: Wiley), 211–247

Goswami, D.C. (1985). Brahmaputra River, Assam, India: Physiography, Basin Denudation, and Channel Aggradation. *Water Resour. Res*., 21(7), 959–978.

Goswami, D.C. (2008). Managing the Wealth and Woes of The River Brahmaputra. *Ishani*, 2(4).

Gupta, A. (1995). Magnitude, Frequency, And Special Factors Affecting Channel Form and Processes in the Seasonal Tropics. *Natural and anthropogenic influences in fluvial geomorphology,* 89, 125-136

Gupta, A., Lim, H., Huang, X. & Chen, P. (2002). Evaluation of Part of the Mekong River Using Satellite Imagery. *Geomorphology,* 44, 221–239.

IWFM, (2007). *Effectiveness of Bandal-Like Structures Assustainable Solution to River Erosion in Bangladesh- Report.*

Jagers, H.R.A. (2003). *Modelling Planform Changes of Braided Rivers*. University of Twente.

Klaassen, G.J. & Masselink, G. (1992) Planform Changes of a Braided River with Fine Sand as Bed and Bank Material. *Proc. 5th Int. Symp. River Sedimentation, Karlsruhe*, 459 – 471.

Milton, E.J., Gilvear, D.J. & Hooper, I.D. (1995). Investigating Change in Fluvial Systems Using Remotely Sensed Data. *Changing river channels* ed A Gurnell and G Petts (Chichester: Wiley), 276–301

Muller, E., Decamps, H. & Dobson, M.K. (1993). Contribution of Space Remote Sensing to River Studies. *Freshwater Biology,* 29, 301-312.

Ollero, A. (2010). Channel Changes and Floodplain Management in The Meandering Middle Ebro River, Spain. *Geomorphology,* 117, 247–260.

Rahman, M.M., Nakagawa, H., Ishigaki, T. & Khaleduzzaman, A.T.M., (2003). Channel Stabilization Using Bandalling. *Annuals of Disaster Prevention Research Institute*, 613-618.

Sarker, M.H., Akter, J. & Ruknul, M. (2011). River Bank Protection Measures in the Brahmaputra-Jamuna River: Bangladesh Experience. *International Seminar on 'River, Society and Sustainable Development, At* Dibrugarh University, India.

Tandon, S. K. & Sinha, R. (2007). Geology of Large River Systems. *Large rivers: geomorphology and management*, 7-28.

Thorne, C.R., Russell, A.P. & Alam, M.K. (1993). Planform Pattern and Channel Evolution of The Brahmaputra River, Bangladesh. *Geological Society, London, Special Publications*, *75*(1), 257-276.

Uddin, M.N. & Rahman, M.M. (2012). Flow and Erosion at a Bend in The Braided Jamuna River. *International Journal of Sediment Research,* 27(4), 498-509.

Yang, X., Damen, M.C.J & Zuidam, R.A.V. (1999). Satellite Remote Sensing and GIS for The Analysis of Channel Migration Changes in The Active Yellow River Delta, China. *International Journal of Applied Earth Observation and Geoinformation,* 1(2), 146–157.

 

Proceedings of the 37th IAHR World Congress
August 13 – 18, 2017, Kuala Lumpur, Malaysia

# PHYSICAL MODELLING OF THE FLUVIAL PROCESS OF THE YANGJIANAO-BEINIANZIWAN REACH IN THE MIDDLE YANGTZE RIVER DOWNSTREAM OF THE TGP

YONGHUI ZHU [(1)], MING TAO [(2)], LI HUANG [(3)] & LIHUA GU [(4)]

[(1,2,3,4)] Key Laboratory of River Regulation and Flood Control of MWR,
Changjiang River Scientific Research Institute, Wuhan, China
yhzhu75@yahoo.com; tm0720@sina.com; hl_hls@163.com; 498022695@qq.com

## ABSTRACT

Construction and operation of the Three Gorges Project (TGP) and the upstream Xiluodu Project (XLDP) and Xiangjiaba Project (XJBP) in the Yangtze River have already changed and will further change the flow and sediment process of the downstream river, and consequently bring far-reaching impacts to the fluvial process of the downstream channel. In this study, physical model tests are performed to predict the scour and siltation of the downstream river channel from Yangjianao to Beinianziwan after joint operation of the three gigantic projects, and to predict the tendency of river regime development as well. Results of the physical model tests indicate that, from 2011 to 2022, significant scour (amount $1.61\times10^8 m^3$ or averaged scour depth 1.12m) occurs to the river channel from Yangjianao to Beinianziwan. The thalweg of the channel shows a general tendency of scour and downcutting, and the river bed near the bank where thalweg closely nestling against suffers significant scour. The overall river regime of the investigated river reach does not change very strongly during the modeling period, despite of the significant scour arisen. However, relatively significant adjustment of the river regime occurs locally at certain sub-reaches.

**Keywords:** The Three Gorges Project; physical model tests; fluvial process; river regime; Yangtze River.

## 1 INTRODUCTION

The Three Gorges Project (TGP), as one of the largest hydropower-complex project in the world, ranks as the key project for improvement and development of the Yangtze River. With a normal storage level of 175m, the total capacity of the reservoir reaches 39.3 billion $m^3$, of which 22.15 billion $m^3$ is the effective flood control capacity. In June 2003 the storage level of the reservoir reached 135m, then 156m in September 2006, and 175m in October 2010, indicating realization of the integrated targets of the project in terms of flood protection, electricity generation, and navigation, etc. Besides the TGP, two other gigantic hydropower projects upstream, the Xiangjiaba Project (XJBP) and the Xiluodu Project (XLDP), began reservoir operation in October 2012 and May 2013, respectively. The XLDP is located in the upper reach of the Yangtze River, 770km apart from the TGP, has a normal storage level of 600m of the reservoir and a total capacity of 11.6 billion $m^3$, of which 4.65 billion $m^3$ is the flood control capacity. The XJBP is situated between the TGP and the XLDP (156.6km downstream). The normal storage level of the reservoir of the XJBP is 380m and the corresponding capacity is 4.98 billion $m^3$.

Construction and then operation of the TGP, the XLDP and XJBP in the Yangtze River have already changed and will further change the hydrological regime of the downstream river, and consequently brings significant impacts to the scour and siltation of the downstream channel. In particular, the river reach from Yangjianao to Beinianziwan in the middle Yangtze, about 128km long (see Figure 1), closely (about 115km) downstream of the TGP, is affected relatively earlier and significant (see e.g. CRSRI, 2011; Xu et al., 2013; CRSRI, 2016). In this study, physical model tests are performed to predict the fluvial process of the river channel from Yangjianao to Beinianziwan after joint operation of the three gigantic projects, and to predict the tendency of river regime development as well.

## 2 HYDROLOGICAL REGIME VARIATIONS AFTER THE TGP OPERATION

Since the operation of the TGP in 2003, the flow and sediment conditions (i.e. the hydrological regime) of the river reach from Yangjianao to Beinianziwan already changed significantly so far (CRSRI, 2016). Operation of the TGP (and later the XLDP and XJBP) reduces the peak of big floods and increases the flow rate for dry season. Generally, the flow process is flattening within the year. According to statistics, comparing with the situations before the TGP operation, the annual runoff of the river reach is about 5% less after the operation. Yet, the sediment load decreases dramatically (85%, see Table 1).

 

Due to the significant scour of the downstream river channel (especially the low water channel, see Section 3) after the TGP operation, water levels decline clearly at the same flow rates, see e.g., Table 2 for the Shashi Hydrological Station (control station for the river reach from Yangjianao to Beinianziwan). From 2003 to 2015, the decline of water level at the flow rate of 6000$m^3$/s is 1.74m. Along with the increase of the flow rate, this decline of water level tends to get smaller. The decline drops to 1.14m when the flow rate increases to 14000$m^3$/s.


**Figure 1**.Modeling area of the Changjiang River Flood Protection Physical Model (blue shading indicates the river reach from Yangjianao to Beinianziwan).

**Table 1**. Variations of runoff and sediment load at Shashi Hydrological Station.

| | By 2002 ① | 2003-2015 ② | 2015 ③ | Variation 1 ④=(②-①/①) | Variation 2 ⑤=(③-①/①) |
|---|---|---|---|---|---|
| **Averaged annual runoff（$10^8m^3$）** | 3940 | 3760 | 3645 | -5% | -7% |
| **Averaged annual sediment load** | 43400 | 6340 | 1420 | -85% | -97% |

**Table 2**. Decline of water level at same flow rate (Shashi Hydrological Station, unit: m).

| **Period** / **Flow rate($m^3$/s)** | **2003-2008** | **2008-2010** | **2010-2015** | **2003-2015** |
|---|---|---|---|---|
| **6000** | -0.43 | -0.58 | -0.73 | -1.74 |
| **10000** | -0.28 | -0.41 | -0.78 | -1.47 |
| **14000** | -0.23 | -0.19 | -0.72 | -1.14 |

## 3 SCOUR AND SILTATION OF THE CHANNEL AFTER TGP OPERATION

Based on analysis of the prototype topographical survey data of the river channel, since the operation of the TGP (2002-2013), the quantity of scour occurred in the bank full channel for the river reach from Yangjianao to Beinianziwan amounts to 2.56×$10^8m^3$, while this quantity amounts to 2.19×$10^8m^3$ for the low water channel (see Table 3). It is therefore indicated from Table 3 that the scour occurs mainly in the low water channel so far after the TGP operation, and the averaged scour intensity is about 0.17×$10^6m^3$/km·a.

 

Among the statistical 11 years (2002-2013), the periods of 2008-2011 and 2006-2008 show the first and second largest scour intensity (which are $0.22\times10^6 m^3/km\cdot a$ and $0.20\times10^6 m^3/km\cdot a$), respectively, even larger than that of the first period of 2002-2006 after the TGP operation ($0.15\times10^6 m^3/km\cdot a$). This illustrates that the scour by clear flow to the channelis developing from upstream to downstream after the TGP operation. As about 115km downstream of the TGP, the river reach from Yangjianao to Beinianziwan does not suffer the largest scour intensity in the first few years after the project operation, instead, a few more years later.

## 4 PHYSICAL MODEL PREDICTIONS OF THE FLUVIAL PROCESS

### 4.1 Brief introduction of the physical model

The experiments were conducted with the Changjiang River Flood Protection Physical Model (CRFPPM) in Wuhan, China. The CRFPPM is mainly via large range physical model tests to investigate the flood protection situation after the operation of the TGP and the countermeasures for the middle reach of the Changjiang River (formerly named the Yangtze River), and to provide scientific basis for the flood protection planning, engineering construction and flood protection decision, etc. (Zhu et al., 2014). The CRFPPM was broke ground in March 2004. In December 2005, construction of the model was completed.The modeling area of the CRFPPM covers the Yangtze River from Zhicheng to Luoshan (380km long, among which from Zhicheng to Lianhuatang, about 340km long, is called the Jingjiang Reach), the Dongting Lake, the downstream ending reaches of the four main tributaries of the lake (i.e. rivers of Xiang, Zi, Yuan and Li, see Figure 1), and the many small channels connecting the Yangtze River and the Dongting Lake. The horizontal scale of the model is 1:400, and the vertical one is 1:100. Figure 2 shows the experimental hall of the CRFPPM.

**Table 3**.Scour quantity of river channel from Yangjianao to Beinianziwan after the TGP operation ($10^6$ $m^3$)

| | 2002-2006 | 2006-2008 | 2008-2011 | 2011-2013 | 2002-2013 |
|---|---|---|---|---|---|
| **Low water channel** | -71.9 | -47.3 | -77.7 | -22.5 | -219.4 |
| **Bank full channel** | -76.1 | -51.2 | -69.7 | -58.6 | -255.6 |

Note: “+” indicates siltation, “-” indicates scour.


**Figure 2**.Experimental hall of the CRFPPM.

### 4.2 Model verification

The initial river bed topography adopted in the verification tests for the movable bed model is the prototype topographic data measured in November 2008. In the model tests, the flow and sediment process of the Yangtze River from November 2008 to October 2011 is first converted according to similarity scales and then discharged, to reproduce the prototype river bed topography measured in October 2011, and to reproduce the prototype measured water surface profile, cross-sectional flow velocity distribution, flow rate

 

diversion ratio at bifurcated channels, etc. The verification results show that the model can reproduce well the prototype measurements, indicating the model design, the model sand selection and the model scales are reasonable. After the model verification, the sediment concentration scale is fixed as 1:0.75, and the time scale of the river bed scour and siltation is fixed as 1:135, see Table 4 (CRSRI, 2016). For more details about the model, readers are referred to CRSRI (2011) and Zhu et al. (2014).

4.3 Experimental conditions

For the physical modeling of the fluvial process of the Yangjianao-Beinianziwan reach, the initial topography of the river bed for the movable bed model adopted the prototype topographic data measured in October 2011. During the tests, existing river regulation works were modeled (see e.g. Figure 3).

The flow and sediment boundary conditions at the inlet and outlet of the model were provided by the long-term simulation of the river-lake network mathematical model of the CRSRI, which was applied for the justification of the TGP decades ago and was continually improved ever after, see e.g. CRSRI (2002). The prediction period of the physical model tests was from October 2011 to December 2022. In the tests, the process of river channel scour and siltation and the adjustment tendency of the river regime were predicted.

**Table 4.**Summary of the model scales.

| Similarities | Scales | Value of scale |
|---|---|---|
| **Geometrical similarity** | horizontal scale ($\alpha_L$) | 400 |
| | vertical scale ($\alpha_H$) | 100 |
| **Flow dynamic similarity** | velocity scale ($\alpha_v$) | 10 |
| | roughness scale ($\alpha_n$) | 1.08 |
| | discharge scale ($\alpha_Q$) | 400000 |
| **Sediment dynamic similarity** | time scale ($\alpha_{t1}$) | 40 |
| | incipient velocity scale ($\alpha_{V0}$) | 10 |
| | particle size scale ($\alpha_d$) | 0.9 |
| | fall velocity scale ($\alpha_\omega$) | 2.5 |
| | sediment concentration scale ($\alpha_s$) | 0.75 |
| | time scale ($\alpha_{t2}$) | 135 |

**Figure 3**.Photo taken for the model ready for tests (with blue model sands in the channel, and the white ones simulate groynes).

 

## 4.4 Experimental results

### 4.4.1 Quantity and distribution of channel scour

According to the physical model predictions, when the TGP, XLDP and XJBP operate jointly to 2022, the quantity of scour occurred in the bank full channel for the modeling river reach amounts to$1.93\times10^8m^3$, while it amounts to $1.61\times10^8m^3$ for the low water channel. It is therefore indicated that the scour occurs mainly in the low water channel, with less scour above the low water level and even slight siltation at some local positions. It is also observed that different river sub-reaches show different intensities of scour. If sub-divide the modeling river reach into five sub-reaches (see Table 5 and Figure 1), it can be seen that the Haoxue sub-reach has the largest intensity of scour ($1.88\times10^8m^3$/km) and the Gongan sub-reach has the smallest ($0.80\times10^8m^3$/km). Assuming an averaged channel width of 1200m for the modeling river reach, the quantity of scour occurred in the low water channel from 2011 to 2022 can be converted into an averaged depth of scour of 1.12m.

If compare the scour of $1.61\times10^8m^3$ in 2011-2022 to the $2.19\times10^8m^3$ in 2002-2013, one can infer that the intensity of scour is reduced after 2013 or so (from $0.17\times10^8m^3$/km·a to $0.12\times10^8m^3$/km·a) for the Yangjianao-Beinianziwan reach.

**Table 5**.Physical model predictions of low water channel scour from 2011 to 2022 in Yangjianao~ Beinianziwan reach.

| River sub-reach | Yuanshi (6.8km) | Shashi (31.8km) | Gongan (20.1km) | Haoxue (32.5km) | Shishou (28.6km) | Full reach (119.8km) |
|---|---|---|---|---|---|---|
| **Quantity scour ($10^6m^3$)** | 10.0 | 43.0 | 16.0 | 61.0 | 31.0 | 161.0 |
| **Intensity scour ($10^6m^3$/km)** | 1.47 | 1.35 | 0.80 | 1.88 | 1.08 | 1.34 |
| **Depth scour (m)** | 1.23 | 1.13 | 0.66 | 1.56 | 0.90 | 1.12 |

### 4.4.2 Longitudinal variations of Thalweg

Physical model predictions indicate that (Figure 4), when the TGP, XLDP and XJBP operate jointly to 2022, the thalweg of the channel from Yangjianao to Beinianziwan shows a general tendency of scour and downcutting. Positions with relatively strong scour include the downstream part of the concave of river curves (e.g. the Yuanshi curve, Gongan curve, Haoxue curve, and Shishou curve), confluence zone at the end of bifurcated channels (e.g. the Sanbatan bifurcated channel). Experimental results also show that, due to the insufficient sediment supply from the upstream, river bed near the bank where thalweg closely nestling against all suffers significant scour, with low-elevation local scour pits formed and developed, which may threaten the safety of bank slopes.

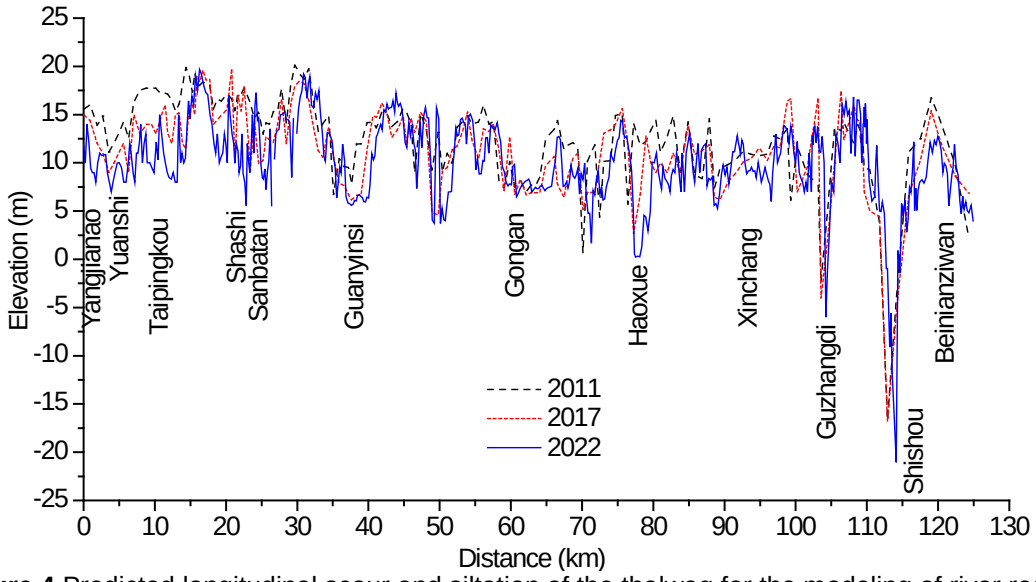


**Figure 4**.Predicted longitudinal scour and siltation of the thalweg for the modeling of river reach.

### 4.4.3 Development of typical cross-sections

Following the cross-sections of S4, J73 and G1 are taken as examples to analyze the development of typical cross-sections after the joint operation of the TGP, XLDP and XJBP (see Figures 1 and 5). The three cross-sections are parts of the conventional cross-sections of the Yangtze River whose section configurations are measured regularly yearly.

 

The S4 section locates at a bifurcated channel (see Figures 1 and 7). With the operation of the TGP, XLDP and XJBP, the left-side channel is scoured down and expands, and the maximum scour depth amounts to 6.9m. Correspondingly, the right-side channel is silted up. The central bar is washed from an original elevation of 35.9m down to about 31m (Figure 5(a)).

The J73 section locates in the upper part of the Haoxue reach (see Figure 1). Generally, this part of river reach is mainly characterized by scouring of the channel and silting of the floodplain. After the operation of the TGP, XLDP and XJBP, the main channel is scoured down from a minimum elevation of 16.7m in 2011 to 10.5m in 2022, indicating a scour depth of 6.2m. Correspondingly, the right-side floodplain is silted by a depth of 3.9m. The section configuration shifts from a “U” shape to a bias “V” shape.

The G1 section locates in the lower part of the Haoxue reach (see Figure 1). As affected by the swing of the thalweg, the right-side channel is scoured down. The elevation drops from originally 21.9m in 2011 to 13.2m in 2022, indicating a scour depth up to 8.7m. The left-side of the section is silted and the section configuration shifts from a wide-shallow “U” shape to a narrow-deep bias “V” shape.

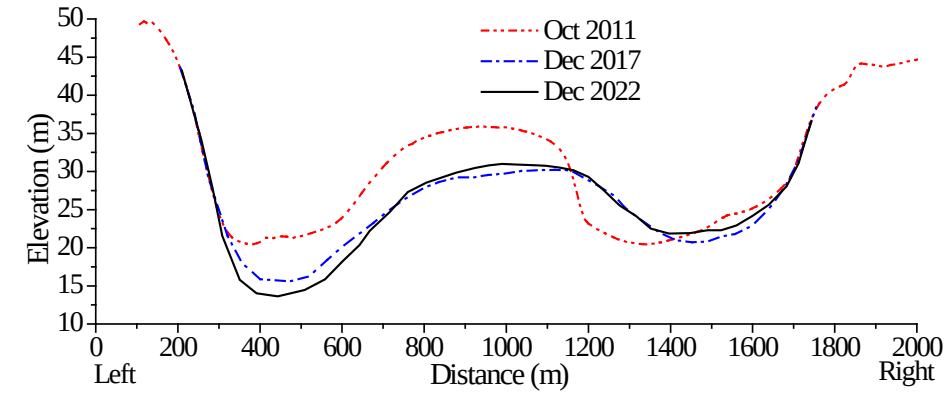


(a) S4 section

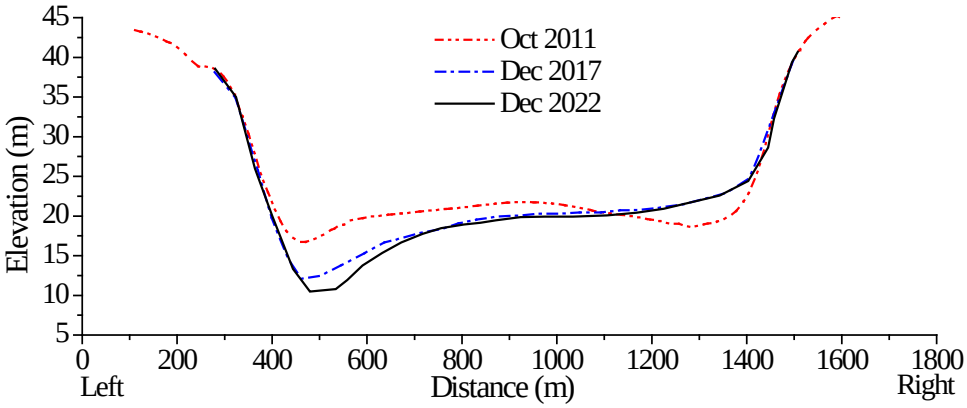


(b) J73 section

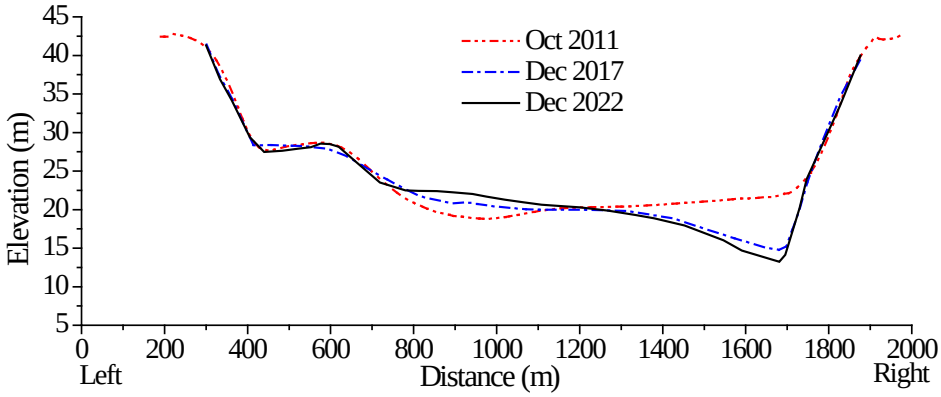


(c) G1section

**Figure 5.** Variation of typical cross-sections.

4.4.4 Tendency of river regime variation

Figure 6 shows a photo of the model after tests. The physical model predictions show that when the TGP, XLDP and XJBP operate jointly to 2022, on the whole, the overall river regime of the investigated river reach (Yangjianao~Beinianziwan) does not change very strongly compared with that in October 2011 (i.e. the initial conditions of the model tests), despite significant scour occurs to the channel. With the lengthening of the projects operation period, in general, the river channel is incised down; the thalweg at transitional river sections swings and moves downstream integrally. However, at certain river sub-reaches, e.g. the bifurcated sub-reach of Shashi, relatively remarkable adjustment of the river regime occurs locally. The sub-reach of Shashi is taken as an example to illustrate the tendency of river regime variation.

It is predicted from the model tests that when the projects operate to 2022, the upper part of Shashi sub-reach shows no large variation of the river regime with only small range of swing of the thalweg (see Figure7). At the end of the Yuanshi curve, the point of flow-split moves downstream by 1.2km from 2011 to 2022. At the Taipingkou section, the bifurcation structure of the river holds continually, with only slight move towards the middle of the river for both the left- and right-side channels due to the shrinkage of the Taipingkou central bar. However, with the change of the flow and sediment conditions from upstream, the Sanba bifurcation section is marked by the expansion of the right-side channel and siltation of the entrance of the left-side channel. To 2022, the thalweg does not go through both channels anymore, instead it flows downstream via the right-side channel only, shows a relatively remarkable adjustment of the river regime.

**Figure 6**.Photo of the model taken after tests.

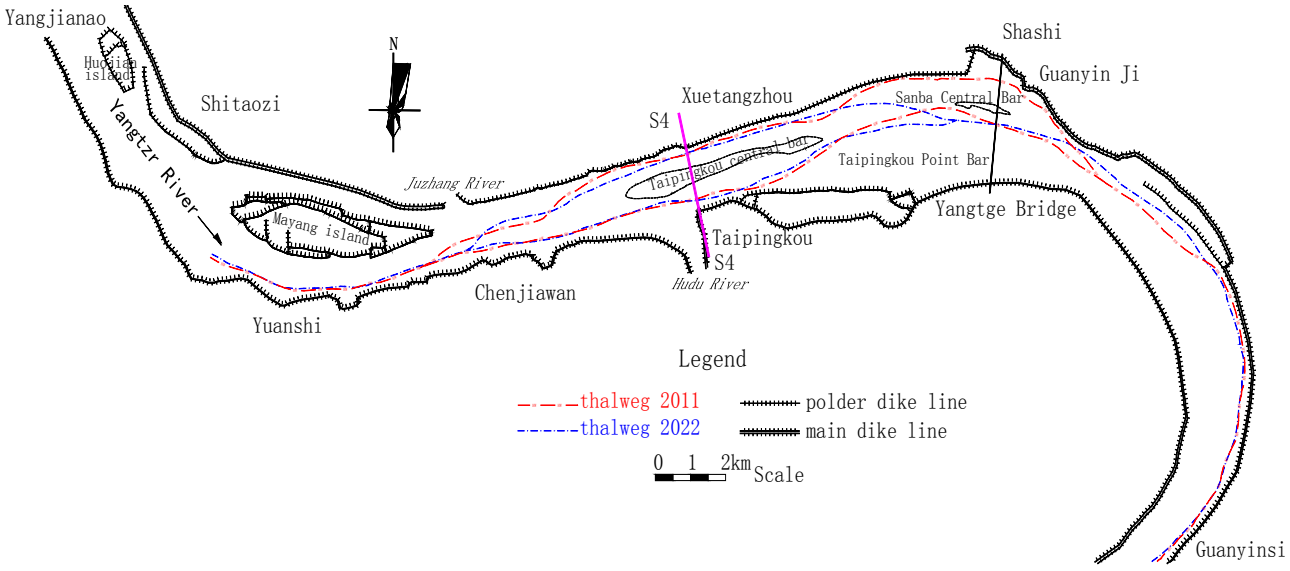


**Figure 7**.Variation of thalweg from Yangjianao to Guanyinsi.

 

## 5 CONCLUSIONS

Construction and operation of the TGP and the upstream XLDP and XJBP in the Yangtze River have already changed and will further change the flow and sediment conditions of the downstream river, and consequently bring significant impacts to the fluvial process of the channel. In this study, physical model tests are performed to predict the scour and siltation of the downstream river channel from Yangjianao to Beinianziwan after joint operation of the three gigantic projects, and to predict the tendency of river regime development as well.

Results of the physical model tests indicate that, from 2011 to 2022, significant scour occurs to the river channel from Yangjianao to Beinianziwan, and the scour occurs mainly in the low water channel, with less scour above the low water level and even slight siltation at some local positions. The quantity of scour occurred in the low water channel amounts to $1.61\times10^8$ $m^3$, about 1.12m in terms of averaged scour depth of the channel. The thalweg of the channel shows a general tendency of scour and down cutting. River bed near the bank where thalweg closely nestling against suffers quite significant scour, imposing potential threat to the safety of bank slopes. The overall river regime of the investigated river reach does not change very strongly during the modeling period, despite significant scour occurs to the channel. However, relatively remarkable adjustment of the river regime occurs locally at certain river sub-reaches, e.g. the bifurcated sub-reach of Shashi.

Since more hydropower projects with large reservoirs are still under construction in the upper reach of the Yangtze River, it is expected that the hydrological regime of the downstream river will suffer further change and the channel evolution will become more complicated. Further research on the fluvial process of the downstream river is still necessary and meaningful.

## ACKNOWLEDGEMENTS

This study was financially supported by the National Natural Science Foundation of China (Grant No. 51339001), the National Key Research and Development Program of China (Grant No. 2016YFC0402305 and 2016YFC0402310), and the Public Welfare Scientific Research Funding Project of the MWR of China (Grant No. 201401011).

## REFERENCES

CRSRI. (2002). *1D Mathematical Modeling of the Scour and Siltation of the River Channel from Yichang to Datong Downstream of the TGP, In Expert Panel on Sediment Problems of TGP (Ed.)*, *Research on the Sediment Problems of the TGP (1996-2000)*. Intellectual Property Press, Beijing, China. (In Chinese)

CRSRI. (2011). *Evolution and Regulation of the Jingjiangriver in The Early Operation Phase of the Three Gorges Project*, The Changjiang River Scientific Research Institute, Wuhan, China. (In Chinese)

CRSRI. (2016). *Riverbed Reformation Process and Influences of the Jingjiangriver After the Operation of the Three Gorges Project*, The Changjiang River Scientific Research Institute, Wuhan, China. (In Chinese)

Xu, Q.X., Zhu, L.L. & Yuan, J. (2013). Research on Water-Sediment Variation and Deposition-Erosion in Middle and Lower Yangtze River. *Yangtze River*, 44(23), 16-21. (In Chinese)

Zhu, Y.H., Lu J.Y. & Fan, B.L. (2014). On The Progress of Research of the Changjiang River Flood Protection Physical Model. *Proceedings of 2013 IAHR World Congress*, Chengdu, China.

 

Proceedings of the 37th IAHR World Congress
August 13 – 18, 2017, Kuala Lumpur, Malaysia

# EXPERIMENTAL STUDY ON TIDAL BASIN MANAGEMENT: A CASE STUDY OF BANGLADESH

ROCKY TALCHABHADEL[(1)], HAJIME NAKAGAWA[(2)], KENJI KAWAIKE[(3)] & NASSIM SAHBOUN[(4)]

[(1)]Department of Civil and Earth Resources Engineering, Kyoto University, Japan
rocky@uh31.dpri.kyoto-u.ac.jp
[(2,3)] Disaster Prevention Research Institute, Kyoto University, Kyoto, Japan
nakagawa@uh31.dpri.kyoto-u.ac.jp; kawaike.kenji.5n@kyoto-u.ac.jp
[(4)]Grenoble INP-Ense3, Grenoble Institute of Technology, France
nassimsahboun@gmail.com

## ABSTRACT

The presence of coastal polders has aggravated the siltation problem in tide-dominated rivers and has reduced the conveyance of the rivers significantly leading to large-scale water-logging problems inside the peripheral polders. Tidal Basin Management (TBM) is the initiative to address this problem. It involves temporary de-poldering by cutting embankment in selected tidal basin. During high tides, muddy water enters into selected tidal basin and during low tides, clear water comes back eroding the riverbed. Sedimentation determines the life span of a basin and the rate of raising the land. It is essential to understand the process efficiently for sustainable operation and rotation of tidal basins. One of the key governing factors affecting the flow and sedimentation is the opening size of link canal that connects tidal basin with a river. In this research, attempts have been made to investigate the effectiveness of TBM exploring different opening sizes of link canal through laboratory experiments and numerical simulations. Four different cases with opening sizes of link canal varying from 0.7 times river width to thrice the river width are investigated. Our finding shows even sediment carrying capacity is the function of velocity, only increasing the opening size will not allow more sediment to deposit in selected tidal basin. A natural force will tend to restore the equilibrium condition. It is recommended that the opening size equals to river width of a tidal river in tidal equilibrium works efficiently. Developed numerical model has good agreement with experimental results and can be used in a real scenario to better understand the effectiveness of the process.

**Keywords:** Beel; opening size; suspended sediment; TBM; TRM.

## 1 INTRODUCTION

Bangladesh is the biggest delta of the world. The rivers of the southwestern region in Bangladesh are characterized by active deposition of sediment. The estuarine rivers witness two cycles of tides every day (Kibria, 2011). In earlier decades before the 1960s, when polders were not constructed, low-lying areas (*beels*) of coastal zone were frequently flooded by saline water during high tide (Islam *et al.*, 2013). In order to increase agricultural production, a series of polders enclosing the *beels* were built (BWDB, 2003).

They had initially created good scope for growing agricultural crops by preventing the intrusion of saline water. But the presence of such polders de-linked the flood plain leading to gradual silting up of rivers. As the land development of the *beels* stopped, these lands became lower than river beds and vast area under the polders became permanently waterlogged rendering large tract of lands uncultivable(Leendert, 2013). To solve this issue, temporary de-poldering by cutting embankment is done (Talchabhadel *et al.*, 2016a) and certain areas are to be kept aside as tidal floodplain. A link canal so created connects the tidal basin (selected *beel*) with the river (Ibne Amir *et al.*, 2013). Muddy water enters the tidal basin during high tide with a thick concentration of sediments, depositing a major portion of suspended sediments before flowing back towards the sea during low tide (Ibne Amir *et al.*, 2013; Khadim *et al.*, 2013; Kibria, 2011).

Tidal basin acts as tidal storage basin which allows natural tidal flows up and down in the river system. This sedimentation would occur into the riverbed if it is not utilized for storage as a sedimentation trap (Ibne Amir *et al.*, 2013; Paul *et al.*, 2013; Rahman and Salehin, 2013). Over time, the depositions of sediment raise a land level in the selected tidal basin. Such tidal basins are to be rotated among various lowlands within the system so that farmers of one tidal basin do not have to suffer a long time, the process known as TBM. Since this process does not allow sediment to be deposited on the riverbed, the depth of the riverbed also increases and makes the river congestion free. Such process of river management is named as Tidal River Management (TRM) (Kibria, 2011; Shampa and Pramanik, 2012).

Three tidal basins were operated successfully in Khulna-Jessore Drainage Rehabilitation Project (KJDRP) shown in Figure 1[right]. Proposed long-term plan for rotational tidal in KJDRP could not happen due to some social and technical problems. On the other hand, Kobadak basin TBM has also similar rotational plan, of which Pakhimara *beel* is currently operational. Field visit to both locations was done in May 2016 as

 

shown in Figure 1 and Figure 2. Google images on 2013 and 2015 shown in Figure 2 clearly show that during operation of TBM, the embankment is cut and natural movement of high and low tides is allowed.

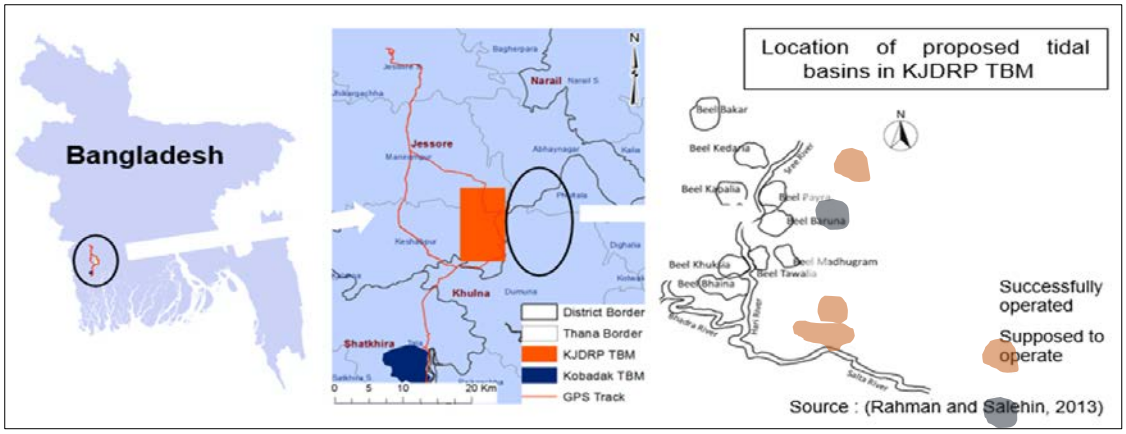


**Figure 1.** Successfully operated TBM and operational TBM in Bangladesh.

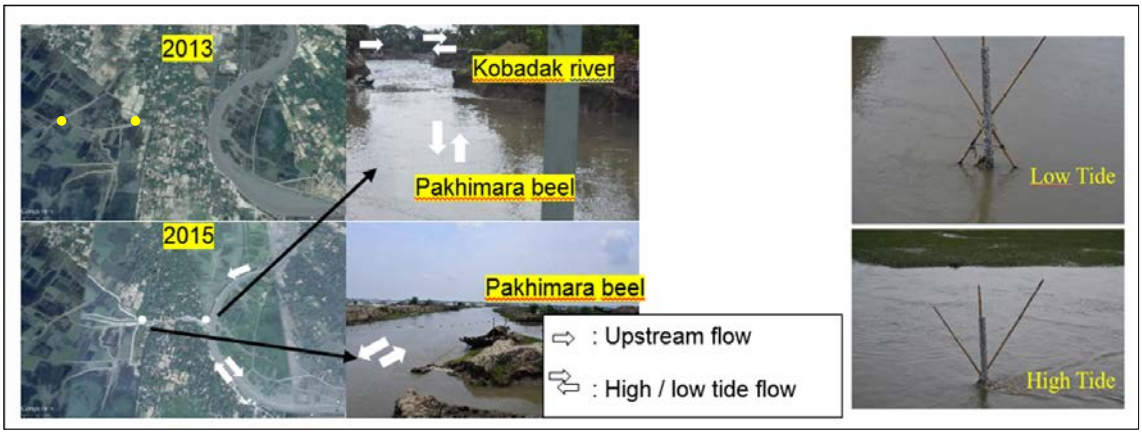


**Figure 2.** Operational Kobadak River TBM effective from 11 July 2015 [Google images on 2013 and 2015 & Field based photographs taken on 9 May 2016].

Since sedimentation determines the life span of a basin and the rate of raising the land, better understanding of sedimentation process is necessary. One significant hydraulic fact is that the faster the river flow is, the more sediment it can carry with it (Talchabhadel *et al.*, 2016b). One of the key governing factors of the flow is the opening size of link canal. The general dimensions of the opening size are carried out by establishing a consistent relation with tidal prism (Rezaie, 2013; Talchabhadel *et al.*, 2017). In this research, this paper has attempted to inspect the effectiveness of TBM exploring different opening sizes of link canal through laboratory experiments and numerical simulations.

## 2 EXPERIMENTAL SETUP

The experiments were carried out at Ujigawa Open Laboratory (UOL) of Disaster Prevention Research Institute, Kyoto University. The experimental setup was prepared considering simplified version of TBM. The experiment flume was made with an acrylic plastic material. The experimental facilities are illustrated in schematic view in Figure3 and photographic view in Figure 4 [left]. All experiments were carried out in fixed and flatbed using a constant discharge of 5.1 l/s as upstream river flow ($Q_{river}$) whereas 2.8 l/s as downstream tidal flow ($Q_{tide}$). To represent alternative high and low tidal flow, an adjustable gate was used. To represent high tide, the gate was closed for 2 mins and downstream flow from water pump was supplied along with dry sediment supply from sediment feeder. After then, the gate was opened for the next 2 min. At that time, downstream supply of water and sediment were stopped representing low tide. Same processes were repeated. Two complete tidal cycles in a day in the real case of Bangladesh (Kibria, 2011) here is attempted to represent with 8 min experimental case (i.e. 2 min high tide and 2 min low tide for one tidal cycle).

The dry sediment of mean diameter equal to 94 µm and density 2.65 gm/cc was fed from sediment feeder (Spiral Feeder, NX-3000M) with a speed of 2gm/s. The critical shear velocity was calculated by using the Iwagaki Formula (Iwagaki, 1956). The details of hydraulic conditions are shown in Table 1. With the Rubey's Formula (Rubey, 1933), the sediment falling velocity was estimated to be $w$=0.75 cm/s. Four cases were investigated by varying the size of the opening canal towards tidal basin. Three blocks namely 1, 2 and 3 shown in Figure2 were adjusted to control the opening size of link canal.

 

Case I: 1000 mm openingCase II: 700 mm opening
Case III: 400 mm openingCase IV: 200 mm opening

All of the four cases were done for 10 hrs each. During that time, measurements of flow velocity, suspended sediment concentration (SSC) and final bed level were done. An electromagnetic current meter was used to measure flow velocity and turbidimeter to measure SSC. For measurement of final bed level data, laser displacement sensor was used. Additionally, photogrammetric processing of digital images taken by Nikon 1 J5 was also investigated using Agisoft PhotoScan Professional Edition Version 1.0.4 Multi-view 3D reconstruction.

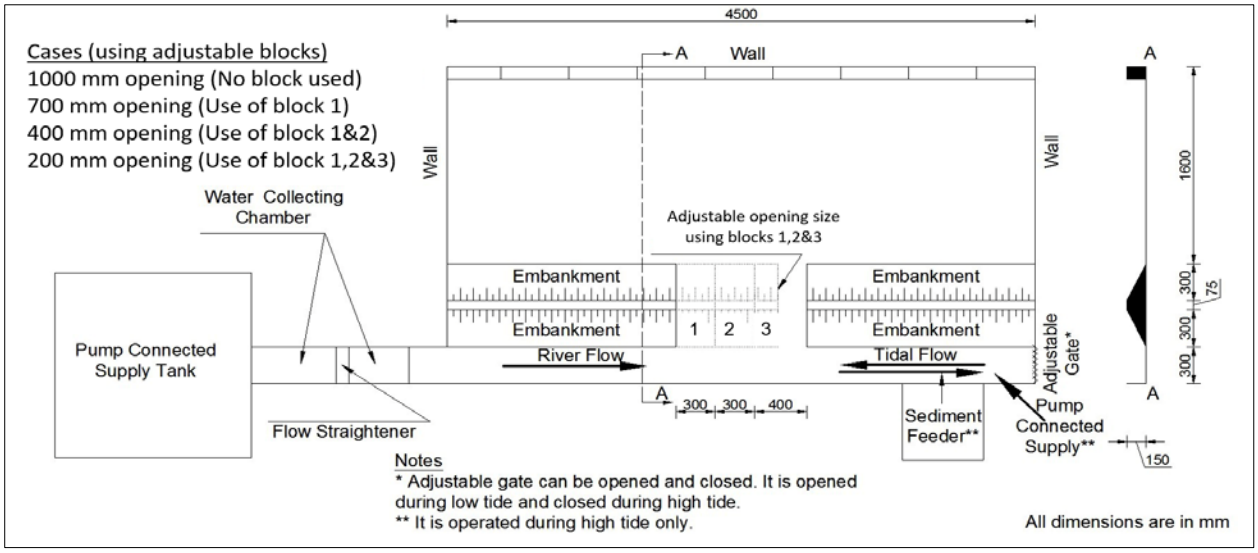


**Figure 3.** Schematic view of the experimental setup.

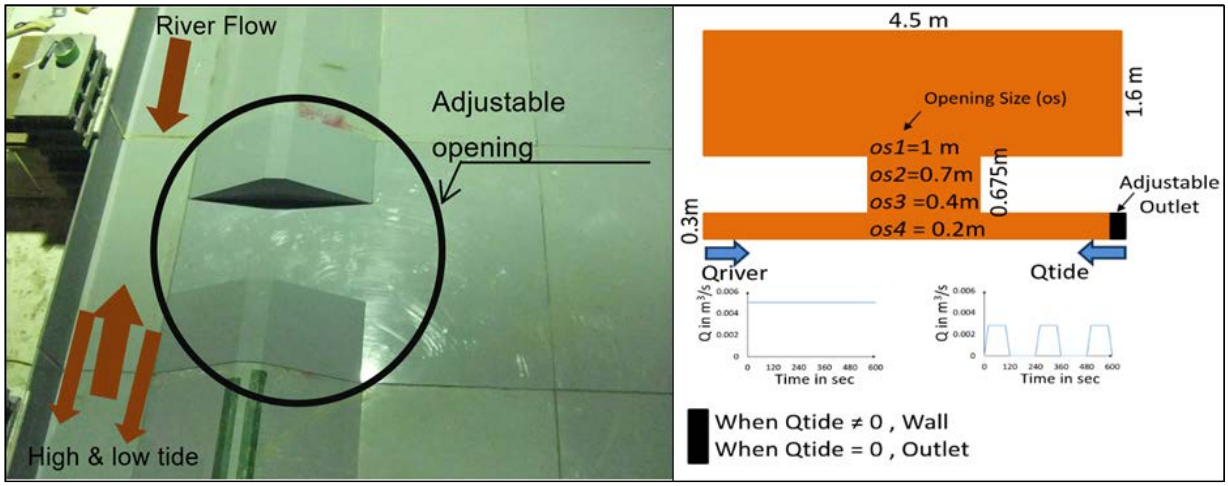


**Figure4.** Experimental facility [left] and Boundary condition treatment in numerical simulation [right].

**Table 1.** Details of Hydraulic Conditions.

| River Discharge | Tidal Discharge | Mean velocity [fluctuating due to tide] | Flow Depth | Shear Velocity | Shear Velocity Ratio | Reynolds | Froude | Rouse |
|---|---|---|---|---|---|---|---|---|
| $Q_{river}$(l/s) | $Q_{tide}$(l/s) | u (cm/s) | h (cm) | $u_*$ (cm/s) | $(u_*/u_{*c})$ | number | number | number |
| 5.10 | 2.80 | 12.00 [Take] | 10.00 | 1.30 | 0.92 | 7169 | 0.15 | 1.38 |

## 3 NUMERICAL MODEL

Efforts have been made to develop a numerical model to simulate experimental conditions. Constant $Q_{river}$ from upstream and alternating $Q_{tide}$ from downstream are provided (shown in Figure 4[right]). The experimental boundary condition was applied in downstream boundary: when $Q_{tide}$ was supplied for 2 min, the boundary treated as wall representing closing of experimental gate whereas during no supply of $Q_{tide}$ for next 2 min, the boundary treated as opening of gates and allowed to flow freely representing the experimental gate was open as shown in Figure 4. Sediment was supplied constantly at downstream boundary as in the case of

 

dry sediment supply from sediment feeder in the experiment. Same process was repeated throughout the simulation.

The simulation model used in this study was structural gridded (grid size 10cm x 10cm) two-dimensional (2D) unsteady flow model based on a shallow-water equation:

$$\frac{\partial h}{\partial t}+\frac{\partial M}{\partial x}+\frac{\partial N}{\partial y}=0 \quad [1]$$

$$\frac{\partial M}{\partial t}+\frac{\partial (uM)}{\partial x}+\frac{\partial (uM)}{\partial y}=-gh\frac{\partial H}{\partial x}-\frac{gn^2u\sqrt{u^2+v^2}}{h^{1/3}} \quad [2]$$

$$\frac{\partial N}{\partial t}+\frac{\partial (uN)}{\partial x}+\frac{\partial (VN)}{\partial y}=-gh\frac{\partial H}{\partial y}-\frac{gn^2v\sqrt{u^2+v^2}}{h^{1/3}} \quad [3]$$

Where, *h* is the water depth (m), *M* and *N* are fluxes in the *x* and *y* directions ($m^2/s$), *u* and *v* are velocities in the *x* and *y* directions (m/s), *H* is the water level (m) and *g* is the acceleration of gravity ($m/s^2$). To solve this equation, leap frog difference scheme was employed. Suspended sediment transport was simulated using the equations:

$$\frac{\partial (Ch)}{\partial t}+\frac{\partial (CM)}{\partial x}+\frac{\partial (CN)}{\partial y}=D\left(\frac{\partial^2 (Ch)}{\partial x^2}+\frac{\partial^2 (Ch)}{\partial y^2}\right)+E+Cw \quad [4]$$

$$w=\sqrt{\frac{2}{3}\left(\frac{\sigma}{\rho}-1\right)gd+\frac{36v^2}{d^2}}-\frac{6v}{d} \quad [5]$$

$$E=wC^* \quad [6]$$

$$C^*=0.015\frac{dT^{1.5}}{aD_*^{0.3}} \quad [7]$$

$$D_*=d\left[\frac{\left(\frac{\sigma}{\rho}-1\right)g}{v^2}\right]^{1/3} \quad [8]$$

$$T=\frac{\tau-\tau_c}{\tau_c} \quad [9]$$

where *C* is the concentration of sediment ($g/m^3$),*D* is a coefficient of diffusion ($m^2/s$), *E* is the parameter of flowing up ($g/m^2s$), *w* is the settling velocity (m/s), $\sigma$ is the density of sediment particles ($kg/m^3$), $\rho$ is the water density ($kg/m^3$), *d* is the diameter of sediment particles (m) and $\nu$ is the coefficient of kinematic viscosity of water ($m^2/s$), $C^*$ is the equilibrium concentration of sediment using (Van Rijn, 1984),$a$ is the reference level taken 0.01*H*, $D_*$ is the particle size parameter, *T* is an excess bed shear stress parameter, $\tau$ is the bottom shear stress ($g/ms^2$) and $\tau_c$ is the critical bottom shear stress ($g/ms^2$) according to Shields . Given the situation, D was set to 0.1 $m^2/s$. Bed load transport rate was calculated by the equation of (Ashida and Michiue, 1972).

$$\frac{q_b}{\sqrt{\left(\frac{\sigma}{\rho}-1\right)gd^3}}=17\tau_*^{\frac{3}{2}}\left(1-\frac{u_{*c}}{u_*}\right)\left(1-\frac{\tau_{*c}}{\tau_*}\right) \quad [10]$$

Where $q_b$ is the bed load discharge ($m^2/s$),$\tau_*$ and $\tau_{*_c}$ are dimensionless shear stress and critical shear stress(Iwagaki, 1956),$u_*$ and $u_{*_c}$ are friction velocity and critical friction velocity(m/s). These parameters were calculated through following relations:

$$\tau_* = \frac{{u_*}^2}{\left(\frac{\sigma}{\rho}-1\right)gd} \quad [11]$$

$$\tau_{*c}=\frac{{u_{*c}}^2}{\left(\frac{\sigma}{\rho}-1\right)gd} \quad [12]$$

 

$$\tau_{*c}=\begin{cases}0.05 & \text{if } R_* \geq 671.0\\ 0.00849R_*^{3/11} & \text{if } 162.7 \leq R_* < 671.0\\ 0.034 & \text{if } 54.2 \leq R_* < 162.7\\ 0.195R_*^{-7/16} & \text{if } 2.14 \leq R_* < 54.2\\ 0.14 & \text{if } R_* < 2.14\end{cases} \quad [13]$$

$$R_*=\frac{\sqrt{\left(\frac{\sigma}{\rho}-1\right)gd^3}}{\nu} \quad [14]$$

The bed level changes were computed from the information of bed load and suspended load transport rates using the mass-balance equation.

$$(1-\lambda)\frac{\partial z_b}{\partial t}+\frac{\partial q_{bx}}{\partial x}+\frac{\partial q_{by}}{\partial y}+(E-Cw)=0 \quad [15]$$

Where $\lambda$ is the sediment porosity, $q_{bx}$and $q_{by}$ are bed load transport rates in the x and y directions.

## 4 EXPERIMENTAL RESULT AND DISCUSSION

During the entire experiment, it is very difficult to repeat same conditions of sediment and water flow from downstream as high tide representation throughout. Averaging of measured SSC is done in all sampling points to determine the SSC at different sampling points. Sampling points [P1-P36] for case IV are shown in Figure 5. The density of sampling points around link canal is made very higher [P1-P15] to better understand spatio temporal SSC distribution. SSC variation during high tides [2 min] and low tides [2 min] for those 36 sampling points for case IV are shown in boxplots in Figure 6. In all other cases, SSC measurement is done similarly.

SSC during high tides are shown in brown and during low tides in black for 36 sampling points [P1-P36] for case IV in boxplots in Figure 6.SSCs during high tides are quite higher than during low tides. Moreover, SSC fluctuations from mean values during high tides are quite larger than during low tides. Around link canal, SSC decreases as the distance from tidal source increases. SSC around [P1-P5] is greater than SSC around [P6-P10] is again greater than SSC around [P11-P15]. According to measured SSC around tidal basin [P16-P36], the lateral distribution of SSC is more or less symmetrical and it also shows a similar result of greater the distance, lesser the SSC. But wall effects are clearly seen around the sampling points near to side walls. The more the distance from tidal source increases, SSC decreases but due to wall effects, SSC around [P16-P18] is greater than SSC around [P19-P21]. Similarly, SSC around [P18,P21,P24,P27,P30,P33,P36] is greater than SSC around [P17,P20,P23,P267,P29,P32,P35]. In all other cases, it has similar patterns.

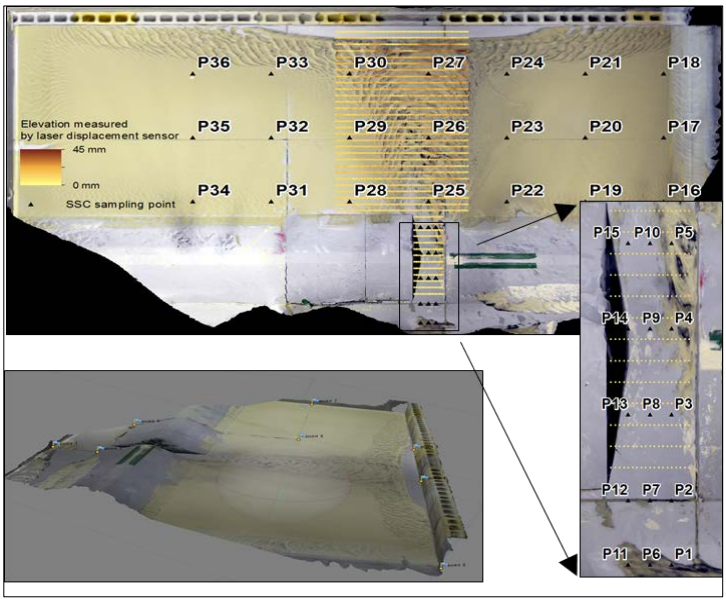


**Figure 5.** Sampling points for SSC measurement [P1 – P36], laser measurement points [yellow to brown] over background of 3D analysis by photogrammetric processing for case IV.

 

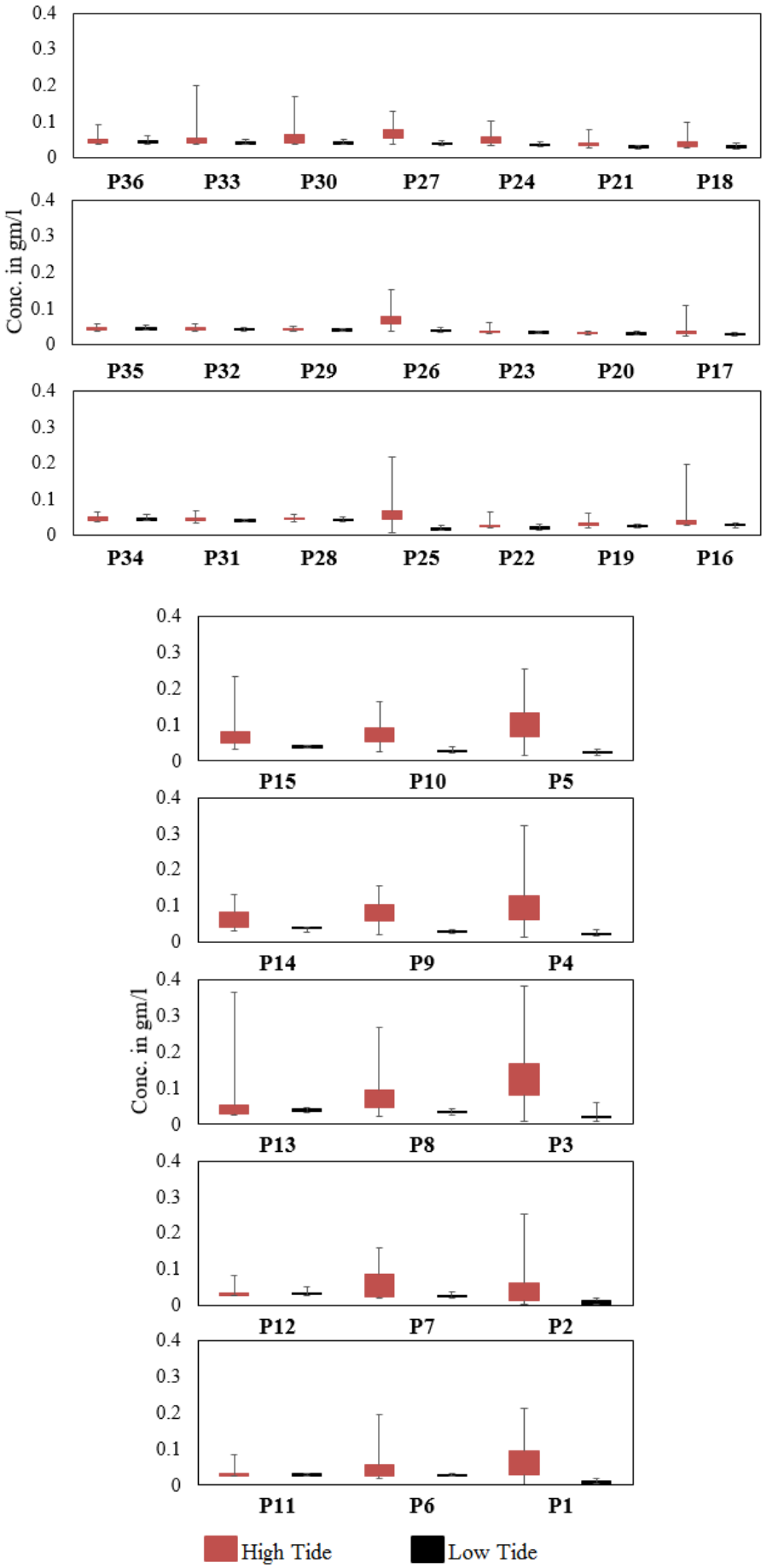


**Figure 6.** Box plots of SSC during high and low tide at 36 sampling points [P1- P36] for case IV.

The spatially distributed SSC at a time during high tide is shown in Figure 7[left]. The line graph at top of Figure 7[left] shows temporal variation of SSC at black dotted location. Similar patterns of temporal distribution of SSC are seen in all sampling points in all four cases. Figure 7[right] is the final bed level after 10 hrs of repetitive high and low tides for case IV. Digital images with 5568 X 3712 pix [pixel size (mm) = 0.00239464 X 0.00239464] and focal length (10 mm) were taken from different angles and heights. 164 images were processed photogrammetrically to generate three-dimensional (3D) spatial data. Generated 3D topographical data was geo-referenced at known control points as shown in Figure 5 (bottom left). The accuracy of photogrammetry analyzed bed level is checked with laser displacement sensor at 2711 points and they both have an acceptable agreement with 2.45 percent bias, 0.4 mm mean error and regression coefficient 0.82.

Bed level measurement from the laser displacement sensor was done around link canal. Figure 8 shows the final bed level condition after 10 hrs in all four cases. In case I, it is quite clear the spacious width has not been properly consumed for sediment transport and deposition. In case II, sediment has been transported and deposited in a substantial amount. But on the link canal itself, a huge amount of sediment gets deposited. The flow during low tide, when it flows out from tidal basin, is not sufficient to erode sediment around link canal. In the case of case III, a significant amount of sediment has been transported and deposited along with significant erosion during low flow coming out. In case IV, the deposited sediment around link canal during high tide has been significantly eroded by the flow of low tide. The flow coming out of tidal basin has sufficient shear stress to erode deposited sediment around link canal and river which effectively solves drainage congestion in the river downstream. To suggest the optimum size of opening size, more experiments are needed with varying opening sizes between case III and case IV. The current research has demonstrated effective TBM processes in narrower opening cases [case III and case IV] than wider opening cases [case I and case II].

In all cases, vortex-like formations have occurred with high shear stress at the embankment nearer to the tidal source where high tide directly hits during flowing towards tidal basin and low tide during flowing out of the tidal basin. In a real case of TBM, it also happens like that. To prevent lateral erosion in link canal in a real case, concrete blocks are normally used. One of the existing problems in raising of land by TBM in real field scenario is non-uniform and unequal sedimentation around selected tidal *beel* which is also seen in experiment.

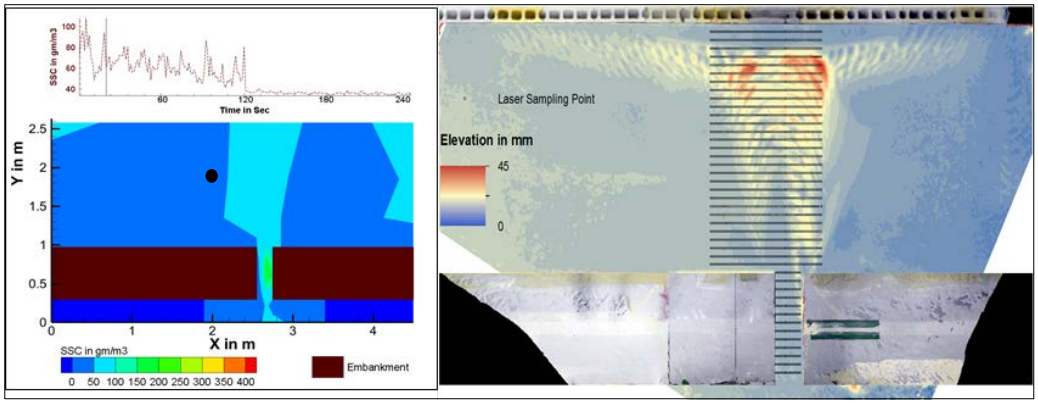


**Figure 7.** SSC [left] and bed level [right] for case IV.

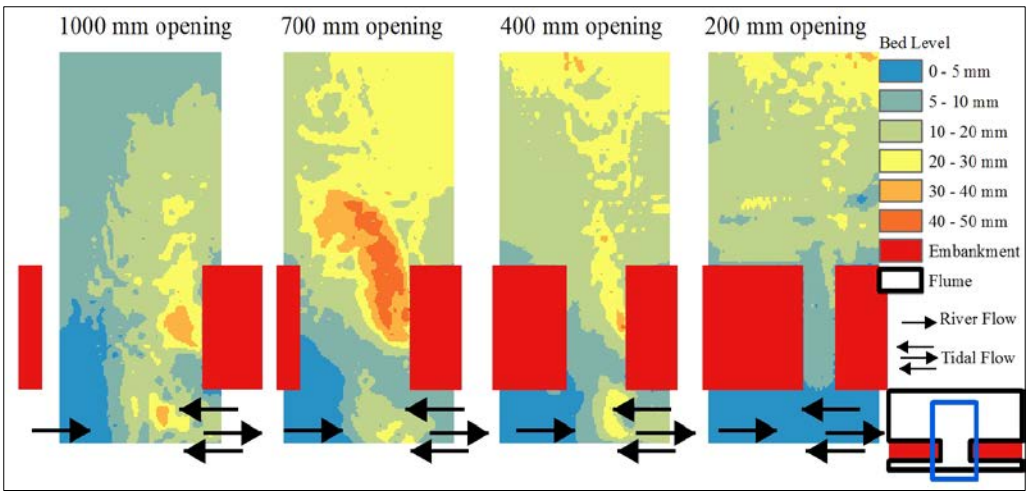


**Figure 8.** Final bed level after 10 hrs of experiment in all four cases.

## 5 NUMERICAL MODEL RESULT AND DISCUSSION

The current experimental condition has been simulated preliminary with a numerical model. Water level and SSC fluctuations have been simulated which have good agreement with experimental data for all four cases. Figure 9 shows the sample simulation result of water level, SSC fluctuations and deposited sediment for case III and case IV. The line graphs show temporal variation of water level, SSC and deposited sediment at a black square location shown in Figure 9. In all cases, numerical simulations could not show instantaneous peak value of SSC and rapid temporal fluctuation of SSC. The sample result of comparison between experimental and simulated SSC at P7 is shown in Figure 10. In the narrower opening in case III and case IV, flow velocity at link canal during low tide is quite high as accumulated water starts coming out from the tidal basin which erodes sediment demonstrating an effective process of TBM. Due to the limited size of the tidal basin in current experimental condition, the wall effect has clearly been seen in all four cases.

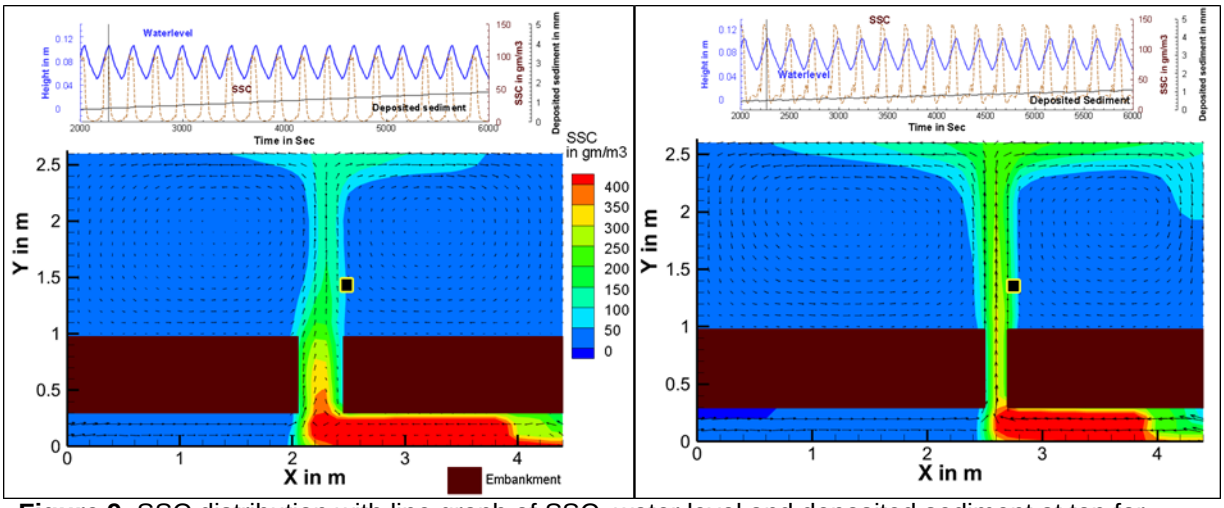


**Figure 9.** SSC distribution with line graph of SSC, water level and deposited sediment at top for case III (left) and case IV (right).

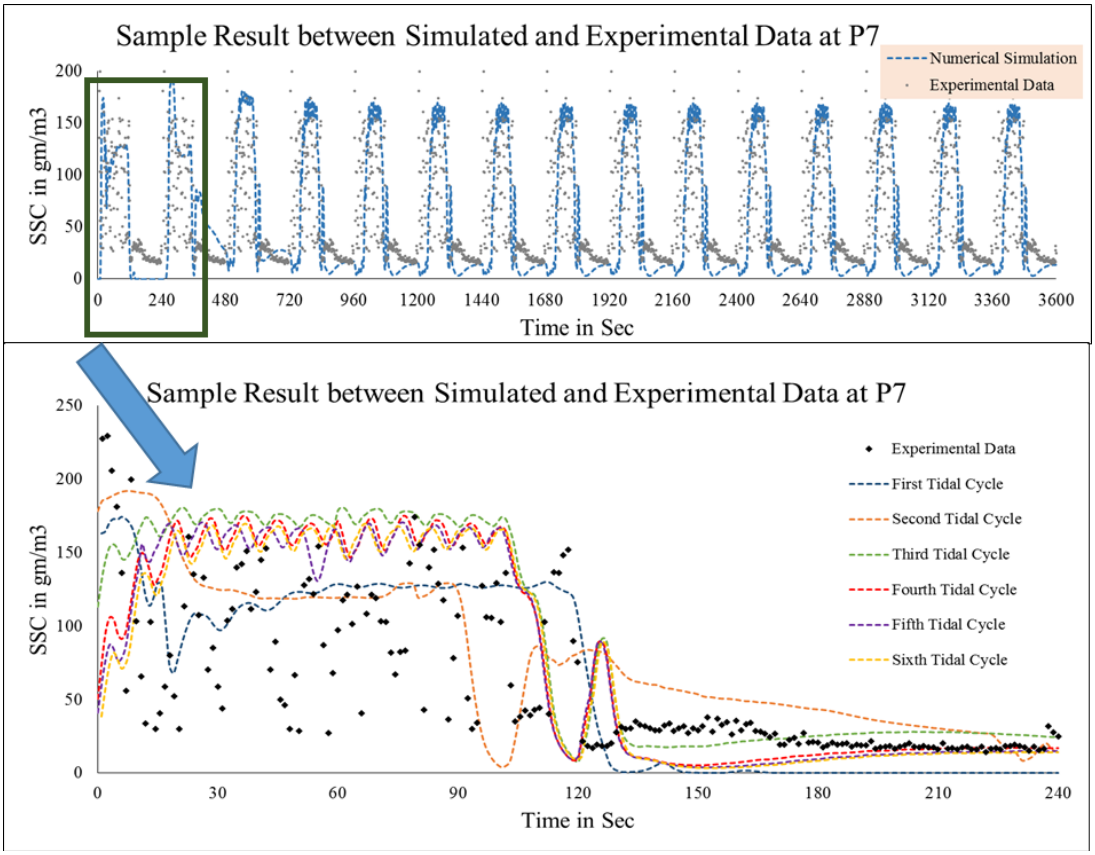


**Figure 10.** Comparison of simulated and experimental SSC for case IV at P7.

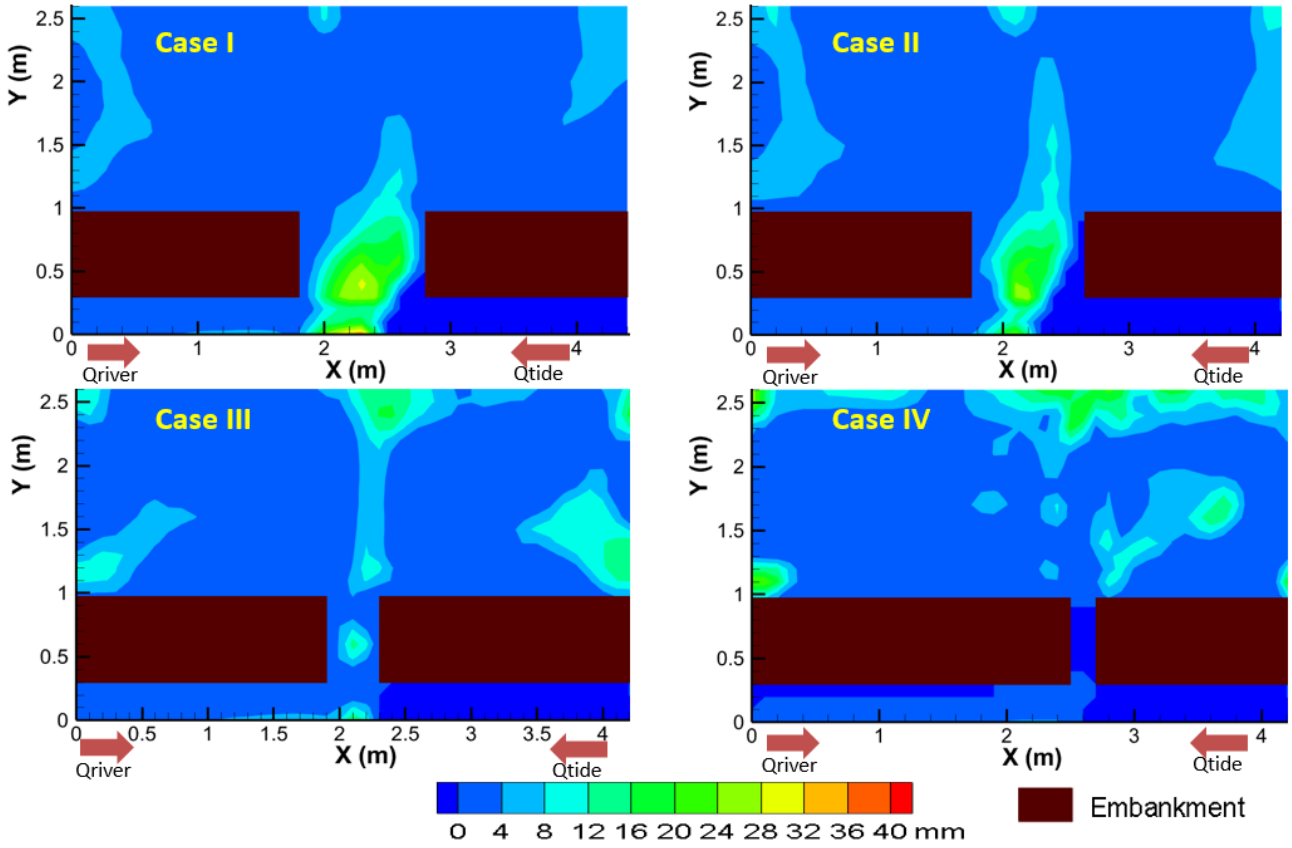


**Figure 11.** Final simulated bed level after 10 hrs. of repetitive high and low tides in different cases.

The simulated final bed level after 10 hrs of repetitive high and low tides are shown in Figure 11. The complex vortex formation at embankment where tidal flow enters during high tide and leaves during low tide, could not be simulated by this 2D simulation model. Depositions of sediment on the course of link canal are seen in wide opening sizes [case I and case II]. Without increasing the tidal prism, just increasing the opening size results in an unsustainable solution. Even the bed deformations have not been simulated in a realistic experimental pattern, effective operation of TBM has clearly been simulated in narrower opening size like in case III and case IV. From this simulation, it can be inferred that the effective operations of TBM are seen when the opening size is more or less equivalent to the natural width of a river. [River width = 30 cm, case III's opening size = 40 cm and case IV's opening size = 20 cm].

## 6 CONCLUSIONS

TBM involves taking full advantages of the natural tide movements in rivers. During high tide, the tide is allowed to enter into selected tidal basin where sediment is deposited and in low tide, water flows out with greatly reduced sediment load and eventually erodes the downstream riverbed. TBM maintains proper drainage capacity in the river. Sediment carrying capacity is a function of velocity. Moreover, only increasing the width of link canal will not allow more sediment to deposit in selected tidal basin. The natural force will tend to restore the equilibrium condition by siltation in spacious opening of link canal. A consistent relationship among tidal prism and a minimum cross-sectional area can be established for which abundant amount of field-based data of the tidal river is needed.

Case III and case IV have represented TBM process quite acceptably so from the current research, it can be inferred if the existing river is not constrained by any civil structure and human interventions (i.e. it is in tidal equilibrium), then the recommended opening size of link canal is almost equaled to the natural width of river. The current research has limitations of fixed and flatbed, the limited size of the tidal basin, perpendicular alignment of link canal, an unrealistic tidal-like representation using adjustable gates etc. in the experiment. The current findings have to be extended in the next stage of experiments.

The accuracy of photogrammetry analyzed bed level has been checked with laser displacement sensor. In the case of experimental measurement, the mean error is less than 1 mm which is satisfactory. For spatially large area and when different experimental circumstances do not permit to measure with high precision or when it is difficult to measure with sophisticated instruments like laser displacement sensor throughout the area of interest, photogrammetric processing of digital images seems a wise decision for topographical data preparation. Next plan is to examine the precision of photogrammetric analyzed elevation to compare with topographical data in real field based case of floodplain topographic measurement.

 

The numerical simulation shows acceptable agreement for water level and SSC in experimental case. Model parameters need to be improved by considering flow-up parameter for sediment transport to better simulate bed load transport and bed level change. TBM process has been simulated successfully in varying the sizes of openings. The next plan is to simulate TBM process numerically with real field based data of Bangladesh which is currently in progress. *East Beel Khuksia* TBM is taken as a case study area after the field visit around South West region of Bangladesh. One of the pertaining problems in raising of land by TBM in real field scenario is non-uniform and unequal sedimentation around selected tidal *beel*. The next stage of research will try to address this issue. Simultaneously, for the replication of local erosion and deposition, complex vortex formation and precise bed load transport and deformation process, a 3D numerical model is also in progress.

## ACKNOWLEDGMENTS

The research is supported by JST/JICA SATREPS program on disaster prevention/mitigation measures against floods and storm surges in Bangladesh (PI: Dr. H. Nakagawa).The authors wish to thank Tai Shuichi (Undergraduate's student in Kyoto University) and Jun Nakagawa (staff in UOL) for their help in conducting the experiment. The authors warmly thank Dr. Masakazu Hashimoto for his valuable advice, discussion and friendly help during the development of numerical simulation model. The first author is pleased to acknowledge a Monbukagakusho scholarship for graduate students.

## REFERENCES

Ashida, K. & Michiue, M. (1972). Study on Hydraulic Resistance and Bedload Transport Rate in Alluvial Streams*. Transactions of Japan Society of Civil Engineering*, 206, 59-69. (In Japanese)

BWDB. (2003). *Bangladesh* Water Development Board Khulna-Jessore Drainage Rehabilitation. *Project Final Report,* Part A: Monitoring and Integration,

Ibne Amir, M.S.I., Khan, M.S.A., Kamal Khan, M.M., Golam Rasul, M. & Akram, F. (2013). Tidal River Sediment Management - A Case Study in Southwestern Bangladesh. *International Journal of Civil Science and Engineering,* 7(3), 175 - 185.

Islam, M.S., Alam, R., Khan, M.Z.H., Khan, M.N.A.A. & Nur-A-Jahan, I. (2013). Methodology of Crest Level Design of Coastal Polders in Bangladesh*. 4th International Conference on Water & Flood Management.*

Iwagaki, Y. (1956). Fundamental Study on Critical Tractive Force. *Transactions of Japan Society of Civil Engineering,* 41, 1 - 21.

Khadim, F.K., Kar, K.K., Halder, P.K., Rahman, M.A. & Morshed, A.K.M.M. (2013). Integrated Water Resources Management (IWRM) Impacts in South West Coastal Zone of Bangladesh and Fact-Finding on Tidal River Management (TRM). *Journal of Water Resource and Protection*, 5(10), 953–961.

Kibria, Z. (2011). *Tidal River Management (TRM) Climate Change Adaptation and Community Based River Basin Management and in Southwest Coastal Region of Bangladesh.* Rivers & Communities, 1(1).

Leendert, F.D. (2013). Tidal River Management Temporary Depoldering to Mitigate Drainage Congestion in the Southwest Delta of Bangladesh, *M.Sc. Thesis.*

Paul, A., Nath, B. & Abbas, R. (2013). Tidal River Management (TRM) and its Implication in Disaster Management : A geospatial Study on Hari-Teka River Basin Jessore, Bangladesh. *International Journal of Geomatics and Geosciences*, 4(1), 125–135.

Rahman, R. & Salehin, M. (2013). *Flood Risks and Reduction Approaches in Bangladesh, Disaster Risk Reduction Approaches in Bangladesh*. Springer Japan: Tokyo, 65–90.

Rezaie, A.M. (2013). Tidal River Management : An Innovative Approach for Terminating Drainage Congestion and Raising Land Through Sedimentation in The Bhabodaho Area, Bangladesh. 1363 - 1375.

Rubey, W.W. (1933). Settling Velocity of Gravel, Sand, and Silt Particles. *American Journal of Science*, 325 - 338.

Shampa & Pramanik, M.I.M. (2012). Tidal River Management (TRM) for Selected Coastal Area of Bangladesh to Mitigate Drainage Congestion. *International Journal of Scientific & Technology Research*, 1(5), 1–6.

Talchabhadel, R., Nakagawa, H. & Kawaike, K. (2016a). Tidal River Management (TRM) and Tidal Basin Management (TBM): A case study on Bangladesh. *3rd European Conference on Flood Risk Management.*

Talchabhadel, R., Nakagawa, H. & Kawaike, K. (2016b). Experimental Study on Suspended Sediment Transport to Represent Tidal Basin Management. *Journal of Japanese Society of Civil Engineers*, Ser B1 (Hydraulic Engineering), 60, 847–852.

Talchabhadel, R., Nakagawa, H., Kawaike, K., Hashimoto, M. & Sahboun, N. (2017). Experimental Investigation on Opening Size of Tidal Basin Management: A Case Study in Southwestern Bangladesh. *Journal of Japanese Society of Civil Engineers*, Ser B1 (Hydraulic Engineering), 61.

Van Rijn, L.C. (1984). Sediment Transport, Part II: Suspended-Load Transport. *Journal of Hydraulic Engineering*, ASCE, 110(11), 1613–1641.

 

Proceedings of the 37th IAHR World Congress
August 13 – 18, 2017, Kuala Lumpur, Malaysia

# APPLICATION OF ACOUSTIC DOPPLER TECHNOLOGY IN ESTIMATING SUSPENDED SEDIMENTS

DANIEL WAGENAAR[(1)] & XUE FAN[(2)]

[(1)]SonTek, San Diego, United States of America
daniel.wagenaar@xyleminc.com
[(2)] SonTek, San Diego, United States of America
xue.fan@xyleminc.com

## ABSTRACT

The application of acoustic doppler instruments has expanded into various facets of catchment hydrology and water engineering and this paper will demonstrate the successful integration of the technology within existing practices in determining suspended-sediment concentration. The traditional methodology that is applied over the past century in defining these key parameters has number of limitations due to the available technology and resources required to perform field measurements and often resulted in insufficient and unreliable data sets for model development and yield calculations. Research is done by the USGS and U.S. Army Corps of Engineers to identify the most effective surrogate for suspended-sediment concentration (SSC). The methodologies that are identified for the study consist of turbidity, laser diffraction and acoustic backscatter principles. During the initial investigation, it is found that the most promising technique is the measurement of acoustic backscatter strength with an acoustic doppler velocity meter (ADVM). A surrogate model is developed based on the SSC samples taken over a two year period in both the Clearwater and Snake Rivers from 2008 -2010. ADVM measurements are performed during the same period and the acoustic backscatter surrogate displays the best relation with the measured SSC during the development of the model. The acoustic surrogate model provides improved estimation of SSC and load than the traditional sediment-transport curves based on discharge during different time scales when sediment concentration is variable (Wood and Teasdale, 2013). The acoustic doppler velocity meters (ADVM) demonstrates during the acoustic surrogate model development the robustness of the technology. The study results also highlight that a higher frequency instrument shows the best estimation of SSC of all technologies. The application of acoustic doppler technology in catchment hydrology is becoming an important criterion in the application science in the various spheres of hydrology.

**Keywords:** Acoustic; velocity; sediment; bathymetric; watercube.

## 1 INTRODUCTION

The application of acoustic doppler instruments has expanded into various facets of catchment hydrology and water engineering and this paper will demonstrate the successful integration of the technology within existing practices in determining suspended-sediment concentration.

The traditional methodology that was applied over the past century in defining these key parameters had a number of limitations due to the available technology and resources required to perform field measurements and often resulted in insufficient and unreliable data sets for model development and yield calculations.

Research was done by the USGS and U.S. Army Corps of Engineers to identify the most effective surrogate for suspended-sediment concentration (SSC). Different technologies were evaluated in the Clearwater River at Spalding, Idaho, and the Snake River near Anatone, Washington study area represented in Figure 1 to help quantify sediment transport to Lower Granite Reservoir in northern Idaho and eastern Washington.

The methodologies that are identified for the study consisted of turbidity, laser diffraction and acoustic backscatter principles. During the initial investigation, it is found that the most promising technique is the measurement of acoustic backscatter strength with an acoustic doppler velocity meter (ADVM).

A surrogate model is developed based on the SSC samples taken over a two year period in both the Clearwater and Snake Rivers from 2008 -2010. ADVM measurements are performed during the same period and the acoustic backscatter surrogate displays the best relation with the measured SSC during the development of the model. The acoustic surrogate model provides improved estimation of SSC and load than the traditional sediment-transport curves based on discharge during different time scales when sediment concentration is variable (Wood and Teasdale, 2013).

 

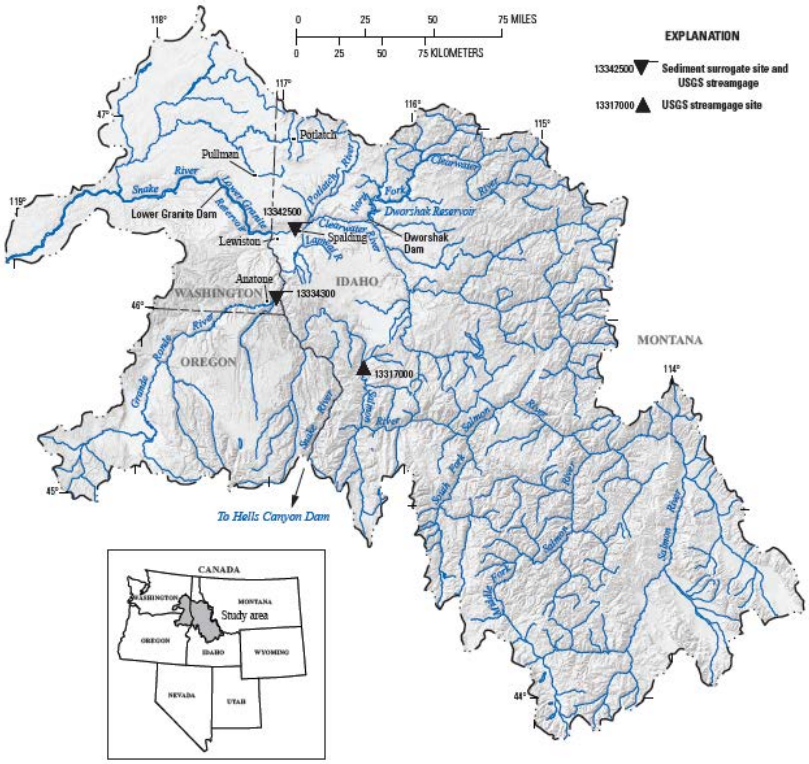


**Figure 1.** Study area and locations of sediment surrogate and U.S. Geological Survey (USGS) stream gage sites in the Clearwater River, Idaho, and Snake River, Washington, May 2008–September 2010.

## 2 METHODS

### 2.1 Suspended-sediment concentration

#### 2.1.1 Sediment sample collection

Suspended-sediment samples were collected by the USGS and U.S. Army Corps of Engineers based on the equal-width-increment (EWI) sampling method (U.S. Geological Survey, 2006). The sampling was targeted at three different areas during the hydrograph, rising limb, peak and falling limb for each river. A total of thirty three suspended-sediment samples were collected during the period at each site in the Clearwater and Snake Rivers from 2008 -2010 (Wood and Teasdale, 2013) summarized in Table 1.

**Table 1.** Suspended-sediment and Streamflow data collected in the Clearwater River, Idaho, and Snake River, Washington, May 2008–September 2010.

| Characteristic | USGS Streamgage | | Units |
|---|---|---|---|
| | Clearwater River (13342500) | Snake River (13334300) | |
| Number of sediment samples collected during study period | 33 | 33 | Na |
| Mean annual Streamflow, period of record [1] | 417 | 976 | m3/s |
| Annual mean Streamflow | | | |
| 2008 | 459 | 887 | m3/s |
| 2009 | 454 | 937 | m3/s |
| 2010 | 307 | 825 | m3/s |
| Total suspended-sediment concentration | | | |
| Mean | 26 | 70 | mg/L |
| Median | 13 | 40 | mg/L |
| Ranges | | | |
| Total suspended-sediment concentration | 3 – 210 | 6 – 414 | mg/L |
| Sand concentration | 0.3 - 122 | 0.5 – 232 | mg/L |
| Fines concentration | 2 – 88 | 5 – 206 | mg/L |
| Flows during sample collection | 135 – 2234 | 422 – 4389 | m3/s |
| Flows during study period (May 2008–September 2010) | 62 – 2257 | 309 - 4899 | m3/s |

[1] Based on published period of record for Streamgage, water years 1972–2010 for Clearwater River, 1958–2010 for Snake River.

 

2.1.2 Surrogate instrument data corrections

The acoustic backscatter data or signal-to-noise ratio (SNR) measured by the ADVM cannot be applied directly for determining the SSC and need to be corrected into a more appropriate estimator of SSC. The acoustic backscatter of each cell measured by the ADVM was corrected for the following losses:

- Beam spreading;
- Transmission losses owing to absorption by water;
- Absorption or attenuation by sediment.

The methodology applied for correcting acoustic backscatter data during this study are discussed in detail in Wood and Teasdale (2013) report. The corrected acoustic backscatter, $ABS_{corr,}$ was calculated using a form of the sonar equation from Urick (1975) given in Eq. [1].

$$ABS_{corr} = K(E - E_r) + 20log_{10}(R) + 2 \propto_w R + 2 \propto_s R \quad [1]$$

where, $ABS_{corr}$ is the range-normalized acoustic backscatter corrected for two-way transmission losses in dB,
K is a scale factor used to convert uncorrected ABS in counts to dB,
E is the raw amplitude of the uncorrected ABS as reported by the acoustic device (counts),
Er is the received signal strength indicator reference level or instrument noise floor (counts),
R is the slant distance along the acoustic beam to the measurement location incorporating beam angle (25 degrees for SonTek™/YSI ADVMs) (m),
$\alpha_w$ is the water absorption coefficient (dB/m), and
$\alpha_s$ is the sediment attenuation coefficient (dB/m).

The different steps involved for correcting acoustic backscatter data for each measurement cell from the ADVM is graphically presented in Figure 2 (Wood and Teasdale, 2013).

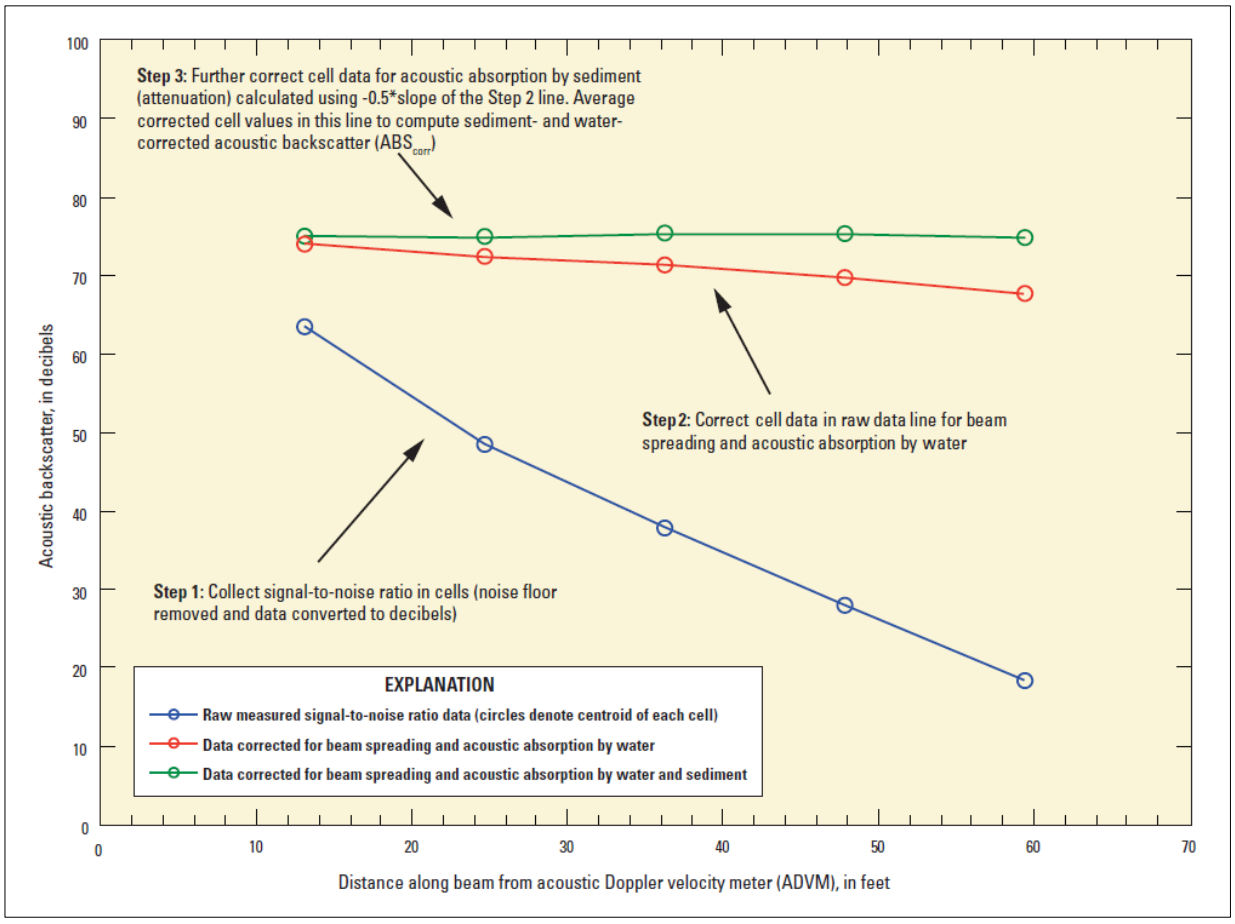


**Figure2.** Process for calculation of range-normalized acoustic backscatter corrected for two-way transmission losses in the Clearwater River, Idaho and Snake River, Washington.

 

2.1.3 Surrogate model development

The samples collected at each site in the Clearwater and Snake Rivers from 2008 – 2010 were used to develop surrogate models with the acoustic backscatter data during the same period. The acoustic backscatter data was averaged in 1-hour time frames to overlap the suspended-samples that were analyzed.

Models were developed for each site in the Clearwater and Snake Rivers between SSC and acoustic backscatter data using stepwise ordinary least- squares regression techniques. Regression models were selected based on statistical significance (p-values) of explanatory variables and various regression statistics, such as high coefficient of determination ($R^2$), low standard error, constant variance and random patterns in residuals plots, and low relative percent difference. Surrogate regression models for total suspended sediment, sand, and fines concentrations based on acoustic backscatter are graphically presented in Figure 3 (Wood and Teasdale, 2013).

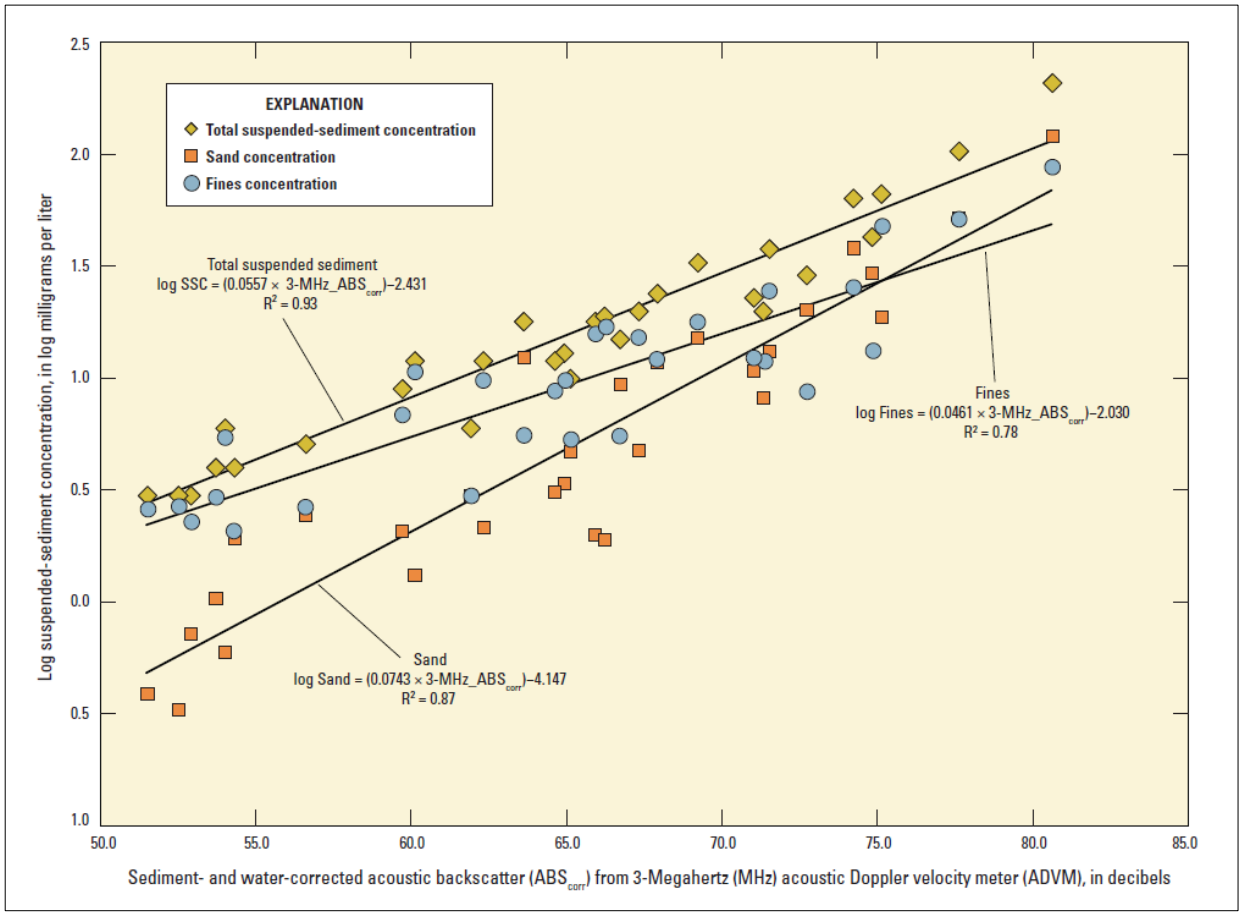


**Figure 3.** Surrogate regression models for total suspended sediment, sand and fines concentrations based on acoustic backscatter for the Clearwater River near Spalding, Idaho.

## 3 FINDINGS

3.1 Suspended-sediment concentration

The acoustic doppler velocity meters (ADVM) demonstrated during the acoustic surrogate model development the robustness of the technology. The study results between the 3Mhz and 0.5Mhz also highlighted that a higher frequency instrument showed the best estimation of SSC of all technologies at the monitoring location.

The acoustic surrogate model based on the 3-MHz acoustic backscatter represented 93 percent of the variability in the SSC and 8.6 percent average between measured and estimated SSC. The standard error and variance for the 3-MHz acoustic surrogate model were lower and more consistent than all the other models summarized in Table 2.

 

**Table 2.** Surrogate model results and regression statistics for the Clearwater River at Spalding, Idaho, May 2008–September 2010.

| Sediment Surrogate | Number of samples used for regression | Model | R2 | Average RPD (percent) | Standard Error (mg/L) | BCF |
|---|---|---|---|---|---|---|
| 3Mhz ADVM Backscatter | 30 | SSC | 0.93 | +8.6 | 1.34 | 1.040 |
| | | Sand Concentration | 0.87 | +34 | 1.71 | 1.146 |
| | | Fines Concentration | 0.78 | +19 | 1.58 | 1.097 |
| Turbidity | 30 | SSC | 0.64 | +48 | 1.92 | 1.202 |
| 2008-10 Sediment Transport Curve | 33 | SSC | 0.54 | +64 | 2.10 | 1.284 |
| 1970 Sediment Transport Curve[1] | 135 | SSC | 0.52 | +54 | 2.69 | na[2] |
| 0.5Mhz ADVM Backscatter | 30 | SSC | 0.007 | +204 | 2.97 | 1.916 |
| Laser Diffraction | 15 | SSC | 0.003 | +119 | 2.73 | 1.560 |

[1]As published in Jones and Seitz (1980).
[2]Bias correction factor was not used in the computation of concentrations and loads in Jones and Seitz (1980).

[**Sediment surrogate:** ADVM, acoustic Doppler velocity meter; MHz, megahertz. **Model:** SSC, suspended-sediment concentration in milligrams per liter (mg/L); ABScorr, acoustic backscatter corrected for beam spreading and attenuation by water and sediment in decibels (dB); Turb, turbidity in Formazin Nephelometric Units (FNU); *Q*, streamflow in cubic feet per second (ft3/s); LISST, suspended-sediment concentration estimated by the LISST StreamSide in microliter per liter (µL/L). **R**2: Coefficient of determination. **Average RPD**: Relative percent difference. **BCF:** Duan's bias correction factor. **Abbreviation:** na, not applicable]

The 3-MHz acoustic surrogate model results with sediment transport curves and physical samples are graphically presented in Figure 4.

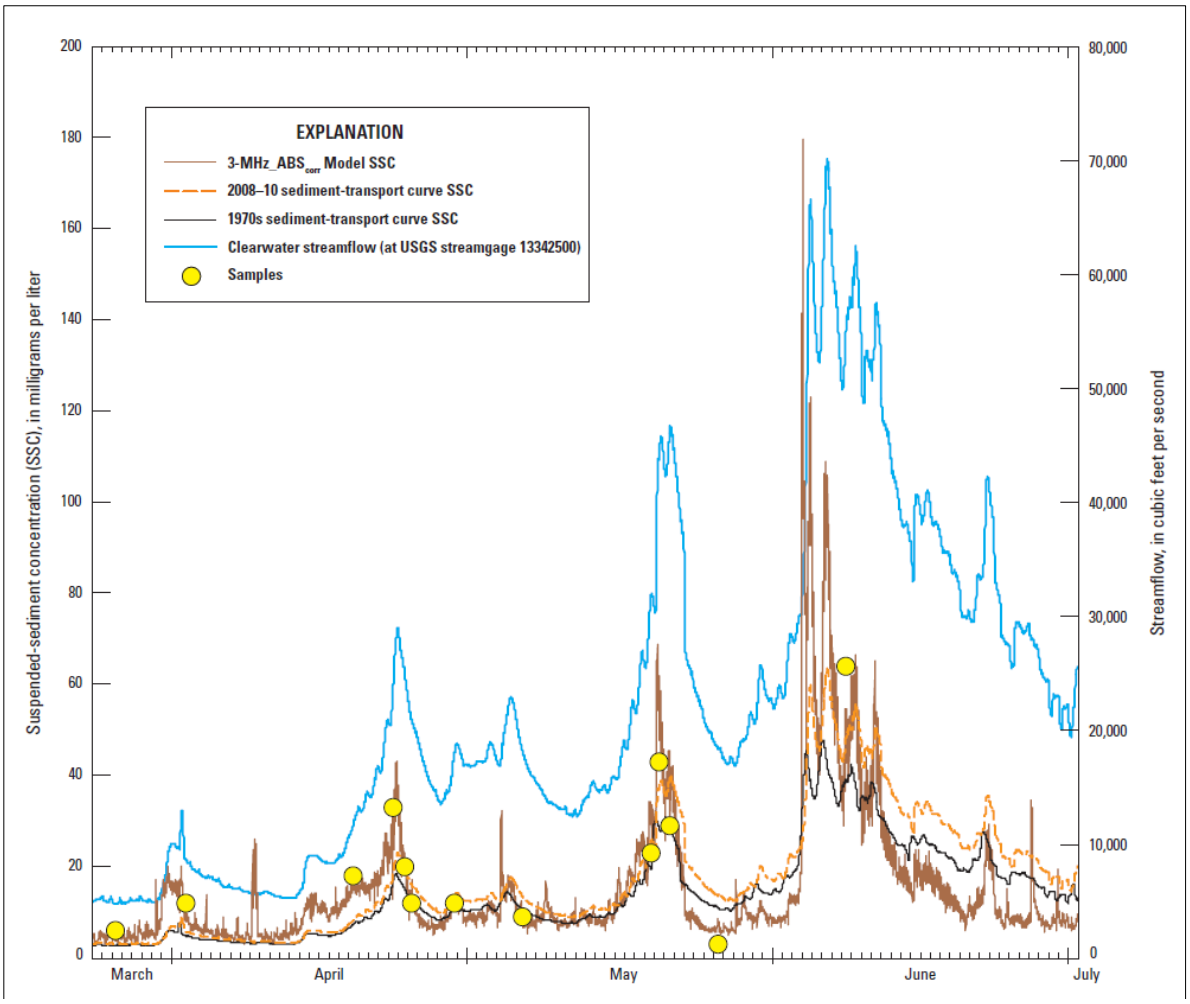


**Figure 4.** 3-MHz acoustic surrogate model results with sediment transport curves and physical samples.

## 4 CONCLUSIONS

The application of acoustic doppler technology in catchment hydrology or the impact thereof is becoming an important criterion in the application science in the various spheres of hydrology. Information has never in the past so accessible or cost effective than now with the use of acoustic doppler technology.

The use of Geographic Information Systems (GIS), Digital Elevation Models (DEM) or Hydrological Models requires significant amount of data to enable the user to develop a model based on the catchment characteristics and the hydrological processes involved. The individual measurements performed on an ad hoc basis are not sufficient for these purposes and a more comprehensive monitoring program is required.

The SonTek acoustic doppler range enables the user to perform a range of monitoring techniques with the following methods defined:

- Instantaneous point velocity measurement
- Continuous point velocity measurement
- Instantaneous velocity measurements at a cross section;
- Continuous velocity measurements at a cross section
- Bathymetry and velocity mapping of a channel reach

There are continuous developments done on both technology and methodology for the application in catchment hydrology and acoustic doppler technology will have a much larger role in the science and management of catchment hydrology in the future.

## ACKNOWLEDGEMENTS

The research and content illustrating the SonTek SL performance as an appropriate surrogate for Suspended Sediment Concentration are supplied by the USGS.

## REFERENCES

Jones, M.L. & Seitz H.R. (1980). *Sediment Transport in the Snake and Clearwater Rivers in the Vicinity of Lewiston, Idaho,* U.S. Geological Survey Open-File Report 80–690, 179.

Wood M.S. & Teasdale G.N. (2013). *Use of Surrogate Technologies to Estimate Suspended Sediment in the Clearwater River, Idaho, and Snake River, Washington,* 2008–10, 1-26.

 

Proceedings of the 37th IAHR World Congress
August 13 – 18, 2017, Kuala Lumpur, Malaysia

# EXPERIMENTAL INVESTIGATION OF BEDLOAD SEDIMENT TRANSPORT AND BED EVOLUTION IN DOUBLE-PEAKED HYDROGRAPH

LE WANG[(1)], ALAN CUTHBERTSON[(2)], DEYU ZHONG[(3)], GARETH PENDER[(4)] & ZHIXIAN CAO[(5)]

[(1,3)]State Key Laboratory of Hydroscience and Engineering, Tsinghua University, Beijing, China,
[(2,4,5)]Institute of Infrastructure and Environment, Heriot-Watt University, Edinburgh, UK,
[(5)]State Key Laboratory of Water Resources and Hydropower Engineering Science, Wuhan University, Wuhan, China.
lewang2016@mail.tsinghua.edu.cn; a.cuthbertson@hw.ac.uk; zhongdy@mail.tsinghua.edu.cn; g.pender@hw.ac.uk; zxcao@whu.edu.cn

## ABSTRACT

In natural rivers, significant bedload transport and variability in sediment bed geomorphology are generally observed to occur under unsteady flows, especially during flood events. In this study, a double-peaked hydrograph event, consisting of two identical and consecutive flood waves (i.e. sub-hydrographs), is performed in a large titling flume to investigate the behavior of bedload transport and response of sediment bed change within both quasi-uniform and fine-graded sediment beds, respectively. The results indicate that the total bedload transport rates for both quasi-uniform and fine-grained sediment beds tend to be reduced during the second sub-hydrograph, in comparison to the first sub-hydrograph, with more significant reductions observed to occur during the rising limb compared to the falling limb. In terms of fractional transport rates for the fine-graded sediment, the results also show that the bedload transport rates for the coarsest fraction are most significantly reduced in the second sub-hydrograph, compared to the first, during the rising limb. A similar overall trend is also shown for the corresponding fine and medium sediment fractions. In terms of the bed evolution over the duration of the double-peaked hydrograph, detailed measurement of bed surface elevation within both quasi-uniform and graded sediment beds runs reveals that the well-defined alternate bars are generated in quasi-uniform sediment bed, while only slight variations in elevation are found to occur in the fine-graded sediment bed with no indication of the generation of bed forms.

**Keywords:** Bedload transport; double-peaked hydrograph; bed elevation; quasi-uniform and graded sediments; flume experiments.

## 1 INTRODUCTION

The flow conditions that sediment beds are subject to prior to entrainment are defined as antecedent flows (Saadi, 2002; Haynes, 2005; Haynes & Pender, 2007; Piedra, 2010; Ockelford, 2011; Haynes et al., 2012; Ockelford & Haynes, 2013). The effect of these antecedent flow conditions on the subsequent sediment transport behavior was firstly highlighted by Reid et al. (1985), who commented that “long periods of inactivity (at low flow) encourage the channel bed to consolidate sufficiently so that bedload is largely confined to the recession limb of the next flood wave, but when floods follow each other closely, the bed material is comparatively loose and offer less resistance to entrainment, in this case, substantial amounts of bedload generated on the rising limb”. Thus, it is implied that the duration of inter-flood antecedent flow conditions will influence the bedload transport behavior during the consequent flood event.

In order to better identify and quantify the effects of antecedent flow on the development of sediment bed stability and bedload sediment transport (during subsequent flood events), many detailed experiments have been undertaken in recent years (Reid & Frostick, 1984; Reid et al., 1985; Saadi, 2002; Haynes, 2005; Haynes & Pender, 2005; Saadi, 2008; Piedra, 2010; Ockelford, 2011; Hassan, 2015). These studies considered two main types of antecedent flow conditions, namely: (i) steady antecedent flow (Saadi, 2002; Haynes & Pender, 2005; Haynes, 2005; Haynes & Pender, 2007; Ockelford, 2011; Haynes et al., 2012; Ockelford & Haynes, 2013); and (ii) unsteady antecedent flow (Saadi, 2002; Piedra, 2010; Hassan, 2015), while all experiments focused on two aspects of antecedent flow, namely duration and magnitude (i.e. under-threshold or over-threshold flows). These combined effects are referred to as the antecedent flow history or stress history (Haynes & Pender, 2005; Haynes, 2005; Haynes & Pender, 2007). In laser-based experiments conducted by Saadi (2002); Ockelford (2011); Haynes et al. (2012) and Ockelford & Haynes (2013), evidence was provided to help explain some of the physical bed mechanisms leading to increased sediment bed stability, as a result of prolonged antecedent flow conditions. These physical processes were found to include: (i) particle repositioning, including rearrangement of bed-surface grain orientation, increased particle imbrication and the formation of structured surface bed grain clusters, and (ii) vertical grain settlement and, sediment bed compaction. Antecedent flow effects are thus clearly significant to the development of sediment bed structure and composition within natural fluvial channels prior to the onset of a flood event.

 

The emerging research into antecedent flow effects on sediment bed stability and transport has so far been mostly concerned with steady (i.e. constant) sub-threshold flows. As such, there remains a significant knowledge gap on the influence of unsteady antecedent flow conditions, particularly associated with the effect of an above-threshold flow history [i.e. prior flood hydrograph(s)] on bedload sediment transport and bed structure evolution during a subsequent flood event (Gomez, 1983). In addition, recent studies (e.g. Ockelford & Haynes, 2013) have noted that the degree of structural bed development depended on the most recent flow history, implying that the bed evolution during the preceding flood will influence strongly the sediment transport during a subsequent flood event when there is a short (or no) inter-flood period between events. On this basis, the current study considers a set of experimental runs with double-peaked hydrograph flow conditions generated from two identical sub hydrographs with no inter-flood period. These runs are conducted specifically to investigate the effect of unsteady, above-threshold, antecedency (i.e. passage of the first hydrograph) on the variability in bedload sediment transport characteristics observed during the subsequent similar flood event (i.e. passage of the second hydrograph).

## 2 EXPERIMENTAL SETUP

### 2.1 Flume set-up and bed sediments

The experimental studies were performed in a 22 m-long, 0.75-m wide and 0.5 m-deep flow-recirculating flume with an adjustable bed slope (Figure 1). The flume was equipped with a computer-controlled pump invertor capable of producing repeatable, unsteady hydrograph flow conditions along the channel with flow rates up to 100 $l \cdot s^{-1}$ at 50 Hz, measured in the delivery pipe by a Micronics ultrasonic flow meter.

A graded sediment (sand-gravel mixture) was sieved into eight fractions ranging in size from d = 1.5 mm to 14.6 mm. These fractions were tested individually (or in pairs) as quasi-uniform sediment bed conditions, or combined in appropriate fractions to provide a design mixture for graded sediment runs. The quasi-uniform sediment bed ($d_{50}$ = 1.95 mm) reported herein was composed of two fine fractions (d = 1.50 mm and 2.40 mm), while the corresponding design fine-graded sediment mixture was generated by adding proportions of coarser fractions (d = 3.4 $\rightarrow$ 11.6 mm) to the quasi-uniform fine sediment. The grain size distribution of design fine-graded mixture is illustrated in Figure2 (a), where $d_{50}$ = 2.64 mm and $\sigma_g$ = 2.09.

The initial 5 m inlet section of the flume bed and the last 3 m at the downstream end of the channel were artificially-roughened with coarse open-work gravel grades (i.e.$d_{50}$ = 40 mm and 20 mm, respectively, see Figure 1) to the aim of (i) preventing upstream scour and mass transport and the channel inlet, and (ii) providing favorable bed conditions to promote fine sediment deposition prior to its transfer into the sump tank.

The remaining 14 m-long test section of the flume was covered with a uniform layer of either the quasi-uniform or fine-graded sediments, which was screeded to a uniform bed thickness of ~11 cm, matching the mean surface elevation of the upstream and downstream coarser, immobile bed sections.

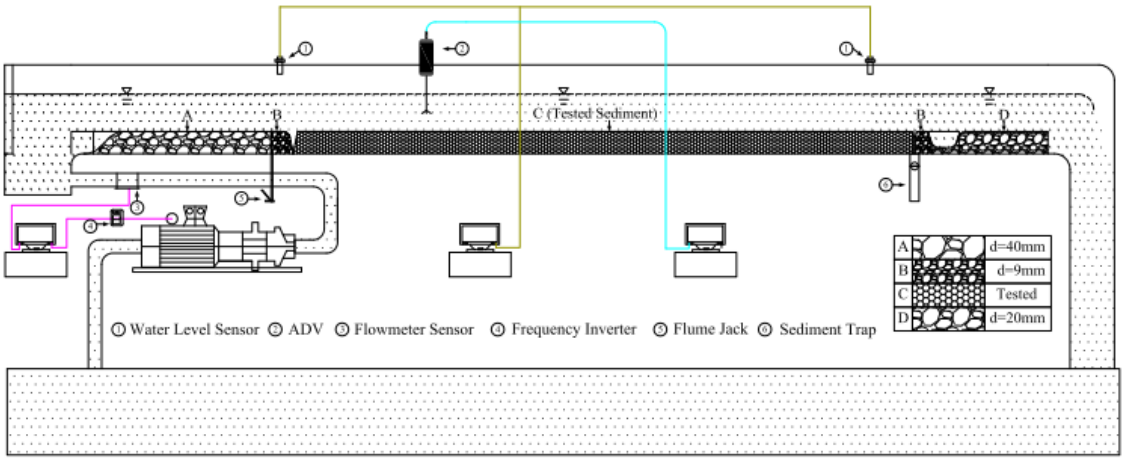


**Figure 1**. Schematic representation of experimental flume set-up.

### 2.2 Experimental procedure

All experimental runs were conducted at a longitudinal bed slope of 0.002. Prior to each test, the downstream tailgate was almost closed and the sump tank water depth checked. The pump was then switched on and set to a low flow rate (~3.0 $l \cdot s^{-1}$) to ensure minimum disturbance to the sediment bed during the initial wetting stage. Once the bed was fully submerged, the flow rate was programmed to increase slowly to sub-threshold, antecedent flow conditions (~17.0$l \cdot s^{-1}$), which were established in the flume to work on sediment bed for a relatively short period (~15.0 minutes). During the establishment of antecedent flow, the downstream tailgate was opened to diminish backwater effects and develop steady, uniform (base) flow

 

conditions along the channel. Initial, transverse bed elevation profiles were measured by an ADV at high spatial resolution (~5.0 mm intervals) across the channel [Note: its use as a bed surface profiler is possible through the utilization of a separate echo sounder mode for distance measurements (to an accuracy of $\pm$ 0.1 mm) at a given sampling interval of 10 Hz]. These transverse bed profiles were recorded at predefined cross-sections located 0.25 m, 0.75 m and 1.25 m downstream from the start of the erodible test bed section.

During each flood hydrograph test, variations in the inflow rate and water surface elevations at the channel inlet and outlet were measured synchronously (in real-time) by the ultrasonic flow meter and level sensors. Sediment bed-load samples were collected at regular intervals (typically every 5 – 15 minutes, according to the sediment transport intensity and test duration) from the sediment trap located towards the downstream end of the erodible bed section (see Figure 1). These sediment samples were dried and sieved to determine the total and fractional (where applicable) transport rates during each unsteady hydrograph flow cycle. Bed elevation transects at the three downstream locations were also measured at similar time intervals to coincide with this bed-load sampling regime.

Once an entire hydrograph flow process was completed and the base flow was re-established, the downstream tailgate was partly closed to generate a backwater effect (i.e. increased flow depth) to stabilize the final sediment bed structure within the erodible test section. At this point, the ADV probe was again utilized to measure transverse bed elevation profiles at 0.25 m intervals along the full length of the erodible sediment bed section of the channel.

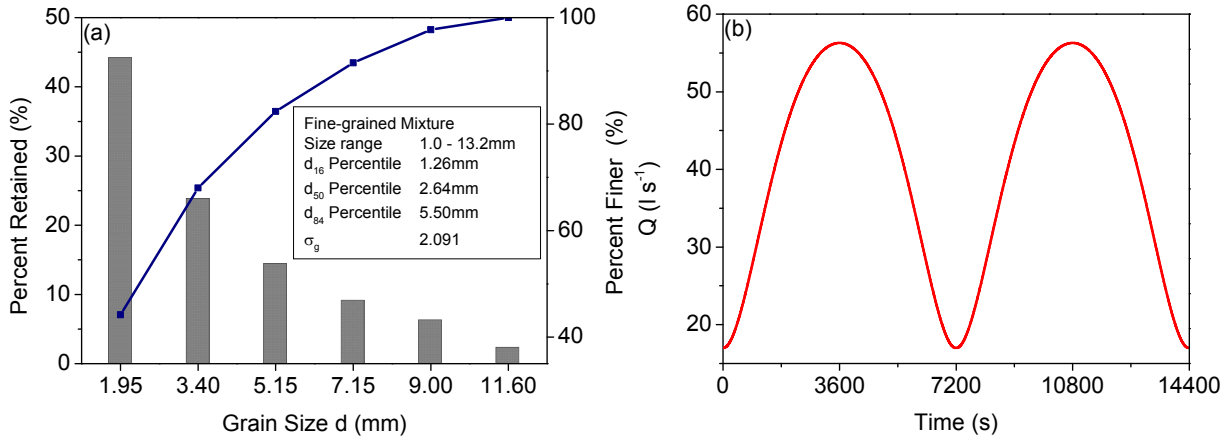


**Figure 2.** Composition of (a) fine-graded sediment and (b) double-peaked hydrograph employed in this study.

2.3 Design double-peaked hydrograph (DPUF)

The double-peaked hydrograph (Figure 2(b)) had the same overall hydrograph duration ($T_h$ = 14,400 s) and total unsteady water volume (Vol$\approx$ 332.88 $m^3$, i.e. excluding the base flow). These unsteady double-peaked hydrograph flows were characterized by (i) little or no sediment transport under base flow conditions $q_{base}$ = 17.0l·$s^{-1}$ (i.e. antecedent flow), (ii) significant bed-load transport rates under peak unsteady flow conditions $q_{peak}$ = 56.0 l·$s^{-1}$, and (iii) the incipient motion of bed-load transport for all size fractions under threshold flow conditions in the regime: $q_{base}<q_{threshold}<q_{peak}$. In fact, this double-peaked hydrograph was designed and generated on the basis of the symmetrical and single-peaked hydrograph characterized by the same duration and peak flow magnitude in the study from Wang et al. (2014) without scale effects associated with any specific field prototype event.

## 3 SCALING CONSIDERATIONS

It should be noted that the elapsed times at which bedload transport rates $q_b$ were measured during the DPUF runs, corresponded exactly to the same discharge *Q* condition during the rising and falling limbs of each hydrograph. Hence, the differences in $q_b$ rates measured at equivalent times and flow conditions in both hydrographs could be compared directly. This difference can be defined quantitatively by the ratio $\Lambda$ of the transport rate $q_{b,1}$ measured during the first hydrograph to the corresponding $q_{b,2}$ transport rate measured during the second hydrograph, i.e.

$$\Lambda = \frac{q_{b,1}}{q_{b,2}} \quad [1]$$

The total sediment flux entrained during the unsteady hydrograph flow can be represented by a non-dimensional total bed-load transport $W_t^*$ (e.g. Bombar et al., 2011), such that:

 

$$W_t^* = \frac{W_t}{\rho_s b d_{50}^2} \quad [2]$$

where $W_t$ is the dimensional bed-load transport (kg) collected in the sediment trap over the duration of the hydrograph, and $b$ is the sediment trap width (m) (i.e. differs from flume width $B$). This $W_t^*$ parameter thus provides information on the cumulative response of the sediment bed to different unsteady hydrograph flows.

Furthermore, in order to analyze sediment sorting associated with the fine-graded sediment transport runs, the current study utilized the classification system proposed by Frey et al. (2003), whereby experimental graded bed-load transport was split into three size-dependent classes defined as *fine*, *medium* and *coarse*. For the design graded sediment mixture tested (Figure 2(a)), the fine sediment class was defined for particle diameters d = 1.0 → 2.8 mm, while grain sizes from d = 2.8 → 6.3 mm were defined as the medium size class, and the coarse size class was defined for gravel particle sizes with d > 6.3 mm. Within the undisturbed design graded sediment mixture, the relative proportions of the fine, medium and coarse fractions were thus approximately 44%, 38%, 18%, respectively.

## 4 RESULTS

### 4.1 Bedload sediment transport rates

#### 4.1.1 Quasi-uniform sediment

Bedload transport rates for the quasi-uniform sediment were measured over the full duration of the double-peaked hydrograph (DPUF) via trapped sediment samples collected throughout the duration of the unsteady flow event. The resulting variation in transport rate $q_b$ for the DPUF flow condition is shown in Figure 4(a) and indicates that the peak $q_b$ values occur on the falling limb of both hydrographs, with the peak $q_b$ shown to be slightly higher during the first hydrograph (i.e. $q_b$ = 78.8 g m$^{-1}$ s$^{-1}$) compared to the second hydrograph (i.e.$q_b$ = 75.6 g m$^{-1}$ s$^{-1}$). Direct plots of bedload rate $q_b$ versus corresponding flow rate Q throughout the tests [Figure 3(b)] reveal (i) a clockwise hysteresis in the sediment transport rates during the first hydrograph (i.e. larger $q_b$ values during rising limb compared to falling limb) and (ii) a no/mixed hysteresis during the second hydrograph. Again, the clockwise hysteresis during the first hydrograph can be attributed to the initial sediment bed conditions. By contrast, the no/mixed hysteresis observed during the second sub hydrograph is thought to result from a more stabilized initial bed condition at the onset of the second hydrograph (i.e. following its response to the passage of the first hydrograph). This is in contrast to the findings from Reid et al. (1985) who noted that floods that followed others comparatively quickly are typically characterized by substantial bedload during the second rising limb. However, the results presented herein may also be due to an initial lag in the sediment transport response during rising limb of the second hydrograph, potentially resulting in greater availability for sediment transport during the falling limb of second hydrograph. This transport behavior therefore shows distinct differences from the findings of Reid et al. (1985).

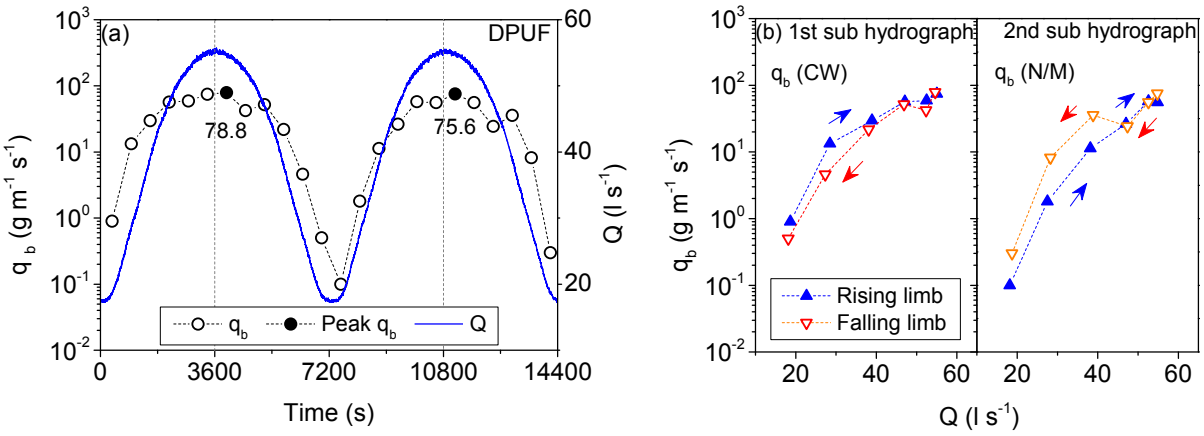


**Figure 3.** Bedload transport rates of quasi-uniform sediment in the DPUF hydrograph test: (a) flow hydrograph and sedimentograph; and (b) bedload transport rate hysteresis over two sub identical hydrographs.

Figure 4 presents the relationship between Λ(Eq. [1]) and flow rate Q for the quasi-uniform sediment transport during the double-peaked hydrograph (DPUF) runs. This indicates that Λ is considerably higher (Λ = ~10) at the initial stage of the rising limb (i.e. lower Q), reducing continually (Λ → ~1) as the flow increases

 

towards the peak flow Q. This suggests that transport rates on the rising limb of the first hydrograph are generally significantly higher than those occurring during the same period of the second hydrograph. By contrast, the $\Lambda$ values on the falling limb are considerably lower and fluctuate around $\Lambda$ = 1.0 (i.e. between about 0.6 – 2.1), meaning that the bedload transport rates $q_b$ on falling limbs of the two hydrographs exhibit smaller differences overall, with transport rates during the second hydrograph on occasion exceeding corresponding rates during the first hydrograph (i.e. $\Lambda$< 1.0).

Figure 5(a) and (d) shows the corresponding temporal variation in total and fractional (i.e. coarse, medium and fine size classes) bedload rates $q_b$ for the fine-graded bed sediment over the DPUF hydrograph, while Figure 5(b) and (c) shows the corresponding hysteresis patterns for total $q_b$ versus Q plots during the first and second sub-hydrographs, respectively. Evidently, the total bedload rate $q_b$ in the two sub-hydrographs exhibits strong clockwise hysteresis, even though the peak bedload rates are generated after the peak flow (i.e. during the receding limb) in both cases. In relation to the bedload transport for the individual size classes, the peak bedload rate $q_b$ for the coarse size class during the first hydrograph typically occurs earlier (prior to peak flow $Q_{peak}$) compared to the medium and fine size classes, which occur after peak flow $Q_{peak}$. These coarse, medium and fine fractional results also all indicate an obvious clockwise hysteresis [Figures 5(e)]. However, this fractional behavior is different in the second sub-hydrograph [Figures 5(f)], namely: (i) the medium size class attains its peak bedload rate $q_b$ before the fine and coarse size classes, and (ii) the coarse size class demonstrates no/mixed hysteresis, while the fine and medium size classes demonstrate clockwise hysteresis. It can thus be deduced both from the temporal lag and hysteresis patterns that (i) the fine size class becomes active during the first sub-hydrograph (i.e. no/mixed hysteresis), continues to be available during the rising limb of the second sub-hydrograph before becoming less active/available in the falling limb of the second sub-hydrograph (i.e. clockwise hysteresis), (ii) the coarse size class is relatively more active in the rising limb of first sub-hydrograph (i.e. clockwise hysteresis) and falling limb of second sub-hydrograph (i.e. no/mixed hysteresis). In this context, the inter-granular effects (i.e. exposure of coarse particles and hiding of fine grains in the graded sediment beds) and temporal-varied availability of various size class particles for entrainment, resulting in changes in bedload transport behavior, can be hypothesized as follows: (i) the coarse size class is preferentially active and available at the bed surface for entrainment during the rising limb of the unsteady hydrographs flow; (ii) its protective role on fine size classes is accordingly reduced during this entrainment, leading to an active response of the fine size class, which becomes increasingly available in the bed surface layer (i.e. during the falling limb of the first sub-hydrograph); (iii) the fine size class remains preferentially active during the rising limb of the second sub-hydrograph; (iii) the resulting preferential transport of fine size class (i.e. during the rising limb of the second sub-hydrograph) leads to bed surface coarsening and increased protection of the fine size class by the coarse size class, and (iv) the coarse size class then becomes more active over the peak flow and into the falling limb of second sub-hydrograph. This hypothesis is strongly supported by the temporal variations in bed-surface $d_{s50}$ as shown in Figure 6.

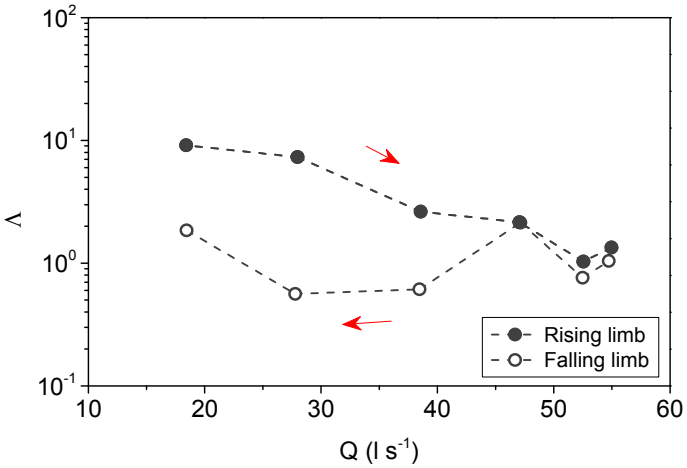


**Figure 4.** Relations of $\Lambda$ with Q for quasi-uniform bedload transport in the DPUF hydrograph test.

The relationships between total and fractional (i.e. coarse, medium and fine size classes) values of $\Lambda$ with Q for fine-grained sediment mixture are presented in Figure 7. It is apparent that the coarse size class has higher bedload rates $q_b$ during the first sub hydrograph than measured in the second sub hydrograph [i.e. $\Lambda$> 1.0, especially during the rising limb, where $\Lambda$ = 3 – 10, Figure 7(d)]. By contrast, although the fine size class is also shown to have higher bedload rate $q_b$ during the first sub hydrograph (i.e. $\Lambda$> 1), this tends to be more prevalent during the falling limb [i.e. Figure 7(b)]. As a consequence, the total bedload transport, demonstrates

 

no clear trend on the relative magnitude of $\Lambda$ during the rising and falling limbs [Figure 7(a)], following a similar pattern to that found for the medium size class [Figure 7(c)].

In general, it is shown that the intergranular interactions (e.g. exposure of coarser particles and sheltering of finer grains in mix-sized sediment) influence temporal lag and hysteresis patterns under double-peak hydrograph DPUF conditions, as well as the form of the relationship between transport rate ratio $\Lambda$ and flow rate Q.

4.2 Bed evolution

Figure 8 shows detailed bed elevation maps measured within the section of the erodible test bed between ~3.5 and 12.5 m. These plots indicate that distinct bed structures form for quasi-uniform and fine-graded sediments under same DPUF hydrograph flow conditions. Specifically, quasi-uniform sediment runs are shown to result in the formation of alternate bars along the channel, with overall localized net erosion depths of up to 30 mm [see Figure 8(a)]. By contrast, the fine-graded sediment bed showed no evidence of bar or ripple formation under the same DPUF flow condition [Figure 8(b)], instead revealing a patchier spatial variation in net deposition and erosion. This is, to some extent, similar to the quasi-uniform and graded bed development observed for the single-peaked hydrograph flow experiments reported in Wang et al. (2014). Comparatively, however, the alternate bars structure developed under the DPUF hydrograph conditions is more regular in spatial formation than within corresponding single-peak tests from Wang et al. (2014). For the fine-graded bed sediments, the erodible bed section downstream between 3.5 m $\rightarrow$ 12.5m indicates relatively low levels of bed erosion, with net final bed profiles often remaining close to the initial bed elevation. This can be attributed to the significantly lower bedload yields obtained from the fine-graded sediment mixture compared with the quasi-uniform sediment bed.

4.3 Bedload yields

Bedload transport yields from the quasi-uniform and fine-graded sediment beds are also studied under the same double-peaked (DPUF) hydrograph comprising with two identical sub hydrographs. The variation for total and fractional (i.e. coarse, medium and fine size classes) bedload rate in two sub hydrographs has been analyzed in detail. In this section, the total and fractional (i.e. coarse, medium and fine size classes) bedload yields generated in the two sub hydrographs will be compared and discussed.

For total bedload transport yields measured from both the quasi-uniform and fine-grained, mixed sediment beds, it is shown from Table 1 that the bedload yields during the first sub hydrograph $W^*_{t\,(1)}$ is considerably higher (up to 2.5 times) than occurs during in second, subsequent sub hydrograph (i.e. $\chi_{12} = W_t^*{}_{(1)} / W_t^*{}_{(2)} > 1.0$). As for fractional bedload yields observed from the fine-grained, mixed sediment transport, one can see that the bedload yields for fine, medium and coarse size classes are always higher in the first sub hydrograph than in second sub hydrograph, which is similar to total bedload yields. However, the ratio $\chi_{12}$ for the three size classes varies as coarse size class > medium size class > fine size class (i.e. Table 1), indicating that a larger proportion of the coarser particles is transported during the first sub hydrograph than during the second sub hydrograph (i.e. $\chi_{12}$ = 2.48), compared to the finer size class (i.e. where $\chi_{12}$ = 1.64). This finding is also in good accordance with that found for total and fractional bedload rate presented with respect to the plots of $\Lambda \sim Q$.

**Table 1.** Total and fractional (i.e. coarse, medium and fine size classes) bedload yields $W_t^*$ for quasi-uniform and fine-grained sediment transport in the two identical sub hydrographs within the DPUF run.

| Sediment | Total/Fractional | Bedload yields $W_t^*$ in 1st unit hydrograph $W^*_{t\,(1)}$ | Bedload yields $W_t^*$ in 2nd unit hydrograph $W^*_{t\,(2)}$ | $\chi_{12}$ |
|---|---|---|---|---|
| **Quasi-uniform (d=1.95mm)** | Total | 25868.78 | 20976.87 | 1.23 |
| **Fine-grained** | Total | 2332.37 | 1339.20 | 1.74 |
| | Fine | 2237.45 | 1366.66 | 1.64 |
| | Medium | 439.71 | 240.59 | 1.83 |
| | Coarse | 8.80 | 3.55 | 2.48 |

 

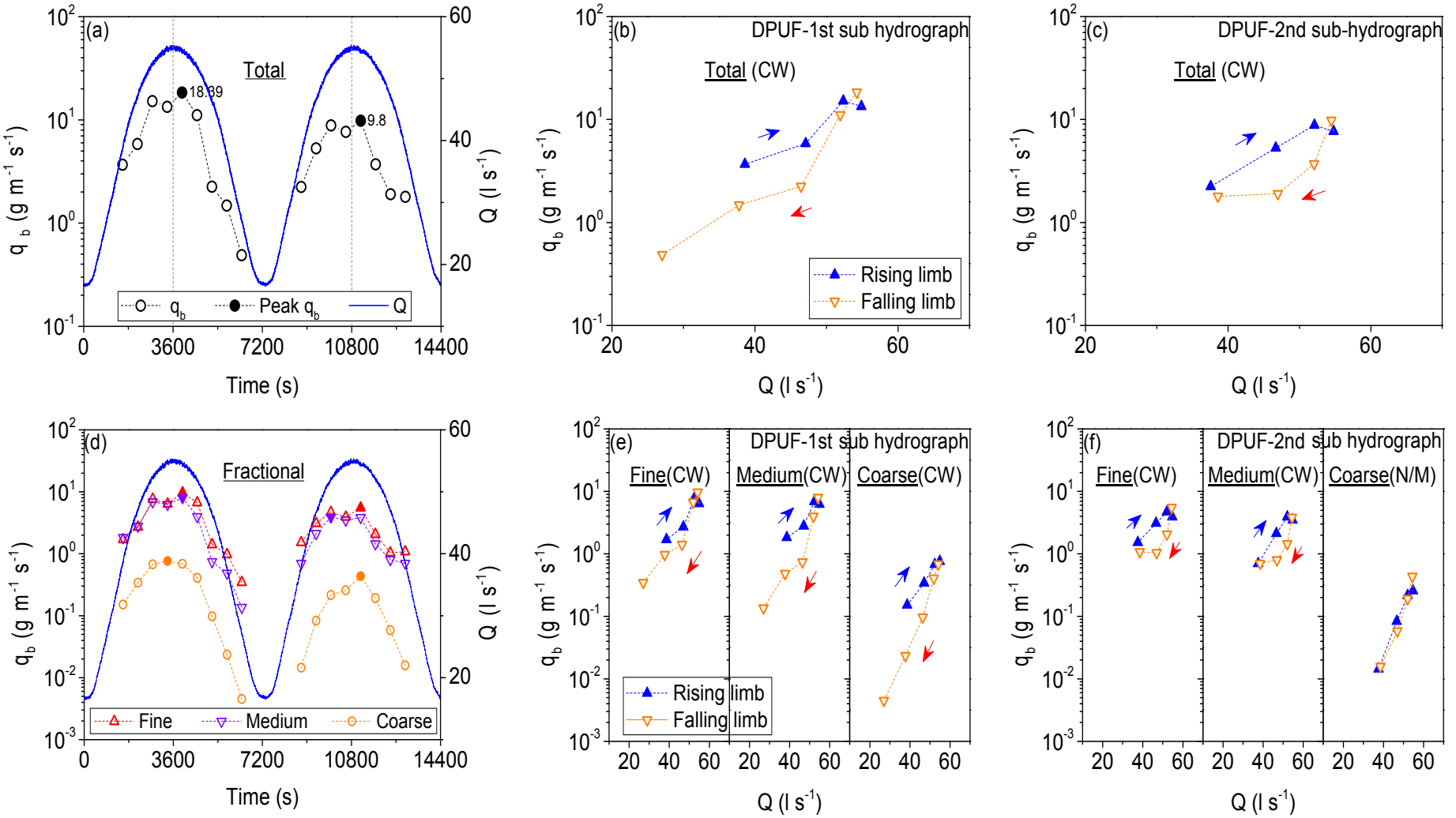


**Figure 5.** Fine-grained sediment transport in the DPUF hydrograph with respect to total and fractional (i.e. coarse, medium and fine size classes) bedload rate.

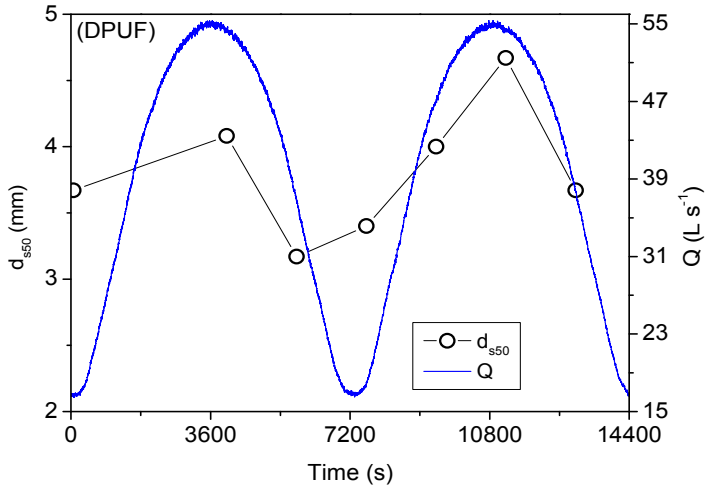


**Figure 6.** Temporal variations in $d_{s50}$ measured for fine-grained sediment bed surface subject to the DPUF hydrograph.

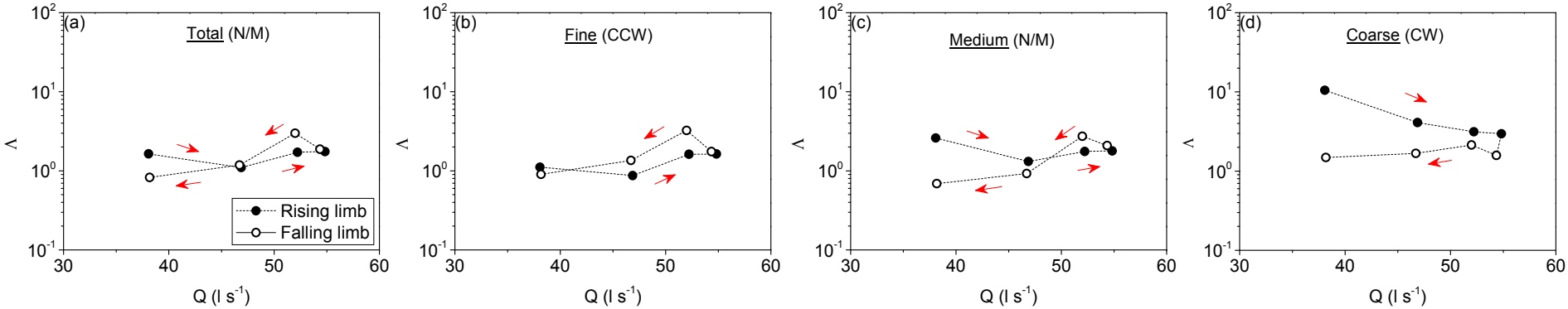


**Figure 7.** Fine-grained sediment transport in the DPUF hydrograph with respect to total and fractional (i.e. coarse, medium and fine size classes) bedload rate.

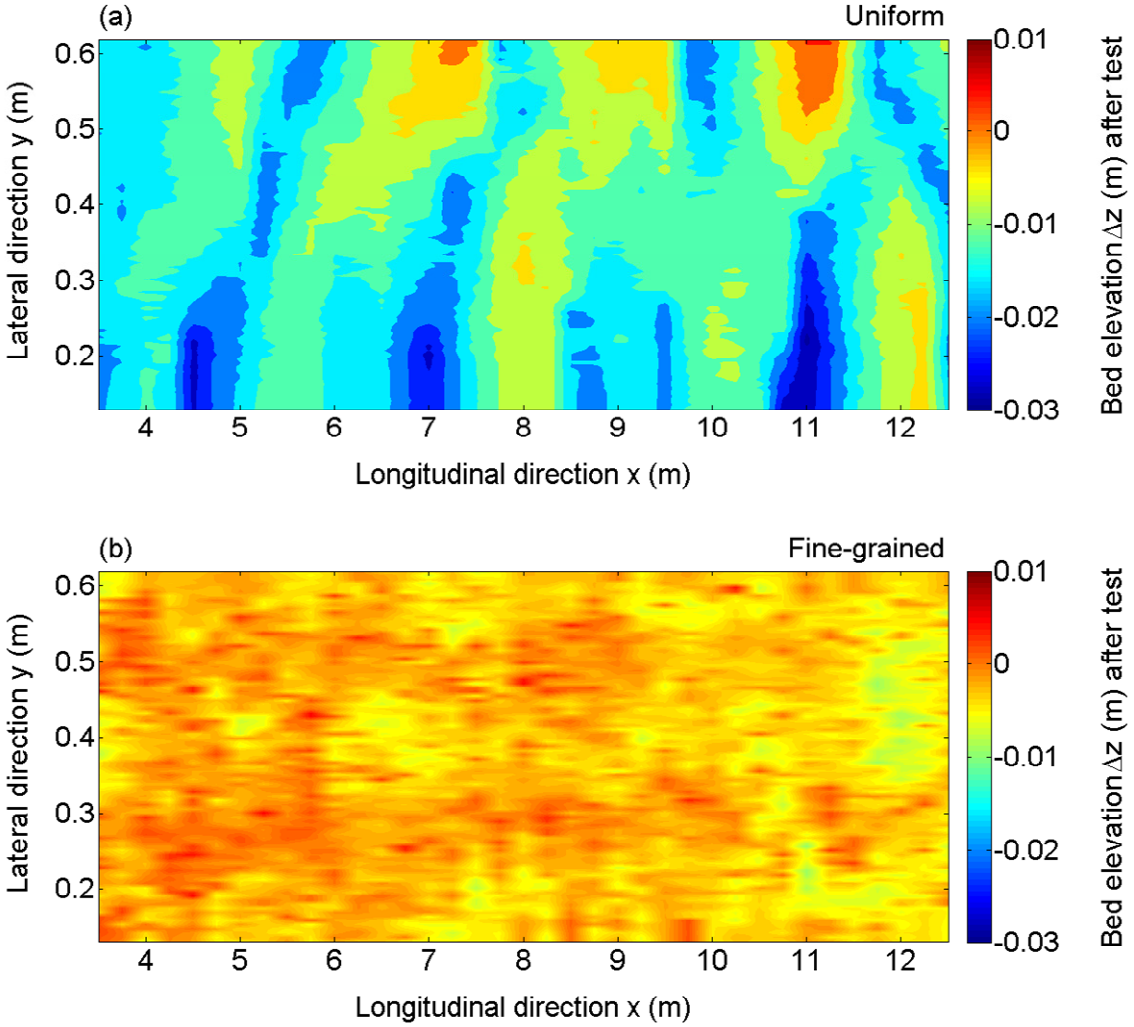


**Figure 8.** Detailed maps of bed surface elevation (relative to initial bed elevation) obtained for both quasi-uniform sediment bed (a) and fine-grained sediment bed (b) following the DPUF hydrograph test.

## 5 CONCLUSIONS

Experiments have been conducted to investigate the response of quasi-uniform and fine-graded sediment beds to an unsteady flow event consisting of two consecutive hydrographs. For the quasi-uniform sediment, direct comparisons of bedload rates measured during the two identical sub hydrographs indicates that the bedload transport rate declines significantly during rising limb compared to more equal transport occurring during the falling limb. For fine-graded sediment transport under the same DPUF hydrograph condition, the measurements indicate that: (i) the temporal lag and hysteresis pattern for three size classes in the first sub hydrograph vary in the way as fine-grained sediment transport in single-peaked hydrographs. In the second sub hydrograph, the hysteresis patterns for three size classes in second sub hydrograph are exactly opposite to what observed in the first sub hydrograph, namely, the coarse size class is shown no/mixed hysteresis, while the fine and medium size classes demonstrate clockwise hysteresis; and (ii) the fractional decline from first to second sub hydrograph can be proportionally ordered as coarse class > medium class > fine class;

Comparison of quasi-uniform and fine-graded sediment transport yields in double-peaked hydrograph (DPUF) event shows that the bedload yields observed in the first sub hydrograph are higher than in the second sub hydrographs, particular to the fine-grained sediment [if compared with quasi-uniform sediment (d=1.95mm)] and coarse and medium size classes [if compared with fine size class] with lower magnitude of bedload yields;

Because of difference in bedload yields obtained from quasi-uniform and fine-grained sediment beds, the quasi-uniform sediment bed undergoes massive bedload transport and bed erosion, the well-defined alternate bars are consequently formed. In contrast, the fine-grained sediment bed experiences lower level of bedload transport and demonstrates no evident bed change as compared to initial sediment bed.

**ACKNOWLEDGEMENTS**

Financial support for LW is provided by UK Overseas Research Student Awards Scheme (ORSAS) and a James Watt Scholarship tenable in the Institute of Infrastructure and Environment at Heriot-Watt University, Edinburgh, UK.

**REFERENCES**

Bombar, G., Elçi, Ş., Tayfur, G., Güney, M.Ş. & Bor, A. (2011). Experimental and Numerical Investigation of Bed-Load Transport under Unsteady Flows. *Journal of Hydraulics Engineering*, 137(10), 1276-1282.

Frey, P., Ducottet, C. & Jay, J. (2003). Fluctuations of Bed Load Solid Discharge and Grain Size Distribution on Steep Slopes with Image Analysis. *Experiments in Fluids*, 35(6), 589-597.

Gomez, B. (1983). Temporal Variations in the Particle Size Distribution of the Surficial Bed Material: The Effect of Progressive Armouring. *Geografiska Annaler*, 65, 183-192.

Hassan, I.K. (2015). MEMORY STRESS: Physical and Mathematical Modelling of the Influence of Water-Working on Sediment Entrainment and Transport, *PhD Thesis*. University of Glasgow.

Haynes, H. (2005). Experimental Investigation into the Effect of Antecedent Flow Conditions on the Stability of Graded Sediment Beds: Stress History, *PhD Thesis*. Heriot-Watt University.

Haynes, H. & Pender, G. (2007). Stress History Effects on Graded Bed Stability. *Journal of Hydraulics Engineering*, 133(4), 343-349.

Haynes, H., Ockelford, A.M., Vignaga, E. & Holmes, W.M. (2012). A New Approach to Define Surface/Sub-Surface Transition in Gravel Beds. *Acta Geophysica*, 60(6), 1589-1606.

Ockelford, A.-M. (2011).The Impact of Stress History on Non-Cohesive Sediment Bed Stability and Bed Structure, *PhD Thesis.* University of Glasgow.

Piedra, M.M. (2010). Flume Investigation of the Effects of Sub-Threshold Rising Flows on the Entrainment of Gravel Beds, *PhD Thesis.* University of Glasgow.

Reid, I. & Frostick, L.E. (1984). Particle Interaction and its Effect on the Thresholds of Initial and Final Bedload Motion in Coarse Alluvial Channels.

Reid, I., Frostick, L.E. & Layman, J.T. (1985). The Incidence and Nature of Bedload Transport during Flood Flows in Coarse-Grained Alluvial Channels. *Earth Surface Processes and Landforms*, 10(1), 33-44.

Saadi, Y. (2002). The Influence of Different Time Varying Antecedent Flows on the Stability of Mixed Grain Size Deposits, *PhD Thesis*. University of Sheffield.

Wang, L., Cuthbertson, A., Pender, G. & Cao, Z.X. (2014). The Response of Bed-load Sediment Transport and Bed Evolution under Unsteady Hydrograph Flows. River Flow 2014 – *7th International Conference on Fluvial Hydraulics, edited, Lausanne, Switzerland.*

 

Proceedings of the 37th IAHR World Congress
August 13 – 18, 2017, Kuala Lumpur, Malaysia

# LONGITUDINAL CHANGES IN SUSPENDED SEDIMENT LOADING AND SEDIMENT BUDGET OF MERBOK RIVER CATCHMENT, KEDAH, MALAYSIA

WAN RUSLAN ISMAIL[(1)], MOHD NAZRUL IBRAHIM[(2)] &
SUMAYYAH AIMI MOHD NAJIB[(3)]

[(1,2,3)]HydroGeomorphology Research Group, Section of Geography, School of Humanities, Universiti Sains Malaysia,
11800 Minden, Penang, Malaysia.
wruslan@usm.my

## ABSTRACT

Merbok River catchment situated in the Kedah State receives its input from Bongkok River and Puntar River flowing down and joining Sg.Lalang River to flow down to the Merbok Estuary. The Merbok catchment (440 $km^2$) is experiencing several degrees of complex land use activities that affect the suspended sediment production of the Merbok River. A study is conducted to investigate the suspended sediment loading of rivers draining the Merbok catchment from January to December 2013. Suspended sediment budget of the Merbok catchment is estimated. The river SSC and SS loads increase during wet season compared to dry season. The SS loads increase from upper catchment to the river mouth. The sediment loadings are divided into three segments- the upstream, middle segment and lower segment. The SS loads increase from 10 t/yr in the upper part of Bongkok River to 3336 t/yr in the upper segment. The sediment loading then increases to to 4299 t/yr in the middle segment of the catchment (at Bongkok 4), and then exiting the Merbok Estuary, as the lower segment, with a total amount of sediment output estimated at 7156 t/yr. Based on the findings, Merbok River catchment is experiencing a lot of sediment removal. Most of the sediment sources originate from the tributaries; Bongkok River, Puntar and Lalang River, which is much higher than its proportion in terms of its length and drainage area. As a conclusion, the inconsistency of SSC in the river is influenced by the various anthropogenic activities (especially agriculture and urbanization activities) in the catchment area which necessitate future land use and sediment control to avoid sediment and possible nutrient loading into the estuary.

**Keywords:** Land use changes; sediment load; sediment budget; Merbok River catchment; Kedah.

## 1 INTRODUCTION

Sediment eroded from slope land, bare land and agricultural lands, all ended up in the rivers draining the whole of the world's landscape. Sediments play an important role in the river ecosystem where they are responsible for transporting many materials and contaminants to the river (Ismail, 1996). Sediment ended up in water bodies could also bring damages to water quality when eroded soil enters surface waters. The characterization of suspended sediment transport in rivers is difficult due to the rapid human exploitation and unpredictable natural hydrologic events. Excessive soil loss is linked to lack of the sustainable use of natural resources, land exploitation and degradation and poor land management.

Concerns regarding the effects of human activities on degradation in river systems, erosion and sedimentation have frequently been raised. High sediment loads can, in particular, result in major problems for human such as affecting flood risk and boat traffic (Sheffield et al., 1995); reducing water quality and water supply, increasing the cost of treating water and other related purposes (Walling, 2009). Sediment suspended in the river can kill or irritate fish gills and suffocate organisms if significant concentrations and durations occur (Bash et al., 2001).

A sediment budget is an application of the continuity equation and it can be regarded as a form of geomorphic accountancy (Slaymaker, 2003). It is also considered as a quantitative inventory of all the sediment inputs, outputs and storage within a defined system. An understanding of the sources of sediment delivered to, stored within, and exported from, an estuary is important for a number of environmental issues including maintenance of navigational channels, light availability for primary productivity, reduction of dissolved oxygen concentrations and the transport and accumulation of particle-bound nutrients and contaminants and their eventual transport to the continental shelf (Cloern, 1987; Balls, 1992; Eyre & McConchie, 1993).

The sediment production is expected to increase in the near future due to rapid economic activities which could lead to the widespread changes in erosion rates, sediment flux and sediment loads transported by the world's rivers shown by the high frequency of human activities and unstable earth climate. The amount of the sediment loads transported by rivers in the catchment area has a very important implications on the biology, geomorphology and hydrology system. In addition, the sediment input from several catchments is important in the management of rivers and water resources, particularly in the context of integrated water resources for

 

domestic use, ecotourism, biodiversity of rivers, hydrology and hydraulics as well. The sediment loads may influence crop productivity and food security, changes in nutrient cycling and flux of many key elements and nutrients, water quality, river channel morphology, delta development and also the aquatic ecosystems and numerous of habitats supported by the river (Walling, 2009). The sediment loads can be estimated by developing a sediment budget. The budget is used for identifying and accounting of the sediment movement, into and out of a site on the catchment. Developing sediment budget is an attempt to identify the sources, sinks and pathways of eroded material content within catchment area (Slaymaker, 2003). For many years, sediment budget has been developed at scales ranging from small catchment to a large catchment (Owens et al., 1997; Walling et al., 2002).

This paper aims to estimate the simple sediment budget in the Merbok catchment area in Kedah, and to assess the various pathways and sediment sources from various land uses and tributaries in the catchment. This study also investigates the role of seasonal effect and the impact of human activities on variations in the concentration of SSC and the amount of input/output of suspended-sediment (SS) load.

## 2 MATERIALS AND METHODS

### 2.1 Study area

The investigation focused on the Merbok River Catchment area from Gurun area down to the Merbok River at Kampong Sg. Lalang, Kedah within latitudes of 5° 39' N to 5° 41' N and longitudes of 100° 20' E to 100° 24' E, respectively (Figure 1). The catchment area of Merbok River is 440 $km^2$. Figure 1 shows all the 15 sampling sites in the Merbok River catchment. They were chosen in this research based on the relation between the main river and its tributaries. The river was classified into the upper, middle and lower segments longitudinally according to the dominant gradient of the river (Rosgen 1994), where the uppermost segment called segment Aa+ should have a slope of more than 10%; followed by A between 4-10%, B between 2-4%; C having less than 2% and so on. Table 1 shows the classification carried out for Bongkok and Merbok Rivers.

**Table 1.** The distance, highest and lowest altitude, and the gradient of the river segment.

| Segment | River | Distance (km) | River Gradient (%) |
|---|---|---|---|
| Upper | Bongkok 1 | 2.05 | 20.46 |
| | Bongkok 2 | 4.42 | 18.56 |
| | Bongkok 3 | 7.27 | 11.28 |
| Midlle | Bongkok 4 | 14.15 | 5.54 |
| Lower | Merbok 1 | 18.9 | 1.16 |
| | Merbok 2 | 26.65 | 3.08 |

### 2.2 Land use

Land use shows the land usage in an area. The land use ranges from development, conservation, or mixed uses. The different types of land cover can be managed or used quite differently. Land use in the Merbok River catchment (440 $km^2$) is very complex. The catchment is experiencing several degrees of complex land use activities ranging from some major activities for example oil palm (24%), urban and residential (22%) and rubber (9.7%) and swamp and mangrove (9.4%). Other activities include forest (6.7%); industries (5.5%) and paddy (5.9%) and mixed horticulture (3%) (Figure 2) (Malaysia, 2010).

### 2.3 The sampling protocol

The water quality and physical parameters sampling was carried out every fortnight at selected river cross sections (15 sites) throughout the catchment area from January to December 2013. Figure 3 shows the five main river cross sections for the main tributary of the Bongkok River. The river width ranging from 3 m at B1; 10-15 m at B2 and B3; 40 m at B4 and nearly 60 m at M1.

Water samples were collected in three replicates representing a river cross-section segments and preserved in a polyethylene bottle. The water sampling procedure was done together with an *in situ* water quality monitoring scheme using YSI 556 multi-parameter. The water samples were collected at depths of about 0.5 m from water surface, and at the center of each segment, after dividing the river width into 3 equal segments. Water samples were transported in an ice-cooled container to the Hydrology laboratory, School of Humanities, Universiti Sains Malaysia for further analysis.

River discharge which is the volume of water that flows past a certain point in a stream over a specific period of time was calculated based on the velocity area method (Shaw et al., 2010) and the calculation of SS loading was based on Littlewood (1992).

 

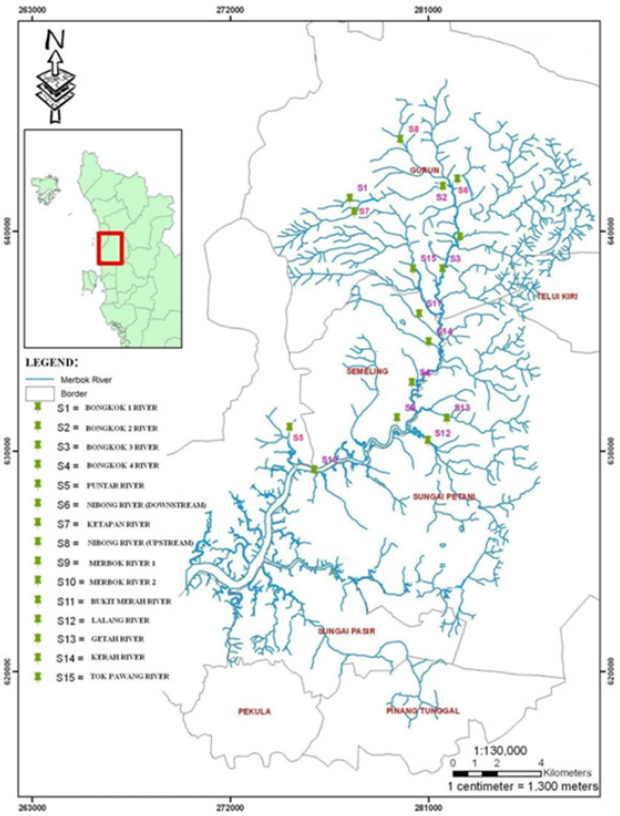


**Figure 1.** Location of the sampling stations from the upper Merbok to the estuary.

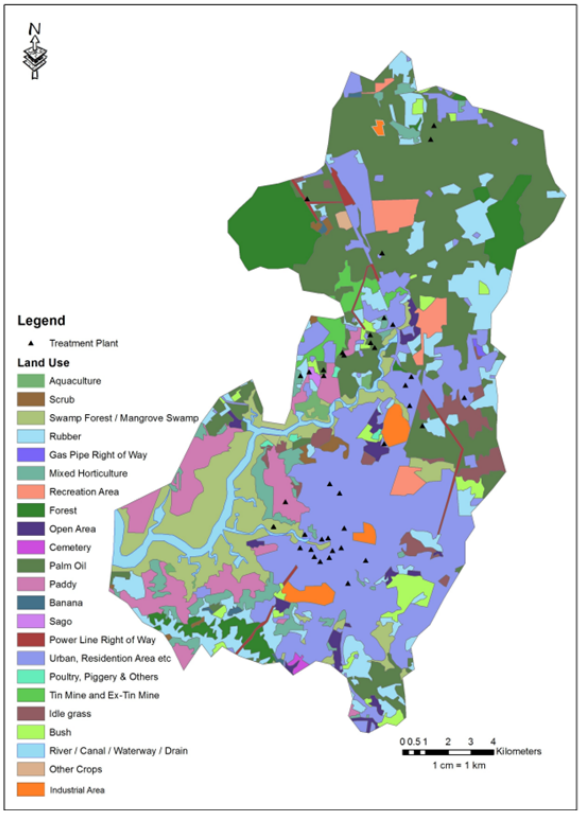


**Figure 2.** The land uses in the catchment area of Merbok (Malaysia, 2010).

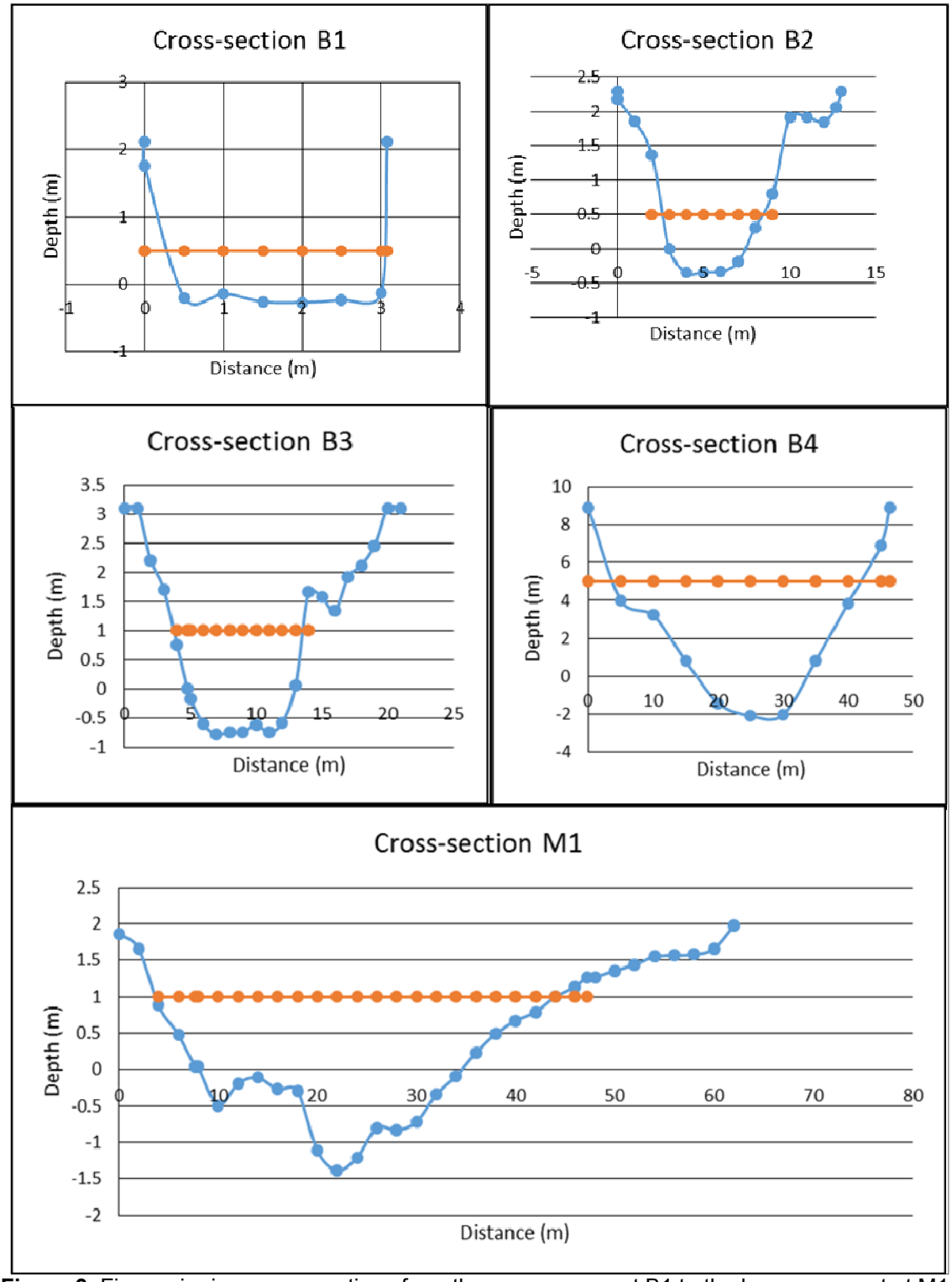


**Figure 3.** Five main river cross sections from the upper segment B1 to the lower segment at M1.

2.4 Determination of suspended sediment concentration (SSC)

The determination SSC was carried out using filtration methods using membrane Glass Fiber Filter ADVANTEC 47mm. After filtration, the membrane filter was placed in a Petri dish for drying in an oven at 105ºC and was left overnight. The membrane filter was cooled at room temperature before being weighed for it final weight. SSC in the sample was calculated by using an equation following APHA (1992). To obtain an estimate of SSC, the difference between weight of filter + dried residue and weight of filter was calculated (APHA, 1992).

 

2.5 Sediment loading calculation

The sediment loading is based on calculating the product of suspended sediment concentration (SSC) with river flow (Q) in a given period. The total amount of suspended load (in tonnes/year) was calculated by multiplying the weighed sediment concentrations (SSC) in mg/L with the stream discharge ($m^3s^{-1}$) with an

interval of 14 days.

To calculate the sediment loading, the average sample load estimation was used. The load of sediments transported through a river cross-section during a time interval was based on calculation described by Littlewood (1992);

$$L = K\left(1/n\sum_{i=l}^{n} Q\ (i).C(\mathrm{i})\right)$$

where:
L = load
K = the period of load estimation
C = sample concentration
Q = discharge

The accuracy of estimating the sediment load depended upon the availability of the river flow and concentration data at a sufficiently high frequency (relative to the variation in flow and concentration during the period of estimation) (Littlewood, 1992).

## 3 RESULTS

3.1 The suspended sediment load

From Table 2, the result shows the sediment loading of each station and was placed into three segments of the catchment i.e. the upstream segment, middle segment and the lower segment towards the river estuary (Table 2). The main river of the Merbok catchment which originated from the Bongkok River, was the upper, middle and part of the third segment, before the Merbok River. So the longitudinal flow was from Bongkok 1 (B1) to Bongkok 4 (B4) and Merbok 1 (M1) (Table 2).

The total SS loads increased from 10 t/yr in the upper part of B1 to 261 t/yr at B2.This was about 25 fold increase in the SS loads. Then the SS loads further increased downstream to 3337 t/yr at Bongkok 3 (B3). This represented an increase of only 12 fold between B2 and B3. The sediment loading then increased to 4299 t/yr at Bongkok 4 (B4). The increase in SS load was only about 0.3 fold but later it increased to 0.66 fold at Merbok 1, where the sediment loading was estimated at 7156 t/yr. Based on the total SS load, Merbok River catchment is experiencing a lot of sediment removal. Most of the sediment sources originate from the tributaries like the Puntar River and Lalang River, which are much higher than its proportion in terms of its length and drainage area.

In wet season, the SS loads were found to increase. Much higher increases were noted in the upper segment (34 and 26 folds, respectively). However, the wet period loading decreased slightly (0.25 fold) between B2 and B3, but later increased 0.8 fold between B4 and M1. In the dry season, however, the SS loadings were much lower due to the lower rainfall activity that drives the hydrological processes in the catchment. The SS loadings were very minimal ranging from 12 fold in the upper segment, 9 and 0.13 fold between B2 and B3, and 1.6 fold in the lower segment (Table 2).

The overall SS loading increment, from the upper to lowest segment, was almost 700 fold for total SS load ranging from 400 fold in the dry period to about 1250 fold increases in the wet period. The SS load was higher at M1 because it received all the sediment from the upper tributaries.

The overall loading between wet and dry periods was not much different with only about 26 tonnes (3.5%). However, there were very significant differences in SS loadings between the wet and dry periods observed at B3 (123%) and B4 (48%). These two stations were located in the middle part of the catchments which is highly active in human activities and land use changes. With a characteristic of great seasonal variations and precipitation in an alternation between wet and dry periods, the annual sediment load from the Merbok River catchment being discharged into the sea showed a very high SS load (ca. 7000 t/year) exported to the river mouth. However, this amount was considered small compared to that of SgKurau (51, 270 t/year) feeding into Bukit Merah reservoir (Ismail and Najib, 2011); but comparable to those of Sg. Jarum (5,400 t/year) and Pelarit River (11,400 t/year) (Rahaman and Ismail, 2010) discharging into Timah Tasoh lake which are also flowing through agricultural land use activities.

 

**Table 2.** Summary of suspended sediment (SS) loading of Merbok River catchment at the main channel of Bongkok and Merbok Rivers in Wet and Dry Seasons.

| Catchment Segment | Sites | Total Loads (t/yr) | Wet Season (t) | Dry Season (t) | Increase in total SS load (fold) | Increase in SS load in wet season (fold) | Increase in SS load in dry season (fold) |
|---|---|---|---|---|---|---|---|
| | Bongkok 1 | 10 | 0.6 | 1.8 | | | |
| | Bongkok 2 | 261 | 20.8 | 23.4 | | | |
| **(B2-B1)/B1** | | | | | 25.1 | 33.7 | 12.0 |
| | Puntar | 2924 | 469.7 | 206.5 | | | |
| **Upper Segment (S1)** | Ketapan | 242 | 34.8 | 19.7 | | | |
| | Nibong 1 | 384 | 40.2 | 30.7 | | | |
| | Nibong 2 | 483 | 61.8 | 43.9 | | | |
| | Bongkok 3 | 3337 | 557.0 | 248.7 | | | |
| **(B3-B2)/B2** | | | | | 11.8 | 25.8 | 9.63 |
| | Bukit Merah | 208 | 23.6 | 14.2 | | | |
| **Middle Segment (S2)** | Getah | 310 | 68.6 | 24.3 | | | |
| | Kerah | 241 | 33.8 | 13.0 | | | |
| | TokPawang | 284 | 45.5 | 25.4 | | | |
| | Bongkok 4 | 4299 | 415.6 | 280.7 | | | |
| **(B4-B3)/B3** | | | | | 0.29 | -0.25 | 0.13 |
| | Lalang | 1370 | 1442.7 | 115.1 | | | |
| **Lower Segment** | Merbok 1 | 7156 | 748.5 | 722.6 | | | |
| **(M1-B4)/B4** | | | | | 0.66 | 0.80 | 1.57 |
| **(M1-B1)/B1** | | | | | 714.6 | 1246.5 | 400.4 |

## 4 DISCUSSION

Naturally, the sediments are transported from land surfaces and slopes to river channel during rainy season. The sediment sources may originate from sources such as landslides in cleared areas (Collison& Anderson, 1996); slope collapses along rivers (Madej, 2001); raindrop impact and subsequent surface wash of exposed soils on roads, agricultural area and open area with poorly compacted soil (Ziegler & Giambelluca, 1997). The understanding of the pattern of sediment delivery and its pathways related to hydrological processes is needed in these investigations of sediment budget. It is very difficult to develop prudent long-term management plans for limitation and reduce the sediment budget in large catchments (Walling, 1983).

Human disturbance, such as agriculture and urbanization activity, makes sediment available for transport during rainfall events (Ismail and Hashim, 2014). The SS load showed an increasing trend during wet season but declined during dry season. The annual SS load also showed an increasing trend from the upper segment to lower segment. However, the rate of increases in sediment loading slightly reduced between the middle to lower segment by about 29%, but toward the lower end of the segment of the catchment, the percentage of sediment load increased by 66%, suggesting a higher sediment loading happened in the lower part of the catchment, where a lot of urbanization is taking place. The increase in human activities, for example a lot of housing and industrial development takes place in the lower part of the catchment.

Changes in the sediment load of a river can give rise to numerous problems. Erosion and sediment transport processes are sensitive due to their close links to climate, wide range of human activities, land cover, land use and the hydrology of a river catchment (Walling, 2009). This reflects a combination of factors. Human activities that affect the river ecosystem by sedimentation and high suspended solids originate from forest cutting and land-clearance, the expansion of agriculture, land use practices, urbanization and infrastructural development and dam construction (Walling & Fang, 2005). These impacts have been especially severe in river ecosystems. Ziegler *et al*. (2000) found that agricultural roads are the main source of sediment to the river and their surface erosion rates were more than eight times higher than those from footpaths and agricultural lands.

In the future, the variability in sediment loading necessitates the need for long-term monitoring of sediment yield. River management is imperative to promote harmonious relationship between humans and nature in reducing sediment input to the river systems. Sediment budgeting approach facilitates in identifying the sediment sources that urgently need attention. The variations of discharge flow and runoff due to seasonal factors showed difference in SS load related to sediment concentration during the wet season period compared to that during the dry season period. Other than that, SSC contents in the river are also affected by the influence of anthropogenic activities in the catchment area as well.

 

## 5 CONCLUSION

This study shows that the sediment load increases from the upper segment of river catchment (B1) which has very little disturbances in terms of land use activities as compared to those in the catchment, between B3, B4 and M1. The downstream changes in SS loads and increasing loading suggest that sediments are being added to the main river from various tributaries in the catchment. The total suspended sediment loading is around 7000 tonnes per year and is comparable to other Malaysian river fluxes associated with agricultural activities. The various land uses in the catchment area contribute to the varying SS loads as shown by the results. The loading in wet period is almost 50% or more than the dry period loads especially in the middle segment of the catchment due to varying land uses in this region. This suggests the effect of rainfall on the eroding of land surfaces with varying land cover. The inconsistencies in SSC in the river are influenced by the various anthropogenic activities (especially agriculture and urbanization activities) in the catchment area which necessitate future land use and sediment control to avoid sediment and possible nutrient loading into the estuary.

## ACKNOWLEDGEMENTS

The authors would like to thank Mohamad Khushairy Mohamad Zahir and Mohamad Adam Omar for their assistance during field sampling. We would also like to acknowledge Universiti Sains Malaysia for RU Grant no.1001/PHUMANITI/816229.

## REFERENCES

APHA. (1992). *Standard Methods for the Examination of Water and Wastewater*. 18th ed. Washington, DC: American Public Health Association.

Bash, J., Berman, C.H. & Bolton, S. (2001) *Effects of Turbidity and Suspended Solids on Salmonids,* Seattle, United States: University of Washington Water Center.

Balls, P.W. (1992). Nutrient Behaviour in Two Contrasting Scottish Estuaries, the Forth and Tay. *Oceanologica Acta*, 15, 261–277.

Cloern, J.E. (1987). Turbidity as a Control on Phytoplankton Biomass and Productivity in Estuaries. *Continental Shelf Research* 7, 1367–1381.

Collison, A.J.C. & Anderson, M.G. (1996). Using a Combined Slope Hydrology/Stability Model to Identify Suitable Conditions for Landslide Prevention by Vegetation in the Humid Tropics. *Earth Surface Processes and Landforms,* 21(8), 737-747.

Eyre, B.D. & McConchie, D. (1993). The Implications of Sedimentological Studies for Environmental Pollution Assessment and Management: Examples from Fluvial Systems in North Queensland and Western Australia. *Sedimentary Geology* 85, 235–252.

Ismail, W.R. (1996). The Role of Tropical Storms in the Catchment Sediment Removal. *Journal of Bioscience*, 7(2), 153-168.

Ismail, W.R. & Najib, S.A.M. (2011). Sediment and Nutrient Balance of Bukit Merah Reservoir, Perak (Malaysia). *Lakes and Reservoirs: Research and Management*, 16, 179-184.

Ismail, W.R. & Hashim, M. (2014). Changing Trends in Rainfall and Sediment Fluxes of Kinta River, Perak, Malaysia, Sediment Dynamics from the Summit to the Sea. *Proceedings of a Symposium held in New Orleans, Louisiana, USA,* 11–14 December 2014 (IAHS Publ.367, 2014), 340-346.

Littlewood, I.G. (1992) *Estimating Contaminant Loads in Rivers: A Review*, Institute of Hydrology Report No.17, Institute of Hydrology, Wallingford, UK.

Madej, M.A. (2001). Erosion and Sediment Delivery following Removal of Forest Roads. *Earth surface Processes and Landforms,* 26(2), 175-190.

Malaysia, (2010). Department of Agriculture Malaysia, 2010. Putrajaya.

Owens, P.N., Walling, D.E., He, Q., Shanahan, J.O. & Foster, I.D. (1997). The Use of Caesium-137 Measurements to Establish a Sediment Budget for the Start catchment, Devon, UK. *Hydrological Sciences Journal,* 42(3), 405-423.

Rahaman, Z.A. & Ismail, W.R. (2010). Spatial and Temporal Variation of Sedimentation Rate in the Timah Tasoh Water Reservoir, Perlis, Malaysia. *Annals of Warsaw University of Life Sciences- SGGW, Land Reclamation,* 42(1), 127-138.

Rosgen, D.L. (1994). A classification of Natural Rivers. *Catena,* 22, 169-199.

Shaw, E.M., Beven, K.J., Chappell, N.A. & Lamb, R. (2010). *Hydrology in Practice.* Spon Press, Taylor and Francis, UK.

Sheffield, A.T., Healy, T.R. & McGlone, M.S. (1995). Infilling Rates of a Steep Land Catchment Estuary, Whangamata, New Zealand. *Journal of Coastal Research*, 11(4),1294-1308.

Slaymaker, O. (2003). The Sediment Budget as Conceptual Framework and Management Tool. *Hydrobiologia,* 494, 71–82.

Walling, D.E. (1983). The Sediment Delivery Problem. *Journal of Hydrology,* 65, 209–237.

Walling, D.E. (2009). *The impact of Global Change on Erosion and Sediment Transport by Rivers: Current Progress and Future Challenges*. UNESCO.

 

Walling, D.E. & Fang, D. (2003). Recent Trends in the Suspended Sediment Loads of the World's Rivers. *Global and Planetary Change*, 39(1), 111-126.

Walling, D.E., Russell, M.A., Hodgkinson, R.A. & Zhang, Y. (2002). Establishing Sediment Budgets for Two Small Lowland Agricultural Catchments in the UK. *Catena*, 47(4), 323-353.

Ziegler, A.D. & Giambelluca, T.W. (1997). Importance of Rural Roads as Source Areas for Runoff in Mountainous Areas of Northern Thailand. *Journal of Hydrology*, 196(1-4), 204-229.

Ziegler, A.D., Sutherland, R.A. & Giambelluca, T.W. (2000). Runoff Generation and Sediment Production on Unpaved Roads, Footpaths and Agricultural Land Surfaces in Northern Thailand. *Earth Surface Processes and Landforms*, 25(5), 519-534.

 

Proceedings of the 37th IAHR World Congress
August 13 – 18, 2017, Kuala Lumpur, Malaysia

# OBSERVATION OF BEDFORMS IN THE DOWNSTREAM REACH OF THE TOYOHIRA RIVER DURING FLOOD

SATOMI YAMAGUCHI[(1)], RYOSUKE AKAHORI[(2)] & HIROKI YABE[(3)]

[(1, 3)]Civil Engineering Research Institute for Cold Region, Sapporo, Japan,
kawamura-s@ceri.go.jp
[(2)] Aichi Institute of Technology, Toyota, Japan

## ABSTRACT

Small-scale riverbed forms enhance form resistance against channel flow and greatly affect a rising water level during flood, so it is quite important to comprehend changes in riverbed topography from the standpoint of river disaster prevention. Further, form resistance decreases tractive force, which greatly influences sediment movement during flood. Thus, the comprehension of riverbed topography during flood is all the more crucial in order to foresee inundated sediment movement. However, few studies have investigated the relation between small-scale riverbed forms and their form resistance on the basis of actual riverbed observation data because riverbed forms are difficult to measure during flood. In this study, the riverbed topography in the lower reach of the Toyohira River is investigated through the observation method proposed by the authors, with the aim of grasping the characteristics of riverbed forms during flood. Small-scale riverbed forms which developed during a relatively large-scale flood is observed and commensurate form resistance is examined.

**Keywords:** Riverbed form; flow resistance; bed form observation; the Toyohira River; bed form evolution.

## 1 INTRODUCTION

Small-scale riverbed forms which develop during flood are a controlling factor of form resistance against channel flow, and greatly affect a rising water level. For this reason, it is quite important to comprehend changes in riverbed topography from the standpoint of river disaster prevention. Further, form resistance decreases flow velocity and weakens tractive force to transport sediment, thus exerting an influence on sediment movement during flood. Therefore, the comprehension of riverbed topography during flood is inevitable in order to foresee inundated sediment movement. There are many experimental studies and theoretical studies on the development of small-scale riverbed forms and the enhancement of hydraulic resistance (For example, Miwa and Daido, 2011; Kikkawa and Ishikawa, 1979; Yalin and Karahan, 1979;

Nakagawa and Tsujimoto, 1976; Kishi and Kuroki, 1973; Engelund, 1966). However, few studies have been conducted on the basis of actual riverbed observation data because riverbed forms are difficult to measure in full during flood.

Figure1 illustrates small-scale riverbed forms observed in Chiyoda Experimental Channel on June 24, 2012). Small-scale riverbed forms, called dunes, emerged. This figure shows the longitudinal profiles along a traverse line across the center of the channel (Tobita et al., 2013). The length and height of sand waves increased with time. In Figure 3, dimensionless total shear force $\tau^*$ and dimensionless effective shear force $\tau^{*'}$ derived by Kakinuma et al. (2013) from hydraulic parameters and bed materials in the experimental flow, are compared with the result of an estimated equation for form resistance of small-scale riverbed forms proposed by Kishi and Kuroki (1973). Here, the effective shear force is defined as a shear force where the roughness height of riverbed surface is limited only to riverbed materials, whereas the total shear force is a shear force which is the sum of effective shear force and form resistance of riverbed forms. When small-scale riverbed forms are absent bringing about no form resistance, roughness height depends largely on riverbed materials. In this case, the total shear force is almost equal to the effective shear force. By contrast, with the appearance of small-scale riverbed forms, form resistance generates shearing force, where the total shear force exceeds the effective shear force as the solid lines of DUNE I and DUNE II in Figure 2 indicate (Kishi and Kuroki, 1973). From Figure 2, it is figured out that riverbed forms observed in the Chiyoda Experimental Channel were small-scale riverbed forms classified as DUNE I, which were accompanied by their commensurate form resistance. Although sand waves of nearly life size were observed in the Chiyoda Experimental Channel, few studies have investigated the relation between small-scale riverbed forms and their form resistance on the basis of actual observation data of inundated riverbed.

Figure 3 illustrates the datum high water level (DHWL) of a flood event in September 2001 of the Toyohira River which is a feeder of the Ishikari River system, and the values calculated by Yoshikawa and Watanabe (2008) from the equation of one-dimensional unsteady flow in a river channel with a compound cross-section. The diagram resulted from the calculation with a fixed value of Manning roughness coefficient, which significantly underestimated the DHWL in the sections between KP 6 and 10. Where, KP in the

 

Toyohira River indicates the longitudinal distance (km) from the downstream end joining the Ishikari River. They proved that the DHWL could be simulated to some extent by allowing for increasing roughness along with the development of small-scale riverbed forms (Yoshikawa and Watanabe, 2008), from which it can be inferred that the sections from KP 6 to 10 possessed a property of developing sand waves during flood. This implies that the water level fluctuated intricately in the lower reach of the Toyohira River during flood and the water surface profile during flood is possibly controlled by the development of sand waves to a considerable degree. Because tractive force to transport sediment downstream may significantly attenuate in a section where water surface gradient greatly decreases, attention needs to be paid not only to a rise in water level but to sediment deposit within a channel during flood. Figure 4 demonstrates the sediment budget within the channel of the Toyohira River before and after the 1981 flood which set the historical maximum discharge (Ooyama and Watanabe, 2002). The diagram indicates that sedimentation took place upstream from KP 7 in the lower reach (erosion downstream from KP 6 is considered to result from the influence of drop-down, but details unknown), suggesting that flood on a larger scale allows a greater amount of soil to be transported from the upper reach and sediment easily.

As the above mentioned reports have suggested, fluctuations of water level and sediment movement during flood are very intricate in the lower reach of the Toyohira River and the development of sand waves made the matter much more complicated. Yet, riverbed forms and form resistance in these sections during flood have not been investigated on the basis of concrete measurement data. Thus, their characteristics have yet to be clarified. In this study, riverbed forms in the lower reach of the Toyohira River during flood are observed with the aim of grasping the characteristics of its riverbed topography.

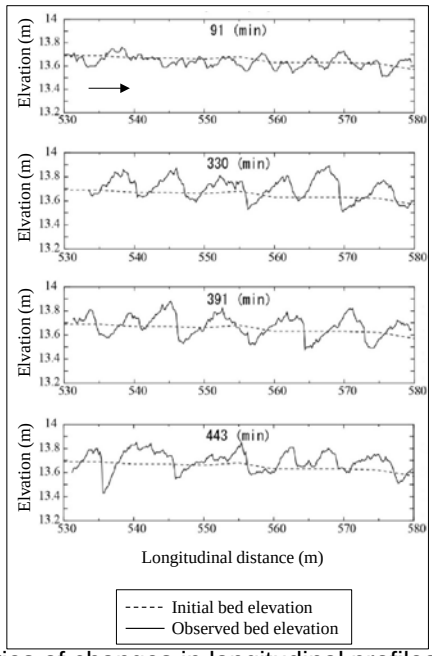


**Figure 1.** Time series of changes in longitudinal profiles of riverbed forms (Chiyoda Experimental Channel in June 2012 (Tobita et al., 2013)).

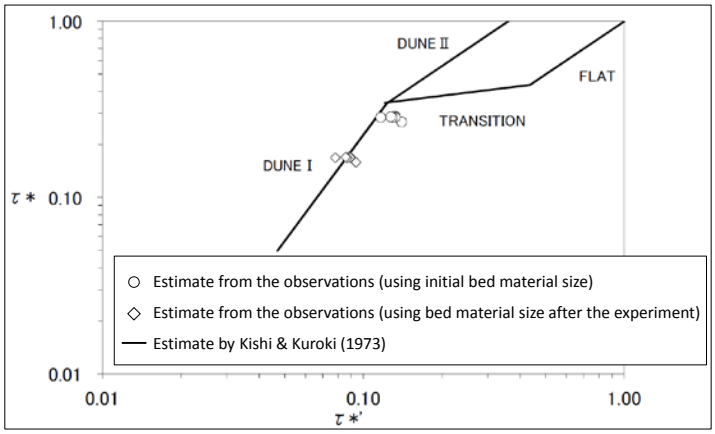


**Figure 2.** Total shear force and effective shear force observed in the Chiyoda Experimental Channel (Kakinuma et al., 2013).

 

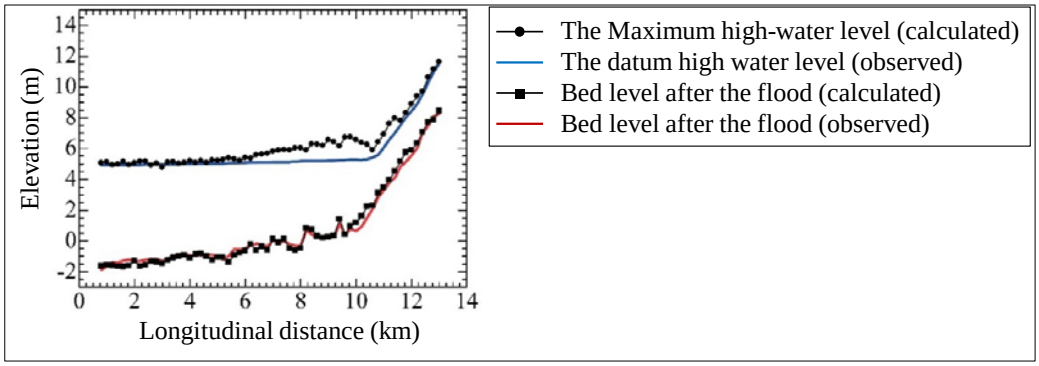


**Figure 3.** Datum high water level (DHWL) and values derived from the equation of one-dimensional unsteady flow with a compound cross-section for the flood event of the Toyohira River in September 2001 (Yoshikawa and Watanabe, 2008).

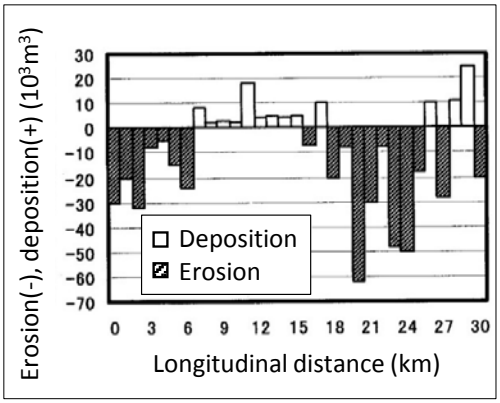


**Figure 4.** Sediment budget in the Toyohira River before and after the 1981 flood (Ooyama and Watanabe, 2002).

## 2 OBSERVATION METHOD

To understand the mechanism of riverbed topography changing during flood, attempts had been made continuously as an important issue for river disaster prevention (Kinoshita, 1989). In some of recent studies, riverbed forms were surveyed by taking advantage of highly advanced planar observation technologies including a multi-beam sonar system (Akahori and Shimizu, 2011). However, these technologies had not yet been applied to an investigation during flood because of difficulty in dealing with economical and personal costs. The authors had proposed a reasonable low-risk method for observing riverbed topography, by applying a commercially available fish detector to an echo-sounding system and installing it on a radio-controlled boat (Akahori et al., 2012). This device was used to survey riverbed topography in the estuary of the Rumoi River and the results were compared with those obtained by a multi-beam sonar system, where the effectiveness of this device was recognized. In this study as well, riverbed topography during flood was observed in the same method.

As Figure 5 shows, an echo sounding system adapted from a fish detector was installed in CERI's radio-controlled air boat to observe riverbed topography. The observation apparatus was based on the commercially available fish detector (Lowrance HDS-8) installed inside the boat. The other devices connected with the HDS-8 terminals are: an echo sounding oscillator (50/200 kHz skimmer transducer) and a simple Structure Scan sonar imaging system, which were fixed to the boat bottom; and a data logger to record observed information (Hydro Systems). The data logger registered soundings, GPS time and other observation data. With the aim of acquiring spatial characteristics of riverbed topography more accurately, a RTK-GPS (Nikon Trimble5700) was used together. The RTK-GPS is capable of acquiring accurate positional information of a mobile station relative to a reference station by exchanging communications between a base station built on the ground and a mobile station on the boat. By assigning a point with known positional information as a reference point (the KP6.8 distance mark on the right bank of the Toyohira River was assigned as a reference point in this study), an absolute positional information of the boat can be figured out from its relative position. The HDS-8-based sounding system and the RTK-GPS were not directly linked in this mechanism, but HDS-8 sounding information stored in the data logger and RTK-GPS positional information were synchronized later according to GPS time of the both systems to produce the survey result with accurate positional information (Akahori et al., 2012). In order to carry out a safe and swift observation during a flood event, an air boat was employed in this study.

 

Because the sounding system installed on HDS-8 collects sounding information as a single beam sounder, only one-dimensional information was generated when the observation boat moves linearly. For this reason, an attempt was made to grasp planar riverbed topography, by running the radio-controlled boat in a longitudinal direction back-and-forth multiple times to scan depth information.

The sounding data obtained in this manner were processed with RTK-GPS information about horizontal direction and water level. Then, the riverbed elevation was figured out planarly. Here, the riverbed elevation was calculated as follows: (the elevation of GPS antenna registered at RTK-GPS) minus (HDS-8 sounding, distance from draft to oscillator, and height from GPS antenna to draft.)

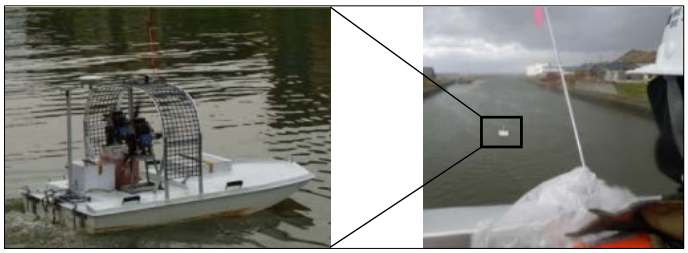

**Figure 5.** An echo sounding system adapted from a fish detector installed in the radio-controlled air boat to observe riverbed topography.

## 3 OBSERVATION RANGE AND PERIOD

The observation range extended from the Kariki Ohashi Bridge at KP 7 in the lower reach of the Toyohira River to nearly 150m downstream (Figure 6 and Figure 7). As stated above, this is the section where a water level was likely to rise with the formation of sand waves during flood. The low-flow channel width in this section was approximately 90m. For the safe operation of the observation boat, a length of nearly 50m around the center of the channel was appointed as a cross-sectional width of the observation range.

The investigation was conducted during floods from a snowmelt season to a summer/fall in 2014 and 2015. Although the observation boat was unmanned, special care was directed to the safe operation by avoiding the research in the nighttime and on windy days. In that situation, the research was conducted seeking the water level as high as possible. The observation was carried out five times in all, on the date and time listed in Table1. Table1 indicates the water levels at an observation time registered at the Kariki observation station (KP 11.1.)

The 2014 and 2015 data of the water level at the Kariki observation station are illustrated in Figure 8. Among all the floods observed during these two years, only the second event in September, 2014, was relatively large in scale. Figure 9 shows observation points obtained by running the radio-controlled boat. In the diagram, observation points (dotted white lines) from Observation No. 2 were depicted as an example. Within the observation range, the radio-controlled boat was run in a longitudinal direction back-and-forth about 15 times (approx. 30 sidings) and the planar riverbed elevation data were collected.


**Figure 6.** Observation range (aerial photo of the Kariki Ohashi Bridge over the Toyohira River). The background photo by Geospatial Information Authority of Japan, 2008.

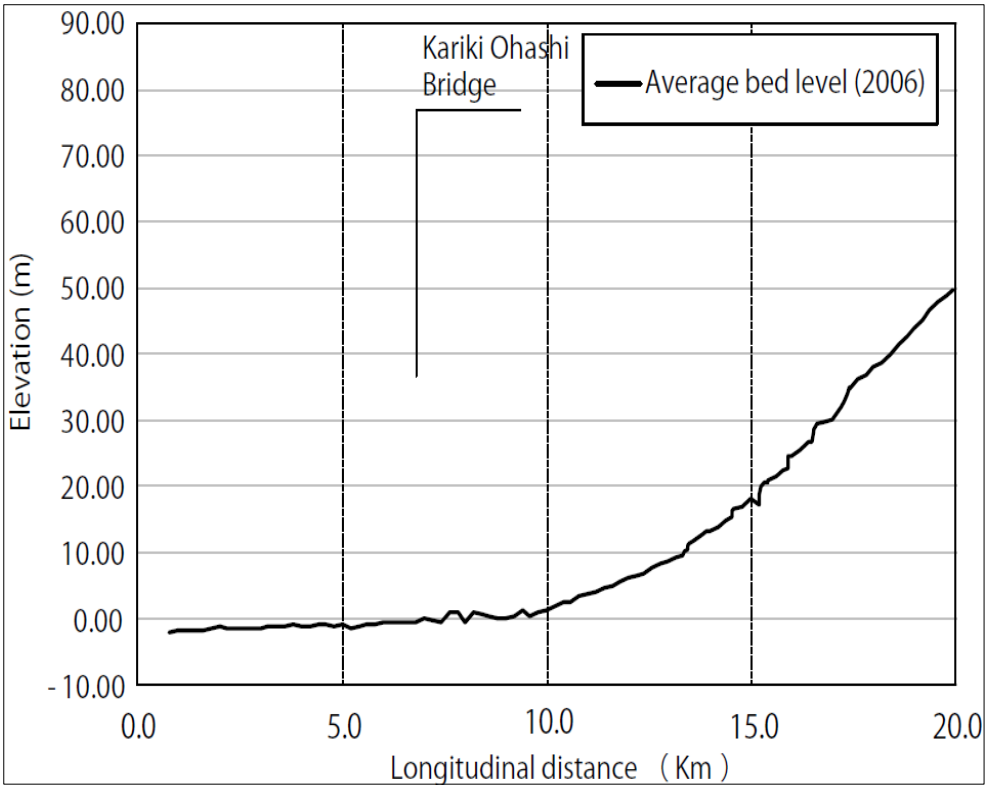


**Figure 7.** Longitudinal profile of the Toyohira River

**Table 1.** The observation date and the water levels at observation time.

| Observation No. | Date and time | Water level at Kariki observation station |
|---|---|---|
| **1** | 2014/4/24 9:00 | 4.6 m |
| **2** | 2014/9/11 13:00 | 5.2 m |
| **3** | 2015/4/28 10:00 | 5.1 m |
| **4** | 2015/10/10 7:00 | 4.8 m |
| **5** | 2015/11/18 10:00 | 4.3 m |

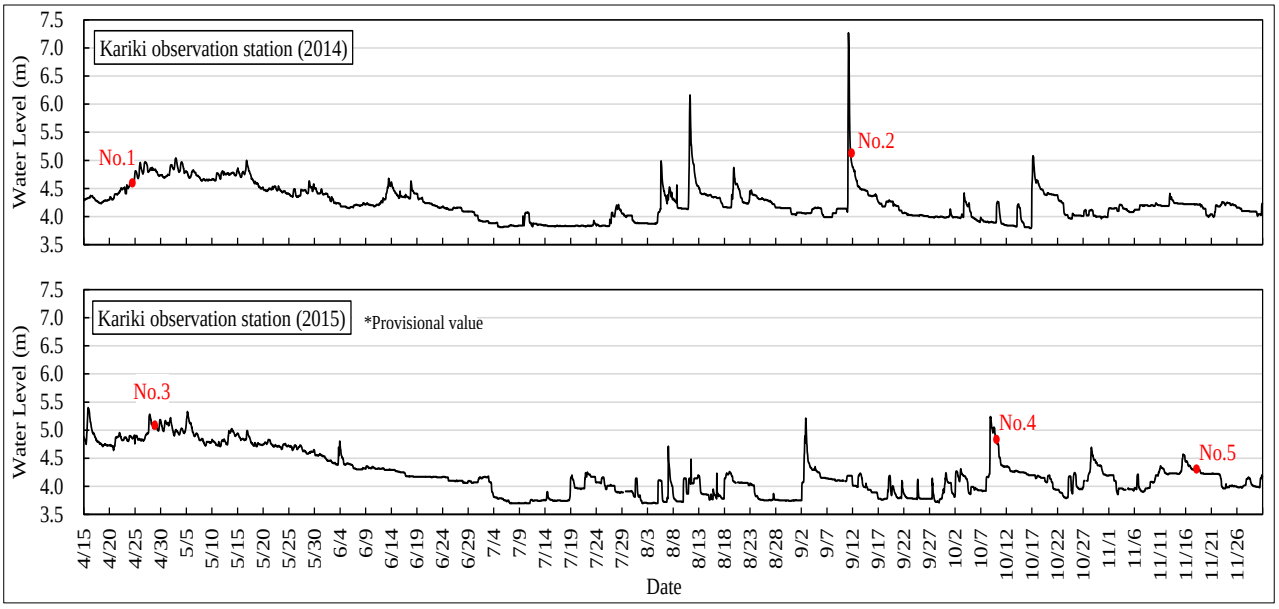


**Figure 8.** Data of the water level at the Kariki observation station (2014 and 2015).

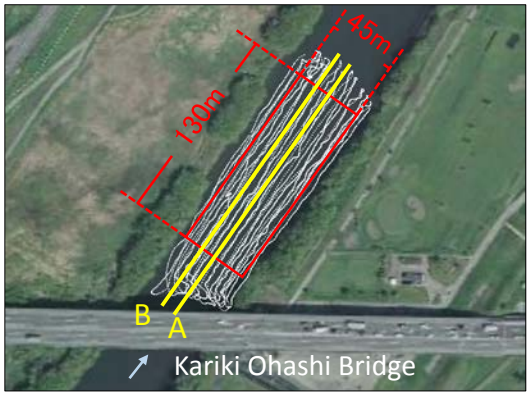


**Figure 9.** Observation points obtained by running the radio-controlled boat (dotted white lines from Observation No. 2). The background photo by Geospatial Information Authority of Japan, 2008.

## 4 OBSERVATION RESULTS

The images of riverbed topography obtained through Observation No. 1 to No. 5 were illustrated in Figure10. They were mapped out of the area within the red rectangle in Figure 9, using a preprocessor, iRIC v.2.3 (http://i-ric.org/). Regarding the longitudinal sections A and B shown in Figure 9, different observation outcomes in longitudinal riverbed profile were compared in Figure 11.

In the riverbed topography observed on April 24, 2014 (Observation No. 1 in Figure 10 (a)), the shape of alternate bars was seen but no small-scale riverbed forms were detected. From the longitudinal profile in Figure 11, no sand waves were confirmed either.

By contrast, the riverbed topography observed on September 11, 2014 (Observation No. 2 in Figure 10 (b)) was more distinctive, from which the development of small-scale riverbed forms like those seen in the Chiyoda Experimental Channel as in Figure 1 was recognized. The longitudinal profile in Figure 11 insinuated the formation of sand waves with a wave length of 10m to 20m, attaining a maximum wave height of 30cm. It was also found that the riverbed elevation on September 11, 2014 (Observation No.2) was generally higher than that observed on April 24, 2014 (Observation No. 1). Within the observation range, the riverbed rose 0.32m at the highest and 0.13m on cross-sectional average.

Riverbed topography observed on April 28, 2015 (Observation No. 3 in Figure 10 (c)) and that on October 10, 2015 (Observation No. 4 in Figure 10 (d)) exhibited the formation of alternating bars similar to those on April 24, 2014 (Observation No. 1 in Figure 10 (a)), as well as considerably small sand waves. But, these sand waves were no higher than 10cm and nothing reached its full growth.

Alike in the riverbed topography observed on April 24, 2014 (Observation No. 1 in Figure 10 (a)), no sand waves were presented on November 18, 2015 (Observation No. 5 in Figure 10 (e)).

On September 11, 2014 (Observation No. 2), when the formation of sand waves was confirmed, a peak water level of 7.3m was observed at 5:00 at the Kariki observation station as shown in Figure 8. The peak levels in the other flood events during the investigation period reached no higher than 5.3m with no development of sand waves. This implied that the observed area was characterized as not to produce sand waves unless the scale of a flood grew to a certain degree. The slope of the observed section was gentle, allowing sediment to accumulate easily, which was counted as one of the characteristics in longitudinal profile of the Toyohira River. Decreased flow velocity as a result of the formation of small-scale riverbed forms possibly encourages sediment deposit. This section was considered to be a place where the water level tends to rise during flood due to the development of small-scale sand waves and sediment deposit.

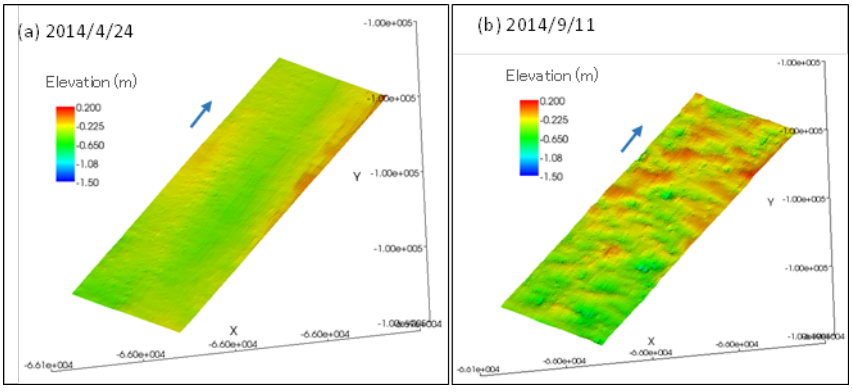

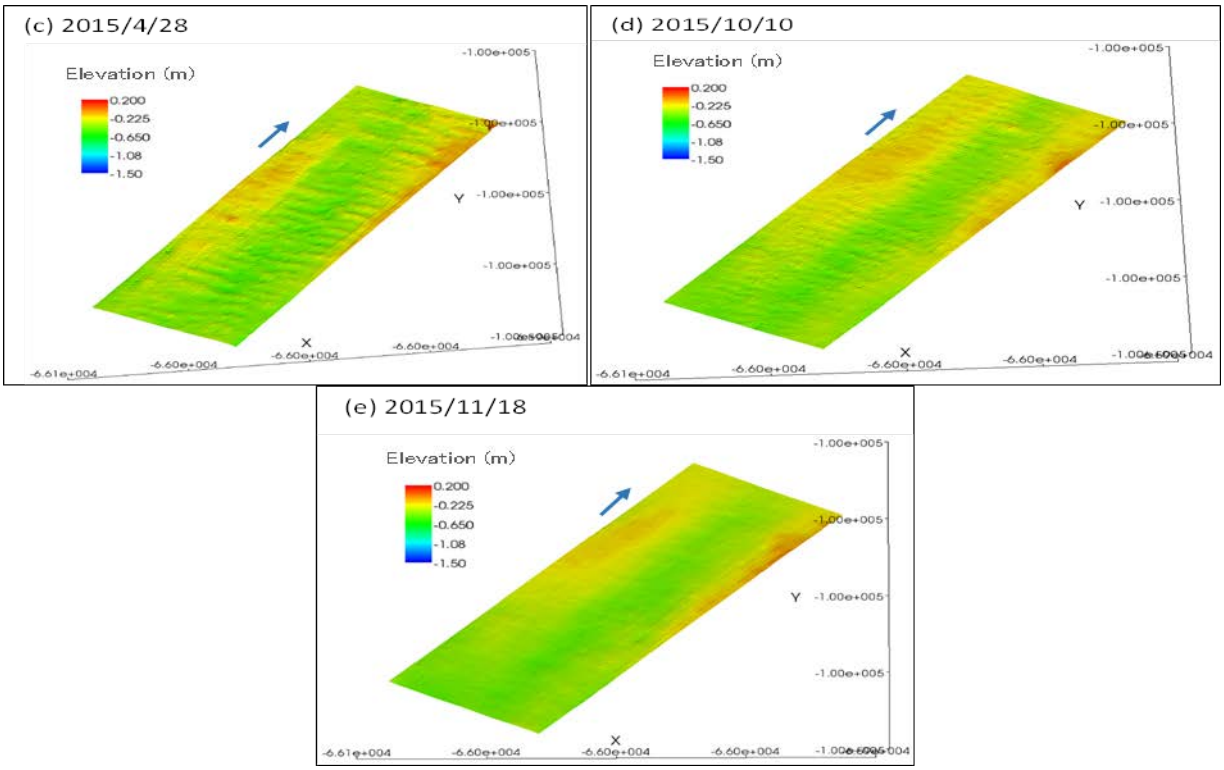


**Figure 10.** Riverbed topography on (a) April 24, 2014 (No. 1), (b) September 11, 2014 (No. 2), (c) April 28, 2015 (No. 3), (d) October 10, 2015 (No. 4) and (e) November 18, 2015 (No. 5).

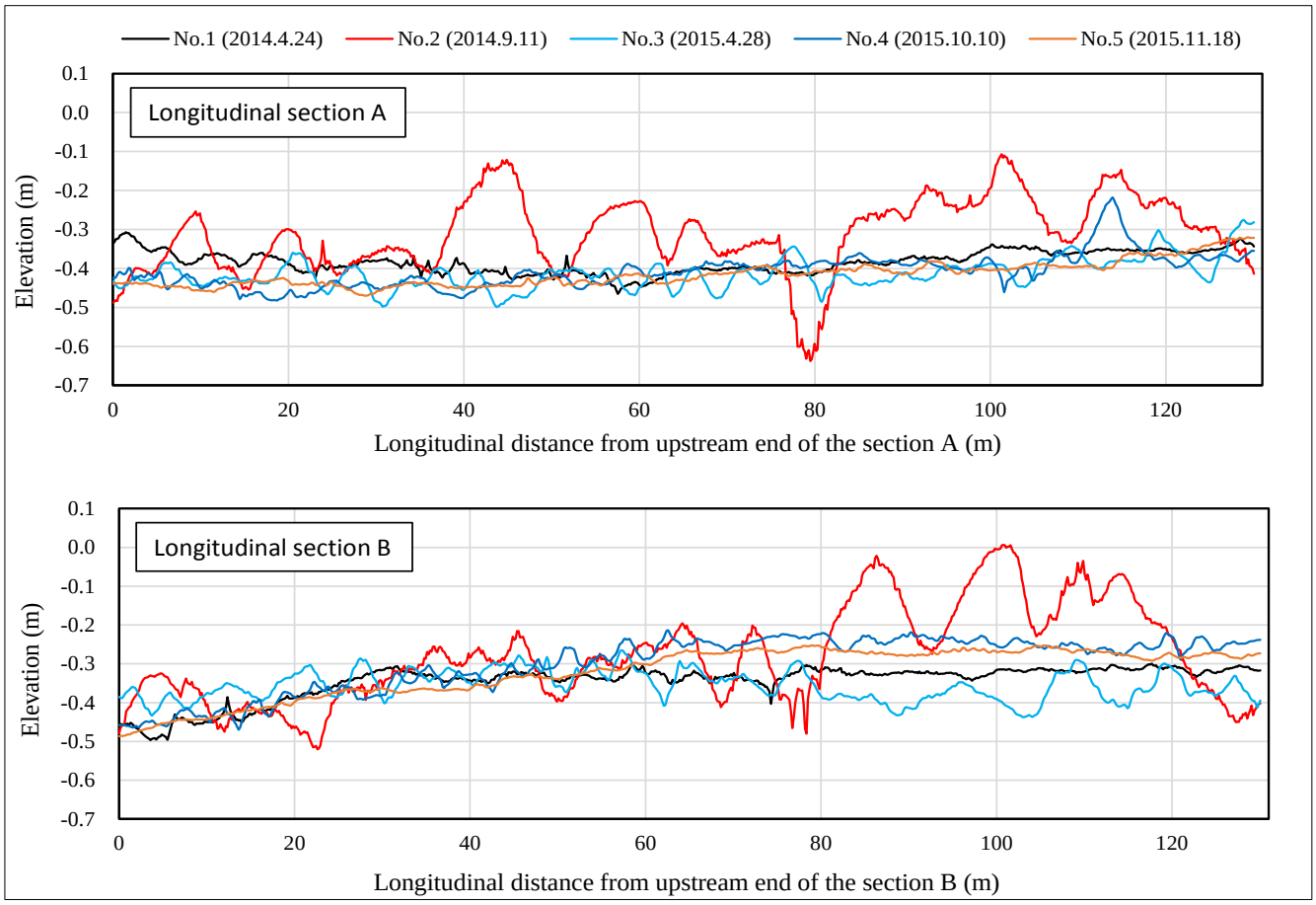


**Figure 11.** Longitudinal riverbed profile (longitudinal sections A and B in Figure 9).

## 5 DISCUSSION

The flows both at peak and at an observation time during floods of Observations No. 1 (April 24, 2014) and No.2 (September 11, 2014) are listed in Table 2. These data were registered at the Kariki observation station. No. 3 through No.5 are omitted because the flow data for FY 2015 has not yet been released by the time this paper is completed. Table 2 also includes mean depth, dimensionless effective shear force $\tau_*'$ and dimensionless total shear force $\tau_*$ derived from observation data. The value of shear force is calculated from flow rate, mean depth, low-flow channel width, bed slope and representative grain-diameter of riverbed materials (Yoshikawa and Watanabe, 2008). In Figure 12, the relationship between effective shear force $\tau_*'$ and total shear force $\tau_*$ derived from the observation result is compared with the result of estimated equation for form resistance of small-scale riverbed forms proposed by Kishi and Kuroki (1973).

According to Figure 12, on September 11, 2014 (Observation No. 2) when the development of sand waves is seen, small-scale riverbed forms categorized as DUNE I appeared, bringing about their form resistance. In the meantime, although the development of small-scale riverbed forms is not observed on April 24, 2014 (Observation No. 1), the value of total shear force is considerably large. This can be attributed to the influence of backwater of the Ishikari River into which the Toyohira River flows. The observation range in this study constituted the backwater section of the Ishikari River, where the flow regime is particularly subject to the water level of the Ishikari River as well as to the flow rate of the Toyohira River. In this regard, the water level is assumed to have risen under the influence of backwater of the Ishikari River on April 24, 2014 (Observation No. 1.)

It is already known that sand waves occur when the Froude number is relatively small and that they tend to disappear as the Froude number increases. In other words, sand waves develop with a relatively low flow rate and disappear when the flow rate increases to a certain level as a general rule. However, in the backwater section observed in this study, the water level in the lower reach possibly affected the developmental properties of sand waves. Thus, it is our future task to clarify the relationship between developmental properties of sand waves and riverbed resistance in the section like this.

**Table 2.** The discharge and the shear force under observation.

| Observation No. | Discharge at Kariki observation station ($m^3/s$)(*1) (at peak of the food) | (at the observation time) | Observed mean depth (m) | Total shear stress $\tau_*$ | Effective shear stress $\tau_*'$ |
|---|---|---|---|---|---|
| **1** | 76.63 | 76.28 | 1.47 | 0.68 | 0.14 |
| **2** | 694.52 | 198.92 | 2.78 | 1.29 | 0.24 |

(*1) Water information system by Ministry of Land, Infrastructure, Transport and Tourism, Japan

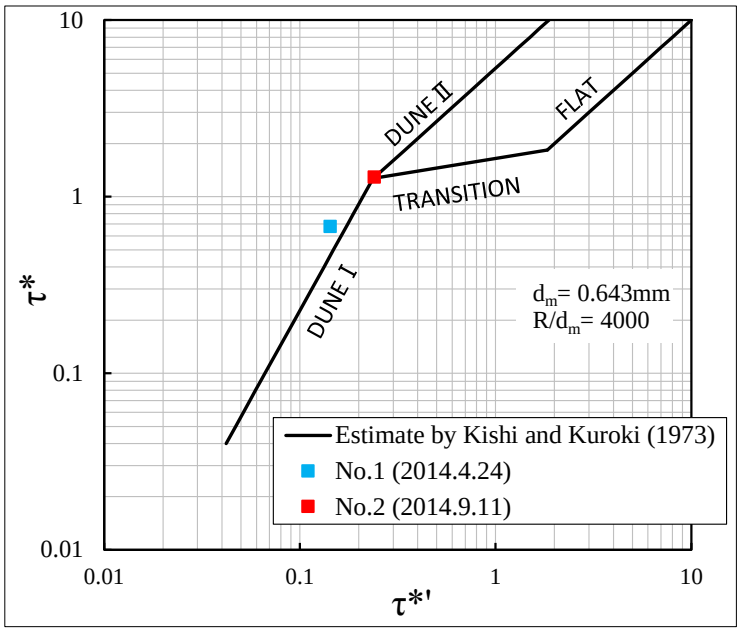


**Figure 12.** Total shear force and effective shear force under observation.

 

## 6 CONCLUSION

In this study, the riverbed topography in the lower reach of the Toyohira River is investigated, with the aim of grasping characteristics of riverbed forms during flood. The development of small-scale riverbed forms is observed in the event of large flood. Their subsequent form resistance is estimated. On this occasion, a rise in mean riverbed height is confirmed along with the development of small-scale riverbed forms. The growth of small-scale riverbed forms possibly encourage sediment deposit. Because few studies have carried out on the basis of actual observation data as to the development of small-scale riverbed forms, the water level increased with form resistance, and properties of sediment movement, our future task is to build up actual measurement data.

## REFERENCES

Akahori, R. Hirai, Y. & Kondo, M. (2012). *Observation of Bedforms in the Downstream Reach of Rumoi River by Using A Brief Acoustic Bathymetric System.* Advances in River Engineering, 18, 137-142. (In Japanese)

Akahori, R. & Shimizu, Y. (2011). Bedforms in the Kushiro River: Wavenumber Analysis of a High-Resolution DEM Obtained from A Multi-Beam Survey. *Proceedings of the 7th IAHR Symposium on River, Coastal and Estuarine Morphodynamics*, 1987- 460.

Engelund, F. (1966). Hydraulic Resistance of Alluvial Streams. *Journal of the Hydraulics Division, ASCE, Proc. ASCE,* 92(HY2), 315-326.

Kakinuma, K., Inoue, T., Akahori, R. & Takeda, A. (2013). A Research on the River Bed Resistance of Chiyoda Experimental Flume. *Journal of Japan Society of Civil Engineers, Ser. B1 (Hydraulic Engineering),* 69(4), 1087-1092.

Kikkawa, H. & Ishikawa, T. (1979). Hydraulic Resistance of Streams over Dunes and Ripples. *Proceedings of the Japan Society of Civil Engineers*, 1979(281), 55-63. (In Japanese)

Kinoshita, R. (1989). Changes in the Sand-Bed Formation During Flood. *Proceedings of the Japanese Conference on Hydraulics,* 33, 439 - 444.

Kishi, T. & Kuroki, K. (1973). Bed Forms and Resistance to Flow in Erodible-Bed Channel (1): Hydraulic Relations for Flow over Sand Waves. *Bulletin of the Faculty of Engineering, Hokkaido University*, 67, 1-23. (In Japanese)

Miwa, H. & Daido, A. (2011). Mechanism of Flow Resistance in Alluvial Streams with Sand Waves and Prediction of Sediment Transport System. *Journal of Japan Society of Civil Engineers, Ser. B1 (Hydraulic Engineering),* 67(4), 757-762. (In Japanese)

Nakagawa, H. & Tsujimoto, T. (1976). Experimental Study on Evolution of Sand Waves Form an Initially Flattened Bed. *Disaster Prevention Research Institute Annuals*, 19(B), 289-309. (In Japanese)

Ooyama, F. & Watanabe, Y. (2002). Study on Bar Formation Under Unsteady Flow Conditions In Rivers. *Monthly Report of Civil Engineering Institute for Cold Region*, 587, 30-45. (In Japanese)

Tobita, D., Kakinuma, K. & Takeda, A. (2013). Observation of Riverbed Form Characteristics in the Chiyoda Experimental Flume. *Hokkaido Development Bureau Technical Research Paper (H24)*. (In Japanese)

Yalin, M.S. & Karahan, E. (1979). Steepness of Sedimentary Dunes. *Journal of Hydraulics Division, ASCE,* 105(HY4), 381-392.

Yoshikawa, Y. & Watanabe, Y. (2008). *Examine of Manning's Coefficient and the Bed-Load Layer for One-Dimensional Calculation of Be Variation*, Monthly Report of Civil Engineering Research Institute for Cold Region, 662, 11-20.

 

# SOIL EROSION IN A CHANGING LANDSCAPE OF PULAU PINANG, MALAYSIA.

SUMAYYAH AIMI MOHD NAJIB[(1)] & ZULLYADINI A RAHAMAN[(2)]

[(1)] Department of Geography and Environment,
Faculty of Human Sciences,Universiti Pendidikan Sultan Idris, Tanjung Malim, Perak
sumayyahaimi@gmail.com
[(2)]Research Centre for Environmental Sustainability, Department of Geography and Environment,
Faculty of Human Sciences,Universiti Pendidikan Sultan Idris, Tanjung Malim, Perak
zully@fsk.upsi.edu.my

## ABSTRACT

Landscape change as the alteration of land use considerably affects the environment and its processes. Land use has changed significantly in the last century, mostly due to human activities. Soil erosion as one of these processes is particularly affected by changes in land use. As soil erosion depends on surface runoff, which is regulated by the structure of land use, the effects of changes in slope length due to landscape change on erosion displacement can be significant. Pulau Pinang which has limited sources of land, has been undergoing a rapid land use changes through agriculture, settlement, and urbanisation and many other human activities. This study utilizes GIS software and topographic maps to examine the changes that occur in the Barat Daya Pulau Pinang during the time points of 1974, 1984,2004 and 2012. Landscape metrics analysis is used to investigate which land uses are dominant and the spreading of the land uses affecting soil erosion. The Universal Soil Loss Equation is used to estimate past soil erosion.The results from Shannon Diversity index show that there is a significant relation between land use changes and Soil loss data with $R^2$=0.92. This study concludes that soil erosion is reflected by changes in land use.

**Keywords:** Soil Erosion; land use; changing landscape; Pulau Pinang.

## 1 INTRODUCTION

Land use change refers to the changes in an area due to any activities and directly changes the landscape (Meyer and Turner, 1994). Changes in land use and land cover is one of those major challenges that affect the natural landscape and also has a direct relationship with natural processes, including soil productivity, species diversity, climate, biogeochemical and hydrological cycles (De Girolamo and Lo Porto, 2012). Land use is also one of the important factors that affect the quantity and quality of water (Wang et al., 2008; Tong et al., 2002). Assessing the impact of land use change on water quantity and quality is fundamental to the sustainable development (Lenhart et al., 2003; Lin et al., 2007) and important component in the river basin and water resource management. Soil erosion is a natural and inevitable process that can become a serious environmental and economic problem (López et al., 1998). Erosion is natural process and can be speeded up by changes in land use. Changes in land use can act as triggers for increases in hill slope soil erosion and catchment sediment yield (Wicks and Bathurst, 1996). After independence in 1957, Malaysia began to move towards a rapid development both in terms of economy, social and urbanisation. The effect of this action is causing some problems such as irregular development and affecting the quality of the physical environment (Ismail Ibrahim, 2000). Significant changes in land use can alter sediment delivery and discharge of a river basin, thus also affecting geomorphological processes in the river (Kondolf et al., 2002).

While spatial metrics are a tool for measuring the structure and style of the thematic map, the analysis of spatial structures and patterns are central to geographic research. Spatial primitives such as location, distance, direction, orientation, linkage, and pattern have been discussed as general spatial concepts in geography. In geography, these concepts have been implemented in a variety of different ways (Wu & Hobbs, 2002). In this study, these basic spatial concepts and the analysis of spatial structure and pattern will be approached from the perspective of spatial metrics. Under landscape metrics, spatial metrics are already commonly used to quantify the shape and pattern of vegetation in natural landscapes (Gustafson, 1998; McGarigal and Marks, 1994). Analysis of landscape metrics have already been widely used such as the number of Patch (NumP), Mean Patch Size (MPS), Edge Density (ED), Total Edge (TE) and determination of the Shannon Diversity Index (SHDI). Research on changes in land use and landscape spatial is important and is the foundation for studies exploring the natural and cultural landscape of a region. This paper describes how land use and landscape pattern have changed in the area of study for the past 38 years and how they affect soil erosion.

 

## 2 STUDY AREA & METHODOLOGY

### 2.1 Study area

Barat Daya District of Pulau Pinang was selected as the study area, which consisted of 19 river catchments. The sampling station of each catchment is shown in Figure 1. The list of the selected rivers are the Upstream and Downstream of Relau River, Upstream and Downstream of Ara River, Bayan Lepas River, TelukKumbar River, PulauBetong River, Nipah River, Burung River, Kuala Jalan Baru River, Buaya River, TitiTeras River, Pak Long River, Ayer Puteh River, Rusa River, Pinang River, TitiKerawang River, and Teluk Bahang Upstream and Downstream River. Barat Daya area was selected as the research area due to the lack of data in terms of sediment and discharge, and also the diversity of land uses compared to the Timur Laut which was dominated by build-up land use. In addition, there were no comprehensive sediment studies in the Barat Daya area. According to the Malaysian Meteorological Department data, the temperature of the northern part of Penang ranges between 29◦C and 32◦C and the mean relative humidity lies between 65% and 70%. The highest temperature is from April to June, while the relative humidity is lowest in June, July and September. Rainfall in Penang Island averages between 2000 and 3000 mm per annum, respectively. The highest annual rainfall was recorded in September, which was 384.66 mm (rain gauged school of physics), while at Bayan Lepas was 376.9 mm (Sumayyah & Zullyadini, 2015).

## 3 DESCRIPTION OF THE DATABASE

### 3.1 Modeling using universal soil loss equation (USLE)

For predicting soil erosion in this study, the Universal Soil Loss Equation (USLE) method was used (Wischmeier and Smith, 1965; 1978). USLE is probably the best-known empirical formula for predicting long-term (annual, monthly) gross erosion and is used frequently by soil conservationists around the world (Brath et al., 2002). It is an, efficient method for soil loss assessment and universally accepted method for monitoring soil loss. The USLE model integrated with GIS could be used to calculate soil erosion at any point in catchment experiencing net erosion. Mathematically, the equation is denoted as:

$$A \text{ (tons/ha/year)} = R*K*LS*C*P \quad [1]$$

Where:A is annual soil loss ,R is rainfall and runoff erosivity factor, K is soil-erodibility factor, L is length of slope factor, S is degree of slope factor, C is cropping-management factor and P is conservation practice factor

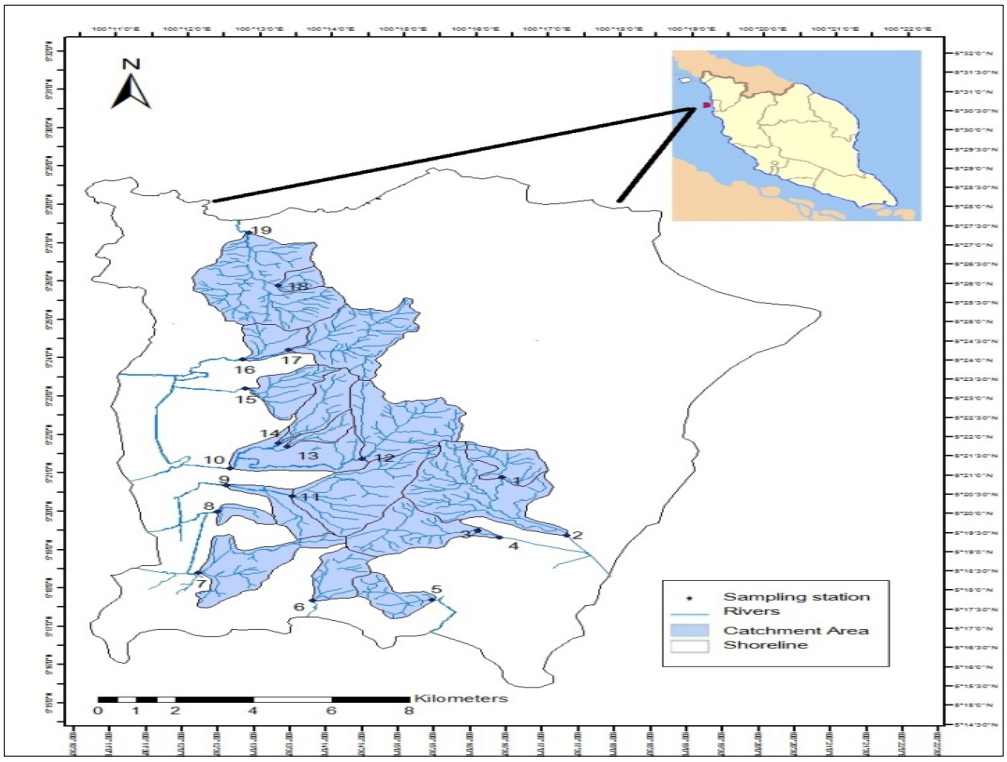


**Figure 1**. Sampling stations for 19 catchments.

 

3.2 Landscape metrics analysis modelling using universal soil loss equation (USLE)

This study analyzed land use changes from 1974 to 2012 for 19 river basins where landuse maps were obtained from the Department of Agriculture. Land use map in JPEG format was registered in RSO and subsequently digitized. The classification of land use was based on the Ministry of Agriculture and the five categories of land uses were forest, agriculture, built-up area, mining and others. (Table 1) shows the details of land uses used in this study. A set of landscape metrics was used for evaluating landscape spatial pattern. Patch analysis were used to obtain the changes in statistical metric analysis by class and landscape using Arc GIS 10.1. Landscape metrics analysis or pattern analysis was used to compare the changes in patterns between years, from 1974 to 2012. The description of the landscape metrics used in this study is shown in Table 2.

**Table 1.** Classification of land uses in this study based on the Ministry of Agriculture Malaysia.

| Land Use | Classifications |
|---|---|
| Forest | Forest |
| Built-up area | Urban area &Housing |
| Agriculture | Rubber, orchards, coconut, oil palm |
| Mining | Mining area, quarry |
| Others | Dam, schrub, grassland |

**Table 2.** FRAGSTAT metrics (McGarigal et al., 1994).

| Index | Formula | Description |
|---|---|---|
| **NumP (Number of Patch)** | $\sum_{i=1}^{n} Pi$ | P*i refers to the number of patches for one class of land use* |
| **ED (Edge Density)** | $\frac{TE}{TLA}$ | *TE* refers to the total perimeter of the land use of the same class, TLA refers to the total area of the land use of the same class<br>*Edge density* is a measurement of the multiple forms of patches involved. The higher the ED, the higher the degree of diversity and complexity |
| **SHDI (Shanon Diversity Index)** | $\sum_{i=1}^{m} (Pi * \ln Pi$<br>m = the number of patches that are involved<br>Pi = area by class | SHDI value increases if the number of patches also increases and wide distribution of borders between classes increases through time. The value of this statistic is very useful for the spatial study especially for landscaping basin which aims to evaluate the process of change as a result of development. |

## 4 RESULTS AND DISCUSSION

4.1 Changing in landscape 1974-2012

Figure 2 and 3 shows the change in land use for the past 38 years in the study area. Based on land use map in 1974, agriculture is the most dominant land use there. The percentage of agricultural land was 71.37%, forest 28.4%, while built up area only covered less than 1% of total area. In 1984, percentage of agricultural land use was 68.06%, and percentage of forest decreased to 24% and other land uses, mining and built up area just began to develop. After 20 years, the land use pattern began to change significantly. Even in 2004, agricultural land use was still dominant with percentage of land use change of 72.86%, while forest land use reduced to 17.8%. Percentage of built up area also increased from only 1% to 5.93%. In line with the development of Penang, land use patterns also began to dractically change in 2012. Percentage of built-up area increased to 18.87%, agricultural land use decreased to 63.12%, forest decresed to 12% and the rest for other land uses. In the Barat Daya region, the main human activities were agricultures because they have paddy, oil palm, orchard as their source of income.

4.2 Metrics analysis

4.2.1 Number of Patches (NUMP), Mean Patch Size (MPS) & Edge Metrics Study Area

NUMP is the total number of patches, while Mean Patch Size (MPS) is the average of patch size which includes analysis of Patch Density and Size Metrics. This land use changes depend on the number of patches where the higher the value, the higher the changes occurring in any land use category. Based on the analysis

 

in this study area (Table 3), the highest patches was from agricultural land use with 251 patches. Built-up area showed increasing value from 1 patch in 1974 to 87 patches in 2012. Forest decreased the most from 60 patches to 9 patches. With regards to mean patch size, the mean built-up area and forest increased, while agriculture decreased from 48.82 in 1974 to 22.46 in 2012. According to mean patch size of mining, the value reached its peak in 2004 and fell to its bottom in 2012 from 64.74 to 1.64, suggesting that human activities had high impact on the land use change. Edge Density and Total Edge (TE) is an analytical edge metrics to observe the diversity of the boundaries between land use categories. For example, if the Edge Density is high, then the degree of diversification of land use and its distribution is uneven. That means the higher the value of the ED, the higher the degree of diversification of land use in a basin. On the other hand, if ED value is reduced, it illustrates the lack of land use in the area. Similarly, if the TE is high, then the composition of the land use is also high and uneven. Based on Table 4, the density of ED value for built up area shows increasing value from 1974 to 2012, while the ED value for forest land use decreases from 1974 to 2012. The density of agriculture increases slightly in 1984 and decreases from 2004 and 2012. Overall landscape fragmentation is greatest in 1984.

4.2.2 Soil loss and and use change relationship

Soil erosion is one of the most critical environmental hazards of modern times (Manoj et al., 2010). In many watersheds or regions, land use changes and climate variability are the major forces behind hydrological variability (Tomer and Schilling, 2009). Land use, which relates to land cover, is one of the influential factors that affect soil erosion. The change in land use has caused the acceleration of erosion such as the clearance of the dense forest into agricultural land has increased soil erosion by 3000 times (Morgan, 2005). Zhou et al. (2008) suggested that in a mountainous area watershed, high erosion tends to occur when more than 30% of soil is exposed, the soil vegetation cover of more than 78% can greatly reduce erosion by water.

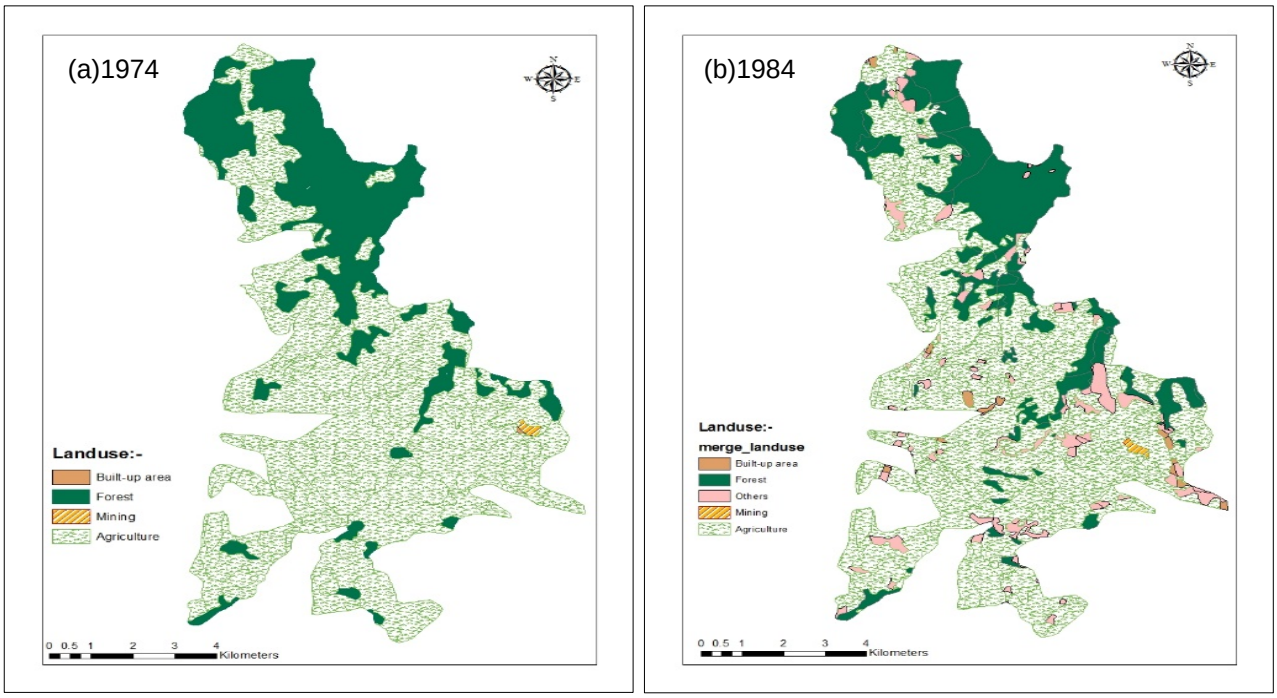


**Figure 2.** The changing of landscape from (a) 1974 to (b) 1984 in the area of study.

Soil Loss from USLE model is estimated at 110.18 ton/km$^2$/year in 1974 and 116.89 ton/km$^2$/year in 1984, respectively, then increases slightly to 117.87 ton/km$^2$/year in 2004 and 122.44 ton/km$^2$/year in 2012. On the other hand, based on the Shannon Diversity Index (SHDI) analysis, this value is found to increase from 1974 to 2012. The changing trends are shown in Figure 4. This situation illustrates that the higher the SHDI value, the higher the composition of the land use. This is because the land use pattern is illustrated by the growing number of patches and also refers to the diversity of land uses activities within a river basin. In this study, the SHDI in 1974 is 0.61 and slightly increases to 0.84 in 1984. The SHDI value in 2004 is 0.94 and thenit further increases to 1.17 in 2012. The results from theShannon Diversity index show that there is a significant relationship between land use changes and soil erosion with $R^2$=0.92.

 

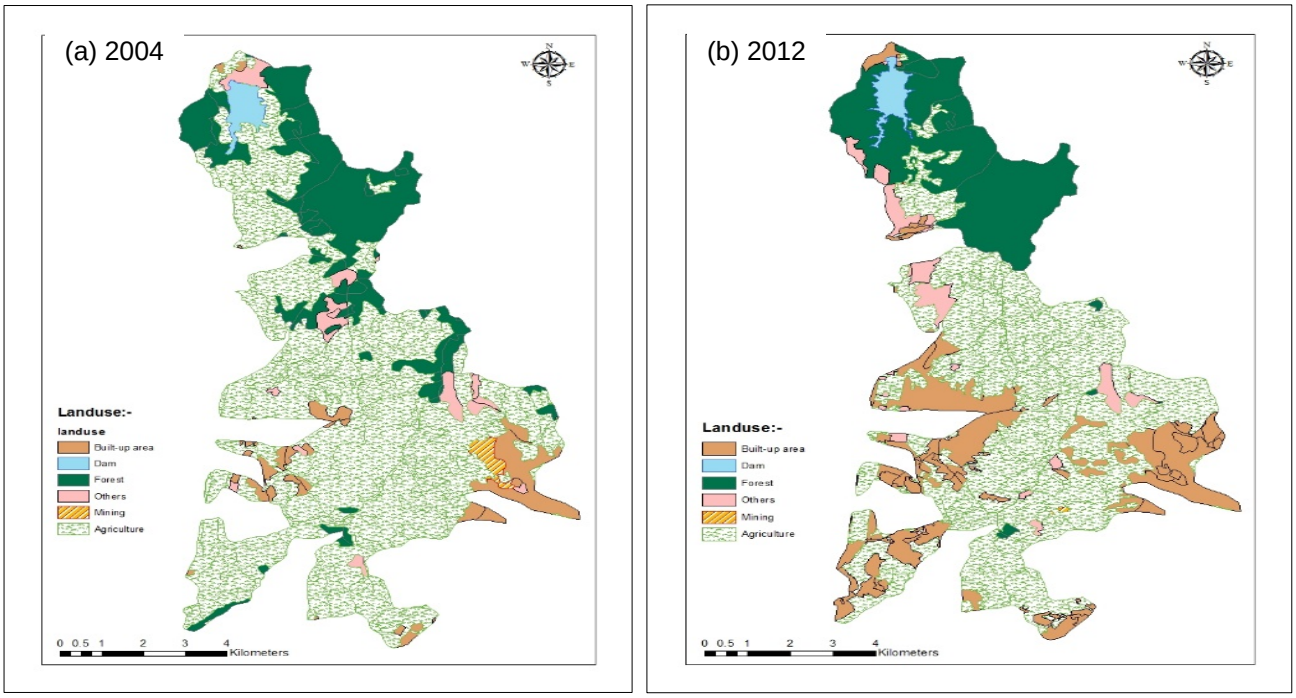


**Figure 3.** The changing of landscape from (a) 2004 to (b) 2012 in the area of study.

**Table 3.** Statistics of metrics analysis *"Patch Analyst" - NumP & MPS.*

| | Number Patch (NumP) | | | | Mean Patch Size (MPS) | | | |
|---|---|---|---|---|---|---|---|---|
| **Landuse** | 1974 | 1984 | 2004 | 2012 | 1974 | 1984 | 2004 | 2012 |
| **Built-up area** | 1.00 | 18.00 | 31.00 | 87.00 | 2.15 | 3.58 | 14.91 | 16.76 |
| **Forest** | 60.00 | 63.00 | 53.00 | 9.00 | 36.91 | 30.02 | 30.08 | 177.72 |
| **Agriculture** | 114.00 | 251.00 | 199.00 | 191.00 | 48.82 | 21.17 | 26.99 | 22.46 |
| **Mining** | 1.00 | 2.00 | 1.00 | 3.00 | 15.17 | 10.82 | 64.74 | 1.64 |
| **Others** | x | 98.00 | 16.00 | 24.00 | x | 5.29 | 11.71 | 13.57 |

**Table 4.** Statistics of metrics analysis *" Patch Analyst "- ED.*

| | ***Edge Density (ED)*** | | | |
|---|---|---|---|---|
| **Landuse** | 1974 | 1984 | 2004 | 2012 |
| **Built-up area** | 0.13 | 1.82 | 6.81 | 23.56 |
| **Forest** | 22.43 | 20.82 | 16.95 | 9.23 |
| **Agriculture** | 57.87 | 85.16 | 70.66 | 64.51 |
| **Mining** | 0.23 | 0.45 | 0.77 | 0.20 |
| **Others** | x | 12.93 | 3.17 | 5.21 |

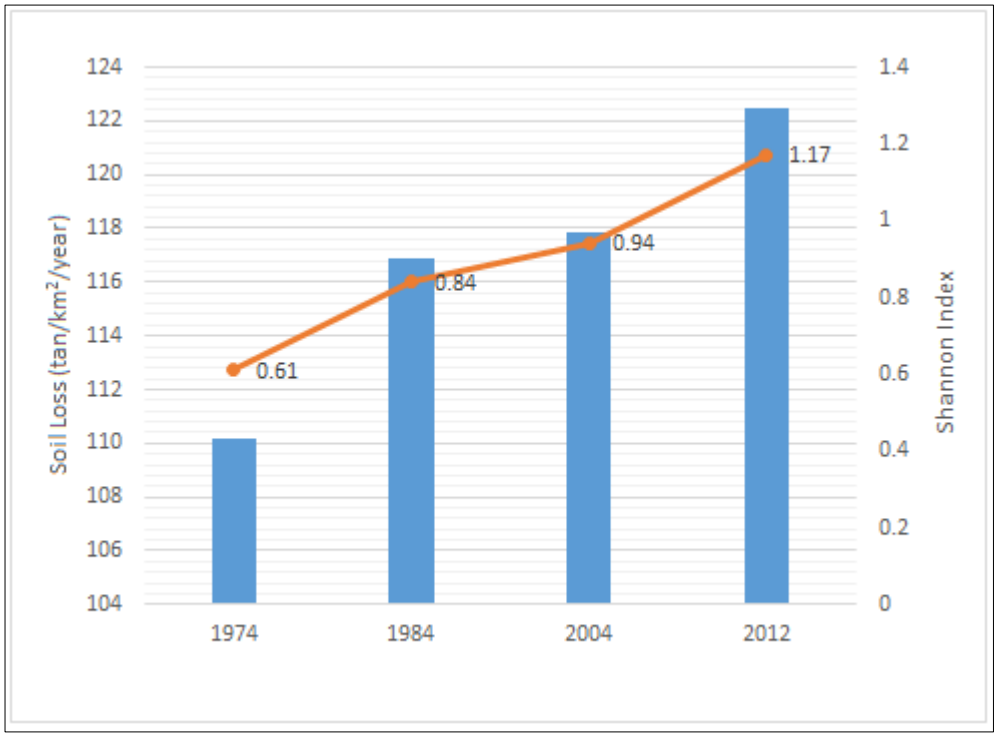


**Figure 4.** Soil Loss and SHDI values from 1974 to 2012.

## 5 CONCLUSION

Following over 38 years composition of the different land use types and the spatial form of the landscape in the study area show rapid and vast developments but as drastic as compared to the Timur-Laut region. However, it is expected that in the next few years there will be increasing development pressures and higher demand of land use especially for residential areas and so on.The soil erosion value and landscape changes show a significant relationship and this new finding from an ungauged catchments in the Barat Daya region is a significant contribution of this study and could be a source of reference for other ungauged catchment studies.

## ACKNOWLEDGEMENT

We would like to thank Universiti Sains Malaysia for supporting this study under the Post-Graduate Research Grant (RU-PRGS), grant number 1001/PHUMANITI/846039.

## REFERENCES

Brath, A., Castellarin, A. & Montanari, A. (2002). Assessing the Effects of Land-Use Changes on Annual Average Gross Erosion. *Hydrology and Earth System Sciences*, 6(2), 255-265.

De Girolamo, A. M. & Lo Porto, A. (2012). Land Use Scenario Development as a Tool For Watershed Management within the Rio Mannu Basin. *Land Use Policy*, 29(3), 691-701.

Golledge, R. G. (1995). *Primitives of Spatial Knowledge*,*Cognitive Aspects of Human-Computer Interaction for Geographic Information Systems*. Kluwer Acedemic Publisher, 29-44.

Gustafson, E.J. (1998). Quantifying Landscape Spatial Pattern: What is the State of the Art? *Ecosystems 1*, 143-156.

Ismail, I. (2002). *Pengenalan kepada Prosedur dan Amalan Perancangan Bandar dan Desa*, DBKL. Kuala Lumpur.

Kondolf, G.M, Piegay, H. & Landon, N. (2002). Channel Response to Increased and Decreased Bedload Supply From Land Use Change: Contrasts Between Two Catchments, *Geomorphology*, 45, 35-51.

Lin, Y.P., Hong, N.M., Wu, P.J., Wu C.F. & Verburg, P.H. (2007). Impacts of Land Use Change Scenarios on Hydrology and Land Use Patterns in the Wu-Tu Watershed in Northern Taiwan. *Landscape Urban Plan*, 80,111-126.

Lenhart, T., Fohrer, N. & Frede, H.G. (2003). Effects of Land use Changes on the Nutrient Balance in Mesoscale Catchments. *Physics Chemistry Earth,* 28, 1301-1309.

Lopez, T. D.M, Aide, T.M, & Scatena, F.N. (1998). The Effect of Land Use on Soil Erosion in the Guadiana Watershed in Puerto Rico, Caribbean. *Journal of Science*, 34(3-4), 298-307.

Mcgarigal, K & Marks, B.J. (1994). Fragstats: Spatial pattern analysis programe for quantifying landscape Structure. Retrieved from *https://www.fs.fed.us/pnw/pubs/pnw_gtr351.pdf*

 

Meyer, W.B. & Turner, B.L. (1994). *Changes in Land Use and Land Cover: A Global Perspective, Cambridge University EROSION 2D/3D: A Computer Model for the Simulation of Soil Erosion by Water.* Land Use Map for 1974, 1984, 2004, Parameter Catalog 2001. Ministry of Agriculture, Malaysia.

Sumayyah A., Mohd, N. & Zullyadini, A. R. (2015). An Estimation of Sediment Yield using USLE and Rating Curve in Barat Daya, Pulau Pinang. *Proceedings of International Conference on Development and Socio Spatial Inequalities at Bayview Beach Resort, 19-20 August, 2015*. 143-15.

Tomer, M.D. & Schilling, K.E. (2009). A Simple Approach to Distinguish Land-Use and Climate Change Effects on Watershed Hydrology. *Journal of Hydrology,* 376, 24-34.

Wicks, J.M. & Bathurst, J.C. (1996). SHESED: A Physically-Based, Distributed Erosion and Sediment Yield Component for the She Hydrological Modelling System. *Journal of Hydrology,* 175(1-4), 213-238.

Wischmeier, W.H. & Smith, D.D. (1965). *Predicting Rainfall-Erosion Losses from Cropel and East of the Rocky Mountains*: USDA-ARS, Agriculture Handbook, 282 pp.

Wischmeier, W.H. & Smith, D.D. (1978). *Predicting Rainfall Erosion Losses: A Guide to Conservation Planning*. Agriculture Handbook, 537pp.

Wu, J. & Hobbs, R. (2002). Key Issues and Research Priorities in Landscape Ecology: An Idiosyncratic Synthesis. *Landscape Ecology*, 17(4), 355-365.

Zhou P., Luukkanen O., Tokola T. & Nieminen J. (2008). Effect of Vegetation Cover on Soil Erosion in a Mountainous Watershed. *Catena*, 75, 319-325.

 

Proceedings of the 37th IAHR World Congress
August 13 – 18, 2017, Kuala Lumpur, Malaysia

# GRAVEL CAPPING FOR TURBIDITY CONTROL DURING SEDIMENT SLUICING UPSTREAM OF OOUCHIBARU DAM BY THE USE OF EJECTOR PUMP SYSTEM

DAISUKE TSURUSAKI[(1)], MASAKI KIYOTA[(2)], KATSUYUKI ASAZAKI[(3)], YUJI NAKAMURA[(4)], TOSHIYUKI TEMMYO[(5)], MICHIHIRO MIZUNUMA[(6)], AHMAD MOUSSA[(7)], SAMEH A. KANTOUSH[(8)] & TETSUYA SUMI[(9)]

[(1,2,3)]Mimikawa Hydro Power Development Office, Kyushu Electric Power Company, Japan,
daisuke_tsurusaki@kyuden.co.jp, Masaki_Kiyota@kyuden.co.jp, Katsuyuki_Asazaki@kyuden.co.jp

[(4,5)] Hazama Ando Corporation, Civil Engineering Division, Japan,
temmyo.toshiyuki@ad-hzm.co.jp, nakamura.yuji@ad-hzm.co.jp

[(6)] West Japan Engineering Consultants, Japan,
m-mizunuma@wjec.co.jp

[(7)] School of Engineering, Monash University. Selangor, Malaysia,
ahmad.mousa@monash.edu@kyuden.co.jp

[(8,9)] Water Resources Research Center, Disaster Prevention Research Institute, Kyoto University, Japan,
kantoush.samehahmed.2n@kyoto-u.ac.jp, sumi.tetsuya.2s@kyoto-u.ac.jp

## ABSTRACT

Successful control of sediment sluicing for river and dam systems requires adopting integrated management plans. Minimizing sediment flow at an early stage is, therefore, important for efficient sediment sluicing as the resuspension of silty sediment could be extremely detrimental to the downstream environment. Gravel capping is one of the common countermeasures that are used effectively for turbidity control during sluicing process. It involves forming a layer of gravel and sand over the silt deposited at the bottom of the reservoir to minimize its resuspension and subsequent flow to the downstream reaches below dam. In this study, a hopper-type of an ejector system is used to execute capping in the reservoir of Oouchibaru dam in Japan. Trial experiments have first been carried out coupled with field investigation of the system design and performance for comparison and gauging efficiency of the implementation. The outcomes of the study are used to propose a final layout plan to effectively carry out sluicing operation. The Mimi River Basin Integrated Sediment Flow Management Plan is presented as a success story for gravel capping by the use of the Ejector system. In this project, a total volume of 107,600 $m^3$ of gravel and sand is projected, of which approximately 28,200 $m^3$ of gravel capping has been completed by monitoring water turbidity in 2016.

**Keywords:** Sediment sluicing; ejector pump; water turbidity control; gravel capping.

## 1 INTRODUCTION

Coupled with the more stringent environmental requirements, the aging of Japan's dams and continuous loss of storage capacity due to reservoir sedimentation instigates growing concerns on several fronts: social, economic, and environmental. Retrofitting and upgrading such aged dams are inevitable remedial measures to recover reservoirs storage capacities (Kantoush and Sumi, 2016). Minimizing flow of existing sediment at an early stage and throughout retrofitting works is one of the key goals of efficient sediment flow management by sluicing. Resuspension of silty sediment causes adverse impact to the downstream environment. One of the restoring countermeasures is capping which involves forming a layer of gravel and sand over the silt deposited at the bottom of the reservoir. This approach is deemed to be effective in minimizing silty sediment discharged to the downstream. The first implementation in river engineering was controlling the turbidity of sluiced sediment volume by using gravel capping. There is a little evidence of forming a uniform layer of gravel and sand over the targeted reservoir area. Therefore, the selection of the most effective method is yet to be investigated.

Due to the Typhoon Nabi in 2005, a huge sediment inflow to the Mimi River Basin and its four power plants of Kamishiiba, Tsukabaru, Yamasubaru and Saigou were flooded. Concurrently, rainfall and water volume flowing towards dams exceeded the flood storage capacity of the reservoirs for all of the seven dams of Mimi River. The floods were accompanied by landslides amounting to approximately 10.60 Million Cubic Meter (MCM) of sediments and driftwood flowing to the river. Miyazaki Prefecture, the river administrator, has subsequently evaluated the current status of the complex Mimi River sediment and proposed the "Mimi River Basin Integrated Sediment Flow Management Plan". The resolution of sediment control exhibited a good balance considering flood control, water usage and environmental conservation. Kyushu Electric Power Company (KEPCO), being in charge of dam installations, is integral prime partner of the Management Plan aiming to restore the original sediment flow intercepted by the dams.

 

Spreading gravel and sand to confine silty sediment in the reservoir was conducted to further minimize silt sedimentation at an early stage. This is referred to as gravel capping (Yamagami et al., 2012; Sumi et al., 2015). A proposed Ejector Pump Dredger System (EPDS) comprises two types: Suction-EPDS and Hopper-EPDS. The suction–type is responsible for hydraulic removal and transportation of the deposited sediment to the downstream area, while the hopper-type involves sediment transportation from a specific site to a disposal site without suction (refer Figure 1). The EPDS system employs high pressure water jet discharged through nozzle to create a negative pressure in the ejector house and, subsequently, produces adequate energy to suck the suspended slurry from reservoir through a suction pipeline. The sediments entering the ejector house is pushed into the transport pipeline under the high pressure water jet introduced through the nozzle.

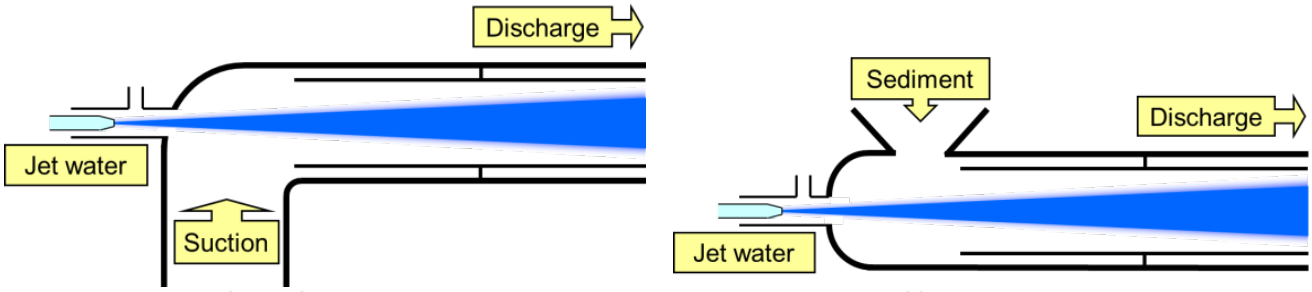


a) Suction-type b) Hopper-type

**Figure 1**.Ejector pump system

Preliminary experimental efforts conducted on two-phases flow (water and sediment) have experienced occasional sediment blockage in the transport section, especially when low pressure water jet is used. The air injection into the transport pipeline is found to be very efficient in assisting sediment transportation. The presence of air into the transport pipe, however, creates a three-phase flow (Meshkati et al., 2011; Meshkati et al., 2012). Hopper type ejector system is used to execute gravel capping in the reservoir. Trial experiments have first been carried out together with field investigations of the system specifications and performance. Ultimately, final layout plan is proposed to successfully carry out sediment transport. However, one of the implementation concerns is water turbidity control. During the Mimi River gravel capping project, the governing criteria and turbidity limits for the flow are established. This paper describes gravel capping by use of an ejector system executed in Mimi River Basin as part of its integrated sediment flow management plan. Several measures against turbidity are taken to maintain high water clarity of the river. The key countermeasures for controlling turbidity can be summarized as follows:

1) Washing the capping material (gravel and sand) before spreading to the river.
2) Using telescopic boom casing to control the distance between the river bed and the ejector.
3) Introducing volcanic-ash-derived as a flocculation agent to settle down the suspended sediments.
4) Installing silt screen to store the turbid water in a specific region.

## 2 GRAVEL CAPPING AT MIMI RIVER

Mimi River in Miyazaki Prefecture, in the southeast of Kyushu, Japan, flows almost due east toward the Pacific Ocean (Figure 2). With a total length of 94.8km and a watershed area of 884.1 km$^2$, the river is one of the largest “Class B” rivers in the prefecture. Making use of an abundant volume of water and large drop, between the 1920’s and 1960’s, seven dams and hydropower stations were built to generate a combined power of 340MW, and an output of 900 million kWh making Mimi river basin one of the most energy strategic areas in the Kyushu region.

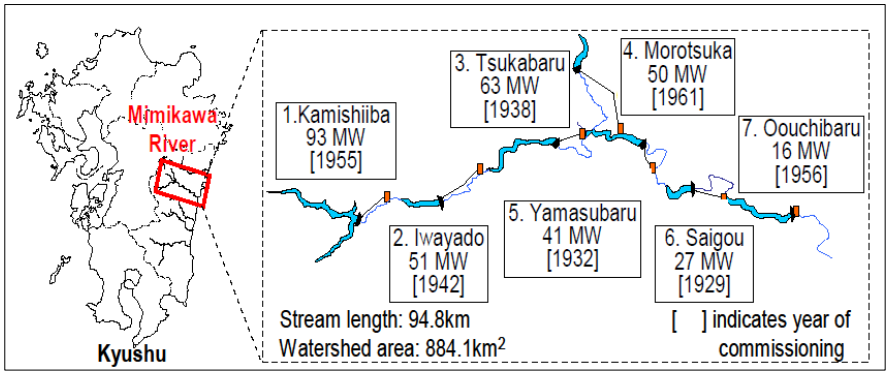


**Figure 2**. Mimi river basin – Overview

In September 2005, Typhoon Nabi (0514) hits Japan, leaving behind massive damage in several parts of the nation, including Miyazaki Prefecture. For Mimi River, this extreme rainfall in the basin and the water inflow volume exceeds the designed flood storage capacity of reservoir. Flood damage is the worst known, and especially in the central area of Morotsuka located on the upstream edge of the Yamasubaru Dam regulating reservoir, the damage caused by flooding is extensive. Flood damage is coupled with numerous mountain slope failures in approximately 500 locations. The failures cause a huge amount of sediments and driftwood flow into the river and dam-regulating reservoirs in the Mimi River Basin.

In October 2011, Miyazaki Prefecture, the river administrator, in a rescue effort compiled the “Mimi River Basin Integrated Sediment Flow Management Plan” to resolve these problems while balancing flood control, water usage and environmental conservation. KEPCO, being in charge of dam installations, has drawn up a plan for sediment sluicing, incorporating Yamasubaru Dam, Saigou Dam, and Oouchibaru Dam and integrate it into the Management Plan aiming to restore the original sediment flow. Sediment sluicing is the temporary lowering of the high dam water levels triggered by flooding (due to typhoons) to the original flow of water in dam-regulating reservoirs, thereby allowing sediment that runs into the upstream to flow downstream of dams (Figure 3).

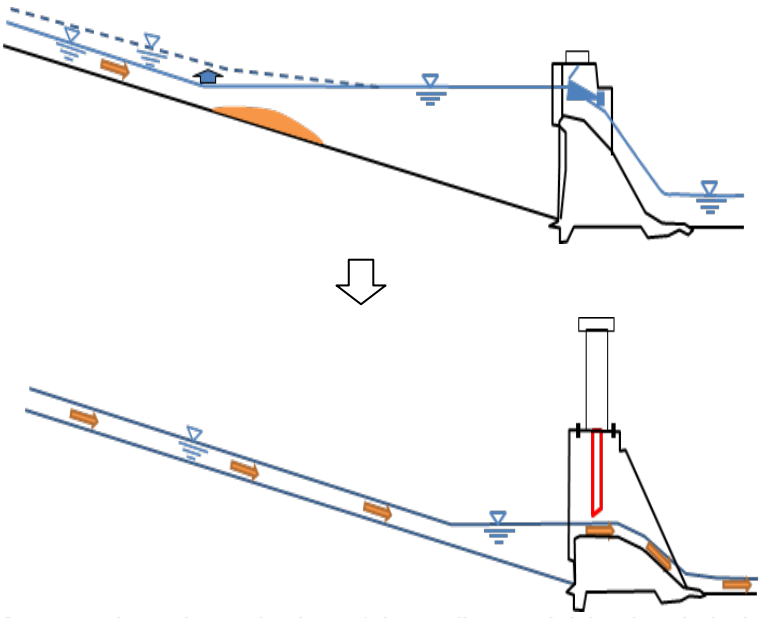

**Figure 3**.The Schematic view of the sediment sluicing in Mimi River

For Yamasubaru and Saigou Dams, it is not possible to perform the necessary drawdown for sediment sluicing without lower spillway gate. For this reason, sluicing functions are now being added to these dams by partially cutting down their overflow sections without jeopardizing the structural integrity of the dam. It will be the first time in Japan that an existing dam, 80 years after commissioning, will be modified by the addition of a new sluicing function. For Oouchibaru Dam, the furthest downstream, a relatively low gate exists as the dam is short, changing dam operation and sediment sluicing will be possible without retrofitting the dam structure.

In the transition to dam sediment flow operation, after completion of dam retrofitting work, proper consideration must be given to flood control and sudden changes to the river environment. As a measure to deal with this, after appropriately assessing factors such as future riverbed form and riverbed material particle size within dam-regulating reservoirs through model experiments and numerical simulations, the relocation of existing accumulated sediment in dams will be carried out in parallel with dam retrofitting work. In the reservoir of the Oouchibaru dam, which is located at the most downstream of the retrofitted dams in Mimi River, the auxiliary sediment management method for the purpose of the resuspension of existing silty sediment at the beginning of sediment sluicing operation (countermeasure for the winding-up of silty sediment) is carried out. As a countermeasure, capping is conducted by placing a layer of gravel and sand, obtained from the upstream of the reservoir, over the silt deposited at the bottom of the reservoir.

This approach is implemented for the first time in Japan to control the amount of sluiced sediment in river engineering. Therefore, since there is a little evidence of forming a uniform layer of gravel and sand over the targeted reservoir area, EPDS is applied as described before. For sites characterized by sediment composed mainly of coarse sand, gravel and buried driftwood, or limited conditions in the site, the application of conventional submersible pump or grab dredging methods is difficult. Therefore, a paradigm shift to EPDS as the most applicable technology is foreseen.

 

## 3 GRAVEL CAPPING using HOPER-TYPE EJECTOR PUMP DREDGER SYSTEM (EPDS)

### 3.1 System configuration

The prime components of the EPDS system are shown in Figure 4. The experiences of authors in previous projects (Nakamura et al., 2012; Temmyo et al., 2013) were taken into account. The following figure summarizes the functionality of each component.

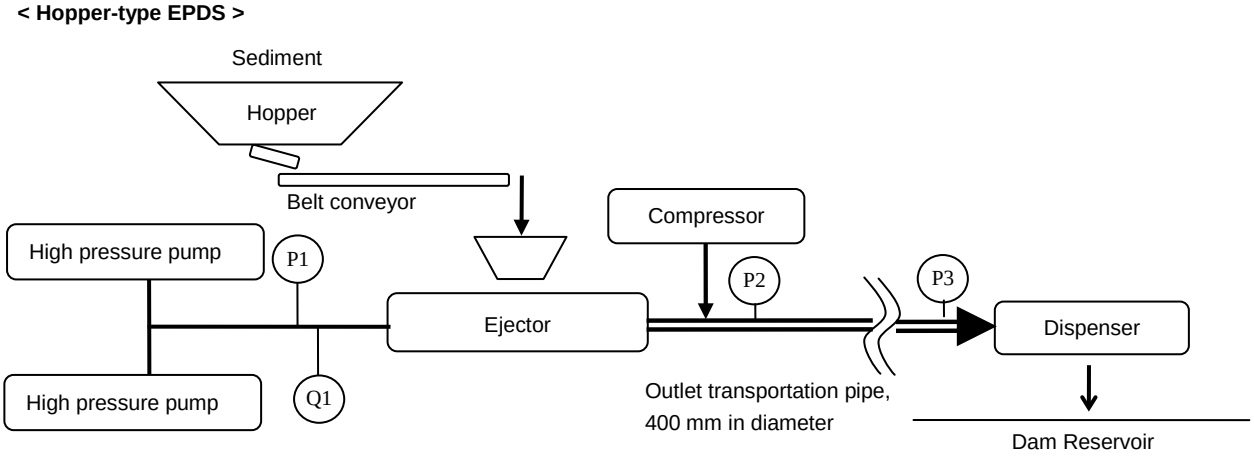


**Figure 4.** Schematic of the hopper-type EPDS

#### 3.1.1 EPDS system on shipboard

The EPDS is distinguished by several unique innovations including special ejector as well as its structurally simple components and easy to maintain system. Contrary to conventional dredger systems, the rotary components (impeller wheel) inside the ejector are eliminated. The energy required to vacuum sediment is provided by creating a differential pressure between inside of special ejector and bottom of reservoir. The EPDS is set on the shipboard hosting a hopper for gravel and sand supply, air compressor and belt conveyor (Figure 5).

As for the commencement of the gravel capping, the high pressure pump of EPDS operated after the shipboard moved to predetermined location. After measuring the clear water flow rate at the end of the transportation pipeline, vibrating feeder under the material supply hopper and belt conveyor started operation, and then material was supplied to the ejector pump through the hopper. The material for gravel capping was placed by wheel loader and excavator into the hopper. Additional material was supplied after monitoring the progress of placed gravel.

#### 3.1.2 High pressure pump

A pressure pump operated with 220 kW power engine supplies high velocity water jet into the EPDS (Figure 5 (2)). This unit is capable of producing an equivalent pressure of 1.95 (MPa) and flow rate up to 5 ($m^3$/minute).

#### 3.1.3 Ejector pump

The ejector pump plays the main role of EPDS, see Figure 5(3). The ejector is equipped with two specific accessories: air controller inlet and a straight inner pipeline to eliminate cavitation in the system and abrasion of the pump. To create a negative pressure domain inside of ejector, the high pressure pump should discharge water jet with high velocity into the ejector through a tiny nozzle. The pressure gradient between the entrance of suction pipeline and inside of ejector vacuums the mixture of sediment and water into the system. The sucked sediments are subsequently pushed forward into the inner pipeline to finally get disposed in the downstream area.

#### 3.1.4 Air compressor and air installation equipment

In order to transport sediment effectively, air was injected into the system by air compressors. Air was introduced at the beginning of transport pipeline just after special ejector Figure 5(4).

#### 3.1.5 Transportation pipeline

The transport section consists of a 6 m long 400-mm pipe sections connected to each other by 1-m length rubber pipe (Figure 6). To float the transport pipeline on the water surface, two sets of float tube were attached to the individual tubes.

 

(1) (2) (3) (4)

**Figure 5**.EPDS shipboard and equipments (high pressure pump, ejector pump and air installation equipment)

3.1.6 Distributing shipboard

In order to release the transported sediment into the reservoir, a distributing shipboard was installed on the reservoir (Figure 7). Distributing shipboard has four winch-operated wire ropes at the corner vessel. The shipboard navigates at a constant speed by using the operating wires to create equal-thickness gravel capping. Operation position is confirmed by automatic tracking total station. At the end of the transportation pipeline on the distributing shipboard, rectangular typed telescopic casing is installed in the expectation of energy dissipation at the discharge of water, gravel and sand.

**Figure 6**.Transportation pipeline

**Figure 7**. Distributing shipboard

3.2 Sediment (Material for gravel capping)

Sediment was excavated at Morotsuka dam, located upstream of the Mimi River (Figure 2). Fixed type vibrating sieving machine was installed to classify the excavated sediments for two sizes less than 100 (mm) and over than 100 (mm). Oversized material was transported to the Oouchibaru reservoir for gravel capping. Material used for gravel capping was washed in order to reduce the impact of water turbidity during gravel capping.

3.3 Trial experiment for sediment transportation by EPDS

Trial experiment had first been carried out together with close investigation of the system specifications and performance. The materials used for the trial experiment were classified by a 120 (mm) sieve mesh depicted in Figure 8 as D=150 mm and 80 (mm) mesh called D 100 (mm). Both grain sizes distributions are shown in Figure 8. The trial was conducted using different transport lengths, sediment grain size, nozzle diameter and inner pipeline diameter. The investigated parameters in the trial case are summarized in Table 1.

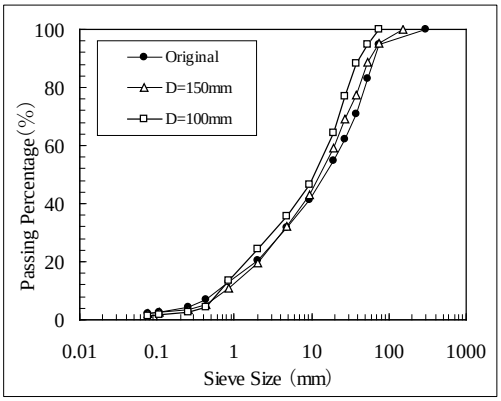


**Figure 8**.Particle size distribution of sediment

**Table 1.** Trial test configurations.

| | Mark | Unit | Case | | |
|---|---|---|---|---|---|
| Transport length | L | m | 200 | 600 | 1,000 |
| Maximum size | Gmax | mm | 150 | 150 100 | 100 |
| Ejector Nozzle | Dn | mm | | 58-70 | |
| Ejector Inner pipe | Di | mm | | 200-250 | |
| Air content | A | $Nm^3$/min | | 0-72 | |

 

Water flow rate (Q) and high pressure pump (P1), pressure at the beginning and ending point of transportation pipeline, (P2) and (P3), respectively, and air content (A) were measured during the trial experiment. The velocity of the water flow in the transportation pipeline was also measured by floating ball distance over the trip time. Results of the trial experiment are summarized in Table 2.

The relation between the pressure at the starting point of the transportation pipeline (P2) and sediment transportation rate (S) in every case of the transportation length L (200 m, 600 m, except 1000 m) is shown in Figure 9. For any transport length, the sediment transportation rate is directly proportional to pump pressure. The results imply that the maximum size of sediment is significant. Influence of the air content to the sediment transportation rate seems to be quantitatively dormant, but it is pivotal to prevent blockage in the pipeline.

**Table 2.**Results of experimental trial investigations.

| **Trial No.** | | Unit | 1 | 2 | 3 | 4 | 5 | 6 | 7 | 8 | 9 | 10 |
|---|---|---|---|---|---|---|---|---|---|---|---|---|
| **Transportation length** | L | m | | | 200 | | | | | 600 | | |
| **Maximum size** | d | mm | | 150 | | | 150 | | | | 100 | |
| **Sediment Concentration** | C | % | - | 12.9 | 12.8 | 16.9 | 6.7 | 6.7 | 7.0 | 7.3 | 7.3 | 7.6 |
| **Sediment transportation rate** | S | $m^3/h$ | - | 65.9 | 63.8 | 91.4 | 33.0 | 33.0 | 38.3 | 39.6 | 47.1 | 48.9 |
| **Ejector Nozzle** | Dn | mm | 61.0 | 61.0 | 61.0 | 61.0 | 61.0 | 61.0 | 61.0 | 61.0 | 70.0 | 70.0 |
| **Ejector Inner pipe** | Di | mm | 250 | 250 | 250 | 250 | 250 | 250 | 200 | 200 | 200 | 200 |
| **Ejector Flow rate** | Q | $m^3/s$ | 8.9 | 8.5 | 8.3 | 9.0 | 8.2 | 8.2 | 9.1 | 9.0 | 10.8 | 10.7 |
| **Ejector Pressure** | P1 | MPa | 1.30 | 1.25 | 1.20 | 1.40 | 1.20 | 1.20 | 1.50 | 1.45 | 1.40 | 1.40 |
| **Air content** | A | $m^3/s$ | 0 | 18 | 36 | 54 | 36 | 54 | 36 | 54 | 36 | 54 |
| **Pressure (starting point)** | P2 | MPa | 0.11 | 0.13 | 0.15 | 0.16 | 0.17 | - | 0.21 | 0.22 | 0.25 | 0.23 |
| **Pressure (ending point)** | P3 | MPa | - | 0.02 | 0.04 | - | 0.02 | - | 0.03 | 0.04 | 0.04 | 0.04 |
| **Pressure differential** | P4 | MPa | - | 0.11 | 0.11 | - | 0.15 | - | 0.18 | 0.18 | 0.21 | 0.19 |
| **Average velocity of flow** | $V_{ave}$ | m/s | - | - | - | - | - | - | 4.0 | 3.6 | 4.9 | 5.2 |
| **Estimated P (starting point)** | T | Mpa | $7.7\times10^{-2}$ | $7.4\times10^{-2}$ | $7.1\times10^{-2}$ | $8.3\times10^{-2}$ | $7.1\times10^{-2}$ | $7.1\times10^{-2}$ | $1.4\times10^{-1}$ | $1.35\times10^{-1}$ | $1.72\times10^{-1}$ | $1.72\times10^{-1}$ |

Next, the relation between P2/L and sediment transportation rate S is shown in Figure 10. The results indicate a liner directly proportional relation. It should be noted that this implies positive and negative proportion with respect to P2 and L, respectively.

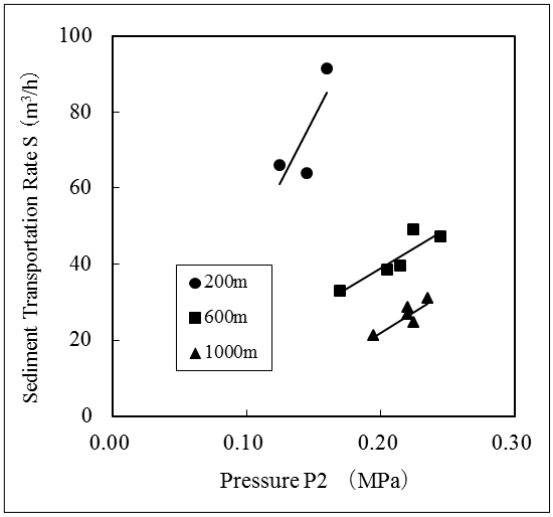


**Figure 9.**Pressure P2 and sediment transportation

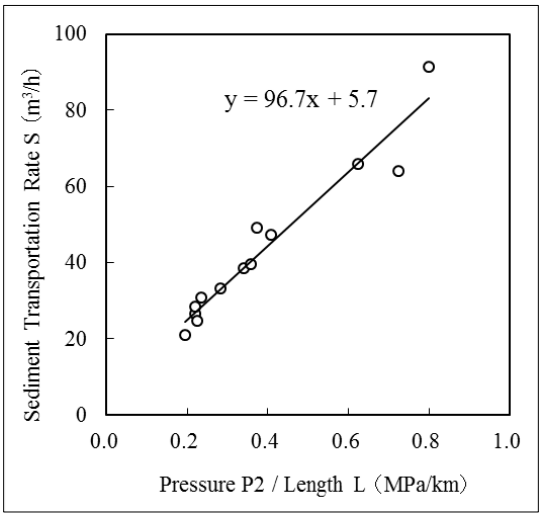


**Figure 10.** P2/L and sediment transportation rate S

It is assumed that the maximum water head of the ejector pump is proportional to the ratio of the nozzle and inner pipe section area and pressure of the high pressure pump. Then, estimated pressure at the starting point of the transportation pipeline T (MPa) is equal to the ratio of nozzle and inner pipe section $Dn^2/Di^2$ (Dn (mm): diameter of the nozzle, Di (mm): diameter of the inner pipe) multiplied by the pressure of high pressure pump P1 and the constant α, it is as shown in formula [1].

 

$$T = \frac{Dn^2}{Di^2} \times P1 + \alpha \quad [1]$$

Here, if α = 0.067, estimated pressure at the starting point of the transportation pipeline T is almost equal to the pressure P2 as shown in Figure 11. This assumption holds that the range of the diameter of nozzle and inner pipe are from 58 mm to 70 mm and from 200 mm to 250 mm, respectively. In this range, the high pressure pump conveys its energy on the proportional basis of $Dn^2/Di^2$.
The relation between estimated T/L and S is depicted in Figure 12. The sediment transportation rate (S) can be related to the estimated T/L as:

$$S = 93.8 \times \frac{T}{L} + 7.71 \quad [2]$$

Substituting formula [1] into [2] yields formula [3].

$$S = 93.8 \times \frac{\frac{Dn^2}{Di^2} \times P1 + \alpha}{L} + 7.71 \quad [3]$$

By simple manipulation of equation [3], the required pressure of the high pressure pump P1 in the current system can be estimated as follows:

$$P1 = \left[ (S - 7.71) \times \frac{L}{93.8} - \alpha \right] \times \frac{Di^2}{Dn^2} \quad [4]$$

For example, if the sediment transportation rate (S) of 50 $m^3/h$ is required at the transportation length (L) of 1000 m, 3.1 MPa of pressure is needed by the high pressure pump. In case that S is 40 $m^3/h$, the required pressure P1 is equal to 2.3 MPa.

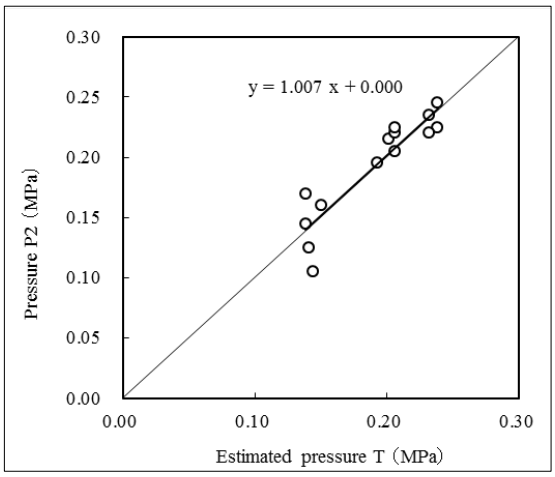


**Figure 11**. Estimated pressure at the starting point of the transportation pipeline P2 and sediment transportation rate S

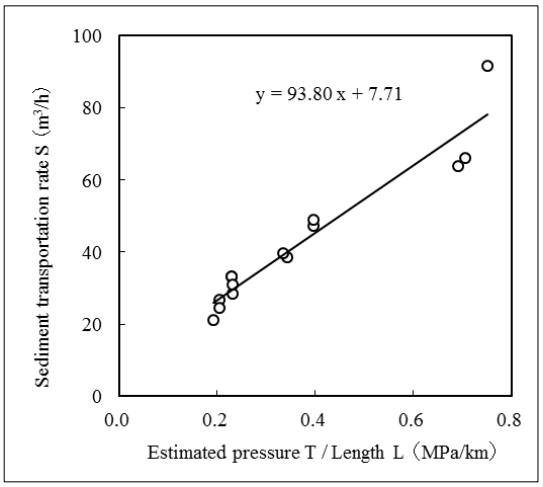


**Figure 12**. T/L and P2 and sediment transportation rate S

3.4 Gravel capping project

A total volume of 107,600 $m^3$ of gravel and sand capping was planned. In 2016, 28,200 $m^3$ of gravel capping had been implemented while controlling and monitoring turbidity. Record of executed placement of gravel capping from October 2015 to March 2016 is shown in Figure 13.

 

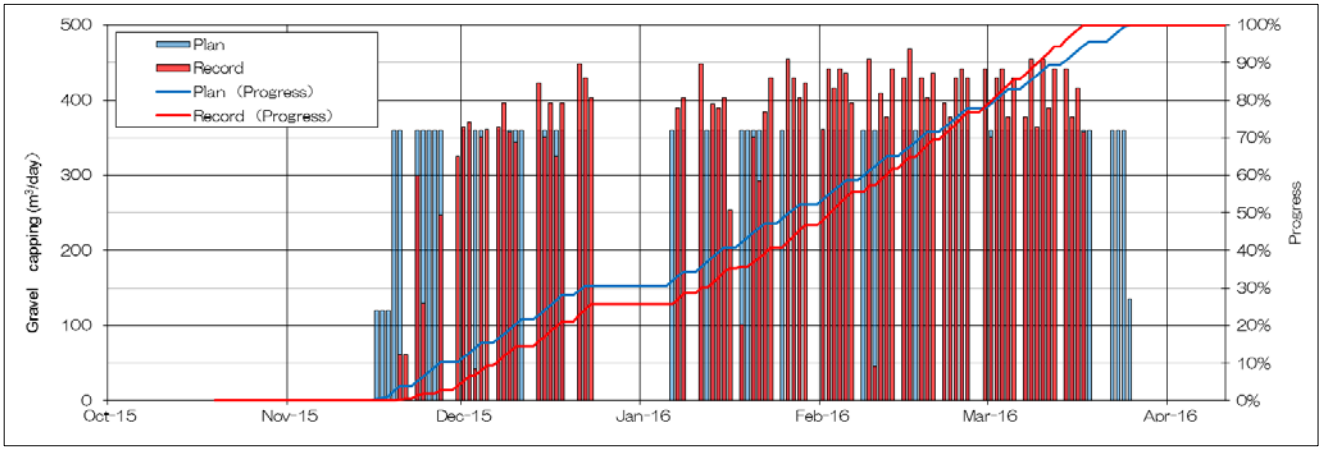


**Figure 13**. Timeline of gravel capping at Oouchbaru reservoir in Mimi River

## 4 TURBIDITY CONTROL DURING GRAVEL CAPPING

### 4.1 General information

It is necessary to perform turbid water measures in the reservoir when carrying out gravel capping. Turbid water generation is analyzed and estimated considering material of gravel capping, method of execution, and diffusion properties of turbid water outflow. Apparently, two challenges have arisen: the suppression of the surface layer floating of turbid water and suppression of turbid water outflow to the downstream. Four scenarios are accordingly presented including washing material for gravel capping, installing telescopic casing, volcanic-ash-derived new flocculation agent, and silt fence.

### 4.2 Washing capping material

Washing excavated material is carried out before, during and after classification by sieving. Only sediments that once or three times washing are checked through particle size distribution test. The test results indicated that particle sizes less than 75 mm of fine fraction are decreased by approximately 40 %. Such washing process is efficiently reducing the fine particle of placed sediments before capping. Sediment excavation and washing process are shown in Figures 14.and 15, respectively.

### 4.3 Telescopic casing

As contrivance at the end of the transportation pipeline, focus is placed on the depth of the casting positions of sediment. Therefore, by performing a simple model experiments the effect of suppressing the surface layer floating in turbid water is examined. As a result, spraying sediment from more deep-water position was able to confirm the reduction of the surface floating of turbid water during gravel capping. Therefore, the telescopic (expansion and contraction) casing was developed and installed at the end of the transportation pipeline. The telescopic casing can be stretched up to a maximum depth of 9.3 m by winch operation. The drawing photograph of the telescopic casing is shown in Figure 16. Actual casting position was set to 4 m by field observation.

### 4.4 Volcanic-ash-derived new flocculation agent

The flocculation method is one of the main processes of the water treatment. Flocculation agent is used in the coagulation process. In general, flocculation agent is artificially manufactured, and the discharged sludge in the water processing plant contains in relatively considerable quantity of aluminum that is the component of the flocculation agent. Therefore, recycling of the sludge is difficult, and it is mainly disposed as industrial waste. For similar reasons, it is difficult to use this flocculation agent in the treatment of environmental turbidity of dam lakes. In this gravel capping project, volcanic-ash-derived new flocculation agent is developed and applied. This agent contains natural mineral without an artificial material, and has the equal cohesion to conventional flocculation agent. The turbid water treatment by this new flocculation agent such as at water treatments and dam lakes is highly expected in situ.

 

**Figure 14.** Sediment excavation

**Figure15.** Vibrating sieving machine

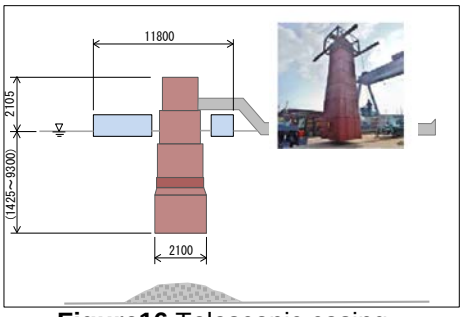


**Figure16.**Telescopic casing

4.5 Silt fences

In order to control the muddy water flowing out downstream, this study investigated the installation of silt fences by settling turbid water in the lower part of the reservoir. The position of the silt fences were determined based on the numerical analysis, which encompassed topographical conditions of the reservoir.

The numerical analysis used two-dimensional multi-layer model (three-dimensional model obtained by simplifying the vertical motion equation), and a model is reproducible by using field investigation results. Factors for numerical analysis are shown in Table 3. The location of the silt fences is shown in Figure 17. Results show that for maximum inflow, so far 60 $m^3$/s into the reservoir as a parameter for the numerical analysis, installing three sets of 7-m long silt fences can effectively reduce turbid water flowing out downstream (Figure 18).

**Table3.** Factors for numerical analysis.

| Parameter | Unit | Value |
|---|---|---|
| **In/Out flow rate** | $m^3$/s | 60 |
| **Sediment placing rate** | $m^3$/h | 70 |
| **Roughness of the bottom of the reservoir** | - | 0.04 |
| **Horizontal eddy diffusivity of momentum** | $cm^2$/sec | $5.0x10^2$ |
| **Vertical eddy diffusivity of momentum** | $cm^2$/sec | 10 |

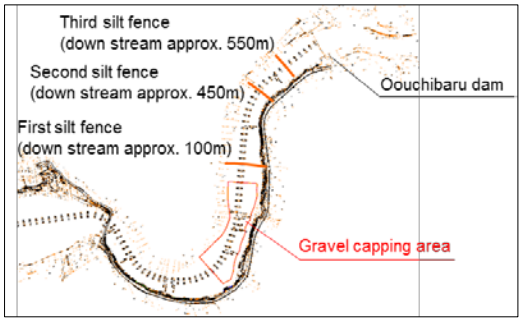


**Figure 17.** Location of the silt fences.

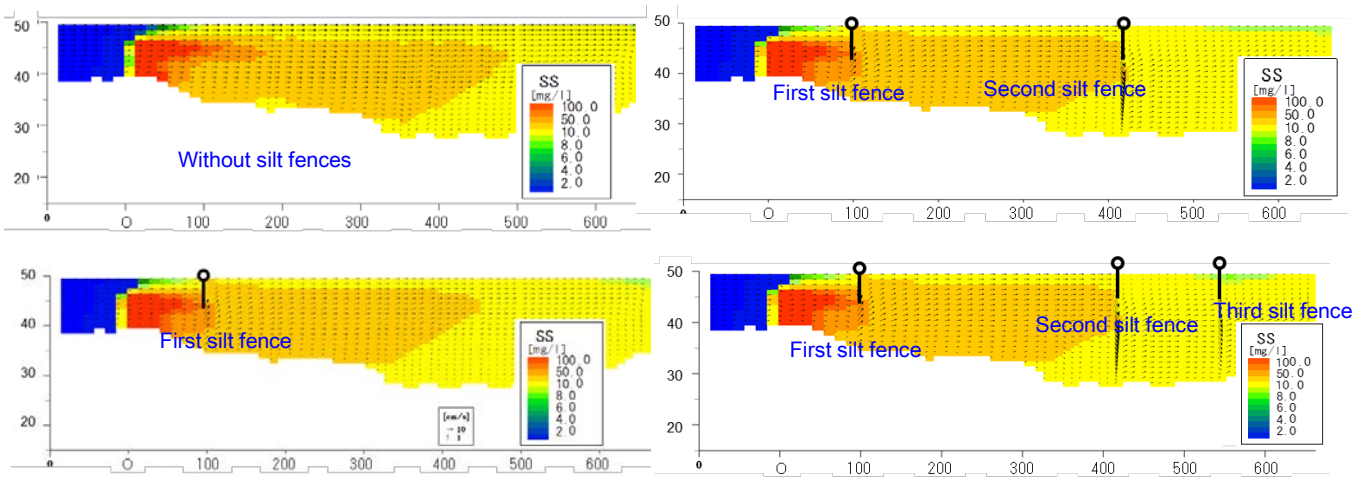


**Figure 18**.Results of numerical analysis.

4.6 Verification by the monitoring record

During the in situ gravel capping works, by monitoring the outflow turbidity and the surface turbidity, and downstream in the vicinity of the gravel capping place, we verified the effect of measures for turbid water and managed that turbid water does not exceed the management regulation value. The regulation value was the same as the turbidity 10 NTU, the target value in this study. If the turbidity exceeded the regulation value, it was decided to interrupt the gravel capping works. As a result, except for the period of torrential rain, water turbidity was well controlled at both locations within the regulation value.

## 5 CONCLUSIONS

This paper describes gravel capping for turbidity control during sediment sluicing upstream of Oouchibaru Dam by the use of the ejector pump system. The study underscores the utility of gravel capping particularly at early stages of sediment sluicing. The system is utilized to remove sediment efficiently with controlled turbidity. Trial experiments are conducted first. Full scale gravel capping project is carried out while performing the turbid water control. The following summarizes the key findings from field investigation:

1) It is necessary to increase the pressure of high pressure pump when sediment transport rate is increased; also the transportation length is longer. Required pressure of the high pressure pump can be determined by sediment transport rate, transport distance and the area ratio of the nozzle and the inner pipe of the ejector. Necessary pressure for the high pressure pump in the current system can be estimated by using Eq. [4].

2) Controlling water turbidity during the gravel capping works requires washing gravel capping material/sediment, adoption of the telescopic casing, the use of volcanic-ash-derived new flocculation agent, and installation of silt fences applied to the project. For all measures, the effect can be verified; it is found that these measures are effective.

Total capping volume is estimated to be around 107,600 $m^3$ of gravel and sand. In 2016, 28,200 $m^3$ of gravel capping is completed with continuous monitoring of turbidity at Mimi River. It is hoped that the proposed method can be adapted to similar sediment management projects.

## ACKNOWLEDGEMENTS

The authors would like to give their sincere thanks to Mr. Inada of Pojet Co. (in Taiwan) for providing technical expertise regarding the ejector pump system.

## REFERENCES

Kantoush, S.A. & Sumi, T. (2016). The Aging of Japan's Dams: Innovative Technologies for Improving Dams Water and Sediment Management. *International Symposium on River Sedimentation (ISRS 2016), Stuttgart, Germany, September 19 - 22, 2016*.

Meshkati, S.M., Sumi, T.,Kantoush, S.A. & Temmyo, T. (2011). "The Effect of Air Injection on Sediment Transport Efficiency in Ejector Pump Dredger System", *Proceedings of the Thirteenth International Summer Symposium, International Activities Committee Japan Society of Civil Engineers,* 135-138.

Meshkati, S.M.,Sumi, T., Kantoush, S.A. & Temmyo,T. (2012).Influence of Air Injection on Suction Power and Pressure Gradient in Dredger System. *Japan Society of Civil Engineering Journal, Series B1 (Hydraulic Engineering)*, 68(4), I37-I42.

Nakamura, Y., Okabe T., Temmyo, T., Yamashita, T., Kaku M., Yamagami Y., Kuroki O., SumiT., Kantoush, S.A. & Meshkati S.M. (2012). A Method of Sediment Transportation by Special Ejector Pump System in the Dam Reservoir, *International Symposium on Dams for Changing World, ICOLD Kyoto.*

Sumi, T., Yoshiymura, T., Asazaki, K., Kaku, M., Kashiwai, J. & Sato T. (2015). Retrofitting and Change in Operation of Cascade Dams to Facilitate Sediment Sluicing in the Mimi River Basin, Japan. *Conference: 25rd Congress, International Commission on Large Dams, At Stavanger, Norway, Volume:* Q99-R45.

Temmyo, T., Nakamura, Y., Yamagami, Y., Kaku, M., Sumi, T. & Meshkati, S.M. (2013). Sediment relocation trial by ejector pump system (EPDS) in a dam reservoir, *ISRS 2013 Advances in River Sediment Research – Fukuoka*, 1241-1247.

Yamagami, Y. Kaku, M., Asazaki, K., Tashiro, Y., Yamashita, T., Nishida, K., Oshikawa, J., Nonaka, K., Kodama, H. & Sugio, S. (2012). Approaches for Integrated Sediment Flow Management at Dams in the Mimi River Basin, *International Symposium on Dams for a Challenging World, ICOLD Kyoto*.

 

Proceedings of the 37th IAHR World Congress
August 13 – 18, 2017, Kuala Lumpur, Malaysia

# RIVER SAND MINING CAPACITY IN MALAYSIA

FANG YENN TEO[(1)], MD. NASIR MD. NOH[(2)], AMINUDDIN AB. GHANI[(3)], NOR AZAZI ZAKARIA[(4)] & CHUN KIAT CHANG[(5)]

[(1,2)]Department of Irrigation & Drainage Malaysia, Jalan Sultan Salahuddin, Kuala Lumpur,Malaysia
teofy@water.gov.my; drnasir@water.gov.my; ngks@water.gov.my
[(3,4,5)]River Engineering and Urban Drainage Research Centre (REDAC), Universiti Sains Malaysia, NibongTebal, Penang, Malaysia
redac01@usm.my; redac02@usm.my; redac10@usm.my

## ABSTRACT

In recent years, urbanisation and land development have led to an increase in river sand mining activities. These activities have given rise to various problems including: river bank erosion, river bed degradation, river buffer zone encroachment and deterioration of river water quality. Excessive removal of sand may significantly distort the natural equilibrium of a river system. Thus, it is important to further investigate on the river sand mining capacity as recommendations for long-term management of sand mining activities. This paper therefore presents a study that includes the assessment of the river morphology, hydraulic and sediment transport modelling, which covers three rivers with different levels of sand mining activities in Malaysia i.e. Muda River, Langat River and Kurau River. Field works on selected sites of the three rivers are made to assess the capacity of the rivers to convey both water and sediment. Data collection on bed material is made to identify the physical characteristics of sediment in terms of river response to erosion and deposition. A detailed sediment transport analysis is conducted to determine the suitability of existing sediment transport equations for use in the selected sediment transport models. Through the analysis, it is found that Yang and Engelund-Hansen equations are able to predict the trend of sediment transport for these three rivers. Hydraulic and sediment transport modelling study are also carried out to determine possible locations of deposition along the rivers. The depth and volume of deposition will in turn determine the viability of sand extraction taking into account the ability of the rivers to replenish the sediment. The findings of this study have provided a proposal on the minimum and maximum levels of sand extraction for each river, and it is also an invaluable planning and management tool for authorities to make effective and timely decisions on sand mining applications and operations in Malaysia.

**Keywords:** River sand mining capacity; river morphology; hydraulic and sediment transport; replenishment rate.

## 1 INTRODUCTION

Sand and gravel have long been used as aggregates for construction of roads and buildings. In recent years, rapid development has led to an increased demand for river sand as a source of construction materials. In Malaysia, the main source of sand is mostly from in stream mining. In stream sand mining is a common practice because the mining locations are usually sited along the transportation route, hence reducing transportation costs. However, in-stream sand mining can damage private and public properties as well as aquatic habitats. Excessive removal of sand may significantly distort the natural equilibrium of a stream channel. By removing sediment from the active channel bed, in stream mines interrupt the continuity of sediment transport through the river system, disrupting the sediment mass balance in the river downstream and inducing channel adjustments extending considerable distances beyond the extract site itself. These include river bank erosion, river bed degradation, river buffer zone encroachment and deterioration of river water quality. Very often, over-mining occurs which jeopardises the health of the river and the environment in general. The magnitude of the impact basically depends on the magnitudes of the extraction relative to bed load sediment supply and transport throughout the reach (Kondolf et al., 2001; Collins and Dunne, 1990; Rovira et al., 2005; Rinaldi et al., 2005).

The objectives of the present study include the assessment of the river morphology, hydrological and sediment transport modelling and development of river register database. It is important to ensure that sand and gravel extraction is carried out in a sustainable way and to maintain the river equilibrium with the application of sediment transport principles in determining the locations, period and quantity to be extracted. Field works on selected sites of the rivers are made to assess the capacity of the river to convey both water and sediment. Data collection on bed material is made to characterize the physical characteristics of sediment responsible for sediment transport that determines the river response in terms of erosion and deposition. The three rivers are clearly composed of bed material size in the sand-gravel ranges based on the data collected in the study.

 

## 2 STUDY AREA

The study was carried out to cover three main rivers in Malaysia i.e. Muda River, Langat River and Kurau River, which had different levels of sand mining activities. Muda River has a long history of sand mining activity along the upper reach. Langat River recently has been a major source of sand for construction with the development of Putrajaya. Fewer activities of sand mining are ongoing in Kurau River at the upstream of Bukit Merah reservoir.

### 2.1 Muda River

Muda River originates in the mountainous areas of the State of Kedah as shown in Figure 1. The watershed is adjacent to Thailand and covers a drainage area of 4,210 km$^2$. At the upstream end of Muda River is the Muda Dam which acts as an extra storage for the Pedu dam. The two dams are part of the Muda Irrigation Scheme. The upper and middle reaches of Muda River belong to the State of Kedah, while the river downstream with a length of about 30 km forms the boundary between the states of Kedah and Pulau Pinang. The main channel of Muda River has a length of about 180 km with a slope of 1/2300 from the river mouth to Muda Dam. The channel width is typically around 100m and widens up to about 300m near the river mouth. The channel tends to erode due to the sand mining operations, aggravating bank erosion and riverbed degradation. As refer to the surveys in year 2000, the shallowest point in the river is located 2.5 km upstream of the river mouth, and causes difficulty to navigation during low tides. Bed load transport is the most influential mode of sediment transport for sandy riverbed like the Muda River. It was estimated that the annual bed load discharge of Muda River is about 10,000 m$^3$ (JICA, 1995).

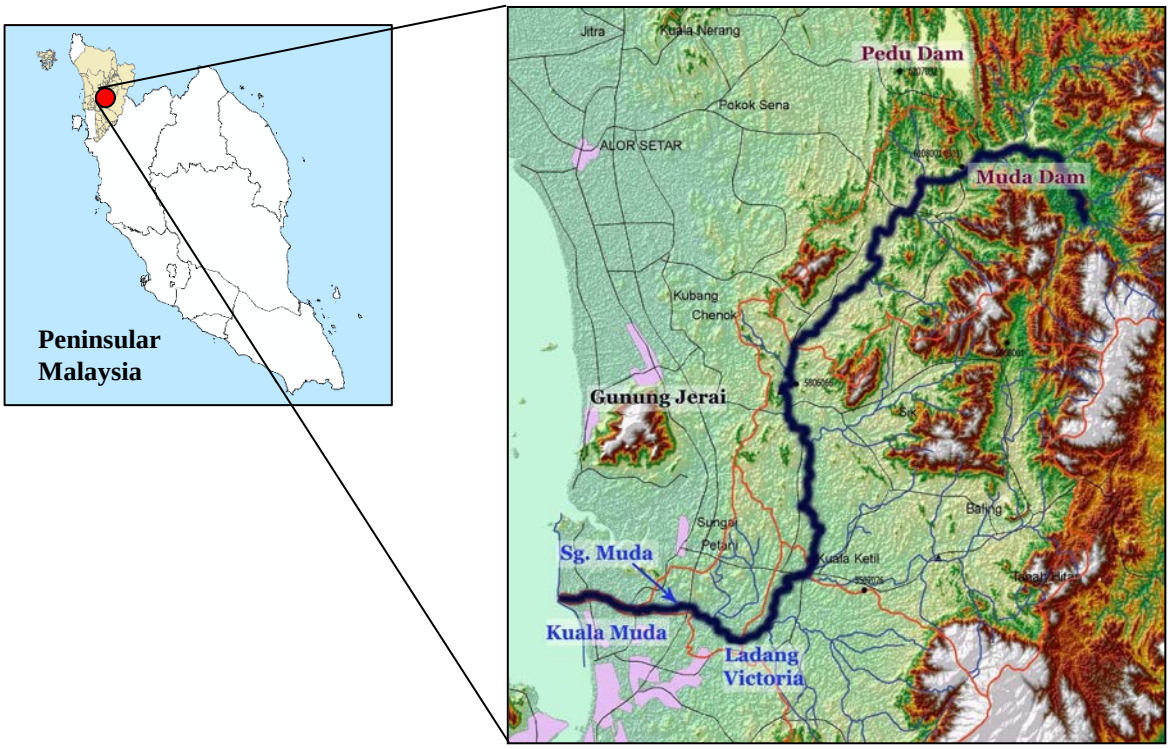


**Figure 1.** Muda River Catchment.

### 2.2 Langat River

The Langat River watershed has a total catchment area of 2350 km$^2$, occupies the south and south-eastern parts of the State of Selangor and small portions of Negeri Sembilan and Federal Territory of Putrajaya. Langat River reaches for 200 km and has average annual flows of 35 m$^3$/s and mean annual floods of 300 m$^3$/s. The watershed is bounded on the east by the Main Range and the Straits of Malacca on the west. The watershed has a diverse topography ranging from mountainous areas in the north-east, low rolling hilly areas in the middle to lowlands in the south-west part of the watershed. The geographic area of the Basin is shown in Figure 2.

 

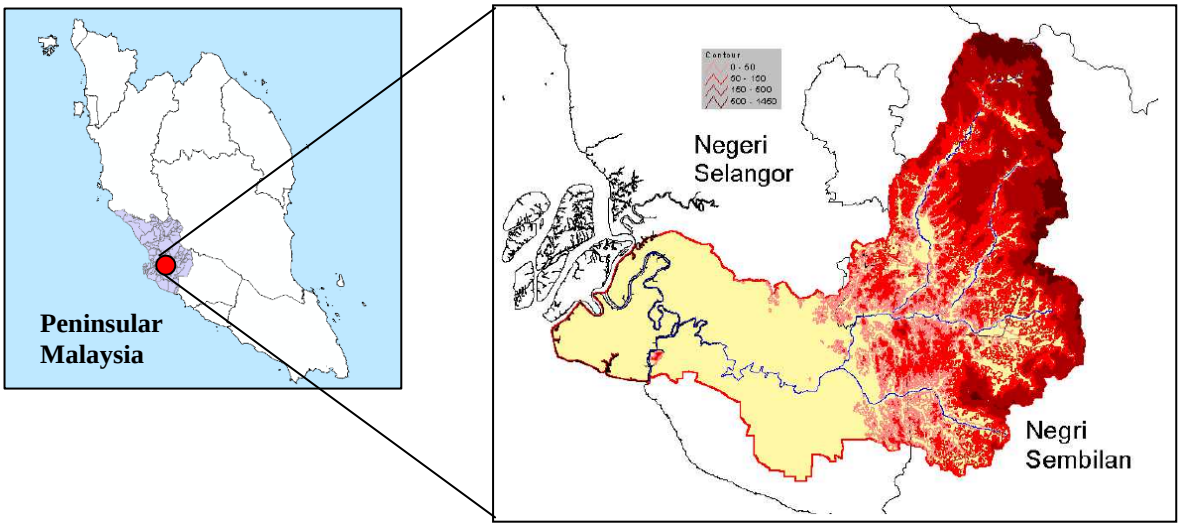


**Figure 2.** Langat River Catchment.

2.3 Kurau River

Kurau River (See Figure 3) represents the main drainage artery of the basin, draining an area of approximately 682 km$^2$ that is generally low lying. The river originates partly in the Bintang Range and partly in the Main Range where the terrain in the upper reaches is steep and mountainous. Mid valleys of the river are characterized by low to undulating terrain, which give way to broad and flat floodplains. Ground elevations at the river headwaters are moderately high, being 1200m and 900m, respectively in Batu Besar and Batu Ulu Trap. The slopes in the upper 6.5km of the river averaged 12.5%, whilst those lower down the valleys are much lower, of the order of 0.25% to 5%. A dam has been constructed at 65km upstream at the mid section of the rivers to form the Bukit Merah Reservoir. This operates principally to irrigate the paddy areas immediately below the Reservoir. Upstream of the Reservoir are two sub-catchments, namely the Kurau River sub-catchments and the Merah River sub-catchments. Both rivers drain through undulating to steep terrain.

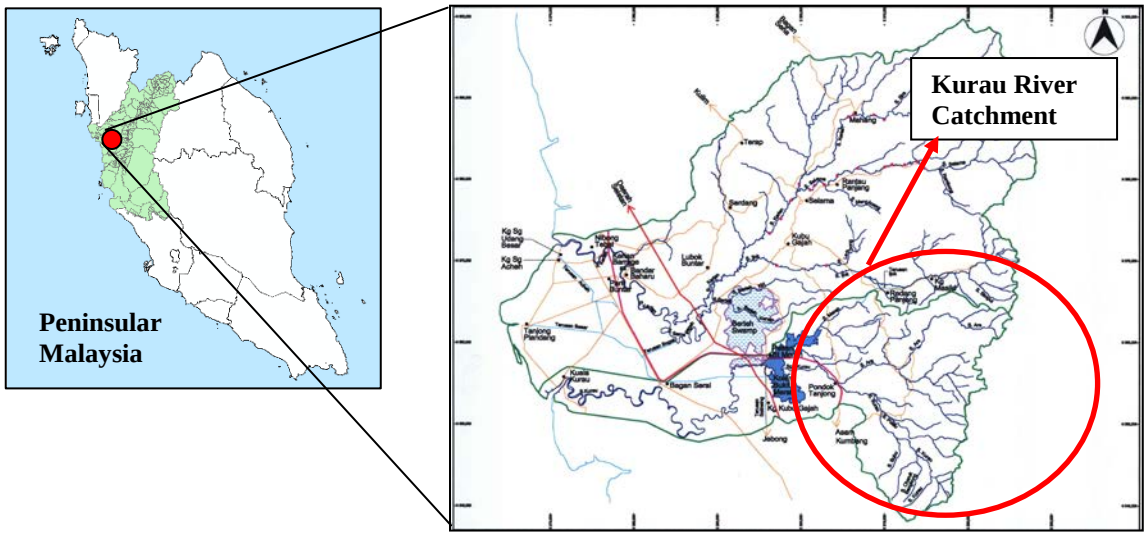


**Figure 3.** Kurau River Catchment

## 3 STUDY APPROACH

The loose boundary (i.e. consisting of movable material) of an alluvial channel deforms under the action of flowing water and the deformed bed with its changing roughness (i.e. bed forms) interacts with the flow. A dynamic equilibrium state of the boundary may be expected when a steady and uniform flow has developed (Nalluriand Featherstone, 2001). One of the principal causes of environmental impacts from in-stream mining is the removal of more sediment than the system can replenish. Coarse material transported by a river (i.e. bed load) commonly is moved by rolling, sliding, or bouncing along the channel bed. Some researchers believe that environmental impacts from in-stream mining can be avoided if the annual bed load is calculated and aggregate extraction is restricted to that value or some portion of it. To accurately limit extraction to some portion of bed load, the amount of sediment that passes the in-stream mining site during a given period of time

 

must be calculated. There is a large amount of uncertainty in the process of calculating annual rates of bed load transport (National Research Council, 1983). How much coarse material is moved, how long it remains in motion and how far it moves depends on the size, shape and packing of the material and the flow characteristics of the river. Downstream movement commonly occurs as irregular bursts of short-distance movement separated by longer periods when the particles remain at rest. Because bed load changes from hour to hour, day to day and year to year, estimating annual bed load rates is a dynamic process involving careful examination.

3.1 River conveyance capacity

Six sites (See Table 1) from each river were chosen for detailed analysis on sediment transport capacity. All cross sections were single thread channel with the top width ranging between 22.75 and 134.0 m representing medium size rivers. According to Department of Irrigation and Drainage's existing guideline (DID, 2008), these ranges of river width are suitable for sand mining purpose with the allowable mining depth up to 1.5 m. The bank full width was determined from the top of the bank as defined by Julien (2002). All three rivers slopes are between 0.00008 and 0.0021 indicating the cross sections are still natural. The ranges of average sediment size ($d_{50}$) show that Muda River is made up of sand and gravel with sizes between 0.29 and 3.00mm, while Langat River and Kurau River river bed is mainly composed of coarse sand with a mean particle size ($d_{50}$) between 0.30 and 1.90mm. The Manning's flow resistance coefficient (*n*) appears to be consistent with those of natural rivers.

**Table 1.** Main morphological and hydrological descriptors.

| Sites | Parameter | | | | |
|---|---|---|---|---|---|
| | Bank full width (m) | Bank full discharge ($m^3/s$) | Channel slope | Manning *n* | Bed material, $d_{50}$ (mm) |
| Muda River | | | | | |
| MU1 | 111 | 778.16(≈ 5-year ARI) | 0.000235 | 0.051 - 0.108 | 0.49 - 2.10 |
| MU2 | 94 | 1407.66 | 0.00021 | 0.021 - 0.089 | 0.70 - 2.20 |
| MU3 | 114 | 1596.3 | 0.00022 | 0.028 - 0.103 | 0.30 - 3.00 |
| MU4 | 122 | 1838.5 | 0.00032 | 0.023 - 0.040 | 0.32 - 1.90 |
| MU5 | 134 | 463.83 | 0.00008 | 0.027 - 0.070 | 0.29 - 0.90 |
| MU6 | 116 | 3177.81 | 0.00075 | 0.032 - 0.037 | 0.55 - 1.10 |
| Langat River | | | | | |
| LA1 | 40 | 89.5(<2-year ARI) | 0.00065 - 0.001 | 0.077 - 0.195 | 0.31 - 3.00 |
| LA2 | 50.2 | 158.59 | 0.001 - 0.00185 | 0.077 - 0.165 | 0.33 - 0.55 |
| LA3 | 28.5 | 71.54 | 0.00115 | 0.040 - 0.112 | 0.70 - 1.10 |
| LA4 | 22.75 | 120.27 | 0.00075 - 0.00135 | 0.038 - 0.064 | 0.80 - 1.80 |
| LA5 | 27.65 | 99.21 | 0.0012 | 0.044 - 0.061 | 0.60 - 1.60 |
| LA6 | 32.4 | 375.26 | 0.0016 | 0.034 - 0.041 | 1.20 - 1.80 |
| Kurau River | | | | | |
| KU1 | 40 | 15.524 | 0.00065 | 0.014 - 0.066 | 0.50 - 1.30 |
| KU2 | 37 | 14.661 | 0.0005 | 0.02 - 0.034 | 0.65 - 1.00 |
| KU6 | 30 | 8.92(<2-year ARI) | 0.00076 | 0.023 - 0.034 | 0.65 - 1.00 |
| KU11 | 28.7 | 7.366 | 0.001 | 0.019 - 0.034 | 0.61 - 1.50 |
| KU12 | 25.8 | 10.882 | 0.0021 | 0.019 - 0.045 | 0.41 - 1.70 |
| A5 | 37.5 | 9.411 | 0.001 | 0.015 - 0.036 | 0.60 - 1.90 |

3.2 Sediment transport capacity

A detailed sediment transport study at six sites of each river was conducted to determine the suitability of existing sediment transport equations for use in the selected sediment transport models. It was found that Yang and Engelund-Hansen equations were able to predict the trend of sediment transport for the three rivers. The data collection included flow discharge (Q), suspended load ($T_t$), bed load ($T_b$) and water surface slope ($S_o$). Besides that, bed elevation, water surface and thalweg measurement (the minimum bed elevation for a cross section), were also carried out at the selected cross sections. Details of measurement methodology were given in Ab. Ghani et al. (2003).

The replenishment rate was determined from either measured or computed sediment rating curve. Figure 4 shows the comparison of the measured sediment rating curves or replenishment rates for the three rivers in the present study. It can be seen that a steeper curve was obtained for Langat River as compared to Muda River and Kurau River. Hence, it is expected that Langat River has a good replenishment rate for the purpose of sand extraction. For a flow discharge of $100m^3/s$, Figure 4 shows that the replenishment rates for Muda River, Langat River and Kurau River are 2.9 kg/s, 48.3 kg/s and 4.6 kg/s, respectively.

 

**Table 2.** Ranges of field data collection.

| Locations | Q ($m^3/s$) | V (m/s) | B (m) | $Y_o$ (m) | A ($m^2$) | R (m) | $S_o$ | $T_b$ (kg/s) | $T_t$ (kg/s) | $T_j$ (kg/s) | $d_{50}$ (mm) |
|---|---|---|---|---|---|---|---|---|---|---|---|
| Muda River | | | | | | | | | | | |
| MU1 | 46.27 - 209.84 | 0.27 - 0.75 | 88.0 - 90.0 | 4.61 - 6.90 | 174.29 - 278.34 | 2.52 - 3.90 | 0.000235 | 0 - 0.125 | 0.423 - 15.614 | 0.423 - 15.644 | 0.49 - 2.10 |
| MU2 | 30.33 - 343.71 | 0.25 - 1.45 | 64.0 - 68.0 | 3.46 - 6.24 | 88.70 - 240.69 | 1.32 - 3.02 | 0.00021 | 0 - 0.056 | 0.360 - 6.688 | 0.360 - 6.688 | 0.70 - 2.20 |
| MU3 | 10.57 - 110.92 | 0.14 - 0.78 | 68.0 - 70.0 | 3.86 - 4.85 | 71.41 - 142.09 | 1.00 - 1.82 | 0.00022 | 0 - 0.017 | 0.367 - 2.280 | 0.367 - 2.291 | 0.30 - 3.00 |
| MU4 | 31.26 - 129.13 | 0.65 - 1.37 | 26.0 - 34.0 | 4.16 - 5.14 | 44.50 - 94.05 | 1.58 - 2.59 | 0.00032 | 0 - 0.014 | 0.163 - 2.646 | 0.163 - 2.660 | 0.32 - 1.90 |
| MU5 | 7.20 - 26.69 | 0.16 - 0.49 | 30 | 3.17 - 3.70 | 31.20 - 55.26 | 0.98 - 1.73 | 0.00008 | 0.004 - 0.011 | 0.096 - 5.667 | 0.099 - 5.675 | 0.29 - 0.90 |
| MU6 | 2.59 - 8.50 | 0.51 - 0.85 | 9 | 0.73 - 1.34 | 5.12 - 9.99 | 0.55 - 0.98 | 0.0008 | 0.102 - 0.191 | 0.024 - 0.664 | 0.173 - 0.809 | 0.55 - 1.10 |
| Langat River | | | | | | | | | | | |
| LA1 | 17.56 - 120.76 | 0.23 - 0.79 | 35.0 - 37.6 | 3.33 - 5.77 | 78.05 - 153.57 | 2.14 - 3.68 | 0.00065 - 0.001 | 0.027 - 0.057 | 4.065 - 99.351 | 4.092 - 99.398 | 0.31 - 3.00 |
| LA2 | 6.86 - 45.06 | 0.25 - 0.69 | 23.7 - 32.9 | 2.15 - 3.74 | 26.98 - 67.44 | 1.09 - 1.93 | 0.001 - 0.00185 | 0.206 - 0.320 | 0.794 - 21.096 | 0.999 - 21.385 | 0.33 - 0.55 |
| LA3 | 6.11 - 19.39 | 0.29 - 0.61 | 21.5 - 23.5 | 1.05 - 2.69 | 13.71 - 35.81 | 0.60 - 1.42 | 0.00115 | 0.247 - 0.460 | 0.670 - 9.319 | 0.936 - 9.654 | 0.70 - 1.10 |
| LA4 | 2.75 - 20.95 | 0.30 - 1.01 | 18.0 - 18.7 | 0.64 - 1.48 | 8.31 - 20.76 | 0.45 - 1.06 | 0.00075 - 0.00135 | 0.208 - 0.304 | 0.2860 - 18.915 | 0.525 - 19.124 | 0.80 - 1.80 |
| LA5 | 8.07 - 23.30 | 0.60 - 0.75 | 18.1 - 20.7 | 1.25 - 2.22 | 13.21 - 32.14 | 0.69 - 1.44 | 0.0012 | 0.173 - 0.363 | 0.630 - 5.663 | 0.874 - 5.867 | 0.60 - 1.60 |
| LA6 | 5.19 - 9.85 | 0.64 - 0.85 | 16.4 - 16.9 | 0.76 - 1.00 | 8.17 - 12.25 | 0.47 - 0.70 | 0.0016 | 0.208 - 0.354 | 1.237 - 4.643 | 1.590 - 4.858 | 1.20 - 1.80 |
| Kurau River | | | | | | | | | | | |
| KU1 | 2.37 - 11.64 | 0.27 - 0.87 | 18.00 - 26.00 | 0.36 - 0.86 | 4.39 - 16.09 | 0.189 - 0.614 | 0.00065 | 0.084 - 0.488 | 0.013 - 1.311 | 0.232 - 1.799 | 0.50 - 1.30 |
| KU2 | 2.56 - 28.94 | 0.47 - 0.89 | 16.0 - 24.0 | 0.41 - 1.91 | 5.04 - 33.45 | 0.313 - 1.349 | 0.0005 | 0.197 - 0.460 | 0.020 - 2.660 | 0.217 - 2.970 | 0.65 - 1.00 |
| KU6 | 1.19 - 7.32 | 0.44 - 0.78 | 9.00 - 13.50 | 0.38 - 1.15 | 2.68 - 10.75 | 0.294 - 0.766 | 0.00076 | 0.083 - 0.291 | 0.006 - 0.466 | 0.089 - 0.684 | 0.65 - 1.00 |
| KU11 | 0.63 - 3.71 | 0.40 - 0.79 | 6.30 - 8.70 | 0.38 - 1.24 | 1.43 - 4.70 | 0.215 - 0.630 | 0.001 | 0.080 - 0.255 | 0.001 - 0.163 | 0.094 - 0.268 | 0.61 - 1.50 |
| KU12 | 1.25 - 14.71 | 0.46 - 1.12 | 10.40 - 14.25 | 0.51 - 1.85 | 2.61 - 13.19 | 0.185 - 0.859 | 0.0021 | 0.087 - 0.328 | 0.010 - 1.280 | 0.209 - 1.450 | 0.41 - 1.70 |
| A5 | 1.58 - 10.66 | 0.52 - 0.94 | 12.00 - 16.63 | 0.50 - 1.40 | 2.95 - 12.41 | 0.177 - 0.679 | 0.001 | 0.126 - 0.367 | 0.015 - 1.706 | 0.239 - 1.832 | 0.60 - 1.90 |

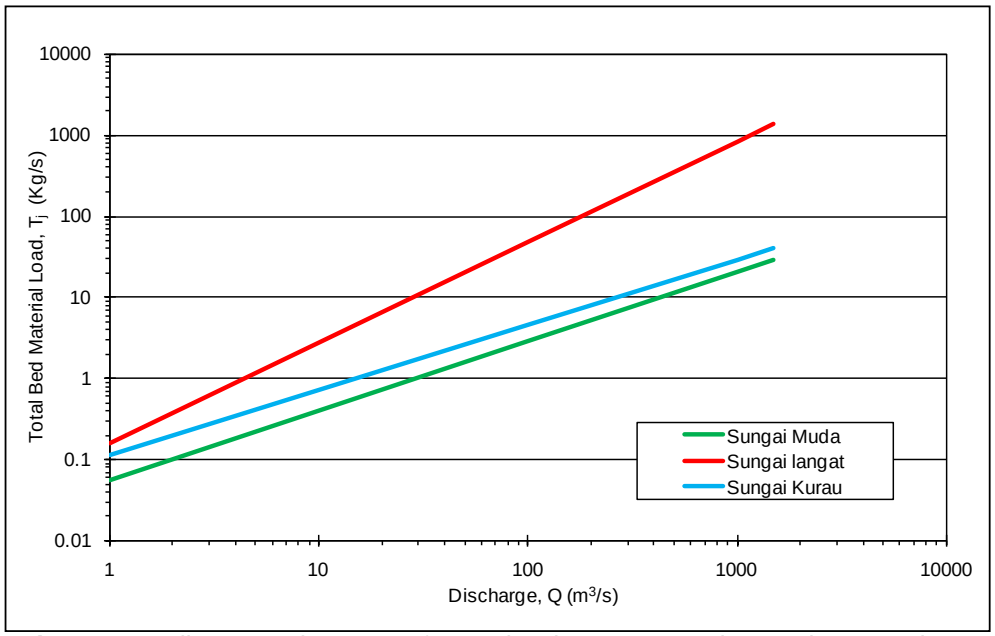


**Figure 4.** Sediment Rating Curve for Muda River, Langat River and Kurau River.

## 4 RESULTS AND DISCUSSIONS

### 4.1 Assessment of sediment transport equations

The assessment of two existing sediment transport equations: Yang and Engelund-Hansen equations, was made for the 214 sets of data from the study as in Tables 3 and 4. The assessment was based on average size of sediment ($d_{50}$). The performances of the equations were measured using the discrepancy ratio (DR), which is the ratio of the predicted load to measured load (DR=predicted/measured). A discrepancy ratio of 0.5 and 2.0 (DR=0.5-2.0) was used as a criterion in the evaluation of the selected equations. It was found that Yang and Engelund-Hansen equations were able to predict the trend of sediment transport for the three rivers.

**Table 3.** Summary of Discrepancy Ratio Using Yang Equation.

| River | Location | Total of Data | Discrepancy Ratio between 0.5-2.0 | |
|---|---|---|---|---|
| | | | No. of data | % |
| Muda River | MU1 (Jambatan Ladang Victoria) | 14 | 4 | 28.57 |
| | MU2 (Jambatan Dato Syed Omar) | 14 | 5 | 35.71 |
| | MU3 (Jambatan Teloi) | 14 | 3 | 21.43 |
| | MU4 (Jambatan Jeniang) | 14 | 2 | 14.29 |
| | MU5 (Jambatan Gajah Putih) | 10 | 0 | 0 |
| | MU6 (Jambatan Nami) | 10 | 2 | 14.29 |
| | **Overall** | **76** | **16** | **21.05** |
| Langat River | LA1 (Dengkil) | 10 | 1 | 20.00 |
| | LA2 (Jenderam) | 10 | 6 | 60.00 |
| | LA3 (UKM) | 10 | 6 | 60.00 |
| | LA4 (Kg. Dusun Nanding) | 10 | 3 | 30.00 |
| | LA5 (Cheras) | 10 | 4 | 40.00 |
| | LA6 (Semenyih) | 10 | 10 | 100.00 |
| | **Overall** | **60** | **30** | **50.00** |
| Kurau River | KU1 (Main Sg Kurau) | 13 | 10 | 76.92 |
| | KU2 (Kurau Tributaries) | 13 | 6 | 46.15 |
| | KU 6 (Batu 14) | 13 | 6 | 46.15 |
| | KU 11 (Kg. Perak) | 13 | 7 | 53.85 |
| | KU 12 (Kg. Cheruk Pelanduk) | 13 | 1 | 7.69 |
| | A5 (Sg. Ara) | 13 | 3 | 23.08 |
| | **Overall** | **78** | **33** | **42.31** |

**Table 4.** Summary of Discrepancy Ratio Using Engelund-Hansen Equation.

| | Location | Total of Data | Discrepancy Ratio between 0.5-2.0 | |
|---|---|---|---|---|
| | | | No. of data | % |
| Muda River | MU1 (Jambatan Ladang Victoria) | 14 | 6 | 42.86 |
| | MU2 (Jambatan Dato Syed Omar) | 14 | 5 | 35.71 |
| | MU3 (Jambatan Teloi) | 14 | 8 | 57.14 |
| | MU4 (Jambatan Jeniang) | 14 | 0 | 0 |
| | MU5 (Jambatan Gajah Putih) | 10 | 0 | 0 |
| | MU6 (Jambatan Nami) | 10 | 0 | 0 |
| | **Overall** | **76** | **19** | **25.00** |
| Langat River | LA1 (Dengkil) | 10 | 3 | 30.00 |
| | LA2 (Jenderam) | 10 | 3 | 30.00 |
| | LA3 (UKM) | 10 | 10 | 100.00 |
| | LA4 (Kg. Dusun Nanding) | 10 | 4 | 40.00 |
| | LA5 (Cheras) | 10 | 3 | 40.00 |
| | LA6 (Semenyih) | 10 | 8 | 80.00 |
| | **Overall** | **60** | **31** | **51.67** |
| Kurau River | KU1 (Main Sg Kurau) | 13 | 11 | 84.62 |
| | KU2 (Kurau Tributaries) | 13 | 8 | 61.54 |
| | KU 6 (Batu 14) | 13 | 6 | 46.15 |
| | KU 11 (Kg. Perak) | 13 | 8 | 61.54 |
| | KU 12 (Kg. Cheruk Pelanduk) | 13 | 1 | 7.69 |
| | A5 (Sg. Ara) | 13 | 4 | 30.77 |
| | **Overall** | **78** | **38** | **48.72** |

 

4.2 Hydraulic and sediment transport modeling

HEC-RAS model was used to predict erosion and deposition in rivers for different hydrological conditions. The results from these models were then used to provide required information for sand mining purposes such as level of deposition, location for extraction and maximum allowable mining depth.The depth and volume of deposition will in turn determine the viability of sand extraction taking into account the ability of the rivers to replenish the sediment.

4.2.1 Muda River

The geometric input was derived from the 2001 surveyed plan for the Proposed Muda River Flood Mitigation Project provided by the DID in the CAD format. The study stretch was approximately 40 km from the upstream most at Ladang Victoria to the river mouth. The survey data were reasonably dense with the distance range between detail cross-section of river and floodplain of about 200 to 250 m. Figure 5 shows that Muda River will experience deposition throughout the river reach utilising the 2003 hydrograph as inflow. The results in Figure 6 show that the invert level changes at the end of simulation on 31 December 2003 and the rate of deposition is higher at the downstream reach. The redline can be drawn for the purpose of setting the minimum envelope level below which no extraction can be made such as 1.0 meter above thalweg level of the 2001 survey.

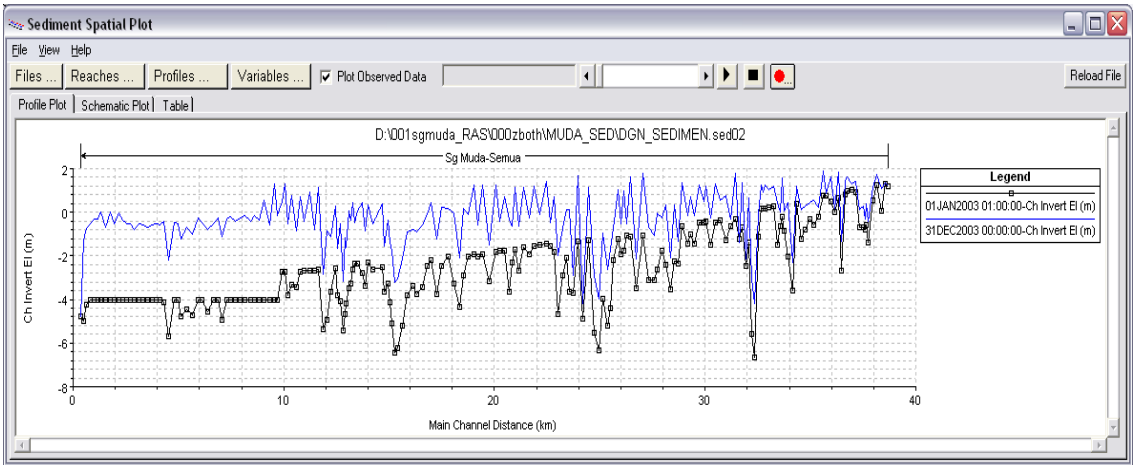


**Figure 5.** Bed Levels of Muda River Before and After Simulation (1 year).

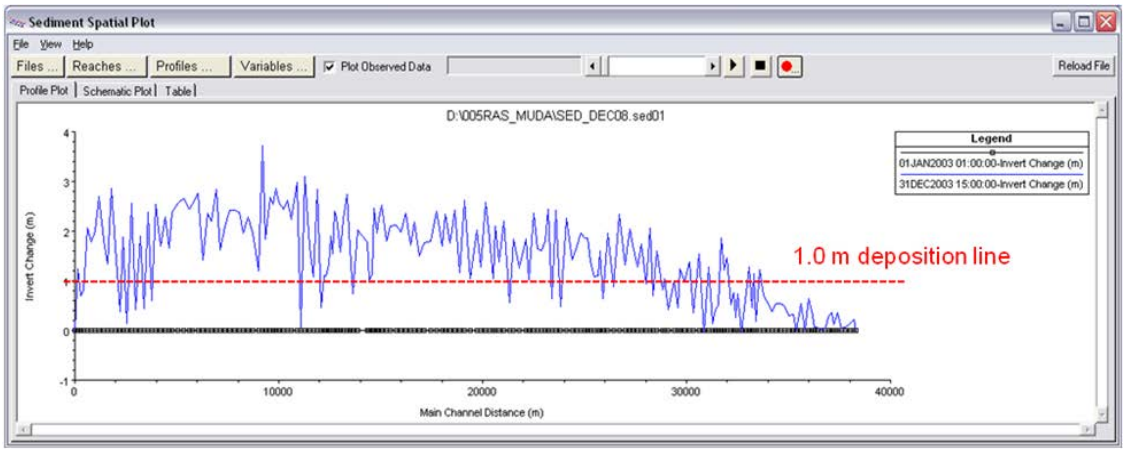


**Figure 6.** Invert Changes Before and After Simulation (1 year).

4.2.2 Langat River

The geometric input was derived from the 2003 surveyed plan provided by the DID in the CAD format. The study site was a stretch of 120 km along the Langat River. Average distance range between detail cross-section of river and floodplain was about 2.0 km and 200 m to 300 m interval for river section only. For both cross-sections, the river sections were represented by only 5 verticals.The simulation results indicate that Langat River has sufficient amount of sediment that can be extracted. From the sediment spatial plot view, comparisons of invert changes between simulation time at 30 Jun 2003 and 31 December 2003 were made. The result as shown in Figure 7 depicts that for most of the river stations, deposition on 31 December 2003 is thicker than the deposition on 30 June 2003. This suggests that there will be some sediment supply to compensate the extracted sand especially the reaches downstream of river station 60000.

 

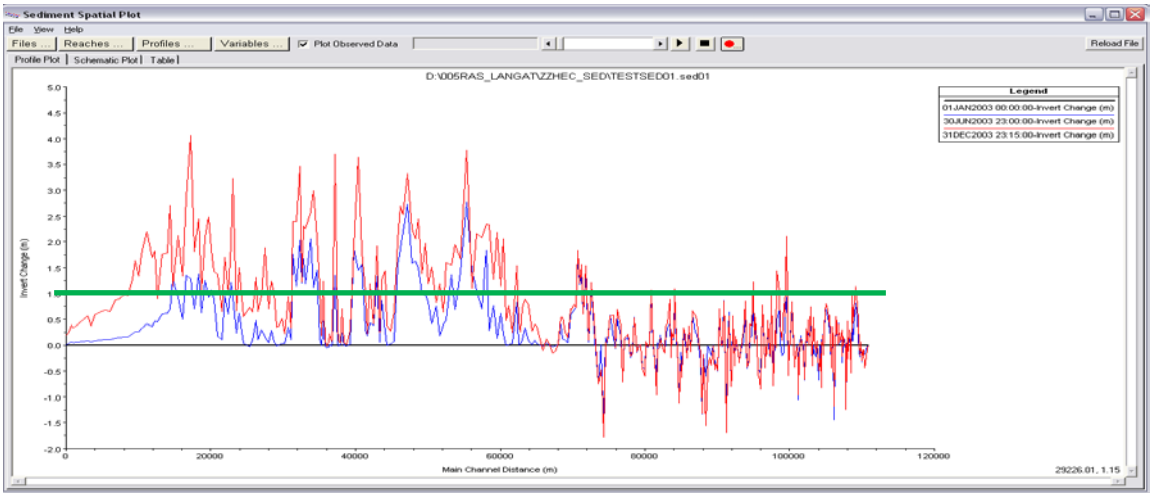


**Figure 7.** Deposition at 31 December 2003 is thicker than the deposition at 30 June 2003 in River Station 60000m.

4.2.3 Kurau River

In this study, there was no survey data available for Kurau River. The geometric data was prepared by estimating the average cross-sections of particular river reaches based on the measured cross-sections at 23 sites along Kurau River. The sections were then engraved into the Digital Terrain Model (DTM) produced by interpolating the contours and spot-heights of the topographical maps in HEC-RAS. Figure 8 shows that after 1 year simulation period, erosion and deposition occur at the upper half of the simulated reach and only slight changes of the bed level at the lower half of the reach. The thickest deposition is less than 0.5 m. This may indicate that Kurau River is in equilibrium state. If the redline is set at 1.0 m, there will be no site that is suitable for sand extraction.

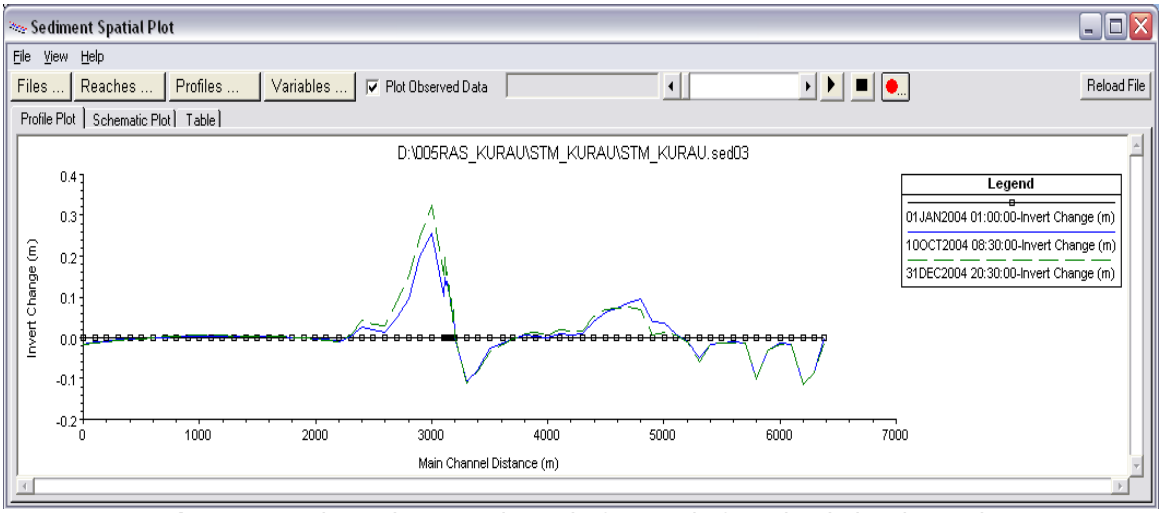


**Figure 8.** Bed Level Comparisons before and after Simulation (1 year).

4.3 Minimum and maximum envelope lines

The suitable sand mining reaches can be determined by drawing the predetermined bed level, or the minimum deposition thickness based on HEC-RAS modelling. The minimum envelope level or redline adopted for the sand extraction was 1.0 m above the design bed levels as shown in Figure 6 and Figure 7. The modelling results for Kurau River as shown in Figure 9 indicate that no sand mining should be allowed if the redline is set at 1.0 m above the present thalweg level. Proposals on the minimum level or redline and maximum level for sand extraction are given based on the HEC-RAS modelling results. It is proposed that the minimum depth of the excavation or redline must be at 1 m deposition above natural channel thalweg elevation, while the maximum allowable mining depth is 1.5 m (See Figure 9). The extraction is allowed for the whole active channel width after taking into consideration of the required setback to avoid bank erosion, and buffer zone encroachment. Allowing the channel wide extraction will increase the volume of the extraction for a particular site. Hence, few mining sites are allocated for each river which will minimize the disturbance to river equilibrium and environment. Based on the sedimentation trend as predicted by HEC-RAS model and after applying the 1 m redline, it can be concluded that Langat River is viable for sand extraction purpose,

 

while Kurau River should be prohibited from any sand extraction activity. Since Muda River is being widened for flood mitigation purpose, it is recommended that deposition should be allowed to occur first after a major flood before any sand extraction activity is allowed in the 40-km lower part of the river.

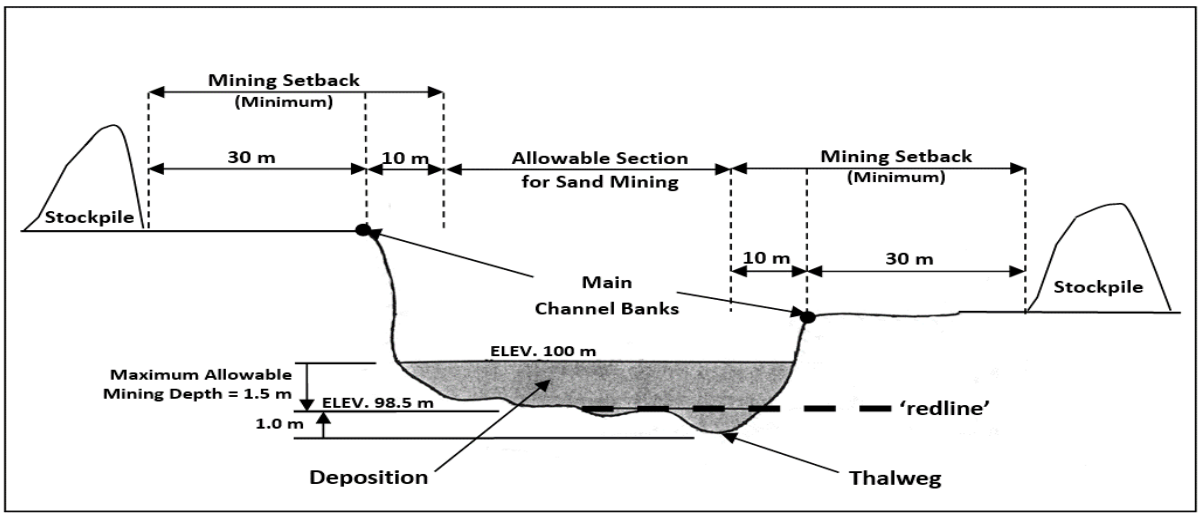


**Figure 9.** Setback, redline and maximum allowable mining depth for in-stream mining (DID, 2009).

## 5 CONCLUSIONS

The replenishment rate as determined from the measured sediment rating curves for the three rivers shows that a steeper curve is obtained for Langat River as compared to Muda River and Kurau River. Hence, it is expected that Langat River has a good replenishment rate for the purpose of sand extraction compared to Muda River and Kurau River. As a result, the findings of this study are invaluable to the local regulatory authorities as planning and management tools to make effective and timely decisions on sand mining applications and operations in Malaysia. A new guideline on river sand mining management is proposed to emphasize the impacts of sand mining and several recommendations for a sustainable sand extraction, including discussions on appropriate extraction methods and floodplain mining as an alternative to in stream mining. Also, Geographical Information System can be utilized for the study areas in the development of river register database.

## REFERENCES

Ab. Ghani, A., Zakaria, N.A., Abdullah, R., Mohd Sidek, L., Sinnakaudan, S.K. & Chang, C.K. (2003). *Guidelines for Field Data Collection and Analysis of River Sediment*, Department of Irrigation and Drainage Malaysia, Kuala Lumpur, 35.

Collins, B. & Dunne, T. (1990). *Fluvial Geomorphology and River-Gravel Mining: A Guide for Planners*, Case Studies Included. Special Publication 98, California Department of Conservation, Division of Mines and Geology.

Department of Irrigation and Drainage, (DID). (2008). *Garis Panduan untuk Memproses Permohonan dan Menetapkan Syarat-Syarat Pengambilan Pasir Sungai*. <http://www.water.gov.my/images/river_section/pengambilan%20pasir%20sungai.pdf> (accessed on Nov. 20, 2016).

Department of Irrigation and Drainage (DID). (2009). *River Sand Mining Management Guideline*. DID, Kuala Lumpur.

Japan International Cooperation Agency, (JICA). (1995). *Comprehensive Management Plan of the Muda River Basin*, Final Report.

Kondolf, G.M., Smeltzer, M. & Kimball, L. (2001). *Freshwater Gravel Mining and Dredging Issues.* Washington Departments of Fish and Wildlife, Ecology, and Transportation, Olympia.

Nalluri, C. & Featherstone, R.E. (2001). *Civil Engineering Hydraulics: Essential Theory with Worked Examples.* Blackwell Science Ltd, Great Britain, 448.

National Research Council. (1983). *Risk Assessment in the Federal Government: Managing the Process.* Washington, DC: The National Academy Press.

Rinaldi, M., Wyzga, B. & Surian, N. (2005). Sediment Mining In Alluvial Channels: Physical Effects and Management Perspectives. *River Research and Applications*, 21, 805–828.

Rovira, A., Batalla, R.J. & Sala, M. (2005). Response of a River Sediment Budget after Historical Gravel Mining (The Lower Tordera, Ne Spain). *River Research and Applications*, 21, 829–847.

 

# CALIBRATION AND DISCHARGE MEASUREMENT USING 0.127 METRE (5") PARSHALL FLUME

ASIS MAZUMDAR[(1)], PRASUN DUTTA[(2)], MILAN NAYEK[(3)], SUBHASISH DAS[(4)] & RAJIB DAS[(5)]

[(1,2,3,4,5)]Jadavpur University, Kolkata, India
asismazumdar@yahoo.com, ju.prasun13@gmail.com, milannayek@gmail.com,
subhasishju@gmail.com, rajibdas79@gmail.com

## ABSTRACT

In the flow measuring structures with control section such as Parshall flumes, a relationship would be produced between water depth and discharge. The advantages of this structure include minimal head loss, low construction cost, adaptability to a variety of channel types, and ability to measure wide ranges of flows with custom-designed structures. In the present study, a series of detailed laboratory measurements are made under steady-state flow conditions through a Parshall flume of throat width 0.127 m (5″) and length 1.352 m. From the literature study very few, in fact no data are available for 5″ throat width for any flume length. Free flow and submerged flow calibration are done within the flow range of 0.005 $m^3/s$ to 0.027 $m^3/s$. Hence forth, equations applicable for both free flow and submerged flow regime are proposed and hence producing Ditchrider's table for field implementation of the flume. The result of the calibration shows that under favorable operating conditions of the discharge within calibrated flow, the proposed equation can determine accurately the discharge with maximum deviation up to ±5 % in both free flow and submerged flow regime.

**Keywords:** Flume; Parshall flume; free flow; submerged flow.

## 1 INTRODUCTION

In the present day situation, accurate flow measurement is an essential component in the collection, distribution, delivery and application of these resources. One of the important problems in irrigation is measuring irrigation water that flows in open channels. Several devices have been used for measuring irrigation water including weirs and flumes. One of the main disadvantages of weirs and flumes in canals of flat gradients is the reduction of the capacity of the canal leads to the further reduction of the gradient. Out of different kinds of flumes, Parshall flume is one flume, which is studied in the present study.

Parshall flumes were developed between 1915 and 1922, and have been widely used in the western United States (USBR 2001) as a simple way to measure discharge in open channels (Parshall 1936; Cone 1917). Parshall flumes can be purchased commercially or built to design specifications given by Parshall (1926), USBR (2001). Because Parshall flumes are not geometrically similar, each specified flume size has its own calibration and corresponding rating curve. Parshall flumes can be accurate up to ±3 to 5% in case of flumes having 3″ throat width for up to 50% submergence; and also ±3 to 5% in case of flumes having 8′ throat width for up to 80% submergence (USBR, 2001).

Parshall flumes are empirical devices for the measurements of water in open channels. They were developed by Parshall (1926) after whom the device was named. The flume consists of a converging section with a level floor, a throat section with a downward sloping floor, and a diverging section with an upward sloping floor. Parshall flumes are calibrated against a piezometric head, measured at a prescribed location in the converging section and the 'downstream' piezometric head measured in the throat (Bos, 1989). Parshall flumes are not the hydraulic scale models of each other, so each Parshall flume must be calibrated separately.

Parshall flumes operate under both free and submerged flow condition. Free flow and submerged flow condition in Parshall flume was described by Skogerboe et al. (1967). Free flow exists in a Parshall flume when a change in the water surface elevation downstream of the flume does not cause a change in water surface elevation upstream of the flume and submerged flow exists in a Parshall flume when a change in the water surface elevation downstream of the flume causes a change in water surface elevation upstream of the flume. In case of free flow only, the depth of upstream flow at $h_a$ is required to determine the flow rate or discharge and for submerged flow, the depths of flow at both upstream $h_a$ and downstream $h_b$ must be measured to determine the flow rate or discharge.

Parshall flumes may be small (0.254, 0.0508, 0.076, 0.152 and 0.23 m or 1, 2, 3, 6 and 9 inch) throat widths, Parshall (1936) and Robinson (1957), medium (0.30, 0.61, 0.91, 1.22, 1.83, and 2.44 m or 1, 2, 3, 4, 6 and 8 ft.) throat widths, Parshall (1936) and large (3.05 m or 10 ft. and greater) throat widths, Parshall (1953). The degrees of submergence are found to be 60%, 70% and 80% for small, medium and larger flumes, respectively (Bos, 1989).

 

In the development of small Parshall flume for measuring discharge of farm laterals, there is no information about the 0.102 m, 0.127 m, 0.177 m and 0.2032 m (4 inch, 5 inch, 7 inch and 8 inch) throated Parshall flume. To improve the undiscovered areas of 0.127 m or 5 ″ Parshall flume, the present study is taken up.

Discharge equation for the Parshall Flume is given by.

For free flow condition:

$$Q = C_f h_a^{n_f} \quad [1]$$

where,

$Q$= discharge, $C_f$ = co-efficient of free flow and $n_f$ = free flow exponent

For submerged flow condition:

$$Q = \frac{C_s \left(h_a - h_b\right)^{n_f}}{\left[-\log S + K\right]^{n_s}} \quad [2]$$

where,

$C_S$= co-efficient of submerged flow, $n_s$= submerged flow exponent, $S$= submergence ratio ($h_0/h_s$) and K= constant for reducing errors in equation

In the present work, an attempt has been made to design and construct a Parshall flume of 5″ throat width, and subsequently to propose equations both for free and submerged flow to calculate the discharge through the flume.

## 2 EXPERIMENTAL FACILITIES

The Parshall flume was constructed at the Fluvial Hydraulics Laboratory of the School of Water Resources Engineering, Jadavpur University. The flume (Figure 1) was installed in a recirculation transparent flume. The recirculating transparent flume was 4 m long, 0.355 m wide and 0.5 m deep.

One centrifugal pump of 3.7 kW rated power and 1420 rpm rated speed was used which was capable of delivering a maximum flow rate of approximately 0.027 $m^3/s$. The flow rate was regulated by means of a valve located on the delivery line and bypass line. Discharge was measured with the help of Dashmesh water meter attached to delivery pipe. The unsteadiness of water before entering the flume was removed by installing one baffle wall across the length of the flume, just after the delivery pipe outlet. The flow passed through the flume and was discharged into the 3.5 m long, 0.4 m wide and 0.6 m deep reservoir from where it was recirculated. Stilling wells were employed on both sides of the flume in upstream and downstream side for measuring the water depth. The upstream flow depth and downstream flow depth measured using the stilling well was indicated as $h_a$ and $h_b$, respectively. A Point Gauge mounted on a movable trolley was used to measure the water level profile or water depth in the flume. Downstream water depth was increased and desired submergence ratio was obtained by regulating the tail gate. The upstream flow depth and downstream flow depth measured using the point gauge was indicated as $h_u$ and $h_d$, respectively. The flow depth taken using the point gauge was utilized to draw the water flow profile for different discharge in the flume. Figure 1 shows the picture of the Parshall flume.

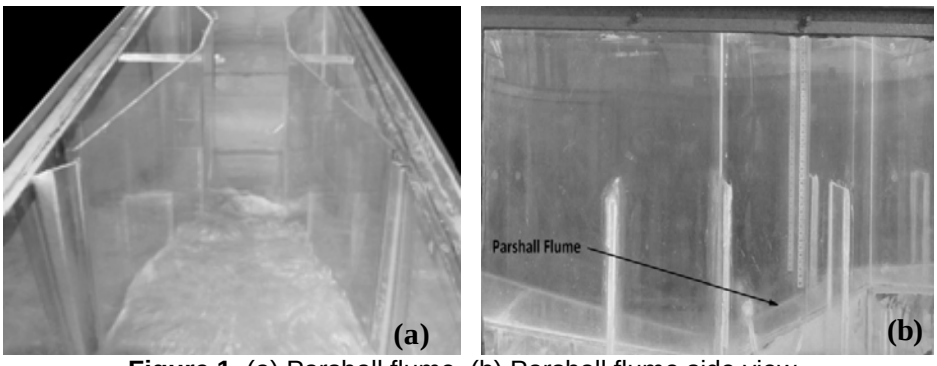


**Figure 1.** (a) Parshall flume, (b) Parshall flume side view.

 

## 3 DESIGN

The Parshall flume was made of 0.006 m thick transparent acrylic sheet of throat width ($b$) 0.127 m and length ($L$) 1.352 m. The vertical side wall height was kept 0.5 m considering 0.2 m free board.

### 3.1 Design of converging inlet section

The axial length of converging inlet section was taken as 0.54 m and the bed of the converging inlet section was horizontal. In the inlet section, the side walls converged with an angle $\theta = tan^{-1}$ (1/5). Width of the entrance cross section of the inlet converging section ($b_1$) was taken as 0.343 m. The width of the recirculating flume ($B$) was 0.355 m and the thickness of the transparent acrylic fiber sheet was 0.006 m. So, the Parshall flume was operated in no wing wall condition. The stilling well to measure the upstream head $h_a$ was placed at a distance of two-third the length of the side wall, upstream of the throat section.

### 3.2 Design of throat section

The length of the throat section ($l$) was taken as 0.272 m and the bed had a downward slope with an angle = $tan^{-1}$ (1/3). Stilling well to measure the downstream head $h_b$ was placed at a horizontal distance of 0.051 m upstream of the end of the throat section.

### 3.3 Design of diverging inlet section

The axial length of the diverging outlet section was taken as 0.54 m and the bed of the diverging outlet section had an upward slope with an angle = $tan^{-1}$ (1/6). Width of the exit cross section of the outlet diverging section ($b_2$) was taken as 0.307 m.

## 4 RESULT AND DISCUSSION

Number of free flow experiments carried out was 23. Discharges were varied from 0.005 $m^3$/s to 0.027 $m^3$/s and the corresponding upstream and downstream heads were measured from stilling well as well as point gauge. The submerged flow calibration was done for the same discharges as for free flow calibration. A total of 92 experiments was carried out in case of submerged flow calibration. Desired Submergence ratio was obtained by regulating the tail gate.

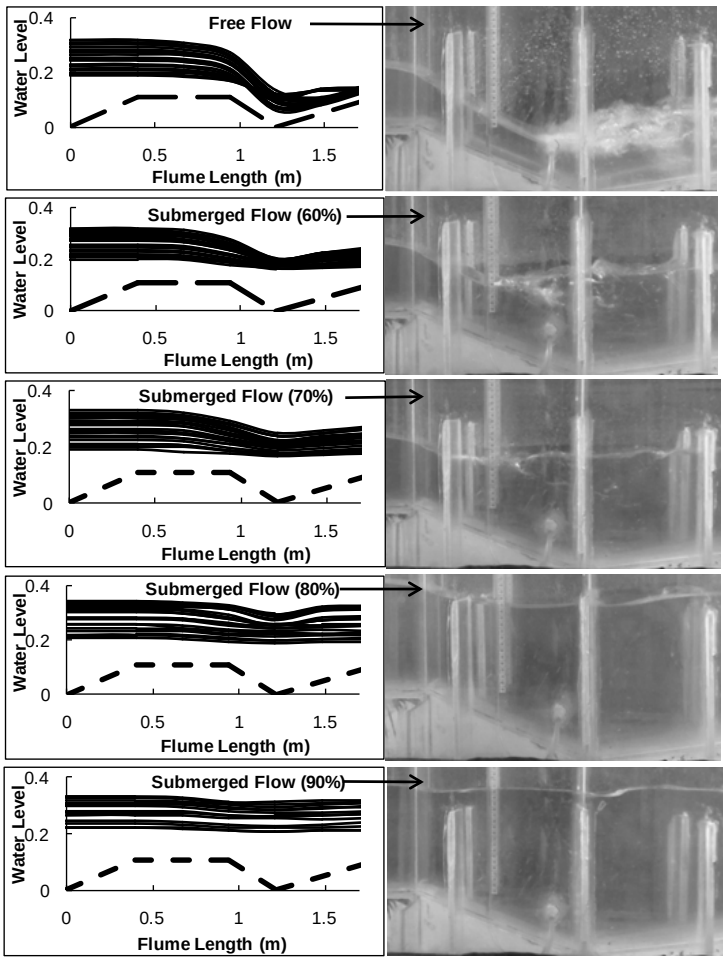


**Figure 2.** Water Profile for all discharges showing free and submergence conditions.

 

For plotting of Water Surface Profile for free flow, 60%, 70%, 80% and 90% submergence, the gauge data was taken at several points of entire Parshall flume. Figure 2 shows the water profile of all the experiments carried out. In Figure 2, the x-axis indicates the flume length and y-axis indicates the water level measured using the point gauge. In the figure, the free flow condition and the different submergence can be seen very clearly.

4.1 Rating equation using stilling well data

In case of rating equation using stilling well data, the upstream and downstream heads ($h_a$ and $h_b$) were measured from the stilling wells for all the experiments. For free flow, a rating curve was obtained by plotting the measured discharge, $Q_m$ against the upstream flow depth $h_a$ obtained from stilling well in logarithmic scale with $Q_m$ as ordinate and $h_a$ as abscissa as shown in Figure 3.

The free flow rating equation for Parshall flume of throat width 0.127 m (5″) is proposed, and is given by:

$$Q_c = 0.4349 h_a^{1.7136} \quad [3]$$

where,

$Q_c$= Calculated discharge

In case of submerged flow, the submergence calibration curve was obtained by plotting the measured discharge against the difference between upstream head ($h_a$) and downstream head ($h_b$) for different submergence ratio 60%, 70%, 80% and 90% as shown in Figure 4.

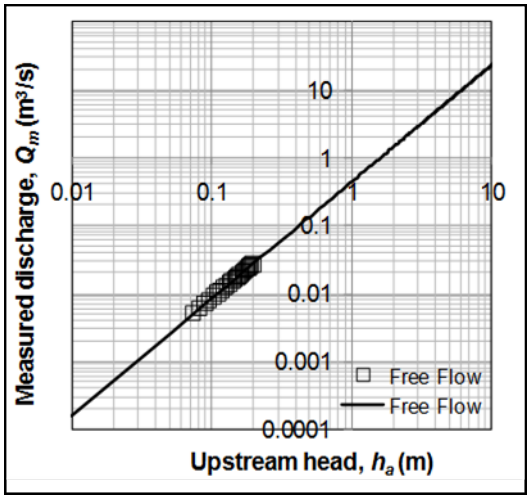


**Figure 3.** Free Flow Calibration Curve (using stilling well data).

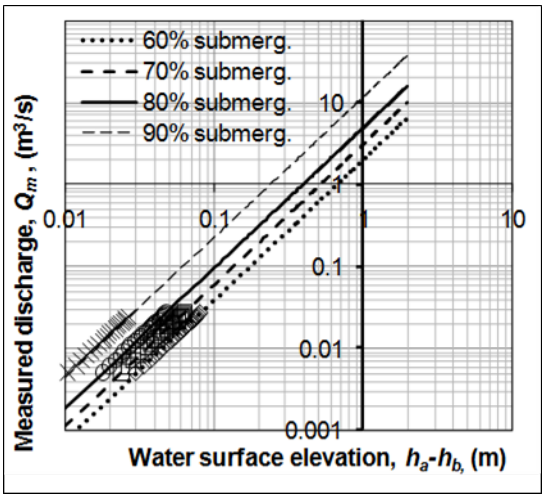


**Figure 4.** Submerged flow rating curve (using stilling well data).

From the submerged flow calibration curve, the discharges at different submergence ratio were obtained for head difference at 1 m. Discharges obtained from Figure 4 for different submergence 60%, 70%, 80% and 90% were 2.008 $m^3$/s, 3.0212 $m^3$/s, 4.892 $m^3$/s and 11.786 $m^3$/s. respectively. Submerged flow discharge parameter $C_s$ and exponent $n_s$ obtained were 0.4063 and 1.0468, respectively. The calculated data obtained

from rating equations (3) and (4) were compared with the measured data as shown in Figure 5. From the figure, it is evident that the calculated data matches very well with the measured data, only few points deviate more than ±5% from the perfect agreement line.

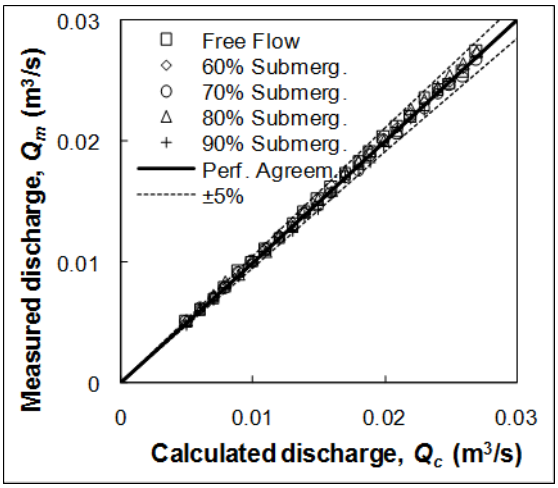


**Figure 5.** Comparison of free and submerged flow calculated data with measured data (stilling well).

$$Q_c = \frac{0.4063\left(h_a - h_b\right)^{1.7136}}{\left[-\log S + 0.0055\right]^{1.0468}} \qquad [4]$$

The Ditchrider's table was prepared with the help of proposed equations. Dichrider's table is necessary for field implementation of the flume. For a person working in the field, Ditchrider's table is very useful to estimate the discharge very easily by simply measuring the head without solving these equations explained above. The range of the table was prepared considering the present experimental range (0.005 $m^3$/s to 0.027 $m^3$/s). In Table 1, the first column represents the upstream head $h_a$ (m), where the upstream head ($h_a$) increases by 0.01 m (1 cm) as it goes downwards in the column. In the same table in 1st row, the upstream head increases by 0.001 m (1 mm) as it goes from left to right. The corresponding discharges in $m^3$/s for a specific upstream head ($h_a$) are indicated in the table from 2nd column and row. It means that this table represents the discharge for a minimum of 1 mm change in $h_a$. Similarly, same kinds of tables are developed for submerged flow (60% - 90%) as shown in Table 2 to Table 5.

**Table 1.** Free flow discharge in $m^3$/s.

| Head ($h_a$) m | 0 | 0.001 | 0.002 | 0.003 | 0.004 | 0.005 | 0.006 | 0.007 | 0.008 | 0.009 |
|---|---|---|---|---|---|---|---|---|---|---|
| **0.07** | | | | 0.0048 | 0.005 | 0.0051 | 0.0052 | 0.0053 | 0.0054 | 0.0056 |
| **0.08** | 0.0057 | 0.0058 | 0.0059 | 0.0061 | 0.0062 | 0.0063 | 0.00649 | 0.0066 | 0.0067 | 0.0068 |
| **0.09** | 0.007 | 0.0071 | 0.0072 | 0.0043 | 0.0075 | 0.0077 | 0.00784 | 0.0079 | 0.0081 | 0.0082 |
| **0.1** | 0.0084 | 0.0085 | 0.0087 | 0.0085 | 0.009 | 0.0015 | 0.0093 | 0.0045 | 0.0096 | 0.0097 |
| **0.11** | 0.0099 | 0.01 | 0.0102 | 0.0138 | 0.0105 | 0.0169 | 0.01085 | 0.0101 | 0.0111 | 0.0113 |
| **0.12** | 0.0115 | 0.0116 | 0.0118 | 0.012 | 0.0121 | 0.0133 | 0.0125 | 0.0167 | 0.0128 | 0.013 |
| **0.13** | 0.0131 | 0.0133 | 0.0135 | 0.0172 | 0.0138 | 0.0107 | 0.01425 | 0.014 | 0.0146 | 0.0147 |
| **0.14** | 0.0149 | 0.0151 | 0.0153 | 0.0153 | 0.0157 | 0.0159 | 0.01609 | 0.0128 | 0.0164 | 0.0166 |
| **0.15** | 0.0168 | 0.017 | 0.0172 | 0.0143 | 0.0176 | 0.0182 | 0.01801 | 0.0121 | 0.0184 | 0.0186 |
| **0.16** | 0.0188 | 0.019 | 0.0192 | 0.0141 | 0.0196 | 0.0182 | 0.02003 | 0.0223 | 0.0204 | 0.0206 |
| **0.17** | 0.0208 | 0.021 | 0.0212 | 0.0219 | 0.0217 | 0.0291 | 0.02213 | 0.0234 | 0.0225 | 0.0227 |
| **0.18** | 0.0229 | 0.0232 | 0.0234 | 0.0235 | 0.0238 | 0.0209 | 0.0243 | 0.0253 | 0.0247 | 0.02497 |
| **0.19** | 0.0252 | 0.0254 | 0.0256 | 0.0258 | 0.0261 | 0.0263 | 0.0265 | 0.0268 | 0.027 | 0.02726 |

 

**Table 2.** For submerged flow (S=60%), discharge in $m^3/s$.

| HEAD $(h_a - h_b)$m | 0 | 0.001 | 0.002 | 0.003 | 0.004 | 0.005 | 0.006 | 0.007 | 0.008 | 0.009 |
|---|---|---|---|---|---|---|---|---|---|---|
| **0.03** | 0.0049 | 0.00523 | 0.00553 | 0.0058 | 0.0061 | 0.00645 | 0.0067 | 0.0071 | 0.0074 | 0.0077 |
| **0.04** | 0.0081 | 0.00847 | 0.00883 | 0.0091 | 0.0095 | 0.00994 | 0.0103 | 0.0107 | 0.0111 | 0.0115 |
| **0.05** | 0.0119 | 0.01231 | 0.01273 | 0.0131 | 0.0135 | 0.01401 | 0.0144 | 0.0148 | 0.0153 | 0.0158 |
| **0.06** | 0.0162 | 0.01672 | 0.0172 | 0.0176 | 0.0181 | 0.01864 | 0.0191 | 0.0196 | 0.0201 | 0.0206 |
| **0.07** | 0.0211 | 0.02167 | 0.02219 | 0.0227 | 0.0232 | 0.02379 | 0.0243 | 0.0248 | 0.0254 | 0.0259 |
| **0.08** | 0.0265 | 0.02711 | | | | | | | | |

**Table 3.** For submerged flow (S=70%), discharge in $m^3/s$.

| HEAD $(h_a - h_b)$ m | 0 | 0.001 | 0.002 | 0.003 | 0.004 | 0.005 | 0.006 | 0.007 | 0.008 | 0.009 |
|---|---|---|---|---|---|---|---|---|---|---|
| **0.02** | | | | | 0.0049 | 0.0053 | 0.0057 | 0.006 | 0.0048 | 0.0068 |
| **0.03** | 0.0073 | 0.0077 | 0.0081 | 0.0086 | 0.009 | 0.0095 | 0.0099 | 0.0107 | 0.0109 | 0.0114 |
| **0.04** | 0.0119 | 0.0124 | 0.013 | 0.0135 | 0.014 | 0.0146 | 0.0152 | 0.0157 | 0.0163 | 0.0169 |
| **0.05** | 0.0175 | 0.0181 | 0.0187 | 0.0193 | 0.0199 | 0.0206 | 0.0212 | 0.0219 | 0.0225 | 0.0323 |
| **0.06** | 0.0239 | 0.0245 | 0.0252 | 0.0259 | 0.0266 | 0.0273 | | | | |

**Table 4.** For submerged flow (S=80%), discharge in $m^3/s$.

| HEAD $(h_a - h_b)$m | 0 | 0.001 | 0.002 | 0.003 | 0.004 | 0.005 | 0.006 | 0.007 | 0.008 | 0.009 |
|---|---|---|---|---|---|---|---|---|---|---|
| 0.01 | | | | | | | | 0.0046 | 0.0055 | **0.0058** |
| 0.02 | 0.006 | 0.0066 | 0.0071 | 0.007 | 0.0083 | 0.0089 | 0.0095 | 0.0102 | 0.0108 | **0.0115** |
| 0.03 | 0.0122 | 0.0129 | 0.0136 | 0.014 | 0.01514 | 0.0159 | 0.0166 | 0.0174 | 0.0183 | **0.0191** |
| 0.04 | 0.0199 | 0.0208 | 0.0217 | 0.0226 | 0.0235 | 0.0244 | 0.02535 | 0.02629 | 0.02725 | **0.02822** |
| 0.05 | 0.0292 | 0.0302 | | | | | | | | |

**Table 5.** For submerged flow (S=90%), discharge in $m^3/s$.

| HEAD $(h_a - h_b)$ m | 0 | 0.001 | 0.002 | 0.003 | 0.004 | 0.005 | 0.006 | 0.007 | 0.008 | 0.009 |
|---|---|---|---|---|---|---|---|---|---|---|
| 0.01 | 0.0043 | 0.0051 | 0.0059 | 0.0068 | 0.0078 | 0.0087 | 0.0098 | 0.0109 | 0.012 | 0.0131 |
| 0.02 | 0.0143 | 0.0156 | 0.0169 | 0.0182 | 0.0196 | 0.021 | 0.0225 | 0.024 | 0.0255 | 0.0271 |

The additional graph has been plotted using Ditchrider's table as shown in Figure 6 and 7. Figures 6 and 7 will be very helpful as it is very easy to evaluate the discharge from those graphs.

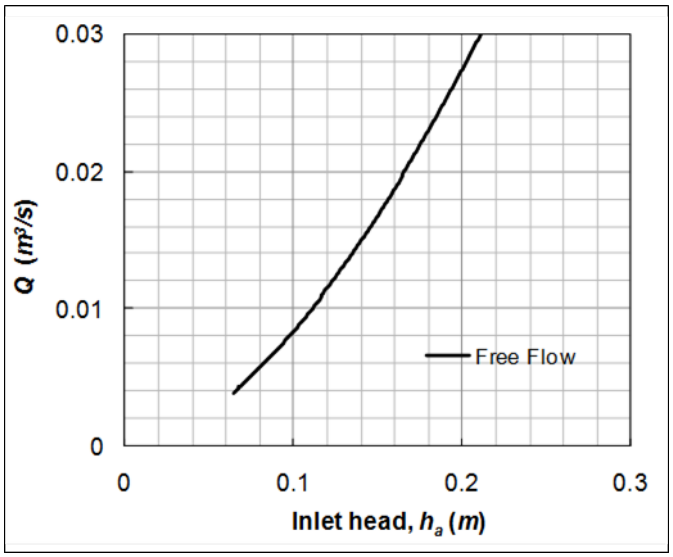


**Figure 6.** Free flow curve (using stilling well data).

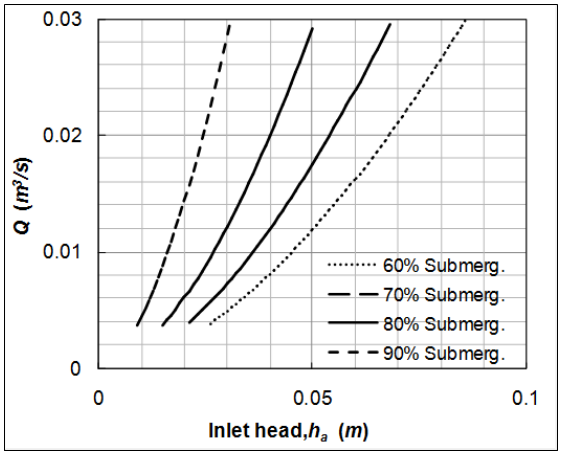


**Figure 7.** Submerged flow curve (using stilling well data).

4.2 Rating equation using gauge data

In case of rating equation using gauge data, the upstream and downstream heads ($h_u$ and $h_d$) were measured using the point gauge for all the experiments both for free flow and submerged flow conditions. Similar elaborations and graphs were plotted as was carried out in case of stilling well data. The graphs for free flow and submerged flow are plotted and shown in Figures 8 and 9. The free flow and submerged flow rating equations for Parshall flume of throat width 0.127 m (5 inch) obtained using the gauge data are given below:

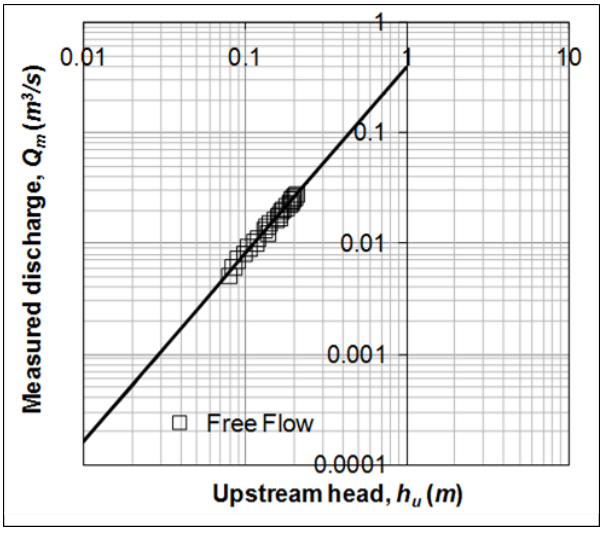


**Figure 8.** Free Flow Calibration Curve (using gauge data).

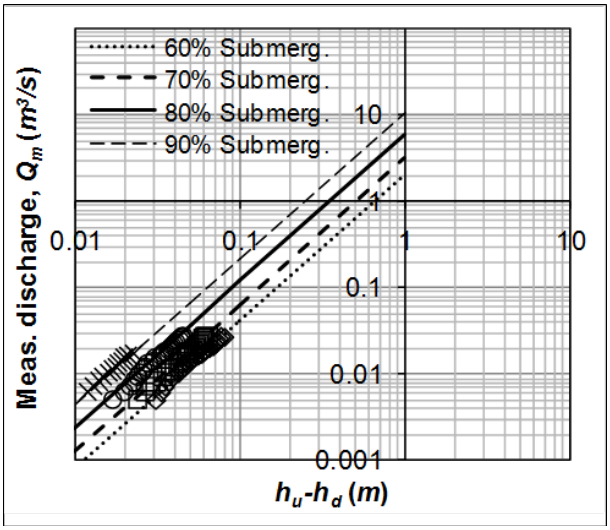


**Figure 9.** Submerged Flow Calibration Curve (using gauge data).

For free flow condition:

$$Q_c = 0.3906 h_u^{1.692} \quad [5]$$

For submerged flow condition:

$$Q_c = \frac{0.4615\left(h_u - h_d\right)^{1.692}}{\left[-\log S + 0.0055\right]^{1.0004}} \quad [6]$$

The calculated data obtained from rating equations (5) and (6) were compared with the measured data as shown in Figure 10. From the figure, it is evident that the calculated data matches considerably with the measured data, only few points deviate more than ±10% from the perfect agreement line. However, after comparing Figures 5 and 10, it is evident that the equations proposed and prediction using the stilling well data are more accurate than the equation proposed using the gauge data. However, the Ditchrider's Table is also developed using the gauge data and the graphical representation of the Ditchrider's Table is shown in Figures 11 and 12.

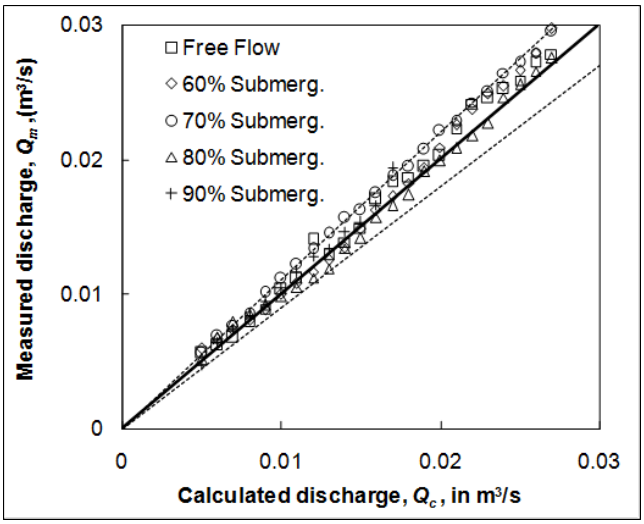


**Figure 10.** Comparison of free flow and submerged flow calculated data with measured data (gauge).

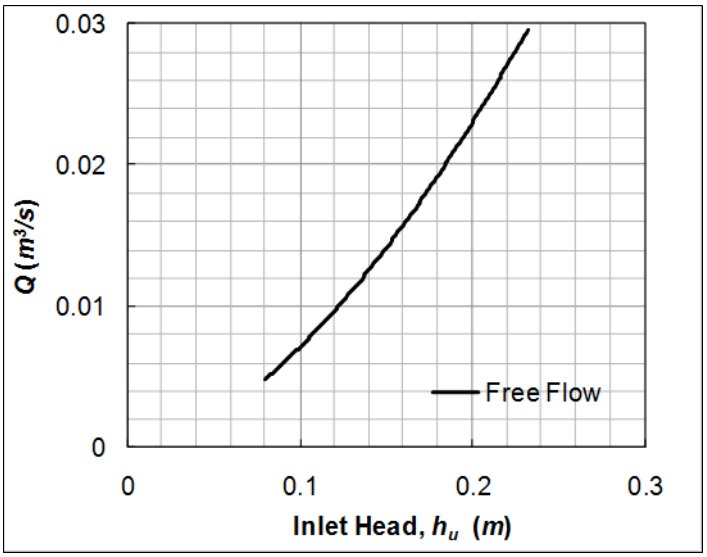


**Figure 11.** Free flow (using gauge data).

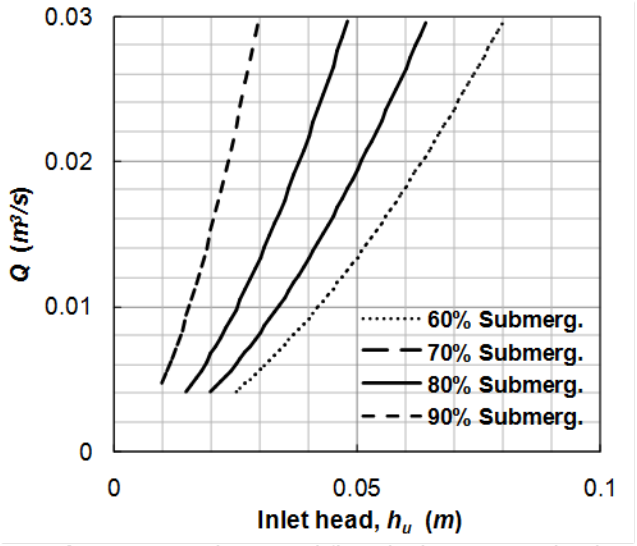


**Figure 12.** Submerged flow (using gauge data).

## 5 CONCLUSIONS

The calibration of Parshall flume is tested and the results of the experiments have been presented in this work. The measured depth-discharge relationships for free flow and submerged flow are plotted within a limited range of discharge (5 $m^3$/s to 27 $m^3$/s) for Parshall flume. From the experimental results, equations are proposed both using the stilling well data as well as the data measured using the point gauge.

- The flexibility of these flumes and the simplicity of developing, calibrating, and constructing effective, economical designs make them the best structure for most open channel flow measurement applications.
- The Ditchrider's Table is necessary for field implementation of flumes. Using this table, a graph is plotted for discharge measurement in lps vs upstream head in cm for free flow and difference of head in cm in case of submerged flow. It is to be noted that the units are taken as lps for discharge and cm for head for simplicity of understanding by the unskilled persons working in the field.

The accuracy of the discharge measurement can be enhanced by increasing the calibration flow range, and also avoiding error in observation of flow depth and flow rate measurements.

## NOTATIONS

| | |
|---|---|
| B | = Width of the recirculation flume. (m) |
| $B$ | =Widths of the throat section. (m) |
| $b_1$ | =Width of the entrance cross section. (m) |
| $b_2$ | = Width of the exit cross section. (m) |
| $h_a$ | =Flow depth at the inlet (upstream) measured from stilling well. (m) |
| $h_b$ | =Flow depth at the outlet (downstream) measured from stilling well. (m) |
| $h_d$ | =Flow depth at the outlet (downstream) measured using point gauge. (m) |
| $h_u$ | =Flow depth at the inlet (upstream) measured using point gauge. (m) |
| $L$ | =Length of the Parshall flume. (m) |
| $l$ | =Length of the throat section. (m) |
| $l_1$ | =Axial length of converging inlet section. (m) |
| $Q$ | =Discharge. ($m^3$/s) |
| $Q_c$ | =Calculated discharge. ($m^3$/s) |
| $Q_m$ | =Measured discharge. ($m^3$/s) |
| $S$ | =Submergence ratio = $h_b/h_a$ |
| $C_f$, $n_f$ | =Free flow discharge parameter and exponent, respectively. |
| $C_s$, $n_s$ | =Submerged flow discharge parameter and exponent, respectively. |

## REFERENCES

Bos, M.G. (1989). Discharge Measurement Structures, *International Institute for Land Reclamation and Improvement/ILRI, Wegeningen*. 3rd Ed. Publication No. 20, Netherlands, 224-248.

Cone, V.M. (1917). The Venturi Flume. *Journal of Agriculture Research*, 9(4). 115-123.

Indian Standard (1996). *Measurement of Liquid Flow in Open Channels,* Parshall and Saniiri Flumes.

Parshall R.L. (1926). The improved Venturi Flume. *Trans. ASCE.* 89. 841-851.

Parshall R.L. (1936). The Parshall Measuring Flume. *Colorado Experiment Station,* Bulletin 423, Colorado.

 

Parshall R.L. (1953). Parshall Flumes of Large Size. *Colorado Agricultural Experiment Station*, Reprint Bulletin 386, Colorado State University, Colorado.

Robinson A.R. (1957). Parshall Measuring Flumes of all Sizes. *Colorado Agricultural Experiment Station*, *Bulletin 61,* Colorado State University, Colorado.

Skogerboe, G.V. Hyatt. M.L., England. J.D. & Johnson, J.R. (1967). *Design and Calibration of Submerged Open Channel Flow Measurement Structures,* Utah Water Research Laboratory, Part 2 Parshall Flumes, Report WG31-*3,* Utah State University, Utah.

U.S. Dept. of the Interior, Bureau of Reclamation, (USBR). (2001). *Water Measurement Manual, 3rd Ed.* U.S. GPO, Washington, D.C.

 

# WATER AND SEDIMENT VARIATIONS AND THEIR INFLUENCE FACTORS IN THE YELLOW RIVER BASIN

YAN-GUI WANG [1] KANG CHEN [2] & YIN CHEN [3],

[1, 2, 3] International Research and Training Center on Erosion and Sedimentation, Beijing, China
wangyg@iwhr.com; ChenKangcp3@163.com; iwhrchenyin@163.com

## ABSTRACT

In order to study the water and sediment variations in the Yellow River, annual runoff and sediment discharge in the stem river and main tributaries from 1950 to 2015 were investigated. This paper applied the cumulative curve analysis method and the Mann-Kendall test method. It is pointed that there are no obvious changing trend for annual runoff and sediment discharge of the Tangnaihai Station in the Upper Yellow River. Significant decrease trends are also observed for the other stations in the stem Yellow River. For the tributaries of the Yellow River, runoff of the Beiluohe River reduces slightly, and runoff and sediment discharge of other tributaries and the sediment discharge of the Beiluohe River reduces significantly. Combined with the characteristics of runoff and sediment in the stemriver and main tributaries of the Yellow River, the influence factors such as precipitation changes, soil and water conservation, silt trapping by reservoirs, and water and sediment diversions on the runoff and sediment variations are analyzed in this paper.

**Keywords:** The Yellow River basin, stem river and tributaries, variation in runoff and sediment, influence factors.

## 1 INTRODUCTION

The Yellow River has a total length of about 5464 km and the catchment area of about 752,000 km$^2$. It is the famous sandy river with prominent characteristics of less water with more sand, and different sources for water and sediment, and with the most sediment discharge and the largest sediment concentration in the world. In the Yellow River basin, human activities frequently occur, such as building the Sanmenxia, Liujiaxia, Longyangxia and Xiaolangdi reservoirs in the upper and middle reaches, implementing a large area of soil erosion control measures and warping-land dams in the Loess Plateau of the Middle Yellow River, and carrying on water and sediment diversions, which changes the water and sediment process. These result in a significant reduction in the runoff and sediment discharge in the stem river and tributaries of the Yellow River Basin. In recent years, there are many researches on water-sediment variations of the Yellow River (Wang, et al., 2010; Liu, et al., 2008; Gao, et al., 2009; Chu et al., 2013). These researches show that the runoff and sediment discharge of the reach above the Longyangxia reservoir have no obvious change. Remarkable decrease trend was observed for the other reaches, and the runoff and sediment discharge of the typical tributaries have a significant tendency to decrease with time. However, these studies are mostly limited to the runoff and sediment variation in the stem Yellow River with limited results on the tributaries. Therefore, using data provided in Gazette of River Sediment in China and Sediment Bulletin of the Yellow River (MWR of China, 2001-2004; MWR of China, 2005-2015; Yellow River Conservancy Commission), the water and sediment variations and their main influence factors in the stem river and tributaries of the Yellow River are studied. This paper applied the hydrological cumulative curve method and the Mann-kendall test method (MK method in short). The Yellow River tributaries and the main control hydrological stations are shown in Figure 1.

The hydrologic accumulation curve method is described as the change in the process line of the cumulative hydrological variables. The changing trend of hydrological variables is analyzed according to the changing characteristics of the accumulation curve (Wang et al., 2010). When the accumulation curve is a straight line, there is no obvious change trend for the hydrological variables. When the curve is convex, the hydrological variables gradually decreases. On the contrary, when the curve is concaved, the hydrological variables gradually increases.

For the MK method, standardized variables M of water and sediment are calculated, and compared with critical variable under a confidence level of 0.05 and 0.02 (Wang et al., 2010), respectively. When $|M| \le 1.96$, it implies that there is no increase or decrease trend for the hydrological variables. When $|M| \ge 3.01$, it is considered that there is an obvious change trend for the hydrological variables. While, variation exists when the hydrological variable are $1.96 < |M| < 3.01$.

 

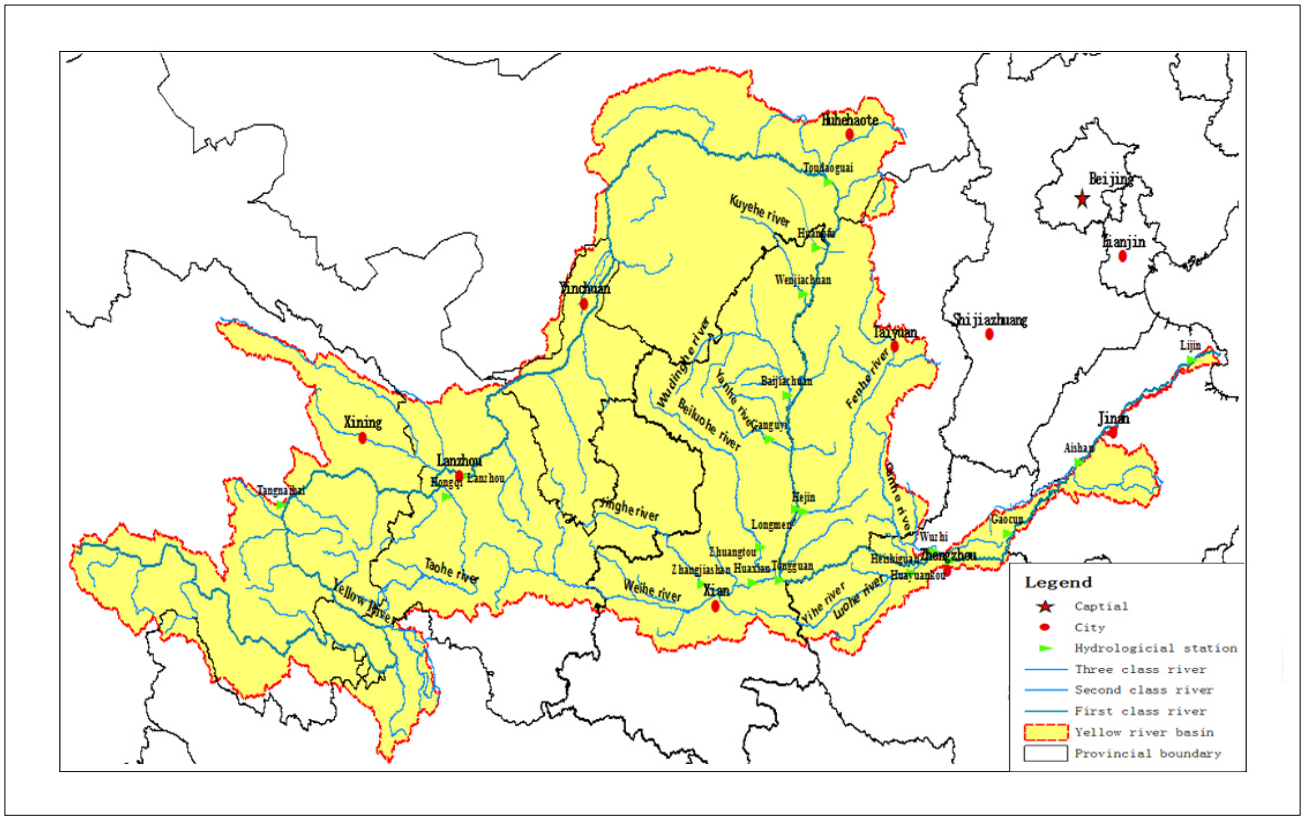


**Figure 1.** Distribution diagram of the hydrological stations and river system in the Yellow River basin

## 2 RUNOFF AND SEDIMENT VARIATIONS IN THE YELLOW RIVER BASIN

### 2.1 Runoff and sediment variation in the stem river

Table 1 lists the characteristics values and standardized variables M of water and sediment in the Stem Yellow River. While Fig 2 shows single cumulative curve of hydrological variables in the Stem Yellow River.

#### 2.1.1 Upper river

The Tangnaihai Station in the Upper Yellow River belongs to the source control station, and single accumulation process curves of runoff and sediment discharge are in a straight line. The corresponding standardized variable M values are -0.946 and -0.561, respectively. This shows that the annual runoff and annual sediment discharge have no change trends because there is little human activity in the basin above Tangnaihai Station. The annual runoff and annual sediment discharge of Tangnaihai Station fluctuate around the mean value of $20.6\times10^9$ $m^3$ and $11.9\times10^6$ t.

In the Lanzhou station and the Toudaoguai station, the standardized M values of runoff respectively are -2.086 and -4.045. The corresponding cumulative curves show an upward convex shape, more obvious for the Toudaoguai station. This shows that the runoff of the Lanzhou station has a decreasing trend, and the runoff of the Toudaoguai station is reduced significantly, especially after 1990's. The annual runoff of the two stations decreases from $33.08\times10^9$ $m^3$ and $24.62\times10^9$ $m^3$ before 1990 to $27.37\times10^9$ $m^3$ and $16.00\times10^9$ $m^3$ after 1990. The standardized variable M values of the sediment discharge of the two stations are -6.182 and -5.684 respectively. While the corresponding cumulative curves are convex, which shows that the sediment discharge of the two stations reduces significantly with similar variation characteristics. The annual sediment discharges of the two stations decreases from $99.6\times10^6$ t and $183\times10^6$ t in 1960s to 21.7×106 t and $40\times10^6$ t in 2000s.

**Table 1.** Trend change of runoff and sediment at hydrological stations in the Stem Yellow River

| Station | Years | 1950s | 1960s | 1970s | 1980s | 1990s | 2000s | 2010~2015 | Average value | M-K analysis | |
|---|---|---|---|---|---|---|---|---|---|---|---|
| | | | | | | | | | | M | Evaluation |
| Tangnaihai | W | 188.1 | 216.4 | 203.9 | 241.3 | 176.0 | 174.5 | 205.9 | 200.6 | -0.946 | NT |
| | $W_S$ | 0.071 | 0.118 | 0.122 | 0.198 | 0.109 | 0.075 | 0.104 | 0.119 | -0.561 | NT |
| Lanzhou | W | 315.3 | 357.9 | 317.9 | 333.6 | 259.8 | 267.6 | 314.0 | 309.2 | -2.086 | DT |
| | $W_S$ | 1.333 | 0.996 | 0.574 | 0.447 | 0.516 | 0.217 | 0.157 | 0.633 | -6.182 | OD |
| Toudaoguai | W | 245.6 | 271.0 | 233.2 | 239.1 | 156.7 | 146.8 | 194.7 | 213.5 | -4.045 | OD |
| | $W_S$ | 1.53 | 1.83 | 1.15 | 0.98 | 0.41 | 0.40 | 0.49 | 1.00 | -5.684 | OD |
| Longmen | W | 305.9 | 336.6 | 284.6 | 276.2 | 198.1 | 170.5 | 211.1 | 257.3 | -5.174 | OD |
| | $W_S$ | 11.89 | 11.32 | 8.68 | 4.70 | 5.09 | 1.77 | 0.98 | 6.67 | -7.178 | OD |
| Tongguan | W | 427.7 | 451.0 | 357.4 | 369.1 | 248.8 | 210.4 | 268.4 | 335.5 | -5.035 | OD |
| | $W_S$ | 18.26 | 14.23 | 13.18 | 7.80 | 7.90 | 3.10 | 1.66 | 9.78 | -6.340 | OD |
| Huayuankou | W | 485.7 | 506.0 | 381.5 | 411.7 | 256.9 | 231.6 | 292.9 | 371.1 | -5.706 | OD |
| | $W_S$ | 15.60 | 11.13 | 12.36 | 7.75 | 6.84 | 1.03 | 0.81 | 8.36 | -6.824 | OD |
| Gaocun | W | 473.4 | 497.2 | 360.2 | 373.9 | 222.1 | 211.2 | 271.2 | 344.7 | -5.585 | OD |
| | $W_S$ | 14.95 | 11.06 | 10.86 | 7.02 | 4.92 | 1.42 | 1.17 | 7.49 | -7.439 | OD |
| Aishan | W | 485.5 | 505.2 | 344.6 | 344.2 | 195.5 | 191.5 | 247.5 | 330.9 | -5.739 | OD |
| | $W_S$ | 13.73 | 11.12 | 9.74 | 7.08 | 5.00 | 1.57 | 1.30 | 7.23 | -7.057 | OD |
| Lijin | W | 474.0 | 501.2 | 311.2 | 286.0 | 140.7 | 140.9 | 190.8 | 292.8 | -6.130 | OD |
| | $W_S$ | 13.68 | 10.89 | 8.98 | 6.39 | 3.90 | 1.34 | 1.13 | 6.74 | -6.999 | OD |

Note:W- annual runoff, $10^8$ $m^3$; $W_S$- annual sediment discharge, $10^8$ t.; NT-No change trend; DT-decrease trend; OD: obvious decrease trend.

2.1.2 Middle river

In the Longmen station and Tongguan station, the standardized variable M values of runoff respectively are -5.174 and -5.850. While the corresponding cumulative curves show an obvious upward convex, which implies that the runoff of the two stations reduces significantly. The annual runoff of the two stations decreases from $33.66\times10^9$ $m^3$ and $45.10\times10^9$ $m^3$ in 1960s to $17.05\times10^9$ $m^3$ and $21.04\times10^9$ $m^3$ in 2000s. The standardized variable M values of the sediment discharge in the two stations are -6.182 and -5.684, respectively. The corresponding cumulative curves are obviously convex, especially from the early 1980s where obvious deflection is observed. This shows that the sediment discharges of the two stations reduces significantly, especially after the early 1980s. The annual sediment discharge of the two stations decreases respectively from $1.19\times10^9$ t and $1.83\times10^9$ t in 1950s to $470\times10^6$ t and $780\times10^6$ t in 1980s, to 177×106 t and $301\times10^6$ t in 2000s, and only $98\times10^6$ t and $166\times10^6$ t after 2010.

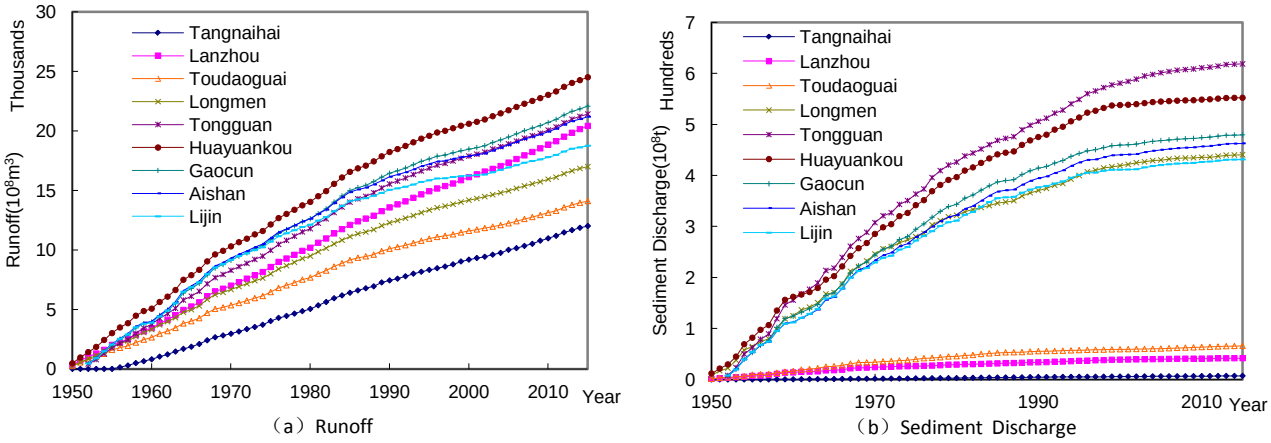


**Figure 2.** Single cumulative curves of hydrological variable in the Stem Yellow River

2.1.3 Lower river

The runoff and sediment discharge of the Huayuankou, Gaocun, Aishan and Lijin stations in the Lower Yellow River have similar change in characteristics. The standardized variable M values of the runoff in the four stations are between -6.5 and -5. While their absolute values are much greater than 3.01, and the

 

corresponding cumulative curves are upward convex with obvious downward deflection in 1969 and 1989,. This shows that the runoff of the four stations significantly reduces with a downward trend. For example, the annual runoff of the Lijin station significantly decreases from $50.12\times10^9$ $m^3$ in 1960s to $28.60\times10^9$ $m^3$ in 1980s, and to $14.09\times10^9$ $m^3$ in 2000s. The standardized variable M values of the sediment discharge of the four stations are between -7.5 and -6.5, and their absolute values are much larger than 3.01. While the corresponding cumulative curves are obviously upward convex, which shows that the sediment discharges in the four stations significantly reduces. The sediment discharge processes are in a downward trend. For example, the annual sediment discharge in the Lijin station decreases obviously from $1.368\times10^9$ t in 1950s to $898\times10^6$ t in 1970s, to $390\times10^6$ t in 1990s and $134\times10^6$ t in 2000s.

**2.2** Runoff and sediment variation in the tributaries

Table 2 lists characteristics values and standardized variables M of water and sediment in the Yellow River tributaries. Figure 3 shows single cumulative curves of hydrological variables in the Yellow River tributaries. Several results from the table and figure are given as follows.

(1) The Hongqi station is a control hydrological station of the Taohe River at the Upper Yellow River. The standardized value M of runoff is -3.031, and the corresponding cumulative curve before 1990 is basically a straight line, and curves downward after 1990. This shows that runoff of the Hongqi station significantly reduces. The annual runoff of the Hongqi station decreases from $4.907\times10^9$ $m^3$ in 1980s to $13.505\times10^9$ $m^3$ in 1990s, and $4.034\times10^9$ $m^3$ after 2010. The standardized variable value M of the sediment discharge in the Hongqi station is -4.635, and the corresponding cumulative curve before 2000 is basically a straight line in shape, and downward deflection after 2000. This implies that the sediment discharge of the Hongqi station significantly reduces. The annual sediment discharge of the Hongqi station decreases from $20.9\times10^6$ t in 1990s to $9.4\times10^6$ t in 2000s, and $3.9\times10^6$ t after 2010.

**Table 2.** Change in trend of runoff and sediment of hydrological stations in the Yellow River tributaries

| Tributary | Station | Years | 1950s | 1960s | 1970s | 1980s | 1990s | 2000s | 2010~2015 | Average annual | M-K analysis | |
|---|---|---|---|---|---|---|---|---|---|---|---|---|
| | | | | | | | | | | | M | Evaluation |
| Taohe | Hongqi | W | 45.50 | 59.15 | 48.51 | 49.07 | 35.05 | 36.32 | 40.34 | 45.10 | -3.031 | OD |
| | | $W_S$ | 0.328 | 0.264 | 0.296 | 0.249 | 0.209 | 0.094 | 0.039 | 0.215 | -4.635 | OD |
| Huangfuchuan | Huangfu | W | 2.65 | 1.72 | 1.76 | 1.27 | 0.90 | 0.36 | 0.28 | 1.25 | -5.789 | OD |
| | | $W_S$ | 0.780 | 0.504 | 0.625 | 0.428 | 0.255 | 0.096 | 0.042 | 0.388 | -5.363 | OD |
| Kuyehe River | Wenjiachuan | W | 8.23 | 7.36 | 7.23 | 5.20 | 4.48 | 1.69 | 2.51 | 5.23 | -6.214 | OD |
| | | $W_S$ | 1.35 | 1.18 | 1.40 | 0.67 | 0.65 | 0.05 | 0.01 | 0.77 | -5.861 | OD |
| Wudinghe River | Baijiachuan | W | 15.82 | 15.21 | 12.10 | 10.36 | 9.34 | 7.54 | 8.61 | 11.01 | -6.990 | OD |
| | | $W_S$ | 2.97 | 1.87 | 1.16 | 0.53 | 0.84 | 0.36 | 0.12 | 1.00 | -6.021 | OD |
| Yanhe River | Ganguyi | W | 2.14 | 2.48 | 2.06 | 2.08 | 2.08 | 1.47 | 1.60 | 2.01 | -2.943 | DT |
| | | $W_S$ | 0.524 | 0.636 | 0.468 | 0.319 | 0.429 | 0.170 | 0.060 | 0.387 | -4.137 | OD |
| Jinghe River | Zhangjiashan | W | 16.24 | 21.67 | 17.45 | 17.12 | 14.01 | 9.97 | 11.68 | 15.68 | -3.924 | OD |
| | | $W_S$ | 2.71 | 2.71 | 2.60 | 1.86 | 2.37 | 1.12 | 0.67 | 2.09 | -3.857 | OD |
| Beiluohe River | Zhuangtou | W | 7.26 | 10.12 | 8.35 | 9.22 | 7.11 | 6.22 | 6.20 | 7.88 | -2.396 | DT |
| | | $W_S$ | 1.05 | 1.03 | 0.89 | 0.50 | 0.90 | 0.22 | 0.09 | 0.69 | -4.890 | OD |
| Weihe River | Huaxian | W | 85.53 | 96.18 | 59.41 | 79.13 | 43.79 | 45.04 | 58.37 | 67.29 | -3.990 | OD |
| | | $W_S$ | 4.29 | 4.36 | 3.84 | 2.76 | 2.76 | 1.38 | 0.70 | 3.00 | -5.208 | OD |
| Fenhe River | Hejin | W | 17.57 | 17.87 | 10.37 | 6.65 | 5.08 | 3.49 | 6.26 | 9.82 | -5.783 | OD |
| | | $W_S$ | 0.700 | 0.344 | 0.191 | 0.045 | 0.032 | 0.003 | 0.003 | 0.199 | -7.941 | OD |
| Yiluohe River | Heishiguan | W | 40.36 | 35.48 | 20.46 | 30.16 | 14.55 | 17.35 | 20.19 | 25.83 | -4.455 | OD |
| | | $W_S$ | 0.360 | 0.181 | 0.069 | 0.089 | 0.009 | 0.007 | 0.005 | 0.109 | -8.063 | OD |
| Qinhe | Wuzhi | W | 15.89 | 14.03 | 6.15 | 5.47 | 3.73 | 5.32 | 4.16 | 8.04 | -4.466 | OD |
| | | $W_S$ | 0.133 | 0.073 | 0.041 | 0.025 | 0.009 | 0.009 | 0.002 | 0.004 | -6.757 | OD |

W-annual runoff, $10^8$ $m^3$; $W_S$- annual sediment discharge, $10^8$ t.; OD- obvious decrease; DT-decrease trend.

 

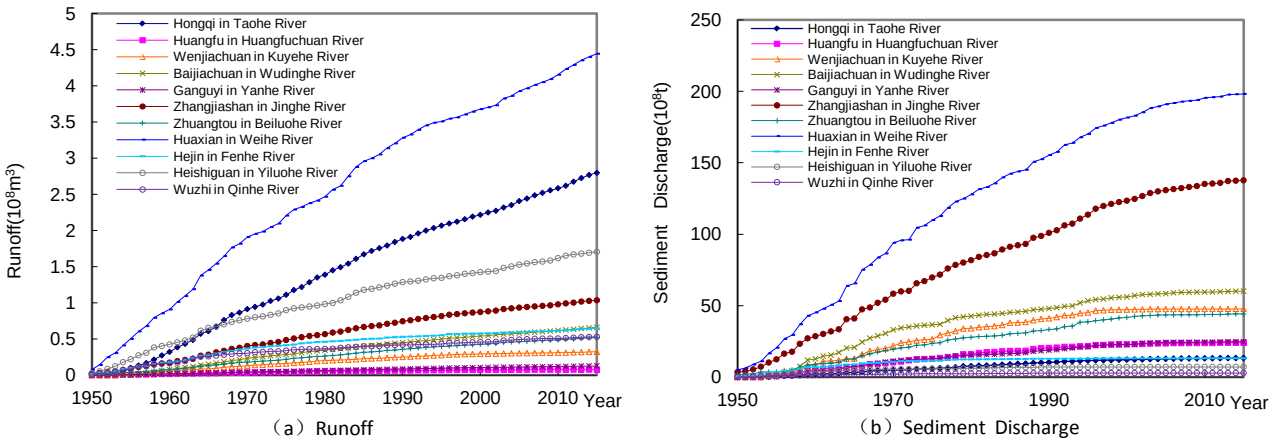


**Figure 3.** Single cumulative curve of hydrological variable in the Yellow River tributaries

(2) In tributaries of the Middle Yellow River, the standardized variable M values of the runoff of the Zhuangtou station in the Beiluohe River and the Ganguyi station in the Yanhe River are -2.396 and -2.943 respectively. While the corresponding cumulative curves before 2000 are basically a straight line in shape, and downward deflection after 2000, which shows that the runoff of the two stations has a tendency to decrease, especially in recent years. The annual runoff of the Zhuangtou station decreases from $711\times10^6$ $m^3$ in 1990s to $622\times10^6$ $m^3$ in 2000s. The standardized variable M values of the runoff in the other tributaries are between -7 and -3.9, and their absolute values are much greater than 3.01. While the corresponding cumulative curves are upward convex, which shows that the runoff of these tributaries significantly reduced. For example, the annual runoff of the Huangfu station in Huangfuchuan River decreases from $265\times10^6$ $m^3$ in 1950s to $127\times10^6$ $m^3$ in 1980s, and $28\times10^6$ $m^3$ after 2010.

(3) In the middle Yellow River, the standardized variable values M of sediment discharge of the 10 tributaries are between -8.5 and -3.8, and their absolute values are much greater than 3.01. The corresponding cumulative curves are upward convex, which shows that the sediment discharges of these tributaries significantly reduced. However, the extent and process of sediment discharge reduction in the tributaries have some differences. The sediment discharges of the Hejin station in the Fenhe River, the Wuzhi station in the Qinhe River and the Heishiguan Station in Yiluohe River reduces in a downward trend. For example, the sediment discharge of the Hejin station decreases from $34.4\times10^6$ t in 1960s to $4.5\times10^6$ t in 1980s, to $0.3\times10^6$ t in 2000. The sediment discharges of the other tributaries in the middle Yellow River decreases gradually with time, and the decrease amount is not significant before the 1970s. However, the amount of sediment reduction is more obvious after the 1970s. For example, the sediment discharge of the Huaxian station in the Weihe River decreases from $429\times10^6$ t in 1950s to $384\times10^6$ t in 1970s, to $276\times10^6$ t in 1990, and $70\times10^6$ t after 2010.

## 3 INFLUENCE FACTORS OF WATER AND SEDIMENT VARIATIONS IN THE YELLOW RIVER

There are several influencing factors related to water and sediment variations in the Yellow River, such as precipitation change, soil and water conservation, silt trapping of reservoir and water and sediment diversion and so on.

### 3.1 Precipitation Changes

Precipitation changes caused by climate change is a direct factor affecting runoff variation. The region above the Lanzhou station is the main runoff areas in the Upper Yellow River. According to the data from 1953 to 2002 (Wang et al., 2004), there are two high water stages (1953-1968, and 1975-1989) and two low water stages (1969-1974, and 1990-2002) in the Upper Yellow River, shown in the table 3. This table shows that the runoff and rainfall are basically similar. In the basin above the Lanzhou station, the rainfall has no significant changes during the period from 1950s to 1980s with a fluctuation of "increase-decrease-increase", and decreases obviously in 1990's and increases again recently, which is consistent with the change of runoff in the Lanzhou station.

**Table 3.** The average annual runoff and rainfall in the Upper Yellow River

| Years | 1950s | 1960s | 1970s | 1980s | 1990s | 2000~02 |
|---|---|---|---|---|---|---|
| Runoff ($10^8m^3$) | 315.3 | 357.9 | 317.9 | 333.6 | 259.8 | 281.1 |
| Rainfall (mm) | 412.5 | 421.0 | 415.9 | 423.6 | 392.2 | 349.9 |

The rainfall data above the Huayuankou station shows that the decrease of precipitation from 1950-1968 and 1969 -1985 to 1986 - 2009 is 4% and 5% respectively, and the reduction of runoff is 19% and 44% in the corresponding period (Shi et al., 2014). Although runoff decreases with rainfall, the decrease in precipitation is

 

significantly less than in runoff. Therefore, the variation of rainfall is an important factor causing the runoff decrease.

**3.2** Soil and water conservation

The soil and water loss in the middle Yellow River is serious. From the late 1960s, large-scale soil and water conservation measures have been carried out in the Loess Plateau. These include trees planting, grass planting and silt dam construction, which have an important influence on the water-retention and sediment-laden and the reduction of runoff and sediment discharge, shown in the Table 4 (Peng et al., 2009). This table shows that the amounts of water reduction and sediment reduction increases with the increase of the soil and water conservation area. While the corresponding runoff and sediment discharge of the river decreases, but the reduction effect of water and sediment decreases after 1990. Before 1960, the sediment reduction amount is not obvious. This is due to the serious soil and water loss that occurs naturally or a small area of soil and water conservation in the middle of Yellow River. In the 1960s, soil and water conservation measures are put into effect, and the soil and water conservation area is 36,000 $km^2$ by 1970s. Therefore, the amounts of water reduction and sediment reduction increases to $2.193\times10^9$ $m^3$ and $287\times10^6$ t, respectively, and the runoff and sediment discharge in the Tongguan station reduces to $35.74\times10^9$ t and $1.318\times10^9$ t. In 1980s, a large area of soil erosion control measures were rapidly carried out in the Middle Yellow River with the soil and water conservation area of 79200 $km^2$. So the amounts of water reduction and sediment reduction increases to $2.935\times10^9$ $m^3$ and $401\times10^6$ t, respectively, and sediment discharge in the Tongguan station reduces to $780\times10^6$ t. After 1990, although the soil and water conservation area continues to grow and large-scale Grain for Green Project was implemented in 1997, sediment reduction and water reduction effect also decreases in the basin because sediment trapping effect of silt dam gradually reduces. Due to the impact of water conservancy construction, the amount of sediment discharge in the Tongguan Station decreases continuously, and is only $282\times10^6$ t after 2000.

**Table 4.** Soil and water conservation area and the amount of water and sediment reduction in the middle Yellow River

| Date | 1950s | 1960s | 1970s | 1980s | 1990s | 2000~05 | Average annual |
|---|---|---|---|---|---|---|---|
| Area of soil and water conservation ($10^4$ $km^2$) | 0.8 | 1.58 | 3.60 | 7.92 | 17.13 | | |
| Runoff reduction ($10^8m^3$) | 7.28 | 9.82 | 21.93 | 29.35 | 29.04 | 27.36 | 20.20 |
| Sediment reduction ($10^8$t) | 0.32 | 1.51 | 2.87 | 4.01 | 4.57 | 4.35 | 2.81 |
| Runoff in Tongguan station ($10^8m^3$) | 427.7 | 451.0 | 357.4 | 369.1 | 248.8 | 229.1 | 338.7 |
| Sediment discharge in Tongguan station ($10^8$t) | 18.26 | 14.23 | 13.18 | 7.80 | 7.90 | 2.82 | 10.06 |

**3.3** Silt Trapping of Reservoir

In order to fully use water resources and make rational allocation of water and sediment resources in the Yellow River, the stem Yellow River and its main tributaries have built or planned a lot of reservoirs. After the construction of the reservoirs, the flow-sediment process will be regulated and the sediment will be deposited in the reservoir, which will make the sediment discharge to reduce in the downstream. According to relevant data (Yellow River Conservancy Commission), by the end of 2006, 171 large and medium-sized reservoirs were built in the Yellow River basin. This consists of 12 large reservoirs in the stem river with a total capacity of $63.037\times10^9$ $m^3$, 4 large reservoirs in the Weihe River with a total capacity of $1.19\times10^9$ $m^3$, and 3 large reservoirs in the Fenhe River with a total capacity of $950\times10^6$ $m^3$. The construction and operation of these reservoirs have important influence on the water and sediment variation in the Yellow River. Such as, (1) Liujiaxia Reservoir and Lijiaxia Reservoir were separately constructed in 1968 and 1997, which result in a significant decrease of the sediment discharge in the Lanzhou Station in 1969 and 2000. (2) In 1969 and 1986, there is a significant decline of the sediment discharge in the Toudaoguai station, which mainly result from water storage and sediment retention of the Liujiaxia Reservoir built in1968 and the Longyangxia Reservoir built in 1986. (3) The water storage and sediment retention of the Sanmenxia Reservoir built in 1960 result in a significant reduce of sediment discharge of the Lower Yellow River. While the operation mode of the Sanmenxia Reservoir changed into the clear water impounding and muddy flow releasing from 1965, the sediment discharge restored. (4) As the Xiaolangdi Reservoir began its water storage and sediment retention in 1999, the sediment discharge in the Lower Yellow River decreases further. (5) In 1960 and 1996, there is a significant decline in sediment discharge in Hejin station, which mainly result from water storage and sediment retention of the Fenhe Reservoir in 1960, the Wenyuhe Reservoir in 1961 and the Fenhe II Reservoir in 1996. (6) The Wangyao Reservoir built in 1972 is also an important reason for the continuous decrease of the sediment discharge of the Yanhe River after 1970s.

In addition, Figure 4 is the relationship between the sediment discharge and the basin cumulative storage capacity in the Lijin station. The figure shows the sediment discharge of the Lijin station which decreases with the increase of the basin cumulative storage capacity. In the stem river, Sanmenxia Reservoir, Liujiaxia

 

Reservoir, Longyangxia Reservoir and Xiaolangdi Reservoir were separately constructed in 1960, 1968, 1986 and 1999, and the cumulative storage capacity increases significantly, which results in the sediment discharges in the lijin station in 1961, 1968, 1986 and 2000 also decreases significantly.

**Table 5.** Large reservoirs conditions in the Yellow River Basin

| River | Numbers of large reservoir | Capacity ($10^8 m^3$) | Typical reservoir |
|---|---|---|---|
| Yellow River | 12 | 630.37 | Sanmenxia, Yanguoxia, Sanshenggong, Qingtongxia, Liujiaxia, Bapanxia ,Tianqiao, Longyangxia, Lijiaxia, Wanjiazhai, Daxia, Xiaolangdi |
| Weihe River | 4 | 11.9 | Bajiazui, Yangmaowan , Fengjiashan, Shitouhe |
| Fenhe River | 3 | 9.496 | Fenhe, Wenyuhe, Fenhe II |
| Yanhe River | 1 | 2.03 | Wangyao |
| Total | 20 | 653.8 | |

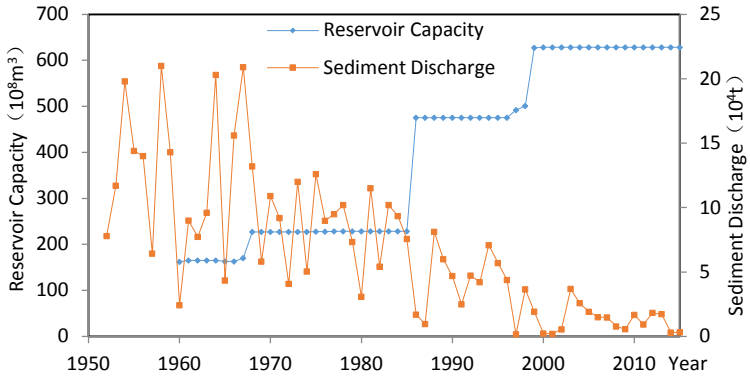


**Figure 4.** Changes of sediment discharge and reservoir capacity in Lijin station

### 3.4 Water and sediment diversion

With the continuous development of social industrial and agricultural production, water and sediment diversion gradually expand in the scale with a gradual water diversion increase in the Yellow River Basin (Peng, et al., 2009). This includes agricultural irrigation, industrial water, ecological water, urban and rural water for life and so on, as shown in Table 6. In the Yellow River from 1950 to 2005 (1962-1965 stop irrigation), the total amount of water diversion is $1384\times10^9$ $m^3$ with an average annual sediment yield of $25.164\times10^9$ $m^3$, accounting for 45.7% of the total runoff of the Yellow River. The total amount of sediment diversion from 1950 to 2005 is $13.31\times10^9$ t with the average annual sediment diversion of $242\times10^6$ t, which accounted for 24.1% of the sediment discharge of the Tongguan station. The water diversion scale of the Yellow River increases gradually with time. The water diversion increases from $15.395\times10^9$ $m^3$ with a water diversion ratio of 24.5% in 1950s to $23.092\times10^9$ $m^3$ in the 1970s with a water diversion ratio of 42.6%, to $31.646\times10^9$ $m^3$ in the 1990s with a water diversion ratio of 69.2%, and to $42.23\times10^9$ $m^3$ with high water diversion ratio of 72.6% from 2000 to 2005. At the same time, the amount of sediment diversion increases before 1980, while decreases gradually after 1980, but the sediment diversion ratio increases. And the sediment diversion increases from $213\times10^6$ t in the 1950s with a sediment diversion ratio of 11.7% to $328\times10^6$ t in the 1970s with a sediment diversion ratio of 24.9%. In the 1990s, the sediment diversion reduces to $229\times10^6$ t and the sediment diversion ratio increased to 29.0%. From 2000 to 2005, the amount of sediment diversion is $204\times10^6$ t, and the sediment diversion ratio is 72.3%. Whether the water diversion ratio or the sediment diversion ratio is very high, the highest ratio is more than 70%, which is very significant influence on runoff and sediment discharge in the Yellow River.

**Table 6** Water and sediment diversion in the Yellow River

| Years | 1950s | 1960s | 1970s | 1980s | 1990s | 2000~05 | Average annual |
|---|---|---|---|---|---|---|---|
| Water diversion ($10^8 m^3$) | 153.95 | 166.12 | 230.92 | 305.42 | 316.46 | 422.3 | 251.64 |
| Water diversion ratio | 0.245 | 0.249 | 0.426 | 0.516 | 0.692 | 0.726 | 0.457 |
| Sediment diversion ($10^8$t) | 2.13 | 1.78 | 3.28 | 2.81 | 2.29 | 2.04 | 2.42 |
| Sediment diversion ratio | 0.117 | 0.125 | 0.249 | 0.360 | 0.290 | 0.723 | 0.241 |

## 4 CONCLUSION

(1) In the Upper Yellow River, due to the relatively less human activity in the source reach, the annual runoff and annual sediment discharge of the Tangnaihai station have no obvious trend change; and the runoff and sediment discharge of the Lanzhou station and Toudaoguai station have a significant decreasing trend. In the Middle Yellow River, the runoff and sediment discharge of the Longmen station and the Tongguan station

 

decreases significantly, and the decreasing trend of sediment discharge is more notable than runoff. In the Lower Yellow River, the runoff and sediment discharge of the Huayuankou station, the Gaocun station, the Aishan station and the Lijin station have a significant decreasing trend, and the nearer the station to the estuary, the higher the decreasing amount is.

(2) In the Upper Yellow River, the runoff and sediment discharge of the tributary Taohe River decreases significantly in recent years. In the Middle Yellow River, the runoff of the Beiluohe River and the Yanhe Rivers decreases slightly, and the runoff of other tributaries decreases significantly. The sediment discharges of all the main tributaries decreases significantly with time, but the decrease range and process have some differences.

(3) Influence factors on runoff and sediment variations in the Yellow River are precipitation changes, soil and water conservation, silt trapping by reservoirs, and water and sediment diversion, of which the latter three human activities are the key factors.

**ACKNOWLEDGEMENTS**

The research is supported by National Natural Science Foundation of China (Grant No.51679259),

**REFERENCES**

Chu, C.J. & Li Y.L. (2013). Variation of runoff, sediment, and Their Driving Factors of the Yellow River Mainstream in the Past 60 Years. *Journal of Soil and Water Conservation*, 27(5), 41-47. (In Chinese)

GAO Hang, YAO Wen-Yi & ZHANG Xiao-Hua (2009). Analysis on short-term variation of runoff and sediment discharge in the upper and middle reaches of Yellow River. J*ournal of North China University of Water Resources and Electric Power*. 30(5), 8-12. (In Chinese)

LIU Cheng, Wang Zhao-Yin & Sui Jue-yi (2008). Variation of flow and sediment of the Yellow River and their influential factors. *Advances in Science and Technology of Water Resources*. 28(3), 1-7. (In Chinese).

MWR of China (2001). *Gazette of River Sediment in China (2000-2004)*, MWR of China, 2001-2005. (In Chinese)

MWR of China (2006). *China Gazette of River Sedimentation (2005-2015)*, Beijing: China Waterpower Press, 2006-2016. (In Chinese)

Peng Jun & Chen Shen-liang (2009). The variation process of water, sediment, and its effect on the Yellow River delta over the six decades. *Acta Geographica Sinica*. 64(11), 1353-1362. (In Chinese)

Shi Hong-ling, Hu Chun-hong & WANG Yan-gui (2014). Analysis on variation trends of runoff and sediment of the Yellow River basin and reasons discussion. *Yellow River*. 36(4), 1-5. (in Chinese)

Wang Yan-gui, Hu Chun-hong & Shi Hong-ling (2010). Variation in water and sediment resources and its influence on utilization of sediment resource in the Yellow River basin. *Journal of China Institute of Water Resources and Hydropower Research*. 8(4), 237-245. (In Chinese)

Wang Yan-gui, Hu Chun-hong & Shi Hong-ling (2010). Nearly 60 years in China's major rivers water and sediment variation characteristics. *The 14th conference on water conservancy science and technology exchanges across the Taiwan straits. Taibei.*

Wang Yun-zhang. Kang Ling-ling & Wang Guo-qing (2004) . Precipitation variations in the middle Yellow River in the last 50 years and its influence on the flow. *Yellow River*. 26(2), 5-7. (in Chinese)

Yellow River Conservancy Commission (2006). *Yellow River Sediment Bulletin*. Zhengzhou: Yellow River Conservancy Commission. (in Chinese)

 

# ENHANCEMENT OF SEDIMENT TRANSPORTATION BY INCREASING SCOUR AROUND A SQUARE PIER WITH VANE ATTACHED ON ONE SIDE

SUBHASISH DAS[(1)], RITAM MUKHERJEE[(2)], RAJIB DAS[(3)] & ASIS MAZUMDAR[(4)]

[(1,2,3,4)] School of Water Resources Engineering, Jadavpur University, Kolkata, India
subhasishju@gmail.com; getritammukherjee@gmail.com; rajibdas79@gmail.com; asism.ju@gmail.com

## ABSTRACT

Stream bank erosion and deposition in small channels are a major resource management problem to hydraulicians. The channel depth reduces significantly in many open channels due to sediment deposition. This in turn makes it non navigable. Hence, if the sediments could be shifted to one side of the bank of the channel, it may help in navigation. In this study, an attempt is made to check whether the sediment could be transported to one side of the pier i.e. the aim is to increase the scour more importantly the dune downstream, to be non-symmetrical. The present study is an experimental work on scour geometry analysis of a square pier with a vane of varying vane angles, flow depths and discharges. Sixty experiments are carried out using a square pier of 7 cm width with a vane fixed to it on one side at different vane angles of 0° (without vane), 15°, 30° and 45°. For each of the four vane angles, three different approaches of flow depths are tested and for each flow depth, five different discharges experiments are carried out. The differences of scour geometry with and without vane are noted. The scour and the dune are found more on the vane side. The dune is not symmetric. The scour depth is more for higher vane angle whereas lower scour depth is observed for higher flow depth. The scour depth increases with increase in densimetric Froude number, it decreases with increase in flow shallowness or relative inflow depth. Effective flow shallowness is calculated and analysed to determine further scour and sediment transportation characteristics. It is also observed that with the decrease of flow shallowness, more sediment is transported towards the downstream alongside the vane.

**Keywords:** Scour; vane angle; flow shallowness; densimetric froude number; effective scour width.

## 1 INTRODUCTION

Sediment control in alluvial channels, in particular the control of sediment movement, scour, and deposition, is one of the most difficult problems encountered by river engineers. Bed scour along the outer bank of river bends frequently causes undermining of the banks and loss of land. Deposition of sediment in the river bed often reduces flood conveyance capacity of river and interferes with navigation. The diversion of flow from one channel to another or to a water intake or to reduce sediment entrainment at water intakes requires sediment management. Vertical wall bridge, abutment of single span bridge, is also affected by deep scour hole around it. The main difficulty in the treatment of these problems is the absence of cost effective, low maintenance and environmentally acceptable sediment control structures with a wide range of applications. The vanes have been developed to meet the above problems and these have been successfully employed in some countries. Vanes are frequently used as vortex generating devices that have several applications, such as protection against bank erosion maintaining depth in navigation channel, sediment control at water intakes, and etc.

The vanes can be laid out to make the water and sediment move through a curve as if it were straight. According to Odgaard (1986a; 1986b), significant changes in depth can be achieved without causing significant changes in cross-sectional area, energy slope, roughness and downstream sediment transport. Odgaard and Mosconi (1987) gave details of a system of submerged vanes for erosion protection for a river bend. Odgaard and Wang (1991) conducted vane experiments for different vane angles of 15° to 25° to observe the change in sediment transport in the area affected by the vanes.

Marelius and Sinha (1998) tried to describe the flow passing a submerged vane at high angles of attack. It was shown that the vane produced the strongest circulation for an angle of attack of about 40°. Later Odgaard (2009) described the submerged vane technique for sediment control in rivers. The structures were installed at an angle of attack of 15° to 25° with the flow, and their initial height was 0.2 to 0.4 times of local water depth at the design stage. It was found that the submerged vanes can produce significant changes in the distributions of velocity and depth in river channels. Johnson et al. (2001) attempted a work on rock vanes with single arm structures, angled to the flow with the pitch into the streambed such that the tip of the vane is submerged even during low flow. Flokstra (2006) concentrated on the development of a morphological simulation system capable to simulate the effect of submerged vanes on an alluvial bed. The results of the simulations were shown and compared reasonably well with experimental results. The measurement outcomes suggest a revision of the theoretical base of the model. The vane description used in the presented

 

morphological model is based on wing theory, as presented by Odgaard (1986a; 1986b). Ghorbani and Kells (2008) studied the effect of a submerged vane on local scour at a cylindrical pier for several vane heights, angles of orientation and flow depths at a constant Froude number. For two vanes attached to the pier, a reduction of 87.7% in scour depth next to the pier was achieved for 15 cm flow depth at 18.5° vane angle and at zero distance upstream from the pier for a vane height of 0 cm.

Behbahan (2011) investigated the effect of vane shapes on river banks protection, a series of experiments on a straight canal with 20 m length, 0.7 m width and 0.6 m depth were carried out using vanes in different shapes. These vanes with 1 mm thickness, 0.15 m width and 0.13 m height were installed on the canal bed such that the vanes height above the river bed was 7 cm. Three types of same sized vanes were used in these experiments. The first type was flat, which were installed in an angle of attack of 20° to flow direction. The second type was angled vanes with an angle of 20° in the middle of vanes, which were installed such that the first half of these vanes were in an angle of attack of 10° and the second half in 30° of flow direction. The third type include two parts flat and cured, these vanes were installed such that the flat part were in an angle of 20° with flow direction. Using measured data, the canal and related vanes were modeled by ANSYS and Surfer softwares. Results show that the curved and angled vanes compared to flat vanes are more effective in river-bank protection by 35% and 20% respectively.

Bejestan et al. (2015) conducted a large number of studies to develop countermeasures to ensure the safety of existing bridges. A submerged vane is a measure that has recently been studied and found to be a promising scour mitigation technique for river bank erosion. Several tests were conducted with and without vanes. Different vane positions and angles were examined. A single vane attached to the upstream nose of an abutment was found to be the most effective at decreasing, shifting, and warding off a scour hole. The results showed that the most appropriate vane angle was 40°. The efficiency of the new measure could reach 95% under some flow conditions.

According to literature, number, size and layout of the vanes depend on the channel morphology, velocity and depth at a meander bend. Vanes stabilize a channel reach without inducing changes upstream or downstream of that reach. Vanes may not be visible in time as they become buried by depositing sediment and aid the stream in doing the work by redistributing the flow energy to produce a more uniform cross-section without an appreciable increase in the energy loss through the reach.

The main function of vane is to generate secondary circulation of flow. The circulation alters magnitude and direction of the bed shear stress and causes a change in the distribution of velocity, depth and sediment transport in the area affected by the vane. The vanes can be used to develop and maintain any desired bed topography of a channel or river. Vanes have been used successfully for protection of stream banks against erosion and amelioration of shoaling problems at water intakes and bridge crossings.

The study reported herein, is based on experiments carried out in the Fluvial Hydraulics Laboratory of the School of Water Resources Engineering at Jadavpur University using a physical hydraulic model. The study is confined to uniform cohesion-less bed material and clear water flow conditions. In the present study, attempts have been made to observe the nature of scour around a square pier with a vane fixed at one side of the pier with varying vane angle, approach flow depth and flow velocity (or discharge). For each vane angle, initially, the discharge is kept constant and the flow depth is changed and then the same experimental run is continued with a different discharge. One of the main aim is to observe whether the scour occurred is symmetric or non-symmetric due to the addition of vane on one side of the pier. If it is non symmetric then it has to be found out on which side of the pier the scour is higher. Comparison of the scour parameters is to be carried out with different vane angles 0°, 15°, 30°, and 45°. It is to be noted here that the 0° represents no vane. Lastly, the variation of scour depth is observed due to different approach flow depths.

## 2 EXPERIMENTAL SETUP AND PROCEDURE

A tilting flume is made up of a steel bottom and Plexiglas side walls along two sides for most of its length to facilitate visual observations. The 0.60 m depth flume has a length of 11 m and a width of ($B$) 0.81 m. A 3 m long sand bed is used as sediment to a uniform thickness of 0.20 m. The sand bed is located at 3 m downstream from the inlet of the flume. The recirculating flow system is served by a centrifugal pump of 10 hp located at the upstream end of the flume. The water flows through a 20 cm diameter inlet pipe line which runs directly into the flume. The median diameter $d_{50}$, 16% finer diameter $d_{16}$ and 90% finer diameter $d_{90}$ of the sand particles are 0.825, 0.5 and 1.78, respectively. Geometric standard deviation of sediment size ($\sigma_g$) is 1.8. Froude number ($F$) and flow Reynolds number ($Re$) for all the experiments were calculated as 0.223 and $1.48\times10^4$-$2.95\times10^4$, respectively.

The pier-vane was first installed in the flume at the desired location (Figure 1). The height and width of the square shaped pier are 45.6 cm and 7 cm, respectively. The vane thickness is 0.5 cm and vane length is 7 cm. Before each experiment or Test, care was taken to level the sand bed throughout the entire length of the flume and perpendicular all around the pier-vane structure. First of all, a sand bed was produced having a smooth uniform surface. A spirit level was used to check the uniformity of the bed surface. Uneven bed surface were levelled using a hand trowel. Then, the bed level was measured by point gauge randomly to check the levelling of the flume. The sand bed preparation is crucial as far as the experiment is concerned.

 

Unevenness or defect in the channel bed can cause damage to the experiment. Experimental conditions for all Tests are shown in Figure 1 and Table 1.

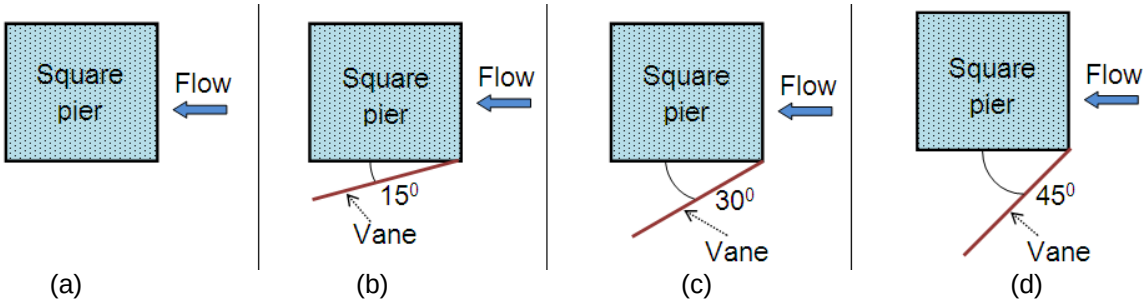


**Figure 1.** Plan view of the experimental setup showing pier and vane positions for Test No. (a) 1-15, (b) 16-30, (c) 31-45 and (d) 41-60.

**Table 1.** Experimental conditions for all tests.

| Test No. | Discharge (*Q*) (l/s) | Flow depth (*h*) (cm) | Vane angle (*φ*) degree) | Flow Reynolds number (*Re*) | Test No. | Discharge (*Q*) (l/s) | Flow depth (*h*) (cm) | Vane angle (*φ*) (degree) | Flow Reynolds number (*Re*) |
|---|---|---|---|---|---|---|---|---|---|
| **1** | 12 | 10 | 0 | 14756 | **31** | 12 | 10 | 30 | 14756 |
| **2** | 12 | 11 | 0 | 18445 | **32** | 12 | 11 | 30 | 18445 |
| **3** | 12 | 12 | 0 | 22134 | **33** | 12 | 12 | 30 | 22134 |
| **4** | 15 | 10 | 0 | 25823 | **34** | 15 | 10 | 30 | 25823 |
| **5** | 15 | 11 | 0 | 29512 | **35** | 15 | 11 | 30 | 29512 |
| **6** | 15 | 12 | 0 | 14756 | **36** | 15 | 12 | 30 | 14756 |
| **7** | 18 | 10 | 0 | 18445 | **37** | 18 | 10 | 30 | 18445 |
| **8** | 18 | 11 | 0 | 22134 | **38** | 18 | 11 | 30 | 22134 |
| **9** | 18 | 12 | 0 | 25823 | **39** | 18 | 12 | 30 | 25823 |
| **10** | 21 | 10 | 0 | 29512 | **40** | 21 | 10 | 30 | 29512 |
| **11** | 21 | 11 | 0 | 14756 | **41** | 21 | 11 | 30 | 14756 |
| **12** | 21 | 12 | 0 | 18445 | **42** | 21 | 12 | 30 | 18445 |
| **13** | 24 | 10 | 0 | 22134 | **43** | 24 | 10 | 30 | 22134 |
| **14** | 24 | 11 | 0 | 25823 | **44** | 24 | 11 | 30 | 25823 |
| **15** | 24 | 12 | 0 | 29512 | **45** | 24 | 12 | 30 | 29512 |
| **16** | 12 | 10 | 15 | 14756 | **46** | 12 | 10 | 45 | 14756 |
| **17** | 12 | 11 | 15 | 18445 | **47** | 12 | 11 | 45 | 18445 |
| **18** | 12 | 12 | 15 | 22134 | **48** | 12 | 12 | 45 | 22134 |
| **19** | 15 | 10 | 15 | 25823 | **49** | 15 | 10 | 45 | 25823 |
| **20** | 15 | 11 | 15 | 29512 | **50** | 15 | 11 | 45 | 29512 |
| **21** | 15 | 12 | 15 | 14756 | **51** | 15 | 12 | 45 | 14756 |
| **22** | 18 | 10 | 15 | 18445 | **52** | 18 | 10 | 45 | 18445 |
| **23** | 18 | 11 | 15 | 22134 | **53** | 18 | 11 | 45 | 22134 |
| **24** | 18 | 12 | 15 | 25823 | **54** | 18 | 12 | 45 | 25823 |
| **25** | 21 | 10 | 15 | 29512 | **55** | 21 | 10 | 45 | 29512 |
| **26** | 21 | 11 | 15 | 14756 | **56** | 21 | 11 | 45 | 14756 |
| **27** | 21 | 12 | 15 | 18445 | **57** | 21 | 12 | 45 | 18445 |
| **28** | 24 | 10 | 15 | 22134 | **58** | 24 | 10 | 45 | 22134 |
| **29** | 24 | 11 | 15 | 25823 | **59** | 24 | 11 | 45 | 25823 |
| **30** | 24 | 12 | 15 | 29512 | **60** | 24 | 12 | 45 | 29512 |

To start the experiment, the flume was slowly filled with water to the required depth from downstream. It should be noted that extra care is required when filling the flume with water, especially for experiment of this nature where no sediment movement is allowed. Any deformity in the bed surface may develop ripples or dunes and general movement of the sand if the shear stress on the smooth bed is close to the critical shear stress. The pump was then turned on and desired flow rate was achieved by controlling the control valve and a bypass valve. Concurrent with getting the pump up to speed, the tailgate was adjusted so as to maintain the correct depth (0.10, 0.11, 0.12 m) of flow in the flume. The discharge (*Q* was also varied in such a way that 12, 15, 18, 21 and 24 l/s at every depth. The vane angle was also varied as 0°, 15°, 30° and 45°. Throughout the experimental period, the location and magnitude of the point of maximum scour depth at the area around the upstream of the pier were observed and measured. The frequency of the scour depth varied throughout each test period. Rate of scouring is maximum in the period of 1$^{st}$ to 12$^{th}$ hour and then less frequently thereafter. The fibre transferring pier-vane model was used in this study. The run duration for all of the experiments was 24 hours. After that, the pump was turned off to allow the water in the flume to drain out

 

slowly without disturbing the scour topography. The flume bed was then allowed to dry, during this time, photos of the scour topography around the pier was taken.

After the run has ended, the maximum equilibrium scour depths were observed at the upstream base of the piers. Then, the maximum scour depth at an equilibrium state was carefully measured by a Vernier type point gauge which was attached to a movable trolley. The contour lines of the scour holes of the square pier with vane angle were plotted by Surfer software.

## 3 Dimensional Analysis

The magnitude that shows interests to the designers for determining pier-vane depth is the maximum equilibrium depth to be attained by scouring process. For this basis, the quantitative study is inadequate to the maximum equilibrium depth $d_s$ reached by scour hole around pier-vane after sufficient time has passed to attain equilibrium. Allowing for a single pier-vane in a rectangular flume, where flow is unidirectional and whose bed materials (sand particles) are cohesion-less, the equilibrium scour depth depends on water (mass density and viscosity), bed particles (mass density and diameter), channel flow (depth, bed slope and gravity) that is section-averaged approaching velocity and the pier-vane geometry (an effective width). The effective width is the smallest diameter of the circle circumscribing the pier-vane. For circular pier, the effective width $b_e$ is same as pier diameter (Yalin, 1977; Das et al. 2014a; Das et al. 2014b).

There is a long list of parameters. Several of them are complex to quantify, like bed-particle size-distribution, the bed-particle form, or bed-materials' cohesion. Therefore, this analysis has been prepared mainly for the following limiting conditions:

Bed particles: the sediment particles are non-cohesive and have uniform size $d_{50}$.

Flow velocity: flume is adequately wide so that significant contraction does not occur at pier-vane.

Pier-vane: perfectly smooth surfaces.

The remaining parameters are:

- for water: mass density $\rho$; kinematic-viscosity $\nu$ and gravitational-acceleration $g$.
- for bed material: particle diameter $d_{50}$ and density $\rho_s$.
- for flow velocity: approaching flow depth $h$; section averaged velocity of undisturbed flow $U$ being equal to $Q/(Bh)$ or shear-velocity $u_*$ being equal to $\sqrt{ghS}$ and
- for pier-vane: its effective width $b_e$.

Therefore the equilibrium scouring depth $d_s$ depends on eight parameters as shown in Eq. [1]:

$$d_s = f\left(\rho, \nu, \rho_s, d_{50}, h, U, g, b_e\right) \qquad [1]$$

The Vaschy-Buckingham $\pi$-theorem allows writing in Eq. [2]:

$$\frac{d_s}{b_e} = f_0\left(\frac{u_* d}{\nu}, \frac{U^2}{\Delta g d_{50}}, \Delta, \frac{h}{b_e}, \frac{d_{50}}{b_e}\right) \qquad [2]$$

The justifications for choosing the dimensionless parameters are as follows:

- $d_s/b_e$ :

  Experiments have apparently exhibited that it was plausible for relating scour depth to effective width of pier-vane. The reason is that scouring is due to horseshoe vortex system whose dimension is a function of pier width (Yalin, 1977; Das et al., 2014a; Das et al., 2014b).

- $u_* d/\nu$ , $U^2/\Delta g d_{50}$ :

  This is the classical non-dimensional parameter for studying bed load. Here densimetric Froude number $F_{d50}$ is equal to $U^2/\Delta g d_{50}$ .

- $h/b_e$ , $d_{50}/b_e$ :

  These non-dimensional ratios relate pier-vane size and shape with flow and sand particles.

  Eq. [2] may be simplified by considering following points:

  - The influence of kinematic-viscosity $\nu$ is insignificant for turbulent flow for rough beds.
  - Shear velocity $u_*$ was kept constant for three different depths 10, 11 and 12 cm.

In sediment-water interaction, the parameters $g$, $\rho$ and $\rho_s$ were merged into single parameter namely non-dimensional submerged weight:

- $\Delta g$ given by $\{(\rho_s/\rho)-1\}g$ , $\Delta$ was kept fixed.

 

The particle diameter $d_{50}$ and section-averaged velocity $U$ were also kept constant for three groups of different depths. Therefore some of these terms can be neglected during analysis for different depths.

Therefore Eq. [2] can be written as in Eq. [3],

$$\frac{d_s}{b_e} = f_1\left(F_{d50}, \frac{h}{b_e}\right) \qquad [3]$$

Therefore the relative maximum-equilibrium scour depth ($d_s/b_e$) can be expressed in non-dimensional form as a function of densimetric Froude number and depth relative to effective pier width ($h/b_e$).

The influence of relative flow depth on the dimensionless scour depth for piers was observed by (Yalin, 1977; Das et al., 2014a; Das et al., 2014b; Das et al., 2016). Sometimes some linear and empirical relations were proposed to correlate the geometrical scour parameters. Here, an initiative has been taken, based on the experimental data, to investigate the relations of pier-vane group based on pier shape.

## 4 RESULTS AND DISCUSSION

A total of 60 experiments were carried out with a square pier. The width of the pier taken was 7 cm. Initially, the scour geometry and scour morphology were studied for the square pier with 7 cm width. Subsequently, a vane was attached to the pier on one side to study the change in the scour geometry and morphology due to the vane. The angle of the vane is also varied to check the effect of the vane angle on the scour. The thickness of the vane was 0.5 cm, 7 cm in length and different vane angles at which the vane attached considered was 0° to 45° with an interval of 15°. The experiments were carried out for different discharge of 12, 15, 18, 21 and 24 l/s and different flow depth of 10 cm, 11 cm and 12 cm for each discharge. It should be mentioned that each experimental run was carried out for 24 hours.

As an example, the scour affected zone and contour lines of the scour holes at the square pier vane group, plotted with the Surfer software, for Test No. 60 are shown in Figure 2 and Figure 3, respectively. Here the scour is non-symmetric due to the effect of one side positioning of the vane.

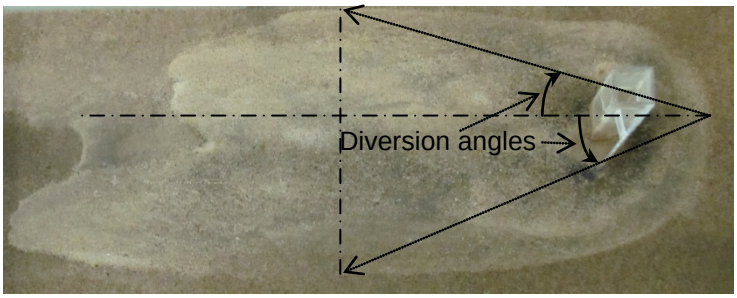


**Figure 2.** Scour affected zone around the pier for Test No. 60 for $Q$ = 24 l/s, $h$ = 12 cm and $\varphi = 45^0$.

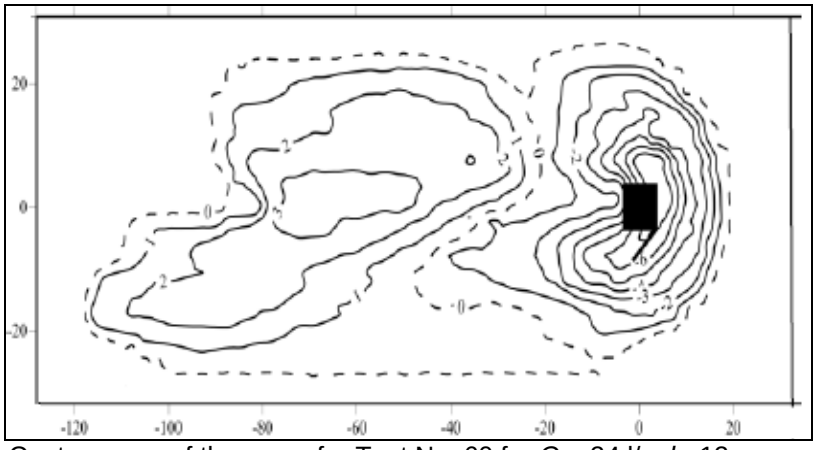


**Figure 3.** Contour map of the scour for Test No. 60 for $Q$ = 24 l/s, $h$=12 cm and $\varphi = 45^0$.

From the experimental results shown in Figures 2 to 8, initially, all the tests from 1 to 15 were carried out using the same pier width of 7 cm without vane angle (0°) at different flow depth of 10, 11, 12 cm at different discharge of 12, 15, 18, 21, 24 l/s. The variation of scour for the same pier is noted. After that, a vane was attached on one side of the pier at an angle of 15°.

 

Then, tests 16 to 30 were carried out at the variation of same discharge and depth as it was done without the vane. Consequently, a vane was attached on one side of the pier at an angle of 30°. Then, tests 31 to 45 were carried out at the variation of same discharge and depth. Lastly, tests 46 to 60 were carried out at the variation of same discharge and depth using a vane attached to one side of the pier at an angle of 45°.

In the case of without vane angle (0°), the morphology of the scour was symmetric at the left and right end of the pier considering from upstream end. However, when the vane was attached to one side of the pier, the scour was non-symmetric at both vane angles i.e. 15°, 30° and 45°. In the case of attached vane angle, the dune is shifted towards the side in which the vane was attached. The shifting of the scour is more for 45° to the vane angles of 15° and 30°.

From Figures 2 to 3, it is clearly observed that the scour is more on the side of the vane. So the diversion angle (as shown in Figure 2) of sediment transportation is found more on the side of the vane as well. Similar observation was found for all experiments conducted at vane angles of 15°, 30° and 45°. However the scour contours were found symmetric for experiments without vane that is at 0° vane angle. It was also observed that the diversion angle at the vane side increases with the increase of vane angle and becomes highest at 45° vane angle. Now keeping 45° vane angle fixed and constant discharge with the decrease of flow shallowness, the diversion angle was also found increasing. Similarly, at 45° vane angle and constant flow shallowness, diversion angle increases with the increase of discharge on the vane side. When the diversion angle increases, the dune shifts towards the side wall of the flume as well as the bed particles (sediment) is transported further downstream. Based on these observations it may be said that the sediment transportation can be increased by increasing scour around a square pier with a vane attached to one side of that pier.

The pier width ($b$) relative to the mean bed particle size is known as the *sediment coarseness* ($b/d_{50}$). The equilibrium scour depth decreases with the decreasing sediment coarseness for values less than about 20 to 25. It also decreases at a greater rate with decreasing flow depth for smaller values of the *flow shallowness* or relative inflow depth $h/b$ which is one of the main parameters influencing the local scour. Yanmaz (1989) addressed that the relative scour depth $d_s/b$ is a function of flow shallowness. The author also presented a relationship between $d_s/b$ and $h/b$ through curves. Such curves were earlier developed by Melville (1975), Breusers et al. (1977), Melville and Sutherland (1988), and Gűnyakti (1989).

Based on the dimensional analysis it is noted that the scour depth varies with densimetric Froude number, flow depth and effective pier width which changes for different vane angles. At first, the non-dimensional scour depth ($d_s/b$) is plotted against densimetric Froude number ($F_{d50}$) for a fixed vane angle with flow depth as parameter as shown in Figure 4(a-d). It is observed that the non-dimensional scour depth ($d_s/b$) increases with the increase of vane angle and decrease of depth that is the flow shallowness ($h/b$). The non-dimensional scour depth ($d_s/b$) becomes highest at 45° vane angle with a maximum magnitude of 1.7 at the flow depth of 10 cm or at the flow shallowness of 1.43.

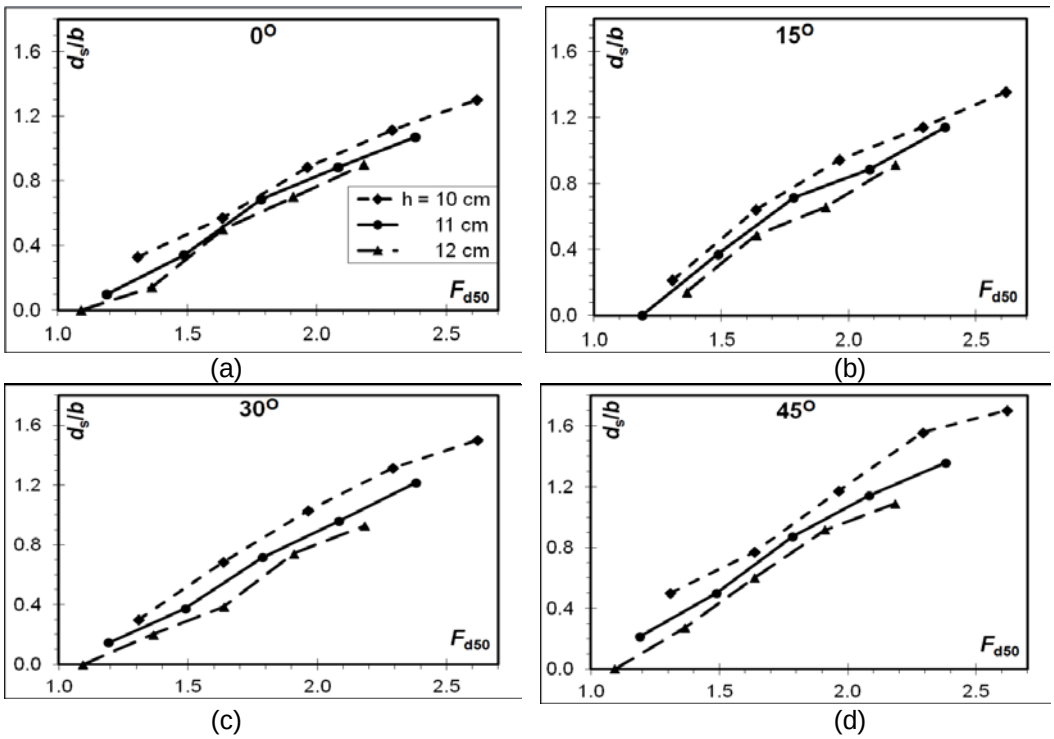


**Figure 4.** Graphical representation of non-dimensional scour depth vs densimetric Froude number at (a) 0°, (b) 15°, (c) 30° and (a) 45° vane angle.

 

To check the influence of the flow depth in a better way, the non-dimensional scour depth was plotted against densimetric Froude number for a particular depth with vane angle as parameter as shown in Figure 5.

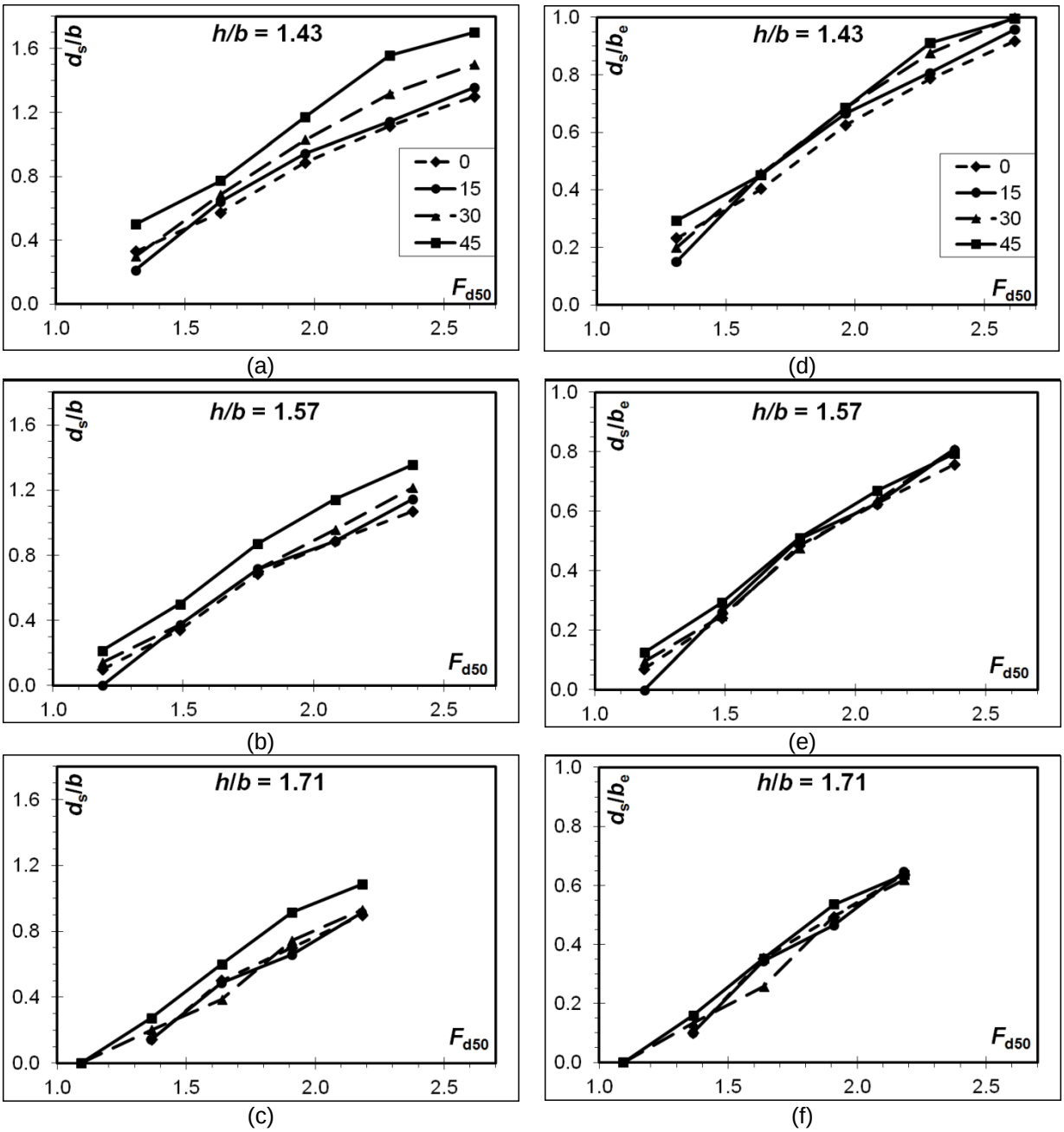


**Figure 5.** Graphical representation of non-dimensional scour depth vs densimetric Froude number at different non-dimensional flow depth (a) *h*/*b* = 1.43, (b) *h*/*b* = 1.57 and (c) *h*/*b* = 1.71 and non-dimensional effective scour depth vs densimetric Froude number at different non-dimensional flow depth (d) *h*/*b* = 1.43, (e) *h*/*b* = 1.57 and (f) *h*/*b* = 1.71.

It is observed that the scour depth increases with increasing densimetric Froude number. This trend is similar for different vane angles of 45°, 30°, 15° and 0°. It is noted that for the same densimetric Froude number, the scour is more for higher angle of vanes i.e. increasing vane angle increases the scour depth. The similar trend is also observed for different approach with flow depths of 10 cm, 11 cm and 12 cm as can be seen in Figure 5a, 5b and 5c. From Figures 5(d) to 5(e), it is observed that the effective scour depth also increases with increasing densimetric Froude number. Here in Figure 5(d to f), the trendlines are overlapping each other compared to Figure 5(a) to 5(c) because the non-dimensional effective scour depth is taking into account the vane angle parameter. Also, an almost linear relationship is observed in Figure 5(d) to 5(f). Therefore, a linear trendline equation may be determined as the scour depth increases with densimetric Froude number for all three tested non-dimensional inflow depths.

 

The non-dimensional effective scour depth or effective flow shallowness are plotted in Figure 6 as a function of densimetric Froude number for three different *h*/*b*. All the linear equations for different vane angles are addressed in Figure 6. The linear trendlines for the curves as given in Figure 6(a to c) indicate their dependence on inflow depths which take the form of Eq. [3].

$$d_s/b_e = C_i F_{d50} - D_i \qquad [3]$$

where, $C_i$ and $D_i$ are arbitrary constants for different effective flow shallowness depending on inflow depths.

In Figure 6, the correlation coefficients $r_1$, $r_2$, $r_3$, $r_4$ represent the values for 0°, 15°, 30° and 45°, respectively. In Figure 6, all the correlation coefficients ($r_i$) are within 0.976-0.998 which implies an almost perfect positive correlation between effective flow shallowness and densimetric Froude number. It is observed from these equations that the arbitrary coefficient $C_i$ and $D_i$ change with effective flow shallowness.

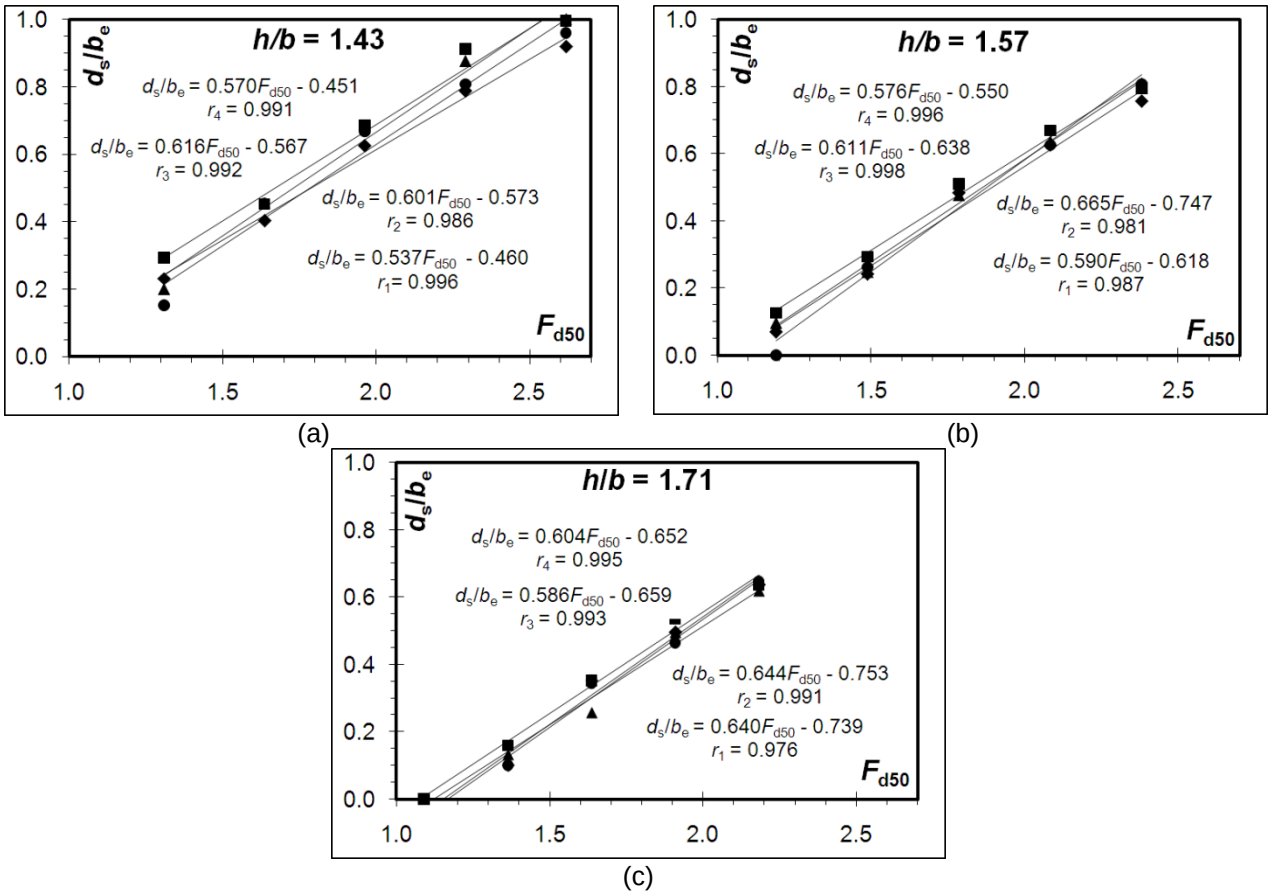


**Figure 6.** Linear relations between non-dimensional effective scour depth vs densimetric Froude number at different non-dimensional flow depth (a) *h*/*b* = 1.43, (b) *h*/*b* = 1.57 and (c) *h*/*b* = 1.71.

Generalized equations for $C_i$ and $D_i$ are further obtained by plotting the different values with their corresponding inflow depths. Hence, these two coefficients can be expressed as a function of effective flow shallowness. Based on the coefficients of the equations addressed in Figure 6, two separate linear trendlines are introduced for $C_i$ and $D_i$ in Figure 7 and expressed in Eqs. [4-5].

$$C_i = 0.1757\left(h/b_e\right) + 0.4282 \qquad [4]$$

$$D_i = 0.767\left(h/b_e\right) - 0.1656 \qquad [5]$$

Here, the correlation coefficient (*r*) for Eq. [4] and Eq. [5] are 0.710 and 0.925 which also imply positive correlation. The equilibrium scour depth for pier-vane arrangement can be expressed as a function of densimetric Froude number and effective flow shallowness as shown in Eq. [6].

$$\frac{d_s}{b_e} = \left\{0.1757\left(h/b_e\right) + 0.4282\right\} F_{d50} - \left\{0.767\left(h/b_e\right) - 0.1656\right\} \qquad [6]$$

For this pier-vane the maximum equilibrium scour depth can be evaluated using Eq. [6].

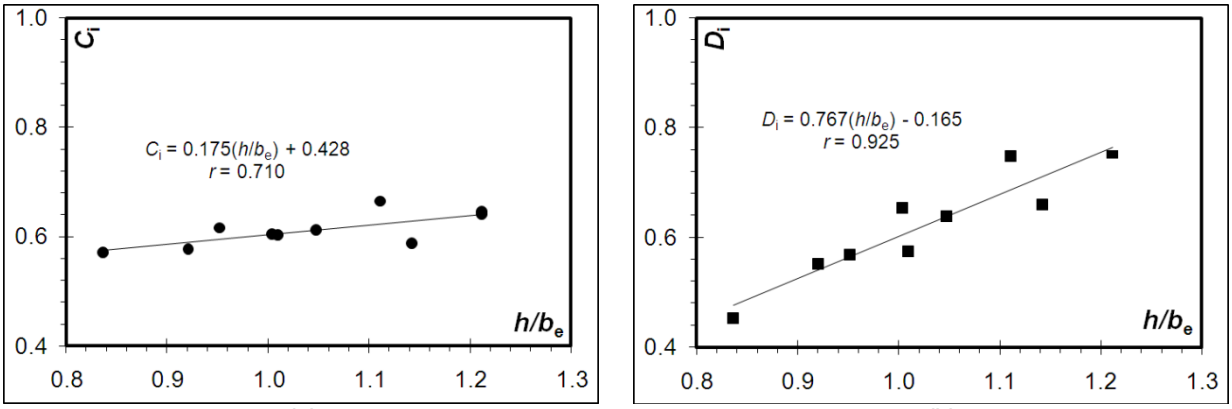


**Figure 7.** Variations of coefficients (a) $C_i$, and (b) $D_i$ with effective flow shallowness.

Therefore, the predicted values of scour depth have been calculated using Eq. [6] for four different vane angles. Figure 8 shows a comparison between observed and predicted values of non-dimensional effective scour depths for experiments 1-60. The ±20% intervals are added as dashed lines in Figure 8. It can be seen from Figure 8 that the deviation between the predicted and measured data is in a range of -20% to 20%. Therefore, the predicted (estimated) scour depths based on Eq. [6] matches very well with the observed (measured) scour depths.

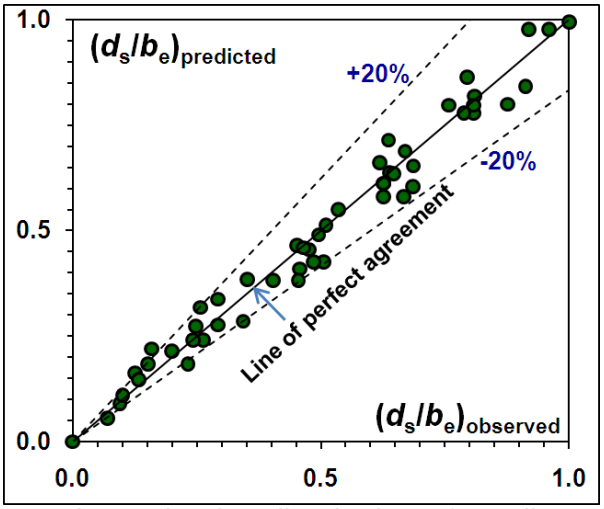


**Figure 8.** Comparison between observed and predicted values of non-dimensional effective scour depth.

Hence, from the above scour values and figures, the effect of densimetric Froude number, effective flow depth, and the vane angle on scour depth around square pier with vane are established.

## 5 CONCLUSIONS

Clear water scour tests have been performed on piers with a vane fixed on one side of it. The pier with a vane attached at 45° is found to be more efficient in terms of causing more scour thereby removing more sediment from the channel bed. Moreover, the sediment removed from the channel bed is deposited on one side of the channel. The diversion angle of the scour and the dune is more on the side of the vane. This is significant as it proves that the transported sediment load in a channel can be shifted towards the bank with the help of a suitable pier-vane combination.

Important results obtained from this study are as follows:

- The experimental results on local scour at square piers with vane under clear water condition have been analysed.
- The scour depth increases with increase in densimetric Froude number ($F_{d50}$) in the present experimental range.
- The scour depth decreases with increase in inflow depth or flow shallowness ($h/b$) in the present experimental range.
- Also, the scour depth decreases with increase in effective inflow depth or effective flow shallowness ($h/b$) in the present experimental range.

 

- Therefore, the scour depth also increases with increasing vane angle.
- Simple new empirical relationship is proposed to evaluate equilibrium scour depth. The proposed equation for such pier-vane is applicable for the following cases: densimetric Froude number is $1.1 \leq F_{d50} \leq 1.6$; the flow shallowness is $1.43 \leq h/b \leq 1.71$; the effective flow shallowness is $0.83 \leq h/b_e \leq 1.22$; and the Reynolds number for pier-vane group is $12{,}000 \leq Re_p \leq 35{,}000$.

The rate of sediment transportation is enhanced further with the increase in vane angle as well as with the increase of flow discharge for particular flow shallowness. These findings are significant as it proves that the transported sediment load in an open channel can be shifted toward the sidewall or bank by self-dredging with the help of suitable pier-vane combination and angle. To decide the location of deposition of removed sediments with respect to centreline of flow, the vane angle parameter must play a key role for this kind of solution.

## REFERENCES

Behbahan, T.S. (2011). Laboratory Investigation of Submerged Vane Shapes Effect on River Banks Protection. *Australian Journal of Basic and Applied Sciences*, 5(12), 1402-1407.

Bejestan, M.S., Khademi, K. & Kozeymehnezhad, H. (2015). Submerged Vane-Attached to the Abutment as Scour Countermeasure. *Ain Shams Engineering Journal*, 6, 775-783.

Breusers, H.N.C., Nicollet, G. & Shen, H.W. (1977). Local Scour around Cylindrical Piers. *Journal of Hydraulic Research*, 15(3), 211-252.

Das S., Ghosh R., Das R. & Mazumdar A. (2014a). Clear Water Scour Geometry Around Circular Piers. *Ecology. Environment and Conservation,* 20(2), 479-492.

Das, S., Das, R. & Mazumdar A. (2014b). Variations of Clear Water Scour Geometry at Piers of Different Effective Widths. *Turkish Journal of Engineering and Environmental Science*, 38(1), 97-111.

Das S., Das R. & Mazumdar A. (2016). Comparison of Local Scour Characteristics around Two Eccentric Piers of Different Shapes. *Arabian Journal for Science and Engineering*, 41(4), 1199-1213.

Flokstra, C. (2006). Modelling of submerged vanes. *Journal of Hydraulic Research,* 44(5), 591–602.

Ghorbani, B. & Kells, J.A. (2008). Effect of Submerged Vanes on the Scour Occurring at a Cylindrical Pier. *Journal of Hydraulic Research,* 46 (5), 610–619.

Gűnyakti, A. (1989). Characteristics of Alluvial Streams and River Training*. Proc. Sediment Transp. Tech. Vol. 2 UNESCO, General Directorate of State Hydraulic Works, Ankara, Turkey*.

Johnson P.A., Hey, R.D., Tessier, M. & Rosgen, D.L. (2001). Use of Vanes for Control of Scour at Vertical Wall Abutments. *Journal of Hydraulic Engineering*, 127(9), 772-778.

Marelius, F. & Sinha, S.K. (1998). Experimental Investigation of flow past Submerged Vanes. *Journal of Hydraulic Engineering* 124(5), 542-545.

Melville, B.W. (1975). *Local Scour at Bridge Sites.* Rep. No. 117. Sch. Eng., Univ. Auckland. Auckland, New Zealand.

Melville, B.W. & Sutherland, A.J. (1988). Design Method for Local Scour at Bridge Piers. *Journal of Hydraulic Engineering*, 114(10), 1210-1226.

Odgaard, A.J. (1986a). Meander Flow Model. i: Development. *Journal of Hydraulic Engineering*, 112(12), 1117-1135.

Odgaard, A.J. (1986b). Meander Flow Model. ii: Applications. *Journal of Hydraulic Engineering*, 112(12), 1137-1149.

Odgaard, A.J. (2009). *River Training and Sediment Management with Submerged Vanes*. USA: ASCE Press.

Odgaard, A.J. & Mosconi, C.E. (1987). Streambank Protection by Submerged Vanes. *Journal of Hydraulic Engineering*, 113(4), 520.

Odgaard, A.J. & Wang, Y. (1991). Sediment Management with Submerged Vanes. *Journal of Hydraulic Engineering*, 117(3), 267.

Yalin MS. (1977). *Mechanics of Sediment Transport*. Elmsford, NY, USA: Pergamon.

Yanmaz, A.M. (1989). Time Dependent Analysis of Clear Water Scour around Bridge Piers, *Ph.D. Thesis*. Middle East Tech. Univ., Ankara, Turkey.

 

# 3D VERSUS 2D CALIBRATION OF A 3D HYDRODYNAMIC MODEL

PARNA PARSAPOUR-MOGHADDAM[1] & COLIN D. RENNIE[2]

[1,2]Department of Civil Engineering, University of Ottawa, Ottawa, Canada
ppars036@uottawa.ca; colin.rennie@uottawa.ca

## ABSTRACT

This study proposes a novel calibration approach to account for the spatial distribution of the fully three-dimensional (3D) flow field. A natural meandering river is simulated using the 3D hydrodynamic model. Fully 3D distributed velocities are employed which are obtained from spatially intensive acoustic Doppler current profiler (ADCP) surveying. Sensitivity analysis is performed on horizontal eddy viscosity as well as the manning roughness to investigate which of these parameters could more influence the model. In the present study, comparison is made between the results of a conventional 2D calibration versus 3D calibration approach. It is shown that the 3D calibration method results in a different optimized model parameterization than the 2D calibration. The 2D calibration approach yields horizontal eddy viscosity of $10 m^2/s$, while the proposed 3D calibration approach results in the horizontal eddy viscosity of $0.1 m^2/s$. The proposed methodology could improve the calibration of a 3D hydro-morphodynamic model in terms of specifically parameterizing it to simulate fully 3D flow field. Moreover, it allows for spatially distributed calibration parameters to better represent physical and turbulent characteristics of the flow. The results of this study suggest that an appropriately calibrated 3D hydrodynamic model could more accurately predict the hydrodynamic processes in a natural meandering river.

**Keywords:** 3D hydrodynamic modeling; 3D calibration; 2D calibration; ADCP; natural meandering river.

## 1 INTRODUCTION

Numerical models should have the capability to simulate dynamics and variability of natural rivers. Models are sensitive to user-defined input parameters. Thus, proper calibration of a model is essential for accurate predictions of flow characteristics and morphological changes. On the other hand, 3D modelling of meandering rivers still has challenges for accurate quantitative prediction of the flow hydrodynamics. Conventional calibration methods mostly used available data measured at a few sections. The calibration process is still disputable and suffers from some inadequacies (Van De Wielet al., 2011). To calibrate the model reliably, it is important to have accurate measurements of the flow field. In particular, the complexity of flow in natural meandering rivers demands that careful attention is paid to 3D model calibration for reliable prediction of the fully 3D flow field.

More recently, acoustic Doppler current profilers (ADCPs) have been extensively applied to estimate the mean water velocity and flow turbulence (Abad et al., 2004; Garcia et al., 2007; Vermeulenet al., 2011; Vermeulen et al., 2014). These instruments can provide spatially dense velocity fields (e.g., Rennie and Millar, 2004; Rennie and Church, 2010), which facilitate numerical model calibration and validation. Parsapour-Moghaddam and Rennie (2015) utilized depth-averaged velocity obtained from an intensive spatial ADCP survey to calibrate a 3D morphodynamic model. They concluded that the developed validated model can be utilized for improved approximation of boundary shear stress and sediment processes. Williams et al. (2013) calibrated their developed 2D model using spatial observations of depth and depth averaged velocity obtained with an ADCP. They showed that proper calibration is critical for accurate prediction of lateral variations in depth-averaged velocity; calibration based only on water level and depth would not be adequate. Kasvi et al. (2015) made a sensitivity analysis of 2D and 3D models in a natural meandering river. They evaluated the model performance with measured ADCP data. They showed that although both 2D and 3D models could agreeably simulate depth-averaged velocity, there was a significant difference between the predicted and measured near-bed flow. The authors suggested improving the calibration and validation data could alleviate the mismatch between simulations and measurements.

Previous studies that used field measurements for evaluation of the model were shown to have problems with quantitative estimation of hydraulic variables (Dargahi, 2004; Rodriguez et al., 2004; Nicholas et al., 2012). This study proposes a novel methodology for calibration of a 3D numerical model. The results of the proposed calibration approach are compared with a typical calibration method commonly used in the literature. Spatially intensive fully 3D ADCP velocity data are employed for calibration of a 3D hydrodynamic model in an attempt to alleviate the existing uncertainties of the calibration procedure.

 

## 2 STUDY AREA

This study aims to simulate hydrodynamic characteristics of Watts Creek, a meandering clay-bed river in the City of Ottawa, Canada (Figure 1).This Creek flows into the Ottawa River at Shirley's Bay in the Kanata region of the Municipality of Ottawa. Watts Creek has been identified as providing important cool water fish habitat (Dillon 1999). It has a bed that consists of a high percentage of clay, i.e., soil particles that are smaller than two to four micrometers. This study focused on part of the reach, M4, which is partially confined by the City of Ottawa rail line. The rail line confines the meander planform, which has exacerbated erosion on the outer bank downstream of bend apices and thereby, is undergoing enhanced erosion. The results of field reconnaissance suggest that M4 has a very active, unstable channel, presumably due to the meander confinement by the rail line.

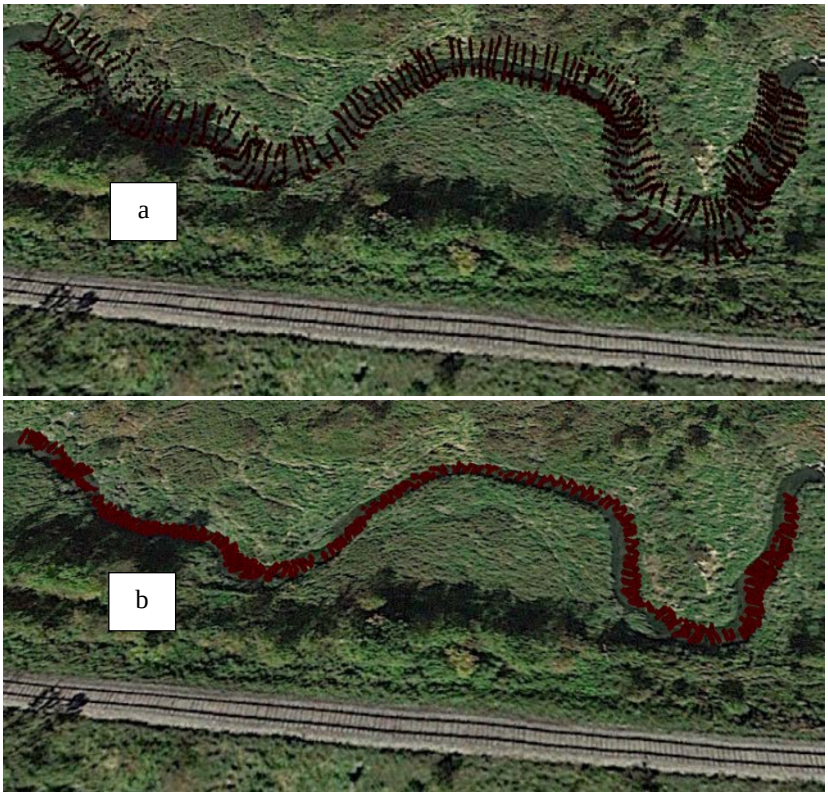


**Figure 1.** (a) Overview of the Watts Creek study reach M4, including surveying points. Flow from left to right. Rail line is immediately adjacent to the south of the river. (b) Track of ADCP survey on the study reach.

## 3 METHODOLOGY

### 3.1 Numerical Model

The Delft 3D_Flow modeling package (Delft-Flow version 4.01.01) was used for 3D hydrodynamic simulation of a natural meandering river. Delft-Flow is an open source code which simulates multi-dimensional (2D or 3D) hydro-morphodynamic processes on a rectilinear or a curvilinear grid (Deltares, 2014). Total Station survey was conducted to collect the topography and bathymetric data. A boundary mesh was generated from the measured digital elevation model. A curvilinear grid was then built with an average grid resolution of 0.35 m and a time step of 0.0025 s to meet the stability condition. Based on the ADCP measurements, a downstream water level of 70.3 m and an upstream discharge of 0.18 $m^3/s$ were specified as the boundary conditions of the reach. 3D k–ε turbulence model was employed to account for the effect of 3D turbulent motions.

### 3.2 Field measurements

Comprehensive spatially distributed fully 3D velocities were acquired by intensive spatial ADCP survey of Watts Creek on 15 August 2015 (Figure 1b). An ADCP is a hydroacoustic instrument that measures the 3D flow velocities using the Doppler effect of backscattered sound waves within the vertical water column. An ADCP deployed on a moving boat can be appropriately utilized to determine the 3D flow field and bathymetric data. Further detailed information on ADCP theory is available in Simpson and Oltman (1993), Morlock (1996), Simpson (2001), Muste et al. (2004), and Rennie and Church (2010). In this study, a Sontek M9 River Surveyor ADCP was mounted on an Ocean Sciences trimaran riverboat. The trimaran was manipulated with

 

ropes by two operators standing at each side of the river, who moved the boat downstream in a zigzag pattern in closely spaced transects (0.5 m to 1 m spacing). It should be noted that the flow depth in the straight portion of the reach was too shallow to be surveyed. Post processing of the measured data was done using in-house Matlab codes (Rennie and Church, 2010). The spatially intensive 3D flow velocity data were then employed for calibration of the 3D hydrodynamic model of a meandering channel.

### 3.3 Model calibration

For 3D calibration of the 3D hydrodynamic model, a Matlab code was developed to compare the co-located simulated and measured 3D velocities throughout the 3D domain. In this code, after post processing, the measured ADCP data to output single bin 3D velocities and their 3D coordinates, the locations of observations are matched to grid points of the 3D numerical model. For each grid point in the boundary mesh, all ADCP measured velocity bin locations were searched. If the horizontal distance between the centres of the model grid point and an individual ADCP velocity bin was less than 5 cm, then the coordinates of the matched points were saved. In the next step, the matched points were compared vertically to co-locate modelled velocity cells and individual ADCP bin points. Specifically, a measured ADCP bin was matched to a modelled cell if the vertical distance between their centres was less than 1cm. This procedure was repeated for all grid points in the boundary mesh to yield a data set of matched co-located measured and predicted 3D velocities throughout the domain. Following, model error statistics were used for evaluation of the model performance:

$$MAE = \sum_i^k \frac{(|x_{mod} - x_{obs}|)_i}{k} \text{ [1]}$$

$$MAE_R = \sqrt{MAE_x^2 + MAE_y^2 + MAE_z^2} \text{ [2]}$$

$$MAE_H = \sqrt{MAE_{\bar{x}}^2 + MAE_{\bar{y}}^2} \text{[3]}$$

$$STD = \sqrt{\frac{\sum_{i=1}^k (|v_{mod_i} - v_{obs_i}| - \mu)^2}{k-1}} \text{[4]}$$

where $x_{obs}$ indicates measured velocity and $x_{mod}$ represents simulated velocity, $MAE$ and $STD$ stand for mean absolute error and standard deviation of the error, respectively. $MAE_R$ is the resultant of $MAE$ for each velocity component in the x (east), y (north), and z (vertical) directions, and $MAE_H$ is the resultant mean absolute error based on depth-averaged velocity components in the horizontal x and y directions. The parameter μ is the mean of all velocity error values and $k$ is total number of co-located points. Sensitivity analysis was done on the user defined input parameters horizontal eddy viscosity ($\nu_H^{back}$)and manning roughness($n$) to determine which of these two parameters most influenced model results. Delft 3D calculates the total horizontal eddy viscosity ($\nu_{H,total}$) based on the below equation:

$$\nu_{H,total} = \nu_v + \nu_H^{back} + \nu_{SGS} \text{[5]}$$

where $\nu_v$ accounts for the 3D turbulence and is calculated by a 3D turbulence closure model. $\nu_H^{back}$ is a background horizontal eddy viscosity which is user defined input file. It is associated with the horizontal turbulence that is not resolved by the Reynolds-averaged shallow-water equations. $\nu_{SGS}$ is referred to as the sub-grid scale turbulence which is not resolved by the horizontal grid (Deltares, 2014). In this experiment, $\nu_H^{back}$, hereinafter referred to as $\nu_H$, is the dominant parameter in Eq. [5] (Parsapour-Moghaddam and Rennie, 2017). This study will illustrate the significance of an appropriate calibration of a 3D hydrodynamic meandering river model using Delft 3D.

## 4 RESULTS

Figure 2 shows the sensitivity analysis on a reasonable range of $n$ (0.01 to 0.07) and $\nu_H$(0.01 to 10). As can be inferred, the horizontal velocity error distributions significantly vary with changes in the horizontal eddy viscosity as opposed to the Manning roughness. This shows that the developed model is more sensitive to the $\nu_H$ compared to $n$. Consequently, horizontal eddy viscosity was used as a calibration parameter for 3D model predictions.

 

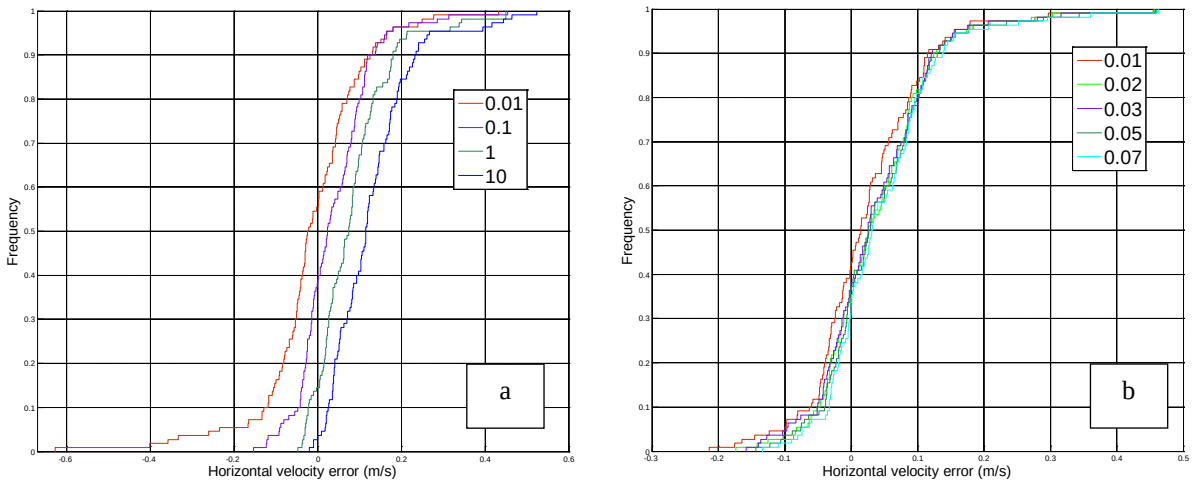


**Figure 2.** Cumulative frequency distributions of the horizontal velocity error for: (a) $\boldsymbol{\nu_H}$, the legend shows different values of $\boldsymbol{\nu_H}$. (b) $\boldsymbol{n}$, the legend shows different values of $\boldsymbol{n}$.

It should be noted that the above analysis (Figure 2) was done based on comparison of the 3D model depth-averaged velocities with those obtained from spatially intensive ADCP surveying. This study calibrated the 3D model based on the proposed calibration approach, whereby simulated 3D velocity components were compared with those obtained by ADCP, both spatially and vertically throughout the water column (3D calibration). Figure 3 shows the results of the proposed calibration approach based on spatially distributed 3D velocity data throughout the model reach. As can be seen, both cumulative frequency distributions of the velocity error and mean absolute error analysis confirmed that $\nu_{\mathrm{H}} = 0.1 m^2/s$ leads to the lowest amount of error.

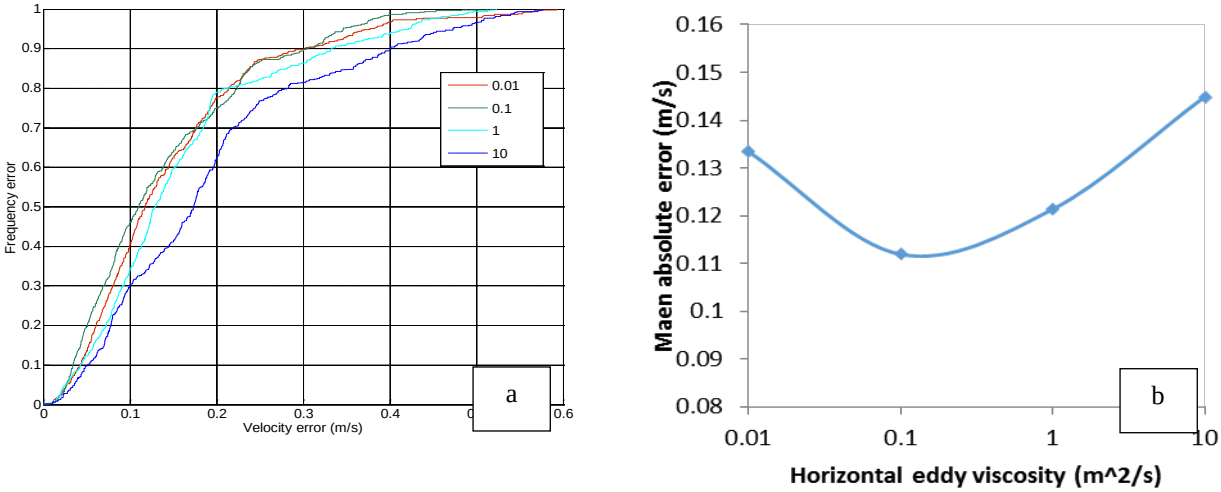


**Figure 3.** Calibration of the 3D model based on spatially intensive 3D velocity vectors throughout the model reach: (a) Cumulative frequency distributions of the velocity error, the legend shows different values of $\nu_H$. (b) Mean absolute error versus horizontal eddy viscosity (log-scale).

The 3D model was also calibrated based on the typical calibration approach in which the available data were used in five discrete sections, equally distributed, through the study area including pools and riffles. As is shown in Table 1, calibration of the 3D model with this method yielded horizontal eddy viscosity of $10 m^2/s$.

**Table 1.** Calibration of the 3D model based on the depth-averaged velocities at discrete locations in the study reach.

| $\boldsymbol{\nu_H(\frac{m^2}{s})}$ | **0 .01** | **0.1** | **1** | **10** |
|---|---|---|---|---|
| $\boldsymbol{MAE}$ | 0.163 | 0.130 | 0.115 | 0.109 |
| $\boldsymbol{STD}$ | 0.149 | 0.079 | 0.065 | 0.072 |

Thus, it can be inferred that different calibration approaches resulted in a different optimized model parameterization, i.e. background horizontal eddy viscosity of $0.1m^2/s$ (based on the proposed 3D calibration) and $10m^2/s$ (based on the 2D calibration). To further study which calibration method can produce more accurate results, modeled versus measured regression statistics were examined for each velocity component based on 2D versus 3D calibration. For each case, the estimated best-fit regression equations are provided in Table 2, where $v_x$ and $v_y$ show the velocity components in East and North directions, respectively. Figures 4 and 5 also illustrate the simulated $v_x$ and $v_y$ versus those obtained from each bin of the ADCP based on 3D calibration using $\nu$=0.1 $m^2/s$ and 2D calibration using $\nu$=10$m^2/s$, respectively.

**Table 2.** Regression parameters based on the best fit analysis in 2D and 3D calibration approaches.

| Velocity Components | Calibration Method | $\nu_H$ $(\frac{m^2}{s})$ | Slope | Intercept | $r^2$ |
|---|---|---|---|---|---|
| $v_x$ | 3D | 0.1 | 0.951 | 0.014 | 0.530 |
| $v_y$ | | | 1.031 | 0.006 | 0.710 |
| $v_x$ | 2D | 10 | 2.392 | 0.027 | 0.358 |
| $v_y$ | | | 2.997 | 0.019 | 0.706 |

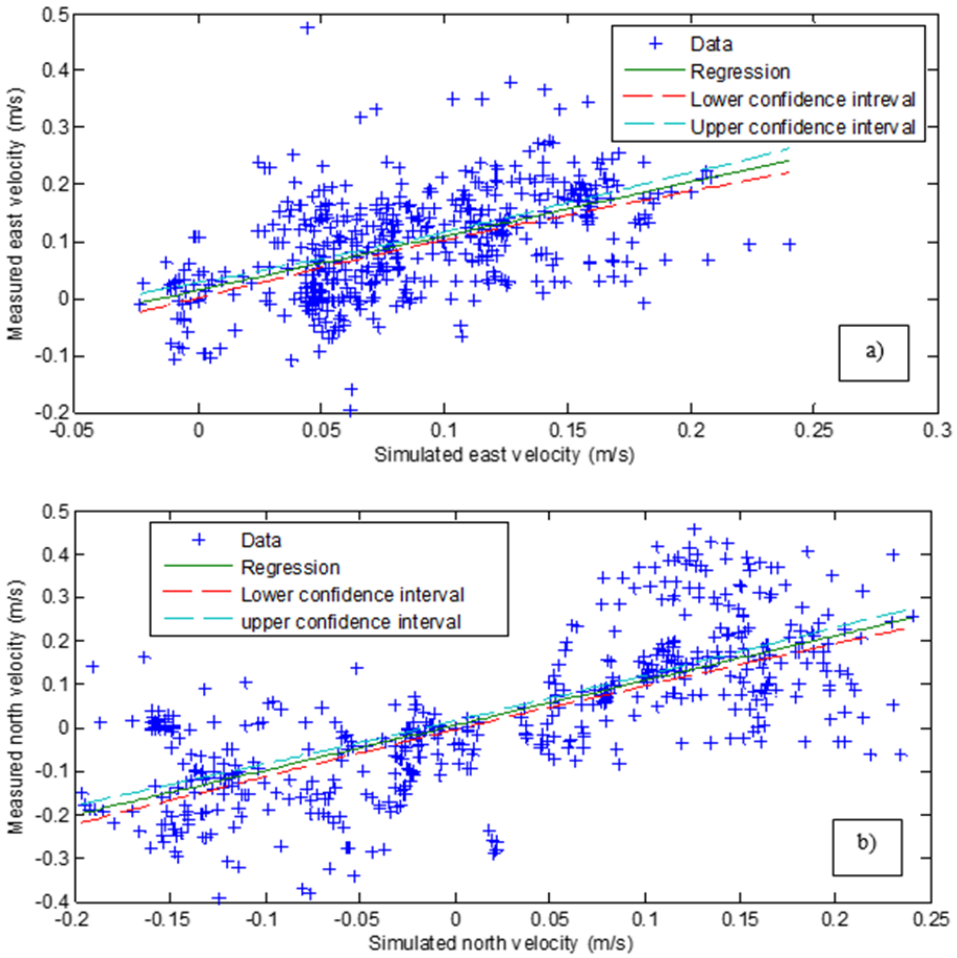


**Figure 4.** Simulated versus measured velocity for $\nu_H$ =0.1$\frac{m^2}{s}$(a) $v_x$ (b) $v_y$.

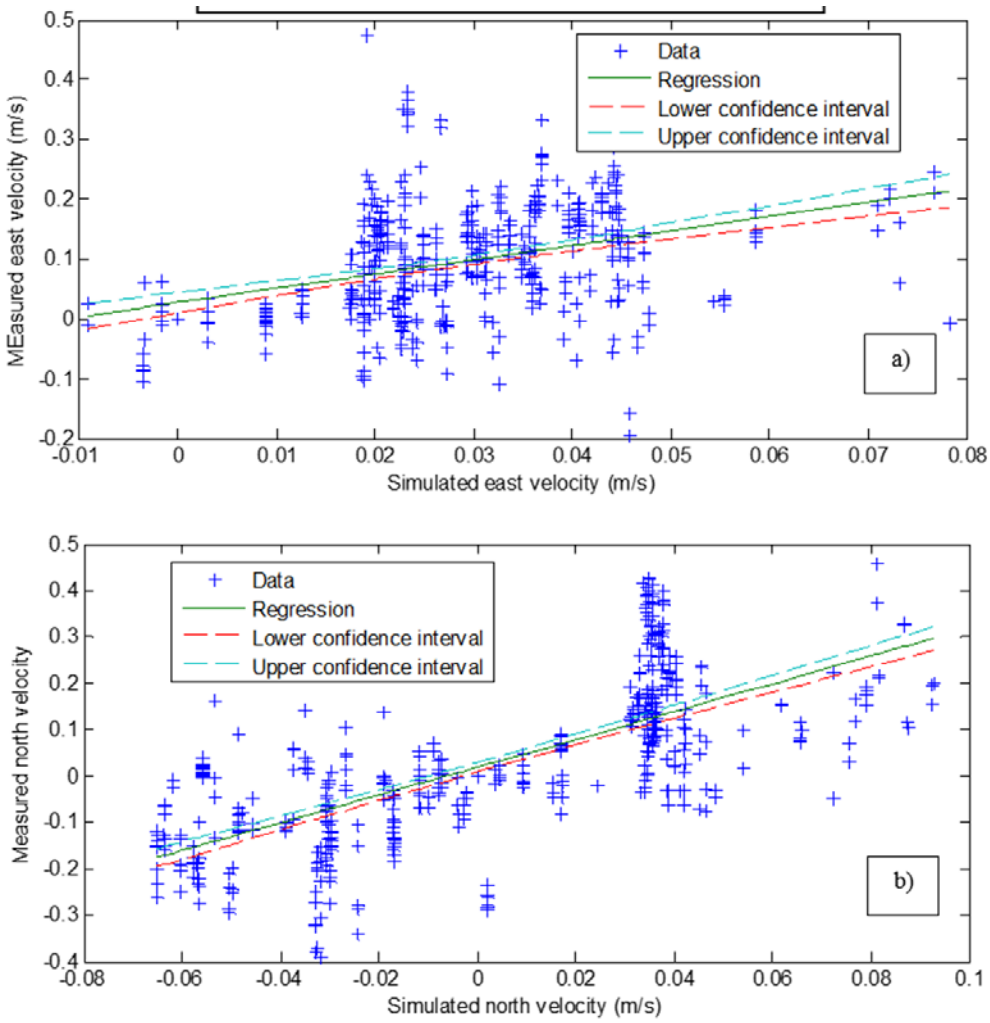


**Figure 5.** Simulated versus measured velocity for $\nu_H$ =10 $\frac{\mathrm{m}^2}{\mathrm{s}}$(a) $v_x$ (b) $v_y$.

As can be inferred from the above regression analysis, 3D calibration approach, which yielded $\nu_H = 0.1m^2/s$ had both better correlation and regression slope (closer to unity) compared to that of the 2D calibration $(\nu_H = 10m^2/s)$. This shows that the 3D calibration could lead to a more accurate model prediction. Figure 6a illustrates the individual velocity vectors, where red and blue vectors show measured and simulated velocities, respectively. Figure 6b specifies the location where the difference between simulated and measured velocity was higher than 0.1 $m/s$. As is shown (Figure 6a-b), most of the errors are less than 0.1 $m/s$ which confirms the acceptability of the model performance. Figure 6b shows that maximum error occurs mostly near the channel margins, which can be due to the compass error (Rennie and Church 2010). These errors may have been caused by inaccuracies in the bathymetric data, interpolation errors, ADCP survey data and numerical model errors. However, considering Figure 6a, one can note that most of the errors are due to the inaccuracies in the ADCP survey data, because in these cases, the direction of the measured velocity does not follow the flow pattern of the reach.

 

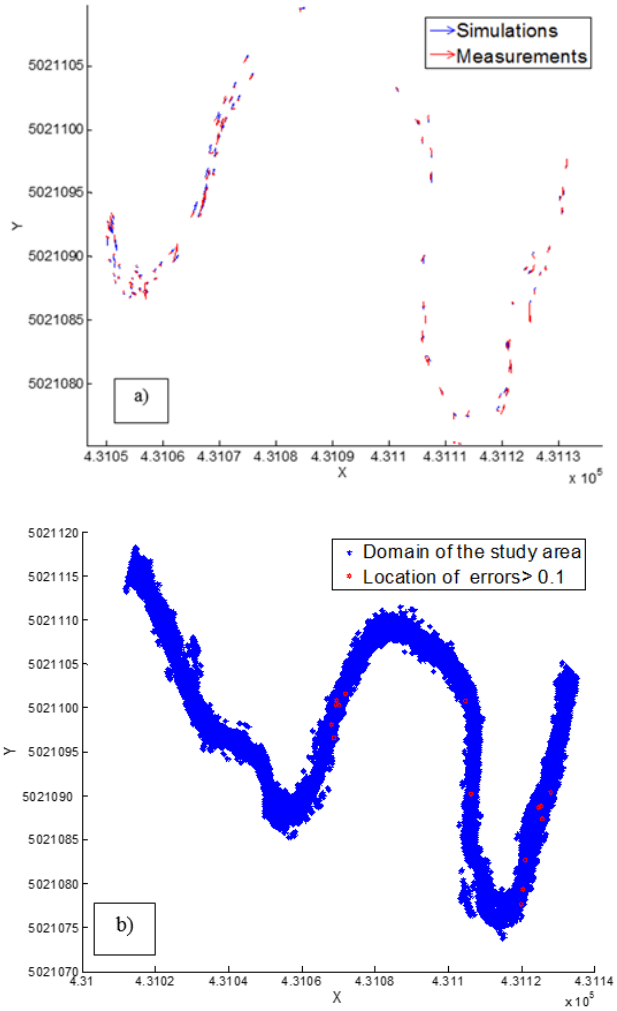


**Figure 6.** Comparison of spatially intensive 3D velocity vectors interpolated to a planar horizontal surface (a) Individual co-located simulated and measured velocity vectors (b) Location of the velocity errors greater than $0.1m/s$ .

## 5 CONCLUSIONS

In the present study, a 3D hydrodynamic model is first developed to simulate the flow characteristics in a natural meandering river. To obtain fully 3D distributed velocities, intensive ADCP surveying is conducted in the study creek. These observations are then employed for 3D calibration of the developed model. For accurate and realistic comparison of the fully 3D predicted and measured velocities, a Matlab code is developed to match the location of each ADCP bin with 3D model grid points. Sensitivity analysis on a reasonable range of Manning roughness and horizontal eddy viscosity shows that the model is highly sensitive to the horizontal eddy viscosity. The results suggest that the commonly used 2D calibration approach (based on the depth-averaged velocities at discrete locations) results in a different calibrated parameter, i.e. horizontal eddy viscosity of $10m^2/s$, while the proposed calibration approach (based on fully spatially distributed 3D velocities) yields horizontal eddy viscosity of $0.1m^2/s$. The results of the best fit regression between the simulations and measurements illustrate better correlation and unbiased acceptable error distributions with the 3D calibration approach. It is shown that the 3D calibration with spatially intensive velocity measurements could lead to a model particularly parameterized to predict the 3D flow field. Moreover, the proposed methodology allows for spatially distributed calibration parameters to better represent physical and turbulent characteristics of the flow.

## REFERENCES

Abad, J.D., Musalem, R.A., García, C.M., Cantero, M.I. & García, M.H. (2004). Exploratory Study of the Influence of the Wake produced by Acoustic Doppler Velocimeter Probes on the Water Velocities within Measurement Volume. *Proceeding of Critical Transitions in Water and Environmental Resource Management,* 1-9.

Dargahi, B. (2004). Three Dimensional Flow Modelling and Sediment Transport in the River Klarälven. Earth Surface Processes and Landforms, 29(7), 821-852.

 

Deltares, Delft3D-FLOW. (2014). *Simulation of Multi-Dimensional Hydrodynamic Flows and Transport Phenomena, including Sediments,* Users Manual, Delft3D-FLOW, 690.

Dillon Consulting Ltd. (1999). Shirley's Brook and Watts Creek Subwatershed Study.

Garcia, C.M., Oberg, K. & García, M.H. (2007). ADCP Measurements of Gravity currents in the Chicago River, Illinois. *Journal of Hydraulic Engineering,* 133(12), 1356-1366.

Kasvi, E., Alho, P., Vaaja M., Hyyppä, H. & Hyyppä, J. (2013). Spatial and Temporal Distribution of Fluvio-Morphological Processes on a Meander Point Bar during a Flood Event. *Hydrology Research,* 44(6), 1022-1039.

Morlock, S.E. (1996). *Evaluation of Acoustic Doppler current Profiler Measurements of River Discharge, US Department of the Interior,* US Geological Survey, 95-4218.

Muste, M., Kim, D. & Merwade, V. (2012). Modern Digital Instruments and Techniques for Hydrodynamic and Morphologic Characterization of River Channels. *Gravel-Bed Rivers: Processes, Tools, Environments,* 315-341.

Nicholas, A.P., Sandbach, S.D., Ashworth, P.J., Amsler, M.L., Best, J.L., Hardy, R.J., Lane, S.N., Orfeo, O., Parsons, D.R., Reesink, A.J. & Smith, G.H.S (2012). Modelling Hydrodynamics in the Rio Paraná, Argentina: An Evaluation and Inter-Comparison of Reduced-Complexity and Physics based Models Applied to a Large Sand-Bed River. *Geomorphology,* 169, 192-211.

Parsapour-Moghaddam, P. & Rennie, C.D. (2017). Calibration of a 3D Hydrodynamic Meandering River Model using Spatially Intensive 3D ADCP Velocity Data. *Journal of Hydraulic Engineering.* In revision.

Parsapour-Moghaddam, P. & Rennie, C.D. (2015). ADCP Validation of 3d Morphodynamic Modelling In Clay-Bed Meandering Rivers. *Proceedings of the 36th IAHR World Congress.*

Rennie, C.D. & Church, M. (2010). Mapping Spatial Distributions and Uncertainty of Water and Sediment Flux in a Large Gravel Bed River Reach using an Acoustic Doppler current Profiler. *Journal of Geophysical Research, Earth Surface,* 115(F3).

Rennie, C.D. & Millar, R.G. (2004). Measurement of the Spatial Distribution of Fluvial Bedload Transport Velocity in Both Sand and Gravel. *Earth Surface Processes and Landforms,* 29(10), 1173-1193.

Rodriguez, J.F., Bombardelli, F.A., García, M.H., Frothingham, K.M., Rhoads, B.L. & Abad, J.D. (2004). High-Resolution Numerical Simulation of Flow through a Highly Sinuous River Reach. Water Resources Management, 18(3), 177-199.

Simpson, M. R. (2001). *Discharge Measurements using a Broad-Band Acoustic Doppler Current Profiler,* US Department of the Interior, US Geological Survey, 123.

Simpson, M.R. & Oltmann, R.N. (1993). *Discharge-Measurement System using an Acoustic Doppler Current Profiler with Applications to Large Rivers and Estuaries,* US Government Printing Office, 32.

Van De Wiel, M.J., Coulthard, T.J., Macklin, M.G. & Lewin, J. (2011). Modelling the Response of River Systems to Environmental Change: Progress, Problems and Prospects for Palaeo-Environmental Reconstructions. *Earth-Science Reviews,* 104(1), 167-185.

Vermeulen, B., Hoitink, A.J.F. & Sassi, M.G. (2011). Coupled ADCPs can Yield Complete Reynolds Stress Tensor Profiles in Geophysical Surface Flows. *Geophysical Research Letters,* 38(6).

Vermeulen, B., Sassi, M.G. & Hoitink, A.J.F. (2014). Improved Flow Velocity Estimates from Moving-Boat ADCP Measurements. *Water Resources Research,* 50(5), 4186-4196.

Williams, R.D., Brasington, J., Hicks, M., Measures, R., Rennie, C.D. & Vericat, D. (2013). Hydraulic Validation of Two-Dimensional Simulations of Braided River Flow with Spatially Continuous ADCP Data. *Water Resources Research,* 49(9), 5183-5205.

 

# EULERIAN-LAGRANGIAN SIMULATION OF BED-MATERIAL LOAD TRANSPORT AROUND PERMEABLE AND IMPERMEABLE SPUR DYKES

KAZUYUKI OTA[(1)], HAJIME NAKAGAWA[(2)] & HAOZHANG[(3)]

[(1)]Central Research Institute of Electric Power Industry, Chiba, Japan
k-ota@criepi.denken.or.jp
[(2)] Prevention Research Institute, Kyoto University, Kyoto, Japan
nakagawa@uh31.dpri.kyoto-u.ac.jp
[(3)] Center for Disaster Prevention Promotion, Kochi University, Kochi, Japan
zhang@kochi-u.ac.jp

## ABSTRACT

This study develops a simulation model consisting of the LES (Large Eddy Simulation), VOF (Volume of Fluid), and practical Eulerian-Larangian approach allowing for resolving motion of flow and bed-material load around a partially permeable (i.e., Bandal-like) spur dyke. The numerical model is applied and validated in the movable bed experiment around four Bandal-like structures. The simulation model well reproduces the scour depth and deposition height around a laboratory experiment of the Bandal-like structures. Furthermore, a comparison of simulation results is made between the Bandal-like and impermeable spur dykes. The coherent structure resolved in the LES shows that the lower opened portion in the Bandal-like structures helps to interrupt development of the HV (horseshoe vortex) which facilitates scour development. In addition, sediment transport simulation shows that the suspended load passing though the lower opened portion plays an important role in facilitating transportation and deposition of the suspended load. The present numerical approach gives possible physical reasons as to why the sediment is likely to deposit around the Bandal-like structure.

**Keywords:** Large Eddy Simulation; bed-material load; Euler-Lagrange; spur-dyke; movable experiment.

## 1 INTRODUCTION

A spur dyke is one of the hydraulic structures used as river training, stream bank protection, and rectifying navigable rivers. Nowadays, social demand increases in those structures not only provide the above functions, but they are also within the local socio-economic condition and environmentally compatible solution as well (Shields et al. 2003). An alternative type of such structure is partially permeable spur dyke called Bandal-like structure. Bandals are one of the local structures developed in the Indian Sub-continent to improve or maintain the flows depth for navigation during low flow season. The main characteristics of Bandal-like structures is that they lead high velocity flow near the water surface to the main channel and allow the reduced velocity flow to pass near the river bed (lower opened portion). In previous experimental study (Teraguchi et al. 2011), flow pattern around a Bandal-like structure was found to have advantage in (1) reducing scour depth around the structure and (2) enhancing sediment deposition at downstream compared to conventional impermeable spur dyke. Figure 1 shows the Bandal-like structure used in field application, where upper plate is removed to be used during next rainy season. The effectiveness of Bandal-like structure to protect the bank erosion is clearly observed in Figure 1. In addition, the Bandal-like structure consists of a framework of naturally available bamboo driven into the riverbed and supported by struts. Thus, the Bandal-like structure is cheaper than conventional structure such as impermeable spur dyke made of concrete or steel.

Although the aforementioned key features of the Bandal-like structures have been demonstrated in previous studies (Zhang et al., 2010; Teraguchi et al., 2011), there are many unknown issues on the effect of the Bandal. Zhang et al. (2010) have measured 3D (three-dimensional) flow velocity around a Bandal-like structure in a field using ADCP (AcousticDoppler Current Profiler) and in a laboratory experiment using PIV (Particle Image Velocimetry). They indicated the importance of understanding 3D flow property, since the vortex system around the Bandal-like-structure is more complicated than a conventional impermeable spur dyke. Teraguchi et al. (2011) have focused on local scour and local deposition around two aligned Bandal-like structures under the condition that the bed load transport is dominative. They have demonstrated that performance of the Bandal-like structures is better than the conventional impermeable spur dyke in both submerged and non-submerged conditions. In spite of these efforts, previous findings on the Bandal-like structures still have some limitations. One unresolved issue is the influence of suspended load on the functions of the Bandal-like structure. Influence of suspended load is an important issue since the suspended load is often dominative in the fields in which the Bandal-like structure has been constructed. Another unresolved issue is

 

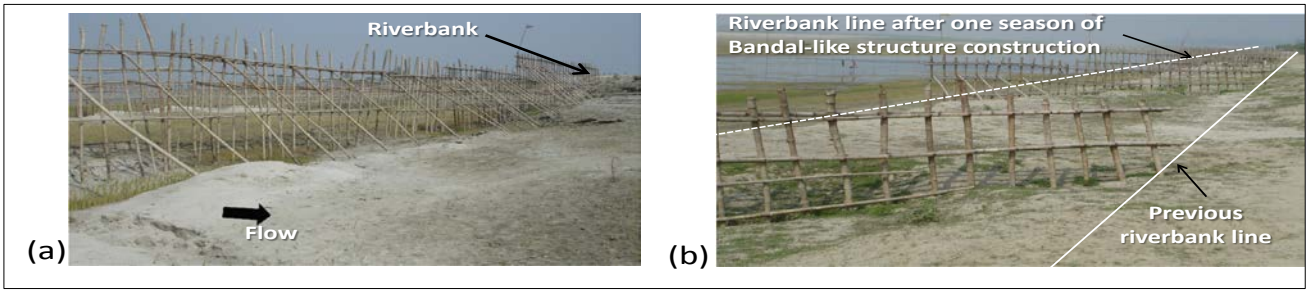


**1**. (a) The Bandal-like structure and (b) deposition influenced by the Bandal. Upper plate is removed to be used during next rainy season. Both (a) and (b) are shown as Figure 1 and Photo 2 in Teraguchi et al. (2011), respectively.

the effect of numbers of Bandal-like structures aligned in the longitudinal direction, as pointed out by Teraguchi et al. (2011). Besides, previous works are mainly conducted by laboratory experiments and field surveys, and numerical approach is limited. Nakagawa et al. (2011) have attempted 3D simulation of sediment transport around the Bandal-like structures by using RANS (Reynolds-Averaged Navier-Stokes) equation. They indicated that the standard k-εmodel captures only limited flow pattern around Bandal-like structures and that more sophisticated approach is preferable for flow and sediment transport models.

In the past decade, state-of-the-art of numerical simulation has successfully clarified the physics of flow and sediment transport around a hydraulic structure. Koken and Constantinescu (2008a, 2008b) have applied LES (Large Eddy Simulation) to resolve 3D turbulence flow around a vertical-wall spur dike on the rigid flat bed and the rigid scoured bed. They demonstrated that coherent flow structures play important roles on morphological change around a hydraulic structure and that formation of the coherent flow depends on the bed condition. However, their simulation lacks sediment transport module and thus temporal variation of the coherent structure and bed topography is not presented. Nagata et al. (2005) coupled RANS equation and bed load model based on the Eulerian-Lagrangian approach. They simulated local scour around a vertical-wall spur dyke with sufficient accuracy. Ota et al. (2016) extended the Eulerian-Lagrangian model proposed by Nagata et al. (2005) to bed-material load by incorporating the suspended load into the model, and the model was successfully applied to local scour around a weir-type structure at which the contribution of the suspended load cannot be neglected. Sediment transport simulation around the Bandal-like spur dyke is much more difficult than that around a conventional spur dykes owing to two factors: more anisotropic turbulence and consideration of the permeable portion. Therefore, further advancement of the numerical simulation technology is preferable to reveal the effect of the Bandal from the view point of turbulence and sediment-laden flow.

This study develops a three-dimensional simulation of sediment transport around permeable spur dyke and examines the effect of the Bandal-like spur dyke. Simulations are applied to Bandal-like and impermeable spur dyke after validation in a laboratory experiment. The simulation model consists of sub modules of (1) Large Eddy Simulation (LES) solving three-dimensional turbulent flow, (2) Volume of Fluid method capturing water surface variation, (3) a Lagrangian model for bed load component integrating the near-bed grain trajectory and the momentum equations, and (4) suspended sediment transport model in the Eulerian grid. The porous media technique is adopted to compute bed deformation to allow for readily changing bed shape without deforming computational cells. Through all numerical simulations, the feature of the Bandal-like structure is discussed from the view point of turbulence and sediment-laden flow.

## 2 NUMERICAL MODEL

### 2.1 Hydrodynamic model

The hydrodynamic model consists of filtered Navier-Stokes equation for the incompressible air-water flow that considers seepage flow and profile evolution in a sediment. The model assumes sufficiently small temporal variation in the porosity $\lambda$ representing the volume fraction of void space in each cell.The porosity becomes $\lambda$=1 for pure fluids, $0 \leq \lambda \leq \eta$ for water-sediment interface, and $\lambda$=$\eta$ for pure sediment region where $\eta$ is the porosity of the sediment itself. The governing equations for continuity and momentum of fluid are given as follows:

$$\frac{\partial\left(\lambda\overline{u_j}\right)}{\partial x_j} = 0 \qquad [1]$$

 

$$\lambda\frac{\partial\left(\rho\overline{u_i}\right)}{\partial t}+\frac{\partial}{\partial x_j}\left(\lambda\rho\overline{u_i}\,\overline{u_j}\right)=-\lambda\frac{\partial p}{\partial x_i}+\lambda\rho g_i+\frac{\partial}{\partial x_j}\left(2\rho\lambda\nu_{eff}\,\overline{D_{ij}}\right)+A\overline{u_i},\ \text{with}\ \nu_{eff}=\nu+\left(c_s\Delta\right)^2\left|\overline{D_{ij}}\right| \quad [2]$$

where $\overline{u_i}$ is GS (grid scale) component of flow velocity; $\overline{D_{ij}}$ is GS component of strain velocity tensor; $A$ is drag coefficient of porous media; $\mathbf{g}$ is the gravitational acceleration vector; $\nu$= kinetic viscosity; and $\nu_{eff}$ is effective kinetic viscosity; $c_s$ = Smagorinsky coefficient (=0.1). Treatment of temporal and spatial gradient of porosity $\lambda$ follows the numerical model of Nakamura and Mizutani (2013) which simulated sediment transport induced by tsunami. To solve the velocity-pressure coupling, the pressure implicit with splitting of operator (PISO) approach was adopted. The finite volume method (FVM) was used for discretization with the second-order central difference method for spatial discretization and the first-order implicit method for temporal discretization. VOF (Volume of Fluid) method was adopted for capturing the water surface. Shear stress acting on the sediment-water interface is specified from the equilibrium wall-law proposed by Nakayama (2012). The Non-slip condition was imposed on the wall boundary.

2.2 Sediment transport model

The Eulerian-Lagrangian simulation of sediment transport starts from sediment pick-up at a stationary bed and its movement as a bed load. The bed load particles picked up from the bed are tracked using the Lagrangian method with the motion equation for a bed load particle. Some of the bed load particles transit to the suspension owing to a fluctuating vertical flow velocity, and conversely the suspended load returns to bed load as a result of gravitational settlement. The suspended load transport is solved using the Eulerian method with a typical advection-diffusion equation. The Lagrangian and Eulerian models are connected through transition between the bedload and the suspended load. The bed surface deforms as a result of sediment exchange between the bed load and the stationary bed (i.e., the pick-up and the deposition).

The volume of sediment pick-up per unit time from a computational grid, $V_p$, is given by

$$V_p=\left(1-\eta\right)dp_sS_b \quad [3]$$

where $p_s$ is the pickup rate; $d$ is the diameter of the sediment particle; and $S_b$= the area of the bed-surface grid; The pickup rate $p_s$ is obtained from the following equation established by Nakagawa et al. (1986), which includes the effect of the local bed slope on the sediment motion:

$$p_s\sqrt{\frac{d}{\left(\rho_s/\rho-1\right)g}}=0.03G_*\tau_*\left(1-0.7\frac{\tau_{*c}}{\tau_*}\right)^3 \quad [4]$$

where

$$\tau_{*c}=\frac{\mu_s\cos\theta_b-\sin\theta_b\cos\alpha}{\cos\psi+k_L\mu_s}\frac{1+k_L\mu_s}{\mu_s}\tau_{*c0} \quad [5]$$

$$G_*=\frac{\cos\psi+k_L\mu_s}{1+k_L\mu_s} \quad [6]$$

where $\tau_{*c}$ and $\tau_{*c0}$ are dimensionless critical bed shear stress on the sloped bed and flat bed, respectively; $G_*$ is a coefficient accounting for the directional deviation between the near-bed velocity and sediment movement; $\psi$ is the angle between the near-bed velocity and sediment movement; $\mu_s$ (= 0.7) is the static friction factor; $k_L$ (= 0.85) is the ratio of lift force to drag force; $\theta_b$ is the local bed slope; and $\alpha$ is the angle between the maximum local bed slope and sediment movement.

Using the velocity vector of the bed load particle, $\mathbf{u_{sed}}$, the position vector of bed load particle $\mathbf{p}_{\mathbf{sed}}^{(n)}$ and the distance of the bed load movement $s_{sed}$ can be calculated, respectively, by

$$\mathbf{p_{sed}}=\int\mathbf{u_{sed}}dt \quad [7]$$

$$s_{sed}=\int\left|\mathbf{u_{sed}}\right|dt \quad [8]$$

The motion of a particle is assumed to follow the local bed plane. Under this assumption, the momentum equation can be simplified. The motion equation of the sediment particle in the $\mathbf{x}^j$($j$ = 1, 2) direction, which is parallel to the local bed surface, is represented by considering fluid drag, submerged particle weight, bed friction, pressure-difference,and added mass as follows:

 

$$\rho\left(\frac{\rho_s}{\rho}+C_M\right)\frac{\pi d^3}{6}\frac{\partial \mathbf{u}_{\mathbf{sed},j}}{\partial t}=\mathbf{D}_j+\mathbf{W}_j+\mathbf{P}_j-\mathbf{F}_j \text{ for } j=1,2 \quad [9]$$

where

$$\mathbf{D}_j=\frac{C_D\rho}{2}\left|\mathbf{u}_{\mathbf{r},j}\right|\mathbf{u}_{\mathbf{r},j}c_e\frac{\pi d^2}{4} \quad [10]$$

$$\mathbf{W}_j=\begin{cases}-W\left(\dfrac{\sin\theta_{bx}\cos^2\theta_{by}}{\sin^2\theta_p}\right) & \text{for } j=1\\ -W\left(\dfrac{\sin\theta_{by}\cos^2\theta_{bx}}{\sin^2\theta_p}\right) & \text{for } j=2\end{cases}, \text{ with } W=(\rho_s-\rho)g\frac{\pi d^3}{6} \quad [11]$$

$$\mathbf{F}_j=\mu_k\left(W\frac{\cos\theta_{bx}\cos\theta_{by}}{\sin\theta_p}-k_L\left|\mathbf{D}_j\right|\right)\frac{\mathbf{u}_{\mathbf{sed},j}}{\left|\mathbf{u}_{\mathbf{sed},j}\right|} \quad [12]$$

$$\mathbf{P}_j=-A_3d^3\frac{\partial p}{\partial \mathbf{x}^j} \quad [13]$$

where $\mathbf{u}_{\mathbf{sed},j}$ is the velocity of a bedload particle in the $j$ direction; $C_M$ (= 0.5) is the coefficient of added mass; $\mathbf{u}_{\mathbf{r},j}$ is the relative velocity of the bedload to the near-bed flow velocity in the $j$ direction; $C_D$(= 0.4) is the drag coefficient; $c_e$= the coefficient accounting for the effective application area of the drag force (where $c_e$= 1.0 for moving particles and $c_e$= 0.4 for static particles); $\mu_k$ (= 0.35) is the coefficient of kinetic friction of bed load particles; $\theta_{bx}$ and $\theta_{by}$= the angles of the local bed inclination in the $x$ and $y$ directions, respectively; $\theta_p$ is the angle between $\mathbf{x}^1$ and $\mathbf{x}^2$, and $p$ = pressure. Through Eqs. [7] and [8], the velocity and trajectory of a sediment particle can be known at any time after being dislodged from the bed, and the motion of sediment particle does not influence the hydrodynamic model. Thus, the bed load particles while in motion are captured in an explicit manner.

Although the Lagrangian model tracks a parcel of bed load particles, in reality all bed load particles included in a parcel does not always behave in the same manner. For example, some of the particles in a parcel continue moving, whereas others may be deposited on the bed surface or transited to the suspension due to fluctuating vertical flow. Since these phenomena are related to fluid turbulence or irregularity of the bed roughness, the stochastic approach is connected to the Lagrangian method. The sediment volume of deposition $V_d$ and transition into suspension $V_t$ along the bed load transport trajectory are computed using the probability density function:

$$V_d^{(n)}=V_{b0}F_s^{(n)}\left(1-F_t^{(n)}\right) \quad [14]$$

$$V_t^{(n)}=V_{b0}\left(1-F_s^{(n)}\right)F_t^{(n)} \quad [15]$$

where

$$V_{b0}=V_p+V_{slide}+V_{settle} \quad [16]$$

where superscript ($n$) represents the $n$th step after a sediment pick-up; $V_{b0}$ is the sediment volume when the computation of the bed load trajectory starts, which is represented as a sum of the sediment volume of the pick-up $V_p$, a sediment slide on a steep slope $V_{slide}$, and gravitational settlement of the suspended load near the bed $V_{settle}$ ($V_{slide}$ and $V_{settle}$ are described later in this section); $F_s^{(n)}$ is the probability of a bedload particle depositing on the bed; and $F_t^{(n)}$ is the probability of a bedload particle being entrained into the suspension. To compute Eqs. [14] and [15], the deposition probability $F_s^{(n)}$ is written as follows:

$$F_s^{(n)}=f_s\left(s_{sed}^{(n)}\right)\Delta s \quad [17]$$

where

 

$$f_s\left(s_{sed}{}^{(n)}\right)=\frac{1}{\Lambda}\exp\left(-\frac{s_{sed}^{(n)}}{\Lambda}\right) \quad [18]$$

where $f_s$ ($s_{sed}{}^{(n)}$) = the probability density function of the step length; $s_{sed}$= the distance that the sediment particle moves from the pickup point, which is computed from Eq. [8]; and $\Lambda$= the average step length, which is estimated using the following formula given by Einstein (1942): To evaluate the transition probability $F_t^{(n)}$ used for Eqs. [14] and Eq. [15], a probability density function with a Poisson distribution is introduced following to Nakagawa et al. (1990) by considering that a transition event can only occur once per bed load particle and at time $\Delta t$. The transition probability $F_t{}^{(n)}$ is written as follows:

$$F_t^{(n)} = f_t\left(t^{(n)}\right)\Delta t \quad \text{with} \quad f_t\left(t^{(n)}\right)= p_t \exp\left(- p_t t^{(n)}\right) \quad [19]$$

where $f_t(t^{(n)})$= the probability density function of the transition from bedload motion to suspension at the $n$th step after a sediment pick-up; and $p_t$= the transition rate representing the reciprocal of the average time until a bed load particle transits into the suspension from time it is picked-up. The transition rate $p_t$ is calculated based on Nakagawa et al. (1990) after modification by Ota et al. (2016) so that fluctuating vertical flow velocity is included in equation as follows:

$$p_t\sqrt{\frac{d}{(\rho_s/\rho-1)g}}=0.0159\left(\frac{\sqrt{\overline{w'^2}}}{w_s}\right)^{0.4}\left[1-\frac{w_s}{\sqrt{\overline{w'^2}}}\right]^{1.1} \qquad \text{for } \sqrt{\overline{w'^2}} > w_s \quad [20]$$

where $w_s$ is the settling velocity,and $w'$ is the fluctuating vertical flow velocity in near-bed flow. Here, the root mean square of $w'$ is computed using the Prandtl's mixing-length formulation:

$$\sqrt{\overline{w'^2}} = \kappa \Delta z \left|\frac{\partial w}{\partial z}\right| \quad [21]$$

where $w$ = ensemble-averaged flow velocity in the vertical direction; $\kappa$(= 0.41) is the von Karman constant; and $\Delta z$ = vertical distance from the bed surface to the center of the first cell near the bed. The velocity gradient is computed through linear interpolation at the center of the first cell. This work uses a standard scalar transport equation for the Eulerian model of suspended load:

$$\frac{\partial \overline{C_s}}{\partial t}+\frac{\partial q_{s,j}}{\partial x_j}=\frac{\partial}{\partial x_j}\left(\nu_{eff}\left(\frac{\partial \overline{C_s}}{\partial x_j}\right)\right) \quad \text{with} \quad q_{s,j}=\left(\overline{u_j}-w_s\frac{g_j}{|\mathbf{g}|}\right)\overline{C_s} \quad [22]$$

where $C_s$ = the sediment concentration; $q_s$ = the flux of the suspended sediment ;$w_s$ = the sediment settling velocity. The source and sink terms are added to the advection-diffusion equation at the bed boundary by considering transition between the bed load and suspended load. The source term represents the transition from the bed load to the suspension, and the volume of transited sediment in a Lagrangian frame is transformed to the entrainment flux into an Eulerian computational cell adjacent to the bed boundary. There is some controversy in the literature as to the range of validity of using a scalar transport equation such as Eq. [22] for modelling sediment transport. Davies (1995) stated that this formulation is valid for concentrations $C_s$< $10^{-3}$ and pointed out that in practice, this formulation has been applied to concentrations as high as 0.01. The present work applied the model for sediment transport with a range of $C_s$< $10^{-3}$.

Deterministic approach to represent reattachment of suspended load to the bed is used for the sink term of the advection-diffusion equation as follows:

$$q_{s,j}\cdot n_j=\frac{\sum_n V_t^{(n)}-V_{settle}}{S_b} \quad \text{with} \quad V_{settle}=w_s C_{s,b} S_b \quad [23]$$

where $C_{s,b}$ is sediment concentration near the bed. The sediment volume settling onto the bed $V_{settle}$ is added to $V_{b0}$, i.e., the sediment volume when the computation of the bed load trajectory is started, at the computational grid where the settling event takes place, as expressed in Eq. [16].

Using the volumes of sediment pickup and deposition, the temporal variation in the bed elevation is expressed as follows:

$$(1-\eta)\frac{\partial z_b}{\partial t}=\frac{\sum_n V_d^{(n)}-V_p}{S_{b,p}} \quad [24]$$

where $z_b$= the bed elevation; and $S_{b,p}$= the area of the bed surface cell projected onto a horizontal plane where the sediment is deposited. The summation of $V_d{}^{(n)}$ represents the total volume of deposited sediment summing up $V_d{}^{(n)}$ for each time step $n$ after pick-up. When the local bed slope $\theta_b$ exceeds a certain critical value $\theta_{bc}$, a

 

sliding of the sediment occurs. Assuming that the sliding event takes place instantly, the sliding sediment volume required to keep the bed slope at its critical value $\theta_{bc}$ is calculated when $\theta_b$ exceeds $\theta_{bc}$ using the method proposed by Sekine (2004). The volume of the sliding sediment is then added to the $V_{b0}$, i. e. the

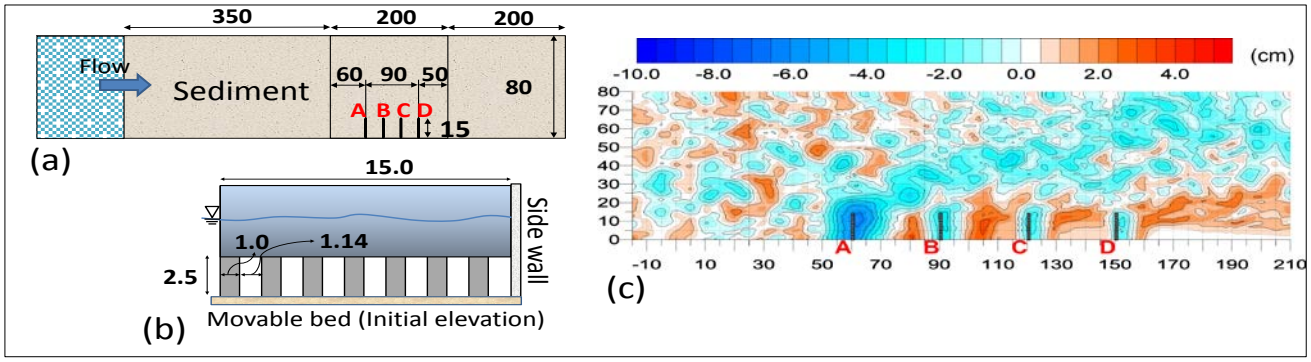


**Figure 2**. (a) Experimental setup, (b) the Bandal-like spur modeled in the experiment, and (c) experimental result of bed elevation in the quasi-equilibrium condition representing aggradation with warm color and degradation with cool color.

sediment volume when the computation of bed load trajectory is started, at the computational grid where the sliding event takes place as expressed in Eq. [16]. In the present scheme, the position at which the deposition or transition volumes were obtained in a Lagrangian frame did not necessarily coincide with the computational grid. Therefore, the deposition and transition volume were distributed proportionally to each cell center and each time step based on the relative location of the particle.

## 3 EXPERIMENTAL DATA AND NUMERICAL SETUP

Two sediment transport simulations around a spur dyke were presented in this study. One was for a Bandal-like structure, and the other was for an impermeable spur dyke. For validation of the numerical model, a physical experiment of sediment transport around a Bandal-like structure was conducted. The experiment was conducted in a straight flume with 12.0 m-long, 0.8 m-wide, and 1/800 slope at Ujigawa Open Labotatory, Disaster Prevention Research Institute, Kyoto University, Japan. Figure 2 shows a schematic view of the experimental apparatus and bed topography after the quasi-equilibrium condition. The Bandal-like structures (A, B, C, and D) having a stream wise thickness of 0.010 m, lateral length on 0.15 m, height of 0.070 m were embedded in the recess with 7.0 m-long, 0.80 m-wide, and 0.10m-deep and were positioned from 3.5 m. The flow rate was 9.18 (L/s), and the approaching cross-sectional flow velocity was 0.230 m/s, **Fr** number was 0.33, and **Re** number was 9225. Uniform sediment with median diameter of 0.093 mm was used in the experiment. Suspended load was supplied at a rate of 2.18 g/s by using feeder apparatus (Spiral Feeder, NX-3000M) installed at upstream end of the flume. As shown in Figure 2(c), a large scour hole existed around the structures A because the structure located in the most upstream directly receives the hydrodynamic force. The structure A changed the flow direction to the main channel and made the bed eroded in the main channel.

In numerical simulations, an inlet boundary was taken at 1.3m upstream of the structure A, which is more than 20-times the approaching water depth. Roughness elements were allocated in the just downstream of the inlet in order to provide fully developed turbulent flow to the computational domain. Hexahedral grids consisting of 1.7 million cells were used. Difference in computational gird between Bandal-like case and impermeable case is only existence of lower opened portion shown in Figure 2(b), which allows for quantifying the effect of lower opened portion through simulations.

## 4 RESULT AND DISCUSSION

Figure 3 shows the numerical results of bed elevation around (a) Bandal-like and (b) Impermeable spur dyke after the quasi-equilibrium condition. A comparison between Figures 1(c) and 2(a) indicated that the numerical simulation well reproduces over all features of bed topography such as scour hole around structure A and deposition between each structure. The maximum scour depths in the experiment and the simulation were 6.5 cm and 5.7 cm, and maximum deposition height in the experiment and the simulation were 3.7 cm and 3.6 cm, respectively. The effects of the Bandal-like spur dyke on morphological change, which will be discussed later, were therefore well captured in the simulation. A comparison between Figures 2(a) and 2(b) indicated that impermeable spur dyke produced larger scour hole than the Bandal-like spur dyke. The maximum scour depth in the impermeable spur dyke was 9.6 cm and thus 1.7 times larger than that in the Bandal-like spur dyke. Furthermore, the impermeable spur dyke produced less deposition height than the Bandal-like spur dyke. The maximum deposition height in the impermeable spur dyke was 1.2 cm and thus 0.3 times lower than that in the Bandal-like spur dyke. These features were consistent with the previous experimental studies. Teraguchi et al. (2011) conducted experiments in which the bed load is dominative, and

 

they showed that the maximum scour depth in the impermeable spur dyke is about 2 times larger than that in the Bandal-like spur dyke under the non-submerged condition. They also mentioned that sediment deposition behind the spur dyke is enhanced

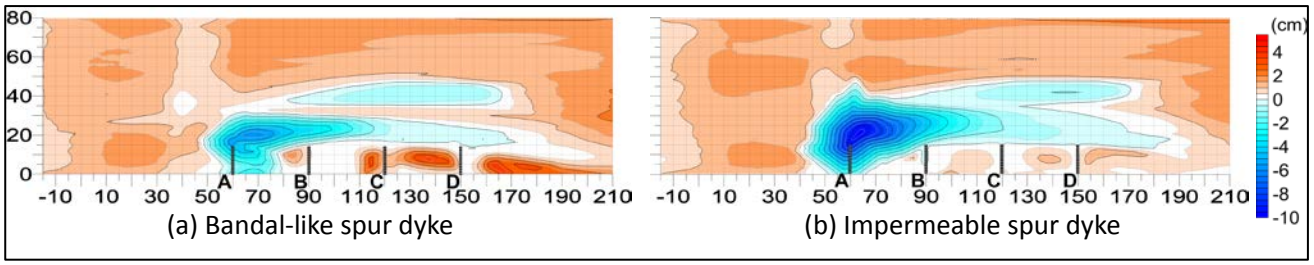


**Figure 3**. Simulation results of bed elevation around (a) Bandal-like and (b) Impermeable spur dykes, which have the same color scale as Figure 2(c).

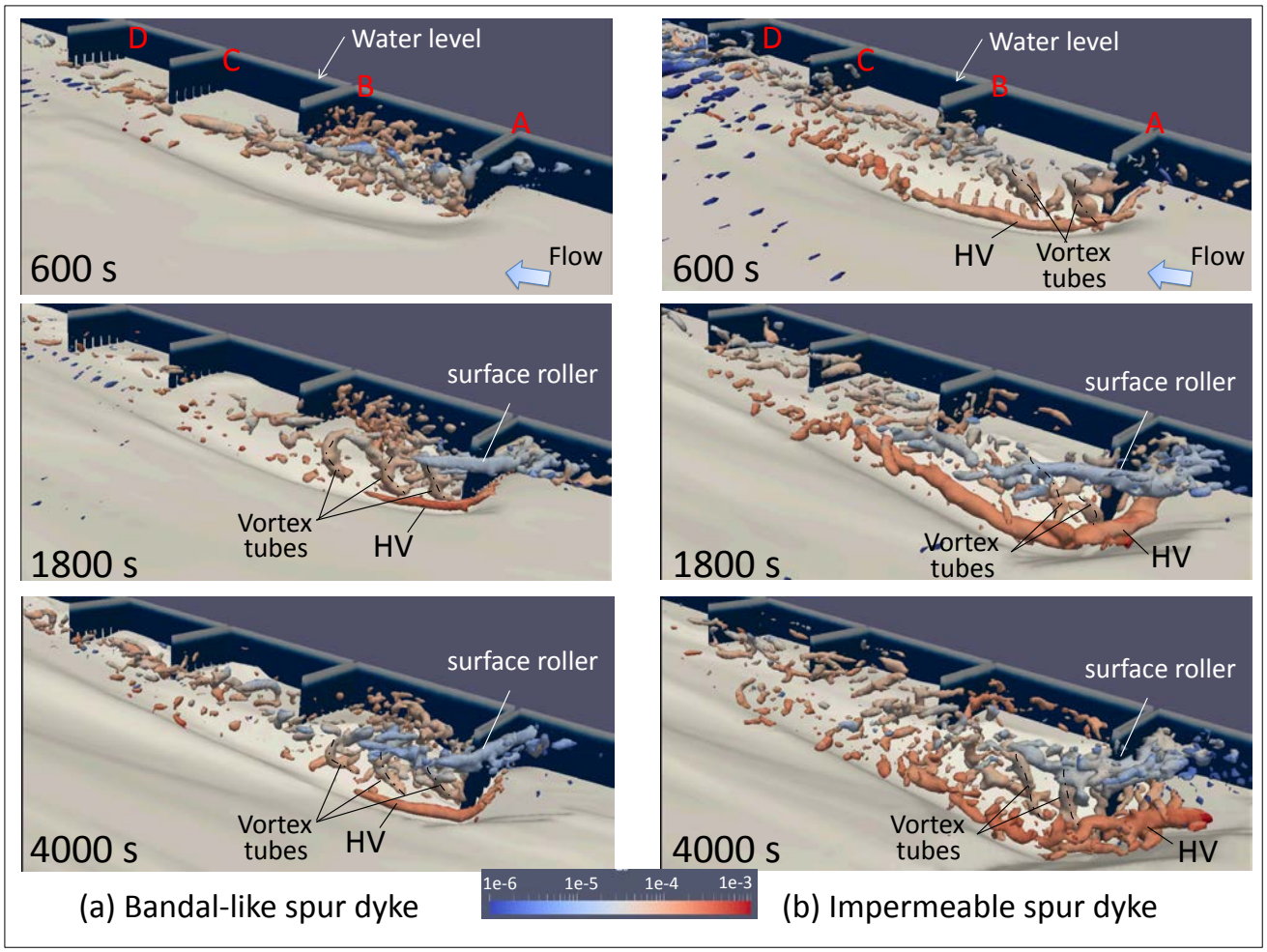


**Figure 4**.Visualization of vortical structure of the instantaneous flow for different elapsed times in numerical simulation of (a) Bandal-like and (b) impermeable spur dykes. The color in the isosurface shows the concentration of the suspended load. Water level is also shown at walls in each figure.

due to lower opened portion even if the bed load component is dominant. However, the maximum deposition heights between Bandal-like and impermeable spur dyke were comparable to the findings of Teraguchi et al. (2011), unlike the present study. Therefore, numerical results of the present work indicated that sediment deposition of the Bandal-like spur dyke is more enhanced in rivers with higher concentration of suspended load.

Figure 4 shows the vortical structure of the instantaneous flow for different elapsed times (600, 1800, and 400 s) in both spur dykes. In Figure 4, the isosurface is drawn by Q criterion (Dubief and Delcayre, 2000) which is the second invariant of the velocity gradient tensor and represents the vortex envelope. The color of the isosurface shows the concentration of the suspended load and warmer color represents higher sediment concentration. In the Bandal-like spur dyke, no clear coherent structure was observed in the early stage (600

 

s), but there were many small vortices between structures A and B. The small vortices are results of wall jet caused by the lower opened portion. Afterwards, the coherent structure develops around the structure A as follows: the HV, the vortex tubes appearing just behind the nose of structure A, and the surface roller appearing near water surface in front of the structure A. As shown at color of the isosurface in Figure 4, the HV has higher concentration of the suspended load and thus entrains bed sediment into suspension in both spur dykes. Most remarkable difference between Bandal-like and impermeable spur dykes is development of

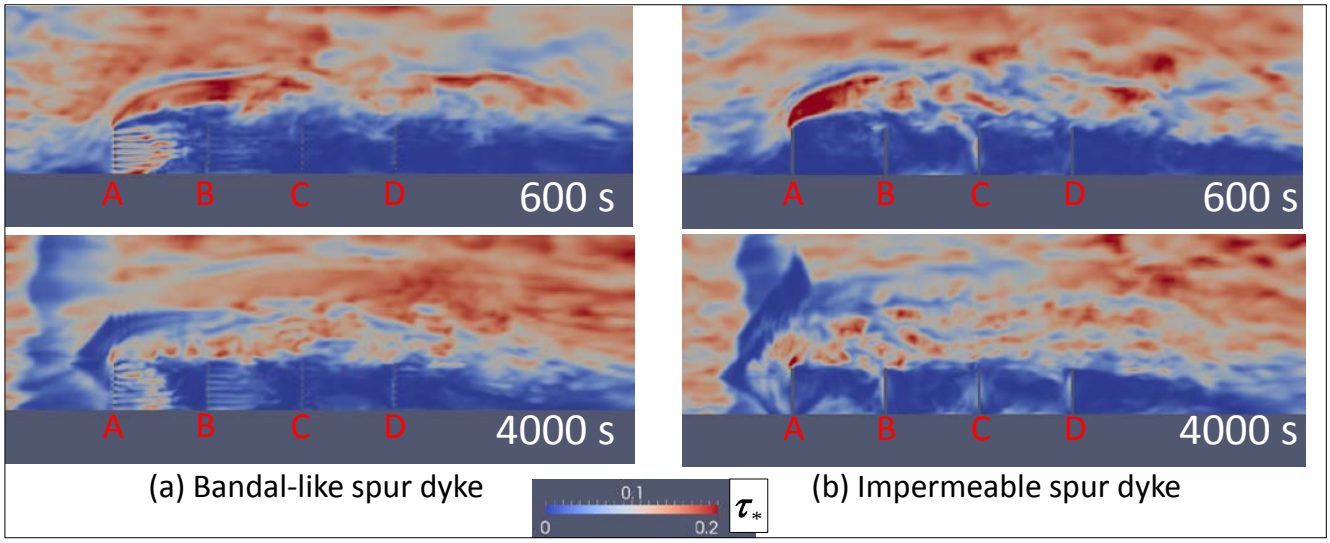


**Figure 5**.Instantaneous dimensionless bed shear stress $\tau_*$ around (a) the Bandal-like and (b) the impermeable spur dykes after 600 and 4000 s.

the HV that is a main cause of the scour development. The HV in the impermeable spur dykes begins to appear in the earlier time and becomes much larger than that in the Bandal-like spur dyke. In the Bandal-like spur dyke, the wall jet going through the structures A dissipates flow energy into small vortices instead of forming large scale HV. This mechanism significantly reduces the scour depth around the spur dyke located in the most upstream.

Koken and Constantinescu (2008a; 2008b) conducted numerical simulation using the LES around an impermeable spur dyke on the rigid flat bed and rigid scoured bed without coupling a sediment transport module. Koken and Constantinescu (2008b) showed that the vortex system becomes unstable and changes with time when the scour achieved equilibrium state. This situation is shown at Impermeable spur dyke after 4,000s in that the HV is not continuous. Furthermore, vortices exist between impermeable spur dykes A and B after 1,800 and 4,000s. This is due to the fluctuating vortex just behind the nose of the spur dyke, and this system conveys sediment into the behind impermeable spur dyke. It should be noted that the present simulation was conducted in relatively low **Re** (=9225) compared to 18,000 used in Koken and Constantinescu (2008a, 2008b). This is why, there is only one HV for both spur dykes in Figure 4, while two HVs were observed in Koken and Constantinescu (2008a, 2008b). Furthermore, simulation by Koken and Constantinescu (2008b) was conducted under the clear-water scour condition, while the present simulation was conducted under the live-ved scour condition. Thus, the numerical result of the coherent structure seen in 4,000s in Fig. 3(b) is more stable and continuous compared to Koken and Constantinescu (2008b).

Figure 5 shows the instantaneous dimensionless bed shear stress $\tau_*$ around the spur dykes after 600 and 4000s in (a) the Bandal-like and (b) the impermeable. The Bandal-like structure A in 600 s gives high $\tau_*$ in the main channel owing to separated flow that changes to the HV afterwards. Furthermore, the wall jet passing through the lower opened portion gives high bed shear stress behind the Bandal-like structure A. The bed shear stress behind the Bandal-like structure becomes less as the structure is located more downstream. The impermeable spur dyke in 600 s has the high $\tau_*$ around the nose of the spur dyke, and it greatly reduces in 4,000 s. It is worth noting that relatively large $\tau_*$ is distributed along the impermeable structures and the side wall in 4,000s compared to that in 600 s. The high $\tau_*$ is caused by the coherent vortex appearing just behind the impermeable spur dyke on the scoured bed owing to the fluctuating HV and vortex tubes (Koken and Constantinescu, 2008b). Such a bed shear stress is not observed on the region between the Bandal structures in spite of the existence of the fluctuating HV. This is because the wall jet passing through the lower opened portion makes the coherent vortex collapse.

To quantitatively evaluate the effect of the Bandal-like spur dyke on sediment deposition, budged of the suspended load in the regions surrounded by structures was evaluated as follows:

 

$$\Phi = \int_{Section} C_s \left( \overline{u_j} \cdot n_{Section,j} \right) ds \qquad [25]$$

where $\Phi$ is the volume of suspended load coming into and out of a region passing through the *Section* per unit time, and $n_{Section}$ is the normal unit vector of the computational face which belongs to the *Section*. That is, the Bandal-like spur dyke has two types of section (i.e., side and lower opened portion) to calculate $\Phi$, and the impermeable spur dyke has only side section. Figure 6 shows the results of $\Phi$ for each section in (a) the

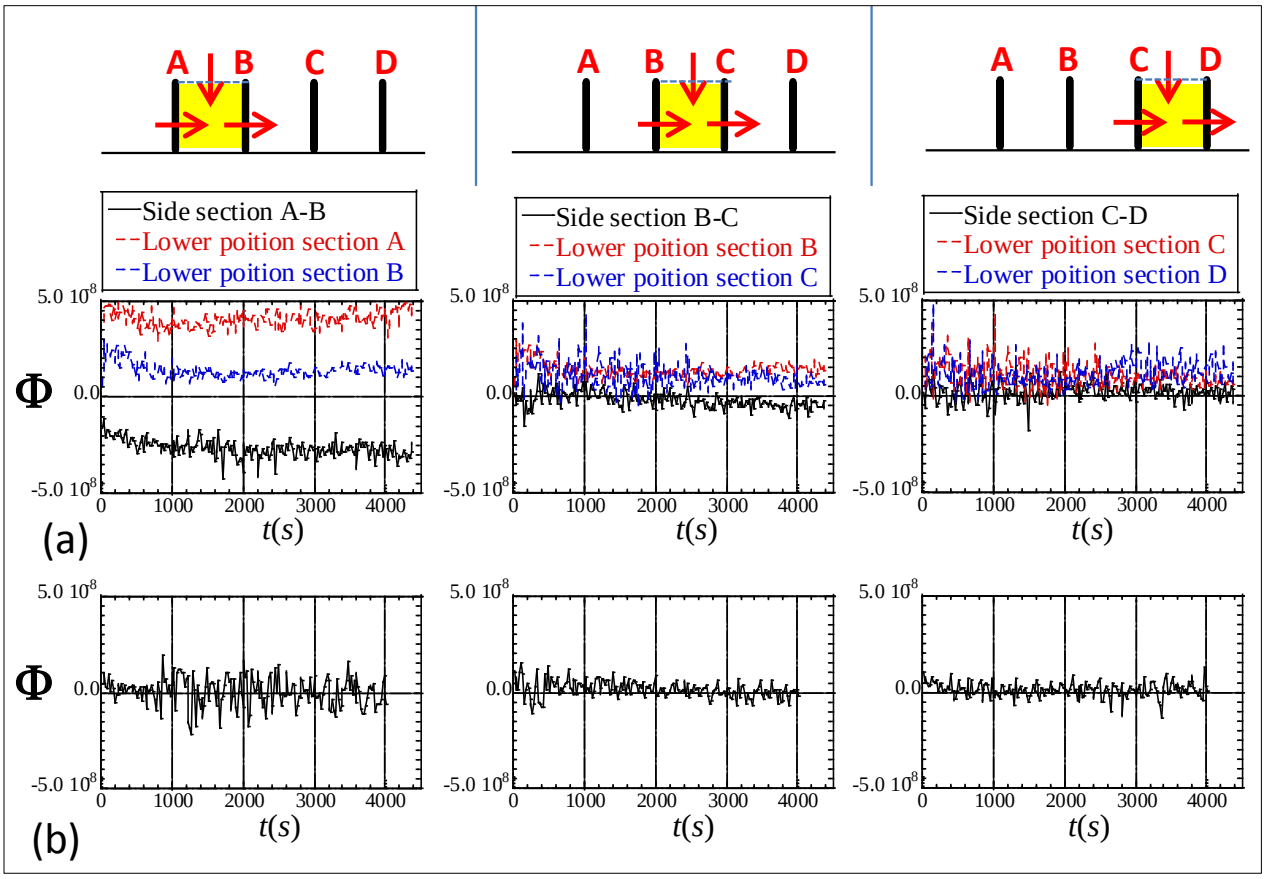


**Figure 6**. Volume of suspended load coming into and out of a region surrounded by (a) the Bandal-like and (b) the impermeable spur dykes, per unit time. The Bandal-like spur dykes have cross sections of the lower opened portion and side section, and the impermeable spur dyke has only the side section.

Bandal-like and (b) the impermeable spur dykes. In the region surrounded by the Bandal-like structures A and B (Left in Figure 6(a)), $\Phi$ for side section has negative value, which means that the suspended load partially goes towards the main channel due to the inverse pressure gradient caused by structure B. Both of lower portion sections A and B have positive values, and the A has larger $\Phi$ than the B. The results also indicates that approximately 50-70 % of suspended load leaves away the spur dyke and that the other passes though the structure B. Computed $\Phi$ at regions B-C and C-D in the Bandal-like spur dyke are similar (Middle and right in Figure 6(a)), and lower portion sections have higher $\Phi$ than side sections. These results indicate that lower opened portion has a dominant role in transportation of the suspended load in the Bandal-like structures. As shown in Figure 5(a), the bed shear stresses on the regions B-C and C-D are relatively low, which also contributes to facilitating deposition of suspended load. It is interesting to note that $\Phi$ obtained at the lower potion sections have similar value (i.e., approximately $10^{-8}$) except the section A. That is, the suspended load passing through the section B is conveyed to the downstream of the section D, as be partially settled in regions B-C and C-D during transportation. In the impermeable spur dyke, $\Phi$ fluctuates around zero and transportation of suspended load is obviously less active compared to the Bandal-like spur dyke. These results indicate that the lower opened portion plays a dominant role in facilitating sediment deposition behind the spur dyke. This mechanism gives a possible reason as to why the sediment is likely to deposit around the traditional Bandal-like structure in the field as observed in Figure 1(b). At the same time, the numerical results imply that design of the Bandal-like structure located in the most upstream is very important for the deposition effect on the downstream because the structure supplies suspended load to the downstream.

 

## 5 CONCLUSIONS

This study develops a simulation model consisting of the LES, VOF, and practical Eulerian-Larangian approach to resolve motion of flow and bed-material load around a permeable (i.e., Bandal-like) spur dyke. The simulation model well reproduces the scour and deposition around a Bandal-like spur dykes. In addition, the coherent structure and suspended load resolved in the present model reveal the advantage of the permeable structures adopted in traditional river works. A comparison with a previous experiment focusing on the bed load transport indicates that higher concentration of suspended load enhances the deposition effects appearing between the Bandal-like structures. In addition, energy dissipation at the lower opened portion interrupts formation of large scale horseshoe vortex that is responsible for scour development. The lower opened portion at the Bandal-like spur dykes plays a dominant a role in transporting highly concentrated suspended load to downstream and facilitating sediment deposition behind structures. This function is beneficial particularly for river bank regions facing the risk of bank erosion. Design of structures located in the most upstream is important because it supplies the suspended load to the downstream.

The present numerical model treats sediment as a porous media to allow for simulating bed deformation around a complicated shaped structure. It is worth noting that a permeable spur dyke is also able to be modeled as porous media in simulation, which allows for a more realistic modeling of the permeable spur dykes used in the field. This should be taken into account in future research.

## ACKNOWLEDGEMENTS

The authors wish to thank Kei Nishio (former Master's student in Kyoto Univ.) and Taku Hashizaki (Master's student in Kyoto Univ.) for their help in conducting the experiment.

## REFERENCES

Davies, A. G. (1995). Modeling Sediment-Turbulent Flow Interactions. *Applied Mechanic Review*, 48(9), 601-609.

Dubief, Y. & F. Delcayre (2000). On Coherent Vortex Identification Inturbulence. *Journal of Turbulence*, 1(1), 11.

Einstein, H. A. (1942). Formulas for the Transportation of Bed Load. *Transaction ASCE*, 2140, 561–597.

Koken, M. & Constantinescu, G. (2008a). An Investigation of the Flow and Scour Mechanisms around Isolated Spur Dikes in a Shallow Open Channel: 1. Conditions Corresponding to the Initiation of the Erosion and Deposition Process. *Water Resources Research*, 44(8), 1-19.

Koken, M. & Constantinescu, G. (2008b). An Investigation of the Flow and Scour Mechanisms around Isolated Spur Dikes in a Shallow Open Channel: 2. Conditions Corresponding to the Final Stages of the Erosion and Deposition Process. *Water resources research*, 44(8).

Nagata, N., Hosoda, T., Nakato, T. & Muramoto, Y. (2005).Three Dimensional Numerical Model for Flow and Bed Deformation Aroundriver Hydraulic Structures. *Journal of Hydraulic Engineering*, 131(12), 1074–1087.

Nakagawa, H., Tsujimoto, T. & Murakami, S. (1986). Non-Equilibrium Bed Load Transport Alongside Slope of an Alluvial Stream. *Proceeding 3rd Int.Symp.on River Sedimentation*, Univ. of Mississippi, Oxford, MS,885–893.

Nakagawa, H., Tsujimoto, T., Murakami, S. & Gotoh, H. (1990). Transition Mechanism from Saltation to Suspension in Bed-Material Load Transport. *Journal of Hydroscience Hydraulic Engineering*, 8(1), 41–54.

Nakagawa, H., Teraguchi, H., Kawaike, K., Yasuyuki, B. & Zhang, H. (2011). Analysis of Bed Variation around Bandal-like Structure, *Annuals Disas. Orev. Res. Inst., Kyoto Univ.*, 54B, 497-510.

Nakamura, T. & Mizutani, N. (2013). Sediment Transport Calculation Considering Laminar and Turbulent Resistance Forces due to Infiltration/Exfiltration and its Application to Tsunami-Induced Local Scouring. In *ASME 2013 32nd International Conference on Ocean, Offshore and Arctic Engineering*, 136(1), 1-9.

Nakayama, A. (2012). Large-Eddy Simulation Method for Flows in Rivers and Coasts Constructed on a Cartesian Grid System. *Memoirs of Construction Engineering Research Institute*, 54, 13-27.

Ota, K., Sato, T., Nakagawa, H. & Kawaike, K. (2016). Three-Dimensional Simulation of Local Scour around a Weir-Type Structure: Hybrid Euler-Lagrange Model for Bed-Material Load. *Journal of Hydraulic Engineering*, 143(4).

Sekine, M. (2004).Numerical Simulation Of Braided Stream Formation On The Basis Of Slope-Collapse Model. *Journal of Hydroscience Hydraulic Engineering*, 22(2), 1–10.

Shields Jr, F. D., Copeland, R. R., Klingeman, P. C., Doyle, M. W. & Simon, A. (2003). Design for Stream Restoration. *Journal of Hydraulic Engineering*, 129(8), 575-584.

Teraguchi, H., Nakagawa, H., Kawaike, K., Yasuyuki, B. A. B. A. & Zhang, H. (2011).Effects of Hydraulic Structures on River Morphological Processes. *International Journal Sed. Research*, 26(3), 283-303.

Zhang, H., Nakagawa, H., Baba, Y., Kawaike, K. & Teraguchi, H. (2010).Three-Dimensional Flow Around Bandal-Like Structures. *Journal of Hydraulic Engineering, JSCE*, 54, 175-180.

 

# STUDIES ON THE PATTERN OF BANK COLLAPSE-RETREAT OF ALLUVIAL RIVERS

YIN CHEN [(1)] & YAN-GUI WANG [(2)]

[(1,2)] International Research and Training Center on Erosion and Sedimentation, Beijing, China
iwhrchenyin@163.com;wangyg@iwhr.com

## ABSTRACT

In order to study and simulate the lateral evolution of alluvial river, the theories of riverbank erosion and stability are used to get the mode of riverbank scour-collapse-retreat (RSCRM) and the rate of riverbank collapse-retreat in this paper. Based on the mechanism of the riverbank collapse-retreat and the different scour process after the riverbank collapse into the water, this paper proposes three kinds of analysis modes, the RSCRM of sinking-slipping failure, the RSCRM of sinking-toppling failure and the RSCRM of falling failure. According to lateral erosion and bank collapse in riverbed evolution, this paper discusses the structure of formula for the average riverbank collapse-retreat rate of alluvial river, and analyzes the main factors that affect the channel collapse-retreat, which are the intensity of the water flow and the properties of the soil. In addition, the calculation method of relevant parameters for three kinds of analysis modes is proposed and tested with measured data from the Yangtze River.

**Keywords**: Collapse-retreat; lateral erosion rate; sinking-slipping failure; sinking-toppling failure; falling failure.

## 1 INTRODUCTION

The lateral evolution of river channel (bank failure) is a harmful natural disaster. Bank collapse is very serious in the middle and lower reaches of the Yangtze River (Wang et al., 2014), and the length of bank collapse account for about 42% of the total length of the river (Li et al., 2008). Many famous scholars have made deep study on the bank collapse by means of theoretical analysis, field observation, physical model experiments and numerical simulation (Thorne C R, 1981; ASCE, 1998; Motta et al., 2012; Henshaw et al., 2013; Deng et al., 2015;). For example, Osman (1988) established the analysis model of cohesive soil bank stability; Wang et al. (2007, 2014) proposed the critical conditions of different bank collapse; Dai et al. (2015) proposed the relationship between the mass of bank erosion, river pattern and bank height. In addition, many scholars (Xia et al., 2000; Darby et al., 2002; Zhong et al., 2008; Jia et al., 2010) established the numerical model to simulate the stability and lateral evolution of river bank. However, due to the complexity of the bank collapse, the studies mentioned above cannot fully explain the internal mechanism, especially the quantitative analysis of the lateral collapse of the riverbank. Based on previous studies, the process of riverbank collapse-retreat is divided into riverbed scouring and riverbank collapse in this paper, and the model and rate of bank collapse-retreat are studied by the theories of caving mechanism and bank stability. The research results are of important values and significances in the analysis of the lateral evolution of the river.

## 2 THE MECHANISM AND PROCESS OF BANK COLLAPSE IN ALLUVIAL RIVERS

Bank collapse of alluvial rivers mainly includes sliding failure, sinking failure and falling failure. The three types of failure have their own unique processes and characteristics, and the corresponding bank collapse process has some differences.

### 2.1 Sliding failure

The mechanical mechanism of sliding collapse is that the sliding moment of the collapse mass is larger than that of anti-sliding moment of soil, and the collapse surface is a curved surface. In addition, the collapse mass volume is generally larger. After the occurrence of collapses, the collapsed body is slowly sliding into the river. If the collapsed mass is small or the river is deep, the collapsed mass will be submerged and form the accumulation body in the river. Then the collapsed soil will be gradually washed away until the next collapse begins. If the slump body is large or the water is shallow, when the slump body slides into the river, only the lower part is submerged and it will be subjected to scour by water flow. When the collapse mass is washed to a certain extent, the upper part of collapsed soil will continue to decline to produce failure. Then the collapsed soil continues to be washed until it is completely washed away.

### 2.2 Sinking failure

The mechanical mechanism of sinking collapse is that the down force is larger than that of resistance forces of collapsed mass due to serious scour of river bed. The failure surface is plane for sinking collapse,

 

and the volume of collapsed mass is slightly smaller than that of the sliding collapse, as shown in Figure 1. Therefore, the critical state of sinking failure can be determined by the critical height of riverbank, which is called the critical scour height of bank (CSHB). For linear slope, Wang et al. (2007) calculated the CSHB of sinking failure by studying the mechanism of collapse:

$$H_{cr} = \frac{S_t}{S_{\Theta\theta} S_\Theta} + \sqrt{\left(\frac{S_t}{S_{\Theta\theta} S_\Theta}\right)^2 - \frac{2 S_t H' - S_{\Theta\theta} S_A}{S_{\Theta\theta} S_\Theta}} \quad [1]$$

$$S_{\Theta\theta} = \frac{1}{2} - \frac{\cos(2\Theta - \theta)}{2\cos\theta}, S_\Theta = \frac{1}{\tan\Theta}, S_A = \frac{H^2 - H'^2}{2\tan\theta} \quad [2]$$

$$H' = \frac{2c \cdot \tan\left(45^0 + \theta/2\right)}{\gamma_s} \quad [3]$$

where, $H_{cr}$ is the CSHB; $S_t$=c/$\gamma_s$; $c$ is the cohesion; $\gamma_s$ is the bulk density; $\theta$ is the internal friction angle; $\Theta$ is the slope of riverbank; $H$ is the height of the bank; $H'$ is the crack depth at the top of cohesive bank; Other parameters are shown in Figure 1(a).

Sinking collapse mainly includes sinking–sliding collapse and sinking–topping collapse. The process and characteristics of sinking–sliding collapse are similar to the sliding failure. When the failure surface is approximated as a plane, sliding failure process can also be analyzed as sinking failure. However, sinking-topping collapsed soil will topple down the river and form a stacked body underwater.

2.3 Falling failure

The caving erosion at the bottom of bank will result in the upper part soil in the suspended state, and when the caving erosion width is larger than the critical value, falling failure will occur, as shown in Figure 1 (b). When lateral erosion leads the river bank to destruction state, the caving erosion width is called the critical caving erosion width (CCEW). For linear slope, the CCEW for falling failure is (Wang, et al. 2014):

$$B_{cr} = \frac{2S_t(H - H')}{H + H_2} + \frac{H_1^2}{(H + H_2)\tan\Theta_1} + \frac{H_2^2 - H_1^2}{(H + H_2)\tan\Theta_2} \quad [4]$$

where $B_{cr}$ is CCEW.

Falling failure mainly includes shear-falling failure and toppling-falling failure. If the weight is greater than the shear strength for the soil which in the suspended state, the soil block will slide down along the vertical section to form shear-falling failure. If the gravity moment for soil body which in the suspended state is greater than the tension moment for the clay layer, toppling-falling failure will occur.

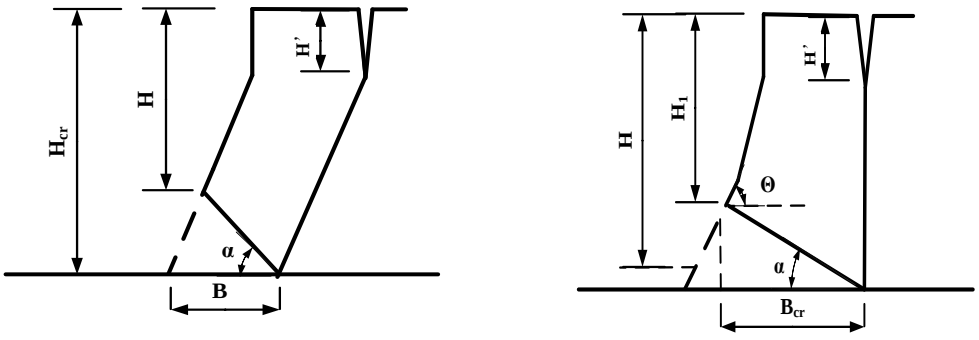


(a) sinking failure (b) falling failure

**Figure 1.** The schematic diagram of bank collapse.

2.4 Collapse into the river and scouring process of collapsed mass

For different types of bank collapse, collapsed mass slips into or topple down the river when collapse occurs. Then the collapsed soil is gradually washed away by water flow. Slipping-collapsed body and topping-collapsed body have different scour processes, respectively. The main features are described below.

 

(i) Scour process of collapsed soil for slipping failure.
Collapsed mass that slides into the river cannot be completely submerged by water because of its large volume. The upper part of the collapsed mass is exposed above the water surface and lies against the riverbank, but the lower part is soaked in the water and eroded by water constantly. Erosion makes the collapsed mass slides continuously until it is washed away completely.

(ii) Scour process of collapsed soil for toppling failure.

As the width of sinking and topping collapsed body are relatively small, collapsed soil topple down the river will be submerged directly and eroded constantly until it is washed away completely. Even the new bank base will be eroded, resulting in continuous bank collapse.

## 3 ANALYSIS OF RIVERBANK SCOUR-COLLAPSE-RETREAT MODE (RSCRM)

Combined with the scour process of collapsed soil after the riverbank failure, the mode analysis of riverbank collapse-retreat can be summarized as the following three cases: the RSCRM of sinking-slipping failure; the RSCRM of sinking-toppling failure and the RSCRM of falling failure.

### 3.1 The RSCRM of sinking-slipping failure

In general, the sinking-slipping collapsed mass slides into the river. As the height of riverbank is much larger than the river depth, the upper part of collapsed mass is not submerged after the collapse of river bank, as shown in Figure 2 ($c_1$). The lower part of the collapsed mass is soaked and washed by water, resulting in collapsed soil sliding into the river continuously until it is washed away. Then the new bank failure will be formed, resulting in continued bank collapse-retreat. If the collapsed mass volume is relatively small, it will be soaked and washed by water after the collapse has occurred, as shown in Figure 2 ($c_2$). The process of the riverbank scour-collapse-retreat can be summarized as: river bed was severely washed → riverbank loses stability and collapsed → collapsed mass slides into the water → collapsed mass scoured by water and slides into the water gradually → collapsed mass washed away completely→ go to the next cycle. This is the RSCRM of sinking-slipping failure, as shown in Figure 2.

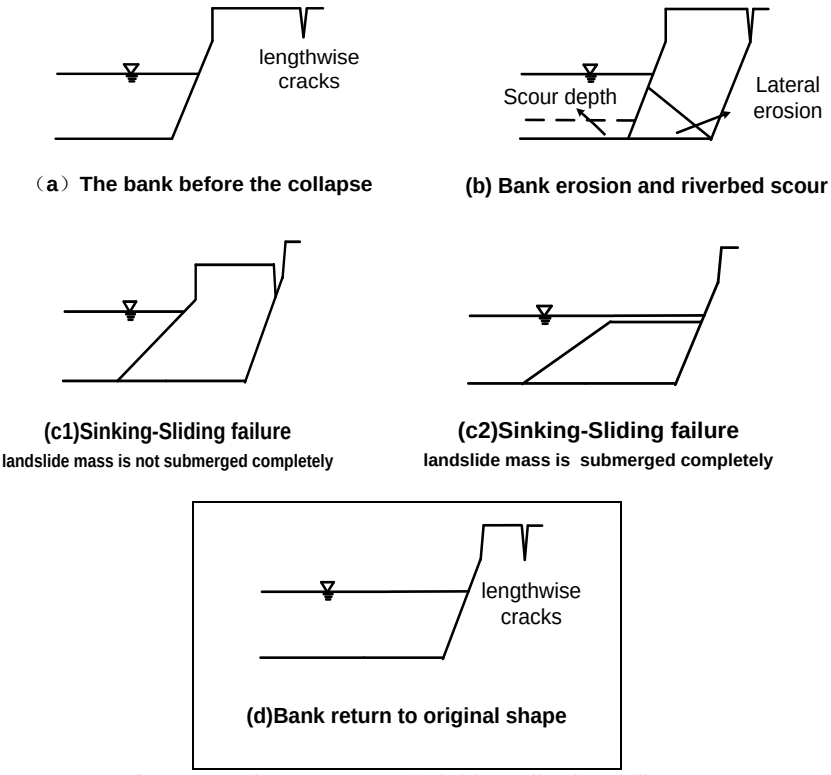


**Figure 2.** The RSCRM of sinking-slipping failure.

### 3.2 The RSCRM of sinking-toppling failure

The collapsed body slides into the river if the sinking failure occurs, but it may also topple over the river sometimes. As the riverbank width of sinking failure is relatively small, the collapsed body that has toppled over the river will be submerged generally. Furthermore, collapsed soil will be scoured continuously until it is washed away. Then the new riverbank failure will be formed, resulting in the continued bank collapse-retreat. The process of the riverbank scour-collapse-retreat can be summarized as: river bed was severely washed

 

→riverbank loses stability and collapses→ collapsed body topples over the river→ collapsed body eroded gradually and washed away→ go to the next cycle. This is the RSCRM of sinking- toppling failure, as shown in Figure 3.

3.3 The RSCRM of falling failure

Because the riverbank width of falling failure is generally small, collapsed mass will be submerged basically no matter what kinds of falling failure occurs. Then the collapsed soil will be scoured continuously until it is washed away, resulting in riverbank failure and continued bank collapse-retreat. The process of the riverbank scour-collapse-retreat can be summarized as: bank base suffers lateral scour→ riverbank loses stability and falling failure occurrs→ collapsed soil falls into the river→ collapsed body eroded gradually and washed away→ go to the next cycle. This is the RSCRM of falling failure, as shown in Figure 4.

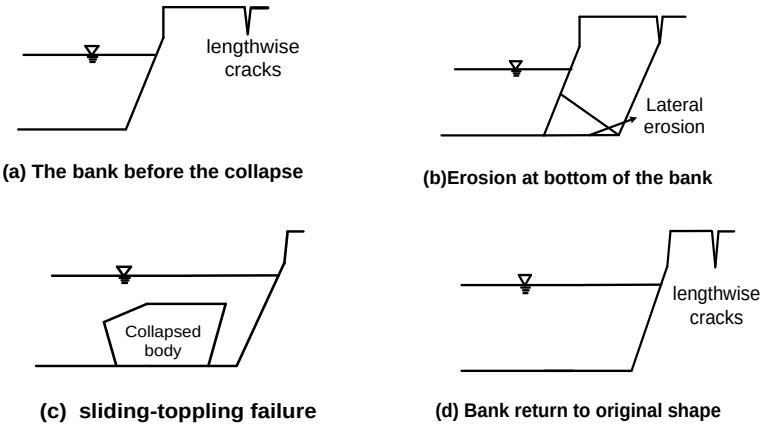


**Figure 3.** The RSCRM of sinking-toppling failure.

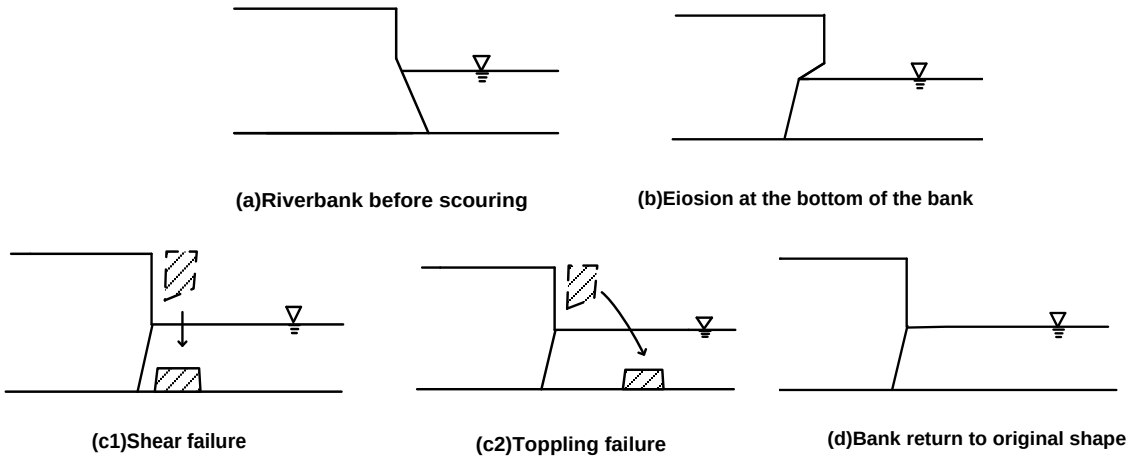


**Figure 4.** The RSCRM of falling failure.

In order to understand the three kinds of models intuitively and thoroughly, combined with the results of previous analysis, the riverbank scour-collapse-retreat model is shown in Figure 5:

 

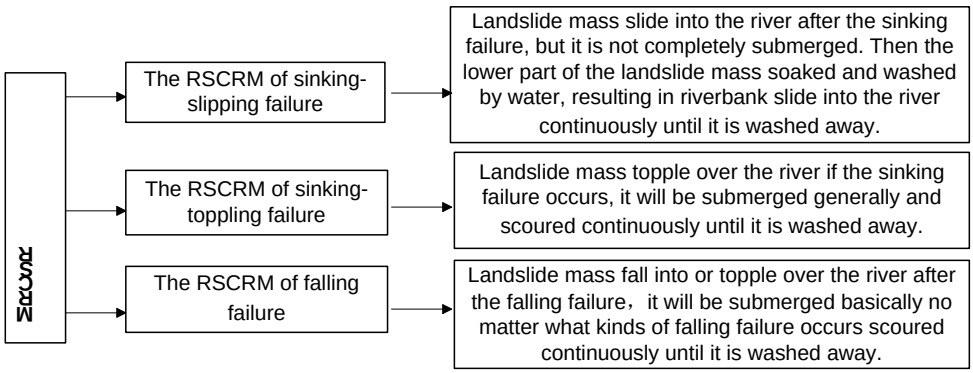


**Figure 5.** The RSCRM of falling failure.

## 4 CALCULATION MODE OF AVERAGE RIVERBANK COLLAPSE-RETREAT RATE OF ALLUVIAL RIVER

The rate of riverbank collapse-retreat is the width of bank retreat at unit interval, and it is equal to the ratio of the distance of bank retreat to the time of collapse process. The lateral widening of alluvial rivers mainly comprises two aspects: Firstly, lateral widening caused by the lateral erosion. When the shear stress of near shore currents is greater than the critical shear stress of soil mass, sediment on the riverbank will be taken away by water, leading to riverbank widening. Secondly, bank collapse resulted in the widening. When the sliding force of riverbank soil is greater than its anti-sliding force, it will be unstable and collapses, resulting in lateral widening. The width and time of the two processes were calculated respectively, and the average collapse rate will be obtained.

### 4.1 Calculation mode

#### 4.1.1 The process of lateral erosion

The lateral erosion of riverbank, especially erosion at bottom of bank base, will cause bank failure. On one hand, the lateral erosion depends on the relationship between the intensity of water which can be measured by shear stress and the riverbank erosion-resisting capacity which can be measured by the critical shear stress of soil. The greater the water intensity, the greater the lateral erosion rate is. On the other hand, it also has a certain relationship with the water depth. Taking into account the principle of factor harmony, the lateral erosion rate of bank ($V_{le}$) can be expressed as follows (HookeJ.M.,1979):

$$V_{le} = (\frac{dB}{dt})_{le} = K_1 \frac{\tau_l - \tau_c}{\tau_b} \sqrt{gH} \quad [5]$$

where $\tau_l$ is the shear stress of near shore currents, N/m$^2$; $\tau_c$ is the critical shear stress of the bank soil, N/m$^2$; $K_1$ is a constant. $\tau_b$ is the shear stress of riverbed.

The corresponding lateral erosion width of riverbank ($\Delta B_{le}$) is

$$\Delta B_{le} = V_{le} T_{le} \quad [6]$$

where $T_{le}$ is lateral erosion time of riverbank.

#### 4.1.2 The process of riverbank collapse

The stability of bank collapse depends on the geometric shape (the slope of riverbank and the height of the bank) and the nature of the soil (volumetric weight, the cohesion, the friction angle) of the riverbank. Taking into account the principle of factor harmony, the average collapse rate of bank can be expressed as follows (HookeJ.M.,1979):

$$V_{fc} = (\frac{dB}{dt})_{fc} = K_2 \frac{\gamma_s H}{c} \frac{\tan\Theta}{\tan\theta} \sqrt{gH} = K_2 \frac{\sqrt{gH}}{N} \quad [7]$$

$$N = \frac{c}{\gamma_s H} \frac{tan\,\theta}{tan\,\Theta} \quad [8]$$

 

where $N$ is the number of bank stabilization (Ponce V.M., 1978), $K_2$ is a constant.

In addition, the average collapse-retreat rate of riverbank can also be estimated according to the model of riverbank scour-collapse-retreat. The longitudinal scour of riverbed and the lateral erosion of riverbank will lead to the bank failure. Therefore, it is possible to determine the bank collapse width by using the critical height of riverbank or the critical caving erosion width of bank failure. In addition, the time that the collapse mass is washed completely can be determined by considering the riverbed scour after collapse mass slides into the river. Thereby, the bank average collapse rate is

$$V_{fc} = \frac{B_{fc}}{T_{fc}} \qquad [9]$$

where $B_{fc}$ is the bank collapse width; $T_{fc}$ is the time that the collapse mass is washed completely.

4.1.3 Average collapse-retreat rate of riverbank

Therefore, the average collapse-retreat rate of riverbank can be calculated by the following formula:

$$V_{bf} = V_{le} + V_{fc} = K_1 \frac{\tau_l - \tau_c}{\tau_b}\sqrt{gH} + K_2 \frac{\sqrt{gH}}{N} \qquad [10\text{-a}]$$

$$V_{bf} = \frac{\Delta B_{le} + B_{fc}}{T_{le} + T_{fc}} = \frac{V_{le}T_{le} + V_{fc}T_{fc}}{T_{le} + T_{fc}} \qquad [10\text{-b}]$$

The formula of bank collapse-retreat rate reflects two aspects, one is that the influence factors of bank collapse-retreat rate are various, mainly include water flow intensity, the soil composition, soil distribution and slope angle of bank etc. The formula indicates that the bank collapse-retreat rate is proportional to flow intensity and the depth of water, but inversely proportional to the number of bank stabilization. Another is that the bank collapse-retreat includes lateral erosion retreat and collapses retreat. The first part of the formula is the function of lateral erosion, and the second part is the influence of river bank collapse.

4.2 Calculation process of different collapse-retreat mode

According to the characteristics of RSCRM proposed in this paper, the calculation process of different types of collapse-retreat rates can be obtained by combining with the calculation method of the average riverbank widening rate. The calculation parameters are shown in Table 1, and the detailed process is as follows:

4.3.1 The RSCRM of sinking-slipping failure

The collapse-retreat process includes the stage of sinking failure and the stage of scour after collapsed mass slides into river. The former is essentially the longitudinal erosion and lateral scouring of the river bank, and the latter refers to the collapsed block sliding into the water gradually in the lateral erosion of water after the bank collapse has occurred, and eventually washed away by water flow. Therefore, the calculation of collapse-retreat rate of sinking-slipping failure requires parameters such as lateral-scouring time before riverbank collapses, the width of riverbank collapse, and the time that collapse mass gradually slides into the water and washed away by water flow.

**Table 1.** Calculation Parameters of the riverbank collapse-retreat rate.

| TYPE | | SINKING-SLIPPING FAILURE | | SINKING-TOPPLING FAILURE | FALLING FAILURE |
|---|---|---|---|---|---|
| | | COLLAPSED BODY NOT SUBMERGED COMPLETELY BY WATER | COLLAPSED BODY SUBMERGED COMPLETELY BY WATER | | |
| LATERAL EROSION | TIME $T_{le}$ | The time that riverbed scour makes the bank reaches the critical state（CSHB） | | | The time that lateral erosion makes the bank reaches the critical state（CCEW） |
| | WIDTH $\Delta B_{le}$ | $\Delta B_{le} = V_{le} \times T_{le}$ | | | It can be obtained by using CCEW and the geometry of the bank |

 

| | | | |
|---|---|---|---|
| **BANK FAILURE** | **TIME** $T_{fc}$ | The time that collapsed body is washed away by water flow (lateral erosion and riverbed scour) | The time that collapsed soil is washed away by water flow (riverbed scour) |
| | **WIDTH** $B_{fc}$ | | CCEW |

4.3.2 The RSCRM of sinking-toppling failure

The process and mechanism of the model of sinking-toppling failure are the same as sinking-slipping failure for the stage of the collapsed mass. However, the process of scour after the bank has collapsed of sinking-toppling failure is very different from sinking-slipping failure. The main aspect is that collapsed soil no longer slides into river but topples down the river when the collapse occurs. Collapsed body will be submerged after topple over the river because the width of it is not great, and it will be washed away by riverbed scour directly.

4.3.3 The RSCRM of falling failure

In general, the soil volume of falling failure is relatively small, so the collapsed mass falling into the river will be submerged completely. However, the soil thickness that used to scour in water of falling collapse is different for toppling failure and shear failure. And the thickness of shear failure is the height of the body, while the thickness of toppling failure is the critical caving erosion width. The time required for this process is related to the intensity of water flow and the volume of collapsed body, which can be calculated as the ratio of collapsed body thickness to riverbed scour rate.

4.3 Test of the calculation mode for collapse-retreat rate

The calculation process of the collapse-retreat model in this paper was very complicated, and it was difficult to obtain all the parameters from the measured data. Therefore, the mode was simplified reasonably and used to test the falling collapse-retreat with measured data from the Yangtze River (Hu et al., 2016). Given space limitations, this paper only provided the final results, as shown in Table 2.

**Table 2.** Calculation results of the riverbank collapse-retreat.

| **COLLAPSE** | **SHEAR FAILURE** | | | **TOPPLING FAILURE** | | | **AVERAGE** |
|---|---|---|---|---|---|---|---|
| **PARAMETER** | $B_{cr}$m | $V_{bf}$ m/s | collapse-retreat distance m/a | $B_{cr}$ m | $V_{bf}$ m/s | collapse-retreat distance m/a | collapse-retreat distance m/a |
| **VALUE** | 0.2 | $3.6\times10^{-7}$ | 11.3 | 1.37 | 8.9×10-7 | 27.6 | 19.45 |

In practical river bed evolution, the two types of falling failures are widespread generally. The average value of two kinds of bank collapse-retreat distance is 19.45m/a, which is close to the average annual collapse distance of 15m/a at Sima Bend of Jiangdu in the Yangtze River (Hu et al., 2016). This shows that the calculation mode of the collapse-retreat rate is consistent with the actual situation. In view of the few measured data, this paper is only a research idea, and related topics should be studied further.

## 5 CONCLUSIONS

Based on the mechanism of riverbank collapse, and combined with the scouring effect after collapse, riverbank scour-collapse-retreat mode of alluvial rivers has been studied preliminarily in this paper. The main conclusions are:

(1) According to the classification of bank collapse and the scour process of collapsed mass after the riverbank failure, analysis modes of riverbank collapse-retreat can be summarized as three cases, which are the RSCRM of sinking-slipping failure, the RSCRM of sinking-toppling failure and the RSCRM of falling failure.

(2) There are some differences among the three modes, but the lateral widening of alluvial rivers can be divided into lateral erosion and bank collapse. Moreover, the calculation mode of average collapse-retreat rate of alluvial rivers is proposed and tested with measured data from the Yangtze River.

(3) Combined with the mode of average collapse-retreat rate of alluvial rivers, the main factors influencing the bank collapse are analyzed, such as the intensity of water flow and bank soil property. The higher the river banks, the smaller the cohesive force of soil and the greater the flow intensity are, the greater the bank collapse-retreat rate will be.

 

**ACKNOWLEDGMENTS**

The research is supported by the National Natural Science Foundation of China (51679259) and National Natural Science Foundation of China (51179208).

**REFERENCES**

ASCE. (1998). Task Committee on Hydraulic, Bank Mechanics and Modeling of Riverbank Width Adjustment. River Width Adjustment I: Processes and Mechanisms. *Journal of Hydraulic Engineering*, 124(9), 881-902.

Dai, J.B., Liu, H.Y. & Dai, H.L. (2015). Field Monitoring and Evaluate Study on Bank Erosion in the Ningxia-Inner Mongolia reaches of the Yellow River. *Journal of Sediment Research,* 5, 63-68. (In Chinese)

Darby, S.E., Alabyan, A.M. & Wiel, M.J.V.D. (2002). Numerical Simulation of Bank Erosion and Channel Migration in Meandering Rivers. *Water Resources Research*, 38(9), 2-1.

Deng, S.S., Xia J.Q., Jie, L.I. & Zhou M.R. (2015). Influence of the Variation of in Channel Water Levels on the Riverbank Stability in the Upper Jingjiang Reach. *Journal of Hydraulic*, 46(7), 844-852. (In Chinese)

Hooke, J.M. (1979). An Analysis of the Processes of River Bank Erosion. *Journal of Hydrology*, 42(1), 39-62.

Henshaw, A.J., Thorne, C.R. & Clifford, N.J. (2013). Identifying Causes and Controls of River Bank Erosion in a British Upland Catchment. *Catena*,100(2), 107-119.

Hu, X.Y., Yao, B.K. & Zhu, C.K. (2016). Formation Mechanism and Prevention Strategies of Bank Collapsingat Sima Bend of Jiangdu in the Yangtze River. *Journal of Geology*, 40(2), 357-362. (In Chinese)

Jia. D., Shao X., Wang H. & Zhou, G. (2010). Three Dimensional Modeling of Bank Erosion and Morphological Changes in the Shi-Shou Bend of the Middle Yangtze River. *Advances in Water Resources*, 33(3), 348-360.

Li, L.G. (2008). Statistics of Bank Collapse and Existing Problems in the Middle and Lower reaches of Yangtze River. *Express Water Resources & Hydropower Information*. 28(2), 11-12. (In Chinese)

Motta, D., Abad, J.D., Langendoen, E.J. & Garcia, M.H. (2012). A Simplified 2d Model for Meander Migration with physically based Bank Evolution. *Geomorphology*, 163–164(4), 10-25.

Osman, A.M. & Thorne, C.R. (1988). Riverbank Stability Analysis, i: Theory. *Journal of Hydraulic Engineering*, 114(2), 134-150.

Ponce, V.M. (1978). Generalized Stability Analysis of Channel Banks. *Journal of the Irrigation & Drainage Division*, 104(4), 343-350.

Thorne, C.R. & Tovey, N.K. (1981). Stability of Composite Riverbanks. *Earth Surface Processes and Landforms*, 6, 469-484.

Wang, Y.G. & Kuang S.F. (2007). Critical Height of Bank Collapse. *Journal of Hydraulic*, 38(10), 1158-1165. (In Chinese)

Wang, Y.G. & Kuang, S.F. (2014). Study on Collapse Mechanism and Critical Caving Erosion Width of Falling Failures in Typical Structure Bank. *Journal of Hydraulic*, 45(007), 767-775. (In Chinese)

Xia, J.Q., Yuan, X. & Wang, G.Q. (2000). Preliminary Simulation of Channel Lateral Widenning in Degradation of Alluvial Rivers. *Journal of Sediment Research*, 6, 16-24. (In Chinese)

Zhong, D.Y., Yang, M. & Ding, Y. (2008). Numerical Simulation of Lateral Evolution of the Lower Yellow River. *Yellow River*, 30(11), 107-109. (In Chinese)

 

# MORPHOLOGICAL SCALE EXPERIMENTS TO LINK RIVER BED STRUCTURE WITH RIVERINE VEGETATION

JÜRGEN STAMM[(1)], NADINE MÜLLER[(2)] & SARAH-CHRISTIN MIETZ[(3)]

[(1,2,3)]University of Technology Dresden, Institute of Hydraulic Engineering and Technical Hydromechanics,
01062 Dresden, Germany
Juergen.Stamm@tu-dresden.de, Nadine_Mueller@tu-dresden.de, Sarah-Christin.Mietz@tu-dresden.de

## ABSTRACT

Most of the rivers in Germany and the EU are still missing the good ecological status (BMU, 2010). Severe reasons are the deviancies in the hydro-morphological status. Generally, this could be improved by the use of vegetation along the river, knowing that it may also affect the flood water table. Vegetation not only has fundamental ecological functions in the fluvial environment, but it also affects the flow pattern, bed-shear stress and hence local sediment deposition, which links back to habitat characteristics. Therefore, a joint research project of university institutes with professional focusing on hydraulic engineering, morphology and hydrobiology, together with administration and engineering consultants in the field of environmental planning, is established with the aim to improve the ecological and flood risk status with simultaneous increase in the level of acceptance by the public when flood risk management is systematically combined with environmental protection goals. The objective of this part of the joint-project is to investigate river bed structures due to the influence of riparian vegetation. This paper reviews the current state and includes investigation of parameters in the morphological scale experiments.

**Keywords:** Morphodynamics; physical model; riverbed structure; sediment transport; vegetated channel.

## 1 INTRODUCTION

Most of the rivers in Germany and the EU are still missing the good ecological status (BMU, 2010; EEA, 2012), although the first period of target achievement of the European Water Framework Directive (EU-WFD, 2000) ended in 2015. Furthermore, between 1995 and 2013, several devastating floods occurred in Europe (Kron, 2015) which underlined the urgent need for improved flood risk management and contributed to an inherent conflict potential for suitable measures.

In the joint research project “In_StröHmunG” (Innovative systems solutions for transdisciplinary and regional ecological flood risk management and natural watercourse development), which is funded by the German Ministry of Education and Research, flood prevention and natural watershed management shall be interconnected (Stamm & Müller, 2015). The goal of the joint research project is to develop instruments in order to achieve the goals of both EU directives: The European Water Framework Directive and the European Floods Directive (EU-FD, 2007) on the assessment and management of flood risks.

In total, seven partners are linked in this project. University institutes with professional focusing on hydraulic engineering, morphology and hydrobiology are equally involved as administration and practical partners of an environmental and a planning agency as well as partners with economical background. The aim of this research is to improve the ecological and flood risk status for several reference watercourses and to increase the level of acceptance by the public when flood risk management is systematically combined with environmental protection goals.

The project is subdivided into four sub-projects: (1) morphology, (2) ecology, (3) implementation and (4) the scientific and administrative project management. The findings of the applied research will be transferred and implemented to selected reference rivers in different model regions (Figure 1). These German rivers reflect the challenges which are typical for numerous rivers due to realization and minimization of trade-offs of both EU directives; all of them fail the good ecological status:

- Mortelbach and Eulitzbach (Saxony, cities of Waldheim and Roßwein, Kriebstein),
- Mutzschener Wasser and Launzige (Saxony, cities of Grimma, Trebsen and Colditz),
- Zwönitz river near Chemnitz (Saxony, district of Einsiedel),
- Allerriver near Celle (Saxony-Anhalt).

In the first sub-project, three different morphological flume experiments are used. Whereas the small rivers (second order rivers) are object of investigation in an experiment at the Technical University in Dresden, a bigger river of first order and a branch is modelled in the laboratory of the Magdeburg-Stendal University of Applied Sciences and investigations of depositions along streams, especially as it appears on the waterway Elbe, are conducted at the Technical University of Braunschweig (Branß & Dittrich, 2016; Branß et al., 2016). All experiments pursue the development of fundamental knowledge about the interaction of hydraulic,

 

vegetation and sediment to enable suggestions for an ecological but also flood oriented watershed management.

The ecology sub-project deals with the effect of bioengineering and stream restoration measures on the quality components of the WFD and the ecological status of the rivers. The hydro-morphology of rivers and their anthropogenic changes have a direct influence on the constitution of fish zoonosis and macrozoobenthos communities. Up to now, measures to improve the structure of rivers have shown only moderate results (Haase et al., 2013). To expand the knowledge about the impact and the need of measures, an extensive sampling of probes of macrozoobenthos and fish has been conducted in the model regions and is still ongoing. Furthermore, the sampling has been extended to probes of the sediment to validate the morphological experiments for small rivers. In addition, research will be done to assess the potential of new settlement of macrozoobenthos and fish in the downgraded rivers. Finally, predictions about the spatiotemporal effectiveness of hydro-morphological improvements in the rivers shall be enabled.

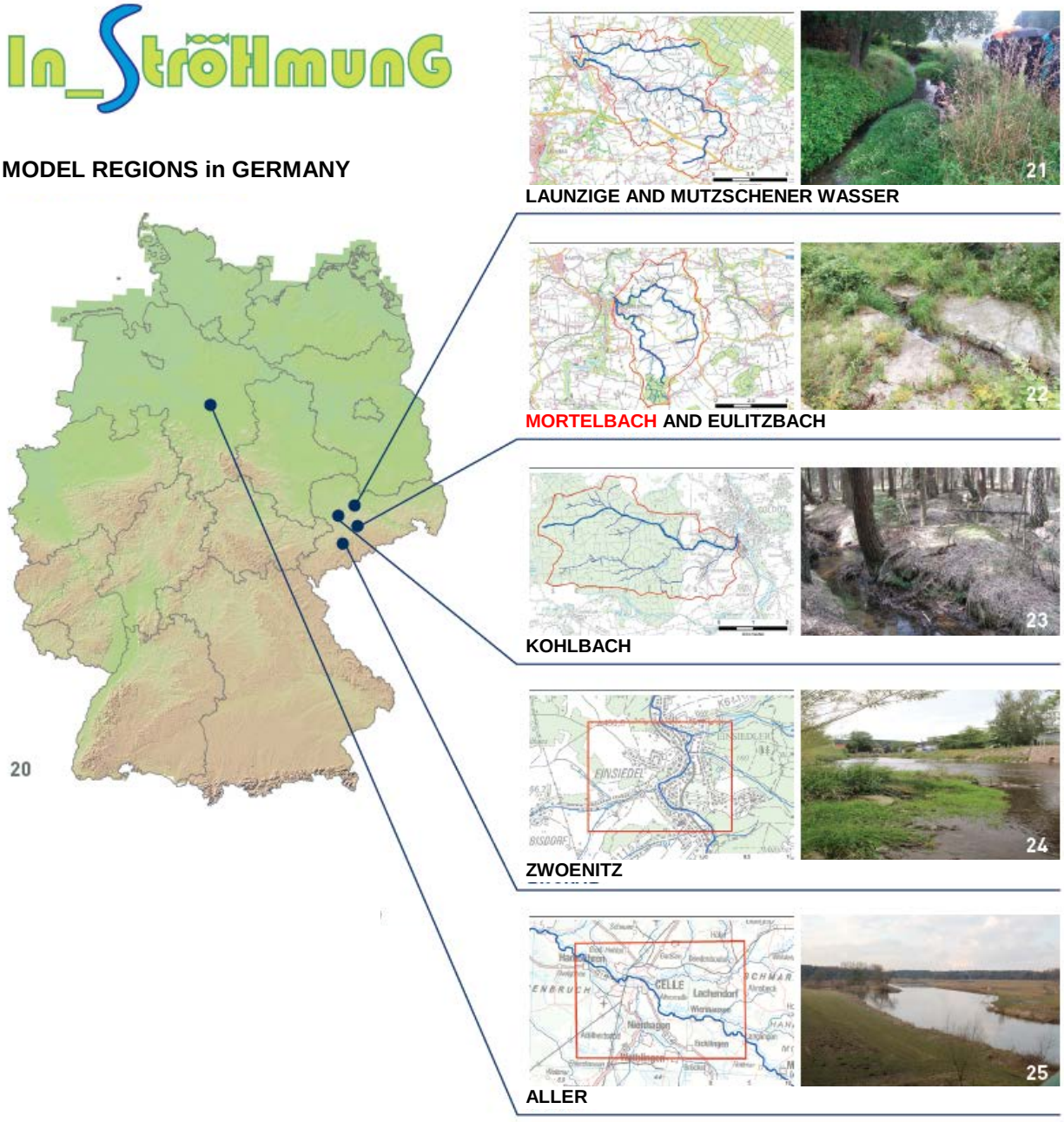


**Figure 1.** Model regions of the joint research project and location of Mortelbach, which is represented in the laboratory experiment (special base data: © Staatsbetrieb Geobasisinformationen und Vermessung Sachsen (GeoSN), 2016; Bundesamt für Kartographie und Geodäsie (BKG), 2016; Landesamt für Geoinformation und Landesvermessung Niedersachsen (LGLN), 2016; Images: 20 © LfuLG; 21 © M. Stengert, ube; 22, 23 © LfuLG; 24 © N. Müller, IWD; 25 © B. Ettmer, HS MD).

Third part of the project focuses on the development of innovative system solutions and concepts for the administrative watershed management as a key element of sustainable regional water resources management. A transdisciplinary approach linked with intensive public relations will help to reach that aim. The main issue is the planning and realization of innovative concepts and measures which integrate flood protection and an enhancement of the ecological status in the model regions (Niemand et al., 2016). To facilitate the maintenance of small rivers in consideration of an ecological orientated flood water prevention, a software will be developed for the cities and municipalities which are responsible for their preservation. In addition, the software will help to inform and get feedback from the citizens (Stowasser et al., 2016).

The main objective of this study is to present the laboratory experiment of the Institute of Hydraulic Engineering and Technical Hydrodynamics (IWD) at the Technical University Dresden, where the riverbed structure is investigated due to the influence of riparian vegetation.

## 2 PROJECT SITE

In order to simulate the results of the laboratory experiment with the natural river condition, a model river needs to be developed. Therefore, several parameters based on channel geometry, hydrology, morphology, grain size curves (Figure 2) etc. were investigated.

One of the selected river sections of the joint research project – the Mortelbach, which is a small river in the middle of Saxony became the examination subject and was schematically modelled in the laboratory. The Mortelbach belongs to the German stream type 5, which means it is rich of coarse material and a silica based low mountain range stream. The stream is rising in Grünlichtenberg and flows 9.5 km later in Waldheim into stream Gebersbach, which itself waters into the Zschopau.

The Mortelbach has a mean channel-width of 3÷7 m, a mean discharge of MQ = 0.14 m³/s and a flood water flow of HQ100 = 12.5 m³/s. The catchment area is 10.3 km².

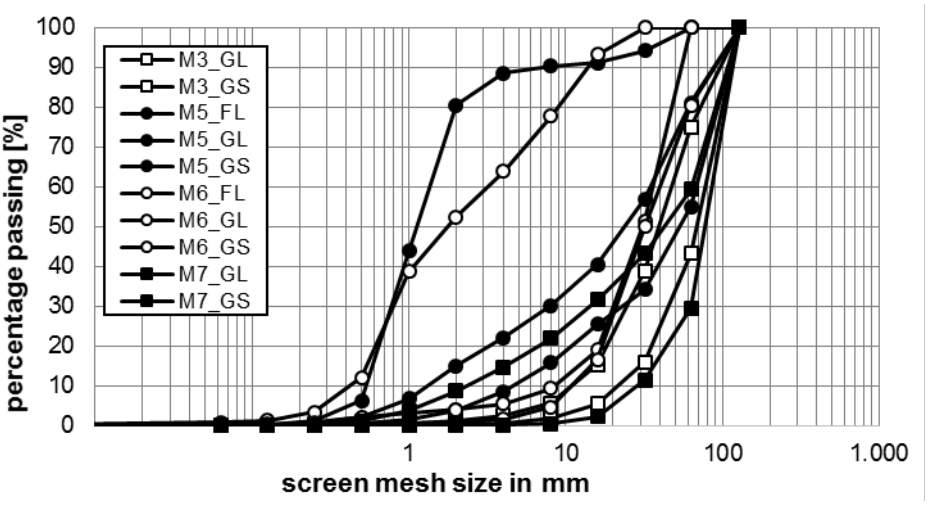


**Figure 2.** Grain size curves on several sampling positions (M3, M5, M6, M7) and mineral substrate types (mineral substrate: G-coarse and F-fine; velocity: L-slow and S-fast in relation to the corresponding patch).

**Figure 3.** Sampling Position M6, Mortelbach (© N. Müller, IWD).

 

## 3 LABORATORY EXPERIMENT

The aim of the flume experiments was to ascertain the influence of riverine vegetation on the bottom structure of rivers, especially small rivers. Small rivers play an important role in the total ecological status, because on one hand the sum of the total length is relevant and on the other they significantly affect the biological status of the larger rivers they are flowing into.

In the Hubert-Engels hydraulic laboratory of the IWDat Technical University of Dresden, Germany, scale experiments with mobile bed and vegetation roughness were in progress. The straight channel used for the morphological experiment was made of concrete angular retaining elements with overall measurements of 30.0 m in length, 2.0 m in width and a height of 0.64 m. Bed width was 1.4 m within embankments with a gradient 1:1 on both sides. The bottom of the flume was covered with mobile sediment with a mean thickness of 0.2 m (Figure 4). The longitudinal slope of the channel was 2.0 ‰. Discharge was conducted through two valves from an underground-tank. The water entered the flume first through a stilling basin and second a set of parallel rectifiers for directing the flow. Downstream at the end of the channel, a sediment trap was constructed, followed by an adjustable overflow weir, which was used to adjust the desired flow depth to reach normal flow conditions. A fixed set of three flow depths (0.2, 0.25, 0.3 m) was adopted for the study. This led to flow capacities up to 0.45 m³/s.

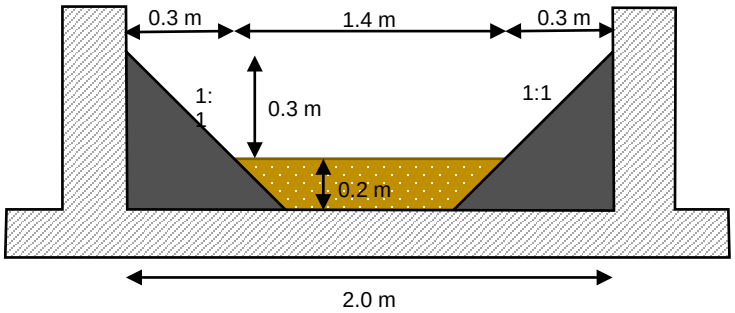


**Figure 4.** Experimental Setup, flume cross-section.

In order to get diverse bottom structures and observe separation of the soil, a specific grain-size curve was used. The material adapted to the conditions of the chosen project site, which was mentioned in chapter 2, with a scale of 1:4 (Figure 5). In order to fit flume experiments to Mortelbach, specifically stream type 5, a method to distinguish the grain-size curve was developed. The sampling method for the WFD had been extended in order to represent the ecological relevant conditions: After determining the substrate type at the sampling position (bedrock type) in 5-percent-steps, one substrate pattern per substrate type had been taken with a cylinder or a Van-Veen-gripper. In the laboratory, the substrate pattern had been dried and sieved in order to get a grain-size curve. If the probes had a not negligible content of fine material, a laser-analysis had been done additionally. Afterwards, the grain-size curve had been scaled and matched with curves of quartz sand and gravel to make it suitable for measurements with the use of three-dimensional photogrammetry system. Sampling Position M6 with a scale of 1:4 was chosen for representation in the laboratory experiments (Fig. 5). For safety reasons due to pump-protection finer sediments, suspension load was neglected.

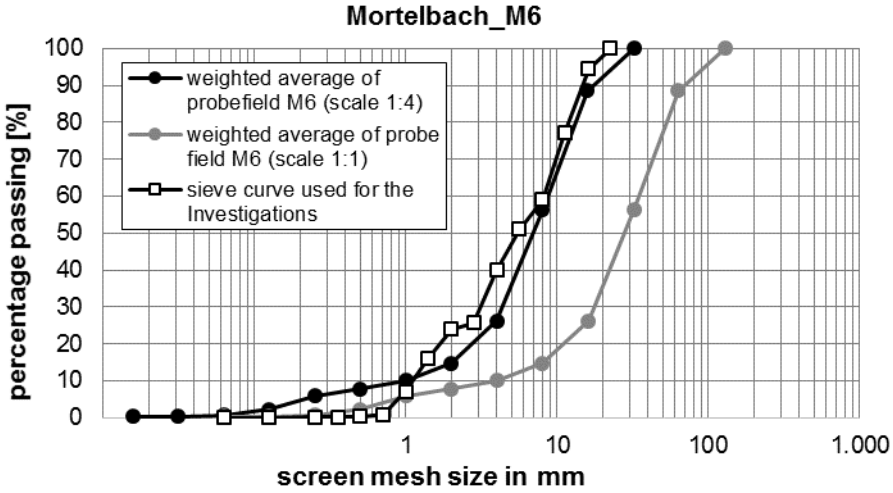


**Figure 5.** Grain size curves on several sampling positions (M3, M5, M6, M7) and mineral substrate types (mineral substrate: G-coarse and F-fine; velocity: L-slow and S-fast in relation to the corresponding patch).

 

To investigate the impact of vegetation at the beginning, experiments without any vegetation (variant 0-A) were conducted. Experimental setups including grass-covered slopes were also executed (variant 0-B). For the mentioned experimental setups, discharges near the beginning of transport were conducted in order to see how the vegetation influenced the bottom structures. Previous analytical calculations for cases of obstacle-free cross-sections showed, that nearly 50.0 % of the sediment-particles were below the critical threshold for particles to move in all stages.

Experiment with diverse vegetation patterns was also carried out (variant 1, 2 etc.). Rigid as well as flexible vegetation will be installed.

## 4 DATA COLLECTION

Bottom structures were measured contact free by using a special photogrammetry system based on correlation measurements, containing three cameras, which were fixed at a movable traverse system. After calibrating the cameras by finding information according to camera-orientation, the system was moved to the area of interest. Reflecting encoded markers, which were fixed along the flume and had predefined positions identified the regions, where the camera system was recording. By means of a software which calculates the bottom height, the structures can be analyzed (Fig. 6 left). To verify the results and increase the data density, additional laser measurements were taken with a movable traverse, which covered an area of 1.4 m × 4.6 m. Laser measurements were taken with a solution of 8 mm × 1 mm (Fig. 6 right).

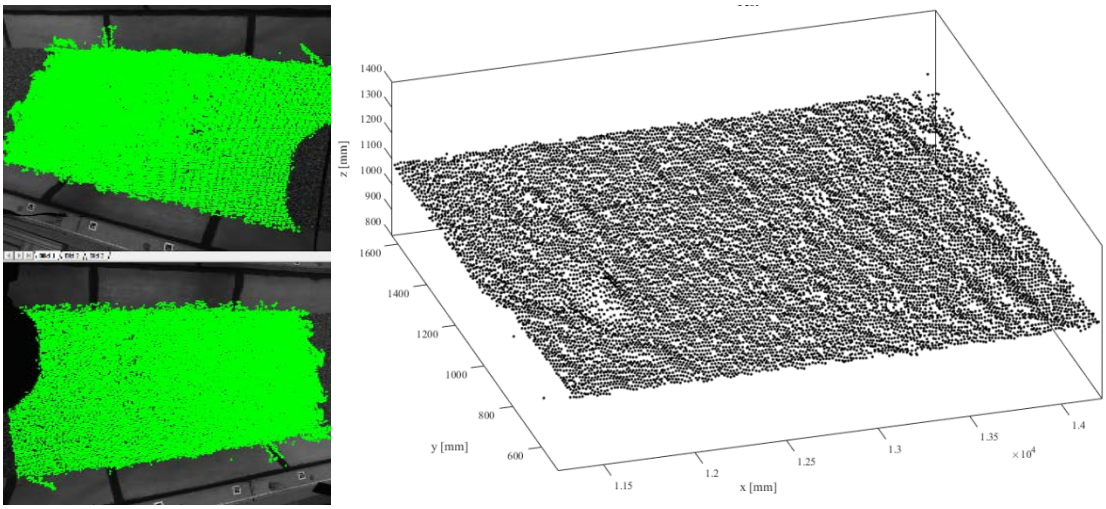


**Figure 6.** Example of photogrammetry analysis, photos with embedded signals (left) and result (right).

Furthermore, grain size distribution on channel bed surface was analyzed using orthogonal photos. The software BASEGRAIN©, developed at ETH Zurich (Detert, 2013), was able to detect the size and position of grains out of photos (Figure 6). The distribution of grains and the sizing induced by the interaction of flow and vegetation were described. The sizing in connection with the three-dimensional bed structure allowed conclusions for the improvement of bed structure and therefore as habitat for macrozoobenthos.

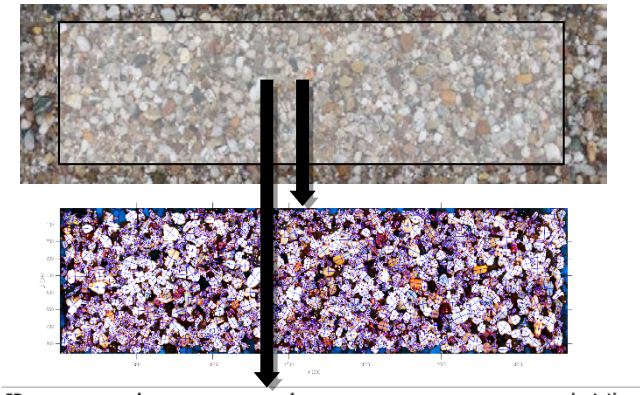

| ID | a | b | a | b | area | x | y | orientation |
|---|---|---|---|---|---|---|---|---|
| [-] | [mm] | [mm] | [px] | [px] | [px] | [px] | [px] | [deg] |
| 1 | 19,841 | 14,513 | 19,841 | 14,513 | 218 | 8,404 | 106,881 | 79,901 |
| 2 | 18,020 | 15,791 | 18,020 | 15,791 | 212 | 11,585 | 395,571 | 35,791 |
| 3 | 16,862 | 12,804 | 16,862 | 12,804 | 164 | 16,677 | 367,122 | 27,029 |
| 4 | 14,713 | 11,209 | 14,713 | 11,209 | 125 | 15,312 | 287,368 | -67,070 |
| 5 | 46,425 | 41,062 | 46,425 | 41,062 | 1447 | 29,351 | 793,143 | -84,023 |

**Figure 7.** Digital grain size analysis by using ortho photos and software BASEGRAIN©.

 

To determine spatial water surface and surface velocity, the photogrammetry system can be used by the principle of partice tracking within a series of images and using tracer particles at water surface. Continuous as well as temporal but local measurements of water level with ultrasound, proofed by needle gauge measurements, were conducted in addition.

A down-looking Acoustic Doppler Velocimeter (ADV), developed by NORTEK, was used to measure the instantaneous three-dimensional velocity components (Figure 8). Errors in the prediction of mean velocities were less than ±2.5 mm/s (or ±1%) (Nortek, 1998). Velocities had been recorded at each point of measurement with a sampling frequency of 200 Hz and sampling duration of 200 seconds for each measurement. WinADV (Wahl, 2000) was used to filter and process velocity and turbulence data. Data with average correlation lower or equal to 70 % and average signal-noise ratio lower or equal to 15 dB were filtered out.

**Figure 8.** Impression of the experimental flume with bare concrete slopes.

## 5 OUTLOOK

Recently, experiments with bare concrete slopes are running to collect basic values for the latter comparative evaluation of the influence of different bank vegetation structures upon the river bed morphology. Investigations including grass covered banks are ongoing. In summer 2017, preliminary results of vegetated banks will be presented.

## ACKNOWLEDGEMENTS

The project „In_StröHmunG“ is funded from Bundes ministerium für Bildung und Forschung (BMBF). It is part of BMBF sponsorship measures „Regionales Wasserressourcen-Management für den nachhaltigen Gewässerschutz in Deutschland (ReWaM)“ in the sponsorship focus „Nachhaltiges Wassermanagement (NaWaM)“.

## REFERENCES

BMU. (2010). *Die Wasserrahmenrichtlinie - Auf dem Weg zu guten Gewässern*. Berlin: Bundesministerium für Umwelt, Naturschutz und Reaktorsicherheit, 75.

Branß, T. & Dittrich, A. (2016). *Erzeugung von Rehnen: Eine experimentelle Studie.*Dresdner Wasserbauliche Mitteilungen, Heft, 57, 275–284.

Branß, T., Dittrich, A. & Núñez-González, F. (2016). Reproducing Natural Levee Formation in an Experimental Flume. *The International Conference on Fluvial Hydraulics, Proceedings of River Flow*, 1122–112.

Detert, M.W. (2013). *User Guide to Gravelometric Image Analysis,* by BASEGRAIN. Advances in Science and Research, 1789–1795.

EEA. (2012). *Europa Waters - Assessment of Status and Pressures,* Copenhagen, Denmark: European Environment Agency, EEA Report No 8/2012, 96.

EU-FD. (2007). Directive 2007/60/EC of the European Parliament.

EU-WFD. (2000). Directive 2000/60/EC of the European Parliament.

Kron, W. (2015). *Sturmfluten - Sturzfluten - Flusshochwasser, Wie gehen wir mit dem Hochwasserrisiko um?* In MunichRe, Hochwasser und Risiko, Stiftung Bauwesen, 39-68.

 

Niemand, C., Bilinski, W., Spänhoff, B. & Müller, U. (2016). *Die gemeinsame Umsetzung von Hochwasserrisiko-management und naturnaher Gewässerentwicklung in Sachsen – Rahmenbedingungen, Restriktionen und Chancen.* Dresdner Wasserbauliche Mitteilungen, Heft 57: 371–382.

NORTEK. (1998). *ADV Operation Manual*. Norway,pp 34.

Stamm, J. & Müller, N. (2015). Innovative Systemlösungen für ein transdisziplinäres und regionales ökologisches Hochwasserrisikomanagement und naturnahe Gewässerentwicklung. Dresdner Wasserbauliche Mitteilungen, Heft 53: 499–510.

Stowasser, A., Stratmann, L., Salim, J. & Lagemann, T. (2016). *PROGEMIS® – „Software as a Service" für das kommunale Gewässermanagement mit Planungs-, Dokumentations- & Kommunikationskomponente.* Dresdner Wasserbauliche Mitteilungen, Heft 57.

Wahl, T.L. (2000). *Analyzing ADV data using Win ADV*. 2000 Joint Conference on Water Resources Engineering and Water Resources Planning &Management, Minneapolis, MN, United States, 1–10.

 

Proceedings of the 37th IAHR World Congress
August 13 – 18, 2017, Kuala Lumpur, Malaysia

# INFLUENCE OF BED-LOAD TRANSPORT ON THE DESIGN OF FLOOD PROTECTION AND RETENTION MEASURES IN GRAVEL-BED RIVERS – APPLICATION OF HYDRO_FT-2D FOR THE TYROLEAN INN RIVER

KATHARINA BAUMGARTNER[(1)], BERNHARD GEMS[(2)], STEFAN WALDER[(3)], MARKUS FEDERSPIEL[(4)] & MARKUS AUFLEGER[(5)]

[(1, 2, 5)] Unit of Hydraulic Engineering, University of Innsbruck, Innsbruck, Austria,
katharina.baumgartner@uibk.ac.at
[(3, 4)] Unit of Protective Water Management and Water Ecology, Office of the Tyrolean Regional Government, Innsbruck, Austria,
stefan.walder@tirol.gv.at

## ABSTRACT

During the last decades, flood risk management has become increasingly important in the Alpine region. Bed-load transport is an important driving factor for riverbed formation. The Inn River located in the Lower Inn valley is a focus of intensive research and the aim is to decrease the flood risk. Morphological changes during flood events significantly influence the channel capacities. The bed-load transport within the river system,or rather the erosion and deposition processes, can have significant impact on the effectiveness of flood protection measures and the dimensioning of retention areas. The work presented in this paper is aimed at the analysis of the influence of the movement of sediments and the associated morphological processes on a large system of flood protection and uncontrolled and controlled retention areas in the gravel-bed river Inn. In order to analyze the impacts of morphodynamic changes on the effectiveness of the planned measures and to identify sensitive areas for retention control, a multi-fractioned bed-load transport simulation is applied. The study focuses on the 75 km long reach of the Inn River between the city of Innsbruck and Kufstein in Tyrol (Austria). The 100-yr design flood hydrograph is analyzed with the numerical model. Grain size distributions are obtained from a field survey along the entire stretch of the Inn River and the relevant tributaries. This study points out that morphodynamic analysis affords an insightful basis for planning of flood protection and retention areas, in particular for retention control of the intake structures. To reach an efficient and optimized peak reduction in the main river and to control fluxes into retention areas, it is crucial to analyze the morphodynamic processes.

**Keywords:** Bed-load transport; flood protection; morphodynamic-numerical-modelling.

## 1 INTRODUCTION

The protection of urban settlement areas, the conservation and restoration of ecologically valuable rivers and the demographic change regarding usable areas in flood hazard-prone areas give importance to many river basin projects in the alpine catchments. In the last decades, many river regulations and course relocations have led to a decline in concern about the water hazard potential and development of new agricultural areas. Floods in mountain and gravel-bed rivers are frequently accompanied by intense sediment transport. Bed-load transport is an important driving factor for riverbed formation, both from a long-term and event-based perspective. Morphological changes during flood events and also sediment loads from the tributaries significantly influence the channel capacities and the extent of flooding of agricultural, infrastructure and settlement areas (Gems, 2011; Plörer, 2012). Also, erosion and deposition processes affect flood protection and retention management and, consequently, have to be prevented in river sections with potentially high losses onto the adjacent flood plain (Habersack, 2000).

As in other Alpine regions, the flood event in August 2005 caused severe damage to infrastructure and settlement areas in the Lower Inn Valley (Godina et al., 2006; Rudolf-Miklau et al., 2006). It revealed the need for regional flood risk management, with further lateral protection structures and retention areas on the densely settled valley floor. This paper presents the application of a sediment transport modelling approach for the planning of flood protection and retention measures in dynamic rivers. The accuracy of the flood forecast and the location of the retention areas relative to the control water gauges are of crucial importance (Fischer, 2008). In this work, the focus is on how river dynamics influence the procedure of activating and controlling fluxes into retention areas.

## 2 STUDY AREA

The study area was located in an alpine valley in Tyrol (Austria); the focus was on the 75 km long reach of the Inn River between the confluence with the Sill River at river km 294.7 in Innsbruck and the city of Kufstein, close to the border with Bavaria (Germany). The main channel of the Inn has a homogeneous,

 

channelized character and features an average channel gradient of about 1.2 ‰. The channel width ranges between 60 m and 130 m. 57 tributaries join the main river in this reach and the catchment rises from 5809 km² up to 9497 km². Nevertheless, the entire valley is characterized by an intensive use for settlements and agricultural purposes. For this paper, the lower Inn valley sub-model 5 between km 251.0 and km 239.8 was considered (Figure 1). The planning of the flood protection and retention measures for this sub-model study site was carried out by ARGE DonauConsult/ILF and included two main retention areas, “Voldöpp” and “Radfeld-Kundl”. Both were selected based on observations of water levels along the Inn River and its important tributaries. A large set of lateral protection measures, object protection and as well retention areas, amongst the two mentioned, are currently planned to protect settlement areas and industrial estate on the valley floor against floods. Retention area “RA Voldöpp” (orographic left) has an available volume of 1.7 million m³ and retention area “RA Radfeld-Kundl” has an optimum volume of 5.4 million m³. Two main tributaries, Brandenberger Ache (282.1 km²) and Wildschönauer Ache (87.2 km²) join the Inn River in this sub-model. The discharge characteristic in flood protection management has changed. Flood areas decrease and several settlement areas are affected. Therefore, flood emergency structures are still necessary to increase the capacity of alpine rivers. The flood protection and retention measures in the study area were designed for a 100-yr design flood.

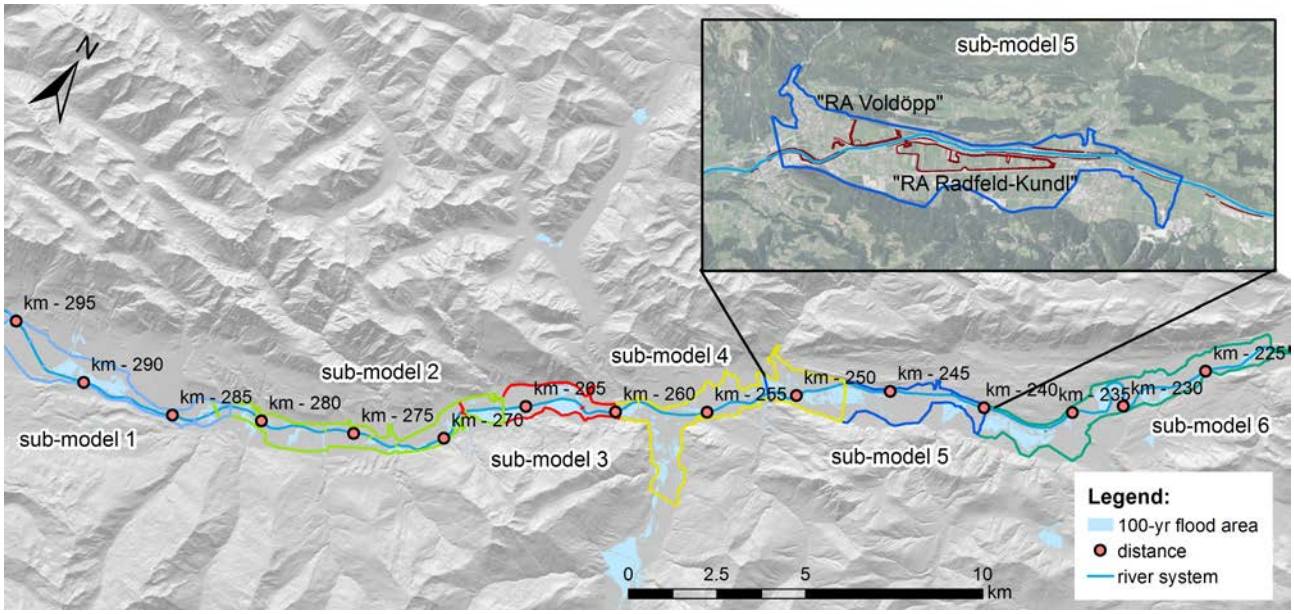


**Figure 1.** Overview of the study area and its sub-models; location of the two retention areas “Voldöpp” and “Radfeld-Kundl” in the sub-model 5 (map section).

## 3 METHODS

### 3.1 Data acquisition

In order to get information about the riverbed composition of the Inn River and its major tributaries, a combination of a line-by-number analysis and volumetric sampling was applied to get grading curves. Data from soil sample sites were selected on site, depending on the soil characteristic in the field. In the case of an existing cover layer, the grain size distribution was analyzed with line-by-number sampling at suitable sites, i.e. gravel banks (Bunte and Abt, 2001). In areas without pronounced cover layers, volumetric sampling was performed. The river bed material was described by characteristic grains sizes ($d_m$, $d_{30}$, $d_{50}$, $d_{90}$).

It was necessary to make an approximation of the grading curves for the multi-fractioned bed-load transport simulation model. Grounded on the study of Umach (2013) and the application of sensitivity analyses, the grading curves were approximated by six fraction classes. The largest grain class results from the maximum grain size. The comparison between the original and the approximated distribution lines was made by comparing the characteristic grain sizes ($d_{50}$, $d_{90}$). Table 1 contains the fraction classes, which were further used in the numerical model both for the characterization of the riverbed composition and the supplied bed-load at the model boundaries.

 

**Table 1.** Grain size classes used for the numerical model, $d_{i,rep}$ = arithmetic mean of grain class i, $d_i$ = maximum grain diameter of grain class i.

| Grain class / fraction i [mm] | 1 | 2 | 3 | 4 | 5 | 6 |
|---|---|---|---|---|---|---|
| $d_{i,rep}$ | 7.5 | 27.5 | 60 | 95 | 150 | 270 |
| $d_i$ | 15 | 40 | 80 | 110 | 190 | 350 |
| $\Delta d_i$ | 15 | 25 | 40 | 30 | 80 | 160 |

3.2 Sediment transport

The applied sediment transport approach for the determination of the supplied bed-load from the major tributaries is based on a model from Rickenmann (1990), see equation [1]. To determine the relevant tributaries, two criteria were selected: (i) the tributary discharge is at least 10 $m^3s^{-1}$ and (ii) a considerable amount of bed-load is expected. The inflow bed-load hydrographs for the model boundaries were performed on the 100-yr design flood hydrograph, the channel topography and the grain size distributions of the bed-load. The latter was obtained from the described field survey along the entire tributaries and a set of "key sections" were defined to calculate the transport rates. The inflow bed-load transport rate into the first sub-model at the Inn River was done according to the method of Meyer-Peter and Müller (1949) (MPM) (eq. 2), with consideration of the form roughness according Wong and Parker (2006).

According to Rickenmann (1990) bed load transport rate $g_{TK}$ is calculated as:

$$g_{TK}= 12.6*\left(\frac{d_{90}}{d_{30}}\right)^{0.2}(q_{spe} - q_{spec,c})*I_{red}^{2}*(s-1)^{-1.6} \quad [1]$$

where, $d_{90}/d_{30}$ = grain size at 90/30% screen underflow, $q_{spe}$ and $q_{spec,c}$ = specific and critical specific discharge, $I_{red}$ = reduced channel slope, s = relation density sediment to density water.

According to Meyer-Peter and Müller (1949), bed load transport rate $g_{TK}$ is expressed as:

$$g_{TK}= \sqrt{(s-1)*g}*d_m^{3/2}*8*(\theta' - \theta_c)^{3/2} \quad [2]$$

where, g=gravity acceleration, $d_m$= characteristic grain diameter, $\theta'$=actual dimensionless shear stress and $\theta_c$ =critical dimensionless shear stress.

3.3 Numerical model

For analyzing the impacts on the effectiveness of the measures under consideration for the Inn River, the unsteady, depth-averaged flow conditions were simulated using the morphodynamic model code of HYDRO_FT-2d (Nujić et al., 2015). The model relies on the two-dimensional Saint Venant equations. The finite-volume-method is used to solve the shallow water equations. The temporal discretization is realized on the explicit and second order Runge-Kutta-scheme. To analyze the bed-load transport, the hydraulic model applies a fractionated multigrain approach. The bed-load transport is based on the fractionated multigrain approach of Meyer-Peter and Müller (1949), adapted by Hunziker (1995). The bed-level changes in the numerical model are calculated by the Exner equation (Exner, 1925). The hiding functions according Hunziker (1995) and the implemented two-layer-technique accounts for grain sorting processes in the riverbed (Nujić et al., 2015).

For this investigation, the focus was the analysis of the influence of bed-load transport and the associated morphological processes on flood protection and retention measures. The computational mesh was provided from the Tyrolean Regional Government. In order to cope with the computational effort, the model was divided into six sub-models with overlap areas to afford stable boundary conditions and a robust transfer of flow conditions between these sub-models. Regarding the numerical stability of the morphodynamic simulations, it was necessary to optimize the computational mesh. The grid resolution values were 8-16 m (in flow direction) by 2-6 m (perpendicular to flow direction).

For the numerical calculation, the upstream boundary condition was set with the 100-years design flood hydrograph for the Inn River in Innsbruck. The discharge time-series for the relevant tributaries and the corresponding sediment bed-load were also set in accordance to the hydrological profile of the design flood at the Inn River. Normal discharge conditions were defined as hydraulic downstream boundary condition. The initial hydraulic condition was considered with wet grid cells. The maximum erosion depth for the riverbed was limited to one meter ($DZ_{max}$ =1 m). Close to bridges and model boundary conditions, such as inflow and outflow areas, erosion was prevented. The characterization of the bed roughness was adopted out of the existing model.

 

Since calibration data for bed-load transport and corresponding changes of channel bed level were not sufficiently available, the model was validated by a sensitivity analysis. River- and model-specific parameters were varied to analyze its influence on the calculation results. Three different scenarios with specific model parameters and sediment loads from the tributaries were finally analyzed, they represented a spectrum of the expected changes in the riverbed during flood events. Subsequent parameter setup had been tested both for the current state situation at the Inn River without the planned flood protection measures and the future situation: critical Shields-parameter $\theta_c$=0.047; Manning roughness $k_{st}$= temporally constant; adaptation length by $\alpha_L$ coefficient =4000 and length $L_{so}$=15. The following three parameter scenarios were simulated with the following variables:

- Scenario 1 represents the "base model" and demonstrates ordinary conditions (exchange layer $d^{ex1}$=0.20 m and scale factor for MPM $k_F$ = 1.0)
- Scenario 2 delivers more dynamics of the riverbed by assuming a minor thickness of the sediment active layer and higher transport rates (exchange layer $d^{ex2} = 0.10$ m and scale factor for MPM$k_F$=1.25)
- Scenario 3 takes higher sediment loads from the tributaries into account (sediment loads according to Scenarios 1 and 2, scaled by the factor 1.4)

## 4 RESULTS

### 4.1 Grain-size analysis and sediment transport

Based on the grain size distributions, five homogeneous sections along the river stretch were defined. Figure 2 shows that the mean grain size decreases with the river length. Downstream of the weir system at Kirchbichl (km 233.4), the smallest grain size can be found. It should be pointed out that the sediment continuum is interrupted through the weir structure of the power plant at Kirchbichl. The critical grain diameters of the surface layer of the Inn River vary between 0.02 m and 0.04 m, and of the sublayer between 0.013 m and 0.032 m. The grain size analyses of the tributaries show a high variability. The characteristic diameters range between 0.014 m and 0.079 m. By use of the data from the field investigations, the grain size analysis and the defined "key-sections", the bed-load transport rates for the tributaries were calculated and verified and reach volumes between 120 m³ to 7700 m³.

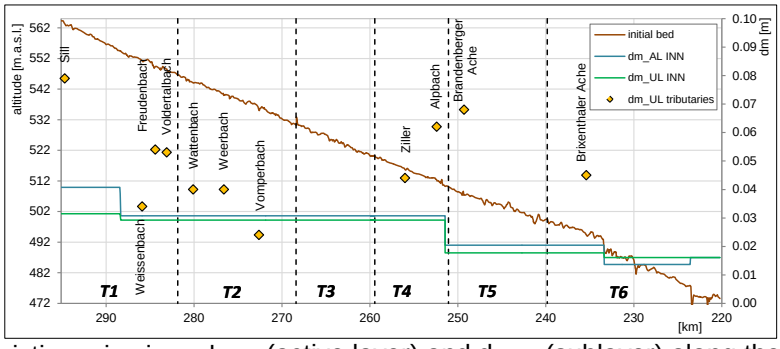


**Figure 2.** Characteristic grain sizes $d_{m,AL}$ (active layer) and $d_{m,UL}$ (sublayer) along the considered reach of the Inn River and its relevant tributaries and the longitudinal initial bed-elevation.

Figure 3 illustrates the inflow discharge (black line) and the associated bed-load transport rate (dotted line) with the associated six fraction layers for the presented sub-model. There is a variation in the delivered sediment load amount depending on the scenario setting. The bed-load input into the sub-model reach varies from about 23800 m³ at scenario 1 to 31800 m³ at scenario 2.

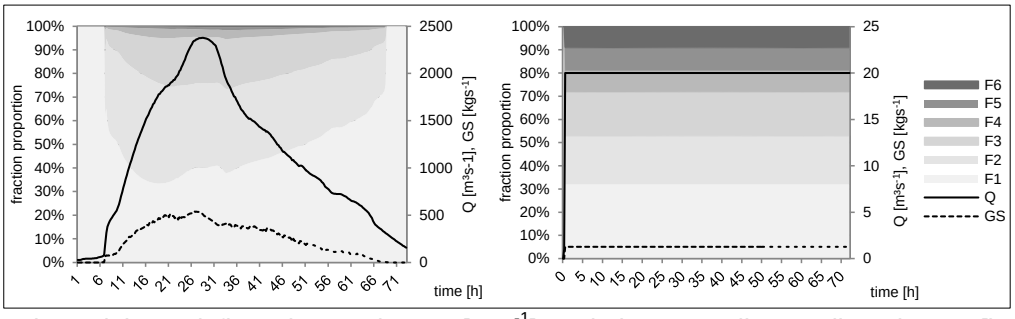


**Figure 3.** Sub-model 5 – inflow time-series Q [$m^3s^{-1}$] and the according sedigraph GS [$kgs^{-1}$] with the proportions of fraction i for the Inn River (left) and the main tributary Brandenberger Ache (282.1 km²) (right).

 

## 4.2 Effect of the river morphodynamics on the efficiency of flood protection and retention measures

### 4.2.1 Sediment volume balance and bed-load transport rates

In the technical planning stage of flood protection and retention measures, the influence of bed-load transport has to be considered. The associated morphological processes (erosion- and deposition developments) are in a close interaction with the event-specific discharges and can lead to problems in protection planning (Habersack et al., 2013). With regard to the temporal and spatial development of the riverbed, a volume analysis approach was made. The sedimentation and erosion volumes and the differences between the three scenarios of the current and future situation, for each kilometer at the simulation end, are plotted in Figure 4. Total volume of sediment inflow in sub-model 5 is approximately 20600 m³ and the outflow amount is around 32000 m³ in the future state condition. Through the simulation, it is estimated that the volume change is around 11400 m³ although the results show that no pronounced trends over the length are visible. The deviation between the current and the future situation can be justified through the planned flood measures and can be confirmed as sensible areas. As expected for section 3 (km 249.5 – km 248.5), where the riverbed is relatively wide, low transport rates occur and are associated with the confluence of the Brandenberger Ache which affects high sediment accumulations. The comparison between the actual and the future state shows a decrease in the sediment volume. It is observed that the upstream located retention areas affect a flood peak reduction and thereby lead to lower water levels. The retention area “Radfeld-Kundl” (km 248.5 – km 247.5) prevents serious damage to settlements. The reason for the reduced erosion in this subsection in the future state can be traced back to the function of the retention area of “Voldöpp”. It can be noted that between km 247.5 and km 240.5, there is no marked difference between the actual and the expected (planned) state. However, the volume change tends to an accumulation and erosion succession.

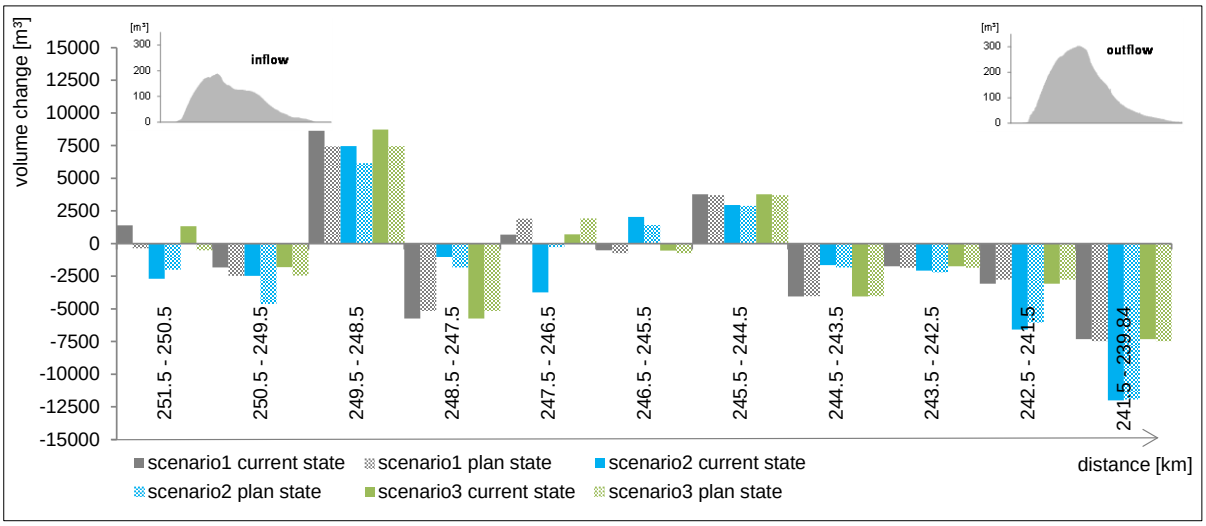


**Figure 4.** Sub-model 5 – volume change for all scenarios for the current and planned state (inflow zone retention areas “Voldöpp” km 249.1 – km 248.9 and “Radfeld-Kundl” km 247.8 – km 247.6).

### 4.2.2 Efficiency of flood protection and retention measures in consideration of bed-load transport and channel bed dynamics in the Inn River

The efficiency of technical measures for flood retention are greatly dependent on the hydrological impacts, predictability and the characteristics of the retention areas, its connectivity to the river channel and the operation mode of the intake structure (Haider, 2014). A stable river bed during flood events without any substantial aggradation and erosion processes at the location(s) of the control gauge(s) in the river is of fundamental importance for the optimum use of the available retention volume. Bed level changes in rivers cause a conforming change of water levels and thus lead to a modification of the stage-discharge-relationship at the control gauge, which is crucial for the operation of the intake structure. Stable channel bed conditions can rarely be ensured in practice and thus an adequate consideration of bed-load transport processes within the planning of flood protection and retention measures is very important.

In the following paragraph, results from morphodynamic numerical modelling for the current state situation at the Inn River and the planning state are discussed for sub-model 5 (Figure 1).

Figure 5 illustrates the differences of channel bed elevations at the times before and after the considered 100-years flood. The presented longitudinal section is based on the analysis of modelling results along the axis of the river channel. Initial channel bed elevations (brown line) and expected morphological changes for the three considered parameter scenarios are shown. In the latter case, the situations without and with protection and retention measures are shown. The surrounding curves (grey lines) denote the minimum and maximum changes in channel bed elevations during the flood event.

 

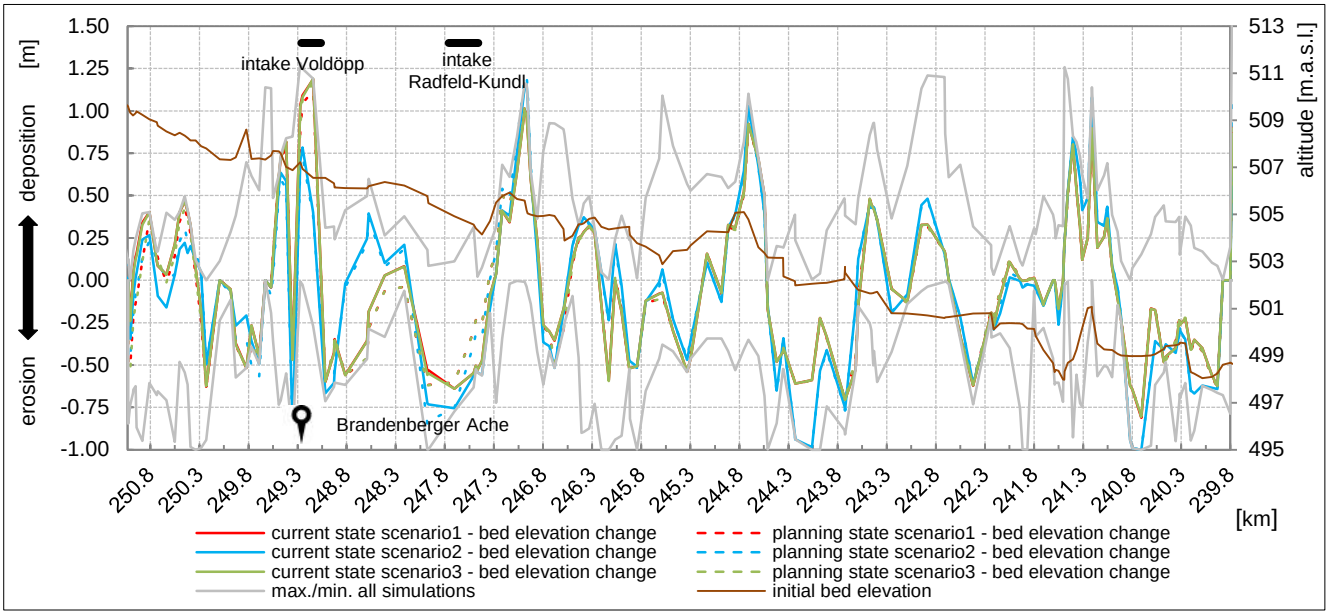


**Figure 5.** Sub-model 5 – differences of channel bed elevations at the times before and after the 100-years flood; modelling results along the channel bed axis; dashed lines represent bed level changes in the planning state (compared to the current state situation); grey lines denote to the minimum and maximum expected bed level changes during the flood event and for the three parameter scenarios.

Again for sub-model 5, Figure 6 illustrates a contour plot of the bed level changes after the 100-years flood and the maximum appearing flood areas for parameter scenario 1. The flood event leads to bed level changes within the range of -1.0 m to +1.3 m. Areas with highest aggradation are thereby observed in calm-water zones such as groin fields or river sections with relatively large channel widths and low gradients. Comparison of the simulation runs for the three considered parameter scenarios shows that the setting of the numerical and water-specific parameters indeed leads to different modelling results. However, the general response of the river sections in terms of erosion or aggradation is not altered. Compared to the parameter settings of scenarios 1 and 3, a lower thickness of the exchange layer of the channel bed ($d^{ex2}$ = 0.10 m) was assumed in scenario 2. This leads to a more substantial exchange of the transported sediments with the soil material and thus higher erosion rates and a finer grain size distribution of the exchange layer material during the flood event (Figure 5). For scenario 3, the amount of bed-load entering the modelled section of the Inn River from the tributaries and at the upstream model boundary is scaled by the factor 1.4 (compared to scenarios 1 and 2). Substantial impacts of this increased input of sediments on the channel bed dynamics are not observed. However, minor changes of water levels in close vicinity to the confluence points, not having any relevant influence on the efficiency of the flood protection measures, appear.

The relevant control gauge for the operation modes of the intake structures of both retention areas is situated close to the upstream sub-model boundary at km 250.8 (Figure 5). Simulation results show that bed-load transport and channel bed dynamics influence the diversion at the intakes and prevent an optimum use of the available retention volumes at the current planning stage. At the control gauge, erosion primarily appears during the rising limb of the hydrograph, subsequent aggradation processes generally lead to final channel bed elevations which are equal to the initial conditions. Due to the channel bed dynamics, water levels are on average 0.06 m below the corresponding values of a hydrodynamic clear-water simulation with a stable channel bed. Consequently, the retention areas are activated comparatively at a later time during the flood event. Diversion to the retention area “Voldöpp” (intake structure at km 249.0) appears within 22.25 hrs and 32.00 hrs of simulation time and leads to a use of 88 % of the available volume of 1.7 million m³. A decrease of the flood peak in the Inn River due to the retention at “Voldöpp” from 2347 $m^3s^{-1}$ to 2301 $m^3s^{-1}$ is achieved. Maximum water depth in the retention area amounts to approximately 3.5 m and is situated to the north of the area (Figure 6). Concerning the bed level elevations close to the intake area, almost no differences between the current state situation and the planning state appear due to the activation of the retention area (after 22.25 hrs of simulation time). The opening of the intake structure leads to substantial aggradation in the downstream section of the Inn River. This process could be observed in all considered scenario simulations.

The flood protection measures along the Inn River, amongst the increase of the embankment heights and the construction of flood walls, generally lead to an increase of flood risk further downstream. In particular, the retention area “Radfeld-Kundl” (Figure 1) with an available volume of 5.2 million m³ and a spatial extent of 4.5 km counteracts this. Under the influence of bed-load transport and channel bed dynamics, 85 % of the

 

available retention volume (or the situation under clear-water conditions) is retained in the area "Radfeld-Kundl". This is again due to erosion processes and a dynamic change of the stage-discharge-relation during the flood event at the control gauge. Thereby, the maximum diverted discharge decreases from 218 $m^3s^{-1}$ (clear-water and stable channel bed) to 185 $m^3s^{-1}$ in the morphodynamic numerical model (parameter scenario 1). Aggradation processes similarly appear downstream of the intake structure. Nonetheless, the retention area "Radfeld-Kundl" leads to a substantial decrease of the flood peak in the downstream section of the Inn River.

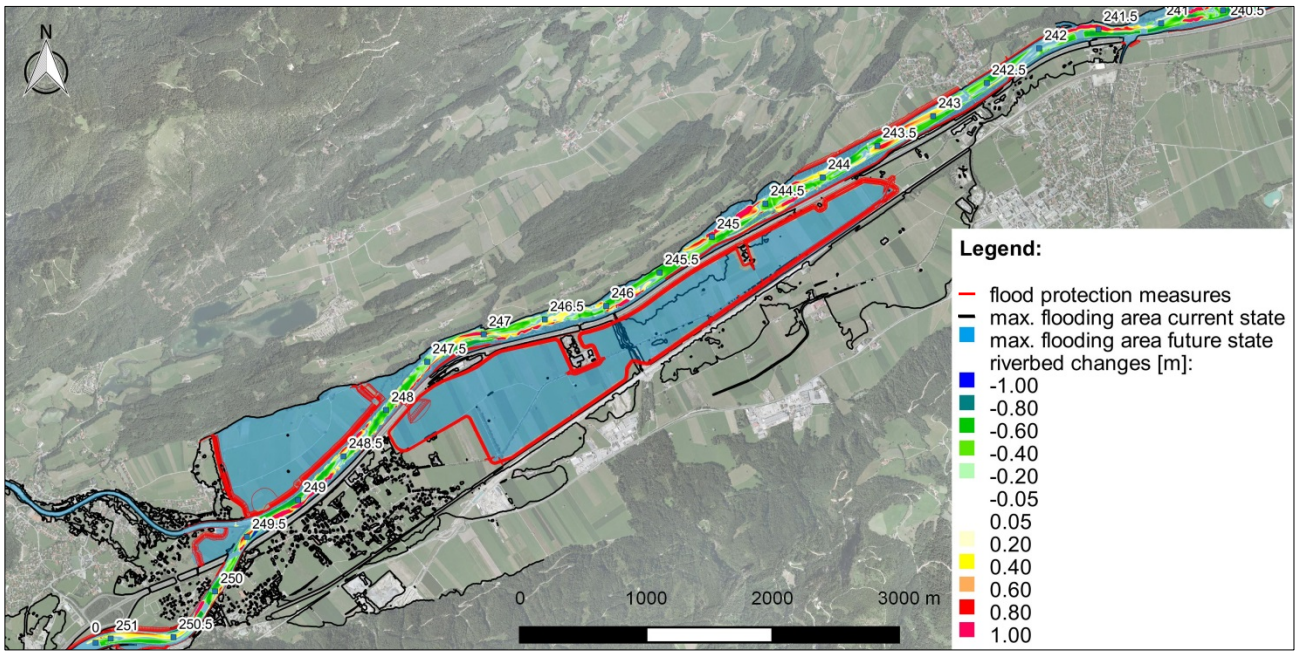


**Figure 6.** Sub-model 5 – contour plot of the final differences of channel bed elevations (scenario 1); comparison of maximum expected flood areas for the current state situation (black surrounding line) and for the planning state (blue area).

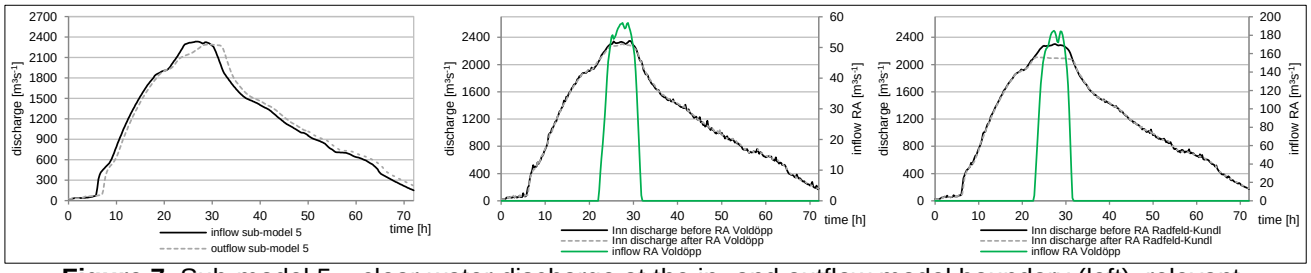


**Figure 7.** Sub-model 5 – clear-water discharge at the in- and outflow model boundary (left), relevant discharge hydrographs at the retention area "Voldöpp" (middle) and at the retention area "Radfeld-Kundl" (right).

With the effects of flood protection and retention measures, the outflow hydrograph of sub-model 5 features a flood peak reduction of 45 $m^3s^{-1}$. Compared to the current state situation, without any technical measures, the simulation shows that the detained volume leads to a peak attenuation of 126 $m^3s^{-1}$. The planned protection and retention measures seem suitable to protect settlement areas and industrial estate on the valley floor against the designed 100-yr design flood.

## 5 CONCLUSIONS

In order to avoid future flood damage at the Inn River in the Lower Inn Valley, the implementation of protection and retention measures is indispensable. This paper analyzes the bed-load related impact on the effectiveness of measures under consideration exemplarily for a selected section of the Inn River. Numerical bed-load transport modelling is performed and with the required data and parameters the model shows that the consideration of morphodynamic processes has to be taken into account for these planning tasks. In this context, due to the lack of databases, the sensitivity analysis is performed which delivers a spectrum of possible bed level changes during a flood event.

The results show that the information about the bed-level changes is very important for the planning state of flood protection and retention measures. For an optimum use of the available retention volume, a stable

 

riverbed during flood events at the locations of the control gauges and at the intake structures into retention areas is of fundamental importance. For dimensioning of the inlet structures, the variation of the riverbed formation must be taken into account. Due to the spatial and temporal variable bed-elevation at the control gauge station, the comparison between pure water flow modeling and the bed-load transport simulation shows that due to erosion processes, a lower water level occurs at the control station and activates the retention area at a later time.

Concerning the parameter setting of the hydraulic model, the thickness of the exchange layer and the grain size distribution of the soil material affect the results. As the thickness of the exchange layer is smaller, erosion and deposition processes increase. The scale factor of the Meyer-Peter and Müller formula is a supplementary factor impacting the morphodynamic changes concerning the bed-load transport rate. The research about the scenario analysis does provide information, that a spatial extension of erosion and deposition areas remains unchanged. The benefit of the applied bed-load transport model shows that the variation of the parameter setup is of crucial importance considering morphodynamic processes. Due to erosion, deposition and downstream transport processes, crucial locations for intake structures into retention areas or sites for control gauge stations, can be determined. The study results are of great interest for determining possible optimization strategies and will be integrated into the detailed planning on flood protection measures and represent a big challenge for planners.

**REFERENCES**

Bunte, K. & Abt, S.R. (2001). *Sampling Surface and Subsurface Particle Size Distributions in Wadable Gravel and Cobble Bed Streams for Analyses in Sediment Transport, Hydraulics, and Streambed Monitoring,* U.S. Department of Agriculture, Forest Service, Rocky Mountain Research Station.

Exner, F.M. (1925). Über die Wechselwirkung zwischen Wasser und Geschiebe in Flüssen. Sitzungsberichte der Akademie der Wissenschaften in Wien. Abt. IIa, Band 134. Wien. (in German)

Fischer, M. (2008). *Ungesteuerte und gesteuerte Retention entlang von Fließgewässern – Beurteilung der Wirksamkeit möglicher Maßnahmen unter Verwendung hydrodynamisch-numerischer Modellierung,* Reports of the Chair of Hydraulic and Water Resources Engineering, Technical University of Munich, Nr. 119. (In German)

Gems, B. (2011). Entwicklung eines integrativen Konzeptes zur Modellierung hochwasserrelevanter Prozesse und Bewertung der Wirkung von Hochwasserschutzmaßnahmen in alpinen Talschaften – Modellanwendung auf Basis einer regionalen Betrachtungsebene am Beispiel des Ötztales in den Tiroler Alpen. Doctoral Thesis, Unit of Hydraulic Engineering, University of Innsbruck (in German).

Godina, R., Lalk, P., Lorenz, P., Müller, G. & Weilguni, V. (2006). Hochwasser 2005 – Ereignisdokumentation, Teilbericht des Hydrografischen Dienstes. Lebensministerium (BMLFUW). Wien (In German)

Habersack, H. (2000). Bedeutung des Feststoffhaushaltes für den Hochwasserschutz. *Conference ProceedingsoftheInterprävent*, Villach, Austria, 317-328. (in German)

Habersack, H., Wagner, B., Schoder, A. & Hauer, C. (2013). Die Bedeutung von Feststoffhaushalt und Sedimentdurchgängigkeit für eine nachhaltige Nutzung der Wasserkraft. *Österreichische Wasser- und Abfallwirtschaft,* 65(9-10), 354-61. (in German)

Haider, S. (2014). Retention in Unseren Flüssen. *Österreichische Wasser- und Abfallwirtschaft, 66(1-2)*, 59-66. (In German)

Hunziker, R.P. (1995). Fraktionsweiser Geschiebetransport, *Doctoral Thesis*. VAW-Reports, Laboratory of Hydraulics, Hydrology and Glaciology, ETH Zürich, Nr. 138, Zürich. (In German)

Meyer-Peter, E. & Müller, R. (1949). Eine Formel zur Berechnung des Geschiebetriebs. *Schweizerische Bauzeitung*, 67, 29-32. (In German)

Nujić, M., Hydrotec Ingenieurgesellschaft für Wasser und Umwelt mbH, Hunziker, Zarn & Partner, A.G. (2015). Benutzerhandbuch HYDRO_FT-2D, Erweiterung zu HYDRO_AS-2D zur Simulation des Stofftransports. Aachen. (In German)

Plörer, M., Achleitner, S., Gems, B. & Aufleger, M. (2012). Uncertainty in 2D Flood Plain Modeling Concerning Varying Distribution of Tributary Bed Loads and Rainfall. *Proceedings of the International Conference on Fluvial Hydraulics, San José. London:* Taylor & Francis, 1203-1210.

Rickenmann, D. (1990). *Bedload Transport Capacity of Slurry Flows at Steep Slopes,* VAW-Reports, Laboratory of Hydraulics, Hydrology and Glaciology, ETH Zürich, Nr. 103, Zürich.

Rudolf-Miklau, F., Ellmer, A., Gruber, H., Hübl, J., Kleemayr, K., Lang, E., Scheuringer, E., Schmid, F., Schnetzer, I., Weber, C. & Wöhrer-Alge M. (2006). Documentation of the Disasters of August 2005 in Austria Caused by Floods and Slope Movements: Methods and Results. Disaster Mitigation of Debris Flows, Slope Failures and Landslides. *International Symposium Interpraevent*, Niigata, Japan.

Umach, L. (2013). Bedeutung der Approximation von Kornverteilungskurven bei der zweidimensionalen numerischen Simulation von Geschiebetransportprozessen, *Doctoral Thesis*. Unit of Hydraulic Engineering, University of Innsbruck. (In German)

Wong, M. & Parker, G. (2006). Reanalysis and Correction of Bed-Load Relation of Meyer-Peter and Müller Using Their Own Database. *Journal of Hydraulic Engineering* 132(11), 1159-68.

 

Proceedings of the 37th IAHR World Congress
August 13 – 18, 2017, Kuala Lumpur, Malaysia

# INFLUENCE OF THE INITIAL VOLUME OF LOCK EXCHANGE GRAVITY CURRENTS ON THE SEDIMENT ENTRAINMENT CAPACITY

JESSICA ZORDAN[(1)]

[(1)] Laboratoire de Constructions Hydrauliques, École Polytechnique Fédérale de Lausanne, Switzerland
jessica.zordan@epfl.ch

## ABSTRACT

In the lock-exchange technique used to produce gravity currents, two fluids of different densities are initially at rest in a tank and separated by a vertical barrier, the lock gate. When this gate is suddenly removed, the two fluids come into contact and, due to differences in the hydrostatic pressure, the denser fluid flows along the bottom boundary of the tank, while the lighter fluid flows in the opposite direction above the gravity current. The initial volume of the denser mixture was found to highly influence the hydrodynamics behavior of the gravity current. The artifacts produced by the geometry of a limited lock exchange release are partly suppressed by increasing the volume of denser fluid and making it, at least, equal to the ambient fluid volume. In the present study the influence of the initial volume release is investigated focusing the attention on the potential capacity of the current to entrain sediments from an erodible bed. In fact, the erosive capacity has found to be a crucial characteristic of these type of flows responsible for the displacement of important sediment volumes. These flows are thus an important mechanisms of distal transport of sediments in the subaqueous environment. In these experiments, the lock gate was placed at three different locations to have three initial volumes of release. Two initial gravity current's densities were tested to have a total of nine experiences to compare. Using 3D instantaneous velocity measurements, the hydrodynamics of the gravity currents are analyzed. The bottom shear stress is estimated from the hydrodynamics measurements. Through the investigation of the instantaneous flow and turbulent quantities, the differences in the potential erosion capacities are discussed as function of the initial conditions of the gravity current.

Keywords**:** Lock-exchange gravity currents, initial volume of release, bottom shear stress, fine sediment entrainment, 3D instantaneous velocity profiles.

## 1 INTRODUCTION

Gravity currents are buoyancy driven flows created by differences in hydrostatic pressure between two fluids of different densities which are coming into contact. In a channel, the denser fluid flows along the bottom boundary, while the lighter fluid flows along the top boundary, in the opposite direction. Gravity currents are characterized by an important exchange at two interfaces, one at the interface with the lighter fluid and one at the bottom with the surface over which they flow. In nature, examples of gravity currents are multiples and in most of the cases, if the lower boundary over which they travel is mobile, they are characterized by a significant interaction with sediments. Consider the cases of lava flows, dust storms or snow avalanches: the presence of sediments entrained from the bed increases the density of the fluid. In water, suspended sediments at relative high concentration cause the formation of turbidity currents. Flowing over a variety of topography and different bed composed of erodible material, entrainment and eventually deposition of sediments can take place at a rate that depends on the characteristic of both the current and of the bed. Field studies have provided quantitative information in the nature of turbidity currents in lakes and reservoirs (De Cesare, 1988; De Cesare et al., 1998), but direct measurements are difficult to perform given the difficulties in handle the instrumentation: gravity currents have a destroying force that often make impossible to keep any type of installation (Parker et al., 1987). Thus, the utility of controlled laboratory experiments becomes evident (Parker et al., 1987). Advanced in experimental technology have increased our understanding from broad description of the gravity current morphology to the inner structure of turbulence in these currents (Kneller and Buckee, 2000).

Gravity currents experiments have been traditionally simulated through the lock-exchange configuration (Huppert and Simpson, 1980; Rottman and Simpson, 1983; Adduce et al., 2012; Nogueira et al., 2014; Theiler and Franca, 2016) that consists on the release of a volume of dense fluid into the lighter one, with the two fluids that are at the beginning at rest and separated by a gate. The aspect ratio of the denser volume is generally of the order of one ($R = h_0/x_0 \approx O(1)$, $h_0$ the water column depth and $x_0$ the lock length). Although partially idealized, such conditions provide and functional initial configuration for both theoretical considerations and numerical simulations (Hogg, 2006) and a closer affinity to real conditions. Continuous release of dense mixture is a second type of experiments that have been developed to produce currents that, by running much longer time periods than lock-exchange currents develop a stationary body. This brings the advantage of using averaging procedures to characterize the current (Tokyay et al., 2011). Recently, in order

 

to overcome the restrictions imposed by both set-up, gravity currents have been more frequently produced by lock-exchange with a lower aspect ratio: the initial volume of heavier fluid is comparable to the volume of the lighter one in the second part of the channel (Shin et al., 2004). This configuration allows the formation of an extended slumping phase in which the front velocity is almost constant. In these conditions, a quasi-steady regime is formed, similar to the steady state observed for constant feed gravity.

Few contributions focus on a detailed description of current's hydrodynamic at the lower boundary and even less on the ability of a gravity current to entrain material from the bed. This relevant characteristic of gravity currents is intended to be reproduced in the laboratory environment. In order to understand which is the influence in the erosion capacity estimation of the volume of release of gravity currents, lock lengths increasingly shorter have been tested. Initial conditions change the hydrodynamic characteristics of the current and so the entrainment potential is affected. The bottom shear stress is highly linked to sediment transport and so it is an indicator of the variation in the erosion capacity of gravity currents formed under different architectures.

Three gravity current initial densities have been tested combined with three lock-lengths. 3D velocity profiles were measured with the ADVP (Acoustic Doppler Velocity Profiler). The velocity field and the vorticity is presented. The bottom shear stress have been calculated through the logarithmic law of the wall theory and its time-development compared among the tests performed.

The present paper is structured as follows: first of all experimental set-up, instrumentations and experimental parameters are presented. Then the velocity field is described through the vector, streamwise velocity and vorticity field plots. The time evolution of bottom shear is also reported and discussed. In the final section the main findings are summarized and particular attention is given to the possible further steps of this research.

## 2 METHODS

### 2.1 Experimental set-up

The flume used to reproduce the gravity currents is 7.5 m long and 0.275 m wide, and it is divided into two sections by a vertically sliding gate. An upstream reach serves as head tank for the dense mixture that is made by dissolving sodium chloride to ambient water. A downstream reach is where the current propagates and where the main measurements are made at a sufficient distance from the gate so to have a completely formed current after the lock opening. The bottom is horizontal and smooth along the whole channel. Three aspect ratios $R = h_0/x_0$ have been tested (Figure 1). The water depth ($h_0$) have been kept constant and equal to 0.2 m, values of $x_0$ (L0, L1, L2 in Figure 1) are summarized in Table 1. Downstream, the current is let to dissipate flowing down into a final large inertial tank.

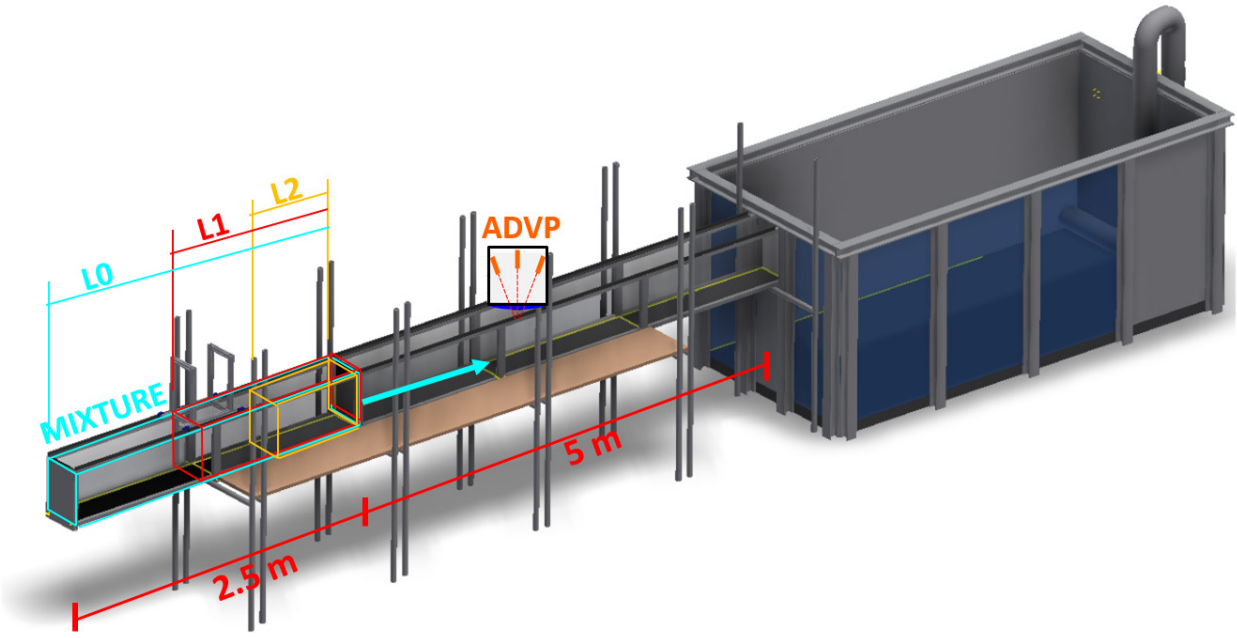


**Figure 1**. 3D view of the experimental set-up.

 

2.2 Measurements and instrumentation

The 3D Acoustic Doppler Velocity Profiler (ADVP) (Lemmin and Rolland, 1997; Franca and Lemmin, 2006) is a non-intrusive sonar instrument that measures the instantaneous velocity profiles using the Doppler effect. It takes 3D instantaneous velocity measurements during the passage of the density current over a vertical, including the upper counter flow. For studies of turbulent flow, a high sampling frequency is desirable. The minimum number of pulse-pairs was here fixed at 32, due to our working conditions, which corresponds to a frequency of acquisition of 31.25 Hz (Lemmin and Rolland, 1997). The instrument consists of a central emitter surrounded by four receivers. The geometric configuration is the result of an optimization of the instrument that allows noise reduction by creating redundancy information for the velocity components (Blanckaert and Lemmin, 2006). This, together with the despiking procedure proposed by Goring and Nikora (2002), leads to a considerable reduction in the noise level of the data set. The velocity data consists of instantaneous 3D velocity profiles along a vertical. The analysis of the power spectra of the raw data collected with the ADVP allows the identification of the noisy frequencies that where furthermore cut off through a low-pass filter of the signal. The maximum time window which allowed to still recognize the characteristic frequencies of the signal was analyzed in order to apply a moving averaging to define the mean velocity field, following Baas et al. (2005).

2.3 Experimental parameters

The experimental parameters of the nine tests performed are shown in Table 1 where $\rho_0$ is the gravity current initial density (as measured with a densimeter in the upstream reach), *g'* is the initial reduced gravity of

$$g' = g\frac{\rho_0 - \rho_a}{\rho_a} \quad [1]$$

the dense fluid defined as:

The lock-length (L) have been varied, the ratio of volume calculated as $V_i/V_0$ ($V_0$ the volume

$$Re_0 = \frac{Uh_c}{\nu} \quad [2]$$

with $U = \sqrt{g'h_c}$ the buoyancy velocity.

correspondent to the longer lock) is calculated and reported in Table 1. Re is the Reynolds number determined as:

Each run have been called *R1, R2* and *R3* to identify the gravity current's initial density, from the lowest one to the greatest, and *L0*, *L1* and *L2* stands for the lock-length as shown in Figure 1.

**Table 1**. Experimental parameters for all experiments.

| | $\rho_0$ kg/m$^3$ | g' m$^2$/s | L m | $V_i/V_0$ - | $Re_0$ x10$^3$ |
|---|---|---|---|---|---|
| **R1.L0** | 1028 | 0.29 | 2.500 | 1.00 | 48.2 |
| **R1.L1** | 1028 | 0.29 | 1.250 | 0.50 | 48.2 |
| **R1.L2** | 1028 | 0.29 | 0.625 | 0.25 | 48.2 |
| **R2.L0** | 1038 | 0.39 | 2.500 | 1.00 | 55.7 |
| **R2.L1** | 1038 | 0.39 | 1.250 | 0.50 | 55.7 |
| **R2.L3** | 1038 | 0.39 | 0.625 | 0.25 | 55.7 |
| **R3.L0** | 1048 | 0.49 | 2.500 | 1.00 | 62.4 |
| **R3.L1** | 1048 | 0.49 | 1.250 | 0.50 | 62.4 |
| **R3.L2** | 1048 | 0.49 | 0.625 | 0.25 | 62.4 |

## 3 RESULTS

3.1 Flow description

The mean streamwise and vertical instantaneous velocity components collected with the ADVP instrumentation are reported in Figure 2 as vector field, for all the tests performed, and for the first 10 seconds. We focus here on the head of the current, the most turbulent part of the current and where the greatest vertical movements are identified. Red dotted lines indicate the contour of the current that on the plot

 

is flowing from the right to the left side. The swirling movements of eddies are identified in correspondence of the high velocity difference at the interface between the heavy and light fluids. These movements are called Kelvin-Helmholtz instabilities that shed from the head of the current as the front advances. The mean vorticity was calculated as:

$$\eta = \frac{\partial w}{\partial x} - \frac{\partial u}{\partial z} \qquad [3]$$

where *w* is the vertical mean velocity component and *u* is the streamwise one. The two terms above have been calculated according to the algorithm proposed by Sveen (2004), Raffel et al. (2013) and used by Nogueira et al. (2013) as follows:

$$\left.\frac{\partial w}{\partial x}\right|_{i,j} = \frac{2w_{i+2,j} + w_{i+1,j} - w_{i+1,j} - 2w_{i-2,j}}{10\Delta x} \qquad [4]$$

$$\left.\frac{\partial u}{\partial z}\right|_{i,j} = \frac{2u_{i,j+2} + u_{i,j+1} - u_{i,j+1} - 2u_{i,j-2}}{10\Delta z} \qquad [5]$$

being *i* and *j* the coordinate of measuring points for streamwise and vertical directions *x* and *z* and indicated as $\Delta x$ and $\Delta z$ are the distances between adjacent points.

The computed vorticity field is shown in Figure 2 as background of the vector field. In general, two regions of opposite vorticity are observed. The structures in the interfacial shear layer rotate clockwise, accelerating towards the back of the current, within the current, and defining a region of negative vorticity. By continuity, the ambient fluid above is accelerated towards the upper layer and a region of positive vorticity is individuated. In Figure 2 for test *R2.L0* the movements are put in evidence with arrows.

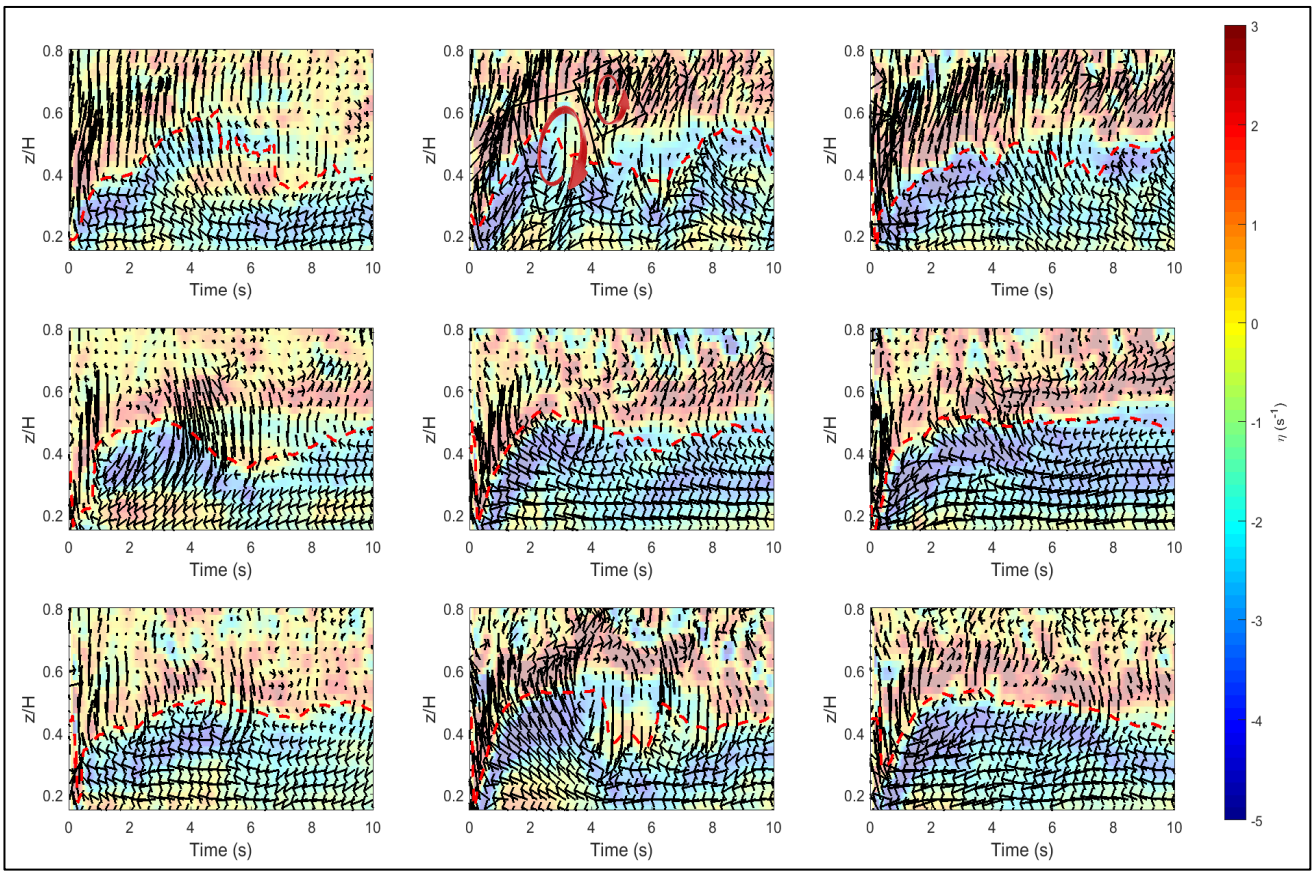


**Figure 2**.Vorticity field $\eta$ $(s^{-1})$ and $(u,w)$ vector plot for all the tests performed with increasing initial densities from column on the left side to column on the right side and decreasing lock-length from first row on the top to the bottom. For test *R2.L0* the movements of the fluid are put in evidence with arrows

### 3.2 Bed shear stress

Under the assumptions of flow gradually varied in the longitudinal direction, essentially two dimensional in vertical plane, and with high relative submersion, the longitudinal velocity in the overlapping layer can be fitted to the logarithmic law of the wall (Eq. [6], Ferreira et al., 2012) following the procedure presented in (Zordan et al., 2016):

$$\frac{u(z)}{u_*} = \frac{1}{\kappa} \ln\left(\frac{z}{z_0}\right) \qquad [6]$$

where *u=u(z)* is the mean longitudinal velocity (generally averaged over a sufficiently long time scale), $u_*$ is the friction velocity, $\kappa$ is the von Kármán constant ($\kappa \approx 0.41$), *z* is the vertical coordinate and $z_0$ is the zero-velocity level (which is the vertical coordinate of the closest velocity measurement to the bottom, as collected with the ADVP).

The fitting procedure of the logarithmic layer is adopted for each instantaneous mean profile collected with the ADVP instrumentation thus an estimation of the bed shear stress is made for each measuring instant. The evolution of the bed shear stress along the streamwise direction is shown in Figure 3 over the current velocity as a background.

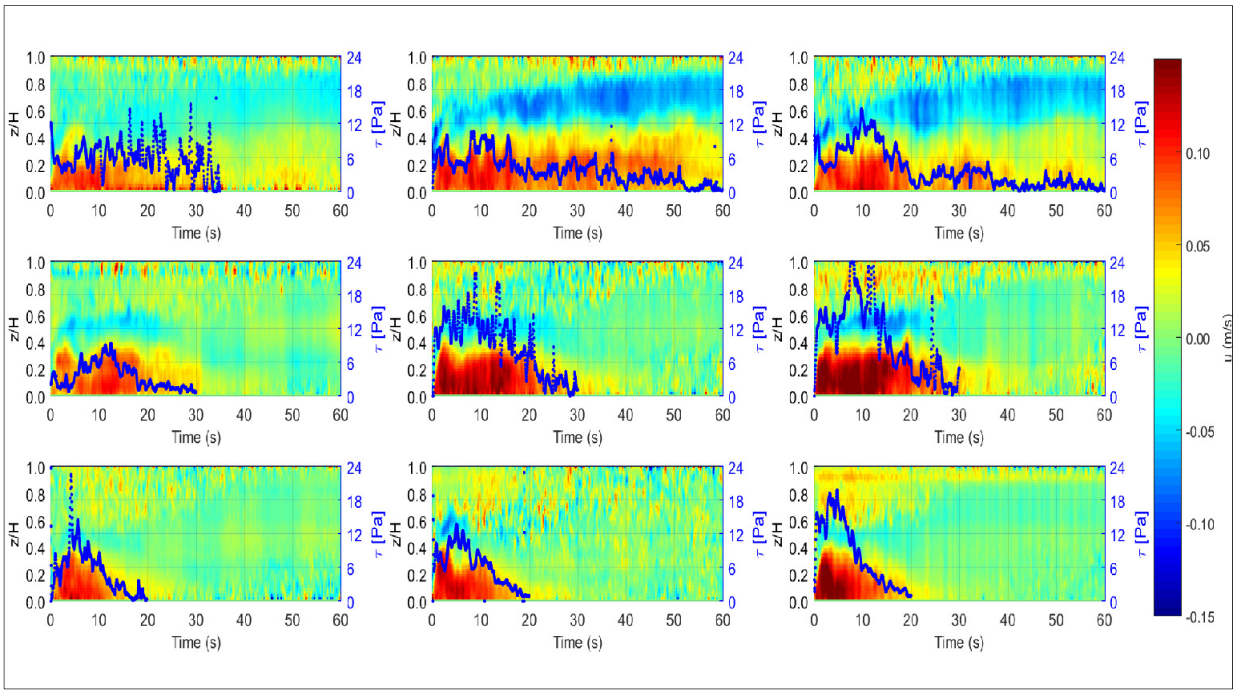


**Figure 3.** Bed shear stress evolution computed after the fitting procedure of the log layer for all the tests performed with increasing initial densities from column on the left side to column on the right side and decreasing lock-length from first row on the top to the bottom.

The bed shear stress generally shows greater values in the frontal region of the current due to the high velocity of the head. Bed shear stress is generally greater for currents of larger initial density. Tests conducted under reduced lock-length produce shorter currents, with a more defined tail and not developed body, and they show a large peak of bed shear stress at the head followed by a steep diminution. The quasi-steady body of the longest lock-length tests present a long-lasting residual bottom shear stress.

## 4 DISCUSSION

Bed entrainment is related to the evolution of bed shear stress. Once the bed shear stress exceed a certain threshold the entrainment takes place. In order to estimate the potential of bed sediment entrainment by the passage of a gravity current, a new quantity has been defined. The evolution in time of the integral of the bed shear stress $\Phi(t) = \int_0^T \tau_b(t)dt$ which, for a fixed advection velocity, represents the work done from *t=0*

 

to *t=T*, per unit surface. The increment in time of this quantity, namely its slope (a power per unit surface), is an indicator of the type of the erosion potential of the gravity current.

In Figure 4, $\Phi(t)$ have been calculated for the nine performed tests. For each geometrical configuration (L0, L1 and L2), the slope of the integral bottom shear stress is increasing with the initial density: steeper lines are identified going from R1 to R3. The slope for the smallest lock-length (L3) grows faster than the other configurations, flattening at around t=10s. At this point the high velocity core of the currents have already passed and consequently the erosion potential is expected to fade.

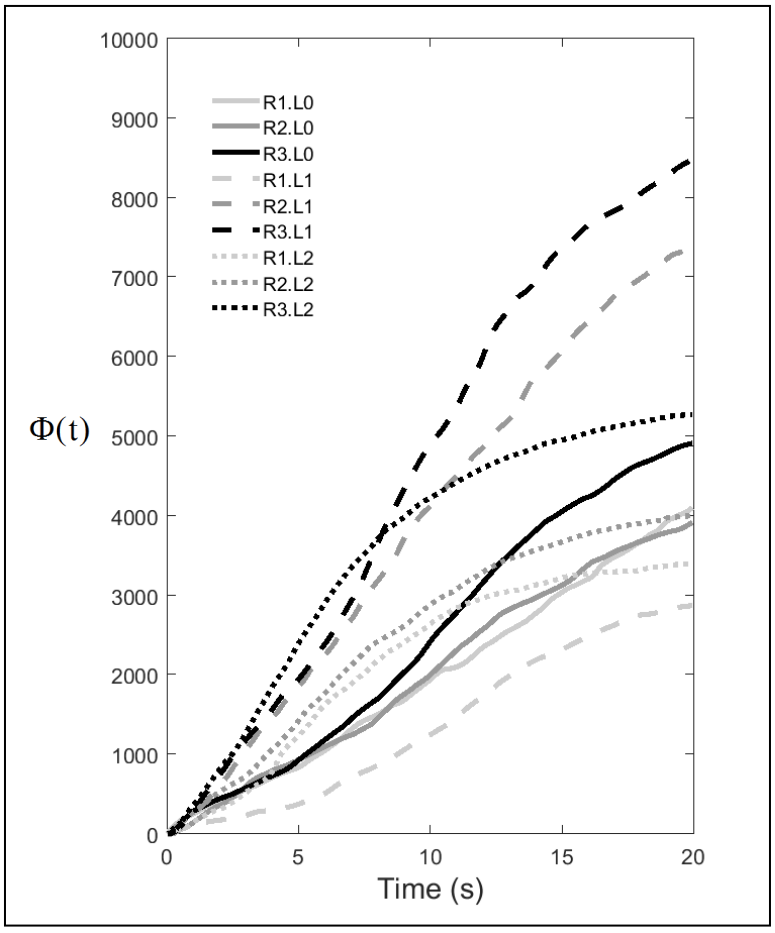


**Figure 4.** Time evolution of the temporal integral of the bed shear stress. In black are the tests with the lowest (*R1*) initial density, dark gray is *R2* and light gray is for the largest initial density (*R3*). The solid line is for tests with the configuration *L0*, dotted line is *L1* and punctuated line is *L2*.

## 5 CONCLUSION

In order to have a quantification of the entrainment capacity of a gravity current, the bed shear stress have to be estimated. At the moment experimental investigation on this subject are very few due to the difficulties of having accurate velocities measurements in the vicinity of the bed (Ooi at al., 2009). The development of bed shear stress is influenced by the initial conditions in which the current form. In this paper the influence of the lock-length on the temporal evolution of bed shear stress due to gravity currents is investigated. The head has been found to be characterized by the highest values of bed shear stress. The body has relevant values of bed shear stresses just when it is well defined, as when the lock-exchange technique to produce gravity currents approach the continuous release, i.e. in the L0 with the highest volume of initial dense fluid tests. An indicator of the type of time-evolution of the bed shear stress has been defined with $\Phi(t)$. The characterization of bed shear stress evolution depending on the set-up configuration was discussed. For the next steps we intend to simulate a mobile bed over which the gravity current flows and entrains sediments. Measurements of volumes of entrained material will be thus possibly related to the herein estimated bed shear stress.

## ACKNOWLEDGMENTS

This research was funded by the European project SEDITRANS funded by Marie Curie Actions, FP7-PEOPLE-2013-ITN-607394 (Multi partner - Initial Training Networks) and supervised by Prof. Anton J. Schleiss and Dr Mário J. Franca.

 

**REFERENCES**

Adduce, C., Sciortino, G. & Proietti, S. (2012). Gravity Currents Produced By Lock Exchanges: Experiments And Simulations With A Two-Layer Shallow-Water Model With Entrainment. *Journal of Hydraulic Engineering*, 138(2), 111-121.

Baas, J.H., Mccaffrey, W.D., Haughton, P.D. & Choux, C. (2005). Coupling between Suspended Sediment Distribution and Turbulence Structure in a Laboratory Turbidity Current. *Journal of Geophysical Research*: Oceans, 110, 1-20

Blanckaert, K. & Lemmin, U. (2006). Means of Noise Reduction in Acoustic Turbulence Measurements. *Journal of Hydraulic Research*, 44(1), 3–17.

Britter, R.E. & Simpson, J.E. (1978). Experiments on the Dynamics of a Gravity Current Head. *Journal of Fluid Mechanics*, 88(02), 223-240.

Cenedese C. & Adduce C. (2008) Mixing in a Density Driven Current Flowing Down a Slope in a Rotating Fluid. *Journal of Fluid Mechanics* 604, 369–388.

De Cesare, G., Portner, N. B., Boillat, J.L. & Schleiss, A.J. (1998). Modelling of Erosion and Sedimentation Based On field Investigations in Alpine Reservoirs of Hydropower Schemes. *Proceedings of the 3rd International Conference on Hydroscience and Engineering, Berlin*, Vol.3, September.

De Cesare, G. (1998) Alluvionnement Des Retenues Parcourant De Turbidité. Doctoral Dissertation, École Polytechnique Fédérale De Lausanne.

Ellison T.H. & Turner J.S. (1959). Turbulent Entrainment in Stratified Flows. *Journal of Fluid Mechanics* 6, 423–448

Goring, D.G. & Nikora, V.I. 2002. Despiking Acoustic Doppler Velocimeter Data. *Journal of Hydraulic Engineering*, 128(1), 117-126.

Franca, M.J. & Lemmin, U. 2006. Eliminating Velocity Aliasing in Acoustic Doppler Velocity Profiler Data. *Measurement Science and Technology*, 17(2), 313-322.

Hogg, A.J. (2006). Lock-Release Gravity Currents and Dam-Break Flows. *Journal of Fluid Mechanics*, 569, 61-87.

Huppert, H.E. & Simpson, J.E. (1980). The Slumping Of Gravity Currents. *Journal of Fluid Mechanics*, 99(04), 785-799.

Kneller, B. & Buckee, C. (2000). The Structure and Fluid Mechanics of Turbidity Currents: A Review of Some Recent Studies and Their Geological Implications. *Sedimentology*, 47, 62-94.

Lemmin, U. & Rolland, T. (1997). Acoustic Velocity Profiler for Laboratory and Field Studies. *Journal of Hydraulic Engineering*, (12): 1089-1098.

Müller,M., De Cesare, G. & Schleiss, A.J. (2014). Continuous Long-Term Observation of Suspended Sediment Transport between Two Pumped-Storage Reservoirs. *Journal of Hydraulic Engineering*, 140(5), 1–9.

Nogueira, H. I., Adduce, C., Alves, E. & Franca, M.J. (2013). Analysis of Lock-Exchange Gravity Currents Over Smooth and Rough Beds. *Journal of Hydraulic Research*, 51(4), 417-431.

Nogueira, H.I.S., Adduce, C., Alves, E. & Franca, M.J. (2014). Dynamics of the Head of Gravity Currents. *Environmental Fluid Mechanics*, 14(2), 519-540.

Ooi, S.K., Constantinescu, G. & Weber, L. (2009). Numerical Simulations of Lock-Exchange Compositional Gravity Current. *Journal of Fluid Mechanics*, 635, 361-388.

Parker, G., Garcia, M., Fukushima, Y. & Yu, W. (1987). Experiments on Turbidity Currents over an Erodible Bed. *Journal of Hydraulic Research*, 25(1), 123–147.

Raffel, M., Willert, C.E., Wereley, S. & Kompenhans, J. (2013). *Particle Image Velocimetry: A Practical Guide*. Springer.

Rottman, J.W. & Simpson, J.E. (1983). Gravity Currents Produced By Instantaneous Releases of a Heavy Fluid in A Rectangular Channel. *Journal of Fluid Mechanics*, 135, 95-110.

Shin, J.O., Dalziel, S.B. & Linden, P.F. (2004). Gravity Currents Produced By Lock Exchange. *Journal of Fluid Mechanics*, 521, 1-34.

Sveen, J.K. (2004). An Introduction to Matpiv V. 1.6. 1. *Preprint Series. Mechanics and Applied Mathematics Http://Urn. Nb. No/URN: NBN: No-23418*.

Theiler, Q. & Franca, M.J. (2016). Contained Density Currents With High Volume Of Release. *Sedimentology*, 63(6), 1820-1842.

Tokyay, T., Constantinescu, G. & Meiburg, E. (2011). Lock-Exchange Gravity Currents with a High Volume of Release Propagating Over a Periodic Array of Obstacles. *Journal of Fluid Mechanics*, 672, 570-605.

Zordan, J., Schleiss, A.J. & Franca, M.J. (2016). Bed Shear Stress Estimation For Gravity Currents Performed In Laboratory. *River Flow 2016,* June 2016, 855-861.

 

# FLOW OVER A WATER-WORKED BED

NADIA PENNA[(1)], ELLORA PADHI[(2)], SUBHASISH DEY[(3)] & ROBERTO GAUDIO[(4)]

[(1,4)] Dipartimento di Ingegneria Civile, Università della Calabria, Rende (CS), Italy,
nadia.penna@unical.it, gaudio@unical.it
[(2,3)] Indian Institute of Technology, Kharagpur, West Bengal, India,
ellora.padhi@yahoo.co.in, sdey@iitkgp.ac.in

## ABSTRACT

In this paper, we present the preliminary results of an extended experimental campaign conducted over both unworked (UW) and water-worked (WW) beds using a non-intrusive Particle Image Velocimetry (PIV) system. The main objective of this study was to explore the differences between the two cases in terms of double-averaged (DA) streamwise velocities, DA normal velocities, DA Reynolds shear stress, form-induced stresses, DA Reynolds normal stresses, form-induced normal stresses, total shear stresses, ratio of form-induced stresses to DA Reynolds shear stresses. This study leads to the conclusion that the flow and turbulence characteristics in wall-shear layer of a WW bed are different from those of an UW bed, while they are almost indifferent in the outer layer of flow. Hence, the results from UW bed experiments need to be treated with caution if applied for the analysis of the near-bed flow field.

**Keywords:** Water-worked bed; gravel bed; 2D flow field; PIV; double-averaging methodology.

## 1 INTRODUCTION

One of the key problems in the research on fluvial hydraulics is the correct reproduction of the flow dynamics over a riverbed in laboratory experiments. Generally, in an experimental setup attention is particularly paid to design of the facility with respect to some hydraulic conditions related to the flow regime, the sediment transport and the bed erosion. In this context, the sediment size of the riverbed to be analysed plays an important role.

It is worth mentioning that several studies demonstrated that the way in which the beds are formed might have, at the same time, an important effect on the flow field (e.g., Koll et al., 2010; Cooper and Tait, 2009; Buffin-Bélanger et al., 2006; Barison et al., 2003). However, it is a common practice to create the bed using a screeded mixture of sediments, with random orientation, packing, spacing and sorting, which could be very different from that observed in natural riverbeds. To overcome this issue and to produce a surface topography that is more representative of the actual conditions, the bed should be water-worked (WW) before the performance of the experimental tests.

Barison et al. (2003) discovered that the near-bed spatial distribution of time-averaged streamwise velocity is significantly different over unworked (UW) beds with respect to WW beds. Cooper and Tait (2008) examined the spatial pattern of time-averaged streamwise velocity in the near-bed region, showing a considerable degree of organization over a WW bed: streamwise streaks of high-speed fluid overlain by spots of low-speed fluid. This pattern indicates the presence of spatially coherent time-averaged flow structures. In their subsequent studies, Cooper and Tait (2009) found that the use of UW bed underestimates the degree of temporal variability in the flow and, in addition to that, the time-averaged streamwise velocities were randomly organized over the UW bed and organized into long streamwise flow structures over the WW beds. They also investigated the level of flow spatial variability and its influence on momentum transfer, considering WW surfaces (Cooper and Tait, 2010). McLelland (2013) performed a series of experiments over a rough WW bed to investigate the development of coherent secondary flow cells. Hardy et al. (2013) quantified simultaneously both the kinematic and dynamic characteristics of coherent flow structures generated over WW gravel surfaces. Finally, Cooper et al. (2013) conducted a detailed study on the influence of submergence on the spatial heterogeneity of key near-bed flow parameters, measuring the flow field over WW beds.

In spite of the existing knowledge on the flow over WW beds, a more detailed description of the turbulent flow characteristics is still required. Thus, this paper presents a novel experimental study designed to contribute to such description over both UW and WW gravel beds by using Particle Image Velocimetry (PIV) measurements as well as to demonstrate the importance of creating WW beds for simulating near-bed flow fields in laboratory model studies.

 

## 2 EXPERIMENTAL FACILITY AND PROCEDURE

### 2.1 Flume and related facilities

The experimental campaign was carried out in a recirculating rectangular 9.66 m-long, 48.5 cm-wide tilting flume, with an initial longitudinal slope $S_0$ = 0.7%, at the *Laboratorio "Grandi Modelli Idraulici"* (GMI) of the *Università della Calabria* (Italy). A 7 m-long, 12 cm-deep recess box was located at about 1 m from the flume inlet. The left wall of the flume was made of PVC, whereas in order to allow the PIV flow field measurements, a 2 m-long glass panel was installed at the right wall of the flume, 6 m downstream of the inlet. The scheme of the experimental setup is shown in Figure 1.

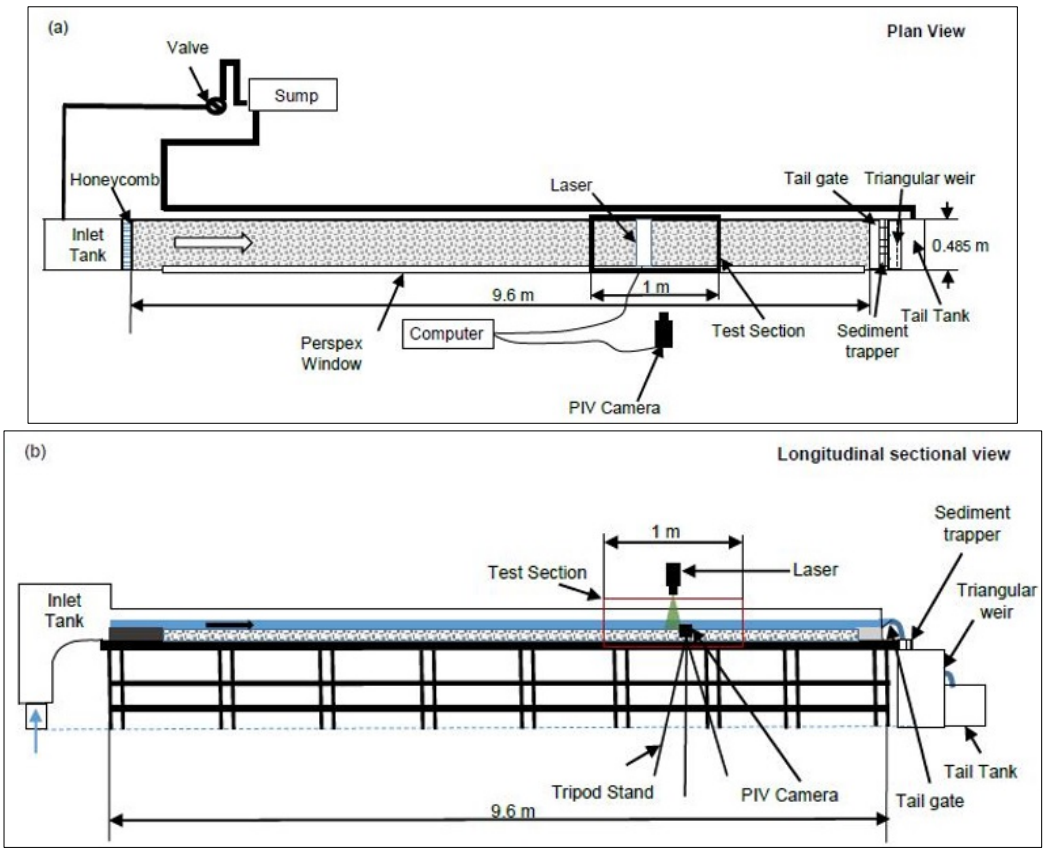


**Figure 1**. (a) Plan view and (b) longitudinal sectional view of the experimental setup.

The inlet of the flume consisted of a stilling tank, an uphill slipway and a honeycomb to reduce the residual pump vibrations. The flow depth was controlled by an adjustable tailgate at the flume outlet. The flow was supplied and measured by an electric pump and a Thomson weir. It was collected in a downstream tank, from which it fell in a restitution channel. At the beginning of the experiments, the hydraulic conditions were fixed such as the slope was adjusted with the help of a hydraulic jack, while the water depth was set with the tailgate. The discharge was easily kept constant without moving the valves regulating the discharge or the tailgate regulating the water depth, but only by switching the pump on/off. However, the flow rate was carefully checked during the experiment through the weir, which has an accuracy of less than 2%.

The recess box was filled with coarse gravel having a unimodal distribution (4 < $d$ < 6 mm), with median diameter $d_{50}$ = 4.81 mm and geometric standard deviation $\sigma_g = (d_{84}/d_{16})^{0.5}$ = 1.18, where $d_{16}$ and $d_{84}$ are the particle sizes finer than 16% and 84% (by weight), respectively. Figure 2 shows the grain-size distribution of the mixture used to create the bed, which was obtained by analysing three gravel samples. The sediments used in the present study were characterized by a specific gravity of 2.71. Initially, the bed was not compacted, but screeded to ensure the same slope as the flume bottom. The same bed material was also glued on the false floors (upstream to and downstream of the recess box) in order to avoid any change in water profile due to change in bed roughness.

### 2.2 Design of the experimental tests

All the measurements were taken starting from the test section 6.3 m downstream the inlet of the flume, where the flow was quasi-uniform, owing to the presence of the tailgate, with water depth $h$~10 cm and constant flow discharge of ~ 0.021 $m^3 \cdot s^{-1}$ (for both the UW and WW beds).

 

The flow depth was selected in order to provide the aspect ratio $B/h$ = 4.8 > 3 (where $B$ is the flume width) and avoid wall effects in the flume centre during the experiments. However, the flow discharge was determined to prevent particle movement during the experiments (clear-water condition) for both UW and WW beds.

In fact, it is necessary to ensure a flow intensity $U / U_c < 0.9$, where $U$ is the approach flow velocity and $U_c$ the threshold value for the inception of sediment movement. A preliminary estimation of $U_c$, using the empirical formulae by Laursen (1963), Neill (1967) and Garde (1970), gave the following values (Eqs. [1], [2] and [3], respectively):

$$U_c = 6h^{1/6} d_{50}^{1/2} = 0.69 \text{ m s}^{-1} \quad [1]$$

$$U_c = \sqrt{2.5\left(\frac{h}{d_{50}}\right)^{0.2} g\Delta d_{50}} = 0.61 \text{ m s}^{-1} \quad [2]$$

$$U_c = \left(0.5\log\frac{h}{d_{50}} + 1.63\right)\sqrt{g\Delta d_{50}} = 0.65 \text{ m s}^{-1} \quad [3]$$

where $g$ is the gravity acceleration and $\Delta$ the relative submerged grain density.

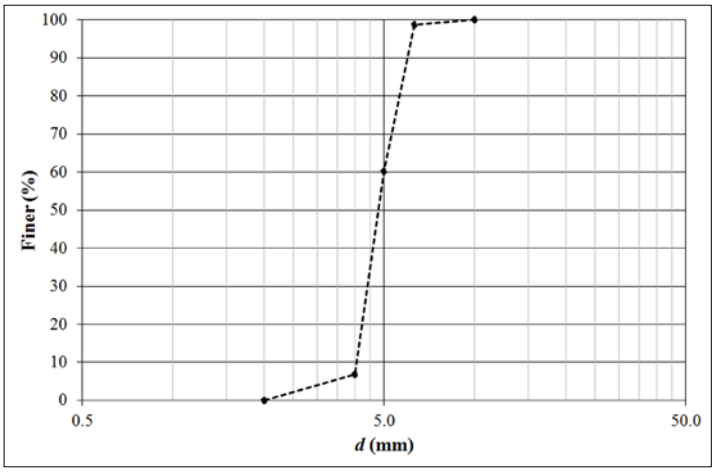


**Figure 2**. Grain-size distribution curve of the bed sediment.

A more accurate estimation of $U_c$ was also carried out through the direct observation of particle movement. Specifically, for $U$ = 0.61 m s$^{-1}$, the particle motion in isolated zones of movable bed was observed. It is may be noted that the average predicted value of $U_c$ by Laursen (1963), Neill (1967) and Garde (1970) was equal to 0.65 m s$^{-1}$, which is close to the observed value. Therefore, the latter was assumed in the present study for $U_c$. This indicates that considering the selected flow discharge for which $U$ is 0.43 m s$^{-1}$, the experiments were performed with flow intensity of $U / U_c$ = 0.71.

The Froude number, $Fr = U / (gh)^{0.5}$, and the Reynolds number, $Re = 4hU/\nu$ (where $\nu$ is the kinematic water viscosity, equal to $1.31 \cdot 10^{-6}$ m$^2$ s$^{-1}$ at the temperature of 10°C), were 0.44 and 93600, respectively. The shear particle Reynolds number $Re^* = 2d_{50}u_* / \nu$ (where $u_*$ is the shear velocity) was found to be 530 > 400, ensuring the fully developed flow condition.

The experimental quantities for the tests in clear-water condition for both UW and WW beds are presented in Table 1.

**Table 1**. Experimental quantities of the tests in clear-water condition for the UW and WW beds.

| $S_0$ (%) | $d_{50}$ (mm) | $\sigma_g$ (mm) | $Q$ (m$^3$ s$^{-1}$) | $h$ (m) | $U$ (m s$^{-1}$) | $U_c$ (m s$^{-1}$) | $U/U_c$ | $Fr$ | $Re$ | $Re^*$ |
|---|---|---|---|---|---|---|---|---|---|---|
| 0.7 | 4.81 | 1.18 | 0.021 | 0.10 | 0.43 | 0.61 | 0.71 | 0.44 | 93600 | 530 |

2.3 Experimental procedure

The first phase of the experiment was aimed to the acquisition of the UW bed surface with a Leica ScanStation P16, which was a time-of-flight style scanner with a 3D accuracy of 3 mm at a distance of 40 m. The bed topography was measured over an area of 200 cm x 40 cm in the streamwise and spanwise directions, respectively. This area was scanned from eight separate stations with different elevations, two at the upstream end, two at the downstream end, two at the right wall and two at the left wall. The raw data were

 

processed using the manufacturer's software, Leica Geosystems Cyclone 9.0. From the resulting cloud of points, a Digital Elevation Model (DEM) of the analysed area was created using the open-source software MeshLab. Thus, the DEM was detrended to remove the longitudinal and transversal slopes, preserving the actual elevations of the bed surface. It was also possible to verify the slope of the bed, equal to the value obtained from the manual measurement (by using a point gauge), as well as to determine the characteristic vertical roughness height $k_s$ (i.e., the standard deviation of the bed elevation with respect to the mean surface elevation, set equal to zero), equal to 1.36 mm.

The second phase of the experiment was focused on the velocity measurements with the PIV system (described in detail in §2.4) over the UW bed, adopting the experimental conditions of Table 1. The flow measurements were taken along the flume centreline at three different longitudinal sections, located at 6.30, 6.80 and 7.30 m from the inlet, respectively, corresponding to the midpoints of the measured vertical planes.

The third phase of the experiment was dedicated to the formation of the WW bed. The screeded bed was water-worked using a flow discharge of about 0.035 $m^3 s^{-1}$, with the tailgate completely lowered. The experimental quantities for the test are furnished in Table 2. Note that in this case, the flow intensity allows the establishment of the live-bed condition ($U / U_c > 1$). The sediment transport took place over a period of 28.5 h, during which its rate declined exponentially from about 72 g $m^{-1} s^{-1}$ to about 0.3 g $m^{-1} s^{-1}$ (Figure 3). There was no sediment input during the sediment transport phase, since the bed degradation (scoured pit) developed at the first meter of the recess box provided continuous sediment feeding to the downstream bed. At the end of this phase, the bed slope decreased to $S$ = 0.4% and the scoured pit was manually filled in to maintain the flow conditions unchanged. Such a steady value of the bed slope was taken to indicate the achievement of the equilibrium condition. Figure 4 shows the bed surface before and after the water-working process.

The fourth phase of the experiment was again aimed to the acquisition of the WW bed surface by using the laser scanner with the same set-up and procedure adopted for the UW bed. Also in this case, the slope of the bed was verified and it was the same as that obtained from the manual measurement. Moreover, the $k_s$ was determined as 1.25 mm.

The fifth and last phase of the experiment was conducted to measure the velocity with the PIV system over the WW bed, adopting the same experimental conditions (Table 1), except the bed slope, and same set-up used for the UW bed, in order to compare the two cases.

**Table 2**. Experimental quantities of the test in live-bed condition.

| $S_0$ (%) | $S$ (%) | $d_{50}$ (mm) | $\sigma_g$ (mm) | $Q$ ($m^3 s^{-1}$) | $h$ (m) | $U$ (m $s^{-1}$) | $U_c$ (m $s^{-1}$) | $U/U_c$ | $Fr$ | $Re$ | $Re^*$ |
|---|---|---|---|---|---|---|---|---|---|---|---|
| 0.7 | 0.4 | 4.81 | 1.18 | 0.035 | 0.09 | 0.84 | 0.58 | 1.44 | 0.92 | 162700 | 502 |

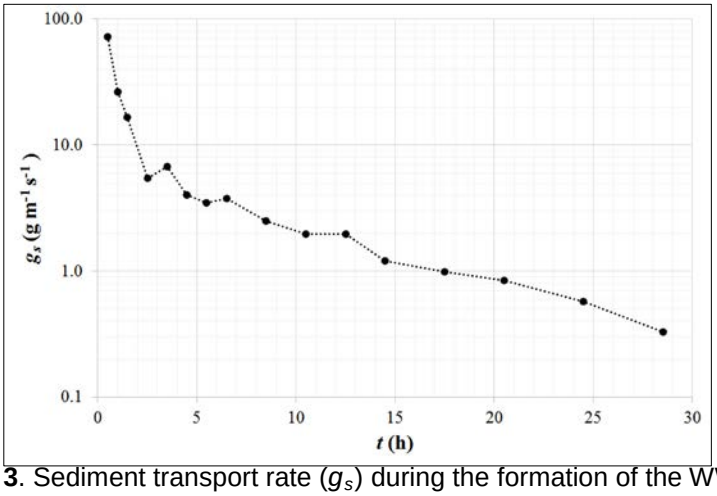


**Figure 3**. Sediment transport rate ($g_s$) during the formation of the WW bed.

2.4 PIV measurements

A TSI® PIV system was used for the velocity measurement. It consisted of a Nikon 12-bit 2048 × 2048 px CCD camera with a frame rate of 15 Hz and a double pulse Nd:YAG laser with pulse energy of 50 mJ, operated at 15 Hz with a time delay of 1000 μs between frames. The PIV system was used at 7.25 Hz, owing to PC port frequency limitation. The flow was seeded with titanium dioxide having a mean diameter of 3 μm and a density of 4.26 g $cm^{-3}$.

The light sheet was set perpendicularly to the bed surface, while the camera was positioned perpendicularly to the glass wall of the flume in order to obtain the instantaneous streamwise and vertical velocities ($u$ and $w$, respectively) for the entire flow depth. Three vertical planes were measured along the centreline of the flume, every 50 cm starting from the abscissa $x$ = 6.30 m in the streamwise direction. For

 

each position, 3000 image couples were acquired, with a measuring area of 140 mm × 140 mm (64 px × 64 px). The image analysis provided about 23 velocity profiles, covering an area of 60 mm × 100 mm, with a spatial resolution of 2.2 mm. Spurious velocity data were despiked using the phase-space thresholding method without spike replacement (Goring and Nikora, 2002).

The resulting instantaneous velocities were used to determine the turbulence and spatial flow characteristics. By combining time and spatial averaging approaches, the double-averaged (DA) characteristics of the flow, for both the UW and WW beds, were analysed.


**Figure 4**. Photographs of the: a) UW, and b) WW beds (the flow is directed from left to right).

## 3 RESULTS AND DISCUSSION

### 3.1 DA velocity

The normalized double averaged (DA) streamwise velocity profiles for the UW and WW beds are shown in Figure 5(a, b). It presents the distribution of normalized streamwise velocity $\langle u^+ \rangle = \langle \bar{u} \rangle + u_*$ over the normalized vertical distance $\tilde{z} = z / h$. Note that angle brackets denote the double averaged quantities. For $z \leq 0$ (below the maximum grain crest), the roughness geometry function $\phi$ (= $A_f/A_0$, where $A_f$ is the area occupied by the fluid at the elevation $z$ and $A_0$ the total area) was used as a multiplier of an intrinsic DA flow quantity contributing to a superficial DA flow quantity (Ferraro et al., 2016; Dey and Das, 2012; Aberle, 2007). The distributions of the geometry function for both the UW and WW beds are shown in Figure 6. The shear velocity was calculated by linearly extrapolating the value of the DA Reynolds shear stress from the region above the bed surface down to the maximum crest of gravels (Manes et al., 2007), determined by using the DEM, for both the cases.

Near the bed the velocity is less, but with an increase in elevation, it also increases and attains the maximum value just below the water surface. The maximum normalized velocity for the UW bed is 17.27, whereas for WW bed, it is found as 17.30. In the present study, the inflection point appearing in the DA streamwise velocity profiles is attributable to the effect of the roughness element rather than to the effect of the mixing layer nature of the near-bed flow. The log-layer does not start immediately above the roughness crest, but it starts from the roughness sublayer.

Figure 5(c) shows the vertical profile of normalized DA streamwise velocity of both the beds. To fit the data plots within the wall shear layer ($z > 0$) above the gravel crests with a logarithmic law, $\langle u^+ \rangle$ and $z$ are scaled by $u_*$ and $\Delta z$, respectively, such that $\langle u^+ \rangle = \langle \bar{u} \rangle + u_*$ and $z^+ = (z + \Delta z)/\Delta z$ where $\Delta z$ is the zero-plane displacement (Nikora et al., 2002). To plot the experimental data, the log-law is expressed as follows:

$$\langle u^+ \rangle = \frac{1}{\kappa} \ln (z^+ / z_0^+) \qquad [4]$$

where $k$ is the von Kármán coefficient, $z_0^+ = z_0 / \Delta z$ , and $z_0$ is the zero velocity level. The values of $\Delta z$, $k$ and $z_0$ were obtained by the regression analysis, as described by Dey and Das (2012). From that analysis, for the UW bed they were found as 0.0044 m, 0.3922, and 0.0037 m, respectively, below the crest. Analogously, the

 

values of $\Delta z$, $k$ and $z_0$ for the WW bed were found as 0.0021 m, 0.4025, and 0.0018 m, respectively, below the crest level. From the analysis of Figure 5c, it is also clearly visible how the normalized DA streamwise velocity of the WW bed is higher than in the UW bed case. However, after a certain distance ($z^+ \geq 2$) the normalized DA streamwise velocity for the UW bed starts increasing and becomes higher than in the WW bed case, up to the free surface. This happens owing to the higher roughness in the UW bed case, which retards the near-bed fluid. With an increase in $z^+$ towards the free surface, the effect of the roughness elements is reduced; hence, the flow accelerates and gains higher values than in the WW bed case.

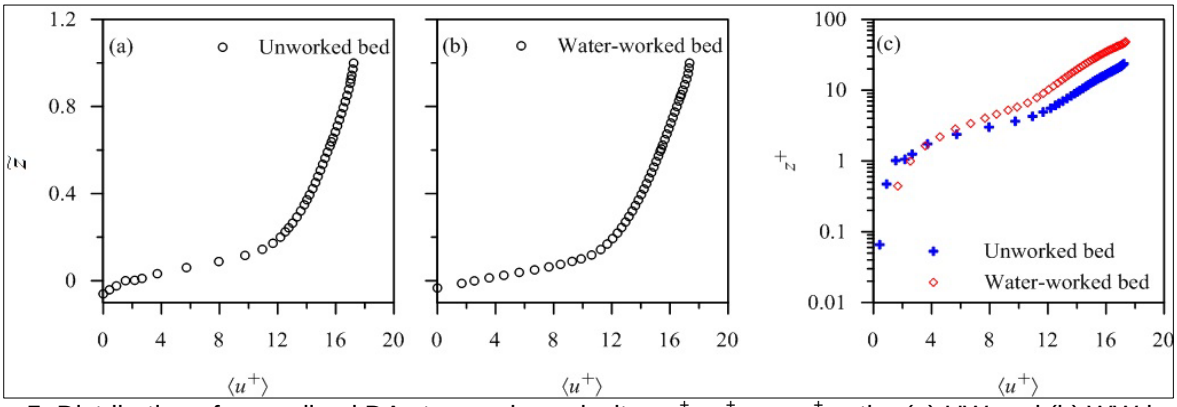


**Figure 5**. Distribution of normalized DA streamwise velocity <u$^+$> $z^+$ over $z^+$ or the (a) UW and (b) WW bed; (c) distribution of normalized DA streamwise velocity <u$^+$> over $z^+$ for the UW and WW beds.

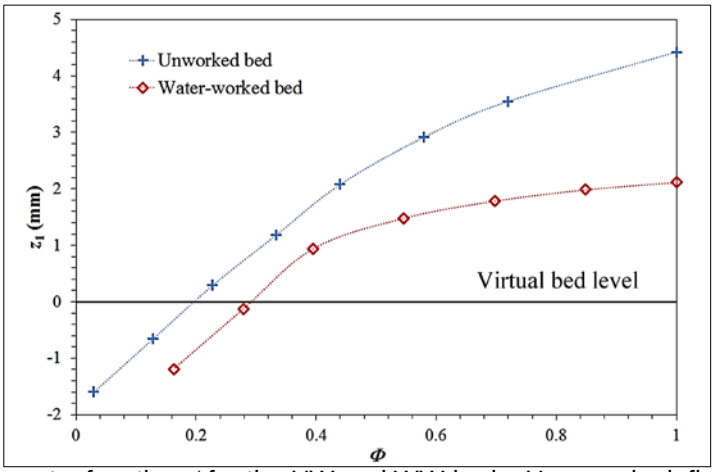


**Figure 6**. Roughness geometry function $\phi$ for the UW and WW beds. Here, $z_1$ is defined as $z + z_c$, where $z_c$ is the maximum grain crest. The virtual bed level is defined as the mean bed level, set to zero.

3.2 DA Reynolds Shear Stress and Form-Induced Shear Stress

The DA total shear stress (TSS) $\langle \tau \rangle$ is the sum of the DA Reynolds shear stress (RSS) $\langle \tau_{uw} \rangle$, form-induced stress (FISS) $\langle \tau_f \rangle$ and viscous shear stress (VSS) $\langle \tau_v \rangle$. The DA total shear stress has to be balanced by the gravity. It has a linear profile for $\langle \tilde{\tau}(\tilde{z} \geq 1) \rangle \times (\rho u_*^2)^{-1} = 1 - \tilde{z}$. The shear stresses are normalized as follows: $\langle \tilde{\tau} \rangle, \langle \tilde{\tau}_{uw} \rangle, \langle \tilde{\tau}_f \rangle, \langle \tilde{\tau}_v \rangle = (\langle \tau \rangle, \langle \tau_{uw} \rangle, \langle \tau_f \rangle, \langle \tau_v \rangle) \times (\rho u_*^2)^{-1}$. The characteristics are discussed as follows.

The distributions of $\langle \tilde{\tau}_{uw} \rangle$ over $\tilde{z}$ for both the UW and WW bed are shown in Figure 7(a). The DA RSS is the governing shear stress across the flow depth. Normalized DA RSS for the UW bed attains its peak at $\tilde{z}$ = 0.15 and then decreases with an increase in $\tilde{z}$. Likewise for the WW bed, it achieves its peak at $\tilde{z}$ = 0.10 and decreases with an increase in $\tilde{z}$. In both the cases, the $\langle \tilde{\tau}_{uw} \rangle$ follows a linear law of RSS distribution, because of the negligible contribution from FISS $\langle \tilde{\tau}_f \rangle$ and VSS $\langle \tilde{\tau}_v \rangle$ (Figures 7b and 7c). Near the bed region, the $\langle \tilde{\tau}_{uw} \rangle$ decreases with a decrease in $\tilde{z}$, owing to a reduction in the temporal velocity fluctuations *u'* and *w'* along *x* and *z*, respectively. Further, in this region the damping in $\langle \tilde{\tau}_{uw} \rangle$ is partially compensated by the appearance of $\langle \tilde{\tau}_f \rangle$. It is noticeable that, near the bed region, the $\langle \tilde{\tau}_{uw} \rangle$ is higher for the WW bed than for the UW bed, probably owing to the effect of roughness characteristics on temporal distribution of streamwise fluctuations (Nezu and Nakagawa, 1993).

 

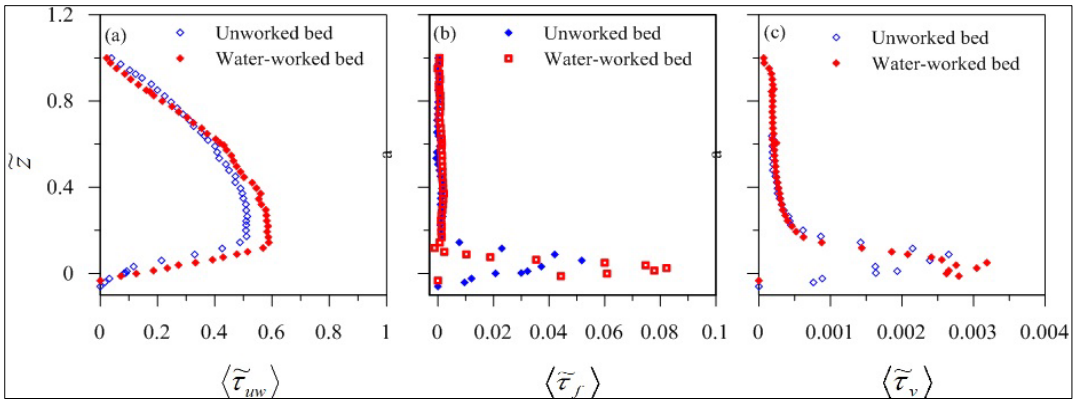


**Figure 7**. Distribution of normalized DA stresses over normalized vertical distance $\tilde{z}$ for the UW and WW: (a) RSS $\langle\tilde{\tau}_{uw}\rangle$; (b) FISS $\langle\tilde{\tau}_{f}\rangle$; (c) VSS $\langle\tilde{\tau}_{v}\rangle$.

Distribution of normalized FISS $\langle\tilde{\tau}_{f}\rangle$ over $\tilde{z}$ for both UW and WW beds is shown in Figure 7(b). FISS $\langle\tilde{\tau}_{f}\rangle$ initiates developing above the roughness crest at $\tilde{z}$ = 0.15 for the UW bed, while for the WW bed it starts developing at $\tilde{z}$ = 0.10. The FISS attains its peak at $\tilde{z}$ = 0.06 for the UW bed, whereas for the WW bed the maximum FISS occurs at $\tilde{z}$ = 0.025. Since the time-averaged flow close to the gravel crest is spatially heterogeneous, the FISS starts developing within the form-induced sublayers and grows sharply with a decrease in $\tilde{z}$. Similar kind of results was obtained by Manes et al. (2007), Sarkar and Dey (2010) and Dey and Das (2012). Within the form-induced sublayer and a zone below the crest level, the spatial velocity fluctuations ($\tilde{u}$ and $\tilde{w}$ along $x$ and $z$, respectively) are high, giving rise to $\langle\tilde{\tau}_{f}\rangle$. In the interfacial sublayer ($z^{+} \leq$ 0), the damping in the $\langle\tilde{\tau}_{f}\rangle$ distribution is associated with a decrease in spatial velocity fluctuations ($\tilde{u}$ and $\tilde{w}$). This indicates that the flow becomes spatially homogeneous in the zone of $z^{+} \leq 0$. Above the log layer, the fluctuations ($\tilde{u}$ and $\tilde{w}$) are negligible, making $\langle\tilde{\tau}_{f}\rangle \approx 0$. Owing to the change in roughness characteristics (shape and orientation of the gravel), $\langle\tilde{\tau}_{f}\rangle$ is higher for the WW than the UW bed.

The distributions of $\langle\tilde{\tau}\rangle,\langle\tilde{\tau}_{uw}\rangle,\langle\tilde{\tau}_{f}\rangle,\langle\tilde{\tau}_{v}\rangle$ over $\tilde{z}$ for both the UW and WW beds are shown in Figure 8, where one can observe that $\langle\tilde{\tau}_{uw}\rangle$ dominates in the most of the flow depth, except close to the roughness elements. In the near-bed region, where the mean flow is highly nonhomogeneous, the decrease of $\langle\tilde{\tau}_{uw}\rangle$ is compensated by the appearance of $\langle\tilde{\tau}_{f}\rangle$ and $\langle\tilde{\tau}_{v}\rangle$. Similar results were obtained by other investigators (e.g., Manes et al., 2007; Mignot et al., 2009a; Dey and Das, 2012). For both the beds, above the roughness layer the total shear stress $\langle\tilde{\tau}\rangle$ follows the linear law, as traditionally found in a uniform flow, and it is approximately equal to $\langle\tilde{\tau}_{uw}\rangle$, with negligible magnitude of $\langle\tilde{\tau}_{f}\rangle$ and $\langle\tilde{\tau}_{v}\rangle$.

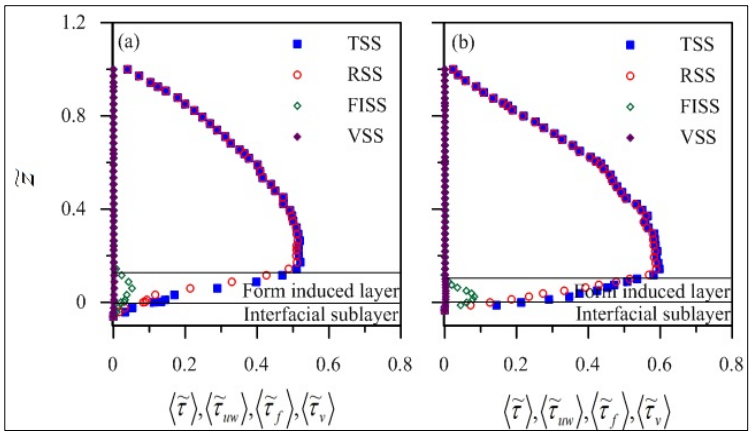


**Figure 8**. Distribution of normalized DA TSS $\langle\tilde{\tau}\rangle$, DA RSS $\langle\tilde{\tau}_{uw}\rangle$, FISS $\langle\tilde{\tau}_{f}\rangle$, DA VSS $\langle\tilde{\tau}_{v}\rangle$ over normalized vertical distance $\tilde{z}$ for the (a) UW and (b) WW beds.

Figure 9 shows the distribution of the ratio $\langle\tilde{\tau}\rangle/\langle\tilde{\tau}_{uw}\rangle$ over $\tilde{z}$ for both the UN and WW beds. It increases with a decrease in $\tilde{z}$, attaining a peak just above the virtual bed level in both the cases. The peak values for the UW and WW beds are found as 0.617 and 0.613, respectively. However, below the virtual bed level a drastic drop of $\langle\tilde{\tau}\rangle/\langle\tilde{\tau}_{uw}\rangle$ occurs due to the reduction in spatial ($\tilde{u}$ and $\tilde{w}$) as well as temporal ($u$' and $w$') velocity

 

fluctuations. More specifically, the reduction of $\langle\tilde{\tau}\rangle/\langle\tilde{\tau}_{uw}\rangle$ in this zone is associated with the reduction of $\langle\tilde{\tau}_f\rangle$, which occurs more rapidly than that of $\langle\tilde{\tau}_{uw}\rangle$.

### 3.3 DA Reynolds Normal Stresses and Form-Induced Normal Stress

The streamwise and vertical DA Reynolds normal stresses (RNSs) are $\langle\sigma_{uu}\rangle = -\rho\langle\overline{u'u'}\rangle$ and $\langle\sigma_{ww}\rangle = -\rho\langle\overline{w'w'}\rangle$, respectively. They are normalized as $\langle\hat{\sigma}_{uu}\rangle,\langle\hat{\sigma}_{ww}\rangle = (\langle\sigma_{uu}\rangle,\langle\sigma_{ww}\rangle)\times(\rho u_*^2)^{-1}$. The normalized DA form-induced normal stresses (FINSs) are $\langle\tilde{\sigma}_{uu}\rangle = -\rho\langle\tilde{u}\tilde{u}\rangle\times(\rho u_*^2)^{-1}$ and $\langle\tilde{\sigma}_{ww}\rangle = -\rho\langle\tilde{w}\tilde{w}\rangle\times(\rho u_*^2)^{-1}$ in the streamwise and vertical directions, respectively.

The distribution of normalized DA streamwise RNS $\langle\hat{\sigma}_{uu}\rangle$ over $\tilde{z}$ for both UW and WW beds is shown in Figure 10(a). Here it is noticeable that $\langle\hat{\sigma}_{uu}\rangle$ increases with an increase in $\tilde{z}$ and attains its peak above the maximum gravel crest and after that it decreases with an increase in $\tilde{z}$. It is visible that $\langle\hat{\sigma}_{uu}\rangle$ is higher for the WW than the UW bed. The possible cause of this is attributed to the effect of roughness elements on RNS in open-channel flows. The peak magnitudes for $\langle\hat{\sigma}_{uu}\rangle$ are 5.298 and 6.325 for the UW and WW beds, respectively.

The distribution of normalized DA vertical RNS $\langle\hat{\sigma}_{ww}\rangle$ over $\tilde{z}$ for both the UW and WW beds are shown in Figure 10(b). It is noticeable that $\langle\hat{\sigma}_{ww}\rangle$ increases with an increase in $\tilde{z}$ and attains its peak above the gravel crest and after that it decreases with an increase in $\tilde{z}$. It is visible that near the boundary $\langle\hat{\sigma}_{ww}\rangle$ is higher for the WW than the UW bed. The peak magnitudes for $\langle\hat{\sigma}_{ww}\rangle$ are 0.85 and 0.997 for the UW and WW beds, respectively. This verifies that near the bed a mixing process in the presence of the roughness elements increases the turbulence level for the WW bed. It is also observed that above the crest level all the profiles have a reduction with an increase in $\tilde{z}$ with a sequence of magnitude $\langle\hat{\sigma}_{uu}\rangle > \langle\hat{\sigma}_{ww}\rangle$. The possible cause of this sequence is attributed to the anisotropic turbulence characteristics in open-channel flows (Nezu and Nakagawa, 1993).

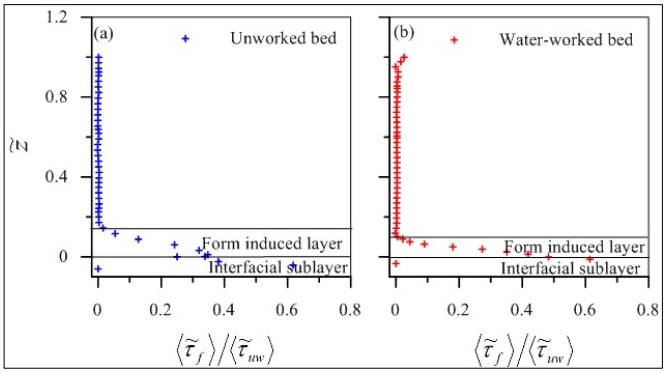


**Figure 9**. Distribution of the ratio of FISS $\langle\tilde{\tau}_f\rangle$ to DA RSS $\langle\tilde{\tau}_{uw}\rangle$ over normalized vertical distance $\tilde{z}$ over the (a) UW and (b) WW beds.

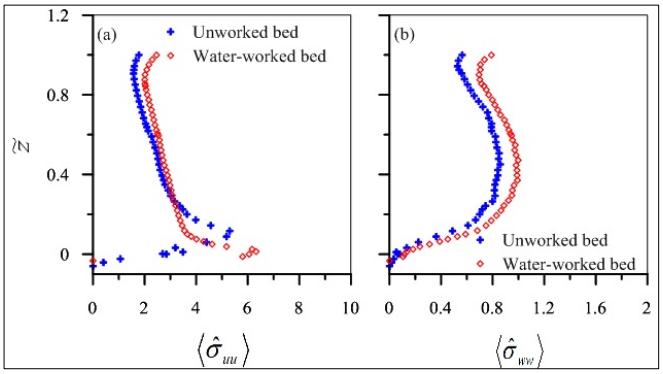


**Figure 10**. (a) Distribution of normalized DA streamwise RNS $\langle\hat{\sigma}_{uu}\rangle$ over normalized vertical distance $\tilde{z}$ for the UW and WW beds; (b) distribution of normalized DA streamwise RNS $\langle\hat{\sigma}_{ww}\rangle$ over normalized vertical distance $\tilde{z}$ for the UW and WW beds.

 

Vertical distribution of normalized streamwise FINS $\langle \tilde{\sigma}_{uu} \rangle$ for the UW bed and WW bed is presented in Figure 11(a). The $\langle \tilde{\sigma}_{uu} \rangle$ starts developing within the form-induced sublayers and grows sharply with a decrease in $\tilde{z}$. The top of the form-induced sublayers can also be recognized from the location at which the FINS profiles approach zero, for instance at $\tilde{z}$ = 0.145 and $\tilde{z}$ = 0.11 for the UW and WW bed, respectively. For the UW bed, the $\langle \tilde{\sigma}_{uu} \rangle$ attains a peak just above the roughness crest ($\tilde{z}$ = 0.06), and for the WW bed, the peak is found almost at the crest level ($\tilde{z}$ = 0.01). It is observed that $\langle \tilde{\sigma}_{uu} \rangle$ is higher for the UW than the WW bed, owing to the higher roughness height of the UW bed and also the different adjustment of the flow around the roughness elements.

The vertical distributions of the normalized vertical $\langle \tilde{\sigma}_{ww} \rangle$ for both the UW and WW beds are presented in Figure 11(b). For the UW bed, the $\langle \tilde{\sigma}_{ww} \rangle$ attains a peak at the crest level, whereas for the WW bed, it attains a peak just above the maximum crest level. It is observed that the $\langle \tilde{\sigma}_{ww} \rangle$ gains higher value for the WW than the UW bed, which is attributed to the influence of the spatial orientation of the grains.

## 4 CONCLUSIONS

An experimental study was carried out in order to explore the difference in turbulence characteristics between manmade (UW bed) and natural open channel (WW bed).

The most important conclusions are summarized as follows, taking into account that further in-depth studies are anyway required and are in progress to analyse other turbulent flow characteristics (Prandtl's mixing length, higher-order correlations, turbulent kinetic energy flux, turbulent kinetic energy budget, quadrant analysis) over both the UW and WW gravel beds by varying also the flow Froude number.

i. There is a change in surface topography due to the water-working process for which the roughness characteristics of both the UW and WW beds is different.
ii. For both the beds, above the roughness sublayer, the vertical distribution of the normalized DA streamwise velocity follows the log-law, whereas within the form-induced and interfacial sublayer it follows the linear law and third order polynomial function, respectively.
iii. Roughness height of the UW bed is higher than that of the WW bed; therefore, near the bed region the velocity of the UW bed is slower than that of the WW bed.
iv. The normalized DA RSS attains a peak above the crest level for both the beds. Near the WW bed, the DA RSS attains the highest values, but near the free surface it is lower than for the UW bed.
v. Within the form-induced sublayer, the FISS attains its peak just above the crest for both the cases and FISS for WW bed is found to be higher than that of the UW bed.
vi. For both the cases, within the form-induced layer, the FISS contributes significantly to the total RSS, whereas viscous stress remains negligible along the entire flow depth.
vii. The normalized DA streamwise RNS components are small near the bed and increases with an increase in vertical distance. It attains a peak just above the roughness crest for both the beds. The normalized DA RNS components for the WW bed attains higher values than that of the UW bed.
viii. The normalized form-induced streamwise normal stress is small near the bed, attaining a peak slightly above the bed. For the UW bed, the normalized form-induced streamwise normal stress is higher than that of the WW bed, owing to the higher spatial velocity fluctuations.

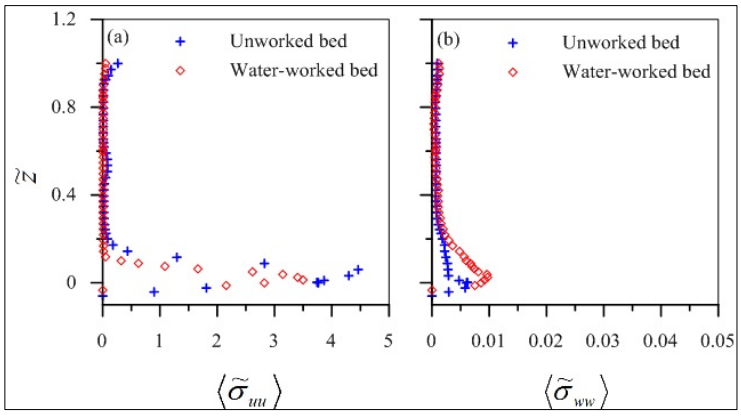


**Figure 11**. (a) Distribution over normalized vertical distance $\tilde{z}$ for the UW and WW beds of (a) normalized streamwise FINS $\langle \tilde{\sigma}_{uu} \rangle$; (b) normalized vertical FINS $\langle \tilde{\sigma}_{ww} \rangle$.

 

**REFERENCES**

Aberle, J. (2007). *Measurements of Armour Layer Roughness Geometry Function and Porosity*. Acta Geophysica, 55(1), pp23-32.

Barison, S., Chegini, A., Marion, A. & Tait, S.J. (2003). Modifications in Near Bed Flow over Sediment Beds and the Implications for Grain Entrainment. *Proceedings of XXX IAHR Congress*, Thessalonki, Greece, 509-516.

Buffin-Bélanger, T., Rice, S., Reid, I. & Lancaster, J. (2006). Spatial Heterogeneity of Near-Bed Hydraulics Above a Patch of River Gravel. *Water Resources Research*, 42(4),1-12.

Cooper, J.R., Aberle, J., Koll, K. & Tait, S.J. (2013). Influence of Relative Submergence on Spatial Variance and Forminduced Stress of Gravel-Bed Flows. *Water Resources Research*, 49(9), 5765–5777.

Cooper, J.R & Tait, S.J. (2008). The Spatial Organisation of Time-Averaged Streamwise Velocity and its Correlation with the Surface Topography of Water-Worked Gravel Beds. *Acta Geophysica*, 56(3), 614–642.

Cooper, J.R & Tait, S.J. (2009). Water-Worked Gravel Beds in Laboratory Flumes – A Natural Analogue? *Earth Surface Processes and Landforms*, 34(3), 384–397.

Cooper, J.R. & Tait, S.J. (2010). Spatially Representative Velocity Measurement over Water-Worked Gravel Beds. *Water Resources Research*, 46(11), 1-15.

Dey, S. & Das, R. (2012). Gravel-Bed Hydrodynamics: Double-Averaging Approach. *Journal of Hydraulic Engineering*, ASCE, 138(8), 707-725.

Ferraro, D., Servidio, S., Carbone, V., Dey, S. & Gaudio, R. (2016). Turbulence Laws in Natural Bed Flows. *Journal of Fluid Mechanics*, 798, 540-571.

Garde, R.J. (1970). Initiation of Motion on a Hydrodynamically Rough Surface - Critical Velocity Approach. *Water and Energy International*, 27(3), 271-282.

Goring, D.G. & Nikora, V.I. (2002). Despiking Acoustic Doppler Velocimeter Data. *Journal of Hydraulic Engineering*, ASCE, 128(1), 117-126.

Hardy, R.J., Best, J.L., Marjoribanks, T.I., Parsons, D.R. & Rosser, N.J. (2013). *Detection and Analysis of Coherent Flow Structures in a Depth-Limited Flow over a Gravel Surface*. *Coherent Flow Structures at Earth's Surface*, Eds. Venditti J.G., Best J.L., Church M. & R.J. Hardy, Wiley, Chichester, 199-214.

Koll, K., Cooper, J.R., Aberle, J., Tait, S.J. & Marion, A. (2010). Investigation into the Physical Relationship Between Water-Worked Gravel Bed Armours and Turbulent in-Channel Flow Patterns. *Proceedings of the HYDRALAB III Joint User Meeting*, Hannover, Germany.

Laursen, E.M. (1963). An Analysis of Relief Bridge Scour. *Journal of the Hydraulics Division*, ASCE, 89(3), 93-118.

Manes, C., Pokrajac, D. & McEwan, I. (2007). Double-Averaged Open-Channel Flows with Small Relative Submergence. *Journal of Hydraulic Engineering*, ASCE, 133(8), 896-904.

McLelland, S.J. (2013). *Coherent Secondary Flows over a Water-Worked Rough Bed in a Straight Channel*, *Coherent Flow Structures at Earth's Surface*, Eds. Venditti J.G., Best J.L., Church M. & R.J. Hardy, Wiley, Chichester, 275-288.

Mignot, E., Barthelemy, E. & Hurther, D. (2009a). Double-Averaging Analysis and Local Flow Characterization of Near-Bed Turbulence in Gravel-Bed Channel Flows. *Journal of Fluid Mechanics*, 618(1), 279-303.

Neill, C.R. (1967). Mean-Velocity Criterion for Scour of Coarse Uniform Bed Material. *Proceedings of the International Association of Hydraulic Research 12th Congress*, Fort Collins, Colorado, USA.

Nezu, I. & Nakagawa, H. (1993). *Turbulence in Open Channel Flows*, Balkema, Rotterdam, Netherlands.

Nikora, V., Koll, K., McLean, S., Dittrich, A. & Aberle, J. (2002). Zero-Plane Displacement for Rough-Bed Open-Channel Flows. *Proceedings of the International Conference on Fluvial Hydraulics River Flow 2002, Louvain-la-Neuve, Belgium*, Eds. Bousmar D. and Y. Zech, Balkema, Lisse, The Netherlands, 1, 83–91.

Sarkar, S. & Dey, S. (2010). Double-Averaging Turbulence Characteristics in Flows over a Gravel Bed. *Journal of Hydraulic Research*, 48(6), 801-809.

 

# NUMERICAL SIMULATION OF A DEEP-SCOUR HOLE IN A TIDAL RIVER CONFLUENCE USING DELFT 3D

WENHONG DAI[(1)], AHMED BILAL[(2)], QIANCHENG XIE[(3)] & YANYAN ZHAI[(4)]

[(1,2,3)]College of Water Conservancy and Hydropower Engineering, Hohai University, Nanjing, China,
wdai@hhu.edu.cn, ahmed.bilal@hhu.edu.cn, qiancheng.xie@hhu.edu.cn
[(1,4)] State Key Laboratory of Hydrology-Water Resources and Hydraulic Engineering,Hohai University,Nanjing, China,
1278983684@qq.com
[(1)]National Engineering Research Center of Water Resources Efficient Utilization and Engineering Safety, Hohai University, Nanjing, China,
[(4)]College of Harbor, Coastal and Offshore Engineering, Hohai University, Nanjing, China.

## ABSTRACT

River confluences have complex hydrodynamic and sediment transport behavior. Research on the interactions including flow, sedimentation and river bed morphology at confluences has long been neglected to some degree in the past years, especially in the tidal river channel confluences. The deep-scour hole is a standard feature of both fluvial and tidal channel confluences. Numerical simulation of the deep-scour hole at tidal channel confluence has not been carried out before as per authors' knowledge. In this study, a tidal channel confluence, namely Sanjiangkou zone, is numerically modeled with a focus to simulate hydrodynamics and deep-scour hole propagation. Sanjiangkou zone is in the Zhejiang Province of China, where two upstream rivers, Yao River and Fenghua River, merge into a downstream river called Yong River. Delft-3D code is applied to simulate the deep-scour hole study. A regular orthogonal grid is used to carry out the simulation. Numerical results are compared with observed measurements. The study indicates that Delft-3D model is useful for simulating a deep-scour hole at tidal river confluences. Such techniques may also be useful in other similar cases.

**Keywords:** Tidal channel confluences; deep-scour hole; delft 3D; hydrologic modeling; sanjiangkou.

## 1 INTRODUCTION

Confluences have complex hydrodynamic and sediment transport behavior in both fluvial as well as tidal channels. Research on the interactions including flow, sedimentation and river bed morphology at confluences has long been neglected to some degree in the past years, especially in the tidal channel confluences. Some studies hypothesized the deep-scour hole, also called deep-hole, with limited field data (Ginsberg and Perillo, 1999, 2004). Ginsberg et al. (2009) analyzed the deep-holes in detail including its genesis and evolution with detailed field investigation.

Structures are often built on tidal channels located within or near growing cities. As a result, tidal channel frequently readjusts its cross section as well as hydrodynamic conditions to achieve equilibrium. It becomes more important to gain a better understanding of complex processes such as deep-holes, to reduce any potential risk for population or infrastructure. Numerical modeling of estuarine channels is a powerful tool to study the morphological evolution and hydrodynamic changes. Numerical simulation of the deep-scour hole at tidal channel confluence has not been carried out before as per authors' knowledge.

In this study, a tidal channel confluence, namely Sanjiangkou zone, is numerically modeled using Delft 3D. The primary focus of the study is to simulate hydrodynamics and deep-hole propagation under heavy sedimentation environment (Chen et al., 2013) of Yong River. Sanjiangkou zone is in Ningbo City, Zhejiang Province of China, where two upstream rivers, Yao River and Fenghua River, merge into a downstream river called Yong River

## 2 STUDY SITE

Yong River is one of the eight central water systems in Zhejiang Province in China. It is of vital importance for Ningbo city, which is located on the east coast of Zhejiang Province and the south to the Hangzhou Bay. Yong River has two tributaries, which originates from Fenghua River in the south and Yao River in the north, as shown in Figure 1. These tributaries join in Ningbo City at their confluence zone, called Sanjiangkou, as its name (in Chinese) suggested. The Yong River is at the downstream of Sanjiangkou, and it flows into the East China Sea at Waiyoushan in Zhenhai. The total length of Yong River is 25.6 km from Sanjiangkou to its mouth at the East China Sea. The Yong River is predominantly tidal in nature.

 

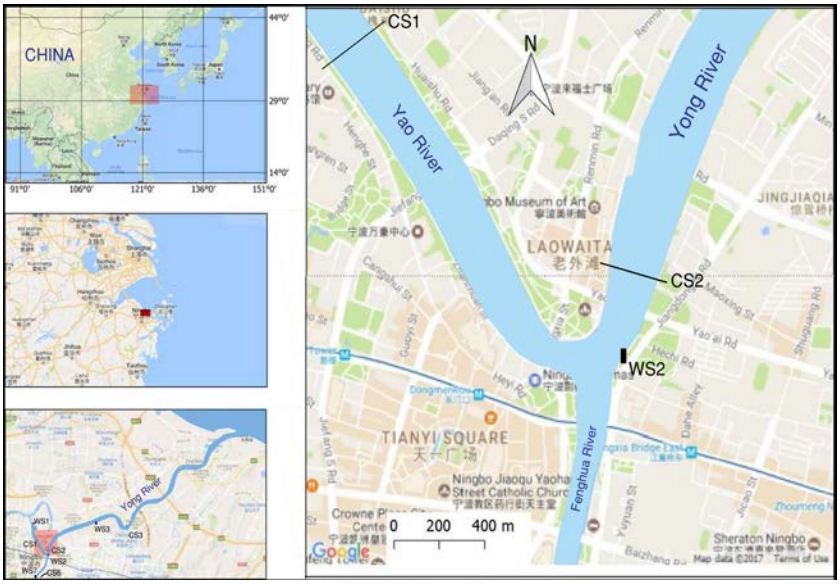


**Figure 1.** Location of Sanjiangkou; the confluence formed by Yao River and Fenghua River in Ningbo City.

The annual average river runoff of Yongjiang from 1973 to 2006 is 2.912 billion $m^3$ (Chen et al., 2013), but the sediment transport in the Yong trunk stream is mainly affected by the tides from the coast. Since 1959, water and sediment characteristics in the Yong River have considerably changed due to the construction of water conservancy projects along the river, especially Yao River's sluice gate, constructed in 1959, which has led to reduced tidal discharge. As a result of the reduced tidal effects, severe deposition within the channel is occurring. After the 1980s, Yong River is affected by human activities, in particular with the increasing building of bridges and wharfs in the area (Chen et al., 2013), which led to severe sediment deposition.

The width of Yao River ranges from 230m to 180m, however just before confluence it forms a constricted section where its width first becomes 140m and then gradually it again broadens to be 180m at the apex of confluence. The width of Fenghua River is relatively smooth before confluence. Its width is 152m at WS7 and then smoothly reduces to 110m before again widening itself to become 154m wide at the apex of the junction region. Bed morphology clearly shows a deep-hole (Figure 2) just after the confluence zone. The deepest point of the deep-hole, or only deep hole, is 17.2m below sea level, while bed level around it is approximately 6.5m below sea level. Data used in this study was acquired during a field survey in 2015 for a particular flood season. Figure 3 shows locations of water level recording stations (WS location) and cross-sections where flow was measured, (CS locations). Both suspended sediments and channel bed material were 95 % consisted of cohesive material, i.e. clayey silt with grain size diameter between 0.5 - 10μm.

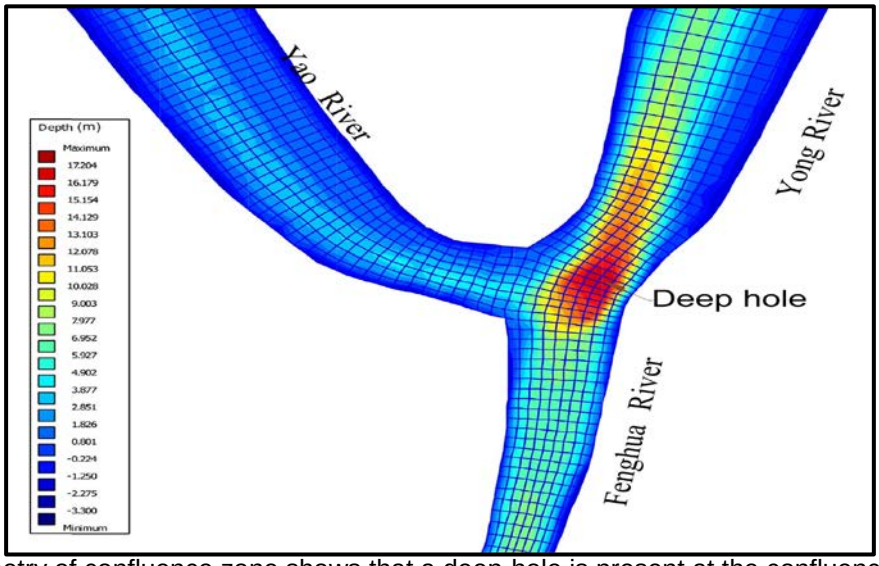


**Figure 2.** Bathymetry of confluence zone shows that a deep-hole is present at the confluence zone and extends into the post confluence zone, i.e. Yong River.

 

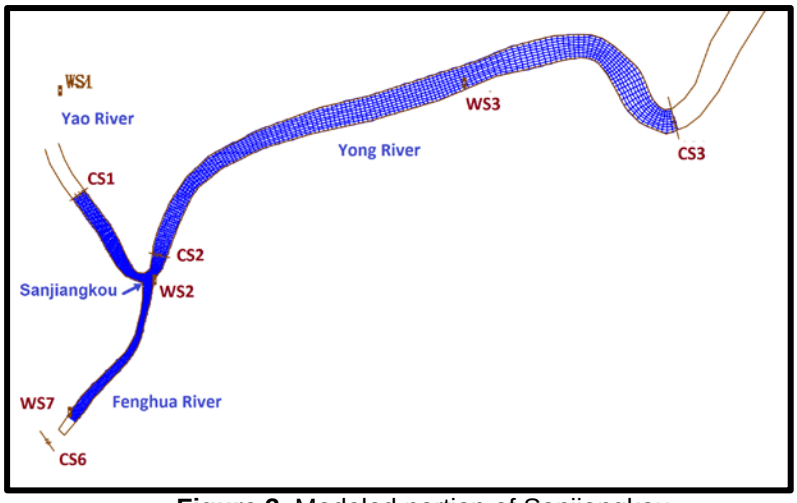


**Figure 3.** Modeled portion of Sanjiangkou.

## 3 MODEL SETUP

### 3.1 Mathematical background

Delft 3D code is based on finite difference method and utilizes the approach to solving Navier-Stokes equation with shallow water and Boussinesq assumption (Deltares, 2014). A deleted description of hydrodynamic and transport equations is described by Lesser et al. (2004) and Deltares (2014). However, a brief summary is presented here

Delft 3D models the three-dimensional suspended sediment transport using a mass balance, advection-diffusion equation (Eq. 1)

$$\frac{\partial c}{\partial t}+\frac{\partial}{\partial x}(uc)+\frac{\partial}{\partial y}(vc)+\frac{\partial}{\partial z}[(w-w_s)c]-\frac{\partial}{\partial x}\left(\varepsilon_{S,x}\frac{\partial c}{\partial x}\right)-\frac{\partial}{\partial y}\left(\varepsilon_{S,y}\frac{\partial c}{\partial y}\right)-\frac{\partial}{\partial z}\left(\varepsilon_{S,z}\frac{\partial c}{\partial z}\right)=0 \quad [1]$$

where,

| | |
|---|---|
| c | is mass concentration of sediment fraction [kg/m$^3$] |
| u,v and w | are longitudinal(x), transversal(y) and vertical(z) components of flow velocity [m/s] |
| $\varepsilon_{S,x}$, $\varepsilon_{S,y}$ and $\varepsilon_{S,z}$ | are eddy diffusivities of sediment fraction [m$^2$/s] |
| $w_s$ | is the settling velocity of sediment fraction [m/s] |

Suspended sediments are cohesive in nature at the Sanjiangkou. Delft 3D uses well known Partheniades-Krone formulations for calculation of erosion and deposition of cohesive sediments.

$$E = MS(\tau_{cw},\tau_{cr,e}) \quad [2]$$

$$D = w_s c_b S(\tau_{cw},\tau_{cr,d}) \quad [3]$$

where,

| | |
|---|---|
| E | is erosion flux [kg m$^{-2}$ s$^{-1}$] |
| M | is erosion parameter [kg m$^{-2}$ s$^{-1}$] |
| $S(\tau_{cw},\tau_{cr,e})$ | is erosion step function |
| D | is deposition flux [kg m$^{-2}$ s$^{-1}$] |
| $w_s$ | is fall velocity [m s$^{-1}$] |
| $c_b$ | is average sediment concentration in the near bottom computational layer [kg/m$^3$] |
| $S(\tau_{cw},\tau_{cr,d})$ | is deposition step function |
| $\tau_{cw}$ | is maximum bed shear stress due to current and wave [N m$^{-2}$] |
| $\tau_{cr,e}$ | is critical erosion shear stress [N m$^{-2}$] |
| $\tau_{cr,d}$ | is critical deposition shear stress [N m$^{-2}$] |

Hydrodynamic conditions vary very quickly (in hours), however significant morphological changes occur in months or years. Practically, detailed data for input is not available in most of the cases. One way to tackle

 

this problem is by introducing morphological scale factor to accelerate the bed change for each hydrodynamic time step. Lesser et al. (2004) conceptually described it in Eq. 4.

$$\Delta t_{morphological} = f_{MOR} \Delta t_{hydrodynamic} \quad [4]$$

where,

$\Delta t_{morphological}$ is morphological time step
$f_{MOR}$ is morphological scale factor
$\Delta t_{hydrodynamic}$ is hydrodynamic time step

3.2 Calibration

A regular orthogonal grid was generated for simulating the deep-hole at the confluence zone. Four layers were used which were skewed towards the bottom to gain more accuracy in the bed change calculations. The model was tested for several different options available for boundary conditions, altering roughness, and grid refinements. Calibration of the model was based on corresponding hourly observed data for spring tide which occurred on interval 2015-06-17 10:00– 2015-06-1816:00, totaling 31 hours. The primary task during the calibration was to adjust roughness, calculation time step, select suitable boundary condition and work on grid refinement so that a reasonable match was found between observed and model-calculated water levels and flows at the end of simulation time.

There are several model evaluation techniques currently being used. Four model evaluation parameters, as well as good visual fit, were selected to check model performance. The four model evaluation parameters include

i. Nash-Sutcliffe efficiency (NSE)
ii. R-Squared ($R^2$)
iii. Percent bias (PBIAS)
iv. RSME-Stander deviation of observations Ratio (RSR)

**Table 1.** Mathematical expressions, range and satisfactory values (Moriasi et al., 2007) for model evaluation parameters.

| | Range | Optimal value | Satisfactory | Equation | |
|---|---|---|---|---|---|
| **NSE** | -∞ to 1 | 1 | >0.5 | $E = 1 - \frac{\sum_{i=1}^{n}(O_i - P_i)^2}{\sum_{i=1}^{n}(O_i - \bar{O})^2}$ | [5] |
| **$R^2$** | 0 to 1 | 1 | >0.5 | $R^2 = \left( \frac{\sum_{i=1}^{n}(O_i - \bar{O})(P_i - \bar{P})}{\sqrt{\sum_{i=1}^{n}(O_i - \bar{O})^2} \sqrt{\sum_{i=1}^{n}(P_i - \bar{P})^2}} \right)^2$ | [6] |
| **PBIAS** | -∞ to ∞ | 0 | ±25% Streamflow<br>±55% Sediment | $PBIAS = \frac{\sum_{i=1}^{n}(O_i - P_i) \times 100}{\sum_{i=1}^{n} O_i}$ | [7] |
| **RSR** | 0 to ∞ | 0 | ≤ 0.7 | $RSR = \frac{\sqrt{\sum_{i=1}^{n}(O_i - P_i)^2}}{\sqrt{\sum_{i=1}^{n}(O_i - \bar{O})^2}}$ | [8] |

Where
O is observed(measured) value
P is predicted (calculated) value by the model
$\bar{O}$ is average of observed values
$\bar{P}$ is average of predicted values
n is total number values

A main criterion adopted to compare model results with observed values was a graphical match. If the observed and the computed values show a reasonable graphical match, then the model evaluation parameters have been calculated for each location. If at least three of four parameters were within acceptable limits, then model results were considered reasonable. The simulated and observed water levels (at WS2 and WS3) and flows (at CS2 and CS6) are shown in Figure 4. The exact location of CS6 does not come under modeled area of Sanjiangkou. However, as CS6 lied close to WS7, predicted flow values by Delft 3D at WS7 were compared with observed flow values at CS6.

3.3 Validation

Validation of the model was done on a neap tide event which occurred on interval 2015-06-24 15:00 – 2015-06-25 22:00. Same principle as used for calibration was adopted to consider a model result as being

 

validated. Validation results are shown in Figure 5. PBIAS for CS6 was more than acceptable. But since a reasonable graphical match and satisfactory value for other three parameters was reached, it was considered acceptable so that this model can be used to analyze the hydraulic and sediment characteristic of Sanjiangkou zone.

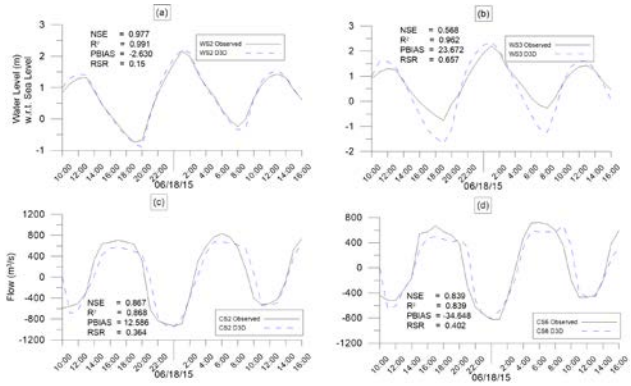


**Figure 4.** Calibration results - Comparison of model results and observed data for a spring tide event (a) WS2, (b) WS3, (c) CS2, and (d) CS6.

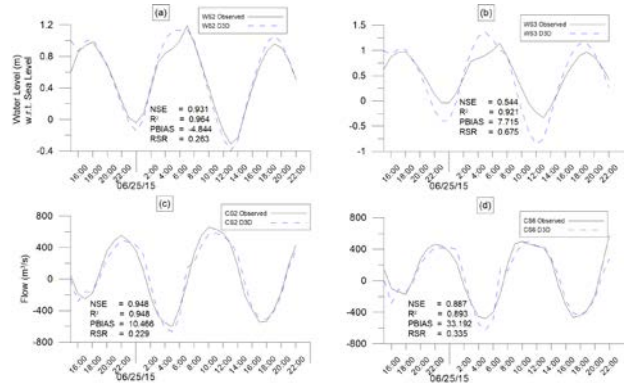


**Figure 5.** Validation results - Comparison of model results and observed data for a spring tide event (a) WS2, (b) WS3, (c) CS2, and (d) CS6.

## 4 RESULTS

After the model was calibrated and validated, it was used to see the channel bed response under current flow and sediment conditions. Morphological scale factor was used to accelerate the erosion and deposition at the channel bed. The scale factor was set to 365 on spring tide data. The results of bed change at the start and three results each after 3-hour break are shown in Figure 6. By analyzing Figure 6, it was visible that all the three rivers were under heavy sedimentation as identified by Chen et al. (2013). The results showed that the maximum depth of the deep-hole changed from an initial 17.2 m below sea level to about 10 m below sea level after one year of development. It may be concluded that under the existing conditions of water, sediment, and river boundary conditions, the depth of the deep-hole has an aggrading tendency. Horizontally, the deep-hole is approximately oval-shaped, which is gradually extending along the flow direction and narrowing along the width of the river (Figure 6). It is estimated that finally, it will result in a deep groove along the Fenghua River and Yong River.

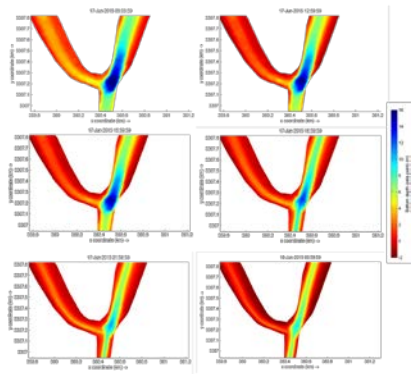

**Figure 6.** Morphological changes under spring tide conditions with Morphological scale factor set to 365.

 

## 5 CONCLUSIONS

Hydrodynamics and sediment transport at tidal channel confluence follow the complicated pattern and are dependent on many other parameters. Deep-holes are one of the results of complex sediment dynamics. In addition to field studies and physical modeling, numerical simulation offers new opportunities to understand hydro-morphodynamics of a tidal river. Broadly, the aim of the study is to use a numerical model Delft 3D to simulate such a complex environment. Specifically, the purpose of this research is to observe the response of the deep-hole qualitatively under heavily depositive environment as identified by Chen et al. (2013).

Delft 3D is successfully used to model the deep-hole at Sanjiangkou confluence. By making use of morphological scale factor, it is confirmed that more sediments are being deposited then being eroded in this system of three rivers. Channel bed level is increasing not only in Yong River but also in Yao and Fenghua Rivers. As also studied by Chen et al. (2013), this aggradation may be linked to the construction of gates upstream of both Yao River and Fenghua River as well as bridges and wharfs built along the reach, which significantly change the natural flow and sediment characteristics. Also, the model predicts that if the situation continues, the deep-hole will be filled slowly and may disappear.

## ACKNOWLEDGEMENTS

The authors are grateful to the Hydrology and Water Resources Survey Bureau of the Lower Yangtze River for proving the data. This research is supported by the NSFC (51479071), the National Key R&D Program of China (2016YFC0402501), the 111 Project (B12032, B17015) and the Priority Academic Program Development of Jiangsu Higher Education Institutions (YS11001).

## REFERENCES

Chen, J., Tang, H.W., Xiao, Y. & Ji, M. (2013). Hydrodynamic Characteristics and Sediment Transport of a Tidal River under Influence of Wading Engineering Groups. *China Ocean Engineering,* 27(6), 829-842.

Deltares. (2014). *Delft3D-FLOW, User Manual*. Delft: Deltares https://oss.deltares.nl/documents/183920/185723/Delft3D-FLOW_User_Manual.pdf.

Ginsberg, S.S., Aliotta, S. & Lizasoain, G.O. (2009). Morphodynamics and Seismostratigraphy of a Deep Hole at Tidal Channel Confluence. *Geomorphology,* 104(3-4), 253-261.

Ginsberg, S.S. & Perillo, G.M.E. (1999). Deep-Scour Holes at Tidal Channel Junctions, Bahia Blanca Estuary, Argentina. *Marine Geology,* 160(1-2), 171-182.

Ginsberg, S.S. & Perillo, G.M.E. (2004). Characteristics of Tidal Channels in a Mesotidal Estuary of Argentina. *Journal of Coastal Research,* 20(2), 489-497.

Lesser, G.R., Roelvink, J.A., van Kester, J.A.T.M. & Stelling, G.S. (2004). Development and Validation of a three Dimensional Morphological Model. *Coastal Engineering,* 51(8-9), 883-915.

Moriasi, D.N., Arnold, J.G., Van Liew, M.W., Bingner, R.L., Harmel, R.D. & Veith, T.L. (2007). Model Evaluation Guidelines for Systematic Quantification of Accuracy in Watershed Simulations. *Transactions of the ASABE,* 50(3), 885-900.

 

# LAGRANGIAN NUMERICAL MODELLING OF LOCAL SCOUR AROUND CIRCULAR PIPE

EHSAN JAFARI NODOUSHAN[(1)], MOHANNA TAJNESAIE [(2)] & AHMAD SHAKIBAEINIA [(3)]

[(1,2)]Department of Civil Engineering, Bijar Branch, Islamic Azad University, Bijar, Iran
emjafari64@gmail.com; mtajnesaie@gmail.com
[(3)] Department of Civil, Geological and Mining Engineering, Polytechnique Montreal, Montreal, Canada,
ahmad.shakibaeinia@polymtl.ca

## ABSTRACT

Mesh-free Lagrangian (particle) methods such as MPS (Moving Particle Semi-implicit) and SPH (Smoothed Particle Hydrodynamics) have proven their capacities in dealing with some the most complex flow systems, especially those with highly distorted and fragmented interfaces. In combination with visco-plastic constitutive relations, these methods can also simulate the solid-liquid multiphase flows, for example in case of sediment-water two phase flow. This provides a unique opportunity for the simulation of the most challenging sediment dynamic problems. Local sediment scours around pipelines, which has many engineering applications, is one of these problems. This paper develops and evaluates a mesh-free Lagrangian model, based on a weakly-compressible version of the MPS method, for 2D modeling of sediment scour around circular pipes. This is a challenging problem for the traditional mesh-based methods due to the highly-dynamic movement of sediments. The flow will be treated as a two-phase system of Newtonian (water) and non-Newtonian (sediment) fluids. A regularized viscoplastic rheological model with a Mohr-Coulomb failure criterion will be used to describe the behavior of sediments. The validation of model results with the available experimental data proves the capability of the developed model for accurate prediction of scour hole under the pipelines.

**Keywords:** Mesh-free Lagrangian method; MPS; sediment dynamics; two-phase flow; scour around circular pipes.

## 1 INTRODUCTION

When pipe, is placed on an erodible bed under water, the effect of the pipe on the flow pattern can cause sediment scouring around the pipe, and loss of the materials that are supporting the pipe weight. This may cause rapture in the pipe with severe economical and environmental consequences.

Traditionally, simulations of sediment-water interaction problems have been based on the Eulerian mesh-based methods such as finite difference and finite element, which are either single-phases or multiphase. Since these methods rely on a background mesh system, these methods have difficulties in predicting the highly-dynamic sediment movements with distorted and fragmented interfaces. In recent years, a newer group of numerical techniques called mesh-free Lagrangian (particle) methods have provided a great opportunity for simulation of multiphase and free-surface flow problems due to their abilities to deal with the interfacial deformations/fragmentations. In these methods, the continuum is represented by a set of free-to-move nodes (called particles), without any connection, in the Lagrangian system. Because of their fully Lagrangian mesh-free nature, no specific method to record or trace interfaces is needed. These advantages make these methods ideal for accurate prediction of sediment dynamics problems such as sediment scouring around pipes.

Smoothed particle hydrodynamics (SPH) (Gingold and Monaghan, 1977) and moving particle semi-implicit (MPS) (Koshizuka and Oka, 1996) are two of the well-studied mesh-free particle methods. The method of this study, MPS method, has been used to solve many fluid flow problems in the past. Kushizukaand et al. (1998) conducted a simulation of wave breaking on slope. Gotoh and Sakai (1999) simulated wave breaking on the various geometries of the seabed. Gotoh and Sakai (2006) developed a multiphase MPS model to simulate fluid and gas or liquid and solid phases of sediment transport and floating objects. Ataei Ashtiani and Farhadi (2006) compared different kernel functions and gave an equation for stability of MPS model. Shakibaeinia and Jin (2010; 2011; 2012a; 2012b) developed a weakly-compressible MPS method (WCMPS) free-surface and multiphase fluid flow problems. In combination with visco-plastic rheological relations, the method was also able to simulate the multiphase sediment-water problems, such as mobile-bed dam-break (Shakibaeinia and Jin, 2011) and sediment jets (Shakibaeinia and Jin, 2012b).

This study aims to develop and evaluate a mesh-free particle model based on the multiphase WCMPS formulation for simulation of sediment scouring under pipes. This method uses a regularized visco-plastic rheological model with a pressure-depended sediment yield criterion (Mohr–Coulomb) to predict the sediment behavior. Unlike the work of Shakibaeinia and Jin (2011; 2012b), a fully dynamic pressure is used for

 

prediction of normal stress between sediment particles. The model results for sediment scouring around a pipe is validated and evaluated in comparison with the available experimental measurements.

## 2 THE GOVERNING EQUATIONS

The equations governing the momentum and continuity conservation are given by (Pope, 2000):

$$\begin{cases} \frac{1}{\rho}\frac{D\rho}{Dt} + \nabla \cdot \mathbf{u} = 0 \\ \rho \frac{D\mathbf{u}}{Dt} = -\nabla p + \nabla . \boldsymbol{\tau} + \mathbf{f} \end{cases} \quad (1)$$

In which, **u** is velocity vector, *t* is time, *ρ* is fluid density, *P* is pressure, **f** is the volume force and **τ** is the shear stress tensor.

### 2.1 Basis MPS formulation

As a Lagrangian method, the governing equations in MPS are converted to particle interaction equations. Each particle possesses a set of field variables and the governing equations are discretized and solved over these particles (Figure 1). Interpolation discretization of spatial derivatives is based on weight averaging (particle smoothing) between a particle of interest and its neighboring particles, locating within a radius of influence, $r_e$. Using this weight averaging process, the spatial derivatives are transformed to equations of particles interaction. The effect of a neighboring particle *j* (with position vector $\mathbf{r}_j$) on the particle of interest i (with position vector $\mathbf{r}_i$) is determined using the weight (smoothing) function W $r_{ij}$,$r_e$), where $r_{ij}=|\mathbf{r}_j - \mathbf{r}_i|$ is distance between particles *i* and *j.*

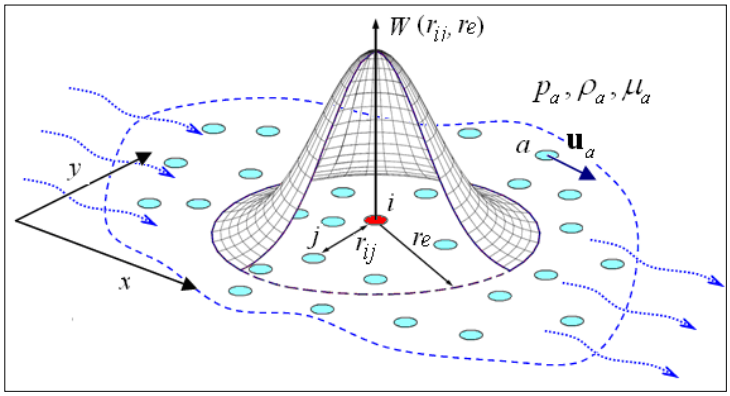


**Figure1.** Position of the particle in the field-solving and interaction with neighboring particles (Shakibaeinia and Jin, 2010).

Parameter *n*, is the number density of particles to show a specific particle density around a particle, is defined as equation 2:

$$\langle n \rangle_i = \sum_{j \neq i} W(r_{ij}, r_e) \quad (2)$$

Assuming that the mass of all particles is equal to *m*, particle density is calculated by Equation 3.

$$\langle \rho \rangle_i = \frac{\sum_{i^{\neq}j} m_i W(r_{ij}, r_e)}{\int_v W(r, r_e) dv} = \frac{m}{\int_v W(r, r_e) dv} \langle n \rangle_i = \frac{\rho \langle n \rangle_i}{n^0} \quad (3)$$

where,$n^0$is initial average particle number density, ⟨−⟩ is weight averaging operator. The kernel function used in this study was a third order, polynomial function, defined by (Shakibaeinia and Jin, 2010)

 

$$W(r_{ij}, r_e) = \begin{cases} (1 - r_{ij} / r_e)^3 & 0 \le \left(r_{ij} / r_e\right) < 1 \\ 0 & \left(r_{ij} / r_e\right) \ge 1 \end{cases} \quad (4)$$

The gradient and Laplacian operators of the flow governing equations are necessary to be discretized in Lagrangian frame. Gradient and divergence operators are based on weighted averaging of gradient and divergence between pair particles (particle *i* and its neighboring particles *j*) as:

$$\left\langle \nabla \phi \right\rangle_i = \frac{d}{n^0} \sum_{i \neq j} \left[ \frac{\phi_i - \phi_j}{r_{ij}} \frac{\mathbf{r}_j - \mathbf{r}_i}{r_{ij}} W(r_{ij}, r_e) \right] \quad (5)$$

$$\left\langle \nabla . \mathbf{u} \right\rangle_i = \frac{d}{n^0} \sum_{i \neq j} \left[ \frac{\mathbf{u}_i - \mathbf{u}_j}{r_{ij}} . \frac{\mathbf{r}_j - \mathbf{r}_i}{r_{ij}} W(r_{ij}, r_e) \right] \quad (6)$$

where *d* is the dimensions of space, and **r** is the position vector. Laplacian formula is calculated by the weighted averaging of distributed physical quantities from the particle *i* to the adjacent particles as: Accordingly, the Laplacian operator is defined as follows:

$$\left\langle \nabla^2 \boldsymbol{\phi} \right\rangle_i = \frac{2d}{\lambda n^0} \sum_{i \neq j} \left[ (\boldsymbol{\phi}_i - \boldsymbol{\phi}_j) W(r_{ij}, r_e) \right] \quad (7)$$

In which $\lambda$ is the defining parameter to maintain equality of increase in variance with the analytical solution. The parameter is defined as:

$$\lambda = \frac{\int_v W(r, r_e) r^2 dv}{\int_v W(r, r_e) dv} \quad (8)$$

2.2 Modeling turbulence

Turbulence is considered as a significant factor in turbulence flow hydraulic calculations. In this study, for turbulence stress modeling in the momentum equation, the relationship presented by Gotoh et al (2001) had been used.

$$\upsilon_t = (C_s \Delta)^2 \sqrt{2 \mathbf{E}_{ij} \mathbf{E}_{ij}} \quad (9)$$

where $\Delta$ is the distance between the particles and $C_s$ is Smagorinsky constant. Also, $\mathbf{E}_{ij}$ is the strain rate tensor-scale solution that is defined as follows:

$$\mathbf{E}_{ij} = \frac{1}{2} \left( \frac{\partial \overline{\mathbf{u}}_i}{\partial \mathrm{x}_j} + \frac{\partial \overline{\mathbf{u}}_j}{\partial \mathrm{x}_i} \right) \quad (10)$$

2.3 Calculation of pressure

The weakly compressible MPS (WC -MPS) method (Shakibaeinia and Jin, 2010) assumes the fluid to be slightly compressible and calculates the pressure of each particle using a stiff equation of state. In this study, Tait's state equation (commonly applied for high pressure water flow) was used as follows:

$$p_i = \frac{\rho c_0^{\,2}}{\gamma} \left[ \left( \frac{\langle \rho \rangle_i}{\rho_0} \right)^{\gamma} - 1 \right] = \frac{\rho c_0^{\,2}}{\gamma} \left[ \left( \frac{\langle n \rangle_i}{n_0} \right)^{\gamma} - 1 \right] \quad (11)$$

where, $\gamma = 7$, c0 is a synthetic sound speed. Since the actual sound speed results were used in very small time steps, a synthetic smaller sound speed was used. To keep the density variations of the liquid ($\rho\Delta/\rho$) to less than 1% of the reference density, the sound velocity should be more than 10 times the maximum fluid velocity ($|\mathbf{u}|_{max}$).

 

2.4 Boundary condition

The MPS method can be used to track the free surface by the particle density. Since there is no particle in the free space outside the area, the density of particles at the surface decreases. Free surface particles are known as particulate that their density is somewhat less than particles standard density. With regard to the issue, this limit may be selected from 80% to 99% and is shown with relationship (12):

$$\left\langle n^{*}\right\rangle_{i} \le n^{0}\beta \tag{12}$$

The pressure of these particles on the free surface will be set zero at each time step. It is required to impose no additional conditions for the MPS method.

In cases such as walls or floors of channels with impenetrable solid boundaries, the wall boundary conditions were used. In the vicinity of the solid boundaries, the density of particles reduced, which can cause disruption in the calculations. Hence ghost particles were stationed abroad to prevent the reduction of unwanted density. This was used for the first time by Kushizuka et al (1995). The thickness of the ghost particles depended on selected influence radius of the kernel function.

## 3 GRANULAR RHEOLOGY

The system of fluid and sediments is a multiphase of solids and liquid, where both phases are treated as continuum. To calculate the viscose term in the momentum equation, dynamic viscosity of each particle (solid or liquid phase) is required. The liquid phase (i.e., water) has a known and constant viscosity (independent of time and stress). However, determination of solid-phase viscosity is not simple.

The sediment phase can be treated as a non-Newtonian visco-plastic fluid that behaves as solid for stresses less than a yield stress and as a viscous fluid for stresses exceeding the yield stress. Bingham plastic, and for more complex cases, Herschel–Bulkley generalized visco-plastic models, are extensively used to describe the behavior sediment flow. In Herschel–Bulkley model, the shear stress tensor is calculated using a stress-dependent effective viscosity given by (Papanastasiou, 1987):

$$\boldsymbol{\tau} = 2\mu_{eff}\mathbf{E} \rightarrow \mu_{eff} = \begin{cases} \dfrac{\tau_{y}}{2\left\|\mathbf{E}\right\|} + \mu_{0}\left(\left\|\mathbf{E}\right\|\right)^{N-1} & \left\|\tau\right\| > \tau_{y} \\ \infty & \left\|\tau\right\| < \tau_{y} \end{cases} \tag{13}$$

In which:

$$\mathbf{E} = \frac{1}{2}\left(\nabla\mathbf{u} + \left(\nabla\mathbf{u}\right)^{T}\right) \;\; ; \;\; \left\|\mathbf{E}\right\| = \sqrt{II_{E}} = \sqrt{\frac{1}{2}\mathbf{E} : \mathbf{E}} \;\; ; \;\; \left\|\boldsymbol{\tau}\right\| = \sqrt{I_{\tau}} = \sqrt{\frac{1}{2}\boldsymbol{\tau} : \boldsymbol{\tau}} \;\; ; \;\; \tau_{y} = p_{mech}sin\phi \tag{14}$$

where, **τ** and **E** are shear stress and rate of deformation tensors, respectively, ($\|E\|$ and $\|\tau\|$ are their magnitude); $\mu_0$ and N are flow consistency and behavior indices (function of grain shape and size), which are determined experimentally; II is second invarient of the tensor, $\tau_y$ is yield stress which is determined using Mohr Coulomb criterion for non-cohesive sediments, Pmech is mechanical pressure; N=1 shows linear behavior (Bingham plastic model).

The ideal form of Herschel–Bulkley model (Eq. 13) is discontinuous when shear rate goes to zero ($\|\mathrm{E}\| \rightarrow 0$). To avoid this and also to avoid determination of yield regions ($\|\tau\| > \tau_y$) and non-yield regions ($\|\tau\| \le \tau_y$), a continuous and regularized forms of the equation proposed by Papanastasiou (1987) is used as:

$$\mu_{eff} = \frac{\tau_{y}\left(1 - exp(-m\left\|\mathbf{E}\right\|\right)}{2\left\|\mathbf{E}\right\|} + \mu_{0}\left(\left\|\mathbf{E}\right\|\right)^{N-1} \tag{15}$$

where parameter m controls the exponential growth of stress. This equation is valid for both yield and non-yield regions. For stresses less than yield stress, which $\|\boldsymbol{E}\|$ gets close to zero, regular effective viscosity B-P (N=1) reaches a maximum value of $\mu_{max} = \mu_0 + 0.5m\tau_y$.

## 4 TIME INTEGRATION AND SOLUTION ALGORITHM

To solve the governing equations, each time step was divided into two pseudo time steps of prediction and correction steps. The velocity at a new time step (k+1) is sum of predicted velocity (u*) and corrected

 

velocity (u') (Jafari et al, 2015):

$$\mathbf{u}_i^{k+1} = \mathbf{u}_i^* + \mathbf{u}'_i \tag{16}$$

where

$$\begin{cases} \mathbf{u}_i^* = \mathbf{u}_i^k + \dfrac{\Delta t}{\rho_i}\left(\mathbf{g} + \mu_{ij}\nabla^2\mathbf{u}_i^k - (1-\alpha)\nabla p_i^k\right) \\ \mathbf{u}' = -\dfrac{\alpha\,\Delta t}{\rho_i}\nabla p_i^{k+1} \end{cases} \tag{17}$$

where $\alpha$ is a relation factor between 0 and 1. Particles were first moved, based on the predicted velocity and the predicted value of the particle number density n* was calculated. n* was then used for calculation of the pressure from the equation of state. The pressure gradient term was then recalculated and used for calculation of corrected velocity. The final solution algorithm, used for each time step, was summarized as follows:

1. Input the initial properties of the particles $\mathbf{r}_i$, $\mathbf{u}_i$, $p_i$, $\rho_i$, $\mu_i$.
2. Time integration

- Calculation of effective viscosity of each particle, $\mu_{eff}$ (for particles of solid phase, Eq. 15 was used)
- Prediction of velocity **u*** by Eq. (17) and calculation of **r*** and *n**
- Calculation of pressure by Eq. (11)
- Calculation of corrected velocity of Eq. (17)
- Calculation of velocity, position of particles (moving particles with own velocity) and numerical density of particles
- Calculation of volume fraction for concentration($\phi$)
- Sending the new results ($\mathbf{r}i^{k+1}$, $\mathbf{u}i^{k+1}$, $pi^{k+1}$, $\phi i^{k+1}$) and preparation for the next time step.

3. Iteration for the next time step

The stability condition of Courant-Friedrichs-Lewy (CFL) should be satisfied. This condition is calculated as:

$$\Delta t = C.min\left\{\frac{\Delta l}{c_0 + |\mathbf{u}|_{max}}, \frac{\rho \Delta l^2}{2d\mu_{max}}\right\} \tag{18}$$

where $\Delta l$ is distance between the particles (size of the particles) and $0 < C \leq 1$ is the Courant number.

## 5 TEST CASES

In this section, the results of physical model Mao (1986) were used for modeling of local scour around circular pipe for the semi-implicit method of moving particles. The sediment martials had a grain size of $d_{50} = 0.00036m$, bulk density of $\rho_s = 2000kg/m^3$ and internal friction angle of ∅=35. The deposited layer had a thickness of 0.25m, the water depth was 0.35 m and the pipeline diameter was 0.1 m. A two-dimensional computational domain with a length of 45D and a height of 6D was used in the simulation. The distance between the pipeline center and the inlet boundary was 15D. The depth-averaged velocity at the inlet boundary was specified as 0.65 m.

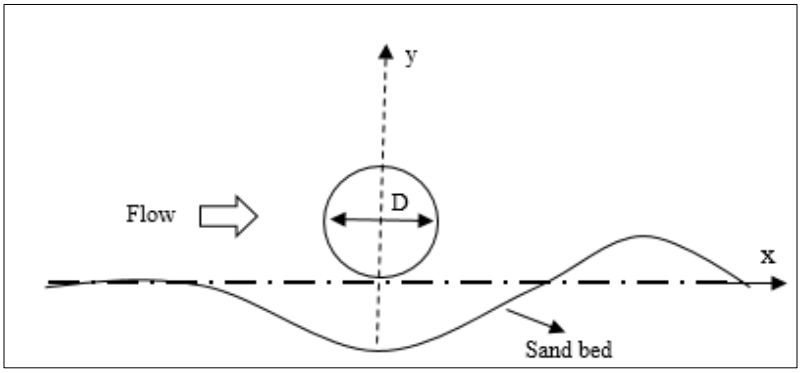


**Figure2.** The forms of motion for the sand grain beneath the pipe.

## 6 LOCAL SCOUR AROUND CIRCULAR PIPE

The computational domain was represented with 28508 particle (with initial distance of 0.01 m). Figure 3 shows the numerical result snapshots of local scour problem around circular pipe at t= 1.5, 2.5 and 5 seconds. The high velocity flow under the pipe and flow circulation created a scour hole that growed as the time went on, until an equilibrium was reached. The eroded materials were deposited further downstream and created a sediment ridge. Comparisons of the experimental and numerical snapshots showed similar scouring and deposition features. Figure 4 provides a quantitative comparison of experimental and numerical sediment surface profiles. The results showed a good compatibility of the profiles, especially for the scour hole. The proposed numerical model has been able to successfully reproduce the shape and size of the scour hole. Figure 5 presents the time evolution of the dimensionless depth of scour hole. The experimental and numerical results are quite compatible. Figure 6 provides a sample snapshot of simulated, volume fraction, velocity magnitude and velocity vectors at *t*= 2 sec.

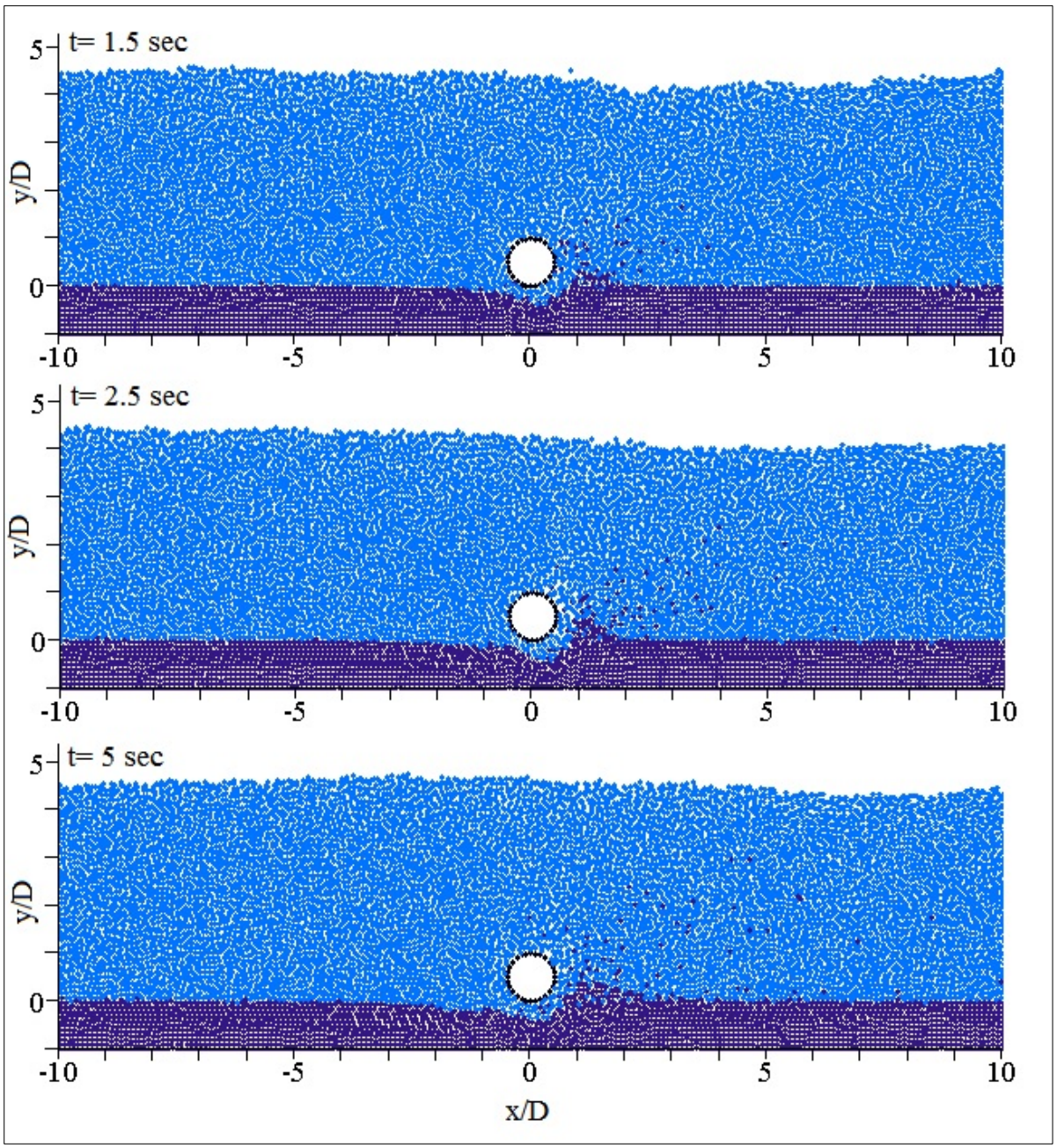


**Figure3.** Results of scour hole for MPS-WC model runs at t= 1.5, 2.5 and 5 seconds.

 

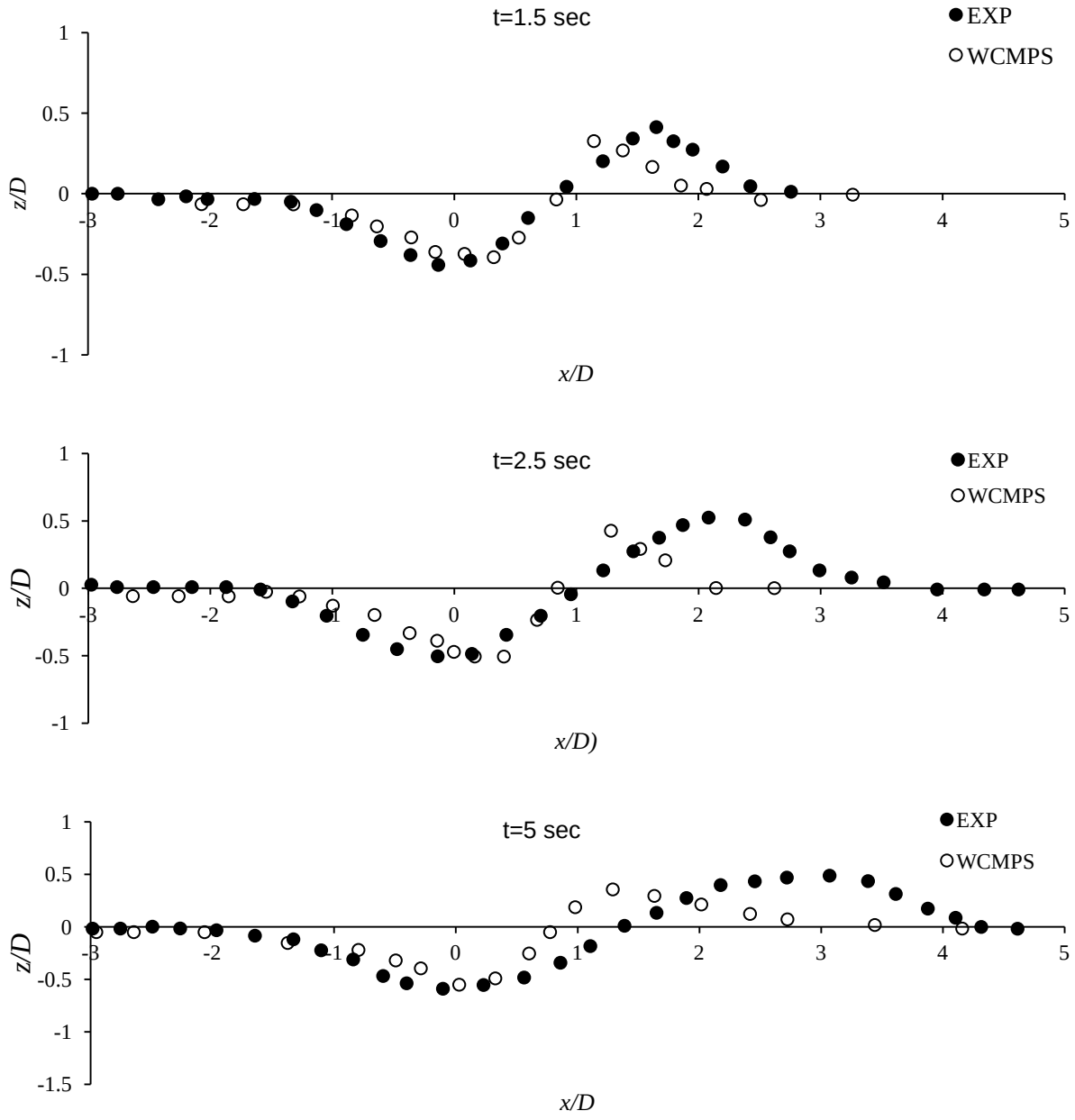


**Figure 4.** Quantitative comparison of scour hole for MPS-WC model and experimental runs at t= 1.5, 2.5 and 5 seconds.

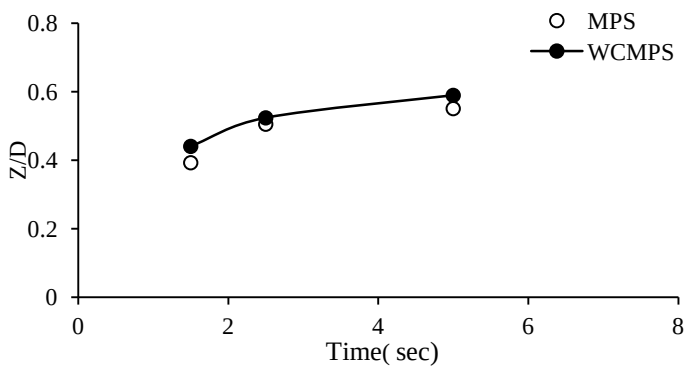


**Figure5.** Comparison of numerical and experimental dimensionless scour depth below the pipe center.

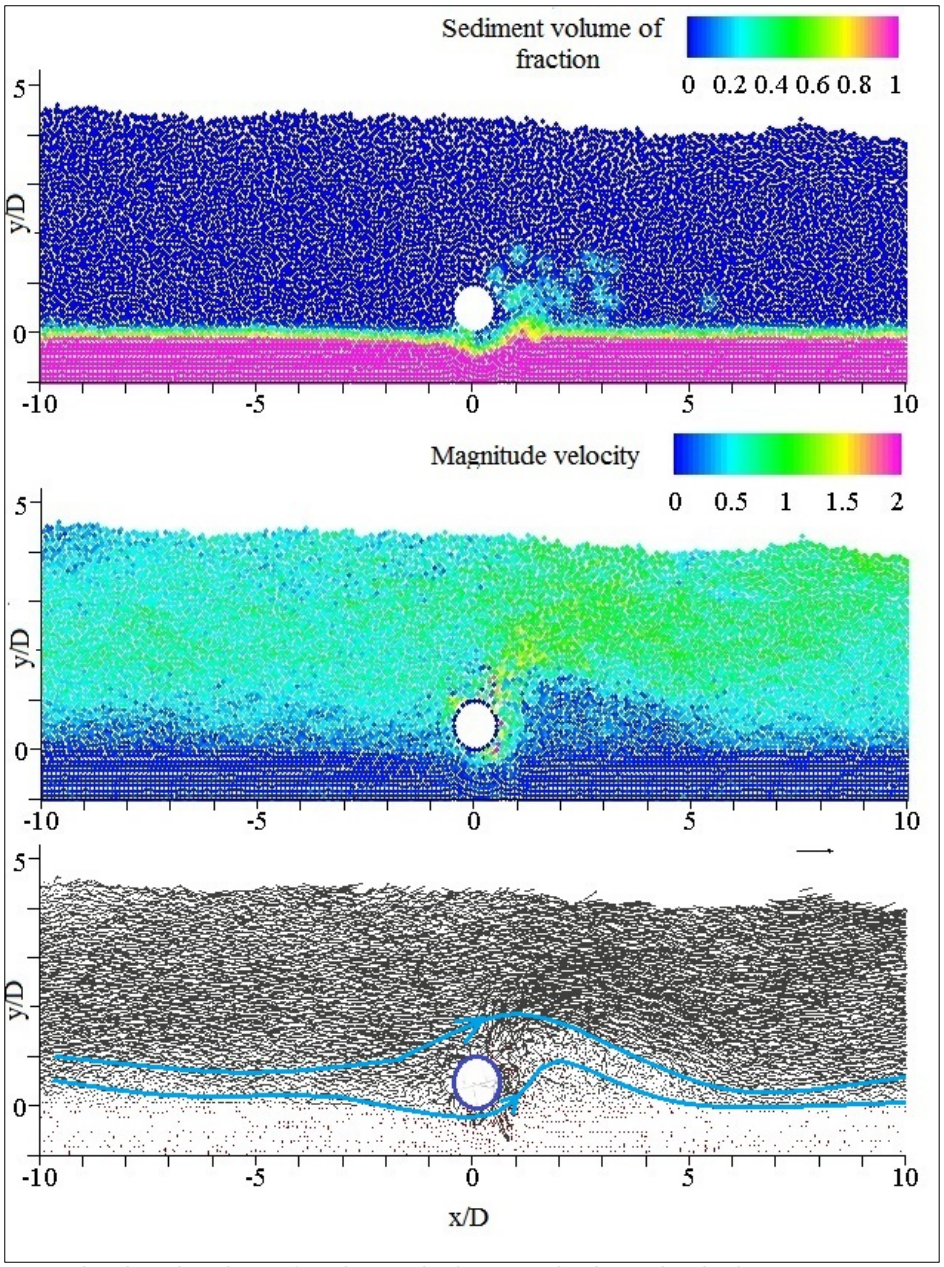


**Figure6.** Simulated, volume fraction, velocity magnitude and velocity vectors at t=2 sec.

## 7 CONCLUSIONS

In this study, a mesh-free Lagrangian model based on a weakly-compressible MPS formulation for simulation of local scour around a circular pipe is developed and evaluated. The developed model treats the two-phase system of Newtonian (water) and non-Newtonian (sediment) fluids, as a multi-density multi-viscosity continuum. A regularized viscoplastic rheological model with a Mohr-Coulomb yield stress is used to predict the non-Newtonian behavior of sediment materials. The model is validated by comparing with the available experimental measurements. Validations prove the capability of the developed model for accurate prediction of the erosion pattern and scour hole shape/dimensions.

## REFERENCES

Ataei-Ashtiani, B. & Farhadi, L. (2006). A Stable Moving Particle Semi Implicit Method for Free Surface Flows. *Fluid Dynamics Research*, 38, 241-256.

Gotoh, H. & Sakai, T. (1999). Lagrangian Simulation of Breaking Wave using Particle Method. *Coastal Engineering Journal,* 41(3-4), 303-326.

Gotoh, H. & Sakai, T.(2006). Key Issues in the Particle Method for Computation of Wave Breaking. *Coastal Engineering Journal,* 53(2-3), 171-179.

Jafari Nodoushan, E. Hosseini, K.H. Shakibaeinia, A. & Mousavi, S.F. (2015). Meshless Particle Modelling of Free Surface Flow over Spillways. *Journal of Hydroinformatics* 18(2), 354-370.

 

Koshizuka, S. & Oka, Y. (1996). Moving Particle Semi Implicit Method for Fragmentation of Incompressible Fluid. *Nuclear Science and Engineering,* 123(3), 421-434.

Koshizuka, S., Nobe, A. & Oka, Y. (1998). Numerical Analysis of Breaking Waves using the Moving Particle Semi Implicit Method. *International Journal of Numerical Methods in Fluids,* 26(7), 751-769.

Liu, G.R. & Liu, M.B. (2003). *Smoothed Particle Hydrodynamics: A Meshfree Particle Method.* World Scientific Publishing, Science, 470.

Mao, Y. (1986). The Interaction between a Pipeline and an Erodible Bed, *Ph.D. Thesis.* Technical Univercity of Denmark, Lyngby, Denmark.

Papanastasiou, T.C. (1987). Flows of Materials with Yield. *Journal of Rheology,* 31, 385-404.

Shakibaeinia, A. & Jin, Y.C. (2010). A Weakly Compressible MPS Method for Simulation of Open Boundary FreeSurface Flow. *International Journal for Numerical Methods in Fluids,* 63(10), 1208-1232.

Shakibaeinia, A. & Jin, Y.C. (2011). A Mesh Free Particle Model for Simulation of Mobile Bed Dam Break. *Advanced Water Resources,* 34, 794-807.

Shakibaeinia, A. & Jin, Y.C. (2012a). MPS Mesh Free Particle Method for Multiphase Flows. Computer Methods in Applied Mechanics and Engineering, 229–232, 13-26.

Shakibaeinia, A., & Jin, Y.C. (2012b). Lagrangian Multiphase Modeling of Sand Discharge into Still Water. *Advances in Water Resources,* 48, 55-67.

Zhao, M. & Cheng, L. (2008). Numerical Modeling of Local Scour below a Piggyback Pipeline in Currents. *Journal of Hydrulic Engineering*, 134,10-1452.

 

# OPERATION OF XIAOLANGDI RESERVOIR AND EVOLUTION RESPONSE OF LOWER YELLOW RIVER

JIAN FU [1], CUIXIA CHEN [2], SHITAO WEI [3], SHENG QIAN [4] & ZENGHUI WANG [5]

[1,2,3,4,5] Yellow River Engineering Consulting Co., Ltd., Zhengzhou, Henan, China 450003
fujian@yrec.cn chencx@yrec.cn, weisht@yrec.cn, qiansh@yrec.cn, wangzh@yrec.cn

## ABSTRACT

Xiaolangdi Reservoir, a crucial project for the control of water and sediment entering into the lower reaches, plays a very important strategic role in the management and development of the Yellow River. Since 1997, when the river is dammed, the amount of sedimentation in Xiaolangdi Reservoir reaches 3.086 billion $m^3$ until April 2016. The reservoir functions in the first stage of the later phase of sediment retaining. During the past 17 years since the impoundment of the reservoir in October 1999, it has played an important part in such aspects as flood control (ice prevention), sedimentation reduction, water supply, irrigation and power generation. The situation of flood control in the lower reaches of the Yellow River has improved effectively. The minimum bankfull discharge of the river channel increases from 1800$m^3$/s before the flood season in 2002 to 4200$m^3$/s before the flood season in 2016, which indicates remarkable benefits for the operation of the Reservoir.

**Keywords**: Xiaolangdi Reservoir; operation of sediment retaining; lower reaches of yellow river; erosion and deposition; effect analysis.

## 1 INTRODUCTION

Located at 130km to the downstream of Sanmenxia Reservoir, Xiaolangdi Reservoir is the last gorge reach of the Yellow River. The drainage area above dam site is 0.694 million $km^2$, accounting for 92.3% of the total, controlling about 90% runoff of the Yellow River and almost all the sediments, so it is critical to settle the flood control and sediment reduction (Jian Fu et al., 2011; Jixiang Liu et al., 2008). The height of the largest dam of Xiaolangdi Water Control Project is 160 m with the normal storage level 275m, the level of dead water 254m, the total capacity of the reservoir 12.65 billion $m^3$, the installed capacity 1.8 million kilowatts, and the annual generating capacity 5.8 billion kilowatt-hours. Figure 1 shows the map of the study area.

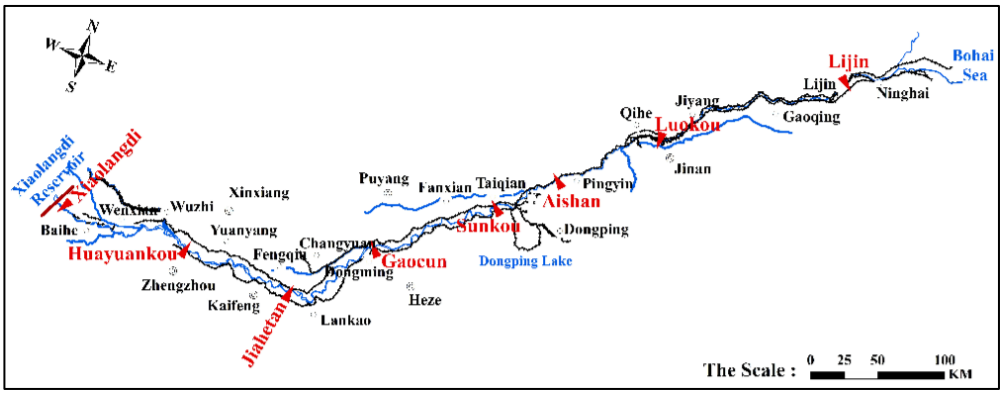


**Figure 1.** Map of the study area.

To develop the work of "Giving priority to flood control (ice prevention) and sedimentation reduction, supported with water supply, irrigation, power generation, water conservancy development and integrative application", Xiaolangdi Reservoir has accumulated a sedimentation volume of 3.086 billion $m^3$ since the cutoff of dam at 1997 until April 2016, and the reservoir functioned in the first stage of the later phase of sediment retaining. Over the past 17 years since the reservoir was put into operation in October 1999, a large amount of observation data, analysis results and valuable experience have been obtained in flood control (ice prevention), sedimentation reduction, water and sediment regulation, water supply, irrigation and power generation (Jianguo Chen et al., 2016; Shujun Liu et al., 2012; Junhua Zhang et al., 2016), which provides a solid foundation for the study of the Yellow River's water and sediment motion law and further deepens the study on modes of the reservoir operation.

 

## 2 CONDITIONS OF INCOMING WATER AND SEDIMENT

With the increasing consumption of industrial and agricultural water since the middle and late 1980s, the influence of reservoir regulation and variations of natural runoff caused by climate factors, the conditions of incoming water and sediment in the Yellow River have been greatly changed. Especially after Xiaolangdi Reservoir was put into operation, the water and sediment conditions have changed more obviously, which is mainly shown in the following aspects: a. the amount of incoming water and sediment decrease dramatically; b. due to the effect of water storage of large reservoirs, annual distribution of the incoming water changes; c. in recent years, the frequency of floods declines and peak discharges decrease.

From July 2000 to June 2015, the average amount of water and sediment entering into Xiaolangdi Reservoir were 22.52 billion $m^3$ and 319 million tons, respectively, with an average sediment concentration of 14.16kg/$m^3$. The amount of water entering into the reservoir was 10.716 billion $m^3$ in the flood season (July to October, similar hereinafter), accounting for 47.6% of the amount during the whole year; while the amount of sediment entering into the reservoir was 297 million tons in the flood season, accounting for 93.1% of the amount during the whole year. The average sediment concentration was 27.72kg/$m^3$ in the flood season. Characteristics of water and sediment entering into Xiaolangdi Reservoir are shown in Table 1.

**Table 1.** Characteristics of water and sediment entering into Xiaolangdi Reservoir from July 2000 to June 2015.

| Items | Flood Season | Non-flood Season | Whole Year |
|---|---|---|---|
| Average Runoff (hundred million $m^3$) | 107.16 | 118.04 | 225.20 |
| Average Sediment Load (hundred million tons) | 2.97 | 0.22 | 3.19 |
| Average Sediment Concentration(kg/$m^3$) | 27.72 | 1.85 | 14.16 |

## 3 OPERATION OF XIAOLANGDI RESERVOIR

### 3.1 Water level variation in front of the dam

Figure 2 shows the water level variation in front of the dam in Xiaolangdi Reservoir from January 2000 to December 2015. It can be seen that the impoundment period of Xiaolangdi Reservoir is from the end of the flood season to March of the next year, during which the water level in front of the dam increases slowly to accumulate water resources for the upcoming water usage peak. From April to May, to meet the water demands for industrial and agricultural production, urban life and ecological balance in the downstream of the Yellow River, the reservoir discharges and the water level in front of the dam begin to decrease. In the flood season, to meet the requirements of flood control, the water level in front of the dam drops beneath the flood control level and water and sediment regulation is conducted if there is a suitable condition. Afterwards, the water level starts to rise up. The highest water level in front of the dam in Xiaolangdi Reservoir was 270.10 m (November 19, 2012) and the lowest was 191.44 m (July 26, 2001) from January 2000 to December 2015.

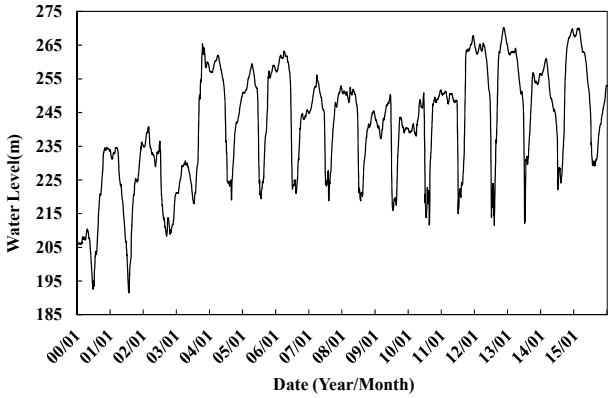


**Figure 2.** Water level variation of Xiaolangdi Reservoir from 2000 to 2015.

### 3.2 Water and sediment characteristics of outflows

Table 2 shows the water and sediment conditions of the outflows since Xiaolangdi Reservoir was put into operation from July 2000 to June 2015. The average annual outflow volume of Xiaolangdi Reservoir was 24.002 billion $m^3$, the corresponding amount of sediment was 67 million tons, and the average sediment concentration was 2.79 kg/$m^3$. The outflow volume was 8.136 billion $m^3$ in the flood season, accounting for 33.9% of the amount during the whole year and the released sediment load was 63 million tons in the flood season, accounting for 94.7% of the amount during the whole year. The average outflow sediment

 

concentration was 7.79 kg/m$^3$ in the flood season.

According to the inflow and outflow of Xiaolangdi Reservoir, the yearly average of incoming sediment was 319 million tons and released sediment was 67 million tons with the reservoir sediment discharge ratio of 21.0% from July 2000 to June 2015.

**Table 2.** Characteristics of water and sediment out of Xiaolangdi Reservoir from July 2000 to June 2015.

| Items | Flood Season | Non-flood Season | Whole Year |
|---|---|---|---|
| **Average Runoff (hundred million m$^3$)** | 81.36 | 158.66 | 240.02 |
| **Average Sediment Load (hundred million tons)** | 0.63 | 0.04 | 0.67 |
| **Average Sediment Concentration(kg/m$^3$)** | 7.79 | 0.22 | 2.79 |

According to "Operation Regulation of Xiaolangdi Project in the Later Phase of Sediment Retaining (First Stage)", reservoir water and sediment regulation should consider the water and sediment conditions, reservoir sedimentation and discharge capacity of the main channel in the downstream of the Yellow River, and make full use of the downstream river channel's sediment transporting capacity. The discharge at Huayuankou Station in the downstream should be controlled lower than 800m$^3$/s or higher than 2600m$^3$/s. After the regulation of Xiaolangdi Reservoir, the frequency of 800m$^3$/s~2000m$^3$/s flow out of the reservoir in the major flood period (July.11-September.30) decreases significantly. The outflow discharge has been polarized. The reservoir sediment is released mainly with the flows above 2000m$^3$/s and the released sediment accounts for 54.0% of that in the main flood period. Due to the water and sediment regulation before the flood season, the frequency of large flows above 2600m$^3$/s nearly double compared with the inflow with the same discharge, as shown in Table 3.

**Table 3.** Frequency of various flows in and out of Xiaolangdi Reservoir and water and sediment statistics (from 1999 to 2015).

| Period | Flow ($m^3/s$) | Days of Various Flows into the Reservoir and Amounts of Water and Sediment | | | | Days of Various Flows out of the Reservoir and Amounts of Water and Sediment | | | |
|---|---|---|---|---|---|---|---|---|---|
| | | Days | Probability (%) | Water ($10^8$ $m^3$) | Sediment ($10^8$ ton) | Days | Probability (%) | Water ($10^8$ $m^3$) | Sediment ($10^8$ ton) |
| **Whole Year (1.1-12.31)** | **0~800** | 262.6 | 71.9 | 101.43 | 0.37 | 255.2 | 69.9 | 102.73 | 0.06 |
| | **800~2000** | 88.6 | 24.3 | 86.06 | 1.06 | 92.0 | 25.2 | 87.03 | 0.16 |
| | **2000~2600** | 7.3 | 2.0 | 14.10 | 0.88 | 6.7 | 1.8 | 13.10 | 0.22 |
| | **above 2600** | 6.8 | 1.9 | 19.23 | 0.72 | 11.4 | 3.1 | 32.65 | 0.19 |
| | **Total** | 365.3 | 100.0 | 220.82 | 3.04 | 365.3 | 100.0 | 235.52 | 0.63 |
| **Main Flood Season (7.11-9.30)** | **0~800** | 40.1 | 48.9 | 14.64 | 0.27 | 63.6 | 77.5 | 23.27 | 0.05 |
| | **800~2000** | 31.3 | 38.1 | 34.14 | 0.69 | 13.7 | 16.7 | 14.15 | 0.12 |
| | **2000~2600** | 5.9 | 7.2 | 11.30 | 0.65 | 2.4 | 2.9 | 4.53 | 0.12 |
| | **above 2600** | 4.8 | 5.8 | 13.45 | 0.45 | 2.4 | 2.9 | 5.95 | 0.08 |
| | **Total** | 82.0 | 100.0 | 73.52 | 2.07 | 82.0 | 100.0 | 47.91 | 0.37 |

3.3 Quantity of reservoir sedimentation

From October 1997 to April 2016 when the river was dammed by Xiaolangdi Reservoir, the deposition in Xiaolangdi Reservoir reached 3.086 billion m$^3$ according to the measurements of cross sections, in which the main stream deposited 2.499 billion m$^3$, accounting for 80.7% of the total and tributaries deposited 587 million m$^3$, accounting for 19.3% of the total. The reservoir sedimentation accounted for about 41% of the designed reservoir sediment storage capacity. According to "Operation Regulation of Xiaolangdi Project in the Earlier Phase of Sediment Retaining" approved officially by Ministry of Water Resources in 2004, when the sedimentation of Xiaolangdi Reservoir reached 2.1~2.2 billion m$^3$, it entered the later phase of sediment retaining. At present, the reservoir is operated in the first stage of the later phase of sediment retaining.

Table 4 shows the result of siltation volume of Xiaolangdi Reservoir, and the sediment in the reservoir area is mainly silted within 64.83km away from the dam.

**Table 4.** Sediment deposition in Xiaolangdi Reservoir from October 1997 to April 2016.

| Sections | Accumulative Deposition($10^8$ m$^3$) |
|---|---|
| **0~33.48km away from the dam** | 19.54 |
| **33.48~64.83km away from the dam** | 10.15 |
| **64.83~123.41km away from the dam** | 1.17 |
| **All of the reservoir regions** | 30.86 |

 

### 3.4 Reservoir sedimentation forms

#### 3.4.1 Main stream sedimentation forms

Due to the separation of sediment by water flow, coarse sand deposits firstly near the end of the backwater area of the reservoir, while finer sand dives into the reservoir and flows to the front of the dam in the form of turbidity currents. Therefore, mainstream sedimentation forms include delta deposits near the end of the backwater area, deposits of turbidity current and muddy pond downstream the delta. Figure 3 shows forms of the main stream sedimentation profiles of Xiaolangdi Reservoir in various periods. It illustrates that the main stream of Xiaolangdi Reservoir presents a form of delta sedimentation. With the use of the reservoir, the delta vertex of the main stream deposits advances gradually to the front of the dam. The sedimentary rate of the reservoir is related to the utilization time of the reservoir and coming water and sediment. The figure also shows that in 2001, 2004 and 2006, due to the narrow channel more than 70 km away from Xiaolangdi Reservoir and the rising water level by the use of the reservoir, there should be sedimentation in this reach. However, when the reservoir operating water level lowered and a certain period of larger flow process occured, sediment deposit in the reach would be soured and moved and thus the sedimentation form could be adjusted. Up to April 2016, the delta vertex was 16.39 km away from the dam and the vertex was 222.36 meters high.

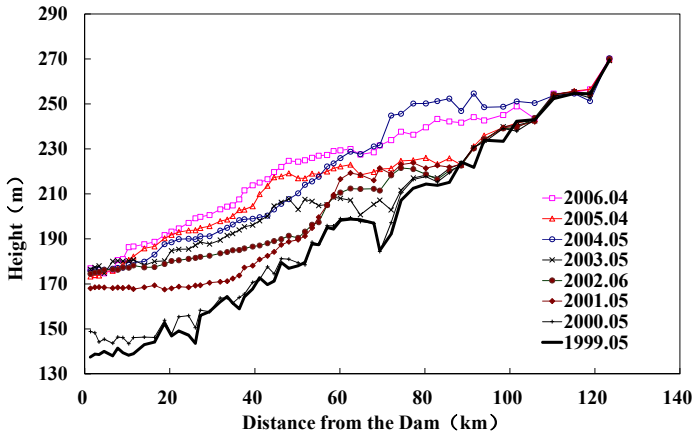


**Figure 3(a).** Forms of sedimentation profiles of Xiaolangdi Reservoir (1999~2006).

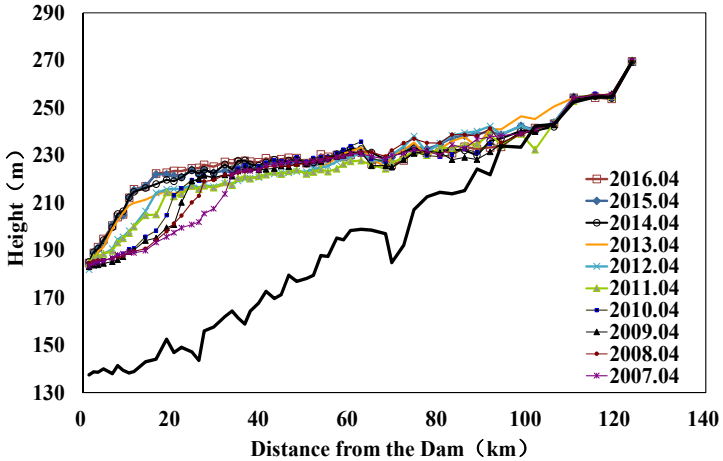


**Figure 3(b).** Forms of sedimentation profiles of Xiaolangdi Reservoir (2007~2016).

#### 3.4.2 Reservoir tributary sedimentation forms

The sedimentation profile changes of tributaries of Xiaolangdi Reservoir (Zhenshui and Boqing River) are shown in Figure 4 and 5. From the profile forms of the reservoir tributaries, sandbars with certain heights that block the tributary mouth are formed in the sedimentation process of Zhenshui and the maximum height is about 10m. However, as time goes by, sandbars are flattened by deposition gradually and therefore there are not severer sandbars formed.

 

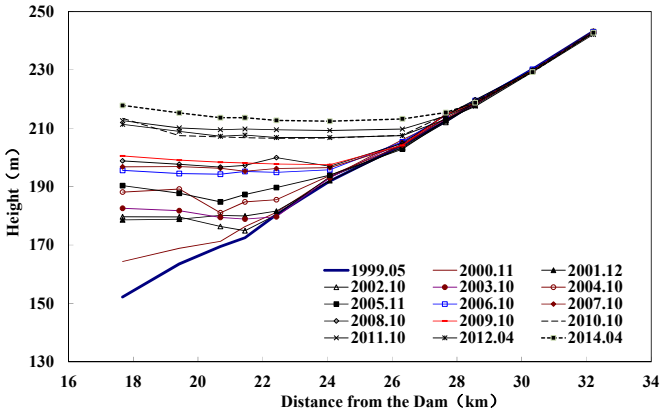


**Figure 4.** Longitudinal profiles of reservoir tributary Zhenshui (17.67km away from the dam).

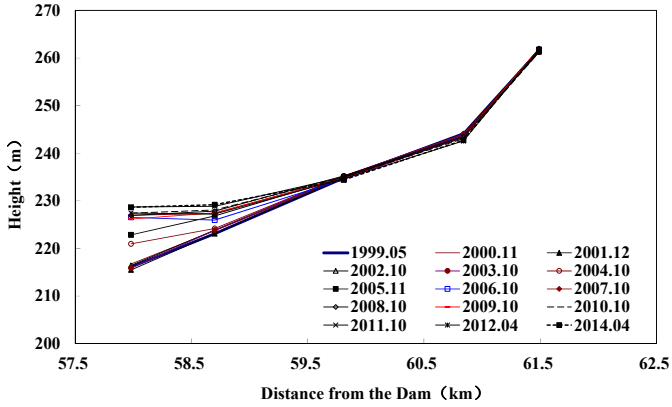


**Figure 5.** Longitudinal profiles of reservoir tributary Boqing River (57.98km away from the dam).

3.5 Water and sediment regulation of the yellow river

Water and sediment regulation tests for three times and operations for sixteen times have been implemented at Xiaolangdi Reservoir from 2002. During the period of water and sediment regulation, water entering into the downstream channel was 71.401 billion $m^3$ and sediment was 655 million tons in total. Water and sediment regulation realized the scouring along the entire main channel downstream and the total sediment entering into the sea was 976 million tons at Lijin Station, and 409 million tons of sediment were scoured in the downstream channel.

## 4 EVOLUTIONARY RESPONSE OF EROSION AND DEPOSITION IN THE DOWNSTREAM CHANNEL

4.1 Quantity of Erosion and Deposition in the Downstream Channel

According to the measurements of cross sections in the downstream channel, all reaches in the downstream of the Yellow River had been scoured since the operation of Xiaolangdi Reservoir and 2.734 billion tons of sediment were scoured in the reach above Lijin, which can be seen in Table 5.

From the perspective of longitudinal distribution, erosion was mainly concentrated in the reaches upstream Gaocun Station and those in downstream Gaocun Station were less scoured relatively. 2.017 billion tons of sediment were scoured in the reaches upstream Gaocun, accounting for 73.8% of the total scouring amount in reaches above Lijin; 368.0 million tons of sediment were scoured in the reach from Gaocun to Aishan, accounting for 13.4% of the total scouring amount in reaches above Lijin; 349.0 million tons of sediment were scoured in the reach from Aishan to Lijin, accounting for 12.8% of the total scouring amount in reaches above Lijin.

From the time distribution, scouring mainly occurred in the flood season; there was 1.745 billion tons of sediment in total that scoured in the downstream river channel in the flood season, including all reaches. In the non-flood season, 989.0 million tons of sediment were scoured in the downstream river channel. Scouring took place in all reaches of upstream Aishan and mainly in the reach from Huayuankou to Gaocun, with the amount 687.0 million tons, accounting for 69.5% of the total in the non-flood season. The scouring weakened downstream gradually and 131.0 million tons of sediment deposited between Aishan and Lijin.

 

**Table 5.** Statistics of erosion and deposition in different downstream reaches according to the measurements of cross sections since the operation of Xiaolangdi Reservoir.

| Period | Reach | Upstream Huayuankou ($10^8$ tons) | Huayuankou-Gaocun ($10^8$ tons) | Gaocun-Aishan ($10^8$ tons) | Aishan-Lijin ($10^8$ tons) | Upstream Lijin ($10^8$ tons) |
|---|---|---|---|---|---|---|
| **Flood Season** | | -3.78 | -5.22 | -3.65 | -4.80 | -17.45 |
| **Non-flood Season** | | -4.30 | -6.87 | -0.03 | 1.31 | -9.89 |
| **Total** | | -8.08 | -12.09 | -3.68 | -3.49 | -27.34 |

4.2 Typical Cross Section Changes

After the operation of Xiaolangdi Reservoir, changes of typical cross sections at Huayuankou and Gaocun stations in the downstream are shown in Figure 6 and Figure 7. The operation of the reservoir made the main channels of all sections in the downstream broader and scour downward.

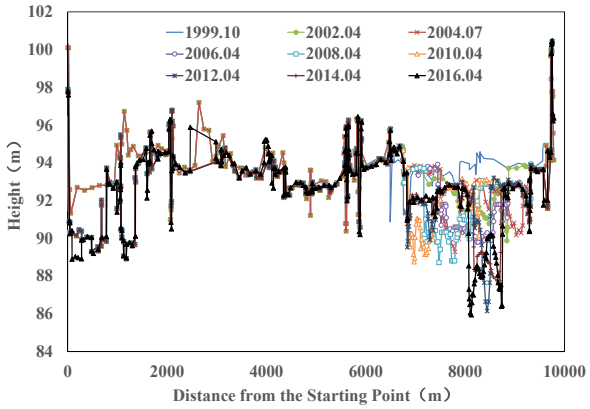


**Figure 6.** Changes of Huayuankou section.

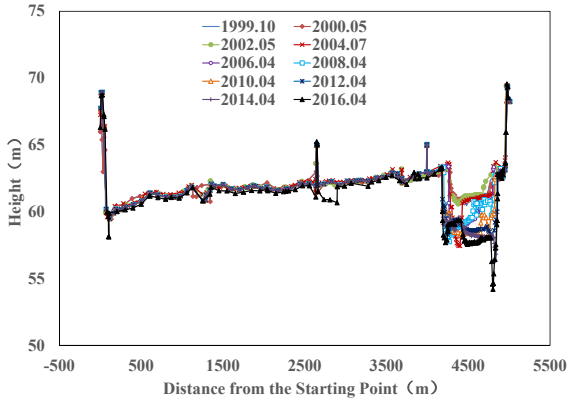


**Figure 7.** Changes of Gaocun section.

4.3 Changes of water level at the same discharge

Changes of water level at the same discharge are the indirect reflection of channel discharge capacity changes in a certain period of time, which means that if the water level at the same discharge lowers, the channel discharge capacity increases. With the continuous scouring of the downstream channel, all water levels at the same discharge are lower in different degrees in the downstream channel. Compared to 1999, the 2000$m^3$/s water levels before flood season in 2016 lowered greatly in the reaches of upstream Gaocun, up to 2.35m~2.77m, and the water levels lowered less in the reaches of downstream Gaocun Village, 1.53m~2.52m, as shown in Table 6.

**Table 6.** Changes of water level at the same discharge (2000 $m^3$/s) in the downstream channel between 1999 and 2016.

| Names of Stations | Huayuankou (m) | Jiahetan (m) | Gao Village (m) | Sunkou (m) | Aishan (m) | Luokou (m) | Lijin (m) |
|---|---|---|---|---|---|---|---|
| **1999** | 93.67 | 76.77 | 63.04 | 48.07 | 40.65 | 30.23 | 13.25 |
| **2016** | 91.32 | 74.00 | 60.52 | 46.21 | 39.08 | 28.32 | 11.72 |
| **Water Level Changes** | -2.35 | -2.77 | -2.52 | -1.86 | -1.57 | -1.91 | -1.53 |

4.4 Changes of Bankfull Discharge

The main channel transports sediment and drains off flood and its discharge capacity directly affects the flood control safety of lower reaches of the Yellow River. Bankfull discharge is an important parameter to reflect the main channel's discharge capacity and also a key technical indicator for maintaining the channel's functions of draining off flood and transporting sediment. The smaller the bankfull discharge is, the lower the main channel's discharge capacity and the constraint on the river regime are and the more difficult the flood control is. Analytically, since the early flood season in 2002, the bankfull discharge in the downstream channel increased by 1700$m^3$/s-4300$m^3$/s after the clear water scouring caused by long time sediment detention by the reservoir and 19 times of water-sediment regulation, and the minimum bankfull discharge had increased to about 4200$m^3$/s from 1800$m^3$/s before the flood season in 2002. Thus, the downstream main channel's abilities of transporting sediment and draining off flood were improved significantly.

**Table 7.** Changes of downstream channel bankfull discharge before the flood season from 2002 to 2016.

| Items | Huayuankou | Jiahetan | Gaocun | Sunkou | Aishan | Luokou | Lijin | Minimum |
|---|---|---|---|---|---|---|---|---|
| **2002** | 3600 | 2900 | 1800 | 2070 | 2530 | 2900 | 3000 | 1800 |
| **2016** | 7200 | 6800 | 6100 | 4350 | 4250 | 4600 | 4650 | 4200 |
| **Accumulative Increase** | 3600 | 3900 | 4300 | 2280 | 1720 | 1700 | 1650 | 2400 |

Unit: $m^3$/s

## 5 CONCLUSIONS

From October 1999 when the reservoir was put into operation to April 2016, the amount of sedimentation in Xiaolangdi Reservoir reaches 3.086 billion $m^3$, in which the main stream deposits 2.499 billion $m^3$ and tributaries deposit 587 million $m^3$, respectively. In the downstream channel of the Yellow River, 2.734 billion tons of sediment are scoured accumulatively in reaches above Lijin, in which 2.017 billion tons of sediment are scoured in reaches above Gaocun and 717 million tons of sediment are scoured in reaches from Gaocun to Lijin. Through sediment detention by the reservoir and water and sediment regulation, the minimum bankfull discharge of the main channel in the lower reaches of the Yellow River has increased to about 4200$m^3$/s from 1800$m^3$/s before the flood season in 2002. The situation for flood control is getting better.

Water and sediment regulation tests for three times and operations for sixteen times have been implemented at Xiaolangdi Reservoir from 2002. During the period of water and sediment regulation, water entering into the downstream channel is 71.401 billion $m^3$ and sediment is 655 million tons in total. Water and sediment regulation realizes the scouring along the entire main channel downstream and the total sediment entering into the sea is 976 million tons at Lijin Station, and 409 million tons of sediment are scoured in the downstream channel.

Before the construction of Xiaolangdi Reservoir, the lower Yellow River channel deposits seriously and the downstream embankment withstands great threat of flood. After the construction of the reservoir, the lower river channel is continuously scoured, 2000$m^3$/s water level at the same discharge decreases by 1.53m ~ 2.77m, greatly reducing the flood control pressure of downstream area.

The adjustment of reservoir sedimentation forms can be achieved by reservoir water–sediment joint operation, which enhances the flexibility of the sediment regulation of Xiaolangdi Reservoir.

Although a variety of researches and explorations have been conducted on operation modes of Xiaolangdi Reservoir in recent years, researches on operation mode of Xiaolangdi Reservoir need to sum up experience in practice and be constantly optimized because of the importance of Xiaolangdi Project and the complexity of sediment problems of the Yellow River, the constantly changing water and sediment conditions of the Yellow River, boundary conditions, economic and social conditions and the continuous improvement of human understanding of natural laws.

## ACKNOWLEDGEMENTS

The study is financially supported by the National Key R&D Program of China (2016YFC0402503).

## REFERENCES

Jian, F., Cuihua, A. & Zhanwei, W. (2011). Effect Analysis of 2000-2006 Operation of Xiaolangdi Reservoir. *Yellow River,* 33(9), 11-13.

Jianguo, C., Wenhao, Z. & Gaohu, S. (2016). Studies on Operation Scheme and Water Sediment Regulation of Xiaolangdi Reservoir. *Journal of Sediment Research,* 4, 1-8.

Jixiang, L. (2008). *The Plan & Design Series of Xiaolangdi Reservoir- Study and Practice on Modes of the Reservoir Operation.* China Water & Power Press, the Yellow River Water Conservancy Press.

Junhua, Z., Tao, L. & Huaibao, M. (2016). Proceeding on Water and Sediment Regulation in Xiaolangdi Reservoir. *Journal of Sediment Research,* 2, 68-75.

Shujun, Liu. (2012). Discussion of Recent Optimal Operation of Xiaolangdi Reservoir. *Yellow River,* 34(10), 23-25.

 

# THE EFFECT OF PATCH SIZE ON GRAIN-SCALE ROUGHNESS PARAMETERIZATION IN FLUVIAL ENVIRONMENTS

JANE GROOM [(1)], STEPHANE BERTIN [(2)] & HEIDE FRIEDRICH [(3)]

[(1,2,3)] Department of Civil and Environmental Engineering, University of Auckland, Auckland, New Zealand
jgro800@aucklanduni.ac.nz

## ABSTRACT

Several disciplines use the term roughness with little clarity. Although there is a general consensus that surface roughness is synonymous of the topography (or structure) of a surface. In fluvial environments, roughness is important due to the interactions between sediment, flow and ecology. River roughness is affected by the surface morphology, composition and structure, acting at different scales superimposed onto one another. There can also be confusion between the term roughness and flow resistance. It is important to differentiate between the two terms and ensure roughness is used as an input parameter for flow resistance equations, rather than a synonymous term. We use the term grain-scale roughness to describe the microtopography of a surface, therefore representing the topography as a result of individual grains. Detailed measurements of the surface were gathered through the collection of digital elevation models (DEMs) of patch-scale fluvial surfaces both in the laboratory and the field, obtained using stereo-photogrammetry. Moving-window detrending applied to the DEMs allowed isolating grain-scale roughness from the underlying larger-scale bedforms. Grain-scale roughness of the gravel patches was derived from the detrended DEMs using a series of surface metrics including skewness, kurtosis, standard deviation, inclination index (degree of imbrication) and roughness lengths obtained from second-order structure functions. These metrics (or roughness parameters) each represent different attributes of the surface. The data presented highlights the spatial variability of grain-roughness parameters at the patch-scale, indicating for a true representation of roughness, an adequate patch size for the surface must be obtained. Due to surface complexity, it can be concluded that a single roughness parameter cannot adequately describe roughness across a surface, even at the patch-scale. Developments to roughness parameterization are still required, however a more defined use of the term is available in the patch-scale fluvial application.

**Keywords:** Roughness; parameterization; scales; microtopography; fluvial.

## 1 INTRODUCTION

Roughness is a term used in the literature throughout a variety of disciplines, however questions have been raised over the issue of whether we know the true meaning of roughness (Morvan et al., 2008; Lane, 2005). The importance of considering surface roughness is frequently stated, alongside ways of measuring and quantifying roughness. Yet, often research uses the term roughness with no clear definition within the context. Although previous authors have suggested there is a need to re-evaluate the meaning of roughness, recent reviews have stated this has not occurred (Lane, 2005; Powell, 2014). Therefore, it seems there is a call for a review in order to take a step back and define the term, rather than focusing on the progression of research in the application of surface roughness.

### 1.1 Defining the roughness term

Roughness is discussed in disciplines ranging from engineering to medicinal applications. For example, research has shown that surface roughness has an influence on the interaction between light beams hitting a surface, the electrical performance of a semiconductor device and a biological cell (Amaral et al. 2002; Lonardo et al. 2002). Biomedical research into surface roughness found a correlation between the surface roughness of cells and the RNA production, suggesting cell morphology and cell processes are sensitive to the microtopography of the cell (Martin et al., 1995). Although not defined outright, the authors indicate that surface roughness relates to the texture of the cell and use the term microtopography as a synonym for surface roughness (Martin et al., 1995). An increase in surface roughness has been found to increase the adhesive strength of ice, in the context of snow removal from road surfaces (Perez et al., 2015). Therefore, roughness is related to the topography of the surface, and is a physical property of the surface of interest. The performance of ships in the water is also related to surface roughness, as increased friction can result from changes to the surface topography, such as corrosion or paint cracking (Amaral et al., 2012). Finally, surface roughness plays an important role in the replacement of bones or joints in the human body. Surface topography of implants or joint replacements influence the life-span and resistance, which is important due to the expense of joint or bone replacements (Lonardo et al., 2002).

 

Throughout different disciplines, authors have identified issues with quantifying roughness, as it is argued that surfaces are complex, which cannot be measured by a single parameter and roughness values are dependent on the scale of measurement (Lonardo et al., 1996; Amaral et al., 2012). These issues are present across disciplines, including Earth sciences and fluvial research (Smith 2014).

In Earth sciences, roughness has been used to represent a surface property, property of flow or in calibration models; however the differences between these applications are infrequently distinguished (Smith, 2014). Areas of Earth sciences which consider surface roughness include, but are not limited to: glaciers, flooding, catchment processes, tectonic activity, aeolian processes, meteorology and ecosystems. A recent review aimed to increase the clarity of the definition of roughness, and throughout the review the applied definition of roughness was the vertical range of sampled elevations and the variability or irregularity of this; thereby surface roughness is a parameter of topography (Smith, 2014).

### 1.2 Roughness in fluvial environments

Roughness is an important aspect within a fluvial system due to its influence on flow properties (including velocity and turbulence), sediment transport and local ecology (Aberle and Nikora, 2006; Hodge et al., 2009; Baewert et al., 2014; Curran and Waters, 2014). Estimations of roughness are important inputs for hydraulic and morphological models, along with models to determine the flow resistance within a channel (Tuijnder and Ribberink, 2012; Aberle and Smart, 2003). There are multiple scales of roughness which result from individual grains (grain-scale roughness) and larger bedform features, such as pebble clusters, which result in bedform roughness (Figure 1); together contributing to the overall surface roughness of the river bed (Smart et al., 2004; Mao et al., 2011; Aberle et al., 2010; Tuijnder and Ribberink, 2012). Dependent on the scale of measurement, the roughness taken into consideration can vary (Morvan et al., 2008; Lane, 2005).

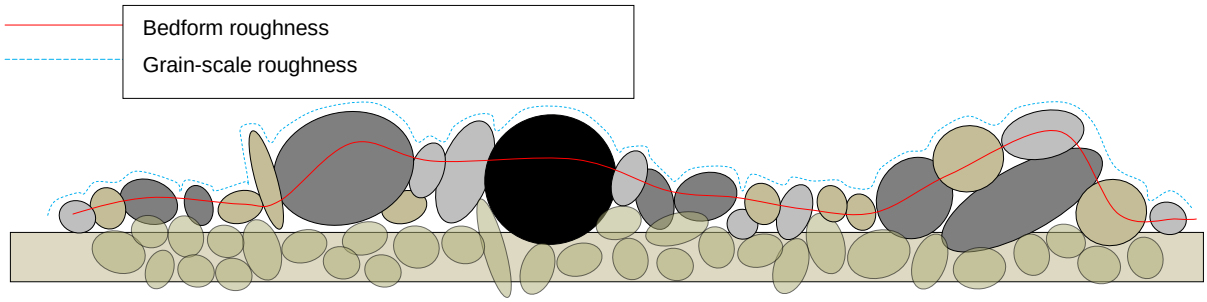


**Figure 1.** Schematic of the differences between grain-scale roughness (microtopography); resulting from individual grains, shown by the blue dashed line and the bedform roughness shown by the red line; reflecting larger scale humps and hollows (bed undulations) in the surface armor layer.

Generally in fluvial research, grain-scale roughness is used inter-changeably with bed microtopography (Smith, 2014). Recently there has been a move away from using the grain-size distribution of the surface sediment to the use of standard deviation of bed elevations to represent surface roughness. This is possible due to research using a random field of bed elevation approach, resulting in high-resolution 3D digital elevation models (DEMs) of the fluvial surface the size of a sediment patch (Mao et al., 2011; Bertin and Friedrich, 2014). Statistical analysis of patch-scale DEMs includes calculating probability distribution functions (including parameters, such as the standard deviation of elevations, skewness and kurtosis) and second-order structure functions. These surface metrics can provide indications of roughness resulting from larger form-scale features such as pebble clusters and can provide an indication of changes in roughness resulting from coarsening of the bed during the armoring process (Bertin and Friedrich, 2014; Qin and Ng, 2012; Coleman et al., 2011).

Several studies have found a linear relationship between certain percentiles of grain size ($D_{50}$, $D_{84}$, $D_{90}$) and the standard deviation of elevations from DEMs (Aberle and Nikora, 2006; Curran and Waters, 2014; Smart et al., 2004; Hodge et al., 2009). However, it should be noted that standard deviation, and therefore roughness, is not only affected by grain size, resulting in no unique relationship between the two; due to variations in packing, burial and imbrication of particles (Mao et al., 2011; Hodge et al., 2009; Powell, 2014). Some research argues that due to the relationship between the two, grain size is still an adequate measure of roughness (Schneider et al., 2015), although most research will now use standard deviation of elevation as an effective roughness parameter (Aberle et al., 2010; Baewert et al., 2014; Aberle and Smart, 2003). However, it is argued that using a single parameter to represent roughness will not be a holistic representation of the overall roughness of the bed, and is likely to underestimate the true roughness (Schneider et al., 2015; Morvan et al., 2008; Powell, 2014).

 

Following clarification of the roughness terminology, and adopting the definition of roughness equating to the microtopography of the surface; this study investigates the effect of patch size (in other words measurement size) on grain-scale roughness parameters obtained during analysis.

## 2 METHODOLOGY

### 2.1 Generating Digital Elevation Models (DEMs)

The microtopography of multiple gravel-bed patches, from both the field and the laboratory are represented by DEMs. Three field patches were collected from the Whakatiwai River in August 2014; which is a small gravel-bed stream in New Zealand. This data is presented in Bertin and Friedrich (2016), and here makes up the surfaces labeled FIELD_1 – FIELD_3, with numbers increasing with distance upstream. Patches were taken on different gravel bars, which differed in sediment size and the structure of the surface. Patches chosen were located on the water edge at the bar head, to ensure water-working and providing consistency in the measurements taken.

Surfaces formed in the laboratory were armored beds resulting from a flow rate of 84L/s (mean flow velocity = 0.82 m/s, shear velocity = 0.077 m/s and uniform water depth = 0.225 m), until the sediment transport rate dropped below 1% of the initial transport rate, when under the condition of sediment starvation. Experimental surfaces formed in a 19 m long, 0.45 m wide and 0.5 m deep non-recirculating flume, set to a slope of 0.5%. Differing bimodal sediment mixtures were used, ranging in size from 0.7 mm to 35 mm. The first sediment mixture contained 85% gravel and 15% sand, compared to 91% gravel and 9% sand in the second sediment mixture. Three DEMs for each sediment size are presented, making a total of six laboratory DEMs (labeled SED1_T1-3 and SED2_T1-3).

A pair of consumable Nikon D5100s (16.4 Mpixel, 23.6 x 15.6 $mm^2$ sensor size) with Nikkor 20 mm lenses were vertically installed in stereo above the gravel patch of interest. Two overlapping images, or stereo photographs, are used to produce DEMs through the following method. Firstly, calibration was completed using the method of Zhang (2000), whereby several stereo photographs of a chequerboard are taken, and using Bouguet (2010)'s calibration toolbox in Matlab®, intrinsic (i.e. camera) and extrinsic (i.e. setup) calibration parameters are obtained. Images are then accurately rectified (with a maximum error < 1 pixel) using the calibration data, whereby corresponding pixels between overlapping images are ideally on a same scanline. Stereo-matching is completed using Gimel'farb (2002)'s symmetric dynamic programming stereo (SDPS) algorithm, which produces point cloud data and ortho-images. Point clouds were interpolated onto regular grids with a 1 mm spacing, which reduces bias from non-uniform data when calculating surface metrics such as the standard deviation of elevations (Hodge et al. 2009a). Outliers were identified using the mean elevation difference parameter and replaced using bi-cubic spline interpolation (Hodge et al. 2009a), before DEMs were normalized to have a mean bed level of zero and rotated to align in the flow direction; which for the field data was determined by eye based on observations of the channel and grain imbrication (Laronne and Carson, 1976; Millane et al., 2006; Bertin and Friedrich, 2016).

Finally, prior to the calculation of surface metrics, a moving-window detrending strategy (Smart et al., 2002; Hodge et al., 2009) was applied to all DEMs. This removed large-scale distortions in the surface, which included those larger than the cluster size; such as hollows and bumps. Following the method of Smart et al. (2002), the trend surface was estimated over a grid with point spacing 1.25 × $D_{90A}$ (where $D_{90A}$ is the $D_{90}$ of the surface material), with the elevation of grid points measured by averaging DEM data points within a circle of diameter 2.5 × $D_{90A}$ centered on the grid point, and removed from the measured DEMs before analysis. This way, data analysis could focus on the grain topography and the properties determined from the detrended DEMs were linked to grain-scale roughness.

### 2.2. Measuring the surface grain size

In order to compare the topographic information derived from DEMs with sediment size, the intermediate (b-) axis of grains was determined for each patch. Here $D_{50A}$ is used to represent the median grain size of the armor surface, for which 50% is smaller by weight; as the armored surface differs from the bulk mixture of the bed. Single, vertical images, containing over 400 detectable grains, were used in the image-analysis tool Basegrain®, whereby automatic grain separation and Fehr (1987)'s line-sampling method are applied for analysis (Detert and Weitbrecht, 2012). Grain sieving was completed on the sediment mixtures from the laboratory in order to determine particle shape, specific gravity and the sediment grading curves.

### 2.3 Calculating surface metrics for grain-roughness parameterization

A total of six surface metrics were calculated in order to assess the effect of DEM size on grain-roughness parameters. Using a moving-window analysis technique, the size of the moving window is indicative of DEM size. Surface metrics were calculated for square windows moving across detrended DEMs, for different window sizes. A large overlap (up to 95%) between moving windows ensured robust statistics even at large window sizes. All window sizes were made proportional to the surface $D_{50A}$ (i.e. calculations

 

were made within windows proportional to the population median grain size determined over the whole DEM). Due to the nature of the DEMs being rectangular in shape, square moving windows were chosen to calculate roughness parameters; in contrast to the circular moving windows used by Scown et al. (2015). The maximum window size for analysis varied between 12 x $D_{50A}$ (i.e. a window size of 12 times the surface $D_{50}$ along both x and y directions) and 26 x $D_{50A}$ due to the differences in DEM areas and bed structure (e.g. sediment size). For clarity, a single value for DEM size normalized by $D_{50A}$ will be used herein, reflecting the dimensions of the DEM in both the x and y directions.

The surface metrics calculated from DEMs are the standard deviation $\sigma_Z$, Skewness $S_K$, Kurtosis $K_u$, horizontal roughness lengths in both streamwise and cross-stream directions ($L_x$ and $L_y$), and the inclination index in the flow direction *I0.* Surface metrics including $\sigma_Z$, $S_K$ and $K_u$ (Eq. 1) are determined from probability distribution functions (PDFs) and have been used in several studies as characteristics of bed roughness (Aberle and Nikora, 2006; Scown et al. 2015). The roughness parameter most used in flow resistance equations is $\sigma_Z$, as it represents the vertical roughness length of a surface (Aberle and Smart, 2003; Noss and Lorke, 2016). The degree of water-working can be gathered from the $S_K$ (degree of asymmetry of PDF), where positive values suggest a water-worked surface whereby fine grains have filled surface depressions, and therefore have reduced the magnitudes of surface deviations below the mean (Aberle and Nikora, 2006). Finally, $K_u$ measures the regularity of the bed, whereby a large kurtosis value (heavy tails and narrow peak distribution) is a result of variance from irregular, extreme deviations. Lower kurtosis values are a result of deviations from the mean occurring frequently; indicating a uniform and compact distribution of the surface (Coleman et al. 2011).

$$\sigma_Z{}^2=\frac{1}{N'}\sum_{i=1}^{N'}(z_i-\langle z_i\rangle)^2$$

$$S_K=\frac{1}{N'\sigma_Z{}^3}\sum_{i=1}^{N'}(z_i-\langle z_i\rangle)^3$$

$$K_u=\left[\frac{1}{N'\sigma_Z{}^4}\sum_{i=1}^{N'}(z_i-\langle z_i\rangle)^4\right]-3 \qquad [1]$$

where, z represents the bed elevation at location (x, y) in a DEM, N' is the total number of DEM points and < > represents the mean value.

Horizontal roughness lengths in both the streamwise and the cross-stream direction ($L_x$ and $L_y$, respectively) are scaling characteristics of a surface and are calculated from second-order structure functions (Eq. 2 & Figure 2):

$$D_{G2}(\Delta x,\Delta y)=\frac{1}{(N-n)(M-m)}\sum_{i=0}^{N-n}\sum_{j=0}^{M-m}\{\left|z(x_i+n\delta x,y_j+m\delta y)-z(x_i,y_j)\right|\}^2 \qquad [2]$$

where, $\Delta x = n\delta x$ and $\Delta y = m\delta y$; $\delta x$ and $\delta y$ are the sampling intervals (i.e. DEM resolution) in the longitudinal and transverse directions respectively; $n$=1,2,3,…$N$ and $m$=1,2,3,…$M$. $N$ and $M$ are the number of DEM points in the same two directions.

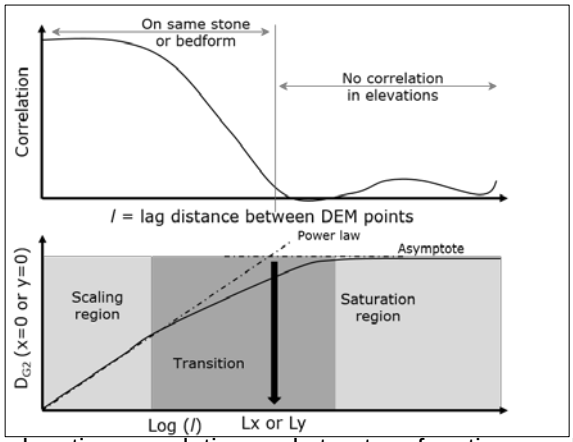


**Figure 2.** Typical gravel-bed elevation correlation and structure function graph for different spatial lags, used to determine horizontal roughness lengths $L_x$ and $L_y$. Adapted from Smart et al. (2002).

Structure functions are used to measure changes in elevation correlations at different spatial lags and in different directions (Figure 2). Here (because of detrending), small values are indicative of areas of similar elevations; suggesting DEM points are on the same grain, whilst larger values suggest surface elevations are no longer correlated and therefore are not of the same grain. Structure functions for gravel-beds have three regions (Figure 2); a scaling region with uniform slope at small lags, a saturation region at large lags, where the slope is zero, with a transition region in between, where the slope decreases (Nikora et al., 1998; Hodge et al., 2009). The scaling region of structure functions provides the horizontal roughness lengths from the slope breakpoint (Figure 2), located at the intersection between the tangent to the scaling region slope and the saturation level asymptote, in both x and y directions (Nikora et al., 1998). The maximum spatial lags for calculating grain-roughness lengths were chosen to be half the window size in both directions.

The inclination index *I0* in the flow direction is calculated using Eq. 3 (Smart et al., 2004). The inclination index is the difference between the fraction of positive and negative inclinations of particles, divided by the total number of positive, negative and zero inclinations at a given lag distance, equal to the resolution of the DEM. Positive slopes are counted as elevation increases with the downstream direction.

$$I0 = \frac{n_+ - n_-}{Ns} \qquad [3]$$

where, $n_+$ and $n_-$ are the number of positive and negative slopes between successive DEM points, respectively, and Ns is the total number of slopes.

Unreliable slope values of below 0.01 were not counted in the numerator of Eq.3 (Millane et al., 2006). Positive inclination index values reflect a predominance of positive slopes in the flow direction, which is the sign of particle imbrication (Laronne and Carson, 1976; Millane et al., 2006). Parameterizing grain imbrication in this manner is informative of the flow direction forming the bed surface; providing insights into both the bed stability and flows that created the surface.

Finally, the variability of the surface was quantified using the coefficient of variation (CV), which is calculated as the standard deviation of the grain-roughness property determined over all moving windows, divided by the mean, and expressed as a percentage. This was completed on all six surface metrics, providing the values were positive; therefore it could not be completed for all DEM sizes considered (particularly the case $S_k$ and *I0).* Furthermore, the error in $\sigma_z$ is calculated in order to quantify surface variability. This was completed by calculating the relative difference between each moving-window $\sigma_z$ and the population $\sigma_z$, averaged over all moving windows of the same size, and expressed as a percentage.

## 3 RESULTS

Roughness parameters for nine DEMs were plotted as boxplots (except for CV, which was plotted as a line graph) in order to visualize the variability in statistics for changing DEM size, using the moving-window analysis technique. Figure 3 presents an example of these boxplots for SED1_T1; which is a laboratory DEM. Plateaus in statistics were observable when the median values stabilized and variability of roughness statistics (e.g. boxplot whiskers) remain similar across increases to DEM size. These plateaus were confirmed statistically with 95% confidence intervals and a paired t-test. As can be seen in Figure 3, and observed across all DEMs studied, an increase in DEM size (and therefore patch size) results in a decrease in the variance of roughness statistics generated across the surface; suggesting at these sizes the patch size is adequate to obtain a representative roughness statistic of the bed surface. At small DEM sizes, the variability is large and therefore statistics obtained from DEMs of this size would be non-representative of the surface topography. Figure 3 shows for this laboratory DEM (SED1_T1) variability plateaus at 14 x $D_{50A}$ for all roughness parameters, with $\sigma_z$ appearing to have the largest variability at the larger DEM sizes.

Plateaus in statistics were observed in the majority of the DEMs, for multiple roughness parameters. These are summarized in Table I below. Generally, for field DEMs, once the DEM size exceeds 16-18 x $D_{50A}$ the roughness statistics are deemed to provide a representative indication of surface roughness, with little effect of inherent surface variability. These plateaus appeared slightly earlier in laboratory DEMs, with plateaus between 14-16 x $D_{50A}$. It is worth noting that not all roughness parameters displayed evidence of a threshold, from both field and laboratory settings (indicated in Table I by a dash [-]). Noticeably, FIELD_2 evidenced plateaus at lower DEM sizes of 10 x $D_{50A}$.

 

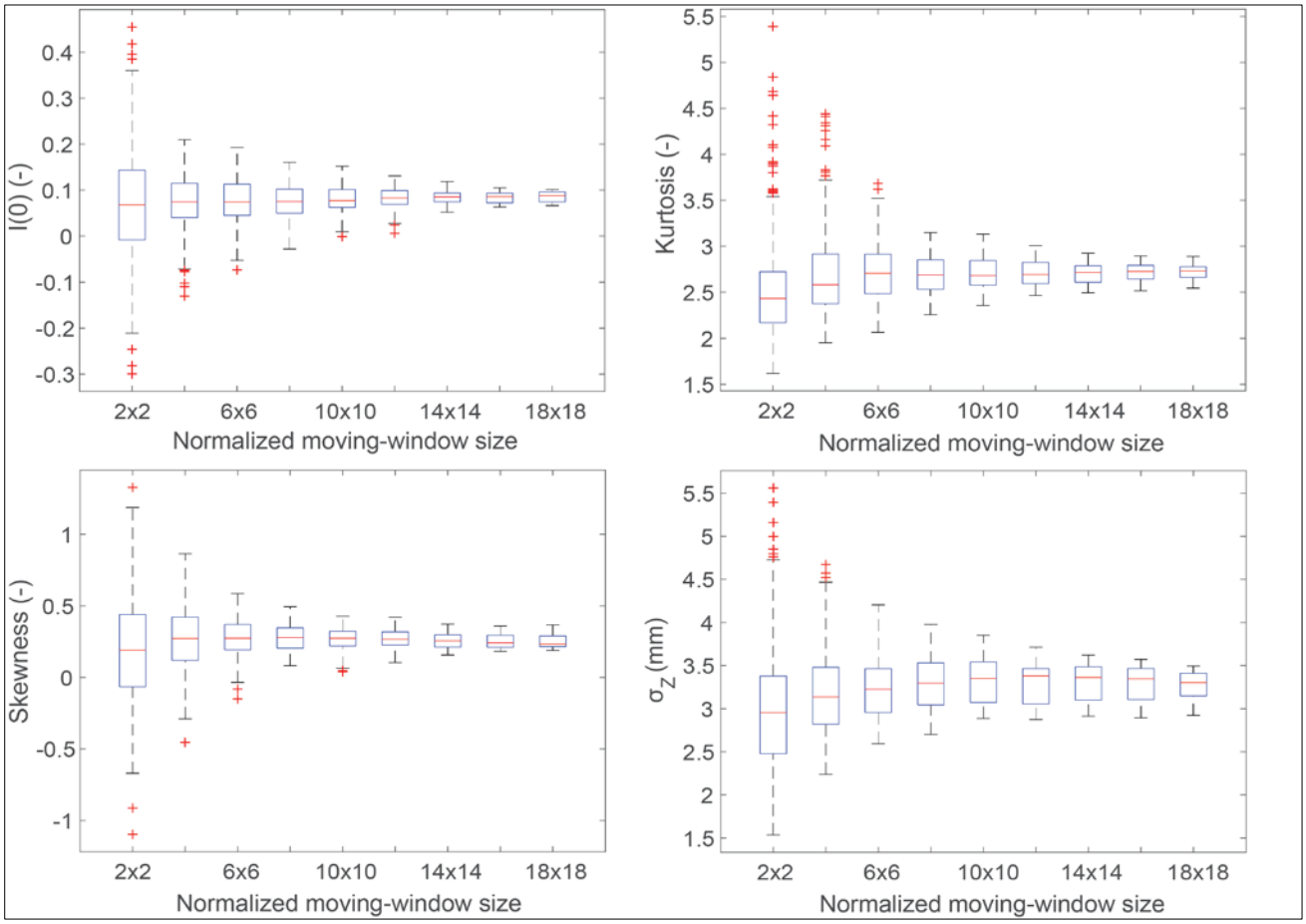


**Figure 3.** Boxplots of roughness statistics for SED1_T1 laboratory DEM, calculated at different moving-window sizes normalized in both directions by $D_{50A}$; showing plateaus in statistics with an increase in DEM size (e.g. at 14 x $D_{50A}$).

**Table I:** Summary table showing plateau values, representing the minimum DEM size (normalized by $D_{50A}$ in both x and y directions) to consider for grain-roughness properties representative of the surface, whereby the mean of the roughness parameter stabilizes and variability is minimum for all nine DEMs studied; from both laboratory and field. The second column provides the $D_{50A}$ value (in mm) for reference.

| DEM name | Location | $D_{50A}$ (mm) | CV | I0 | Ku | Sk | $\sigma_z$ |
|---|---|---|---|---|---|---|---|
| FIELD_1 | Field | 18.7 | 18 | 14 | 18 | 16 | 20 |
| FIELD_2 | Field | 47.2 | - | 10 | 10 | 10 | - |
| FIELD_3 | Field | 19.4 | 18 | 12 | 18 | 16 | 18 |
| SED1_T1 | Lab | 18.0 | 14 | 14 | 14 | 14 | 14 |
| SED1_T2 | Lab | 19.0 | 14 | 12 | - | 14 | 14 |
| SED1_T3 | Lab | 18.5 | 12 | 14 | 16 | 16 | 14 |
| SED2_T1 | Lab | 19.5 | - | 12 | 14 | - | 14 |
| SED2_T2 | Lab | 17.5 | 12 | 10 | 16 | 16 | 14 |
| SED2_T3 | Lab | 18.5 | 16 | 14 | 16 | 16 | - |

The error in $\sigma_z$ for each window size was plotted for each DEM to present the effect of DEM size on all data studied in this paper. Figure 4 presents the error for all nine DEMS over a range of DEM sizes normalized by $D_{50A}$. At smaller DEM sizes, the error in $\sigma_z$ is high for all DEMs (> 15%), with field data displaying the highest values (between 25% and 35%). There is a wider spread in the variability of error values across all DEMs at smaller DEM sizes, however as DEM size increases, the error values decrease (namely below 10% at 14 x $D_{50A}$) and the variability of error values reduces. Note that Figure 4 is restricted to 18 x $D_{50A}$, as following this DEM size, only a few data points are available (e.g. for FIELD_1 and FIELD_3). Further note that for 14 – 18 x $D_{50A}$ there is one less data point, due to FIELD_2 being limited to a size of 12 x $D_{50A}$.

 

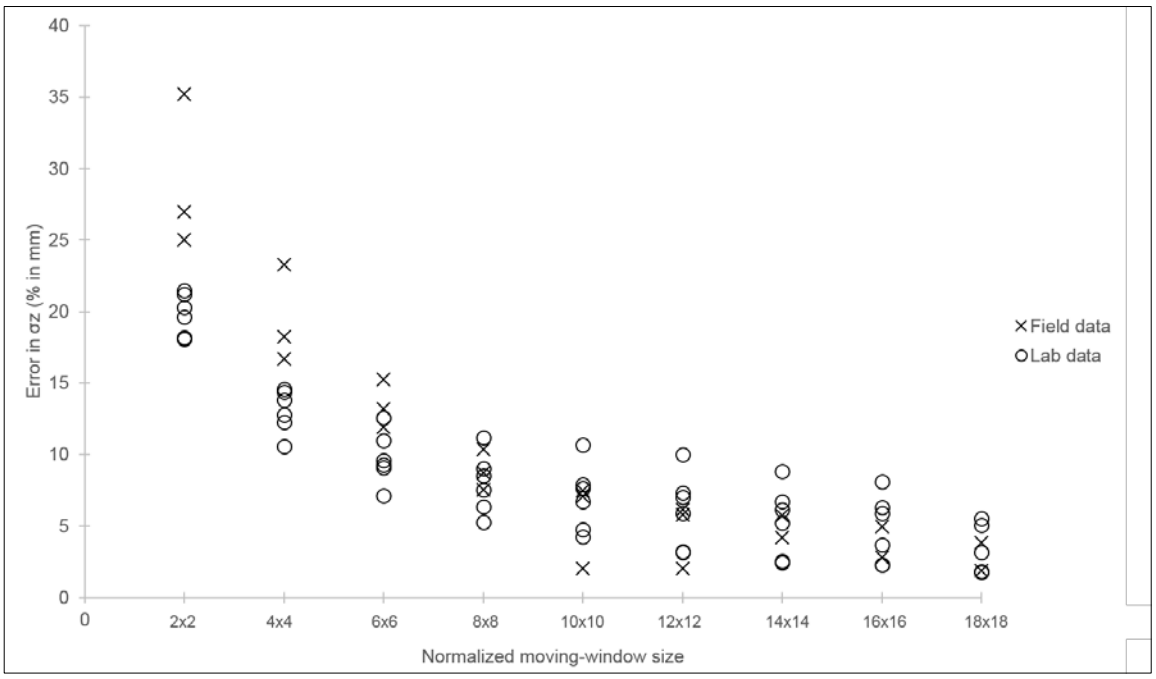


**Figure 4.** Scatter plot of all nine DEMs showing the error in $\sigma_z$ (expressed as a percentage) calculated at different moving-window sizes normalized in both directions by $D_{50A}$. Circular markers represent laboratory data, compared to markers with a cross which are the field data. The presentation of data is limited to 18 x $D_{50A}$, as only a few DEMs provide data exceeding this size. Note there are only two field data points from 14 x $D_{50A}$, due to FIELD_2 only reaching 12 x $D_{50A}$.

## 4 DISCUSSION

Decreases in the variability of statistics were not only seen visually in boxplots (as in Figure 3), but there was a distinct decrease in CV with increases in DEM size. These findings are similar to a study which found an increase sampling density (and therefore spatial coverage) of measurements into bed shear stress and roughness lengths of a gravel-bed channel, were associated with a reduction in CV (Cienciala and Hassan, 2016). In contrast to this, a larger-scale floodplain investigation found an increase in CV with DEM size (Scown et al., 2015), likely due to the difference in scale of analysis in comparison to this study. It is therefore important to consider the scale of roughness under investigation; as mentioned previously, the incorporation of bedform roughness would be non-representative of grain-scale roughness or the microtopography of the surface. This study used a detrending method which aimed at removing the influence of bedform-scale roughness of the surfaces in order to gain solely grain-roughness properties. Isolating the different scales of roughness through a suitable detrending strategy is a key analytical decision which should be dependent on the required application.

Variability in roughness parameters does not completely reduce (Figure 4), as gravel-bed surfaces are non-uniform in nature. Differences in packing, burial, sorting, shape and size of sediment account for a lack of uniformity and contribute to the variability in topography seen across DEM surfaces (Graham et al., 2010). Often, individual roughness parameters display differing degrees of variability (Figure 3); therefore suggesting some parameters are more sensitive to surface variability in comparison to others. This would suggest using a single roughness parameter is inadequate to holistically represent the surface roughness of gravel-beds in fluvial environments.

Plateaus in statistics were taken to be when the median values stabilize and variability remains consistent with further increases to DEM size. Statistical confirmation of these plateaus were completed through 95% confidence intervals, which has previously been used to assess spatial variability in data sample size (Cienciala and Hassan 2016), and a paired t-test to assess for significant differences in the mean values of each DEM size. Both statistical methods were used, as variability could fluctuate whilst median values remained stable and visual observations from boxplots (as in Figure 3) considered both of these factors before a plateau was determined. Some roughness parameters did not display plateaus in statistics; likely due to the surface displaying high spatial variability and/or the maximum DEM size was inadequate to gain a representative statistic.

Differences in the plateaus between field and laboratory DEMs result from differences in the complexity of these surfaces. Whilst laboratory DEMs are reasonably uniform in nature (therefore less variability and lower plateaus), field surfaces were found to have more poorly sorted sediment (Bertin and Friedrich 2016), resulting in increased surface variability. In Table I, some of the field DEMs displayed plateaus at a smaller DEM size in comparison to the other DEMs. In particular this is the case for FIELD_2; likely due to the surface

 

having a larger $D_{50A}$ (of 47 mm in comparison to ~ 20 – 25 mm) than other field DEMS. Previous investigations using this data identified a high number of imbricated grains, poorly sorted sediment and high $\sigma_z$ values (Bertin & Friedrich 2016), highlighting differences between this patch and the other field data.

It can be gathered from Table I, that for both laboratory and field, DEMs would require a DEM with dimensions exceeding 16 x $D_{50A}$ in both directions in order to provide representative roughness statistics. Although, it is important to note that the DEM size will be dependent on the scale of investigation for the application and also on the surface composition and morphology. Making the thresholds dimensionless by $D_{50A}$ allow for easy comparison between surfaces and reduces the effects of differing grain sizes of each surface. However, although the work is dimensionless by $D_{50A}$, differences in microtopography may be as a result of other influences such as sediment shape, sorting and structural arrangement (Smart et al., 2002; Powell, 2014). Therefore surfaces with similar $D_{50A}$ may provide different roughness properties; evidencing why using roughness parameters based on the topography of a surface is superior to using a simple grain size characteristic, as previously undertaken.

Figure 4 reinforces evidence of requiring an adequate DEM size for representative statistics; due to a reduction in error in $\sigma_z$ with increases in DEM size. The error in $\sigma_z$ reduces for all DEMs studied to below 10% from 14 x $D_{50A}$ size. Following this DEM size, further increases in DEM size have a slight reduction in error in $\sigma_z$, however this is not as significant as increases from the small DEM sizes of 2 x $D_{50A}$ for example. Therefore this would suggest there is a plateau across all DEMs for grain-scale roughness statistics becoming representative and with as small error values as possible.

The recommended DEM size in this study would appear lower than the value of 21 x $D_{50}$ suggested as an appropriate patch size in previous literature (Ockelford and Haynes, 2013). Likely this is resulting from the sediment in this study being from the armor layer ($D_{50A}$), in comparison to the assumption that Ockelford and Haynes refer to the bulk mixture $D_{50}$ (of 4.8 mm). Clarity in the literature between the $D_{50}$ values obtained from the bulk sediment or armor layer ($D_{50A}$) is needed for universal comparisons. However differences in threshold values between studies highlight the importance of other surface properties such as sediment sorting. Furthermore, differences in these recommendations may result from different analytical methods used; for example this studied removed the effect of bedforms through a moving-window detrending method. Therefore smaller patch sizes may be indicative of the grain-scale roughness, compared to larger patch sizes required for surface incorporating bedform (or larger scale) roughness. Isolating the influence of these scales of roughness is an important consideration for the required application.

## 5 CONCLUSIONS

Firstly, clarification of the term roughness is presented, whereby the term grain-scale roughness is synonymous with the microtopography of a surface; resulting from individual grains. Larger scale roughness (such as bedform roughness) results from the clustering of particles and forming bed undulations across the surface. It is important to remove these larger scale roughness trends to obtain reflective grain-scale roughness.

There is a clear influence of patch size (e.g. DEM size) on the grain-scale roughness parameters obtained during analysis, with high variability in results using smaller patch sizes. This high variability is also reflected in larger error in $\sigma_z$ at smaller DEM sizes, with reductions in values as DEM size increases. In order to produce representative grain-scale roughness parameters, a DEM size of > 14 x $D_{50A}$ (in both directions) should be used, in both the laboratory and field; albeit larger patch sizes (16 – 18 x $D_{50A}$) are required for field surfaces. Differences between the patch size required in the laboratory and the field is likely due to differences in surface structure and composition (and therefore complexities) between the two environments. Therefore, adequately isolating different scales of roughness (e.g. through a sufficient detrending method) is essential to obtain representative grain-roughness values.

Finally, the variability expressed across surfaces highlights spatial variability in the microtopography; therefore using a single roughness parameter (such as the previously used $\sigma_z$) is not sufficient, and in order to holistically represent the surface complexity and grain-roughness, a combination of parameters, as used in this paper are required. Analysis was undertaken on data from both the laboratory and field environments with the similarities between the effect of patch size in both presented; therefore these trends observed can be generalized over multiple gravel patches in differing environments.

## ACKNOWLEDGEMENTS

The study was partly funded by the Marsden Fund (Grant No. UOA1412), administered by the Royal Society of New Zealand.

## REFERENCES

Aberle, J. & Nikora, V. (2006). Statistical Properties of Armored Gravel Bed Surfaces. *Water Resources Research,* 42, 1-11.

Aberle, J. & Smart, G. (2003). The Influence of Roughness Structure on Flow Resistance on Steep Slopes. *Journal Of Hydraulic Research,* 41(3), 259-269.

Aberle, J., Nikora, V., Henning, M., Ettmer, B. & Hentschel, B. (2010) Statistical Characterization of Bed Roughness Due to Bed Forms: A Field Study in the Elbe River at Aken, Germany. *Water Resources Research,* 46, 1-11.

Amaral, R., Chong, L.H. & Selvaduray, G. (2012). Surface Roughness. *San Jose State University, Http://Www.Sjsu.Edu/Faculty/Selvaduray/Page/Papers/Mate210/Surface.Pdf*

Baewert, H., Bimböse, M., Bryk, A., Rascher, E., Schmidt, K. & Morche, D. (2014). Roughness Determination of Coarse Grained Alpine River Bed Surfaces using Terrestrial Laser Scanning Data. *Zeitschrift Für Geomorphologie, Supplementary Issues,* 58(1), 81-95.

Bertin, S. & Friedrich, H. (2014). Measurement of Gravel-Bed Topography: Evaluation Study Applying Statistical Roughness Analysis. *Journal of Hydraulic Engineering,* 140(3), 269-279.

Bertin, S. & Friedrich, H. (2016). Field Application of Close-Range Digital Photogrammetry (CRDP) for Grain-Scale Fluvial Morphology Studies. *Earth Surface Processes and Landforms*, 41(10), pp.1358-1369.

Cienciala, P. & Hassan, M.A. (2016). Sampling Variability in Estimates of Flow Characteristics in Coarse-Bed Channels: Effects of Sample Size. *Water Resources Research*, 52, 1899-1922.

Coleman, S.E., Nikora, V.I. & Aberle, J. (2011). Interpretation of Alluvial Beds Through Bed-Elevation Distribution Moments. *Water Resources Research,* 47(11), 1-14.

Curran, J.C. & Waters, K.A. (2014). The Importance of Bed Sediment Sand Content for the Structure of a Static Armor Layer in a Gravel Bed River. *Journal of Geophysical Research: Earth Surface,* 119(7), 1484-1497.

Gimel'farb, G. (2002). Probabilistic Regularisation and Symmetry in Binocular Dynamic Programming Stereo. *Pattern Recognition Letters,* 23(4), 431-442.

Graham, D.J., Rollet, A., Piégay, H. & Rice, S.P. (2010). *Maximizing the Accuracy of Image-Based Surface Sediment Sampling Techniques.* Water Resources Research, 46, W02508.

Hodge, R., Brasington, J. & Richards, K. (2009). Analysing Laser-Scanned Digital Terrain Models of Gravel Bed Surfaces: Linking Morphology to Sediment Transport Processes and Hydraulics. *Sedimentology,* 56(7), 2024-2043.

Lane, S.N. (2005). Roughness–Time for a Re-Evaluation?. *Earth Surface Processes and Landforms,* 30(2), 251-253.

Laronne, J. & Carson, M. (1976). Interrelationships between Bed Morphology and Bed-Material Transport for a Small, Gravel-Bed Channel. *Sedimentology,* 23(1), 67-85.

Lonardo, P., Lucca, D. & De Chiffre, L. (2002). Emerging Trends in Surface Metrology. *CIRP Annals-Manufacturing Technology,* 51(2), 701-723.

Lonardo, P., Trumpold, H. & De Chiffre, L. (1996). Progress in 3D Surface Microtopography Characterization. *CIRP Annals-Manufacturing Technology,* 45(2), 589-598.

Mao, L., Cooper, J.R. & Frostick, L.E. (2011). Grain Size and Topographical Differences between Static and Mobile Armour Layers. *Earth Surface Processes and Landforms,* 36(10), 1321-1334.

Martin, J., Schwartz, Z., Hummert, T., Schraub, D., Simpson, J., Lankford, J., Dean, D., Cochran, D. & Boyan, B. (1995). Effect of Titanium Surface Roughness on Proliferation, Differentiation, and Protein Synthesis of Human Osteoblast-Like Cells (MG63). *Journal of Biomedical Materials Research,* 29(3), 389-401.

Millane, R., Weir, M. & Smart, G. (2006). Automated Analysis of Imbrication and Flow Direction in Alluvial Sediments using Laser-Scan Data. *Journal of Sedimentary Research,* 76(8), 1049-1055.

Morvan, H., Knight, D., Wright, N., Tang, X. & Crossley, A. (2008). The Concept of Roughness in Fluvial Hydraulics and its Formulation in 1D, 2D and 3D Numerical Simulation Models. *Journal of Hydraulic Research,* 46(2), 191-208.

Nikora, V.I., Goring, D.G. & Biggs, B.J. (1998). On Gravel-Bed Roughness Characterization. *Water Resources Research,* 34(3), 517-527.

Noss, C. & Lorke, A. (2016). Roughness, Resistance, and Dispersion: Relationships in Small Streams. *Water Resources Research,* 52(4), 2802-2821.

Ockelford, A. & Haynes, H. (2013). The Impact of Stress History on Bed Structure. *Earth Surface Processes and Landforms,* 38(7), 717-727.

Perez, A.P., Wåhlin, J. & Klein-Paste, A. (2015). Effect of Surface Roughness and Chemistry on Ice Bonding to Asphalt Aggregates. *Cold Regions Science and Technology,* 120, 108-114.

Powell, D.M. (2014). Flow Resistance in Gravel-Bed Rivers: Progress in Research. *Earth-Science Reviews,* 136, 301-338.

Qin, J. & Ng, S. (2012). Estimation of Effective Roughness for Water-Worked Gravel Surfaces. *Journal of Hydraulic Engineering,* 138(11), 923-934.

Schneider, J.M., Rickenmann, D., Turowski, J.M. & Kirchner, J.W. (2015). Self-Adjustment of Stream Bed Roughness and Flow Velocity in A Steep Mountain Channel. *Water Resources Research,* 51(10), 7838-7859.

 

Scown, M.W., Thoms, M.C. & De Jager, N.R. (2015). Measuring Floodplain Spatial Patterns using Continuous Surface Metrics at Multiple Scales. *Geomorphology* 245, 87-101.

Smart, G., Aberle, J., Duncan, M. & Walsh, J. (2004). Measurement and Analysis of Alluvial Bed Roughness. *Journal of Hydraulic Research,* 42(3), 227-237.

Smart, G.M., Duncan, M.J. & Walsh, J.M. (2002). Relatively Rough Flow Resistance Equations. *Journal of Hydraulic Engineering,* 128(6), 568-578.

Smith, M.W. (2014). Roughness in the Earth Sciences. *Earth-Science Reviews,* 136, 202-225.

Tuijnder, A.P. & Ribberink, J.S. (2012). Experimental Observation and Modelling of Roughness Variation Due to Supply-Limited Sediment Transport in Uni-Directional Flow. *Journal of Hydraulic Research,* 50(5), 506-520.

Zhang, Z. (2000). A Flexible New Technique for Camera Calibration. *IEEE Transactions on Pattern Analysis and Machine Intelligence,* 22(11), 1330-1334.

 

# RESEARCH ON SYNERGISTIC EVOLUTION BETWEEN THE RIVER CHANNEL AND FLOODPLAIN IN THE LOWER YELLOW RIVER

QIUSHI LUO [(1)], MOXI WU[(2)], ZHANWEI WAN[(3)] &YU QIAN[(4)]

[(1,3,4)] Yellow River Engineering Consulting Co., Ltd., Zhengzhou, China
18655093@qq.com.cn;9321264@qq.com.cn;qianyu@yrec.cn
[(2)] North China University of Water Resources and Electric Power, Zhengzhou, China
1556411654@qq.com.cn

## ABSTRACT

The Lower Yellow River is a typical compound channel in the upper reach with 5-12km in width and 0.6-1.0km wide. It is also a sandy river with 35kg/$m^3$ multi-years averaged sediment concentration. The deposition and erosion in the Lower Yellow River and the bankfull discharge were analyzed based on the measured data of runoff and sediment. The index system was put forward, in which the riverbed erosion and deposition amount in the main channel and floodplain, the bankfull discharge are included. The action of the runoff and sediment on the synergy evolution between the main channel and floodplain in the Lower Yellow River was studied and a relationship model was built to forecast the erosion and deposition amount and bankfull discharge in the Lower Yellow River. Besides, the Lower Yellow River and estuary coupling simulation mathematical model was improved from the erosion/deposition section area division and the bankfull discharge estimation and the model validation was carried out using data from 1982 to 2012.Three different scenarios were designed, and for different scenarios the amount of multi-years averaged sediment into Yellow River of the future 50 years are designed as 8.0×108t, 6.0×108t and 3.0×108t.The synergy evolution between the main channel and floodplain in the Lower Yellow River was simulated by the model built here. The result shows that the multi-years averaged deposition amount in the Lower Yellow River are 1.6×108t, 1.0×108t and 0.01×108t for different scenarios. The minimum bankfull discharge will be reduced to 2900 $m^3$/s~3100 $m^3$/s for the 8.0×108t Case and the 6.0×108t Case, and for 3.0×108t Case, the minimum bankfull discharge can maintain at about 4000 $m^3$ /s.

**Keywords:** Lower Yellow River; synergistic evolution; compound channel; siltation and scouring; bankfull discharge.

## 1 OVERVIEW

The Lower Yellow River flows into the Huanghuaihai Plain from the mountainous area in Mengjin, Henan and then flows into the Bohai Sea in Kenli County, Shandong with the full length 878 km. The Lower Yellow River is a typical wide and shallow compound channel. The reach from Baihe, Mengjin to Taochengpu, Yanggu is 464 km long, and the distances between dikes on the both sides are mostly above 5 km with the widest 24km. The river channel is about 0.8～1.0km wide and two tributaries Yiluo River and Qin River flow into it. For the reaches below Taochengpu, the distances between dikes on the both sides are generally 1～2km with the normal channel width 0.6～0.8km. The width of floodplain between dikes on the both sides in the Lower Yellow River is much larger than the general river. There are 1.9 million people and 3.4 million multi cultivated land on the floodplain. Therefore, the floodplain is not only an important part of the river channel for flood detention and sediment silting, but also the homeland of the people living in it. The profile of the Lower Yellow River is shown in Figure 1.

The Lower Yellow River is a typical wide and shallow compound channel under the joint action of complex water-sediment conditions and human activities. Especially since the 1970s, due to the coordinate relationship of the water and sediment flowing into the Lower Yellow River and the obstruction of human activities on the water and sediment exchange between the channel and floodplains, the sediment deposition in the main river has been aggravated and the bankfull water levels in many sections have been 2-3m higher than the floodplain surface which was 4-6 m higher than the back river ground, showing the secondary suspended river situation of “high channel, low floodplain and low-lying bottom of the embankment”, which is a serious threat to problems. For example, Liu JiXiang, et al. studied the siltation or scouring characteristics of overbank or non-overbank flood with different sediment concentrations in the Lower Yellow River and the siltation and scouring relations between the upper wide river channels and lower narrow river channels (Liu et al, 2000; Liu et al, 2003; Liang, 2012). The researchers also analyzed the effect of water-sediment relationship on the channel evolution from different aspects and studied respectively the water-sediment regulation and the formation of normal channel, the change of water and sediment conditions and riverbed adjustment, lower river channel’s sediment transporting capacity and river type evolution, etc (Hu et al, 2008; Cao et al, 2004; Shen et al, 2008; Chen et al, 2013). Shao (2012) studied the dynamic process of erosion and deposition of

 

channel and floodplain in the Lower Wei River and its mechanism, and put forward the deposition or scouring amount in the floodplain was correlated most to the year's sediment load in the flood season, and the deposition or scouring amount in the channel was correlated most to the year's runoff in the flood season.

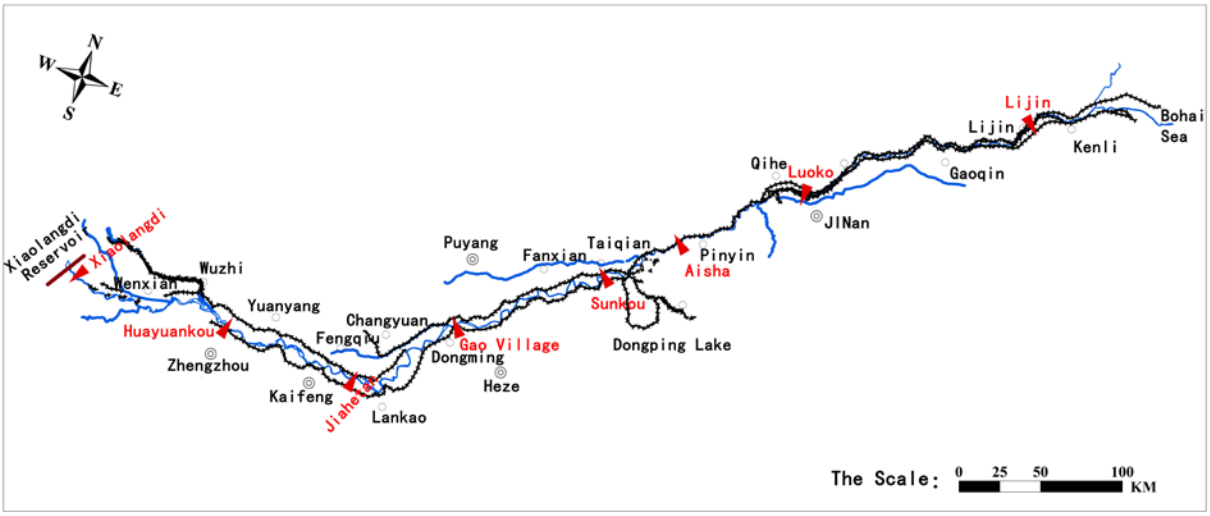


**Figure 1**. Profile of the Lower Yellow River.

The evolution of floodplain and channel in the Lower Yellow River is jointly affected by such factors as the complicated water and sediment relations, the riverbed boundary conditions, the estuary evolution and human activities (Shao et al, 2012; Zhao et al, 2013). Previously, especially since 2000, the water and sediment flowing into the Lower Yellow River have changed greatly, which may have significant impact on the evolution of the river. Under the background of the changed water and sediment conditions, the synergy evolution between the main channel and floodplain in the Lower Yellow River should be studied and the mathematical model should be improved to make scientific predictions of the deposition amount and bankfull discharge in the Lower Yellow River. The work here can not only deepen the comprehension of complex river channel evolution law, but also guide the river channel management of the Yellow River, which is of important scientific value and practical significance.

## 2 CHARACTERISTICS OF WATER-SEDIMENT VARIATION AND RIVER SEDIMENTATION

### 2.1 Characteristics of water-sediment variation

Combined with the operation of the reservoirs in the upper Yellow River and the conditions of water and sediment in the downstream, measured data of Sanmenxia (Xiaolangdi), Heishiguan and Wuzhi are employed to analyze the characteristics of water and sediment into the Lower Yellow River, as shown in Table 1.

**Table 1**. Characteristics of Water and Sediment into the Lower Yellow River (Sanmenxia (Xiaolangdi), Heishiguan and Wuzhi).

| Years | Water ($10^8$ $m^3$) | | | Sediment ($10^8$t) | | | Sediment concentration (kg/$m^3$) | | |
|---|---|---|---|---|---|---|---|---|---|
| | 7~10 | 11~6 | 7~6 | 7~10 | 11~6 | 7~6 | 7~10 | 11~6 | 7~6 |
| 1919.7～1950.6 | 290.5 | 184.1 | 474.6 | 13.26 | 2.63 | 15.89 | 45.65 | 14.27 | 33.48 |
| 1950.7～1968.6 | 297.6 | 207.3 | 504.9 | 12.16 | 2.81 | 14.97 | 40.85 | 13.57 | 29.65 |
| 1968.7～1986.6 | 199.5 | 181.9 | 381.4 | 11.87 | 1.86 | 13.72 | 59.48 | 10.20 | 35.98 |
| 1986.7～2000.6 | 128.9 | 146.1 | 275.0 | 7.31 | 0.40 | 7.71 | 56.69 | 2.77 | 28.04 |
| 2000.7～2012.6 | 85.1 | 159.2 | 244.3 | 0.56 | 0.04 | 0.60 | 6.58 | 0.28 | 2.48 |
| 1919.7～2012.6 | 230.2 | 178.3 | 408.6 | 10.17 | 1.68 | 11.85 | 44.19 | 9.40 | 29.00 |

(a)The measured water and sediment into the Lower Yellow River have characteristics of the insufficient water, excessive sediment and unharmonious of the two. The annual average water into the lower river channel from 1950 to 2012 was 408.6 ×108$m^3$, the annual average sediment was 11.85 ×108t and the average sediment concentration was 29.00kg/$m^3$.

(b)Annual average water and sediment into the Lower Yellow River channel in different periods descended and the descending trend was more obvious after 2000. From 1968 to 1986, 1986 to 2000 and 2000 to 2012, the annual average water into the lower river channel was 381.4×108m$^3$, 275.0×108m$^3$ and 244.3×108m$^3$ and the annual average sediment was 13.72×108t, 7.71×108t and 0.60×108t, respectively. The annual average water into the lower river channel was 19.6%, 42.1% and 48.5% less than 1919-1959 and the annual average sediment was 13.6%, 51.5% and 96.2% less than 1919-1958 with more decreasing percentages than water.

(c)Water allocation have changed during the year. The proportion of water in the flood season decreased. Water in the flood season accounted for 61.2% from 1919 to 1959. After the joint operation of Longyangxia and Liujiaxia Reservoir, water in the flood season accounted for 46.9% and 34.8%, respectively from 1986 to 2000 and from 2000 to 2012.

(d)Proportion of sediment transported in the flood season increased. The proportion (sediment transported in the flood season to the sediment of the whole year) was 83.5% in the flood season from 1919 to 1959. After the joint operation of Longyangxia and Liujiaxia Reservoir, the proportion increased to 94.2% and 92.7%, respectively from 1986 to 2000 and 2000 to 2012.

2.2 Characteristics of river sedimentation and bankfull discharge

As an alluvial channel, the Lower Yellow River has the sediment transport features of “more sediment incoming, more sediment transport and more sediment deposition, and vice versa”. Water and sediment conditions are important factors affecting the evolution of river erosion and deposition. During the natural period before Sanmenxia Reservoir was constructed, there was large water and sediment at average annually into the lower channel with annual average water 475.4×108m$^3$ and sediment 17.9×108t, and the annual amount of sediment deposition was 3.76×108t in the lower river channel. After the operation of Sanmenxia Reservoir, due to the water storage and silt detention, sediment into the lower river channel decreased and scouring occurred in the Lower Yellow River. The annual average sediment scoured was 5.78 ×108t and the bankfull discharge in the lower river channel increased from 6000m$^3$/s to the maximum 7500m$^3$/s. Since the end of the sediment detention period in 1964, the lower river channel was silted up again. From 1964 to 1986, the annual average water into the lower river channel was 422.2×108m$^3$ and sediment is 10.7×108 t. Average 2.22×108t of sediment was silted in the lower river channel annually. During the period of 1964-1973, due to the large sediment release of Sanmenxia Reservoir, the lower river channel was silted again and the bankfull discharge decreased to 3350m$^3$/s. From 1980 to 1985, water was abundant, so the bankfull discharge returned to the maximum of 6800 m$^3$/s. From 1986 to the operation of Xiaolangdi Reservoir, the annual average water into the lower river was 273.0×108m$^3$ and sediment was 7.80×108t with siltation 2.28×108t in the river channel. The proportion of the annual average siltation to the total incoming sediment increased from 20%to about 30% in the natural period. Due to decreasing water, sediment was mainly silted in the main channel, resulting in river channel shrinkage. In 1999, the bankfull discharge was only 2300 m$^3$/s at the minimum. After the operation of Xiaolangdi Reservoir, the annual average sediment into the lower river channel was only 0.71×108t and the lower river channel was scoured continuously again. In October, 2013, 1.73×108t of sediment was scoured annually in the lower river channel and the bankfull discharge increased gradually from less than 1800 m$^3$/s (2002) to about 4000 m$^3$/s which is still maintained. The measured water and sediment and river channel scouring amount of the Lower Yellow River in different periods are shown in Table 2, and bankfull discharge changes are demonstrated in Figure 2.

**Table 2**. Statistics of sedimentation of the Lower Yellow River in Different Periods.

| Periods | Annual Water and Sediment Characteristics | | Annual Scouring ($10^8$ m$^3$t) | Minimum Bankfull Discharge (m$^3$/s) | Estuarine Extension (km) |
|---|---|---|---|---|---|
| | Annual Water ($10^8$m$^3$) | Annual Sediment ($10^8$t) | | | |
| 1950.07～1960.08 | 475.4 | 17.9 | 3.76 | — | 7（1953-1960） |
| 1960.09～1964.10 | 572.6 | 5.93 | -5.78 | 6000～7500 | 7 |
| 1964.11～1986.10 | 422.2 | 10.7 | 2.22 | 3350～6800 | 12（1964-1976）<br>29（1976-1987） |
| 1986.11～1999.10 | 273.0 | 7.8 | 2.28 | 2300～5000 | 9（1987-1996）<br>7（1996-1999） |
| 1999.11～2013.10 | 259.9 | 0.71 | -1.73 | 1800～4100 | 4 |

 

## 3 RESPONSIVE RELATIONSHIP BETWEEN WATER-SEDIMENT VARIATION AND SEDIMENTATION

### 3.1 Responsive relationship between water-sediment variation and sedimentation amount

The siltation and scouring of the Lower Yellow River channel is affected by many factors like water and sediment conditions, riverbed boundary and estuarine siltation and scouring. To analyze the responsive relationship between river channel siltation and scouring and water-sediment change, measured data from 1960 to 2010 are used to establish the relationship between the annual average sedimentation amount and the annual average sediment coefficient (ratio of annual average sediment concentration to annual average discharge) and the relationship between the annual average sedimentation amount and the sediment concentration of the Lower Yellow River. And the results show that the annual average sedimentation amount of the Lower Yellow River channel has a good correlation with the annual average sediment coefficient and the sedimentation amount increases with the annual average sediment coefficient. Second-order polynomial is used to fit the relationship and the formula of river channel siltation and scouring with annual sediment coefficient as the leading factor is obtained:

$$\Delta W_s = 182.44\xi_y^2 + 99.36\xi_y - 5.68 \qquad [1]$$

Where: $\Delta W_s$ denotes the amount of siltation or scouring; $\xi_y$ denotes the annual average sediment coefficient. Formula [1] is used to calculate the lower river channel siltation and scouring from 1960 to 2010, as shown in Figure2. It can be seen that the amount of siltation and scouring calculated with Formula [1] coincides quite well with the actually measured value.

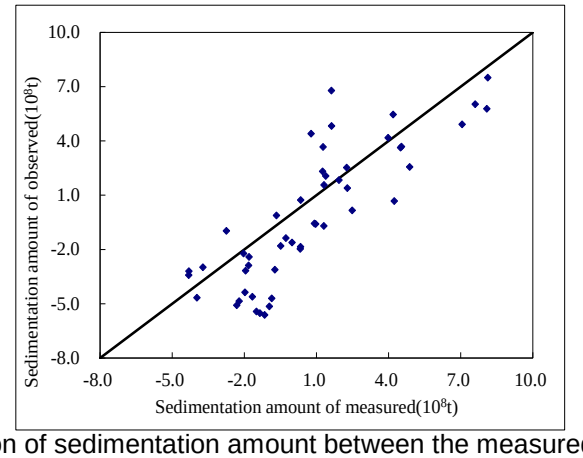


**Figure 2**. Comparison of sedimentation amount between the measured and the calculated.

### 3.2 Responsive relationship between water-sediment variation and bankfull discharge

The existent researches show that the bankfull discharge of the Lower Yellow River changes with the water inflow of Huayuankou. The larger water volume of HuaYuanKou, the more power full the bed-forming capacity will be, and the channel with larger bankfull discharge will be formed (JianGuo Chen et al, 2006).In addition to the year's water inflow and water in the flood season, bankfull discharge changes are also affected by the previous water inflow, the year's flood process and other factors. To study the influence of the previous water inflow on the minimum bankfull discharge of the lower Yellow River, the moving averaged values of the annual average water volume in consecutive two, three, four and five years and the minimum bankfull discharge of the lower river channel are plotted and analyzed, and the results show that the moving averaged value of the lower river channel's annual averaged water in consecutive three years is closely correlated to the minimum bankfull discharge of the lower river channel. Second-order polynomial is further adopted to fit their relationship:

$$\overline{Q} = -0.0113W_{ay}^2 + 18.472W_{ay}^2 - 709.87 \qquad [2]$$

Considering the bankfull discharge changes are not only affected by the annual water volume, but also supposed to be affected by the annual sediment amount. A dimensionless correction coefficient of sediment is introduced into Formula [2]to take into account of the sediment

 

$$\overline{Q_c} = (\frac{S}{\overline{S}})^{\alpha}\overline{Q} \qquad [3]$$

Where: α is a constant. The least square method is used to fit and α=-0.082 is obtained. Formulas [2] and [3] are used to calculate the bankfull discharge, as shown in Figure 3. It can be seen that the bankfull discharge calculated with formula [3] is in better agreement with the measured value.

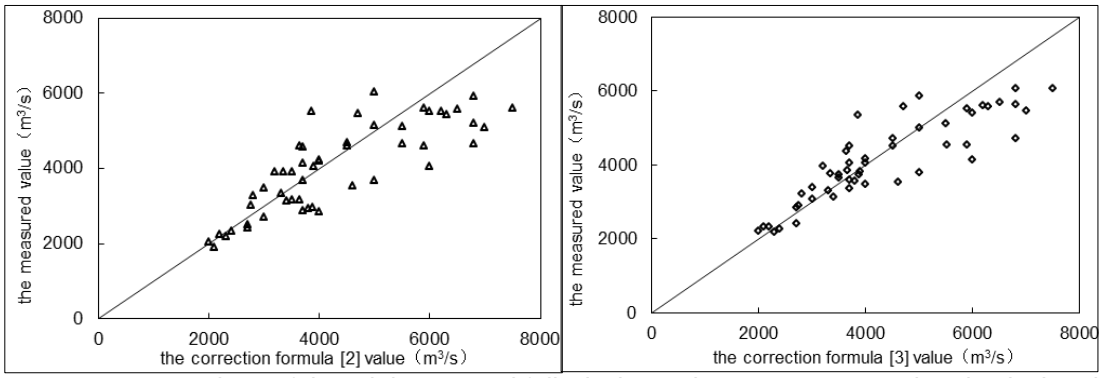


**FIgure3**. Comparison of the Minimum Bankfull Discharge between measured and calculated.

## 4 COUPLING MODEL OF THE LOWER YELLOW RIVER CHANNEL AND ESTUARINE

### 4.1 Mathematical model

(a) Governing Equations of Flow

The governing equations of one-dimensional unsteady flow area follows:

Continuity Equation:

$$B\frac{\partial z}{\partial t} + \frac{\partial Q}{\partial x} = q_l \qquad [4]$$

Momentum equation:

$$\frac{\partial Q}{\partial t} + 2\frac{Q}{A}\frac{\partial Q}{\partial x} - \frac{BQ^2}{A^2}\frac{\partial z}{\partial x} - \frac{Q^2}{A^2}\frac{\partial A}{\partial x}\Big|_z = -gA\frac{\partial z}{\partial x} - \frac{gn^2|Q|Q}{A(A/B)^{4/3}} \qquad [5]$$

where x denotes the coordinates along the flow direction; t denotes the time; Q denotes the discharge; z denotes the water level; A denotes the wetted cross-section area; B denotes the river width; is the quantity of lateral flow into (out of) the river per unit time and unit river length; n is the coefficient of roughness; denotes the acceleration of gravity.

(b)Non-Equilibrium Sediment Transportation Equation of Suspended Load

Suspended load sediment is divided into M groups and $S_k$ denotes the sediment concentration of Group k. The non-equilibrium sediment transportation equation of suspended load sediment is:

$$\frac{\partial(AS_k)}{\partial t} + \frac{\partial(QS_k)}{\partial x} = -\alpha\omega_k B(S_k - S_{*k}) + q_{ls} \qquad [6]$$

In which $\alpha$ is the coefficient of sedimentation; $\omega_k$ denotes the settling velocity of the sediment grain in Group k; $S_{*k}$ denotes the sediment carrying capacity of sediment in Group k; $q_{ls}$ is the quantity of sediment into (out of) the river per unit time and unit river length.

(c)Equation of Riverbed Deformation

Equation of Riverbed Deformation:

 

$$\gamma' \frac{\partial A}{\partial t} = \sum_{k=1}^{M} \alpha \omega_k B\left(S_k - S_{*k}\right) \qquad [7]$$

where $\gamma'$ denotes the dry density of the bed material.

(d)Boundary Condition. The upstream boundary condition is given the flow and sediment concentration process and the downstream boundary condition is set as the water level process.

4.2 Treatment of related Problems

(a)Distribution of cross-section siltation and scouring area

At present, only empirical methods can be adopted for the distribution of cross-section siltation and scouring area. In the numerous empirical methods, distribution along the wetted perimeter is a method easy to be accepted and relatively conforming to reality. Based on this method, this study modifies the method for distribution of siltation and scouring area according to the scouring features of the Lower Yellow River channel.

i. When the deposition appears, deposits are distributed along the wetted perimeter with equal thickness. Considering the large flood in the Lower Yellow River usually deposit in the floodplain and scour in the main channel, if the cross-section discharge is larger than 1.5 times of the bankfull discharge, the deposits are distributed along the floodplain surface with equal thickness.

ii. When scouring happens, if the cross-section discharge is lower than the bankfull discharge, the erosion quantity is distributed with equal depth along the wetted perimeter; when the cross-section discharge is larger than the bankfull discharge, the erosion quantity is distributed with equal depth in the river channel and there is no erosion quantity on the floodplain.

(b) Bankfull discharge estimate

Manning Formula and Floodplain Siltation and Scouring Quantity are used to estimate the bankfull discharge. The bankfull discharge is estimated according to Manning Formula:

$$\overline{Q}_{pt}^{1} = AC\sqrt{RJ} = \frac{1}{n_c^1} B_c^1 \left(H_c^1\right)^{2/3} \sqrt{J_c^1} \qquad [8]$$

- where $\overline{Q}_{pt}^{1}$ denotes the present bankfull discharge;
- $n_c^1$ is the present river channel's roughness coefficient;
- $B_c^1$ denotes the corresponding river width of the present bankfull water level;
- $H_c^1$ denotes the corresponding water depth of the present bankfull water level;
- $J_c^1$ is the corresponding water surface gradient of the bankfull discharge.

4.3 Numerical computation method

The finite volume method is used to discretize the one-dimensional model equations and SIMPLE algorithm based on the staggered grid is adopted to handle the coupling relationship of the discharge and water level. The discrete equations are composed of the water flow movement equation, water level correction equation and sediment transport equation, all of which are solved by using Gauss Iteration.

4.4 Model verification

Topographic Data: measured cross section data of reaches of the Lower Yellow River from Tiexie to Estuary in 1976; there were 104 measured cross sections from Tiexie to Qing-7 in the Lower Yellow River in 1976 and the average distance between cross sections was about 8.3 km.

Hydrologic data: measured water and sediment data at Xiaolangdistation and water and sediment diversion along the Lower Yellow River from 1976 to 2010 are used to verify the computation. From July, 1976 to June, 1999, water into the Lower Yellow River was $343.55\times10^8$ m$^3$ and sediment was $9.35\times10^8$ t; from July, 1999 to June, 2000, water into the Lower Yellow River was $231.1\times10^8$ m$^3$ and sediment was $0.93\times10^8$ t.

The amount of deposition added up to $1.684\times10^8$ t in reaches above Lijin in the Lower Yellow River from 1976 to 2010, including $35.96\times10^8$ t from 1976 to 1999 with the annual sediment silted $1.56\times10^8$ t. From 2000 when Xiaolangdi Reservoir was put into use to 2010, about $19.12\times10^8$ t of sediment was scoured in reaches above Lijin with the annual average scouring $1.74\times10^8$ t. Table 3 shows the comparisons of the amount of erosion and deposition between the calculated values and the measured. Table 3 shows that the calculated results with the mathematical model in different period are in good agreement with the measured results and

 

the errors between the two is less than 20%, indicating that the mathematical model can accurately reflect the changes of sediment deposition and scouring in the studied river reach.

**Table 3**. Results of Model Verification.

| Period | Measured Value ($10^8$t) | Calculated Value ($10^8$t) | Error ($10^8$t) |
|---|---|---|---|
| 1976.10~1999.10 | 35.96 | 36.07 | 0.11 |
| 1999.10~2010.6 | -19.12 | -18.85 | 0.27 |
| 1976.10~2010.6 | 16.84 | 17.22 | 0.38 |

## 5 EVOLUTION AND FLOOD CONTROL SITUATION IN THE FUTURE

### 5.1 Water and Sediment Conditions in the Future

In view of studies on the Loess Plateau erosion background values in historical periods, analysis of water-sediment changes and causes in recent years, sediment reduction effect and characteristics of the water conservancy and soil conservation measures and the incoming sediment load in the continuous low water and sand period from 1922 to 1932, the futuristic sediment load of the Yellow River is considered to be $3.0\times10^8$t, $6.0\times10^8$t and $8.0\times10^8$t. Considering when Guxian and Xiaolangdi Reservoirs went into the normal operation after the sediment trapping period ,the water and sediment conditions into the Lower Yellow River of different water-sediment scenario plans were calculated by the joint operation model of Guxian, Sanmenxia and Xiaolangdi Reservoir, and the results are shown in Table 4.

### 5.2 Scouring and deposition in the Lower Yellow River and the Estuarine

Table 4 and Figure 4 show the quantities of the river channel siltation and scouring in different future incoming sediment scenario plans calculated by using riverbed boundary conditions before the flood in 2012. For the scenario plan with $3.0\times10^8$t of sediment into the Yellow River, the annual average water and sediment into the Lower Yellow River are 248 $.0\times10^8$m$^3$ and $3.21\times10^8$t, respectively. In the next 50 years, the erosion and deposition of the Lower Yellow river will in a state of approximate equilibrium. For the scenario plan with 6 $.0\times10^8$t of sediment into the Yellow River, the annual average water and sediment into the Lower Yellow River are 263 $.0\times10^8$m$^3$ and $6.06\times10^8$t, respectively. The Lower Yellow River channel will be silted cumulatively. In the coming 50 years, the average annual quantity of siltation will be $1.0\times10^8$t according to the mathematical model and $0.84\times10^8$t according to the calculation in Formula [1]. For the scenario planwith$8.0\times10^8$t of sediment into the Yellow River, the annual average water and sediment into the Lower Yellow River are 273 $\times10^8$m$^3$ and $7.70.0\times10^8$t, respectively. The Lower Yellow River channel will be silted cumulatively. In the coming 50 years, the average annual quantity of siltation will be $1.62\times10^8$t according to the mathematical model and $1.78\times10^8$t according to the calculation in Formula [1].

**Table 4**. Water and sediment conditions into the Lower Yellow River.

| Plans | Conditions of Water and Sediment into the Lower Reaches | | | Quantities of the Siltation and Scouring in Reaches above Lijin (hundred million t) | | |
|---|---|---|---|---|---|---|
| | Water ($10^8$m$^3$) | Sediment ($10^8$t) | Sediment Concentration (kg/m$^3$) | Floodplain | Main Channel | total |
| Scenario Plan 1 | 241.36 | 3.47 | 12.9 | 0.05 | -0.03 | 0.01 |
| Scenario Plan 2 | 262.84 | 6.06 | 23.1 | 0.33 | 0.67 | 1.00 |
| Scenario Plan 3 | 272.78 | 7.70 | 28.2 | 0.46 | 1.16 | 1.62 |

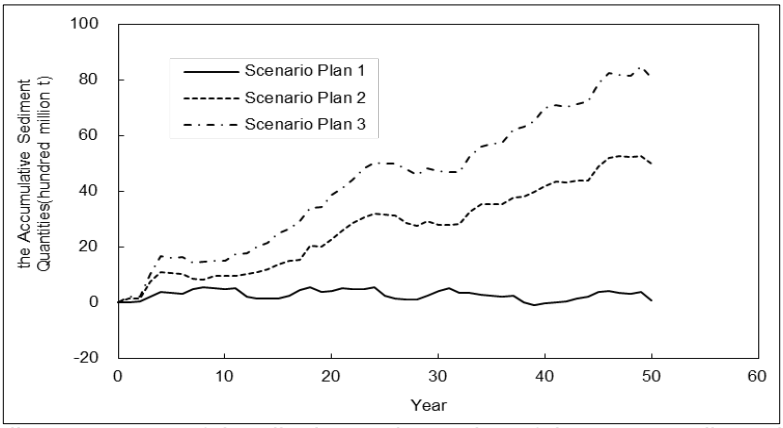


**Figure 4**. Sediment amount of the siltation and scouring of the Lower Yellow River in future.

 

5.3 Minimum bankfull discharge changes

The changes of minimum bankfull discharge of the Lower Yellow River are shown in Figure 5. In the next 50 years, the minimum bankfull discharge of the Lower Yellow River can basically maintain at 4000m3/s or so for the scenario plan of 3.0×108t incoming sediment in the future into the Yellow River. With the channel siltation, the minimum bankfull discharge will decrease to 2900 $m^3$/s and3100$m^3$/s, respectively for the scenarios of 6.0×108t and 8.0×108t of incoming sediment in the future.

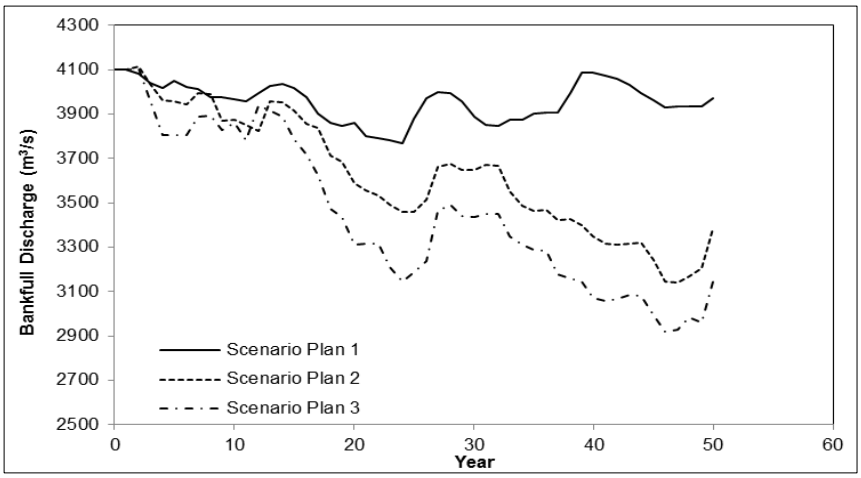


**Figure 5**. Minimum bankfull discharge of the Lower Yellow River in future.

5.4 Changes of water level in the typical cross sections of the lower yellow river

Table 5 shows the changes of water level at the same discharge in the typical cross sections of the lower Yellow River. For 3×108 t sediment incoming of Yellow River (scenario plan 1), the water level of Huayuankou, Gaocun, Aishan and Lijin will not be higher than 0.22 m after 50 years for the slight scouring and silting for the Lower Yellow River and the water level of Xihekou will rise by 0.48-0.60 m because of the estuary siltation extension. For 6×108 t sediment incoming of Yellow River (scenario plan 2), the water level of Huayuankou, Gaocun, Aishan and Lijin will rise by 1.06-1.91mdue to the channel siltation after 50 years and the water level will change the most greatly in Gaocun section. Water level of Xihekou will rise by 0.83-1.04 m because of the estuary siltation and extension. For 8×108 t sediment incoming of Yellow River (scenario plan 3), the water level of Huayuankou, Gaocun, Aishan and Lijin will rise by 1.65-2.81mdue to the channel siltation after 50 years and the water level will change the most greatly in Huayunakou section, followed by Gaocun. Water level of Xihekou will rise by 0.99-1.24m because of the estuary siltation and extension.

**Table 5**. Water Level Changes of the Typical Cross Sections.

| Plans | Discharge ($m^3$/s) | Huayuankou | Gaocun | Aishan | Lijin | Xihekou |
|---|---|---|---|---|---|---|
| Scenario Plan 1 | 4000 | -0.22 | 0.21 | 0.22 | 0.19 | 0.60 |
| | 10000 | -0.17 | 0.17 | 0.18 | 0.15 | 0.48 |
| Scenario Plan 2 | 4000 | 1.31 | 1.90 | 1.72 | 1.56 | 1.03 |
| | 10000 | 1.06 | 1.53 | 1.39 | 1.26 | 0.83 |
| Scenario Plan 3 | 4000 | 2.78 | 2.63 | 2.16 | 2.04 | 1.22 |
| | 10000 | 2.25 | 2.12 | 1.74 | 1.65 | 0.99 |

5.5 Estuary extension and the water level of xihekou

According to the predicted results with the mathematical model, Yellow River Estuary will extend and the water level of Xihekou will rise in the next 50 years. For 3×$10^8$ t sediment incoming of Yellow River, the Yellow River estuary will extend 9.7km and the corresponding water level of Xihekou at 10000$m^3$/s will rise by 0.48m in the next 50 years. For 6×$10^8$ t sediment incoming of Yellow River, the Yellow River estuary will extend14.5km and the corresponding water level of Xihekou at 10000$m^3$/s will rise by 0.83m. For 8×$10^8$ t sediment incoming of Yellow River, the Yellow River estuary will extend16.8km and the corresponding water level of Xihekou at 10000$m^3$/s will rise by 0.99m in the next 50 years.

## 6 CONCLUSIONS

(a)The deposition and erosion in Lower Yellow River and the bankfull discharge were analyzed based on the measured data of runoff and sediment. The action of the runoff and sediment on the synergy evolution

 

between the main channel and floodplain in Lower Yellow River was studied and a relationship model was built to forecast the erosion and deposition amount and bankfull discharge in the Lower Yellow River.

(b)The Lower Yellow River and estuary coupling simulation mathematical model was improved from the erosion/deposition section area division and the bankfull discharge estimation and the model validation was carried out using data from 1982 to 2012. The result shows that the error of sediment erosion and deposition between the measured and the calculated is less than 20%, which indicate that the mathematical model can more accurately reflect and calculate the changes of siltation and scouring in the river channel.

(c)Three different scenarios were designed, and for different scenarios the amount of multi-years averaged sediment into Yellow River of the future 50 years are designed as $8.0\times10^8$t, $6.0\times10^8$t and $3.0\times10^8$t.The synergy evolution between the main channel and floodplain in the Lower Yellow River was simulated by the model built here. The result shows that the multi-years averaged deposition amount in the Lower Yellow River are $1.6\times10^8$t, $1.0\times10^8$t and $0.01\times10^8$t for different scenarios. The minimum bankfull discharge will reduced to 2900 $m^3$/s~3100 $m^3$/s for the $8.0\times10^8$t Case and the $6.0\times10^8$t Case, and for $3.0\times10^8$t Case, the minimum bankfull discharge can maintain at about 4000 $m^3$ /s.

**ACKNOWLEDGEMENTS**

The study was financially supported by the National Key R&D Program of China (2016YFC0402503) and the SpecialScientific Research Fund of MWR Public Welfare Profession of China (Grant No.201401002).

**REFERENCES**

Jixiang, L. & Guoming, G. (2000). Study on Erosion and Deposition Characters of the Lower Yellow River. *Yellow River*, 8, 11-12.

Jixiang, L., Cuihua, A. & Zeng, Q. (2003). Research on the Regulation Discharge of Xiaolangdi Reservoir in the Primary Sediment Impoundment Period. *Yellow River*, 8, 26-27.

Zhiyong, L. (2012). Investigation on the Sedimentation Relation between Upper and Lower Reaches in the Lower Yellow River. *Yellow River*, 34(7), 20-24.

Chunhong, H., Jianguo, C. & Qingchao, G. (2008). Regulation of Water and Sediment Process and Reform of Medium-Size Channel in the Lower Yellow River. *Journal of Tianjin University*, 41(9), 1035-1040.

Wenhong, C. (2004). Relationship between Variation of Sediment Carrying Flows and Readjustment of Riverbed in the Lower Reaches of Yellow River. *Journal of Hydraulic Engineering*, 11, 1-6.

Guanqing, S., Yuanfeng, Z. & Shaojun, Q. (2008). Influence of Flood Wave Type on Sediment Transport in Lower Reaches of Yellow River. *Journal of Hydraulic Engineering*. 39(1), 7-13.

Xujian, C. & Qingyang, C. (2013). Theory of River Pattern Transformation and Change of Channel Sinuosity Ratio in Lower Yellow River. *Journal of Sediment Research*, 1(2), 1-6.

Wenwei, S., Changxing, S. & Xiaoli, F. (2012). Processes and Mechanisms of Sedimentation in Channel and Floodplain in the Lower Weihe River in 1960-1990. *Geographical Research*, 33(10), 1268-1275.

Tianyi, Z. & Tianjiao, C. (2013).Problems Caused by Runoff Decrease in the Lower Yellow River and Countermeasures. *Yellow River*, 35(2), 1-5.

Jianguo, C., Chunhong, H. & Zhandi, D. (2006). Change of Bankfull and Bed-Forming Discharges in the Lower Yellow River. *Journal of Sediment Research*, 10(5), 10-16.

 

# ADVANCES AND PRACTICE OF THE LOWER YELLOW RIVER CHANNELAND FLOODPLAIN TREATMENT RESEARCH

CUIHUA AN[1], SHENGYUN LIU[2], QIUSHI LUO[3] & MOXI WU[4]

[1,2,3] Yellow River Engineering Consulting Co., Ltd., Zhengzhou, China,
anch542@sina.com; hwhlsy@yerc.cn; 18655093@qq.com

[4] North China University of Water Resources and Electric Power, Zhengzhou, China,
1556411654@qq.com

## ABSTRACT

Three important problems about the Lower Yellow River are deeply analyzed. The first is the characteristics of above ground 'secondary suspended river', the second is the 'dual-function' of the floodplain, i.e. the important area for flood release, flood detention, sediment deposition and also the homeland of people living in the floodplain; and the third is the prominent contradiction between floodplain economic and social development and river regulation. The main research and practice of the Lower Yellow River channel and floodplain treatment are reviewed, which include the changing trend of incoming discharge and sediment load of the Lower Yellow River in the future, keeping a broad flood plain with solid embankment or keeping river channel with solid embankment, the existence or abolishment of production levee, the floodplain management mode, the treatment of secondary suspended river, the floodplain safety improvement, river channel reconstruction and so on. The practice and effect of sediment trapping by reservoirs, water and sediment regulation governance of Secondary Suspended River and safety construction of floodplain which were carried out in the Yellow River in recent years were studied. The understanding of governance of the Lower Yellow River channel and floodplain and problems that should be further studied in the next stage is put forward.

**Keywords:** Lower Yellow River; river channel and floodplain; research advance; treatment practice.

## 1 FEATURES OF THE LOWER YELLOW RIVER CHANNEL

### 1.1 Characteristics of the river channel

Main stream of the Yellow River which pours into the Bohai Sea at Kenli County of Shandong Province belongs to the Lower Yellow River from Taohuayu downward (Figure 1). The river channel is 786km long. As the Yellow River has insufficient water coupled with excessive sediment, extreme differences of the two situation give rise to great quantity of sediments being deposited, making the downstream river bed generally 4～6m higher than the ground backing the river, even more than 10m in some reaches. It becomes an above ground suspended river across the North China Plain. Few branches flow into the Lower Yellow River. Branches in plain area are only Tianran Wenyan Channel and Jindi River, a large tributary in hilly area is Wenhe River. Studies on lower river channel and floodplain governance also includes 92km of chanel from Baihe to Taohuayu in general. Distance between dikes and river channel in the lower river channel are wide at the upstream and narrow at the downstream in shape, with a flood discharge capacity being large at the upstream and small at the downstream.


**Figure 1**. Map of Lower Yellow River.

Based on pattern and evolution characteristics of the river channel, the Lower Yellow River channel can be divided into four sections along the flow path:

(a) The first is the river reach from Baihe Town of Mengjin to Gaocun Village of Dongming County, which is 299km long. This reach is a typical braided river channel, with broad floodplain and frequent swinging main flow. Distance between dikes on both banks is generally 5～10km, and 24km at the widest point. The bed slope is 2.56-1.72%. Branches including Yiluo River and Qinhe River ends into the Yellow River in this reach;

(b) The second is the transitional river reach from Gaocun Village of Dongming County to Taochengpu of Yanggu County, which is 165km long. This river channel transforms from braiding to meandering, with minimized change of river regime. Distance between dikes on both banks is 1.4～8.5km, most of which are above 5km. Average bed slope is 1.2%;

(c) The third is meandering reach form Taochengpu of Yanggu County to Ninghai of Kenli County, which is 322km long. There are many river training projects on both banks of this reach, so the river regime is stable. Distance between dikes on both banks is 0.4～5km, and 1～2km in general. Average bed slope of the river channel is about 1%, and the branch of Wenhe River falls in this section;

(d) The fourth is the estuarine reach below Ninghai of Kenli. Due to sedimentation, extension and swinging at the mouth of the Yellow River, give rise to changes in the flow path into the sea. Existing flow path into the sea is the Qingshuigou flow path artificially changed in 1976 which has been running for 40 years.

"Secondary Suspended River" in the Lower Yellow River (Figure 2) started to appear in reach of Dongbatou~Gaocun Village at the beginning of 1970s. Since 1986, due to factors including increased water consumption and regulation of Longyangxia and Liujiaxia Reservoir, the amount of water into lower reaches decreased sharply, especially in the flood season. Besides that, the influence of production of dike in floodplain affected the sedimentation ratio of main channel in reach above Taochengpu which increased from 30% to 70%. More than 90% sediments in reach below Taochengpu were deposited in the main channel and the lower river channel was deposited and shrank. Before flood season in 2002, bank full discharge decreased from 6,000$m^3$/s in the early 1980s to 2,000～3,000$m^3$/s, and only 1,800$m^3$/s in some reaches. At present, the situation of "Secondary Suspended River" from Dongbatou to Taochengpu reaches is at the most serious condition. The floodplain is generally about 3m higher than the foot of river dikes, and 4～5m at the most. Transverse gradient of floodplain reaches about 10%, which is about 10 times as high as the longitudinal slope of river channel. In case that a big flood occurs, the transverse gradient of the channel will be much larger than longitudinal river slope and this increases the likelihood of rushing flow at dikes, flood flowing along dikes and even "rolling river", which would greatly endanger the safety of dike (Yellow River Conservancy Commission, 2013).

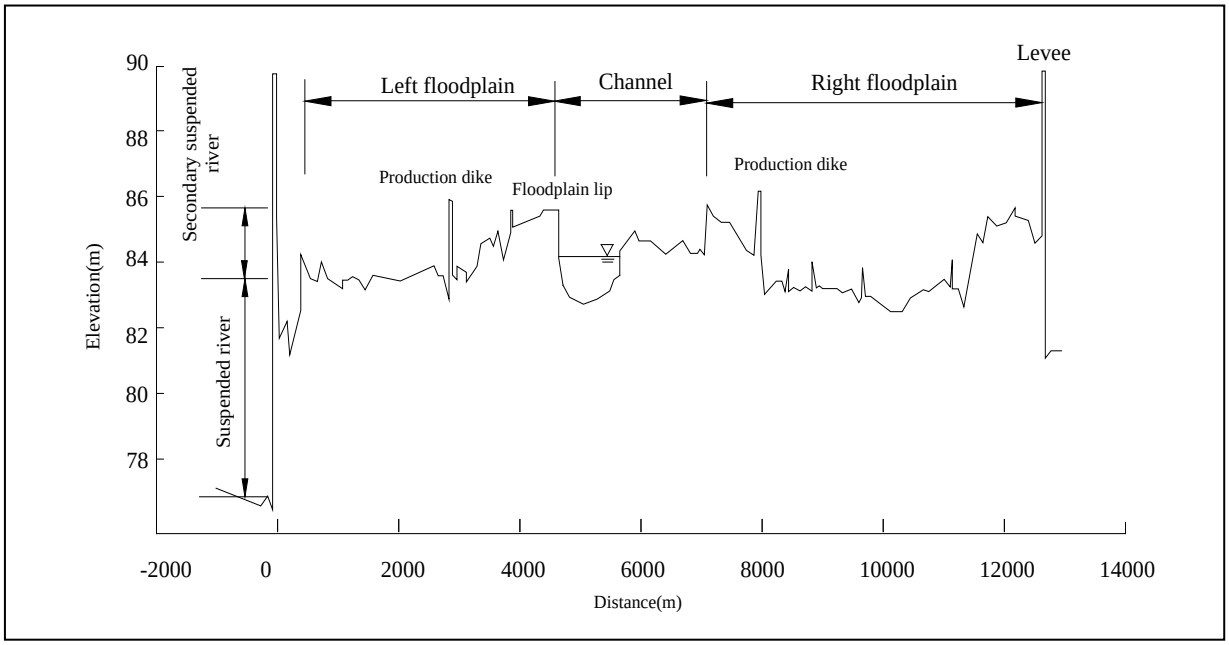


**Figure 2**. Typical Cross Section Profiles of Secondary Suspended River.

1.2 Characteristics of floodplain

The Lower Yellow River channel has a typical compound section with broad floodplains. Total area of the lower river channel is 4860.3km$^2$, and the floodplain area is 3,154km$^2$. So the floodplain occupies about 65% of gross area of the lower reach. Most of the lower floodplain area is situated in reaches above Taochengpu, with its area accounting for more than 78% of the lower floodplain.

The Lower Yellow River floodplain has significant effects of flood detention and peak reducing. In 1958 and 1982, the peak discharges of Huayuankou were 22,300m$^3$/s and 15,300m$^3$/s, and the corresponding peak discharges of Sunkou were 15, 900m$^3$/s and 10,100m$^3$/s respectively. The peak was reduced by 29% and 34%. The channel storage volumes from Huayuankou to Sunkou were 2.59 billion m$^3$ and 2.45 billion m$^3$ respectively.

Sediment deposition effects on the floodplain is an important function for the Lower Yellow River floodplain in distinguishing it from other river floodplains. When the floodplain is flooded, sediments enter the floodplain to deposit, and water goes back to main channel, resulting in exchange of water and sediment in channel and floodplain, and sediment deposition in floodplain. According to statistics of measured data, 9.2 billion t sediments were deposited cumulatively in the Lower Yellow River channel from June 1950 to October 1998 (Table 1), of which, there were 6.37 billion t sediments depositing in the floodplain, which occupied 69% of the deposition amount of the entire lower reach.

**Table 1**. Sediment siltation amount in the Lower Yellow River (from July 1950 to October 1998).

| Items | Amount of Siltation and Scouring (×10$^8$ t) | | | | |
|---|---|---|---|---|---|
| | Tiexie - Huayuankou | Huayuankou-Gaocun | Gaocun-Aishan | Aishan-Lijin | Tiexie-Lijin |
| **Channel** | 1.02 | 13.54 | 6.33 | 7.43 | 28.32 |
| **Floodplain** | 8.82 | 27.38 | 19.74 | 7.76 | 63.70 |
| **Full Cross-section** | 9.84 | 40.92 | 26.07 | 15.19 | 92.02 |

At present, the Lower Yellow River floodplain involves 43 counties (districts) of Henan and Shandong Province with a total population of 1.895 million, where 1.2465 million people stays in Henan Province, and 0.6487 million people stay in Shandong Province. The gross cultivated area at the lower reach is 4.816 million, accounting for 65% of the area of river channel.

The floodplain of the Lower Yellow River is flooded and submerged frequently. According to analysis, at present, flood occurred once every five years at the Lower Yellow River (peak discharge at Huayankou Station is 10,000m$^3$/s) has a population of 764,000 at the floodplain. The 5% frequency of flood (peak discharge at Huayankou Station is 12,370m$^3$/s) has inundated a population of 1.5819 million at the floodplain. There are obvious contradictions between economic and social development and river regulation at the floodplain.

## 2 RECENT RESEARCH ADVANCES

Nearly ten years of scientific and technological works have been carried out and a lot of researches on regulation of channel and floodplain of the Lower Yellow River were studied. Based on different ideas on future changing trend of water-sediment conditions in the Lower Yellow River, now there are three opinions on regulation of the Lower Yellow River: a) the Yellow River will still be a sandy river in the future, considering the need of the flood detention and sediment deposition in the floodplain thus, the current broad river governance should be kept; b) the flood sediments will decrease greatly in future, so the river channel should be narrowed; c) the Lower Yellow River will be dominated by medium and small floods in the future with big flood still existing, and the water-sediment conditions will be polarized. Therefore, the strategy of "water and sediment regulation where gathering of water to transport sediment and reinforcing the dikes of the current broad river" has been proposed. There are three kinds of views focusing on existence and abolishment of the production dikes in the floodplain: a) the production embankment should be abolished gradually; b) the standards of production embankment should be lowered; c) the floodplain should be utilized differently in different regions.

2.1 Research on the Lower Yellow River channel management strategy

Studies have been carried out on the management plans of “the current broad river with reinforced dikes” and “narrowing of the current dikes and river”. The two plans were compared from the following aspects:

From the view of economic and social development, the narrowing of river plan can liberate most floodplains in wide reach plus put an end to the unfavorable frequency of flooding situation. This will better solve the problems in economic and social development of floodplain (He et al., 2013).

From the view of flood treatment, both the current river plan and the narrowed river plan can systematically controlling the flood within existing prevention standards of the Yellow River. However, by

 

contrast, the current flood prevention system under the current river plan has the characteristic of better flood control safety.

From the point of sediment disposal, according to 165-year (2005～2169) series, the calculation results of mathematical modeling shows the amount of accumulative deposition in the current and narrowed river plans to be 18.403 billion $m^3$ and 13.453 billion $m^3$ respectively. It is a known fact that sediment transport efficiency of narrowed river plan is higher, and the uplifting speed of the river bed is faster than that of the current river plan. And the uplifting speed of narrowed river is 1.56 times as big as that of the current river.

Seeing from extension of the river estuary delta, the length of river mouth delta deposition extension of the narrowed river plan is 2.15km larger than that of the current river plan. And the influence of retrogressive aggradation caused by river mouth delta deposition extension of the narrowed river plan is greater. From the perspective of construction management, engineering construction scale of the narrowed river plan is larger, which enforces the need to rebuild existing embankment and channel for improvement on a large scale. It also shall occupy a lot of lands and take a long time from engineering construction towards stability. During flood season, the time of the embankment with high water level increases obviously, and the pressure of flood prevention is high. According to researches, although the total depositing amount of narrowed river plan was lower than that of the current river plan during the 165-year study period, its deposition thickness and rate were greater than that of the current plan. Based on comprehensive consideration, “the current broad river with reinforced dikes” was recommended as the basic plan for regulation of the lower reach.

2.2 Research on governance mode and safety construction of the Lower Yellow River floodplain

According to the requirements of ensuring flood control security and people’s life and property safety of the floodplain, the floodplain’s effect on flood discharge, flood detention and sediment deposition was considered. This paper analyzes the comprehensive governance mode of the lower river floodplain and measures needed for the management of floodplains in different reaches. Based on the principle of economic rationality and technical feasibility, in-depth studies have been conducted on three plans: abolishing the production embankment gradually, low standard production embankment and utilizing the floodplain in regions. In the long run, the Yellow River is still a sandy river and the floodplain plays an irreplaceable role in governance of the Lower Yellow River. Thus, the plan of stabilizing embankment by widening the river is required. In order to reduce the flood threat and realize the floodplain’s function for flood detention and sediment deposition, production embankments should be abolished and the mode of whole floodplain utilization should be implemented. The premise to carry out whole floodplain utilization is that safety problems of the masses at the floodplain area must be solved. For the safety construction of the Lower Yellow River, it is advised to take comprehensive measures of combing partial resettlement with on-the-spot flood avoidance and temporary withdrawal. It is advisable for the safety facilities to create conditions for the floodplain’s economic development. The policy *Interim Measures for the Compensation of the Use of Flood Detention and Impoundment Areas* should be adopted in the Lower Yellow River floodplains.

2.3 Research on flood detention and sediment deposition function of the Lower Yellow River wide floodplain and floodplain disaster reduction technology (Chen et al., 2013)

Three programs were studied, which were comprehensive destruction of production dike, the construction of protection dike according to standards of 6000$m^3$/s, 8000$m^3$/s and 10000$m^3$/s and division utilization. This paper held a view that compares the no protection dike program, the flood detention amount and sediment deposition amount of floodplain for protection dike program and division utilization program to be significantly reduced. The functions of flood detention and sediment deposition of wide floodplain was obviously weakened as well. Meanwhile, the two programs lead to the increase of sediment amount flowing into narrow river channel, which strengthened the sediment deposition at narrow river channel below Aishan, which gave rise to the rising of water level and the discharge being faster, brought adverse effect to flood control of narrow river channel. The affected degree increased as the inflow sediment coefficient increases.

The model test showed that the program of no protection dike performs better at flood detention and sediment deposition, but the total submerged area was larger than that of the protection dike. The sediment transport capacity of the channel with protection dike was stronger, but the sediment deposition amount of newly formed floodplain was larger than that of no protection dike mode. This will aggravate the bad situation of "Secondary Suspended River" where the highest flood water level downstream of Gaocun under protection dike mode was higher than that of no protection dike, which increased the flood control pressure at lower reaches.

The research on flood detention and sediment deposition & disaster reduction effect under the operational mode of different floodplains showed that flood detention and sediment deposition played the best function under the operational mode of no protection dike. The disaster reduction effect was weakened because eventhough the disaster reduction effect under the operational mode of dike, floodgate and division utilization was increased, the flood detention and sediment deposition function was limited to a certain extent.

The research put forward the recommendation of operational program for the future of wide floodplain that will be used to retain the production dike. For floods that were below 6,000$m^3$/s at Huayuankou Station,

 

the floodplain was protected from loss through the production dike; for flood that was over 6,000$m^3$/s at Huayuankou station, all the production dikes were destroyed to play the flood detention and sediment deposition function of wide floodplain. For the loss caused by flood, the floodplain compensation policy should be considered to give reasonable economic compensation to affected areas, and at the same time, special floodplain development risk fund should be funded and established by the central and provincial governments and water conservancy departments jointly to reduce the risks of the floodplain area to withstand the flood.

2.4 Research on river channel regulation and floodplain governance in the Lower Yellow River (Jiang et al., 2016)

This paper analyzed the characteristics and reasons for recent changes of water and sediment in the Yellow River. The research put forward the water-sediment process under three scenarios of different water and sediment amounts into the Lower Yellow River: 24.803 billion $m^3$ and 321 million t, 26.284 billion $m^3$ and 606 million t, and 27.278 billion $m^3$ and 770 million t of 50 years. In addition, four typical flood-sediment process are put forward, which were the measured 96.8 return period flood, the "73" ten-year return period flood, the"58" hundred-year return period flood and the "58" thousand–year return period flood. A typical water-sediment process and the flood-sediment process were put forward here to carry out the Lower Yellow River channel regulation and floodplain governance research.

The lower river channel regulation and floodplain governance program was put forward after the flood release and sediment transport, river channel regulation, floodplain area and location as well as floodplain population distribution and other situations were combined, to be compared in aiding the selection of different mitigation programs. The program is as follows: building protective embankments in the floodplain bounded by the main dikes which reach above Beidianzi. The average distance between protective embankments is 3.7km. Protective embankments should be able to resist 20-year floods in Changyuan Floodplain, 30-year floods in Pingyin Floodplain and Changqing, and 10-year floods in other floodplains. After the protective embankments are built, 22,000 people in the floodplains between protective embankments can be moved out and resettled and people in other floodplains can be evacuated temporarily to be arranged locally or resettled.

According to the parallel calculation results of mathematical models by China Institute of Water Resources and Hydropower Research, Yellow River Institute of Hydraulic Research, Yellow River Engineering Consulting Co., Ltd. and Tsinghua University, in Scenario Program 1, under the present Yellow River channel management mode, the lower reach channel was generally close to siltation and scouring equilibrium. However, under the management mode with protective embankments, the channel is scoured slightly with the average annual erosion amount of -33～-1.0 million t, where the protection dike had silt reduction or scouring strengthening effect. In Scenario Program 2 and Scenario Program 3, the Lower Yellow River channel was in the cumulative siltation state. In the Scenario Plan 2, the annual average sediment deposition was 80 to 107 million t for the present management mode and it is 74 to 92 million t for the protective embankment management mode. In Scenario Program 3, the annual average sediment deposition was 159 to 169 million t for the present management mode and it is 138 to 153 million t for the protective embankment management mode, and the protection dike had a silt reduction by about 11%.

Results of research on the non-engineering and engineering measures conducive to improving the sediment transport capacity of the lower river channel showed that appropriate non-engineering and engineering measures can improve the sediment transport capacity of the river channel to a certain extent. However, the lower course of the Yellow River channel is still in a significant siltation state in case of 800 million t of incoming sediment.

## 3 MANAGEMENT PRACTICE IN RECENT YEARS

3.1 Sediment detention by reservoir and water and sediment regulation

Xiaolangdi Reservoir which dammed the Yellow River in 1997 was put into use in October 1999. From 1997 to April 2016, 3.086 billion $m^3$ sediment was silted accumulatively. Reservoir sediment detention and water and sediment regulation scoured the whole channel of the Lower Yellow River. From November 1999 to April 2016, 2.814 billion t of sediment were scoured accumulatively (Table 2).

**Table 2**. Amount of erosion in different reaches (November 1999 ~ April 2016). Unit: $\times 10^8$ t

| Reach / Period | Above Huayuankou | Huayuankou-Gaocun | Gaocun-Aishan | Aishan-Lijin | Lijin-Estuary | Above Lijin | Whole Lower Reach |
|---|---|---|---|---|---|---|---|
| Flood Season in Total | -3.78 | -5.22 | -3.65 | -4.80 | -1.38 | -17.45 | -18.83 |
| Non-flood Season in Total | -4.30 | -6.87 | -0.03 | 1.31 | 0.58 | -9.89 | -9.31 |
| Whole Year in Total | -8.08 | -12.10 | -3.68 | -3.49 | -0.80 | -27.34 | -28.14 |

 

Seen from the distribution of the scouring amount along the river, the upstream reaches of Gaocun was scoured more, accounting for 71.7% of the total scouring amount of the lower river channel. The scouring amount of the reach from Gaocun to Aishan accounted for 13.1% of the total scouring amount of the lower river channel. The scouring amount of the reach from Aishan to Lijin accounts for 12.4% of the total scouring amount. From the distribution of scouring intensity indicated by the scouring amount per unit river length, the scouring intensity declined gradually along the river. In flood season, the scouring intensity of reaches upstream of Huayuankou was 2.3 times of that of at the estuary reach. From time distribution of the scouring amount, the scouring occurred mainly in flood season. During the flood season, scouring occurred in all the river reaches where the amount was a total of 1.883 billion t. During non-flood season, scouring occurred in reaches upstream of Aishan which had a scouring amount of 1.12 billion t. The silting amount in reaches downstream of Aishan Mountain was 189 million t. During non-flood season, the total scouring amount of the lower river channel was 931 million t.

With the continuous scouring of the lower river channel, water levels at the same discharge at each downstream hydrological station went down in varying degrees. Compared with 1999, the water-rising period during water and sediment regulation in June 2015, was at 2000m$^3$/s and dropped by about 2.3-2.6 m in reaches upstream of Gaocun and 1.5-2.5m in reaches downstream of Gaocun (Table 3).

**Table3**. Water level variations at the same discharge of 2000m$^3$/s in the Lower River Channel (from 1999 to 2015).

| Hydrological Stations | Hydrological Stations | Huayuankou | Jiahetan | Gaocun | Sunkou | Aishan | Luokou | Lijin |
|---|---|---|---|---|---|---|---|---|
| Water Level (m· Dagu) | 1999 ① | 93.67 | 76.77 | 63.04 | 48.07 | 40.65 | 30.23 | 13.25 |
| | 2015 ② | 91.32 | 74.10 | 60.52 | 46.21 | 39.08 | 28.32 | 11.72 |
| Water Level Changes（m） ②－① | | -2.35 | -2.67 | -2.52 | -1.86 | -1.57 | -1.91 | -1.53 |

Since the beginning of the flood season in 2002, due to Xiaolangdi Reservoir's effect on sediment trapping due to the water and sediment regulation, the bankfull discharge of the Lower Yellow River increased by 1650 to 4300 m$^3$/s. The greatest bankfull discharge increase was in reaches upstream of Gaocun, by an average value of 3900m$^3$/s. The bankfull discharge increased by about 1700m$^3$/s in the reach between of Aishan and Lijin. The minimum bankfull discharge of the lower river channel had increased from 1800 m$^3$/s ibefore the flood season of 2002 to 4250m$^3$/s in 2016 (Figure 3).

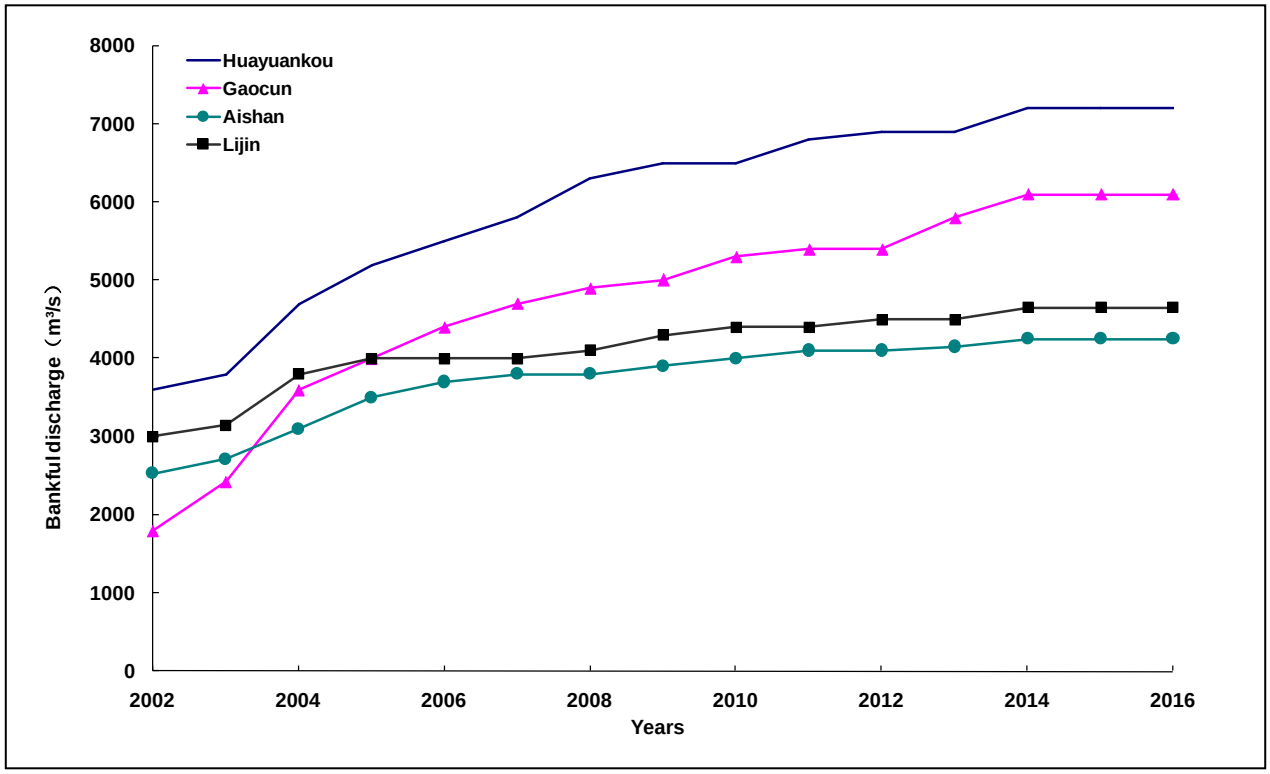


**Figure 3**. Changes of bankfull discharge of the Lower Yellow River Channel since 2002.

 

3.2 Pilot project of secondary suspended river management

Based on research by testing projects such as dredging the lower main channel, blocking divergent grooves and filling the ditches along the dike with siltation were used. Yellow River Conservancy Commission chose the reach from Nanxiaodi to Penglou in Puyang City of Henan Province to conduct the testing project for managing "Secondary Suspended River" by using the river digger in early June 2003.The length of the dredged river channel was 5.2km, and the dredged siltation was 2.202 million $m^3$. The length of the ditches along the dike filled with dredged silt was 8.25km, the area of blocked grooves was 211mu. Through dredging the main channel, blocking divergent grooves and the filling ditches along the dike and other measures, the adverse situation of "Secondary Suspended River" in the reach was improved preliminarily.

3.3 Execution of the floodplain compensation policy

In order to ensure the basic benefits of people in the Lower Yellow River floodplains, improvement of their production and living conditions will help to solve the contradiction between the peace and stability of the Lower Yellow River. The economic, social development and stability of the floodplain were based on plenty of investigations and researches, where compensation policies for the utilization of the floodplains of the Lower Yellow River were approved by the State Council in 2011. In 2012, Ministry of Finance, National Development and Reform Commission and Ministry of Water Resources formulated the Measures of Financial Compensation Funds for the Utilization of Floodplains in the Yellow River, which stipulated explicitly the compensation for the utilization of the floodplains in the Lower Yellow River.

The Measures stipulated that the central government will afford 80% and the provincial governments afford 20% of the compensation. Compensation for crop losses should be rectified according to 60-80% of the annual average outputs per mu in the same quarter of the last three years (not including the year when the floodplain was used) as submitted by the statistical department of the county where the floodplain was located. Residential loss compensation should be assessed based on 70% of the value of main part loss.

3.4 Pilot project for the resettlement of residents in the floodplain

Two batches of pilot resettlement for residents in the floodplain in Henan and Shandong Province in the Lower Yellow River were conducted successively. The first batch of pilot project in Henan Province was launched in 2014, involving 16718 people of four towns in Fan, Fengqiu and Lankao Counties. The total investment was RMB 1.204 billion yuan, including 695 million yuan for housing, 359 million for infrastructure and public service facilities and 150 million yuan for the land occupation compensation in the resettlement areas. Regarding the housing investment, the fund subsidy of central government per household on average was RMB 70,000 yuan and the fund subsidy of local government per household on average was RMB 43,600 yuan. The second batch of pilot project in Henan Province was launched in 2016, involving 40132 people of 11 towns of Zhongmou, Fengqiu, Puyang, Taoqian, Lankao and Changyuan Counties. The total investment was 3.45 billion yuan, 2.09 billion of which was used for housing.

The first batch of pilot project in Shandong Province was launched in 2015, involving 5019 people of Juancheng and Dongping counties. The total investment was 312 million yuan, in which central subsidy fund was 111.65 million yuan and local subsidy was 77.8 million yuan. Other expenses were solved by integrated departmental funds, revenues from “Linking the Decrease in Rural Construction Land with the Increase in Urban Construction Land” policy, self-raised funds by the mass and other measures. In 2016, Pingyin, Liangshan, Dongping and Juancheng were selected as the second batch of pilot counties. The total investment was 533 million yuan, including 183.33 million yuan from the central financial subsidy and 114.33 million yuan from the provincial, municipal and county-level subsidy. Self-raised fund of the mass was 82.3 million yuan and others were solved by integrated departmental funds, revenues from land use policy, and other measures.

## 4 CONCLUSIONS

(a) The Lower Yellow River channel is an above ground suspended river across North China Plain. "Secondary Suspended River" appeared in partial cross sections of the reach from Dongbatou to Gaocun in the early 1970s. Since 1986, due to the factors such as water use increase, regulation and storage of Longyangxia and Liu Jiaxia Reservoirs, water amount flowing into the downstream in flood season decreased sharply. Plus the effect of production dike in floodplains and the increase in siltation of river channel give rise to "Secondary Suspended River" being developed. At present, the "Secondary Suspended River" situation of the reach from Dongbatou to Taochengpu is the most serious one. The floodplain lips are generally about 3m higher than the dike toe and the largest height difference is even up to 4～5m. The floodplain surface transverse gradient increases to around 10%, which is about 10 times of the river channel’s longitudinal gradient. In case that large flood occurs, since the transverse gradient of the river channel is much greater than the longitudinal gradient, the possibilities of rushing at dikes by main streams, occurrence of running along the main

 

dike toe and even occurrence of "rolling river" are increased, which will seriously affect the safety of the dike;

(b) The Lower Yellow River channel is typical compound section river channel with broad floodplain. Total area of the lower river channel is 4860.3km$^2$, and the floodplain area is 3,154km$^2$. So the floodplain occupies about 65% of gross area of the lower reach. The Lower Yellow River floodplain has a significant effect on flood detention and peak clipping. It is an important part of the flood control and siltation reduction system in the Lower Yellow River and also the production and living sites of 1.895 million people. The contradiction between river channel regulation and economic and social development of the floodplain is prominent, which needs coordination to resolve;

(c) In recent years, a lot of researches have been carried out on the governance of the Lower Yellow River channel. In summary, there are three categories of views including broad river by abolishing production dike, narrowed river with low standard production dike, and managing the floodplain in regions. Due to different forecasting of the future water and sediment conditions of the Yellow River, at present, there are still great divergences. As a result, the direction and measures of the Lower Yellow River channel and the floodplain governance should be studied deeply according to the future changes of water and sediment;

(d) In recent years, massive production practices have been carried out around the Lower Yellow River channel governance, such as sediment storage by reservoirs, water and sediment regulation, "Secondary Suspended River" governance, execution of floodplain compensation policy and resettlement of residents in the floodplains. All the production practices have achieved significant results. Especially through the sediment storage and water and sediment regulation by Xiaolangdi Reservoir where the Lower Yellow River main channel is scoured continuously along the whole channel. The minimum bank full discharge of the Lower Yellow River has increased from 1800m$^3$/s to 4250m$^3$/s. The flood discharge and sediment transport capacities of the main channel have been improved greatly. The situation of "Secondary Suspended River" has been relieved and the Lower Yellow River floodplain situation of "floodplain is submerged by small flood" has been improved. The ecology and environment in estuarine regions have been improved effectively as well.

## ACKNOWLEDGEMENTS

The study is financially supported by the National Key R&D Program of China (2016YFC0402503) and the SpecialScientific Research Fund of MWR Public Welfare Profession of China (Grant No.201401002).

## REFERENCES

Yellow River Conservancy Commission (2013). *Integrated Planning of Yellow River Basin*. Zhengzhou: The Yellow River Water Conservancy Press.

He, Y., Cui, M., Liu, S. & Wan, Z. (2013). Study on Strategy of River Training in the Lower Yellow River. *Yellow River*, 35(10), 51-53.

Chen, W., Liu, S., Han, X. & Cui, M. (2013). Research on Yellow River's Downstream Floodplain Comprehensive Treatment Measures. *Yellow River*, 35(10), 63-65.

Jiang, E., Wang, Y., Zhang, Y. & Cao, Y. (2016). New Advancement in Yellow River Sediment Research. *Yellow River*, 38(10), 24-31.

 

Proceedings of the 37th IAHR World Congress
August 13 – 18, 2017, Kuala Lumpur, Malaysia

# FORMATIVE PARAMETERS FOR STABLE ARMOR DEVELOPMENT

STEPHANE BERTIN[1] & HEIDE FRIEDRICH[2]

[1,2] Department of Civil and Environmental Engineering, University of Auckland, Auckland, New Zealand
s.bertin@ymail.com; h.friedrich@auckland.ac.nz

## ABSTRACT

Stable fluvial armors, shaped by surface coarsening during selective sediment transport, received considerable attention over the years. Stable armoring is important in river engineering studies. For example, a classical problem is the riverbed degradation downstream of a dam. Our knowledge of whether stable armors can develop with limited sediment supply is still insufficient, yet this is a condition found in many natural gravel-bed rivers. Practically, given a suitable timeframe that allows sediment transport to reduce to approximately zero under a constant flow of water, stable armors can be re-created in laboratory flumes, allowing controlled studies with precise measurements. This study examines the extent to which armor structure is replicable under identical flow and bulk sediment composition. Two sets of experiments were performed using two different bulk sediment mixtures. Unstructured gravel beds were prepared in a laboratory flume and were water-worked successively with two constant discharges until the formation of stable armors. No sediment was fed and selective sediment transport prevailed. Grain-scale digital elevation models (DEMs), as well as bed-surface and bedload compositions, were obtained to quantify the changes due to armoring and to identify the formative parameters. We found bed structure to be more responsive to changes in flow discharge than bed-surface composition, and both armor composition and surface structure were unique given identical formative parameters. This finding is significant as it shows that bed composition alone is not sufficient to describe armor roughness. We discuss the relationships between a fully-developed stable armor and the flow and sediment forming it. The relationships examine the effects of varying the formative parameters onto the armor properties (e.g., composition and roughness), which were extended with the addition of extensive data from previous research.

**Keywords:** Roughness; remote sensing; photogrammetry; dem; statistical analysis.

## 1 INTRODUCTION

Stable (also called static) fluvial armors commonly occur in poorly sorted gravel-bed rivers in conditions of partial sediment transport with little to no sediment supply from upstream (Proffitt, 1980; Chin et al., 1994; Gomez, 1994; Vericat et al., 2006). The formation of a stable armor is a stability-seeking mechanism, whereby selective entrainment (winnowing) of fine mobile particles uncovers coarse immobile particles forming a layer typically one grain diameter thick, which isolates the underlying bed material from the flow and prevents further bed degradation (Parker and Klingeman, 1982; Gomez, 1983; Parker and Sutherland, 1990; Richards and Clifford, 1991; Gomez, 1993; Pitlick et al., 2008). Stable armors result from a progressive reduction in sediment transport to practically zero (Gessler, 1967).

In comparison, sediment supply from upstream allows for the progressive equalization between the bedload and the subarmor composition for mobile armors (e.g., Paris, 1992; Marion et al., 2003; Mao et al., 2011). Mobile armors can persist over floods (e.g., Parker and Klingeman, 1982; Wilcock and DeTemple, 2005; Clayton and Pitlick, 2008), as eroded grains are replaced by similar-sized grains originating from upstream, whilst stable armors only persist during floods of a lesser magnitude than the formative flow (e.g., Laronne and Carson, 1976; Proffitt, 1980; Gomez, 1983; Chin et al., 1994; Vericat et al., 2006). In the case of flows above the critical armoring discharge or when uniform sediment prevents selective entrainment, all particle sizes present on the bed are in motion and no armor can form (e.g., Chin et al., 1994). Other protective mechanisms are involved, such as a slope reduction.

Field observations reveal that full mobilization of surface grains in gravel-bed rivers is not a frequent event, with examples indicating full mobilization for floods with a 7-year return period or more (Haschenburger and Wilcock, 2003; Vericat et al., 2006). This suggests a possible wide occurrence of stable armors in nature. In the laboratory, recreating stable armoring allows to study bed-flow interactions and the evolution of a gravel streambed under readily recreated experimental conditions (selective transport and no sediment feed).

Using different flow discharges, past work (e.g., Odgaard, 1984; Chin et al., 1994; Garde et al., 2006) examined the armoring effects onto bed grain-size distribution (GSD). The models developed suggest a specific (i.e. replicable) armor composition, dependent on the parent bed material and the formative discharge. More recently, research on the interactions between flow and sediment has evolved to consider no

 

only the armor GSD but the actual surface structure and topography (e.g., Lane, 2005; Hodge et al., 2013), since the latter offers new perspectives on bed stability and roughness. Therefore, it is of interest to test the hypothesis that armor topography is replicable given formative parameters.

## 2 METHODOLOGY

Two sediment mixtures with natural river-worn sands and gravels were used in this study to recreate armored beds in a laboratory flume. For each sediment mixture, three replicated experimental runs were performed, during which an initially screeded flat and poorly-sorted gravel bed was water-worked successively with two discharges until stable armors were formed. Conditions of parallel degradation (i.e. selective entrainment and no sediment feed) prevailed. To assess the reproducibility of our experiments, each run was set up identically and flow conditions were kept as constant as possible within and between runs. In particular, the condition of a constant shear stress despite bed degradation was justified by raising the sediment bed according to the depth of erosion, to maintain bed and water surface slopes steady, a technique used by others before (e.g., Chin et al., 1994; Heays et al., 2014).

### 2.1. Experimental environment

A non-recirculating tilting flume with glass side-walls, 19 m long, 0.45 m wide and 0.5 m deep, shown in Figure 1A, was used for the experiments. A 1.0 m long, 0.45 m wide and 0.13 m deep sediment recess (called the test section), with a vertically adjustable table that supported the movable sediment bed, was installed 10.4 m from the flume inlet. To facilitate the development of a fully turbulent boundary layer and homogeneous hydraulic conditions, the bed upstream and downstream of the test section was artificially roughened. A sediment trap was installed 0.5 m downstream of the test section and allowed collection of all eroded sediment.

Two coarse sediment mixtures, called sediment 1 and sediment 2 (Figure 1B), were prepared from two distinct, slightly bimodal, alluvial sediments, with size ranging from 0.7 to 35 mm, and used as movable bed materials for the development of stable armors in the sediment recess. Median grain size, $D_{50}$, was 8.4 mm and 9.2 mm and the sediment geometric sorting was 3.1 and 2.6, for sediment 1 and sediment 2, respectively.

### 2.2 Experimental procedure

For each run, the well-mixed sediment was placed in the test section, screeded flat to a thickness of 0.13 m, parallel to the flume bed, and leveled with the surrounding fixed beds. The flume slope was held constant at 0.5% throughout the tests.

A short period of low flow was initiated to allow air trapped in the gravel mixture to escape. A constant flow discharge $Q_1$ = 67 L/s was then applied over 100 hours (see Table I). The flume tail gate was not used, allowing the water depth to naturally adjust, while near uniform flow conditions were attained. After a stable armor had formed, a constant flow rate $Q_2$ = 84 L/s was applied over 300 hours. For $Q_1$ and $Q_2$, the flow was stopped when the sediment transport rate dropped to less than 1% of the initial transport rate measured after two hours at a constant discharge.

### 2.3 Bed surface measurement and analysis

Measurement of the bed surface, both through air and water, was performed with digital photogrammetry, using a pair of Nikon D5100s (16.4 Mpixel, 23.6 × 15.6 $mm^2$ sensor size) with Nikkor 20 mm lenses. The cameras were placed 0.3 m apart using a mounting bar and installed 0.65 m vertically above the test section (Figure 1A).

**Table I:** Flow conditions for the formation of the two successive stable armors. H is flow depth; U is flow depth-averaged velocity; Re = $UR_h/v$, where $R_h$ is the hydraulic radius and v is the kinematic viscosity of water (taken as $10^{-6}$ $m^2/s$); $\tau_*$ is Shields stress based on the parent bed $D_{50}$, calculated as $u^{*2}/(SG-1)gD_{50}$; and Re* = $u^*k_s/v$ is the grain Reynolds number. [1,2]is for the two different sediment mixtures. Low transport rates characterized the study. [I]The shear velocity u* and the equivalent roughness height $k_s$ were estimated from the law-of-the-wall and a velocity profile measured in the centerline of the flume over the fixed roughness bed upstream of the test section, using a Vectrino+ acoustic velocimeter (Nortek®), with 200 Hz sampling rate and 120 s sampling time. 15 measurement points along the lower 75% of the water column were recorded (with 5 points along the lowest 10 mm).

| | H (m) | U (m/s) | Re | u* (m/s) | $\tau_*$ | Re* | Duration (hrs) |
|---|---|---|---|---|---|---|---|
| $Q_1$ = 67 L/s | 0.195 | 0.75 | 79,300 | 0.0722[I] | 0.044[1]<br>0.040[2] | 513 | 100 |
| $Q_2$ = 84 L/s | 0.225 | 0.82 | 92,800 | 0.0774[I] | 0.050[1]<br>0.046[2] | 526 | 300 |

 

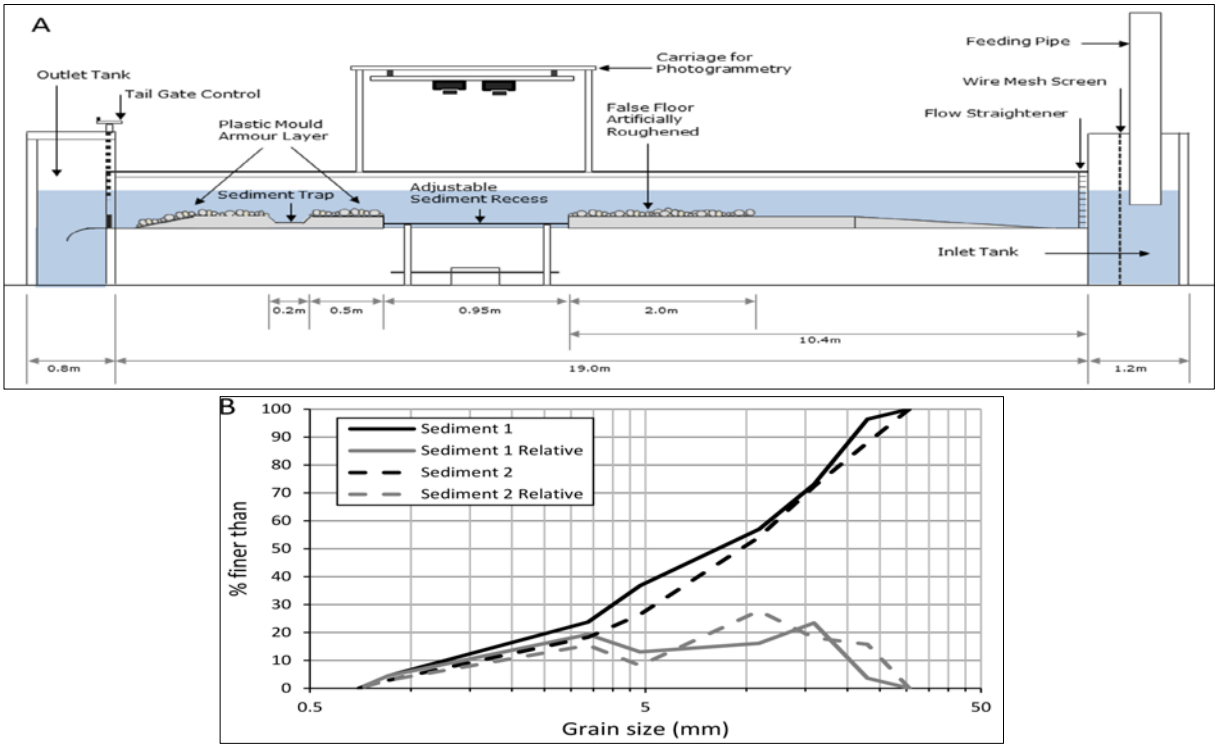


**Figure 1.** (A) Experimental setup. Flow direction is from right to left. (B) Grain-size distributions (GSDs) of the two sediment mixtures used in the study, obtained after sieving and correcting for the square-hole sieves.

Armor composition and gravel orientation were determined using a single photograph (area: 0.65 × 0.35 $m^2$, pixel size: 0.15 mm, number of detected sediment grains ~ 1000) and the image-analysis tool Basegrain®. The latter allows for automatic grain separation in digital images of gravel beds and applies Fehr (1987)'s line-sampling method for the results' analysis (Detert and Weitbrecht, 2012). The method was calibrated to minimize differences with a sieve-based grain-size distribution. Grain-size properties of the armors were indexed with "A", to easily distinguish them from properties of the bulk mixtures. For the screeded beds, the composition was assumed equal to the bulk mixtures. Basegrain® also determined the detected grains' a-axis orientation by fitting an ellipse whose areal normalized second-central moment equals that of the grain and computing the angle formed between the ellipse long axis and the flow-orientated image long axis.

To avoid draining and re-filling the flume during the tests, a common practice potentially disturbing the bed surface (Ockelford and Haynes, 2013), photographs of the bed after armoring with $Q_1$ were obtained through water (H = 0.13 m). The flow rate was reduced substantially to remove surface waves and to record clear images. The armors formed with $Q_2$ were photographed both through water and in air, at the end of each run. The maximum relative difference in terms of $D_{50}$ was 1.4%, demonstrating the intrinsic robustness of the methodology.

High-resolution DEMs of the gravel-bed surface (area: 1 × 0.45 $m^2$, grid spacing: 1 mm, theoretical depth resolution: 0.35 mm) were reconstructed from three overlapping stereo photographs, using the technique presented in Bertin et al. (2015). Camera calibration was performed in-situ at the beginning of a test using a flat chequerboard, before the recess was loaded with sediment, to allow subsequent topography measurements both in air and through water. To measure through water, it was critical to keep the water depth constant (H = 0.13 m was used) for all image acquisition (Bertin et al., 2013). Using photogrammetry, depth is triangulated at each pixel location (pixel size ~0.15 mm), and shadowed points are interpolated based on the assumption of a continuous surface, leaving no voids in the point clouds. Point clouds were interpolated onto raster DEMs with 1 mm grid spacing. Relative DEM accuracy was estimated by comparing DEMs of the armors formed with $Q_2$ measured in air with those measured through water, resulting in MUE = 0.66 ± 0.11 mm, and SDE = 1.01 ± 0.10 mm (i.e. mean ± 1 standard deviation, n = 6). Before analysis, the DEMs were resized to 0.8 × 0.3 $m^2$ to minimize flume wall influence. Similar to previous research, DEMs were detrended to remove any surface trend that could bias the grain-roughness properties of interest (e.g., Aberle and Nikora, 2006; Hodge et al., 2009), such as linear trend surfaces representing the combined effect of flume-bed slope and setup misalignment (when the cameras are not perfectly parallel to the flume bed, causing a tilt in the DEM). Any low-amplitude bedform on the gravel-bed surface, larger than particle clusters,

 

was also removed in a second step, through the application of a moving filter of radius $1.25D_{90A}$ (Smart et al., 2002). DEMs were finally normalized to have a zero-mean bed elevation.

For all experimental runs, detrended DEMs were first analyzed in terms of standard deviation ($\sigma_Z$), range ($\Delta_Z$) and skewness ($S_K$). The latter are bed-elevation moments contained in probability distribution functions (PDFs) and classical descriptors of bed roughness.

Generalized second-order structure functions of detrended bed elevations were also obtained:

$$D_{G2}(\Delta x, \Delta y) = \frac{1}{(N-n)(M-m)} \sum_{i=0}^{N-n} \sum_{j=0}^{M-m} \{ \left| z(x_i + n\delta x, y_j + m\delta y) - z(x_i, y_j) \right| \}^2 \quad [1]$$

where, $\Delta x = n\delta x$ and $\Delta y = m\delta y$; $\delta x$ and $\delta y$ are the sampling intervals (both 1 mm) in the longitudinal and transverse directions respectively; n=1,2,3,…N and m=1,2,3,…M. N and M are the number of samples (801 and 301, respectively) in the same two directions. The maximum spatial lag in both x and y directions was chosen as ±100 mm, being larger than the maximum particle size and sufficient to reach the saturation region. Horizontal (grain-) roughness indices $\Delta X_0$ and $\Delta Y_0$ were determined from 1D structure functions, in both x and y directions (Nikora et al., 1998). Because analyzed DEMs were detrended, observed patterns of statistical elevation correlation indicate characteristics of grain size, shape and 2D arrangement on the bed surface.

Furthermore, the inclination index (I) was evaluated. The inclination index measures grain imbrication, by analyzing the signs of elevation changes between successive pairs of detrended DEM points at different lags, in different directions (Millane et al., 2006):

$$I(d, \theta) = \frac{n_+(d, \theta) - n_-(d, \theta)}{N(d, \theta)} \quad [2]$$

where $n_+$ and $n_-$ are the number of positive and negative slopes, respectively, and N is the total number of slopes, all functions of the separation or lag d between pairs of DEM points and the angle θ formed with the flow direction. A positive slope was defined as increasing elevations along the flow direction. Inclination indices were computed using d = 1 mm, which is the DEM grid spacing. Slopes, whose absolute value was below 0.01, were deemed not reliable, and were not counted in the numerator of Eqn. 2 (Millane et al., 2006). We focused the analysis on I(0°), the inclination index measuring grain imbrication in the flow direction.

To test the hypothesis that stable armors are replicable under identical flow and sediment conditions, we compared the variability between replicated runs with the spatial variability within DEMs (inner variability), in terms of the different DEM properties measured during the study. All detrended DEMs were divided in three parcels of size 266 × 300 $mm^2$ and each DEM subset was analyzed independently. The coefficient of variation (CV) was calculated for each DEM as the standard deviation of the DEM property divided by the mean, and reported as a percentage, using the three DEM subsets, providing there were only positive values. Each DEM of the same sediment and surface type (e.g., all three armors formed with sediment 1 at the discharge $Q_1$) was characterized by the same inner variability for the different DEM properties. Hence, the CVs were averaged using all nine DEM subsets of the same surface type and sediment. We thus (1) compared the variability between replicated runs using the same sediment mixture and the average spatial variability within these same DEMs; (2) concurrently, a MATLAB® routine ensured no significant difference on the mean (i.e. average) values determined using the three subsets of any replicated surface, using paired t-tests at a confidence level α = 0.01. The observation of a similar variability (1) together with no significant difference on the mean (2) would lead to the conclusion that replicated surfaces cannot be distinguished.

## 3 RESULTS

The decline in sediment transport rate with armoring time (Figure 2) was well described by a relationship of the form $q_s = c.t^n$ (with c and n constants), which is characteristic of static armoring (e.g., Proffitt, 1980; Marion et al., 2003). Distinct trends in transport reduction were observed depending on the flow discharge, while no difference was observed between the sediment mixtures. The transport reduction during armoring with $Q_2$ was slower: only 30% of the total bedload charge was removed during the first 20 hours, with erratic transport up to 100 hours of armoring time.

Figure 3 shows the changes in bed-surface composition after armoring. Armoring with $Q_1$ altered the bed surface substantially, with a consistent increase for all percentiles (i.e. $D_{16}$, $D_{50}$ and $D_{84}$). Application of $Q_2$ only

 

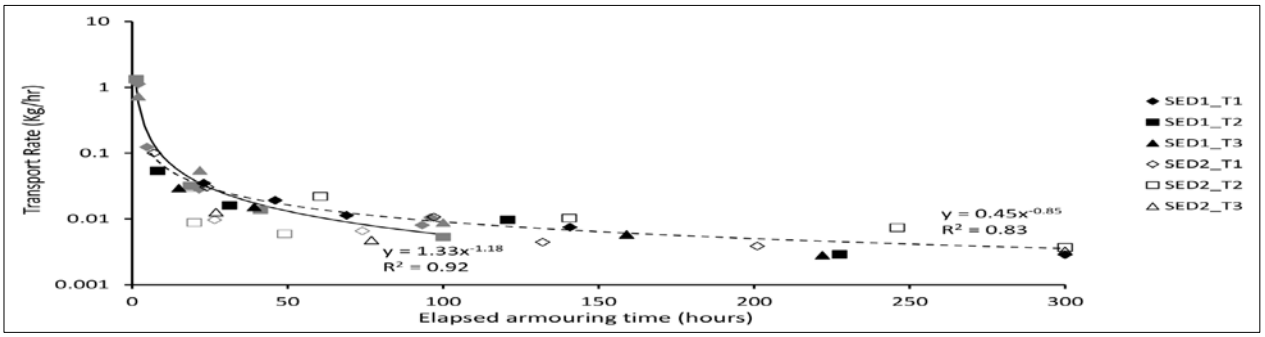


**Figure 2.** Sediment transport for all replicated runs during armoring with $Q_1$ on the initially screeded flat gravel-beds (grey markers and continuous line); and armoring with $Q_2$ on the beds previously armored with $Q_1$ (black markers and dashed line).

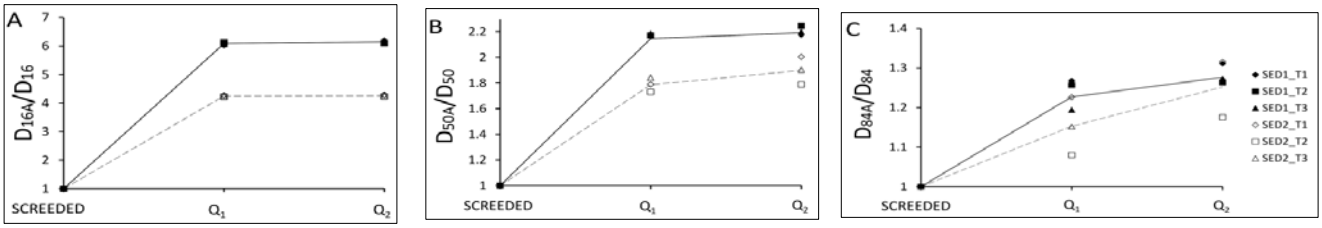


**Figure 3.** Bed surface composition, in terms of (A) $D_{16}$, (B) $D_{50}$ and (C) $D_{84}$, for the different bed states (i.e. screeded, armored with $Q_1$ and armored with $Q_2$). Armor compositions obtained with Basegrain® (associated with the subscript "A") were normalized by the bulk mixture characteristics (Figure 1B). The lines represent the average trends for each sediment mixture (continuous black lines for sediment 1; dashed grey lines for sediment 2).

impacted the coarse end of the GSD. The greater variability in the armor $D_{84}$ (i.e. $D_{84A}$), compared to $D_{16A}$ and $D_{50A}$, likely relates to the preparation of the initial screeded beds and to the availability of coarse particles being uncovered by the flow. Measuring the armor ratio (defined as $D_{50A}/D_{50}$) shows that sediment 1 allowed the surface to armor more than the better-sorted sediment 2 (armor ratio of 2.2 and 1.8, respectively). The armor ratios were virtually unchanged despite re-armoring with $Q_2$ (paired t-test, no significant difference at $\alpha = 0.01$).

Preferential armor grains' orientation is presented in Figure 4. For both sediment mixtures, armor grains preferentially aligned their long axis (i.e. a-axis) with the flow direction during $Q_1$. The proportion of grains perpendicular to the flow was larger after $Q_2$ (Figure 4C).

Bed-elevation moments measured from the detrended DEMs are presented in Figure 5. The analysis reveals that the two sediment mixtures adjusted identically to the imposed flow rates in terms of distribution skewness, but evidences significant differences for the range and standard deviation (paired t-tests, $P < 0.05$).

Sediment 2 formed rougher surfaces for the two discharges, indicated by larger $\Delta_Z$ and $\sigma_Z$ compared with sediment 1 (paired t-tests, $P < 0.05$). Only $\sigma_Z$ changed significantly between $Q_1$ and $Q_2$ water-working (difference significant, $P < 0.05$), for both sediment mixtures, indicating surface roughening with discharge increases (e.g., Aberle and Nikora, 2006), whilst neither $S_K$ nor $\Delta_Z$ values were significantly impacted.

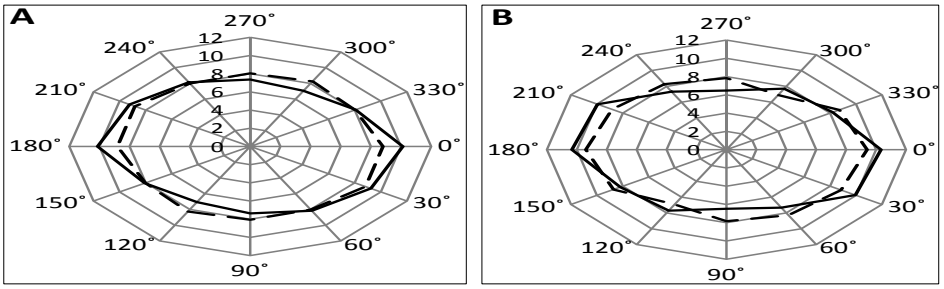


**Figure 4.** Frequency distribution of bed-surface material for different a-axis orientations, with (A) sediment 1 and (B) sediment 2. The general tendency for each discharge is presented (continuous line for $Q_1$; dashed line for $Q_2$), which was obtained by averaging the results over the three replicated runs.

Results obtained from second-order structure functions are presented in Figure 5D and 5E**.** It is shown that both sediment mixtures formed armors with identical horizontal grain-roughness indices (paired t-test, P <

 

0.01), in both the downstream and transverse directions. Grain-roughness indices in the flow direction were on average longer than cross-flow indices, and both indices increased with discharge (differences significant at α = 0.01).

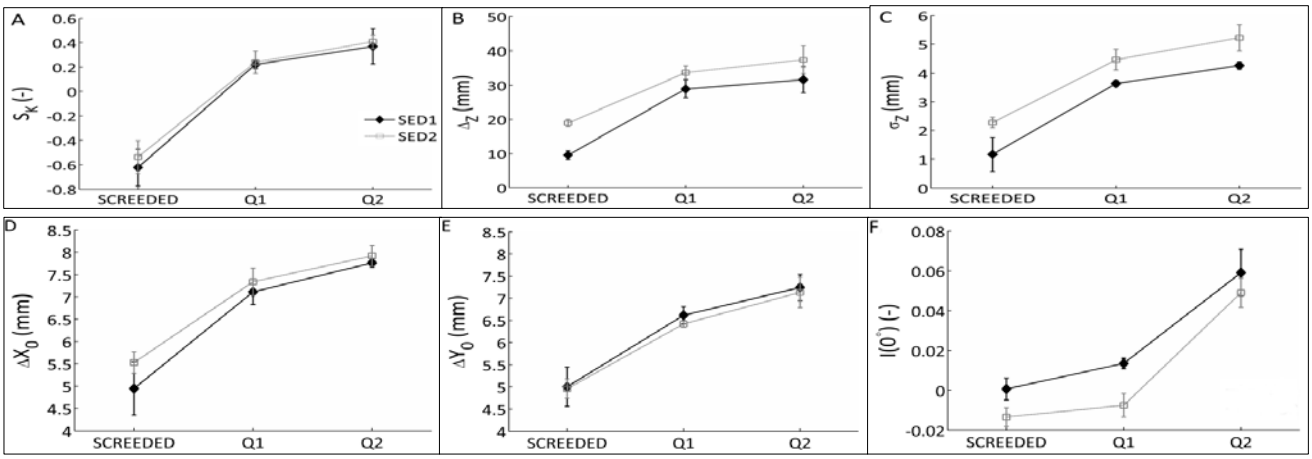


**Figure 5.** (A) skewness ($S_K$), (B) range ($\Delta_Z$) and (C) standard deviation ($\sigma_Z$) of detrended bed elevations for all replicated runs. (D, E) are the horizontal grain-roughness indices ($\Delta X_0$, $\Delta Y_0$) determined from 2$^{nd}$-order structure functions along (D) the downstream (x), and (E) the transverse (y) direction. (F) is the inclination index representing grain imbrication in a direction parallel to the flow (θ = 0°). The trend for each sediment mixture is presented, which was obtained by averaging the results over the three replicated runs. The error bars have a length equal to two times the standard deviations, centered on the mean value.

Figure 5F shows results for the inclination index, measuring grain imbrication in the flow direction. Screeded beds were characterized by a negative or near zero (0°), suggesting no grain imbrication. Only the beds made of sediment 1 showed grain imbrication after armoring with $Q_1$. However, the small inclination index values (≃0.0175) suggest that imbrication was weak and limited to small portions of the bed. $Q_2$ was competent enough to imbricate particles for both sediment mixtures.

Table II compares the variability between replicated surfaces and the average (inner) variability within these same surfaces, for the parameters measured in this study, using the percent coefficient of variation (CV). It shows firstly that armored beds have smaller CVs, therefore are more consistent, both spatially and between replicated runs than screeded beds prepared manually. Secondly, the difference in variability between replicated armors and within DEMs is small, even suggesting a larger variability within DEMs than between replicated runs. In parallel, we verified the hypothesis that the mean (i.e. average) property values determined using the three subsets of any replicated run do not differ statistically using paired t-tests (α = 0.01), for the different DEM properties.

**Table II:** Variability (using the percent coefficient of variation, CV) between and within replicated surfaces. The variability within a DEM was measured using three DEM subsets of size 266 × 300 mm$^2$. N.A stands for non-applicable, because of the existence of negative values, preventing the use of the coefficient of variation.

| | | | $S_K$ | $\sigma_Z$ | $\Delta X_0$ | $\Delta Y_0$ | I(0°) |
|---|---|---|---|---|---|---|---|
| SEDIMENT 1 | Averaged CV | Screeded | *N.A* | 12.7 | 3.5 | 2.5 | *N.A* |
| | within DEMs | After $Q_1$ | 47.1 | 6.1 | 4.0 | 3.1 | 70.6 |
| | | After $Q_2$ | 32.8 | 5.1 | 1.4 | 1.9 | 31.5 |
| | CV between | Screeded | *N.A* | 16.1 | 12.1 | 8.8 | *N.A* |
| | repeat runs | After $Q_1$ | 15.5 | 2.6 | 4.0 | 2.9 | 19.7 |
| | | After $Q_2$ | 38.8 | 4.0 | 1.3 | 4.1 | 19.8 |
| SEDIMENT 2 | Averaged CV | Screeded | *N.A* | 16.1 | 6.0 | 5.0 | *N.A* |
| | within DEMs | After $Q_1$ | 87.6 | 5.2 | 2.6 | 4.1 | *N.A* |
| | | After $Q_2$ | 16.6 | 6.7 | 2.5 | 4.1 | 71.3 |
| | CV between | Screeded | *N.A* | 13.1 | 4.3 | 4.3 | *N.A* |
| | repeat runs | After $Q_1$ | 38.8 | 12.3 | 4.2 | 1.1 | *N.A* |
| | | After $Q_2$ | 13.6 | 1.2 | 2.9 | 4.8 | 15.0 |

## 4 DISCUSSION

The use of a vertically adjustable test section in our tests allowed analysis of bed degradation under consistent bed shear stress, which was critical to study armor replicability. The progressive transport reduction characteristic of static armors (Proffitt, 1980; Marion et al., 2003) was consistent throughout the six runs ($R^2$ =

 

0.92 and 0.83 for $Q_1$ and $Q_2$, respectively), which verified that the sediment recess was correctly adjusted upwards for all runs according to the rate of bed degradation (Figure 2).

In accordance with previous works, which showed that armor composition is specific given the parent bed material and formative discharge during parallel degradation (e.g., Garde et al., 2006), our armor composition replicated well between runs using the same sediment, yet varied substantially between the two sediment mixtures (Figure 3). The latter can be explained by different flow competencies. Increasing the flow discharge from $Q_1$ to $Q_2$ did not alter the degree of armoring (unchanged armor ratio), suggesting the persistence of the armor formed with $Q_1$ and constant roughness effects.

In contrast, we measured changes in grain orientation during $Q_2$, with increasing grains aligned perpendicular to the flow direction (Figure 4). Furthermore, grain roughness increased during $Q_2$, as shown by increasing $\sigma_Z$ values (Figure 5C). This strengthens the argument that fluvial surfaces react to moderate changes in flow strength through a variety of processes.

Likewise, we measured increases in horizontal roughness length with armoring (Figure 5D, 5E), which can be explained by surface coarsening (Figure 3) and particle grouping. Observations of grain imbrication also support surface alterations due to armoring (Figure 5F). Armors formed with $Q_2$ presented accentuated grain imbrication, compared to the armors formed with the lower discharge $Q_1$.

Hence, despite difficulties preparing the screeded beds identically at the beginning of each run, due to the random distribution of coarse particles near the surface after manual preparation of the beds, our experimental data showed that water-working had a notable effect for the initial random sediment organization, creating more pronounced patterns, such as grain packing and grouping, interlocking and imbrication. We observed an augmented surface consistency (Table II), together with a similar variability in armor properties between repeat armors and within these same surfaces. Together with our finding that mean values, measured using the three subsets of any replicated surface, were consistent, this provides strong evidence for armor replicability - for a given formative discharge and parent bed material. This finding has been assumed previously (e.g., Aberle and Nikora, 2006), yet never proven.

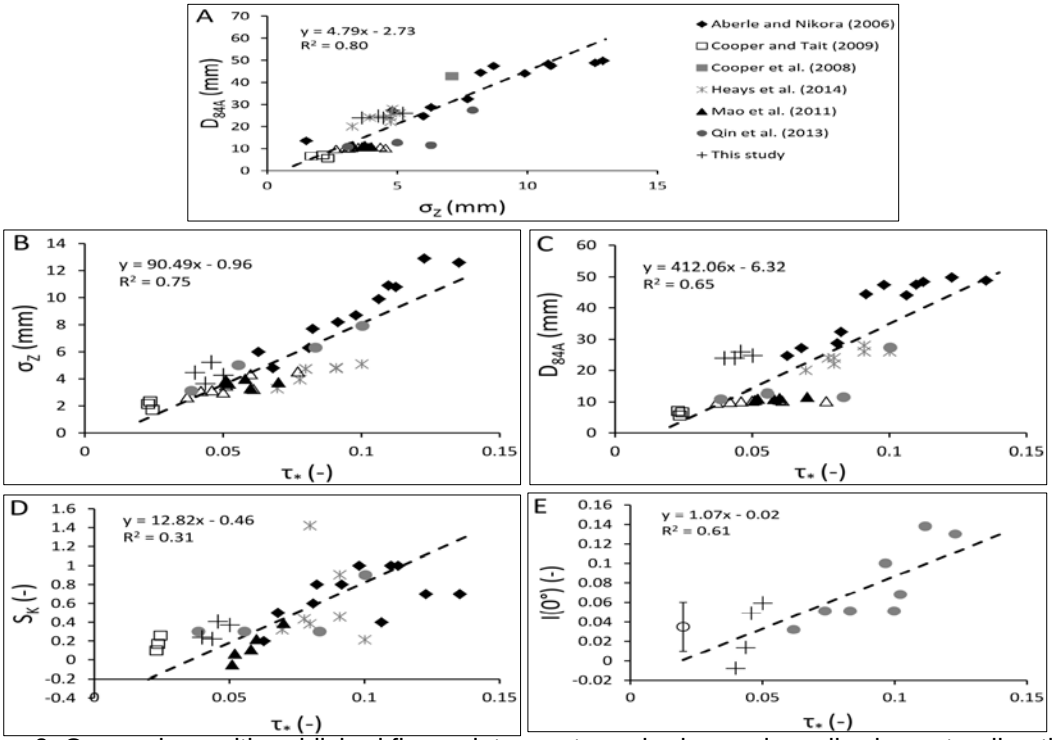


**Figure 6.** Comparison with published flume data on streambed armoring, allowing extending the analysis of the formative controls on gravel-bed armors. Open markers correspond to mobile armors (formed with either sediment feeding or sediment recirculating). The open round marker in subplot (E) corresponds to data from *Pledger et al.* (2014). In the case data was not collated in tables, it was digitized from graphs with the best care possible. Depending on the data source, the Shields stress had to be re-calculated from the shear stress and the bulk mixture $D_{50}$. Dashed lines are the functional lines best representing the data (Mark and Church, 1977).

When compared with previous studies on stable armor composition (e.g., Garde et al., 2006), our experimental results therefore suggest that a gravel-bed's response is specific to the formative parameters. To strengthen this argument and to provide a broader context for our findings, we combined our experimental results with those from previous flume studies on streambed armoring (Figure 6). The combined analysis of 43

 

gravel armors, of which 12 were mobile armors (Cooper and Tait, 2009; Mao et al., 2011; Pledger et al., 2014), extended the range of parent bed ($D_{50}$ = [4 - 11] mm) and formative discharge ($\tau_*$ = [0.02 - 0.14]) and allowed extending the analysis of the effects of discharge and bed composition on the armor properties. The extended dataset presented in Figure 6A confirms the strong link between armor composition and armor topography. A better agreement was observed between $D_{84A}$ and $\sigma_Z$, compared to $D_{50A}$ and $\sigma_Z$ ($R^2$ = 0.80 and $R^2$ = 0.62, respectively), suggesting that the arrangement of coarse grains on the surface, which protrude higher into the flow and form the anchor for small-scale bedforms (e.g., Piedra et al., 2012), is an essential control on gravel-bed topography. Because of the good relationship between armor $\sigma_Z$ and grain-size properties, commonly researchers suggest the interchangeable use of $\sigma_Z$, $D_{50A}$ and $D_{84A}$ as indicators of surface roughness. However, we observed in this study that armor topography is more sensitive to changes in flow discharge than armor composition, and shows a better relationship with the Shields stress (Figures 6B and 7C). The analysis of 43 gravel armors showed that $\sigma_Z$, $S_K$ and I(0°) increase with Shields stress, confirming previous assumptions of a strong control of flow discharge on armor topography (e.g., Aberle and Nikora, 2006; Mao et al., 2011). Figure 6E shows that streamwise particle imbrication increases with transport capacity, supporting past statements that imbrication forms as a result of the entrainment of the coarse sediment fraction in a mixture (Rust, 1972).

## 5 CONCLUSIONS

Experimental gravel beds, water-worked in a laboratory flume under conditions of zero sediment feed and selective transport, have been analyzed using a range of accepted statistical methods in order to examine the formative controls for gravel-bed armors. The use of photogrammetric techniques enabled a detailed characterization of gravel-bed surfaces and their adjustments to competent flows. We presented the efficient and effective measurement of bed composition and topography through water, which obviated the need to drain and refill the flume in-between measurements.

We showed that bed topography (structure) was more responsive to changes in flow discharge and displayed more degrees of adaptability than bed material size alone. Our experimental data supported the hypothesis that stable armor properties are replicable under identical flow and sediment conditions. This suggests that in conditions of parallel degradation, gravel-bed's response to water-work is specific to the formative parameters, even though the inherent mechanisms for the armor layer formation are stochastic. The addition of independent data from previous flume studies on streambed armoring illustrated the importance of two formative controls on armor structure: the Shields stress and the parent bed composition.

Future work may try to further our understanding of the effect of sediment supply and flow duration onto armor properties formed in the laboratory, which would ultimately allow more realistic investigations of field processes.

## ACKNOWLEDGMENTS

The study was partly funded by the Marsden Fund (Grant No. UOA1412), administered by the Royal Society of New Zealand. The authors would like to thank M. Dequidt and S. Stähly for their assistance during the experimental programme.

## REFERENCES

Aberle, J. & Nikora, V. (2006). Statistical Properties of Armored Gravel Bed Surfaces. *Water Resource Research,* 42(11), 1-11.

Bertin, S., Friedrich, H., Delmas, P. & Chan, E. (2013). On the use of Close-Range Digital Stereo-Photogrammetry to Measure Gravel-Bed Topography in a Laboratory Environment. *35th IAHR Congress,* Chengdu, China.

Bertin, S., Friedrich, H., Delmas, P., Chan, E. & Gimel'farb, G. (2015). Digital Stereo Photogrammetry for Grain-Scale Monitoring of Fluvial Surfaces: Error Evaluation and Workflow Optimisation. ISPRS *Journal of Photogramm and Remote Sensing,* 101, 193-208.

Chin, C., Melville, B. & Raudkivi, A. (1994). Streambed Armoring. *Journal of Hydraulic Engineering,* 120(8), 899-918.

Clayton, J.A. & Pitlick, J. (2008). Persistence of the Surface Texture of a Gravel-Bed River during a Large Flood. *Earth Surface Processes and Landforms,* 33(5), 661-673.

Cooper, J.R. & Tait, S.J. (2009). Water-Worked Gravel Beds in Laboratory Flumes - A Natural Analogue? *Earth Surface Processes and Landforms,* 34(3), 384-397.

Detert, M. & Weitbrecht, V. (2012). *Automatic Object Detection to Analyze the Geometry of Gravel Grains*. Riverflow 2012, San Jose, Costa Rica, Taylor And Francis Group.

Fehr, R. (1987). *Geschiebeanalysen in Gebirgsflüssen Translated Analysis of Sedimentary Bed Material in Mountain Rivers*, *Conversion and Comparison of Various Analytical Methods*. Mitteilungen Derversuchsanstalt Fürwasserbau, Hydrologie Und Glaziologie, Eidgenössische Technische Hochschule, Zürich, Nr. 92.

 

Garde, R.J., Sahay, A. & Bhatnagar, S. (2006). A Simple Mathematical Model to Predict the Particle Size Distribution of the Armour Layer. *Journal of Hydraulic Research,* 44(6), 815-821.

Gessler, J. (1967). *The Beginning of Bedload Movement of Mixtures Investigated as Natural Armoring in Channels. Pasadena, Calif*. W.M. Keck Laboratory of Hydraulics and Water Resources, California Institute of Technology.

Gomez, B. (1983). Temporal Variations in Bedload Transport Rates: The Effect of Progressive Bed Armouring. *Earth Surface Processes and Landforms,* 8(1), 41-54.

Gomez, B. (1993). Roughness of Stable, Armored Gravel Beds. *Water Resource Research,* 29(11), 3631-3642.

Gomez, B. (1994). Effects of Particle Shape and Mobility on Stable Armor Development. *Water Resource Research,* 30(7), 2229-2239.

Haschenburger, J.K. & Wilcock, P.R. (2003). Partial Transport in a Natural Gravel Bed Channel. *Water Resource Research,* 39(1), 1-9.

Heays, K.G., Friedrich, H. & Melville, B.W. (2014). Laboratory Study of Gravel-Bed Cluster Formation and Disintegration. *Water Resource Research,* 50(3), 2227-2241.

Hodge, R., Brasington, J. & Richards, K. (2009). Analysing Laser Scanned Digital Terrain Models of Gravel Bed Surfaces: Linking Morphology to Sediment Transport Processes and Hydraulics. *Sedimentology,* 56(7), 2024-2043.

Hodge, R.A., Sear, D.A. & Leyland, J. (2013). Spatial Variations in Surface Sediment Structure in Riffle–Pool Sequences: A Preliminary Test of the Differential Sediment Entrainment Hypothesis (DSEH). *Earth Surface Processes and Landforms,* 38(5), 449-465.

Lane, S.N. (2005). Roughness – Time For A Re-Evaluation? *Earth Surface Processes and Landforms,* 30(2), 251-253.

Laronne, J.B. & Carson, M.A. (1976). Interrelationships Between Bed Morphology and Bed-Material Transport For a Small, Gravel-Bed Channel. *Sedimentology,* 23(1), 67-85.

Mao, L., Cooper, J.R. & Frostick, L.E. (2011). Grain Size And Topographical Differences Between Static And Mobile Armour Layers. *Earth Surface Processes and Landforms,* 36(10), 1321-1334.

Marion, A., Tait, S.J. & Mcewan, I.K. (2003). Analysis of Small-Scale Gravel Bed Topography during Armoring. *Water Resource Research,* 39(12), 1-11.

Mark, D.M. & Church, M. (1977). On the Misuse of Regression In Earth Science. *Journal of the International Association for Mathematical Geology,* 9(1), 63-75.

Millane, R.P., Weir, M.I. & Smart, G.M. (2006). Automated Analysis of Imbrication and Flow Direction in Alluvial Sediments Using Laser-Scan Data. *Journal of Sedimentary Res*earch, 76(8), 1049-1055.

Nikora, V.I., Goring, D.G. & Biggs, B.J.F. (1998). On Gravel-Bed Roughness Characterization. *Water Resource Research,* 34(3), 517-527.

Ockelford, A.-M. & Haynes, H. (2013). The Impact of Stress History on Bed Structure. *ESPL,* 38(7), 717-727.

Odgaard, A.J. (1984). Grain Size Distribution of Riverbed Armor Layers. *Journal of Hydraulic Engineering,* 110(10), 1479-1484.

Paris, E. (1992). Time-Space Bed Load Evolution in Static Armour Formation. *Grain Sorting Seminar*, Ascona, Switzerland, Eidgenössische Technische Hochschule Zürich, Switzerland.

Parker, G. & Klingeman, P.C. (1982). On Why Gravel Bed Streams are Paved. *Water Resource Research.,* 18(5), 1409-1423.

Parker, G. & Sutherland, A.J. (1990). Fluvial Armor. *Journal of Hydraulic Research,* 28(5), 529-544.

Piedra, M.M., Haynes, H. & Hoey, T.B. (2012). The Spatial Distribution of Coarse Surface Grains and the Stability of Gravel River Beds. *Sedimentology,* 59(3), 1014-1029.

Pitlick, J., Mueller, E.R., Segura, C., Cress, R. & Torizzo, M. (2008). Relation Between Flow, Surface-Layer Armoring and Sediment Transport in Gravel-Bed Rivers. *Earth Surface Processes and Landforms,* 33(8), 1192-1209.

Pledger, A.G., Rice, S.P. & Millett, J. (2014). Reduced Bed Material Stability and Increased Bedload Transport Caused by Foraging Fish: A Flume Study with Juvenile Barbel (Barbus Barbus). *Earth Surface Processes and Landforms,* 39(11), 1500-1513.

Proffitt, G.T. (1980). Selective Transport and Armouring of Non-Uniform Alluvial Sediments, *PhD Thesis*. Department of Civil Engineering. Christchurch, University of Canterbury.

Richards, K. & Clifford, N. (1991). Fluvial Geomorphology: Structured Beds in Gravelly Rivers. *Progress In Physical Geography,* 15(4), 407-422.

Rust, B.R. (1972). Pebble Orientation in Fluvial Sediments. *Journal of Sedimentary Research,* 42(2), 384-388.

Smart, G., Duncan, M. & Walsh, J. (2002). Relatively Rough Flow Resistance Equations. *Journal of Hydraulic Engineering,* 128(6), 568-578.

Vericat, D., Batalla, R.J. & Garcia, C. (2006). Breakup and Reestablishment of the Armour Layer in a Large Gravel-Bed River Below Dams: The Lower Ebro. *Geomorphology,* 76(1–2), 122-136.

Wilcock, P.R. & Detemple, B.T. (2005). Persistence of Armor Layers in Gravel-Bed Streams. *Geophysical Research Letter,* 32(8).

 

# LARGE EDDY SIMULATIONS OF THREE DIMENSIONAL SEDIMENT DUNE EVOLUTIONS

HONGWEI FANG[(1)], YAN LIU[(2)], THORSTEN STOESSER[(3)] & CHENWEI ZHAO[(4)]

[(1,2,4)]Department of Hydraulic Engineering, Tsinghua University, Beijing, China
fanghw@tsinghua.edu.cn; yanliu12@mails.tsinghua.edu.cn; zcw16@mails.tsinghua.edu.cn
[(3)]School of Civil Engineering, Cardiff University, Cardiff, United Kingdom
stoesser@cf.ac.uk

## ABSTRACT

Large eddy simulations are performed for open channel flows with sediment dune evolutions. The turbulent flow is simulated with Hydro3D, which has been performed successfully on flow over several complicated geometries. Sediment transport module, consist of bedload transport and bed morphology evolution module are imbedded into the Hydro3D by the current author. The coupling of sediment particles and turbulent flow is achieved by applying the direct-force immerse boundary method on sediment particles. The code is firstly validated on a flow with two dimensional sediment dune evolutions. Simulated dune height and dune length evolution processes are compared with the processes of flume experiments. A well agreement is gained between the simulation and the experiment. Then, two kinds of three dimensional sediment dune initiation processes are simulated, i.e. dune propagation processes from defects and dune instantaneous initiation occurred over the entire bed. For the dune propagation processes, three major feathers are observed during the simulation: new dune crests develop with decreasing H and L with distance downstream, bed form field widens forming a triangular shape, and the dune crests take on a uniform H and L in cross section. While for the dune instantaneous initiation processes, the observed sediment dune crests demonstrate three shapes, i.e. lobe, straight and saddle, which is similar to those found in natural rivers and in coastal areas. Further investigation of the non-dimensional span (NDS) shows that the NDS decreases with time increment, which agrees with those found in flume experiments. In terms of the turbulent events, sweeps and ejections occurs more frequently on dune stoss side than the other two events (inward and outward interactions).

**Keywords**: Large eddy simulation; dune propagation; sediment transport; three dimensional dunes; dune evolution.

## 1 INTRODUCTION

Interactions between the flow, the sediment transport and the bed morphology, often lead to the formation of rhythmic patterns on river beds, such as dunes (e.g. Carling et al., 2000; Parsons et al., 2005). The migration and propagation of three dimensional sediment dunes have major impacts on humans and infrastructure. Despite decades of study of geomorphology and efforts in engineering, there exists no comprehensive theory capable of describing the formation of three dimensional sediment dunes.

Most research on small-scale bedforms suggests that, under low flow conditions, bedforms exhibiting a 2D straight-crested morphology are common and at higher flow velocities, 3D forms are established (Southard & Boguchwal, 1990; Southard, 1992). Some authors have argued that 3D bedforms form under 3D flow conditions, e.g. the transverse velocity affects the direction of bedload rate and thus form the three dimensional dunes (e.g. Ashley, 1990; Southard & Boguchwal, 1990; Southard, 1992). However, seminal works (Baas et al. 1994; Baas et al. 1999) have showed that although in 2D flow conditions, given enough time will observe the development of 3D dunes. Flume experiments by Venditti & Church (2005) also gave evidence that under 2D low conditions 3D bedforms initially developed over a flat bed. They argued that excesses sand pass from one bedform to another is responsible for the transition from 2D dunes to 3D dunes. However, there is no explanation of what causes these excesses sand when 2D dunes forms. Despite these efforts, the actual physical processes responsible for the formation of three dimensional sediment dunes are not well understood.

Recently, increasing computational power has led to reliable numerical codes to simulate dune evolution by solving coupled systems of flow, sediment transport and bed morphology (Tjerry et al., 2005; Nelson et al., 2006; Giri and Shimizu, 2006). These numerical codes are able to predict the time evolution of dune dimensions, dune shapes and dune migration, by associating flow separation and sediment transport to mean flow parameter under the RANS frame. However, many recent work have shown that sediment transport is related to the instantaneous flow conditions, such as the instantaneous downstream velocity, impulse, or force fluctuations (e.g., Nelson et al., 1995; Schmeeckle et al., 2007; Diplas et al., 2008). The numerical modes mentioned above are unable to study the relationship of dune evolution with instantaneous variables.

 

The objectives of the present study include the following:

(a) Establishment of a coupled hydro-morphodynamic numerical model for carrying out large-eddy simulation of stratified, turbulent flow over a mobile sand bed.
(b) Establishment of relationship between instantaneous flow parameters and bed initiations under low and high flow conditions.
(c) Answering how three dimensional sediment dunes develop under two dimensional flow conditions.

## 2 MATERIALS AND METHODS

### 2.1 The hydrodynamic model

Incompressible, unsteady and viscous flow were considered, which is governed by spatially filtered (LES) Navier-Stokes equations. The in-house code Hydro3D is employed for the method of large eddy simulation (LES). The code is based on a finite differences method on a staggered Cartesian grid and it has been validated for and applied to flows over various bed geometries, such as dunes, rough beds, and pool-riffle sequences. The filtered Navier-Stokes equations are expressed as below:

$$\frac{\partial u_i}{\partial x_i} = 0 \qquad [1]$$

$$\frac{\partial u_i}{\partial t} + \frac{\partial u_i u_j}{\partial x_j} = -\frac{\partial p}{\partial x_j} + \frac{\partial (2\upsilon S_{ij})}{\partial x_j} - \frac{\partial \tau_{ij}}{\partial x_j} \qquad [2]$$

where ui and uj are spatial resolved velocity vectors (i or j = 1, 2, and 3 represent x-, y- and z-axis directions, respectively; and similarly $x_i$, $x_j$ represent the spatial location vectors in the three directions; p is the spatial resolved pressure divided by flow density; $\upsilon$ = kinematic viscosity; and $S_{ij}$ denotes filtered strain-rate tensor and is calculated as $S_{ij} = 1/2(\partial u_i / x_j + \partial u_j / x_i)$. The subgrid scale (SGS) stress $\tau_{ij}$ is defined as $\tau_{ij} = -2\upsilon_t S_{ij}$. In this study, the wall-adapting local eddy viscosity (WALE) proposed by Nicoud et al. (1999) is used to calculate the eddy viscosity, $\upsilon_t$ and model the SGS stress.

The convection and diffusion terms in the Navier-Stokes equations are approximated by 4$^{th}$-order accurate central differences. An explicit 3-step Runge-Kutta scheme is used to integrate the equations in time, providing 2$^{nd}$-order accuracy. A fractional step method is employed, i.e. within the time step convection and diffusion terms are solved explicitly first in a predictor step which is then followed by a corrector step during which the pressure and divergence-free-velocity fields are obtained through a Poisson equation. The latter is solved iteratively through a multi-grid procedure. Details of the code are reported in Cevheri et al. (2016).

In terms of the fluid-solid interface, a no-slip condition is applied on the bed surface boundary to mimic mobile sediment-water interface. In order to achieve the no-slip condition, a refined version of the direct forcing immersed boundary method (IBM) proposed by Uhlmann (2005) is used.

### 2.2 Bed morphodynamics model

In this study, the case for which all sediment transport occurs in bed-load mode within a live layer are only considered. The temporal variation of the bed elevation is governed by the sediment continuity equation, the so-called Exner-Polya equation, which reads as follows:

$$(1-\gamma)\frac{\partial z_b}{\partial t} = -\nabla q_{BL} \qquad [3]$$

where $\gamma$ is sediment material porosity, $z_b$ is the bed elevation, $\nabla$ denotes the divergence operator, and $q_{BL}$ is the bed-load flux vector. Similar to the Navier-Stokes equations, equation (3) is solved on the Cartesian grid by the finite difference method. The local bed load transport rate is evaluated through the formula of Meyer-Peter and Muller (1948), including gravitational bed slope effects:

$$q_b = \begin{cases} \alpha(\tau(x) - \tau_c(x))^n (1 + \eta \frac{\partial z_b}{\partial x})^{-1} & if \quad \tau > \tau_c \\ 0 & if \quad \tau < \tau_c \end{cases} \qquad [4]$$

where $\tau$ is the bed shear stress ($m^2s^{-2}$) and $\tau_c$ is the critical bed shear stress. $\tau_c$ is determined using Shield's criterion (using the parameterized relation of Shield's curve (Van Rijn(1984)) as :

 

$$\tau_c = f(D_*) \qquad [5]$$

where $D_* = d_{50}[\frac{(\rho_s - \rho)g}{\rho\upsilon^2}]^{1/3}$

The local near bed shear stresses $\tau$ are difficult to determine. Here we use an empirical formula suggested by Paarlberg et al. (2009) downstream of dune crests as:

$$\tau(x) = \begin{cases} 0 & if \quad x_s < x \le x_r \\ a_3 x'^3 + a_2 x'^2 + a_1 x' + a_0 & if \quad x_r < x \le x_m \end{cases} \qquad [6]$$

in which $x_s$ is the flow separation point, $x_r$ the reattachment point, $x_m$ the x coordinate of the maximum bed shear stress, $x' = x - x_r$ , and $a_0$ … $a_3$ are coefficients.

The coefficients are determined as $a_0 = \tau_c$ . $a_1$ is specified as $a_1 = 2\frac{\tau_m - \tau_r}{x_m - x_r}$ as suggested by Paarlberg et al. (2009). $a_3$ are set to be 0 as suggested by Paarlberg et al. (2009). $a_2$ are calculated through the smooth condition at the dune crest proposed by Paarlberg et al. (2009). Several flume experiments have showed that the reattachment length of the flow is around 5 times of the dune height. Therefore, $x_r = 5H_d$ , in which $H_d$ is the dune height.

The proportionality constant and the exponent n applied in the present study are 5.7 and 1.5 respectively, as suggested by Yager et al. (2007) in the bed load dominant rivers. The bed slope parameter reflects the downhill preference of moving sediment and is inversely related to the tangent of the angle of repose (Sekine and Parker (1992)):

$$\eta = \frac{1}{\tan(\varphi)}. \qquad [7]$$

In order to prevent the bed slope from exceeding the sediment material angle of repose, a mass-conservative sand-slide algorithm has been developed and incorporated. After solving the Exner-Polya equation and computing the new bed elevations, the entire bed is swept to identify bed cells at which the transverse and streamwise bed slope is larger than the angle of repose. The local slope correction procedure of the sand-slide model is then applied only to the identified bed cells.

### 2.3 Description of the experimental test cases

The flow and sediment transport were simulated in a straight laboratory flume studied experimentally in a series of papers by Venditti et al. (Venditti et al. 2005;2005a;2005b;2006). These experiments include detailed and systematic observations of sediment dune initiation, growth and transition from 2D to 3D geometry, as well as quantitative measurements of the temporal variation of bedform characteristics, such as amplitude, wavelength, and celerity. Only a brief introduction of the experimental set-up and flow conditions are given here. For more details, the reader is referred to the original papers, Venditti (Venditti et al. (2005;2005a;2005b)).

Venditti and Church (2005) employed a tilting flume with recirculating flow of water and sediment. The flume dimensions were 15.2 m long, 1.0 m wide and 0.3 m deep. Venditti and Church (2005) carried out five experimental runs under various subcritical turbulent flows ranging from a mean flow velocity of 0.36 to 0.5 m/s and a flow depth of approximately 0.15 m. In their experiment, two kinds of initiate bed geometry were used before experimental runs, carefully flattened bed and flattened bed with an artificial defect. A uniformly graded non-cohesive sand material with a median grain size of d50=0.5 mm and grain density of =2650 kg/m3 was used. Instantaneous images of the evolving bedforms were captured at 10 s time intervals using a high resolution video camera mounted above the flume and focusing on an observation window that covers an area of 1.0 m x 0.92 m and centered at ~10.3 m downstream of the channel's inlet. Two acoustic echo sounders were used to measure the celerity of sand dunes. Once the bedforms reach equilibrium, the average sand dune amplitude is between 19.7 and 47.7 mm and the average sediment wavelength range between 0.3 and 1.2m.

Three of the experiment runs described above conducted by Venditt and Church (2005) were chosen to investigate dune development from flat bed, a negative defect and a positive defect. It is important to mention that the critical threshold for the sand used in these experiments occurs at $\tau$ =0.30 pa. In Run B and Run C, the bed shear stress is just above the critical shear stress and in Run A, the bed shear stress is approximately

 

2.5 times of the critical shear stress. The difference in flow strength (bed shear stress) is thought to cause different types of bed initiation modes (Venditti and Church (2005)). Therefore, the differences of the shear stress were maintained in the different numerical simulations.

## 3 RESULTS AND DISCUSSIONS

### 3.1 Validation

To validate the numerical model, a 2D sediment dune evolution process from flat mobile sand bed was conducted (See Figure 1). The flume experiments were conducted by Naqshband et al. (2016) and the experiment data (amplitude and length) was reported by Naqshband et al. (2016). The experimental set-ups and flow conditions were used in the simulations, which were not shown in this paper. For more details, the reader is referred to the original papers (Naqshband et al. (2016)).

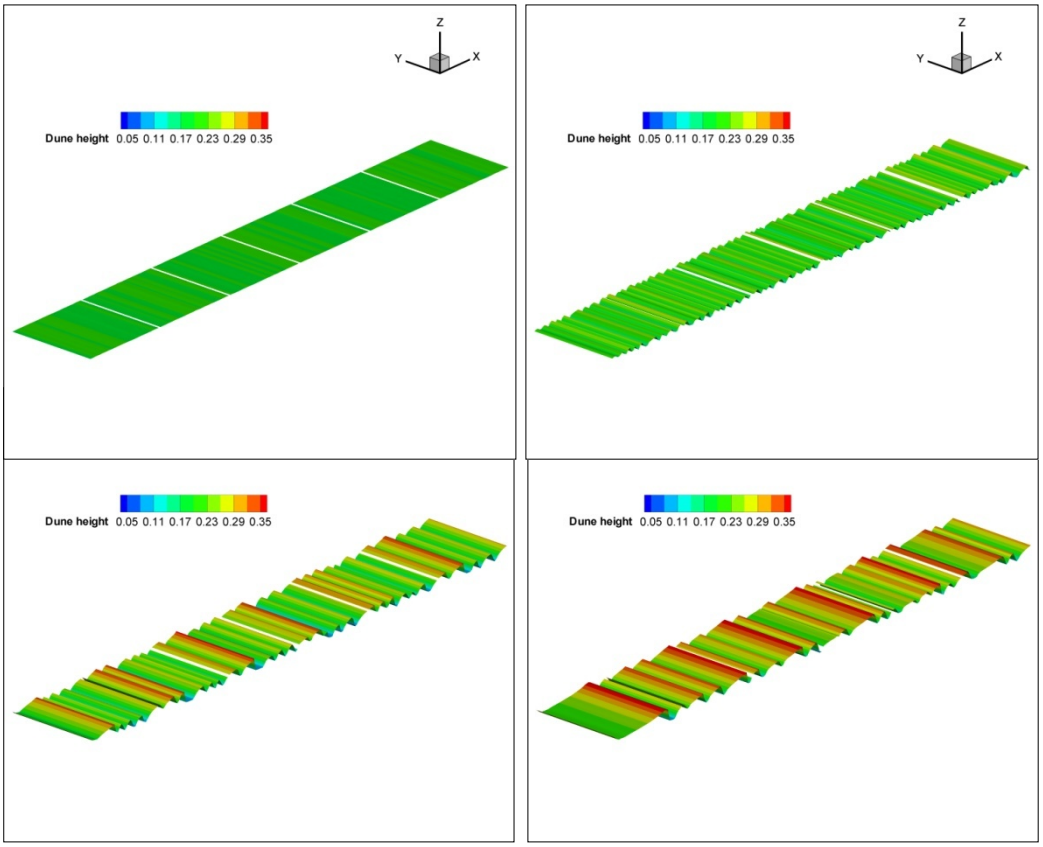


**Figure 1.** 2D sediment dune evolution process.

In Figure 2, the simulated temporal variation of sediment dune characteristics (amplitude and length) was plotted along with the experiment data reported by Naqshband et al. (2016). It was evident that the simulations gave a reasonable good prediction of the sediment dune characteristics development compared with the experimental data except for the very beginning of the simulation. The most significant discrepancies were observed during the early stages of the process when the simulated sand wave appears to grow in amplitude somewhat faster than the measurements. In general, figure 2 showed that the simulations capture sediment dunes whose characteristics were comparable to what was measured in the laboratory.

 

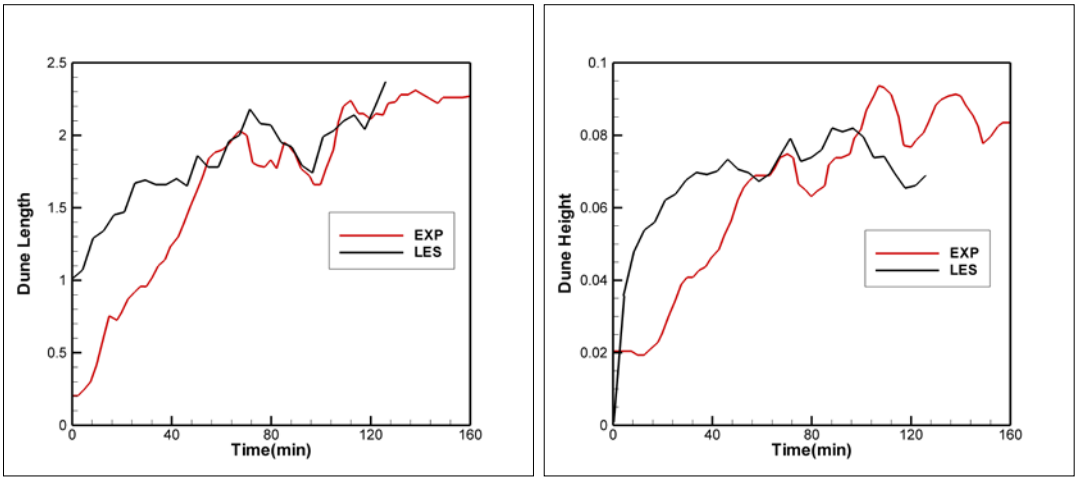


**Figure 2.** Comparison of the simulated and experimental dune length (left) and the dune height (right).

3.2 Dune propagation from defects

The propagation processes from positive defects is shown in Figure 3(a-c). The bed was initially flat but with a positive defect at the place of x/H=1.5 and y/H=1. The defect is 10mm in height and 30mm in circumference (Figure 3. (a)). In Figure 3, three major feathers during the positive defects propagation process is observed: new dune crests develop with decreasing H and L with distance downstream, bed form field widens forming a triangular shape, and the dune crests take on a uniform H and L in cross section. Five new dune crests are formed and the contour showed that H and L of these new dune crests decreases with distance downstream of the defect. The bed form field are widen as a triangular shape for the first three new dune crests. For the last two dune crests, they are not well developed yet and therefore the triangular shape is not observed. The dune crest took on a similar H and L distribution in cross section compared with the experiment. These feathers are also captured for the propagation processes from negative defects as shown in Figure 4. The original negative defect formed a U-shape, scour pit developed downstream of the defects with sediment accumulated at the downstream edge of the scour pit, and the new crests are narrowed incipiently and widened transversely with time.

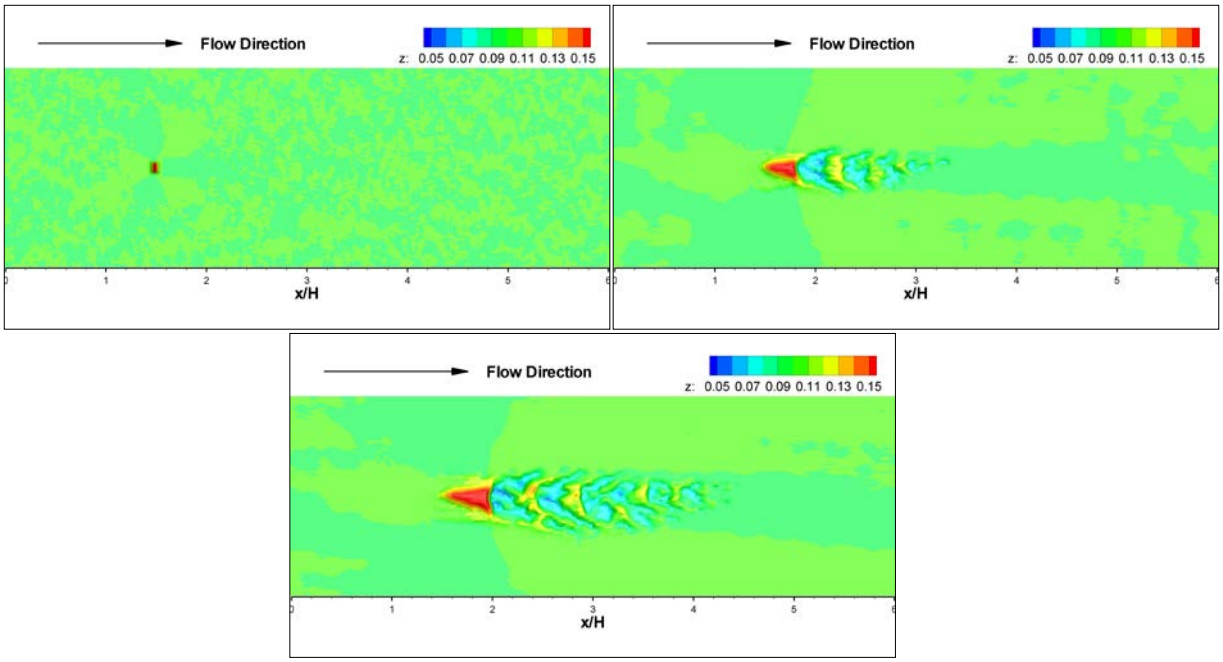


**Figure 3.** Simulated dune propagation processes from positive defects.

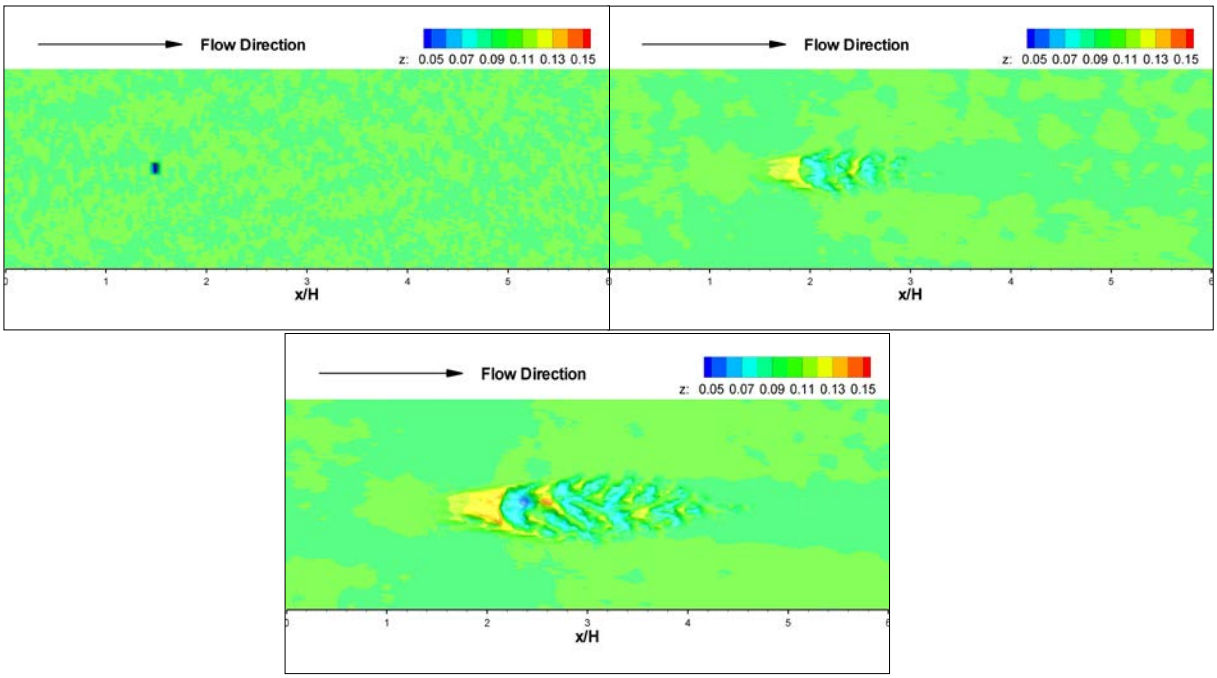


**Figure 4.** Simulated dune propagation processes from negative defects.

3.3 Instantaneous initiation over the entire bed

When flow strength increases, dune instantaneous initiation occurred over the entire bed. The results are shown in Figure 5. Also plotted here (Figure 6) is a picture of the natural three dimensional sediment dunes along the coastal line in Beidaihe City, China. In general, the three dimensional sediment dunes generated in the simulation looked similar to those found along the coastal line, including the curvature, dune height and dune length. From figure 5(a) to figure 5(b), minute sand waves are firstly generated over the flat bed. These minute sand waves are curving and the extent are not very long in the transverse direction. Then, the minute sand waves merged together and forms larger sediment dunes, which occupied the whole computational domain in the transverse direction. The dune crestlines are further extracted in Figure 5 and shown in Figure 7. Three types of dune crestlines are found, straight crestline (transversely perpendicular to the flow direction), saddle crestline (crestline bending against the flow direction) and lobe crestline (crestline bending towards the flow direction).

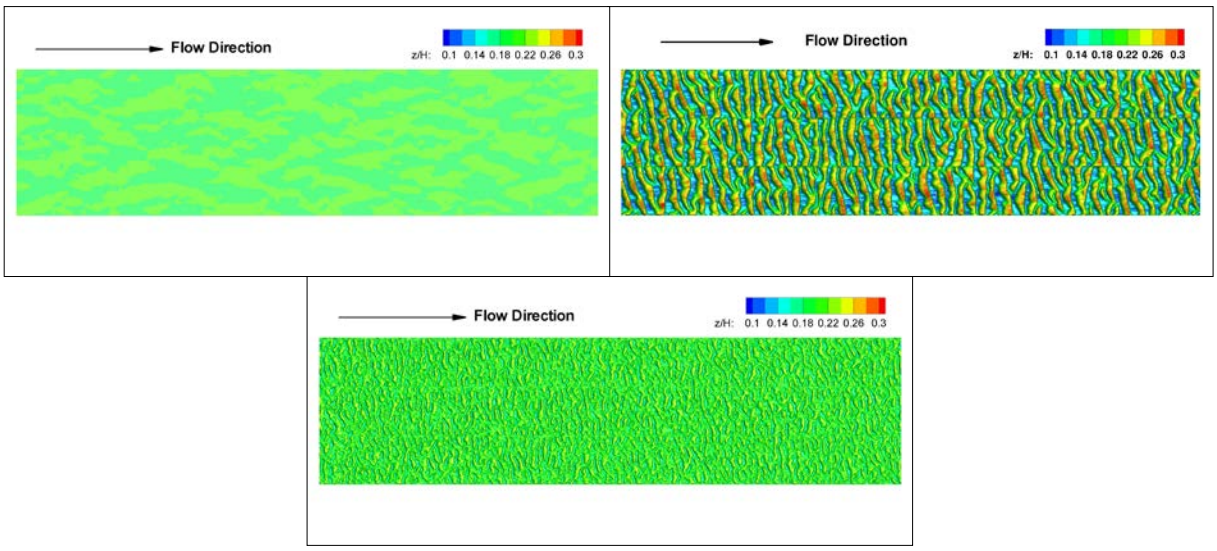


**Figure 5.** Simulated dune instantaneous initiation occurred over the entire bed.

**Figure 6.** A picture of the natural three dimensional sediment dunes along the coastal line in Beidaihe City, China.

Venditti et al. (2005b) defined a simple measure of the crest curvature or sinuosity, the non-dimensional span as NDS=Lc/Ly, where Lc is the length of the crestline and Ly is the length in the transverse direction from the ends of the same crestline (see definition in supporting material (8)). The NDS of the crestline is then calculated from both simulations. The results are plotted in Figure 7. Venditti et al. (2005b) reported that the NDS would decrease from 1.2 to 1.02 in the first 450s during the initial of the dune crest. This phenomenon is observed in these simulations, which revealed that the initial sand wave curves more than the well-developed sediment dunes (also see figure 5).

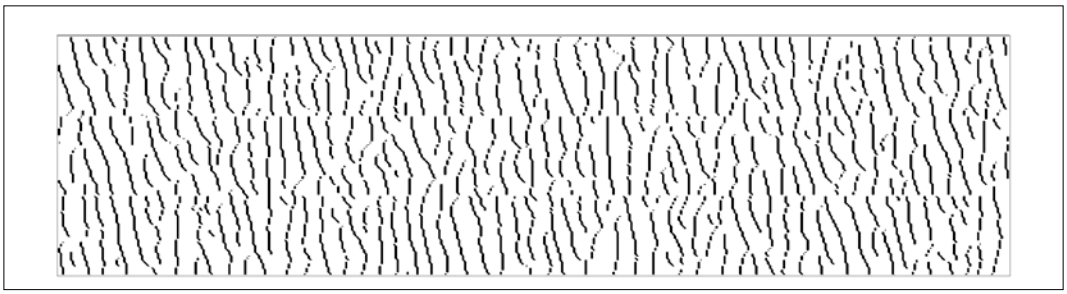

**Figure 7.** Crestlines extracted from the fully developed three dimensional sediment dunes.

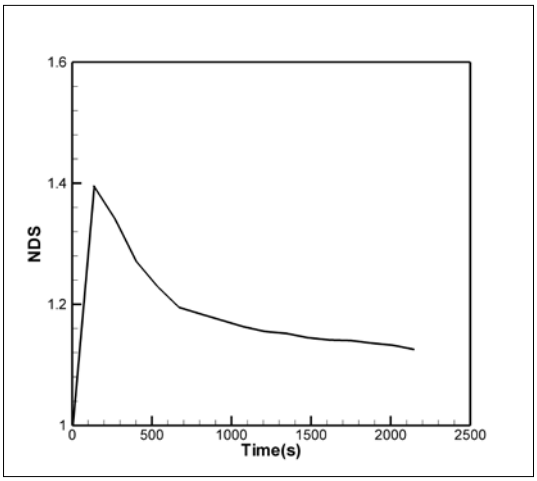


**Figure 8.** Non-dimensional span (NDS) during the simulation of the instantaneous initiation.

3.4 Turbulent events during dune evolution

To better understand the impact of coherent flow structures on dune formation, quadrant analyses of the velocity fluctuations were performed on the LES results. Time series of instantaneous velocities were collected near the dune bed surface. Next, the streamwise and vertical fluctuating components were calculated as

$$u' = u - < u > \quad [8]$$

$$w' = w - < w > \quad [9]$$

where u and w were the instantaneous streamwise and vertical velocities; and <u> and <w> are the time-averaged streamwise and vertical velocities. The joint distribution of u' and w' is divided into four quadrants: busts (u'<0, w'>0), sweeps (u'>0, w'<0), inward interactions (u'<0, w'<0) and outward interactions (u'>0, w'>0). The quadrant results are shown in figure 9. As shown in figure 9, the stoss side of the dune is covered mostly with red (sweeps) and green (bursts) area. Whereas, the blue (inward interactions) and yellow (outward interactions) area occupied much less area.

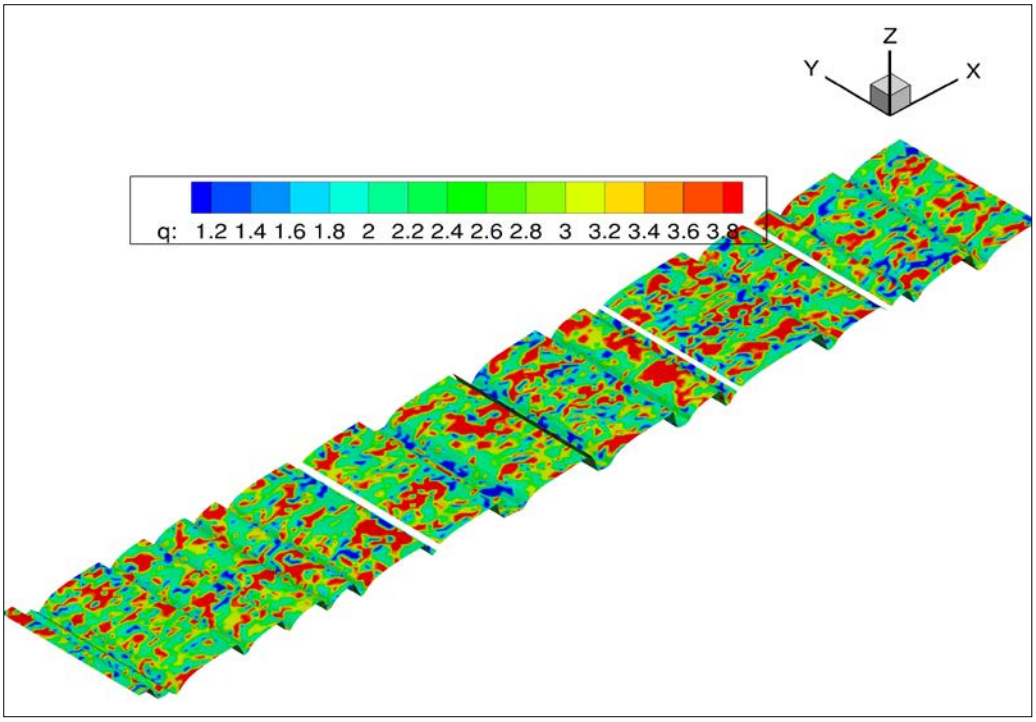


**Figure 9.** Turbulent events near the dune surface.

## 4 CONCLUSIONS

A coupled hydro-morphodynamic numerical model is developed for carrying out large-eddy simulation of stratified, turbulent flow over a mobile sand bed. The code was used to simulate the sediment dune evolution processes. Three kind of sediment dune evolution are investigated, i.e. formation of 2D sediment dune, dune propagation process and formation of 3D sediment dune. Comparison between simulated results and experimental results show that the numerical model captures the dune length and dune height evolution reasonably. For the dune propagation processes, three major feathers are observed during the simulation: new dune crests developed with decreasing H and L with distance downstream, bed form field widened forming a triangular shape, and the dune crests took on a uniform H and L in cross section. While for the dune instantaneous initiation processes, the observed sediment dune crests demonstrates three shapes, i.e. lobe, straight and saddle, which is similar to those found in natural rivers and in coastal areas. Further investigation of the non-dimensional span (NDS) showed that the NDS decreases with time increment, which agreed with those found in flume experiments. In terms of the turbulent events, sweeps and ejections occurred more frequently on dune stoss side than the other two events (inward and outward interactions).

## ACKNOWLEDGEMENTS

This research is supported by the Nature Science Foundation of China (91647210) and Key Research and Development Program of China (2016YFC0402407). Mr. Yan Liu is funded by China Scholarship Council (CSC). The computations were supported by Tsinghua High-performance Computing Center (THPCC).

## REFERENCES

Ashley, G. M. (1990). Classification of Large-Scale Subaqueous Bedforms: A New Look At an Old Problem-SEPM Bedforms and Bedding Structures. *Journal of Sedimentary Research*, 60(1), 160-172

 

Baas, J. H. (1994). A Flume Study on the Development and Equilibrium Morphology of Current Ripples in Very Fine Send. *Sedimentology*, 41, 185-209.

Baas, J. H. (1999). An Empirical Model for the Development and Equilibrium Morphology of Current in Fine Sand, *Sedimentology*, 46, 123-138.

Carling, P. A., Williams, J. J., Golz, E. & Kelsey, A. D. (2000). The Morphodynamics of Fluvial Sand Dunes in the River Rhine, Near Mainz, Germany. II. Hydrodynamics and Sediment Transport. *Sedimentology*, 47(1), 253.

Cevheri, M., Mcsherry, R. & Stoesser, T. (2016). A Local Mesh Refinement Approach for Large ‐ Eddy Simulations of Turbulent Flows. *International Journal for Numerical Methods in Fluids*, 82, 261-285.

Diplas, P., Dancey, C. L., Celik, A. O., Valyrakis, M., Greer, K. & Akar, T. (2008). The Role of Impulse on the Initiation of Particle Movement under Turbulent Flow Conditions. *Science,* 322(5902), 717-720.

Giri, S. & Shimizu, Y. (2006). Numerical Computation of Sand Dune Migration with Free Surface Flow. *Water Resources Research*, 42(10), 1-19.

Meyer-Peter, E. & Mu¨Ller, R. (1948). Formulas for Bed-Load Transport. *IAHR*, Stockholm.

Naqshband, S. Duin, O. V. Ribberink, J. & Hulscher, S. (2016). Modeling River Dune Development and Dune Transition to Upper Stage Plane Bed. *Earth Surface Processes and Landforms*, 41, 323-335.

Nelson, J. M., Shreve, R. L., Mclean, S. R. & Drake, T. G. (1995). Role of Near ‐ Bed Turbulence Structure in Bed Load Transport and Bed Form Mechanics. *Water Resources Research,* 31(8), 2071-2086.

Nelson, J. M., Burman, A. R., Shimizu, Y., Mclean, S. R., Shreve, R. L. & Schmeeckle, M. (2006). Computing Flow and Sediment Transport Over Bedforms. In *4th IAHR Symposium on River, Coastal and Estuarine Morphodynamics, RCEM 2005*.

Nicoud, F. & Ducros, F. (1999). Subgrid-Scale Stress Modelling Based on the Square of the Velocity Gradient Tensor. *Flow, Turbulence and Combustion*, 62(3), 183-200.

Paarlberg, A. J., Dohmen ‐ Janssen, C. M., Hulscher, S. J. & Termes, P. (2009). Modeling River Dune Evolution using a Parameterization of Flow Separation. *Journal of Geophysical Research: Earth Surface*, 114(F1), 1-17.

Parsons, D. R., Best, J. L., Orfeo, O., Hardy, R. J., Kostaschuk, R. & Lane, S. N. (2005). Morphology and Flow Fields of Three ‐ Dimensional Dunes, Rio Paraná, Argentina: Results From Simultaneous Multibeam Echo Sounding and Acoustic Doppler Current Profiling. *Journal of Geophysical Research: Earth Surface*, 110(F4), 1-9.

Schmeeckle, M. W., Nelson, J. M. & Shreve, R. L. (2007). Forces on Stationary Particles in Near ‐ Bed Turbulent Flows. *Journal of Geophysical Research, Earth Surface*, 112(F2003).

Sekine, M. & Parker, G. (1992). Bed-Load Transport on Transverse Slope. I. *Journal of Hydraulic Engineering*, 118(4), 513-535.

Southard, J. B. (1992). Interpreting Primary Physical Bedding Structures. *A Short Course* Given at The University Of Southern California. University Of Southern California, Los Angeles, CA.

Southard, J. B. & Boguchwal, L. (1990). A. Bed Configurations In Steady Unidirectional Water Flow Part 2. Synthesis of Flume Data. *Journal of Sedimentary Research*, 60, 658-679.

Tjerry, S. & Fredsøe, J. (2005). Calculation of Dune Morphology. *Journal of Geophysical Research: Earth Surface*, 110(F4), 1-13.

Uhlmann, M. (2005). An Immersed Boundary Method with Direct Forcing for the Simulation of Particulate Flows. *Journal of Computational Physics*, 209(2), 448-476.

Van, Rijn, L. C. (1984). Sediment Transport, Part I: Bed Load Transport. *Journal of Hydraulic Engineering*, 110(10), 1431-1456.

Venditti, J. G., Church, M. A. & Bennett, S. J. (2005). Bed Form Initiation from a Flat Sand Bed. *Journal of Geophysical Research, Earth Surface*, 110(F1), 1-19.

Venditti, J. G., Church, M. & Bennett, S. J. (2005a). Morphodynamics of Small ‐ Scale Superimposed Sand Waves over Migrating Dune Bed Forms. *Water Resources Research*, 41(10), 1-21.

Venditti, J. G., Church, M. & Bennett, S. J. (2005b). On The Transition between 2D and 3D Dunes. *Sedimentology*, 52(6), 1343-1359.

Venditti, J. G., Church, M. & Bennett, S. J. (2006). On Interfacial Instability as a Cause Of Transverse Subcritical Bed Forms. *Water Resources Research*, 42(7), 1-10.

Yager, E. M., Kirchner, J. W. & Dietrich, W. E. (2007). Calculating Bed Load Transport In Steep Boulder Bed Channels. *Water Resources Research*, 43(7), 1-24.

 

Proceedings of the 37th IAHR World Congress
August 13 – 18, 2017, Kuala Lumpur, Malaysia

# RESEARCH ON RELATIONSHIP BETWEEN FLOW AND SEDIMENT VARIATION AND TAIL CHANNEL EVOLUTION IN YELLOW RIVER ESTUARY

YANJIE LIANG[(1)], CUIHUA AN[(2)] & QIUSHI LUO[(3)]

[(1,2,3)] Yellow River Engineering Consulting Co., Ltd., Zhengzhou, China,
iamlyj_2006@163.com; anch542@sina.com; 18655093@qq.com
[(1)] Institute of Yellow River Engineering Consulting Co. Ltd., Zhengzhou, China

## ABSTRACT

Combined measured data with theoretical analysis, flow and sediment variation and tail channel evolution characteristics in Yellow river estuary and their relationship in Qingshui channel period are studied. The research results showed that Xiaolangdi Reservoir played an important role in sediment detention and reduction of sediment coming in Yellow River estuarine region. The water-sediment regulation changed the annual distribution of flow and sediment. Due to this, the proportion of flood season decreased and the proportion of non-flood season increased. The cross section morphology developed towards deep and narrow, down-cutting of flow effect is obvious. The bankfull discharge is closely related to water amount of flood season where the bankfull discharges increased with flow amount of flood season increasing. The variation trend of 3 years of moving average value of annual water amount and bankfull discharges are same. The bankfull discharge has close relation with 2 years moving average value of flow and sediment collocation coefficient where the former increased and reduced with latter.

**Keywords:** Yellow river estuary; tail channel; bankfull discharge; 3 years moving average water amount; flow and sediment collocation coefficient.

## 1 OVERVIEW

From 1976, the Yellow River flowed into the Bohai Sea through the current flow path of Qingshuigou, which is located in the estuary south. The water and sediment in the estuary of Yellow River began to decrease sharply from 1986 and the river cross section of the tail channels shrunk clearly. The bankfull discharge has become smaller and the water level with the same discharge has risen, all of which put great pressure on the control of river flood. In 1996, the river length of the downstream Xihekou reached 65km, and the channel of Qing-8 was transferred due to oil exploitation, and its direction was slightly transferred to northeast. Afterwards, the function of Xiaolangdi Reservoir combined with the water-sediment regulation of Yellow River, helped optimize the water and sediment condition and contributes to recovering on the function of flood carrying capacity of the tail channel.

The Yellow River estuary's typical characteristic was weak tide and too much sand. When the sand is carried into the estuary, the estuary will extend and even change its channel. The erosion height datum in the lower reaches of the Yellow River will be changed, and the river profile will change correspondingly (Wang et al., 2008; Wang et al.,2013; Zhao et al.,2007). However, the adjustment of the tail channel will have important impact on the sedimentation and the evolution of river bed. The evolution of the tail channel is influenced by factors like the runoff, water-sediment ratio, sand component, and the extending of the estuary (Hu et al., 2009; Hu et al., 2011; Wang et al., 2007). Therefore, the research on the relation between the river channel evolution and the water-sediment variation should be carried out, and the law of evolution of the tail channel in different conditions should be mastered so as to improve the flood control capacity in the lower reaches of the river (Ru et al.,2011).

## 2 VARIATION CHARACTERISTICS OF THE WATER-SEDIMENT IN ESTUARY OF YELLOW RIVER

### 2.1 Annual changes of water and sediment

According to the data statistic analysis of Lijin station from 1950 to 2012, which is shown in Figure 1, the water amount of the Yellow River estuary had declined gradually since 1970s and it had decreased more sharply in 1980's compared to that of in 1950's and 1960's. The annual average water amount after Xiaolangdi Reservoir built had only occupied 35.5% of the water in 1950's. The water flow amount of Lijin station was analyzed by the exponential smoothing method. It can be seen that in Figure 2 there was an obvious fluctuation in 1968 and 1986. There was a continual large flow between 1950 and 1968, and that the flow was decreasing between 1969 and 1985 where the figure dropped sharply between 1986 and 2004, while there was a slight increase since 2005.

 

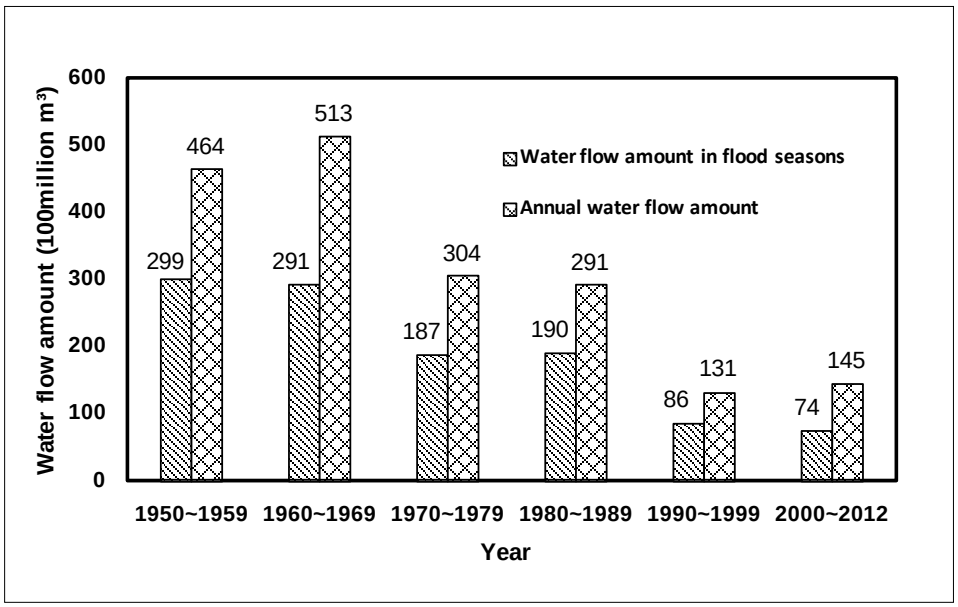


**Figure 1**. Comparison of water flow from1950 to 2012 of Lijin Station.

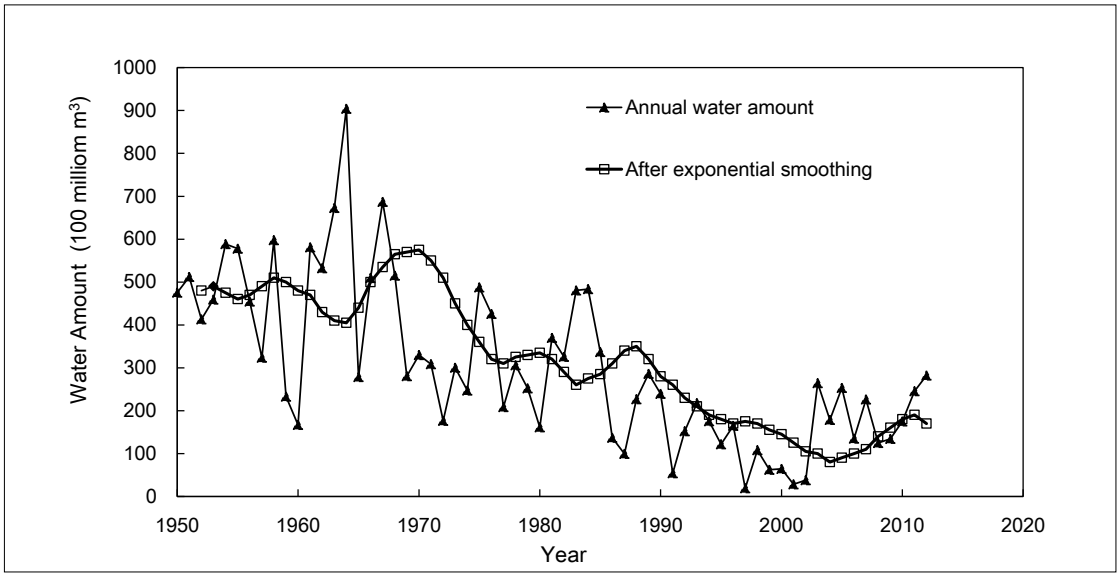


**Figure 2**. Annual water flow amount in Lijin Station.

The actual sediment was in accordance with the changes of water flow in which the sediment transport had shown the downward trend, especially since 1980 (Figure 3). Due to the blocking sediment function of the Xiaolangdi Reservoir, since the reservoir was built, the sediment amount in estuary had reduced to 10.7% of that of 1950's. In 1968 and 1986, the Liujiaxia Reservoir and the Longyangxia Reservoir were put into use respectively, and the Xiaolangdi Reservoir was put into use in 2000, all of which had great impact in the process of the sediment flow. Seen from Figure 4, there was an obvious change in the sediment in 1968, 1986, and in 2000. There was continuous increase in the sediment between 1950 and 1968, while there was a drop in the sediment between 1969 and 1985, and a sharp drop between 1986 and 2004, Finally there was almost no sedimentation in the estuary from 2005.

 

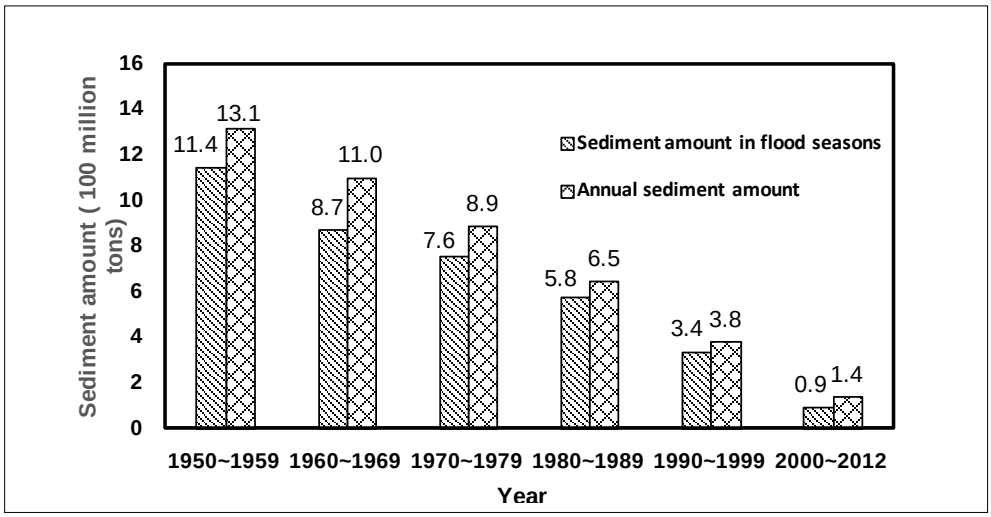


**Figure 3**. Comparison of sediment amount between 1970 and 2012 of Lijin Station.

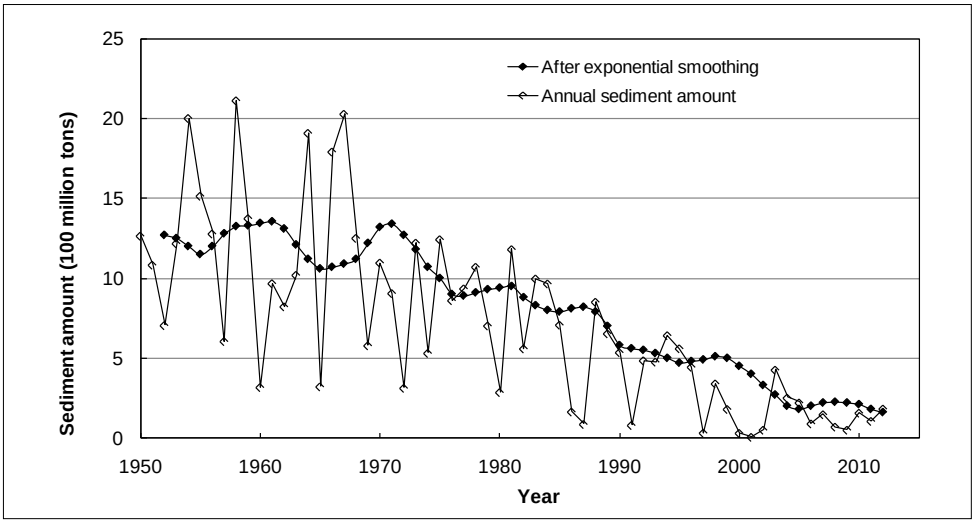


**Figure 4**. Annual sediment amount in Lijin Station.

2.2 Annual allocation changes of water and sediment

After the implementation of water-sediment regulation in Yellow River, there were obvious changes in the allocation of water and sediment entering the estuary. After the Xiaolangdi Reservoir built, the proportion of the water in the flood season and the sediment amount decreased to some extent while the proportion in the non-flood season increased. There was increase in the proportion in the water and sediment amount in June, rising from 0.59% and 1.97% respectively during the period between 1970 and 1979 to 13.84% and17.6% respectively during the period between 2000 and 2012. Slight changes can be observed in other months, and the allocation changes are as follows (Figure 5 and Figure 6).

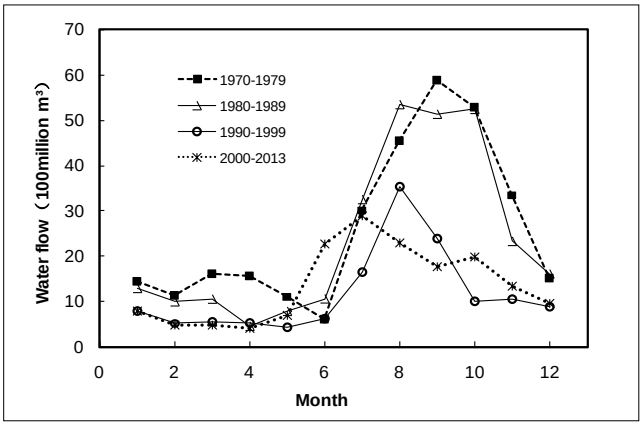


**Figure 5**. Water allocation changes of Lijin.

 

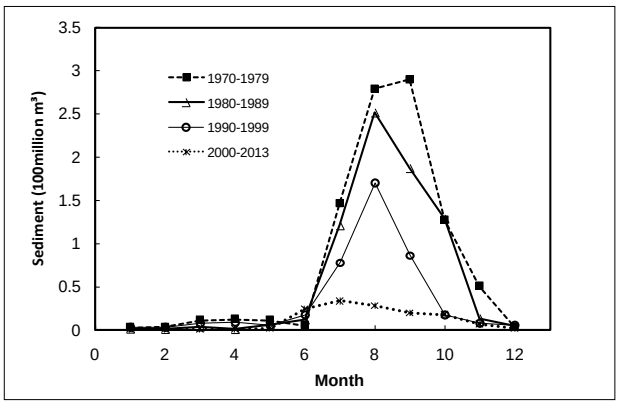


**Figure 6**. Sediment allocation changes of Lijin

2.3 The changes of flow discharge magnitude

Compared to the period from 1976 to 1985, and the period from 1986 to 1999, the period from 2000 to 2012 showed a slight increase in the incoming flow of the estuary of Yellow River, and decrease in the large flow (Figure 7). During the period from 2000 to 2012, the days for flow of 2000~3000$m^3$/s, and the days for flow of 3000~4000$m^3$/s were 11.5 and 2.6 respectively, and there wasn't one day with discharge over 4000$m^3$/s; and the days for flow which was less than 5000$m^3$/s and between 1000 and 2000$m^3$/s were respectively 58.9 and 30.

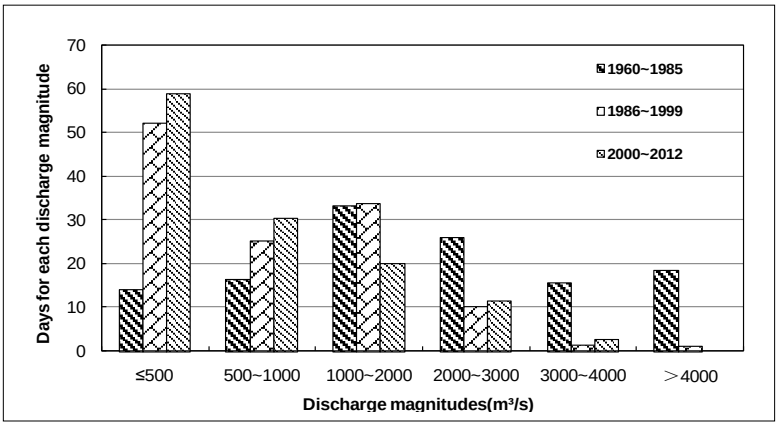


**Figure 7**. Days for different magnitudes of flow in flood season.

2.4 Changes of sediment concentration

Before 2000, with the synchronized decrease of the sediment and the flow in the estuary, the sediment concentration showed almost no changes. In the 1970's, 1980's and 1990's, the annual sediment concentration in Lijin Station was over 20kg/$m^3$ (Figure 8). After Xiaolangdi Reservoir was put into use, there was an increase in the declining sediment concentration in the estuary area, which can be seen in Figure 8. The annual sediment concentration between July 2000 and June 2013 was 8.79kg/$m^3$ and the maximum annual sediment concentration was less than 20kg/$m^3$.

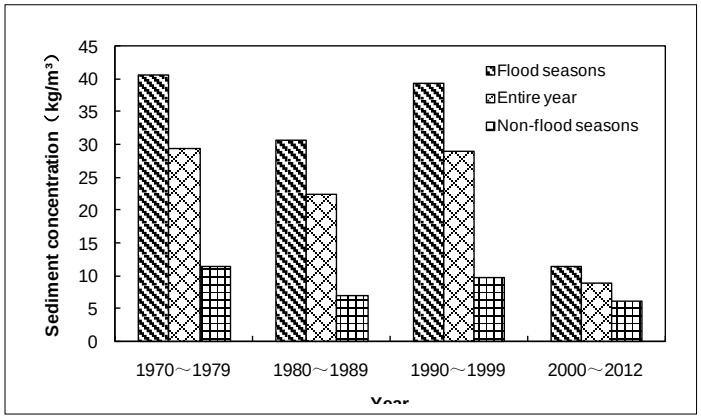


**Figure 8**. Actual sediment concentrations in Lijin Station in different periods.

 

## 3 CHARACTERISTICS OF EVOLUTION OF THE TAIL CHANNEL EVOLUTION OF THE TAIL CHANNEL

### 3.1 Lateral adjustment of the channel

The cross section profile of Lijin is shown in Figure 9 and it can be seen that when compared with that of May, 1976, the discharge area in May, 1985 increased greatly because of the washing of great discharge from 1980 to 1984. Due to the fact that there was low flow since 1986, the cross section area of Lijin was withering and some of the main channel became a high floodplain in May 2001. The lower reaches became smaller with the discharge capacity deducing. In April 2012, the cross section of Lijin obviously became larger and the discharge capacity was higher.

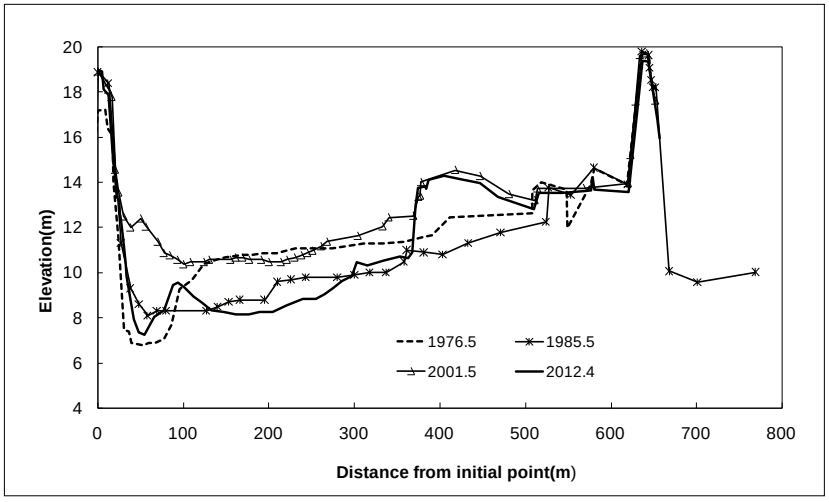


**Figure 9**. Cross section profile of Lijin.

The cross section profile of Yuwa is shown in Figure 10. It can be seen that the width of the main channel increased from 490m in 1976 to 870m in May of 1985. Besides that, the erosion of the flood between 1981 and 1984 could be observed and the erosion effect coming from the source was stronger. In May 2001, the width of the main channel decreased to 450m, and some of the main channel became high floodplain. In April 2012, the main channel's bottom became lower, which was due to the use of the Xiaolangdi Reservoir, and there was no water flow over 4000$m^3$/s. The water flow was mostly less than 1000$m^3$/s, which influenced the scouring of the channel.

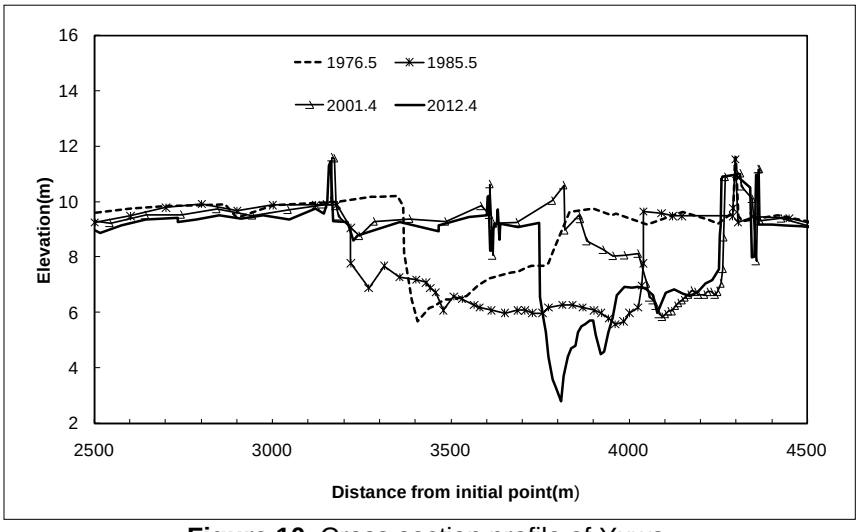


**Figure 10**. Cross section profile of Yuwa.

Figure 11 shows the cross section profile of Qing-2 section. Compared to that in May 1976, the height of the floodplain in May 1986 was rising, and annual siltation thickness was about 2.2m. In May 2001, the channel was showing a shrinking trend and in April 2012, the thalweg of the section was clearly lowered for the fact that the large flow coming into the estuary was less. However, there were more small flows, and the flood flowed almost in the main channel, which means that the channel shape was influenced by the water flow process.

 

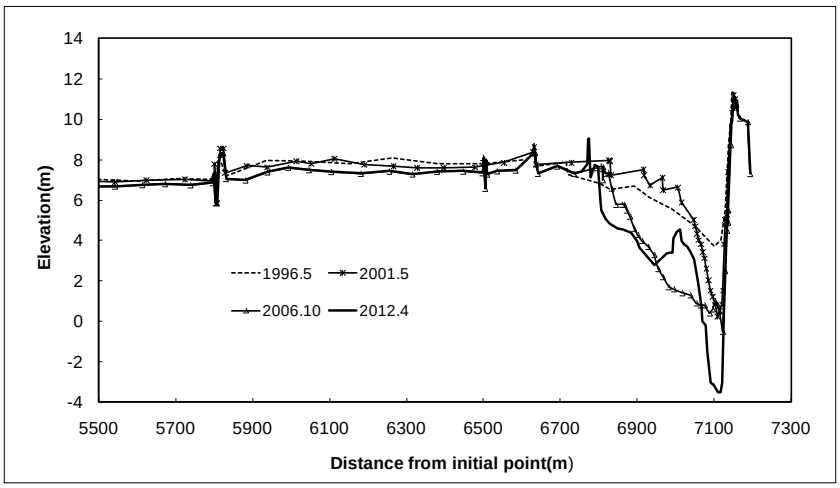


**Figure 11**. Cross section profile of Qing-2.

3.2 The longitudinal adjustment of the channel

Compared to that in May 1976, there was a drop in the bottom elevation along the path below Lijin in May 1985 (Figure 12). When compared with 1985, the bottom elevation fell slightly above the section of Yuwa while it rose clearly below the section of Yuwa, which was due to the fact that the water and sediment coming into the estuary decreased after 1986. The cross section of tail channel shrank, and the bottom elevation increased from the Yuwa to the estuary because of the sedimentation effect coming from the source. In 2012, the bottom elevation decreased sharply below Lijin, and due to the flood discharging function of the Xiaolangdi Reservoir and the erosion effect coming from the source, the gradient of river below Yuwa was larger than that of river from Lijin to Yuwa.

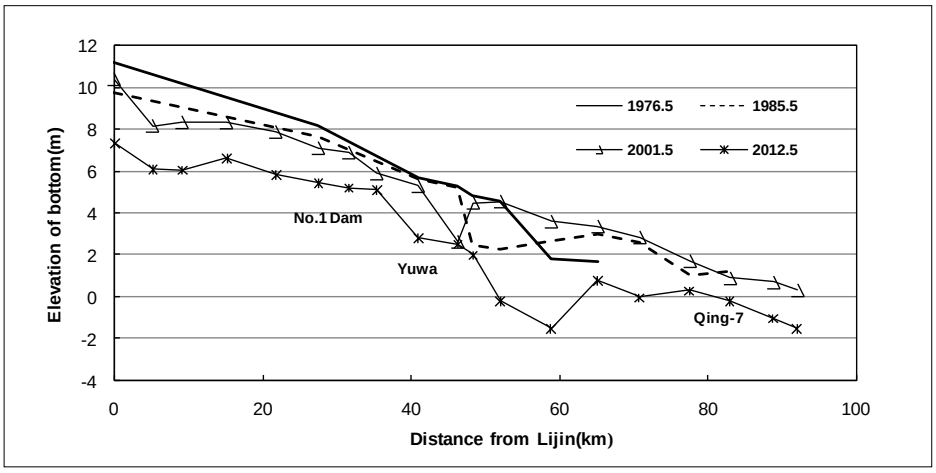


**Figure12**. Changes of the average bottom elevation of the channel.

## 4 RELATIONSHIP BETWEEN RIVER CHANNEL EVOLUTION AND FLOW-SEDIMENT VARIATION

As an important indicator of evaluating the capacity of the river flood conveyance, the bankfull discharges can reflect the flood conveyance capacity of the main channel and the characteristics of the evolution of the channel. The following part analyzes the relation between the bankfull discharge and the flow amount in the flood season, and the collocation of the water and sediment. Meanwhile, the changes of the bankfull discharge and the 3 years moving average value were compared to further explore the influence of the flow changes process of the sediment on the evolution of the tail channel.

4.1 The relation between the bankfull discharge and the water amount in flood seasons

During the period between 1976 and 2012, the annual water amount in flood season of Lijin Station reached 61.2% of the water amount in whole year, and the annual sediment in the flood season reached 80% of the entire year's sediment. It means, the changes of the river channel's erosion and sedimentation usually occur in the flood season. The regression analysis method was used to explore the correlation between the bankfull discharge and the water amount in the flood season. The correlation index reached 0.8, which means that there was close relationship between each other. Seen from Figure13, it can be deduced that with the flow increasing in the flood season, the scouring enhanced the flood carrying capacity and increased the bankfull discharge.

 

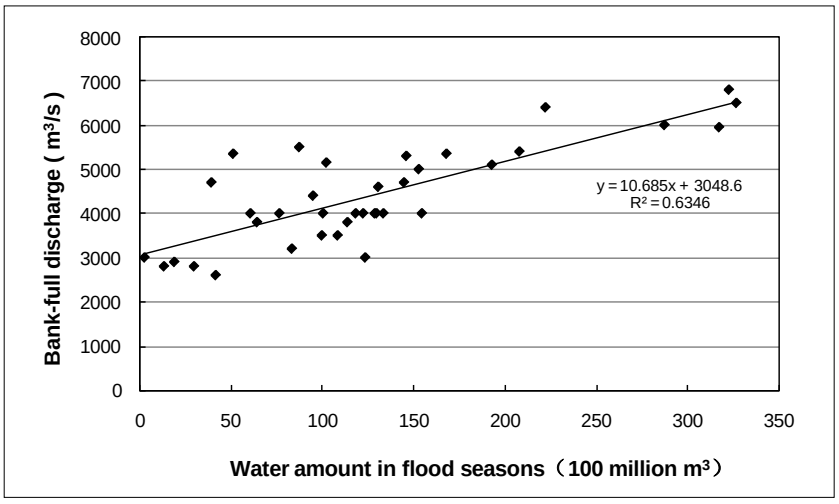


**Figure 13**. The relation between water amount in flood seasons and the bankfull discharge.

4.2 Comparison of the bankfull discharge and the 3 years moving average value of water amount

The bankfull discharge was not only influenced by the water conditions of the current year but also influenced by the flow of the previous years. The changes of the bankfull discharge were compatible with the water conditions and it was a continuous process. Figure 14 showed the changes process of the 3 years moving average value of water amount and the bankfull discharge of Lijin from 1976 to 2012. It can be seen that the changes of the bankfull discharge was basically in accordance with the 3 years moving average value of water amount, which was 26.1 to 43.3 billion $m^3$ between 1980 and 1985. This period could be considered as years with abundance of water. Meanwhile, the bankfull discharge was kept as 6000 to 6500 $m^3/s$' However, from 1986 to 2002, the 3 years moving average value of water amount decreased from 31.9 billion to 4.35 billion $m^3$ while the bankfull discharge decreased from 5500$m^3$/s to 2800$m^3$/s. After 2003, the 3 years moving average value of water amount showed increasing trend and reached 23.4 billion $m^3$ in 2002, while the bankfull discharge rose from 2800$m^3$/s to 4000$m^3$/s.

The bankfull discharge of Lijin showed almost the same change trend as the 3 years moving average value of water amount, which increased and decreased with the water amount. However, the changing trends were not completely consistent and there was slight fluctuation in some years, which indicated that there are other factors influencing the changes of the bankfull discharge such as the riverbed conditions in the early stages, the flood peak and the flood amount and so on.

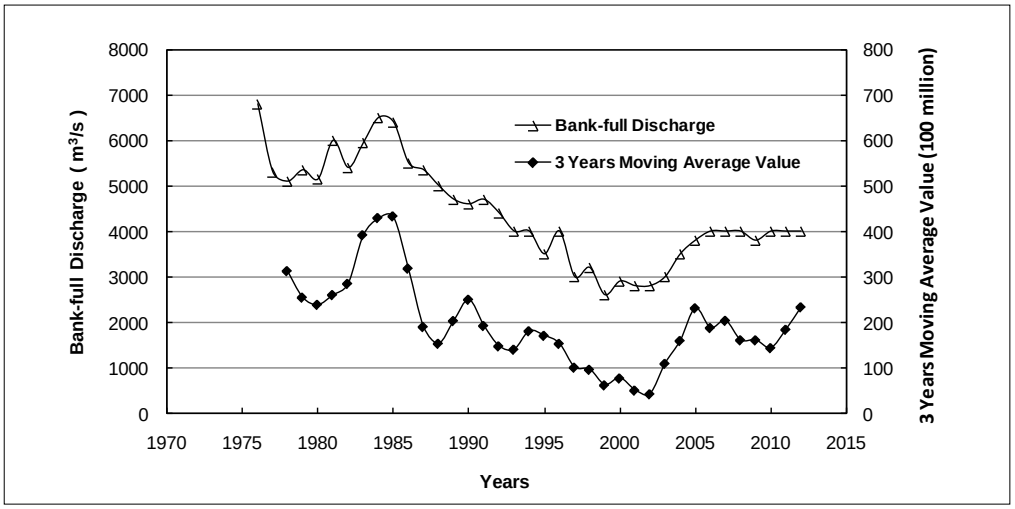


**Figure 14**. Comparison of 3 years flow moving average value and bankfull discharge.

4.3 Relation of the bankfull discharge and flow and sediment collocation coefficient

The collocation of water and sediment was not only related to the value of the average discharge and the sediment concentration, but also linked to the process of discharge and sediment concentration of the river. It was also said, especially the discharge over 2000$m^3$/s has an obvious impact on the erosion of the tail channel. Based on the factors above, the following equation is used to analyze the bankfull discharge, which displays the relation between the water and the sediment:

 

$$K = (Q/Q_{ave})(S_{ave}/S)e^{(W_2/W_f)} \quad [1]$$

As Equation 1 (Ru et al., 2011), K is the coefficient, Q and $Q_{ave}$ are respectively the average discharge in the flood season and the annual average discharge. S and S are respectively the average sediment concentration of the flood season and the annual average sediment concentration; $W_2$ is the water amount over 2000m$^3$/s in the flood season and $W_f$ is the water amount of the flood season.

From the regression analysis of 2 years moving average value of sediment collocation coefficient and the bankfull discharge, it can be found that the correlation coefficient reaches 0.82 which means that their relation is close and shows that the bankfull discharge was not only influenced by the water and sediment conditions of the current year but also influenced by the collocation of the water and sediment in the previous year. Meanwhile, the discharge over 2000m$^3$/s in the flood season helps to maintain the normal channel by channel scouring (Figure 15).

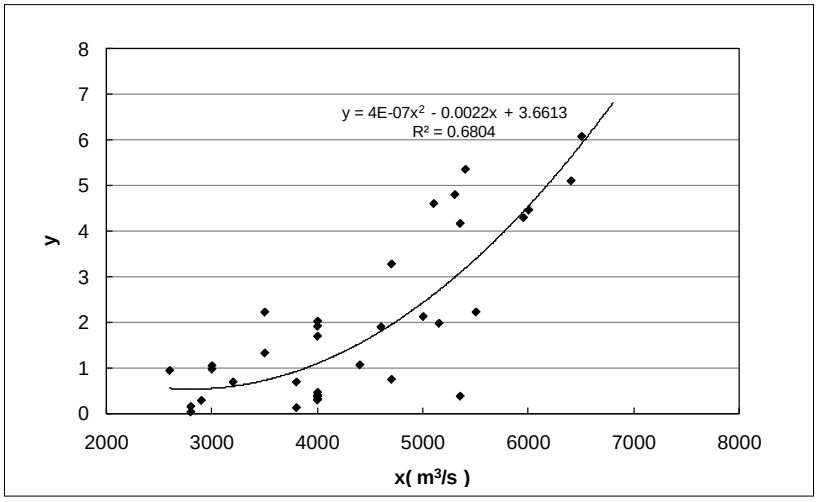


**Figure 15**. Relation between the collocation coefficient and the bankfull discharge (x: bankfull discharge, y: 2 years moving average value of sediment collocation coefficient)

## 5 CONCLUSIONS

After the data analysis of the annual changes of the flow and the sediment, the collocation changes within the years, the magnitudes of the flow and the changes of the sediment concentration are studied. The lateral and longitudinal changes are compared and the relation between the water amount, collocation coefficient and bankfull discharge were also noted. The conclusions are as following:

a. The relation between the bankfull discharge and the water amount in the flood season was built by regression analysis method, and their relation is close. The bankfull discharge increased with the increase of the flow in the flood season;
b. The change process of the 3 years moving average value of annual water amount and the bankfull discharge were drawn and showed a parallel trend where the latter changed with the former;
c. The figure of the relation of the 2 years moving average value of water and sediment collocation coefficient and the bankfull discharge is shown. The latter increased with former, and flow of discharge over 2000m$^3$/s in the flood season plays an important role in maintaining the bankfull discharge.

## ACKNOWLEDGEMENTS

The study is financially supported by the National Key R&D Program of China (2016YFC0402503).

## REFERENCES

Wang, K.C., Wang, K.R. Chen, X.T. & Ru, Y.Y. (2008). Study on Influence of the Yellow River Estuary to Feedback of the Lower Channel. *Yellow River,* 30(1),18-21.

Wang, K.R., Yu, S.B. & Ru, Y.Y. (2013). Study on Change of Flow and Sediment Entering into the Sea and the Yellow River Estuary Evolution Since 2000. *Yellow River,* 35(4),11-13.

Zhao, L., Jiang, E. & Wu, J. (2007). Analysis of Research Advances in Feedback Influence of Estuary Evolution on the River Channel of the Yellow River. *China Rural Water and Hydropower*, 8(4), 5-8.

Hu, C. & Zhang, Z. (2009). Response Relationship between the Bankfull Discharge in Tail Channel and the Process of Flow-Sediment in the Yellow River Estuary. *Advances in Water Science*, 20(2), 209-214.

 

Hu, C. & Zhang, Z. (2011). Relationship between Adjustment of Section Configurationand Flow-Sediment of Tail Channels in theYellow River Estuary. *Journal of Basic Science and Engineering*,19(4), 543-553.

Wang, C., Zhang, S. & Cao, W. (2007). Study on Response of Evolution of Yellow River Mouth on its Trail Channel. *Water Resources and Hydropower Engineering*, 38(9), 16-20.

Ru, Y.Y., Wang, K.R. & Hou, Z.J. (2013). Response of the Reach near the Yellow River Estuaryto the operation of Xiaolangdi Reservoir. *Journal of Sediment Research,* 3, 63-68.

 

# INVESTIGATION OF THE EFFECTS OF VEGETATION ON SEDIMENT DISTRIBUTION AND MORPHODYNAMICS EXPERIMENTALY AND NUMERICALLY

CHANG-LAE JANG[1], ELLIS PENNING[2], GI JUNG KIM[3], HYO HWANG[4] & YONGUK RYU[5]

[1,3,4] Dept. of Civil Engineering, Korea National University of Transportation, Chungju-si, Korea,
cljang@ut.ac.kr; kimgijung@ut.ac.kr; hwanghyo@ut.ac.kr

[2] Deltares, P.O. Box 177, 2600 MH Delft, The Netherlands,
Ellis.Penning@deltares.nl

[5] Korea Institute of Civil Engineering and Building Technology, Goyang-si, Korea,
yuryu@kict.re.kr

## ABSTRACT

This study investigated the effects of vegetation on flow, sediment distribution and morphodynamics through the outdoor laboratory experiments and 2-D numerical simulation. At the dense vegetation zone, flow velocity decreased severely and diverted toward unvegetated channel due to the high drag by vegetation. Flow is accelerated along the patch after diverging flow between the patch and the open channel. Maximum velocity pattern along the channel was meandering. At the sparse vegetation zone, however, the alternated flow pattern was not clear due to the low drag in the vegetation zone. The thalweg of the bed is meandering shape, and was relatively agreed with the maximum velocity pattern. The significant bed changes are vegetated numerically an experimentally. Suspended sediment concentration was high in front of vegetation reach. However, the concentration was low at the outlet of vegetation reach because of the low velocity in the vegetation zone. The bed aggraded in the lee of vegetation patch. At the lee of dense and sparse vegetation regions, bed material size was fine at the aggradation region and coarse at the degradation region. The riparian vegetation reduced the suspended sediment transport capacity and changed the sediment profile of it according to the water depth. The suspended sediment concentration is 50mg/L at 50m from upstream. However, the concentration is reduced to 29.5mg/L at 86m of dense vegetation patch. The vertical profiles of suspended sediment concentration from the bed are that the concentration is higher at 0.4m than at 0.2m in the dense vegetation patch. However, the concentration is lower at 0.4m than at 0.2m in the sparse vegetation patch. The numerical results are in reasonable agreement with the experiment with the experimental results, capturing the most important characteristics of the alternate bar.

**Keywords:** Vegetation; morphodynamics; numerical modelling; suspended sediment concentration.

## 1 INTRODUCTION

Vegetation plays a significant role in flow changes, sediment sorting, and the channel evolution. Riparian vegetation increases hydrodynamic drag, and reduces flow velocity and distribution. Vegetation also decreases the bed stress and Reynolds stresses within the canopy, which lead to sedimentation, sediment sorting and bed changes (Zong and Nepf, 2010; Neary et al., 2012; Bennett et al., 2008). The decreased momentum transfer to the bed in vegetated channel leads to a lower suspended sediment transport capacities in the regions compared to those in unvegetated channel (Lopez and Garcia, 1998). Field investigations in riverine wetlands by Demissie (1990) have indicated that the sediment trapping rate is ranging from 69 to 84%.

Further understanding of its influence on river morphology is of great importance with respect to river restoration (Rominger et al., 2010). The shape of vegetation zone and the density of vegetation also affect the bank erosion, pool and riffle development, the shape of channels, and change of channel sinuosity (Bennett et al., 2008). However, there has been relatively little study of vegetation in this regard and, since the behavior of vegetated rivers is complex, its influence is not yet fully known (Jang and Shimizu, 2007).

Flow velocity and structures are affected by vegetation, the degree to which depends on vegetation density, flexibility, type, and whether it is in a submerged or emergent condition (Nepf and Vivoni, 2002; Defina and Bixio, 2005). Bennett et al. (2002) showed that flow of velocity was decelerated within and near vegetation zones, and flow direction was changed toward the opposite bank. Vegetation also has an influence on the channel processes and morphology by means of its density, type, age, and health, etc. (Thorne, 1990; Bennett et al., 2002).

Change of riparian vegetation zones strongly depends on the flood frequency and the amount of sediment supply due to dam construction and other factors, and accordingly affects the river morphology (Tsujimoto, 1999). Murray and Paola (2003). It is found that high sediment supply leads to the development of braided channel patterns via local destruction of vegetation.

 

The purpose of this study is to investigate the hydraulic characteristics, sediment distributions and the evolution processes of a channel with vegetation by means of the outdoor laboratory experiments at the River Experiment Center, Korea Institute of Civil Engineering & Building Technology in Andong, Korea. Experiments were conducted in an initially straight channel with vegetation, where the density of willows was controlled to form vegetated rivers. The channel was reproduced with an erodible bed composed of non-uniform sandy materials in the laboratory.

## 2 EXPEREIMENTAL METHOD

Within a 600m long outdoor experimental channel a section of 60m in length with a trapezoidal cross section (3m bed width, 2m height and 26.5 degrees side slope) was selected to vegetation channel and 70m of the channel was selected to calibration reach for suspended sediment experiments (Figure 1). The banks were covered with grass. The channel slope was 1/1000 and filled with sand of 0.8mm of median diameter to smoothen the natural graded underlaying river sediment deposits. Water discharge was controlled at a concrete headbox supplied from the Nakdong River. Water ran through the channel and was discharged at the end in the Nakdong River again. Sediment was supplied upstream.

The set-up of the experiment was designed for sand-bed channels with alternate bar patterns which wave lengths when calculated following Ikeda (1984) for a normal flow discharge of 0.5$m^3$/sec, will give rise to the willow saplings being planted on the alternate bar pattern profile (Figure 1). The 4 vegetation patches upstream were designed to have dense vegetation (38 stems/$m^2$), and 3 downstream vegetation patches had sparse density (10 stems/$m^2$). These densities were derived from field measurements on vegetation density in the Nakdong River near the outdoor laboratory at the River Experiment Center, where 1.2 stems/$m^2$, and a diameter of 7cm, were recorded. Height of this natural vegetation was around 5.0 m, and the mean diameter of sediments was 1.5mm. The length of the planted willow saplings was 60 cm, with a stem diameter of 1cm. The sapling/twigs were planted in summer 2014 up to 20cm depth in the natural sandy bed of the outdoor flume, leaving 40cm exposed and left to properly get established. The experiment had been conducted from Aug. 20, 2014 to Sept. 8, 2015.

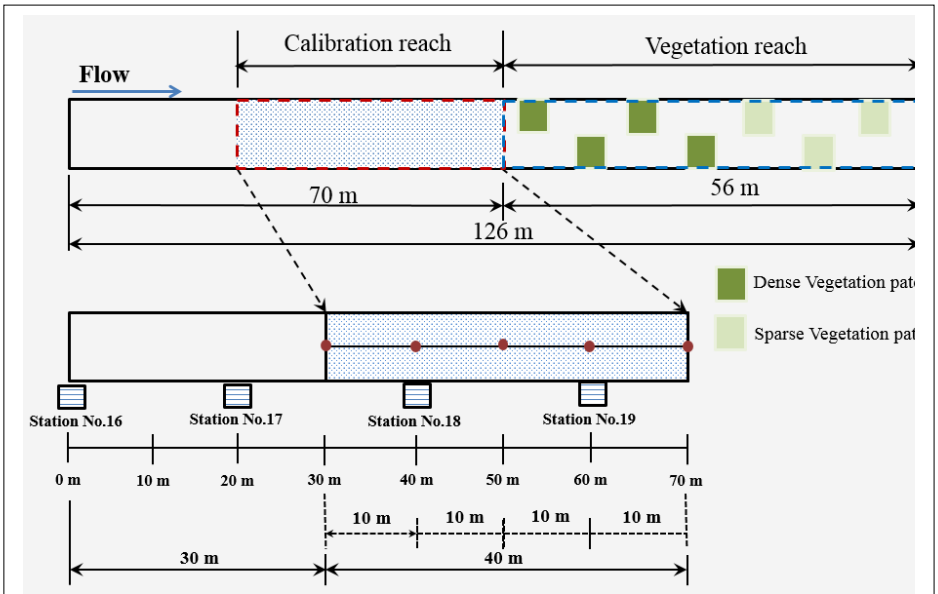


(a) Plan view of experimental outdoor channel

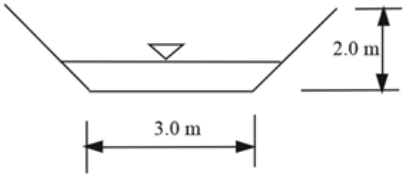


(b) Cross section of experimental channel

**Figure 1**. Sketch of experimental channel.

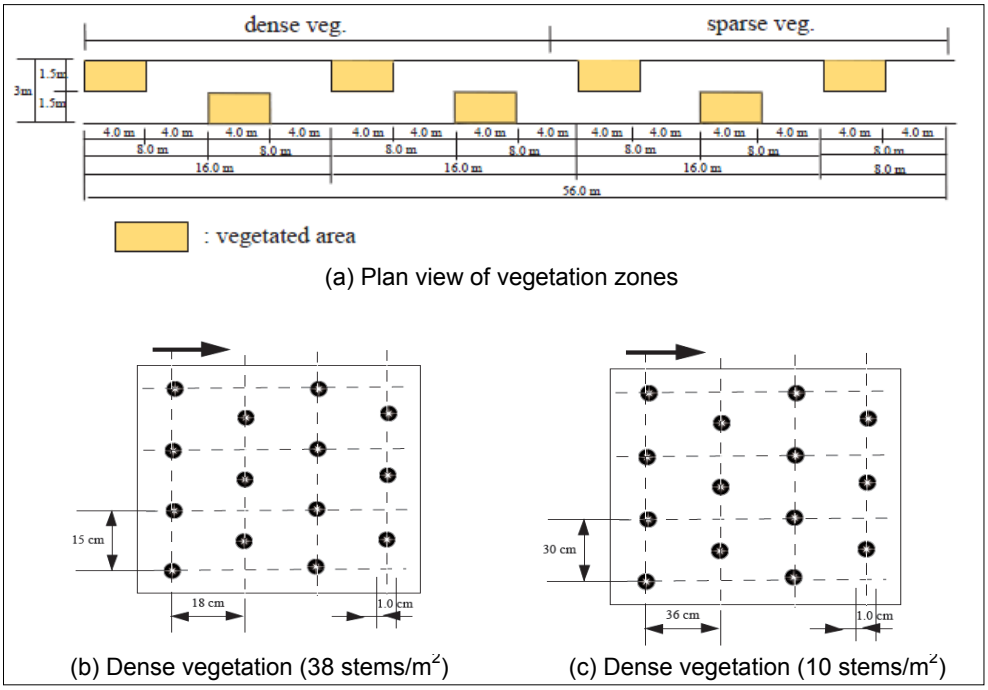


(a) Plan view of vegetation zones

(b) Dense vegetation (38 stems/m$^2$)

(c) Dense vegetation (10 stems/m$^2$)

**Figure 2**. Layout of vegetation zone.

Over the year 2014-2015 the discharge in the experimental channel ranged from 0.5m$^3$/sec to 7m$^3$/sec, and flow and geometric changes were measured after discharges of 0.5m$^3$/sec, 2.5m$^3$/sec and 3.5m$^3$/sec as shown in Figure 2 marked by circles. Vegetation total length was 0.4m from July 8, 2014 to April 6, 2015. The vegetation grew fast in spring and summer season of 2015 where the length was 1.2 m around August 2015. The bed survey was made with Total Station to record channel changes after stopping water flow as showed in Figure 2. The longitudinal bed profile was measured in the experimental reach from the upstream every 1.0m. The transverse bed profile was surveyed every 0.5m. Bed materials of the surface layers were sampled at some places and analyzed after stopping water flow at the end of the experiment, August 25, 2015.

The suspended sediment load at some places was measured by USDH-48 at 20%, 40% and 80% of water depth from the bed to find out the distribution of sediment at dense and sparse vegetation patches. To generate the suspended sediment with the discharge of 1.8m$^3$/sec for 42 hours and 3.2m$^3$/sec for 51 hours, fine sediment was supplied upstream. The suspended sediment concentration was measured at 5 points in the longitudinal direction at calibration reach and 5 points at vegetation reach.

## 3 EXPERIMENTAL RESULTS

### 3.1 Time-averaged flow velocity

To distinguish flow in the vegetated channel reach, laboratory Sontek Micro Acoustic Doppler velocimeters (ADV) was used to measure the three velocity components simultaneously. The ADVs were mounted on a traverse perpendicular to the channel. A longitudinal transect was made through every 1.0m and transverse direction was measured every 0.2m. The velocity was recorded at each point every 30 seconds period with 50Hz.

Figure 3 shows the time averaged by flow velocity distribution in the vegetated channel reach. At the dense vegetation zone, flow velocity decreased severely and diverted toward the unvegetated channel sections because of the vegetation. Flow was separated at a diverging flow zone at the front edge of vegetation patch. Flow sharply decelerated in the lee of vegetation zone, where the meandering flow pattern was reduced. Flow accelerated along the patch after diverging flow between the patch and the open channel, where a shear layer was developed. These strong lateral differences are commonly observed in partially vegetated channels (Bouma et al., 2007; Zong and Nepf, 2010). Moreover, flow was forced around the dense patches, creating a meandering flow pattern due to the obstruction.

 

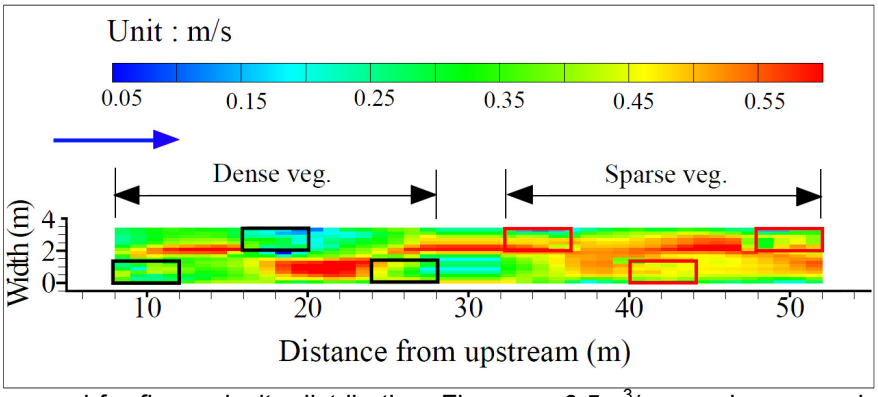


**Figure 3**. Time-averaged for flow velocity distribution; Flow was 0.5m$^3$/sec and measured at Nov. 12, 2014. Squares indicate the vegetation patch. Flow was measured from the second vegetation patch of the high density of vegetation reach upstream toward downstream of the channel.

The downstream velocity accelerated near the edge of the dense vegetation patches, which led to a deep scour at these locations. At the sparse vegetation zone, however, flow passed through the patches with less decelerated speed. Flow direction was also changed at the next vegetation patch downstream. However, the alternated flow pattern was not as pronounced as in the dense vegetation zone because of the low drag in the vegetation zone.

### 3.2 Bed changes

The alternated flow pattern around vegetation region causes the bed changes. The bed scoured deeply along the vegetation region by the enhanced flow between the patch and the open channel as shown in Figure 3 (Tsujimoto, 1999). However, the bed aggradated in the lee of vegetation zone, where flow velocity was dramatically retarded due to the high drag of vegetation. Figure 4 shows planimetric changes of the channel. The alternate bars were developed in the vegetation zones and increased in the downward direction of flow. The thalweg of the bed developed into a meandering shape as shown in Figures 4, and was in agreement with the maximum velocity pattern along the channel as shown in Figure 3, which was similar to that observation by Bennett et al. (2008). Figure 5 shows the cross sectional change in the lee of vegetation at point 1 of dense vegetation zone and point 2 of sparse vegetation zone. At the high vegetation density, the bed scoured deeply as shown in Figure 5, which was due to the enhanced flow around vegetated zones (Neary et al., 2012).

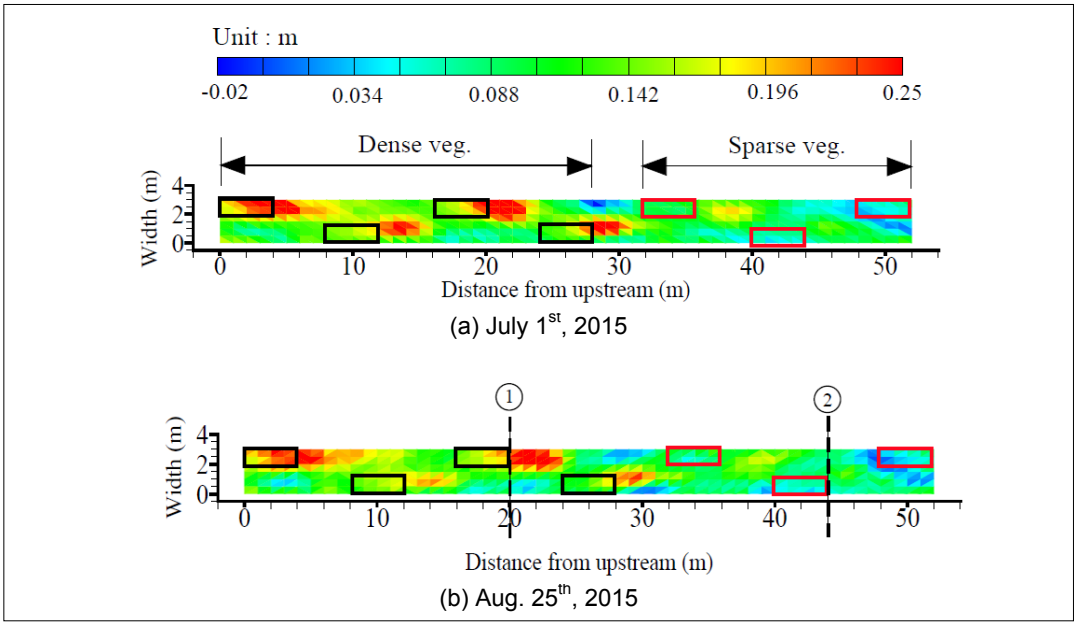


**Figure 4**. Planimetric changes of the channel.

At the dense vegetation zone, the bar length increased with time as shown in Figure 4. At the low vegetation zone, however, the bar length was not increased after July 1st, 2015. Flow velocity sharply decreased in vegetation zone and shear layer vortices developed along the vegetation zone, which led to the change of bed load direction into and from the vegetation zone

 

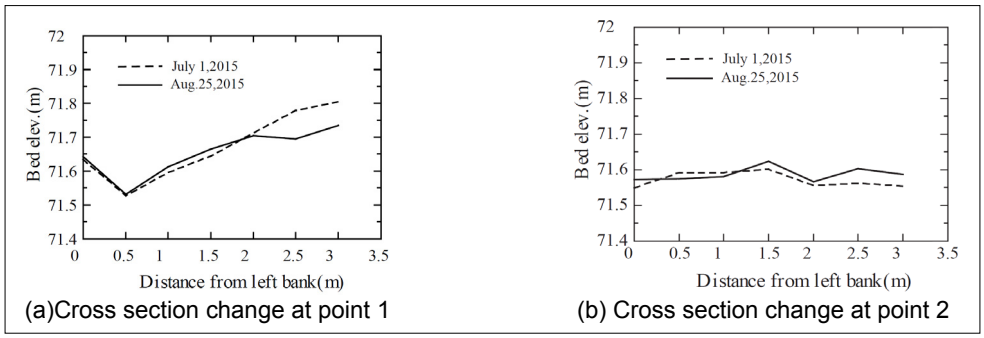


**Figure 5**. Cross sectional changes of the channel at points 1 and 2.

The difference of the transport rate between the vegetation patches and unvegetated area of the channel led to the lateral transport rate toward the vegetation zone from the unvegetated zone. It was also found by Tsujimoto (1999), which caused the bar growth in the vegetation zone. The deep scouring along the dense vegetation zone was source of growing sand bars in success. Tsujimoto (1999) showed that vegetated sand bars increased as the flood number increased.

### 3.3 Sediment sorting

Figure 6 shows the variation of bed material size of surface layer in the lees of dense and sparse vegetation zone. The bed material sorting of the bed surface in the channel with mixed sediment is related to bed changes, variations of sediment supply upstream, and flow structure changes. At the lee of dense vegetation region at point 1, bed material size was fine at the aggradation region near the left bank. Median size of bed materials decreased from 0.8mm at initial condition to 0.67mm near the left bank and increased from 0.8mm initial condition to 1.17mm near right bank. At the lee of sparse vegetation region at point 2, median size of bed materials decreased from 0.8mm at initial condition to 0.66mm near the left bank and increased from 0.8mm to 1.03mm near the right bank. Tsujimoto (1999) found that the aggradation area was composed of fine materials in the vegetation zone numerically.

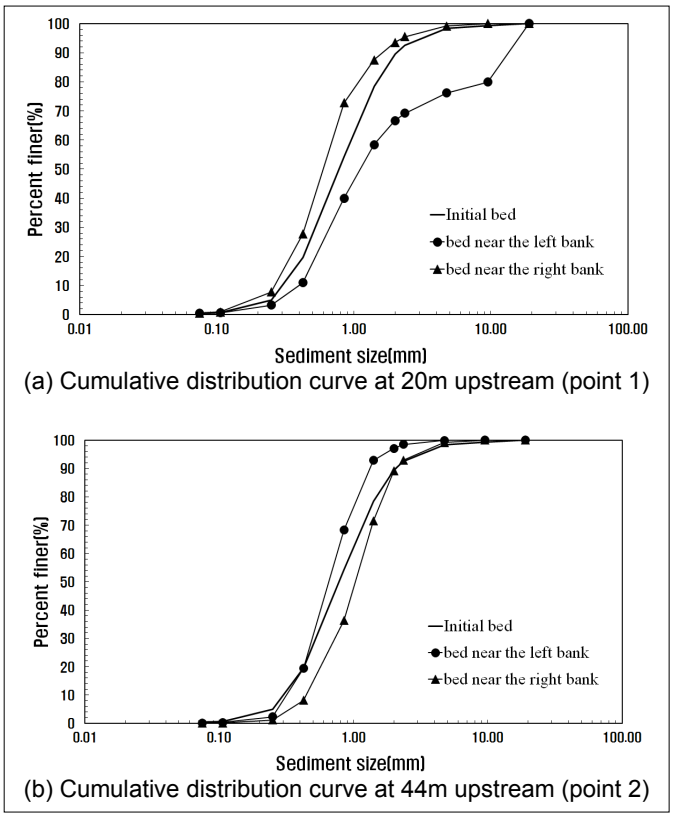


**Figure 6**. Bed material size distribution of the surface at points 1 and 2 shown in Figure 5.

 

3.4 Distribution of suspended sediment

The riparian vegetation reduces the suspended sediment transport capacity and changes the sediment profile of it in water depth. The sediment transport capacity was also affected by sediment particle size. The volumetric water discharge and plant height were kept constant with discharge of 2.5m$^3$/sec and 3.5m$^3$/sec. Figure 7(a) shows concentration profiles of suspended sediment load with distance from upstream. The suspended sediment concentration was 50mg/L at 50m from upstream. However, the concentration was reduced to 29.5mg/L at 86m of dense vegetation patch. Moreover, the concentration recovered to 37.1mg/L at 118m of sparse vegetation patch. Lopez and Garcia (1998) explained that dense vegetation decreased the momentum transfer toward the bed by only small amount, while at the same time requiring a large increase in flow depth because of the increased flow depth.

Figure 7(b) shows the vertical profiles of suspended sediment concentration from the bed without vegetation reach of sparse vegetation patch and dense vegetation patch as shown in Figure 1. The suspended sediment concentration from bed is 50mg/L at 0.4m from bed. However, the sediment concentration is 40mg/L at 0.8m and 25mg/L at 0.2mg/L. The suspended sediment concentration is 35mg/L at 0.4m, 40mg/L at 0.8m and 36mg/L at 0.2m in the sparse vegetation patch. The sediment concentration is 33mg/L at 0.4m, 26.5mg/L at 0.8m and 29.2mg/L at 0.2m in the dense vegetation patch. The suspended sediment concentration is higher at 0.4m than at 0.2m in the dense vegetation patch. However, the concentration is lower at 0.4m than at 0.2m in the sparse vegetation patch.

Figure 7(c) shows the total load with distance from upstream. The total load is higher without vegetation patch than in the vegetation patch. The total load is lower in the dense vegetation patch than in the sparse vegetation patch. This is associated with the lower momentum transfer to the channel bed due to the absorption of momentum by vegetation (Lopez and Garcia, 1998).

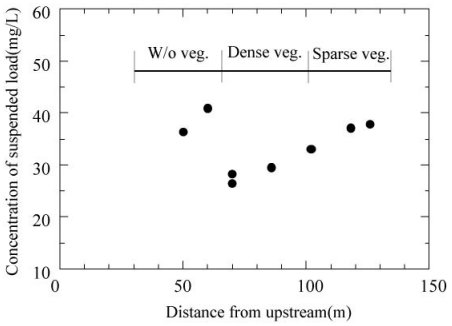


(a) Concentration of suspended sediment load with distance from upstream

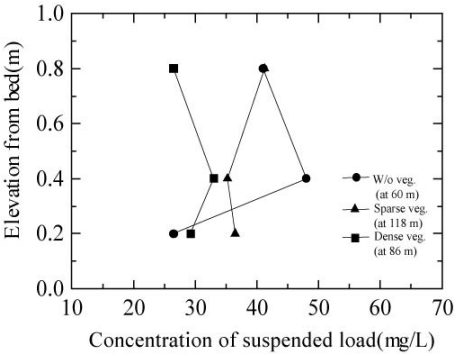


(b) Vertical profile of suspended sediment concentration from the bed

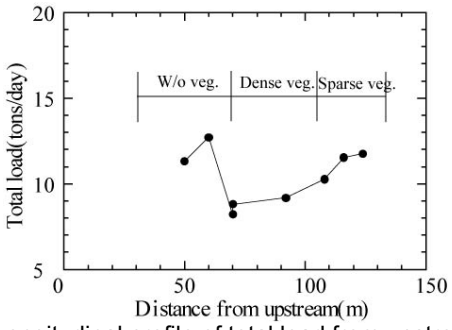


(c) Longitudinal profile of total load from upstream

**Figure 7**. Suspended sediment and total load profiles with and without vegetation reaches.

 

## 4 NUMERICAL SIMULATION

### 4.1 Characteristics of numerical model

This study used a plane 2D-based numerical model, Nays2DH, for simulating the flow and bed changes. Two-dimensional water equations to calculate the resistance due to vegetation must be solved in a boundary-fitted coordinate system. The vegetation is modeled as a rigid circular bar and its density is represented as the projected area of vegetation per unit volume of water. The drag coefficient of the vegetation element is used to 1.0 for round-shaped vegetation with a high Reynolds number.

To simulate bed changes, the two-dimensional sediment continuity equations in a boundary-fitted coordinate system were used. In addition, the sediment transport rate in the stream line was calculated by using the formula of Ashida and Michiue (1972). The bed load transport rate in the stream wise direction is affected by the flow near the bed and local bed slope, and secondary flow was considered to calculate the transverse bedload transport rate.

As a numerical scheme, a splitting technique was used to momentum equations to be decomposed into an advection term and a non-advections term. The continuity equation and the non-advection term of the momentum equations are implicitly solved by an iteration method, and the advection term is explicitly solved it by the cubic interpolated psuedoparticle(CIP) method proposed by Yabe et al.(1990). The numerical method solves boundary problems while introducing little numerical diffusion, and algorithm implementation is more straightforward than for other high-order upwind. Readers are referred to Jang and Shimizu (2007) and Iwasaki et al. (2015).

The computation length in dense vegetation reach is 32m and the equivalent width is 5m for 1.8m$^3$/s. The calculation grid is 64 in streamwise and 16 in the transverse direction. The computational time step is set to 0.01s. In the vegetation zone, the drag that flow through the emergent plants is considered as 1.0.

### 4.2 Numerical results

Figure 8 shows the experimental and numerical results of planimetric changes with discharge of 1.8m$^3$/sec for 42 hours. Both the results show that alternate bars are remarkably developed at lee of vegetation patches, where the flow velocity decreased sharply due to the drag of the vegetation elements. The bed scours deeply at the opposite side and in front of the patch at point 3 shown in Figure 8 due to the concentration of flow. The bed elevation in the patch increases the streamwise, due to the deceleration in the longitudinal direction, which resulted in an increase in lateral velocity. And it is associated with the diversion of flow away from the patch (Zong and Nepf, 2010).

The reproduced thalweg of the channel and the bar size are not satisfactory but, as a whole, the numerical results are in reasonable agreement with the experiment with the experimental results, capturing the most important characteristics of the alternate bar.

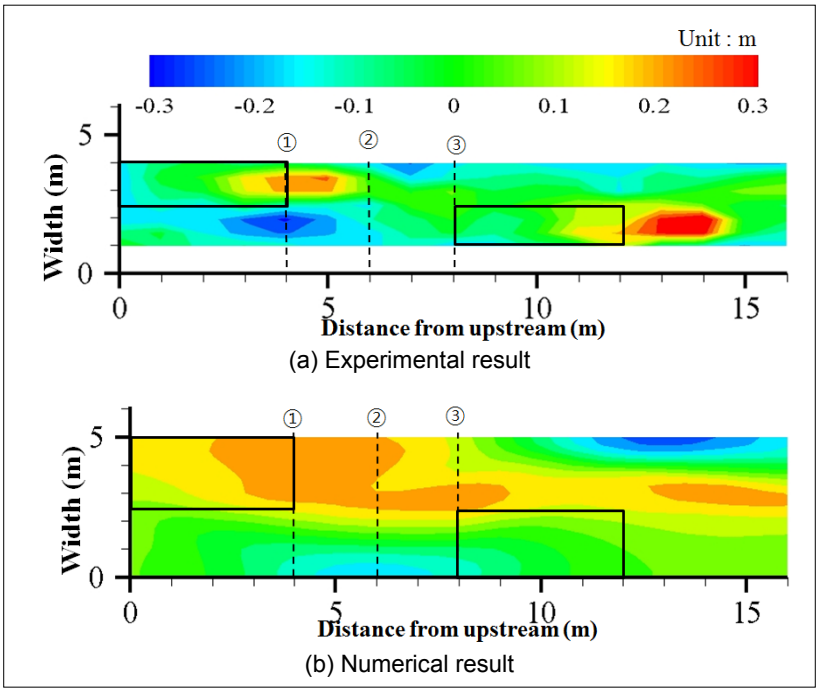


**Figure 8**. Experimental and calculation results of planimetric changes in the dense vegetation reach with discharge of 1.8m$^3$/sec for 42 hours. Rectangles are vegetation patches.

 

Figure 9 shows cross sectional changes at the lee of vegetation patch, point 1, a place between two patches, point 2, and in front of the patch, point 3. At each point the numerical results were relatively in agreement with the experimental results. Meanwhile, the numerical model over predicted slightly the experimental results at point 3.

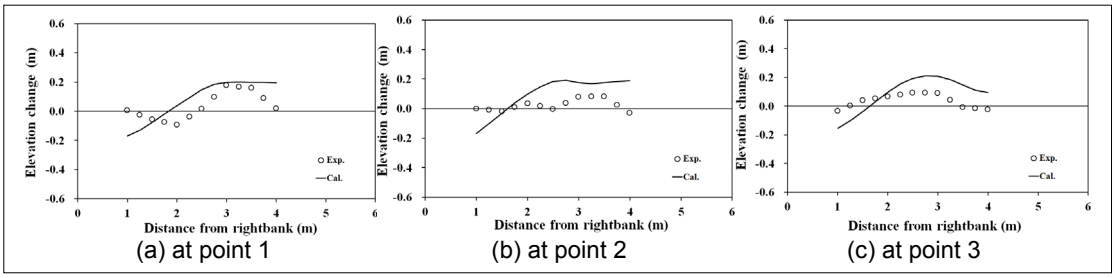


(a) at point 1 (b) at point 2 (c) at point 3

**Figure 9**. Cross sectional changes at each point shown in Figure 9 with the discharge of 1.8m$^3$/sec for 42 hours.

Figure 10 shows the experimental and numerical results of planimetric changes with discharge of 3.2m$^3$/sec for 51 hours. Experimental result shows that alternate bars are remarkably developed at lee of vegetation patches, where the flow velocity decreased sharply due to the drag of the vegetation elements. The bed was scoured deeply at the opposite side due to the concentration of flow. However, the numerical result shows the aggradation of sediment in the lee of vegetation and side of the vegetation patch. The bed scoured in front of the path at point 3 shown in Figure 11. At point 1, the numerical results are relatively in agreement with the experimental results. Meanwhile, the numerical model over predicted slightly the experimental results at point 2 and 3 (Figure 11). This may be due partly to the poorly treated bed shear stress in the vegetation patch, three-dimensional flows of the vegetated channels including the flow structure and exchange at the interface between the vegetation and open channels.

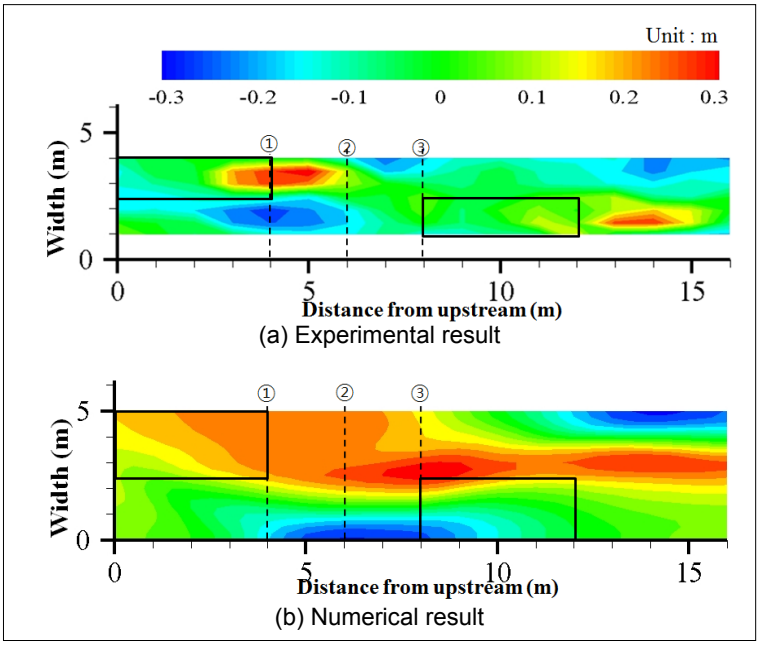


(a) Experimental result

(b) Numerical result

**Figure 10**. Experimental and calculation results in the dense vegetation reach with discharge of 3.2m$^3$/sec for 51 hours. Rectangles are vegetation patches.

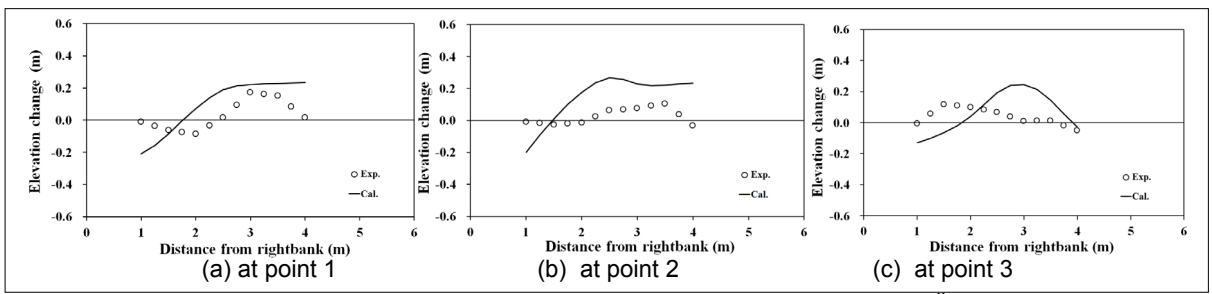


(a) at point 1 (b) at point 2 (c) at point 3

**Figure 11**. Experimental and calculation results with the discharge of 3.2m$^3$/sec for 51 hours.

## 5 SUMMARY AND CONCLUSIONS

Vegetation plays a significant role in flow changes, sediment sorting, and the channel evolution. Riparian vegetation increases hydrodynamic drag, and reduces flow velocity and distribution. At the dense vegetation zone, flow velocity decreased severely and is diverted toward unvegetated channel area because of high drag by vegetation. Flow was separated at a diverging flow zone at the front edge of the dense vegetation patches, and accelerated along these patches after diverging flow between the patch and the open channel. Moreover, flow direction was changed at the next vegetation patch downstream with alternated pattern. Maximum velocity pattern along the channel was meandering. As a result, a meandering flow pattern is observed in this section of the experimental setup. At the spare vegetation zone, however, flow passed through the vegetation patches with less decelerated speed. The meandering flow pattern is not clear because of the low drag in the vegetation zone.

The bed elevation increased in the lee of vegetation zone, where flow velocity is dramatically retarded due to the high drag. The thalweg of the bed is in meandering shape, and is in agreement with the maximum velocity pattern. As the vegetation density increased, the bed scoured deeply.

As flood increased, the sandbar length increased in dense and sparse vegetation zone. At the dense vegetation zone, the bar length increased with time. At the low vegetation zone, however, the bar length was not increased. Shear layer vortices along the vegetation patch were developed along the vegetation zone, which led to the change of bed load direction into and from the vegetation zone.

The sediment sorting of surface in the vegetated channel is related to bed changes, and flow structure changes. At the lee of dense and sparse vegetation regions, bed material size is fine at the aggradation region and coarse at the degradation region. The riparian vegetation reduces the suspended sediment transport capacity and changes the sediment profile of it in water depth. The suspended sediment concentration was 50mg/L at 50m from upstream. However, the concentration was reduced to 29.5mg/L at 86m of dense vegetation patch. Moreover, the concentration recovered to 37.1mg/L at 118m of sparse vegetation patch. The vertical profiles of suspended sediment concentration from the bed were that the concentration was higher at 0.4m than at 0.2m in the dense vegetation patch. However, the concentration was lower at 0.4m than at 0.2m in the sparse vegetation patch. The numerical results were in reasonable agreement with the experiment with the experimental results, capturing the most important characteristics of the alternate bar.

## ACKNOWLEDGEMENTS

This research is supported by a grant (12-TI-C02) from Advanced Water Management Research Program funded by Ministry of Land, Infrastructure and Transport of Korean government. This study is also conducted by participants of Andong River Experiment Forum (AREF) and a joint research between Deltares and KICT.

## REFERENCES

Ashida, K., & Michiue, M. (1972). Study on Hydraulic Resistance and Bed-Load Transport Rate in Alluvial Stream. In *Proceedings of the Japan Society of Civil Engineers,* 206, 59-69, (in Japanese).

Bennett, S.J., Pirim, T. & Barkdoll, B.D. (2002). Using Simulated Emergent Vegetation to Alter Stream Flow Direction within a Straight Experimental Channel. *Geomorphology*: 44(1), 115-126.

Bennett, S.J., Wu, W., Alonso, C.V. & Wang, S.S.Y. (2008). Modeling Fluvial Response to In-Stream Woody Vegetation: Implications for Stream Corridor Restoration. *Earth Surf. Processes Landforms,* 33(6), 890–909.

Bouma, T.J., van Duren, L.A., Temmerman, S., Claverie, T., Blanco-Garcia, A., Ysebaeri, T. & Herman, P.M.J. (2007). Spatial Flow and Sedimentation Patterns within Patches of Epibenthic Structures: Combining Field, Flume and Modeling Experiments. *Continental Shelf Research,* 27(8), 1020–1045.

Defina, A. & Bixio, A.C. (2005). Mean Flow and Turbulence in Vegetated Open Channel Flow. *Water Resources Research,* 41(7).

Demissie, M. (1990). Sediment Yield and Accumulation in the Cache River. Paper presented at *National Hydraulic Engineering Conference*, Am. Soc. Civ. Eng., San Diego, Calif, USA.

Iwasaki, T., Shimizu, Y. & Kimura, I. (2016). Numerical Simulation of Bar and Bank Erosion in a Vegetated Floodplain: A Case Study in the Otofuke River. *Adv. Water. Resour.,* 93, 118-134, http://dx.doi.org/10.1016/j.advwatres.2015.02.001.

Jang, C.-L. & Shimizu, Y. (2007). Vegetation Effects on the Morphological Behavior of Alluvial Channels. *J. Hydraul. Res.,* 45(6), 763-772.

Lopez, F. & Garcia, M. (1998). Open-Channel Flow through Simulated Vegetation: Suspended Sediment Transport Modeling. *Water Resour. Res.,* 34(9), 2341-2352.

Murray, A.B. & Paola, C. (2003). Modelling the Effect of Vegetation on Channel Pattern in Bedload Rivers. *Earth Surf. Proc. Landforms,* 28(2), 131-143.

Nearly, V.S., Constantinescu, S.G., Benett, S.J. & Diplas, P. (2012). Effects of Vegetation on Turbulence, Sediment Transport, and Stream Morphology. *J. Hydraul. Eng.*, 138(9), 765-776.

 

Nepf, H.M. & Vivoni, E.R. (2000). Flow Structure in Depth-Limited, Vegetated Flow. *J. Geophys. Res.: Oceans*, 105(C12), 28547-28557.
Rominger, J.T., Lightbody, A.F. & Nepf, H.M. (2010). Effects of Added Vegetation on Sand Bar Stability and Stream Hydrodynamics. *J. Hydraul. Eng.,* 136(12), 994–1002.
Thorne, C.R. (1990). *Effects of Vegetation on Riverbank Erosion and Stability in Vegetation and Erosion*. Edited by Thornes, J.B., 125-144, John Wiley, New York.
Tsujimoto, T. (1999). Fluvial Processes in Streams with Vegetation. *J. Hydraul. Res.,* 37(6), 789-803.
Yabe, T. & Aoki, T. (1991). A Universal Solver for Hyperbolic Equations by Cubic-Polynomial Interpolation I. One-Dimensional Solver. *Comp. Phys. Comm.*, 66(2-3), 219-232.
Zong, L. & Nepf, H. (2010). Flow and Deposition in and Around a Finite Patch of Vegetation. *Geomorphology* 116(3), 363-372.

 

# GENERATION MECHANISM OF DEEP SCOUR AROUND A NARROWED SECTION IN RIVERS

YUJI HARA[(1)], AKIHIRO TOMINAGA[(2)], YUKA KUNO[(3)] & NAOHIKO SASSA[(4)]

[(1,2,3,4)] Department of Civil Engineering, Nagoya Institute of Technology, Nagoya, Japan
tominaga.akihiro@nitech.ac.jp

## ABSTRACT

A large scoured area with 20 m depth in maximum is observed besides the convex river bank in the Kiso River. Expanding of the scour has possibility of causing destabilization and damage to hydraulic structures. It is necessary for river control and maintenance to make clear the generation mechanism of such a deep scouring. We consider the effect of narrowed section in a river as a trigger of scouring. In this study, we investigate the flow and bed deformation around a narrowed section in an open channel and then the flow structures around a deep hole in an open channel experimentally and numerically. Particularly, to model an erosion proof clay layer, sand was solidified partially with resin spray. The bed shear stress becomes higher so as to erode the clay layer at the center of channel in appropriate condition of the contraction ratio. Finally, scour hole similar to the field observation was reproduced in the laboratory channel. The characteristic flow structures that include vertical and transverse vortices were indicated. It is suggested that these flow structures have potential to maintain and develop the scour hole.

**Keywords:** Local scour; narrowed section; bed shear stress; clay layer; planform vortex.

## 1 INTRODUCTION

River bed degradations are recognized in many rivers in Japan due to a decrease of sediment supply and gravel extraction. Following this phenomenon, erosion of exposed clay layer was occurred and then large local scour of sand layer under the clay layer begun. A large-scale local scour with 20 m depth in maximum was observed in the Kiso River at 37 km from the river mouse (Kurihara et al., 2013). This scour had developed in a term from 1998 to 2007. In this region of the Kiso River, clay layer and sand layer are deposited alternately. Once an exposed clay layer is eroded, the lower sand layer is likely to be scoured. Similar phenomenon is observed in the other region of the Kiso River and in the other large rivers in Japan. The expanding of the scour has possibility of causing destabilization and damage to hydraulic structures. It is necessary for river control and maintenance to make clear the generation mechanism of such a deep scour.

In the section where the large-scale scour occurred in the Kiso River, a decrease of sand supply from the upstream region became significant (Saito et al., 2014, Takaoka et al., 2014). Resultantly a surface layer composed by sand was diminished and a lower clay layer was exposed. This is considered to be one of factors of such a large-scale scouring. The clay layer is difficult to erode and the scour had stopped transiently but large-scale flood over 9000 $m^3/s$ occurred recently could burst through the clay layer and then the deep scour was generated rapidly in the regions where the bed shear stress was increased locally. During the term without large flood flow, the growth of trees on sand bars was developed and this phenomenon sometimes could increase the local bed shear stress.

In the region where the deep scour is observed, there is roundly projected flood plain and slightly bulged sand bar with tree growth as shown in Figure 1. This planar river configuration is considered to increase the local bed shear stress. We consider the effect of such a narrowed section in a river as a trigger of scouring. At first the condition that is possible to generate the local scour was investigated experimentally and numerically changing both-side projections. Next, in order to investigate the effect of a boundary between erosion proof clay layer and loose sand layer, sand was solidified partially with resin spray. The sand layer downstream of an erosion-proof clay layer is likely to be scoured as observed in a region downstream of a groundsill (Iwami et al., 2015). By the combination of channel contraction and solidified bed, we tried to reproduce the similar scouring in a laboratory flume.

## 2 FIELD OBSERVATION

The water depth and velocity components were measured by scanning the target area with ADCP when lower-middle magnitude flood on 5th May 2016. Figure 2 shows the measured water depth contours. The red lines show estimated bulging shore line that narrow the river. The largest scour hole is observed just downstream from the upstream edge of the left bulge and the water depth attains approximately 20 m.

 


**Figure 1.** Aerial photograph in the region where deep local scour is observed in the kiso River. (Tree-grew sand bar on the left bank and roundly bulged flood plain on the right bank).

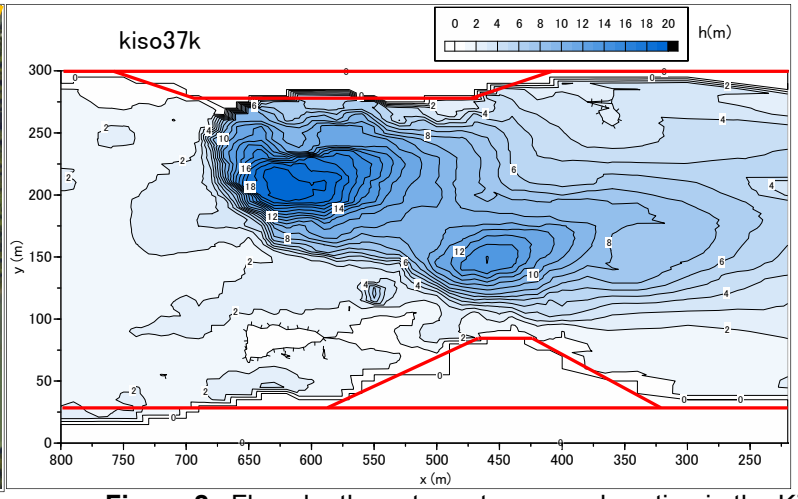


**Figure 2.** Flow depth contour at narrowed section in the Kiso River. (Red lines show estimated shore line narrowing the river).

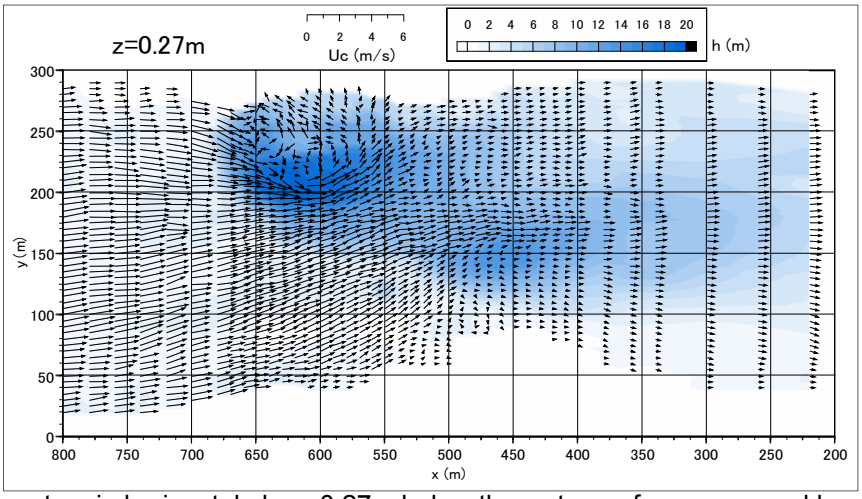


**Figure 3.** Velocity vectors in horizontal plane 0.27m below the water surface measured by a ADCP, discharge was approximately 1500m$^3$/s (This data was provided by the Kiso River Upstream Office, Central Regional Bureau in the Ministry of Land, Infrastructure, Transport and Tourism).

Another smaller scour hole with 13 m depth appears in front of the right bulge. Figure 3 shows the velocity vectors in horizontal plane 0.27m below the water surface measured by using an ADCP. In the upstream area, the flow depth is about 1.7 m and the mean velocity is 1.6 m/s. On the largest scour hole, counter-clockwise planform vortex is observed. This vortex is continuously exist in the vertical direction and rather strong velocity is recognized even near the bottom. In the right-hand side of this vortex, the flow is turned toward left bank and is concentrated on the center of the channel. In the downstream area, the flow depth becomes deep (5m - 6m) and the velocity becomes smaller.

As shown in Figure 3, the flow in the deep scoured area is three-dimensional and these complex flow structures are considered to contribute to the generation and maintenance of the deep scouring. It is important for the river maintenance to make clear the generation mechanism of the deep scour. At first, we notice to the origination of the scouring. Two factors are considered to be the cause of the scouring: one is an increase of the local bed shear stress and the other is the existence of boundaries between scour-proof clay layer and loose sand layer. In this study, these two factors were tested in a stepwise manner.

## 3 LABORATORY EXPERIMENT AND NUMERICAL SIMULATION

Experiments were conducted to test the effects of contraction by side bulges on bed deformation and bed shear stress. The experimental flume was 13m long and 0.6m wide rectangular flume and the slope was set to 0.001. The side bulge models were made of aluminum plate with symmetric trapezoidal shape as shown in Figure 4. Their dimensions were changed as shown in Table 1. The upstream end of the left-bank bulge was located at 7.5m downstream from the channel entrance. The experimental conditions are also shown in Table

 

1. A recess of sediment 6m long and 0.11m deep was filled by uniform sand of mean diameter $d_m$=0.61 mm, in movable bed cases.

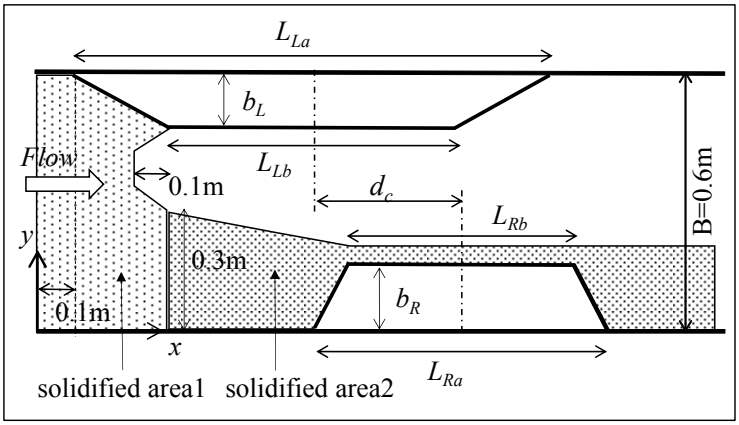


**Figure 4.** Narrowed section condition with bulges (upstream doted area is solidified in case B).

**Table 1** Experimental Conditions.

| Case | $L_{Ra}$ | $L_{Rb}$ | $b_R$ | $L_{La}$ | $L_{Lb}$ | $b_L$ | $d_c$ | discharge $Q$ ($m^3$/s) | mean velocity $U_m$ (m/s) | flow depth $h$ (m) | $Fr$ |
|---|---|---|---|---|---|---|---|---|---|---|---|
| A1 | 0.623 | 0.45 | 0.15 | 0.888 | 0.60 | 0.06 | 0.325 | 0.0085 | 0.287 | 0.050 | 0.41 |
| A2 | 0.519 | 0.45 | 0.06 | 1.120 | 0.60 | 0.15 | 0.325 | 0.0085 | 0.287 | 0.050 | 0.41 |
| A3 | 0.588 | 0.45 | 0.12 | 0.888 | 0.60 | 0.06 | 0.325 | 0.0085 | 0.287 | 0.050 | 0.41 |
| A4 | 0.866 | 0.45 | 0.12 | 0.888 | 0.60 | 0.06 | 0.325 | 0.0085 | 0.287 | 0.050 | 0.41 |
| B0 | - | - | - | - | - | - | - | 0.0080 | 0.333 | 0.040 | 0.53 |
| B1 | 0.640 | 0.12 | 0.15 | 0.785 | 0.60 | 0.05 | 0.30 | 0.0080 | 0.333 | 0.040 | 0.53 |
| B2 | | | | | | | | 0.0050 | 0.281 | 0.030 | 0.52 |
| B3 | | | | | | | | 0.0050 | 0.337 | 0.025 | 0.68 |
| B4 | | | | | | | | 0.0040 | 0.241 | 0.028 | 0.46 |
| B5 | | | | | | | | 0.0040 | 0.270 | 0.025 | 0.55 |
| B6 | | | | | | | | 0.0030 | 0.220 | 0.023 | 0.46 |
| B7 | | | | | | | | 0.0030 | 0.253 | 0.020 | 0.57 |
| B8 | | | | | | | | 0.0080 | 0.333 | 0.040 | 0.53 |

The case A series were set to test the effect of bulge wall on the scour position. In the case B series, a solidified area (area 1) was produced by using resin spray as a solidification agent as shown in Figure4 in order to simulate the erosion-proof clay layer. The boundary was not straight in the transverse direction, a little concave shape was adopted to induce downstream scouring. In the case B0, no bulge wall was placed and the effect of boundary between clay layer and sand layer was tested. Since the case B1 was set to obtain an initial state of scour, the flow was stopped after 15 min. The other cases in the case B series, the discharge and the flow depth were changed starting from the bed form created in the case B1. In the case B8, an additional solidified area (area 2) was made to prevent the local scour around right bulge wall.

The bed deformation was measured with a laser distance meter after 120 min from the beginning of the flow except for the case B1. Since the shear velocity $U_*$ was larger than the critical shear velocity $U_{*c}$, sediment was movable in the main channel. However, sediment was not supplied because the provision of sediment from the upstream region was enough in the observation time of 120min.

Numerical simulations were conducted by using depth averaged 2-D k-ε turbulence model (Tominaga & Sadat 2016, Rodi et al. 1981) to see the bed shear stress distribution. Though it is obvious that a 3-D numerical model is necessary to predict the local scour around the structure, we used 2-D numerical model to evaluate the bed shear stress variation in a channel. Then the prediction of bed deformation was tried by using a sediment continuity equation with Mayer-Peter-Muller equation as a bed load formula and Ashida-Michiue equation as an effective shear stress formula.

## 4 EXPERIMENTAL RESULTS AND DISCUSSION

The bed deformation results in the case A were shown in Figure 5. The expected bed deformation similar to the field observation as shown in Figure 2 was not reproduced in all cases. The local scour is generated around the upstream corner of the bulge wall. The maximum scour depth becomes larger with an increase of the thickness and the attack angle of the bulge wall. The erosion in the middle area of 2cm is recognized in the cases A1 and A2. As the total thickness of bulge becomes smaller, the middle area erosion diminishes.

 

Figure 6 shows the calculated results of bed shear stress, velocity profile and bed deformation in the case A3. The streamwise bed shear stress becomes maximum in a region around the downstream end of the left bulge wall. In this region, the mean velocity is accelerated due to the flow contraction. The spanwise bed shear stress attains peak values at the corner of the bulge walls. The calculated results of bed deformation indicates the deep scours around the corner of the bulge walls similarly to the experiment. This means the spanwise bed shear stress plays more substantial part to the local scour. Although the numerical simulation can reproduce the bed deformation caused by the bulge walls, the observed bed scour in the Kiso River cannot be realized with a set of bulge walls only.

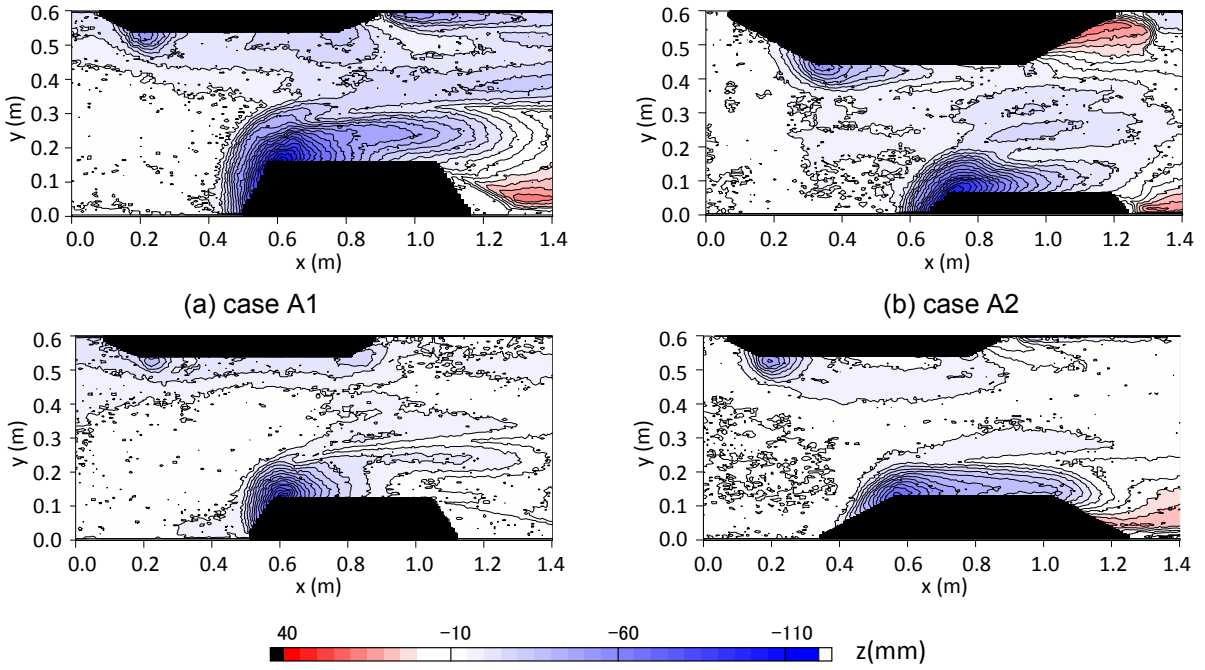


**Figure 5.** Bed elevation contours for case A.

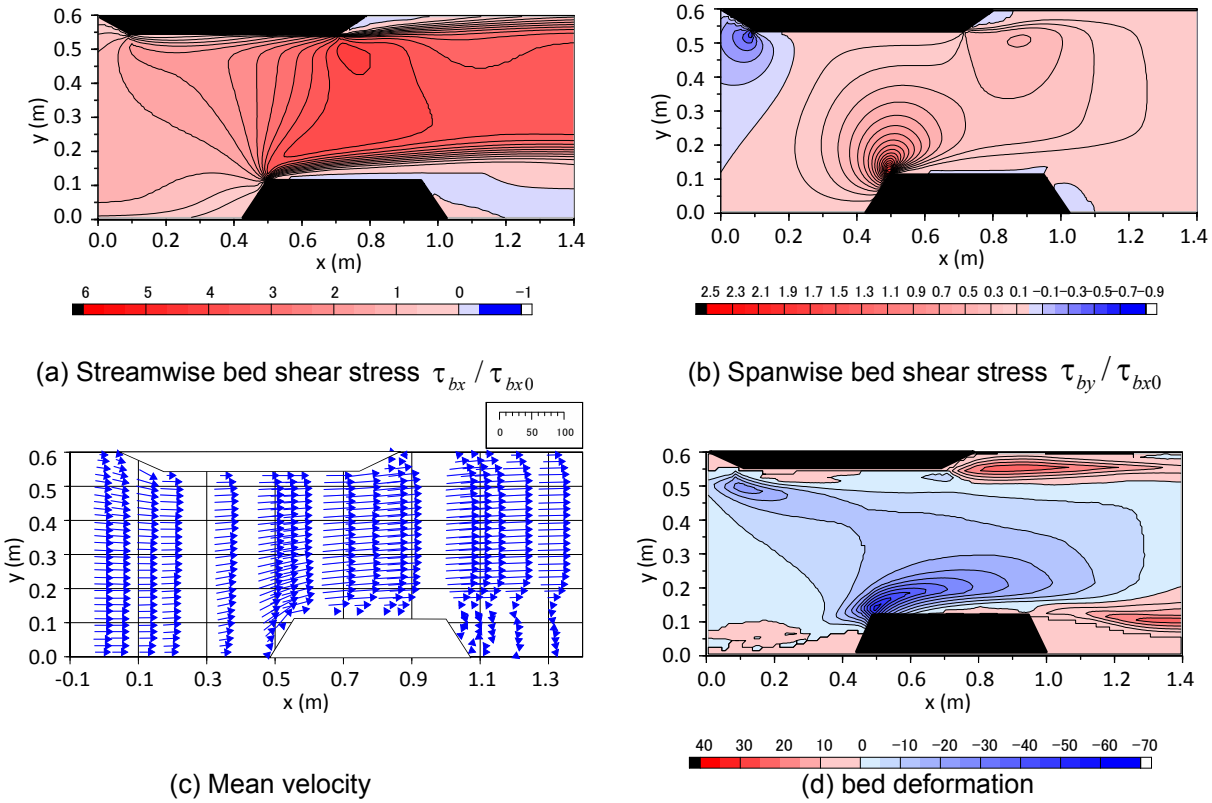


**Figure 6.** Calculated results for the case A3.

Next, we turned attention to the effect of the boundary between clay layer and sand layer. At first, the experiment without bulge wall was conducted (case B0). The downstream area is eroded slightly and the scour depth becomes larger behind the concave boundary near the left bank. The scour depth reaches about 25 mm in maximum after 120 min water discharge. This is rather small in comparison with the actual filed scour. Therefore, bulge walls were set in the same manner as the case A series but the dimension of the bulge was slightly changed. Figure 7 shows the bed deformation result in the case B1 and B3. In the case B1, local scour in front of the right bulge wall becomes significant and then water discharge was stopped after 15 min. The small scour hole is recognized on the left-bank side apart from the left bulge wall. This small scour hole has about 40mm depth and may be regarded as the origination of the deep scour hole as observed in the Kiso River. After this experiment, on the way reducing the discharge, expansion of scour was recognized. Shallow and fast water flow concentrate in the initial scour hole and this deepened the scour hole. Sometime, shallow water flow broke the solidified layer.

So, we conducted the experiment with lower discharge and lower flow depth continuing from the bed form produced in the case B1. Figure 7(b) shows the bed elevation contours in the cases B3. The local scour around the right bulge is developed toward the downstream but the maximum depth hardly changed. The depth of the left-bank side scour hole becomes larger in these cases. The discharge in the cases B2 and B3 is same but the flow depth is smaller and the velocity becomes higher in the case B3. The smaller flow depth and faster velocity make the scour hole larger. This situation is very similar to the scouring generated downstream of the groundsill. The downflow like a submerged jet is generated with a transverse vortex. The The maximum depth of the left-bank side scour hole attains about 80 mm. Figure 8 shows the relation between the maximum depth of the left-bank side scour and the mean velocity. In the range of the present experiments, the maximum scour depth is almost proportional to the mean velocity.

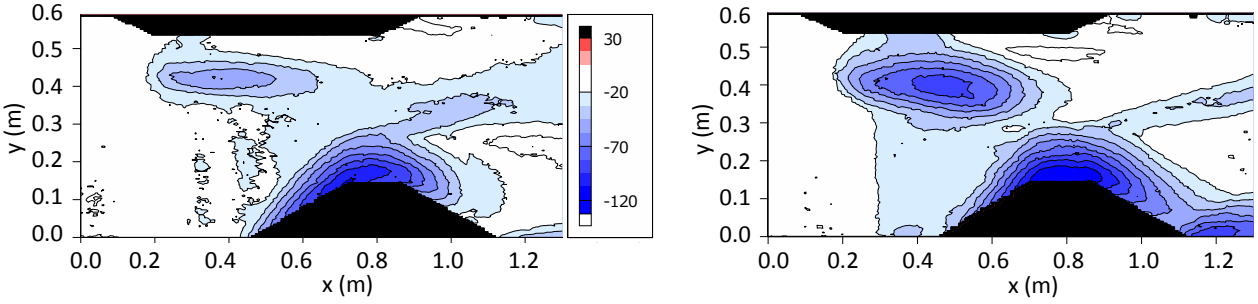


(a) case B1 (b) case B3

**Figure 7.** Bed elevation contours in Case B1 and B2.

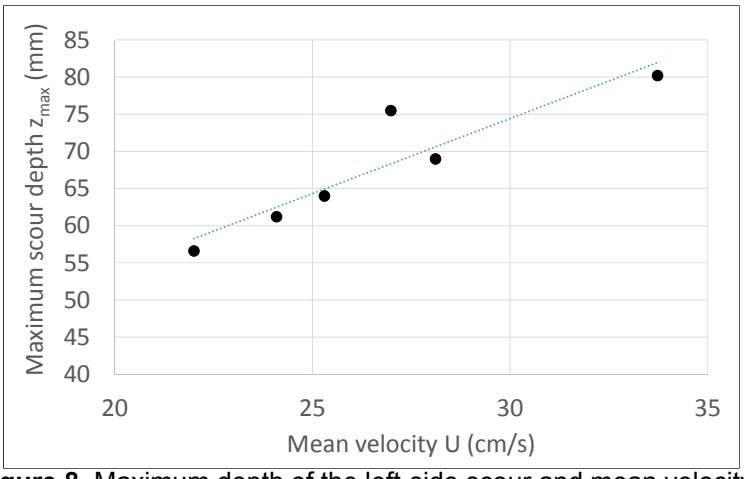


**Figure 8.** Maximum depth of the left-side scour and mean velocity.

For these cases with solidified area, a numerical calculation was attempted. The solidified area is treated as fixed bed and no sediment is supplied from the upstream region. Figure 9 and 10 show the calculated bed deformation and the streamwise bed shear stress, respectively. The scour around the right bulge is predicted but the depth is smaller than the experiment. As to the left-bank side, no scour is reproduced. It is difficult to predict the scour behind the solidified layer by using 2-D numerical calculation because three-dimensional flow structures are important in this case. But the bed shear stress increases on the left-bank side in front of the left bulge wall. This indicates the possibility of scouring on the left-side region.

 

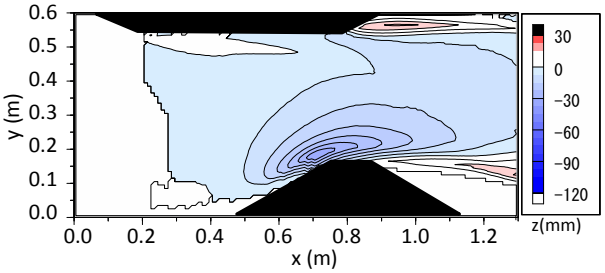


**Figure 9.** Calculated bed deformation (case B3).

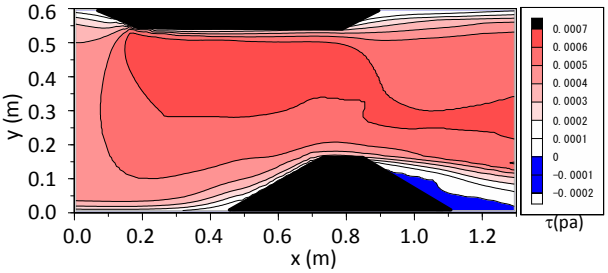


**Figure 10.** Calculated streamwise bed shear stress (case B3).

No significant scour is produced around the right bulge in the narrowed section of the Kiso River as shown in Figure 2. This is because the basement around the right bulge is hard to erode. In the above experiments, noticeable scour is generated around the right bulge and this may affect the scour on the left side. Therefore, in the case B8, the area around the right bulge was also solidified as shown in Figure 3 (area 2). The bed deformation result in the case B8 is shown in Figure 11. The large scale scour hole is generated on the left-side. This scour hole is very similar to the field observation though the downstream scour area is rather small compared to the field data. Figure 12 shows the comparison of bed profile along the deepest streamwise line between the field and experimental data. The streamwise length is normalized by the channel width at the most narrow section and the vertical length is not normalized. The horizontal reduction scale of this model is considered to be around 1/500 but the vertical reduction scale is not exactly determined. The present experiments were not intended to simulate the real situation with satisfying similitude, but were aimed to understand the possibility of the large-scale scouring. The flow depth in the experiment is restricted to keep a certain depth and to be capable of sediment transport. For this reason, the vertical reduction scale is rather smaller than the horizontal reduction scale. If the vertical reduction scale is assumed to be 1/200, the magnitude of this scour in the experiment is almost similar to the field value. But the scoured length in the streamwise direction becomes longer in comparison with the field data.

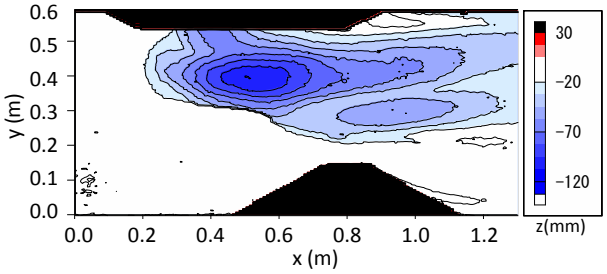


**Figure 11.** Bed elevation contours in the case B8.

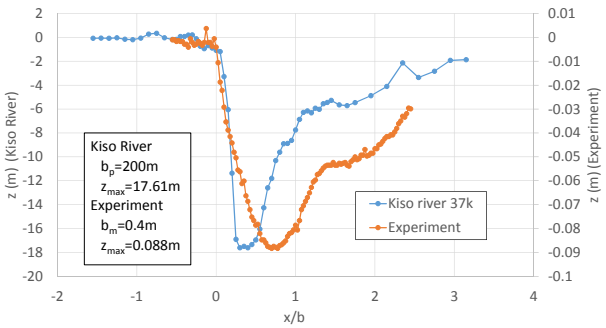


**Figure 12.** Comparison of bed profile between field and experiment (along the deepest line).

The flow structure on the obtained bed configuration in the case B8 was calculated by using 2-D depth-averaged k-ε model. The calculated velocity vectors were shown in Figure 13. In comparison with the observed velocity vectors in Figure 3, the characteristic vortex near the left-side bulge is clearly reproduced. The flow structure upstream from the top area of the right-side bulge is very similar to the field data. The planform vortex is also generated in an open channel with a deep pool (Tominaga et al., 2008). This separation vortex shows cylindrical conformation without much change in size and strength from the bottom to the free surface. It is considered that the increased pressure in the deep pool zone induces the deflecting flow toward the channel center. The observed vortex in the Kiso River has similar feature. This means that a certain level of velocity is generated even near the bottom of the scour hole.

 

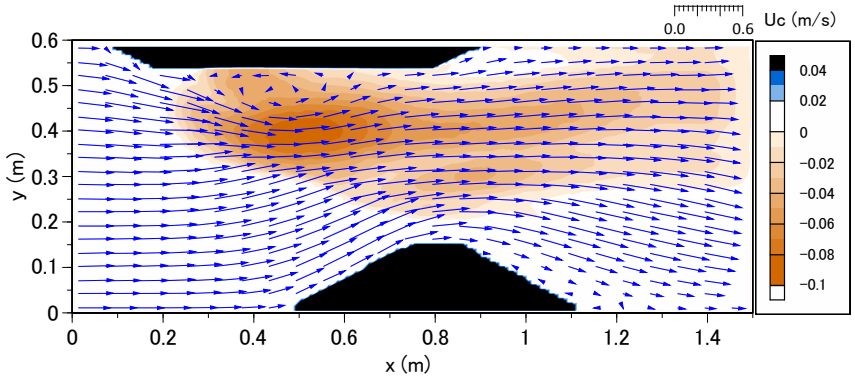


**Figure 13.** Calculated velocity vectors on the solidified bed of case B8.

## 5 CONCLUDING REMARKS

We intended to reproduce the local scoring observed in the Kiso River in a laboratory open channel with contraction. It is expected that the bed shear stress locally increased by narrowing the channel section is capable to generate a scour on the main part of the channel. However, this expected scouring did not occur because another scour caused by the edge part of the bulge structure. In the Kiso River, the basement around the bulge is hard to erode and this should be accounted in the experiment.

When the upstream region was solidified to simulate the clay layer, significant scouring was generated like that in the actual river. Once small-scale scour hole appears, scouring continues even in a low and middle level discharge. The downflow like a submerged jet develop the scouring. Taking into account the hardness of the basement around the right-side bulge, a large scour hole was produced at the similar region of the river. The depth of the scour created in the laboratory flume does not apply to the field value directly, because the similitude of sediment transport was not fitted in the experiment. The existence of planform vortex on the scour hole was suggested in the experiment in the same manner as the field observation. The vortex probably contributes to maintain and develop the scouring. It is necessary to investigate furthermore by field measurement and 3-D numerical simulation for understanding the generation mechanism of a large scale scouring.

## ACKNOWLEDGEMENTS

The field observation data in the Kiso River was provided by the Kiso River Upstream Office, Central Regional Bureau in the Ministry of Land, Infrastructure, Transport and Tourism. We appreciate the kind corporation.

## REFERENCES

Iwami, S., Nishizawa, R., Fukuoka, T., Fukui, O., Kawabe, H., Kasai, R., Itou, Y. & Saito, M. (2015). Estimation of Vortex Structure at the Large Scouring and Causes of Expansion of the Scouring Area in the Kiso River. *Advances In River Engineering*, 21, 137-142 (In Japanese).

Kurihara, T., Asano, K., Kikuti, H., Takahashi, S. & Kuroda, N. (2013). Estimation of Generating Factors for Local Scouring at Kisogawa River. *Advances in River Engineering*, 19, 165-170 (In Japanese).

Rodi, W., Pavlovic, R.N. & Srivatsa, S.K. (1981). *Prediction of Flow and Pollutant Spreading in Rivers*. Transport Models for Inland and Coastal Waters. Academic press, 63-111.

Saito, M., Koga, H., Takahashi, S., Inaba, S., Asano, K., Kuroda, N., Yanasa, S. & Nishizawa, R. (2014). Investigation of Causes for Large Scouring Developing in the Kiso River. *Advances In River Engineering*, 20, 259-264 (In Japanese).

Takaoka, H., Nagayama, S. & Kayaba, Y. (2014). Investigation of River^Bed Morphology and Generating Process of Local Scouring in the Kiso River. *Journal of JSCE, B1*, 70(4), 1015-1020.

Tominaga, A., Hashimoto, N. & Liu, J. (2008). Experimental Study on Three-Dimensional Flow Structures in Straight River Channel with a Pool, *Advances in Hydro-science and Hydraulic Engineering*, 8, 659–666.

Tominaga, A. and Sadat, S. H. (2016). Combination of Permeable and Impermeable Spur Dikes to Reduce Local Scour and to Create Diverse River Bed. *River Sedimentation: Proceedings of the 13th International Symposium on River Sedimentation* (Stuttgart, Germany, 19-22 September, 2016) (p. 101). CRC Press.

 

Proceedings of the 37th IAHR World Congress
August 13 – 18, 2017, Kuala Lumpur, Malaysia

# MORPHOLOGICAL ADJUSTMENT OF THE NORTH FORK TOUTLE RIVER, WASHINGTON STATE AND THE APPLICATION OF THE STREAM EVOLUTION MODEL

SHANZHENG[(1)], COLIN R. THORNE[(2)], SHASHA HAN[(3)] & BAOSHENG WU[(4)]

[(1,3)]State Key Laboratory of Water Resources and Hydropower Engineering Science, Wuhan University, Hubei, China, zhengs@whu.edu.cn; sshan9202@whu.edu.cn.
[(2)] School of Geography, University of Nottingham, Nottingham, NG7 2RD, UK, colin.thorne@nottingham.ac.uk.
[(4)]State Key Laboratory of Hydroscience and Engineering, Tsinghua University, Beijing, China, baosheng@tsinghua.edu.cn.

## ABSTRACT

Channel evolution models (CEMs) are frequently used to explain and predict channel changes in incised streams but they have not yet been applied to volcanically disturbed rivers. The North Fork Toutle River (NFTR) provides excellent opportunity to examine the applicability of the CEM approach to rivers disturbed by volcanic eruptions that introduce heavy large inputs of sediment. In this study, vertical and lateral adjustments in the ~30-km of river channel disrupted by a 2.5 $km^3$ debris-avalanche deposition during the catastrophic eruption of Mount St. Helens in 1980 are investigated. A recent revised channel evolution model named the Stream Evolution Model (SEM) is applied to the NFTR. The results show that the upstream channel reaches generally degrade in the first few years following the eruption, evolving in SEM Stage 4 (i.e. degradation and widening), while the downstream reaches evolve in Stage 5 (i.e. aggradation and widening). Starting in the late-1980s, this simple pattern is disrupted by renewed incision and secondary adjustments. Upstream reaches evolveto stages 5 (aggradation and widening) and 7 (laterally active) as rates of vertical adjustment slow and river valley top widths relax to asymptotic values. Channel evolution at individual cross-sections tends to follow the sequence of stages expected according to the SEM, indicating the applicability of the model. However, stages 4 and 5 are sometimes repeated and stage 6 is sometimes omitted. Stage 8 (anastomosing) only occurrs in the reach furthest downstream, where the valley floor is very wide. As expected from the SEM, lateral adjustment has become predominant since 1990s and now seems largely responsible for persistently high sediment yields from the upper NFTR. According to the SEM, degradation, widening and lateral activity are forecast to continue until stable transverse valley profiles and channel planforms are formed and floodplain and terrace surfaces are stabilized by vegetation.

**Keywords:** Evolution model; evolution stage; degradation and aggradation; lateral adjustment; North Fork Toutle River.

## 1 INTRODUCTION

Incision at river channels can be triggered by evolutionary mechanisms internal to the fluvial system as well as the external disturbances, such as channelization, deforestation, urbanization, base level lowering and alterations to the flow and/or sediment regimes (Knighton, 1998; Simon and Darby, 2002). Despite being caused by different perturbations operating at variable spatial and temporal scales, many studies have found that incised channels tend to follow similar sequences of process-response and morphological adjustment (Schumm et al., 1984; Harvey and Watson, 1986; Simon and Rinaldi, 2006; Hawley et al., 2012). Recognizing this, Channel Evolution Models (CEMs) consisting of selected sequences of evolution stages have been proposed to describe how incised rivers change through space and with time (Schumm et al., 1984; Simon and Hupp, 1986; Cluer and Thorne, 2014).

The CEM approach was first proposed by Schumm et al. (1984) based on the morphological response of unstable streams in North Mississippi. And Simon and Hupp (1986) proposed a CEM based on the evolution of channelized streams in West Tennessee. Since the original work by Schumm et al. (1984) and Simon and Hupp (1986), many studies (Doyle and Shields, 2000; Simon and Darby, 2002; Beechie et al., 2008; Hawley et al., 2012; Cluer and Thorne, 2014) have added to these CEMs and to proposed versions specific to different river systems and contexts. For example, Cluer and Thorne (2014) added one precursor and two successor stages to the CEMs proposed by Schumm et al. (1984) and Simon and Hupp (1986). The resulting Stream Evolution Model (SEM) extends the physical representation of the channel in the CEM by integrating physical changes with habitat and ecosystem benefits and it represents stream evolution as a cyclical, rather than linear, phenomenon (Cluer and Thorne, 2014).

CEMs have been widely used as templates for understanding and predicting the morphological adjustment of incised fluvial systems subjected to various disturbances, such as channelization (Simon and

 

Hupp, 1986), base-level change (Simon and Darby, 2002), alterations to the flow and sediment regime (Simon, 1999), dam construction, torrent-control works and sediment mining (Bollati et al., 2014). Nevertheless, CEMs cannot be assumed to be universally applicable to rivers in different hydrological, geological and geographical settings and that are subject to various forms of disturbance (Doyle and Shields, 2000; Thompson et al., 2016).

The North Fork Toutle River (NFTR), Washington State, provides an excellent opportunity to examine the utility of a CEM in explaining and forecasting channel changes observed in a river disturbed by a volcanic eruption and sudden, heavy input of sediment. In this study, geomorphic changes observed during more than three decades since the eruption are investigated for the first ~30km of the upper NFTR. The SEM proposed by Cluer and Thorne (2014) is applied to this reach of the NFTR to characterize trends of spatial and temporal change and the evolution stages of the channel at cross-sections resurveyed by the US Geological Survey. The SEM is selected because it considers late-stage evolution processes, which feature lateral shifting and planform change in incised rivers, changes not covered in the early, CEMs. In this context, the objectives of this study are to: 1) chronicle trends in vertical and lateral adjustments of the NFTR channel; 2) establish temporal and spatial sequences for the evolutionary stages of channel adjustment and so test the applicability of the SEM, and; 3) identify the recent evolutionary trends in the NFTR and use these to infer how stream evolution may progress in the near to intermediate future.

## 2 STUDY AREA

Prior to the 1980-eruption of Mount St. Helens, the NFTR was a gravel-bed river with relatively steep, meandering and well-developed pool-riffle morphology (Meyer and Martinson, 1989). During the first time of the eruption, the first ~17 km of the upper NFTR was buried by a debris-avalanche with the volume of ~2.5-$km^3$. The maximum depth of burial was ~140 m and the average depth was ~40 m (Simon and Thorne, 1996). The NFTR channel re-formed on the debris-avalanche deposit under the impacts of post-eruption disturbances, such as breaches of ponds and lakes on the hummocky surface of the debris-avalanche/pumice plain, water pumping from blocked lakes, and several lahars (volcanic debris flows).

As shown in Figure 1, the study reach extended ~30 km, from cross-section NF105 to NF375. 11 of the cross-sections resurveyed by the USGSCVO, were included in the study, using data collected over three decades. The study reach can be divided into three sub-reaches, based on the flow, topographic and geological conditions. Sub-reach I extended from NF100 to the confluences of the Coldwater and Castle Creeks with the NFTR. Sub-reach II was between those confluences and the narrow valley constriction near Elk Rock, which was just upstream of NF345. The valley widens markedly downstream of Elk Rock and sub-reach III was between the valley constriction and NF375. The channel in sub-reaches I and II is generally single-threaded, while in sub-reach III it is predominantly braided. Discharges in sub-reaches II and III are greater than that at sub-reach I due to significant inflows from Castle and Coldwater Creeks, and other smaller tributaries. There are no large tributaries in sub-reaches II and III.

The basin drained by the upper NFTR is characterised by cool, wet winters and warm, dry summers. The seasonal hydrograph is driven primarily by prolonged, low-intensity autumn and winter rainfall, augmented by spring melt of high-elevation snowpack (Major and Mark, 2006). Flow series for the upper NFTR at a Sediment Retention Structure (SRS) developed by Simon and Klimetz (2012) showed that three major floods occurred in 1982, 1996 and 2006.

## 3 METHODS

This study used the SEM proposed by Cluer and Thorne (2014) that was developed from the earlier CEMs of Schumm et al. (1984) and Simon and Hupp (1986). Stages 1-6 in the SEM correspond to those in the Simon and Hupp'sCEM, i.e. 1-sinuous single-thread, 2-channelised, 3-degradation, 4-degradation and widening, 5-aggradation and widening, and 6-quasi-equilibrium. In the successor stage 7, the channel develops an asymmetrical cross-section, promoting bar accretion at inner margins, and toe scour and renewed bank retreat along outer margins of expanding/migrating bends that results in the incised channel developing a sinuous planform. A precursor stage 0-anastoming is included in the SEM, based on recognition that many streams are now known to have had low-gradient, multi-threaded courses prior to human disturbance (Cluer and Thorne, 2014). In the end stage, 8-anastomosing, the stream recovers the relatively stable, multi-threaded planform that it featured prior to disturbance. For application in this study, 'anastomosing' in stages 0 and 8 of the SEM had been replaced by 'anabranching', recognising that anabranching is a more likely quasi-equilibrium form than anastomosing in the NFTR, which is a relatively steep fluvial system that drains an active volcano (Nanson and Knighton, 1996).

To perform and generate the necessary data, a MatLab program was coded to calculate the widths of the river channel, the floodplain and the valley at series of incrementally-increasing heights above the thalweg at each resurveyed cross-section. The width at the thalweg (at elevation of $y_0$) is denoted $W_0$ and, by definition, $W_0 = 0$. The elevation at which the width was measured was then increased by an increment of $\Delta y$ and the corresponding width, $W_i$ at the elevation of $y_i = y_0 + i\Delta y$ ($i$=0, 1 …) was calculated until the program reaches the

 

top of the river valley. The width of a channel with multiple anabranches was taken to be the sum of the widths of all the anabranches.

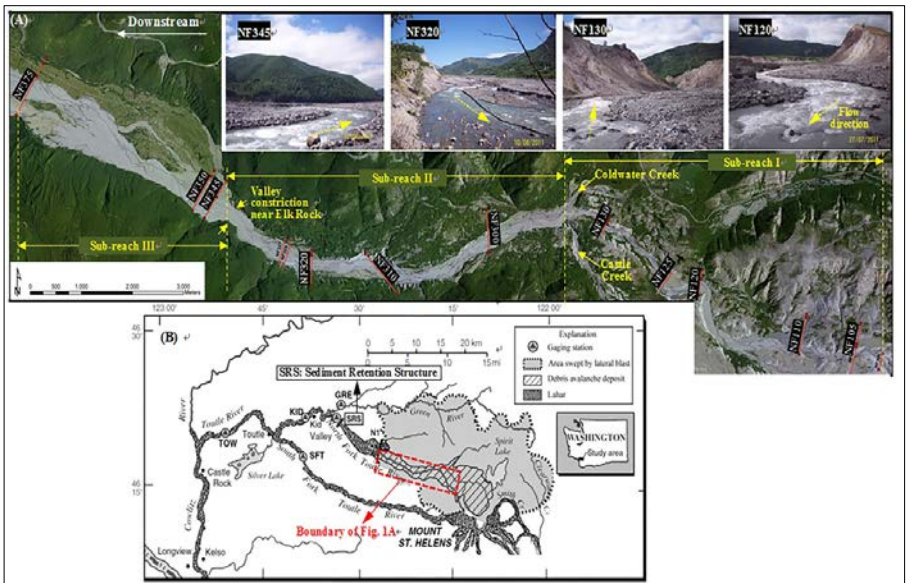


**Figure 1.** Study area: (A) study channel reaches and cross-sections and (B) Toutle River basin (modified from Major (2004)). Note: the image and map of the study reach are modified based on the file provided by Adam Mosbrucker. Photographs are taken by the first and second authors in July-August 2011.

## 4 RESULTS

The temporal and spatial distributions of changes in thalweg elevations at all eleven cross-sections are listed in Figure 2. The time series was divided into five periods: 1980-1982, 1982-1984, 1984-1987, 1987-1999 and 1999-2009. The greater length of the final period reflects the reduced frequency with which cross-sections were resurveyed after 1990. In the context of post-disturbance change in this highly-disturbed system, cross-sections with rates of change in thalweg elevation less than 0.1 m/yr may be regarded as relatively stable and are denoted by 'S/D' or 'S/A' in the Figure 2, where 'D', 'A', 'S' represent Degradation, Aggradation and Stability, respectively.

| Sub-reaches | | Sub-reach I | | | | | Sub-reach II | | | Sub-reach III | | |
|---|---|---|---|---|---|---|---|---|---|---|---|---|
| Cross-sections | | NF105 | NF110 | NF120 | NF125 | NF130 | NF300 | NF310 | NF320 | NF345 | NF350 | NF375 |
| River length upstream of the SRS (km) | | 42.24 | 40.83 | 37.62 | 36.72 | 34.66 | 31.38 | 28.21 | 26.26 | 23.18 | 22.68 | 17.52 |
| Time period | 1980-1982 | D(-7.62) | D(-7.61) | D(-7.41) | D(-10.21) | D(-4.68) | D(-2.32) | D(-4.83) | D(-2.66) | A(2.38) | D(-0.28) | A(5.17) |
| | 1982-1984 | D(-5.80) | D(-6.16) | D(-1.01) | | A(0.12) | S/A(0.02) | D(-2.14) | S/A(0.09) | A(1.20) | A(1.38) | A(2.07) |
| | 1984-1987 | D(-3.84) | A(1.62) | A(0.26) | D(-0.62)[a] | D(-0.36) | D(-1.03) | D(-0.57) | D(-1.11) | D(-0.29) | A(0.36) | D(-1.72) |
| | 1987-1999 | A(0.47) | S/D(-0.05) | A(0.21) | A(0.20) | D(-0.68) | D(-0.85) | D(-0.88) | D(-0.28) | D(-0.31) | D(-0.26) | S/D(-0.05) |
| | 1999-2009 | D(-0.58) | D(-0.30) | S/D(-0.09) | D(-0.33) | S/D(-0.04) | D(-0.38) | D(-0.36) | D(-0.37) | S/D(-0.01) | S/D(-0.06) | S/A(0.05) |

**Figure 2.** Changes in the thalweg elevation at resurveyed cross-sections on the NFTR, 1980-2009. (Note: [a]- Average degradation during 1982-1987)

Broadly, between 1980 and 1987 sediment eroded from sub-reaches I and II was deposited downstream in sub-reach III. Between 1980 and 1982, the hinge zone (between degradation upstream, and aggradation downstream) was located at the downstream limit of sub-reach II: that is between NF320 and NF345. However, between 1982 and 1984, the hinge zone migrated to the upstream end of reach II. This behavior was probably caused by pumping of water out of Spirit Lake to lower the water level and prevent an out-break flood, by the US Army Corps of Engineers, between November 1982 and August 1983.

As high flows exit the geologically-constrained valley in sub-reach II and expand laterally in sub-reach III, both flow depth and stream power per unit bed area decrease, producing an increasing tendency for aggradation. Thus, in the seven years following the eruption, the capacity of the river in sub-reach III to transport sediment was insufficient to carry the very heavy sediment yields being generated by degradation upstream in sub-reaches I and II, leading to rapid aggradation (Zheng et al., 2014).

 

During the period 1987-1999, degradation in sub-reach I slowed, because bed lowering was reducing the channel slope, while selective entrainment was coarsening the bed grain size, tending first to stabilize the bed and then to promote aggradation (Paine, 1984; Simon and Thorne, 1996). Downstream in sub-reach III, aggradation was replaced by degradation because the input of sediment upstream decreased markedly, while the previous aggradational phase had steepened the slope sufficiently to significantly increase sediment transport capacity and trigger degradation in sub-reach III (Simon and Thorne, 1996).

Post-1999, second phase degradation reduced local slopes in sub-reach III to the point that bed elevations were able to again stabilize. Degradation in sub-reach II has continued for almost three decades albeit at slowing rates (Figure 2), mainly due to its relatively narrow valley-floor width and high specific stream powers. This has led Major et al. (2015) to conclude that sub-reach II has now become the predominant source of sediment delivered by the upper NFTR to the SRS. Notwithstanding this, Zheng et al. (2014) noted that during the period 1999-2009, the rate of thalweg elevation change slowed to less than 0.1 m/yr at NF120, NF130, NF345, NF350 and NF375.

In considering lateral adjustments, cross-section NF130 was taken as an example (Figure 3). Over the study period, the upper elevations of all the valley cross-sections generally widened at progressively declining rates, such that top of valley widths had relaxed by 2009. In contrast, in the lower elevations of the valley cross-sections, the widths of the river channel and its floodplain increased at constant or even accelerating rates. Consequently, as rates of vertical adjustment have slowed, bank erosion, channel widening and terrace mass-wasting processes have progressively come to dominate late-stage evolution in the upper NFTR.

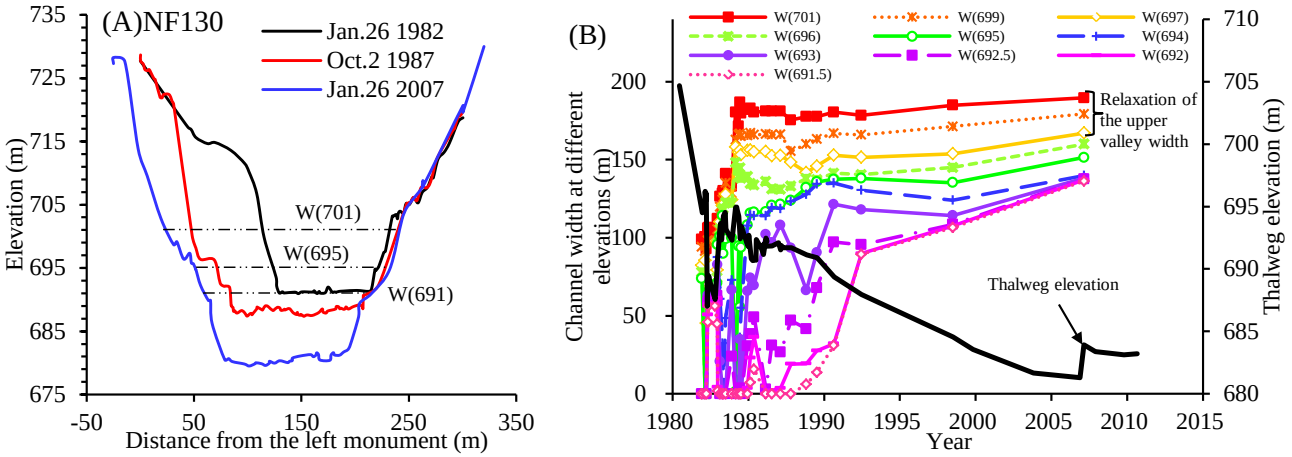


**Figure 3.** Changes in (A) cross-valley profiles and (B) thalweg elevations and valley widths at incremental elevations above the thalweg at NF130.

Based on changes observed at the resurveyed cross-sections, the evolution stages of the river channel were inferred using the SEM and the results are shown in Figure 4. During the first few years after the eruption, most cross-sections in sub-reaches I and II were in stage 4 (degradation and widening), while those at the sub-reach III were in stage 5 (aggradation and widening). However, evolution involving bed lowering upstream and aggradation downstream did not persist into the late-1980s. This is reflected in the SEM through evolutionary progression through the expected sequence of stage 3 or 4, to stages 5, 6 or 7 at several of the cross-sections in sub-reaches I and II. This progression was, however, disrupted by secondary adjustments in the second and third decades after the eruption, as shown in Figure 4.

During and since the late-1980s, stage 7 (laterally active) occurs with increasing frequency in all three sub-reaches. This supports the argument first put forward by Thorne (1999) that the early-CEMs should be modified by adding late-stage evolution involving lateral and planform adjustments in incised rivers. Figure 5 shows examples of the morphological changes typically driven by lateral adjustment. Figure 5A shows how the left bank of NF300 was eroded as the main channel migrated leftwards during1987-1990, reducing the steep transverse slope in the valley floor. Lateral channel evolution in the braided/anabranched reach around NF375 was more complex (Figure3B). The right bank was severely eroded, while the left bank was almost stable between 1990 and 2011, but since then the river seems to be reworking the anabranches within its channel migration zone. These examples illustrate how asymmetrical retreat of either the left or right channel margin may increase planform sinuosity and result in channel planform evolution or metamorphosis, as well as widening the river channel, floodplain and valley floor.

 

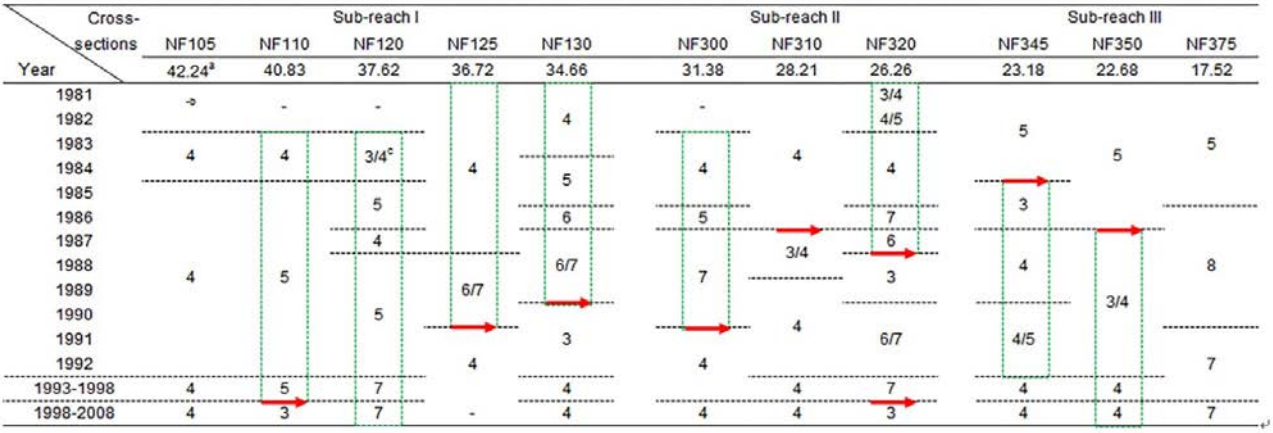


**Figure 4**. Spatial and temporal changes of stream evolution model stage in the NFTR during 1981-2008.(Note: numbers 3, 4…to 8 represent stages in the Stream Evolution Model proposed by Cluer and Thorne (2014). Rectangles indicate full or half-evolutionary cycles at a given cross-section. Arrows indicate renewed incision.)

a -numbers in this row indicate the distance (river kilometre) from the cross-section to the SRS.
b -no data available.
c -the cross-section was in either stage 3 or stage 4.

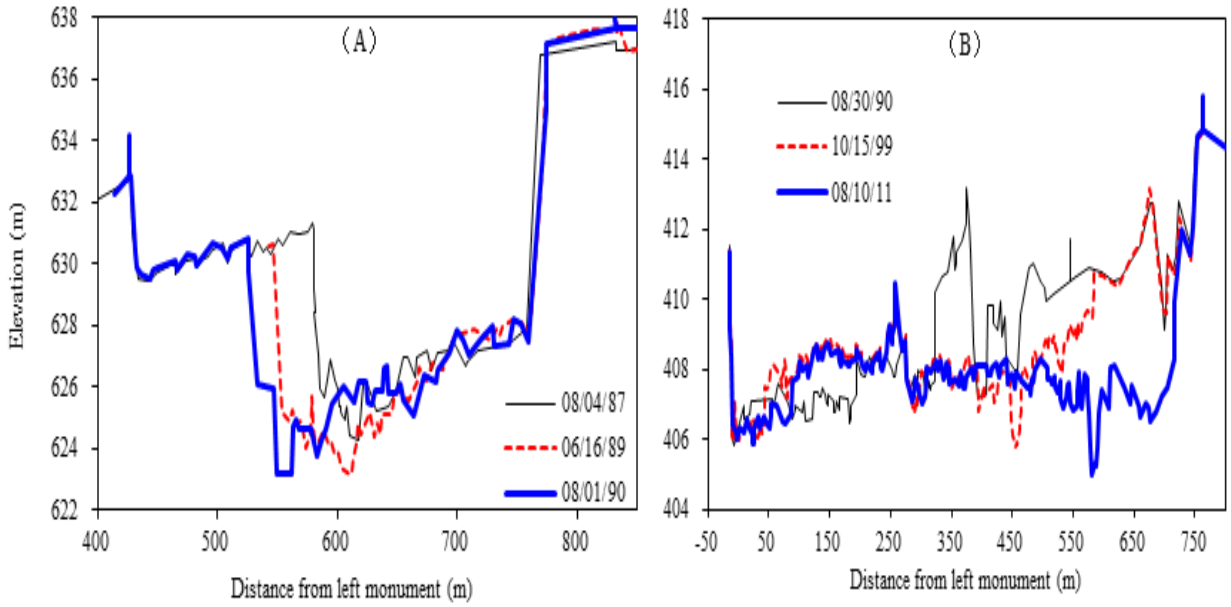


**Figure 5.** Modes of lateral adjustment at: (A) NF300 in sub-reach II, and (B) NF375 in sub-reach III. Note: dates are formatted MM/DD/YY.

As highlighted by the rectangular boxes in Figure 4, channel changes followed the expected sequence evolutionary stages at NF110, NF120, NF125, NF130, NF300, NF320, NF345 and NF350 until incision was renewed during the second cycle of vertical adjustments. Quasi-full evolutionary cycles, from stage 3 to stage 7, were observed at some cross-sections, e.g. NF120and NF320, although within these cycles, stages 6 and 8 may be absent and short-term looping between stages 4 and 5 was commonplace. Half-cycles from stage 3 to stage 5, or from stage 4 to stage 7, also occurred. Quasi-full cycles of channel evolution were generally completed within a few years but sometimes lasted for more than a decade, as was the case at NF120.

Renewed incision (highlighted by the arrows in Figure 4) disrupted evolution (usually at stages 5 or 7) to initiate second or third-phase,evolutionary cycles. Notably, stage 8-anabranching was observed only in the form of braiding/anastomosing at the downstream end of sub-reach III, where the valley is widest and vegetation has been able to partly recolonise the valley floor.

Due to data scarcity, Figure 4 can show only general, longer-term evolutionary stages for the periods 1993-1998 and 1998-2008. Most cross-sections were in stages 4 or 7 during these time periods. This indicated that bed elevations either degraded slightly or stayed almost constant, while the incised channel either continued to widen or migrated laterally. This finding emphasises the significance of lateral activity by

 

the upper NFTR during the second and third decades after the eruption (Simon and Thorne, 1996; Simon and Klimetz, 2012; Meadows, 2014). Renewed incision at NF110 and NF320 (during 1998-2008) may be attributed to floods of 1996 and 2006. However, due to lack of data, the responses of the upper NFTR to major floods cannot be established unequivocally.

## 5 DISCUSSION

Based on the results listed in Figure 4, the number of cross-sections in each evolutionary stage during each time period was tallied and the results are shown in Figure 6. In cases where it was impossible to differentiate between two possible stages of evolution, each stage was assigned a score of 0.5.

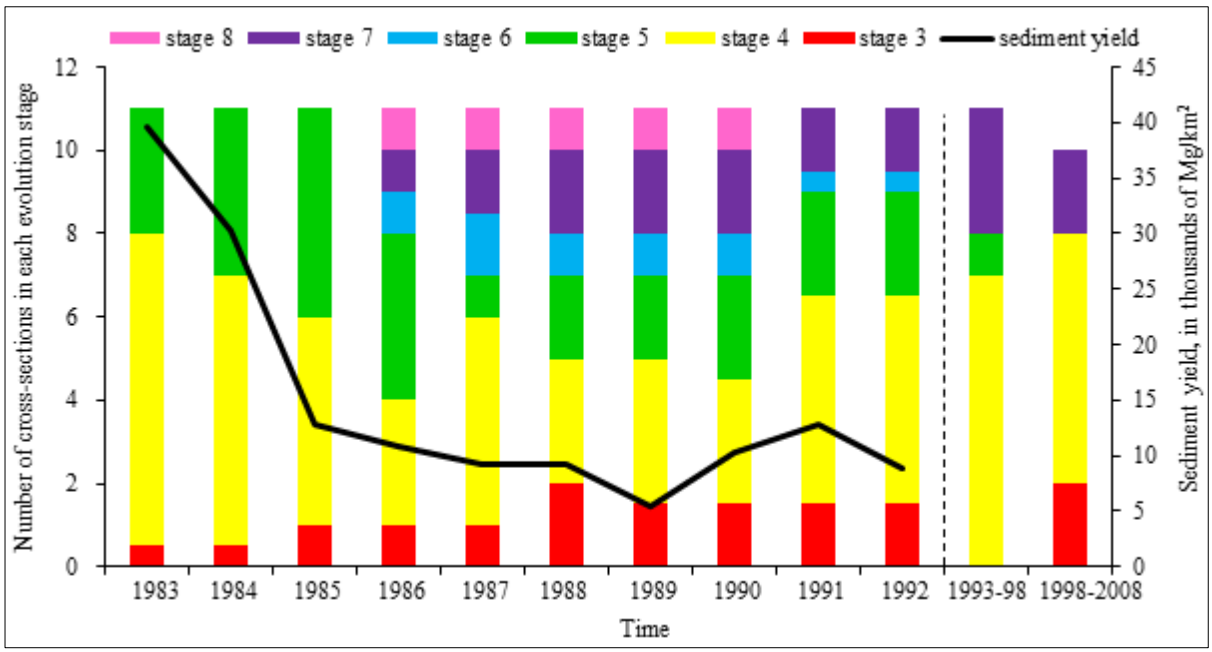


**Figure 6.** Numbers of cross-sections in each SEM stage in each resurvey period. Note: In cases where it was impossible to differentiate between two possible stages of evolution, each stage was assigned a score of 0.5. The sediment yield indicated in the graphic is annual suspended load measured at the USGS Kid Valley station projected in absence of sediment retention structure (adopted from Major et al. (2000)).

Stages 4 and 5 dominated during the first few years after the eruption. This result is consistent with the argument in the last section that sub-reach I (upstream) was generally in stage 4 while downstream, sub-reach III was in stage 5 between 1980 and 1987. In the late-1980s, several cross-sections evolved to stages 6, 7 and 8, implying that adjustments of channel bed elevation had ceased. However, the early-1990s, stages 4 and 5 again became predominant, as the second phase of bed elevation changes took hold, reversing the nonlinear decline in sediment yields from the upper NFTR that occurred during the first decade following the eruption (Major et al., 2000). Interestingly, the temporal trend in annual suspended sediment yields at the Kid Valley gauging station projected to have occurred in absence of the SRS by Major et al. (2000), which is plotted in Figure 8, is closely related to the occurrence frequency of stage 4 evolution. In fact, the correlation coefficient between the sediment yield and the number of cross-sections in stage 4 between 1983 and 1992 is 0.84. This finding is understandable considering that the rate of sediment production is highest when both channel bed and banks are being eroded. In addition, although renewed incision starting in the late-1980s and early-1990s occurred at much lower frequencies and rates than during the first cycle, it played a significant role in introducing a new sequence of channel adjustments in a second evolutionary cycle.

Stages 4 and 7 have now been predominant for over two decades and they may be expected to persist into the near and intermediate future. Secondary aggradation, coupled with lateral activity and planform changes may continue until suitable cross-valley profiles and wide floodplains develop. Through time, the channel-floodplain system should evolve towards a condition of dynamic equilibrium such that the intensity and frequency of lateral inter-action between the river and the terrace/valley sides will decrease, rates of planform adjustment will slow and the floodplain is stabilized by riparian vegetation (Harvey and Watson, 1986; Simon and Thorne, 1996).

Sequential distribution of evolution stages in space (upstream channel reaches in stage 4 and downstream ones in stage 5) during the early-1980s and temporal evolutionary cycles at individual cross-sections indicate general applicability of the SEM to evolution of the NFTR following the eruption of Mount St. Helens in 1980. Nevertheless, there are some evolution characteristics that are different from those expected according to the SEM. For example, while stage 8-anastomosing occurred in the wide, braided channel at the

 

downstream limit of sub-reach III, it was absent everywhere else in the upper NFTR. To date, the channel in sub-reaches I and II has shown no tendency to evolve beyond stage 7-lateral activity. This may because conditions around the upper NFTR have, to date, prevented vegetation from colonizing the valley floor. It is also possible that stage 7 of quasi-equilibrium in bed elevations and continued lateral activity, rather than stage 8, represents the potential evolutionary outcome for the predominantly single-threaded channel of the upper NFTR in sub-reaches I and II. In addition, the sequence of stage numbers observed along the upper NFTR showed no obvious increasing trend during the late-1980s. This may be attributed to the occurrence of second-phase adjustments coupled with the impacts of local geologic, geomorphic and hydraulic conditions at particular cross-sections.

The results reported here shed light on time scales of adjustment and stream evolution in the upper NFTR. As shown in the last section, quasi-full and half cycles of evolution took from a few years to more than a decade and evolution to the end state (anastomosing), has not yet occurred three decades after the eruption. This may imply that stage 7 represents the equilibrium state for this river, or at least that evolution to stage 8 requires a much longer period without further perturbation. This would be consistent with the hypothesis that the stability of multi-threaded, anastomosed river channels is closely related to establishment of dense riparian vegetation, especially trees, and colonisation by such vegetation may take centuries at Mount St Helens.

## 6 CONCLUSIONS

The upper North Fork Toutle River (NFTR) has suffered dramatic morphological adjustments since it is disturbed by deposition of a massive debris-avalanche during the catastrophic eruption of Mount St. Helens in 1980. The Stream Evolution Model (SEM) developed by Cluer and Thorne (2014) is applied to cross-sectional resurveys performed during the three decades since the eruption to characterize spatial and temporal trends in vertical and lateral adjustments in a ~30 km study reach of the upper NFTR. The main conclusions are:

(1) During the first few years after the eruption, upstream cross-sections in sub-reaches I and II evolve predominantly through degradation and widening (stage 4 in the SEM), while evolution at downstream cross-sections in sub-reach III is dominated by aggradation and widening (stage 5). Incision at the upstream cross-sections is rapid immediately following the eruption, resulting in the enlargement of the whole river valley, but it slows during the late-1980s. As bed lowing upstream slows down, reduced sediment outputs trigger degradation to move downstream, in sub-reach III. Short-lived stabilization of bed elevations occurrs locally in the late 1980s but is disrupted by renewed incision. Rates of widening decay rapidly following the eruption and top valley widths appear to have relaxed to asymptotic values. Nevertheless, the lateral activity of the river channel sufficient to continue widening the valley floor has continued for three decades.

(2) Time sequences of evolutionary stages observed at specific cross-sections generally follow those expected from the SEM, indicating the applicability of the approach. Evolutionary progression from stages 3-4 through to stages 5-6-7 is commonplace. Although within these cycles, stage 6-quasi-equilibrium is either short-lived or absent, and the short-circuiting between stages 4 and 5 is a frequent occurrence. The full-cycle takes from a few years to more than a decade to complete. The full-cycle is usually disrupted by renewed incision (i.e. stage 3 or 4), which initiates a new evolutionary cycle. The sequence of evolutionary stages does not increase with distance downstream along the upper NFTR during the late-1980s, probably due to the occurrences of second-phase bed elevation adjustments and local geologic, geomorphic and hydraulic conditions.

(3) Stage 4-degradation and widening, and the stage 7-laterally active dominate stream evolution during the second and third decades following the eruption, emphasising the significant role of channel shifting, widening and slope mass-wasting processes in perpetuating high sediment yields from the upper NFTR. Unlike rates of vertical adjustment and valley top widening, rates of lateral channel activity and widening of the valley floor show no signs of abating. The river will not obtain a condition of quasi-equilibrium until a suitable transverse valley profile is formed, a dynamically-stable planform develops and the floodplain is stabilised by riparian vegetation, which could be decades or centuries.

## ACKNOWLEDGEMENTS

This study is supported by National Natural Science Foundation of China (51409193) and the University of Nottingham. We appreciate the help provided by Jon Major, Kurt Spicer, Adam Mosbrucker and Tami Christianson at the U.S. Geological Survey Cascades Volcano Observatory.

## REFERENCES

Beechie, T., Pess, G., Roni, P. & Giannico, G. (2008). Setting River Restoration Priorities: A Review of Approaches and a General Protocol for Identifying and Prioritizing Actions. *North American Journal of Fisheries Management*, 28, 891-905.

Bollati, I.M., Pellegrini, L., Rinaldi, M., Duci, G. & Pelfini, M. (2014). Reach Scale Morphological Adjustments and Stages of Channel Evolution: The Case of the Trebbia River (Northern Italy). *Geomorphology,* 221,176-186.

 

Cluer, B. & Thorne, C.R. (2014). A Stream Evolution Model Integrating Habitat and Ecosystem Benefits. *River Research and Applications,* 30(2), 135-154.

Doyle, M.W. & Shields, F.D. (2000). Incorporation of Bed Texture into a Channel Evolution Model .*Geomorphology*, 34, 291-309.

Knighton, D. (1998). *Fluvial Forms and Processes: A New Perspective*. Arnold Hodder Headline, PLC, London, UK.

Major, J.J., Mosbrucker, A.R. & Spicer, K.R. (2015). *Geomorphic Response of the Toutle River Basin to the 1980 Eruptions of Mount St. Helens, a 30-year Perspective,* U.S. Geological Survey, Reston, Virginia.

Major, J.J., Pierson, T., Dinehart, R. & Costa, J. (2000). Sediment Yield following Severe Volcanic Disturbance. A Two Decade Perspective from Mount St. Helens. *Geology,* 28(9), 819-822.

Meadows, T. (2014). Forecasting Long-term Sediment Yield from the Upper North Fork Toutle River, Mount St. Helens, USA, *PhD. Thesis.* University of Nottingham, UK.

Meyer, D.F. & Martinson, H.A. (1989). Rates and Processes of Channel Development and Recovery following the 1980 Eruption of Mount St. Helens, Washington. *Hydrological Sciences Journal,* 34(2), 115-127.

Nanson, G.C. & Knighton, A.D. (1996). Anabranching Rivers: Their Cause, Character and Classification. *Earth Surface Processes and Landforms,* 21, 217-239.

Paine, A.D.M. (1984). Canyon and Terrace Formation near Mount St. Helens, Washington, *M.S. Thesis.* Colorado State University, Fort Collins, CO.

Simon, A. & Darby, S.E. (2002). Effectiveness of Grade Control Structures in Reducing Erosion along Incised River Channels: The Case of Hotophia Creek, Mississippi. *Geomorphology,* 42, 229-254.

Simon, A. & Hupp, C.R. (1986). Geomorphic and Vegetative Recovery Processes along Modified Tennessee Streams: An Interdisciplinary approach to Disturbed Fluvial Systems. *Forest Hydrology and Watershed Management*, 167, 251-262.

Simon, A. & Klimetz, D. (2012). *Analysis of long Term Sediment Loadings from the Upper North Fork Toutle River System, Mount St. Helens, Washington,* National Sedimentation Laboratory Technical Report Number 77. U.S. Department of Agriculture. Agricultural Research Service, National Sedimentation Laboratory.

Simon, A. & Thorne, C.R. (1996). Channel Adjustment of AN Unstable Coarse-Grained Stream: Opposing Trends of Boundary and Critical Shear Stress, and the Applicability of Extremal Hypotheses. *Earth Surface Processes and Landforms,* 21,155-180.

Simon, A. 1999. *Channel and Drainage-Basin Response of the Toutle River System in the Aftermath of the 1980 Eruption of Mount St. Helens, Washington*. U.S. Department of the Interior, U.S Geological Survey, Open File Report, 96-633.

Thompson, C.J., Croke, J., Fryirs, K. & Grove, J.R. (2016). A Channel Evolution Model for Subtropical Macro Channel Systems. *Catena,* 139, 199-213.

Thorne, C.R. (1999). *Bank Processes and Channel Evolution in the Incised Rivers of North–Central Mississippi,* in *Incised River Channels*. J Wiley: Chichester, UK, 97-122.

Zheng, S., Wu, B.S., Thorne, C.R. & Simon, A. (2014). Morphological Evolution of the North Fork Toutle River following the Eruption of Mount St. Helens, Washington. *Geomorphology,* 208,102-116.

 

Proceedings of the 37th IAHR World Congress
August 13 – 18, 2017, Kuala Lumpur, Malaysia

# NUMERICAL STUDY ON FORMATION AND EVOLUTION OF GRAVEL TO SAND TRANSITION

WEI HUANG[(1)], HUAIHAN LIU[(2)], BO JIANG[(3)], GUOPING LEI[(4)], ZUPENG GU[(5)], HONGWEI KUANG[(6)] & FEI CHEN[(7)]

[(1,3,4,5,6,7)] Changjiang Waterway Planning Design and Research Institute, Wuhan, China, huangvy@whu.edu.cn
[(1,2,3,4,5,6,7)] National Engineering Research Center for Inland Waterway Regulation, Wuhan, China,
[(2,3)] Changjiang Waterway bureau, Wuhan, China

## ABSTRACT

In natural rivers, bed sediment size tends to decrease from upstream to downstream. Interestingly, sediment size does not decrease gradually. Bed material can change from gravel to sand abruptly with paucity of some sizes accompanying abrupt change in bed slope. Although many studies have investigated features and mechanisms of the gravel to sand transition (GST), details about flow, sediments and bed are not investigated during formation and evolution of GST. In the present paper, a nonuniform sediment transport model is applied to investigate formation and evolution of GST feeding with poor sorted sediments at the upstream inlet. Results show that bed shear stresses, sediment transport, medium size of bed sediment and Shields number all change abruptly at some locations during formation and evolution of GST. It should be noted that abrupt changes for different variables do not appear at the same location, which implies that variations for flow and sediment characteristics exist some spatial lags. Sensitive analyses of flow and sediment discharges on GST show that gravel front migrates downstream further in relation to a larger flow discharges. However, influence of sediment discharge on GST is not monotonous, e.g., in the initial period, GST moves faster in relation to a larger sediment discharge. However, it moves slower after a certain period.

**Keywords:** Poor sorted sediments; gravel to sand transition; numerical study; sensitive analysis.

## 1 INTRODUCTION

Generally, grain size decreases downstream in natural rivers (Sternberg, 1875). Interestingly, bed sediment size does not decrease in exponent along the river, but fines abruptly in a relative short distance which is referred as gravel to sand transition (GST) (Knighton, 1999). Unlike the unimodal sand curve in adjacent gravel bed or sand bed, the sand curve in the GST is bimodal (Sambrook Smith and Ferguson, 1996) with paucity of some size (about 1-5 mm) of sediment (Lamb and Venditti, 2016). Accompanied with abrupt change in sediment size, bed slope, sediment transport rate and bed shear stress change abruptly too (Ferguson, 2003).

Since Yatsu (1955) reported rapid reduction in bed sediment size, abundant works have been carried out to explain the formation mechanics of GST. It can dominantly be categorized into two kinds: a) sediment size fining due to abrasion or broken, b) selective deposition of sediment by flow dynamics.

On one hand, based on observed data from 7 Japanese rivers, (Yatsu, 1955; 1957) proposed the abrasion or broken of sediment was the formation mechanism of GST. Sambrook Smith and Ferguson (1995) analyzed the field observation from the rivers worldwide and thought abrasion of sediment may be one of the formation mechanisms of GST.

On the other hand, Paola et al. (1992) carried out a laboratory flume experiment on downstream fining with feeding bimodal sediment. It reproduced GST observed in the field and pointed out the selective deposition was the mechanism of GST formation because the size decrease in exponent due to abrasion or broken was too small to match that observed in the experiment. Moreover, no obvious abrasion or broken of sediment was observed. Ferguson et al. (1996) analyzed the field data and numerical results, and also concluded that the selective deposition was the reason for GST formation. Ferguson, (2003) employed a simplified numerical model to simulate formation and evolution of GST with two sizes of sediment representing gravel and sand, respectively. The abrupt change in bed slope was also reproduced. The nonlinearity of bedload transport was ascribed to be reason of GST formation. Moreover, general sediment size fining was largely enhanced as the bed shear stress declined rapidly. Recently, Venditti and his cooperators (Venditti et al., 2014; 2015; Lamb and Venditti, 2016) studied GST in the Fraser River. Based on analysis of sources of bed topography, bed material, bed shear stress and sediment flux, GST was thought to result from the combination of decrease in bedload transport and deposition of suspended load. The abrupt change in bed slope was the result of GST formation. As sediment can be transported in different modes, there were critical threshold conditions for different modes. For the paucity of 1-5 mm in bed surface, Lamb and Venditti (2016) quantitatively analyzed thresholds for wash load and for initial sand motion. It demonstrated that the flow

 

dramatically lost its capacity to transport sediment as wash load where bed shear velocity dropped below ~0.1 m/s, resulting in an abrupt transition in bed grain size.

In conclusion, selective deposition by hydrodynamics is the main mechanism of GST formation in spite of the important role of sediment abrasion/broken is not fully excluded. Although features and formation mechanism of GST have been widely investigated (Cui and Parker, 1998; Ferguson et al., 2011; Frings, 2011; Parker and Cui, 1998; Singer, 2010; Wilcock, 1998), the details in the formation and evolution of GST are not well studied yet. In this paper, a coupled water and sediment dynamical model is developed to simulate formation and evolution of GST resulted from feeding poor sorted sediment at the upstream end. Details of bed sediment size, sediment transport rate, bed slope, bed shear stress are analyzed. Impacts of flow discharge and sediment transport rate on the formation and evolution of GST are also investigated.

## 2 MATHEMATIC MODEL

### 2.1 Governing equations

The governing equations are essentially the shallow water equations comprising complete mass and momentum conservation equations for the water-sediment mixture flow and mass conservation equations for sediment transport and bed material, respectively (Huang et al., 2012). The governing equations in a well-balanced conservative form are written as:

$$\frac{\partial \mathbf{U}}{\partial t}+\frac{\partial \mathbf{F}}{\partial x}=\mathbf{S} \tag{1}$$

$$\mathbf{U}=\begin{bmatrix}\eta\\ hu\\ hc_k\end{bmatrix},\quad \mathbf{F}=\begin{bmatrix}hu\\ hu^2+0.5g(\eta^2-2\eta z)\\ huc_k\end{bmatrix}, \tag{2}$$

$$\mathbf{S}=\begin{bmatrix}0\\ -g\eta\dfrac{\partial z}{\partial x}-\dfrac{\tau_b}{\rho}+\varepsilon\nabla^2(hu)-\dfrac{\Delta\rho}{2\rho}\dfrac{gh^2\partial C_T}{\partial x}-\dfrac{(\rho_0-\rho)(E_T-D_T)u}{\rho(1-P)}\\ E_k-D_k\end{bmatrix}, \tag{3}$$

$$\frac{\partial z}{\partial t}=\frac{D_T-E_T}{1-P} \tag{4}$$

$$\frac{\partial(\delta f_{ak})}{\partial t}+f_{Ik}\frac{\partial \varsigma}{\partial t}=\frac{D_k-E_k}{1-P} \tag{5}$$

where $\mathbf{U}$ is a vector of conserved variables; $\mathbf{F}$ is the convective flux vectors of the flow in $x$ direction, respectively; and $\mathbf{S}$ is the source term; $\eta$ is the water surface level above the datum; $z$ is the bed elevation, and the water depth is then evaluated by $h=\eta-z$; $u$ is the velocity; the subscript $k$ indicates the $k$-th sediment class; $c_k$ is the depth averaged volumetric sediment concentration, $C_T=\sum c_k$; $g$ is the gravitational acceleration; $P$ is the bed sediment porosity; $\rho_w$ and $\rho_s$ are densities of water and sediment, respectively; $\rho$ and $\rho_0$ are the densities of water-sediment mixture and saturated bed material, where $\rho=\rho_w(1-C_T)+\rho_s C_T$ and $\rho_0=\rho_w P+\rho_s(1-P)$; $\Delta\rho=\rho_s-\rho_w$; $E_k$ and $D_k$ are sediment entrainment and deposition fluxes across the bottom boundary of flow for the $k$-th class, representing sediment exchange between water column and river bed; $E_T=\sum E_k$ and $D_T=\sum D_k$; $\delta$ is the thickness of active layer; $\varsigma=z-\delta$ is the bottom of the active layer; $f_{ak}$ is the fraction percent of the sediment at the river bed surface, $f_{Ik}$ is the percent at the bottom boundary of active layer. $\nabla^2$ is the Laplace operator; $\varepsilon=\gamma\kappa hu_*$ is the turbulent eddy coefficient, $\gamma$ is a coefficient, $\kappa$ is the von Karman constant 0.4, $u_*$ is the shear velocity; $\tau_b$ is the bed shear stress.

 

2.2 Model closure

To close the governing equations, auxiliary formulae have to be employed to determine bed shear stresses, sediment exchange fluxes. In general, flows are unsteady and non-uniform, featuring boundary resistance substantially different from those of steady and uniform flows. This fact is more pronounced as sediment transport is involved and the bed is rendered mobile, and exhibits bedforms (e.g., dunes). Moreover, as nonuniform sediment transport is included, resistance changes temporally and spatially. Unfortunately, there has been no generally applicable relationship representing boundary resistance in such flows, which has been proven to be able to result in improved results. This limitation is why computational studies of flow over fixed and mobile beds have to date exclusively used resistance relationships originally developed for steady and uniform flows, which involves the Manning roughness, $n$ . The present model follows the same practice in this regard, i.e.:

$$\tau_b = \rho g n^2 u|u| / h^{1/3} \qquad [6]$$

Two distinct mechanisms are involved in the sediment exchange between the flow and bed, i.e., sediment entrainment due to turbulence and particle-particle interactions, and sediment deposition mainly due to gravitational action. Current understanding of these remains far from clear. Inevitably quantification of sediment entrainment and deposition fluxes is largely empirical, and no generally valid formulations are available. As the model includes the nonuniform sediments, it is more complex than that of uniform sediments in the model closure. Given this fact, it is sensible to estimate the fluxes using existing sediment transport formulae and carefully appreciate the uncertainty with a modification coefficient. Accordingly, the entrainment and deposition fluxes are estimated by:

$$E = \alpha_k \omega_k c_e ,\ D = \alpha_k \omega_k c_k \qquad [7a, b]$$

where $\omega_k$ is the settling velocity of a single sediment particle in tranquil clear water, which is calculated using the Zhang formula (Zhang and Xie, 1993). Bed load sediment transport capacity $c_{ek}$ is determined from the local flow regime. The empirical parameter $\alpha_k$ represents the difference between the near-bed concentration and the depth-averaged concentration, which is determined following Cao et al. (2011). The bed load sediment transport capacity $c_{ek}$ is given by:

$$c_{ek} = q_{bk} / (hu) ,\ q_{bk} = 8\sqrt{sgd_k^3}(\theta_k - \theta_{ck})^{1.5} \qquad [8a, b]$$

where $q_b$ is unit-width bed load transport rate at transport capacity status; $s$ is the specific gravity of sediment; $d_k$ is the local sediment medium diameter; $\theta_k$ is the Shields parameter and $\theta_{ck}$ is threshold Shields parameter for initiation of sediment movement, which considered the hiding and exposure effect of nonuniform sediments. There has been a plethora of empirical formulations for $q_{bk}$ in Eq. [6b], and the MPM (Meyer-Peter and Müller, 1948) formula is adopted here.

There are two distinct approaches to determine the thickness of active layer, relating it to the characteristic sediment diameter, e.g., $d_{84}$ (84% percentile size), or depending on the height of river bedforms. $\delta = 2d_{84}$ is adopted following Hoey and Ferguson (1994).

Quantization of $f_{Ik}$ is usually difficult as there are few flume data to validate it. In the present work, it is determined following Hoey and Ferguson (1994) and Toro-Escobar et al. (1996).

$$f_{Ik} = \begin{cases} f_{sk} & \partial\eta/\partial t < 0 \\ \sigma C_k / C_T + (1-\sigma) f_{ai} & \partial\eta/\partial t > 0 \end{cases} \qquad [9]$$

where $f_{sk}$ is fraction of the $k$ -th size in the substrate layer, $\sigma$ is an empirical coefficient, and $\sigma$ =0.7 Toro-Escobar et al. (1996).

2.3 Numerical scheme

The Godunov-type finite volume method incorporating the HLLC (Harten-Lax-van Leer Contact Wave) approximate Riemann solver was used and the MUSCL (Monotone Upstream-centered Schemes for

 

Conservation Laws) method was adopted to reconstruct the face values of the Riemann problem to achieve a second order in space (Toro, 2001). The details of the numerical scheme are described in Huang et al. (2012). The bed evolution (Eq. [4]) was discretized using central difference method and the fractions formulation of the active layer (Eq. [5]) was discretized using iteration method.

### 2.4 Model test

Paola et al. (1992) carried out an experiment on downstream fining of sediments in a laboratory flume. This experiment is the first one which reproduced the formation and evolution of the GST in the flumes scale. It is useful to test the capacity of the present model. The flume was 45 m long, 1.2 m high and 0.3m wide with initial bed slope 0.2%. The sediment size ranged from 0.125 mm to 64 mm with bimodal at 0.35 mm and 16 mm, respectively. Water discharge during the experiment run was held constant at 49 liter/s and sediment feeding rate was held at 11.3 kg/min. The tailgate was kept constant at 0.40 m. The experiment run lasted for 16 hour 50 minutes. The manning roughness was calibrated to 0.025 s/m$^{1/3}$. The results showed the computed (C) bed elevation agreed well with that of measured (M) for all instants. This indicates the present model can reproduce the formation and evolution of GST well and shows applicability of the model to investigate details through the formation and evolution of GST.

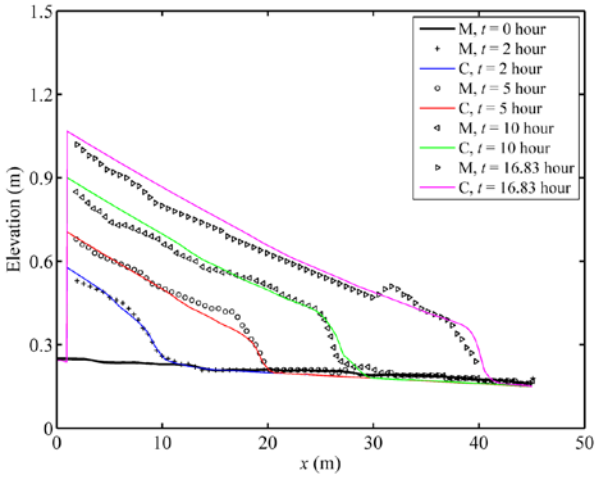


**Figure 1**. Measured (M) and computed (C) bed profiles (Paola et al. 1992).

### 2.5 Numerical experiment setup

A numerical experiment was designed to investigate details about formation and evolution of GST. The river was 122 km long, 12.0 m wide with rectangular cross sections. Initial bed slope of the river was 0.001. Bimodal sediment was fed at the inlet cross section (Table 1). The medium sizes were 0.3 mm and 4.4 mm at initial bed and inlet cross section, respectively (Table 1). Flow discharge and sediment discharge were 20 m$^3$/s and 0.01 m$^3$/s, respectively. The critical Shields number was specified to 0.04. Each experiment run lasted 500 days.

**Table 1**. Sand distributions for initial bed and feeding cross sections.

| Size (mm) | 0.0625 | 0.125 | 0.25 | 0.5 | 1 | 2 | 4 | 8 | 16 | 32 | $d_{50}$ |
|---|---|---|---|---|---|---|---|---|---|---|---|
| **Initial bed (%)** | 10 | 16 | 19 | 25 | 20 | 10 | 0 | 0 | 0 | 0 | **0.3** |
| **Inlet cross section (%)** | 0 | 0 | 0 | 6 | 15 | 20 | 5 | 40 | 12 | 2 | **4.4** |

## 3 RESULTS AND DISCUSSIONS

### 3.1 Results

#### 3.1.1 Flow, sediment transport and bed evolution of GST

Figure 2 shows the water depth and river bed adjustment at $t$=300d. The water depth increased from $x$=0 to 20 km. The upstream reach is aggraded due to over feeding from $x$=0 to 8.3 km and that is scoured from $x$=8.3 to 43.4 km with its minimum -0.54 m at $x$=12.6km. The bed adjustment pattern was similar to those in Sichuan Province reported by Fan et al. (2016). Figure 3 showed that the bed shear stress, bed load transport, $d_{50}$ and Shields number all changed longitudinally. Specifically, bed shear stress and bed load transport rate increased firstly and then decreased. However, bed stress decreased longitudinally with a relative rapid rate, fining of $d_{50}$ was relatively gentle. As bed shear stress decreased to a certain value, $d_{50}$

 

fined dramatically and formed a steep slope. Downstream of GST, bed stress decreased in a slow rate. Bedload transport rate decreased rapidly from the upstream to GST and reached its minimum value just upstream of GST. In contrast to the variation of $d_{50}$, Shields number firstly decreased along the river and reached its minimum value at GST. After that, Shields number increased along the river. As stated above, abrupt change cross sections for bed shear stress, bedload transport rate and $d_{50}$ do not locate at the same site. This means no direct simple relationship among these three factors. Figure 4 shows distribution of water surface gradient and bed slope along the river at $t$ =300d. Both water surface gradient and bed slope decreased from $x$ =0 to 15 km. Moreover, water surface gradient was smaller than bed slope in this range. However, the relative magnitude of water surface gradient and bed slope alternatively appeared ranging from $x$ =15 to 20 km. Downstream of $x$ =20 km, water surface gradient equaled to bed slope and remained to their initial values. This implies the water surface and bed evolution changes in different rate at different locations.

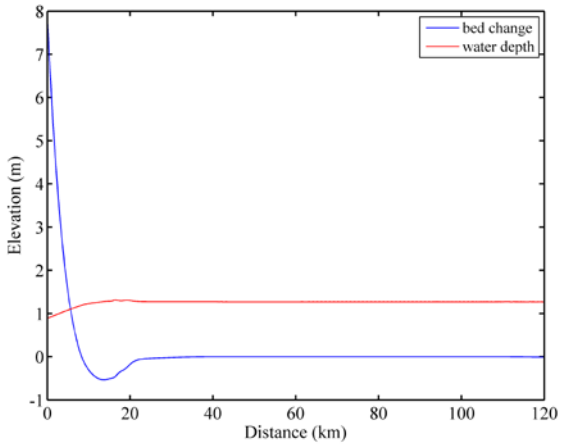


**Figure 2**. Depth and bed change distributions along the river.

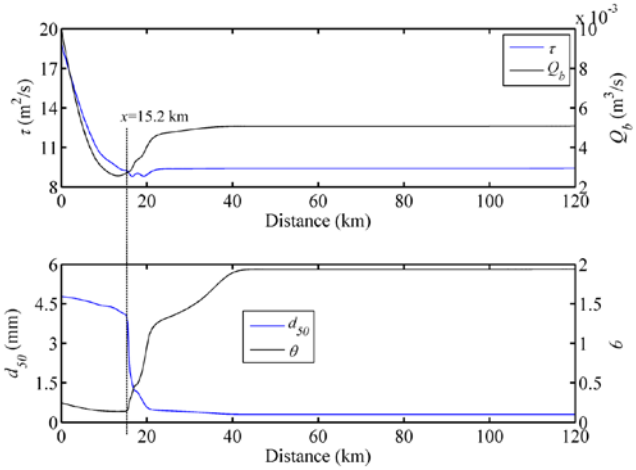


**Figure 3**. Bed shear stresses, bed load transport rate, $d_{50}$ and Shields number based on $d_{50}$ at $t$ =300 d.

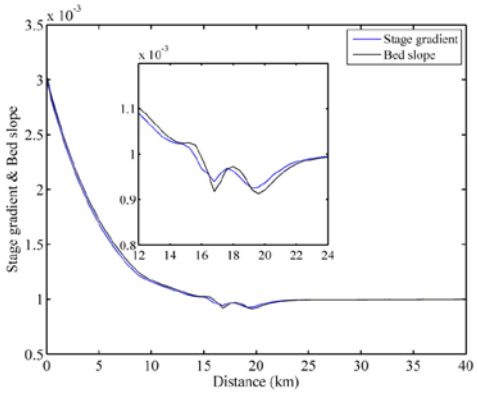


**Figure 4**. Stage gradient and bed slope profiles at $t$ =300d.

3.1.2 Evolution of GST

Figure 5 shows longitudinal distribution of $d_{50}$ at different times. It was shown that $d_{50}$ decreased downstream along the river. The GST migrates downstream and the range of fining diameter narrows with time. As shown in Table 2, generally, the fining range increased with time and the maximum fining rate of diameter decreased with time. However, the fining rate does not change monotonous and there is no simple relation which can represent downstream migration velocity of GST.

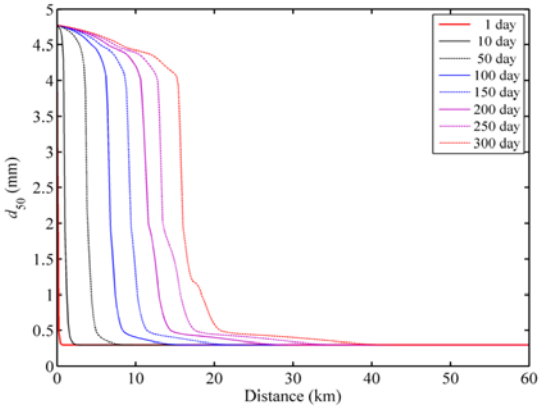


**Figure 6**. $d_{50}$ distributions along the river.

**Table 2.** Characteristics of grain size fining ($q_b$=0.01m$^3$/s).

| Days | Fining starts at $X_1$ (km) | Fining ends at $X_2$ (km) | X_range (km) | Maximum fining rate (mm/km) | Location of maximum fining rate(km) |
|---|---|---|---|---|---|
| **1** | 0 | 0.297 | 0.29 | 17.7 | 0.0 |
| **10** | 0.26 | 1.69 | 1.43 | 11.8 | 0.8 |
| **50** | 2.74 | 4.95 | 2.21 | 8.0 | 3.6 |
| **100** | 5.39 | 8.13 | 2.74 | 4.6 | 6.4 |
| **150** | 8.22 | 10.99 | 2.77 | 3.7 | 9.0 |
| **200** | 10.04 | 13.76 | 3.72 | 2.4 | 11.4 |
| **250** | 12.44 | 16.55 | 4.11 | 3.9 | 13.2 |
| **300** | 15.10 | 19.39 | 4.29 | 3.6 | 15.6 |
| **350** | 17.60 | 19.90 | 2.31 | 3.7 | 18.2 |
| **400** | 19.91 | 22.84 | 2.93 | 3.1 | 20.8 |
| **450** | 22.13 | 24.59 | 3.46 | 2.7 | 23.2 |
| **500** | 24.22 | 28.27 | 4.05 | 2.0 | 25.4 |

Figure 7 shows water surface gradient and bed slope at different times. It was shown that both water surface gradient and bed slope reached their minimum near $x$=7.5 km at $t$=100 d. Compared with bed slope variation, that of water surface gradient was relative small. Likewise, both water surface gradient and bed slope decreased firstly and then increased at $t$=200 d. However, they did not reach the minimum values at the same location.

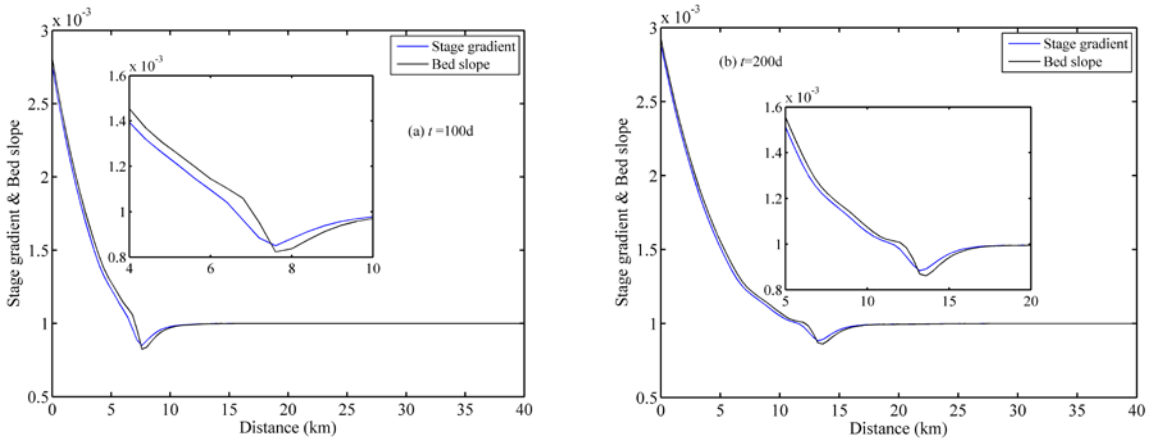


**Figure 7**. Stage gradient and bed slope profiles (a) at $t$=100d and (b) at $t$=200d.

Figure 8 shows longitudinal distributions of bed shear stress, bedload transport rate, $d_{50}$ and Shields number. It was shown bed shear stress, bedload transport rate and Shields number decreased first and then increased. However, $d_{50}$ decreased along the river. At $t$=100d, bed shear stress decreased from $x$=0 km reaches to its minimum at $x$=7.6 km. Downstream this cross section, bed shear stress increased to a constant. Likewise, bedload transport rate decreased from the inlet cross section and reached its minimum at $x$=6.6 km. It increased to a constant downstream from $x$=6.6 km. $d_{50}$ decreased along the river and fined rapidly at $x$=6.2 km. Although the declined rate of bed shear stress was large from $x$=0 to 6.2 km, the fining rate of $d_{50}$ was small. From $x$=0 to 6.2 km, Shield number changed marginally. After it reached its minimum, it increased largely due to $d_{50}$ fining. The tendency of these four variables at $t$=200d was similar to that at $t$=100d, however, locations of abrupt alteration for these variables changed.

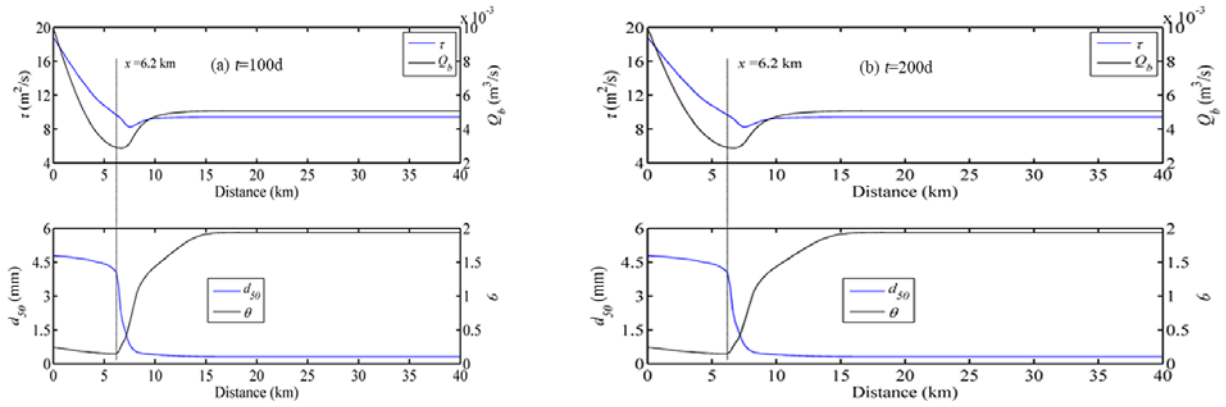


**Figure 8**. Bed shear stress, bed load transport rate, $d_{50}$ and Shields number based on $d_{50}$.

From Figure 9, distributions of different grain sizes differ from each other due to flow capacity on sediment transport. The percentiles of each class changed along the river and render $d_{50}$ changed. In general, the larger size sediment moves downstream in a shorter distance. From the percentile variations of each class, the reason for rapid fining of $d_{50}$ can be demonstrated. It was shown that percentile of $d$ =8.0 mm dominated the fining rate of $d_{50}$. At $t$=100d, the percentile of $d$ =8 mm reached its peak at $x$=6.2km. Downstream that point, the percentile of $d$ =8mm decreased rapidly, and $d_{50}$ reduced rapidly at the same time. Meanwhile, percentiles for $d$ =0.0625~0.5 mm increased in a large amount. It can be inferred that formation of GST is due to rapid decrease in percentile of some coarse gravels and rapid increase in percentiles of fine sands at the same time.

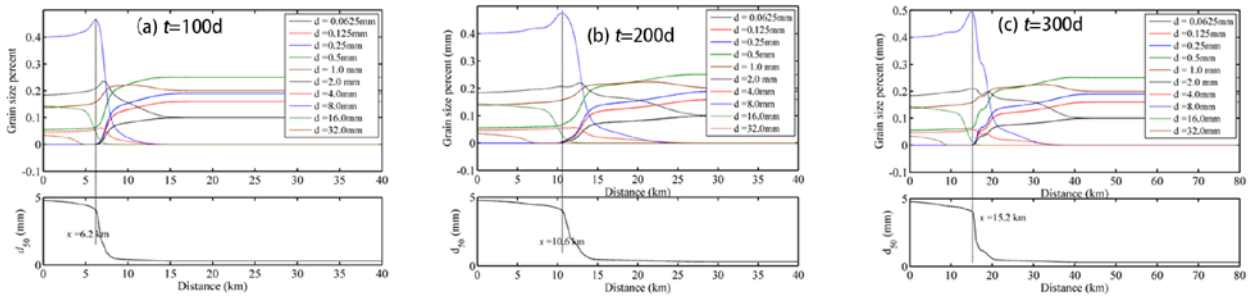


**Figure 9**. Grain size percents and $d_{50}$ profiles.

## 3.2 Sensitivity analysis

### 3.2.1 Impact of Sediment discharge

Figure 10 shows distribution of $d_{50}$ along the river under different sediment discharge with the same flow rate. In general, medium size near the inlet cross section is larger, the range of sediment fining is larger and the fining rate is larger in relation to a smaller sediment discharge. In a certain range, the abrupt GST migrates downstream faster corresponding to a larger sediment discharge at the inlet. However, the migration rate of

 

lager sediment discharge is slower than that of small sediment discharge after a certain moment. This implies the impact of sediment discharge on migration rate of GST is not monotonous, and is rather complex.

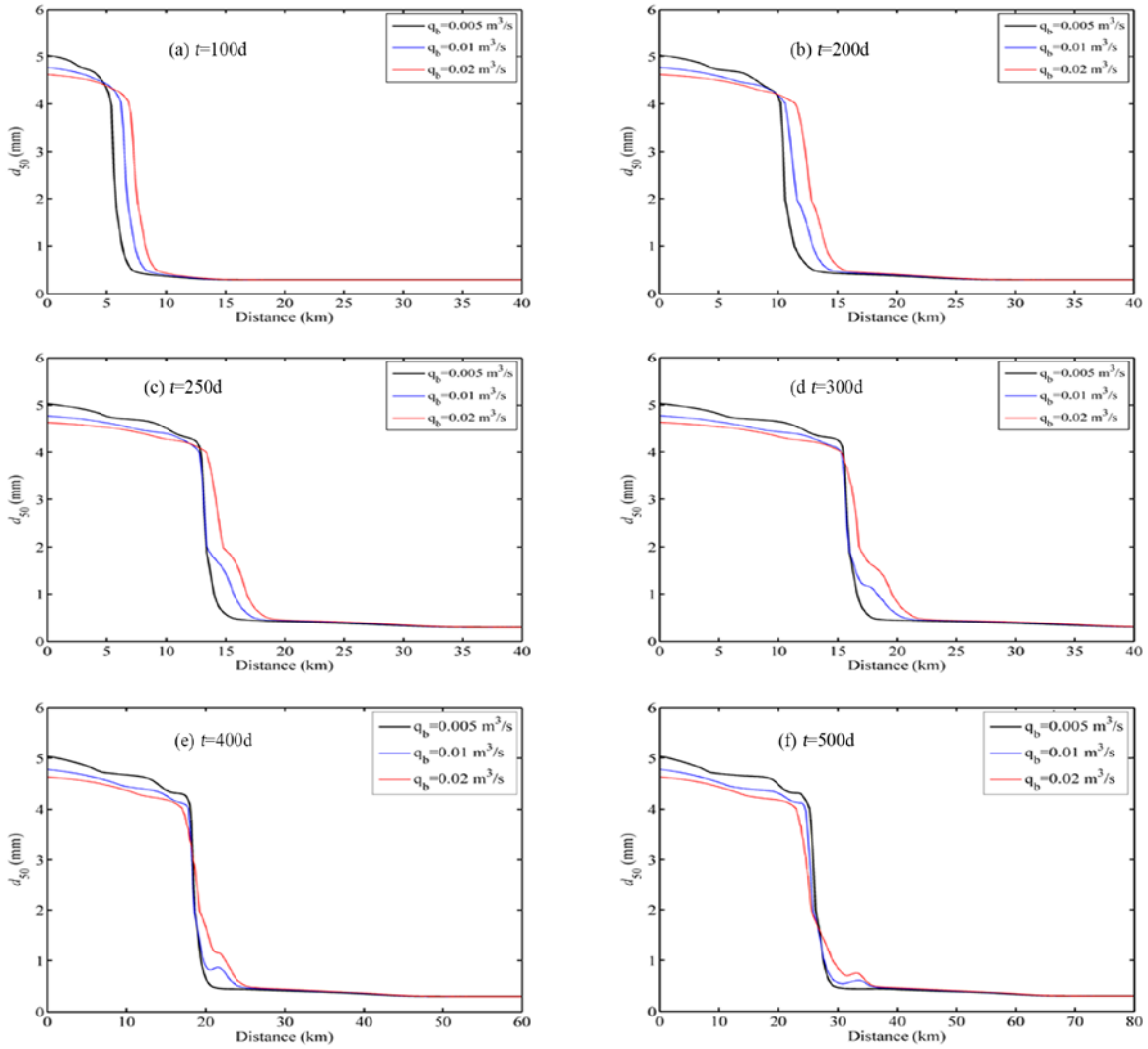


**Figure 10**. Profiles of $d_{50}$ for different inlet sediment discharge.

3.2.2 Impact of flow discharge

Figure 11 shows the impact of flow discharge on bed sediment diameter along the river. As shown in Figure 11, GST migrates downstream faster in relation to a larger flow discharge, which implies that there is a monotonous relationship between flow discharge and GST. Moreover, the space between different discharges enlarges with time. It means the influence of the flow discharge reinforced as GST migrating downstream.

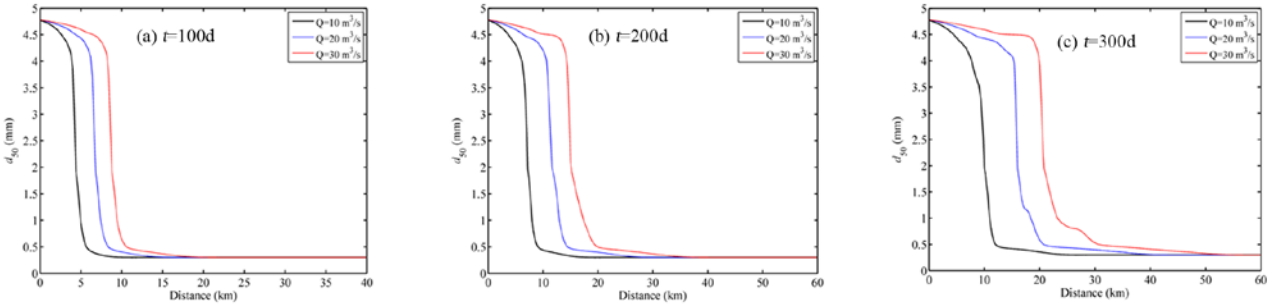


**Figure 11**. Profiles of $d_{50}$ for different inlet discharge at *t*=100d.

## 4 CONCLUSIONS

The present model well reproduces the laboratory experiment of GST, which indicates its ability in modeling formation and evolution of GST. Details during formation and evolution of GST have been investigated through numerical experiments on a generalized river case. The results show bed shear stress, bedload transport rate, $d_{50}$ and Shields number change in tendency along the river. Moreover, the abrupt change points for these factors are not always at the same location, which implies no direct and simple relationships exist among them. Analysis of grain percentiles has shown rapid decrease of certain coarser gravel (mostly the size with largest percentile at the inlet cross section) and rapid recover of some fine sands form GST in combination. Sensitive analyses of flow and sediment discharges on evolution of GST demonstrate that migration of GST is faster in regard to a larger flow discharge. However, migration of GST is not monotonous to sediment discharge. In the initial period, GST moves faster in relation to a larger sediment discharge. However, it moves slower after a certain period.

## ACKNOWLEDGEMENTS

This work is funded by Natural Science Foundation of China (11502032) and National Key Research and Development Program of China (2016YFC0402106).

## REFERENCES

Cao, Z., Yue, Z. & Pender, G. (2011). Landslide Dam Failure and Flood Hydraulics. Part II: Coupled Mathematical Modelling. *Natural Hazards*, 59(2), 1021-1045.

Cui, Y. & Parker G. (1998). The Arrested Gravel Front: Stable Gravel-Sand Transitions in Rivers Part II: General Numerical Solution. *Journal of Hydraulic Research*, 36, 159–182.

Fan, N., Nie, R., Wang, Q. & Liu, X. (2016). *Dramatic undercutting of Piedmont Rivers after the 2008 Wenchuan Ms 8.0 Earthquake,* Scientific Reports, 6(37108), 1-6.

Ferguson, R.I. (2003). Emergence of Abrupt Gravel to Sand Transitions along Rivers through Sorting Processes. *Geology*, 31(2), 159–162.

Ferguson, R.I., Bloomer, D.J. & Church, M. (2011). Evolution of an Advancing Gravel Front: Observations from Vedder Canal, British Columbia. *Earth Surface and Processes Landforms*, 36, 1172–1182.

Ferguson, R., Hoey, T., Wathen, S. & Werrity, A. (1996). Field Evidence for Rapid Downstream Fining of River Gravels through Selective Transport. *Geology*, 24, 179–182.

Frings, R.M. (2011). Sedimentary Characteristics of the Gravel-Sand Transition in the River Rhine. *Journal of Sedimentary Research*, 81, 52–63.

Hoey, T. B. & Ferguson, R. (1994). Numerical Simulation of Downstream Fining by Selective Transport in Gravel Bed Rivers: Model Development and Illustration. *Water Resource Research*, 30(7), 2251-2260.

Huang, W., Cao, Z., Yue, Z., Pender, G. & Zhou, J. (2012). Coupled Modelling of Flood due to Natural Landslide Dam Breach. *Proceedings of the ICE - Water Management*, 165(10), 525-542.

Knighton, A.D. (1999). The gravel–Sand Transition in a Disturbed Catchment. Geomorphology, 27, 325-341.

Lamb, M.P. & Venditti, J.G. (2016). The Grain Size Gap and Abrupt Gravel-Sand Transitions in Rivers due to Suspension Fallout. *Geophysical Research Letter*, 43, 1-13.

Meyer-Peter, E. & Müller, R. (1948). Formulas for Bed-Load Transport. *IAHR 2nd meeting,* IAHR Stockholm, 39-64.

Paola, C., Parker, G., Seal, R., Sinha, S.K., Southard, J.B. & Wilcock P.R. (1992). Downstream Fining by Selective Deposition in a Laboratory Flume. *Science*, 258, 1757–1760.

Parker, G. & Cui Y.T. (1998). The Arrested Gravel Front: Stable Gravel-Sand Transitions in Rivers - Part 1: Simplified Analytical Solution. *Journal of Hydraulic Research*, 36(1), 75–100.

Sambrook Smith, G.H. & Ferguson, R.I. (1995). The Gravel-Sand Transition along River Channels. *Journal of Sedimentary Research*, A65, 423–430.

Sambrook Smith, G.H. & Ferguson, R.I. (1996). The Gravel-Sand Transition: Flume Study of Channel Response to Reduced Slope. *Geomorphology*, 16, 147–159.

Singer, M.B. (2010). Transient Response in Longitudinal Grain Size to Reduced Gravel Supply in a Large River. Geophysical Research Letter, 37(L18403), 1-5.

Sternberg, H. (1875). Untersuchungen Uber Langen-und Querprofil geschiebefuhrender Flusse. *Zeitschrift fur Bauwesen*, 25, 483–506.

Toro, E.F. (2001). *Shock-capturing Methods for Free-Surface Shallow Flows*. John Wiley, England.

Toro-Escobar, C.M., Paola, C. & Parker, G. (1996) Transfer Function for the Deposition of Poorly sorted Gravel in Response to Streambed Aggradation. *Journal Hydraulic Research*, 34(1), 35-53.

Venditti, J.G. & Church, M. (2014). Morphology and Controls on the Position of a Gravel-Sand Transition: Fraser River, British Columbia. *Journal of Geophysical Research: Earth Surface*, 119, 1959–1976.

Venditti, J.G., Domarad, N. Church, M. & Rennie, C.D. (2015). The Gravel-Sand Transition: Sediment Dynamics in a Diffuse Extension. *Journal of Geophysical Research: Earth Surface*, 120, 943–963.

Wilcock, P.R. (1998). Two-Fraction Model of Initial Sediment Motion in Gravel-Bed Rivers. *Science,* 280, 410–412.

 

Yatsu, E. (1955). On the Longitudinal Profile of the Graded River. American Geophysical Union Transactions, 36, 655-663.

Yatsu, E. (1957). On the Discontinuity of Grain Size Frequency Distribution of Fluvial Deposits and its Geomorphological Significance. *Proceedings of the International Geophysical Union Regional Conference,* Tokyo, Japan, 224–237.

Zhang, R. & Xie, J. (1993). *Sedimentation Research in China: Systematic selections,* China Water and Power Press, Beijing.

 

Proceedings of the 37th IAHR World Congress
August 13 – 18, 2017, Kuala Lumpur, Malaysia

# MODELING THE SEDIMENT DYNAMICS OF SUPPLIED SAND AND GRAVEL IN ARMORED RIVER DOWNSTREAM OF A DAM

NORIO TANAKA[1] & KOSUKE MATSUO[2]

[1,2] Graduate School of Science and Engineering, Saitama University, Saitama, Japan,
[1] International Institute for Resilient Society, Saitama University, Saitama, Japan,
e-mail tanaka01@mail.saitama-u.ac.jp

## ABSTRACT

Sediment supply downstream of a dam by dredging sediment in a reservoir and placing the sediment in a downstream flood basin of the river is recently tested for solving a riverbed environmental problem caused by armoring. The objective of this study is to clarify the dynamics of artificially supplied sand quantitatively in armored bed by proposing a new model for calculating a reduced bed shear stress in the armored, boulder or stone (BS) layer. Quasi-three dimensional (Q3D) model has been developed considering the force balance, i.e., sheltering effect by boulders and reduction of bed shear stress. The flow is divided into two layers vertically and the velocity in the armored layer is solved by continuity equation and momentum equations in between the two layers. Both the two dimensional (2D) depth averaged flow model and Q3D model were applied downstream of the Futase dam, Japan. For verifying the effectiveness of the Q3D model, middle class flood event in September 2009 was selected because the gravels or stones with different color were set in the three locations before the flood event. The threshold values of gravel/stone movement and the percentage of movement in different gravel/stone were investigated. Simulated results indicated that friction velocity derived in 2D model exceeds the threshold value of movement of the stones in most of the river grids. However, Q3D model showed similar or smaller values of bed friction in most of the river. After the verification, the difference of 2D model and the Q3D model were compared in the flood events in October 2006. The Q3D model can express the sedimentation at the inner side of meandering part of the river well. On the contrary, 2D model cannot express the bed aggradation that actually occurred.

**Keywords:** Two-layered model; sediment budget; improvement of stream ecology; reduction in friction velocity.

## 1 INTRODUCTION

Dams affect the ecological habitat of aquatic plants and insects in the downstream through sediments' input change to the downstream (distribution of the material size, river morphology). Sediment supply performed by dredging sediment in a reservoir and placing it in a downstream flood basin of the river is recently tested in many rivers for improving dam-downstream river ecosystem and mitigating erosion. As the sediment movement greatly affects the invertebrate dynamics (Gibbins et al., 2010; Gomi et al., 2010; Tanaka et al., 2016), the response of a river ecosystem to the disturbance needs to be clarified to design a suitable amount and size of supplied sediment. The dynamics for flood disturbance are usually discussed in relation with the mean diameter of sand and gravel at the habitat; although the mean-diameter particles are assumed not to be moved by flooding at the invertebrate growing season from autumn to next spring. The increase in the movability of small size particles may affect the drift of invertebrates.

Tanaka et al. (2016) reported the change of invertebrate dynamics after the sediment supply to the downstream of the Futase dam, Japan. Fig.1 shows the pictures of the river bed after sediment supply. The supplied material just downstream of the Futase dam (which is located upstream of the Arakawa River, Japan) were accumulated around boulders (Fig.1a) and in between the boulders or stones especially the inner side of meandering part of the river (Fig.1b). Although the velocity structures at the armored bed are assumed to greatly affect the sedimentation, not many studies have been conducted especially for armored bed. Previous experiments showed the reduction of velocities and friction in the armor layer, as a result of which the sand motion in the armored layer progressed very slowly. However, there are many unknown factors regarding how the sediment supply affects the bed material size and its dynamics at a flood event.

Therefore, the objective of this study is to clarify the dynamics of artificially supplied sand quantitatively in armored bed by proposing a new model for calculating a reduced bed shear stress in the armored, boulder or stone (BS) layer. For the objective, new numerical model has been developed to express the reduced friction velocity in the armored layer. The applicability of the reduced friction velocity was verified by the previous available field test data, where the difference of the depth-averaged two dimensional (2D) model and quasi-three dimensional (Q3D) model were compared. Sediment accumulation were calculated by the measured cross-section around 1 km length of the downstream river.

 

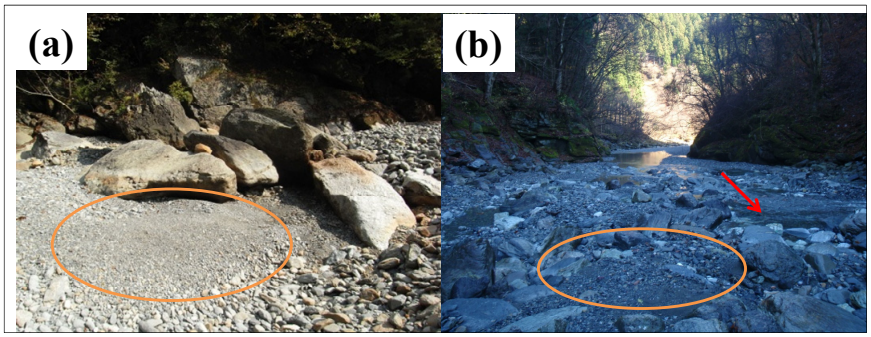


**Figure 1**. Sedimentation after sand and gravel supply (in circle). Arrow is the flow direction at low flow. (a) around boulders, (b) in between stones at inner side of meandering part (Photos are from the Ministry of Land, Infrastructure, Transport and Tourism, Japan (MLIT)).

## 2 MATERIAL AND METHODS

### 1.1 Two dimensional (2D) river flow analysis

In order to compare the two-layered flow model (quasi-three dimensional model: Q3D) with the previous two-dimensional depth averaged flow model, a two-dimensional hydrodynamic model was used. The basic equations used in the hydrodynamic model are the conservation of fluid mass equation and the momentum equation (Reynolds equation). The basic governing equations in Cartesian coordinates are shown below.

The continuity equation:

$$\frac{\partial h}{\partial t}+\frac{\partial M}{\partial x}+\frac{\partial N}{\partial y}=0 \qquad [1]$$

Momentum equations in x and y directions:

$$\frac{\partial M}{\partial t}+\frac{\partial Mu}{\partial x}+\frac{\partial Mv}{\partial y}=-gh\frac{\partial Z_s}{\partial x}-\frac{\tau_{0x}}{\rho}-\frac{f_x}{\rho}+\frac{\partial}{\partial x}\left(-\overline{u'u'}h\right)+\frac{\partial}{\partial y}\left(-\overline{u'v'}h\right) \qquad [2]$$

$$\frac{\partial N}{\partial t}+\frac{\partial Nu}{\partial x}+\frac{\partial Nv}{\partial y}=-gh\frac{\partial Z_s}{\partial y}-\frac{\tau_{0y}}{\rho}-\frac{f_y}{\rho}+\frac{\partial}{\partial x}\left(-\overline{u'v'}h\right)+\frac{\partial}{\partial y}\left(-\overline{v'v'}h\right) \qquad [3]$$

where $t$ is the time; $h$ is the water depth; $u$ and $v$ are the depth-averaged velocities in $x$ and $y$ directions, respectively; $M$=$uh$ and $N$=$vh$ are the flux in $x$ and $y$ directions, respectively; $\tau_{0x}$ and $\tau_{0y}$ are the bed shear stress in $x$ and $y$ directions, respectively; $f_x$ and $f_y$ are the drag forces per unit area in $x$ and $y$ directions, respectively; $-\overline{u'^2}$, $-\overline{u'v'}$, and $-\overline{v'^2}$ are depth-averaged Reynolds stresses; $g$ is the gravitational acceleration, $\rho$ is the fluid density, and $Z_s$ is the water level.

Reynolds stresses were modeled using the method of Hosoda (2002). To transform the grid from Cartesian coordinates to a generalized coordinate system, the method of Hosoda et al. (1996) was applied. The finite volume method was used for solving the partial differential equations. The applicability of the model was validated for river flow by Tanaka and Yagisawa (2009).

### 1.2 Decomposition to two layers for solving the shear stress in the armored layer

Considering the experiment by Tanaka et al.(2015), the flow structure on the armored bed characterized by boulders or stones is decomposed in two layers as shown in Fig.2. For the upper layer, following equations can be derived considering force balance as:

$$\tau_{g2}=\tau_{as} \qquad [4]$$

$$\tau_{g2}=\rho g(H-h_{cob})I_e \qquad [5]$$

$$\tau_{as}=\rho f_{ask}(u_2-u_1)^2 r_{A-noncob} \qquad [6]$$

Where, $\tau_{g2}$: slope component of the gravity force in upper layer, $\tau_{as}$: apparent shear force at the boundary between upper and lower BS layer by the momentum exchange, $H$: water depth, $h_{cob}$: height of the cobble

 

from the lower bed, $I_e$: energy gradient, $f_{ask}$: mixing coefficient at the boundary, $u_1$: average velocity in BS layer, $u_2$: average velocity in upper layer, $r_{A\text{-}noncob}$: ratio of water area (total area – stone area) and total area.

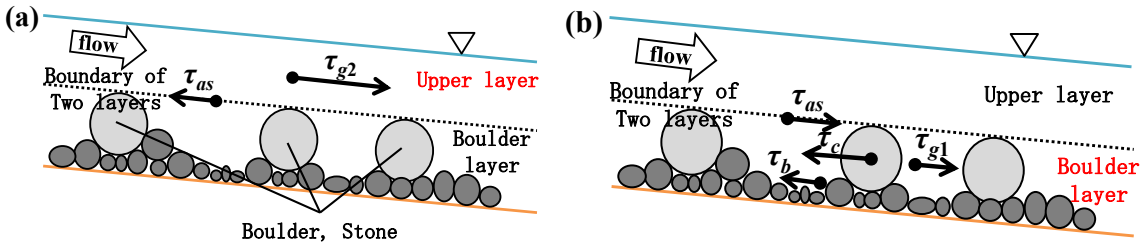


**Figure 2**. Modeling the force balance as a two-layered flow. $\tau_{g1}$: slope component of gravity force in boulder and stone (BS) layer, $\tau_{g2}$: slope component of gravity force in upper layer, $\tau_c$: drag force, $\tau_b$: bed shear stress, $\tau_{as}$: shear stress in between two-layers

For the lower layer (in boulder or stone (BS) layer)

$$\tau_{g1} + \tau_{as} = \tau_c + \tau_b \qquad [7]$$

$$\tau_c = 0.5 M \rho . \ {}_D u_1^2 S_{cob} \qquad [8]$$

Where, $\tau_{g1}$: slope component of the gravity force in BS layer, $\tau_b$: bed shear stress in the BS layer, $\tau_c$: drag force by boulders or stones in the BS layer, $C_D$: drag coefficient, $S_{cob}$: projected area of the boulders and stones, $M$: the number of boulders and stones in the unit area.

In addition, the continuity equation can be derived as:

$$u \cdot H = u_1 \cdot h_{cob} + u_2 \cdot (H - h_{cob}) \qquad [9]$$

Where, $u$: depth averaged velocity derived from Eqs.(1)-(3).

From the equations, the unknown variables, $u_1$, $u_2$ and $\tau_b$ can be solved, and the movement of the supplied sand can be simulated.

For the judgement of critical movement of sand, Iwagaki's equation (Iwagaki, 1956) was used:

$$d_{cri} = u_* / 80.9 \times 10^5 \qquad [10]$$

Where, $u_*$: friction velocity and $d_{cri}$: critical diameter of sand or gravels at the friction depth velocity.

For the friction velocity, Eq (11) and (12) were used for 2D and Q3D calculations, respectively

.

$$u_* = \sqrt{gHI_e} \qquad [11]$$

$$u_* = \sqrt{\tau_b / \rho} \qquad [12]$$

1.3 Simulation condition

1.3.1 Verification of the threshold of gravel movement using field test data

Both the two dimensional (2D) depth averaged flow model and Q3D model which have 378 and 41 grids in streamwise and cross-stream direction, respectively, were applied downstream of the Futase dam in generalized grid system (average grid length in two directions are around 5m in each). Averaged height of the BS layer was investigated and the 2 km river was classified into three sections considering the stone size. The height of the BS layer in the three sections was set 24, 17 and 15 cm from the upstream. The velocity and friction in the BS layer were calculated by the force balance in case of Q3D model and sand/gravel movement was solved by the reduced friction velocity. Firstly, for verifying the applicability of the Q3D model, 2008-September flood was selected (peak discharge was around 50$m^3$/s), at which flood gravel movement was investigated by using colored stone by the Ministry of Land, Infrastructure, Transport and Tourism, Japan (MLIT). After verifying the applicability, the model was applied to 2006-October flood (peak discharge was around 200 $m^3$/s) at which the change of river bed situation was investigated (but only photo was taken,

detailed measurement of the cross section was not conducted). Although the measurement was not conducted, gravel bars were generated at the flood site, and the simulated sedimentation situation can be compared qualitatively with the actual situation. Supplied sediment amount at the flood event was assumed by the annual flood discharge and annual sand supply amount in the year.

1.3.2 Analysis on the river bed change at a flood event using 2D and Q3D model

The 2D and Q3D model were applied to 2006-October flood by changing the assumed sediment amount. In 2006, there were two major floods and the total sediment amount was 5350 $m^3$ per year. Using the rate of peak discharge of both the floods, 1530 $m^3$ per target flood (total sediment volume) was decided. In order to discuss the sensitivity of the sediment input, half the amount, i.e 700 $m^3$ per flood was also set. For the input sediment characteristics in the simulation, the sediment characteristics ($d_{50}$ =4 cm, $d_{16}$ =0.5cm, $d_{84}$ =8cm) measured at the upstream of the dam where the input sediment was collected, was used. The total sediment volume was divided in time correlating with the discharge from the dam. As the sediment input was conducted just downstream of the dam which has no major tributaries, all the amount was put from the upstream boundary condition. So, the initial stage data in 2006 was selected for the analysis. This study only analyzed bed load as most of the input sediment was assumed to transport in the bed load motion in the reduced shear stress in BS layer calculated by the Eqs.(1)-(12). At the flood event, the armored layer was not destructed and the boulder position was not much changed. Therefore, the bed aggradation was calculated by the continuity equation of sediment.

1.4 Differences of sediment accumulation after different type of floods in 2014 and 2015

At the downstream of the Futase dam, sediment supply countermeasure was conducted from 2005 to 2010 (Phase 1), and stopped for two years later. Considering the effectiveness to the stream biota, the sediment supply restarted from 2013 (Phase 2). Detailed measurement of the cross section was taken before restarting and the measurement continued once a year. So, the sediment dynamics can be discussed after 2013. This study analyzes the data in Phase 2, and compares the analyzed sediment dynamics.

## 3 RESULTS AND DISCUSSION

a. Verification of the difference between 2D and Q3D model for expressing the critical movement of the gravels using a previous field experiment data

For verifying the effectiveness of the Q3D model, middle class flood event in September 2009 (peak discharge was around 50 $m^3/s$) was selected because the gravels or stones with different color were set in the three locations in Fig.3 before the flood event. The threshold values of gravel/stone movement and the percentage of movement in different gravel/stone were investigated. Simulated results indicated that friction velocity derived in 2D model exceeds the threshold values of movement of the stones (around 120 mm in diameter) in most of the river grids (Fig.3a). However, Q3D model shows similar or smaller values of bed friction in most of the river (Fig.3b). The actual field experiment showed that 60% of the stone (around 120-300 mm size) did not move at the flood event. The 2D model overestimates the movement of the bed material but Q3D does not. Therefore, Q3D model has high possibility to express the sand or gravel movement of the armored river.

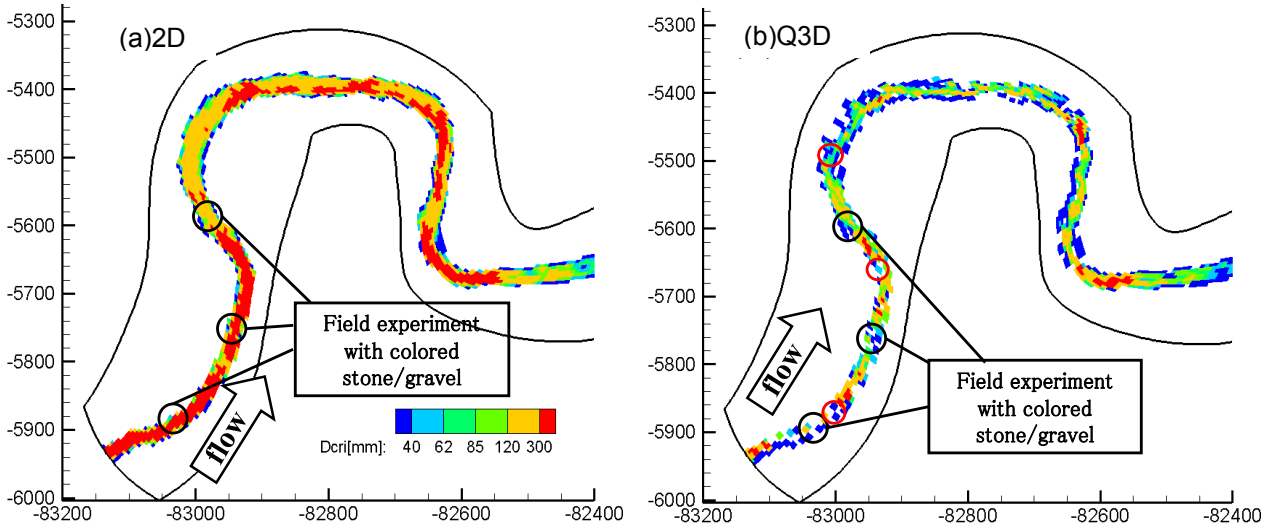


**Figure 3**. Comparison the Critical diameter of movement ($D_{cri}$) with (a) 2D and (b) Q3D model

b. Analysis of sediment supply to the armored gravel bed in the downstream of a dam

i. The difference of sedimentation height and the location during the flood event between 2D and Q3D

After the verification, the difference of 2D model and the Q3D model was compared in the flood events in October 2006 (peak discharge was around 200 $m^3/s$). Dynamics of sedimentation height and the deposited mean diameter were analyzed in the simulation. Fig.4 shows simulated sedimentation height from October-2006 flood. Fig.4a shows the result by 2D model (supply amount: left= 700 $m^3$, right=1530$m^3$) and Fig.4b by Q3D model (supply amount: left= 700 $m^3$, right=1530$m^3$). For both the models, the accumulation in region A, which was just downstream of the sediment input location that was actually observed, were reproduced well. The height in Region A was not much changed by the models and sediment input amount. However in Fig.4b, after the accumulation in Region A, sediment accumulation occurred in Region B, C and D by Q3D model, where actually gravel bars were generated after the flood event.

ii. The characteristics of sedimentation in the Q3D model

Fig.5 shows the average diameter of the sediment material simulated in 2006-October flood (Fig.5a and 5b show the results by 2D model and Q3D model respectively). From Fig.5b, sediment having size of more than 7cm becomes the core in the sediment accumulated region and afterwards, whereas, 4cm and less than 4cm sediment were accumulated in Region B, C and D, especially in Q3D model. On the contrary, 2D model can easily pass the larger size sediment because of the large shear stress in the river. The Q3D model can express the sedimentation at the inner side of meandering part of the river well. However, 2D model cannot express the bed aggradation that actually occurred. The Q3D model has a possibility to express the dynamics of supplied sediment motion in armored rivers. From the Q3D simulation, 7-4cm class gravel are assumed to be important materials for the sediment input, especially the downstream condition of the Futase dam. Further study is needed in this area.

For clarifying the sedimentation process further, simulated results at the peak for 2006-October flood (supply amount = 700 $m^3$) is shown from the point; (a) friction velocity by Q2D model, (b) friction velocity by Q3D model and (c) average diameter accumulated and velocity vector calculated by Q3D model. Compared with Fig.6a, friction velocity in Fig.6b is mostly less than 0.1 m/s in the dashed line region where sediment accumulation occurred. Fig.6a shows quite larger values than Fig.6b. Fig.6c shows that the direction of the velocity vector is forward on the inner side, and the flow contracted region can be confirmed in the red dashed line. In Fig.6b, by the reduced friction velocity, sediment accumulation occurred upstream of the contracted region (Fig.6c). Similar trend was also confirmed in Region C and D. So, the modeling of reduced friction velocity by considering the sheltering effect by boulders is very effective for analyzing the dynamics of sediment motion in the armored layer.

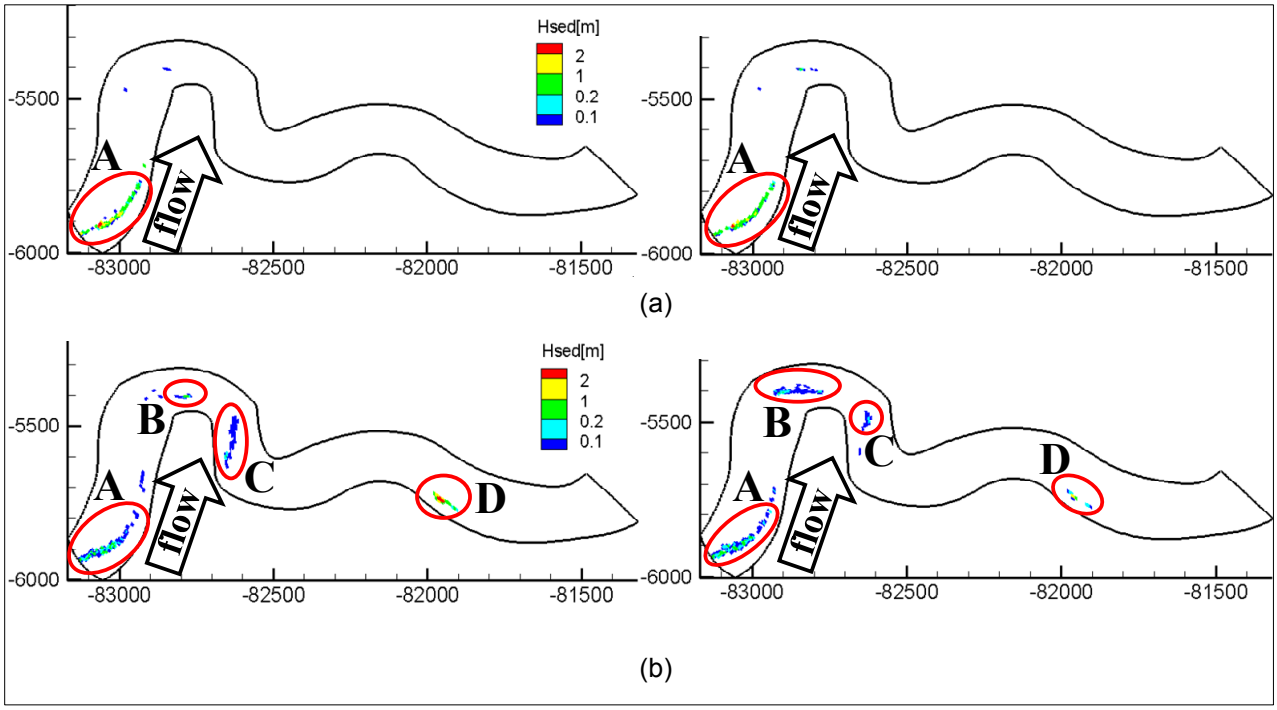


**Figure 4**. Simulated sedimentation height by October 2006 flood. (a) 2D model (supply amount: left= 700 $m^3$, right=1530$m^3$), (b) Q3D model (supply amount: left= 700 $m^3$, right=1530$m^3$)

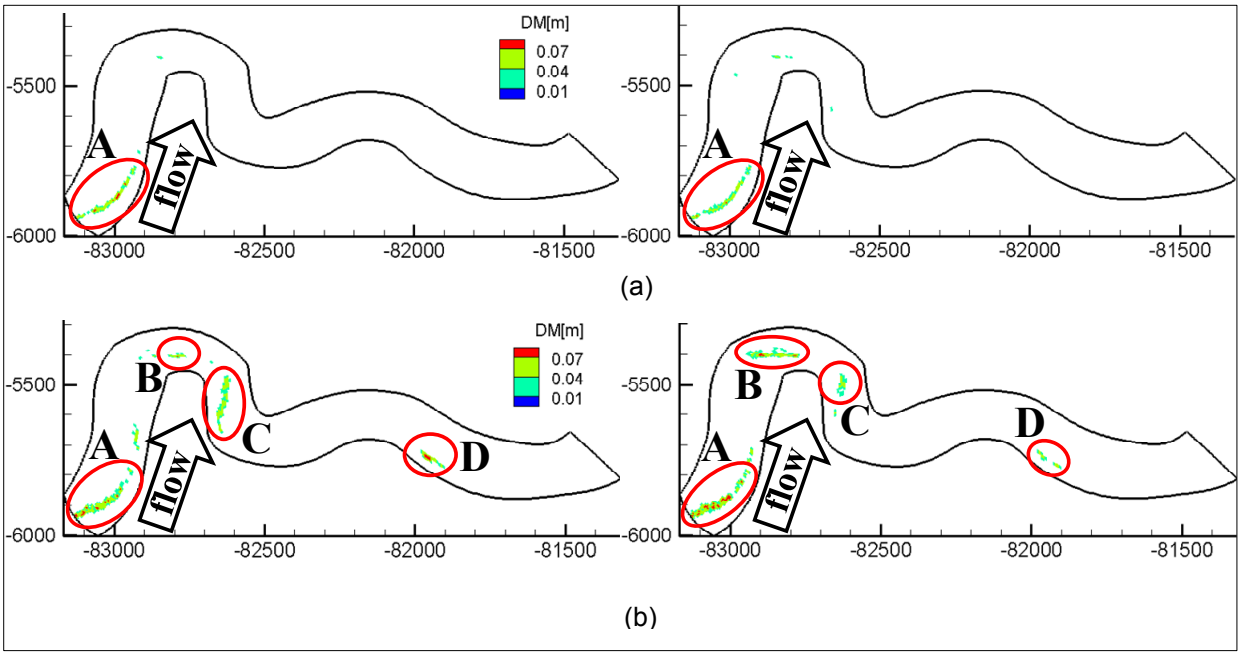


**Figure 5**. Average diameter of the sediment material simulated in October 2006 flood. (a) 2D model (supply amount: left= 700 $m^3$, right=1530$m^3$), (b) Q3D model (supply amount: left= 700 $m^3$, right=1530$m^3$)

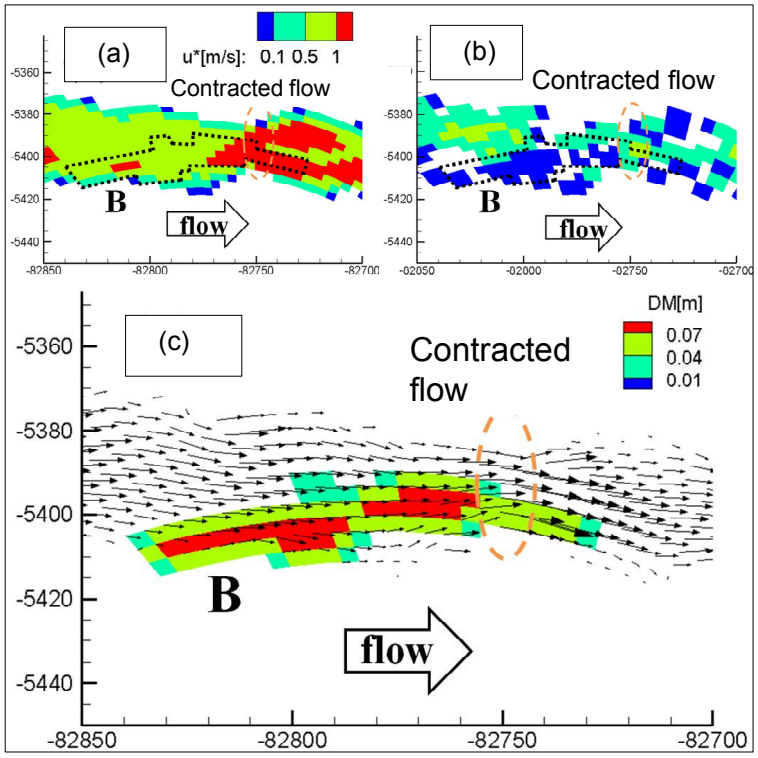


**Figure 6**. Simulated results at the peak for October 2006 flood (supply amount = 700 $m^3$). (a) friction velocity by Q2D model (dashed line shows the fringe of Location B in Fig.6), (b) friction velocity by Q3D model, (c) average diameter and velocity vector calculated by Q3D model

c. Change of the cross section

Fig.7 shows the change of cross section in the downstream of Futase dam from 2013 to 2015 after the flood season each year at (a) Location B and (b) Location C. As shown in Fig.1, at Location A (Fig.1b) and Location B (Fig.1c), the bed aggradation can be clearly confirmed. Although the measurement time of cross section was different, the change of cross section can be confirmed at Location B and Location C. Fig. 8 show the time series of the flow discharge at the locations and Table 1 summarizes the peak discharge and sediment input in 2014 and 2015. The accumulation largely occurred in 2014 although the sediment input and peak discharge was smaller than those in 2015. Especially at Location B, bed degradation also occurred after

 

2014 by the 2015 floods. In 2014, just after the restart of the sediment input, some pocket for accumulating the sediment is assumed to exist. Another important difference between the two years' flood is the difference in the flood wave shape. In 2014, flood peak was small and a decreasing trend of discharge slowly occurred as compared to the 2015 flood which was large and sharp. So, the sediment dynamics is supposed to be related to not only the peak discharge but also the flood wave characteristics, and the previous year's sediment remains in the river section. The sediment budget should be clarified not only to the input but also sediment amount that existed in the armored bed and is movable for the next floods. So the analysis should be conducted not only for one year's flood event but consecutive several floods. In future, for clarifying the relationship between the sediment input and the river habitat through the invertebrate and/or periphyton dynamics (Tanaka et al., 2016) further, the effect of sediment supply to downstream of dam should also be discussed in the successive years.

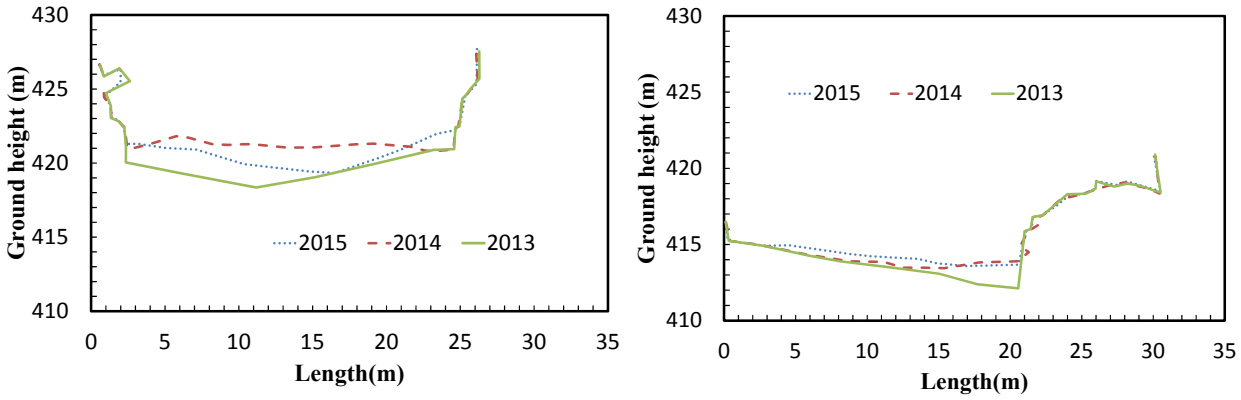


**Figure 7**. Change of cross section in the downstream from 2013 to 2015. (a) Location B, (b) Location C

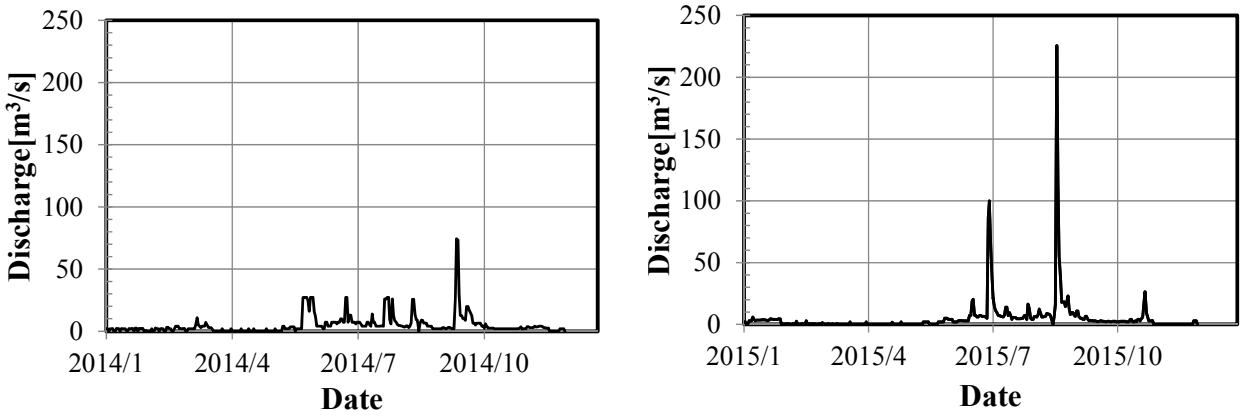


**Figure 8**. Discharge from the Futase dam. (a) 2014, (b) 2015

**Table 1**. Comparison the amount of supplied sediment and deposited amount in the investigated region (0.85-1.70 km from the downstream of Futase Dam. Spacing of the cross-section data is around 50 m)

| Year | Supply amount of sediment $m^3$ | Amount of deposition $m^3$ | Maximum discharge in the year $m^3/s$ |
|---|---|---|---|
| **2014** | 4200 | 3416.7 | 74.3 |
| **2015** | 11000 | 1272.3 | 225.6 |

## 4 CONCLUSIONS

The Q3D model can express the sedimentation at the inner side of meandering part of the armored river well. On the contrary, 2D model cannot express the bed aggradation that actually occurred. The Q3D model has a possibility to express the dynamics of supplied sediment motion in armored rivers. However, from the river cross section analysis, the sediment remains in the previous years' flood has a possibility to affect sediment dynamics in the river. This should be discussed in more detail in the successive years' analysis and sediment budget by using the Q3D model.

 

**ACKNOWLEDGMENTS**

This research was supported in part by the River Foundation, Japan. Authors acknowledged the Futase dam Office, the Ministry of Land, Infrastructure, Transport and Tourism, Japan (MLIT)), for providing data.

**REFERENCES**

Gibbins, C., Batalla, R. J. & Vericat, D. (2010). Invertebrate Drift and Benthic Exhaustion during Disturbance: Response of Mayflies (Ephemeroptera) to Increasing Shear Stress and River-Bed Instability. *River Research and Applications*, 26, 499-511.

Gomi, T., Kobayashi, S., Negishi, J. & Imaizumi, F. (2010). Short-Term Responses of Macroinvertebrate Drift Following Experimental Sediment Flushing in a Japanese Headwater Channel. *Landscape and Ecological Engineering*, 6, 257-270.

Hosoda, T. (2002). *River Flow Analysis by Generalized Coordinate System*. In: Programme Library for Hydraulic Engineering (in Japanese). CD-ROM (ISBN 4-8106-0203-6)

Hosoda, T., Nagata, N. & Muramoto, H. (1996). Numerical Analysis of Unsteady Open Channel Flows By Means of Moving Boundary Fitted Coordinated System (in Japanese with English abstract). *Journal of Hydraulic Engineering*, 533(34), 267-272.

Iwagaki, Y. (1956). Hydrodynamical study on critical tractive force. *Japanese Society of Civil Engineers Journal*, 41, 1-21.

Tanaka, N. & Yagisawa, J. (2009). Indices for Evaluating the Breaking and Wash-Out Condition of Trees on Gravel Bar At Flood Events*. Proceedings of 33rd IAHR, Vancouver, Canada*.

Tanaka, N., Yoshizawa, Y. & Habib, S. (2015). Boundary Layer Development in Roughness Layer at Modeled Armored Gravel Bed Stream and the Sand Movement in the Region, *E-proceedings of the 36th IAHR World Congress, Hague, Netherlands.*

Tanaka, N., Shinyama, H. & Sakata, R. (2016). Invertebrate Dynamics in The Downstream of A Dam After Sediment Supply, *11th Int. Symposium on Ecohydraulics (ISE) 2016, Melbourne, Australia.*

 

Proceedings of the 37th IAHR World Congress
August 13 – 18, 2017, Kuala Lumpur, Malaysia

# ASSESSMENT OF SEDIMENT RATING CURVES FOR MOUNTAIN RIVERS IN MALAYSIA

SHANKER KUMAR SINNAKAUDAN[(1)], MOHD RIZAL SHUKOR[(2)], MUNYATI MOHAMMED[(3)] & AZWIN ZAILITI ABDUL RAZAD[(4)]

[(1, 2, 3)] Faculty of Civil Engineering, Universiti Teknologi MARA Pulau Pinang, Permatang Pauh, Penang, Malaysia, mohdrizal50@yahoo.com; drsshan@yahoo.com; munyatimohammed@gmail.com

[(4)] TNB Research Sdn. Bhd., 1, Lorong Air Hitam, Kawasan Institusi Penyelidikan, 43000 Kajang, Selangor, Malaysia, azwinzailiti.arazad@tnbr.com.my

## ABSTRACT

Sediment transport measurements at the inflowing rivers into reservoirs which are located at the mountainous catchment area have been always a daunting task. However, to meet the continuous requirement on reservoir sedimentation monitoring and management initiatives, Total Sediment Load (TL) rating curves are developed mostly based on low flow data and TL equations area is adopted to give reliable prediction for medium to high flow data. However, with the present state of knowledge, the selection of best TL equation for natural rivers remains a major doubt among engineers and practitioners. Thus, the present study attempts to evaluate applicability of the 10 existing TL equations to predict the sediment rating curves specifically for 2 inflowing rivers namely Sungai Senang Berangan and Sungai Kenyir into Kenyir Reservoir which is the largest man-made reservoir in Peninsular Malaysia. A total of 48 sets sediment and hydraulic data which covers low to high flow ranges have been obtained from Sinnakaudan and Abdul Razad (2014) and is adopted in the analysis. The study streams data encompass a wide range of flow discharge ($0.034m^3/s$ – $23.96m^3/s$) with diverse particle size ranging from fine sand to boulder size of bed material (d50). The accuracy of existing equations is assessed by discrepancy ratio (DR) analysis whereby the predicted and measured TLs are compared and accepted if the ratio is within the acceptable range from 0.5 - 2.0. It is found that Shen and Hung (1972) and Sinnakaudan et al. (2010) equations can predict more than 10% of data for coarse bed river. However, Shen and Hung (1972) shows consistency in prediction for both river morphologies and is adopted for TL rating curve development for the said rivers.

**Keywords:** Sediment transport; sediment rating curve; mountain rivers; discrepancy ratio test.

## 1 INTRODUCTION

Mountain River (MR) is the critical issue in the river management because it may function as the potential part for the reservoir or dam construction. Sedimentation problem at MR may disturb the dam construction and operation whenever the dam is filled with sediment (Sulaiman, 2009). In the general knowledge of sediment study, sediment rating curve is used to estimate total sediment load (TL) transported by a river. The TL is estimated by fitting a curve of plot between sediment and river discharge (Ahanger et al., 2013). Besides that, sediment rating curve is also beneficial when there is an absence of actual TL data. TL is determined by extrapolating the data through existing recorded TL rating curve. The most challenging task in estimating TL is when there is no historical rating curve available at all for study reaches. Alternatively, empirical equation was adopted. Adopting any of empirical TL equations in any study reaches is not an easy task for engineers or practitioners because currently none of the existing equations have received universal acceptance.

At present, major studies have been focused on the lowland rivers. A good appraisal for the existing and commonly used sediment transport equation which were given by Meyer-Peter and Muller (1948), Toffaleti (1969), Yang (1972), Ackers and White (1973), Engelund and Hansen (1967) and Laursen (1958). As reported, the existing equation was developed by using the data which is not native to Malaysian river condition. In Malaysia, Ariffin (2004) and Sinnakaudan et al. (2006) was among the researchers that developed equations that are native to local river conditions. Both equations were developed by regression analysis of the local lowland rivers data. An attempt has been made by Sinnakaudan et al. (2010) to develop a specific equation for MR in Malaysia. The equation was reported to be successful in predicting 55% of local MR data. The equation has been further tested with 16 MR data by Sinnakaudan and Abdul Razad (2014), unfortunately none of the data were successfully predicted with confident. Therefore, this study attempts to evaluate the applicability of existing TL equations to local MR and propose the best predictor for TL.

 

## 2 RESEARCH APPROACH

### 2.1 Study area

As part of the requirement for sediment transport study at Kenyir Hydroelectric Scheme, sediment samplings and total sediment load calculations are required on two rivers which are located near to the water intake point for the power generation as listed below:

- Sungai Senang Berangan (approximately 500m from intake of Kenyir Lake);
- Sungai Kenyir (further away from Kenyir Intake).

The location of the sampling site is shown in Figure 1.

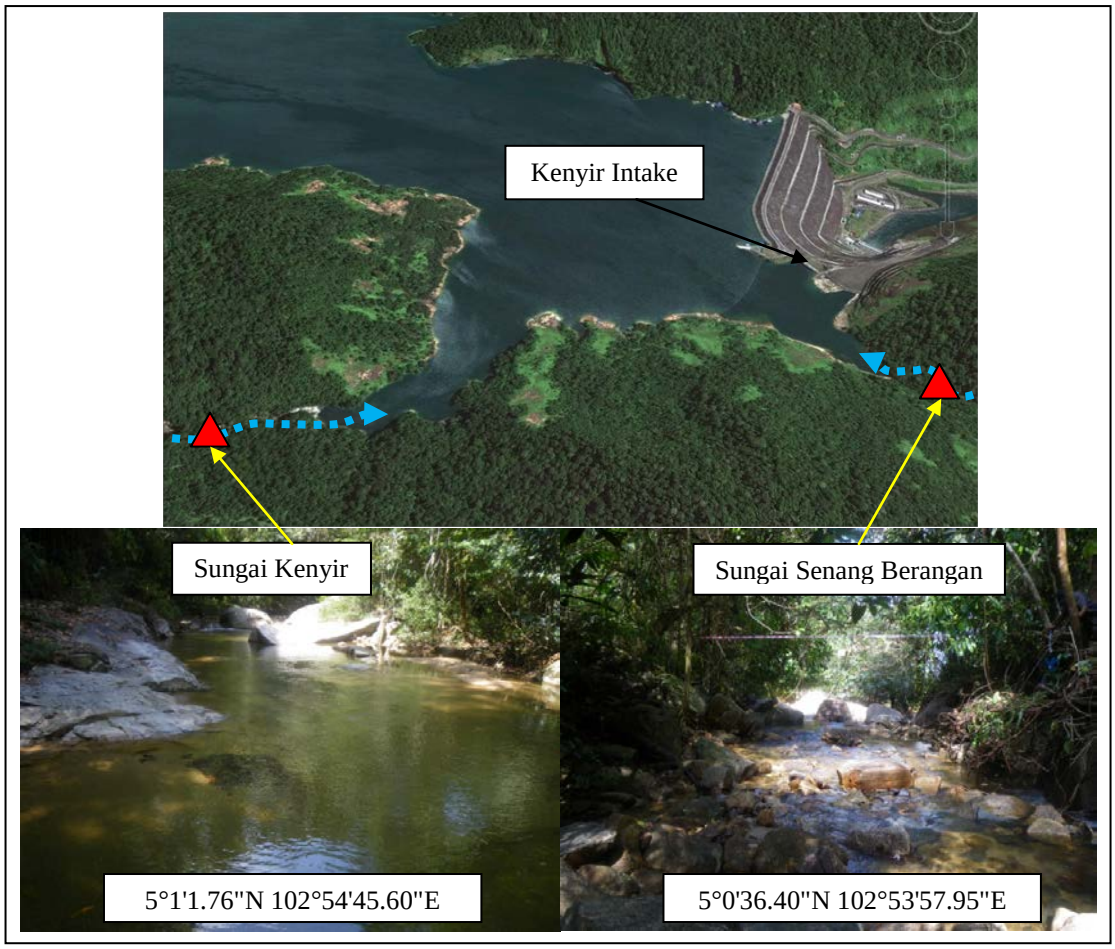


**Figure 1**. Locations of study reach.

Sungai Senang Berangan located 147 meters above mean sea level (MSL) is a plane bed channel which having a moderate water surface slope. The median size of bed material is ranging from cobble to boulder with limited depth of flowing water during the dry season. Conversely, Sungai Kenyir is less coarse compared to Sungai Senang Berangan by which sand and fine gravel dominate upper layer of the riverbed. It is a single thread channel with moderate width to depth ratio where a formation of pool visible near to the river confluence. As shown in Figure 1, Sungai Kenyir is having stable river morphology with underlying rigid bedrocks with slowly moving the upper layer of sand and fine gravels. Table 1 summarizes the hydraulic condition of study sites.

 

**Table 1**. Hydraulic condition of study reaches.

| | | Discharge Q ($m^3/s$) | Velocity V (m/s) | River width B (m) | River depth $Y_0$ (m) | Water slope $S_0$ (m/m) | Sediment Size $D_{50}$ (mm) |
|---|---|---|---|---|---|---|---|
| Sungai Kenyir | Minimum | 0.15 | 0.05 | 5.63 | 0.31 | 0.0212 | 1.46 |
| | Average | 5.01 | 0.38 | 10.74 | 0.56 | | 1.84 |
| | Maximum | 23.96 | 1.18 | 16.55 | 1.12 | | 2.88 |
| Sungai Senang Berangan | Minimum | 0.03 | 0.03 | 3.37 | 0.12 | 0.0415 | 62.30 |
| | Average | 2.40 | 0.59 | 5.79 | 0.29 | | 90.89 |
| | Maximum | 18.70 | 3.69 | 7.17 | 0.79 | | 113.58 |

2.2 Data collection and laboratory analysis

The sampling work was started on 16th April 2014. Low flow data was collected from April to May 2014 while medium to high flow data was collected during monsoon season from November to December 2014. During low flow event (dry season), the flow is relatively low for both rivers therefore all the measurements were done by wading technique. For medium to high flow data, suspended bridge was used to collect the data. Channel geometry and hydraulic properties such as water surface slope (S0), flow depth (Y0) and flow velocity (V) were measured for each river. The flow discharge then was calculated by using Mid-Section Method by utilizing the measured data.

There are two types of sediment data collected in this study namely suspended load and bed load. Suspended load (Ts) was sampled using DH 48 during low flow event and DH 59 for medium to high flow events. Bed load (Tb) was sampled using Helley Smith sampler and the sampler was deployed 10 minutes for measurement. The suspended load concentration was analyzed using Spectrophotometer for TSS and for samples not within the acceptable range of the equipment, gravimetric method was employed. The bed load concentration was analyzed according to the Manual on Operational Methods for the Measurement of Sediment Transport, World Meteorological Organization – Operational Hydrology Report No 29" and DID (2003). Total sediment load, Tj was calculated by the summation of Suspended Load (Ts) and Bed Load (Tb).

A standard grab sampler (Van Veen) was used to collect bed material at Sungai Kenyir while Wolman Pebble Counts Method employed for Sungai Senang Berangan. Samples are bagged, labeled and sent to the laboratory for particle size distribution analyses to determine the respective sizes and average diameter of the sediment particles.

2.3 Selected roughness coefficient equations

The analysis for a total of 48 sets of data was made for selected 10 TL equations. These equations can be grouped into two main categories namely: 1) equations based power function; 2) equations based on regression analysis.

Category 1: Equations based on power function

Bagnold (1966)

$$W'_T U = \frac{P}{b}\left[\frac{e_b}{\tan\phi} + \frac{e_s(1-e_b)}{\tan\phi_s}\right] \quad [1]$$

Engelund and Hansen (1967)

$$q_s = \frac{0.05\rho_s g^{1/2} V^2 d_{50}^{1/2}\theta^{3/2}}{(S_s-1)^{1/2}} \quad [2]$$

Yang (1972) for sand

$$\log C_T = 5.435 - 0.286\log\frac{\omega_s D_{50}}{\nu} - 0.457\log\frac{U_*}{\omega_s} + \left(1.799 - 0.4909\log\frac{\omega_s D_{50}}{\nu} - 0.314\log\frac{U_*}{\omega_s}\right) x \log\left(\frac{VS_o}{\omega_s} - \frac{V_c S_o}{\omega_s}\right) \quad [3]$$

Ackers-White (1973)

$$C_v = \left[\frac{V}{\frac{K\sqrt{g(S_s-1)D_{50}}}{J}} - 1\right]^m \quad [4]$$

 

Yang (1984) for gravel

$$\log C_T = 6.681 - 0.633\log\frac{\omega_s D_{50}}{\nu} - 0.4816\log\frac{U_*}{\omega_s} + \left(2.784 - 0.305\log\frac{\omega_s D_{50}}{\nu} - 0.282\log\frac{U_*}{\omega_s}\right) x \log\left(\frac{VS_o}{\omega_s} - \frac{V_c S_o}{\omega_s}\right) \quad [5]$$

Category 2: Equations based on regression analysis

Laursen (1958)

$$C_T = 0.01\gamma\sum_i p_i\left(\frac{d_i}{D}\right)^{7/6}\left(\frac{\tau'}{\tau_{ci}} - 1\right) f\left(\frac{U_*}{\omega_i}\right) \quad [6]$$

Graf (1971)

$$\phi = \frac{C_V VR}{\sqrt{g(S_s - 1)d_{50}{}^3}} \quad [7]$$

Shen and Hung (1972)

$$\log C_T = -107404.459381 + 324214.747340Y - 326\,309.589\,08739Y^2 + 109503.87232539Y^3 \quad [8]$$

Sinnakaudan et al. (2006)

$$C_v = 1.811*10^{-4}\left(\frac{VS_o}{\varpi_s}\right)^{0.293}\left(\frac{R}{d_{50}}\right)^{1.390}\left(\frac{\sqrt{g(S_s - 1)d_{50}{}^3}}{VR}\right) \quad [9]$$

Sinnakaudan et al. (2010)

$$C_V = 2.138\times10^{-11}\times\left[\frac{\left(\frac{\omega_s d_{50}}{\nu}\right)^{1.117}\times\Omega^{0.603}\times\xi_i^{-0.336}}{VR}\right]\times\left[g(S_s - 1)d_{50}^3\right]^{1/2} \quad [10]$$

## 3 RESULTS AND DISCUSSIONS

### 3.1 Sediment rating curve performance

The TL rating curves for 24 sets of data for each river are given in Figure 2 and 3. The linear function is used as a fitting function for measured data. It was found that linear function yielded good correlation coefficient for both rivers. A strong correlation existed between river discharge and total sediment load for both rivers. Sungai Kenyir is a wide river that tends to have a curve with gentle slope and smaller y-intercept. This phenomenon indicates that the wider river has less capacity to carry sediment compared with narrower river. The trend of TL transport is almost identical for both rivers during low flow event. However, when the river discharge exceeded its base flow level, the capacity of both rivers to carry sediment varies. Sungai Senang Berangan is recorded to transport more sediment compared to Sungai Kenyir at equivalent discharge. Even Sungai Kenyir is surrounded by a lot of potential mobile sand however, the morphological condition of the site restricts the movement of sediment. Besides a wide channel, gauging location which is also associated with moderate depth pool, where most of the sediment gets trapped therefore greater force, is required to transport all the sediment.

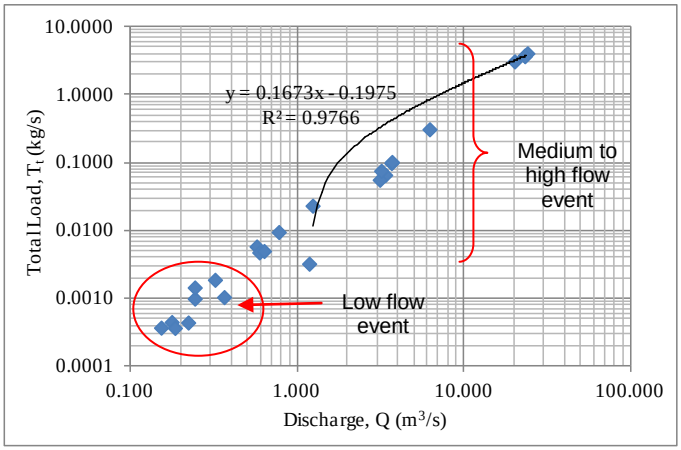


**Figure 2**. Sediment rating curve for Sungai Kenyir.

 

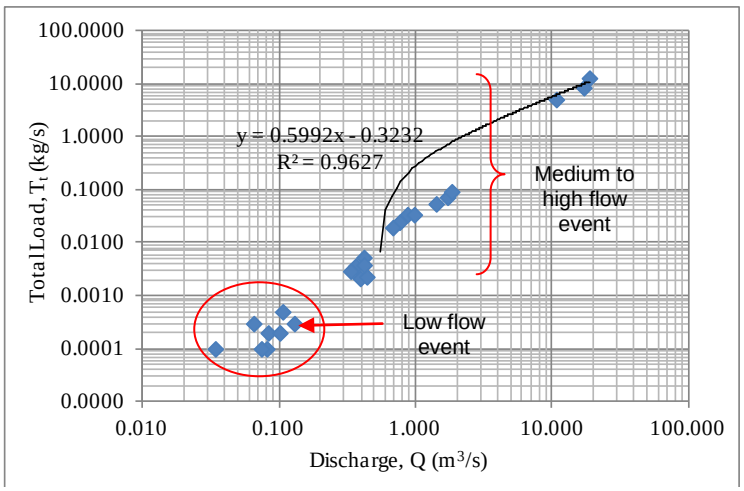


**Figure 3**. Sediment rating curve for Sungai Senang Berangan.

3.2 Evaluation of Various TL Equations

The selected TL equations were applied to the selected data to calculate TL for respective reach. Calculated TL is then compared with measured TL as discrepancy ratio (DR). In this study, acceptable TL equations should have DR within range of 0.5 to 2.0. Recorded DR below than 0.5 is categorized as under-predicted while for DR greater than 2.0 can be categorized as over-predicted.

Table 1 and 2 summarizes the performance of various TL equations at different river morphologies. For a pool-riffle channel represented by Sungai Kenyir, it was found that Shen and Hung equation successfully predicted 37.5% of total data. There is a strong correlation existed between predicted and measured TL for Shen and Yung approach. However, the average deviation of predicted value from measured value was a bit high at which RMSE recorded was 31.05kg/s. Besides, Yang equation can only predict 1 data out of 24 sets while the other equations were unable to predict the TL within the acceptable range at all. The majority of the equations have a tendency to over-predict the TL values where Graf approach contributed the largest error of prediction for given data.

The capability of TL prediction using Shen and Hung equation is consistent for a plane-bed channel. However, there is reduction in number of data predicted. Only 3 data were successfully predicted out of 24 sets of data measured. The average deviation from measured data was recorded much higher compared to the predicted values for the pool-riffle channel. Sinnakaudan et al. (2010) equation was reported as the best TL predictor for the plane-bed channel in this study. 20.83% of data were successfully predicted with small error recorded. Unfortunately, the prediction is not linearly consistent since recorded correlation coefficient, $R^2$ equal to 0.45. As shown in Table 3, the other equation such as Bagnold (1966), Engelund and Hansen (1967), Graf (1971), Yang for sand (1972), Ackers-White (1973), Yang for gravel (1984) and Sinnakaudan et al. (2006) were unable to predict TL at all. All of them consistently over-predict the TL values where Ackers-White equation recorded the highest error of prediction. Laursen equation continuously underestimated the value of TL for both river morphologies, pool-riffle and plane-bed channel, therefore, it is not recommended to be used for recent study reaches.

**Table 2**. Discrepancy ratio test for Sungai Kenyir.

| | | Under predicted | | Acceptable | | Over predicted | | Total Data | Descriptive Statistics | |
|---|---|---|---|---|---|---|---|---|---|---|
| | | No. of Data | % | No. of Data | % | No. of Data | % | | $R^2$ | RMSE |
| Laursen | 1958 | 14 | 58.33 | 0 | 0.00 | 10 | 41.67 | 24 | 0.99 | 328.18 |
| Bagnold | 1966 | 0 | 0.00 | 0 | 0.00 | 24 | 100.00 | 24 | 0.96 | 8.12 |
| Engelund and Hansen | 1967 | 0 | 0.00 | 0 | 0.00 | 24 | 100.00 | 24 | 0.99 | 140.74 |
| Graf | 1971 | 0 | 0.00 | 0 | 0.00 | 24 | 100.00 | 24 | 0.96 | 9093.37 |
| Yang for Sands | 1972 | 0 | 0.00 | 0 | 0.00 | 24 | 100.00 | 24 | 0.99 | 59.54 |
| Sheng and Hung | 1972 | 2 | 8.33 | 9 | 37.50 | 13 | 54.17 | 24 | 1.00 | 31.05 |
| Ackers-White | 1973 | 0 | 0.00 | 0 | 0.00 | 24 | 100.00 | 24 | 0.98 | 105.06 |
| Yang for Gravel | 1984 | 23 | 95.83 | 1 | 4.17 | 0 | 0.00 | 24 | 0.98 | 1.46 |
| Sinnakaudan et al. | 2006 | 0 | 0.00 | 0 | 0.00 | 24 | 100.00 | 24 | 0.95 | 3.51 |
| Sinnakaudan et al. | 2010 | 24 | 100.00 | 0 | 0.00 | 0 | 0.00 | 24 | 0.33 | 1.50 |

**Table 3**. Discrepancy ratio test for Sungai Senang Berangan.

| | | Under predicted | | Acceptable | | Over predicted | | Total Data | Descriptive Statistics | |
|---|---|---|---|---|---|---|---|---|---|---|
| | | No. of Data | % | No. of Data | % | No. of Data | % | | $R^2$ | RMSE |
| Laursen | 1958 | 21 | 87.50 | 0 | 0.00 | 3 | 12.50 | 24 | 0.83 | 341.67 |
| Bagnold | 1966 | 0 | 0.00 | 0 | 0.00 | 24 | 100.00 | 24 | 0.94 | 14.51 |
| Engelund and Hansen | 1967 | 0 | 0.00 | 0 | 0.00 | 24 | 100.00 | 24 | 0.99 | 17.71 |
| Graf | 1971 | 0 | 0.00 | 0 | 0.00 | 24 | 100.00 | 24 | 0.83 | 87.89 |
| Yang for Sands | 1972 | 0 | 0.00 | 0 | 0.00 | 24 | 100.00 | 24 | 0.95 | 116.71 |
| Sheng and Hung | 1972 | 5 | 20.83 | 3 | 12.50 | 16 | 66.67 | 24 | 1.00 | 70.71 |
| Ackers-White | 1973 | 0 | 0.00 | 0 | 0.00 | 24 | 100.00 | 24 | 0.96 | 1577.97 |
| Yang for Gravel | 1984 | 0 | 0.00 | 0 | 0.00 | 24 | 100.00 | 24 | 0.98 | 12.07 |
| Sinnakaudan et al. | 2006 | 3 | 12.50 | 0 | 0.00 | 21 | 87.50 | 24 | 0.86 | 2.25 |
| Sinnakaudan et al. | 2010 | 19 | 79.17 | 5 | 20.83 | 0 | 0.00 | 24 | 0.45 | 3.32 |

3.3 Applicability ranges of selected TL Equations

It was found that Sinnakaudan et al. (2010) and Shen and Hung (1972) were the only equations that capable to predict a part of the given data. However, the trend of TL prediction for both equations varies at different flow discharge. As shown in Figure 4, Sinnakaudan et al. (2010) able to predict TL for a range of discharge that less than 0.1m$^3$/s. The equation tends to underestimate the TL value when the river discharge exceeded 0.1m$^3$/s. On the other hand, Shen and Hung (1972) equation has shown a good TL prediction for the range of discharge between 0.1m$^3$/s to 1.0m$^3$/s (refer Figure 5). However, the prediction ranges need further investigation because there are few data showing the uncertain prediction for the same flow discharge ranges. For the range of discharge below than 0.1m$^3$/s, the equation tends to underestimate the TL values. As well when the dis-charge value exceeded 1.0m$^3$/s, the TL values were overestimated.

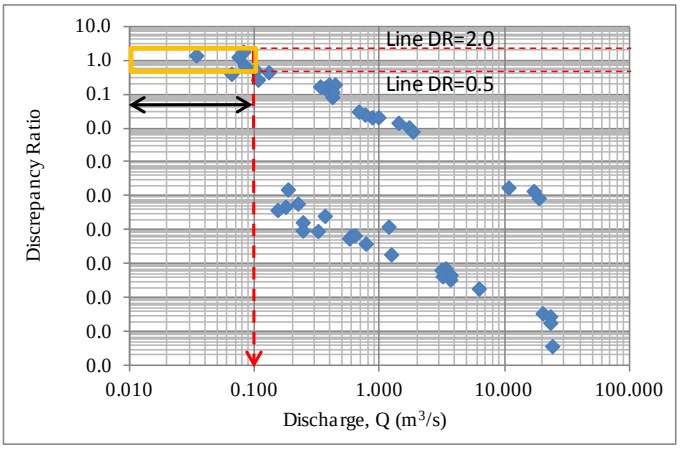


**Figure 4**. Discrepancy ratio test for Sinnakaudan et al. (2010) Equation.

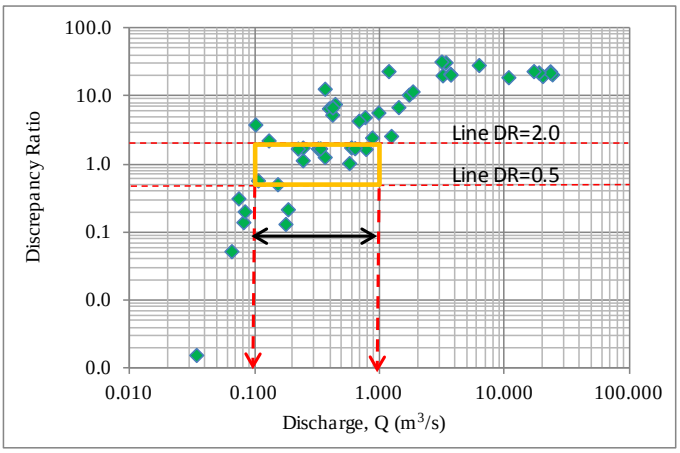


**Figure 5**. Discrepancy ratio test for Shen and Hung (1972) Equation.

 

## 4 CONCLUSIONS

Ten well-known TL equations were used to examine their predicting ability over Mountain Rivers in Malaysia. It was found that majority of the equations tend to over predict the TL for given data. Shen and Hung (1972) equation was the only equation that is capable of predicting TL for two different river morphologies. Besides, a local equation namely Sinnakaudan et al. (2010) equation has shown a reasonable prediction for plane bed channel. However, the prediction is restricted to low flow event. It is interesting to note that none of the equations show a satisfactory prediction for medium to high flow data. As such, it is proposed that the new TL equations need to be developed specifically for Malaysian Mountain River in order to promote suitability for wide range of usage. At the moment, it is suggested that some careful technical consideration needed before adopted any of the TL equations in field design activities.

## ACKNOWLEDGEMENTS

We would like to thank the Ministry of Higher Education Malaysia for funding this research through MyBrain15 scholarship. Part of the data for this study was obtained from contract research awarded by TNB Research Sdn. Bhd. in 2014 through project TNBR/D03/2014-MTC-paperNo10/2014 and project TNBR/T8/2014. Many thanks also due to Water Resources Engineering and Management Research Centre (WAREM), Faculty of Civil Engineering and Research Management Institute, Universiti Teknologi MARA for their support and encouragement to conduct this research successfully.

## NOTATION

| | |
|---|---|
| $\phi$ | Angle of repose |
| $\theta$ | Correction factor |
| $\omega_i$ | Fall velocity of particles of mean size $d_i$ in water |
| $\gamma$ , $\gamma_s$ | Specific weight of water, sediment |
| $\tau^{'}$ | Bed shear stress |
| $\tau_{ci}$ | Critical tractive force for sediment size $d_i$ as given by the Shields diagram. |
| $\rho_s$ | Density of sediment |
| b, Tb | Bed load |
| $C_V$ | Volumetric sediment concentration |
| $C_T$ | Total load concentration |
| *D* | Mean diameter of the sediment ($D_{50}$) |
| DID | Department of Irrigation and Drainage Malaysia |
| DR | Discrepancy ratio |
| $d_{50}$ | Sediment diameter where 50% of the material are finer |
| $e_b$ | Bed load transport efficiency coefficient |
| $e_s$ | Suspended load transport efficiency coefficient |
| g | Acceleration due to gravity (m/s$^2$) |
| *n* | Manning roughness coefficient |
| *P* | Power required to maintain bed movement provided by the flow |
| $p_i$ | Percentage of materials available in size fraction, *i* |
| $q_s$ | Sediment transport rate |
| *R* | Hydraulic radius |
| $R^2$ | Correlation coefficient |
| RMSE | Root Mean Square Error |
| $S_0$ | Water surface slope |
| $S_s$ | Specific gravity of sediment |
| TSS | Total suspended solids |
| $U_*$ | $(gDS)^{1/2}$ |
| *V* | Average flow velocity |
| $VS$ | Unit stream power |

 

| | |
|---|---|
| $V_{cr}S$ | Critical unit stream power required at incipient motion |
| $\nu$ | Kinematics viscosity |
| $W'$ | Immersed weight of particles |
| $Y$, $Y_0$ | Average flow depth |

**REFERENCES**

Ackers, P. & White, W.R. (1973). Sediment Transport: New Approach and Analysis. *Journal of Hydraulic Division*, 99(HY11), 2041-2060.

Ariffin, J. (2004). Development of Sediment Transport Models for Rivers in Malaysia Using Regression Analysis and Artificial Neural Network, *PhD Thesis*. Universiti Sains Malaysia, Penang.

Bagnold, R.A. (1966). An Approach to the Sediment Transport Problem from General Physics. *U.S. Geological Survey Professional Paper,* No. 422-J.

Department of Irrigation and Drainage Malaysia (DID). (2003). *River Sediment Data Collection and Analysis Study (Final Report)*, Department of Irrigation and Drainage Malaysia, Kuala Lumpur, 66.

Engelund, F. & Hansen, E. (1967). *A Monograph on Sediment Transport in Alluvial Streams*. Teknisk Vorlag, Copenhagen.

Graf, W.H. (1971). *Hydraulics of Sediment Transport*. McGraw-Hill, New York.

Laursen, E.M. (1958). The Total Sediment Load of Streams. *Journal of the Hydraulic Division,* 84(HY1), 1-36.

Meyer-Peter, E. & Muller, R. (1948*).* Formulas for Bed Load Transport*, International Association of Hydraulic Research*, 2nd Meeting Documents, Stockholm.

Shen, H.W., & Hung, C.S. (1972). *An Engineering Approach to Total Bed Material Load By Regression Analysis,* Proceedings of Sedimentation Symposium, Chapter 14, 1-7.

Sinnakaudan, S.K. & Abdul Razad, A. (2014). *Sediment Transport Study of Sungai Senang Berangan and Sungai Kenyir into Kenyir Lake Intakes (Final Report)*, TNB Research Sdn. Bhd., Kajang, Selangor, Malaysia. Unpublished manuscript.

Sinnakaudan, S.K., Ab Ghani, A., Ahmad, M.S.S. & Zakaria, N.A. (2006). Multiple Linear Regression Model for Total Bed Material Load Prediction. *Journal of Hydraulic Engineering*, 132(5), 521-528.

Sinnakaudan, S.K., Sulaiman, M.S. & Teoh, S.H. (2010). Total Bed Material Load Equation for High Gradient Rivers. *Journal of Hydro-Environment Research*, 4, 243-251.

Sulaiman, M.S. (2009). Sediment Transport Equation Development for Highland Rivers in Malaysia, *MSc Thesis*. Universiti Teknologi MARA, Malaysia.

Toffaleti, F.B. (1969). Definitive Computation of Sand Discharge in Rivers. *Journal of Hydraulics Engineering*, 95(HY1), 225-246.

Yang, C.T. (1972). Incipient Motion and Sediment Transport. *Journal of Hydraulics Division*, 99(HY10), 1679-1704.

Yang, C.T. (1984). Unit Stream Power Equations for Gravel. *Journal of Hydraulics Engineering*, 110(HY12), 1783-1797.

 

Proceedings of the 37th IAHR World Congress
August 13 – 18, 2017, Kuala Lumpur, Malaysia

# EVALUATION OF SELECTED ROUGHNESS COFFIECIENT EQUATIONS FOR MOUNTAIN RIVERS IN MALAYSIA

MOHD RIZAL SHUKOR[(1)], SHANKER KUMAR SINNAKAUDAN[(2)], MUNYATI MOHAMMED[(3)], SITI ISMA HANI ISMAIL[(4)] & MOHD SOFIYAN SULAIMAN[(5)]

[(1,2,3,4)] Faculty of Civil Engineering,
Universiti Teknologi MARA Pulau Pinang, Permatang Pauh, Penang, Malaysia
mohdrizal50@yahoo.com; drsshan@yahoo.com; munyatimohammed@gmail.com; sitiismai@ppinang.uitm.edu.my
[(5)] Faculty of Engineering and Technology Infrastructure, Infrastructure University Kuala Lumpur
mohd.sofiyan@yahoo.com

## ABSTRACT

At present state of knowledge, the selection of roughness coefficients, *n* for natural rivers are remains a major doubt among engineers and practitioners. In common practice, roughness values are obtained either by referring to the typical tabulated values listed in any hydraulic textbooks or handbook manuals or by using empirical equations. However, the values obtained are mostly unfit for all river morphologies. Various studies has been reported to quantify the Manning's *n* values for diverse river conditions, however similar studies are still limited in Malaysia particularly for mountain river reaches. Thus, the present study evaluates the applicability of the existing roughness coefficient equations to the Mountain Rivers of Malaysia. 12 selected roughness coefficient equations were tested in present study whereby 4 equations are developed locally. The roughness value recommended by DID (2012) also included in the analysis for comparison purposes. Selected roughness coefficient values were used to predict the velocity for 178 sets of data from 27 Mountain Rivers in Malaysia. The accuracy of existing equations was assessed by discrepancy ratio analysis whereby predicted and measured velocities from field are compared. It was found that none of local equations can predict more than 50% of total number of data. So far, Jarrett (1984) equation has shown satisfactory prediction of flow velocity over Malaysian Mountain Rivers with 63% of data lies within the acceptable discrepancy ratio (0.5 to 2.0).

**Keywords:** Roughness coefficient; Mountain River; coarse-bedded river; discrepancy ratio test.

## 1 INTRODUCTION

Roughness coefficient, often denoted as *n*, is an expression of flow resistance towards surface of a river such as bed or flood plain (Jarrett, 1985). Generally, most of hydraulic calculations of flow in rivers and overbank areas require an evaluation of roughness characteristics of the channel. The procedure of estimating *n* values is subjective and largely dependent on a hydrologist's or engineer's experience (Coon, 1998). Estimation of n values becomes a very complex and challenging task when dealing with mountainous rivers whereby coarse river-bed materials are pronounced. Studies on roughness coefficients over Mountain Rivers or coarse bed rivers had becoming a global interest. One of the early works was done by Strickler (1923) whereby roughness coefficient has been related with median particle size of bed material. Because of its importance, similar studies continued to receive vital attention among the other researchers. Among them are Mayer-Peter & Muller (1948), Henderson (1966), Limerinos (1970), Griffiths (1981), Jarrett (1984), Bray and Davar (1987), Julien (2002), and many more.

In Malaysia, River Engineering and Urban Drainage Research Centre (REDAC) have pioneered the research on roughness coefficient since year 2000 (Ab. Ghani et al., 2007). Abdul Ghaffar et al. (2004) and Ab. Ghani et al. (2007) were among the local researchers that developed equations for roughness coefficient by utilizing data from sand bedded rivers in Malaysia. Despite intensive research that have been carried out on roughness coefficient, none of the published roughness coefficient equations have gained universal acceptance confidently in hydraulic calculations. In addition, applying existing equations to Malaysian Mountain Rivers produce wide range of results particularly in estimating mean velocity of flow for the same set of data (Sinnakaudan and Abdul Razad, 2014). Therefore, the primary motivation of this study is to evaluate and propose the best roughness coefficient equation that suited with Malaysian Mountain Rivers.

## 2 DATA SOURCE

This study had focused on 27 Mountain Rivers in Malaysia. A total of 178 sets of data from 5 different states of Malaysia were used in the analysis as tabulated in Table 1. The data used covering wide range of flow characteristics whereby 55 sets of data are taken from published work done by Sinnakaudan et al.

 

(2010). The remaining data are obtained from intensive field works conducted at various locations. The range of hydraulic properties for study reaches are summarized in Table 2.

**Table 1.** Study reaches.

| No. | State | River's Name | No. of Data |
|---|---|---|---|
| 1 | Kedah | Sungai Ulu Paip | 9 |
| 2 | | Sungai Reyau | 9 |
| 3 | | Sungai Sedim (Kg Sedim) | 4 |
| 4 | | Sungai Sedim | 2 |
| 5 | | Sungai Bukit Hijau | 1 |
| 6 | | Sungai Rambai | 1 |
| 7 | P.Pinang | Sungai Air Putih | 4 |
| 8 | Sarawak | Sungai Abang | 1 |
| 9 | | Sungai Giam | 1 |
| 10 | | Sungai Semadang | 1 |
| 11 | Terengganu | Sungai Kemia | 3 |
| 12 | | Sungai Sayap | 5 |
| 13 | | Sungai Kenyir | 24 |
| 14 | | Sungai Lata Tembakah | 1 |
| 15 | | Sungai Rasi | 1 |
| 16 | | Sungai Senang Berangan | 24 |
| 17 | | Sungai Keruak 3B | 1 |
| 18 | | Sungai Lubuk Permata | 1 |
| 19 | | Sungai Lagus | 1 |
| 20 | | Sungai Loh | 1 |
| 21 | | Sungai Kacong | 1 |
| 22 | | Sungai Besut | 2 |
| 23 | Pahang | Sungai Lemoi, C.Highlands | 25 |
| 24 | | Sungai Bertam, C.Highlands | 25 |
| 25 | | Sungai Telom, C.Highlands | 25 |
| 26 | | Sungai Terla, C.Highlands | 3 |
| 27 | | Sungai Telom (upstream), C.Highlands | 2 |

**Table 2.** Data ranges.

| | Discharge Q ($m^3/s$) | Velocity V (m/s) | River width B (m) | River depth $Y_0$ (m) | Water slope $S_0$ (m/m) | Sediment Size $d_{50}$ (mm) |
|---|---|---|---|---|---|---|
| Minimum | 0.03 | 0.03 | 3.37 | 0.12 | 0.0001 | 0.34 |
| Average | 3.93 | 0.68 | 10.59 | 0.50 | 0.0197 | 91.98 |
| Maximum | 23.96 | 3.69 | 21.30 | 1.41 | 0.0415 | 472.53 |

## 3 RESEARCH APPROACH

### 3.1 Selected Roughness Coefficient Equations

The analysis for a total of 178 sets of data was made for selected 12 roughness coefficient equations. These equations can be grouped into three main categories namely; 1) equations based on bed sediment size, $d_i$; 2) equations based on water surface slope, $S_0$; and 3) equations based on ratio between flow depth or hydraulic radius and bed sediment size, $Y_0/d_i$ or $R/d_i$. Among all the equations tested, there are four equations were developed locally. Two of the equations were developed by Abdul Ghaffar et al. (2004) while the other two equations obtained from Ab. Ghani et al. (2007). Besides, recommended $n$ value by Department of Irrigation and Drainage Malaysia (DID) through Urban Storm Management Manual for Malaysia is also included in the analysis. For steep mountain streams, the suggested $n$ value is 0.07 (DID, 2012).

*Category 1*: Equations based on bed sediment size, $d_i$

Strickler (1923), $$n = d_{50}^{1/6} / 21.1 \quad [1]$$

Meyer-Peter & Muller (1948), $n = d_{90}^{1/6} / 26$ [2]

Henderson (1966), $n = 0.031 d_{75}^{1/6}$ [3]

Julien (2002), $n = 0.062 d_{50}^{1/6}$ [4]

*Category 2*: Equations based on water surface slope, $S_0$

Jarrett (1984), $n = 0.39 S_0^{0.38} R^{-0.16}$ [5]

Bray & Davar (1987), $n = 0.094 S_0^{1/6}$ [6]

*Category 3*: Equations based on ratio of flow depth or hydraulic radius and bed sediment size, $Y_0/d_i$ or $R/d_i$.

Limerinos (1970), $n = 0.0926 R^{1/6} / (1.16 + 2.0 \log (R/d_{84}))$ [7]

Griffiths (1981), $n = 0.113 R^{1/6} / (0.76 + 1.98 \log (R/d_{50}))$ [8]

Abdul Ghaffar et al. (2004), $n = 2\text{x}10^{-8}(Y_0/d_{50})^2 - 3\text{x}10^{-5}(Y_0/d_{50}) + 0.0511$ [9]

$n = 3\text{x}10^{-8}(R/d_{50})^2 - 4\text{x}10^{-5}(R/d_{50}) + 0.0537$ [10]

Ab. Ghani et al. (2007), $n = 4\text{x}10^{-8}(Y_0/d_{50})^2 - 5\text{x}10^{-5}(Y_0/d_{50}) + 0.0582$ [11]

$n = 5\text{x}10^{-8}(R/d_{50})^2 - 7\text{x}10^{-5}(R/d_{50}) + 0.0622$ [12]

3.2 Assessment Method

The selected bed roughness coefficient equations are applied to the selected data and mean flow velocity are calculated. Calculated velocities are then compared with measured velocity as discrepancy ratio. Accuracy of each equation was assessed in two ways:

1) Discrepancy ratio, DR should lies between ranges of 0.5 to 2.0.
2) Statistical parameters like correlation coefficient, $R^2$ and root mean square error, RMSE.

## 4 RESULT AND DISCUSSION

4.1 Discrepancy Ratio Test

Discrepancy ratio, DR was used to measure performance of those equations in present study. DR is defined as ratio between predicted velocity and measured velocity. A good roughness coefficient predictor should have DR equal to 1.0. In Figure 1, perfect line of agreement represents DR of 1.0. In reality, there is no such a perfect velocity predictor. As such an acceptable range of DR is adopted at range of 0.5 to 2.0. The data that lies above the line of DR = 2.0 is categorized as over predicted while for data below DR = 0.5 line is considered as under predicted.

Figure 1 and Figure 2 illustrates performance of various roughness coefficient equations on mean velocity prediction. Overall, all the equation shows a non-linear pattern of velocity prediction over measured velocity. Most of the equations tend to over predict flow velocity except for Jarrett equation and DID recommended value. It is interesting to note that none of the local equations can predict more than 35% of total data (Table 3). The recommended value by DID able to predict 45% out of 178 data. Jarrett is the only equation that capable of predicting more than half of the velocity data by which 63% of data lies within acceptable ranges. Jarrett equation recorded the best prediction for velocity range from 0.2 to 2.0 m/s. When velocity exceeded 2.0 m/s, it tends to underestimate the actual velocity values. As such, other equations should be used for fast flowing river. Conversely, all the local equations had show good prediction over fast flow data. However, only four sets of data available for that velocity range for the test and all the local equations successfully predict three of the data close to actual values (Figure 2(c – f)). The worst prediction comes from Meyer-Peter & Muller equation followed by Hendersen equation and Strickler equation. It is not a surprise that none of tested equations capable of predicting velocity for slow flowing river (velocity below than 0.2 m/s). For Mountain Rivers, morphological feature that typically associated with slow moving flow is pool. Predicting velocity for a pool is quite challenging due to water flow which is too slow. Empirical equation typically developed from medium ranges of velocity. Therefore it tends to over predict the velocity when applied to the ranges which is lower than it was initially developed.

 

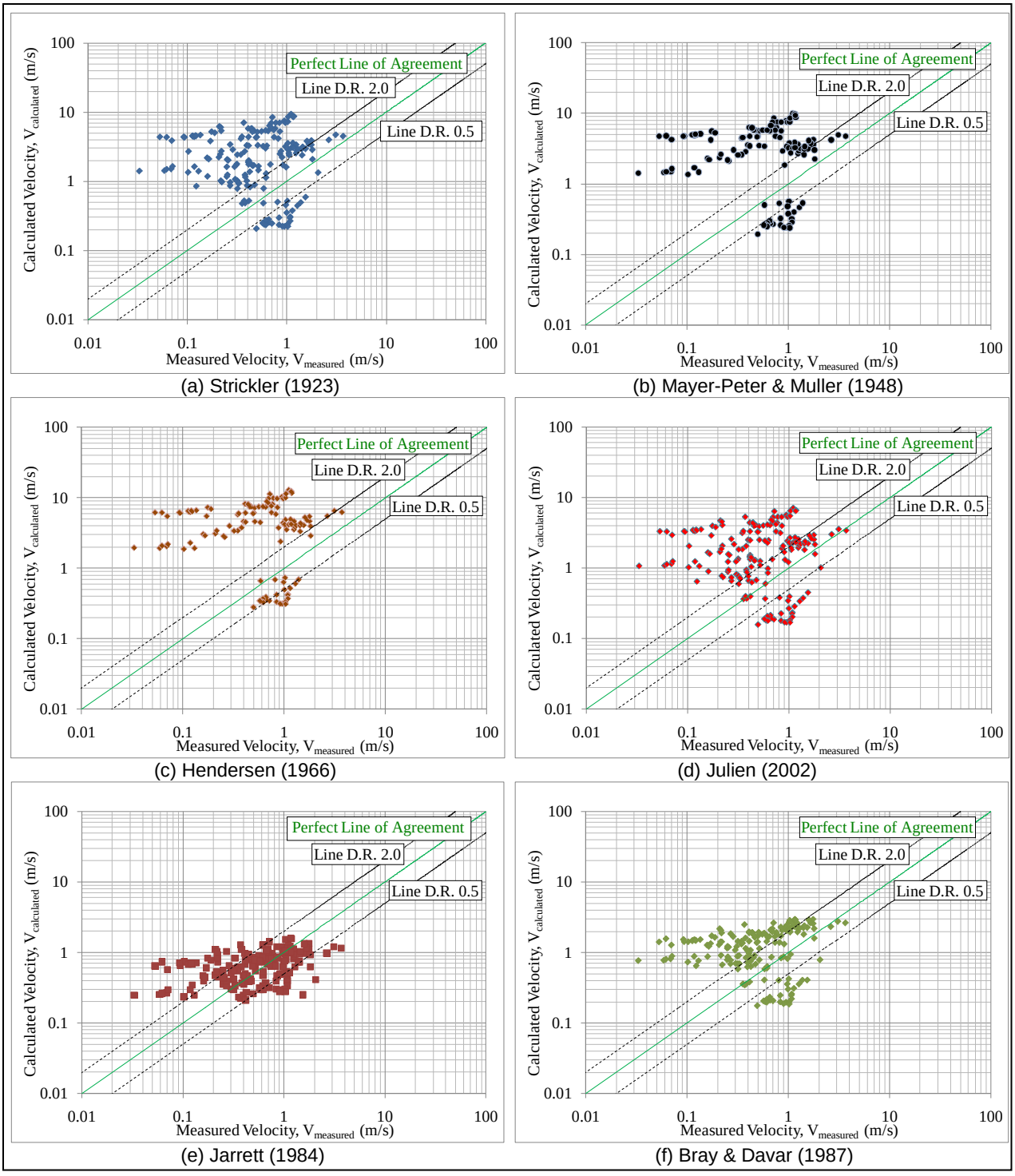


**Figure 1.** Discrepancy ratio test.

 

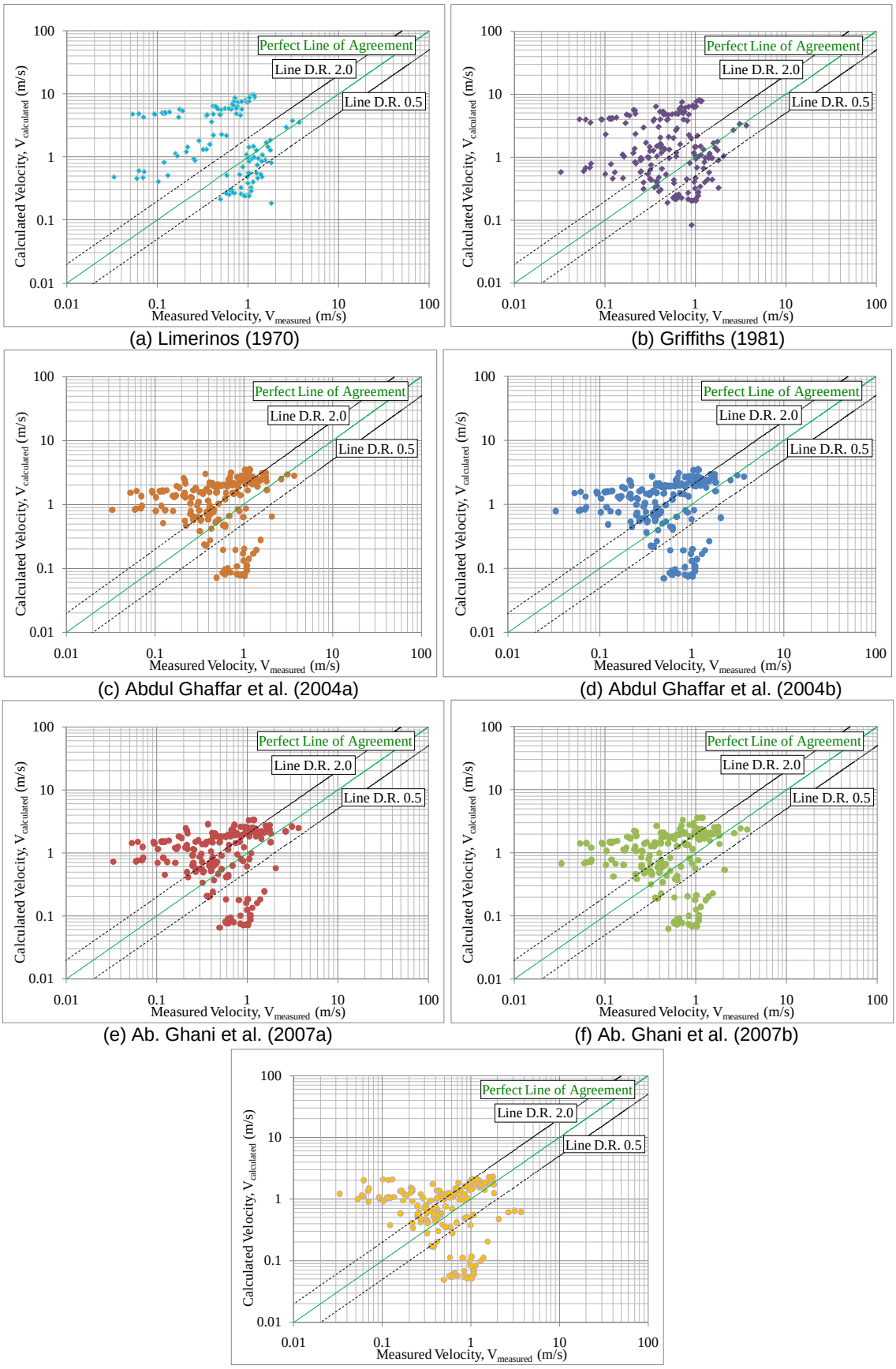


(a) Limerinos (1970)

(b) Griffiths (1981)

(c) Abdul Ghaffar et al. (2004a)

(d) Abdul Ghaffar et al. (2004b)

(e) Ab. Ghani et al. (2007a)

(f) Ab. Ghani et al. (2007b)

(g) DID (2012)

**Figure 2.** Discrepancy ratio test value.

**Table 3.** Summary of performance test.

| Authors | | Underpredicted | | Acceptable | | Overpredicted | | Total |
|---|---|---|---|---|---|---|---|---|
| | Year | No. of Data | % | No. of Data | % | No. of Data | % | |
| **Strickler** | 1923 | 23 | 12.92 | 22 | 12.36 | 133 | 74.72 | 178 |
| **Mayer-Peter & Mueller** | 1948 | 22 | 17.89 | 9 | 7.32 | 92 | 74.80 | 123 |
| **Hendersen** | 1966 | 12 | 9.76 | 15 | 12.20 | 96 | 78.05 | 123 |
| **Limerinos** | 1970 | 27 | 21.95 | 26 | 21.14 | 70 | 56.91 | 123 |
| **Griffiths** | 1981 | 28 | 15.73 | 47 | 26.40 | 103 | 57.87 | 178 |
| **Jarrett** | 1984 | 20 | 11.24 | 112 | 62.92 | 46 | 25.84 | 178 |
| **Bray & Davar** | 1987 | 26 | 14.61 | 45 | 25.28 | 107 | 60.11 | 178 |
| **Julien** | 2002 | 26 | 14.61 | 37 | 20.79 | 115 | 64.61 | 178 |
| **Abdul Ghaffar et al.** | 2004a | 27 | 15.17 | 51 | 28.65 | 100 | 56.18 | 178 |
| **Abdul Ghaffar et al.** | 2004b | 27 | 15.17 | 53 | 29.78 | 98 | 55.06 | 178 |
| **Ab. Ghani et al.** | 2007a | 27 | 15.17 | 61 | 34.27 | 90 | 50.56 | 178 |
| **Ab. Ghani et al.** | 2007b | 27 | 15.17 | 62 | 34.83 | 89 | 50.00 | 178 |
| **DID** | 2012 | 37 | 20.79 | 80 | 44.94 | 61 | 34.27 | 178 |

4.2 Statistical Analysis

Table 4 tabulates results for correlation test and RMSE determination. In this study, relationship between predicted and measured velocity is described by correlation coefficient. A good correlation coefficient should have $R^2$ value close to 1.0. It can be seen that, there is almost no correlation existed towards measured velocity for all equations. The highest correlation coefficient value was recorded by Jarrett equation at 0.175. The poor correlation value indicates that even Jarrett equation recorded satisfactory prediction of velocity as reported earlier, however the prediction is not consistent. The recommended value by DID also cannot perform well with selected rivers and recorded small $R^2$ value which is 0.018. RMSE is the measure of average magnitude of error associated with predicted values to the measured values. As illustrated in Table 4, Jarrett equation recorded the smallest error compared to other equations. Nevertheless, the average deviation value of 0.51 m/s is still quite high for the range of velocity measured.

**Table 3.** Statistical analysis.

| Equation | | $R^2$ | RMSE |
|---|---|---|---|
| Strickler | 1923 | 0.010 | 3.101 |
| Mayer-Peter & Muller | 1948 | 0.029 | 3.785 |
| Hendersen | 1966 | 0.034 | 5.124 |
| Limerinos | 1970 | 0.008 | 2.638 |
| Griffiths | 1981 | 0.001 | 2.674 |
| Jarrett | 1984 | 0.175 | 0.510 |
| Bray & Davar | 1987 | 0.134 | 1.001 |
| Julien | 2002 | 0.010 | 2.278 |
| Abdul Ghaffar et al. | 2004a | 0.111 | 8.929 |
| Abdul Ghaffar et al. | 2004b | 0.110 | 1.098 |
| Ab. Ghani et al. | 2007a | 0.096 | 1.027 |
| Ab. Ghani et al. | 2007b | 0.089 | 1.032 |
| DID | 2012 | 0.018 | 0.819 |

## 5 CONCLUSIONS

Twelve well-known equations of roughness coefficient together with proposed value by DID (2012) are used to examine their predicting ability of mean velocity by using wide range of Mountain Rivers data. It was found that, majority of equations tested unable to predict not even half of total data. Jarrett (1984) equation was the only equation that gives satisfactory velocity prediction for study site. However, it is still far away from perfection whereby 37% of data not fitted well with the measured data. Recommended *n*-value for steep mountain rivers by DID have show inconsistent prediction over diverse morphological stream characters and flow conditions. As such, it is proposed that existing *n*-value need to be reevaluated with larger sets of data in order to promote suitability for wide range usage. It is suggested that some careful technical consideration

 

needed before adopted any of the existing roughness coefficient formulas in field design activities. For future study, it is important to have a site specific equation for Malaysian Mountain River in order to correctly predict the mean flow velocity.

**ACKNOWLEDGEMENTS**

We would like to thank the Ministry of Higher Education Malaysia for funding this research through MyBrain15 scholarship. Part of the data for this study was obtained from contract research awarded by TNB Research Sdn Bhd in 2014 through project TNBR/D03/2014-MTC-paperNo10/2014 and project TNBR/T8/2014. Many thanks also due to Water Resources Engineering and Management Research Centre (WAREM), Faculty of Civil Engineering and Research Management Institute, Universiti Teknologi MARA for their support and encouragement to conduct this research successfully.

**NOTATION**

| | |
|---|---|
| DID | Department of Irrigation and Drainage Malaysia |
| DR | Discrepancy ratio |
| $d_{50}$, $d_{75}$, $d_{84}$, and $d_{90}$ | Sediment diameter where 50, 75, 84 and 90 % of the material are finer |
| $n$ | Manning roughness coefficient |
| R | Hydraulic radius |
| $R^2$ | Correlation coefficient |
| RMSE | Root mean square error |
| $S_0$ | Water surface slope |
| $Y_0$ | Average flow depth |

**REFERENCES**

Abdul Ghaffar, A.B., Ab. Ghani, A., Zakaria, N.A., Abu Hasan, Z. & Chang, C.K. (2004). Determination of Manning's Flow Resistance Coefficient for Rivers in Malaysia. *1st International Conference on Managing Rivers in the 21st Century: Issues and Challenges. 21st - 23rd September, Penang, Malaysia*, 104-110.

Ab. Ghani, A., Zakaria, N.A., Chang, C.K., Ariffin, J., Abu Hasan, Z. & Abdul Ghaffar, A.B. (2007). Revised Equations for Manning's Coefficient for Sand-Bed Rivers, *International Journal of River Basin Management*, 5(4), 329-346.

Bray, D.I. & Davar, K.S. (1987). Resistance to Flow in Gravel-Bed Rivers. *Canadian Journal of Civil Engineering*, 14, 77-86.

Department of Irrigation and Drainage Malaysia (2012). *Urban Storm Water Management Manual for Malaysia – 2nd Edition*, Department of Irrigation and Drainage Malaysia, Kuala Lumpur.

Griffiths, G.A. (1981). Flow Resistance in Coarse Gravel Bed Rivers. *Journal of the Hydraulic Division,* 107, 899-918.

Henderson, F.M. (1966). *Open Channel Flow*. New York, Macmillan, 552 pp.

Jarrett, R.D. Hydraulics of High Gradient Streams. *Journal of Hydraulic Engineering*, 110(11),

Julien, P.Y. (2002). *River Mechanics*. Cambridge: Cambridge University Press UK.

Limerinos, J.T. (1970). *Determination of the Manning Coefficient for Measured Bed Roughness in Natural Channels*. Water Supply paper 1898-B, U.S.Geological Survey, Washington D.C.

Meyer-Peter, E. & Muller, R. (1948). Formulas for Bed-load Transport*. Proceeding for Third Meeting of IAHR,* Stockholm, Sweden, 39–64.

Sinnakaudan, S.K. & Abdul Razad, A. (2014). *The Engagement of Contractor to Undertake Sediment Analysis for High Gradient Rivers of Sungai Senang Berangan and Sungai Kenyir (progress report)*, TNB Research Sdn. Bhd., Kajang, Selangor, Malaysia.

Sinnakaudan, S.K., Sulaiman, M.S. & Teoh, S.H. (2010). Total Bed Material Load Equation for High Gradient Rivers. *Journal of Hydro-environment Research*, 4, 243-251.

Strickler, A. (1923). *Beitrage zur frage der geschwindigkeitsformel und der rauhigkeitszahlen fuer stroeme kanaele und geschlossene leitungen*. Mitteilungen des eidgenossischen Amtes fuer Wasserwirtschaft 16. Bern, Switzerland. (in German) (Translated *as "Contributions to the question of a velocity formula and roughness data for streams, channels and closed pipelines"* by Roesgan, T. and Brownie, W. R., Translation T-10, W. M. Keck Lab of Hydraulics and Water Re-sources, Calif. Inst. Tech., Pasadena, Calif. January 1981.

 

# GEOMORPHIC IMPACTS OF THE OPERATION OF XIAOLANGDI RESERVIOR ON THE LOWER YELLOW RIVER

JUNQIANG XIA[(1)], JIE LI[(2)], SHIYUAN ZHANG[(3)] & TAO LI[(4)]

[(1-3)] State Key Laboratory of Water Resources and Hydropower Engineering Science, Wuhan University, Wuhan, China, xiajq@whu.edu.cn
[(4)] Yellow River Institute of Hydraulic Research, Yellow River Conservancy Commission, Zhengzhou, China

## ABSTRACT

The operation of the Xiaolangdi Reservoir has altered the flow and sediment regime downstream of the dam, and causes a channel re-establishment process in the Lower Yellow River (LYR). Recent significant channel evolution in the LYR has led to longitudinal variability in different geomorphic variables at section-scale. Therefore, it is necessary to describe the variations in these geomorphic variables of the LYR using a reach-averaged method. In this study, an integrated approach is proposed for calculating reach-scale geomorphic variables such as bankfull channel geometry and bankfull discharge. Based on the observed hydrological data and cross-sectional profiles during the period from 1999 to 2015, the processes and characteristics of recent channel adjustments in the LYR are investigated, including: (i) The average annual sediment load entering the LYR is only $0.88\times10^8$ tonnes/a, and the cumulative volume of channel scour is $18.6\times10^8$ $m^3$, with the value of the braided reach accounting for 72%; (ii) Substantial adjustments in channel geometry occur in the LYR, with the channel becoming narrower and deeper. The process of channel widening is prominent in the braided reach, with the bankfull width increasing from 972 m in 1999 to 1275 m in 2015, while there is little variation in the bankfull width in transitional or meandering reach. The reach-scale bankfull discharges in these three reaches increase dramatically from 3229, 2339, 3080 $m^3/s$ in 1999 to 7321, 5065, 5494 $m^3/s$ in 2015, respectively; and (iii) the reach-scale bankfull channel dimensions and bankfull discharge in each reach are closely related to the previous 4-year average fluvial erosion intensity, with the power functions between them being developed in these reaches.

**Keywords:** Channel adjustment; bankfull channel geometry; bankfull discharge; reach-scale; Lower Yellow River.

## 1 INTRODUCTION

Bankfull usually refers to the level in a channel at which the flow fills the channel to the level of the active floodplain with the corresponding flow being defined as bankfull discharge, which is considered to be effective in controlling channel shape (Leopold and Maddock, 1953; Williams, 1978; Xia et al., 2014a; Xia et al., 2014b). Therefore, bankfull (channel) geometry in an alluvial river usually refers to channel dimensions associated with the bankfull discharge, which can be represented by the channel width, cross-sectional area, and the corresponding mean depth under bankfull. Bankfull geometry is closely related to the concept of hydraulic geometry introduced earlier by Leopold and Maddock (1953), which is usually represented in the form of downstream hydraulic geometry. It can vary between various reaches because of the variations in discharge, sediment load and size distribution, bed slope, bank soil composition and other boundary conditions. However, the dominant factors that cause the change in bankfull geometry of an alluvial river are the water discharge and sediment load, as independent variables that integrate the basin conditions and upstream flow regulation.

According to the degree of morphological changes, two kinds of methods are used for predicting bankfull dimensions and bankfull discharges in alluvial rivers. One method is based on the hydraulic geometry equations usually for alluvial rivers in equilibrium or quasi-equilibrium, which are typically represented by empirically fitted power functions (Leopold and Maddock, 1953; Wohl et al., 2004; Stewardson, 2005; Wohl and Wilcox, 2005; Harman et al., 2008). Another method is based on the empirical relations or delayed response equations for alluvial rivers undergoing severe channel evolution, which are usually expressed by a function of incoming flow and sediment conditions (Wu et al., 2008a; Wu et al., 2008b; Xia et al., 2014a; Xia et al., 2014b).

A wide range of human activities, including withdrawal of water for irrigation and municipal uses, land-use changes and dam construction, can significantly alter the natural flow and sediment regimes in rivers, with important consequences for channel morphology (Williams and Wolman, 1984; Petts and Gurnell, 2005; Ma et al., 2012). Many case studies of downstream response to water impoundment have shown that these major changes included significant variations in bankfull geometry and bankfull discharge (Wu et al., 2008a; Wu et al., 2008b; Shin and Julien, 2010; Xia et al., 2014a; Xia et al., 2014b). Therefore, some empirical relations or

 

equations for alluvial rivers undergoing severe aggradation or degradation have been developed to predict the variation in bankfull geometry and discharge caused by the altered flow and sediment regime. For example, Wu et al. (2008a) investigated the accumulative effect of previous years' flow and sediment conditions on the channel adjustments in the Lower Yellow River (LYR), and a methodology for the prediction of bankfull cross-sectional area was developed based on a general delayed response equation. It is found that these relations for the predictions of bankfull geometry are only applicable to a specified cross section in a river reach under disequilibrium, and the obtained results can be unrepresentative of the bankfull characteristic parameters of a total river reach. Therefore, a reach-scale concept is more appropriate to describe the bankfull channel dimensions and bankfull discharge in a river because reach-based values can provide more representative geometry and statistics characterising longitudinal variability in the channel (Wohl et al., 2004; Stewardson, 2005; Wohl and Wilcox, 2005; Harman et al., 2008). Harman et al. (2008) developed a geometric mean method based on the log-transformation to calculate the reach-scale bankfull geometry in a river, which satisfied the condition of flow continuity for reach-averaged bankfull parameters. However, reach-based bankfull geometry studies require considerably more data of surveyed cross-sectional profiles in the reach, with the bankfull level and the corresponding main-channel zone at each section being carefully identified manually.

For an alluvial river undergoing severe degradation such as the LYR, the bankfull channel geometry and bankfull discharge have adjusted owing to the recent operation of the Xiaolangdi Reservoir, which has led to significant variability in the section-scale bankfull geometry and discharge. In order to investigate the variation in reach-scale bankfull geometry and discharge in the LYR, a general description of the study reach is first stated, as well as the recent flow and sediment regime entering the LYR and the corresponding characteristics of fluvial processes in different reaches. The main aims of the current study are to (i) propose a procedure to calculate reach-scale bankfull characteristic parameters; (ii) calculate the recent reach-scale bankfull parameters and discharges in different reaches of the LYR; and (iii) develop empirical relationships between the reach-scale bankfull parameters and the corresponding incoming flow and sediment conditions.

## 2 STUDY AREA

The Yellow River, as the second longest river in China, is well known for its high concentrations of suspended load. At Sanmenxia, the average annual natural runoff of the Yellow River is 58 billion $m^3$, and the average annual suspended load is 1.6 billion tonnes, ranking it first of all the world's rivers in terms of sediment load (Wu et al., 2008a; Wu et al., 2008b; Xia et al., 2010). In general, the Lower Yellow River is defined as the reach between Mengjin in Henan province and Lijin in Shandong province, with a total length of about 740 km (see Figure 1). Heavy soil erosion on the Loess Plateau upstream led to intensive sedimentation in the LYR channel. According to observed data, the total deposition volume in the LYR was about 5.52 billion $m^3$ during the period from 1950 to 1999, of which 60% was deposited in the braided reach. One effect of the heavy sedimentation in the LYR was an obvious shrinkage of the main channel accompanied by a sharp decrease in flood discharge capacity (Wu et al., 2008b; Xia et al., 2014b). The heavy sedimentation also led to a phenomenon of 'secondary perched river' in local reaches of the LYR (Xia et al., 2010).

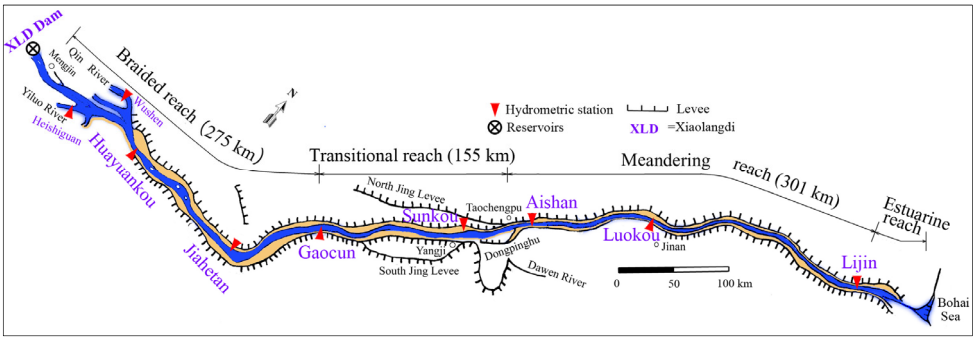


**Figure 1.** Plan view of the Lower Yellow River.

In order to reduce the sedimentation rate in the LYR, the Xiaolangdi Reservoir was built in the late 1990s as a key engineering measure for flood and sediment control and it started to operate in 2000. The dam is located at the exit of the last gorge in the Middle Yellow River, 130 km downstream of the Sanmenxia Dam. The release from the Xiaolangdi Reservoir and the contribution of the two tributaries immediately below the dam comprise the inflow to the LYR, and the contribution of the tributaries is considerably limited. Owing to the operation of the Xiaolangdi Reservoir, the flow and sediment regime entering the LYR has been altered dramatically, which has led to significant geomorphic adjustments in the LYR, including the variations in bankfull channel geometry and bankfull discharge (Wu et al., 2008a; Wu et al., 2008b, Xia et al., 2014a; Xia et al., 2014b).

 

The river reach selected for this study was the Lower Yellow River, as shown in Figure 1. In this study, the total LYR was divided into the following three different channel-pattern reaches, incorporating the reference hydrometric sections of Gaocun and Aishan according to the classification of channel pattern. The reach upstream of Gaocun is called the braided reach, with a length of 284 km; the reach lying approximately between Gaocun and Aishan is called the transitional reach with a length of 184 km; and the reach roughly from Aishan to Lijin is called the meandering reach with a length of 272 km. Notably, this kind of reach division was slightly different from the previous division based on the geomorphological characteristics of the reach. For convenience, all the following analyses were concentrated on these three reaches.

## 3 DATA AND METHODS

### 3.1 Data collection

Since the reservoir operation, the sediment discharge entering the LYR has been reduced greatly, and the LYR channel is undergoing significant degradation because of the flows with low sediment concentrations released from the reservoir. In order to investigate the geomorphic adjustments in the above-mentioned three reaches, hydrological data were collected over the period from 1999 to 2015, including the mean discharges and sediment concentrations during non-flood and flood seasons at several hydrometric stations. Furthermore, the post-flood cross-sectional profiles at 91 sedimentation sections over this period were also collected.

The channel evolution of an alluvial river is a direct result of erosion and deposition caused by the non equilibrium transport of sediment. Water discharge and sediment load are the two dominant factors that determine the geomorphic adjustments in alluvial rivers (Leopold and Maddock, 1953; Wu et al., 2008a; Xia et al., 2014a; Xia et al., 2014b). In this study, the flow and sediment regime entering the LYR accounted for the effect of the contribution of two tributaries immediately below the Xiaolangdi dam. The average annual water discharge entering the LYR was $25.5\times10^9$ $m^3$/yr over the period from 1999 to 2015 after the reservoir operation, which approximated 61.7% of the long-time average before 1999. During this period, the average annual sediment discharge was significantly reduced to about $0.88\times10^8$ tonnes/yr because the majority of sediment was deposited in the reservoir, with a cumulative sedimentation volume of $3.1\times10^9$ $m^3$. The flood-season average water volume accounted for 37% of the average annual water volume, while the flood season average sediment amount comprised 96% of the average annual amount entering the LYR. Therefore, the sediment load entering the LYR since the completion of the dam was transported mainly during flood seasons.

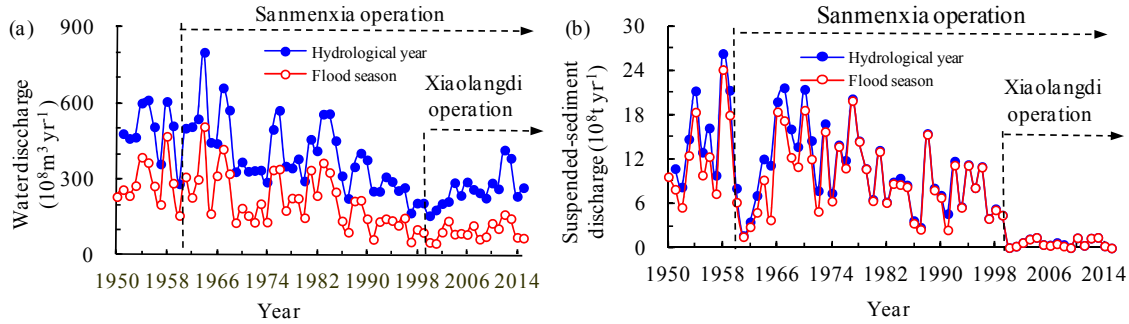


**Figure 2.** Temporal variations in the annual flow and sediment regime entering the LYR of: (a) water discharge; (b) sediment discharge.

### 3.2 Methods

A procedure was proposed herein to calculate the reach-scale bankfull channel geometry and discharge in the LYR, based on the determination of section-scale bankfull parameters using a suitable identification method of bankfull level and main-channel zone (Xia et al., 2014a; Xia et al., 2014b). In this procedure, the first step was to determine the bankfull parameters at a section with a specified bankfull level and main-channel zone, and the second step was to calculate the reach-scale bankfull channel dimensions and discharge using an appropriate reach-averaged method. Notably, the proposed reach-scale bankfull geometry differed from the original concept of downstream hydraulic geometry, and the latter usually referred to the relationship between bankfull geometry and characteristic discharge in an alluvial river under equilibrium. The aim of this study was to investigate the response of the reach-scale geomorphic variables to the altered flow and sediment regime in the LYR undergoing continuous channel degradation.

#### 3.2.1 Determination of section-scale bankfull geometry and discharge

The identification of bankfull level was one of the key steps, which was also associated with the concept of bankfull discharge. Bankfull discharge in the LYR often means the flow at which water just fills a main channel without overtopping the banks of the floodplain or the farm dyke tops, and these farm dykes are inner

 

embankments adjacent to the main channel constructed by local inhabitants. Therefore, the level of the lip top of an active floodplain is usually defined as the bankfull level at a section in terms of flood control, and the main passage between the two lips of the active floodplains on both sides is often defined as the zone of the main channel (Xia et al., 2010). The width between these two lips on both sides is defined as the bankfull channel width ($W_{bf}$), with the corresponding main channel area under the bankfull level being equal to the bankfull cross-sectional area ($A_{bf}$). Therefore, the mean bankfull channel depth ($H_{bf}$) is equal to the ratio of $A_{bf}$ to $W_{bf}$. In cases where the bankfull indicators are not obvious, earlier and later measurements of the cross-sectional profiles were used as reference information to determine the bankfull level at a section (Wu et al., 2008a). For the section whose main channel is restricted closely by local farm dykes, the effect of local water retention by those dykes needs to be considered in the calculation. For this specific case, the bankfull level was often equal to the elevation of the floodplain lip plus a partial height of the farm dyke.

The magnitude of bankfull discharge is equal to the product of the wetted cross-sectional area and the corresponding average velocity as the water level at a section just rises to the bankfull level. These bankfull parameters at a section are also influenced by the downstream channel geometry and flood discharge capacity. In this method, a relatively long reach with a specified channel pattern, including several hydrometric sections and a number of cross-sections, was selected as a study reach. Water levels under different discharges at each section in the study reach can be simulated by a one-dimensional hydrodynamic model, with the observed post-flood profiles of cross-sections being taken as the channel boundary condition. The bankfull discharge at each section ($Q_{bf}$) can be calculated using the determined bankfull level and the simulated stage-discharge relation (Xia et al., 2010). The advantage of this method lies in its capacity to obtain the simulated stage-discharge relation at any section, and all the bankfull discharges can then be obtained at these sections. The disadvantage of this method is that the Manning's roughness coefficients in the main channel and on the floodplain need to be calibrated according to the observed data at hydrometric sections for each investigation.

Cross sections in the LYR are usually characterized by a compound geometric profile, which is composed of a narrow main-channel zone and two wide floodplain zones on both sides, especially in the braided reach. The cross-sectional geometry in the braided reach has changed significantly since the 1970s because of the continuous channel evolution from the previous geometric profile with a high floodplain and low channel to the profile with a high channel and low floodplain in a perched reach in the late 1990s (Xia et al., 2010). To identify the main channel zone and bankfull level is relatively difficult at such sections with complex geometry in the braided reach. Figure 3a shows the post-flood channel geometry at the Mazhai section of a secondary perched reach measured in 1999. The identified bankfull level at this section was 68.84 m, with the effect of a farm dyke constructed on the left floodplain being included, and the calculated bankfull channel dimensions were $W_{bf}$ = 438 m, $H_{bf}$ = 2.2 m, and $A_{bf}$ = 956 $m^2$, respectively, with the corresponding bankfull discharge of $Q_{bf}$ = 2572 $m^3/s$. In the transitional and meandering reaches, the bed level difference between the main channel and the floodplain is very distinct and is characterized by a lower bed level for the main channel and a higher level for the active floodplain. To identify the bankfull level and main-channel zone is relatively easy at such a section in these two reaches. Figure 3b shows the post-flood channel geometry at the Liujiayuan section of a local meandering reach measured in 1999, and the bankfull characteristics were identified of $W_{bf}$ = 385 m, $H_{bf}$ = 2.4 m, and $A_{bf}$ = 911 $m^2$, respectively, with the corresponding bankfull discharge of $Q_{bf}$ = 2991 $m^3/s$.

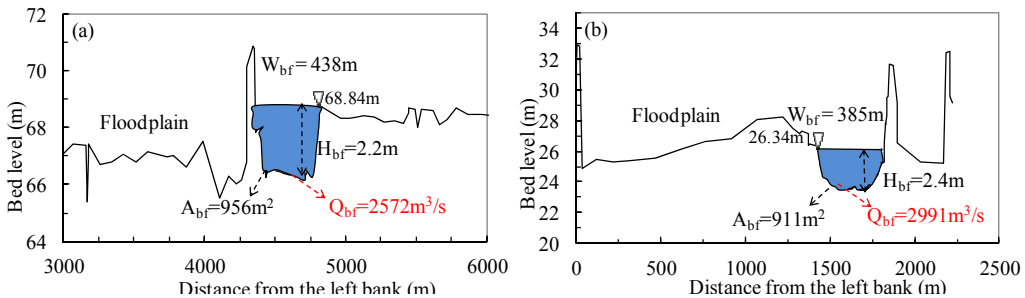


**Figure 3.** Calculated bankfull channel dimensions and bankfull discharges in 1999: (a) at the Mazhai section, 35.2 km upstream of Gaocun; and (b) at the Liujiayuan section, 131.8 km upstream of Lijin.

### 3.2.2 Calculation of reach-scale bankfull geometry and discharge

Adoption of an appropriate method is necessary to calculate the reach-scale bankfull geometry and discharge in a specified channel-pattern reach. Based on the method by Harman et al. (2008), an improved approach was proposed in this study to calculate the reach-scale bankfull characteristic parameters in a river by integrating the geometric mean based on the log-transformation with the weighted average based on the spacing between two consecutive sections. This method assumed that the study reach with a channel length of L covers a number of cross sections, and the bankfull channel dimensions and discharge at the *i*th section

 

can be determined using the proposed procedure, including the bankfull width ($W_{bf}^{i}$), depth ($H_{bf}^{i}$), and cross-sectional area ($A_{bf}^{i}$), and discharge($Q_{bf}^{i}$) . Using the integrated method, the corresponding reach-scale bankfull geometry of $\overline{W}_{bf}$, $\overline{H}_{bf}$ and $\overline{A}_{bf}$ and bankfull discharge $\overline{Q}_{bf}$ can be written as:

$$\overline{W}_{bf} = \exp\left(\frac{1}{2L}\sum_{i=1}^{N-1}(\ln W_{bf}^{i+1} + \ln W_{bf}^{i}) \times (x_{i+1} - x_i)\right) \quad [1]$$

$$\overline{H}_{bf} = \exp\left(\frac{1}{2L}\sum_{i=1}^{N-1}(\ln H_{bf}^{i+1} + \ln H_{bf}^{i}) \times (x_{i+1} - x_i)\right) \quad [2]$$

$$\overline{A}_{bf} = \exp\left(\frac{1}{2L}\sum_{i=1}^{N-1}(\ln A_{bf}^{i+1} + \ln A_{bf}^{i}) \times (x_{i+1} - x_i)\right) \quad [3]$$

$$\overline{Q}_{bf} = \exp\left(\frac{1}{2L}\sum_{i=1}^{N-1}(\ln Q_{bf}^{i+1} + \ln Q_{bf}^{i}) \times (x_{i+1} - x_i)\right) \quad [4]$$

where $x_i$ is the longitudinal distance at the *i*th section downstream of the dam; and *N* is the number of cross sections included in the study reach. Eqs. [1] - [3] indicate that the calculated reach-scale bankfull geometry can guarantee the continuity of channel dimensions, which means that $\overline{A}_{bf} = \overline{W}_{bf} \times \overline{H}_{bf}$ always holds true using the proposed procedure. In addition, this approach can also account for the effect of varied spacing between two sections on the reach-scale bankfull parameters.

## 4 RESULTS AND DISCUSSION

### 4.1 Variation in cumulative channel evolution volume

The water impoundment and sediment detention of the Xiaolangdi Reservoir has led to continuous channel degradation in the LYR. Based on the repeated surveys of sedimentation sections, the cumulative volume of channel scour in the LYR was calculated to reach 18.66×10$^8$ m$^3$ during the period from 1999 to 2015, with the corresponding values of 13.37×10$^8$ m$^3$ in the braided reach, 2.69×10$^8$ m$^3$ in the transitional reach, and 2.60×10$^8$ m$^3$ in the meandering reach (Figure 4). Therefore, the channel evolution in the braided reach played a key role in the fluvial processes of the LYR during this period. Figure 4 also indicates that the cumulative channel scour volume during non-flood seasons (6.5×10$^8$ m$^3$) was comparable to the value during flood seasons (6.9×10$^8$ m$^3$) in the braided reach, while the cumulative volume of channel scour was 3.4×10$^8$ m$^3$ during flood seasons, with the cumulative channel deposition volume of 0.8×10$^8$ m$^3$ during non-flood seasons in the meandering reach.

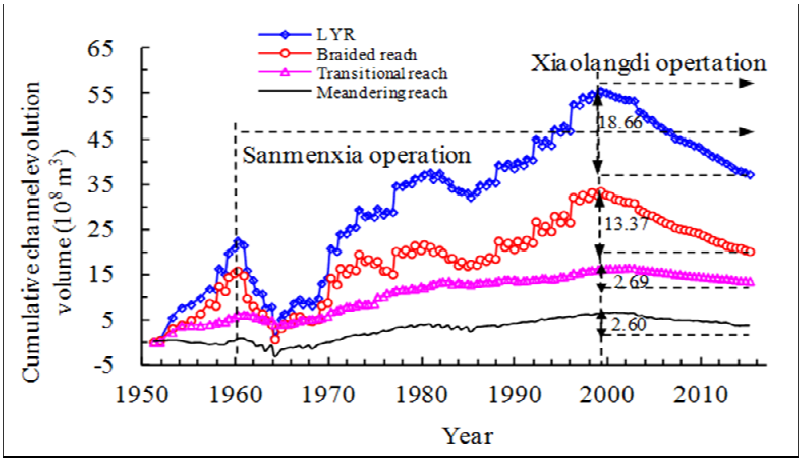


**Figure 4.** Cumulative channel evolution volume in the different reaches of the LYR.

### 4.2 Changes in cross-sectional profiles

A substantial change in the cross-sectional geometry of the LYR occurred as a result of the continuous channel degradation during this period. However, the adjustment characteristics of the cross-sectional geometry were different in the aforementioned different channel-pattern reaches. These measurements of cross-sectional profiles indicated that channel widening owing to bank erosion was considerably prominent in the braided reach, especially in the reach between two sections of Huayuankou and Jiahetan because of imperfect river training works and floodplain protection works; and channel incision was considerably

 

dominant in the transitional or meandering reach because of the effective control of various river training works.

Figure 5a shows the change of cross-sectional profile at the section of Heishi in the braided reach. This section is located about 46 km downstream of Huayuankou, and the left bank of this section is close to a water intake site on the Yuanyang floodplain. A lot of floodplain protection works has been constructed around this site, which keeps the left bank relatively stable. However, on the right bank of the Heishi section, no river training works existed on the floodplain, which led to an accumulated bank retreat width of 1948 m over the past 16 years, with the bankfull cross-sectional area increasing from 1847 to 12540 $m^2$. During the 2004 flood season, the right bank at this section retreated by 465 m caused by the large incoming discharges. Therefore, bank erosion plays a key role in channel degradation of the braided reach, and the variation in the bankfull geometry is characterized by the adjustments in both bankfull width and bankfull depth.

However, the phenomenon of channel incision was dominant in the reaches downstream of Gaocun, with a negligible variation in bankfull width being observed especially in the meandering reach. Figure 5b shows the change of cross-sectional profile at a typical section of Zhujuan in the meandering reach. This section is located about 20 km downstream of Aishan, and continuous river training works on both sides restrict the shifting of the main channel in the local region. The bankfull width at this section changed little over the period from 1999 to 2015 with a mean width of 273 m because of the effect of the training works, while the corresponding bankfull depth increased from 3.8 to 5.1 m, with a downcutting depth in the lowest bed level of 4.4 m. Therefore, bed incision makes a significant contribution to the channel evolution of the meandering reach, and the variation in bankfull geometry behaves mainly the variation in the component of bankfull depth.

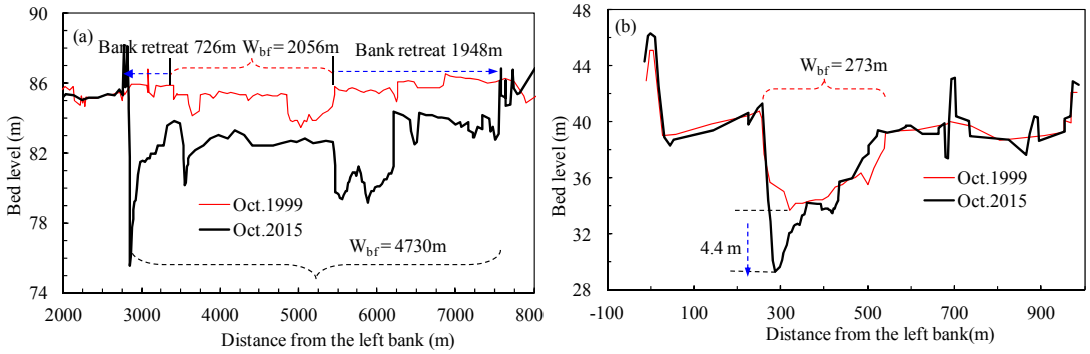


**Figure 5.** Changes of cross-sectional profiles at two sections of: (a) Heishi in the braided reach; (b) Zhujuan in the meandering reach.

4.3 Adjustment in reach-scale channel geometry

The post-flood cross-sectional profiles at 91 sedimentation sections in the LYR were surveyed annually over the period from 1999 to 2015, and the corresponding bankfull channel parameters at these sections were then determined using the proposed procedure. The section numbers for the reach-average calculation were 28, 28, and 35 in the braided, transitional, and meandering reaches, respectively. The reach-scale bankfull channel dimensions ($\overline{W}_{bf}$, $\overline{H}_{bf}$ and $\overline{A}_{bf}$) in these reaches of the LYR were then calculated using Eqs. [1] - [3]. These results indicate that the bankfull geometry varied significantly along the LYR and also changed with the recent channel degradation.

Previous studies have shown that the magnitude of the bankfull cross-sectional area in the LYR is a function of the previous years' flow and sediment conditions during flood seasons, and these conditions are usually represented by the previous several years' average discharge and incoming sediment coefficient during flood seasons (Wu et al., 2008a; Wu et al., 2008b; Xia et al., 2014a; Xia et al., 2014b). However, Figure 4 also indicates that different channel evolution processes occurred in different reaches during both non-flood and flood seasons. Therefore, it is assumed that similar relations also apply to predict the reach-scale bankfull geometry in the LYR, with the effects of the flow and sediment regimes during both non-flood and flood seasons being considered. Therefore, empirical relations were developed between the reach-scale bankfull geometry and the previous years' average of an integrated flow and sediment factor in different reaches. The integrated flow and sediment factor is defined as the average fluvial erosion intensity during a hydrological year, and the intensity during the $i^{th}$ hydrological year is generally represented by the parameter $F_i$, which can be expressed by:

$$F_i = (\overline{Q}_i^2 / \overline{S}_i) / 10^4 \qquad [5]$$

where $\overline{Q}_i$ and $\overline{S}_i$ are the mean discharge [$m^3/s$] and suspended sediment concentration [$kg/m^3$] over the $i^{th}$ hydrological year. In an alluvial river reach under quasi-equilibrium, there is an empirical power function

between water discharge and sediment discharge at a hydrometric station. Based on the hydrological data measured at Huayuankou, Jiahetan and other stations in 1950-2015, the calibrated exponent in the sediment rating curve is around 2.0. Therefore, $\overline{Q}_i^2$ in Eq. [5] approximately represents the sediment transport capacity at a specified section, and the term $\overline{Q}_i^2 / \overline{S}_i$ in Eq. [5] is regarded as a comprehensive parameter, which represents the ratio of sediment transport capacity to incoming sediment concentration at a given discharge.

Previous studies indicated that morphological responses to perturbations in alluvial rivers are usually the result of the cumulative effect of earlier flow and sediment conditions (Wu et al., 2008, 2012; Xia et al., 2014a; Xia et al., 2014b). In this study, the previous *n* year average fluvial erosion intensity ( $\overline{F}_n$ ) can be expressed by:

$$\overline{F}_n = \frac{1}{n}\sum_{i=1}^{n} F_i \qquad [6]$$

where *n* is the number of years for the moving average. The following analysis confirms that an empirical function of $\overline{F}_n$ can be applied to estimate the channel adjustments in the LYR, with the corresponding correlation coefficients reaching their maximum values at *n* = 4. Therefore, the reach-scale bankfull geometry in a river is closely related to the 4-year average fluvial erosion intensity, and the relation for predicting the reach-scale bankfull geometry in a specified channel-pattern reach can be expressed by:

$$\overline{G}_{bf} = \alpha(\overline{F}_4)^{\beta} \qquad [7]$$

where $\overline{G}_{bf}$ is a variable representing one of the reach-scale bankfull dimensions, such as $\overline{W}_{bf}$, $\overline{H}_{bf}$ and $\overline{A}_{bf}$; $\alpha$ is a coefficient; and $\beta$ is an exponent. Using the measured hydrological data and the reach-scale bankfull channel dimensions in 1999-2015, the parameters $\alpha$ and $\beta$ in Eq. [7] were calibrated for each reach using the method of regression analysis, with the calibrated parameters being shown in Figure 6 and Table 1.

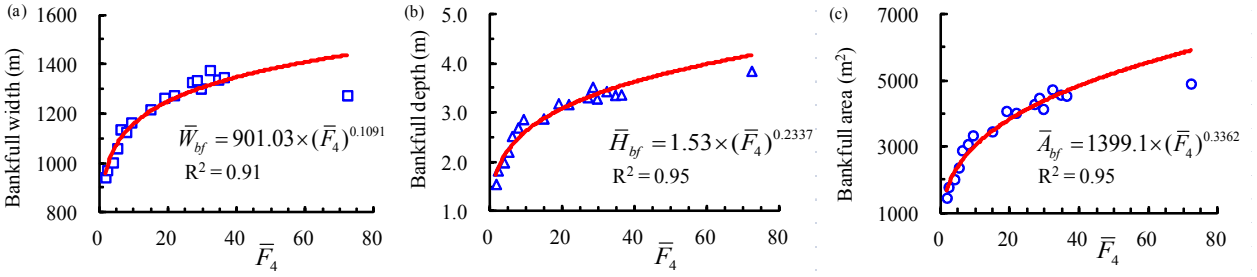


**Figure 6.** Relationships between the 4-year average fluvial erosion intensity at Huayuankou and the reach-scale bankfull dimensions in the braided reach of (a) width; (b) depth; and (c) area.

During the parameter calibration, the previous 4-year average fluvial erosion intensities at Huayuankou, Gaocun and Aishan were used as the incoming flow and sediment conditions for the braided, transitional and meandering reaches, respectively. As shown in Table 1, only the correlation degrees betweem $\overline{W}_{bf}$ and $\overline{F}_4$ were lower in the transitional and meandering reaches because the bankfull widths did not change at a large scale owing to the control of various river training works in these two reaches. Figure 6 and Table 1 show that: (i) a high value of correlation degree ($R^2$) between $\overline{G}_{bf}$ and $\overline{F}_4$ is obtained in the braided reach, with the values of $R^2$ ranging from 0.91 to 0.95; (ii) the correlation coefficients between $\overline{H}_{bf}$ (or $\overline{A}_{bf}$) and $\overline{F}_4$ are relatively higher in the transitional and meandering reaches, with the value of $R^2$ ranging between 0.91 and 0.97; (iii) there is significant variability in the calibrated parameters in Eq. [7] for these different reaches as a result of the particular fluvial processes in these reaches; and (iv) the calibrated parameters $\alpha$ and $\beta$ for any bankfull variable in each reach are greater than zero, which means that the reach-scale bankfull channel dimensions increase with a higher $\overline{F}_4$. These results also show that: the effect of the substantially reduced sediment load on the reach-averaged bankfull channel geometry; and the adjustments in bankfull channel geometry tend to behave a narrower and deeper profile in each reach of the LYR.

 

**Table 1.** Calibrated parameters in Eqs. [7]-[8] for different reaches of the LYR.

| Bankfull parameters | Different reaches of the LYR | | | | | | | | |
|---|---|---|---|---|---|---|---|---|---|
| | Braided | | | Transitional | | | Meandering | | |
| | $\alpha$ | $\beta$ | $R^2$ | $\alpha$ | $\beta$ | $R^2$ | $\alpha$ | $\beta$ | $R^2$ |
| $\overline{W}_{bf}$ (m) | 901.03 | 0.1091 | 0.91 | 473.82 | 0.0302 | 0.24 | 374.96 | 0.0028 | 0.02 |
| $\overline{H}_{bf}$ (m) | 1.53 | 0.2337 | 0.95 | 1.84 | 0.3064 | 0.95 | 3.17 | 0.1790 | 0.91 |
| $\overline{A}_{bf}$ ($m^2$) | 1399.10 | 0.3362 | 0.95 | 872.54 | 0.3367 | 0.97 | 1187.80 | 0.1818 | 0.93 |
| $\overline{Q}_{bf}$ ($m^3/s$) | 3186.7 | 0.2333 | 0.85 | 1819.2 | 0.3043 | 0.84 | 3008.0 | 0.1467 | 0.70 |

4.4 Adjustment in reach-scale channel discharge

The post-flood bankfull discharges at the selected 91 sedimentation sections in the LYR were calculated annually from 1999 to 2015, using the presented method, and the reach-scale bankfull discharges in these reaches were then calculated using Eq. [4], as shown in Figure 7. Due to the continuous channel degradation in the LYR, the reach-scale bankfull discharges in different reaches increased gradually over the period. For example, the reach-scale bankfull discharge in the braided reach increased from 3229 $m^3/s$ in 1999 to 7321 $m^3/s$ in 2015, and this value in the transitional or meandering reach increased to about 5000 $m^3/s$ in 2015. However, the mean reach-scale bankfull discharge in the transitional reach was less than the value in the braided or meandering reach before 2011.

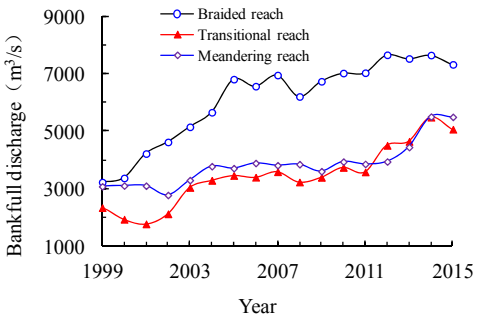


**Figure 7**. Temporal variations in the reach-scale bankfull discharges in different reaches

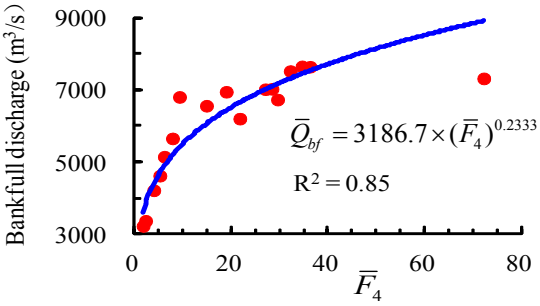


**Figure 8.** Relationship between the 4-year average fluvial erosion intensity and the reach-scale bankfull discharge in the braided reach.

where the parameters $\alpha$ and $\beta$ need to be calculated using the measurements. Figure 8 indicates the relationship between the reach-scale bankfull discharge ($\overline{Q}_{bf}$) and the four-year moving fluvial erosion intensity ($\overline{F}_4$) in the braided reach. The correlation degree between $\overline{Q}_{bf}$ and $\overline{F}_4$ is relatively high, and the value of $\overline{Q}_{bf}$ in the braided reach would generally increase with an increase in $\overline{F}_4$. The calibrated parameters $\alpha$ and $\beta$ in Eq. [8] in each reach are also presented in Table 1.

## 5 CONCLUSIONS

With the operation of the Xiaolangdi Reservoir, the flow and sediment regime entering the Lower Yellow River has been altered dramatically, and the LYR channel is undergoing continuous degradation, leading to significant variations in bankfull channel geometry and bankfull discharge. However, the section-scale bankfull parameter at a specified site can be unrepresentative of the total reach because of longitudinal variability in the cross-sectional profiles. The reach-scale concept is appropriate to describe the bankfull characteristic parameters in the LYR. The conclusions obtained from this study are as follows:

(i) An improved approach is proposed to calculate the reach-scale bankfull geometry and discharge in the LYR by integrating the geometric mean method based on the log-transformation with the weighted average method based on the spacing between two consecutive sections.

(ii) Using the proposed approach, the reach-scale bankfull channel dimensions and discharges in three reaches of the LYR are calculated annually in 1999-2015. These results indicate that: the reach-scale bankfull geometry varies significantly along the LYR, changing in the components of bankfull width and bankfull depth in the braided reach and mainly in the component of bankfull depth in the transitional and meandering reaches; and the reach-scale bankfull discharge in the braided reach increases from 3229 $m^3/s$ in 1999 to 7321 $m^3/s$ in 2015, with the increase magnitude in this reach being greater than that in the transitional or meandering reach.

 

(iii) Empirical power functions are developed between the reach-scale bankfull characteristic parameters and the previous 4-year average fluvial erosion intensity in three reaches, with the coefficients and exponents in the proposed relations being calibrated by the measurements in 1999-2015, with higher correlations being obtained for these reaches.

**ACKNOWLEDGEMENTS**

The study reported herein is supported by the National Natural Science Foundation of China (Grant Nos. 51379156 & 51579186), and it is also supported by the Scientific Special Expenditure for Non-profit Public Industry from the MWRC (Grant Nos. 201401038 & 201401023).

**REFERENCES**

Harman, C., Stewardson, M. & Derose, R. (2008). Variability and Uncertainty in reach Bankfull Hydraulic Geometry. *Journal of Hydrology*, 351(1-2), 13-25.

Leopold, L.B. & Maddock, T. (1953). *The Hydraulic Geometry of Stream Channels and Some Physiographic Implications.* Professional Paper No. 252, U.S. Geological Survey, Washington, DC, 57.

Ma, Y.X., Huang, H.Q., Nanson, G.C., Li, Y. & Yao, W.Y. (2012). Channel Adjustments in Response to the Operation of Large Dams: The Upper reach of the Lower Yellow River. *Geomorphology,* 147-148: 35-48.

Petts, G.E. & Gurnell, A.M. (2005). Dams and Geomorphology: Research Progress and Future Directions. *Geomorphology,* 71(1-2), 27-47.

Shin, Y.H. & Julien, P.Y. (2010). Changes in Hydraulic Geometry of the Hwang River below the Hapcheon Re-regulation Dam, South Korea. *International Journal of River Basin Management,* 8(2), 139-150.

Stewardson, M. (2005). Hydraulic Geometry of Stream Reaches. *Journal of Hydrology*, 306(1-4), 97-111.

Williams, G.P. (1978). Bankfull Discharge of Rivers. *Water Resources Research,* 14(6), 1141-1154.

Williams, G.P. & Wolman, M.G. (1984). *Downstream Effects of Dams on Alluvial Rivers.* Professional Paper 1286, U.S. Geological Survey, Washington, DC, 83.

Wohl, E. & Wilcox, A. (2005). Channel Geometry of Mountain Streams in New Zealand. *Journal of Hydrology,* 300(1-4), 252-266.

Wohl, E., Kuzma, J. & Brown, N.E. (2004). Reach Scale Channel Geometry of a Mountain River. *Earth Surface Processes and Landforms*, 29(8), 969-981.

Wu, B.S., Wang, G.Q., Ma, J.M. & Zhang, R. (2005). Case Study: River Training and its Effects on Fluvial Processes in the Lower Yellow River, China. *ASCE Journal of Hydraulic Engineering,* 131(2), 85-96.

Wu, B.S., Xia, J.Q., Fu, X.D., Zhang, Y.F. & Wang, G.Q. (2008a). Effect of Altered flow Regime on Bankfull Area of the Lower Yellow River, China. *Earth Surface Processes and Landforms,* 33(10), 1585-1601.

Wu, B.S., Wang, G.Q., Xia, J.Q., Fu, X.D. & Zhang, Y.F. (2008b). Response of Bankfull Discharge to Discharge and Sediment Load in the Lower Yellow River. *Geomorphology,* 100(3-4), 366-376.

Xia, J.Q., Li, X.J., Li, T., Zhang, X.L. & Zong, Q.L. (2014a). Response of Reach Scale Bankfull Channel Geometry in the Lower Yellow River to the altered flow and Sediment Regime. *Geomorphology,* 213, 255–265.

Xia, J.Q., Li, X.J., Zhang, X.L. & Li, T. (2014b). Recent Variation in Reach Scale Bankfull discharge in the Lower Yellow River. *Earth Surface Processes and Landforms,* 39(6), 723–734.

Xia, J.Q., Wu, B.S., Wang, G.Q. & Wang, Y.P. (2010). Estimation of Bankfull Discharge in the Lower Yellow River using Different Approaches. *Geomorphology,* 117(1-2), 66-77.

 

Proceedings of the 37th IAHR World Congress
August 13 – 18, 2017, Kuala Lumpur, Malaysia

# EFFECT OF RACK ANGLE OF TYROLEAN TYPE INTAKES ON SEDIMENT CAPTURE EFFICIENCY OF THE SYSTEM

MUSTAFA GOGUS [(1)], ABIDDIN BERHAN MELEK [(2)] & KUTAY YILMAZ [(3)]

[(1, 2, 3)] Middle East Technical University Civil Engineering Department Hydromechanics Laboratory, Ankara, Turkey,
mgogus@metu.edu.tr
berhanmelek@gmail.com
ktyylmz@gmail.com

## ABSTRACT

Tyrolean type water-intake structures are commonly constructed on steeply sloped mountain rivers to divert water with the minimum amount of sediment. There are various parameters affecting the amount of diverted water and sediment among which the most important ones are the length and inclination angle of the rack, and the distance between the rack bars. In this study, on a Tyrolean type intake model constructed in a channel 7 m long and 1.98 m wide at the laboratory, a series of experiments were conducted with water and sediment of various gradations. Three different racks having various bar spacing; 3mm, 6 mm and 10 mm were tested at the rack angles of θ=19° and θ=23° and the sediment capture capacities of each rack were determined. The results of the experiments were compared with the previously obtained results, and the effect of rack inclination on the sediment capture efficiency of the system was determined.

**Keywords:** Open channel flow; run-of-river type hydropower plants; sediment capture efficiency; tyrolean type intakes; intake racks.

## 1 INTRODUCTION

Run-of-river type hydropower plants are preferred where the construction of a reservoir is not possible because of the environmental issues. Although it is a practical alternative to the conventional dams, there are some difficulties in the operation of the run-of-river hydropower plants. The complications in the operation of run-of-river hydropower plants arise from the sediment carried by the flow. The facility especially the parts which are open to corrosion like turbines, may take damage due to sediment transmitted to the facility.

As a water inlet structure, Tyrolean weir is a convenient solution to reduce sediment transmission to the power generation system. Tyrolean weir separates considerable amount of sediment from the system by a trash rack and direct required amount of water to the system. There are limited number of studies in the literature about the variables affecting the sediment capture efficiency of Tyrolean weir (Kamanbedast and Bejestan, 2008; Yilmaz, 2010). This is a follow up study of Yilmaz (2010) to determine the most efficient variables of the system which will provide minimum sediment capture.

The aim of this study was to investigate the effect of rack angle on the sediment capture efficiency of the Tyrolean weir. For this reason, a series of experiments were conducted in a hydraulic model of a Tyrolean weir with trash racks having various lengths, bar spacing and two different rack angles. The results of the experiments were compared with those of Yilmaz (2010) which had been obtained from the same physical model having three different rack slopes.

## 2 METHODOLOGY

### 2.1 Experimental Setup

A physical model was constructed at the laboratory to observe the effects of the properties of Tyrolean weirs on the water capture efficiency and sediment capture efficiency (Figure 1). This model has a reservoir at the upstream end which is connected to an elevated constant head tank with a 30 cm diameter pipe. Water was supplied from this constant head tank and required discharge was adjusted by a mechanical valve at the end of the water intake pipe. An ultrasonic flow meter located upstream of the mechanical valve was used to measure the amount of the total discharge supplied to the system. The reservoir of the channel has 1.98 m width, 2m length and 1.5m depth. Water directed from the reservoir to the channel passes through bricks to regulate the flow and decrease turbulence of the flow. The main channel is 7m in length, 1.98 m in width which is the same as the reservoir width and has a slope of 0.001. At the downstream part of the channel, Tyrolean weir was placed to divert water and sediment. The experiments were performed with 3 screens having different bar openings ($e_1$=3 mm, $e_2$=6 mm, $e_3$=10 mm) and two different rack inclinations (θ=19°, θ=23°). A thin metal plate was used to arrange the screen length. The screens were made up of aluminum bars with circular cross section 1 cm in diameter and different bar openings as mentioned before. Under the

 

Tyrolean weir, a collection channel with a slope of 10% was located to direct the sediment and water to sediment trap reservoir (Figure 2). 20 cm high barrier was provided to keep the sediment in the sediment trap reservoir and clear water was transmitted to the intake structure with the 6.5m long and 0.7m wide side channel. Two manometers were used which were located just downstream of the reservoir and downstream section of the side channel to measure the water depths and calculate the discharges.

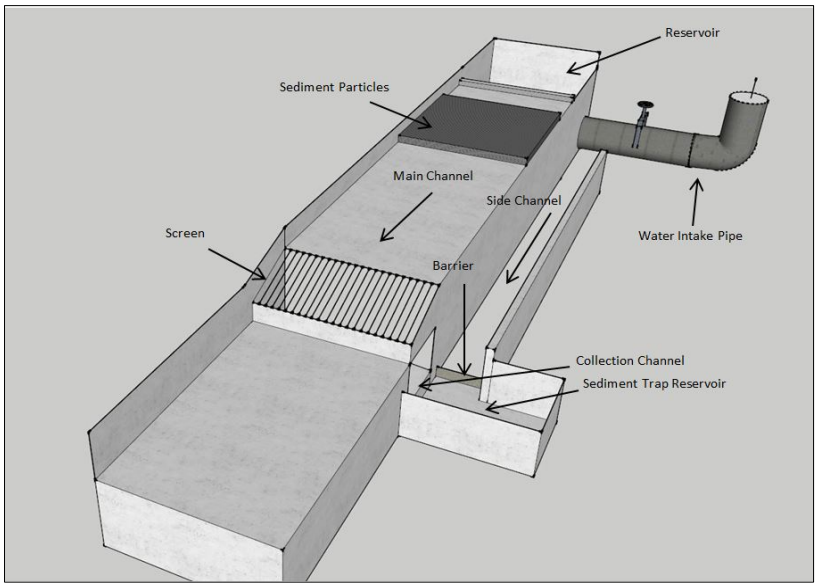


**Figure 1**. Schematic representation of the experimental setup.

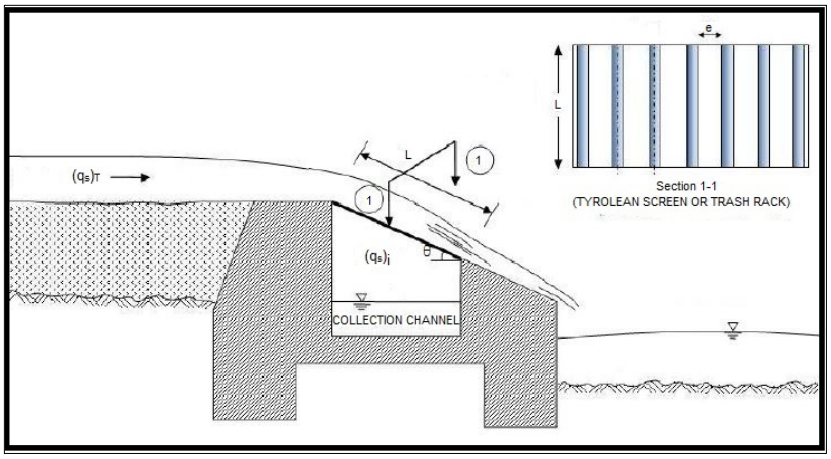


**Figure 2**. Schematic representation of the collection channel and thrash rack.

Three different sediment mixtures were prepared using sediments of various size ranges. To provide the conformance with the past studies, the same amount of sediment was used in the experiments. Table 1 shows the size ranges, amount of the sediments and total weights of the mixtures as a function of the screen types tested in the experiments.

**Table 1**. Size ranges and amounts of sediments in the mixtures used in the experiments.

| Bar spacing of the tested screen, e(mm) | Weight of the sediment(kg) Size ranges (mm) | | | | Total weight of sediment mixture (kg) |
|---|---|---|---|---|---|
| | 0-3 | 3-6 | 6-9 | 9-15 | |
| 3 | 50 | 50 | 50 | - | 150 |
| 6 | 50 | 50 | 50 | 50 | 200 |
| 10 | 50 | 50 | 50 | 50 | 200 |

 

2.2 Experimental Procedure

This experimental study aims to observe the effects of the bar openings, inclination of the screen and the screen length on the sediment capture efficiency. After the preparation of the sediment mixture, it was heaped up to upstream of the main channel to model the river bottom. At the beginning of the experiment, 10 lt/s discharge was given to the system for 4 minutes. The discharge was gradually increased to 30 lt/s, and during 4 minutes this discharge was maintained. This procedure was repeated to create an artificial flood regime in the main channel; in every stage, the discharge was gradually increased by 20 lt/s and kept constant for 4 minutes until the sediment mixture in the main channel was completely carried with the flow (Figure 3). Duration of the experiment, the main channel discharge and side channel discharge were recorded during the experiment with 1 minute time intervals. Side channel discharge was obtained by the water depth read by the manometer placed at the downstream of the side channel. From the calibration curves prepared before the experiments, the discharge transmitted by the side channel could be obtained from the depth. After the experiment was completed, sediment passed from the rack and accumulated on the rack and main channel was collected and weighed to determine the sediment capture efficiency, $(q_s)_i/(q_s)_T$ of the tested screen where $(q_s)_i$ is the weight of the sediment passing through the openings of the screen and $(q_s)_T$ is the total weight of the sediment in the main channel. This procedure was performed for three screens with bar openings of 3 mm, 6 mm, 10 mm, with two inclination angles of 19°, 23° and for three screen lengths of 20 cm, 40 cm and 60 cm.

**Figure 3**. Tyrolean screen with $e_1$=3 mm clear distance before and after clogged during the experiment.

## 3 ANALYSIS OF THE EXPERIMENTAL DATA AND DISCUSSION OF THE RESTULTS

The results of the experiments conducted with sediment were presented in Figures 4-6 in the form of sediment capture efficiencies as function of rack angle and rack lengths for bar openings of $e_1$=3 mm, $e_2$=6 mm, $e_3$=10 mm, respectively, along with the data of Yilmaz (2010). From these figures it can be stated that for a screen of known bar opening, e, the sediment capture efficiency of the screen gradually decreases with increasing angle of rack, θ, for a given rack length, and increases with increasing rack length, L, for a given angle of rack. The observed minimum and maximum sediment capture efficiencies for the screens of e=3 mm, 6 mm and 10 mm are 23.00 and 43.00 %, 39.00 and 52.75 %, 64.00 and 80.00 %, respectively for θ and L values tested. If the same figures are analyzed for the effect of bar spacing on the values of sediment capture efficiency of the screen having fixed L and θ values, it is seen that as the bar opening increases, the sediment capture efficiency increases significantly (Figures 7-9). For a Tyrolean weir of given screen length and bar opening, the sediment capture efficiency, in general, gradually decreases as the rack angle increases, except for the screens of $e_3$=10 mm. At the bar opening of $e_3$=10 mm which was the largest value tested, the sediment capture efficiency do not change significantly with the angle of rack.

In order to see the effect of the clogging of the bar openings with sediment on the water capture efficiency of the screen, the related data are presented in Figures 10-12, for screens of e=3 mm, 6 mm and 10 mm, respectively, along with the data of Yilmaz (2010). These figures reveal that water capture efficiencies do not significantly change at small θ values tested for a given screen length, even if the bar spacing of the screen increases. However, as θ values increase, θ≥19°, the water capture efficiency has a tendency to increase. The increment in the water capture efficiency is also logical as the length of the rack increases because, the possibility of clogging the rack bar openings reduces. The most severe reduction in the water capture efficiency is observed in the screen of $e_1$=3 mm even when the rack length tested was maximum L=60 cm. It means that the small bar openings can easily be clogged by sediment and about 80 % water capture efficiency is obtained from the longest screen instead of the expected value of 100 %. To show the rate of clogging of the rack bar opening, Figures 13-21 were plotted using some of the data of tested screens. From these figures it is clearly seen that as time passes, the water capture efficiency of the screen drops to

 

minimum values observed at the end of the time periods of the experiments as a function of the screen type used.

During flood times the main channel carries lots of bed load and since they will all pass over the weir rack, clogging of the rack bar openings will occur. This phenomenon results in a reduction in the amount of flow to be diverted from the main channel. Therefore, as a final conclusion it can be stated that in practice, the lengths of the rack bars should be kept about 20-30 % longer than the values to be calculated to be in the safe side.

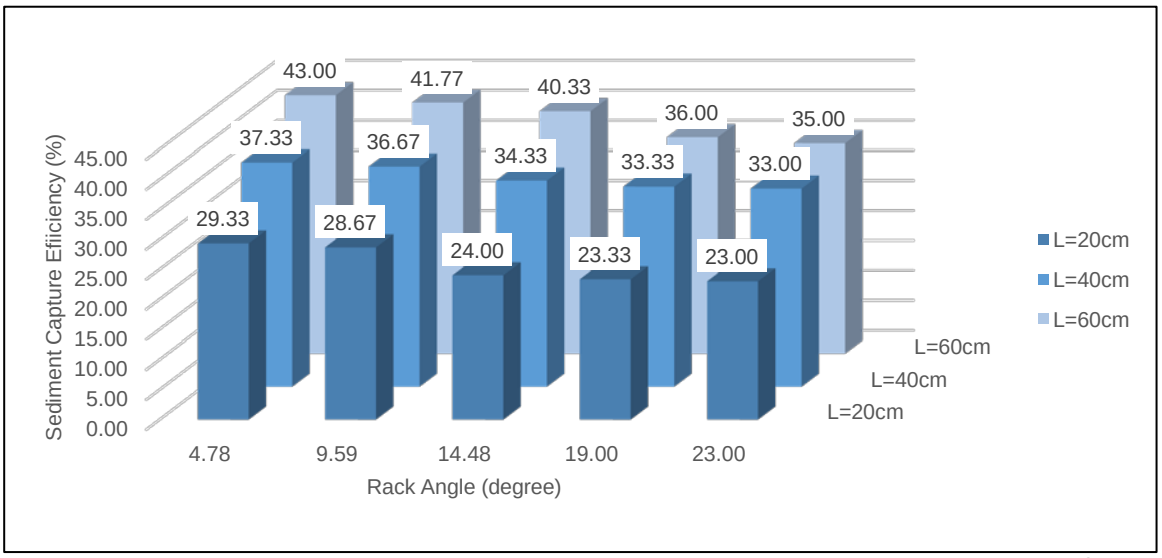


**Figure 4**. Variation of sediment capture efficiency with rack angle and length ($e_1$=3 mm).

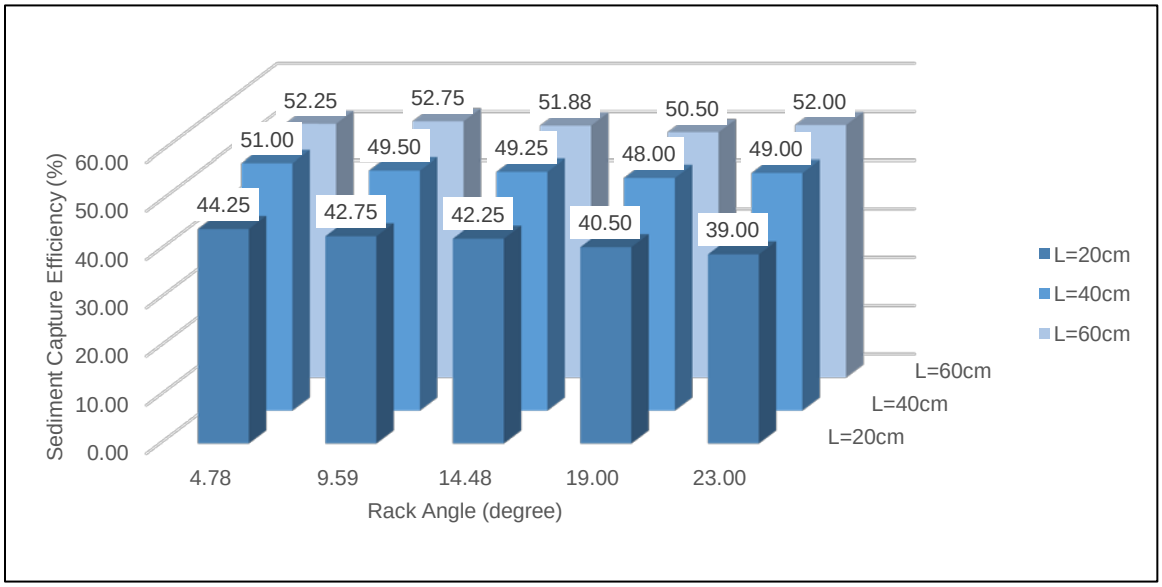


**Figure 5**. Variation of sediment capture efficiency with rack angle and length ($e_1$=6 mm).

 

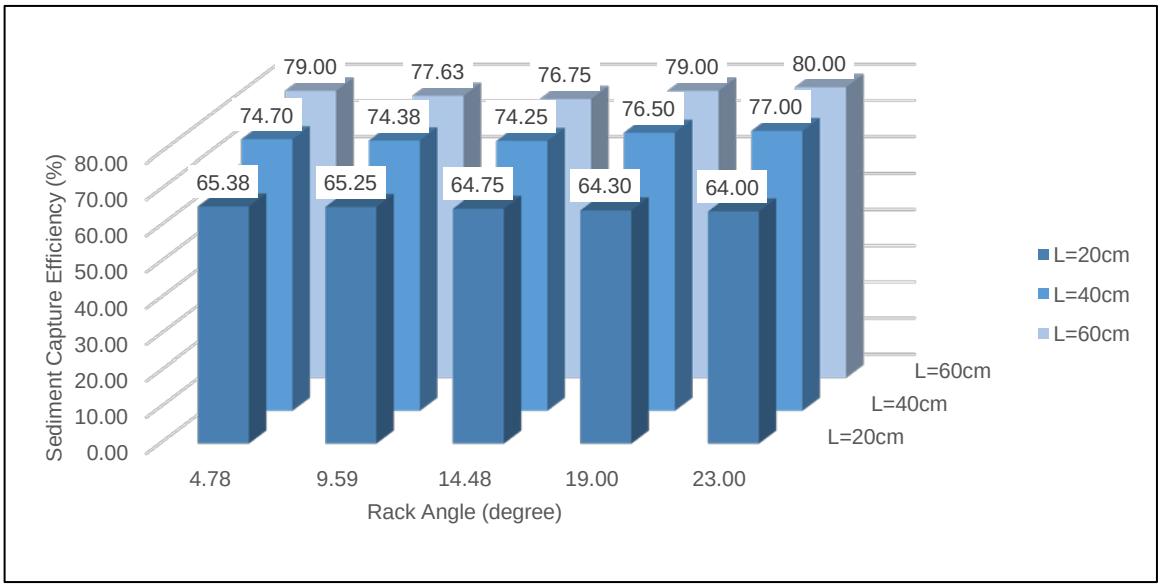


**Figure 6**. Variation of sediment capture efficiency with rack angle and length ($e_1$=10 mm).

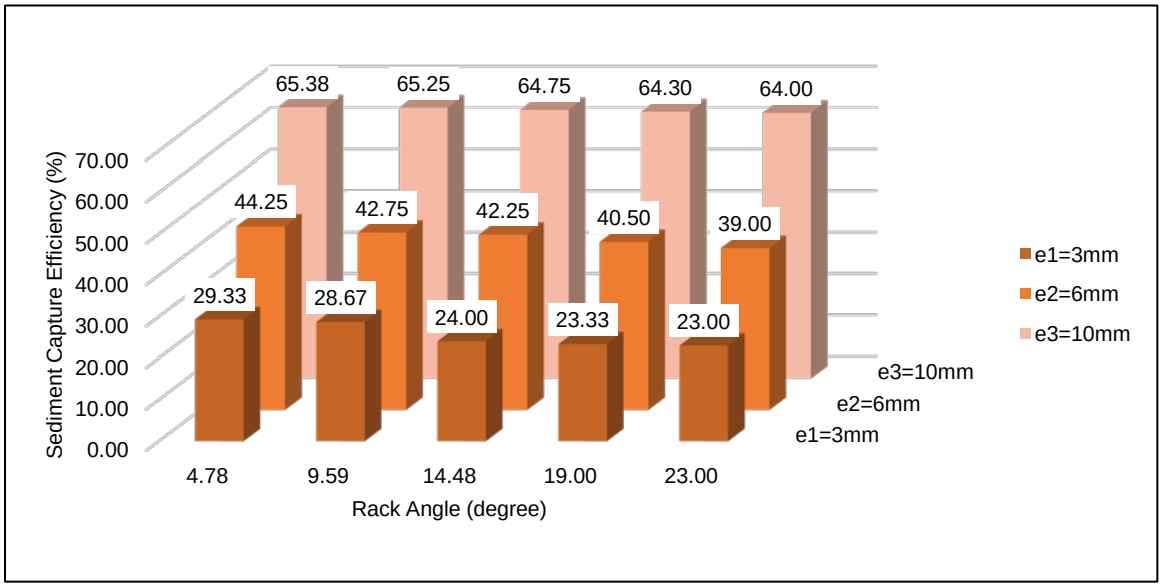


**Figure 7**. Variation of sediment capture efficiency with rack angle and bar spacing (L=20 cm.

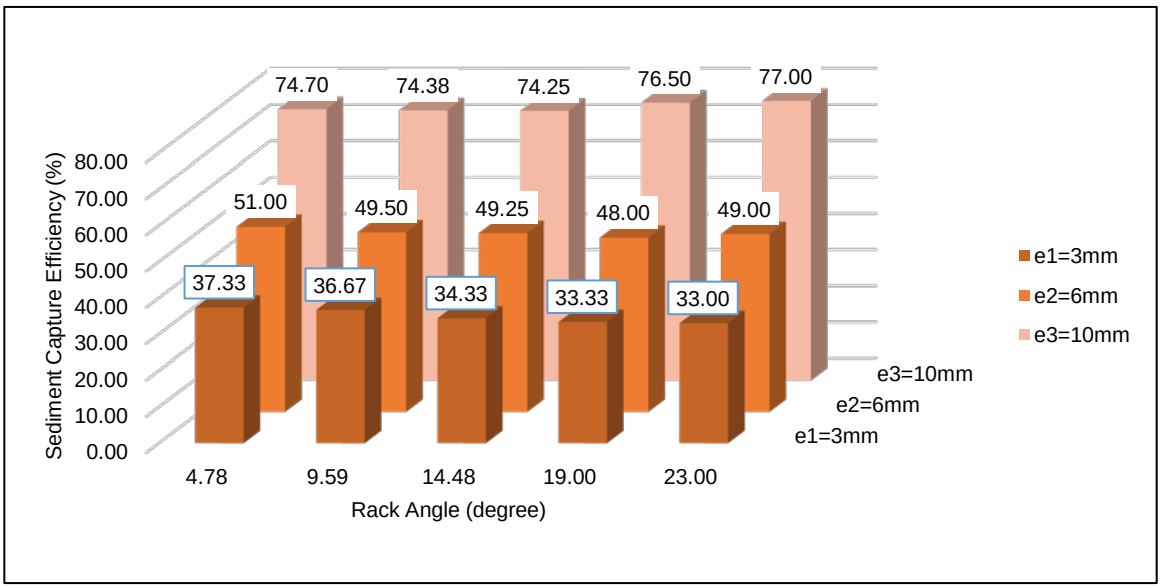


**Figure 8**. Variation of sediment capture efficiency with rack angle and bar spacing (L=40 cm).

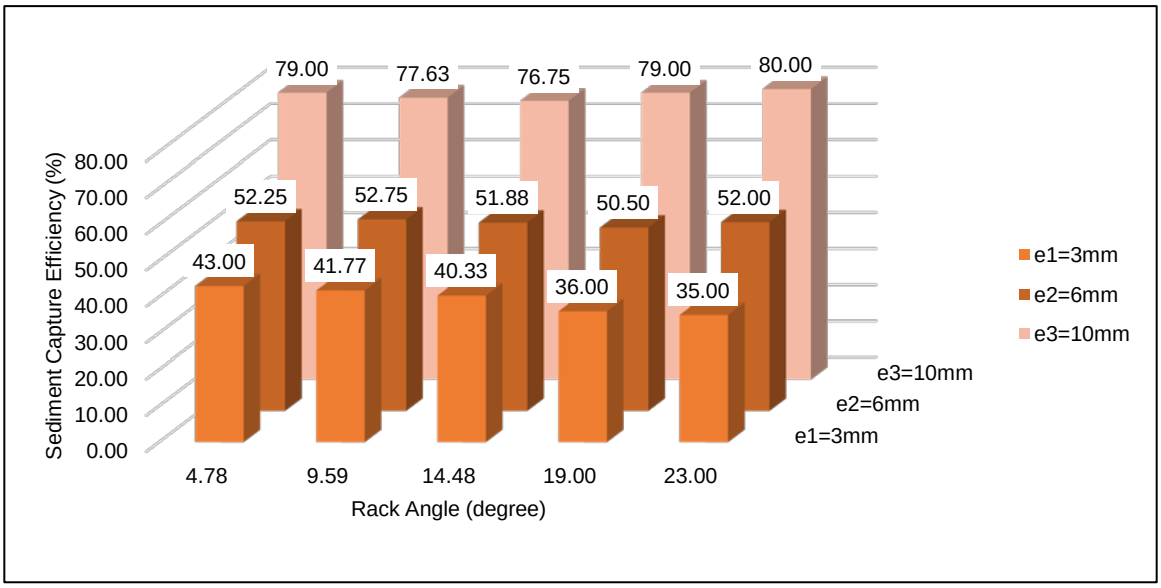


**Figure 9**. Variation of sediment capture efficiency with rack angle and bar spacing (L=60 cm).

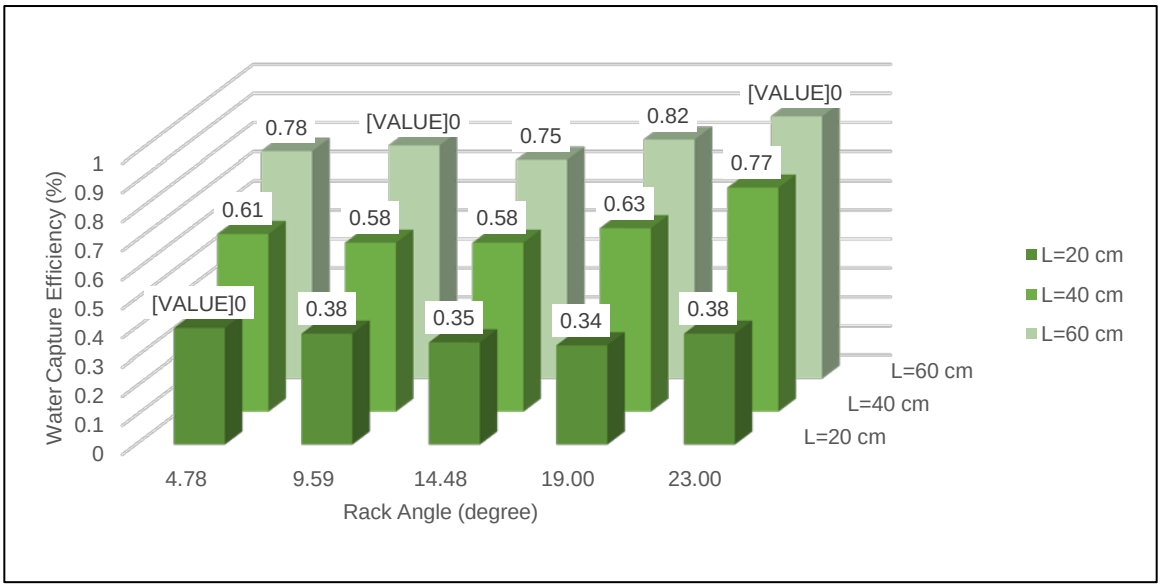


**Figure 10**. Variation of water capture efficiency with rack angle and length ($e_1$=3 mm).

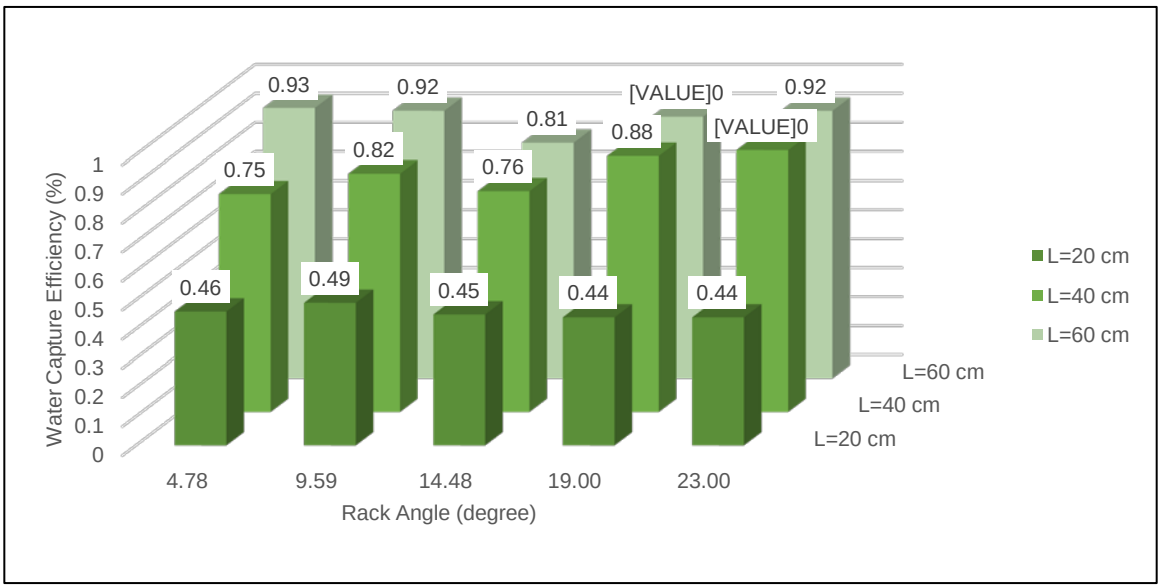


**Figure 11**. Variation of water capture efficiency with rack angle and length ($e_2$=6 mm).

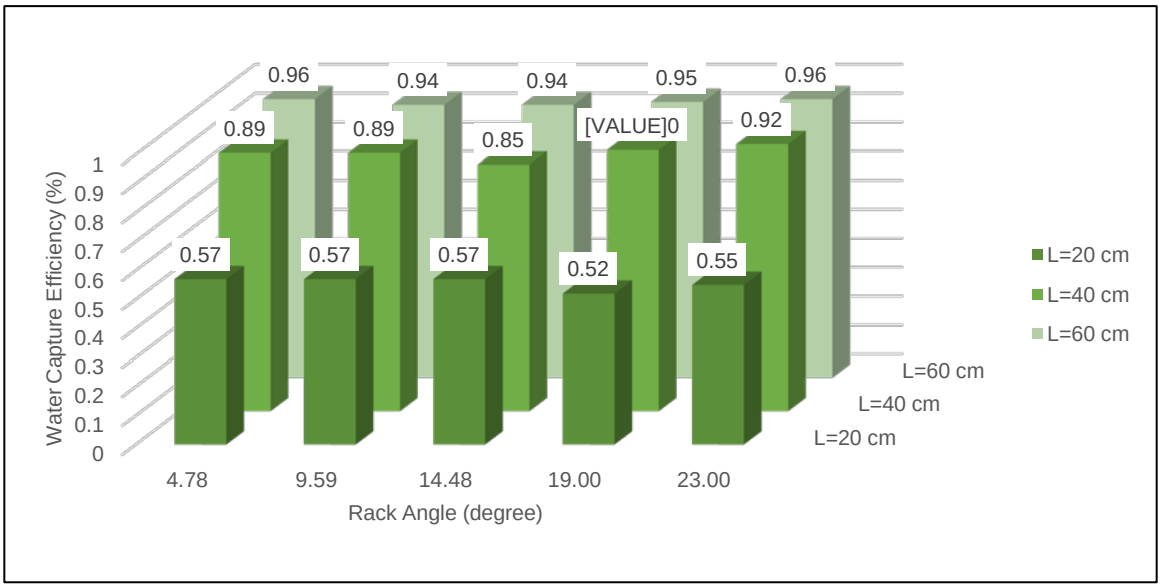


**Figure 12**. Variation of water capture efficiency with rack angle and length ($e_3$=10 mm).

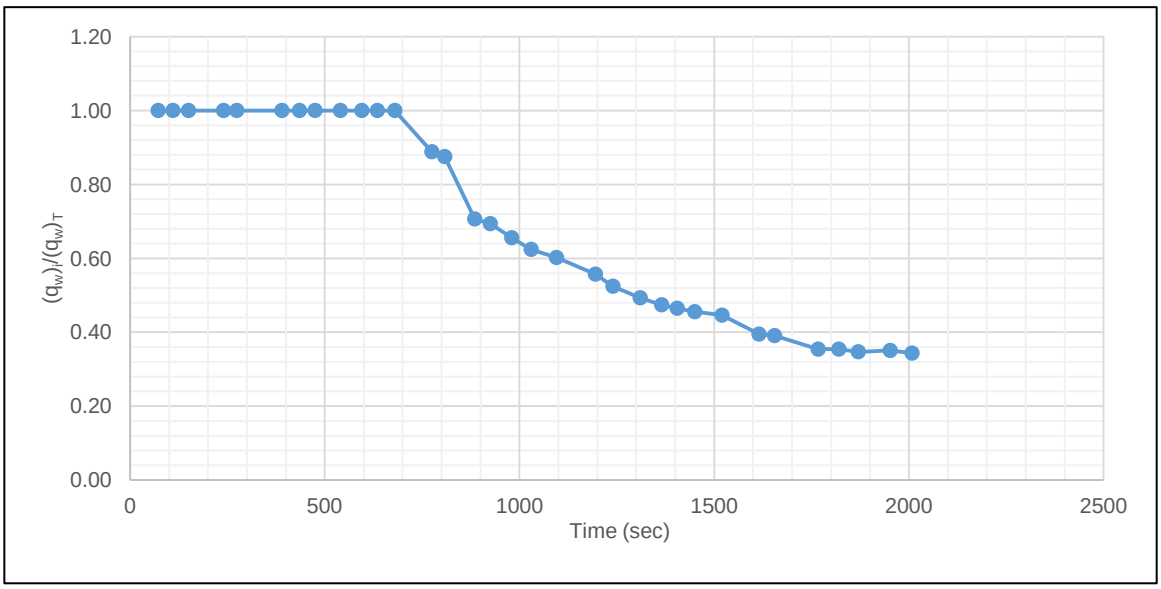


**Figure 13**. Variation of $(q_w)_i/(q_w)_T$ with time for the Tyrolean screen of e=3 mm, L=20 cm and θ=19°.

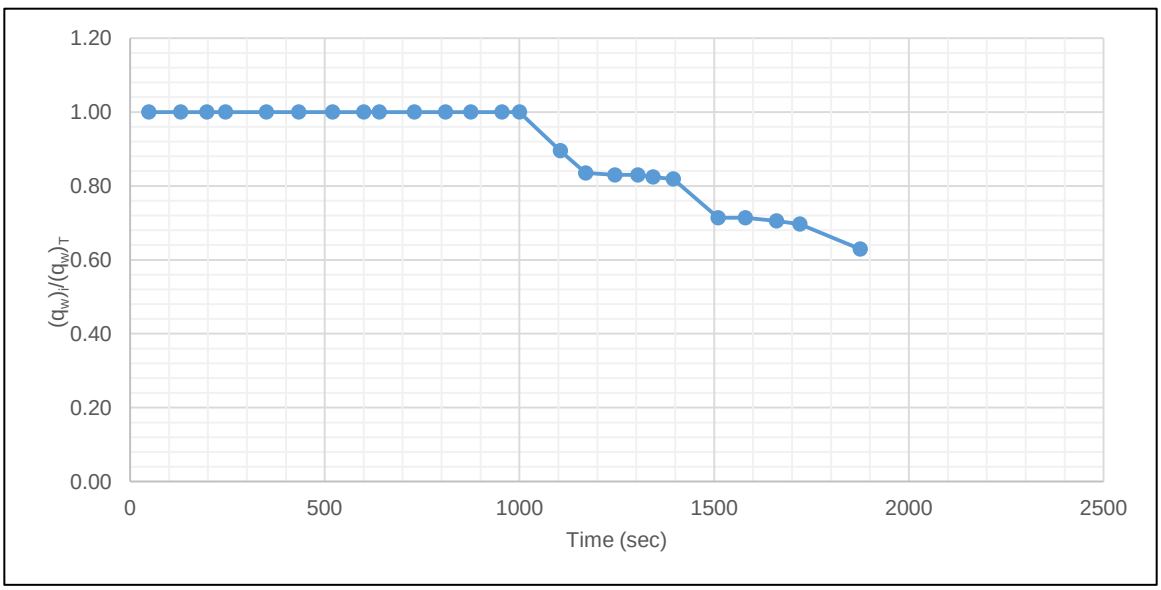


**Figure 14**. Variation of $(q_w)_i/(q_w)_T$ with time for the Tyrolean screen of e=3 mm, L=40 cm and θ=19°.

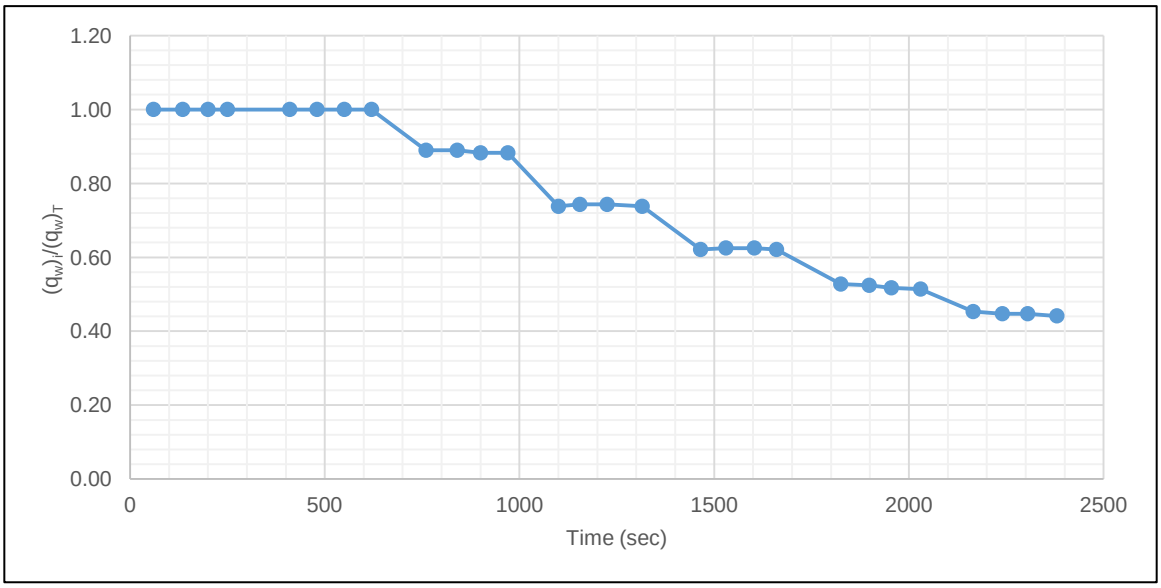


**Figure 15**. Variation of $(q_w)_i/(q_w)_T$ with time for the Tyrolean screen of e=6 mm, L=20 cm and θ=19°.

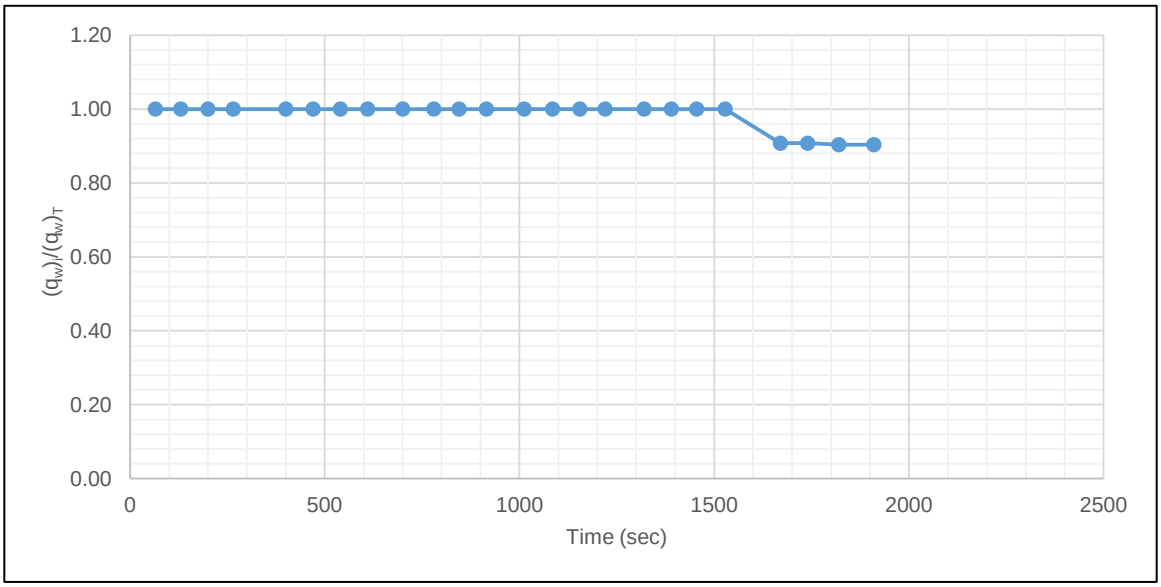


**Figure 16**. Variation of $(q_w)_i/(q_w)_T$ with time for the Tyrolean screen of e=6 mm, L=60 cm and θ=19°.

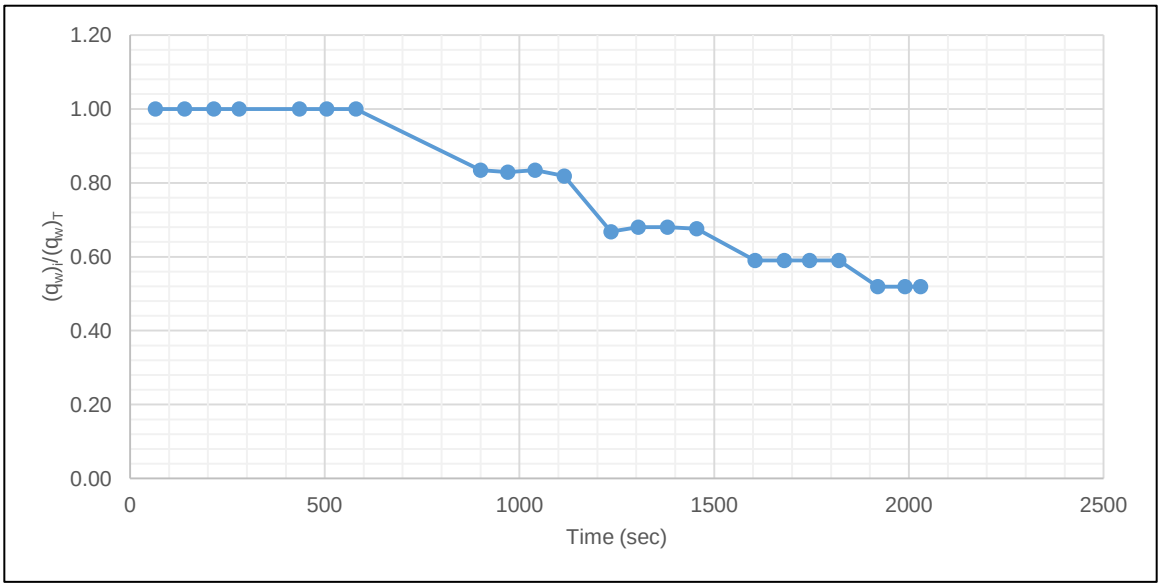


**Figure 17**. Variation of $(q_w)_i/(q_w)_T$ with time for the Tyrolean screen of e=10 mm, L=20 cm and θ=19°.

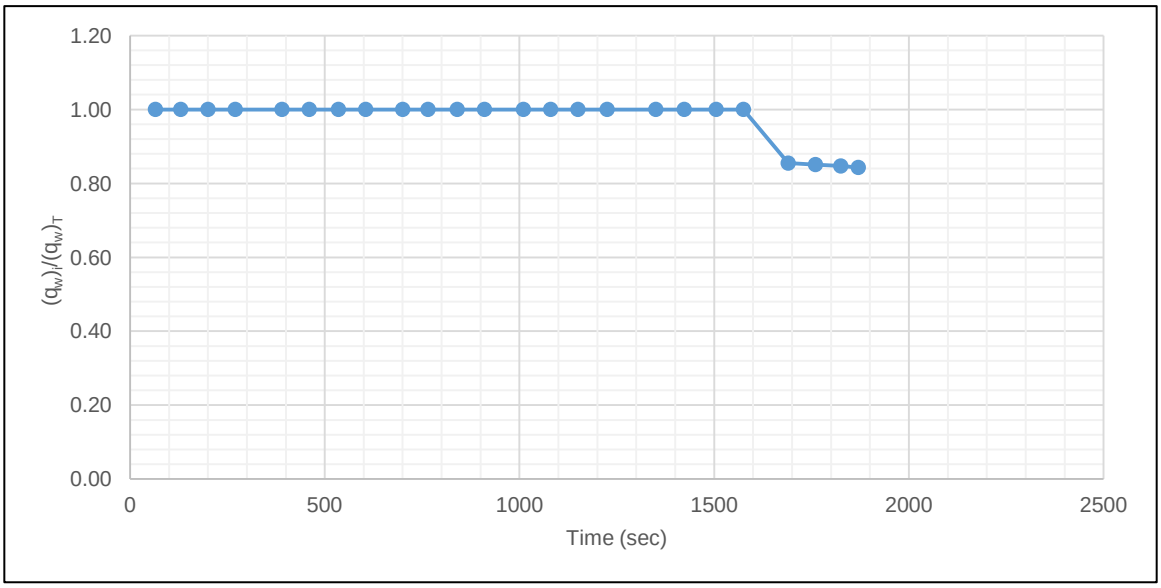


**Figure 18**. Variation of $(q_w)_i/(q_w)_T$ with time for the Tyrolean screen of e=10 mm, L=40 cm and θ=19°.

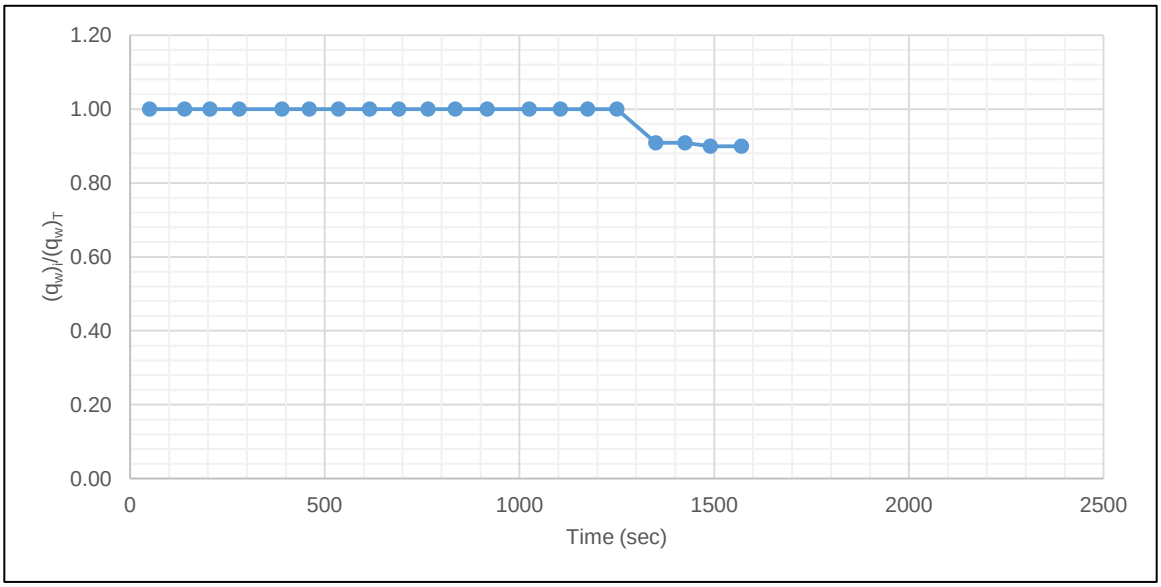


**Figure 19**. Variation of $(q_w)_i/(q_w)_T$ with time for the Tyrolean screen of e=3 mm, L=60 cm and θ=23°.

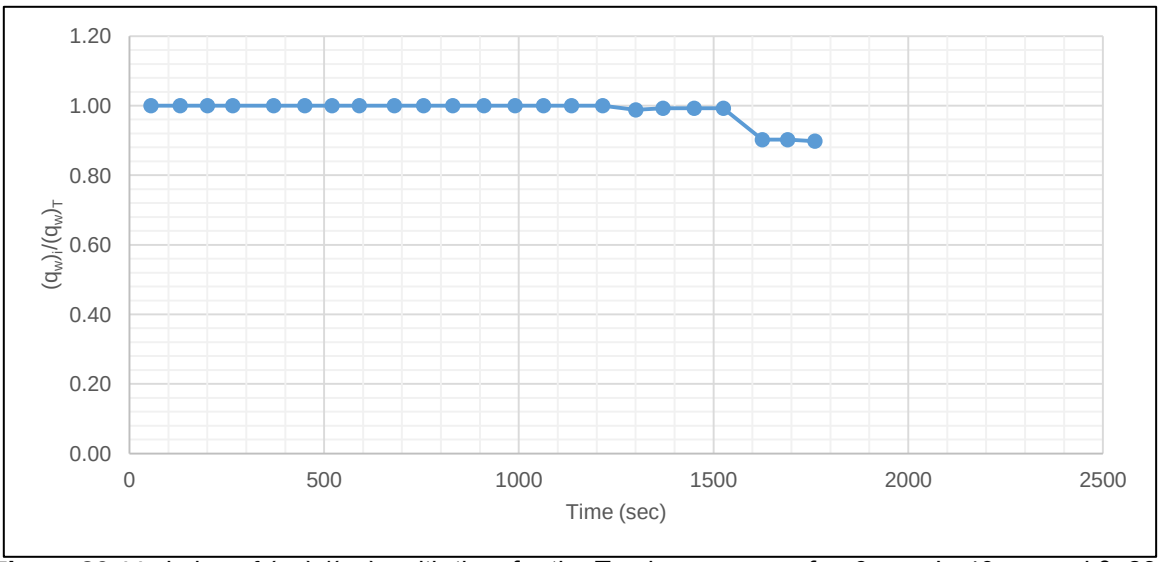


**Figure 20**. Variation of $(q_w)_i/(q_w)_T$ with time for the Tyrolean screen of e=6 mm, L=40 cm and θ=23°

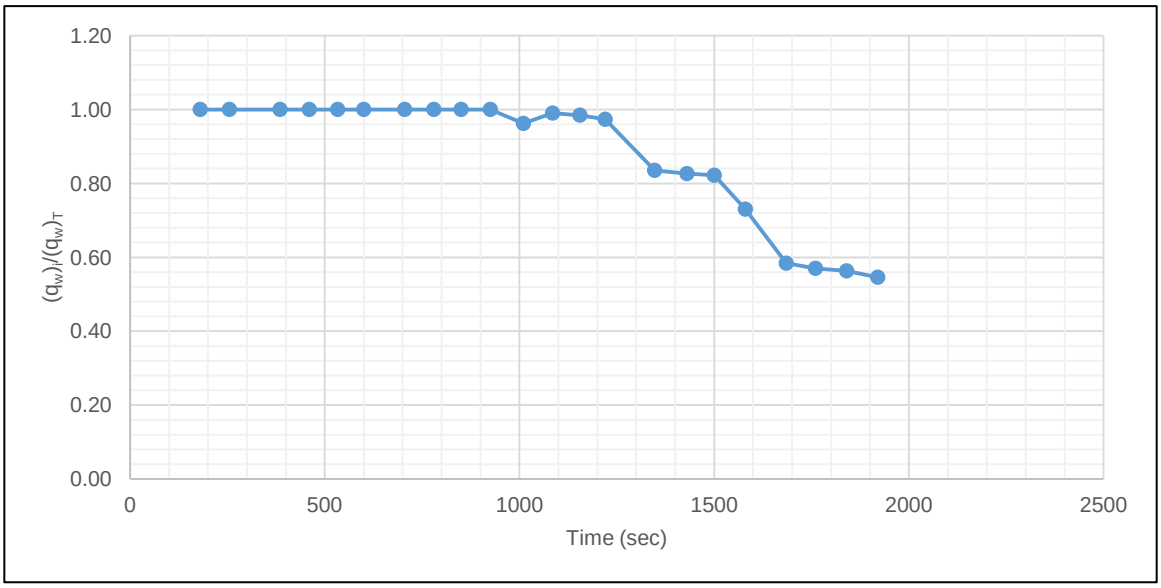


**Figure 21**. Variation of $(q_w)_i/(q_w)_T$ with time for the Tyrolean screen of e=10 mm, L=20 cm and θ=23°.

## 4 CONCLUSIONS

From the analysis of the experimental results, the following conclusions can be drawn:

- For a Tyrolean weir of given screen length and bar opening, the sediment capture efficiency, in general, gradually decreases as the rack angle increases, except for the screens of $e_3$=10 mm. At the bar opening of $e_3$=10 mm which was the largest value tested, the sediment capture efficiency do not change significantly with the angle of rack.
- Bed load carried by the main channel very seriously affects the performance of Tyrolean screens by clogging the openings between the rack bars and this results in reduction in the water capture efficiencies of the screens. Therefore, in practice the rack bar lengths to be calculated should be multiplied by a safety factor of about 1.2-1.3.
- Among the rack angles tested the one of θ=23° gives the minimum sediment capture efficiency and maximum water capture efficiency for almost all the bar openings and lengths investigated.

## ACKNOWLEDGEMENTS

This work was supported by TUBITAK, The Scientific and Technological Research Council of Turkey (Grant No. 214M028), which is gratefully acknowledged here.

## REFERENCES

Kamanbedast, A. A. & Bejestan, M. S. (2008). Effects of Slope and Area Opening on the Discharge Ratio in Bottom Intake Structures. *Journal of Applied Sciences*, 8(14), 2631-2635.

Yilmaz, N. A. (2010). Hydraulic Characteristics of Tyrolean Weirs, *MSc Thesis.* Middle East Technical University, Ankara, Turkey

 

Proceedings of the 37th IAHR World Congress
August 13 – 18, 2017, Kuala Lumpur, Malaysia

# VARIATION IN BANKFULL GEOMETRY IN A GRAVEL-TO-SAND BED REACH UNDERGOING CHANNEL DEGRADATION

MEIRONG ZHOU[(1)], JUNQIANG XIA[(2)], SHANSHAN DENG[(3)] & FENFEN LIN[(4)]

[(1, 2, 3, 4)] State Key Laboratory of Water Resources and Hydropower Engineering Science, Wuhan University, Wuhan 430072, China, ZMR@whu.edu.cn; xiajq@whu.edu.cn; dengss@whu.edu.cn; fflin@ whu.edu.cn

## ABSTRACT

Since the onset of the Three Gorges Project (TGP), remarkable geomorphic adjustments have occurred in the Yizhi reach (YZR) downstream of the dam. Due to the differences in channel pattern and bedform, the YZR is divided into the Yichang reach (YCR) and the Yidu reach (YDR). A special attention has been paid on the variation in bankfull channel geometry. The section-scale bankfull dimensions were firstly calculated annually from 2002 to 2015 in these two reaches, and then a reach-average method is adopted to calculate the reach-scale bankfull channel dimensions. Calculated results indicate that: (i) the reach-scale bankfull widths changed slightly; (ii) the adjustments in channel geometry occurred mainly in the component of bankfull depth, with the value increasing respectively by 1.57m and 3.28m in each reach, as well as a corresponding increase in bankfull cross-sectional area of about 6% and 17%. Furthermore, empirical relationships for the YCR and the YDR are developed between these reach-scale bankfull dimensions and the previous 5-year average fluvial erosion intensity during flood seasons at Yichang. It is found that: (i) the relationships between the reach-scale bankfull width and the previous flow and sediment conditions are relatively weak in these two reaches, with the corresponding correlation degrees of 0.16 and 0.04; (ii) the bankfull depth and cross-sectional area responded well to the altered flow and sediment regime, with the correlation degrees both being equal to 0.98 in the YDR, which are higher than those of 0.61 and 0.71 in the YCR where the bed material suffered significant coarsening process. Therefore, a comprehensive empirical relationship both the concerning previous flow and sediment regime and the bed material coarsening process is further proposed, with much higher correlations of 0.93 for bankfull depth and 0.91 for bankfull area being obtained in the YCR.

**Keywords:** Geomorphic adjustments; flow and sediment regime; bed-material coarsening; gravel-sand bed reach; Three Gorges Project.

## 1 INTRODUCTION

Upstream damming can significantly alter the natural flow and sediment regimes entering the downstream rivers, which usually lead to important consequences for geomorphic adjustments (Williams and Wolman, 1984; Petts and Gurnell, 2005; Phillips, 2009; Ma et al., 2012). Especially in a gravel-sand bed reach, the channel adjustment is more complicated owing to the effect of bed-material coarsening process. For example, the process of bed-material coarsening can restrict the degree of channel incision to some extent (Galay, 1983; Luo et al., 2007), and it can also increase the bed roughness and the in-channel water levels, which consequently affects the navigation conditions (O'Hare et al., 2010; Tanny et al., 2011). Therefore, better understanding of morphological adjustments in a gravel-sand bed reach downstream of a dam is required in current river management.

Common methods for the investigation into geomorphic adjustments in a gravel-sand bed reach mainly include analysis of field measurements, physical modeling, as well as numerical modeling. The former two methods are usually adopted to investigate the variation in bedforms and the formation of armour layer (Kleinhans et al., 2002; Wilbers and Brinke, 2003; Kuhnle et al., 2006; Venditti and Church, 2014), while numerical modeling is often used to calculate the transport rate of sand or gravel, and the process of channel deformation (Wu and Chou, 2003; Curran and Wilcock, 2005; Wilcock and Detemple, 2005; Orrú et al., 2015). For example, Kleinhans et al. (2002) conducted a series of flume experiments to study the sediment supply-limited bedforms in a gravel-sand bed river, with the results showing that the sediment-supply limitation determined the bed morphology. Bedforms were also investigated respectively in the Goodwin Creek and a laboratory flume channel by Kuhnle et al. (2006), which reveals that the bedforms were controlled by the amount of sediment available for transport. Wu and Chou (2003) developed a numerical model to investigate the response of gravel-sand bed to flushing flows, and the simulation results indicated that the transport rates of sand and gravel declined very fast in the beginning but approached asymptotically to small values. However, these studies rarely investigate the detailed channel geometry, and a quantitative analysis is required to study the intensive variation in channel geometry caused by upstream damming.

Previous studies usually investigated the adjustments in channel geometry, with hydraulic geometry relations being developed between the channel dimensions and the incoming flow and sediment regime (Wu

 

et al., 2008; Shin and Julien, 2010; Shibata and Ito, 2014). It should be noted that these studies mainly concentrated on the geomorphic adjustments at specified sections and the results cannot be representative of a total reach. Therefore, a reach-averaged method is required to investigate the morphological adjustments of a total study reach (Stewardson, 2005; Harman et al., 2008; Xia et al., 2014a). In addition, adjustments in channel geometry are the result of a set of complex natural processes that depend on both in-channel hydrodynamic conditions and bed-material properties (Piegay et al., 2005; Bartley et al., 2008; Xia et al., 2014b), especially in a gravel-sand bed reach. Therefore, bed-material coarsening should be considered when developing empirical relationships to describe the channel adjustments in the gravel-sand bed reach.

The Yizhi reach is a typical gravel-sand bed reach in the Middle Yangtze River, and remarkable channel adjustments have occurred since the operation of the Three Gorges Project (TGP). Therefore, this reach is selected as the study region. The main purposes of the current study are to: (i) investigate the variations in the incoming flow and sediment conditions, channel deformation process, and bed-material coarsening process in the study reach in response to the TGP operation; (ii) determine the adjustment characteristics of bankfull channel geometry by calculating the section- and reach-scale bankfull dimensions; (iii) analyze quantitatively the impacts of the altered flow and sediment regime and bed-material coarsening process on the adjustments in bankfull channel geometry.

## 2 STUDY AREA

The Yangtze River is the longest river in China with a total length of 6300km, and it is usually divided into the upper, middle and lower reaches. The Yizhi reach (YZR) is located about 43km downstream of the Three Gorges Dam (TGD) in the Middle Yangtze River, covering the region between Yichang and Zhicheng, as shown in Figure 1. With the boundary at Huyatan, the total reach is often divided into the Yichang reach (YCR) and the Yidu reach (YDR), with a respective length of 19.4 and 39.6km (Figure 1). The YCR is generally straight and the YDR consists of two bends named the Yidu and the Baiyang bends, with a tributary called the Qingjiang Reach flowing into the main stream at the Yidu bend. In addition, the riverbanks of the YZR are mainly controlled by low hills and terraces, as well as the bank-protection works with a length of 6.8 km along the reach (Cao and Wang, 2015). As to the bed-material composition, the riverbed in the YCR is mainly composed of gravel and fine sand with a thin sand layer; while the riverbed in the YDR comprises predominantly of fine sand with a thick sand layer of about 10 m and a subordinate layer of gravel, and the proportion of gravel deceases gradually along the reach (CRWC, 2015).

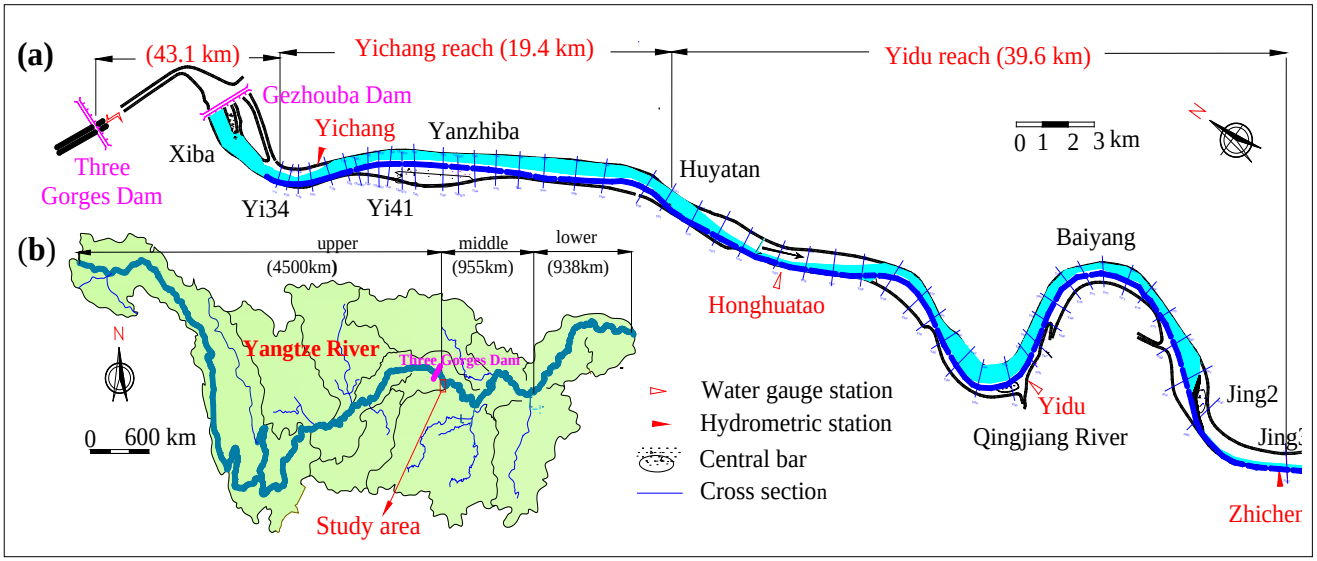


**Figure 1**. Map of the Yangtze River Basin and sketch of the Yizhi reach.

## 3 DATA AND METHODS

### 3.1 Data collection

In order to investigate the geomorphic adjustments of the study reach, the following data sources were collected, including:

(i) For analyzing the variation in the incoming flow and sediment conditions, hydrological data were collected from the Changjiang Water Resources Commission (CRWC), covering the daily mean discharge, sediment concentration and water stages at the hydrometric station of Yichang since 1955. This station is located at about 44 km downstream of the TGD, and it is at the inlet section of the YZR, as shown in Figure 1;

 

(ii) For the sake of investigating the channel erosion and deposition processes, the annual channel scour volumes in the YCR and the YDR were also collected after the operation of the TGP. In addition, the median diameters of bed material at specified cross-sections from 2002 to 2010 were used to analyze the bed-material coarsening process.

(iii) With the purpose of observing the variation in channel geometry, topographic data of the YZR were collected mainly including the topographic map with a scale of 1:10,000 measured in 2002 and the post-flood cross-sectional profiles at 50 fixed sites in 2002–2015, with the numbers of surveyed sections of 22 in the YCR and 28 in the YDR, respectively.

### 3.2 Methods

Since the operation of the TGP, remarkable geomorphic adjustments have occurred in the YZR, especially the variation in bankfull channel geometry. In the current study, the adjustments in channel geometry were investigated by developing hydraulic geometry relations between the bankfull channel dimensions and the relevant influencing factors.

#### 3.2.1 Procedure for calculating the bankfull channel geometry

- Determination of section-scale bankfull geometry

Bankfull channel geometry commonly includes the bankfull width, depth, cross-sectional area and etc. To determine these dimensions, the bankfull level at each section needs to be determined first. When the lip top of an active floodplain is obvious, the level of the lower lip is generally defined as the bankfull level; otherwise, it should refer to the bankfull level of adjacent sections, making sure that the bankfull level doesn't suffer big changes (Xia et al., 2014a). The distance between the two lips of the active floodplains on both sides and the main passage under the bankfull level are respectively regarded as the bankfull width ($W_{\mathrm{bf}}^{i}$) and cross-sectional area ($A_{\mathrm{bf}}^{i}$), with the ration of area to width defined as the bankfull depth ($H_{\mathrm{bf}}^{i}$) (Xia et al., 2014a). It should be noted that the riverbanks of the YZR are mainly controlled by low hills and terraces, and the lip tops are not obvious at some fixed sites, such as the Yi41 section in the YCR (Figure 2a). In this case, the measured cross-sectional profiles at Yi41 were adopted to determine the bankfull level, and the profiles at the adjacent sections should be used for reference. Finally, the bankfull level at this section is comprehensively determined to be 48.93m in 2015, with the bankfull width and cross-sectional area being of 1318m and 25177m$^2$, respectively. However, the lip top at Jing2 is relatively obvious so that the bankfull level can be determined directly to be 47.77m and then the corresponding bankfull channel dimensions can also be calculated (Figure 2b).

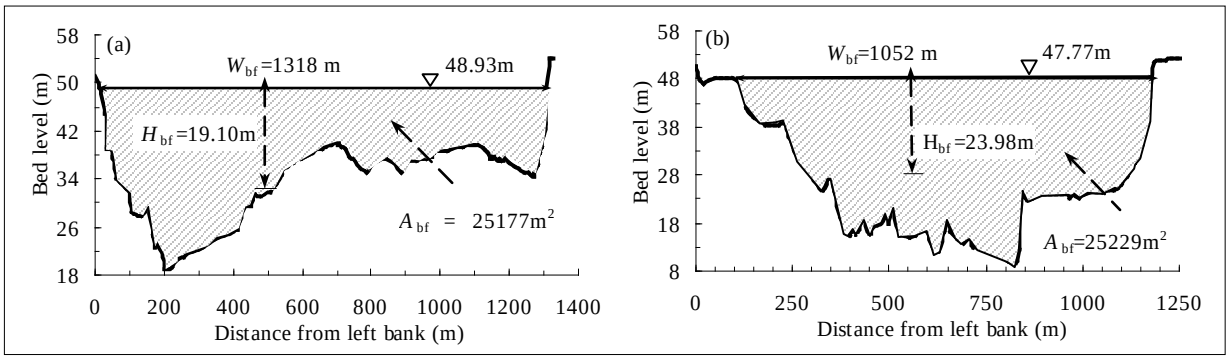


**Figure 2**. Calculated bankfull channel dimensions at two sections of: (a) Yi41; (b) Jing2.

- Calculation of reach-scale bankfull geometry

A reach-averaged method is adopted to calculate the reach-scale bankfull channel dimensions to investigate the channel adjustment characteristics of a whole reach, which integrates a geometric mean based on the log-transformation with a weighted average based on the spacing between two consecutive sections (Xia et al., 2014a). This method assumes that the study reach with a channel length of *L* covers a number of cross-sections, and the bankfull channel dimensions at the *i*th section ($G_{\mathrm{bf}}^{i}$) can be determined by the first step, including the bankfull width ($W_{\mathrm{bf}}^{i}$), depth ($H_{\mathrm{bf}}^{i}$), and cross-sectional area ($A_{\mathrm{bf}}^{i}$). Using the reach-averaged method, the corresponding reach-scale bankfull geometry ($\bar{G}_{\mathrm{bf}}$) can be written as:

$$\bar{G}_{\mathrm{bf}} = \exp\left(\frac{1}{2L}\sum_{i=1}^{N-1}(\ln G_{\mathrm{bf}}^{i+1} + \ln G_{\mathrm{bf}}^{i}) \times (x_{i+1} - x_i)\right) \qquad [1]$$

 

where $x_i$ is the longitudinal distance at the *i*th section downstream of the TGD; and *N* is the number of cross-sections, with *N*=22 in the YCR and *N*=28 in the YDR. $\bar{G}_{bf}$ covers the reach-scale bankfull width ($\bar{W}_{bf}$), depth ($\bar{H}_{bf}$) and cross-sectional area ($\bar{A}_{bf}$). The reach-averaged method can guarantee the continuity of channel dimensions, which means that $\bar{A}_{bf}=\bar{W}_{bf}\times\bar{H}_{bf}$ always holds true.

3.2.2 Method for developing hydraulic geometry relations

In terms of an alluvial river, bankfull channel geometry was mainly determined by the incoming flow and sediment regime, as well as the bed-material composition. Many hydraulic geometry relations have been proposed to describe the bankfull dimensions in stable or quasi-stable rivers, using empirically fitted power functions of a characteristic discharge or a controlled drainage area (Leopold and Maddock, 1953; Stewardson, 2005; Wohl and Wilcox, 2005; Lee and Julien, 2006; Harman et al., 2008; Navratil and Albert, 2010). However, in terms of an alluvial river especially a gravel-sand bed river, adjustments in bankfull channel geometry were not only determined by the incoming flow and sediment regime, but also the bed-material composition. Therefore, the hydraulic geometry relations associated with these two influencing factors are developed further using the multiple nonlinear regression in the current research. This analysis method was a commonly applied statistical technique for relating a set of two or more variables (Vecchia and Cooley, 1987; Adamowski et al., 2012). In a multivariate setting, the dependent variable (Y) can be related to a set of p explanatory variables ($X_1$, $X_2$, …, $X_p$). In this study, the bankfull channel dimensions (Y) were determined by both the incoming flow and sediment regime ($X_1$) and the bed-material composition ($X_2$), with the hydraulic geometry relations being written in the following form:

$$Y=a(X_1)^b+c(X_2)^d \qquad [2]$$

where a, c are coefficients; and b, d are exponents.

## 4 RESULTS

4.1 Variation in the flow and sediment regime

Runoff and sediment entering the YZR mainly comes from the main stream and tributaries in the Upper Yangtze River, which were transported intensively during flood seasons lasting from May to October (Xia et al., 2014a). The incoming flow and sediment regime can be represented by the regime measured at the hydrometric station of Yichang, because the water and sediment discharges converging into the struck stream from the Qingjiang Reach were limited. Figure 3 shows the temporal variation in water volume and sediment load during flood seasons at Yichang from 1955 to 2015. The average water volume was about 2992×$10^8$ $m^3$/a in 2002–2015, with a decrease of 14% as compared with the average value of 3464×$10^8$ $m^3$/a during the pre-dam period from 1950 to 2002. This happened mainly because of the climate change and drastic evaporation in the reservoir (Cao and Wang, 2015). Whereas the flood-season average sediment load was significantly reduced to 0.53×$10^8$ tonnes/a in 2002–2015, with a remarkable reduction of 89% as compared with that before the TGP operation (CWRC, 2015). This phenomenon was attributed to the implementation of soil and water conservation projects and the construction of upstream dams, especially the TGD.

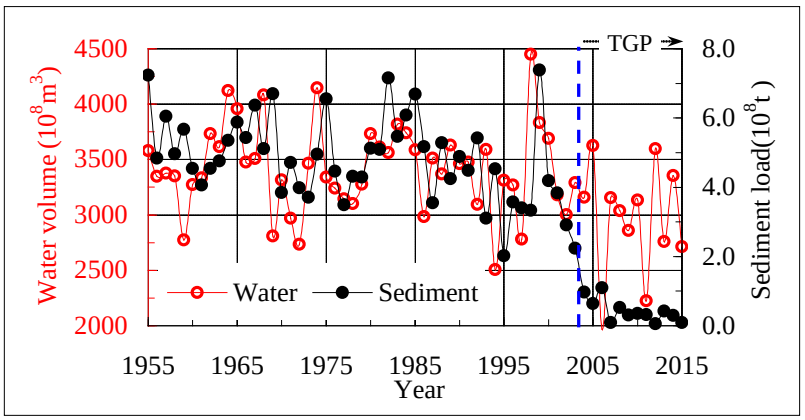


**Figure 3**. Temporal variations in water volume and sediment load during flood seasons at Yichang from 1955 to 2015.

Owing to the characteristics of incoming flow and sediment regime, the channel adjustments in the YZR occurred mainly during flood seasons, and the intensity of the channel evolution during non-flood seasons

 

was negligible in this investigation (Wu et al., 2008; Xia et al., 2014a). The average fluvial erosion intensity during the *i*th flood season ($F_{fi}$) was usually adopted to represent the incoming flow and sediment conditions in an alluvial river with low sediment concentrations (Xia et al., 2016), which can be written as:

$$F_{fi} = (\bar{Q}_i^2 / \bar{S}_i) / 10^8 \quad [3]$$

where $\bar{Q}_i$ and $\bar{S}_i$ are the mean discharge [$m^3/s$] and suspended sediment concentration [$kg/m^3$] during the *i*th flood season. The hydrological data at Yichang were used to calculate the flood-average fluvial erosion intensity in the YZR, and the results indicate that the parameter $F_{fi}$ increased gradually varying from 8.10 in 2002 to 358.68 in 2015. This means that the fluvial erosion intensity increased significantly since the operation of the TGP.

4.2 Variation in channel erosion and deposition processes

Owing to the clear-water scoring after the TGP operation, the YZR suffered significant channel degradation process with the average annual scour volume of about $0.12\times10^8$ $m^3$/a under the bankfull level, much greater than the value of $0.05\times10^8$ $m^3$/a during the pre-dam period from 1975 to 2002 (CWRC, 2015). Furthermore, it can be observed from Figure 4 that there existed a significant difference in the channel evolution processes of the YCR and the YDR. Firstly, the cumulative volume of channel scour reached $1.59\times10^8$ $m^3$ in the whole YZR from 2002 to 2015, with the values of $0.18\times10^8$ $m^3$ in the YCR and $1.41\times10^8$ $m^3$ in the YDR. Therefore, the scour intensity was relatively higher in the YDR whose cumulative channel score volume accounted for 89% of the value in the whole reach. Secondly, the channel degradation in the YCR mainly occurred during the first year of the TGP operation, whose cumulative scour volume accounted for 75% of the total value in 2002-2015. As the bed-material coarsening degree increased, the armor layer was formed in the YCR and then the channel underwent alternate and slight degradation or deposition during the period of 2004–2015, with the average annual scour volume of about $0.014\times10^8$ $m^3$/a. By contrast, the YDR suffered continuous and significant degradation in 2002–2015, with its average annual scour volume of about $0.11\times10^8$ $m^3$/a. The reason was that the bed-material coarsening process was faster and more obvious in the YCR, with the channel basically achieving the equilibrium state since 2004. However, the riverbed in the YDR is mainly composed of fine sand, owning a sufficient sand supply to support the channel degradation. Thus, it is more difficult to form an armor layer in this reach owing to a relatively uniform bed-material composition.

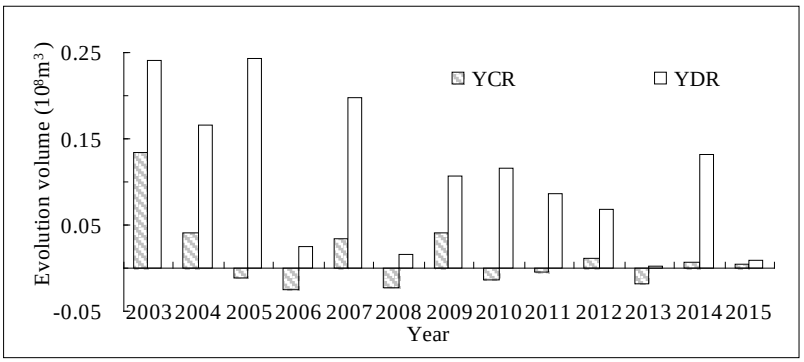


**Figure 4**. Annual channel evolution volume in the YCR and the YDR from 2002 to 2015.

4.3 Variation in bed-material coarsening process

Due to the significant channel degradation after the TGP operation, the bed-material composition in the study reach was adjusted subsequently. Nevertheless, the related measurements of bed material were not measured since 2010 so that the adjustment process was investigated during the period 2002–2010 only. During the response period to the interruption of its sediment supply caused by dam construction, a phenomenon of bed-material coarsening occurred, with coarser sediment particles becoming predominant on the bed. Based on the bed-material composition data at 23 cross sections in the study, the reach-averaged median diameters of bed material ($\bar{D}_{50}$) in the YCR and YDR were calculated during the period 2002-2010. Calculated results indicate that $\bar{D}_{50}$ increased significantly from 0.51 to 35.11mm in the YCR, while the value increased from 0.29 to 29.99mm in the YDR, as shown in Figure 5. Therefore, $\bar{D}_{50}$ in the YCR was greater than that in the YDR, with the coarsening rate of bed material also being higher than the value in the YDR.

 

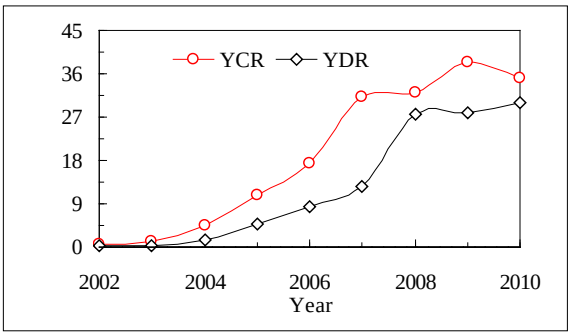


**Figure 5**. Temporal variations in the reach-averaged median diameter of bed material in the YCR and the YDR.

The relative roughness can reflect the bed friction, as well as the coarsening degree of bed material, which was represented by the dimensionless parameter $\bar{H}/\bar{D}_{50}$, where $\bar{H}$ is the average flow depth in m and $\bar{D}_{50}$ is the reach-averaged median diameter of bed material in mm. The increase in the value of $\bar{H}/\bar{D}_{50}$ means the decrease in the riverbed friction. Based on the measured bed material data and the water stages at Yichang, the values of $\bar{H}/\bar{D}_{50}$ in the YCR and the YDR were calculated during the period 2002-2010. The results show that due to the coarsening processes in these two reaches, the values of $\bar{H}/\bar{D}_{50}$ decreased from 27.79 to 0.40 in the YCR and 48.30 to 0.47 in the YDR.

## 4.4 Variation in bankfull channel geometry

### 4.4.1 Variation in section-scale bankfull geometry

Based on the presented method in Section 3.2.1, the post-flood cross-sectional profiles collected at 50 fixed locations in the YCR and the YDR from 2002 to 2015 were used to determine the bankfull channel geometry at section-scale. The calculated results at the end of the 2015 flood season (Figure 6) show that: (i) the section-scale bankfull widths changed considerably along these two reaches, and there was a minimum value of 716m and a maximum value of 1490m in the YCR and these widths varied between 780-1827m in the YDR; (ii) the bankfull depths varied significantly along the reach, ranging between 18.70m and 24.21m in the YCR and between 14.71m and 27.84 in the YDR; (iii) the bankfull cross-sectional areas also varied greatly because of the variability in width and depth. It turned out that the variation in bankfull channel geometry at a specified section cannot represent that of a total study reach.

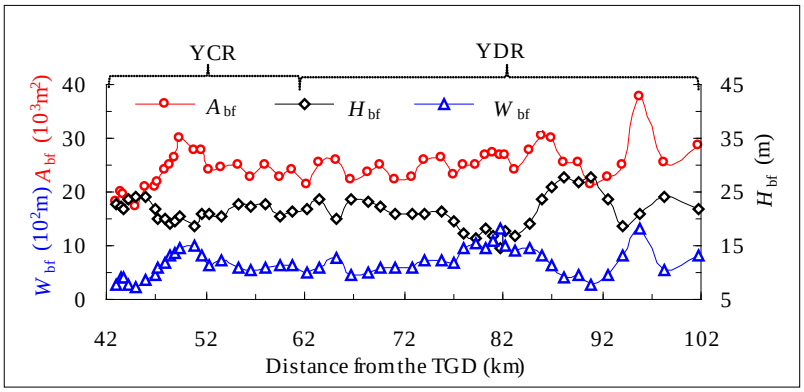


**Figure 6**. Calculated bankfull channel dimensions in the YCR and the YDR after the 2015 flood season.

### 4.4.2 Variation in reach-scale bankfull geometry

Due to the significant longitudinal variability in the cross-sectional geometry, the reach-scale bankfull dimensions $\bar{G}_{bf}$ ($\bar{W}_{bf}$, $\bar{H}_{bf}$ and $\bar{A}_{bf}$) in the study reach were then calculated using Eq. [1]. Calculated results indicated that: (i) the reach-scale of bankfull widths of both reaches changed slightly, owing to the high erosion-resistant capacity of riverbanks and the construction of bank-revetment works; (ii) the adjustments in channel geometry occurred mainly in the component of bankfull depth, with the values increasing by 1.57m and 3.28m in these two reaches, respectively; and (iii) the corresponding reach-scale bankfull cross-sectional area respectively increased about 6% and 15%. In general, the adjustments in bankfull channel geometry behaved more dramatically in the YCR than in the YDR. Furthermore, the reach-scale in bankfull depth and

 

area mainly increased during the period of 2002–2005 in the YCR, with the increase rate decreasing from then on. The YDR underwent more significant increase in bankfull geometry, with the reach-scale bankfull area increasing by 3.32m in 2002-2009 and only 0.19m in 2009-2015.

## 5 DISCUSSIONS

It is widely accepted that the variation in channel geometry of an alluvial river was the result of a set of complex natural processes that depend on in-channel hydrodynamic conditions and bed-material properties (Piegay et al., 2005; Bartley et al., 2008; Wilkerson and Parker, 2011; Xia et al., 2014b). In the current study, the average fluvial erosion intensity during a flood season ($F_{fi}$) and the mean relative roughness ($\bar{H}/\bar{D}_{50}$) were selected as the key influencing factors. The bed-material composition in the YZR was not measured after 2010, and only the measurements in 2002–2010 were used for investigating the adjustments in bankfull channel geometry.

### 5.1 Impact of the altered flow and sediment regime on bankfull channel geometry

Previous studies (Knighton, 1998; Wu et al., 2008; Xia et al., 2014a) reveal that the variation in bankfull channel geometry was usually the result of the cumulative effect of earlier flow and sediment conditions, which can be expressed by the previous *n*-year average fluvial erosion intensity during flood seasons ($\bar{F}_{nf}$):

$$\bar{F}_{nf} = \frac{1}{n}\sum_{i=1}^{n} F_{fi} \qquad [4]$$

where *n* is the number of moving years; and $F_{fi}$ is the average fluvial erosion intensity during the *i*th flood season (Section 4.1). Based on the calculated reach-scale, bankfull dimensions of the YCR and the YDR in 2002–2015, as well as the average fluvial erosion intensity at Yichang, the relations between $\bar{G}_{\mathrm{bf}}$ and $\bar{F}_{nf}$ were plotted with the parameter *n* varying from 1 to 8, and the correlation degree reached the maximum at *n*=5. The relationship can be expressed by:

$$\bar{G}_{\mathrm{bf}} = \alpha_1(\bar{F}_{5f})^{\beta_1} \qquad [5]$$

where $\alpha_1$ is a coefficient; and $\beta_1$ is an exponent. The results presented in Figure 7 show that: (i) the relationships between the reach-scale bankfull widths ($\bar{W}_{\mathrm{bf}}$) and the previous flow and sediment conditions were relatively weak in these two reaches, with the corresponding correlation degrees of 0.16 and 0.04; (ii) the reach-scale bankfull depths ($\bar{H}_{\mathrm{bf}}$) and cross-sectional areas ($\bar{A}_{\mathrm{bf}}$) responded well to the altered flow and sediment regime caused by the TGP, with the correlation degrees both being equal to 0.98 in the YDR and being of 0.61 and 0.71 in the YCR; and (iii) these correlation degrees for the YDR were higher than those for the YCR. It can be explained that the channel evolution is not only closely related to the flow and sediment regime, but also the composition of bed material. The formation of an armor layer led to a weaker effect of the flow and sediment regime on the channel adjustments in the YCR.

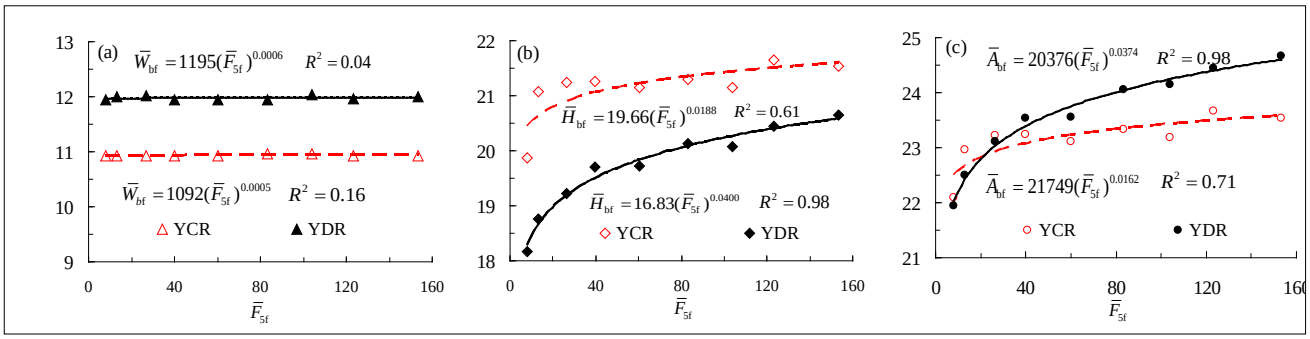


**Figure 7**. Relationships between the 5-year average fluvial erosion intensity during flood seasons and the reach-scale bankfull dimensions of: (a) bankfull width; (b) bankfull depth; (c) bankfull area.

### 5.2 Impact of the bed-material coarsening on bankfull channel geometry

Therefore, a comprehensive empirical relation is proposed to account for the effects of both the previous flow and sediment regime and the bed-material coarsening on the variation in reach-scale for bankfull

 

geometry. According to the multiple nonlinear regression method (Section 3.2.2), a comprehensive relation between $\bar{G}_{bf}$ and these variables can be written in the following form:

$$\bar{G}_{bf} = \alpha_1(\bar{F}_{5f})^{\beta_1} + \alpha_2(\bar{H}/\bar{D}_{50})^{\beta_2} \quad [6]$$

where $\alpha_1$ and $\alpha_2$ = coefficients; and $\beta_1$ and $\beta_2$ = exponents. The values of $\bar{G}_{bf}$, $\bar{F}_{5f}$ and $\bar{H}/\bar{D}_{50}$ in two subreaches during the period of 2002–2010 were used to calibrate the parameters in Eq. [6] by using the software SPSS, as shown in Figure 8. The calibration results indicated that: (i) the correlations for bankfull depth and cross-sectional area in the YCR increased to 0.93 and 0.91, which were much higher than those being obtained from the Eq. [5] by merely considering one influencing factor; (ii) the correlation degree for the bankfull depth or area in the YDR reached 0.99. Therefore, Eq. [6] can used to reflect the variation in bankfull geometry at reach-scale in a gravel-sand reach.

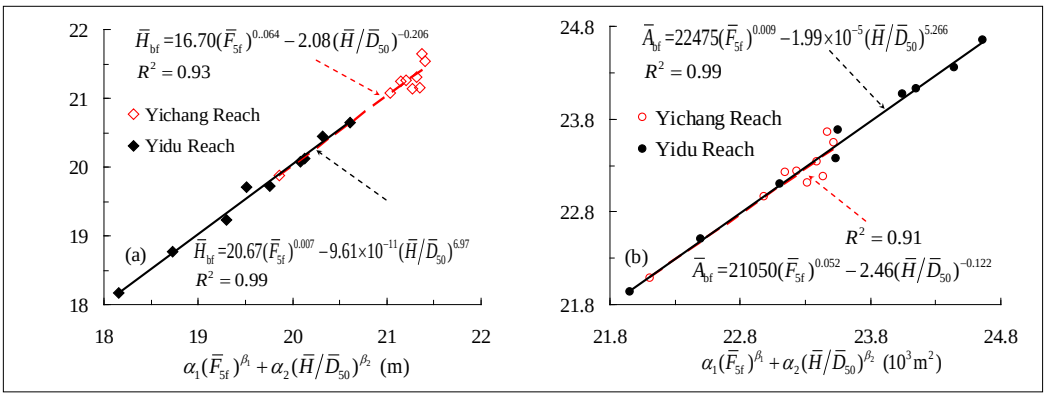


**Figure 8**. Relationships between the two influencing factors ($\bar{F}_{5f}$ and $\bar{H}/\bar{D}_{50}$) and the reach-scale bankfull dimensions of: (a) bankfull depth; (b) bankfull area.

## 6 CONCLUSIONS

As a result of the recent TGP operation, the flow and sediment regime entering the YZR in the MYR has been altered significantly. The dramatic decrease of sediment load led to considerable adjustments in various fluvial variables of this gravel-sand bed reach. Therefore, the geomorphic response of the YZR to the TGP operation were investigated quantitatively, and the conclusions obtained include the following:

(i) The reduced sediment load entering the study reach led to a sharp increase in the fluvial erosion intensity, but also caused remarkable channel degradation and bed-material coarsening. The cumulative bankfull channel scour volume reached $1.59\times10^8$ m$^3$ in the YZR in 2002–2015, with the scour intensity being much greater in the YDR whose cumulative scour volume took up 89% of the value of the whole YZR. Besides, the riverbed in the YZR suffered significant bed-material coarsening since the TGP operation, and the coarsening degree of the bed material in the YCR was higher than that in the YDR;

(ii) The section-scale and reach-scale of bankfull channel dimensions are calculated annually from 2002 to 2015 in the YCR and the YDR. The reach-scale of bankfull widths changed slightly, owing to the high erosion-resistant capacity of riverbanks and the construction of bank-revetment work where the bankfull depths increased respectively by 1.57m and 3.28m, with a corresponding increase in bankfull area of about 6% and 17% in these reaches. In general, the adjustments in bankfull channel geometry are more dramatic in the YDR than in the YCR;

(iii) Empirical relationships for the YCR and YDR are developed between the reach-scale bankfull dimensions and the previous 5-year average fluvial erosion intensity during flood seasons at Yichang in 2002–2010. The relationships for the reach-scale bankfull widths were relatively weak in these two reaches, with weak correlation degrees of 0.16 and 0.04. However, the bankfull depth and area responded well to the altered flow and sediment regime, with the correlation degrees for both being equal to 0.98 in the YDR, which were higher than those of 0.61 and 0.71 in the YCR. This is due to such a fact that the bed-material coarsening process reduced the effect of the flow and sediment regime on the channel adjustments in the YCR;

(iv) A comprehensive empirical relationship is further proposed, with the previous flow and sediment regime and the bed-material coarsening both being considered. The correlation degrees for bankfull depth and cross-sectional area in the YCR increased to 0.93 and 0.91, respectively which is much higher than those obtained from the empirical equation which is merely considered for one influencing factor.

 

**ACKNOWLEDGEMENTS**

This work is supported by the National Natural Science Foundation of China (Grant Nos. 51579186 & 51339001). It is also partly supported by the National Key Research and Development Program of China (Grant No. 2016YFC0402303/05).

**REFERENCES**

Adamowski, J., Chan, H.F., Prasher, S.O., Ozga‐Zielinski, B. & Sliusarieva, A. (2012). Comparison of Multiple Linear and Nonlinear Regression, Autoregressive Integrated Moving Average, Artificial Neural Network, and Wavelet Artificial Neural Network Methods for Urban Water Demand Forecasting in Montreal, Canada. *Water Resources Research*, 48(1), 273-279.

Bartley, R., Keen, R.J., Hawdon, A.A., Hairsine, P.B., Disher, M.G. & Kinsey-Henderson, A.E. (2008). Bank Erosion and Channel Width Change in a Tropical Catchment. *Earth Surface Processes and Landforms*, 33(14), 2174-2200.

Cao, G.J. & Wang. J. (2015). *Measurements and Studies of Hy-Drological and Sediment Data in the Three Gorges Projec*t. Science press, Beijing. (In Chinese)

Curran, J.C. & Wilcock, P.R. (2005). Effect of Sand Supply on Transport Rates in a Gravel-Bed Channel. *Journal of Hydraulic Engineering*, 131(11), 961-967.

Changjiang Water Resources Commission (CWRC). (2015). *Analysis of Channel Degradation Downstream of the Three Gorges Dam*. Scientific Report of CWRC, Wuhan. (In Chinese)

Galay, V.J. (1983). Causes of River Bed Degradation. *Water Resources Research*, 19(5), 1057-1090.

Harman, C., Stewardson, M. & DeRose, R. (2008). Variability and Uncertainty in Reach Bankfull Hydraulic Geometry. J*ournal of Hydrology*, 351(1), 13-25.

Kleinhans, M.G., Wilbers, A.W.E., De Swaaf, A. & Van Den Berg, J.H. (2002). Sediment Supply-Limited Bedforms in Sand-Gravel Bed Rivers. *Journal of Sedimentary Research*, 72(5), 629-640.

Knighton, D. (1998). *Fluvial Forms and Processes*. Wiley, New York.

Kuhnle, R.A., Horton, J.K., Bennett, S.J. & Best, J.L. (2006). Bed Forms in Bimodal Sand-Gravel Sediments: Laboratory and Field Analysis. S*edimentology*, 53(3), 631-654.

Lee, J.S. & Julien, P.Y. (2006). Downstream Hydraulic Geometry of Alluvial Channels. *Journal of Hydraulic Engineering*, 132(12), 1347-1352.

Leopold, L.B. & Maddock T. (1953). *The Hydraulic Geometry of Stream Channels and Some Physiographic Implications*. US Geological Survey Professional Paper No. 252, Washington, DC.

Luo, X.L., Zeng, E.Y., Ji, R.Y. & Wang, C.P. (2007). Effects of In-Channel Sand Excavation on the Hydrology of the Pearl River Delta, China. *Journal of Hydrology*, 343(3), 230-239.

Ma, Y.X., Huang, H.Q., Nanson, G.C., Li, Y. & Yao, W.Y. (2012). Channel Adjustments in Response to the Operation of Large Dams: The Upper Reach of the Lower Yellow River. *Geomorphology,* 147, 35-48.

Navratil, O. & Albert, M.B. (2010). Non-Linearity of Reach Hydraulic Geometry Relations. J*ournal of Hydrology,* 388(3), 280-290.

O'Hare, M.T., Mcgahey, C., Bissett, N., Cailesc, C., Henvillec, P. & Scarlettc, P. (2010). Variability in Roughness Measurements for Vegetated Rivers Near Base Flow, in England and Scotland. *Journal of Hydrology,* 385(1), 361-370.

Orrú, C., Chavarrias, V., Ferrara, V., Stecca, G. & Blom, A. (2015). *A Laboratory Experiment on the Evolution of a Sand Gravel Reach under a Lack of Sediment Supply,* paper presented at the 36th IAHR World Congress, 28 June - 3 July 2015, The Hague, The Netherlands.

Petts, G.E. & Gurnell, A.M. (2005). Dams and Geomorphology: Research Progress and Future Directions. *Geomorphology*, 71(1), 27-47.

Phillips, J.D. (2009). Changes, Perturbations, and Responses in Geomorphic Systems. *Progress in Physical Geography,* 33(1), 17-30.

Piegay, H., Darby, S.E., Mosselman, E. & Surian, N. (2005). A Review of Techniques Available for Delimiting the Erodible River Corridor: A Sustainable Approach to Managing Bank Erosion. *River Research and Applications,* 21(7), 773-789.

Shibata, K. & Ito, M. (2014). Relationships of Bankfull Channel Width and Discharge Parameters for Modern Fluvial Systems in the Japanese Islands. *Geomorphology,* 214, 97-113.

Shin, Y.H. & Julien, P.Y. (2010). Changes in Hydraulic Geometry of the Hwang River below the Hapcheon Re-regulation Dam, South Korea. *International Journal of River Basin Management*, 8(2), 139-150.

Stewardson, M. (2005). Hydraulic Geometry of Stream Reaches. *Journal of Hydrology,* 306(1), 97-111.

Tanny, J., Cohen, S., Berger, D., Teltch, B., Mekhmandarov, Y., Bahar, M., Katul, G.G. & Assouline, S. (2011). Evaporation from a Reservoir with Fluctuating Water Level: Correcting for Limited Fetch. *Journal of Hydrology,* 404(3), 146-156.

Vecchia, A.V. & Cooley, R.L. (1987), Simultaneous Confidence and Prediction Intervals for Nonlinear Regression Models with Application to a Groundwater Flow Model. *Water Resources Research,* 23(7), 1237-1250.

 

Venditti, J.G. & Church, M. (2014). Morphology and Controls on the Position of a Gravel-Sand Transition: Fraser River, British Columbia. *Journal of Geophysical Research: Earth Surface,* 119(9),1959-1976.

Wilbers, A.W.E. & Ten Brinke, W.B.M. (2003). The Response of Subaqueous Dunes to Floods in Sand and Gravel Bed Reaches of the Dutch Rhin. *Sedimentology*, 50(6), 1013-1034.

Wilcock, P.R. & DeTemple, B.T. (2005). Persistence of Armor Layers in Gravel-Bed Streams. *Geophysical Research Letters,* 32(8).

Williams, G.P. & Wolman, M.G. (1984). *Downstream Effects of Dams on Alluvial Rivers.* Professional Paper 1286, US Geological Survey, Washington DC.

Wohl, E.E. & Wilcox, A. (2005). Channel Geometry of Mountain Streams in New Zealand. *Journal of Hydrology,* 300(1), 252-266.

Wu, B.S., Xia, J.Q., Fu, X.D., Zhang, Y.F. & Wang, G.Q. (2008). Effect of Altered Flow Regime on Bankfull Area of the Lower Yellow River, China. *Earth Surface Processes and Landforms,* 33(10), 1585-1601.

Wu, F.C. & Chou, Y.J. (2003). Simulation of Gravel-Sand Bed Response to Flushing Flows Using a Two-Fraction Entrainment Approach: Model Development and Flume Experiment. *Water Resources Research*, 39(8).

Xia, J.Q., Deng, S.S., Lu, J.Y., Xu, Q.X., Zong, Q.L. & Tan, G.M. (2016). Dynamic Channel Adjustments in the Jingjiang Reach of the Middle Yangtze River. *Scientific Reports*, 6, Doi:10.1038/srep22802.

Xia, J.Q., Li, X.J., Li, T., Zhang, X.L. & Zong, Q.L. (2014a), Response of Reach-Scale Bankfull Channel Geometry in the Lower Yellow River to the Altered Flow and Sediment Regime. *Geomorphology*, 213, 255-265.

Xia, J.Q., Zong, Q.L., Zhang, Y., Xu, Q.X & Li, X.J. (2014b). Prediction of Recent Bank Retreat Processes at Typical Sections in the Jingjiang Reach After the TGP Operation. *Science China (Technological Sciences),* 57(8), 1490-1499.

 

Proceedings of the 37th IAHR World Congress
August 13 – 18, 2017, Kuala Lumpur, Malaysia

# DETERMINATION OF OPTIMUM RACK ANGLE OF TYROLEAN TYPE INTAKES TO INCREASE WATER CAPTURE EFFICIENCY

MUSTAFA GOGUS[(1)], KUTAY YILMAZ[(2)] & ABIDDIN BERHAN MELEK[(3)]

[(1,2,3)] Middle East Technical University Civil Engineering Department Hydromechanics Laboratory, Ankara, Turkey, mgogus@metu.edu.tr; ktyylmz@gmail.com; berhanmelek@gmail.com

## ABSTRACT

Run-of-river type power plants are preferred for locations where the construction of a reservoir is not possible or economic. Tyrolean weir is a water inlet structure in which water is abstracted from the main channel through a screen over a collection channel. Tyrolean weirs are known to be a very suitable solution to separate major part of the sediment in the river flow while it diverts the desirable amount of water to the system. Within the current study, a physical model of a Tyrolean weir was constructed in a channel of 7m long and 1.98m wide at the laboratory. By varying the dimensions of the various components of the Tyrolean model; the length and inclination angle of the rack and the distance between the rack bars and the amount of water entering the system was measured. Based on a dimensionless expression derived by applying dimensional analysis to the related parameters for water capture efficiency of the system, its variation with the relevant parameters is presented. The results of these studies are compared with those previously obtained and the range of the rack angle which gives the maximum water capture efficiency is determined as 22°-25°.

**Keywords:** Open channel flow; run-of-river type hydropower plants; tyrolean type intakes; intake racks; water capture efficiency.

## 1 INTRODUCTION

Hydropower is the most common and reliable renewable clean energy source. Considering the country's hydraulic potential, hydropower plants are one of the best ways of producing electricity. In addition, all possible big dams are either under construction or in operation. Therefore, remaining hydropower potential is expected to be used by means of small hydropower plants.

Run-of-river type power plants are preferred for locations where the construction of a reservoir is not possible or economically unfeasible. The main problem of the run-of-river type power plants is the sediment transported by flow from the river to the plant. Even the smallest size of the sediment can cause serious damages on the parts of a power plant, especially on the turbines.

Tyrolean weir is a water inlet structure in which water is abstracted from the main channel through a screen over a collection channel. Tyrolean weirs are known to be a very useful tool for separating considerable amount of the sediment from the flow that reaches to turbines while it conveys desirable amount of water to the system. The slope of the screen is one of the important parameters of a Tyrolean weir influencing the amount of water to be diverted from the main channel. If the screen slope is too small, the amount of water to be diverted from the main channel increases for sediment-free main channel flows, but at the same time, the risk of having the screen bar openings clogged by the incoming sediment increases if the upstream flow is carrying sediment. On the other hand, larger screen slopes for both the water and sediment capture capacities of the system decreases. Therefore, the determination of optimum screen slope is important from hydraulics point of view.

In the literature there are limited number of studies related to the effect of screen slope of Tyrolean weirs on the water capture efficiency of the system (Brunella and Hager, 2003; Kamanbedast and Bejestan, 2008; Yilmaz, 2010; Sahiner, 2012). Based on the experimental data provided from a physical model of a bottom intake Kamanbedast and Bejestan (2008) stated that the ratio of the diverted discharge to the total incoming discharge is function of only the area spacing of the bars and the rack slope, and the discharge ratio reaches maximum at a slope of about 30% ($\theta$=16.7°) and then the discharge ratio decreases. Yilmaz (2010) and Sahiner (2012) conducted similar experiments to the present study in the same physical model with various screen slopes as to be stated in the following sections and demonstrated the effect of screen slope on the variation of water capture efficiency. They observed that the optimum screen slope would be between $\theta$=14.5° and 27.8°. In the current study, a series of experiments are conducted in a Tyrolean weir model which had been used by Yilmaz (2010) and Sahiner (2012), with two screens of different slopes, $\theta$=19° and $\theta$=23°, which had not been covered by the previous researchers, to determine the optimum rack angle to obtain the maximum amount of water into the channel that conveys water to the turbines for electricity purposes.

 

## 2 THEORETICAL ANALYSIS

For a Tyrolean weir of which the hydraulic and geometric parameters are described in Figure 1 and the following equation for the diverted discharge $(q_w)_i$ through the bottom racks can be written as a function of the appropriate variables, assuming that the screen comprises of the circular bars and surface tension where effects of viscosity and fluid compressibility are negligible.

$$(q_w)_i = f[\,(q_w)_T, e, a, L, \theta, g, \rho_w] \qquad [1]$$

where $(q_w)_T$ is the total water discharge of the flow approaching the rack per unit channel width, e is the clear distance between bars, a is the distance between centers of the two adjacent trash rack bars, L is the rack length, θ is the angle of inclination of the rack, g is the gravitational acceleration and $\rho_w$ is the density of water.

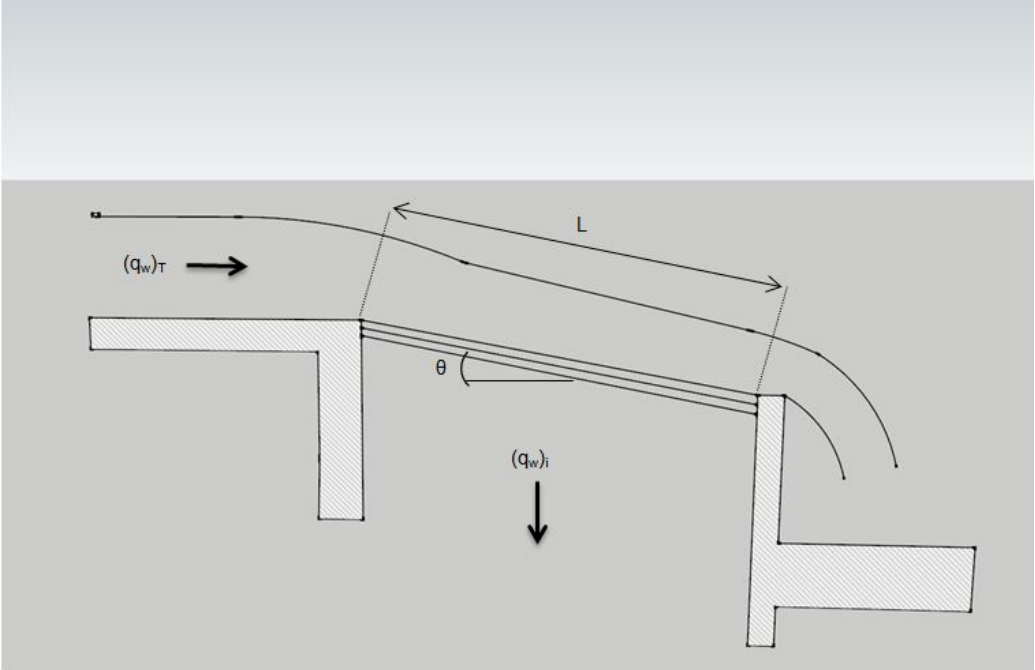


**Figure 1**. Definition sketch for a Tyrolean weir.

Selecting $(q_w)_T$, e and $\rho_w$ as the repeating variables and applying the Buckingham's π theorem, the following relationship is obtained.

$$\frac{(q_w)_i}{(q_w)_T} = f_1\left[\frac{(q_w)_T{}^2}{e^3 g}, \frac{L}{e}, \frac{a}{e}, \theta\right] \qquad [2]$$

where $[(q_w)_i/(q_w)_T]$ can be named as "water capture efficiency" of the Tyrolean weir and $(q_w)_T{}^2/e^3 g$ is the square of the Froude number $(F_r)_e$ based on bar opening. Equation 2 can also be written as

$$\frac{(q_w)_i}{(q_w)_T} = f_1\left[(F_r)_e, \frac{L}{e}, \frac{a}{e}, \theta\right] \qquad [3]$$

## 3 EXPERIMENTAL SETUP AND PROCEDURE

A physical model was built at the Hydromechanics Laboratory of the Civil Engineering Department in the Middle East Technical University. The model, shown in Figure 2, consists of a water intake pipe, a reservoir at the head of the main channel, a main channel, water and sediment intake screen, collection channel located just below the intake screen and a side channel with a sediment trap reservoir located at the head of the side channel.

 

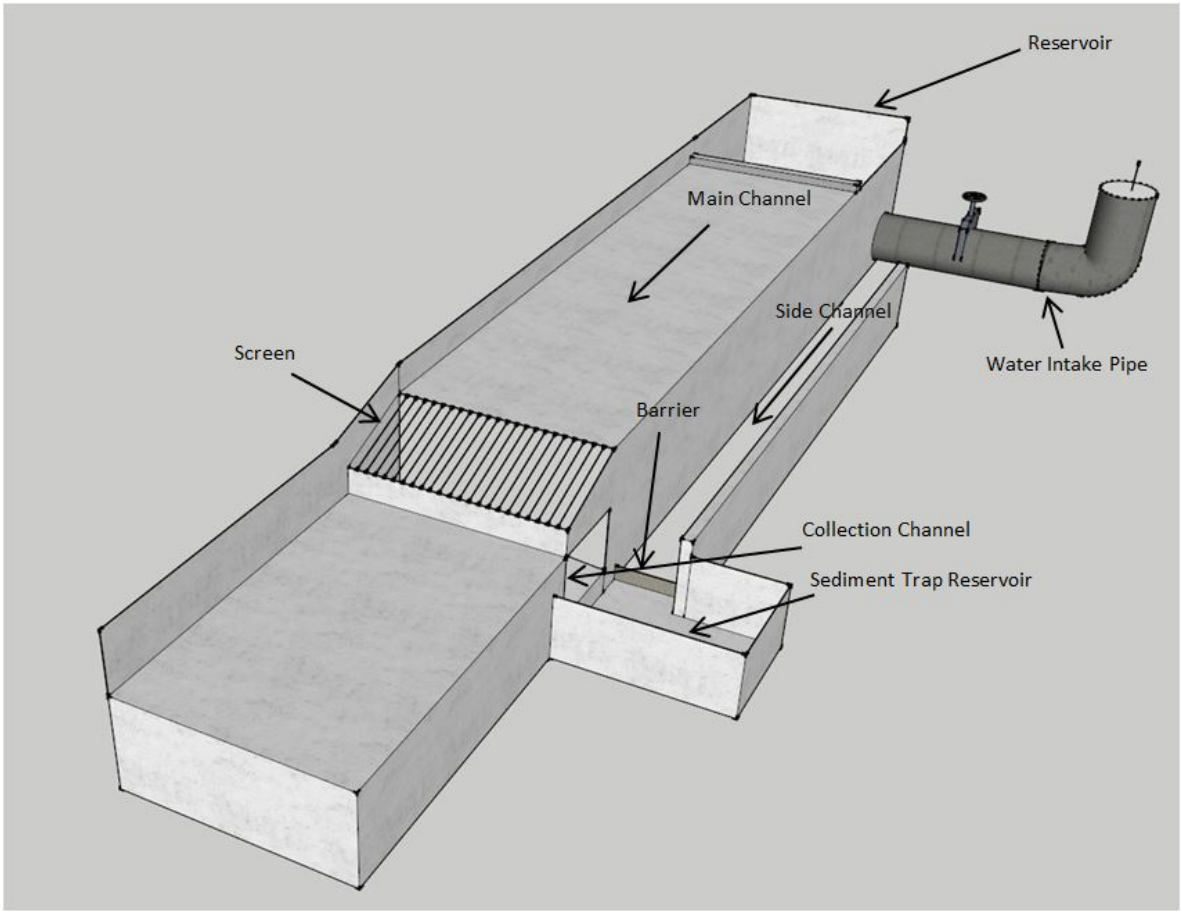


**Figure 2**. Schematic representation of the experimental setup.

Water was supplied to the system by a large, elevated, constant head reservoir through a water intake pipe which is 30cm in diameter. A mechanical valve was placed at the end of a water intake pipe to adjust the discharge. In addition, an ultrasonic flow meter was installed on water intake pipe to measure the total discharge on the system. Intake pipe directs water to a reservoir which is 2.0m in length, 2.0m in width and 1.5m in height. From the reservoir which was placed at the head of the main channel, after having the water passed through a filter layer formed by bricks to reduce turbulence of the water, water was directed to the main channel which is 1.98m in width, 7.0m in length and has a slope of $S_0$=0.001.

The Tyrolean screen was placed at the downstream end of the main channel. The screen was made of aluminum bars of circular cross section that are 1 cm in diameter. Experiments were repeated for three different screens each one having different clear distances between bars ($e_1$=3mm, $e_2$=6mm and $e_3$=10mm) and at two different screen slopes ($\theta$=19˚ and 23˚).

The collection channel with 1.98m in length, 0.60m in width and 0.33cm in height was placed just below the Tyrolean screen and has a bottom slope of 10%. Water and sediment from the main channel are directed to the sediment trap reservoir via collection channel. To keep incoming sediment particles within the sediment trap reservoir, 0.20m high barrier was placed at the downstream part of the sediment trap reservoir.

After the sediment trap reservoir, water enters the side channel that conveys water to the turbines. The side channel is 0.70m in width and 6.50m in length.

In this experimental setup, the similar investigations were conducted with the same screens ($e_1$=3mm, $e_2$=6mm and $e_3$=10mm) at different screen angles by Yilmaz (2010); $\theta$=4.8˚, 9.6˚ and 14.5˚, and Sahiner (2012); $\theta$=27.8˚, 32.8˚ and 37.0˚. The purpose of the experiments was to determine the water capture efficiencies $[(q_w)_i / (q_w)_T]$ of the given Tyrolean screen lengths L. The surface area of the screens was to be tested which covers at desired lengths with a thin steel plate from downstream to upstream to obtain the desired partial length. For the Tyrolean screen with 3mm clear distance between bars, the first screen length was 5cm. After placing the screen and the steel plate, the valve on the water intake pipe was opened to give the system a discharge corresponding to 3cm flow depth at the upstream section of the main channel. Using the manometer readings in the main channel and side channel, the total discharge and the discharge of the side channel respectively were calculated by means of the rating curves derived earlier. The manometer readings were recorded for each 1cm increment in the flow depth at the main channel until 13cm flow depth corresponding as to the maximum discharge was reached. After completing the experiment of the initial screen length, the screen length was increased to 10cm. The experiments were repeated with 5cm

 

increments in the screen length until the total discharge corresponds to 13cm flow depth in the main channel was diverted by the Tyrolean screen. The experimental procedure was similar for each screen having different angles of inclination (θ=19° and θ=23°) and clear distance between bars ($e_1$=3mm, $e_2$=6mm and $e_3$=10mm).

## 4 ANALYSIS OF THE EXPERIMENTAL DATA AND DISCUSSION OF THE RESULTS

The analyses of the experimental data related to the water capture efficiency are presented in the following sections.

### 4.1 Relationship between the Water Capture Efficiencies (WCE) and the related dimensionless parameters for steel racks

Referring to the relationship for the water capture efficiency of a Tyrolean screen expressed in Equation 3, the data of the related parameters for each experimental setup tested were plotted. Figures 3 and 4 show only the ones related to the first screen ($e_1$=3mm) with two different screen angles of θ=19˚ and θ=23˚. All of the figures plotted for the variation of $[(q_w)_i / (q_w)_T]$ with $(F_r)_e$ showed that the WCE depends on L/e and $(F_r)_e$ for a setup of known e/a and θ. For a screen of given slope and L/e, the WCE value decreases with increasing $(F_r)_e$. As the value of L/e decreases, the dependency of the WCE on $(F_r)_e$ decreases and becomes almost negligible and approaches to the value of 1.0 for L/e values greater than about 83.33.

When the bar spacing of the screen is increased from $e_1$ to $e_2$ or from $e_2$ to $e_3$ while keeping the screen inclination and bar length constant, the related figures reveal that the numerical value of $(F_r)_e$ becomes smaller for a given main channel discharge, and this change in the value of e results in higher WCE values. The similar results were obtained by Yilmaz (2010) and Sahiner (2012) for the variation of WCE with the related dimensionless parameters.

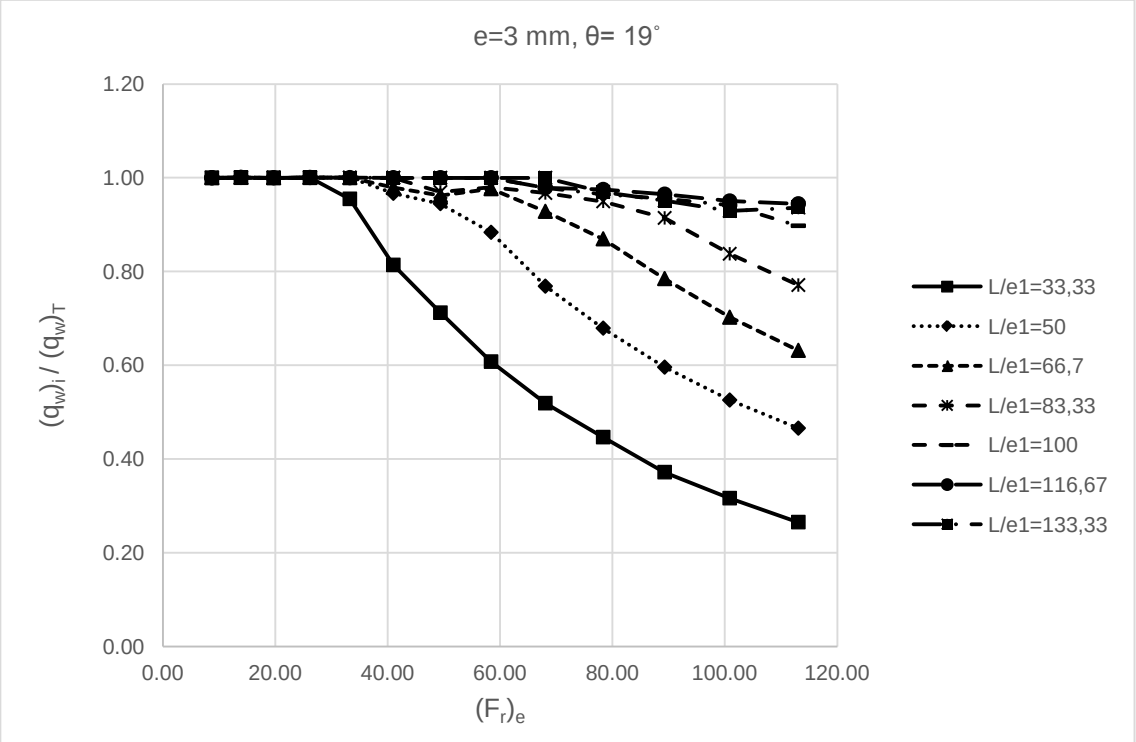


**Figure 3**. Water capture efficiency for the Tyrolean screen of $e_1/a_1$=0.23 and θ=19˚.

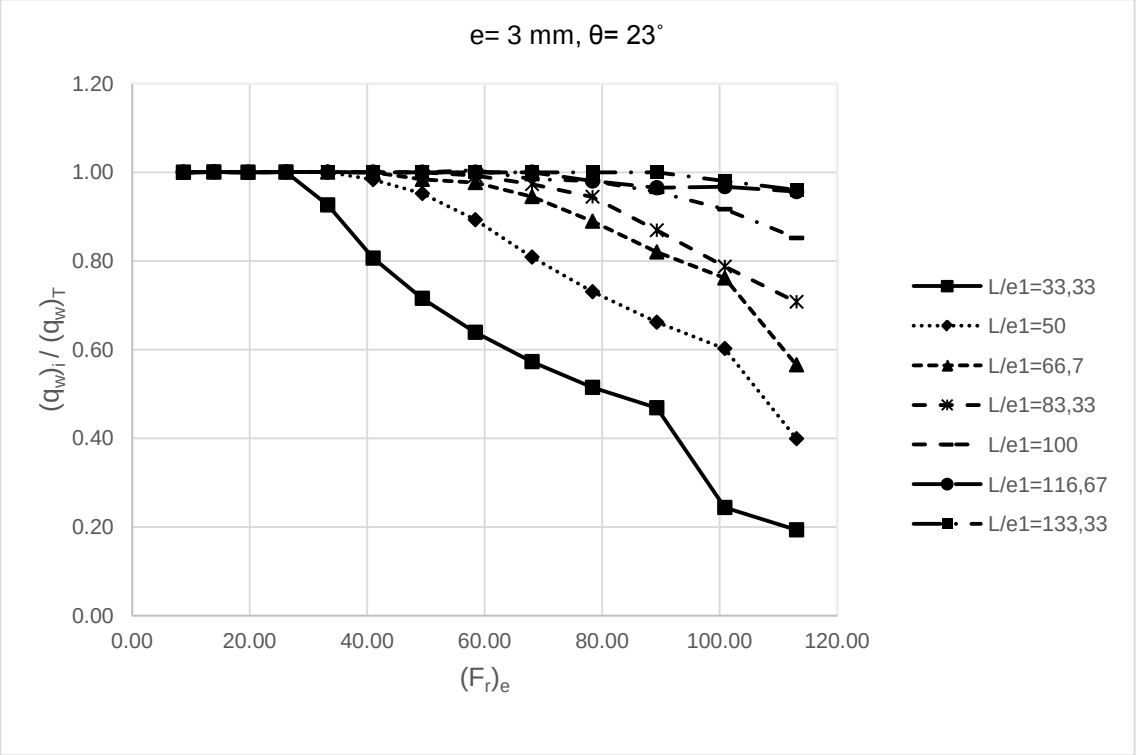


**Figure 4**. Water capture efficiency for the Tyrolean screen of $e_1/a_1$=0.23 and θ=23˚.

4.2 Variation of water capture efficiency with screen angle

The water capture efficiency data of the present study and those of Yilmaz (2010) (θ=14.5°, 9.6° and 4.8°) and Sahiner (2012) (θ=27.8°, 32.8° and 37.0°) were plotted as a function of screen slope θ and $(F_r)_e$ for given values of L/e and e/a. Some of these plots for three different screens tested in this study were presented in Figures 5-12. In all of these figures it is seen that for the smallest $(F_r)_e$ tested which correspond to the small main channel discharges, the variation of WCE with θ is almost negligible at any screen length tested. As the value of $(F_r)_e$ increases, the effect of θ on WCE becomes more significant in such a way that the value of WCE first decreases with increasing θ up to the value of about 15° and then increases with increasing value of θ up to the value of about 20°, and finally decreases again with increasing θ. In all the figures presented here it is observed that the value of WCE for the screen of θ=5° and θ=20° attain almost the same maximum values for a given $(F_r)_e$. For screens of known rack bar openings e/a and slope θ, if the dimensionless screen length L/e increases, the water capture efficiency of the screen attains larger values as expected.

The range of the rack angle which will provide the maximum WCE among the θ values tested can be stated as 22˚-25˚ for the ranges of the parameters tested within this study and those of Yilmaz (2010) and Sahiner (2012).

 

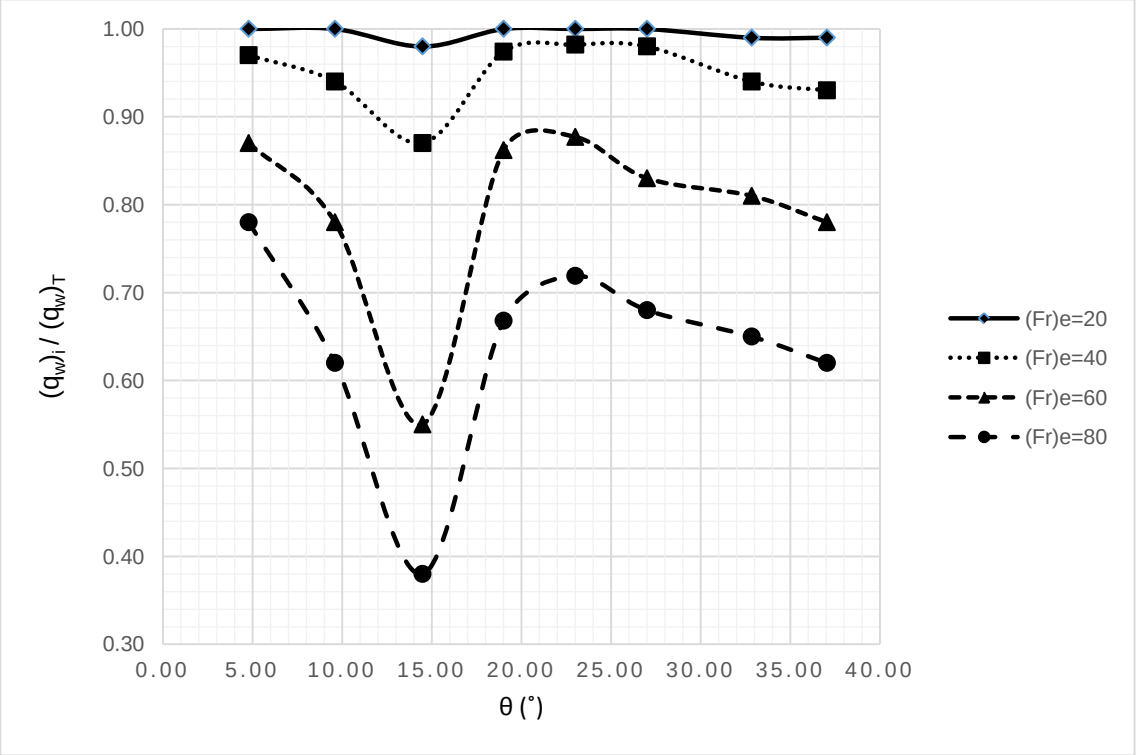


**Figure 5**. Variation of water capture efficiency with θ and $(F_r)_e$ for the screen of $L/e_1$=50.00 and $e_1/a_1$=0.23.

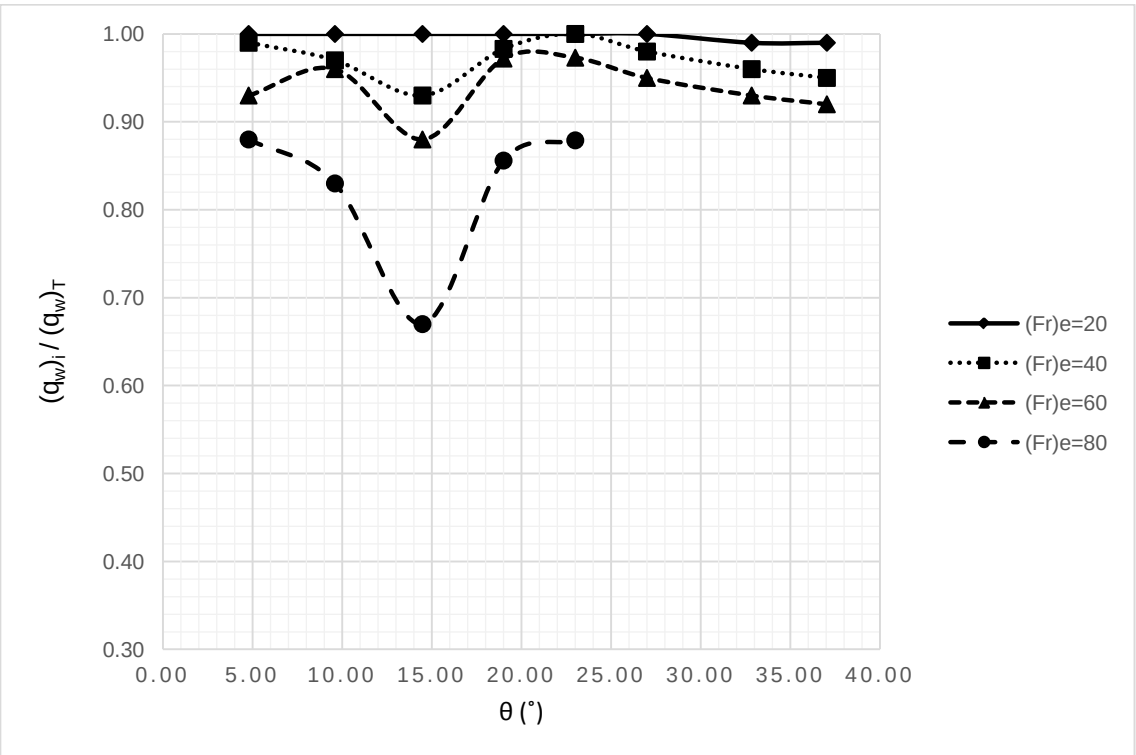


**Figure 6**. Variation of water capture efficiency with θ and $(F_r)_e$ for the screen of $L/e_1$=66.67 and $e_1/a_1$=0.23.

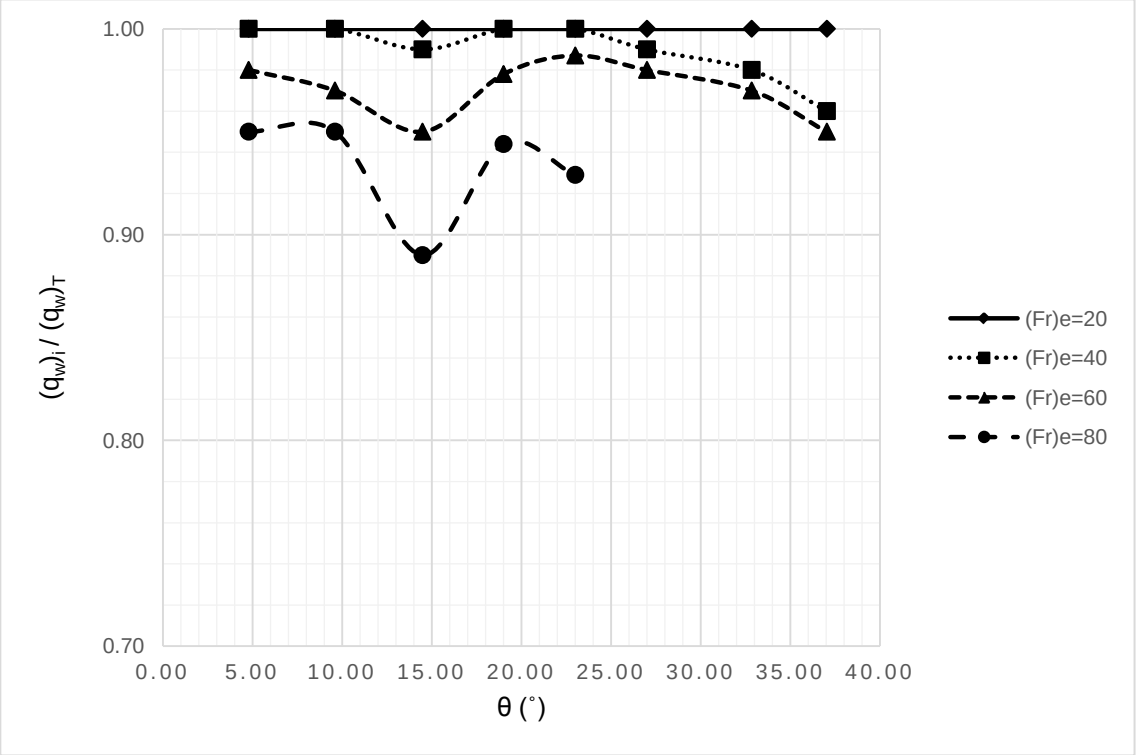


**Figure 7**. Variation of water capture efficiency with θ and $(F_r)_e$ for the screen of $L/e_1$=83.33 and $e_1/a_1$=0.23.

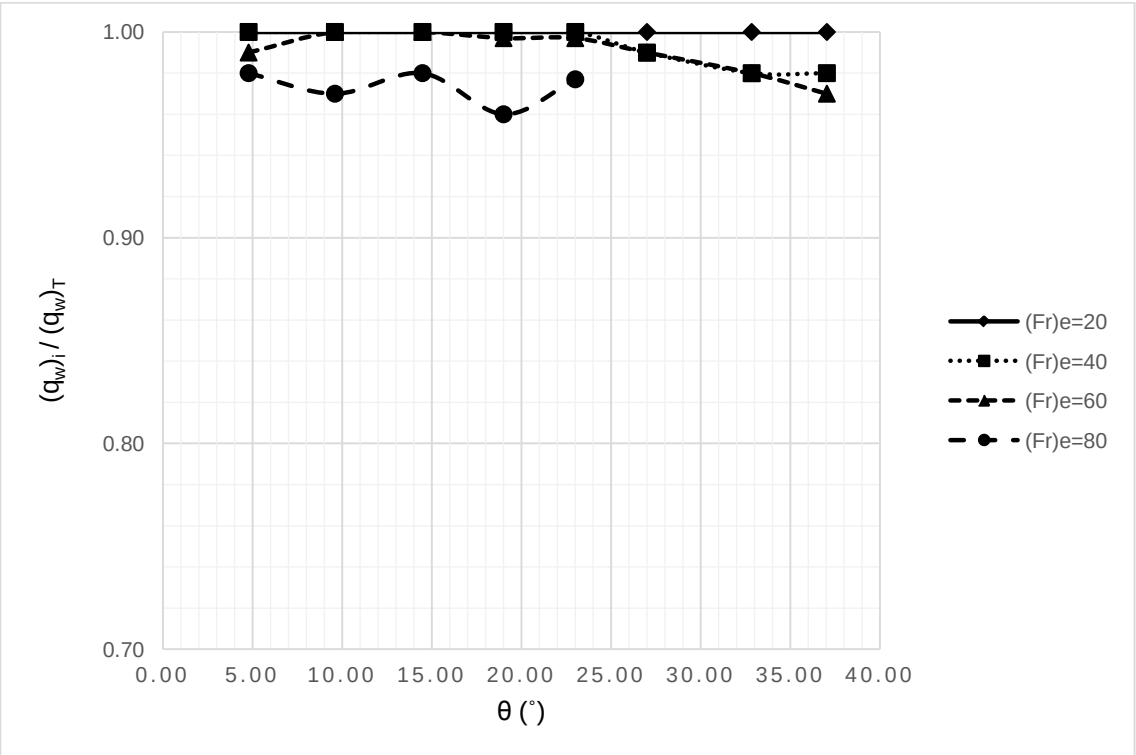


**Figure 8**. Variation of water capture efficiency with θ and $(F_r)_e$ for the screen of $L/e_1$=100.00 and $e_1/a_1$=0.23.

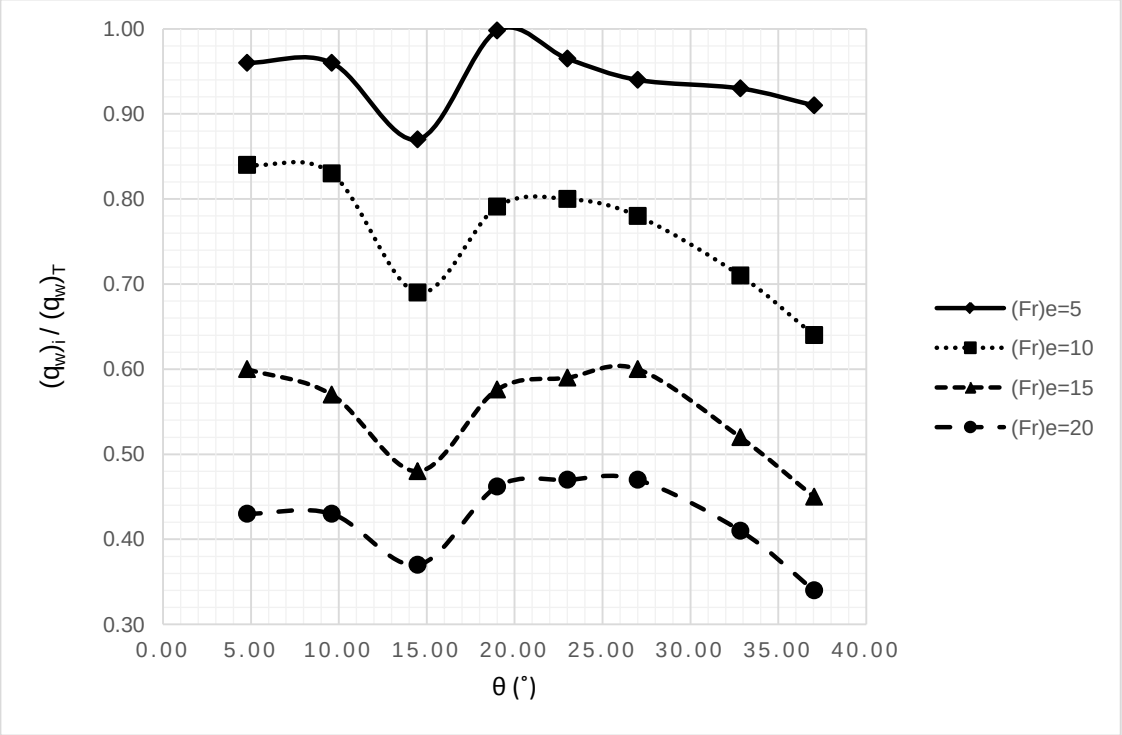


**Figure 9**. Variation of water capture efficiency with θ and $(F_r)_e$ for the screen of $L/e_2$=8.33 and $e_2/a_2$=0.375.

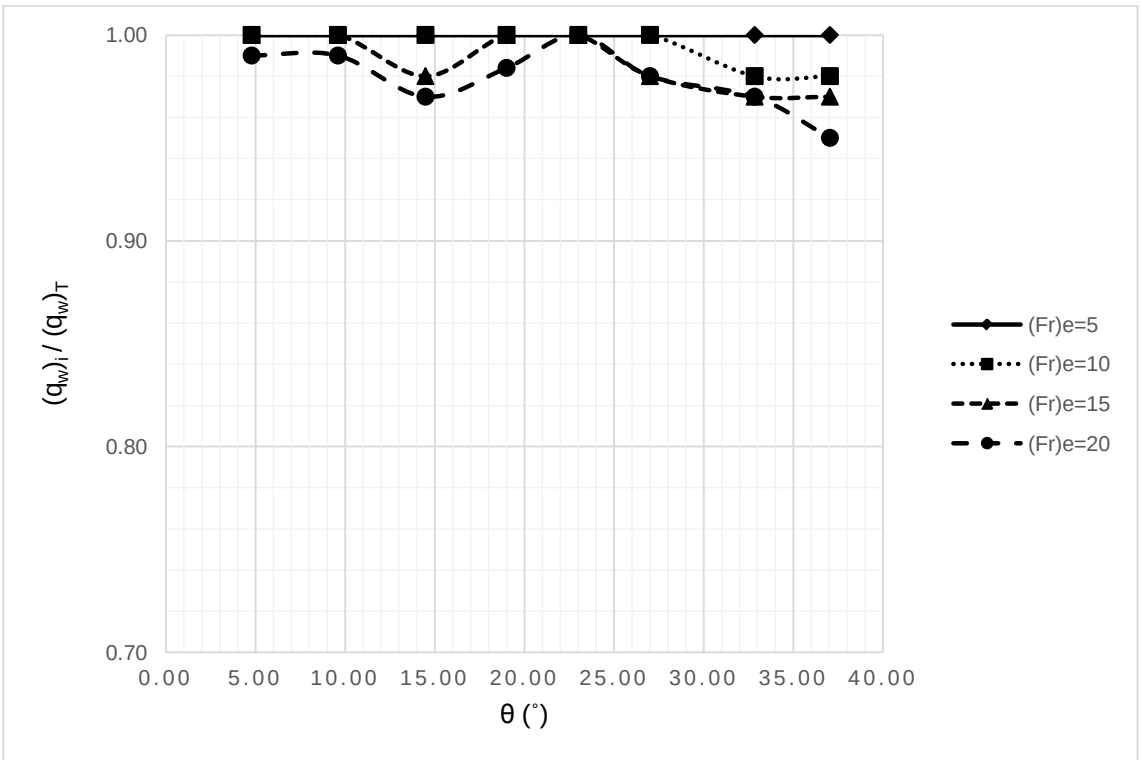


**Figure 10**. Variation of water capture efficiency with θ and $(F_r)_e$ for the screen of $L/e_2$=33.33 and $e_2/a_2$=0.375.

 

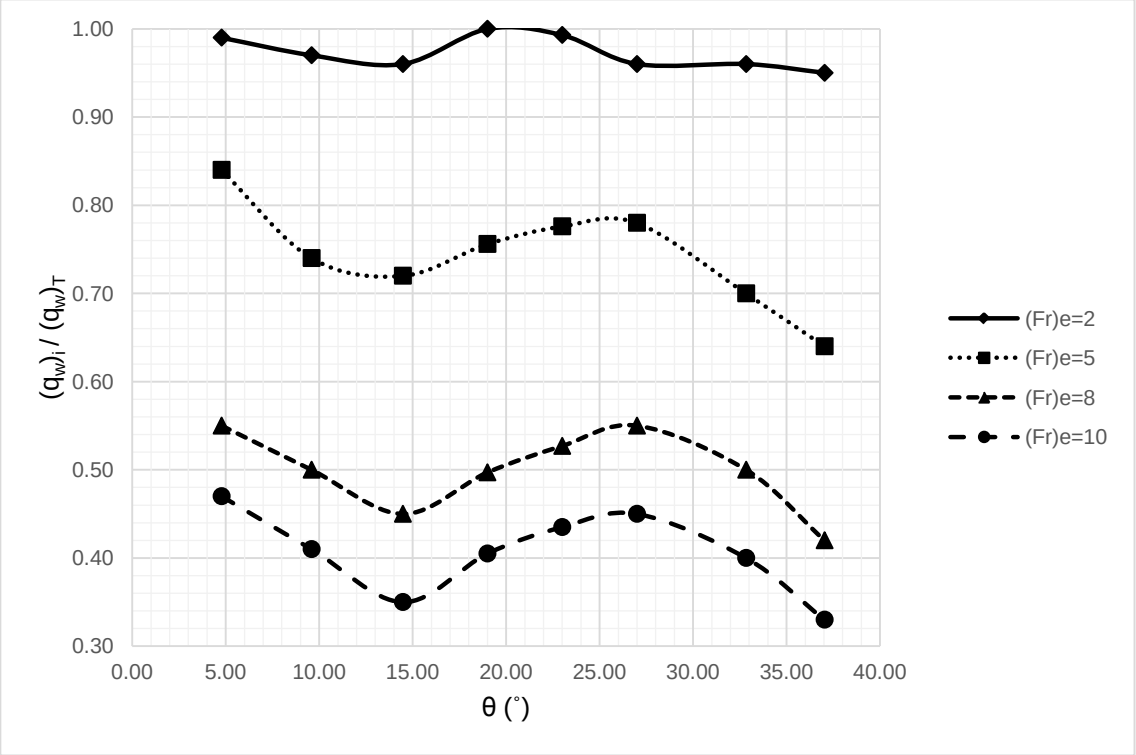


**Figure 11**. Variation of water capture efficiency with θ and $(F_r)_e$ for the screen of $L/e_3$=5.00 and $e_3/a_3$=0.5.

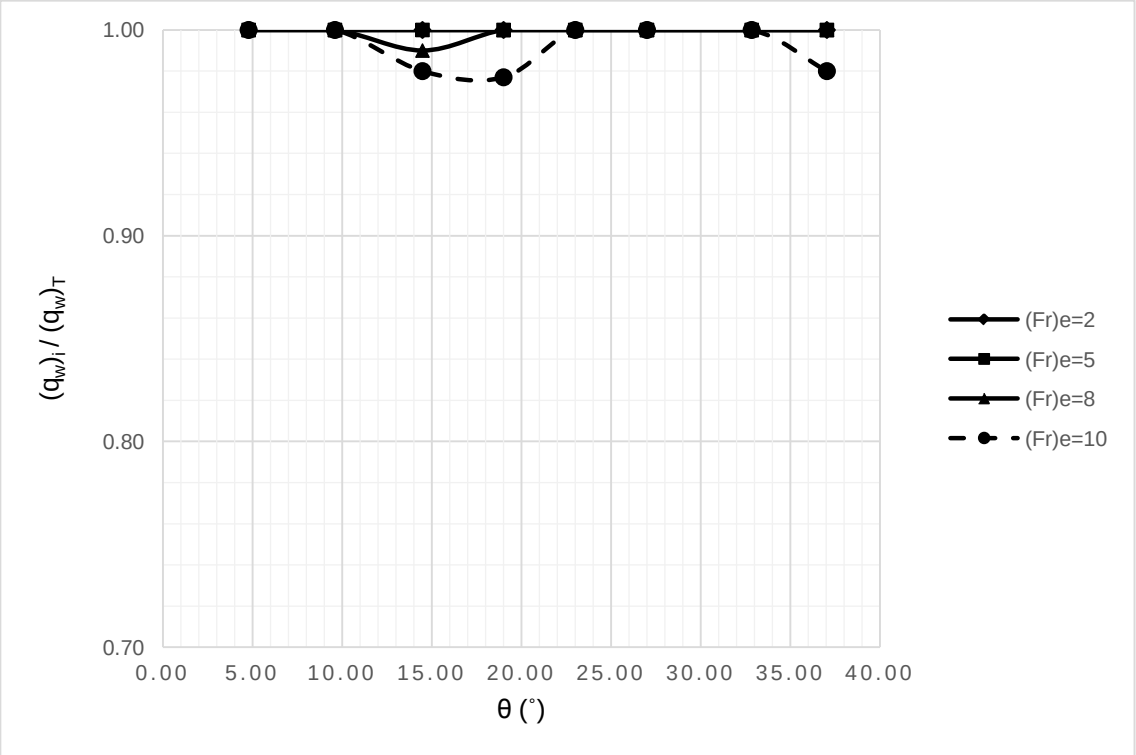


**Figure 12**. Variation of water capture efficiency with θ and $(F_r)_e$ for the screen of $L/e_3$=20.00 and $e_3/a_3$=0.5.

## 5 CONCLUSIONS

From the analysis of the experimental results the following conclusions can be drawn:

- Water capture efficiency of Tyrolean weirs were presented as a function of dimensionless parameters $(F_r)_e$, L/e, e/a and θ using the dimensional analysis.
- The water capture efficiency, WCE of a Tyrolean screen strongly depends on L/e and $(F_r)_e$ for a screen of known e/a and θ. For a given L/e the value of WCE decreases with increasing $(F_r)_e$ .

 

- With increasing θ, WCE decreases for a screen of given bar spacing of L/e and $(F_r)_e$.
- When the bar spacing of the screen increased while keeping the screen inclination and bar length constant, for a given main channel discharge WCE values increase.
- Based on the tests conducted on Tyrolean weirs within the scope of this study and those by Yilmaz (2010) and Sahiner (2012) it can be stated that the racks having the inclination angles between 22˚ and 25˚ produce the maximum WCE values within the ranges of experimental parameters tested in this study.

**ACKNOWLEDGEMENTS**

This work is supported by TUBITAK, The Scientific and Technological Research Council of Turkey (Grant No. 214M028), which is gratefully acknowledged here.

**REFERENCES**

Brunella, S., Hager, W.H. & Minor, H.E., (2003). Hydraulics of Bottom Rack Intake. *J. of Hydraulic Engineering*, 129(1), 2-10.

Kamanbedast, A.A. & Bejestan, M.S. (2008). Effects of Slope and Area Opening on the Discharge Ratio in Bottom Intake Structures. *Journal of Applied Sciences*, 8(14), 2631-2635.

Sahiner, H. (2012). Hydraulic Characteristics of Tyrolean Weirs Having Steel Racks and Circular-Perforated Entry. *MSc Thesis,* Middle East Technical University, Ankara, Turkey.

Yilmaz, N.A. (2010). Hydraulic Characteristics of Tyrolean Weirs. *MSc Thesis,* Middle East Technical University, Ankara, Turkey.

 

Proceedings of the 37th IAHR World Congress
August 13 – 18, 2017, Kuala Lumpur, Malaysia

# MATHEMATIC MODEL FOR FLOW AND SUSPENDED SEDIMENT TRANSPORT WITH BIOFILMS

HAOJIE LAI[(1)], GUOJIAN HE [(2)], HONGWEI FANG[(3)], WEI CHENG[(4)] & LEI HUANG[(5)]

[(1,2,3,4,5)] State Key Laboratory of Hydro-science and Engineering,
Department of Hydraulic Engineering, Tsinghua University, Beijing, China
laihj14@mails.tsinghua.edu.cn; fanghw@mail.tsinghua.edu.cn; dgjjcw@163.com; huangl05@mails.tsinghua.edu.cn

## ABSTRACT

Sediment erosion, transport and deposition play an essential role in the natural river succession, pollutants transport and habitats changes. Mathematical modeling is an effective tool to enhance our understanding of sediment transport. Previous models for sediment transport have been proposed based on clean sediment without biological process. However, sediment is pervasively coated by microorganisms and extracellular polymeric substances (EPS), which significantly increase erosion threshold due to the role of biological cohesion. In this paper, a mathematical model for flow and suspended sediment transport for biofilm coated sediment (bio-sediment) is proposed. In the hydrodynamic module, the bed resistance and bedform dynamics for bio-sediment are applied to the river bed boundary. In the suspended sediment transport module, the critical erosion velocity, settling velocity and reference concentration for bio-sediment are integrated for sediment transport. The proposed model is applied to flume experiments for bio-sediment and results show that the proposed model can reasonably reflect the flow and suspended sediment transport with biofilm coating.

**Keywords:** Biofilm; bedform dynamics; suspended sediment transport; mathematic model.

## 1 INTRODUCTION

In the aquatic system, release and relocation of contaminants are associated with sediment erosion, transport, and deposition, which is critical to the river succession and the aquatic environment (Förstner et al., 2004; Paterson et al., 2000). Previous studies on sediment transport were mainly based on laboratory experiments using clean sediment (Jepsen et al., 1997; Mcneil et al., 2004). Over the past several decades, a variety of sediment transport models have been proposed without considering the effects of biological materials (Papanicolaou et al., 2008). However, most natural sediment is prevalently coated by biofilms (Gerbersdorf et al., 2009; Righetti and Lucarelli, 2007), which are composed of microorganisms (e.g., bacteria, microalgae and fungi) and their metabolic products extracellular polymeric substances (EPS) (Flemming and Wingender, 2010; Gerbersdorf and Wieprecht, 2015), especially in eutrophic water bodies. Biofilms generate biological cohesion and increase erosion threshold by preventing sediments from moving independently, resulting significant influence on sediment transport (Fang et al., 2016; Fang et al., 2015).

In recent years, researches on the biofilm coated sediment (bio-sediment) have been proposed in marine systems (Black et al., 2002; Stal, 2003; Underwood and Paterson, 2003), and in freshwater (Battin and Sengschmitt, 1999; Cyr and Morton, 2006; Droppo and Amos, 2001; Hirst et al., 2003). The basic physical properties such as the architecture, size gradation and the morphology of bio-sediment have been proposed by environmental scanning electron microscope (ESEM) (Fang et al., 2012; Zhao et al., 2011) as show in (a) Original sediment. (b) Bio-sediment (Zhao et al., 2011).

Figure 1, in which, biofilms cover fine sediment and bind the sand grain and organic materials. In addition, transport characteristics such as settling velocity, critical erosion velocity and the bed resistance have been studied for bio-sediment (Fang et al., 2017; Fang et al., 2014; Shang et al., 2014) . Most of these studies focus on several aspects of the effects of biofilms on hydrodynamics and sediment transport. However, there is very little research about the sediment transport model for bio-sediment.

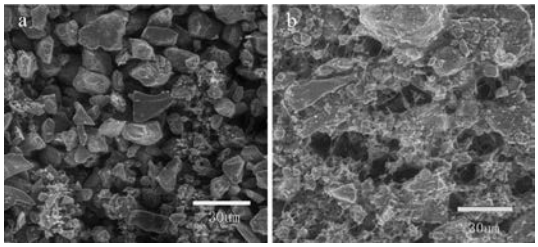


(a) Original sediment. (b) Bio-sediment (Zhao et al., 2011).
**Figure 1.** ESEM images of sediment samples.

 

In this paper, the basic physical properties and the transport characteristics are integrated to propose a mathematic model for flow and sediment transport with biofilm coating. In the hydrodynamic module, the bed resistance for bio-sediment are used for establishing a new river bed boundary condition. Furthermore, the settling velocity and reference concentration for bio-sediment are integrated in sediment transport model. The proposed model is tested by flume experiments and then applied to evaluate the effects of biofilms on sediment transport.

## 2 HYDRODYNAMIC MODEL

### 2.1 Equations for hydrodynamics

The basic equations are the Reynolds-averaged Navier-Stokes equations for incompressible flow as follow:

Continuity equation:

$$\frac{\partial u_i}{\partial x_i} = 0 \qquad [1]$$

Momentum equation:

$$\frac{\partial u_i}{\partial t} + \frac{\partial \left(u_i u_j\right)}{\partial x_j} = -\frac{1}{\rho}\frac{\partial P}{\partial x_i} + \frac{1}{\rho}\frac{\partial \tau_{ij}}{\partial x_j} + F_i \qquad [2]$$

where $U_i$ ($i$=1,2,3) are the velocity components; $\rho$ is fluid density; $P$ is pressure; $F_i$ is the gravity force per unit volume;. $\tau_{ij}$ are the turbulent stresses calculated with the $k$- $\varepsilon$ turbulence model as follow

$$\tau_{ij} = \rho v_t \left(\frac{\partial ui}{\partial xj} + \frac{\partial uj}{\partial xi}\right) - \frac{2}{3}\delta_{ij}k \quad with \;\; v_t = c_u k^2 / \varepsilon \qquad [3]$$

where the turbulent kinetic energy $k$ and its dissipation rate $\varepsilon$ can be derived from the following equations:

$$\frac{k}{t} + \frac{\partial \left(u_j k\right)}{\partial \left(x_j\right)} = \frac{\partial}{\partial x_j}\left(\frac{v_t}{\sigma_k}\frac{\partial_k}{\partial x_j}\right) + G - \varepsilon \qquad [4]$$

$$\frac{\partial \varepsilon}{\partial t} + \frac{\partial \left(u_j \varepsilon\right)}{\partial x_j} = \frac{\partial}{\partial x_j}\left(\frac{v_t}{\sigma_\varepsilon}\frac{\partial \varepsilon}{\partial x_j}\right) + \left(c_{\varepsilon 1} G - c_{\varepsilon 2}\varepsilon\right)\frac{\varepsilon}{k} \qquad [5]$$

where $G = \upsilon_t\left(\left(\partial u_i / \partial x_j\right) + \left(\partial u_j / \partial x_i\right)\right)\partial u_i / \partial x_j$ is the production of $k$. The model coefficients are given as follow: $c_\mu$=0.09, $c_{\varepsilon 1}$=1.44, $c_{\varepsilon 2}$=1.92, $\sigma_k$=1.0, $\sigma_\varepsilon$=1.3.

### 2.2 Boundary conditions

At the free surface, the shear stress and the gradient of turbulent energy $k$ are specified as zero without wind shear. The pressure is set as the atmospheric one and the dissipation rate $\varepsilon = k^{2/3}/\left(0.4h\right)$, where $h$ is the water depth.

For the river bed, the wall-function approach is used and the details are described in Fang and Rodi (2003). The log-law relation for the velocity employed mainly involves the roughness Reynolds number $k_s^+ = u_* k_s / \upsilon$, where $k_s$ is the equivalent roughness height, which can be expressed as the sum of roughness due to particle $k_s'$ and roughness due to bedforms $k_s''$. The equivalent roughness due to particle $k_s'$ is related to the particle size and the equivalent roughness due to bedforms is related to the height and length of the sand waves. The empirical relations proposed by van Rijn (1984) are widely used for $k_s$ for clean sediment. However, biological cohesion stabilizes sediment by inhibiting sand grains from moving independently and a larger flow intensity is needed to form the same bedforms for bio-sediment, which changes relations between the equivalent roughness due to bedforms and bedform dimensions for bio-sediment. Fang et al., (2017) proposed the following relations for calculating $k_s$ for bio-sediment.

$$k_s = k_s' + k_s'' \quad with \quad k_s' = 3d_{90} \quad and \quad k_s'' / \Delta = 1.2\left(1 - e^{-40\Delta/\lambda}\right) \qquad [6]$$

where, $\Delta$ and $\lambda$ are the height and length of the sand waves for bio-sediment respectively, which would be

 

discussed in the next section.

2.3 Bedform dynamics for bio-sediment

The development of bedform for bio-sediment is affected by biological cohesion due to EPS (Malarkey et al., 2015). In our previous researches, the following expressions of the height $\Delta$ and length $\lambda$ of the sand waves were presented for bio-sediment (Fang et al., 2017)

$$\frac{\Delta}{\lambda}=0.0127\left(\eta-1\right)e^{-0.195\left(\eta-1\right)} \quad with \quad \lambda=3.2h \tag{7}$$

where $\eta = \Theta / \Theta_c$ is a transport stage parameter, where $\Theta$ and $\Theta_c$ are the Shields parameter and the threshold Shields parameter respectively. $\Theta_c$ will be discussed in the next section, and $\Theta$ is derived from

$$\Theta=\frac{\tau_0}{\left(\rho_s-\rho\right)gd}=\frac{\rho u_*^2}{\left(\rho_s-\rho\right)gd} \tag{8}$$

where $\tau_0$ is the shear stress near the river bed; $u_*=U\,g^{0.5}/C$ is the shear velocity, where $U$ is mean velocity; $C=18\log\left(12.27\chi R_b/k_s\right)$ is the Chézy coefficient; $\chi$ is Einstein correction factor; $R_b$ is the hydraulic radius.

2.4 The incipient velocity for bio-sediment

The incipient velocity for bio-sediment is essential to compute the development of bedforms. In consideration of the effects of biofilm on sediment erosion, the following formulas for incipient velocity for bio-sediment were suggested by Fang et al. (2014)

$$\Theta_C=\Theta_{C0}+\Theta_{C*}+\Theta_{CA} \;\; with \;\; \Theta_{C*}=C_*\cdot\Theta_{C0} \;\; and \;\; \Theta_{CA}=\Theta_{C0}\left(A(t)/\alpha_3\left(\rho_s-\rho\right)gd\right) \tag{9}$$

where $\Theta_C$ is the total Shields number for bio-sediment; $\Theta_{C0}$ is the Shields number for non-cohesive sediment; $\Theta_{C*}$ is the Shields number that represents physical cohesive force; $\Theta_{CA}$ is the Shields number that represents biological cohesive force; $C_*$ is a dimensionless coefficient for physical cohesion that is equal to $9.06\times10^{-5}/(\rho_s-\rho_w)d^2$ (Fang et al., 2014; Righetti and Lucarelli, 2007). $\alpha_3$ is the volumetric shape factor, which is equal to π/6 for sphere. The biological cohesive force $A(t)$ is given as:

$$A(t)=0.898\cdot d_{50}^{-0.449}t\cdot\exp\left(1-0.357t\right) \tag{10}$$

where $d_{50}$ is the median particle diameter (cm); $t$ represents the cultivation time (in weeks). In order to distinguish the physical cohesion and biological cohesion, the comprehensive threshold Shields curves are presented, as shown in Figure 2. where the dimensionless particle parameter $d_*$ is defined as: $d_*=d_{50}\left[\left(s-1\right)g/\upsilon^2\right]^{1/3}$, where $s$ is the relative density of sediment ($s=\rho_s/\rho_w$).The shields curve and van Rijn curve represent the erosion threshold of non-cohesive sediment and cohesive sediment respectively, and the curve of Fang represents the erosion threshold of bio-sediment with cultivation time for 6 weeks.

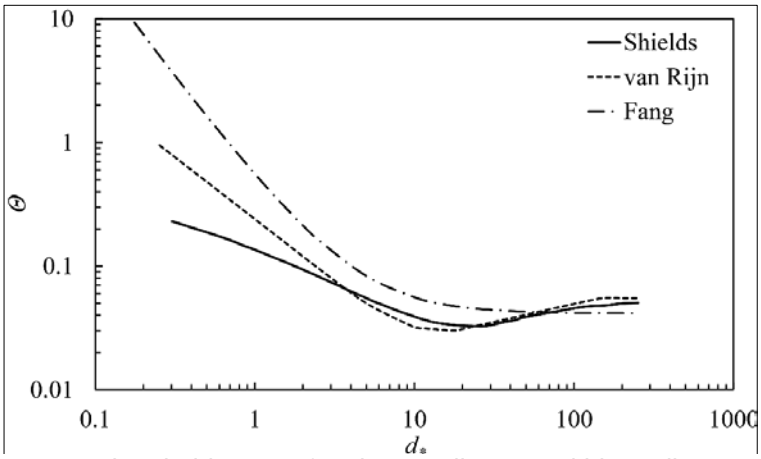


**Figure 2**. Threshold curves for clean sediment and bio-sediment (Fang et al., 2014).

 

However, the biological cohesive force A (t) related to cultivation time in Eq. (10) cannot be used in natural water with different eutrophication degrees and microbial community structures. It is generally believed that both the quantity and structuring of EPS play a dominant role in biostabilization (de Brouwer et al., 2005). With the certain strains, the biological cohesive force *A* is related to the quantity of EPS (Malarkey et al., 2015). In most biofilms, EPS account for more than 90% of the dry biofilm mass. Loss on ignition (LOI) was used to measure the biofilm mass after the biofilm growth to represent the mass of EPS (Fang et al., 2015). Therefore, the biological cohesive force *A* is related to the biofilm mass, as shown in Figure 3, and the relation is written as:

$$A = 0.514 Biomass \quad [11]$$

where biomass is the dry biofilm mass (mg/g).

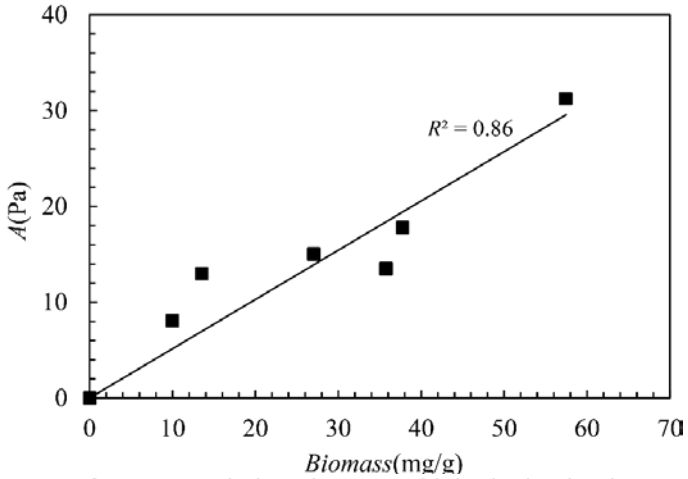


**Figure 3**. Relations between biological cohesive force *A* and biofilm mass *biomass* ($R^2$=0.86)

Above all, in the aquatic system with certain water and sediment conditions, the measured dry biofilm mass can be applied to calculate the biological cohesive force A, then the Shields number for bio-sediment $\Theta_C$ can be calculated for the erosion threshold of bio-sediment. Then the height $\Delta$ and length $\lambda$ of the sand waves can be computed, and the equivalent roughness height $k_s$ is derived. Therefore, the hydrodynamic model is established for bio-sediment.

## 3 SUSPENDED SEDIMENT TRANSPORT MODEL

### 3.1 Equations for suspended sediment transport

The distribution of sediment concentration is determined by the following convection diffusion equation:

$$\frac{\partial c}{\partial t} + u_j \frac{\partial c}{\partial x_j} = \frac{\partial}{\partial x_j}\left(\frac{\nu_t}{\sigma_s}\frac{\partial c}{\partial x_j}\right) + \frac{\partial}{\partial x_j}\left(\omega \delta_{j3} c\right) \quad [12]$$

where $\sigma_s$ is turbulent Schmidt number relating the turbulent diffusivity of sediment to the eddy viscosity $\nu_t$, $c$ is sediment concentration; $\omega$ is settling velocity of sediment.

### 3.2 Boundary conditions

At the free surface, the boundary condition for the vertical sediment flux is zero:

$$\frac{\nu_t}{\sigma_c}\frac{\partial c}{\partial z} + wc = 0 \quad [13]$$

At the lower boundary of suspended-load layer, the boundary condition is the net exchange near the bed as follow

$$D_b - E_b = \omega\left(c_b - c_{b*}\right) \quad [14]$$

where the deposition rate and entrainment rate are defined as: $D_b = \omega c_b$ and $E_b = \omega c_{b*}$, respectively, where $c_b$ and $c_{b*}$ are the actual and equilibrium concentration at the interface respectively. In the finite-volume procedure for numerical solving, the concentration $c_b$ at $z' = \delta_b$ has to be related to the value $c_2$ at the first grid point above the bed ($z' = z'_2$) as follow:

$$c_b = c_2 + c_{b*}\left[1 - e^{-(\omega\sigma_c/\nu_t)(z'_2 - \delta_b)}\right] \quad [15]$$

In sediment transport model, the equilibrium concentration $c_{b*}$ provides boundary conditions and the settling velocity determines sediment deposition, which are important for sediment transport. The two parameters would be discussed for bio-sediment in next section.

3.3 The equilibrium concentration for bio-sediment

Due to biostabilization, the equilibrium concentration for bio-sediment is quite different from clean sediment. Fang et al. (2016) proposed the following formula of the equilibrium concentration near bed for bio-sediment base on the measurement of bio-sediment saltation by PTV.

$$c_{b*} = 0.00363\frac{D_f}{a}T^{1.5}D_*^{0.2} \quad [16]$$

where, $a$ is the reference height that is usually taken as $k_s$. $D_* = D_f\left((s-1)g/v^2\right)^{1/3}$ is the particle parameter for bio-sediment; $T = u_*'^2/u_{*cr}^2 - 1$ is a transport stage parameter, where $u_{*cr}$ is the threshold shear velocity for bio-sediment and $u_*'$ is the shear velocity due to bio-particle roughness defined as $u_*' = U\left(g^{0.5}/C'\right)$, where $C'$ is the Chézy coefficient due to bio-particle roughness defined as $C' = 18\log\left(4R/D_f\right)$.

3.4 Settling velocity

Biofilm growth changes the density, structure and sediment size. The decrease of the density and the change of the structure cause the decrease of settling velocity, but the significant increase of sediment size causes the increase of settling velocity. All things considered, the settling velocity becomes much larger than that of primary particles, and the following formula suggested by Shang (2014) is applied to calculate the bio-sediment settling velocity.

$$w_f = \left[\frac{g d_f^{1.754} v^{-0.754}}{47.52}\frac{\left(\rho_f - \rho_w\right)}{\rho_w}\right]^{1/1.246} \quad [17]$$

where $\omega_f$ is the settling velocity of bio-sediment; $\rho_f$ is density of bio-sediment; $\rho_w$ is density of water.

## 4 RESULTS AND DISCUSSION

4.1 Calibration

The proposed model is tested by flume experiments, which were conducted in the flume as shown in Figure 4. In the region 0 m < x < 6 m and 8 m < x < 14 m the channel width are 0.16 m and 0.5 m, respectively, and the channel width extended from 0.16 m to 0.5 m in the region 6 m < x < 8 m. The sediment samples ($d_{50}$=0.033 mm) were deposited at 2 to 4 m (in gray bar) with the depth of 1.5~2.0 cm. After the biofilm growth, the water was added to the flume and the discharge was gradually increased until the bio-sediment was eroded. During the erosion, the distribution of velocity and sediment concentration were measured. The water depth is 0.14 m, the mean velocity is 0.77 m/s, the median sediment diameter $d_{50}$ is 0.033 mm and the measured dry biofilm mass is 51.8 mg/g after the biofilm growth.

 

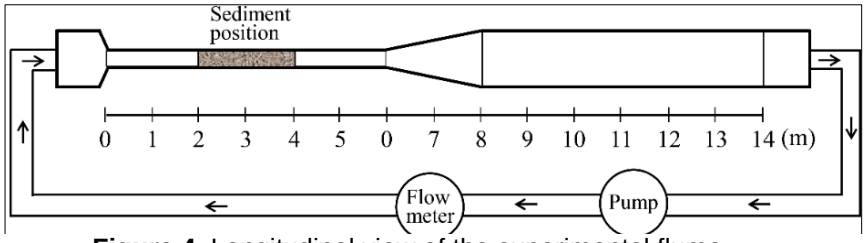


**Figure 4.** Longitudinal view of the experimental flume.

The simulated and measured velocity profiles at several locations (i.e., x=1m, 3m, 4m, 10m) in the longitudinal section are compared in Figure 5. The agreement of the flow show well, which is the premise for simulating suspended sediment transport. The simulated and measured distributions of suspended sediment concentration at several locations (i.e., x=3m, 4m, 5.8m, 8m, 10m, 12m) in the longitudinal section are compared in Figure 6. The results are in good agreement with the experiments, which gives confidence in the modification for suspended sediment transport model, especially the settling velocity and the equilibrium concentration near bed for bio-sediment. It is evident that the proposed model can be used for the suspended sediment transport for bio-sediment.

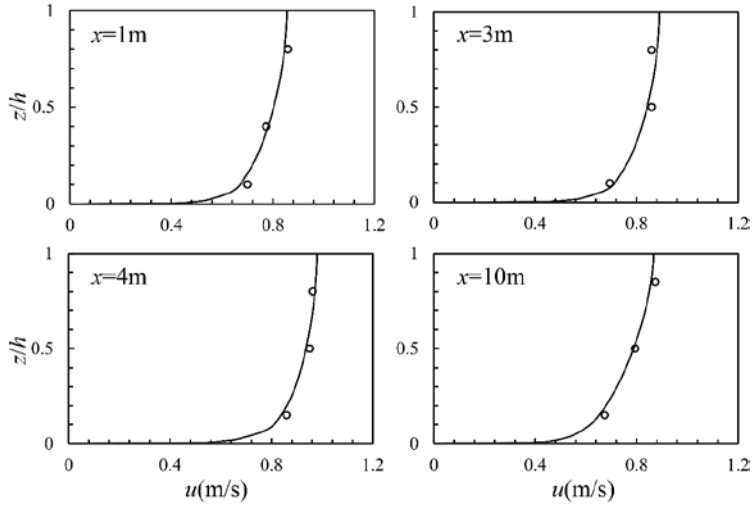


**Figure 5.** Comparison of velocity profiles between the experiments and simulations in the longitudinal section for bio-sediment. —Simulations, Experiments.

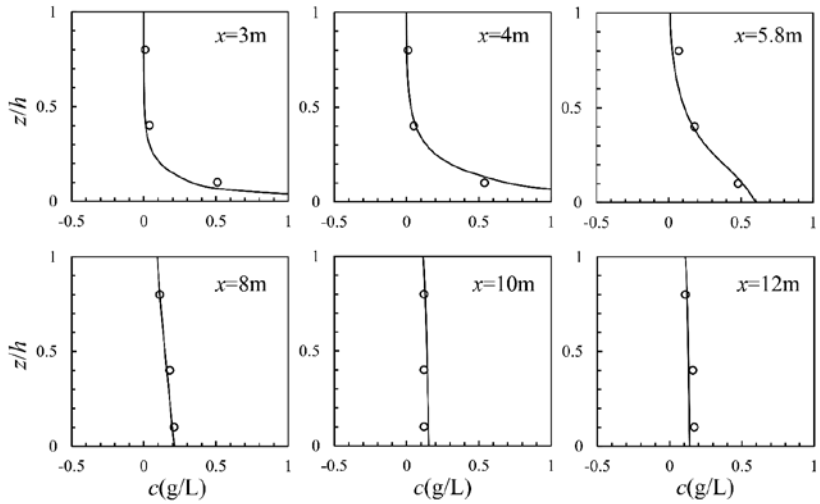


**Figure 6.** Comparison of distributions of suspended sediment concentration between the experiments and simulations for bio-sediment. —Simulations, Experiments.

 

4.2 Discussion

In order to investigate the effects of biofilms on suspended sediment transport, both clean sediment and bio-sediment have been simulated under the same flow conditions. The mean velocity is 0.75 m/s at the inlet boundary, the mean water depth is 0.09 m and the median sediment diameter $d_{50}$ is 0.033 mm in the numerical simulations.

The suspended sediment concentration at longitudinal section for clean sediment and bio-sediment are shown in Figure 7. Overall, the entrainment is observed in the region from 2m to 4m in flume and then the sediment concentration decreased due to sediment deposition. Since the sediment erosion threshold increase due to biostabilization, the average concentration of bio-sediment is significantly less than that of clean sediment. Moreover, the suspended sediment concentration of bio-sediment drops more quickly than that of clean sediment due to the much larger settling velocity.

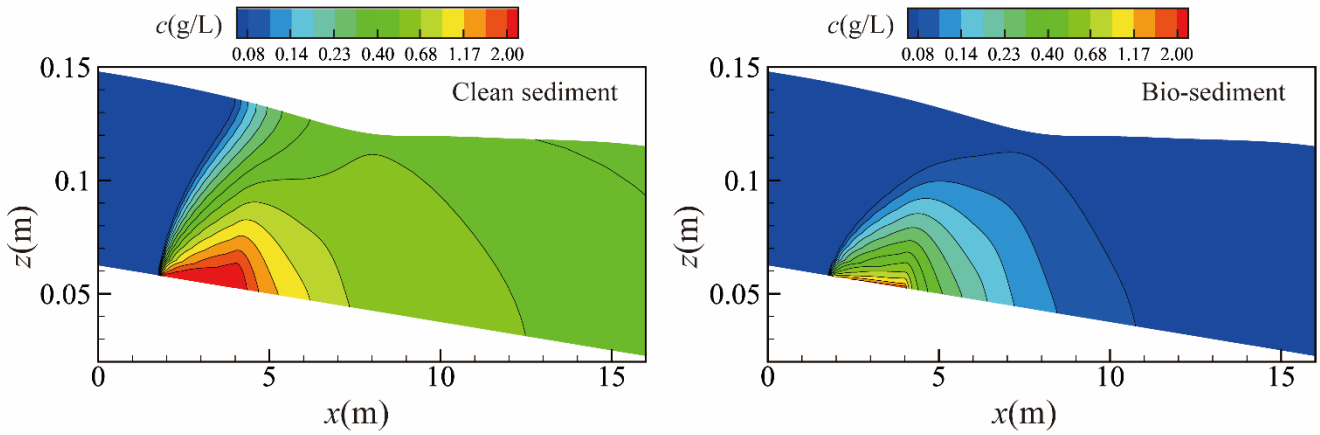


**Figure 7.** Distribution of suspended sediment concentration in the longitudinal section for clean sediment and bio-sediment.

## 5 CONCLUSIONS

In this paper, a mathematic model for flow and suspended sediment transport with biofilms is proposed. In the hydrodynamic module, the relation between the biological cohesion and biofilm mass is established, then the method for computing the bedform dynamics and the bed resistance are presented for bio-sediment. Meanwhile, settling velocity and the equilibrium concentration of bio-sediment are integrated in the sediment transport model. The proposed model is tested by flume experiments and the results are in good agreement with the experiments. Then, the proposed model is applied to evaluate the effects of biofilms on suspended sediment transport. The results show that the sediment concentration of bio-sediment is significantly smaller than that of clean sediment under the same hydrodynamic conditions. In addition, due to the much larger settling velocity of bio-sediment, the suspended bio-sediment concentration drops more quickly. Therefore, it is more difficult for sediment erosion and transport with biofilm. In conclusion, the proposed model can reasonably reflect the flow and suspended sediment transport with biofilm.

## ACKNOWLEDGEMENTS

This investigation was supported by the National Natural Science Foundation of China (No. 91647210) and National Key Research and Development Program of China (No. 2016YFC0402407).

## REFERENCES

Battin, T.J. & Sengschmitt, D. (1999). Linking Sediment Biofilms, Hydrodynamics and River Bed Clogging: Evidence from a Large River. *Microbial Ecology*, 37(3), 185-196.

Black, K.S., Tolhurst, T.J., Paterson, D.M. & Hagerthey, S.E. (2002). Working with Natural Cohesive Sediments. *Journal of Hydraulic Engineering*, 128(1), 2-8.

Cyr, H. & Morton, K.E. (2006). Distribution of Biofilm Exopolymeric Substances in Littoral Sediments of Canadian Shield Lakes: The Effects of Light and Substrate. *Canadian Journal of Fisheries and Aquatic Sciences*, 63(63), 1763-1776.

de Brouwer, J.F.C., Wolfstein, K., Ruddy, G.K., Jones, T.E.R. & Stal, L.J. (2005). Biogenic Stabilization of Intertidal Sediments: The Importance of Extracellular Polymeric Substances produced by Benthic Diatoms. *Microbial Ecology*, 49(4), 501-512.

Droppo, I.G. & Amos, C.L. (2001). Structure, Stability and Transformation of Contaminated Lacustrine Surface Fine-grained Laminae. *Journal of Sedimentary Research*, 71(5), 717-726.

Fang, H.W. & Rodi, W. (2003). Three-dimensional Calculations of flow and Suspended Sediment Transport in the Neighborhood of the Dam for the Three Gorges Project (TGP) Reservoir in the Yangtze River. *Journal of Hydraulic Research*, 41(4), 379-394.

 

Fang, H.W., Cheng, W., Fazeli, M. and Dey, S. (2017). Bedforms and flow resistance of cohesive beds with and without biofilm coating. *Journal of Hydraulic Engineering*, 06017010.

Fang, H.W., Fazeli, M., Cheng, W. and Dey, S. (2016). Transport of biofilm-coated sediment particles. *Journal of Hydraulic Research*, 54(6), 631-645.

Fang, H.W., Fazeli, M., Cheng, W., Huang, L. & Hu, H.Y. (2015). Biostabilization and Transport of Cohesive Sediment Deposits in the Three Gorges Reservoir. *PLoS One*, 10(11).

Fang, H.W., Shang, Q.Q., Chen, M.H. & He, G.J. (2014). Changes in the Critical Erosion Velocity for Sediment Colonized by Biofilm. *Sedimentology*, 61(3), 648-659.

Fang, H.W., Zhao, H.M., Shang, Q.Q. & Chen, M.H. (2012). Effect of Biofilm on the Rheological Properties of Cohesive Sediment. *Hydrobiologia*, 694(1), 171-181.

Flemming, H. C. & Wingender, J. (2010). The Biofilm Matrix. *Nature Reviews Microbiology*, 8(9), 623-633.

Förstner, U., Heise, S., Schwartz, R., Westrich, B. & Ahlf, W. (2004). Historical Contaminated Sediments and Soils at the River Basin Scale. *Journal of Soils and Sediments*, 4(4), 247-260.

Gerbersdorf, S.U., Westrich, B. & Paterson, D.M. (2009). Microbial Extracellular Polymeric Substances (EPS) in Fresh Water Sediments. *Microbial ecology*, 58(2), 334-349.

Gerbersdorf, S.U. & Wieprecht, S. (2015). Biostabilization of Cohesive Sediments: Revisiting the role of Abiotic Conditions, Physiology and Diversity of Microbes, Polymeric Secretion and Biofilm Architecture. *Geobiology*, 13(1), 68-97.

Hirst, C.N., Cyr, H. & Jordan, I.A. (2003). Distribution of Exopolymeric Substances in the Littoral Sediments of an Oligotrophic Lake. *Microbial Ecology*, 46(1), 22-32.

Jepsen, R., Roberts, J. & Lick, W. (1997). Effects of Bulk Density on Sediment Erosion Rates. *Water, Air and Soil Pollution*, 99(1-4), 21-31.

Malarkey, J., Baas, J.H., Hope, J.A., Aspden, R.J., Parsons, D.R., Peakall, J., Paterson, D.M., Schindler, R.J., Ye, L., Lichtman, I.D., Bass, S.J., Davies, A.G., Manning, A.J. & Thorne, P.D. (2015). The Pervasive Role of Biological Cohesion in Bedform Development. Nature Communications, 6, 6257.

Mcneil, J. & Lick, W. (2004). Erosion Rates and Bulk Properties of Sediments from the Kalamazoo River. *Journal of Great Lakes Research*, 30(3), 407-418.

Paterson, D.M., Tolhurst, T.J., Kelly, J.A., Honeywill, C., de Deckere, E., Huet, V., Shayler, S.A., Black, K.S., de Brouwer, J. & Davidson, I. ( 2000). Variations in Sediment Properties, Skeffling Mudflat, Humber Estuary, UK. Continental Shelf Research, 20(10-11), 1373-1396.

Papanicolaou, A.T.N., Elhakeem, M., Krallis, G., Prakash, S. & Edinger, J. (2008). Sediment Transport Modeling Review: Current and Future Developments. *Journal of Hydraulic Engineering*, 134(1), 1-14.

Righetti, M. & Lucarelli, C. (2007). May the Shields Theory be extended to Cohesive and Adhesive Benthic Sediments? *Journal of Geophysical Research*, 112(C5).

Shang, Q.Q., Fang, H.W., Zhao, H.M., He, G.J. & Cui, Z.H. (2014). Biofilm Effects on Size Gradation, Drag Coefficient and Settling Velocity of Sediment Particles. *International Journal of Sediment Research*, 29(4), 471-480.

Stal, L.J. (2003). Microphytobenthos, their Extracellular Polymeric Substances and the Morphogenesis of Intertidal Sediments. *Geomicrobiology*, 20(5), 463-478.

Underwood, G.J.C. & Paterson, D.M. (2003). The Importance of Extracellular Carbohydrate Production by Marine Epipelic Diatoms. *Advances in Botanical Research*, 40(05), 183-240.

van Rijn, L.C. (1984). Sediment Transport, part III: Bed Forms and Alluvial Roughness. *Journal of Hydraulic Engineering*, 110(12), 1733-1754.

Zhao, H.M., Fang, H.W. & Chen, M.H. (2011). Floc Architecture of Bio Flocculation Sediment by ESEM and CLSM. *Scanning*, 33(6), 437-45.

 

Proceedings of the 37th IAHR World Congress
August 13 – 18, 2017, Kuala Lumpur, Malaysia

# INVESTIGATING THE IMPACT OF THE HEAVY RAINFALL OF 1999 AND LAND COVER CHANGES ON SOIL LOSS AND SEDIMENTATION OF FRASER HILL CATCHMENT IN MALAYSIA USING REMOTE SENSING AND GIS

ZHOOBIN RAHIMI[(1)] & FARIDAH OTHMAN[(2)]

[(1)] Department of Civil Engineering, University of Malaya, Kuala Lumpur, Malaysia,
zhrahimi@siswa.um.edu.my; faridahothman@um.edu.my

## ABSTRACT

Rainfall intensity and human activity accelerate soil erosions. According to the southern oscillation index (SOI), a La Nina period occurred during 1999. As a result, a series of heavy rainfall events were recorded over peninsular Malaysia. Meanwhile, human activities such as mining and dam construction at this area has heavily changed the land cover during 1990s. Geographic information systems (GIS) and satellite images are two important tools that enable us to overlay these factors to observe the spatial distribution of erosion process. This study shows the effect of the heavy rainfalls of 1999 and human activities on soil loss and sedimentation at highlands of Fraser hill in Malaysia. In this study, we used a GIS-based universal soil loss erosion (USLE) model to study the spatial changes of land cover as a result of human activities. We generated two land cover maps using Landsat images in 1990 and 1999. The results of generated land cover products show that due to increasing construction and mining activities the forest area has decreased by 600km$^2$. As a result, the land cover maps show a significant increase of soil loss in 1999. Moreover, according to the collected data from Department of irrigation and drainage (DID), the accumulated annual sediment at the downstream of Fraser hill watershed significantly increases from 3.2 tons per hectare per year in 1990 up to 7.3 tons per hectare per year in 1999 while the average rainfall at these two occasions slightly increases by 3mm. This results shows that land cover changes have a greater impact on sedimentation when compared with rainfall intensity. Finally, comparing the estimated annual sediment by USLE model with collected data shows 0.3 ton per year bias which indicate that Landsat images can be an alternative source of data to map the geomorphological processes.

**Keywords:** Soil loss assessment; climate cycles; land use conversation; annual sediment; southern oscillation index.

## 1 INTRODUCTION

Soil erosion process includes detachment, transport, and deposition of soil particles by erosive elements such as wind and water (Morgan, 2005). The eroded and transported soil mass by shear force of water that are accumulated at the downstream of basin produce delivered sediment. The relationship between erosion and delivered sediment is based on transport capacity of runoff water and soil erodibility. The transport capacity of runoff depends on, slope, rainfall intensity, and shape of the watershed. At steep slope area of Hulu Selangor, with high rainfall intensity will give rise to the transport capacity being extremely high. According to figure 1, a La Nina event with magnitude of 0.8 occurred in 1999. This led to a series of heavy rainfall events and a sequence of floods in peninsula Malaysia.

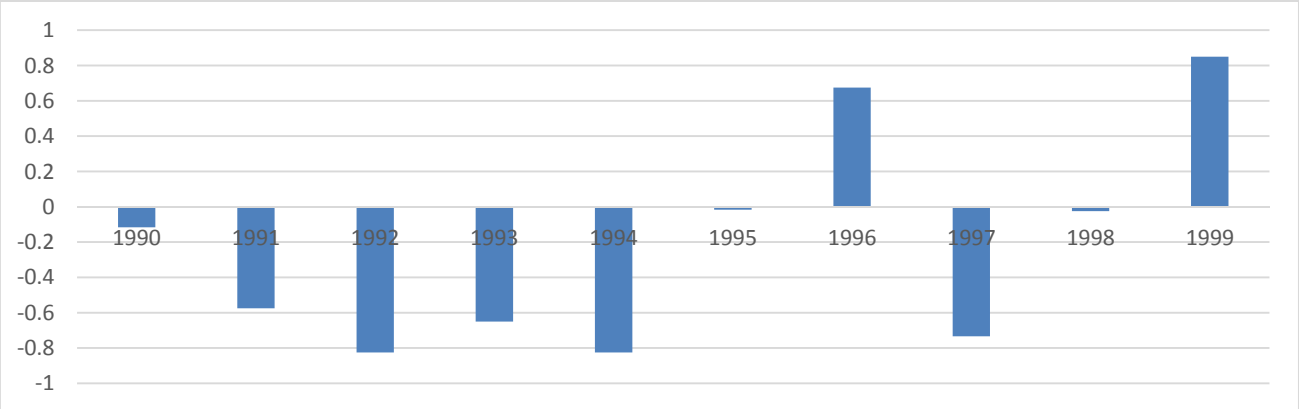


**Figure 1**. The average of southern oscillation index (SOI) between 1990 and 1999. The value above +0.8 indicates a LA Nino period whereas any value below -0.8 indicates El Nino period in the corresponding years.

 

In addition, human activities such as agriculture, mining, urbanization, and logging accelerate this geomorphic process. In 1998, federal authorities started construction of Selangor Dam to increase the capacity of water supply to Selangor state. The rapid construction of dam caused a significant land cover change in Hulu Selangor district. Furthermore, an increase in delivered sediment at downstream of Hulu Selangor catchment in subsequent years is expected to occur. Estimation of soil erosion and sediment delivery are important issues for decision makers.

A valid estimation of erosion via USLE model (Wiscgmeier and Smith, 1978) is a good source of information to calculate the delivered sediment within the catchment. However, as a result of Heterogeneity in rainfall intensity and land cover, the magnitude of estimated soil erosion varies spatially. Reviewing previous studies show that employing remotely sensed data along with GIS can significantly increase the spatial accuracy of estimated soil erosion (Jain et al., 2010).

## 2 STUDY AREA

Selangor River is the main river in the state of Selangor which carries over 100 million liters water per year. The Hulu Selangor watershed is located at the upstream of Selangor River in Hulu Selangor district of Selangor state, peninsula Malaysia (Figure 2). This watershed lies between Geographical coordinates of 101.539˚E, 3.239˚N and 101.945˚E, 3.82˚N. The maximum and minimum temperature varies between 33.4 C and 22.8 C. Most part of this watershed is occupied by granitic rocks with small isolated areas of Siluran meta-sediments. The river starts from the slopes near Fraser's Hill and flows in a southwest direction towards Hulu Selangor district.

The total area of hulu Selangor watershed is approximately 15600km$^2$. According to department of agriculture (DOA) 2001, the land use of Hulu Selangor catchment in 1990, consisted of large area of forest that has been planted with rubber for agriculture with approximately 97km$^2$ area of scattered tin mining. However, due to dam construction, sand mining, and rapid development of road and highways in 1999, the forest area has been reduced by 600km$^2$ from 15400km$^2$ to 14800km$^2$.

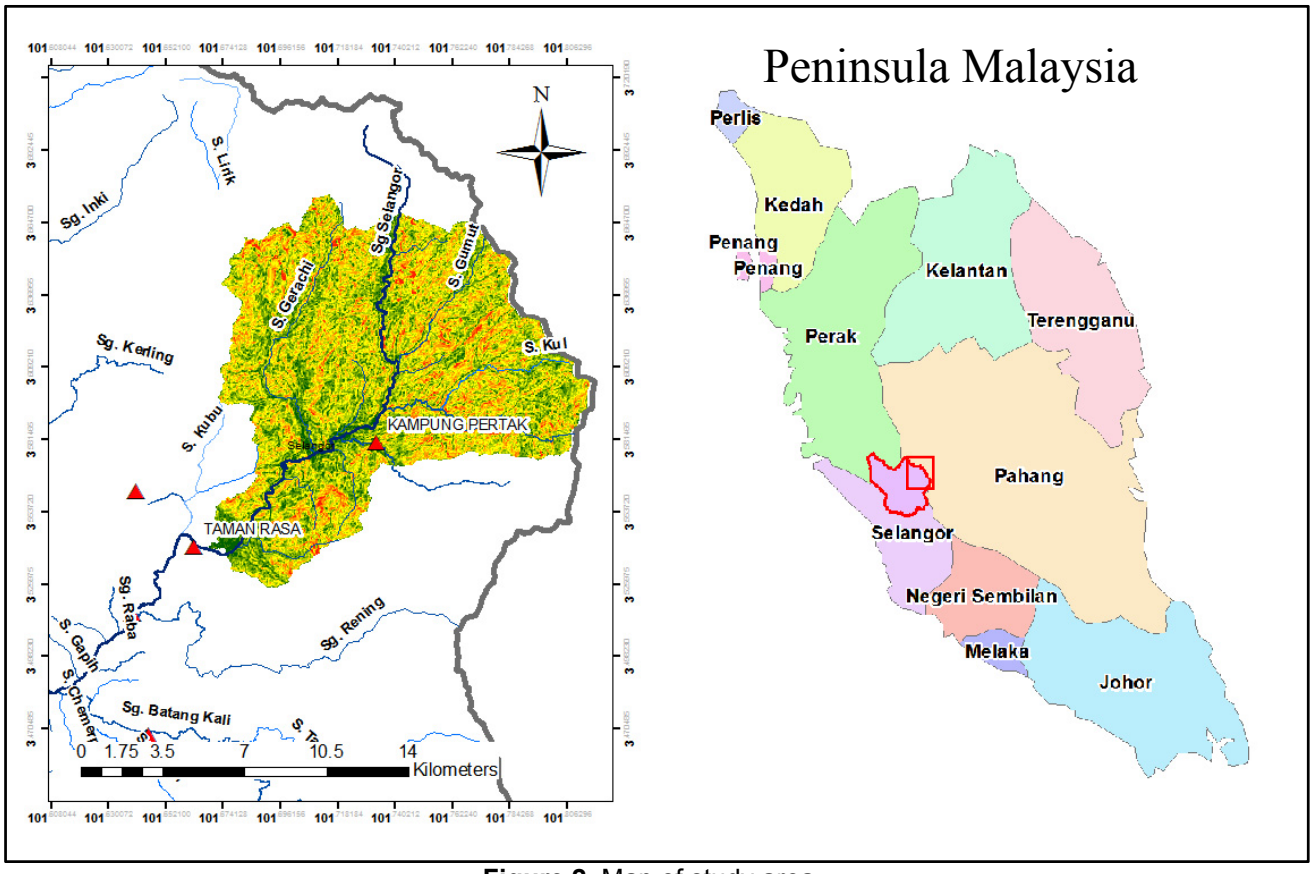


**Figure 2**. Map of study area.

## 3 METHODOLOGY

### 3.1 Image processing

The thematic mapper sensor installed on Landsat 5 (TM5) is one of the most common used resources in remote sensing studies. TM5 started its mission in early 1980s and have been capturing satellite images for over two decades. This long period of time has allowed researchers to conduct many change detection

 

analysis all over the world. In the present study, TM5 images were utilized to assess the land cover changes within the study area with 30-meter spatial resolution. Two captured images on 1990 and 1999 were collected to monitor land cover changes in 10 years. The landcover maps of satellite images were processed and analyzed by Erdas8.1 software. The processing steps of satellite images starts with applying the atmospheric and radiometric corrections. To apply the corrections rescale, gain coefficients were used along with sun elevation angle to convert Digital numbers to reflectance (Jensen, 2007). The supervised maximum likelihood classification method was applied to classify the landcover into six different categories. The overall accuracy of conducted classification shows 89.4% and 92.6% correlation for 1990 and 1999 images, respectively.

3.2 Universal soil loss erosion model

The soil erosion was calculated using the universal soil loss model (Wiscgmeier and Smith, 1978) expressed in Eq. [1].

$$A=R*K*LS*C*P \quad [1]$$

where, A is the soil loss, R is rainfall erosivity factor, K is the soil erodibility, LS is slope length factor, C is the vegetation cover index, and P is soil conservation practices.

3.3 Rainfall runoff erosive factor (R)

The rainfall factor (R), calculates the kinetic energy of rain which depends on the rainfall intensity at a certain area. There a few different models that calculate (R). (Islam et al., 2010). After comparing different methods, it was concluded that (Morgan, 2005) model in Eq. [2] is the most suitable model for Malaysia. (Figure 3 shows spatial variation of R factor in 1990 and 1999.)

$$R= [(9.28P-8838.15)*75]/1000 \quad [2]$$

where, P is the rainfall average in mm.

Rainfall erosivity was defined using isolines. The monthly average rainfall data were collected from 4 rainfall stations adjacent to the study area. The data were collected from the department of irrigation and drainage from 1990 to 1999. Figure 3 compares the distribution of rainfall erosivity within 1990 and 1999.

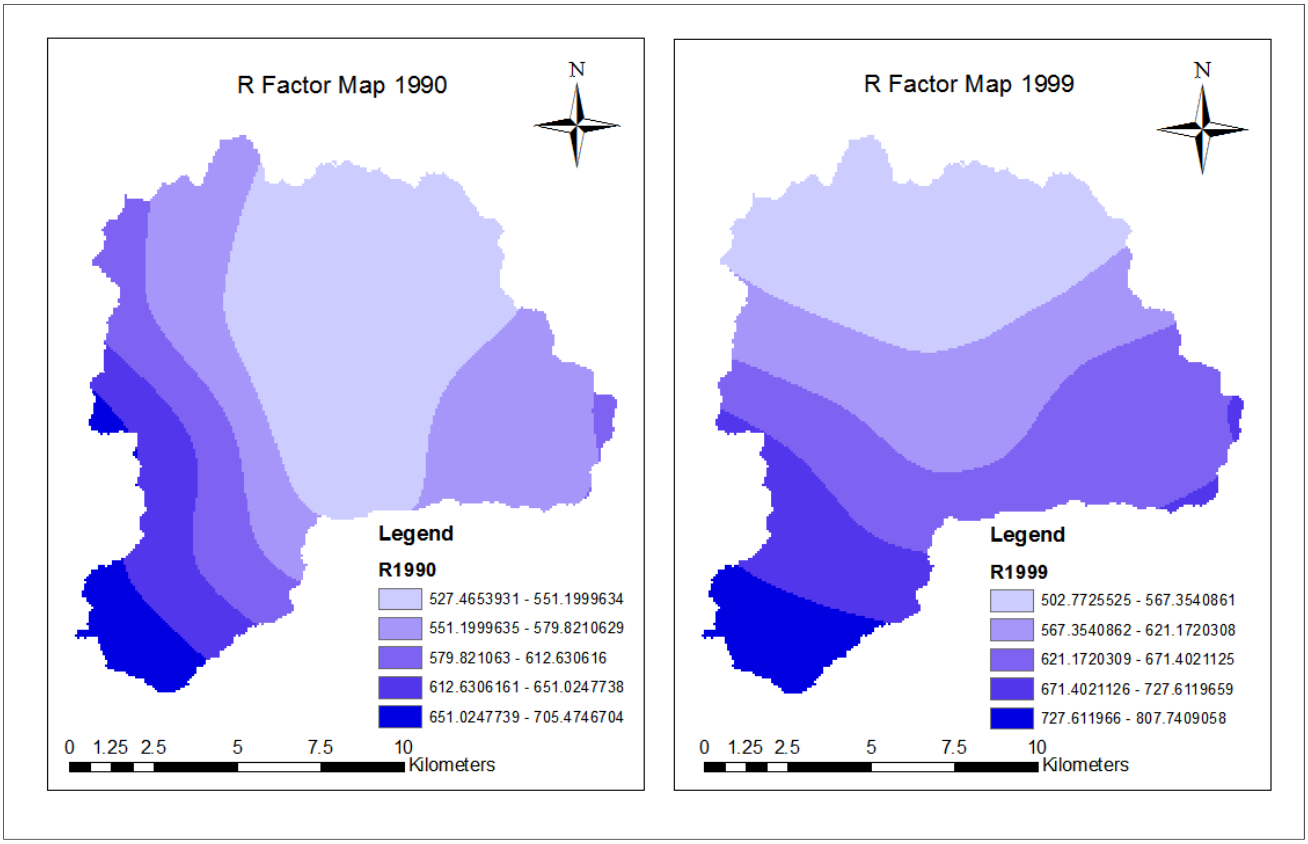


**Figure 3**. Distribution of R factor within the study area based on collected average rainfall in 1990 and 1999.

3.4 Soil erodibility (K)

Soil erodibility is the rate of eroded soil which depends on soil structure, and size of the composition. The soil series map of Malaysia generated by DOA was used to prepare a lookup table for (K) factor. Table 1 shows the available soil series and calculated K values based on the soil type. Spatial analysis tool was used to generate the soil erodibility map in raster format (Figure 4).

**Table 1**. Show available soil series in study area.

| Soil series | Soil group | K factor | Soil properties | Hydrologic soil group |
|---|---|---|---|---|
| **Serdang** | 1 | 0.310 | Sandy clay loam | C |
| **Muchong** | 2 | 0.347 | Sandy clay loam | C |
| **Rengam** | 6 | 0.103 | Clay | D |
| **Steep land** | 7 | 0.110 | Clay | D |

Among all soil types, steep land with almost 86km$^2$ and Rengam52 km$^2$ have the lowest level of soil erosion.

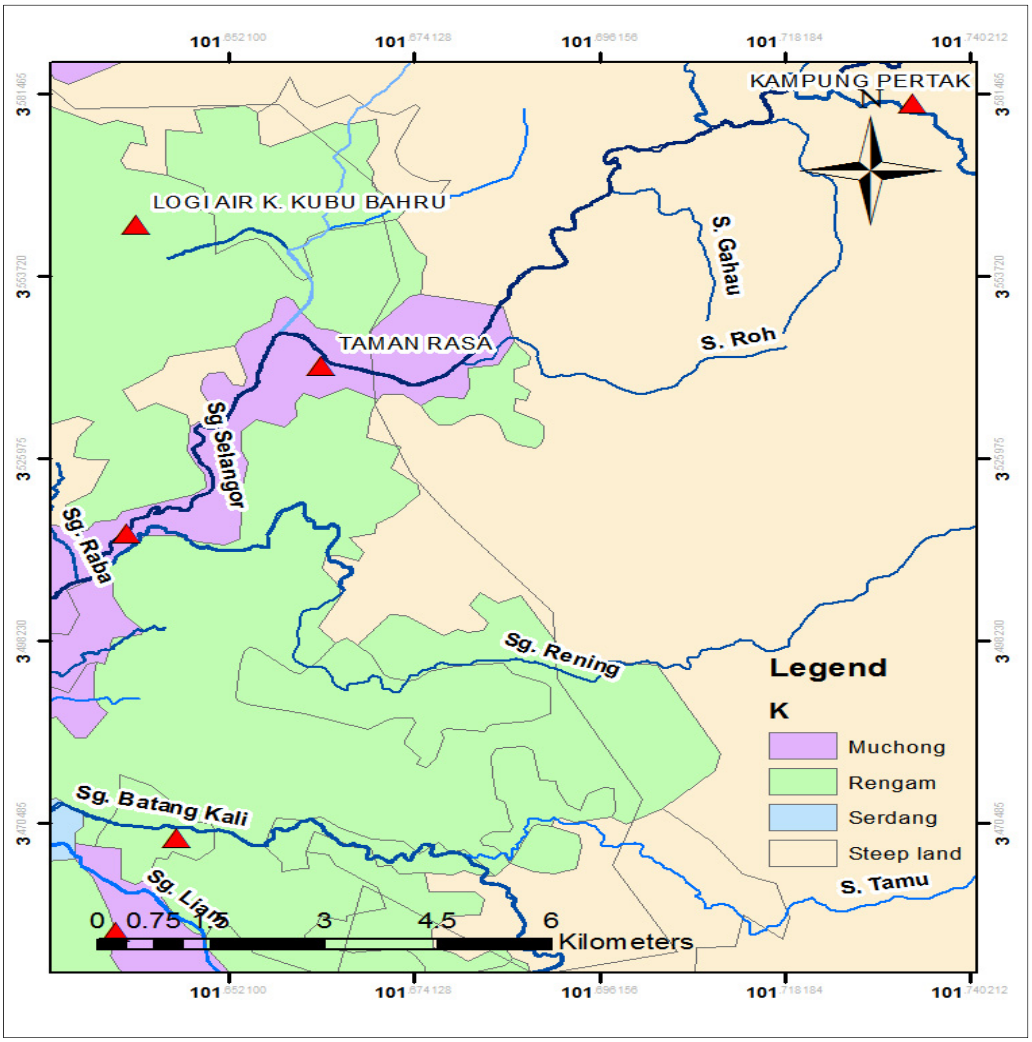


**Figure 4**. Spatial distribution of Soil series at Hulu Selangor.

3.5 Topographic factor (LS)

As it was discussed in the previous section, the topography of a watershed that consists of combined slope gradient and slope length has an important effect on erosion. The estimated LS factor in this study is based on a raster based format (Moore and Wilson, 1992) expressed in Eq. [3].

$$LS=(A/22.13)^n+(\sin \beta/0.0896)^m \quad [3]$$

where, A is the specific area, defined as upslope contributing area for overland grid per unit width normal to flow direction. $\beta$ was the slope gradient in degrees n=0.4 and m=1.3. The generated slope map has been shown in figure 5.

 

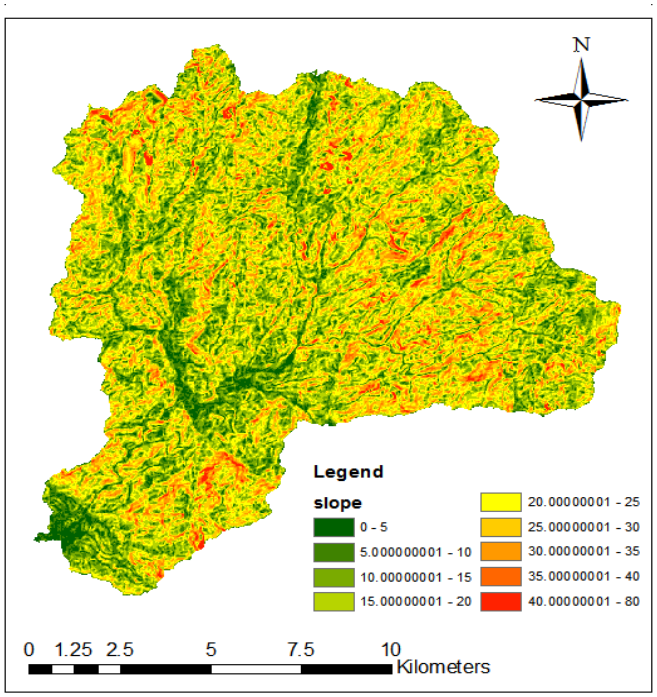


**Figure 5**. Spatial distribution map of slope in degree.

3.6 Cover factor (C)

The density of vegetation cover affects the magnitude of soil loss. The C value that represents vegetation density is close to 0 value when there is a highly dense vegetation landcover and 1 represents bare lands (Table 2). Figure 6 shows the spatial variation of cover factor in Hulu Selangor.

**Table 2**. Erosion control treatment.

| | Land cover | C factor |
|---|---|---|
| **1** | Bare land &Mining areas | 1.00 |
| **2** | Agricultural crop | 0.38 |
| **3** | Rubber | 0.20 |
| **4** | Forest area | 0.03 |
| **5** | Urbanized areas & Residential | 0.01 |
| **6** | Water bodies | 0.00 |

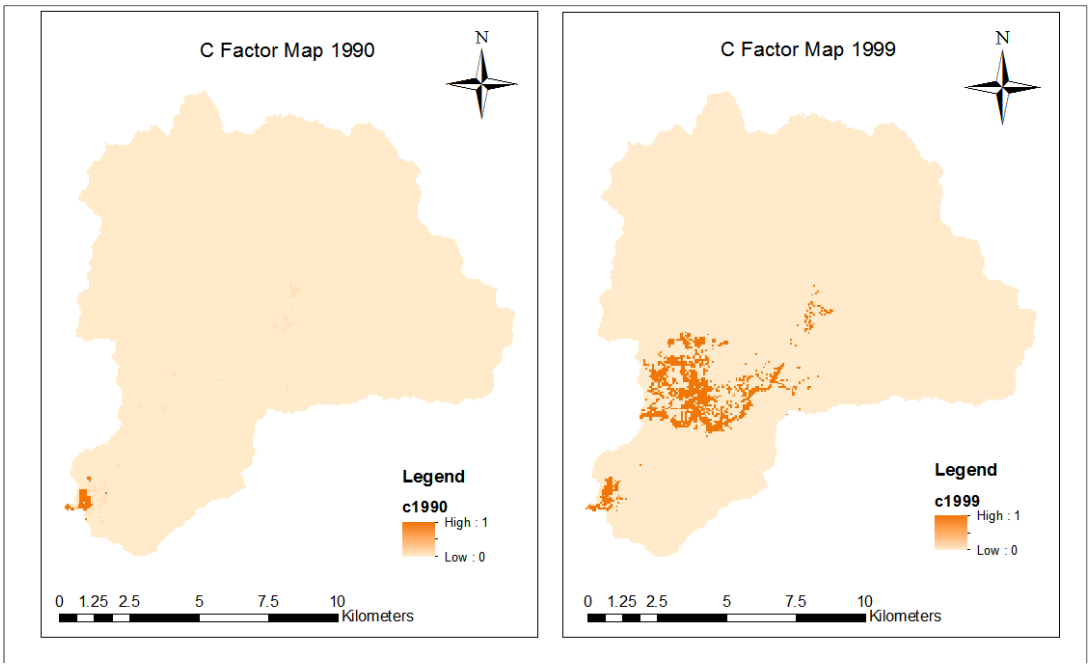


**Figure 6**. Map of C factor shows the effect of vegetation loss on erosion. Areas with darker color presents deforested areas.

3.7 Conservation practices factor (P)

The practice factor (P) represents land loss ratio. The values of the P is defined by DOA. Table 3 presents the conservation practice values that were assigned to the land cover maps. The 30 meter resolution land cover map generated by Landsat 5 had significantly helped us to assign corresponding practice factors for each category (Figure 7).

**Table 3**. Conservation Practices Factor (P).

| Landuse | P-factor | Landuse | P-factor |
|---|---|---|---|
| **Agricultural Stations** | 0.4 | Orchards | 0.4 |
| **Coconut** | 0.5 | Mining Area | 1 |
| **Diversified Crops** | 0.45 | Paddy | 0.5 |
| **Estate Buildings** | 0.4 | Recreational Area | 0.6 |
| **Fish & Hyacinth Ponds** | 0.5 | Rubber | 0.4 |
| **Forest** | 0.1 | Scrub | 0.2 |
| **Mixed Horticulture** | 0.4 | Swamps | 0.5 |
| **Newly Cleared Land** | 0.7 | Urban Area | 1 |
| **Lowland Forest** | 0.1 | Water | 0.5 |

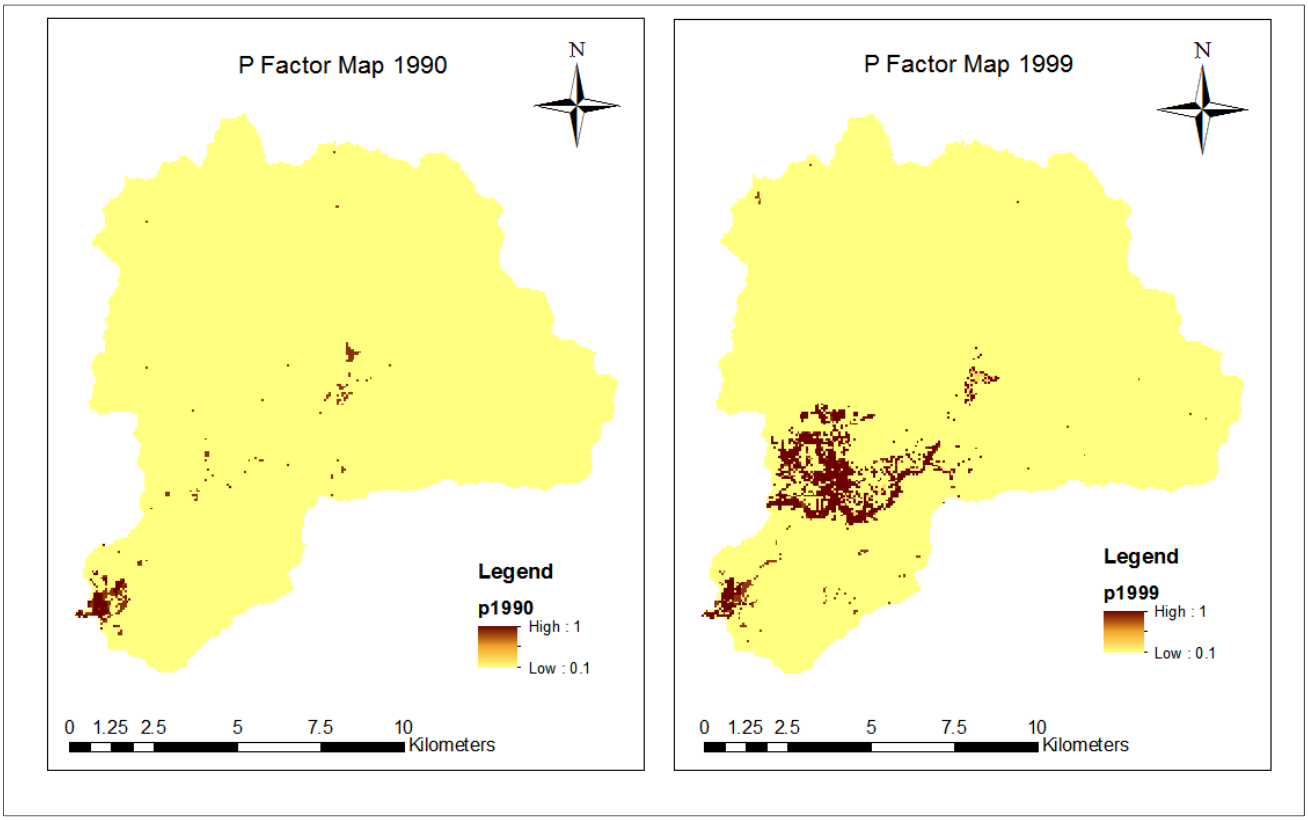


**Figure 7**. Map of conservation practices Factor (P).

## 4 RESULTS AND DISCUSSIONS

In this study, integrating the remotely sensed satellite images with the GIS tools has made the job easier to calculate the soil erosion intensity and to demonstrate the spatial distribution of eroded soil within the Hulu Selangor watershed. The results of the intersection of different layers such as soil types, land cover, vegetation, and topography with respect to the influence of each layer shows a comprehensive view on water soil erosion.

4.1 Monitoring land use change

Vegetation cover is mostly the dominant coverage in Malaysia. However, changing in land cover between 1990 and 1999 shows significant deforestation in middle parts of Hulu Selangor. This vast area of deforestation was as a result of rapid road development and dam construction in that area which leads to a rapid increase of soil erosion in 1999 (Figure 8).

 

4.2 Soil erosion analysis

The intensity of soil erosion highly depends on land cover and rainfall intensity. In this study, two important factors such as deforestation and La Nina had directly affected the land cover and average rainfall. According to final results of USLE model, although the estimated soil loss in 1990 was insignificant the maximum amount of estimated soil loss in 1999 is 17.3 tons per hectare per year. Most of soil erosion was located in deforested areas by mining and construction activity. Figure 9 demonstrated the spatial distribution of eroded area in Hulu Selangor catchment. Zones with red color were labeled as very high correspond with above 10 ton per hectare per year soil loss.

4.3 Estimating of sediment delivery

The relationship between soil erosion and sediment was expressed in many studies. Eq. [4] developed by (LIM et al., 2005) calculates sediment delivery ratio.

$$SDR = 0.4724 * A^{-0.125} \qquad [4]$$

where, SDR is the calculated annual sediment delivery ratio in percentage. A is the area of the catchment.

According to this model, the magnitude of delivered sediment was dependent on the area of the watershed. The larger the watershed the lower the sediment will be estimated. The area of Hulu Selangor catchment is approximately 156 $km^2$. The estimated area is converted into 1.5 hectare. According to Eq. [4], the sediment delivery ratio for Hulu Selangor catchment is 44% which means 44% of eroded soil was washed away and delivered to the sediment outlet at downstream. Multiplying this ratio by amount of estimated soil erosion shows 7.7 ton per hectare sediment yield in 1999. In general, the sediment delivery has significantly increased from 3.2 to 7.7 ton per hectare between 1990 and 1999. The average annual soil loss and sediment yield results in similar conditions which were validated by other researchers. However, comparing the results of SDR model and USLE model with hydrologic data is necessary to validate and assess the accuracy of this study.

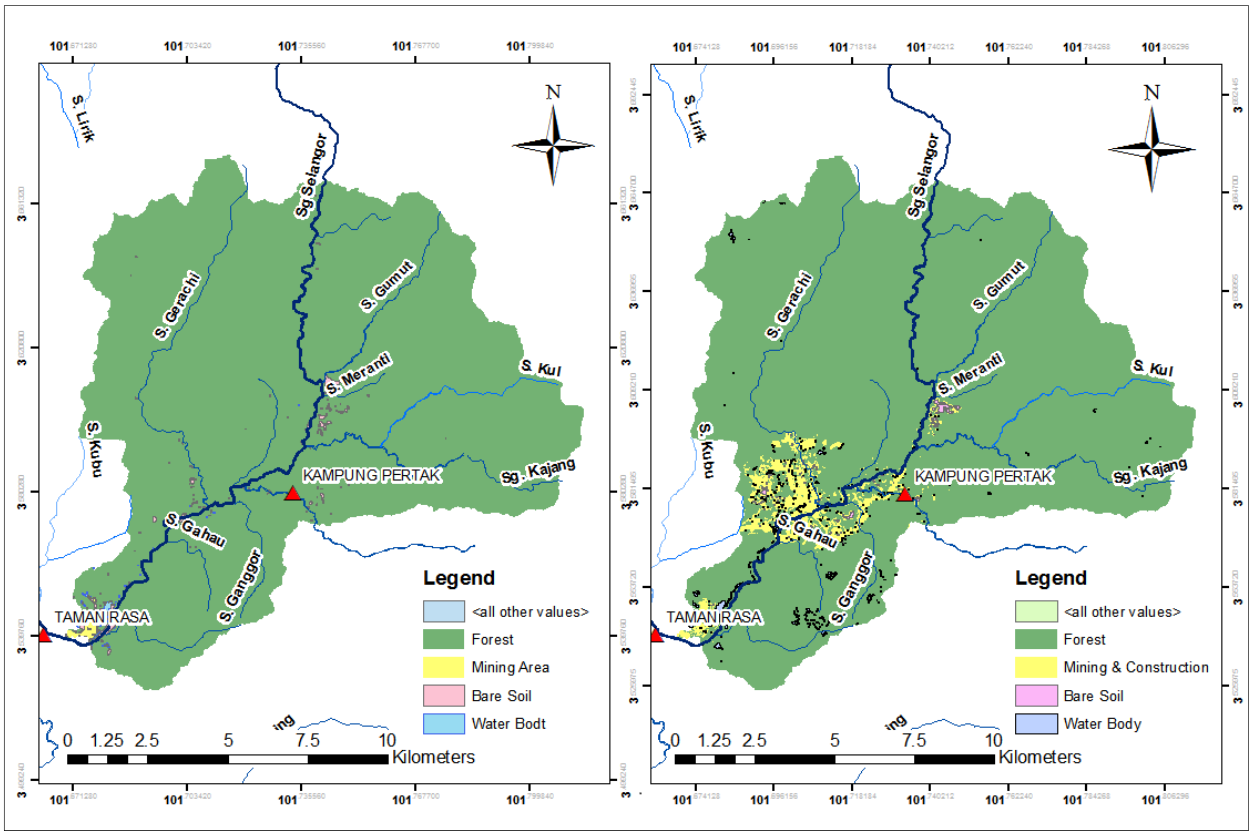


**Figure 8.** Land cover maps in 1990 (on left hand side) and 1999 (on right hand side).

 

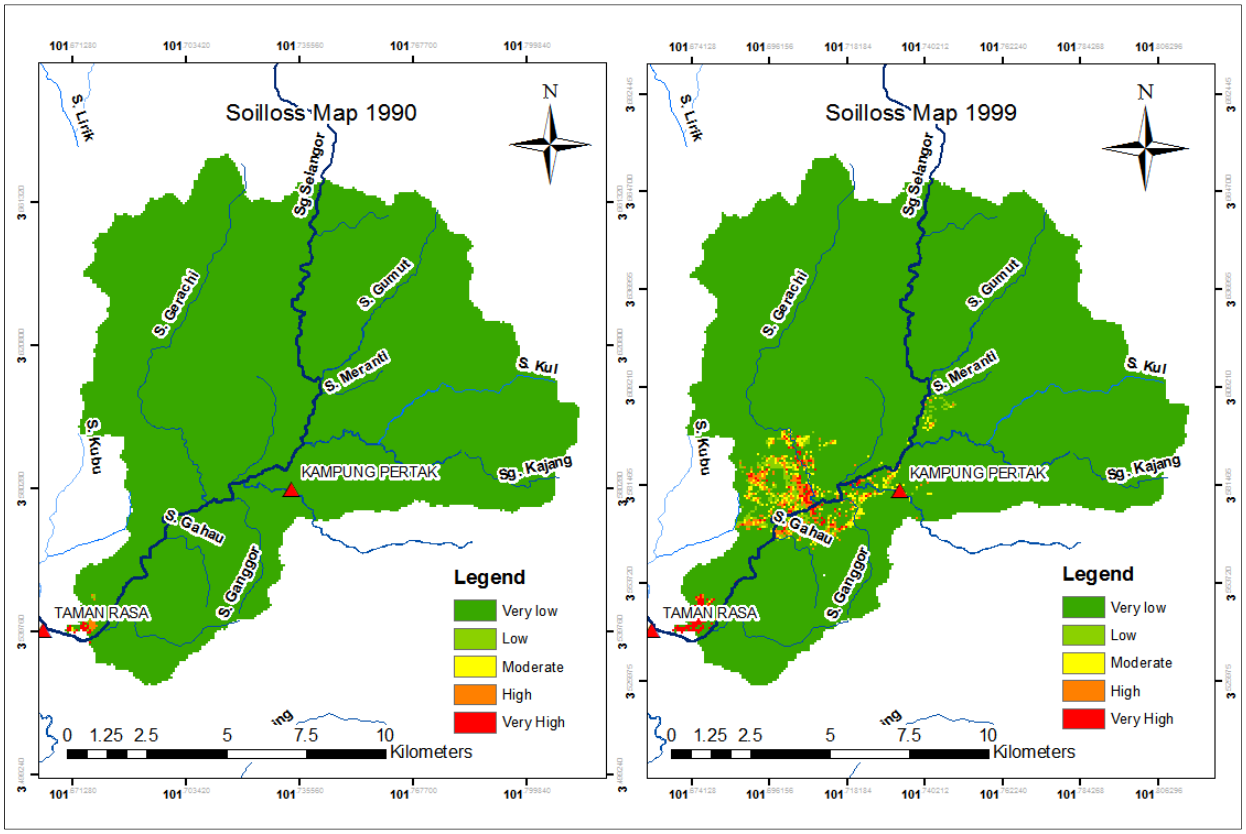


**Figure 9.** Soil loss map in 1990 and 1999.

4.4 Hydrological data and validation

The annual sedimentation data collected from department of irrigation and drainage (DID) at Taman Rasa, to the downstream of Hulu Selangor watershed, shows a dramatic increase from 2.8 to 7.4 ton per hectare per year. Table 4 compares the calculated sediment yield and amount of measured sediment at Taman Rasa sediment station. Comparing the estimated sediment yield by USLE model with collected data varies between 0.3 and 0.4 ton per hectare per year, which indicate the accuracy of the estimated results. Consequently, such a strong accuracy shows that Landsat images can be used as a good alternative source of data to map the geomorphological processes.

**Table 4**. Annual sediment rate for 1990 and 1999.

| | Calculated Sediment yield (Ton/Hec/yr) | Measured sediment at Taman Rasa (Ton/Hec/yr) | Calculated sediment - Measured sediment (Ton/Hec/yr) |
|---|---|---|---|
| 1990 | 3.2 | 2.8 | 0.4 |
| 1999 | 7.7 | 7.4 | 0.3 |

Meanwhile, the effect of differences in the sequence of rainstorm intensities on soil erosionwass rarely considered in soil loss predictions. The annual average rainfall collected from 4 rainfall stations (Kampung Pertak, Taman Rasa, Lembah Beringin, Logi Air K. Kubu Bahru) at upstream of Selangor river shows a slight increase of rainfall from 11.86 to 12.43mm (Figure 10). The average rainfall was slightly increased by 3mm. This result showed that land cover changes have a greater impact on sedimentation in comparison with variation of rainfall intensity.

 

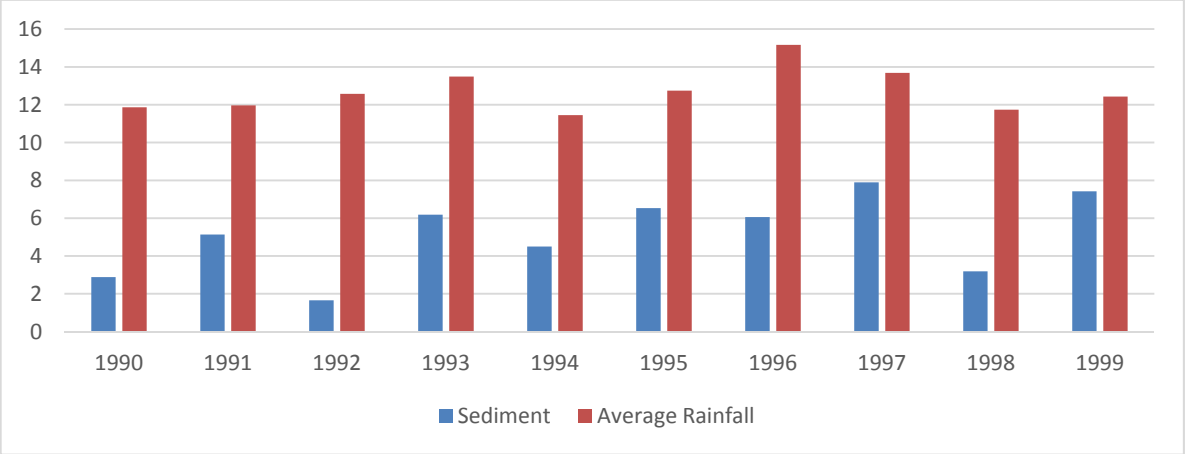


**Figure 10**. Comparison of the average rainfall and annual sediment delivery rates in Hulu Selangor Catchment.

## 5 CONCLUSIONS

In conclusion, two satellite images were collected to generate land cover maps of 1990 and 1999. The generated landcover maps show a significant deforestation (approximately 600km$^2$) within 10 years. Such a huge change in land cover has affected the magnitude of sediment delivery by 4.1 ton per hectare per year. Moreover, comparing the obtained results with hydrological data validated the final results. The small biasness between estimated sediment and collected data indicate that integrating remotely sensed images with GIS tools can be an alternative solution to estimate sediment delivery in forest areas.

## ACKNOWLEDGEMENTS

The authors acknowledge the financial support provided by University of Malaya under Resource Grant (RP017C-15SUS). The comments from anonymous referees are also highly appreciated. Furthermore, the authors are grateful for the assistance by Department of Drainage and Irrigation (DID) and Department of Agriculture (DOA) for providing the necessary hydrological data and charts to validate the results.

## REFERENCES

Islam, S., Gasim, B.M., Rahim, S.A. & Toriman, M.E. (2010). Soil Loss Assessment in the Tasik Chini Catchment, Pahang, Malaysia. *Bull. Geol. Soc. Malaysia*, 56, 1–7.

Jain, M.K., Mishra, S.K. & Shah, R.B. (2010). Estimation of Sediment Yield and Areas Vulnerable to Soil Erosion and Deposition in a Himalayan Watershed using GIS. *Curr. Sci*., 98(2), 213–221.

Jensen, J.R. (2007). *Remote Sensing of the Enviroment: An Earth Perspective*. 3rd ed. Practice Hall Series.

Lim, K.J., Sagong, M., Engel, B.A., Tang, Z., Choi, J. & Kim, K.S. (2005). GIS-Based Sediment Assessment Tool. *Catena*, 64(1), 61–80.

Moore, I.D. & Wilson, J.P. (1992). Length Slope Factor for the Revised Universal Soil Loss Equatin Simplified Method of Solution. *J. Soil Water Conserv.,* 47(5), 423–428.

Morgan, R.P.C. (2005). *Soil Erosion and Conservation.* 3rd ed. Wiley, Blackwell, UK.

Wiscgmeier, W.H. & Smith, D.D. (1978). *Predicting Rainfall Erosion Losses,* USDA Agricultural Research Service Handbook.

 

# SIMULATION OF TRAP EFFICIENCY FOR SRIRAMSAGAR RESERVOIR USING ARTIFICIAL NEURAL NETWORK TECHNIQUES

QAMAR SULTANA [(1)] & M. GOPALNAIK [(2)]

[(1)] MuffakhamJah College of Engineering & Tech, Hyderabad, India,
qamarsultana4@gmail.com
[(2)] University College of Engineering (UCE) OU, Hyderabad, India.
mgnaikc@gmail.com.

## ABSTRACT

The storage reservoirs built across rivers and streams, undergo deposition of sediment. This deposition which takes place progressively in time reduces the active capacity of the reservoir to provide the outputs of water through passage of time. A major portion of the silt that is carried along with the river water settles down in the reservoir, which causes the reduction in its storage capacity, which in turn reduces the benefits from the reservoir projects which were constructed with a huge investment. Thus reservoir sedimentation has become a major problem all over the world. There are a number of methods for estimation of reservoir sedimentation but all these methods differ in terms of their complexity, inputs and other requirements. In the simplest way, the fraction of sediment deposited in the reservoir can be determined through the knowledge of its trap efficiency. In this study, the empirical formulae are used for estimating the trap efficiency of Sriramsagar reservoir which is located on Godavari river in Nizambad district of Telangana State, in India. The observed trap efficiency is calculated using empirical equation suggested by Heinemann and compared with the Brune, Brown method which uses the capacity-inflow ratio for medium sediment depending upon the size of the reservoir and also compared with Gill method which is used for estimation of medium sediment. An attempt has also been made to develop the Artificial Neural Network Model (ANN) to simulate the trap efficiency of the reservoir using the Matlab software. It is observed from the values of several performance statistical indicators that the ANN model predicted the trap efficiency of the reservoir with better accuracy and less effort than that of the conventional method. Based on the simulation results it concludes that the developed ANN model has more advantages over the conventional methods.

**Keywords:** Reservoir sedimentation; trap efficiency; artificial neural network.

## 1 INTRODUCTION

Reservoir sedimentation is caused due to many reasons. The important factors effecting the reservoir sedimentation are the watershed, sediment and river characteristics. The significant factors influencing the rate of siltation in a reservoir are: (a) Capacity to Inflow Ratio (C/I), (b) sediment content in the flowing water, (c) texture and size of the sediment, (d) trap efficiency ($T_e$) of the reservoir, and (e) the reservoir operation method. Methods to predict reservoir sedimentation have been the subject of several empirical studies since the 1950's. There are several methods to estimate the amount of sediments accumulated in reservoirs. One of these methods is trap efficiency method proposed by Brune (1953), Gill (1979), Dendy (1974), Heinemann (1981), and Garg et al. (2008). The trap efficiency method is used to estimate the amount of sediments accumulated in reservoirs by using the reservoir capacity-inflow ratio.

Neural networks models have proved useful for better definition of the relationship between hydrologic parameters and sediment concentration. The neural networks model is essentially a nonlinear black box that correlates outputs to inputs by training its internal algorithms and their weighting schemes against a calibration data set (Hammerstrom, 1993). It is a highly nonlinear tool that can capture complex interactions among the input and output variables without any prior information about the nature of the relations between them. When ANN's are compared with the conventional methods, they can tolerate imprecise or incomplete data and approximate information (Haykin, 1999).

In this paper the trap efficiency has been estimated using the empirical methods, the artificial neural network technique and the conventional regression methods. The ANN model has been developed using Matlab tool and the available input parameters for the estimation of the trap efficiency ($T_e$). The input parameters such as annual inflow ($I_a$), annual rainfall ($R_a$) and the age of the reservoir ($A_g$) were considered and the trap efficiency ($T_e$) was considered as an output parameter.

 

## 2 STUDY AREA DISCRIPTION

The Sriramsagar Project (SRSP), formerly known as the Pochampadu irrigation project has been built on Godavari river. The Godavari river is one of the major peninsular rivers in southern India. This irrigation project is located at Pochampadu village (18°-58' N latitude and 78°- 20' E longitudes) in Nizamabad district of Telangana State (TS) of southern India at a distance of about 200Km from Hyderabad city the location of which is shown in the Figure 1. This project has been built to utilize Godavari river water for irrigation and drinking purposes in Telangana state. It was intended to create irrigation facilities to about 4.0lakhs hectares in addition to generate power up to 36 MW. The regions such as Nizamabad, Adilabad, Karimnagar, and Warangal districts of Telangana State are covered under this project.

Construction of the SRSP project was taken up in 1964, with an elevation up to 322.48 m. In the year 1970, the irrigation benefits started, when the first impounding of the reservoir took place. Subsequently after the Godavari Water Dispute Tribunal Award, the gates on the reservoir were provided and the full reservoir level was raised to 332.537 m. Full benefits of this project were achieved by 1984 after the water was stored up to 332.537 m. The estimated capacity of reservoir at FRL +332.537m is given as 3,172 Mcum. As a result of sedimentation, the live storage capacity of the reservoir came down to 2166.10 Mcum and the Minimum Draw Down Level (MDDL) storage capacity of the reservoir came to 10.10 Mcum.

A provision for silting made at the time of construction was based on Khosla's formula for evaluation of sediment inflow at the rate of 3.57 H m/100 SqKm/year of catchment area and assuming the life of the reservoir as 100 years, a provision of dead storage to an extent of 849 Mcum (30 TMC) corresponding to E.L +324.307m was made in the original proposal. This has been revised taking the recommended silt rate of 1.20 Acres ft/Sq mile/year by the Central Water Commission. Based on this, it is expected that 35 TMC silt gets deposited in the first 50 years and 65 TMC in next 100 years.

The data of the annual inflows into and the annual outflows from the reservoir has been acquired from the Sriramsagar Reservoir Camp Office (SRSP-I) .The sediment inflow and outflow data for the Sriramsagar reservoir were collected from CWC (Central Water Commission), Hyderabad. The reservoir capacity, reservoir annual inflows and reservoir outflows data were obtained from SRSP -I (Sriramsagar Camp) Office, Hyderabad and the reservoir sedimentation data were obtained from Andhra Pradesh Engineering Research Laboratory presently renamed as Telangana State Engineering Research Laboratory (TSERL), Hyderabad. The location of the Sriramsagar reservoir project is shown in Figure 1.

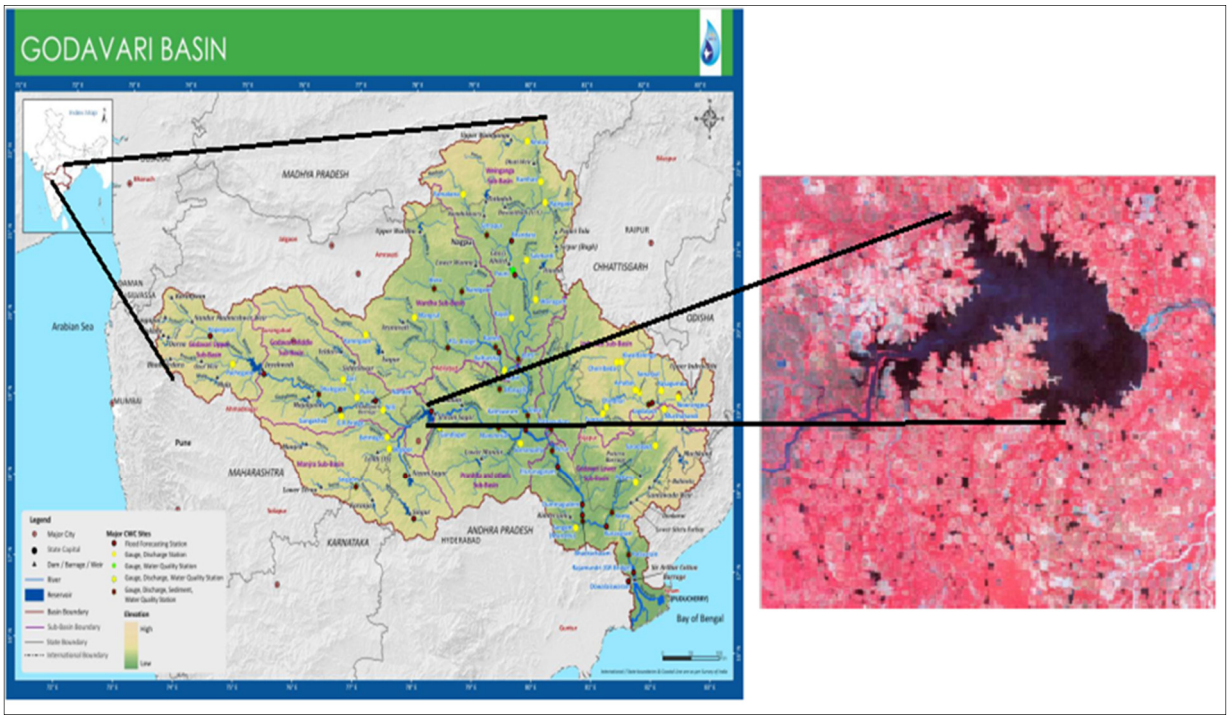


**Figure 1**. Location of Sriramsagar Reservoir.

## 3 METHODOLOGY AND MODEL DEVELOPMENT

Trap efficiency ($T_e$) is the proportion of the incoming sediment that is deposited, or trapped, in a reservoir or pond. The different methods of estimating trap efficiency that is the empirical methods and the artificial neural network (ANN) techniques are used to estimate the trap efficiency of the reservoir. The empirical

 

methods estimate the amount of sediments accumulated in a reservoir depending on reservoir capacity and inflow to the reservoir.

3.1 Empirical Methods

The different empirical methods used for the estimation of the trap efficiency are as follows:

3.1.1 Heinemann's Method:

Heinemann (1981) considered trapping efficiency to be the most informative descriptor of a reservoir. This value is the proportion of the incoming sediment that is deposited or trapped in a pond, reservoir, or lake, often expressed in percentage as given in Eq. [1].

$$\mathrm{Te} = \left[\frac{\mathrm{V_I - V_O}}{\mathrm{V_I}}\right] \mathrm{X}100 \qquad [1]$$

where, $V_I$ is the inflowing sediment load and $V_O$ is the out flowing sediment load.

3.1.2 Brown's Method*:*

The first trap efficiency ($T_e$) estimation method was the pioneer work by Brown in 1944. USACE (1989) expressed this method as Capacity-Watershed method because Brown's curve relates the ratio of the reservoir capacity ($C$) and the catchment/watershed area ($A$) to trap efficiency ($T_e$). The general equation represented by Brune Curve is given by the Eq. [2].

$$\mathrm{Te} = 1 - \frac{1}{[1+\mathrm{K}\left(\frac{\mathrm{C}}{\mathrm{A}}\right)]} \qquad [2]$$

where $C$, is capacity of the reservoir in acre ft.; $A$, is area of the catchment above the reservoir in sq. mile and K is a coefficient which varies from 0.046 to 1.0. A value of K = 0.1 was recommended for average conditions, and values of K = 1.0, 0.1 and 0.046 may be used for coarse, medium and fine sediments, respectively (Gill, 1979). The major advantage of Brown's method is that only two parameters i.e., catchment area and reservoir capacity are required.

3.1.3 Brune's Curve (Capacity-Inflow Method):

This method is probably the most widely used method for estimating the trap efficiency of reservoirs. Brune's curves were drawn based on data from 44 normal ponded reservoirs in the United States. Brune plotted $T_e$ against the reservoir C/I ratio. The graph plotted by Brune has three curves consisting of one median and two envelop curves. Brune developed an empirical relationship between trap efficiency and the ratio of reservoir capacity to mean annual inflow, both in the same volume units as shown in the Eqs [3] to [6].

(i) Primarily highly flocculated and coarse grained sediments.

$$T_e = \frac{8000 - 36\left(\frac{\mathrm{C}}{\mathrm{I}}\right)^{-0.78}}{78.85 + \left(\frac{\mathrm{C}}{\mathrm{I}}\right)^{-0.78}} \qquad [3]$$

(ii) Median curve (for medium sediments)

$$T_e = \frac{\left(\frac{\mathrm{C}}{\mathrm{I}}\right)}{0.00013 + 0.01\left(\frac{\mathrm{C}}{\mathrm{I}}\right) + 0.0000166\sqrt{\frac{\mathrm{C}}{\mathrm{I}}}} \qquad [4]$$

Heinmann (1981) developed Brune method as

$$T_e = 100\left[\frac{\mathrm{K}}{0.012 + 1.02\mathrm{K}}\right] \qquad [5]$$

where,
K = sedimentation index (S.I) x acceleration due to gravity (g),
the value of SI calculated using the relationship:

$$S.I = \frac{\left(\frac{\mathrm{C}}{\mathrm{I}}\right)^2}{\mathrm{L}} \qquad [6]$$

 

where,
L= the reservoir length

A best fit equation based on the original Brune (1953) Primarily Highly Flocculated and Coarse Grained Sediments envelope curve was developed for Gobind Sagar Reservoir to calculate the $T_e$ by Garg et al. (2008) which is given in the Eq. [7].

$$T_e = \frac{\left(\frac{C}{I}\right)^2}{\left(\frac{C}{I}\right)^2 + 0.0025x\left(\frac{C}{I}\right) + 0.00003} \quad [7]$$

3.1.4 Gill's Equations

Gill (1979) developed empirical equations for different grain sizes which provided a very close fit to the three curves proposed by Brune which are presented in the Eqs. [8] to [10].

(i) Primarily Highly Flocculated and Coarse Grained Sediments:

$$T_e = \frac{\left(\frac{C}{I}\right)^2}{0.994701\left(\frac{C}{I}\right)^2 + 0.006297\left(\frac{C}{I}\right) + 0.3x10^{-5}} \quad [8]$$

(ii) Median Curve (for Medium Sediments) Morris and Wiggert (1972):

$$T_e = \frac{\left(\frac{C}{I}\right)}{0.012 + 1.02\left(\frac{C}{I}\right)} \quad [9]$$

(iii) Primarily Colloidal and Dispersed Fine-grained Sediments*:*

$$T_e = \frac{\left(\frac{C}{I}\right)^3}{1.02655\left(\frac{C}{I}\right)^3 + 0.02621\left(\frac{C}{I}\right)^2 - 0.133x10^3\left(\frac{C}{I}\right) + 0.1x10^{-5}} \quad [10]$$

3.2 Artificial Neural Network

Artificial Neural Network (ANN) is widely applied in the forecasting of hydrology and water resource variables. In ANN, the feed-forward artificial neural network structure with a back-propagation algorithm (BP) is common to engineers. Figure 2 shows the different steps of the training process in the form of a flow chart.

3.2.1 Developing ANN model*:*

Designing of ANN model consists of five steps such as data collection, pre-processing of the data, building of the network, training the network and test performance of model. Collection and preparation of the sample data is the first step in designing of the ANN models. The data of the annual inflows into and the annual outflows from the reservoir has been acquired from the Sriramsagar Reservoir Camp Office (SRSP-I). The reservoir sediment inflow and outflow date is acquired from CWC, Hyderabad. The data for 26 years period from 1986 to 2012 have been used to carry out the current study along with annual inflow, annual rain flow and age of the reservoir.

After data collection, in the data pre-processing procedure, there are three steps for the efficient training of the ANNs which includes solving the problem of missing data, normalization of data and randomization of data. The gaps in the data are replaced by the average of neighbouring values during the same period. Normalizing the data before giving the input data to the network is generally a good practice, since mixing variables with large and small values will cause confusion to the learning algorithm on the weightage of each variable and the variables with the smaller values may be forced to be rejected .The data used is normalized between 0 and 1 using the Eq. [11].

$$r_j = \frac{R_j - R_{min}}{R_{max} - R_{min}} \quad [11]$$

where $r_i$ is the respective normalized value, $R_i$ is the actual value, $R_{min}$ and $R_{max}$ are the minimum and maximum of the total values of the data.

 

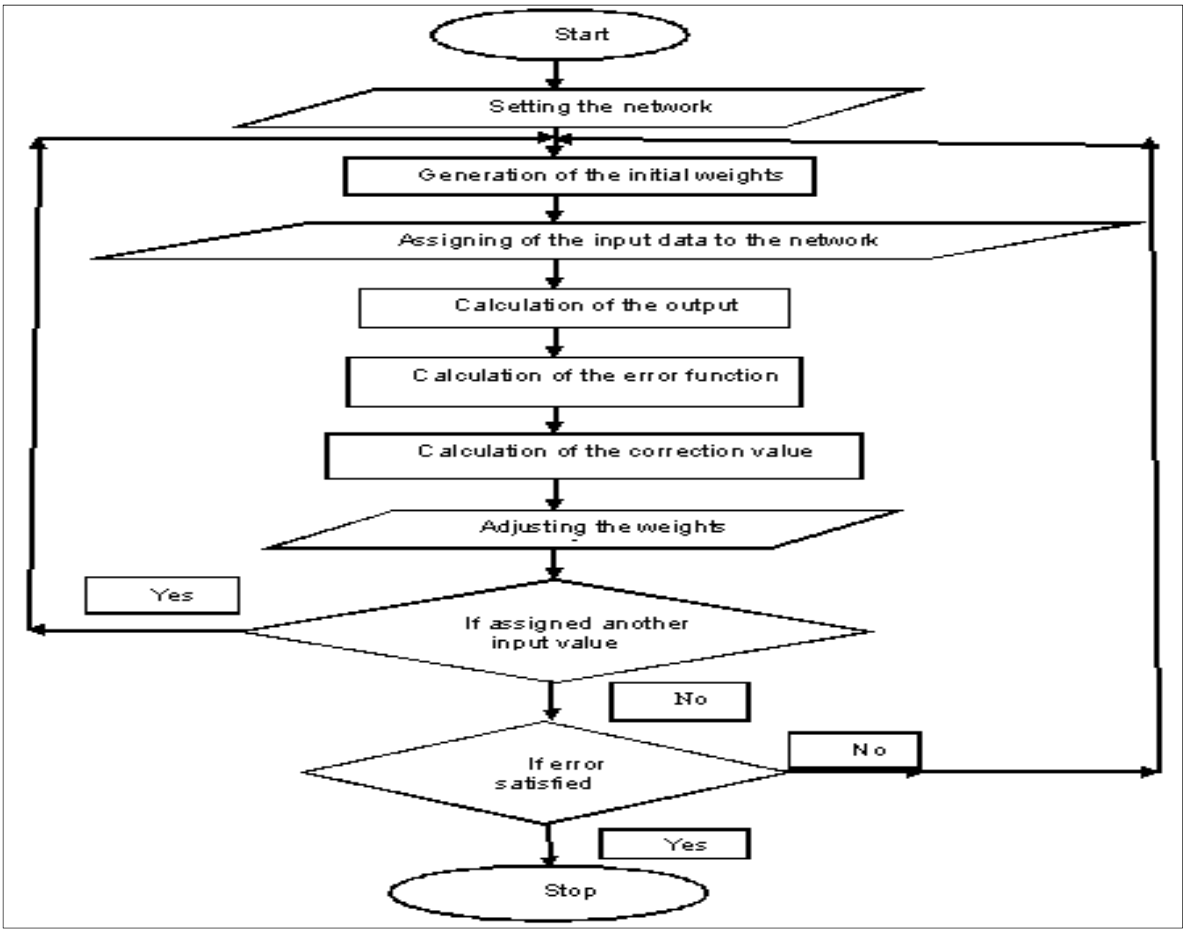


**Figure 2**. Flow Chart for the simulation of the trap efficiency using the ANN technique.

Building of the network at this stage includes the selection and specification of the number of hidden layers, neurons, transfer function, training function in each layer, weight/bias learning function, and performance function to the network. In this study, a Multilayer Perceptron (MLP) network is used. A three-layered feed forward neural network (FFNNs), which is usually used in forecasting hydrologic time series, provide a general framework for representing nonlinear functional mapping between a set of input and the output variables. The term "feed-forward" means that a neuron connection exists only in the forward direction from one layer to another and the neurons within a layer are not interconnected to each other. Thus, a three layer BP network model trained by Levenberg Marquardt optimization algorithm is chosen for this study.

During the training process, the weights are adjusted in order to make the actual outputs (predicted) close to the target (measured) outputs of the network. MATLAB provides built-in transfer functions which are used in this study i.e. the linear (purelin), Hyperbolic Tangent Sigmoid (logsig) and Logistic Sigmoid (tansig) transfer function. The next step is to test the performance of the developed model. In order to evaluate the performance of the developed ANN models quantitatively, statistical analysis involving the coefficient of determination ($R^2$), mean-square-error (MSE), the root mean square error (RMSE) were conducted. RMSE provides information on the short term performance which is a measure of the variation of predicted values from the measured data. The lower the RMSE, the more accurate is the estimation.

3.3 Conventional Regression method.

A conventional regression analysis is conducted, between the output parameter ($T_e$) and the input parameters ($I_a$, $R_a$, and $A_g$), using RegressIt software that performs multiple linear regression analysis.

## 4 RESULTS AND DISCUSSIONS

4.1 Empirical Methods

The trap efficiency which is a measure of the proportion of the sediment trapped in the reservoir is determined by using the empirical equations given by Brune, Brown and Gill. These equations make use of the original capacity (C) of the reservoir, and the average annual inflows (I) as the input data. The trap efficiencies calculated by using the various methods along with the observed trap efficiency is shown in the Table 1. The observed trap efficiency is calculated using the equation given by Heinemann, which uses the

 

parameters, volume of sediment inflow into and outflow from the reservoir. The Brown's equation used for the determination of the trap efficiency uses the capacity-area ratio and the K factor whose value is adopted as 1 as K=0.1 is showing underestimated values. The trap efficiency by Brune method which uses the capacity-inflow ratio is selected for the medium sediment depending upon the size of the reservoir. The trap efficiency by Gill method is obtained by using the equation for medium sediment.

It is seen that the trend of the results of the Gill's and Brune's method for medium sediment follows that of the observed trap efficiencies as shown in the Figure 3. but on an average are giving higher values. The results of the trap efficiency estimated by Brown's method with K=1 is found to be well suitable for the estimation of the trap efficiency values for the reservoir which is shown from the values displayed in the Table 1.

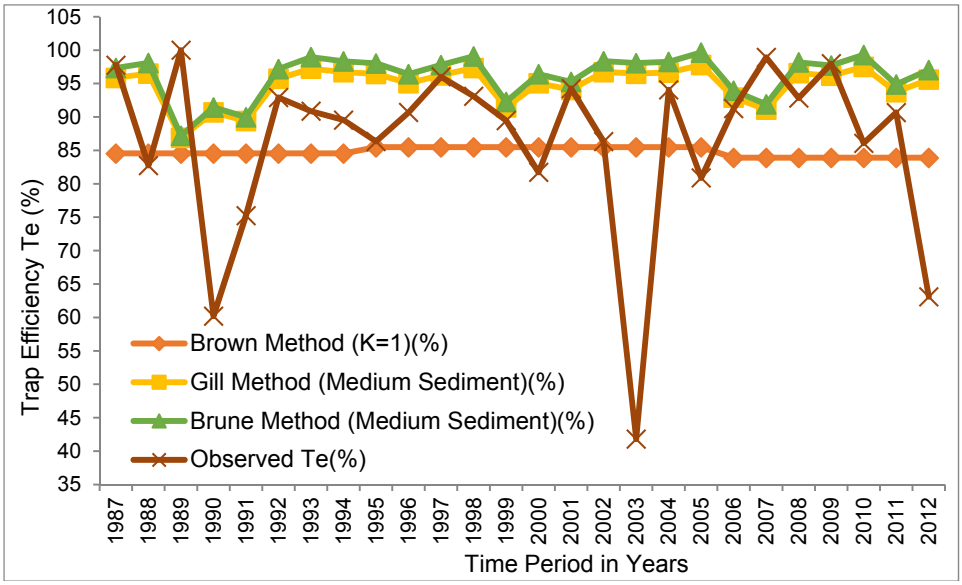


**Figure 3.** Comparative plot of Te (%) estimation by different methods.

**Table 1.** Comparison of Observed and Estimated Trap efficiencies by different methods.

| Year | Capacity (C in x$10^6$ $m^3$) | Annual Inflows (I in Mcum) | (C/I) Ratio | (C/A) Ratio | $T_e$ (%) Brown Method (k=1) | $T_e$ (%) Gill Method (Medium Sediments) | $T_e$ (%) Brune Method (Medium Sediments) | $T_e$ (%) Observed |
|---|---|---|---|---|---|---|---|---|
| 1987 | 2377.37 | 4593.95 | 0.52 | 5.47 | 84.54 | 95.86 | 97.33 | 97.76 |
| 1988 | 2377.37 | 3215.82 | 0.74 | 5.47 | 84.54 | 96.50 | 98.09 | 82.74 |
| 1989 | 2377.37 | 25900.39 | 0.09 | 5.47 | 84.54 | 86.90 | 87.18 | 99.99 |
| 1990 | 2377.37 | 16351.96 | 0.15 | 5.47 | 84.54 | 90.70 | 91.43 | 60.19 |
| 1991 | 2377.37 | 19509.94 | 0.12 | 5.47 | 84.54 | 89.41 | 89.97 | 75.24 |
| 1992 | 2377.37 | 4863.10 | 0.49 | 5.47 | 84.54 | 95.74 | 97.18 | 92.91 |
| 1993 | 2377.37 | 1666.60 | 1.43 | 5.47 | 84.54 | 97.24 | 98.96 | 90.86 |
| 1994 | 2377.37 | 2775.15 | 0.86 | 5.47 | 84.54 | 96.71 | 98.33 | 89.54 |
| 1995 | 2557.25 | 3586.79 | 0.71 | 5.88 | 85.47 | 96.45 | 98.02 | 86.33 |
| 1996 | 2557.25 | 6815.24 | 0.38 | 5.88 | 85.47 | 95.06 | 96.40 | 90.67 |
| 1997 | 2557.25 | 4049.05 | 0.63 | 5.88 | 85.47 | 96.25 | 97.78 | 96.01 |
| 1998 | 2557.25 | 1583.05 | 1.62 | 5.88 | 85.47 | 97.33 | 99.07 | 93.11 |
| 1999 | 2557.25 | 15672.72 | 0.16 | 5.88 | 85.47 | 91.45 | 92.27 | 89.47 |
| 2000 | 2557.25 | 6815.07 | 0.38 | 5.88 | 85.47 | 95.06 | 96.40 | 81.72 |
| 2001 | 2557.25 | 9185.72 | 0.28 | 5.88 | 85.47 | 94.06 | 95.25 | 94.26 |
| 2002 | 2557.25 | 2947.73 | 0.87 | 5.88 | 85.47 | 96.73 | 98.35 | 86.33 |
| 2003 | 2557.25 | 3505.65 | 0.73 | 5.88 | 85.47 | 96.48 | 98.06 | 41.80 |
| 2004 | 2557.25 | 3147.25 | 0.81 | 5.88 | 85.47 | 96.64 | 98.25 | 94.07 |
| 2005 | 2557.25 | 541.16 | 4.73 | 5.88 | 85.47 | 97.80 | 99.65 | 80.88 |
| 2006 | 2264.15 | 10622.35 | 0.21 | 5.21 | 83.89 | 92.91 | 93.93 | 91.25 |
| 2007 | 2264.15 | 14625.44 | 0.15 | 5.21 | 83.89 | 91.11 | 91.90 | 98.91 |
| 2008 | 2264.15 | 2920.04 | 0.78 | 5.21 | 83.89 | 96.57 | 98.17 | 92.84 |
| 2009 | 2264.15 | 3707.05 | 0.61 | 5.21 | 83.89 | 96.19 | 97.71 | 97.99 |
| 2010 | 2264.15 | 1061.09 | 2.13 | 5.21 | 83.89 | 97.50 | 99.28 | 86.07 |
| 2011 | 2264.15 | 8848.57 | 0.26 | 5.21 | 83.89 | 93.73 | 94.87 | 90.67 |
| 2012 | 2264.15 | 4896.58 | 0.46 | 5.21 | 83.89 | 95.61 | 97.04 | 63.10 |
| | | Average | | | 84.75 | 94.85 | 96.19 | 86.34 |

4.2 Artificial Neural Networks Method

A conventional regression analysis is done relating the output parameter (Trap Efficiency ($T_e$)) with the input parameters (Annual Rainfall ($R_a$), Annual Inflows ($I_a$), Age of the reservoir ($A_g$)). The regression equation of the three input variables with the output parameter which gave the best result is shown in the Eq. [17].

Estimated Trap Efficiency from regression method =

$$80.342 + (0.034 * A_g) - (0.0000004857 * I_a) + (0.004882 * R_a) \quad [17]$$

The value of R, the correlation coefficient for three input variables is 0.207 which is shown in the Table 3 which is not very satisfactory, and hence an attempt is made by using Artificial Neural Network (ANN) technique for the better results.

A Multilayer Perceptron (MLP) ANN architecture consisting of three layers with 10 neurons in the hidden layer is developed using the MATLAB tool. Twenty six years data is used, out of which 70% is used for testing and the rest 30% is used for training and validation. Based on the values of R, the correlation coefficient generated (0.9766), it is seen that a Feed Forward, Back Propagation (BP ANN) model shown in the Figure 4 with the structure 3-10-1 generated the trend of the trap efficiency values very well with TRAINLM - training function, TRAINGDM - learning function and TANSIG - transfer function. The performance statistics of the ANN model in comparison to the conventional regression method is shown in the Table 3 .It is observed from the calculated values of trap efficiency in the Table 2 and the Figure 5. that the pattern of trap efficiency is well depicted by the ANN model.

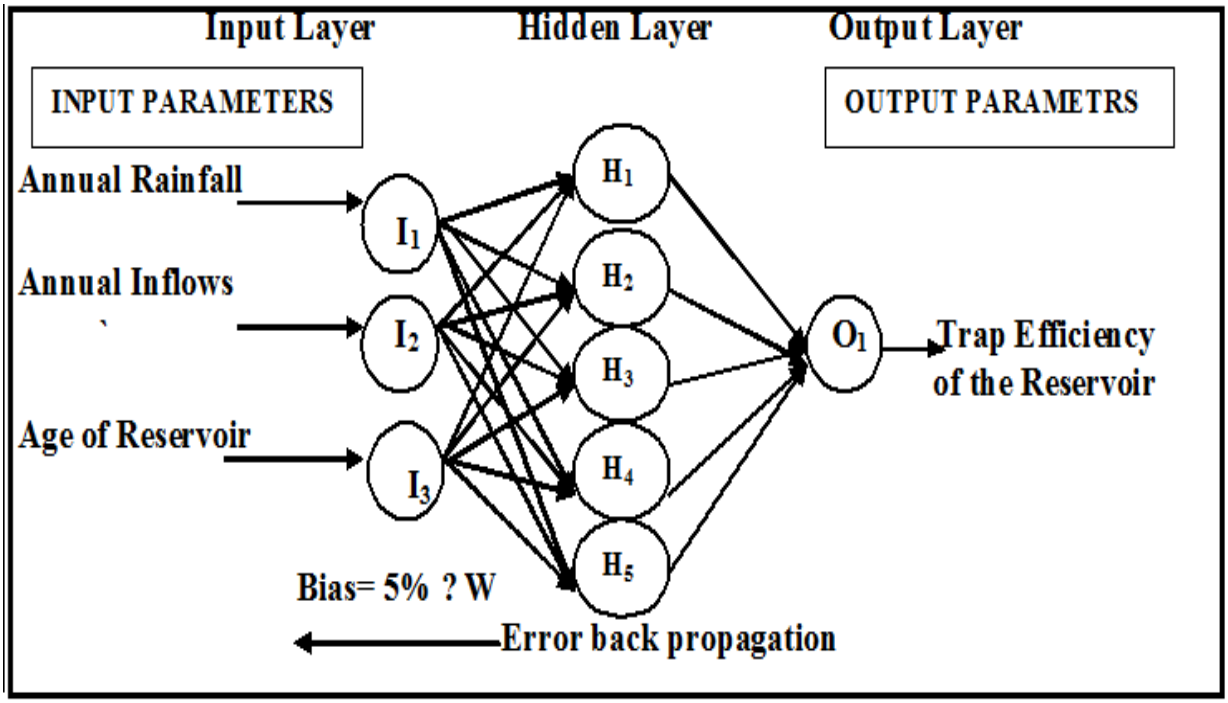


**Figure 4.** Neural network architecture used for prediction of trap efficiency.

 

**Table 3.** Observed, Predicted (ANN Model) and the Estimated (Regression Analysis) values of Trap Efficiency of the reservoir.

| Year | Age Of the Reservoir | Annual Inflows ($10^6$ $m^3$) | Annual Rainfall (mm) | Observed Trap Efficiency(%) | Predicted (ANN)Trap Efficiency(%) | Estimated (Regression) Trap Efficiency (%) |
|---|---|---|---|---|---|---|
| 1986-1987 | 17 | 43137.58 | 3828.96 | 97.76 | 89.75 | 99.32 |
| 1987-1988 | 18 | 3215.82 | 818.20 | 82.74 | 106.48 | 84.67 |
| 1988-1989 | 19 | 25900.39 | 1166.99 | 99.99 | 98.62 | 86.40 |
| 1989-1990 | 20 | 16351.96 | 1028.22 | 60.19 | 60.29 | 85.76 |
| 1990-1991 | 21 | 19509.94 | 1040.55 | 75.24 | 75.49 | 85.85 |
| 1991-1992 | 22 | 4863.10 | 833.75 | 92.91 | 90.43 | 84.89 |
| 1992-1993 | 23 | 1666.60 | 835.42 | 90.86 | 94.58 | 84.93 |
| 1993-1994 | 24 | 2775.15 | 947.89 | 89.54 | 89.63 | 85.51 |
| 1994-1995 | 25 | 3586.79 | 1008.65 | 86.33 | 87.00 | 85.84 |
| 1995-1996 | 26 | 6815.24 | 1248.73 | 90.67 | 92.97 | 87.05 |
| 1996-1997 | 27 | 4049.05 | 1201.49 | 96.01 | 94.38 | 86.85 |
| 1997-1998 | 28 | 1583.05 | 853.92 | 93.11 | 98.92 | 85.19 |
| 1998-1999 | 29 | 15672.72 | 1150.78 | 89.47 | 89.05 | 86.67 |
| 1999-2000 | 30 | 6815.07 | 872.89 | 81.72 | 87.02 | 85.35 |
| 2000-2001 | 31 | 9185.72 | 1031.16 | 94.26 | 92.86 | 86.15 |
| 2001-2002 | 32 | 2947.73 | 823.50 | 86.33 | 83.67 | 85.18 |
| 2002-2003 | 33 | 3505.65 | 798.66 | 41.80 | 41.80 | 85.09 |
| 2003-2004 | 34 | 3147.25 | 733.10 | 94.07 | 93.00 | 84.80 |
| 2004-2005 | 35 | 541.16 | 1197.80 | 80.88 | 77.52 | 87.11 |
| 2005-2006 | 36 | 10622.35 | 1066.60 | 91.25 | 94.14 | 86.49 |
| 2006-2007 | 37 | 14625.44 | 917.60 | 98.91 | 96.87 | 85.80 |
| 2007-2008 | 38 | 2920.04 | 959.30 | 92.84 | 92.60 | 86.04 |
| 2008-2009 | 39 | 3707.05 | 689.70 | 97.99 | 101.31 | 84.76 |
| 2009-2010 | 40 | 1061.09 | 1192.70 | 86.07 | 85.47 | 87.25 |
| 2010-2011 | 41 | 8848.57 | 962.90 | 90.67 | 91.81 | 86.16 |
| 2011-2012 | 42 | 4896.58 | 845.40 | 63.10 | 59.45 | 85.62 |
| Average | | | | 86.34 | 87.12 | 86.34 |

**Table 4.** Comparison of Performance Statistics of ANN Model and Conventional Regression Method.

| Statistical Parameter | ANN Model | Conventional Regression Method |
|---|---|---|
| R | 0.9766 | 0.207 |
| $R^2$ | 0.9537 | 0.043 |
| MSE | 0.0024 | 164.02 |
| RMSE | 0.0493 | 12.81 |

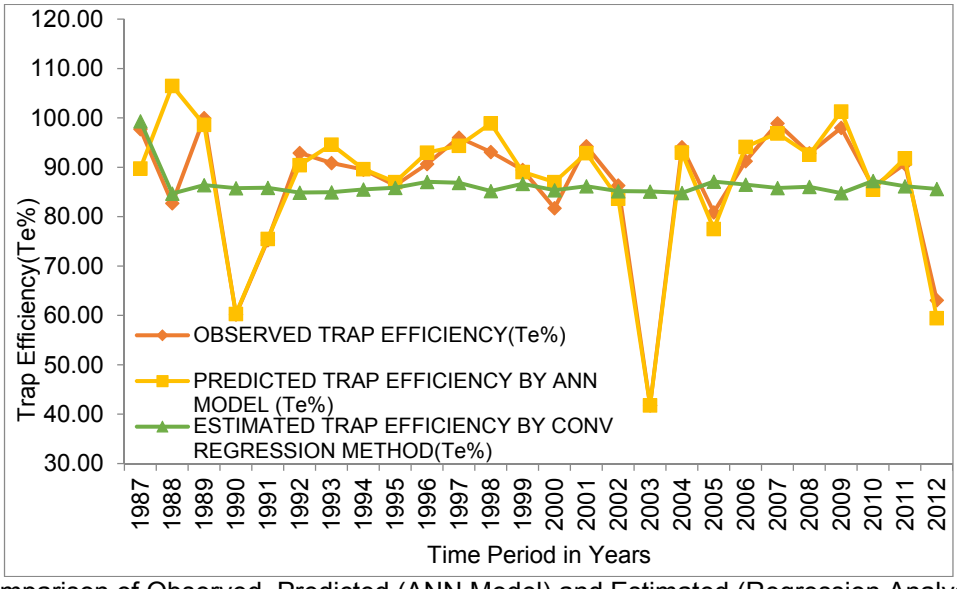


**Figure 5.** Comparison of Observed, Predicted (ANN Model) and Estimated (Regression Analysis) values of Trap Efficiency.

## 5 CONCLUSIONS

It is seen that the trend of results of Gill's method closely follow the Brune's method and the Brown's method was showing lower values but on an average the Brown's method is simulating well with the observed values of the trap efficiency. The limitation of these methods is, they are applicable only to long-term average conditions but in India where the sediment inflow and outflow data are usually not measured, these empirical approaches are the best suitable approach to estimate sediment retained in the reservoirs and the major advantage of these empirical methods are to estimate fairly reasonable results from very limited data such as, the capacity, average annual inflow and catchment area.

The developed ANN model such as a three layered ANN network with three inputs, ten neurons in the hidden layer and one output with a feed forward back propagation (FFBP) network generated the trend of the trap efficiency values reasonably well with TRAINLM - training function, TRAINGDM - learning function and TANSIG - transfer function. The input parameters used are annual inflow, annual rainfall and age of the reservoir and the output parameter considered is the trap efficiency ($T_e$) of the reservoir. Twenty six years of data pertaining to Sriramsagar reservoir is used in this study. It is observed from the values of several performance statistical indicators that the ANN model predicted the trap efficiency of the reservoir with better accuracy and less effort and also captured the trend of the variation of trap efficiency very well when compared to the traditional regression approach. Based on the simulation results, it concludes that the developed ANN model has more advantages over the conventional methods.

## REFERENCES

Brown, C.B. (1944). Discussion of Sedimentation in Reservoirs.Ed. J. Witzig. *Proceedings of the American Society of Civil Engineers*, 69, 1493-1500.

Brune, G.M. (1953). Trap Efficiency of Reservoirs. *Transaction of America. Geophysical Union*, 34(3), 407-418.

Dendy, F.E. (1974). Sediment Trap Efficiency of Small Reservoirs. *Transaction of the America Society of Agricultural Engineers*, 17(5), 898-988.

Garg, V. & Jothiprakash, V. (2008). Trap Efficiency Estimation of a Large Reservoir. *ISH Journal of Hydraulics*, 14(2), 88-101.

Garg, V. & Jothiprakash, V., (2009). Reservoir Sedimentation Estimation Using, Artificial Neural Network. *Journal of Hydrologic Engineering*, 14(9), 1035-1040.

Gill, M.A., (1979). Sedimentation and Useful Life of Reservoirs. *Journal of Hydrology*, 44, 89-95.

Heinemann, H.G. (1981). A New Sediment Trap Efficiency Curve for Small Reservoirs. *Water Resources Bulletin*, 17(5), 825-830.

Hammerstrom, D. (1993). Working with Neural Networks. *IEEE Spectrum*, 30(7), 46–53.

Haykin, S. (1999). *Neural Network: A Comprehensive Foundation*. Prentice-Hall, Upper Saddle River, N.J.

 

Proceedings of the 37th IAHR World Congress
August 13 – 18, 2017, Kuala Lumpur, Malaysia

# DETERMINATION OF GRAIN SIZE DISTRIBUTION ALONG AREAS OF SAND DEPOSITION: A CASE STUDY OF HIJI RIVER

ITANI DALE NDWAMBI[(1)], AKIHIRO KADOTA[(2)] & OMAR MAHMOUD SELEEM[(3)]

[(1,2,3)] Ehime University, Matsuyama, Japan,
itanidalendwambi@gmail.com; akado@cee.ehime-u.ac.jp; akado@cee.ehime-u.ac.jp

## ABSTRACT

In order to clarify several phenomena occurring in rivers such as river bed changes and flood flows, accurate information on grain size distributions is very crucial. Determination of grain size affects the accuracy of numerical flow and river bed configuration analysis. The most used method to measure grain size distributions is by sampling sand and gravel at selected sites in a river. However, this method is tedious and costly. The current study proposes an efficient method to accurately estimate the distribution of grain size by means of surface images of sand deposition areas (taken by drone) such as a sand bar. Image analysis is based on estimation of each particle size using BASEGRAIN which is a code in MATLAB. In this study, the accuracy of the image analysis is verified by comparing it with the sampling results and the applicability of the method is discussed.

**Keywords:** Grain size; drone; image analysis; BASEGRAIN; Hiji River.

## 1 INTRODUCTION

Recently, temperatures have been increasing so high, which caused a lot of extraordinary typhoons and heavy rains in Japan. This has increased the frequency of natural disasters such as flooding and inundation. Information on rivers such as time variation of flood discharge, water depth, riverbed morphology, riverbed roughness and vegetation are very crucial to be collected in order to assess natural phenomena in rivers (flood flow, flood inundation and river bed changes). Together with these, the information on grain size distributions from riverbed surface is also important to determine which will enable numerical analysis and hydraulic experiment of river flow, riverbed changes and flood inundation. In addition, evaluation of the sand deposits is essential for classification of aquatic habitats. However, ancient estimation of grain size distributions on riverbed surfaces require gravel excavation, collection and screening and this procedure is tedious and costly.

In this study, an efficient method of grain size distribution determination is proposed. This method covers aerial photography of riverbed surfaces and the BASEGRAIN program analysis developed by Detert and Weitbrecht (2012), which is referred to image processing techniques and analysis. The grain distributions estimated by the proposed method are discussed by comparing with the screened results of excavated sand and gravel, and its applicability is also discussed. Few studies have been done for estimating grain size distributions using image processing techniques.

Kozakiewicz (2013) used automated image analysis for measuring size and shape of Martian sand grains in USA, Arizona. In this study, image analysis tool for grain detection and measurement was established. The automated approach was based on the algorithm which enabled to detect individual grains and measured their size and shape. The algorithm used a set of image processing techniques related to filtering extraction and segmentation is implemented in Wolfrain Matematica.

Chang and Chung (2012) used an image processing method of fusing feedback pulse coupled with neural network and multilevel thresholding. The I-FM method, which is proposed for automatic extraction of grain size distribution is based on digital photographs taken from a riverbed. A decisive image-emerging technique was also developed for improving the quality of image segmentation in grain size measurements.

## 2 METHODOLOGY

The setting of the study is in Hiji River in Ozu City of Ehime Prefecture in the Northwestern side of Shikoku Island of Japan. The catchment area is 1, 210km$^2$, length of 103km and annual rainfall of 1, 800mm. The Hiji River is well known for its many tributaries and narrow river mouth, resulting in frequent flooding as shown in Figure 1.

There is deposition of the riverbed, with an area of sand deposition developed on the east side of the river, as shown on the left in Figure 2, which resulted in flow to be concentrated into a narrow channel found on the west side of the river.

 

**Figure 1**. Narrow river mouth in Hiji River.


**Figure 2**. Developed sand depositions.

According to the flow pattern, sediment was transported to the area of deposition on the east side of the river and deposition advances progressively. By doing so, risk of flooding increases. In order to solve this deposition problem, data of grain size distributions in the deposition area is needed. Accurate grain size data ensures that there is a reasonable analysis, such as estimation of tractive force for sediment particles, riverbed roughness for flow, bed load and riverbed variation. The current study used images of the surface of the deposition area by means of photographs shot using a drone (unmanned Aerial Vehicle, DIJ phantom 2 vision, Figure 3). The drone was equipped with a digital camera including a GPS logger, so that the surface image and position of the image can be recorded.

For the purpose of measurement, 3 shooting points were selected in the deposition area, as shown in Figure 2, and 4 positions for drone height were chosen at 1m, 2m, 3m, and 4m. Resolution effects and accuracy of grain size distributions were also discussed in the present study. Figure 4 shows the image analysis procedure for determining the particle size distributions.

The procedure includes five steps: (1) data import; (2) pre-processing; (3) parameter adjustment; (4) post-processing; and (5) particle size distribution analysis. As for step (1), an appropriate resolution was derived from the images taken by the drone as initial control parameters as shown in Figure 5. Improving the analytical efficiency for large volume images by downscaling to the range of the minimum detectable diameter was accomplished at this step. Then, the ratio in mm was determined for the pixels from the 1m × 1m square frame shown in Figure 1, if the image scale is already known. The actual geographical coordinates were also extracted from the position information of the image, which is given in latitude and longitude by the GPS logger. These three bits of information were saved as the initial control parameters. At step (2), a cropped

 

area of the image was outlined by a square shown with a yellow line in Figure 5. In the same way, some other scales of the image were selected for the area (approximately 5 repeating) with inputting accurate distance for end of this area. At step (3), voids in the gravel were evaluated in the parameter adjustment as shown in Figure 6. The area between voids was discriminated, and then the long axis and short axis of each identified gravel particle were evaluated by object detection processing (Figure 7). At step (4), post-processing to correct excessive segmentation of particles for incorrectly divided particles was done as shown in Figure 8. The different particle region was also corrected in the same procedure. As a result, particle size distributions were obtained from the above analysis and compared with data from excavated and collected samples in order to evaluate the effectiveness of the particle size distribution analysis by this image analysis procedure.

**Figure 3**. Drone (DIJ phantom 2 vision).

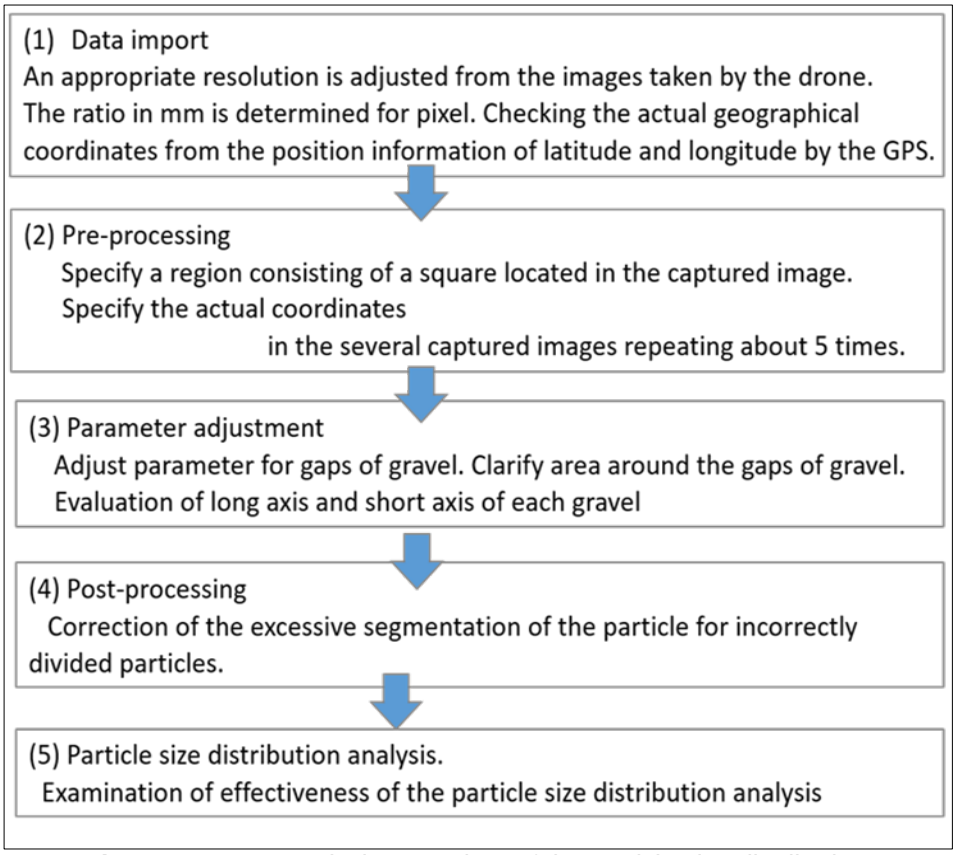


**Figure 4**. Image analysis procedure of the particle size distribution

 

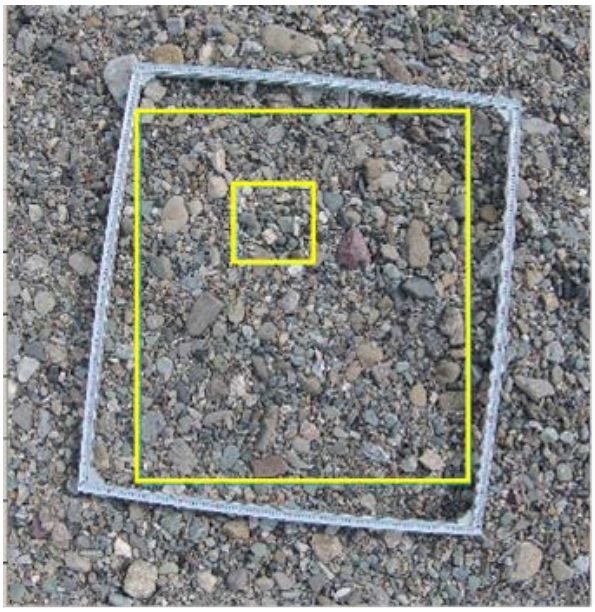

**Figure 5**. An image on bed surface of sand deposition area.

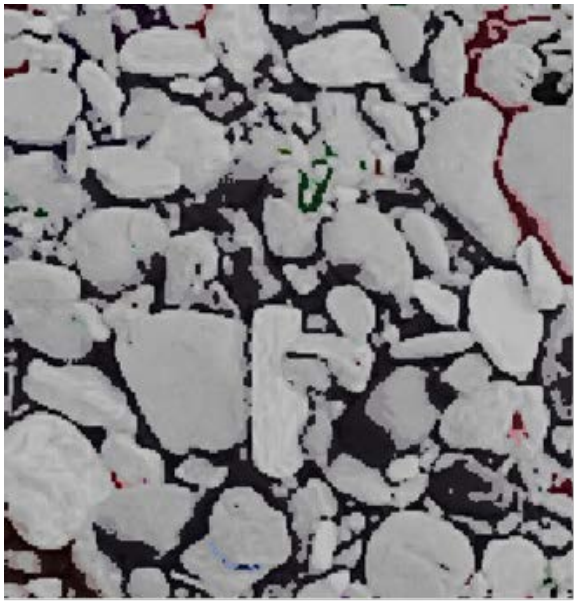

**Figure 6**. Evaluated gap/voids of gravels.

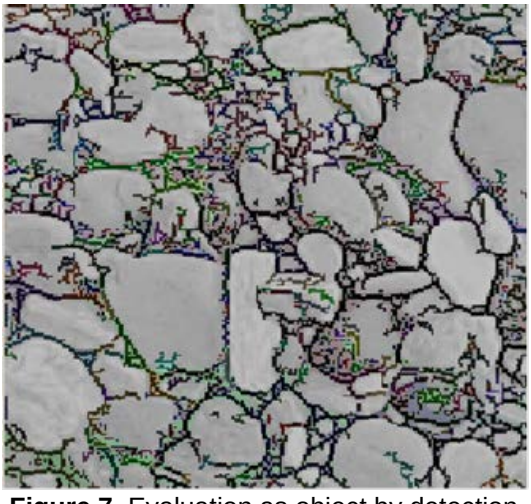

**Figure 7**. Evaluation as object by detection of each gravel.

**Figure 8**. Correction of the excessive particle-segmentation.

**Figure 9**. Shooting image on the bed surface at shooting point 2 in Figure 2.

**Figure 10**. Analyzed result of image calculated by means of BASEGRAIN.

**Table 1**. Resolution due to different height at fixed point.

| Height (m) | Resolution (mm/px) | Mean Size (mm) | Minimum Size (mm) |
|---|---|---|---|
| 1 | 0.7732 | 20.9955 | 10.007 |
| 2 | 0.9016 | 21.0597 | 10.0012 |
| 3 | 1.4164 | 23.8002 | 10.0203 |
| 4 | 1.9275 | 25.0933 | 10.0371 |

## 3 RESULTS AND DISCUSSIONS

### 3.1 Comparison of analyzed results with survey data

Figure 9 shows an image of the riverbed surface at shooting point 2 in Figure 2. The analyzed result of the image as calculated by BASEGRAIN is shown in Figure 10. The gravel was well represented by the major (longest) axis and minor (shortest) axis directions. However, smaller sand particles were undetectable due to the limitations of spatial resolution. Verification of the grain sizes obtained by the above image analysis was discussed by comparing with data generated by the volumetric method. The latter was obtained from field surveys conducted by Ministry of Land, Infrastructure and Transportation of Japan.

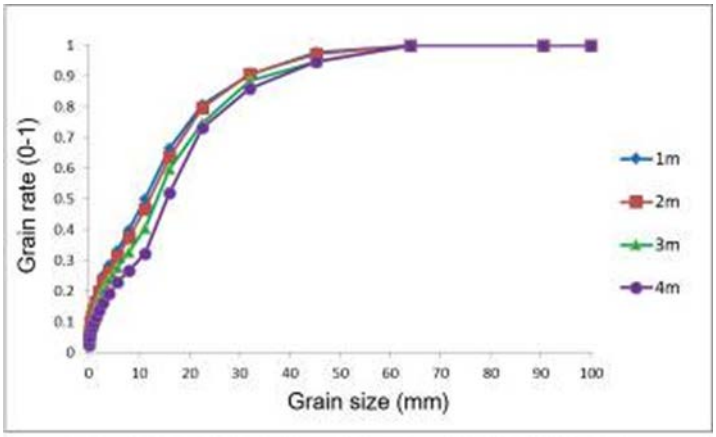


**Figure 11**. Image analyzed results for different shooting height and different position.

### 3.2 Effects of shooting height at fixed point

In order to discuss the effects of different shooting heights on the accuracy of the particle size distributions, survey point 1 shown in Figure 2 was selected. The results shown in Table 1 were obtained by the above-mentioned image analysis procedure. The resolution of the analyzed image decreases over the range from 1m to 4m in height. As expected, the image resolution was lower at the higher shooting height, and was highest at the lowest height. Mean grain diameter and minimum diameter were shown for each height. Figure 11 is a comparison of estimated grain distributions at the different heights (1m, 2m, 3m, and 4m). The grain size distributions from the 1m and 2m heights had similar profiles. However, small differences were seen in the case of the 3m and 4m heights, with about 0.064 and 0.14, respectively, due to progressively lower resolution.

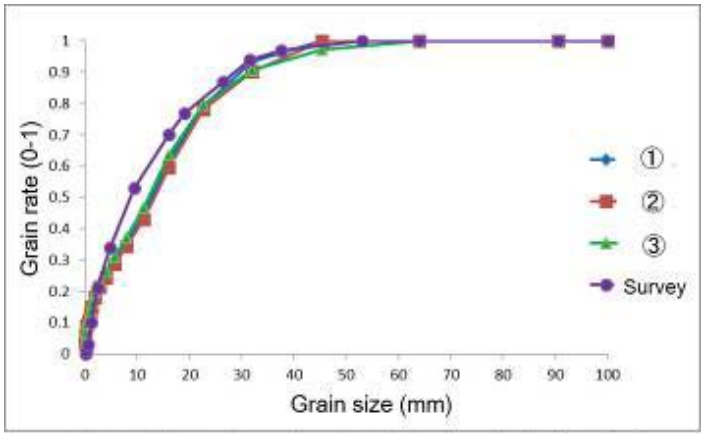


**Figure 12**. Comparison of analyzed grain size distribution for 3 shooting points measured by field survey (2m).

3.3 Effects of different shooting position

Figure 12 shows the comparison of grain size distributions analyzed for 3 shooting points (at 2-m height) and measured by field survey. Small differences were seen for finer grains, but similar profiles were obtained from the results for each of the 3 points. Therefore, the analyzed results will be applicable for estimation of grain size distributions. Figure 13 showed the image analysis results for the 3 different shooting positions at the height of 4m. The finer grains could not be detected for the highest position, consistent with the lower resolution at the height of the shooting position.

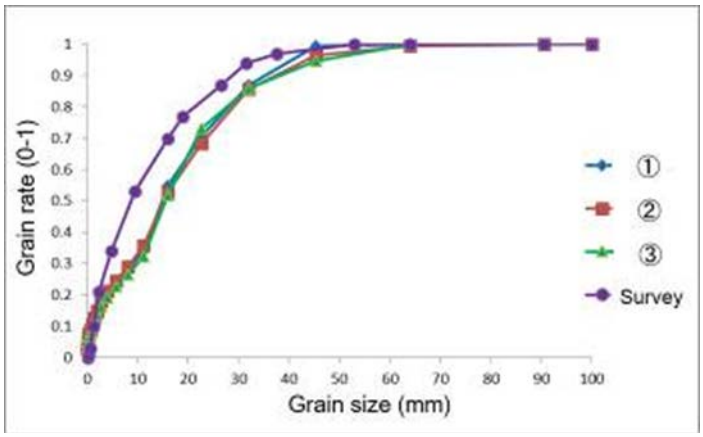


**Figure 13**. Comparison of analyzed grain size distribution for 3 shooting points with measured by field survey (4m).

## 4 CONCLUSIONS

The present study applied an efficient method to estimate grain size distributions from the analysis of surface images of a deposition area in a river. The accuracy of the analysis was evaluated using field measurements by excavation, and the applicability of the method is discussed.

## ACKNOWLEDGEMENTS

The authors would like to thank the Land, Infrastructure and Transportation Ministry, Ozu River and National Highway office for providing the field survey data for the particle size distributions and river bed profiles.

## REFERENCES

Chung, C.H. & Chang, F.J. (2013). A Refined Automated Grain Sizing Method for Estimating Riverbed Grain Size Distribution of Digital Images. *Journal of Hydrology*, 486, 224-233.

Detert, M. & Weitbrecht, V. (2012). Automatic Object Detection to Analyze the Geometry of Gravel Grains a Free Stand-Alone Tool. *River Flow*, 595-600. Murillo (Ed).

Kozakiewicz, J. (2013). Automated Image Analysis for Measuring Size and Shape of Martian Sand Grains: A Tool to Estimate Threshold Shear Velocities and to Compare Different Sand Samples. *44th Lunar and Planetary Science Conferece*, 2906.

 

# EXPERIMENTAL INVESTIGATION OF THE INTERACTION BETWEEN FINE HEAVY PARTICLES AND ORGANIZED TURBULENT FLOWS IN OPEN CHANNEL

YI LU[(1)] & KIT MING LAM[(2)]

[(1)] Department of Civil Engineering, The University of Hong Kong, Pokfulam, Hong Kong
e-mail: Helen-199307@outlook.com
[(2)] Department of Civil and Environmental Engineering, The Hong Kong University of Science and Technology, Hong Kong
kitminglam@ust.hk

## ABSTRACT

This paper reports an experimental investigation on the settling velocities of heavy particles of sub-millimeter size in a water flow with organized eddy motions. The eddies are generated in the flow of a laboratory flume using a set of vibrating shutters. Instantaneous movements of the fluid phase and the solid particle phase are measured with time-resolved particle image velocimetry (PIV) and particle tracking velocimetry (PTV), respectively. The averaged settling velocity of the heavy particles is found to be reduced with increasing vibration frequency of the shutters, probably due to the vortex trapping effect. At the highest vibration frequency, the settling velocity becomes about 15% lower than that in still water.

**Keywords:** Sediment transport; settling velocity; turbulent flow; particle image velocimetry (PIV); particle tracking velocimetry.

## 1 INTRODUCTION

Sediment is defined as the particulate material on earth surface and it can be transported by wind, water or ice (Crook, 1997). Almost all the rivers in nature carry sediments of different sizes and materials. Transportation of sediments will contribute to the new formation of landform. The motions of sediments determine the emerging geomorphy. Particle settling in a turbulent flow contributes a lot to the transport of sediments in river. It remains an unsettled problem as the averaged settling velocity of the heavy particles has been reported to be either increased or decreased by the turbulence. The objective of this paper is to investigate the interaction between movement of sediments and turbulence in a flow.

Recent experimental studies show that a pair of oscillating grids can be used to generate homogeneous and isotropic turbulence in a laboratory setting (Zhou and Cheng, 2009; Doroodchi et al., 2008; Yang and Shy, 2003). The work conducted by Shy et al. (1997) concluded that the area in the core region of a pair of oscillating grids can be considered as stationary and nearly isotropic turbulence. Zhou and Cheng (2009) studied settling of a single particle in grid turbulence and claimed that the relative settling velocity under turbulence appears smaller than the terminal velocity in quiescent water.

Some related investigations on the topic of particle settling in turbulent flow were based on experiments in a laboratory flume with roughness installed on the channel bed. Cuthbertson and Ervine (2007) measured the settling rates of fine sand particles and showed that they are strongly affected by the turbulent flow, being enhanced in the near-bed and intermediate regions and disputed in the outer flow region. Explanations for the observed phenomena are the interaction mechanisms behind the solid particles and fluid phase. Four main mechanisms which influence the settling velocity were summarized by Nielsen (1993). The nonlinear drag, vortex trapping and the loitering effect lead to the reduction of settling velocity while fast tacking between vortices contributes to the enhancement of settling velocity conversely. There have been some experimental data to verify these postulations but data with wide range of particle size and other parameters are still limited and not sufficient.

In this study, a specified form of turbulent fluid motion is generated in the flow stream of a laboratory flume. Organized eddy structures are produced by a set of horizontal shutters oscillating in the flow. Simultaneous measurement of the fluid phase and solid phase is made to observe the structure of the turbulence flow and trajectory of the falling fine heavy particles in the organized turbulent flow.

## 2 EXPERIMENTAL TECHNIQUES

### 2.1 Experiment setup

Experiments were carried out in a laboratory flume measuring 13 m long and 0.4 m wide and with water filled to 0.3 m depth. The sketch of the setup is shown in Figure 1. A set of vibrating shutters with rocking motion placed in the beginning of the flume was used to generate organized eddies. A fetch of roughness blocks were placed on the bottom of the flume to help maintain the turbulence from rapid decay. The rectangular blocks had a height $D$ = 30 mm and the area density of the blocks were 7.04% of the channel bed. Five groups of

 

experiments were conducted with different oscillating speeds of the shutters between 0.00 Hz and 1.00 Hz to obtain different turbulence structures. The group of experiments with the shutters stationary was taken as the reference case for comparison. In all experiments, the amplitude of the rocking shutters at their tips was kept constant at ±2 cm. The freestream velocity in the flume upstream of the vibrating shutters was set at 0.0125 m/s in all experiments

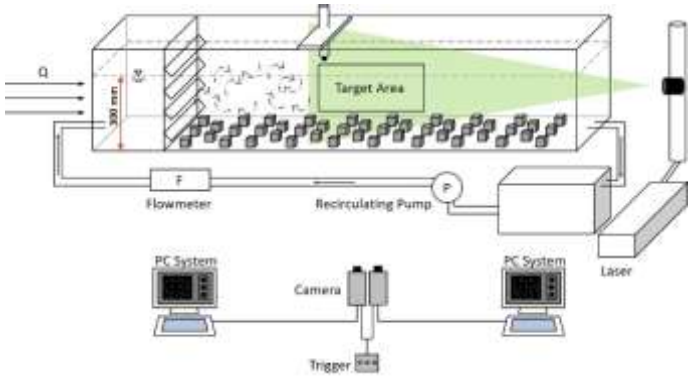


**Figure 1.** Sketch of the experimental setup.

The heavy particles were released from an hourglass above the flume with a magnetic valve controlling the amount of particles released in each run. The solid particles used were glass beads with density 2500 kg/m$^3$. In the experimental investigation of single particle settling in turbulence (Zhou and Cheng, 2009), particles had diameter between 6.35 mm and 7.94 mm and it claimed that more efforts should be put on the small-sized particles. Therefore, in this project, sub-millimeter particles were adopted. The properties of the solid particles used in the present study are listed in Table 1.

**Table 1.** Properties of particles.

| Type | Density (kg/m$^3$) | Dia. Range (μm) | Median Diam. (μm) | $w_s$ from Stokes law (m/s) |
|---|---|---|---|---|
| GP6 | 2500 | 176.9-256.9 | 220.0 | 0.0367 |

2.2 Measurement of fluid phase and solid particle phase

The middle longitudinal section of the flow in the flume was illuminated by a laser sheet generated from a continuous wave Argon-ion laser (Spectra-Physics Stabilite, 2017). The laser beam was transmitted to a laser sheet with uniform density using a submersible laser-sheet optic. Images of the target area on the illuminated plane were captured by two high speed CCD cameras. The two cameras were of the same model (PCO model 1200hs) with resolution of 1280 × 1024 pixels. They were aligned closely to capture the same target area to make sure the solid phase of heavy particles and fluid phase were measured simultaneously.

To separate the solid phase and fluid phase, different optical filters were used as similar to the setup in a related study (Liu and Lam 2015; 2013). The water flow was marked with very fine neutrally buoyant seeding particles which scatter the light from the laser at the original wavelength at 514.5 nm. On the other hand, the heavy solid particles coated with fluorescent dye scatter light with the highest emission wavelength around 607 nm. Using an optical filter to cut out wavelength smaller than 570 nm, a camera captured only the images of the heavy particles. The other camera was fitted with a band-pass filter which only allowed light centered at wavelength 514.6 nm to pass through, so that it captured only the seeding particles following motions of the fluid phase. The two sets of flow images were taken at a rate of 45 images per second and for a record of 1424 images in each test run.

The images of solid fine heavy particles were analyzed with the PTV technique, in which Lagrangian approach was used to track the trajectory of the solid particles. The velocity of each particles was subsequently calculated. For the fluid phase, the images of seeding particles were analyzed with the usual cross-correlation PIV algorithm, in which the Eulerian fluid field velocity field is obtained from two successive images. The PTV and PIV computations were carried out with the commercial software Dantec DynamicStudio.

## 3 RESULTS AND DISCUSSION

3.1 Behavior of fine heavy particles in turbulent flow

Four different vibration frequencies of the shutters at 0.25 Hz, 0.50 Hz, 0.75 Hz and 1.00 Hz, were tested in the experiments and the group at 0.00 Hz was conducted as the control group. Twenty runs of drops of heavy particles were released under each vibration frequency and the measured mean settling velocity of each group were all within the uncertainty of 10%. Figure 2 shows the mean settling velocity of fine heavy particles varies

 

with the vibration frequencies. The terminal velocity of a solid particle in still water is 0.0367 m/s as calculated by the Stokes' law,

$$V = \frac{2}{9}\frac{(\rho_p - \rho_f)}{\mu}\, g\, R^2 \qquad [1]$$

where $\rho_p$ is the density of the heavy particles, $\rho_f$ is the density of fluid flow, $\mu$ is the viscosity of fluid and R is the radius of the solid particle.

In the control group, the mean settling velocity of solid particles was measured at 0.0286 m/s. It was similar but smaller than the value calculated by the Stokes' law. This is probably because the settling of bulk particles would induce the interaction between them. Furthermore, there is some ambient turbulence in the flow inside the flume even when the shutters are stationary

Figure 2 shows that the mean settling velocity of the fine heavy particles decreases with the increase of the frequency of the vibrating shutters. It can be seen that at the highest vibration frequency in this study, the settling velocity descends by 15% when compared with that in normal open channel flow without extra added fluctuations. This supports that the settling of the fine particles is strongly affected by the characteristics of the eddy structures in this form of turbulent flow.

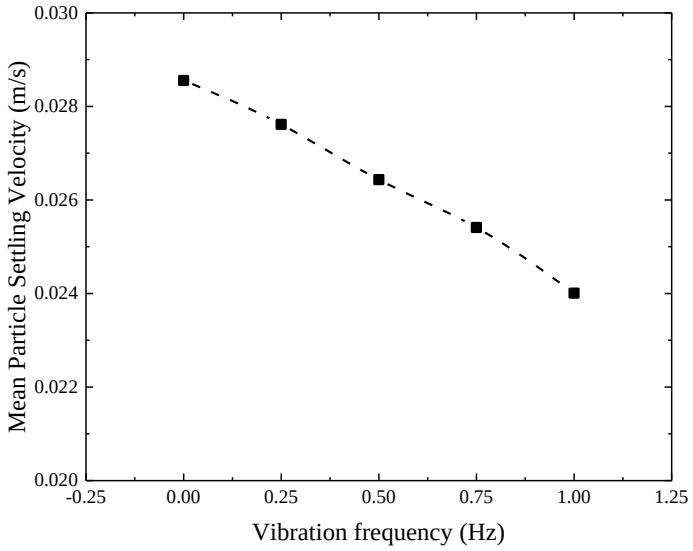


**Figure 2.** Mean setting velocity versus vibration frequency

3.2 Characteristics of time-averaged fluid phase

The first investigation of fluid phase is focused on the characteristics of the time-averaged mean flow. The mean flow is computed from all 1424 PIV snapshots obtained over the duration at about 30 seconds. Five vertical sections are selected from the target area to plot the profiles of the mean velocities of fluid flow. As shown in Figure 3, the profiles at the five sections collapse well into one curve at each group of experiments which means the flow field is near homogenous.

 

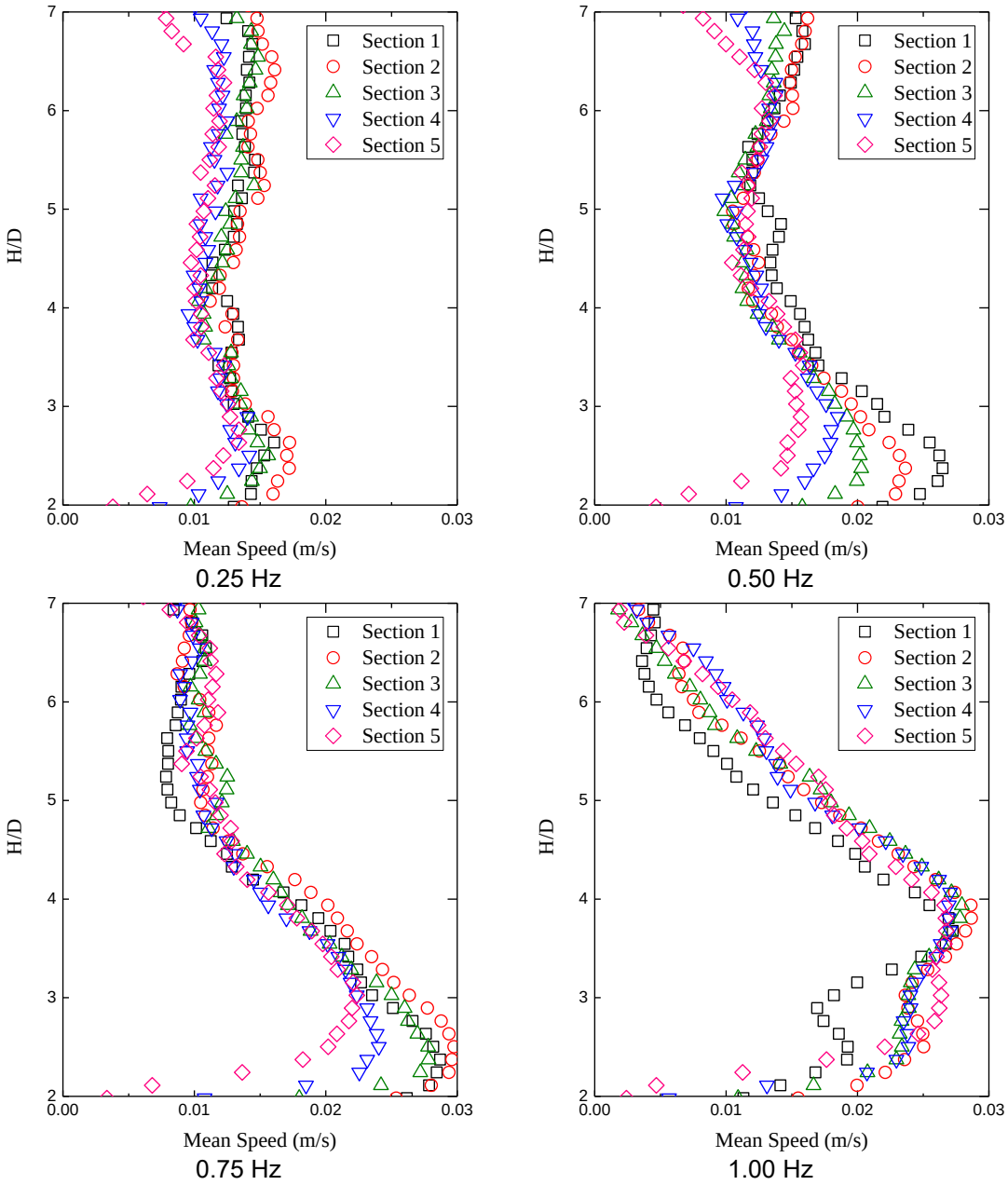


**Figure 3.** Mean velocity of fluid under different vibration frequencies.

At the lowest shutter vibration frequency, $f$ = 0.25 Hz, the mean flow velocities are nearly uniform across the water depth. However, at higher shutter vibration frequencies, the flow is found to re-distribute itself and results in higher velocities near the channel bed. Going down from the free surface, the mean velocities increases and reaches a maximum value in the lower part of the water depth. At deeper locations approaching the wake region of the bed roughness blocks, the velocities decreases again.

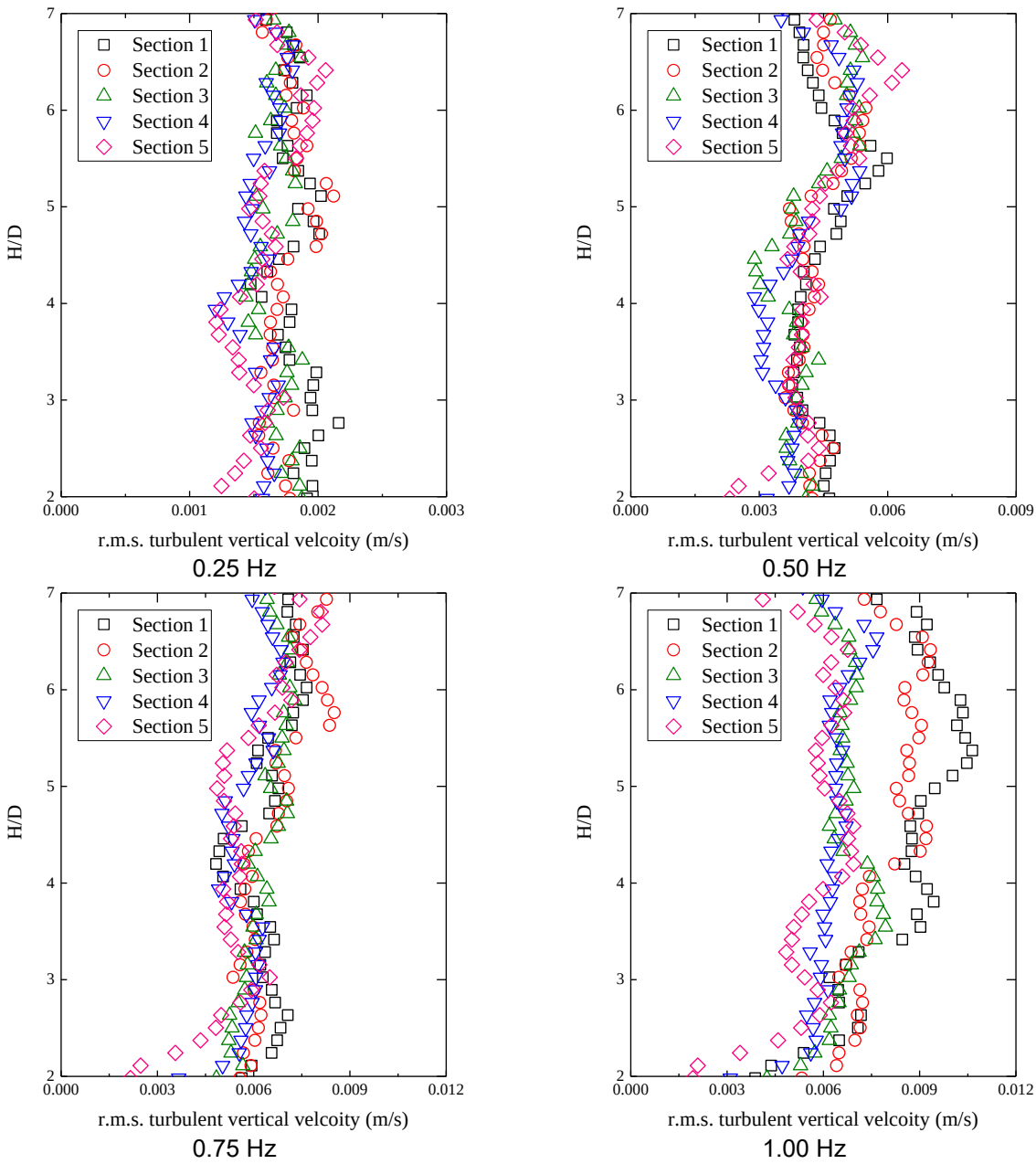


**Figure 4.** Fluctuation of vertical velocity under different vibration frequencies.

In addition to the mean velocities, the root-mean-square (r.m.s.) value of the turbulent vertical velocity is used to analyse the turbulence characteristics. The r.m.s. value $v'$ is defined by the first order statistics of the velocity field of the fluid phase as the standard deviation $\sqrt{v^2}$ of the fluctuating vertical velocity component $v$. Figure 4 shows the r.m.s. fluctuation of vertical velocity under different vibration frequencies of the shutters. It can be seen from the four individual graphs that $v'$ is enhanced with the increase of shutter vibration frequency. The value of $v'$ at the highest shutter frequency is nearly five times that at the lowest shutter frequency. The profiles in Figure 4 also show that unlike the mean fluid velocities, the distribution of $v'$ is rather uniform across the water depth.

The postulation of vortex trapping is proposed by Tooby et al. (1977) to explain the reduction of the settling velocity of particles in a turbulent flow. The postulation is based on the assumption that the settling velocity of the particle is equal to the terminal velocity of the particle in still water plus the velocity of the turbulent flow at that point. When particle falls into a forced vortex, it will be trapped and the settling velocity will be reduced accordingly.

### 3.3 Characteristics of instantaneous fluid phase

To observe the structures of the fluid field, instantaneous fluid vector fields in each PIV snapshot are analyzed to explain the motion of the falling particles. Figure 5 shows four typical graphs of the fluid field. It can be observed that the flow is disturbed by the vibrating shutters and organized eddy structures are formed downstream. At the higher shutter vibration frequencies, some form of interaction among the eddy structures

 

may result in the formation of eddies of larger sizes. The interaction may be also responsible for the re-distribution of mean velocities which leads to higher flow velocities towards the channel bed. The greater strengths of the large-sized vortices and the stronger induced circulating flow may trigger the vortex trapping effect, leading to the observed reduction in particle settling velocity.

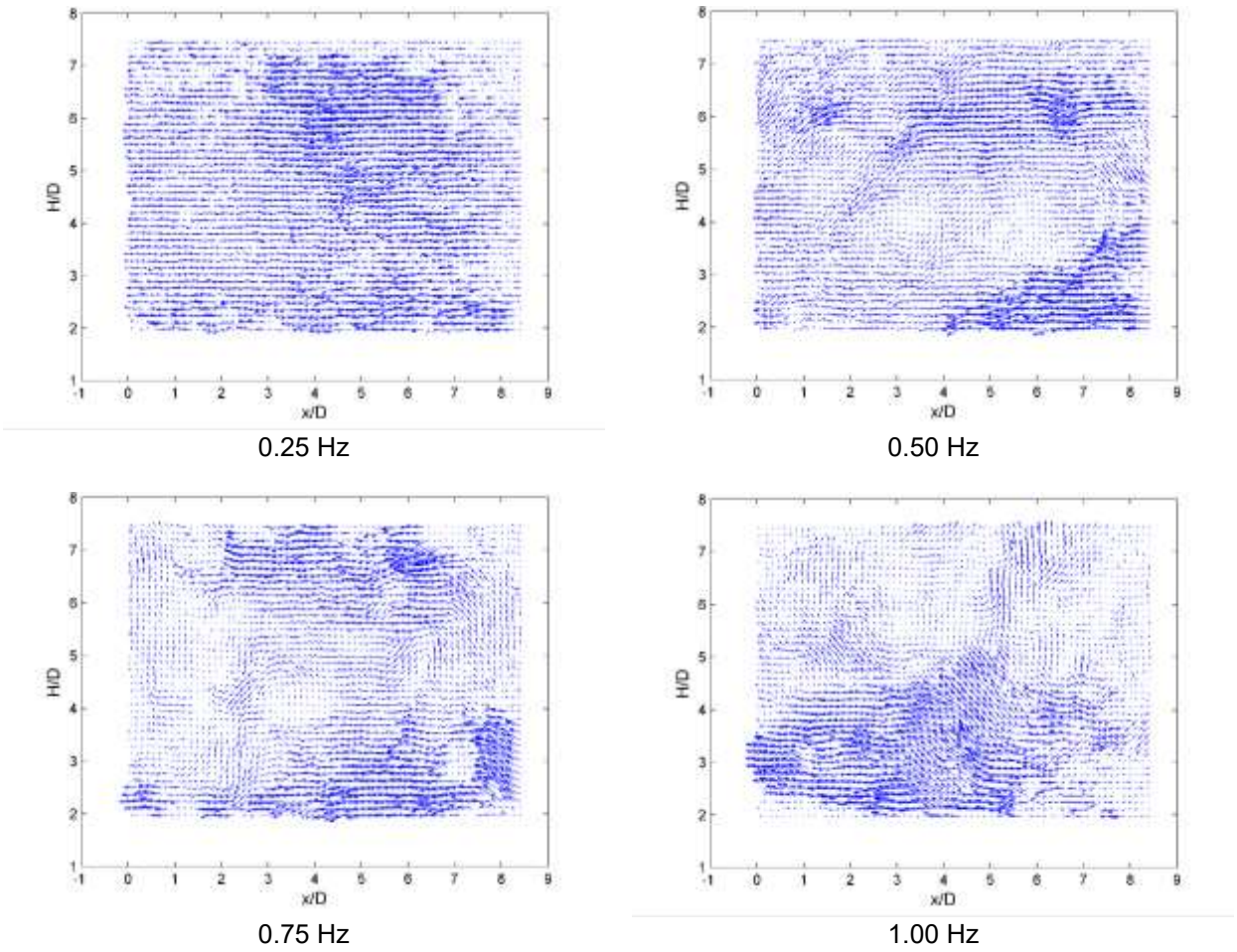


**Figure 5.** Instantaneous fluid vector field.

3.4 Relationship between solid particle and turbulent flow

The degree of vertical turbulence generated is represented by the r.m.s. turbulent velocity, $v'$. Figure 6 shows the relationship between the particle settling velocity and this vertical turbulence intensity. In this study, the experimental results suggest that settling velocity reduced with the enhancement of vertical turbulence intensity.

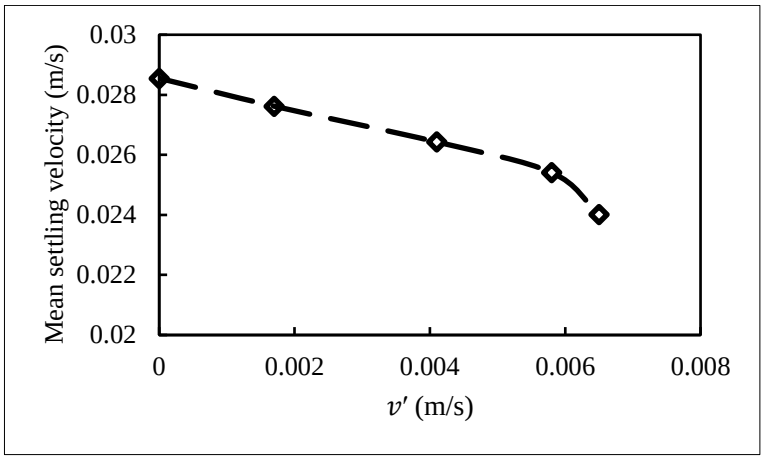


**Figure 6.** Relationship between settling velocity and vertical turbulence intensity $v'$.

 

## 4 CONCLUSION

The effect of organized eddies on the settling velocities of sub-millimeter heavy particles in a water flow is investigated experimentally with time-resolved PIV and PTV measurements. The organized eddies are generated by vibrating a set of horizontal shutters in the flow. It is found that the average settling velocity of the heavy particles is reduced with higher vibration frequencies of the shutters. In the present setup, the largest reduction in the average settling velocity, observed at the highest shutter vibration frequency tested, is about 15% when compared with the case of no shutter vibration. The vortex trapping theory is proposed to explain this effect. The fluctuations of the vertical turbulent velocities in the region downstream of the shutters are found to depend on the vibration frequency. The experimental results infer that the turbulence structures, such as the induced circulations by large-scale vortices, govern the settling behaviors of the heavy particles as they fall through the turbulent water column.

## ACKNOWLEDGEMENTS

This study is supported by a research grant provided by the Research Grants Council of Hong Kong (GRF No. 17204114).

## REFERENCES

Crook, K.A. (1997). *Sedimentary Geology: An Introduction to Sedimentary Rocks and Stratigraphy.* WH Freeman and Company, New York, 1996, Elsevier, 575.

Cuthbertson, A. & Ervine D. (2007). Experimental Study of Fine Sand Particle settling in Turbulent Open Channel flows over Rough Porous Beds. *Journal of Hydraulic Engineering,* 133(8), 905-916.

Doroodchi, E., Evans, G., Schwarz, M., Lane, G., Shah, N. & Nguyen, A. (2008). Influence of Turbulence Intensity on Particle Drag Coefficients. *Chemical Engineering Journal,* 135(1), 129-134.

Liu, P. & Lam, K.M. (2013). Two-phase Velocity Measurement in a Particle-laden Jet. *Journal of Hydro-environment Research,* 7(1), 18-29.

Liu, P. & Lam, K.M. (2015). Simultaneous PIV Measurements of Fluid and Particle Velocity Fields of a Sediment-laden Buoyant Jet. *Journal of Hydro-environment Research,* 9(2), 314-323.

Nielsen, P. (1993). Turbulence Effects on the settling of Suspended Particles. *Journal of Sedimentary Research* 63(5), 835-838.

Shy, S., Tang, C. & Fann, S. (1997). A nearly Isotropic Turbulence Generated by a Pair of Vibrating Grids. *Experimental Thermal and Fluid Science,* 14(3), 251-262.

Tooby, P. F., Wick, G. L. & Isaacs, J. D. (1977). The Motion of a Small Sphere in a Rotating Velocity Field: A Possible Mechanism for Suspending Particles in Turbulence. *Journal of Geophysical Research,* 82(15), 2096-2100.

Yang, T. S. & Shy, S. S. (2003). The settling Velocity of Heavy Particles in an Aqueous near Isotropic Turbulence. *Physics of Fluids,* 15(4), 868.

Zhou, Q. & Cheng, N.S. (2009). Experimental Investigation of Single Particle settling in Turbulence Generated by Oscillating Grid. *Chemical Engineering Journal,* 149(1-3), 289-300.

 

Proceedings of the 37th IAHR World Congress
August 13 – 18, 2017, Kuala Lumpur, Malaysia

# EXPERIMENTAL EVALUATION FOR EFFECT OF SABO FACILITIES ON BED VARIATIONS IN DOWNSTREAM REACH

HARUKI WATABE[(1)], KAZUHIKO KAITSUKA[(2)], MINORU SUGIYAMA[(3)], HIROHISA MURAMATSU[(4)], TAKAHIKO NAGAYAMA[(5)], HIROSHI OGAWA[(6)], TSUTOMU MIIKE[(7)], AYUMI MIYAMOTO[(8)], YUUCHI YAMADA[(9)], TAKAHIRO ITOH[(10)] & TAKAHISA MIZUYAMA[(11)]

[(1,2,3,10)] Research and development center, Nippon koei Co., Ltd., Tsukuba, Japan,
a6809@n-koei.co.jp
[(4,7,8)] Sabo Department, Nippon koei Co., Ltd., Tokyo, Japan,
a4282@n-koei.co.jp, a5405@n-koei.co.jp, a7329@n-koei.co.jp
[(5)] Hokuriku Office, Nippon koei Co., Ltd., Ishikawa, Japan,
a4619@n-koei.co.jp
[(6)] Overseas Consulting Administration, Nippon koei Co., Ltd., Tokyo, Japan,
a4257@n-koei.co.jp
[(9)] Sabo Frontier Foundation, Tokyo, Japan,
a7003@n-koei.co.jp
[(11)] National Graduate Institute for Policy Studies, Tokyo, Japan,
byk01260@nifty.com

## ABSTRACT

Two patterns of bed erosion are in downstream reach of the Sabo dam, one is the local scouring by an overflow in between main and counter dams, and the other is bed erosion due to imbalance of sediment transportation along downstream reach of the counter dam. Apron and counter dam are usually applied for countermeasure of erosion in downstream reach of the dam. More effective countermeasure in downstream reach is desired, because a horizontal distance and an overlapping height of the Sabo dam are determined empirically in Japanese standard of Sabo dam design. In present study, influences of Sabo facilities on the bed variations in downstream area of the dam are discussed experimentally for combinations of overlapping height, horizontal distance between dams and apron. Bed erosion depth is not noticeable around the counter dam, if the counter dam is set behind main dam such that the over flow from main dam can attack on the top of the counter dam in case of large magnitude of floods. Differences of overlapping height affect bed erosions in long downstream reach of the counter dam, and do not affect the sediment runoff at downstream end. Smaller overlapping height is desired to protect bed erosions around the counter dam. Apron protects bed surface between main and counter dams in small or middle magnitude of discharge in present flume tests, because the overflow attacks on the surface of the counter dam in large magnitude of discharge.

**Keywords:** Bed variation; overlapping height; distance between dams; Sabo facilities; weir.

## 1 INTRODUCTION

Bed erosions take place in downstream reach of the Sabo facility in floods. There are two kinds of erosion patterns. One is the local scouring by overflow from the dam, and the other is bed erosion in long reach by imbalance of sediment transportation along the channel. Longitudinal profile has typical bed formation either rotational or parallel degradation due to hydraulic conditions. Those bed erosions are well-known phenomena, and countermeasures against those erosion problems are basic and classic matters. Maximum erosion depth in equilibrium condition was evaluated by ASCE Committee (1962), and there are many researches concerning to local scouring due to rapid flow (e.g., Suzuki et al., 1982; Hayashi 1983; Lenzi et al., 2003). Though the view of our research is different, one research (e.g., Martin et al., 2006) is discussed the gradient of between sills in comparison with that of no sills for bed erosion. Bed slope become milder due to the local head loss for sediment transportation if sills are set properly, it brings to stop degradation. This research is a little different from our study, it is discussed the adequate interval of main dam and counter dam, overlapping height, bed variation behind the counter dam for the bed erosion in this study. A Sabo dam which is located in the mountainous region designed with some structures for bed erosions and to ensure its stability such as wing, counter dam, apron, and side bank protection wall... Facilities related to bed erosions around the dam are mainly counter dam, and some setting in both upstream and downstream of the counter dam such as to the horizontal length between main and counter dam and the overlapping height between dams. However, preferable countermeasures and related structured are not seem to be completed due to interaction between Sabo facilities and bed variations around them depends on the effects of local water flow and sediment discharge, longitudinal water level profiles, and sediment transport mode..., and the layout of those facilities is not uniquely determined. In Japan, that horizontal length and overlapping height are proposed experimentally in the manual for the design of Sabo dams by Ministry of Land as described below (Figure 1), and the longitudinal length and the overlapping height correspond to $L_{mc}$ and $H_{oh}$, respectively.

 

The horizontal length and the overlapping height are determined by empirical formula proposed by Angerholzer (e.g., Hand buch des Wasserbaus, 1962) and the value of Hoh is 1/4 to 1/3 times of the dam height. The design for dimension of the horizontal length and the overlapping height between dams and apron is conducted under the plan size of discharge. The horizontal length, $L_{mc}$, can be interpreted as the flying distance of drop flow water from a dam, and the overlapping height, $H_{oh}$, can be interpreted as distance from the center of total water pressure to the bed. Additionally, Mizuyama et al. (1990) proposed experimentally design standard for an apron in case of slit type Sabo dam. More effective countermeasures for erosion in downstream reach of Sabo dams need to be conducted based on hydraulic and sediment transport conditions. In present study, erosion in downstream reach of Sabo facilities such as Sabo dam, between main and counter dam and the apron is discussed experimentally focusing on the combination of overlapping height and longitudinal length between dams. Geographical and hydraulic conditions are determined, supposing steep slope torrents in mountainous basin in Japan. Additionally, new idea for the outline of the setting for those dimensions and layout can be discussed experimentally in magnitude of plan size of discharge in steady and unsteady flows.

## 2 LAYOUT OF SABO DAM

Figure 1 shows the schematics layout of Sabo facilities around a Sabo dam, where, $L_{mc}$ = length between main dam and counter Sabo dam; $H_1$ = height of main Sabo dam from bed surface; $h_3$ = overflow depth; $H$ = height of main Sabo dam; and $H_{oh}$ = overlapping height. Equation [1] was proposed by shown in the handbook in German (1962). Depth of embedment is also set as 2 m, and it is assumed that height of Sabo dam is 10 m. Preferable setting for $H_{oh}$, $L_{mc}$ and pattern with apron can be tried to find through flume tests, and, in present flume tests, overlapping height and length between Sabo dams are specified as follows; $H_{oh}$ = 1.25 m, 2.50 m, 5.00 m and $L_{mc}$ = 9.5 m, 14.1 m, 28.2 m. Herein, the values for $H_{oh}$ and $L_{mc}$ are calculated as 2.5 m and 14.1 m, respectively, in case of $H$ = 10 m and 1/4 in Eq.[2] and $Q_{wp}$, peak discharge rate, 230 $m^3/s$ and 1.5 in Eq.[1]. Present settings were carried out such as 0.5th or 2nd times of basic dimensions for $H_{oh}$ (2.5 m) and $L_{mc}$ (14.1 m).

$$L_{mc} = (1.5 \text{ to } 2.0)(H_1+h_3) \quad [1]$$

$$H_{oh} = (1/3 \text{ to } 1/4)H \quad [2]$$

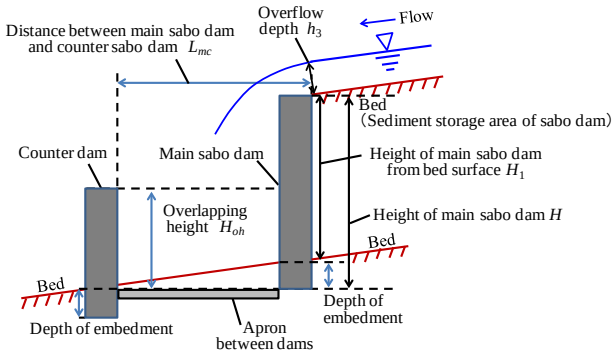


**Figure 1.** Schematics of layout of Sabo dam.

## 3 EXPERIMENTAL FLUME

Representative values are specified for bed slope, flow width and size of bed materials supposing steep slope torrents in mountainous basin in Japan as follows: 1/20 in longitudinal bed slope, 45 m in flow width. Figure 2 shows an experimental flume with following dimensions: 7 m in effective flume length; 0.3 m in width; and 0.4 m in depth. Water and sediment are supplied at upstream of flume, and groundsill is set at flume end to maintain bed elevation. The setting for those dimensions are determined by a model scale (1/75), because it is specified to reproduce the minimum grain diameter of model sediment, as described below.

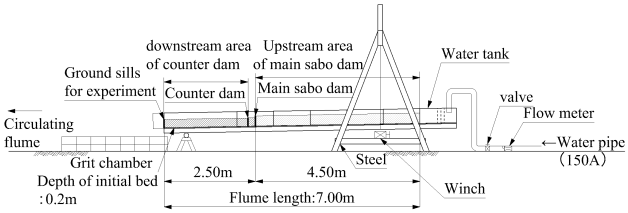


**Figure 2.** Experimental flume.

## 4 EXPERIMENTAL CONDITIONS

### 4.1 Sediment and Hydraulic Conditions

Grain diameter has range from 7.5 mm to 800 mm, and representative values of sediment are as follows: $d_{95}$ =428 mm and $d_{60}$=91 mm, $d_{30}$=34 mm (see Figure 3). Model scale is specified as 1/75 to reproduce the minimum grain diameter of 7.5 mm as bed load. Flux sediment concentration, $c_f$, is set as equilibrium value (=0.012) for bed slope. Flux sediment concentration $c_f$ is defined as $c_f = q_s / q_m$ (e.g., Egashira et al., 1997) and in which $q_s$ is the sediment discharge rate in unit width and $q_m$ is the mixture discharge rate of clear water and sediment in unit width. Flow discharge is 230 $m^3$/s in magnitude of maximum value and 127 $m^3$/s of critical discharge of movement of $d_{95}$. Three kinds of flow discharge and shape are used for steady flow in 127 $m^3$/s and 230 $m^3$/s, and for unsteady flow with 230 $m^3$/s of peak discharge as shown in Figure 4. Hydraulic and sediment parameters are satisfied with Froude and geometric similarity, respectively. Modeled sand has the following physical characteristics: $d_{95}$ = 5.71 mm; $d_{60}$ = 1.21 mm; $d_{30}$ = 0.453 mm; $\sigma/\rho$ = 2.66; $\varphi_s$ = 38.6 degrees; $c_*$ = 0.523, $\sigma$= mass density of sediment particles; $\rho$= mass density of water; $\varphi_s$ = interparticle friction angle; and $c_*$ = volumetric sediment concentration in the sediment deposition layer.

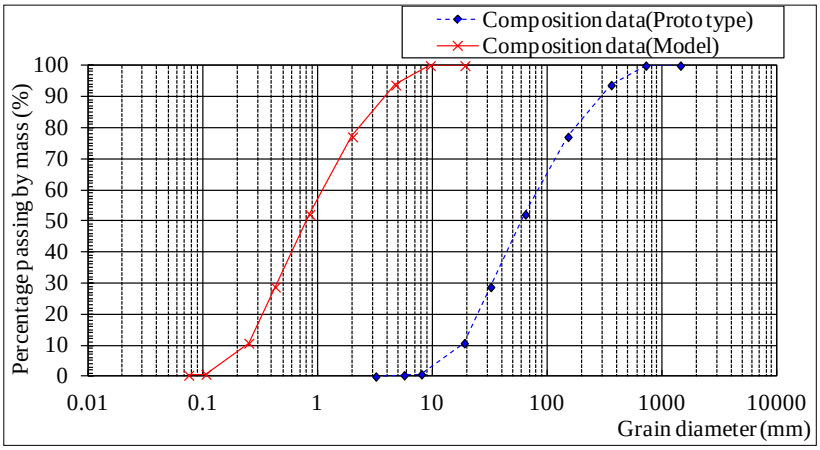


**Figure 3.** Sediment grain size distributions.

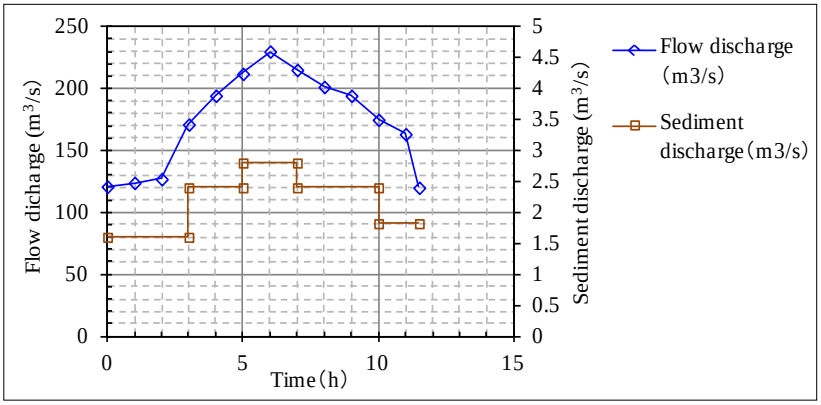


**Figure 4.** Hydrograph and sedigraph from the upstream end.

### 4.2 Experimental Runs

Table 1 shows experimental runs. Runs for evaluating differences of the horizontal length, $L_{mc}$, are as follows: Run 5 (9.5 m), Run 9 (14.1 m) and Run4 (28.2 m) in steady flow and Run7 (9.5m) and Run1 (14.1 m) in unsteady flow. Runs for differences of the overlapping height, $H_{oh}$, are Run3 ($H_{oh}$ = 1.25 m), Run9 (2.5 m) and Run2 (5 m) under the condition of $L_{mc}$ =14.1 m in steady flow. Additionally, runs for differences with and without apron are Run6 (with apron) and Run5 (without apron) under the condition of $H_{oh}$ = 2.5 m and $L_{mc}$ =9.5 m in steady flow. In unsteady flow, comparisons of runs for differences with and without apron are Run10 (with apron) and Run7 (without apron) under the condition of $H_{oh}$ = 2.5 m and $L_{mc}$ =9.5 m.

 

**Table 1**. Experimental runs.

| | $\theta$(DEGREES) | $Q_{WP}$ ($M^3/S$) | $H_{OH}$ (M) | $L_{MC}$ (M) | $c_F$ | APRON |
|---|---|---|---|---|---|---|
| **Run1** | 2.58 | 230* | 2.5 | 14.1 | 0.012 | × |
| **Run2** | 2.58 | 230 | 5.0 | 14.1 | 0.012 | × |
| **Run3** | 2.58 | 230 | 1.25 | 14.1 | 0.012 | × |
| **Run4** | 2.58 | 230 | 2.5 | 28.2 | 0.012 | × |
| **Run5** | 2.58 | 230 | 2.5 | 9.5 | 0.012 | × |
| **Run6** | 2.58 | 230 | 2.5 | 9.5 | 0.012 | ○ |
| **Run7** | 2.58 | 230* | 2.5 | 9.5 | 0.012 | × |
| **Run8** | 2.58 | 127 | 2.5 | 9.5 | 0.012 | × |
| **Run9** | 2.58 | 230 | 2.5 | 14.1 | 0.012 | × |
| **Run10** | 2.58 | 230* | 2.5 | 9.5 | 0.012 | ○ |

4.3 Measurement

Outflow of water and sediment are sampled by buckets at downstream end. Level of free surface and bed are measured by a gauge. Bed variations from the plan and longitudinal views are taken by a digital camera. Sabo facilities are made by woods, and depth of embedment of a main Sabo dam and counter dam is set deeply to evaluate maximum erosion depth in flume tests.

## 5 RESULTS AND DISCUSSIONS

5.1 Longitudinal bed variation and local scouring in downstream of dams

5.1.1 Temporal changes of bed variations

Let us discuss on bed variations in steady and unsteady flow. Figure 5 shows temporal changes of longitudinal water level and bed elevation for differences of $L_{mc}$ : 9.5 m (Run5), 14.1 m (Run9), 28.2 m (Run4). Figure 6 is temporal changes of longitudinal water level and bed elevation in comparison with Run1($L_{mc}$= 14.1m) and Run7($L_{mc}$= 9.5m). Herein, overflow water from the main Sabo dam directly hit on the top of the counter dam in 230 $m^3$/s in case of $L_{mc}$ = 9.5 m (Run5). Bed erosions take place between dams and downstream reach of the counter dam in Run4 and Run9. While, bed erosion between a main and a counter dam in Run5 is smaller than that in Run4 and Run9. Bed degradation in downstream reach in Run5 takes place within around 50 m from the counter dam. Those result in the energy dispersion due to attacking of overflow from the main Sabo dam to the surface of counter dam.

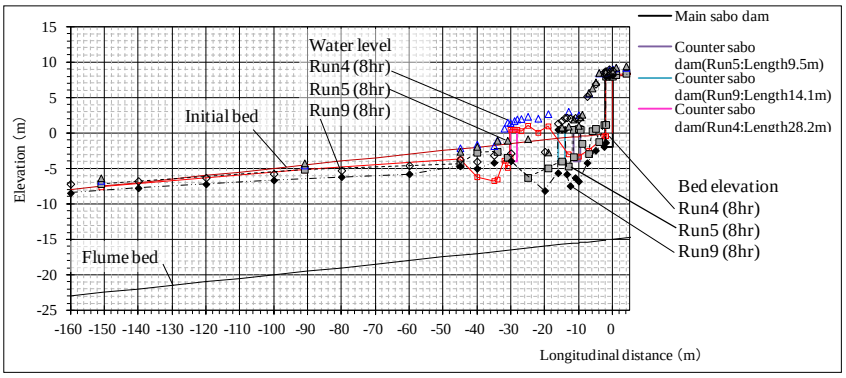


**Figure 5.** Temporal changes of longitudinal water level and bed elevation (Run4, Run5, Run9).

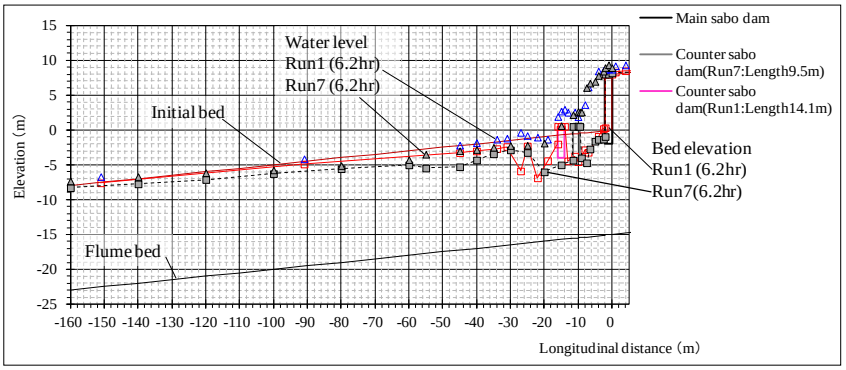


**Figure** 6. Temporal changes of longitudinal water level and bed elevation (Run1, Run7).

 

Rotational degradations take place in Run4 and Run9 due to bed erosion on the downstream reach of the counter dam. In Run4, sediment transportation in downstream of the counter dam becomes actively because of formation of quite mild bed slope in upstream reach of the counter dam due to long setting of $L_{mc}$.

Large overlapping height contributes the protection for embedment of main Sabo dam, and large erosion takes place the downstream reach (Run2). While, erosions in both upstream and downstream reach take place in case of small overlapping height (Run3 and Run9). The maximum of erosion depth in those reaches become thinner as seen in Figure 7 (Run2,Run3). Local scoring depth in downstream of the counter dam tends to be large if the overlapping height is higher. However, scouring over the depth of embedment takes place at downstream of the counter dam.

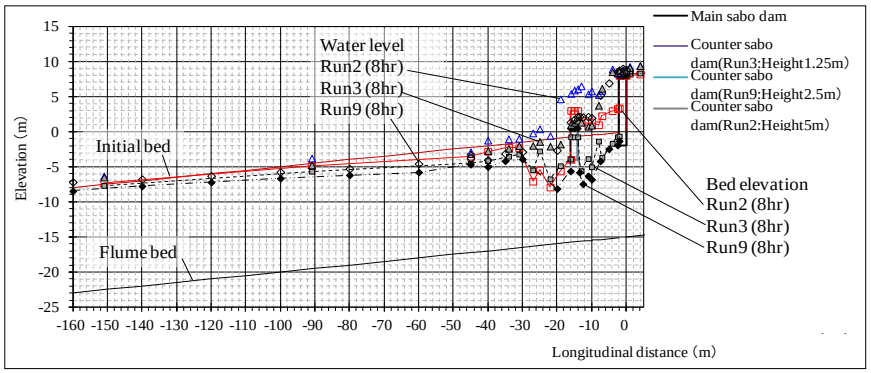


**Figure 7**. Temporal changes of longitudinal water level and bed elevation (Run2, Run3, Run9).

5.1.2 Sediment concentration at downstream of dams

Let us discuss on sediment concentration and unsteady flow, runoff and grain size in steady and unsteady flow. Figure 8 shows temporal changes of flux sediment concentration obtained at downstream end for differences of $L_{mc}$ : 9.5 m (Run5), 14.1 m (Run9), 28.2 m (Run4). Figure 9 shows temporal variations of flux sediment concentration at downstream end in comparison with Run1 ($L_{mc}$= 14.1m) and Run7 ($L_{mc}$= 9.5m). Figure 10 shows temporal variation of flux sediment concentration obtained at downstream end in case of Run3 ($H_{oh}$ = 1.25 m), Run9 (2.5 m) and Run2 (5 m) with $L_{mc}$ =14.1 m.Focused flux sediment concentration in 8hr in Figure 10, sediment concentration has relation; Run2 < Run3 < Run9, and bed slope at downstream reach of counter dam is steep in order of Run2 < Run3 < Run9. Those tendency depend on bed slope at downstream reach of counter dam.

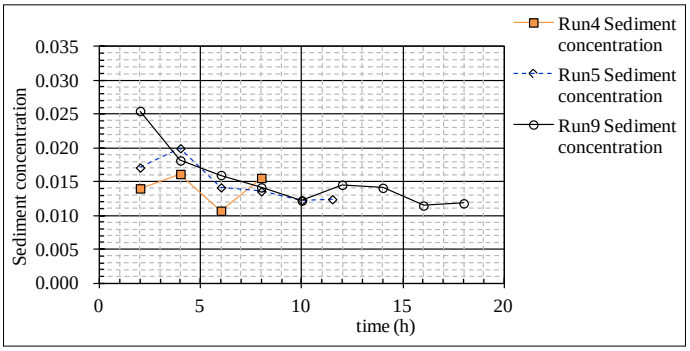


**Figure 8**. Temporal variations of flux sediment concentration at downstream end (Run4, Run5, Run9).

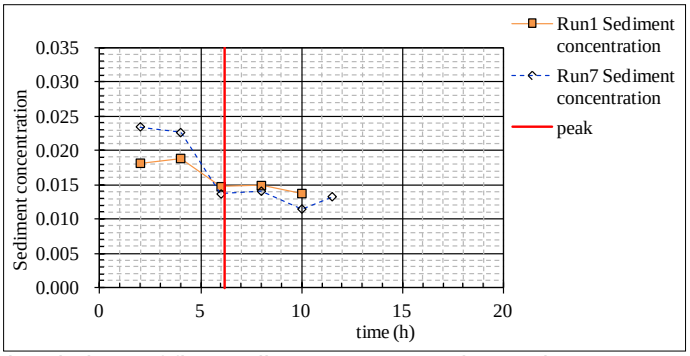


**Figure 9**. Temporal variations of flux sediment concentration at downstream end (Run1, Run7).

 

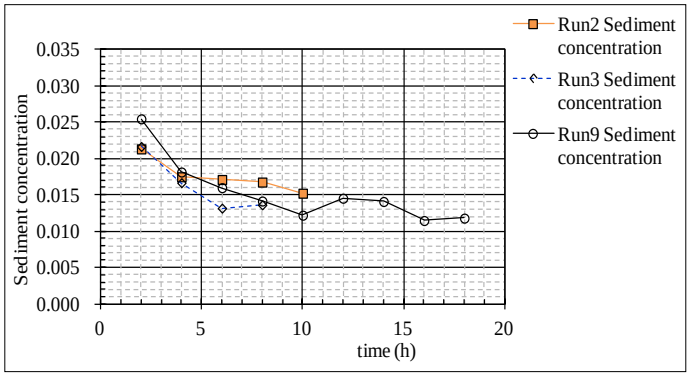


**Figure 10**. Temporal variations of flux sediment concentration at downstream end (Run2, Run3, Run9).

5.1.3 Grain size at downstream of dams

Figures12 show temporal changes of grain size in sediment discharge. Those data are obtained in steady flow with high magnitude of flow discharge for differences of $L_{mc}$ : 9.5 m (Run5), 14.1 m (Run9), 28.2 m (Run4). Figures 13 are temporal changes of grain size at downstream end, respectively, in case of Run3 ($H_{oh}$ = 1.25 m), Run9 (2.5 m) and Run2 (5 m) with $L_{mc}$ =14.1 m.

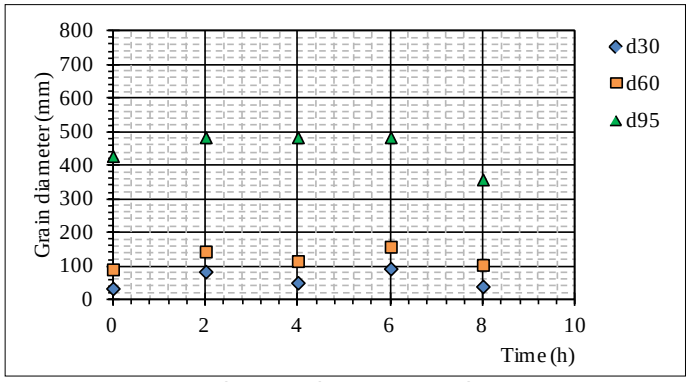


a) Run4 ($L_{mc}$= 28.2 m)

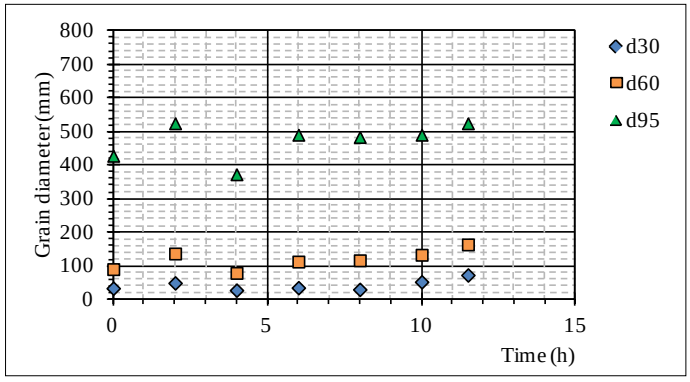


b) Run5 ($L_{mc}$= 9.5 m)

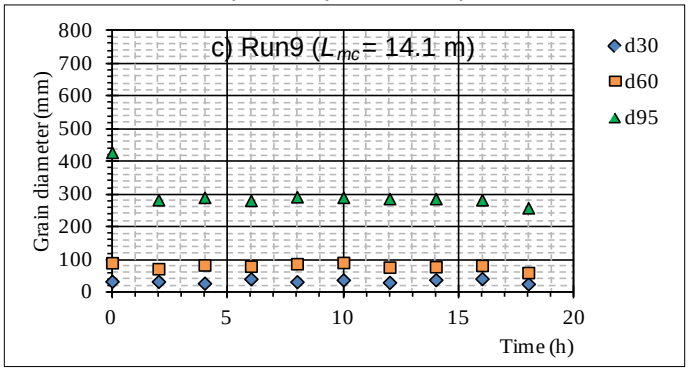


**Figure 11**. Temporal changes of grain size at downstream end (Run4, Run5, Run9).

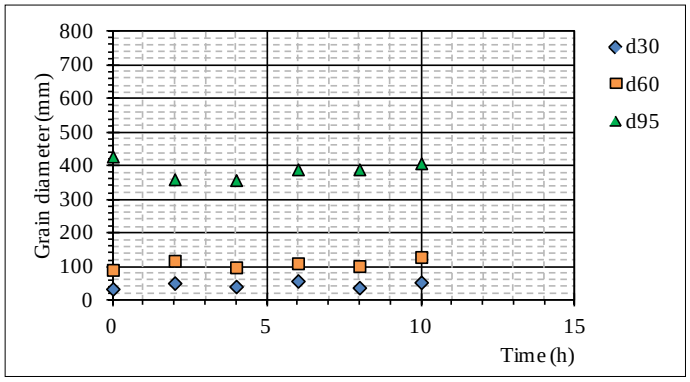


a) Run2 ($H_{oh}$= 5.0 m)

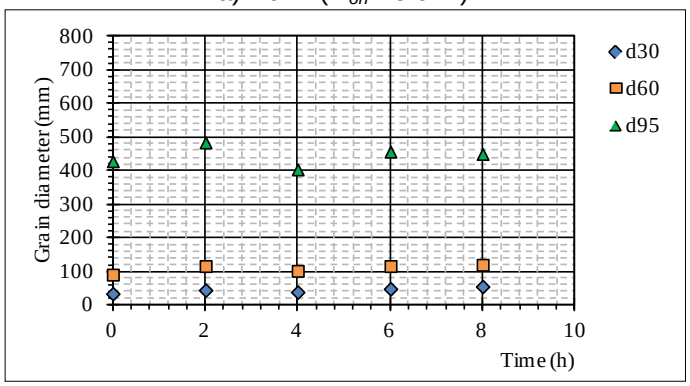


b) Run3 ($H_{oh}$= 1.25 m)

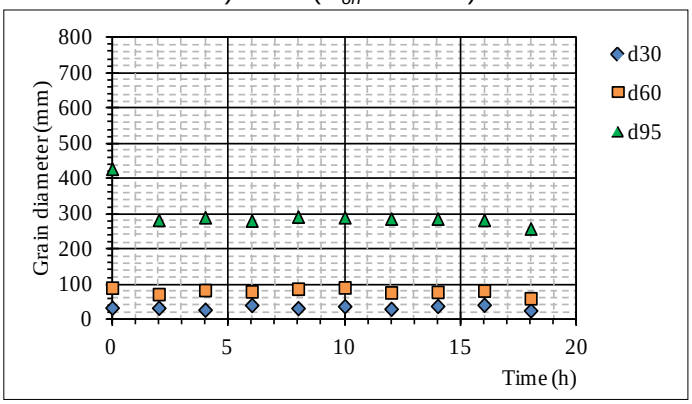


c) Run9 ($H_{oh}$= 2.5 m)

**Figure 12**. Temporal changes of grain size at downstream end (Run2, Run3, Run9).

Coarse component of sediment, $d_{95}$, becomes somewhat larger, and the differences of overlapping height are depending on changes of components of sediment. The size can be controlled if the overlapping height is set appropriately as shown in Run9 ($H_{oh}$=2.5m). The temporal changes of coarse sediment are due to the stable condition of the bed erosion. However, there is a little differences of sediment runoff for the three patterns of overlapping height. That means the small overlapping height is effective for embedment protection to both upstream and downstream of the counter dam. Differences of overlapping height do not effect on sediment runoff at downstream end.

In case of Run9, grain size decreases due to time developing, and the reason is why armoring takes place for long reach in downstream of the counter dam. Temporal changes of grain size in Run4 and Run5 seem to be similar with each other. However, fine and middle components of sediment such as $d_{30}$ and $d_{60}$ do not change due to time progressing and coarse component of sediment, $d_{95}$, has somewhat large value comparison to initial value because the bed slope of downstream reach is similar to initial bed slope. Those indicate that erosion for long reach of the counter dam does not take place in Run5 ($L_{mc}$ = 9.5 m). Sediment transportation of downstream reach of a counter dam depends on the combination of the main and counter dam. Water flow is controlled by between dams, and free surface profile (Run5) is steeper than those of Run4 and Run9, and coarse component of sediment become small (Run4, Run9) due to decreasing of bed slope by developing armor coat on the surface. While, coarse component of sediment is still active in Run5 and result in steady bed slope in downstream reach of counter dam.

 

5.2 Effect of apron between dams on local scouring and bed variation

Let us discuss the function of apron against the bed erosion. Figures 14 to 16 show temporal changes of longitudinal water level and bed elevation, flux sediment concentration and grain size obtained at downstream end in a steady flow with high magnitude of discharge ($Q_{wp}$=230 $m^3$/s) . Figures 16 to 18 show the data corresponding to Figure 13 to 15 in unsteady flow. Those data are obtained in combination of $L_{mc}$ = 9.5 m and $H_{oh}$ = 2.5 m. The difference of existence of apron yields bed erosion between the main and counter dam. While, bed variation except between dams is not different to each other in an unsteady flow, and sediment runoff and grain size are not similar in comparison with Run7 and Run10. That means the apron is effective for bed degradation between main and counter dam. In case of steady flow as shown in Figure 15, grain size, especially for $d_{95}$ in Run5, becomes larger than that of Run6, because coarse component of sediment is transported from main dam and between dams and because inclination of free surface in downstream reach of a counter dam is noticeable in comparison with Run5 due to apron and a counter dam.

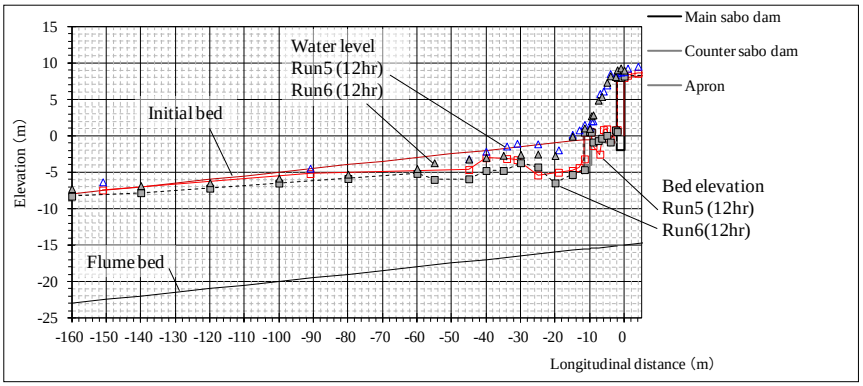


**Figure 13**. Temporal changes of longitudinal water level and bed elevation (Run5, Run6).

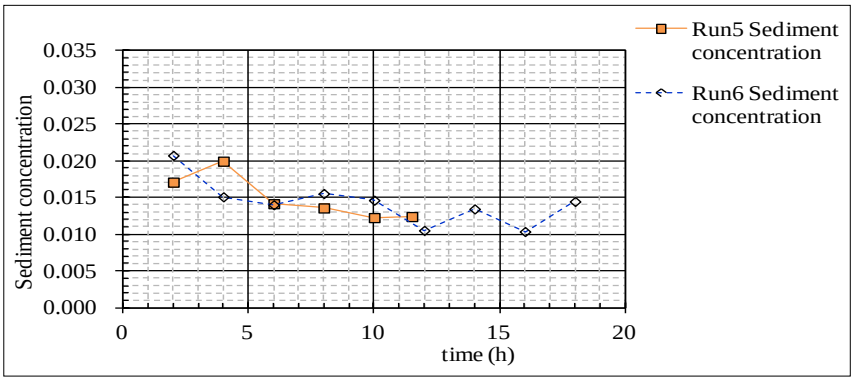


**Figure 14**. Temporal variations of flux sediment concentration at downstream end (Run5, Run6).

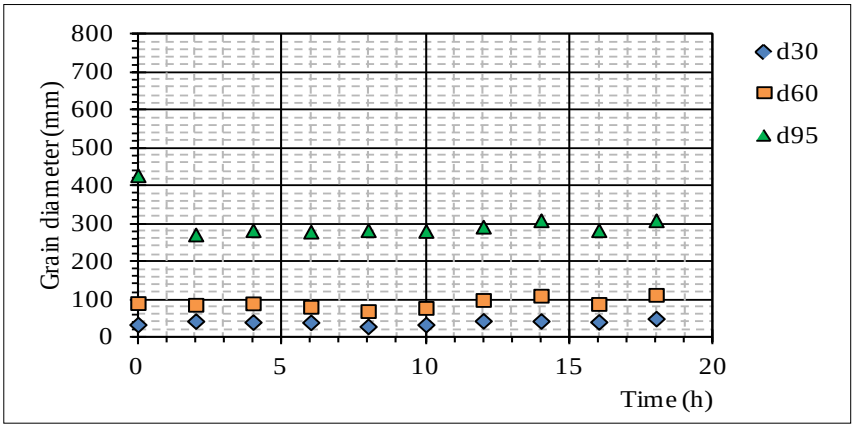


**Figure 15**. Temporal changes of grain size at downstream end (Run6, $L_{mc}$=9.5m, $H_{oh}$= 2.5 m).

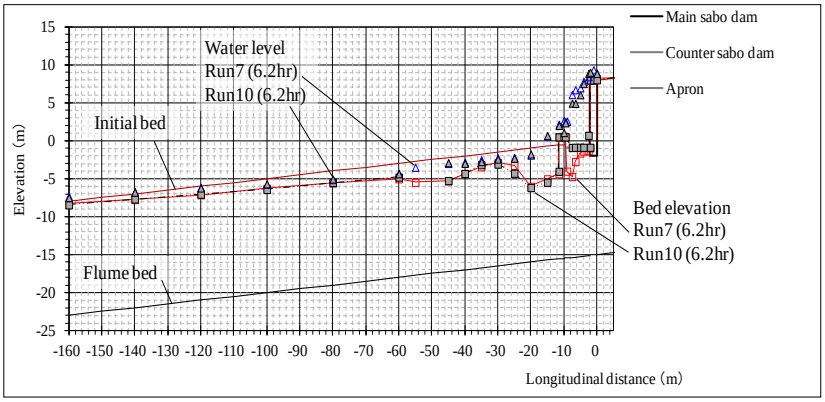


**Figure 16**. Temporal changes of longitudinal water level and bed elevation (Run7, Run10).

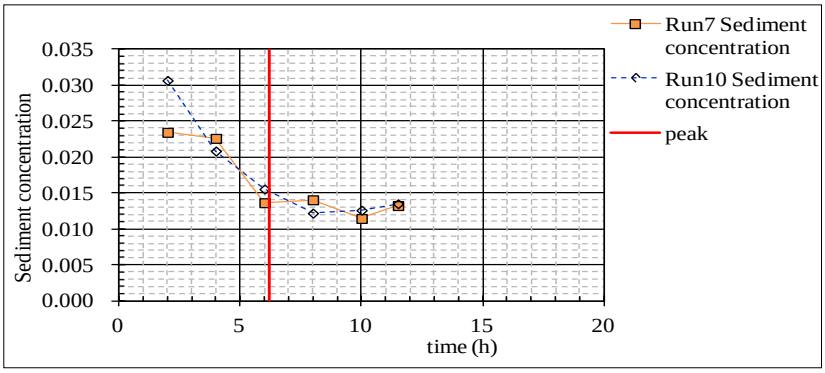


**Figure 17**. Temporal variations of flux sediment concentration at downstream end (Run7, Run10).

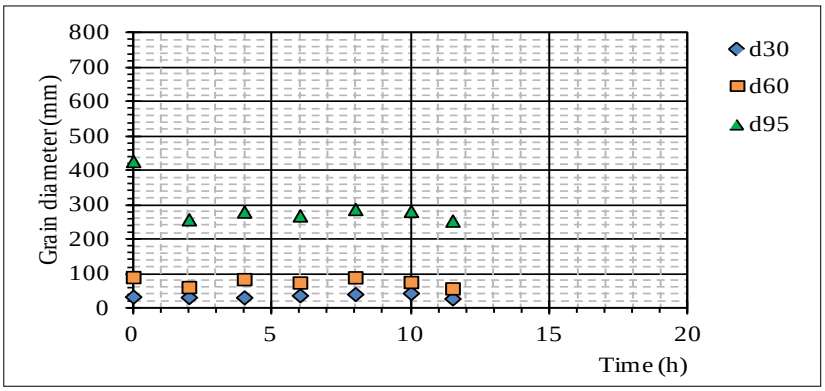


**Figure 18**. Temporal changes of grain size at downstream end (Run10, $L_{mc}$=9.5m, $H_{oh}$= 2.5 m).

5.3 New idea for setting of the layout of Sabo facilities

Erosion in downstream area and reach of Sabo dam and between main and counter dam are examined experimentally for Sabo facilities such as the combinations of overlapping height and horizontal length between dams. In present flume tests, the following results are obtained for combination of $H_{oh}$ and $L_{mc}$ in high magnitude of discharge as follows: The length between main and counter dams is shorter and the overlapping height of those dams become smaller such that the embedment is not eroded, though the magnitude of flood is large corresponding to design discharge. One of preferable suggestions for the setting of length between dams is set in position so that overflow from main dam hits to the top of counter dam in case of large magnitude of flow discharge. Flow intensity of drop water from the main dam will be decreased due to collision to the top of the counter dam, and results in decrease of local scouring of bed and longitudinal bed degradation in downstream reach of the counter dam. The suggestion needs to be evaluated for small and middle magnitude of flood flow.

## 6 CONCLUSIONS

In present study, erosion in downstream area and reach of Sabo dam and between main and counter dam are examined experimentally for Sabo facilities such as the combinations of overlapping height and horizontal length between dams. The results are summarized as follows;

 

(1) One of preferable way of the setting of length between dams is set in position so that overflow from main dam hits to the top of counter dam in case of large magnitude of flow discharge. It is important to decide the magnitude of design flow discharge.
(2) Differences of overlapping height affect bed erosions in long downstream reach of the counter dam, and does not affects the sediment runoff at downstream end. Smaller overlapping height is desired to protect bed erosions because of smaller erosion depth downstream of the counter dam.
(3) Apron is effective to prevent the erosion between dams. Apron protects bed surface between main and counter dams in small or middle magnitude of discharge in present flume tests, because the overflow attacks on the surface of the counter dam in magnitude of discharge (Run5, Run7). Maximum erosion depth in downstream of the counter dam becomes deeper in case of large magnitude of flow discharge with an apron. Erosion depth needs to be evaluated during flood water supplying in long time in case of small and middle magnitude of floods such that erosion between dams is active.
(4) Sediment flux concentration and grain size of sediment discharge rate are affected by bed slope in a reach of downstream of the counter dam. The horizontal length and overlapping height between main Sabo dam and counter dam need to be considered based on hydraulic and sediment transport characteristics, supposing that longitudinal bed variations and grain size are taken into account for layout of Sabo facility.

In present flume tests, flow condition is mainly steady flow with large magnitude of flood corresponding to design flow discharge. In order to evaluate influences of Sabo facilities on local scouring and bed variations, flume tests need under the flow condition for unsteady flow with small and middle magnitude of flow discharge.

**REFERENCES**

Armin, S. (1962). *Handbuch des Wasserbaues*, Vienne: Springer, 3. Aufl, 540-541.

Hayashi, S. (1983). *Hydraulic Studies on the Phenomenon of Scour at the Base Caused By Free Falling Nappe Over Sediment Control Dams*. The Bulletin of the Faculty of Agriculture, Mie University, 66, 101-189 (In Japanese).

Egashira S. & Miyamoto K. & Itoh T. (1997). Constitutive Equations of Debris Flow and Their Applicability. *Proceedings of the 1st International Conference on Debris-Flow Hazards Mitigation*, San Francisco, CA, USA, 340- 349.

Lenzi, M. A. & Comiti, F. (2003). Local Scouring and Morphological Adjustment in Steep Channels with Check-Dam Sequense. *Geomorphology*, 55, 97-109.

Martin-Vide, J.P. & Andreatta, A. (2006). Disturbance Caused By Bed Sills on the Slope of Steep Streams. *Journal of Hydraulic Engineering*, 132(11), 1186-1194.

Mizuyama, T. (1990). *Design of Slits Sabo Dam Apron.* Report of PWRI (National Research and Development Agency Public Works Research Institue), 183(3), 71- 156. (In Japanese)

Suzuki, K., & Michiue, M. & Kawatsu, K. (1982). Study on the Local Scour and Flow Downstream of a Consolidation Work. *Proceedings of the Japanese Conference on Hydraulics*, 2, 75- 80. (In Japanese)

Task Committee on Preparation of sedimentation Manual, ASCE. (1962). Sediment transportation mechanics, erosion of sediment, *Proc. ASCE*, HY, 88.

 

Proceedings of the 37th IAHR World Congress
August 13 – 18, 2017, Kuala Lumpur, Malaysia

# SUSPENDED SEDIMENT FLOW CHARACTERISTICS IN NON-UNIFORM OPEN CHANNEL

BAMBANG AGUS KIRONOTO [(1)], BAMBANG YULISTIYANTO[(2)], BUDI WIGNYOSUKARTO[(3)], BAMBANG TRIATMODJO[(4)], ERWIN NUR AFIATO[(5)] & RAHMAT BANGUN GIARTO[(6]

[(1,2,3,4)] Civil and Environmental Engineering Department, Faculty of Engineering, Universitas Gadjah Mada, Indonesia, Jl.Grafika 2, Yogyakarta, Indonesia.
kironoto@ugm.ac.id; yulis@ugm.ac.id; budiws@ugm.ac.id; btriatmodjo@ugm.ac.id
[(5,6)] Alumni of Graduate Program of Civil Engineering, Civil and Environmental Engineering Department, Faculty of Engineering, Universitas Gadjah Mada, Jl.Grafika 2, Yogyakarta, Indonesia,
shaa.erwin718@gmail.com; bangungiarto@gmail.com

## ABSTRACT

The characteristics of suspended sediment flow in open channel flows are often required in hydraulic engineering design, such as, in irrigation-canals design, design of reservoirs, river improvement, etc. The suspended sediment data, however, is often unavailable, or if there is, the availability of such data is very limited due to the complex and costly procedure in obtaining the data during the field measurements. The existence of non-uniformity of the channel is expected to affect the characteristics of suspended sediment flow, especially when compared to those known in uniform open channel flow and thus need to be studied in more detail. The suspended sediment characteristics in non-uniform open channel flow, such as velocity distribution, friction velocity, and suspended sediment concentration distribution, are studied based on 144 of velocity and suspended sediment concentration profiles. They are measured in narrowed and widened channels, at three different locations on Mataram Irrigation Channel, in Yogyakarta, Indonesia. The suspended sediment concentration profiles were measured by using Opcon Probe, while the velocity profiles were measured by using propeller current meter probe. The findings of the research showed that closer to the edge of the channel, the velocity profile become fuller and smaller, as well as the suspended sediment concentration profile become smaller closer to the side walls. The equations of Rouse and of Tanaka-Sugimoto give good predictions for the concentration of suspended sediment measured in the center of the channel, while near to the edge of the channel, the equations require a correction factor, namely, β-value. The existence of suspended sediment concentration and the changes of flow velocity due to narrowed and widened channels influence the friction velocity values. The results of the friction velocity, $u_*$, by Clauser's method for the data evaluated in this study show a specific pattern in narrowed and widened channels.

**Keywords:** Non uniform open channel flow; velocity; suspended sediment; field measurement.

## 1. INTRODUCTION

Studies of suspended sediment are essential in environmental study problems of water resources since the knowledge of sediment transport is very necessary, especially in terms of planning, designing and operating hydraulic structures such as irrigation channels, dams, water treatment plants of drinking, installation of waste water disposal, and others. Suspended sediment flows in natural rivers or artificial channels can be regarded as uniform or non-uniform of suspended sediment flow. It depends on how far the influence of non-uniformity applies to the flow. For example, flows that occur under a bridge with narrowing and widening of the channel might be considered as non-uniform of suspended sediment flow. The existence of suspended sediment and of non-uniformity of flow in open channel can influence the flow characteristics, such as velocity profiles, suspended sediment concentration profiles, etc. These flow characteristics - which are very important in hydraulic engineering - can be significantly different compared with those in the clear water of uniform and non-uniform flows.

In an effort to obtain accurate information about the transport of sediment suspension, the method of calculation using empirical formulas or a combination of theoretical-empirical formulas have been developed. However, due to the complexity of the sediment problems, the results obtained from the various formulations are often unsatisfactory. So as to study the characteristics of suspended sediment in open channels, especially in a non-uniform flow, field sampling method is often more reliable than the method of calculation.

Based on the issues raised above, this study was conducted using direct measurements in the field on Mataram irrigation channel in Yogyakarta, Indonesia, which is an artificial channel. The measurement location was taken on the narrowing and widening of channels representing non-uniform flow conditions.

 

## 2. LITERATURE REVIEWS

Various researches related with suspended sediment can be found in the literature, such as done by Coleman (1981, 1986), Muste & Patel (1997), Wu et al. (2008), Shah-Fairbank et al. (2011), Gray & Landers (2014), and Lv et al. (2015). Coleman (1981, 1986) reported that the existence of suspended sediment can affect the shape of velocity distribution, although it still follows the logarithmic velocity distribution in the inner region. Kironoto and Graf (1994; 1995) examined the characteristics of turbulence in the flow of uniform and non-uniform of clear water of rough open channel flow, and analyzed the effects of acceleration and deceleration to velocity profiles and turbulent. Cardoso et al (1991) and Kironoto and Graf (1995) studied non-uniform clear water flows and showed that there are significant differences between the flow characteristics of uniform and non-uniform open channel flow, although, some similarities between the two flows were also reported. Kironoto (2007) conducted a laboratory and field study of suspended sediment flow in square-shaped channels which showed that the position where the suspended discharge ratio is equal to one, occurs at position $z/B$ = 0.2, where $B$ is the width of the channel. While Kironoto and Yulistiyanto (2016) conducted a similar study but in trapezoidal field channel obtained the value of at $z/B$ = 0.25. Kironoto and Yulistiyanto (2009) also showed that Rouse's equation can predict the profiles of the suspended sediment concentration data satisfactorily well for the measured data at the center area of the channel, either for laboratory or field data. However, away from the center of the channel, the equation deviates significantly from the measured data.

## 3. THEORETICAL CONSIDERATION

### 3.1. Velocity distribution

In open channel flow, the velocity profiles are often distinguished in the inner region and the outer regional areas. The inner region area is the region near the wall where the logarithmic velocity distribution is valid. While the outer region is the region far from the wall, where the velocity data slightly but systematically deviate from the logarithmic velocity distribution. Kironoto and Graf (1995) showed that the theory of uniform clear water flow remains valid for non-uniform flow, and thus, the logarithmic velocity distribution in the inner region, *i.e.*, in $y/D$ < 0.2 where $D$ is the flow depth, can be defined by the equation:

$$\frac{u}{u_*} = \frac{1}{\kappa}\ln\left(\frac{y}{k_S}\right) + Br \qquad [1]$$

where $u$ is the average point velocity at a distance $y$ from the reference point, $u_*$ is the shear velocity; $\kappa$, a universal constant of Von-Karman ($\kappa$ = 0.4); $Br$, integration constant of logarithmic velocity distribution, and $k_s$ is the equivalent sand roughness of Nikuradse.

The Nikuradse roughness value, $k_s$, can be evaluated from the following equation:

$$\frac{C}{\sqrt{g}} = \sqrt{\frac{8}{f}} = 5.6\log\left(\frac{R}{k_S}\right) + 6.25 \qquad [2]$$

where $C$ is the Chezy coefficient, $f$ is the friction coefficient, and $R$ is the hydraulic radius.

### 3.2. Suspended sediment concentration

The depth-averaged of suspended sediment concentration, $C_y$, can be calculated using the following equation:

$$C_y = \frac{1}{D-a}\int_a^D C\,dy \qquad [3]$$

where $D$ is flow depth (m), $a$ is a reference level, and $C$ is average concentration point of sediment suspension. Suspended of sediment concentration distribution, $C$, can be predicted by using Rouse's equation and by Tanaka-Sugimoto's equation. Rouse Equation (1937, in Yang, 1996) is based on a logarithmic velocity distribution, and assuming that the diffusion coefficient of the sediment has an equal value to the momentum transfer coefficient, it can be expressed as.

$$\frac{C}{C_a} = \left[\frac{D-y}{y}\frac{a}{D-a}\right]^z \qquad [4]$$

 

Tanaka and Sugimoto equation can be given as (Garde and Ranga Raju, 1977):

$$\frac{C}{C_a} = \left[\left(\frac{\sqrt{D}+\sqrt{D-y}}{\sqrt{D}-\sqrt{D-y}}\right)\left(\frac{\sqrt{D}-\sqrt{D-a}}{\sqrt{D}+\sqrt{D-a}}\right)\right]^{\frac{w_S}{\kappa u_*}} \quad [5]$$

where $D$ is the flow depth, $C$ is the suspended sediment concentration at a distance $y$ from the channel bed, $C_a$ is the reference of suspended sediment concentration at a certain distance, a, from the bed, $w_s$, is the fall velocity of suspended sediment, and $\kappa$ is a Von Karman's constant, $z = w_s/(\kappa\, u_*)$ is defined as the Rouse parameter.

Suspended sediment discharge, $Q_s$, can be formulated as a result of multiplication of the depth-averaged velocity, $\bar{U}_y$ and the depth-averaged suspended sediment concentration, $\bar{C}_y$, from the left to the rigth edges of the channel:

$$Q_S = \int_0^B \bar{U}y.\bar{C}y.dB \quad [6]$$

## 4. RESEARCH METHODOLOGY

Study of suspended sediment flow characteristics in non-uniform open channel flow was conducted by direct measurement of suspended sediment flow in Mataram Irrigation Channel, in Yogyakarta, Indonesia. The measurement locations were taken at three (3) different locations on the narrowing and widening channels representing non-uniform flow conditions. The sketch of measuring locations at three (3) different locations in Mataram Irrigation is given in Figure 1.

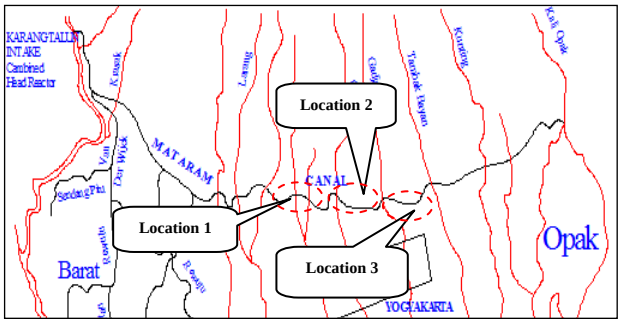


Description Location Coordinates:

Location 1 : 7°44'51"S ; 110°19'35"E
Gombang, Mlati, Sleman
Location 2 : 7°44'45"S ; 110°20'3"E
Nambongan, Mlati, Sleman
Location 3 : 7°45'40"S 110°21'39.8"E
Kutuasem, Mlati, Sleman

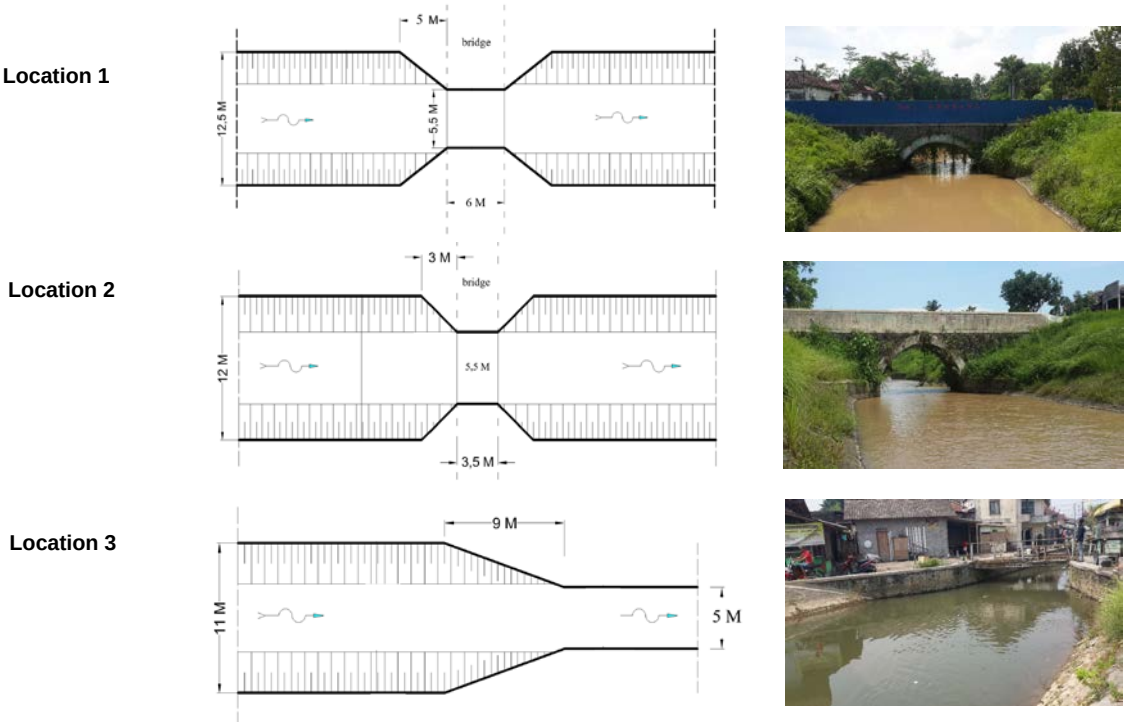


**Figure 1.** Measurement locations along Mataram Irrigation Channel, Yogyakarta, Indonesia.

Several variables were measured in this study; they are grouped as the mean point-velocity and the suspended-sediment measurements, and the other measurements, such as flow depth, water temperature, and free water surface slope. The mean point-velocity profiles were measured by using a calibrated Propeller Current meter C2 type 10".150" No.95384. The suspended sediment concentration profiles were measured by using Opcon probe coupled with the Opcon control-unit of a signal processor with an output capacity of 0-10 volts DC and connected with a computer for data acquisition and further data processing. Signal processor has a frequency response of 1 Hz with accuracy level or zero stability 0.4%/24 hours.

The measuring locations were conducted at 3 different locations along Mataram Irrigation Channel (L1, L2, and L3) as shown in Figure 1 above. For locations 1 (L1) and location 2 (L2), the measurements were conducted at 9 different sections (S1, S2, …, S9) from the upstream of narrowing section to the downstream of widening section. While for Location 3, the measurements were conducted at 6 different sections (S1, S2, …, S6) from the upstream of narrowing section to the downstream uniform section. Measurement points of velocity and suspended sediment concentration, conducted at each section in transversal direction are shown in Figure 2. Starting from the edge of the channel to the center of the channel, *i.e*., respectively at position, $z$ = 2*B*/32, 3*B*/32, 4*B*/32, 5*B*/32, 10*B*/32, and 16*B*/32; thus, for each section, there are 6 profiles of velocity and of suspended sediment concentration.

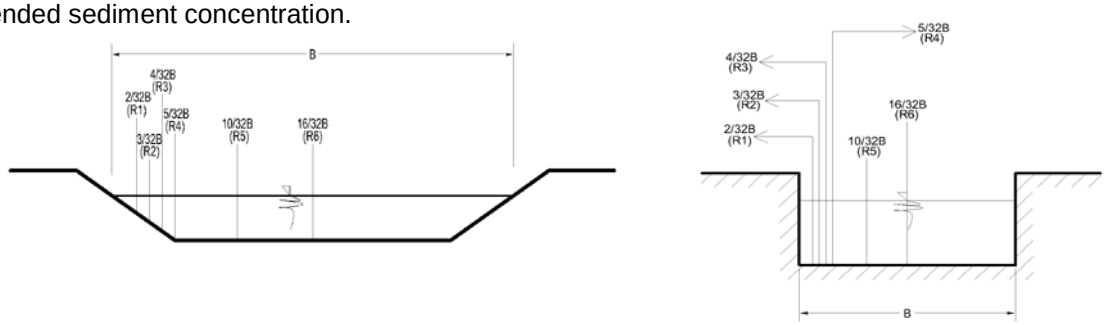


**Figure 2.** Transversal measurement points on trapezoid and rectangle channel sections.

One hundred and forty-four profiles of both velocity and suspended sediment concentration have been measured in the present study. Each running profiles have a code name with 6 different alphabets. The first alphabet represents the Location (L1, L2 dan L3), the second and the third alphabets represent the measuring sections (S1, S2, …, S9 for Location 1 and 2, and S1, S2, …, S6 for location 3), and the fourth and the fifth alphabets represent the measuring vertical positions in transversal direction at each cross sections (V1, V2, …, V6). The most relevant hydraulic variables and suspended sediment parameters obtained in this study are summarized in Table 1. It should be noted here that, due to the measurement for all sections (S1, S2, …, S9), each location could not be completed within one (1) day, thus, the flow discharge for each measuring sections may change from day to day at the time where the measurements were conducted; the presentation of the data analyzed in this study were then given in non-dimensional values.

4.1. Velocity distribution

Figure 3 presents a typical example of velocity profiles obtained at location 1, section 3 (L1S3) for 6 different measuring verticals (from the left to the center of the channel; V1, V2, …, V6); it can be seen from the figure that the highest velocity occurs at the center of the channel, and then decreases at the locations near the channel edge. It can be noted also from the figure, that the velocity profile in the center of the channel tends to get slender, while closer to the edge of the channel, the velocity profiles tend to get fuller.

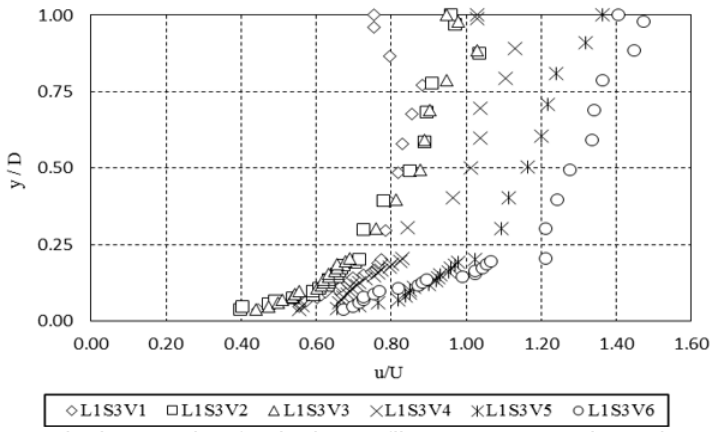


**Figure 3.** Typical example of velocity profiles at cross section 3 (Location 1).

**Table** 1. Summary of basic measurement data, flow and suspended sediment parameters (Kironoto and Yulistiyanto, 2016).

| Location, L, and Section, S | $m$ (V:H) | $b$ | $B$ | $D$ | $S_w$ | $u_*$ | $k_s$ | $\overline{U}$ | $\bar{C}$ | $Q$ | $Q_S$ | Channel section shape | Type of channel side wall | Date of measurements |
|---|---|---|---|---|---|---|---|---|---|---|---|---|---|---|
| | ( - ) | (m) | m | m | ( - ) | (m/s) | (m) | (m/s) | (gr/l) | ($m^3$/s) | (gr/s) | ( - ) | ( - ) | ( - ) |
| L1S1 | 1 : 2 | 7.2 | 9.5 | 0.82 | 0.000250 | 0.042 | 0.052 | 0.531 | 0.597 | 3.840 | 2292.046 | Trapezoid | Stone masonry wall | 3-Feb-16 |
| L1S2 | 1 : 2 | 7.2 | 8.9 | 0.75 | 0.000175 | 0.034 | 0.129 | 0.353 | 1.141 | 2.297 | 2620.077 | Trapezoid | Stone masonry wall | 9-Feb-16 |
| L1S3 | 1 : 2 | 7.1 | 7.1 | 1.02 | 0.000125 | 0.031 | 0.097 | 0.352 | 1.662 | 2.543 | 4227.241 | Trapezoid | Stone masonry wall | 5-Mar-16 |
| L1S4 | - | 5.6 | 5.6 | 0.96 | 0.000175 | 0.035 | 0.054 | 0.438 | 1.115 | 2.364 | 2636.084 | Rectange | Plastered concrete wall | 8-Feb-16 |
| L1S5 | - | 5.6 | 5.6 | 1.04 | 0.000150 | 0.033 | 0.024 | 0.490 | 1.181 | 2.839 | 3351.744 | Rectange | Plastered concrete wall | 29-Feb-16 |
| L1S6 | - | 5.5 | 5.5 | 0.99 | 0.000320 | 0.048 | 0.027 | 0.681 | 1.448 | 3.710 | 5373.031 | Rectange | Plastered concrete wall | 14-Feb-16 |
| L1S7 | 1 : 2 | 5.9 | 7.9 | 0.93 | 0.000125 | 0.032 | 0.020 | 0.485 | 1.305 | 3.509 | 4579.989 | Trapezoid | Stone masonry wall | 15-Feb-16 |
| L1S8 | 1 : 2 | 6.2 | 9.6 | 0.99 | 0.000125 | 0.031 | 0.120 | 0.340 | 1.430 | 2.772 | 2903.360 | Trapezoid | Stone masonry wall | 27-Feb-16 |
| L1S9 | 1 : 2 | 7.0 | 10.0 | 0.89 | 0.000067 | 0.022 | 0.032 | 0.308 | 1.218 | 2.418 | 2946.080 | Trapezoid | Stone masonry wall | 28-Feb-16 |
| L2S1 | 1 : 2 | 8.7 | 9.6 | 0.56 | 0.000400 | 0.047 | 0.021 | 0.666 | 0.503 | 3.664 | 1842.646 | Trapezoid | Stone masonry wall | 9-Apr-16 |
| L2S2 | 1 : 2 | 7.2 | 8.6 | 0.55 | 0.000350 | 0.042 | 0.089 | 0.437 | 0.737 | 1.979 | 1459.126 | Trapezoid | Stone masonry wall | 20-Mar-16 |
| L2S3 | 1 : 2 | 8.0 | 8.0 | 0.81 | 0.000333 | 0.047 | 0.050 | 0.593 | 0.577 | 3.837 | 2212.675 | Rectange | Stone masonry wall | 9-Apr-16 |
| L2S4 | - | 5.6 | 5.6 | 0.72 | 0.000425 | 0.049 | 0.064 | 0.562 | 0.816 | 2.281 | 1860.867 | Rectange | Plastered concrete wall | 20-Mar-16 |
| L2S5 | - | 5.5 | 5.5 | 0.94 | 0.000571 | 0.062 | 0.052 | 0.784 | 0.504 | 4.063 | 2047.958 | Rectange | Plastered concrete wall | 9-Apr-16 |
| L2S6 | - | 5.6 | 5.6 | 0.82 | 0.000425 | 0.052 | 0.091 | 0.570 | 1.128 | 2.630 | 2967.066 | Rectange | Plastered concrete wall | 19-Mar-16 |
| L2S7 | - | 6.8 | 6.8 | 0.73 | 0.000333 | 0.044 | 0.076 | 0.501 | 1.304 | 2.499 | 3256.887 | Rectange | Stone masonry wall | 19-Mar-16 |
| L2S8 | 1 : 2 | 6.9 | 8.7 | 0.60 | 0.000350 | 0.043 | 0.069 | 0.486 | 1.240 | 2.381 | 2951.482 | Trapezoid | Stone masonry wall | 19-Mar-16 |
| L2S9 | 1 : 2 | 7.2 | 9.5 | 0.59 | 0.000200 | 0.032 | 0.018 | 0.456 | 1.112 | 2.262 | 2515.411 | Trapezoid | Stone masonry wall | 19-Mar-16 |
| L3S1 | 1 : 2 | 6.3 | 8.0 | 0.47 | 0.000150 | 0.025 | 0.038 | 0.296 | 0.190 | 0.997 | 189.130 | Trapezoid | Stone masonry wall | 24-Nov-15 |
| L3S2 | 1 : 2 | 6.3 | 8.2 | 0.58 | 0.000200 | 0.032 | 0.069 | 0.351 | 0.313 | 1.528 | 478.040 | Trapezoid | Stone masonry wall | 17-Nov-15 |
| L3S3 | 1 : 2 | 6.3 | 8.7 | 0.83 | 0.000150 | 0.033 | 0.137 | 0.335 | 0.338 | 2.225 | 752.969 | Trapezoid | Stone masonry wall | 28-Nov-15 |
| L3S4 | - | 6.8 | 6.8 | 0.86 | 0.000150 | 0.032 | 0.120 | 0.339 | 2.023 | 1.983 | 4011.936 | Rectange | Plastered concrete wall | 22-Nov-15 |
| L3S5 | - | 5.0 | 5.0 | 0.82 | 0.000200 | 0.035 | 0.040 | 0.444 | 0.392 | 1.827 | 716.714 | Rectange | Plastered concrete wall | 17-Nov-15 |
| L3S6 | - | 5.0 | 5.0 | 0.95 | 0.000200 | 0.037 | 0.071 | 0.431 | 0.632 | 2.052 | 1297.064 | Rectange | Plastered concrete wall | 4-Des-15 |

$b$: channel width, $m$ : slope of side wall, $B$ : the channel width at the free water surface, $D$ : flow depth, $S_w$ : free water surface slope, $k_s$ : Nikuradse Roughness Coeff., $\overline{U}$ : cross-section mean velocity, $\bar{C}$: cross-section averaged suspended sediment concentration; $u_*$ : friction velocity, $Q$ : flow discharge; $Q_S$ : Suspended sediment discharge

Figure 4 shows a typical example of the normalized of depth-averaged velocity, $U_y$, to the cross-section averaged velocity, $U$, measured at Location 3. The depth-averaged of velocities at each measuring vertical were calculated by integrating the measured velocity profiles from the bed to the free water surface and divide it by the flow depth. As shown in Figure 5, the depth-averaged velocity at the center of the channel is greater than that closer to the edge of the channel, which is indicated by the ratio value of $U_y/U$, is greater than one at the center of the channel, and smaller to one at the area closer to the edge of the channel. This is due to the influence of friction of the side walls to the flow. For measuring location 3, as shown in Figure 5, the position where $U_y/U$=1 occur at $z/B$ = 0.24.

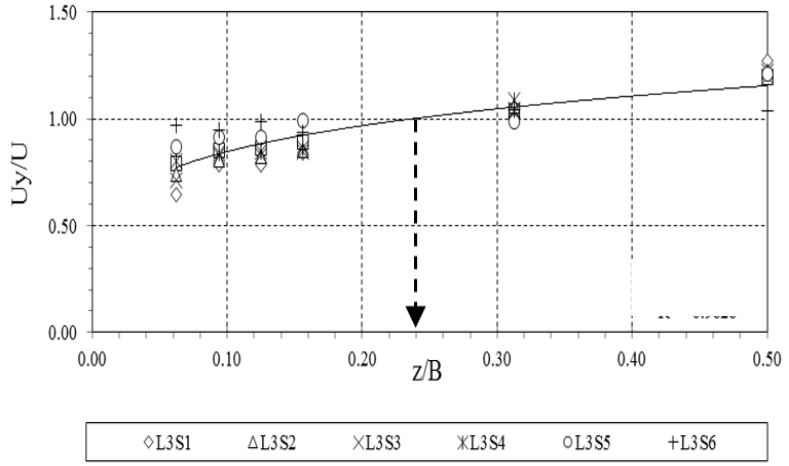


**Figure 4**. Typical example of the normalized of
the depth-averaged velocity to the cross-section averaged velocity (Location 3)

4.2. Friction velocity, $u*$

Friction velocity, $u*$, can be determined by applying the Clauser Method, using the measured data of the velocity profile in the inner region together with logarithmic velocity distribution. To obtain the friction velocity, $u_*$, the velocity profiles obtained from the measurements were plotted against their positions from the channel bed in Cartesian coordinate, where ln($y/ks$) are plotted against $u$, as given in Figure 5 for profile L1S1V6 as a typical example.

The non-dimensional values of friction velocity, $u*/u_{*\text{cross-section}}$, in the transversal direction of each section are given in Figure 6 (for Location 3), in which the friction velocity, $u_{*\text{cross-section}}$, is defined as the average value of friction velocity at each cross section. As can be seen in Figure 6, the value of $u*/u_{*\text{cross-section}}$ = 1 occurs at $z/B$ = 0.17, that means that the friction velocity at $z/B$ ≈ 0,17 represent the average friction velocity at the cross section.

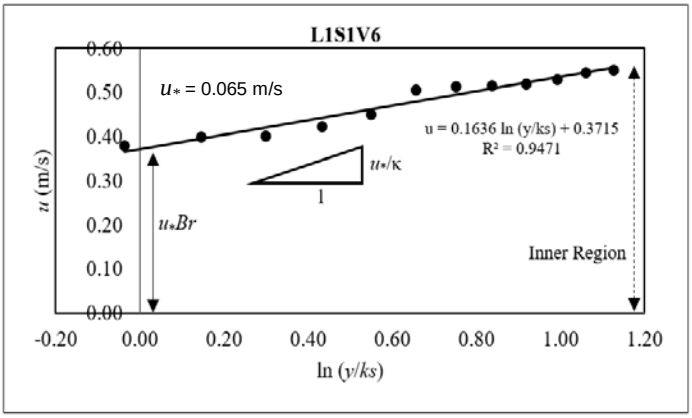


**Figure 5.** Typical example of friction velocity, $u*$, calculated using Clauser Method (profile L1S1V6).

The non-dimensional values of friction velocity, $u*/u_{*\text{cross-section}}$, along the channel sections at Location 1, 2, and 3, respectively, are given in Figure 7a, 7b dan 7c. As can be seen from the figures, the non-dimensional values of friction velocity at location 1 and 2, where the channels are narrowing and widening, they have similar trends, where the friction velocities at the center area of the channel (for example at sections V5 and V6) are higher than those of averaged value at each cross section, *i.e.*, $u*/u_{*\text{cross-section}}$ >1, and even more on the widening section and behind the section; and they tend to be smaller closer to the channel edge, *i.e.*

$u_*/u_{*\text{cross-section}}$ <1 (i.e. at sections V1 and V2) and even less on the widening section and behind the section. The different trend is observed at Location 3, where the channel is narrowing, the non-dimensional friction velocity, $u_*/u_{*\text{cross-section}}$, at cross section behind the narrowing channel is slightly more uniform.

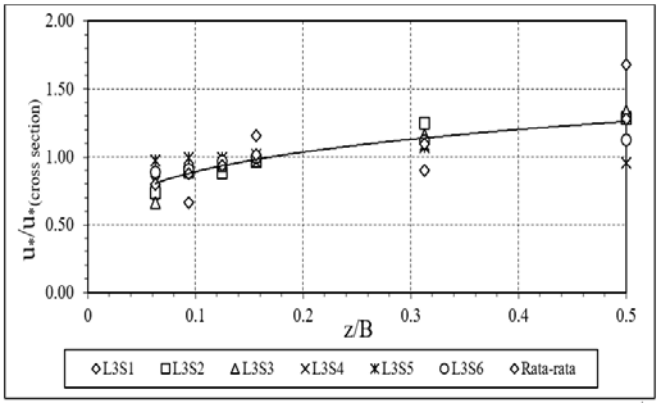


**Figure 6.** The non-dimensional friction velocity in transversal direction at Location 3.

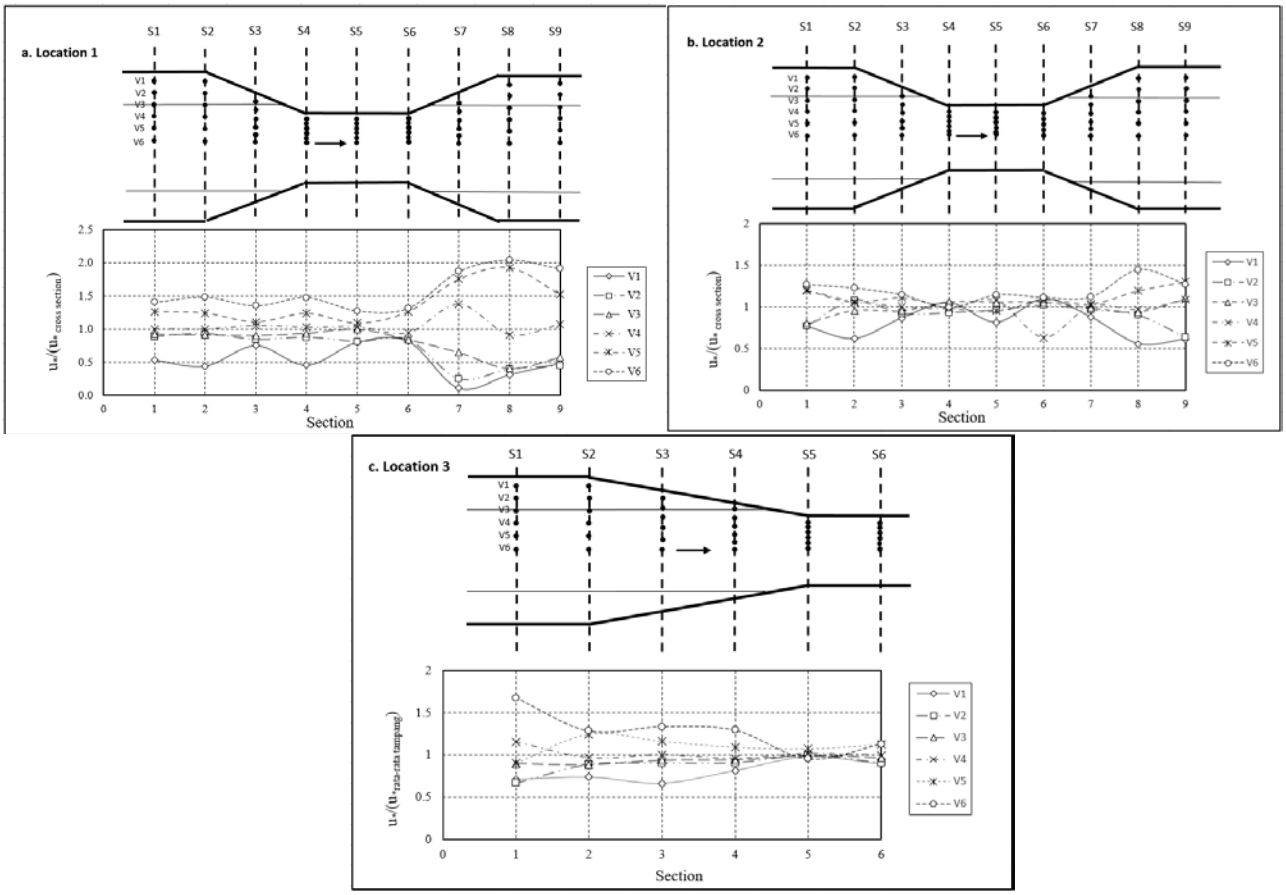


**Figure 7.** Non-dimensional friction velocity along the Mataram Irrigation Channel;
a). Location 1, b). Location 2, c). Location 3.

4.3. Suspended sediment concentration

A typical example of suspended sediment concentration profile obtained in this study is shown in Figure 8, for profiles at Section 3 (Location 1). It can be shown from the figure that the suspended sediment concentration in the center part of the section tends to be higher than those closer to the wall.

Figure 9 presents the comparison between the calculated of suspended sediment concentration profiles — by Rouse's and by Tanaka-Sugimoto's equations — with the data measured for profile L1S1V5, which show that the equations are not valid for the data measured at the left side of the center of the channel. However, by applying correction parameters — called as $\beta$-Rouse and $\beta$ -Tanaka-Sugimoto —, both equations can represent the measured data more satisfactorily. Kironoto and Yulistiyanto (2009) which have

 

measured suspended sediment concentration profiles in a transverse direction of rectangular channels, either for laboratory or irrigation channels, showed similar results to those observed in this study.

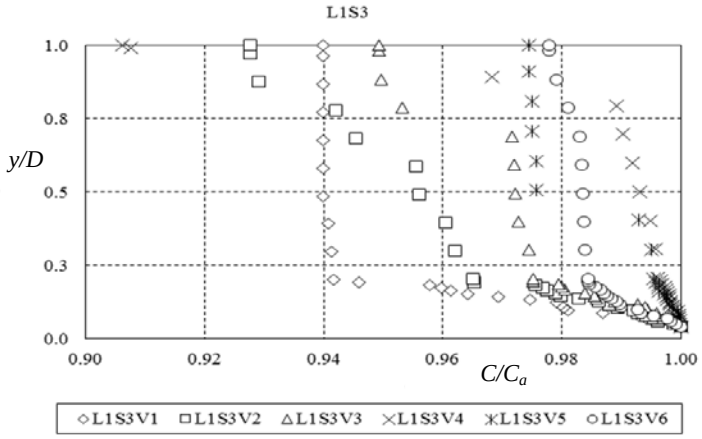


**Figure 8.** Typical example of suspended sediment concentration profiles, $C/C_a$, at Section 3 (Location 1).

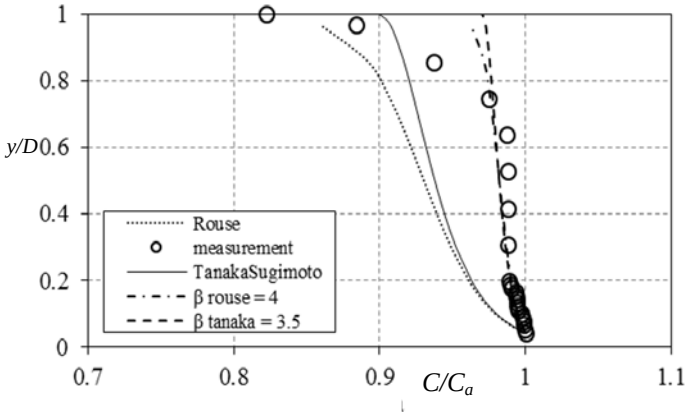


**Figure 9.** Comparison of the measured of suspended sediment concentration profiles (L1S1V5) with the equation of Rouse and of Tanaka and Sugimoto.

4.4. Suspended sediment discharge

In Figure 10, it is shown that the ratio of the depth-averaged suspended sediment concentration, $C_y$, to the cross-section averaged suspended sediment concentration, $C$, from the edge to the center of the channel. Scattering is more pronounced for the measurement data closer to the edge of the channel. From Figure 10, it can also be seen that $C_y/C$ = 1 occurs at $z/B$ = 0.30, which means that measuring of suspended sediment concentration at $z/B$ = 0.3 will give the mean value of suspended sediment concentration at the cross section.

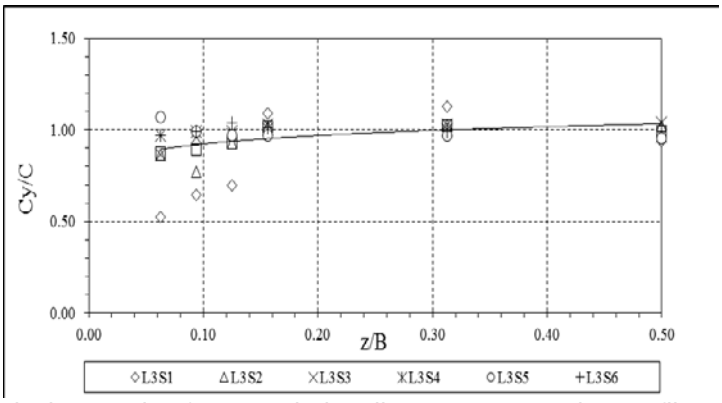


**Figure 10.** Typical example of suspended sediment concentration profiles at Location 3.

In Figure 11, it is shown that the non-dimensional values of suspended sediment discharge, $(U_yC_y)/(UC)$, plotted against $z/B$, where the position of $(U_yC_y)/(UC)$ = 1 occur at $z/B$ = 0.25. This means that the suspended sediment discharge can be calculated based on the measurement of $U_y$ and $C_y$ at $z/B$ =1. Based on the curve given in Figure 11, it can also determine the suspended sediment discharge from the measurements of $U_y$ and

$C_y$ at any positions in the transverse direction, by applying the correction factor according to the curve given in Figure 11.

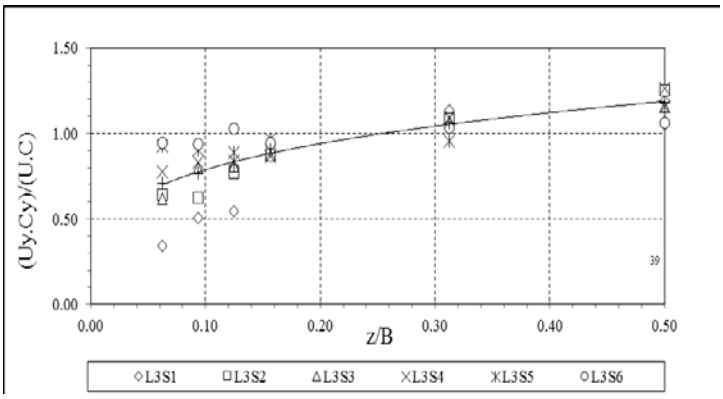


**Figure 11.** Typical example plot of $(U_yC_y)/(UC)$ *vs*. $z/B$ at Location 3.

## 5 CONCLUSIONS

Based on the data analyzed from this study, some conclusions can be obtained as follow:

1. From the data of velocity profiles obtained in this study, it can be observed that the highest velocity profile generally occurs at the center of the channel, and then decreases at the locations near the channel edge. It can also be noted that the velocity profile in the center of the channel tends to get slender, while closer to the edge of the channel, the velocity profiles tend to get fuller.
2. Friction velocity, $u*$, can be determined by applying the Clauser Method, using the measured data of velocity profiles in the inner region together with logarithmic velocity distribution.
3. The non-dimensional values of friction velocity at the center area of the channel, where the channels are narrowing and widening, are higher than those of averaged values at each cross section, and even more on the widening section and behind the section. They also tend to be smaller closer to the channel edge and even less on the widening section and behind the section. For narrowing channel, the non-dimensional friction velocity at cross section behind the narrowing channel is slightly more uniform.
4. The Rouse's and Tanaka and Sugimoto's equations can still be used to represent the measured data of suspended sediment concentration in the center part of the channel. However, a parameter should be applied, named as β-parameter if it used in the edge part of the channel.
5. The ratio of suspended sediment discharge, $(U_yC_y)/(UC)$ = 1 occur at $z/B$ = 0.25, which means that the suspended sediment discharge can be calculated based on the measurement of $U_y$ and $C_y$ at $z/B$ =1.

## ACKNOWLEDGMENTS

Great thanks and awards are granted to the Research and Community Service Institution (LPPM) Universitas Gadjah Mada on funding of this study (Kironoto and Yulistiyanto, 2016)

## REFERENCES

Cardoso, A.H., Graf, W.H. & Gust, G. (1991). Steady Gradually Accelerating flow in a Smooth Open Channel. *Journal of Hydraulic Research*, 29(4), 525–543.

Coleman, N.L. (1981). Velocity Profiles with Suspended Sediment. *Journal of Hydraulic Res*earch, 19(3), 211–229.

Coleman, N.L. (1986). Effects of Suspended on the Open Channel Velocity Distribution. *Water Resources Research*, 22(10), 1377-1384.

Garde, R.J. & Ranga Raju, K.G. (1977). *Mechanics of Sediment Transportation and Alluvial Streams Problems*. Wiley Eastern Limited, New Delhi.

Graf, W.H. (1984). *Hydraulics of Sediment Transport*. McGraw-Hill Book Company, New York.

Gray. J.R & Landers, M.N. (2014). Measuring Suspended Sediment. *Comprehensive Water Quality and Purification.* 1, 157-204.

Kironoto, B.A. & Graf, W.H. (1994). Turbulence Characteristics in Rough Uniform Open Channel Flow. *Proceeding of Institution of Civil Engineers Water, Maritime & Energy*, 106, 333-344.

 

Kironoto, B. A. & Graf, W. H. (1995). Turbulence Characteristics in Rough Non Uniform Open Channel Flow. *Proceeding of Institution of Civil Engineers Water, Maritime & Energy*, 112, 336-348.

Kironoto, B.A (2007). Study of Suspended Sediment Sampling Location in Transverse Direction for Determination of Cross-Section Suspended Sediment Concentration (Comparison of Laboratory and Field Data). *Dinamika Teknik Sipil*, 7(2). (in Indonesia)

Kironoto, B.A. & Yulistiyanto, B. (2009). The Validity of Rouse Equation for Predicting the Transversal Suspended Sediment Concentration Profiles ın Uniform Open Channel Flow. *International Conference on Sustainable Development for Water and Wastewater Treatment*, MUWAREC-YK09, Gadjah Mada University, Yogyakarta, Indonesia.

Kironoto, B.A. & Yulistiyanto, B. (2016). *Suspended Sediment Sampling Method for Determining Suspended Sediment Discharge in Artificial Channel and Natural River*, Competitive Research Grant Report, Research and Community Service Institution (LPPM), Universitas Gadjah Mada, Yogyakarta. (in Indonesia)

Lv, S., Tang, H., Xue, Y., Yuan, S. & Bai, X. (2015). Laboratory Measurement of Suspended Sediment Concentration by using ADV. *Proceedings of the 6th International Asia Conference on Industrial Engineering and Management Innovation*, 91-100.

Muste, M. & Patel, V.C. (1997). Velocity Profiles for Particles and Liquid in Open Channel Flow with Suspended Sediment. *Journal of Hydraulic Eng*ineering, 123(9), 742-751.

Shah-Fairbank, S., Julien, P. & Baird, D. (2011). Total Sediment Load from Semep using Depth Integrated Concentration Measurements. *Journal of Hydraulic Engine*ering, 137(12), 1606–1614.

Wu, B., van Maren, D.S. & Li, L. (2008). Predictability of Sediment Transport in the Yello River using Selected Transport Formula. *International Journal of Sediment Res*earch, 23(4), 283–298.

Yang, C.T. (1996). *Sediment Transport Theory and Practice*. The McGraw-Hill Companies Inc., USA.

 

Proceedings of the 37th IAHR World Congress
August 13 – 18, 2017, Kuala Lumpur, Malaysia

# CONVEX BANK VEGETATION SUCCESSION AND ITS EFFECT OF FORMING POINT BAR OF MEANDERING RIVER IN THE YELLOW RIVER SOURCE REGION

HAILI ZHU [(1)], XIASONG HU [(2)], ZHIWEI LI [(3)] & YANTING LI[(4)]

[(1,4)] Qinghai Institute of Salt Lakes, Chinese Academy of Sciences, Xining, China,
[(1,4)] University of Chinese Academy of Sciences, Beijing, China,
qdzhuhaili@163.com; 17835012@qq.com
[(1,2,4)] Department of Geological Engineering, Qinghai University, Xining, China,
huxiasong@sina.com;
[(3)]School of Hydraulic Engineering, Changsha University of Science & Technology, Changsha, China
253616927@qq.com

## ABSTRACT

Alpine meadow is generally developed well in meandering river of the Yellow River source region. Riparian vegetation plays a critical role on river stability and river bed evolution. The aim of this paper is to make a further study of riparian vegetation succession law and explicate the process of synchronous transverse migration of meandering rivers. In 2013-2016, field investigation and experimental work are conducted on quadrat survey, plant species identification, vegetation coverage degree, vegetation distribution characteristics and testing sediment grain size of point bar. The results show that from inside to outside of inner bank in study area, the riparian vegetation is generally divided into four distinct ribbon zonings or arcuation zonings: *hydrophyte*, *hygromesophytes*, *mesophytes*, and *subshrub*. The vegetation types of the four vegetation zones are abundant step by step, and the coverage degree takes the tendency of increasing. *Potamogeton pectinatus L.* and *Halerpestes tricuspis Hand.-Mazz* are pioneer plants in convex bank, and the main dominant plants are cyperaceae *Blysmus sinocompressus Tang et Wang*, *Kobresia tibetica Maxim* and *subshrub Potentilla fruticosa L.* From the first vegetation zone to the fourth zone, sediment grain size progressively becomes smaller in convex bank, and the clay content increases with increasing vegetation coverage. The plants endured by flood in point bar have the effects on receding near-bank flow velocity in flood period and stabilizing the new forming point bar. The herb and subshrub in middle and outside zone of the inner bank have the effects on developing riparian meadow, entrapping sediment during flood period, stabilizing point bar, increasing soil fertility, and promoting the growth of point bar. In such a way, the velocity of forming inner bank can remain consistent with the speed of concave bank failure.

**Keywords:** Source region of the Yellow River; vegetation zone; sediment composition; riparian meadow; convex bank.

## 1 INTRODUCTION

Riparian vegetation acts as a key parameter in river health condition, riverbed and riverbank stability indices (Huang and Nanson, 1997; Ma et al., 2006). Some conditions such as riparian vegetation structure, root system development and river bank material composition can recede river bank scouring (Zhu et al., 2015), reduce near bed current velocity of inner bank to some extent (Li et al., 2016), restrict channel migration arbitrarily and keep long term stability of river bend (Gregory et al., 1991; Abernethy and Rutherfurd, 1998; Zhang and Peng, 2003; Dong, 2003; Huang et al., 2007; Ni and Gao, 2011). Besides these, the increasing of vegetation coverage may result in the evolution of channel pattern (Wang et al., 2000; Bennett et al., 2002). Because of meandering characteristics of rivers, a large variety of aquatic ecological environments can be formed such as concave bank, convex bank, transition section, rapids and riffle etc., which created conditions for diversity of species (Wang et al., 2000; Zhang and Peng, 2003; Huang et al., 2007) and provided hydrological conditions for riparian vegetation succession from *hydrophytes* to *mesophytes* and terrestrial plants (Nilsson et al., 1997; Ma et al., 2006). Fluvial landforms and hydrogeomorphic processes drive the evolution of riparian plant communities. However, biological communities may significantly control geomorphic processes and have strong impacts on landform dynamics (Corenblit et al., 2007). River migration also controlled the soil texture of river bank and influenced the soil moisture balance, thereby influenced the establishment of riparian vegetation. Reciprocal adjustments between hydrogeomorphic processes and landforms and vegetation communities are usually intense along fluvial corridors (Steiger et al., 2005; Tabacchi et al., 2005). Mechanical processes of submersion, sediment erosion, transportation and deposition, plant destruction, import and export of new pioneer species by flow dynamics (Tabacchi et al., 1998) drives regressive or progressive vegetation successions (Bendix, 1998). In turn, plant structures can strongly interact with water flow and sediment transport (Samani and Kouwen, 2002) to impart significant control on river channels and margins.

 

Riparian vegetation plays an important role in river landform forming processes in the Yellow River source region. Vegetation and bed load transport capacity of channel constitute the main factors of forming different river pattern (Li et al., 2016). The source region of the Yellow River located in Qinghai-Tibet Plateau interior, is the important water conservation area of Yellow River basin. Alpine meadow and alpine steppe meadow are wide spread in meandering river banks (Zhu et al., 2013), they are the most important cover types of vegetation and take up about 80 percent of source region area (Zhang et al., 2006). On channel bars, vegetation roots bind bar sands and gravels into a cohesive 'skin' thereby increasing the shear stress required to mobilize bar particles. Lots of continuous river bends are well developed and of regular morphology in source region of Yellow River, such as Zequ River and Lanmucuoqu River. Meandering rivers are formed by the interplay between erosion of the outer bend and deposition on the point bars in the inner bend. Highly sinuous rivers are formed when the point bars are stabilized, i.e. by vegetation development, thereby preventing chute cut-offs and promoting lateral expansion of the meander bends (Schuurman et al., 2015). But the extent of vegetation stabilization and thereby the formation of river floodplain strongly depends on the type of vegetation. Besides these, vegetation can alter the flow field and subsequently the sediment balance through hydraulic resistance, which is determined by parameters such as plant density, plant thickness, plant height and flexibility (Järvelä, 2002). It is well known that vegetation stabilizes substrate and encourages sediment retention, but it is rarely known of the identification of riparian vegetation control on sediment deposition dynamics as a key biogeomorphic function. Vegetation development take on an phenomena of gradual succession on the point bar, but the studies of characteristics of meadow communities succession and the mutual effects of vegetation structure and sedimentation remains unclear. Which has the greater influence on the magnitude of sediment deposition: biological structures (plant morphotypes) or location of stands along the hydrogeomorphic transverse gradient from the main channel to the floodplain? In order to provide the basis for transverse evolution rule of meandering river and offer scientific references for river ecological restoration in Yellow River source region, some field investigations and tests will be conducted to analyze the vegetation succession regulation and the correlation with river bank sediments in Lanmucuoqu River.

## 2 STUDY AREA AND METHODS

### 2.1 General situation of study area

Lanmucuoqu River located in northeast part of Qinghai-Tibet plateau, belongs to Henan County of Huangnan Tibetan Autonomous Prefecture. The geographical coordinates are 34°26′-35°02′ N, 101°23′-101°35′ E. The region belongs to subrigid zone and humid regions of plateau bearing features of plateau continental climate. The weather is warm and rainy from May to October, and is cold, dry and windy in other months of each year, the cold season is long and cold and warm season is short and rainy. The elevation of this region is 3400-4200 m. Annual average temperature is minus four degrees centigrade, average annual precipitation is 597.1-615.5 mm (Lin et al., 2016). The precipitation forms mainly are snowfall and rainstorm and concentrate on May to September each year, which take up 75 percent to 85 percent of the full year precipitation. Typical meandering rivers are developed in the study area (see Figure 1), and the vegetation forms mainly are alpine meadow and alpine steppe meadow, alpine cushion-like vegetation and sparse vegetation distributed locally in some high attitude terrain (Zhu et al., 2013).

### 2.2 Field investigation methods

Field investigation and in situ tests were carried annually on three chosen river bends from 2013 to 2016, with the width of the river channel is about 6-8 m. At first, pulling a section line using trap along the centre line of river bend, the length was found to be almost 80-120m (see Figure 2); then carrying out some field investigations and experimental work along the pulled section line at certain sites, the tested sites were mainly influenced by the changes of plant species and bank material. The vegetation and bank material sampling locations in meander-1 were shown in Figure 2, where at least three sampling locations were made at each vegetation zoning. The experimental work included plant quadrat (0.5m×0.5m) survey, plant species identification, vegetation coverage estimation and plant height measurement, plant species distribution survey and bank material sampling etc. About 60 pieces of plant specimens were made and more than 40 plant species were identified during four years. The sediment samples were taken back to the laboratory of Qinghai University. Sieve analysis method and laser particle analyzer (Mastersizer 2000) were used to test the bank material particle size more than 2 mm and less than 2 mm, respectively.

 

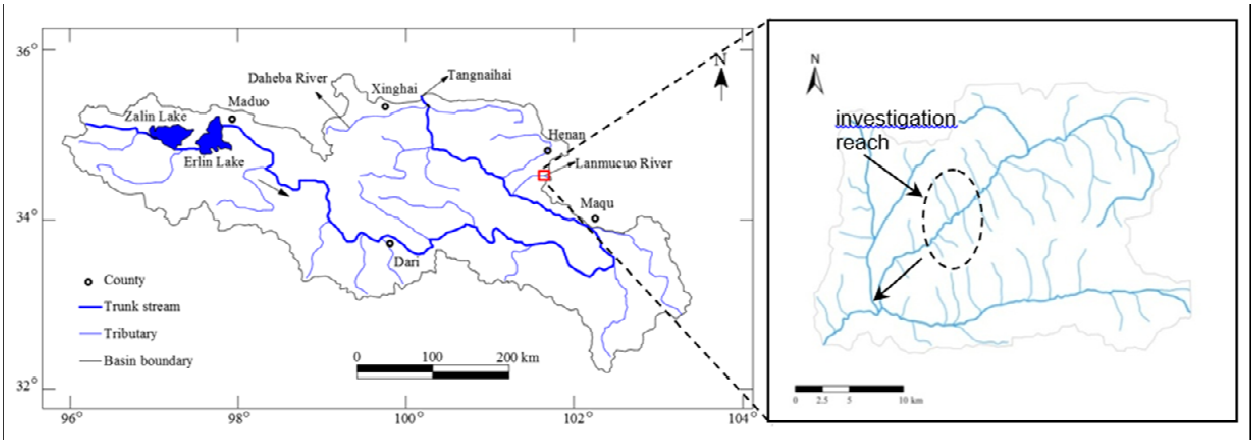


**Figure 1**. Location of Lanmucuo River and continuous meanders (July 2016).

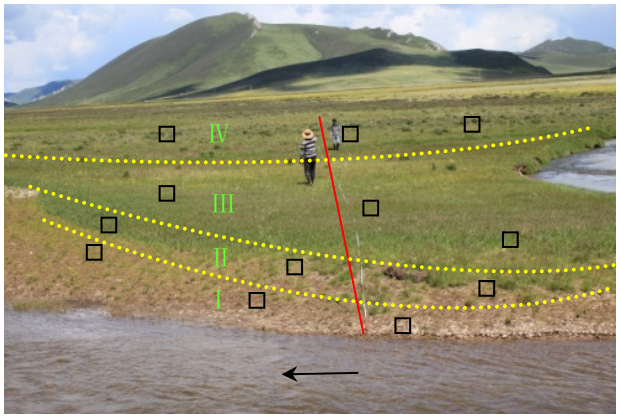


**Figure 2**. Measured profile and vegetation sampling locations in Meander-1.

## 3 RESULTS AND ANALYSIS

### 3.1 Vegetation zoning of convex bank

Plant species, vegetation coverage, sediment grain size distribution and soil water content along the section line took on a regular change through field survey and tests. The riparian vegetation was generally divided into four distinct ribbon zonings or arcuation zonings that were parallel to the river bends (see Figure 3). The width of the four zonings was increased from the water edge to the outside of inner bank, and increased with the widening of river channel. The plant species presented the gradual transition of *hydrophyte*, *hygromesophytes*, *mesophytes*, and subshrub. There were obvious differences among the four vegetation zonings of plant species, vegetation coverage and height. The basic features of the four vegetation zonings are summarized in Table 1.

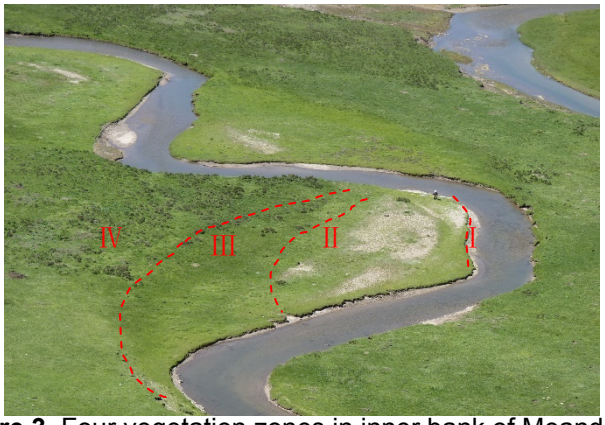


**Figure 3**. Four vegetation zones in inner bank of Meander-1.

**Table 1**. Feature of vegetation zonings in convex bank.

| Zoning | Mean horizontal distance/m | Mean vegetation coverage/% | Main plant composition | Mean plant height/cm | Mean height difference |
|---|---|---|---|---|---|
| **I** | 0-2.1 | 8-15 | *Potamogeton pectinatus L.*<br>*Hippuris vulgaris L.*<br>*Halerpestes tricuspis Hand.-Mazz.* | 4.6 | / |
| **II** | 2.1-16.6 | 40-65 | *Blysmus sinocompressus Tang et Wang*<br>*Poa annua L.*<br>*Elymus nutans Griseb.*<br>*Potentilla anserina L.*<br>*Halerpestes tricuspis Hand.-Mazz.*<br>*Pedicularis megalochila Li*<br>*Blysmus sinocompressus Tang et Wang*<br>*Kobresia tibetica Maxim* | 10.5 | about 10cm Between zone I-zone II |
| **III** | 16.6-34.9 | 60-85 | *Poa annua L.*<br>*Kobresia capillifolia C. B. Clarke*<br>*Double-stigma Bulrush*<br>*Elymus nutans Griseb.*<br>*Potentilla anserina L.*<br>*Trollius pumilus D. Don*<br>*Caltha scaposa Hook. F. et Thoms.*<br>*Aonitum tangutium Stapf*<br>*Ranunculus tanguticus Ovcz.* | 14.6 | about 6cm Between Zone II-zone III |
| **IV** | ＞34.9 | 90-100 | *Kobresia capillifolia C. B. Clarke*<br>*Carex kansuensis Nelmes*<br>*Carex moorcroftii Falc. ex Boott*<br>*Elymus nutans Griseb.*<br>*Poa annua L.*<br>*Potentilla fruticosa L.*<br>*Potentilla glabra Lodd.*<br>*Hippophae thibetana Schlechtend.*<br>*Polygonum viviparum L.*<br>*Ligularia virgaureaMattf*<br>*Ranunculus tanguticus Ovcz.*<br>*Nardostachys chinensis Batal.*<br>*Oxytropis ochrocephala Bunge*<br>*Potentilla anserina L.*<br>*Gentiana dahurica Fisch*<br>*Leontopodium pusillum Hand.-Mazz.*<br>*Cremanthodium lineare Maxim.*<br>*Geranium pylzowianum Maxim.*<br>*Dxytropis coerulea*<br>*Aonitum tangutium Stapf* | 21 | about 25cm Between Zone III-zone IV |

 

Some colonized *hydrophyte* or wetland plants recently grow on the vegetation zoning I. And with many new deposits constituting the bank, the width of the zone is between 1.7-2.5 m. The vegetations are sparse and plant species are single or less relatively, with vegetation coverage only reaches 8%-15%. This bank is always covered with water during the period of 5-9 month, so *Potamogeton pectinatus L.* is the main plant which is a kind of submerged plant. The plants can grow in both sandy bottom of oxygen-rich environment and ooze bearing organics of oxygen deficit environment, which has developed root system and play a key role of intercepting sediment. The biomass of overground parts is focused on water surface (Liu, 1996). When the bank deposits accumulate gradually, the main vegetation is perennial herb *Halerpestes tricuspis Hand.-Mazz*. (see Figure 4a). Its prostrate stem is slender and arising roots and clusters leaves from the node, therefore the plant exerts a role of intercepting and stabilizing the sediment.

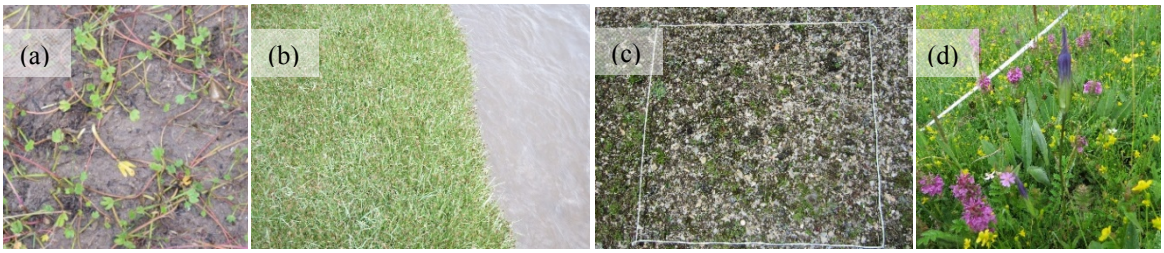


**Figure 4**. (a) *Halerpestes tricuspis Hand.-Mazz*. in zone I (b) community of *Blysmus sinocompressus Tang et Wang* near bank of zone II (c) Sand-gravel shoal in zone II (d) forb in zone IV

The main vegetations of second zone are *hydrophyte* and *hygromesophytes*, with width of between 11.6-18.3m, and coverage of about 45%-65%. The dominant plant is *Blysmus sinocompressus* Tang et Wang, which belongs to *cyperaceae*, and swamp, sandy loam and swamp meadow soils are all fit for its growth. *Blysmus sinocompressus Tang et Wang* has developed rhizome and nodes with roots. Because this plant has strong capacity of vegetative propagation and competition, it can form a special plant community by the single plant (Liu, 1996). At the study area, *Blysmus sinocompressus Tang et Wang* mostly distributes at the river bank near to the first vegetation zone, 2-3 m wide and 45%-55% of coverage. Besides this, the plant community made up of single plant *Blysmus sinocompressus Tang et Wang* is distributed on the two sides of river bank, its width is 4-6 m, length is 20-25 m, coverage reach up to 100% (see Figure 4b). Small amount of gramineous plants such as *Poa annua L.* and *Elymus nutans Griseb*. are found at the second zone. Potentilla anserina *L*. are also distributed rarely. Irregularly shaped patch covered with sand and gravel can be found at the zone, the area is about 20-40 $m^2$ and the vegetation coverage is only about 5%-10% (see Figure 4c).

*Hydrophyte* and *hygromesophytes* are the main vegetations of third zone, width is 12.4-18.9m, and coverage is about 55%-80%. Some of gramineous plants and *cyperaceae* plants are well distributed at the zone, such as *Kobresia tibetica Maxim*, *Kobresia capillifolia C. B. Clarke, Poa annua L.* and *Elymus nutans Griseb*. These plants coverage degree take up about 35%-45% of the total.

Plant species increases obviously at the fourth zone, some subshrubs like *Potentilla fruticosa L., Potentilla glabra Lodd*. and *Hippophae thibetana Schlechtend.* appear. *Mesophytes* are increasing, with vegetation coverage degree more than 95%, and width of the zone reaching up to 50m. Gramineous plants increase relatively, while cyperaceae plants decrease, with the coverage degrees of both taking up 40%-50% of the total. Weeds invasion (see Figure 4d) leads to alpine meadow degeneration (Sun et al., 2013).

The height difference between the first and second zone is 10cm, while the second and third zone, third and fourth zone height difference is 6cm and 25cm, respectively. Vegetation of the fourth zone is well developed, especially the root system of *Blysmus sinocompressus Tang et Wang* and *Carex moorcroftii Falc. ex Boott*. These plants have long creeping rhizome, developed fibrous roots and arising roots from the node, so they play an important role of protecting the riverbank. The root system can reach up to 0.4-1.1m of the lower part of the riverbank, and average length of roots is 0.6m. The interlocking root networks of meadow vegetation reinforce soils by adding tensile strength to the bank soil matrix (Zhu et al., 2015). The very fine root networks typical of sedges, for example, comprise large numbers of randomly oriented roots less than 1 mm in diameter. We observed that this dense root reinforcement creates a tough sod layer ranging in thickness from 0.45 to 0.65 m.

### 3.2 Relationship between bank material composition and vegetation succession of convex bank

According to the results of sieve analyses and laser particle analyses (Mastersizer 2000), we calculated the mass percentage of less than some particle size, clay content of each zone, coefficient of uniformity and coefficient of curvature, and then drew the particle size distribution curve of four zones at inner bank, as shown in Figure 5 and Table 2. From the first to fourth vegetation zone, the clay content takes on the increasing trend. The particle size distribution curve of the first and second zones shows discontinuity ($C_c < 1$ or $C_c > 3$), where the difference of particle size is large and $C_u$ is big, which means the middle particle size is

 

lack. Silty sand and silty gravel are the main soil types of the first and second zone. In contrast, along with the gradual transition of vegetation zone, the particle size distribution curve of the third and fourth vegetation zones shows continuity ($C_c$ is between 1 and 3), where difference of particle size is less, and the main type is silt.

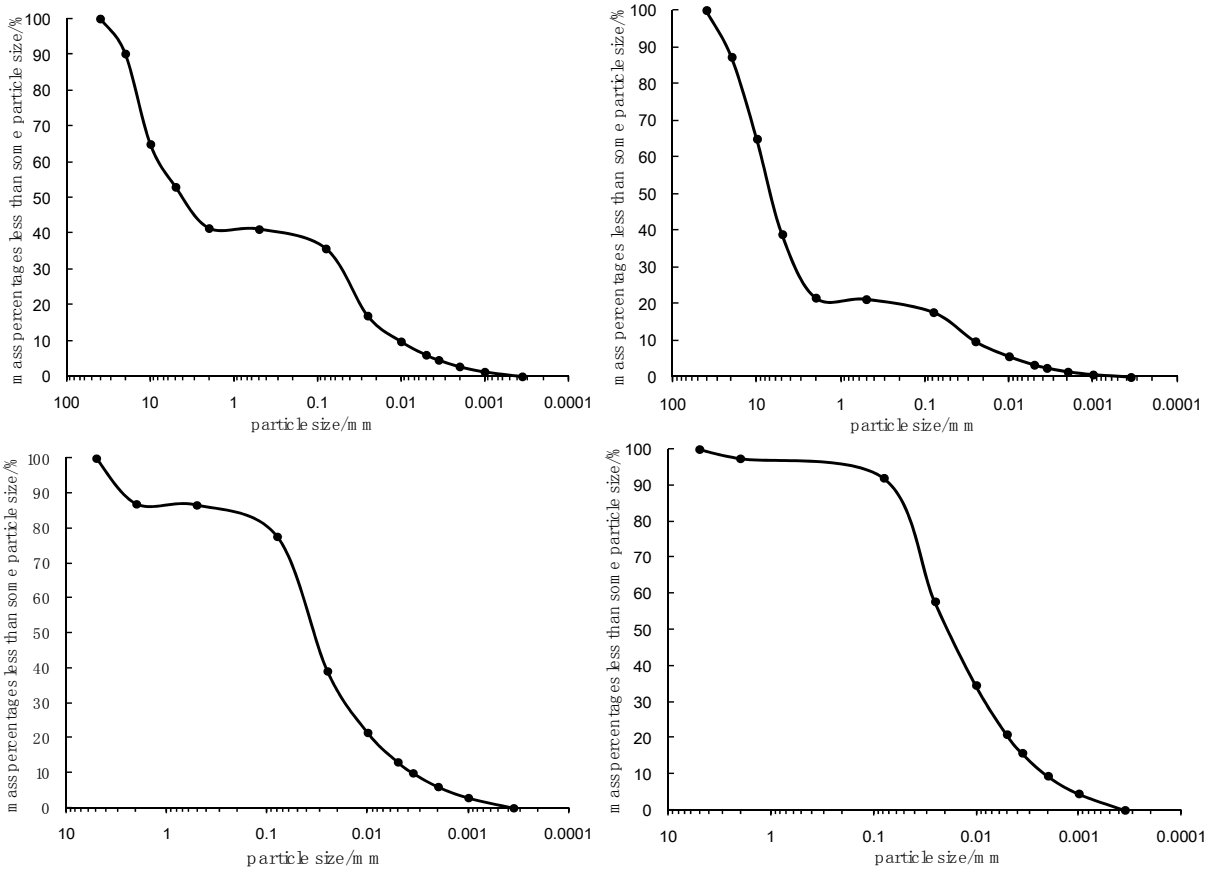


**Figure 5**. Particle size distribution curve of four zones at inner bank of Meander-2 (a) Zone I (b) Zone II (c) Zone III (d) Zone IV.

**Table 2**. Sediment properties in convex bank of three typical meanders.

| Serial number | horizontal distance | naming soil sample | $d_{50}$/mm | clay content/% | $C_c$ | $C_u$ | vegetation coverage/% |
|---|---|---|---|---|---|---|---|
| $T_{1-I}$ | 0.2 | silt | 0.029 | 17.32 | 1.33 | 14.41 | 15 |
| $T_{1-I}$ | 1.6 | silt | 0.035 | 12.95 | 1.64 | 12.59 | 10 |
| $T_{1-II}$ | 2.5 | silt | 0.033 | 14.65 | 1.35 | 13.97 | 65 |
| $T_{1-II}$ | 3.6 | silt | 0.029 | 15.12 | 1.6 | 13.14 | 75 |
| $T_{1-II}$ | 7.8 | silt | 0.034 | 13.92 | 1.5 | 14.03 | 70 |
| $T_{1-II}$ | 11 | silty gravel | 3.951 | 6.03 | 0.04 | 727.9 | 60 |
| $T_{1-III}$ | 18.5 | silt | 0.028 | 16.69 | 1.49 | 13.64 | 85 |
| $T_{1-IV}$ | 31 | silt | 0.026 | 18.02 | 1.31 | 13.98 | 100 |
| $T_{2-I}$ | 0.1 | silt | 0.034 | 14.11 | 1.58 | 13.72 | 15 |
| $T_{2-I}$ | 1 | silty gravel | 6.718 | 3.33 | 42.25 | 334.41 | 8 |
| $T_{2-II}$ | 7.5 | silt | 0.035 | 13.12 | 1.46 | 13.2 | 70 |
| $T_{2-II}$ | 14.5 | silty gravel | 11.493 | 3.43 | 64.22 | 597.65 | 55 |
| $T_{2-III}$ | 22 | silt | 0.024 | 17.13 | 1.32 | 13.86 | 80 |
| $T_{2-IV}$ | 37 | silt | 0.018 | 20.99 | 1.11 | 12.92 | 100 |
| $T_{3-I}$ | 0.4 | silty sand | 0.123 | 9.81 | 0.07 | 479.25 | 18 |
| $T_{3-II}$ | 9 | silty gravel | 6.701 | 4.14 | 39.43 | 568.53 | 45 |
| $T_{3-III}$ | 26 | silt | 0.027 | 15.44 | 1.41 | 14.26 | 85 |
| $T_{3-IV}$ | 66 | silt | 0.025 | 16.31 | 1.3 | 13.33 | 100 |

note : "T" in the serial number refers to convex bank, subcript"1, 2, 3"refers to the meander1, 2, 3, respectively, the roman number "I, II, III, IV" after the en dash refers to the first, second, third and fourth vegetation zones, respectively; horizontal distance refers to the horizontal distance from inside to outside of the inner bank; $d_{50}$ :median size of soil sample; *Cc*: coefficient of curvature; *Cu*: coefficient of uniformity.

 

The results show that the bank material of the first and second vegetation zones is influenced greatly by seasonal rainfall. During flood period, most of the sand and gravel grains deposit at the zones, where the environment are unstable relatively, and the hydrodynamic condition prepares plant seeds and nutrient material for the riverbank and thus creates the condition for plant germination and growth. While during drought period, the hydrodynamic condition is weakened, and a little fine grain is deposited, so the difference of particle size is large and particle size distribution curve shows discontinuity.

As shown in Table 2, there was a corresponding relation between sediment composition change and vegetation succession at convex bank. From the first vegetation zone to fourth zone, sediment particle size is decreasing gradually. The clay content reduced at first and then increased, especially at the second zone reaching up to the least 10%. The vegetation coverage degree takes on an increasing trend correspondingly along with the sediment which accumulates constantly. Vegetation increases gradually, so the coverage degree increases with the horizontal distance to the riverbank of inner bank increasing (see Figure 6). The results indicated that colonized vegetation at convex bank possesses the capability of intercepting sediment, consolidating soil, building bank and forming riverbank, besides the root system which play a good role of improving the soil structure. Within the meandering channel, when the main current flowed forward in a spiral along the arc direct of convex bank, the bed load entered into the channel at upstream were deposited at the same bank alone the arc point bar. In such a way, arcuate sediment belt can be formed by the deposited material, which then created the conditions for colonized vegetation and formed arc vegetation zone at convex bank.

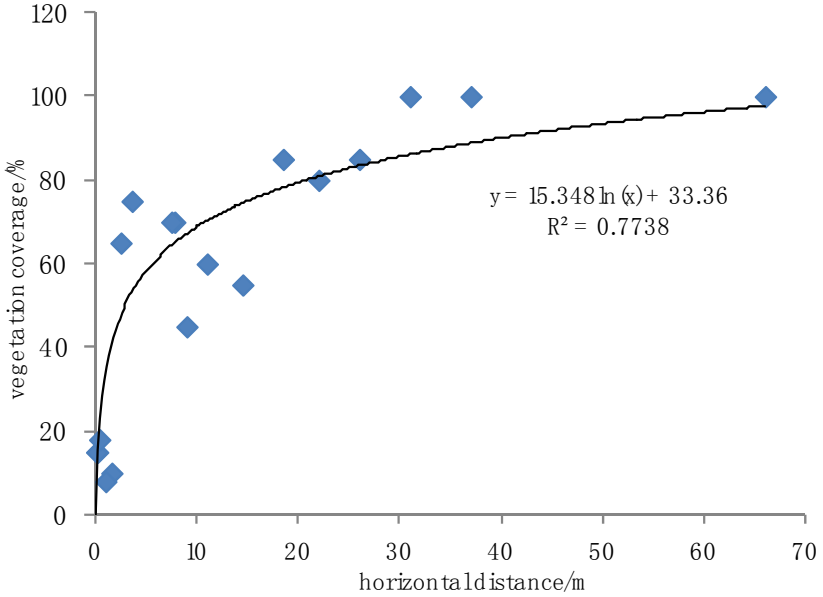


**Figure 6**. Correlativity between vegetation coverage and horizontal distance from inner bank.

The height difference was increased from inside to outside of inner bank, and the water content of bank sediment was decreased with the increase of horizontal distance to the riverbank. As a consequence, the vegetation takes on a succession from *hydrophyte* and *hygromesophytes* to *mesophytes*. The vegetation growing at the inner sides of the convex bank possesses developed root system, especially some developed creeping rhizomes and fibrous roots along the horizontal direction of riverbank providing for the sediment interception and deposition. Furthermore, the dominant plant *Halerpestes tricuspis Hand.-Mazz*. exerts an important role of stabilizing the riverbank by its abundant roots and shear resistant characteristics.

## 4 CONCLUSIONS AND DISCUSSION

(1) According to the change rule of vegetation and bank material composition, the riparian vegetation is generally divided into four distinct arcuate zonings: *hydrophyte*, *hygromesophytes*, *mesophytes*, and subshrub. The vegetation types change more abundantly gradually and the coverage degree is increasing from the first zone to fourth zone. *Potamogeton pectinatus L.* and *Halerpestes tricuspis Hand.-Mazz*. are pioneer plants in convex bank, and the main dominant plants are *cyperaceae Blysmus sinocompressus Tang et Wang, Kobresia tibetica Maxim* and *subshrub Potentilla fruticosa L.*

(2) The vegetation zoning of meandering channel convex bank reflects the different succession stages. Different vegetation located in different area has different roles. The water tolerant plants are pioneer plants colonized at the sediment at the earliest, they can weaken the near bank scouring during drought flood period; the herbaceous plants in the middle part of the point bar are the earlier stage plants, which play a role of constituting riparian meadow and intercepting coarse and fine sediment, stabilizing bank and enhancing soil

 

fertility; the herbaceous plants and subshrubs are the late stage growing plants at the outside of the point bar, and they can incept the sediment during flood period.

(3) The herbaceous plants in the middle zone are earlier stage vegetations, which have the effects on developing riparian meadow, entrapping sediment during flood period, stabilizing point bar, increasing soil fertility and promoting the growth of point bar. The herb and subshrub in the outside zone of the inner bank are the end-stage vegetations, where the sediments in low-frequency flood period are intercepted. Because the riparian vegetation works with current under the action of circulating current in curved channels, point bar is deposited gradually and comes into new banks, which continuously extended and pushed alone to the concave bank. As a result, the new forming banks width of convex bank remains at the same level with bank failure width of concave bank per year, and keeps the transverse migration of meandering rivers synchronous.

The interlocking root networks of meadow vegetation reinforce soils by adding tensile strength to the bank soil matrix (Zhu et al., 2015). The very fine root networks typical of sedges comprise large numbers of randomly oriented roots less than 1 mm in diameter. We observe that this dense root reinforcement creates a tough sod layer ranging in thickness from 0.45 to 0.65 m. Therefore, it provides the condition for riverbank forming and keeping consistent migration speed of concave bank failure and convex bank forming, especially by the plants of second and third zones. Micheli and Kirchner (2002) suggested that rushes appear better than sedges at stabilizing coarse bar surfaces, while sedges are far more effective at stabilizing actively eroding cut banks. Many studies have been made about the interplay between vegetation and morphodynamics, and the study objects are mainly shrubs or trees (Corenblit et al., 2007; Gurnell, 2014; Perucca et al., 2006). Perucca et al. (2006) suggested that the interactions exist among river movement, process of sedimentation and vegetation, then arcuation zoning of trees paralleled with river centre line can be formed. Several Salicaceae species such as willows and cottonwoods have different seed dispersal windows resulting in a vegetation zonation at different elevations on river bars and banks (Van Splunder et al., 1995). Along the hydrogeomorphic transverse gradient from the main channel to the floodplain in the study area, the riparian vegetation generally takes on the continuous succession from *hydrophyte* to *hygromesophytes*, *mesophytes*, and subshrub. These are in agreement with the results of Nilsson et al.(1997) and Ma et al. (2006) etc.. The arc-shaped zones of meadow are the outcome of interplay of river dynamics, sedimentary processes and riparian vegetation. Gregory et al. (1991) put forward that the plant species generally presents a parabolic shape distribution from riverbank to two sides upland, and forms a succession, and considered that the river ecosystems are the products of interaction of river-terrestrial ecosystem at three dimensions (lengthways, transversal and vertical direction). Perucca et al. (2006) also come up with the same conclusion that the riparian vegetation forms an arc shaped forested ribbon paralleled to the river centre line. The characteristics of patchiness at the second and third vegetation zones in the study area accord with the features of vegetation distribution proposed by Harris and Olson in 1997. They considered that patchiness of riparian vegetation is the product of frequent flood effect, because complex changes of landform and soil texture occur frequently at riparian zone. According to the basis of this study, further analyses should consider the influence of flow dynamics on vegetation succession, and for this reason establish an interactive mechanism of plateau meandering river and terrestrial ecosystem.

This study takes the typical meandering channel of Lanmucuoqu River in the source region of Yellow River as an example, where continuous field investigation and study are made to analyze the vegetation zoning characteristics and succession rules. The findings will have scientific significances for vegetation protection and restoration at the source region. A further study should analyze the quantitative relation between channel evolution speed and vegetation growth by continuous field investigation and in situ tests, and then explain vegetation succession rule from the community aspect.

## ACKNOWLEDGEMENTS

The research reported herein is funded by the Natural Science Foundation of China (NSFC, 41302258) and project of Qinghai Science and Technology Department (2017-ZJ-776).

## REFERENCES

Abernethy, B. & Rutherfurd, I.D. (1998). Where along a River's Length will Vegetation most Effectively Stabilise
Stream Banks? *Geomorphology*, 23(1), 55-75.

Bendix, J. (1998). Impact of a Flood on Southern California Riparian Vegetation. *Physical Geography,* 19(2), 162-174.

Bennett, S.J., Pirim, T. & Barkdoll, B.D. (2002). Using Simulated Emergent Vegetation to alter Stream Flow Direction within a Straight Experimental Channel. *Geomorphology*, 44(1), 115-126.

Corenblit, D., Tabacchi, E., Steiger, J. & Gurnell, A.M. (2007). Reciprocal Interactions and Adjustments between Fluvial Landforms and Vegetation Dynamics in River Corridors: A Review of Complementary Approaches. *Earth-Science Reviews,* 84(1-2), 56-86.

Dong, Z.R. (2003). Diversity of River Morphology and Diversity of Bio-Communities. *Journal of Hydraulic Engineering*, 34(11), 1-6.

 

Gregory, S.V., Swanson, F.J., Mckee, W.A. & Cummins, K.W. (1991). An Ecosystem Perspective of Riparian Zones. *Bioscience*, 41(8), 540-551.

Gurnell, A. (2014). Plants as River System Engineers. *Earth Surface Processes and Landforms,* 39(1), 4-25.

Harris, R. & †, C.O. (1997). Two-Stage System for Prioritizing Riparian Restoration at the Stream reach and Community Scales. *Restoration Ecology*, 5(4S), 34-42.

Huang, H.Q. & Nanson, G.C. (1997). Vegetation and Channel Variation: A Case Study of Four Small Streams in Southeastern Australia. *Geomorphology*, 18(3-4), 237-249.

Huang, K., Guo, H.C., Liu, Y., Yu, Y.J. & Zhou, F. (2007). Research Progress on the Degradation Mechanisms and Restoration of Riparian Ecosystem. *Chinese Journal of Applied Ecology*, 18(6), 1373-1382.

Järvelä, J. (2002). Flow Resistance of Flexible and Stiff Vegetation, a Flume Study with Natural Plants. *Journal of Hydrology*, 269, 44–54.

Li, Z.W., Yu, G.A., Brierley, G. & Wang, Z.Y. (2016). Vegetative Impacts upon Bedload Transport Capacity and Channel Stability for Differing Alluvial Planforms in the Yellow River Source Zone. *Hydrology & Earth System Sciences Discussions*, 20(200), 3013-3025.

Lin, C.Y., Li, X.L., Liu, K. & Xue, Z.P. (2016). Vegetation change Characteristics during Degradation succession in Floodplain Wetlands of the Yellow River Source Zone. *Chinese Agricultural Science Bulletin*, 32(19), 115-119.

Liu, S.W. (1996). *Qinghai Flora.* People's Publishing House of Qinghai, Book.

Ma, X.B., Wang, Z.Y., Cheng, D.S. & Deng, J.Q. (2006). Diversity Evaluation of Riparian Vegetation in Middle reaches of the East River. *Journal of Hydraulic Engineering*, 37(3), 348-353.

Micheli, E.R., Kirchner, J.W. & Larsen E.W. (2004). Quantifying the Effect of Riparian Forest versus Agricultural Vegetation on River Meander Migration Rates, Central Sacramento River, California, Usa. *River Research & Applications*, 20(5), 537-548.

Ni, J.R. & Gao, X.W. (2011). Comprehensive approach for Classification of River Systems and Identification of Ecological Characteristics I: Methodology. *Journal of Hydraulic Engineering*, 42(9), 1009-1016.

Nilsson, C., Jansson, R. & Zinko, U. (1997). Long Term Responses of River Margin Vegetation to Water Level Regulation. *Science*, 276(5313), 798-800.

Perucca, E., Camporeale, C. & Ridolfi, L. (2006). Influence of River Meandering Dynamics on Riparian Vegetation Pattern Formation. *Journal of Geophysical Research Biogeosciences,* 111(G1), 338-356.

Samani, J.M.V. & Kouwen, N. (2002). Stability and Erosion in Grassed Channels. *Journal of Hydraulic Engineering,* 128(1), 40-45.

Schuurman, F., Shimizu, Y., Iwasaki, T. & Kleinhans, M.G. (2016). Dynamic Meandering in Response to Upstream Perturbations and Floodplain Formation. *Geomorphology*, 253, 94-109.

Steiger, J., Tabacchi, E., Dufour, S., Corenblit, D. & Peiry, J. (2005). Hydrogeomorphic Processes Affecting Riparian Habitat within Alluvial Channel-Floodplain River Systems: A Review for the Temperate Zone. *River Research & Applications,* 21(7), 719-737.

Sun, H.Q., Zhai, D.P., Li, C.H. & Li, X.L. (2013). Analysis of Vegetation Characteristics of Different Types of Wetlands in Three Rive Source Region. *Journal of Henan Agricultural Sciences*, 42(11), 124-128.

Tabacchi, E., Correll, D.L., Hauer, R., Pinay, G., Planty-Tabacchi, A.M. & Wissmar, R.C. (1998). Development Maintenance and Role of Riparian Vegetation in the River Landscape. *Freshwater Biology,* 40(3), 497–516.

Tabacchi, E., Planty-Tabacchi, A.M., Roques, L. & Nadal, E. (2005). Seed Inputs in Riparian Zones: Implications for Plant Invasion. *River Research & Applications,* 21(2-3), 299-313.

Van Splunder, I., Coops, H., Voesenek, L. & Blom, W. (1995). Establishment of Alluvial Forest Species in Floodplains: The Role of Dispersal Timing, Germination Characteristics and Water Level Fluctuations. *Acta Botanica Neerlandica,* 44(3), 269–278.

Wang, S.J., Ni, J.R. & Wang, G.Q. (2000). Temporal and Spatial Evolution Models of Fluvial Channel Patterns and their Interrelation. *Journal of Tsinghua University (Science & Technology)*, (S1), 96-100.

Zhang, Y.L., Liu, L.S., Bai, W.Q., Shen, Z.X., Yan, J.Z., Ding, M.J., Li, S.C. & Zheng, D. (2006). Grassland Degradation in the Source Region of the Yellow River. *Acta Geographic Sinica*, 61(1), 3-13.

Zhang, J.C. & Peng, B.Z. (2003). Study on Riparian Zone and the Restoration and Rebuilding of its Degraded Ecosystem. *Acta Ecologica Sinica*, 23(1), 56-63.

Zhu, H.L., Li, Z.W., Hu, X.S., Li, G.R., Song, L. & Fu, J.T. (2015). Cantilever Bank Failure Mechanism of Meadow Meandering River in the Yellow River Source Region. *Journal of Hydraulic Engineering*, 46(7), 836-
843.

Zhu, H.L., Wang, Z.Y. & Li, Z.W. (2013). Influence of Riparian Meadow to the Meandering Rivers Evolution in the Yellow River Source Region. *Yellow River*, 35(4), 41-44.

Zong, L., Nepf, H. (2011). Spatial Distribution of Deposition within a Patch of Vegetation. *Water Resources Research*, 47(3), 1-12.

 

# LARGE AND VERY LARGE SCALE MOTIONS IN ROUGH-BED OPEN-CHANNEL FLOW

STUART CAMERON[(1)], VLADIMIR NIKORA[(2)] & MARK STEWART[(3)]

[(1,2,3)] University of Aberdeen, Aberdeen, United Kingdom,
v.nikora@abdn.ac.uk

## ABSTRACT

Long duration PIV measurements in rough-bed open-channel flow (OCF) reveal that the pre-multiplied spectra of the streamwise velocity has a bimodal distribution due to the presence of large and very large scale motions (LSMs and VLSMs, respectively). The existence of VLSMs in boundary layers, pipes and closed channels has been acknowledged for some time, but strong supporting evidence for their presence in OCF has been lacking. The data reported in this paper fill this gap. Length scales of the large and very large scale motions in OCF exhibit different scaling properties; whereas the streamwise length of the LSM scales with the flow depth, the VLSM streamwise length does not scale purely with flow depth and may additionally depend on other scales such as the channel width, roughness height, or viscous length. The origin and nature of LSMs and VLSMs are still to be resolved, but differences in their scaling suggest that VLSMs in rough-bed open-channel flows form independently rather than as a spatial alignment of LSMs.

**Keywords:** Open channel flow; turbulence; hydraulic resistance; sediment transport; flow-biota interactions.

## 1 INTRODUCTION

Kim & Adrian (1999) discovered a bimodal distribution in the streamwise velocity pre-multiplied spectrum of pipe flow and described the two apparent scales as large and very large scale motions. They proposed that very large scale motions (VLSMs) may result from a streamwise alignment of large scale motions (LSMs) which themselves might represent a collection of smaller hairpin shaped vortices. Subsequently, VLSMs have been discovered in other flow types although their origin remains unclear, with other authors proposing that VLSMs could form independently due to large-scale instability (e.g. Hwang & Cossu, 2010). In the case of boundary layers, Hutchins & Marusic (2007) introduced the term 'superstructures' although it is possible that these have the same origin as VLSMs albeit different characteristics due to fundamental differences in the boundary conditions of pipe, closed channel, and boundary layer flows. Comparing pre-multiplied spectra across these three flow types, Monty et al. (2009) found a remarkable resemblance between pipe and closed-channel flows; boundary layers in comparison exhibit superstructures in the logarithmic layer, being significantly suppressed in the outer layer.

The presence of VLSMs in open-channel flow (OCF) has not been firmly established yet although such a test would be important as a number of specific OCF features (e.g., free water surface) make them distinctly different from pipes, closed channels and boundary layers. Most studies of VLSMs and superstructures in pipes, closed channels, and boundary layers have been undertaken with smooth-wall conditions. Although smooth wall conditions are also relevant to open-channel flows, most practical situations involve rough-bed OCFs and thus their study is of the utmost importance. There are many engineering challenges such as the assessment of bed stability, sediment transport, mixing, and hydraulic resistance in rivers and canals that require the advanced understanding of rough-bed OCF turbulence. Therefore, the focus of this study is on rough-bed OCF. If VLSMs are confirmed in OCF, then the assessment of their roles in processes occurring in river flows and important for hydraulic engineering may lead to significant scientific advances and much improved engineering models.

The objective of this study is to identify and quantify VLSMs in rough-bed open-channel flow using long duration (2 hour) particle image velocimetry (PIV) measurements. The focus is on OCFs at low and intermediate submergences, which remain the least studied flow configurations in spite of their ubiquitous occurrence in nature and engineering. Section 2 outlines the experimental facility, instrumentation, and procedures. Section 3 summarises the background hydraulic conditions including bulk statistics, velocity correlations, spectra, and turbulence scales. Finally, the main findings are briefly outlined in Section 4.

## 2 EXPERIMENTAL SETUP

### 2.1 Open-channel and flow configurations

Experiments were conducted in the Aberdeen Open-Channel Facility (AOCF). The facility consists of a 1.18m wide and 18m long re-circulating open-channel flume and a motorised instrumental carriage which

 

houses a PIV system and supporting instrumentation. A vertical slat weir regulates the backwater curve which we measure by profiling the water surface with an ultrasonic displacement sensor attached to the instrumental carriage. The entire bed of the flume and part of the entrance tank (19.2m total length) was covered for these experiments with a single layer of 16mm diameter ($D$) glass spheres. The spheres were precisely aligned in a hexagonally close packed arrangement with the help of perforated stainless steel plates. The installed plates were levelled using shims to within +/-0.25mm. Experiments were conducted with relative submergences ($H/D$) between 1.9 and 7.5 (table 1) and constant shear velocity ($u_*$=0.042m/s). The roughness Reynolds number $D^+=Du_*/\nu$ was 605 for all experiments indicating fully rough flow conditions. The friction Reynolds number $H^+=Hu_*/\nu$ varied between 1140 and 4540. The Froude number was well below 1.0 securing a flat-water surface without visible surface waves; measured standard deviations of water surface level varied within 0.28-0.45mm. The flows were uniform, with water surface slope deviating from the bed surface slope by a maximum of $2.5\times10^{-5}$, and steady to within a flowrate standard deviation of 0.0002m$^3$/s.

**Table 1**. Flow conditions used for the experiments. $H$ is flow depth above the roughness tops, $B$ is the width of the channel, $D$ is sphere diameter, $Q$ is flowrate, $S_0$ is channel slope, $U=Q/BH$ is the bulk velocity, $u_*=(gHS_0)^{0.5}$ is shear velocity, $R=UH/\nu$ is the bulk Reynolds number, $Fr=U/(gH)^{0.5}$ is the Froude number, the + superscript denotes normalization with the viscous length scale $\nu/u_*$, $\nu$ is the fluid kinematic viscosity, and $g$ is acceleration due to gravity.

| RUN | $H$ (mm) | $Q$ (m$^3$/s) | $U$ (m/s) | $S_0$ | $u_*$ (m/s) | $R$ | $H^+$ | $D^+$ | $H/D$ | $B/H$ | $Fr$ |
|---|---|---|---|---|---|---|---|---|---|---|---|
| **H030** | 30.1 | 0.0153 | 0.431 | 0.00600 | 0.042 | 11700 | 1140 | 605 | 1.9 | 39.2 | 0.79 |
| **H050** | 50.3 | 0.0275 | 0.463 | 0.00360 | 0.042 | 21000 | 1900 | 605 | 3.1 | 23.5 | 0.66 |
| **H070** | 70.5 | 0.0404 | 0.486 | 0.00257 | 0.042 | 30800 | 2670 | 605 | 4.4 | 16.7 | 0.58 |
| **H095** | 94.9 | 0.0569 | 0.508 | 0.00189 | 0.042 | 43400 | 3590 | 605 | 5.9 | 12.4 | 0.53 |
| **H120** | 120.1 | 0.0745 | 0.526 | 0.00150 | 0.042 | 56900 | 4540 | 605 | 7.5 | 9.8 | 0.48 |

2.2 Stereoscopic particle image velocimetry

A four-camera stereoscopic PIV system was used to measure all three velocity components in a wall-normal transverse plane (figure 1). The measurement plane covered the full flow depth, extended 330mm across the flow and was positioned 12.7m (>100$H$) downstream from the flume entrance. Under equivalent flow conditions Stewart (2014) demonstrated that this distance was sufficient for fully developed conditions to exist at the test section. The four cameras (Dalsa 4M60, 2352×1728 pixels, 7.4 micron pixel pitch, 60% effective fill factor, 8 bits per pixel, Nikon 60mm lens at f/16 aperture) were positioned symmetrically with respect to the light sheet at angles of ±45° and ±38° for cameras 1/4 and 2/3 respectively (figure 1). The laser (Oxford Lasers dual cavity Nd:YAG, 532nm, 100mJ per pulse) output was formed into a 2.4mm thick sheet using a series of spherical and cylindrical lenses. Silver coated hollow glass microspheres manufactured by Microsphere Technology Ltd were used as tracer particles (20-32 micron diameter, 0.8-1.0g/cm$^3$ density) at a concentration of 11mg/l which resulted in PIV records with particle image diameters of 2.0 pixels and a particle image concentration of 0.02 particles per pixel. Water prisms in the optical path were used to reduce distortion and total internal reflection at the air/water interface. Images were recorded directly to a fast disk array at a rate of 32 image pairs per second per camera for a continuous duration of 120 minutes at each of the 5 flow configurations identified in table 1.

Analysis of the recorded images proceeds by first ‘de-warping’ images from each camera onto a common grid and then extracting 2-component vector fields independently for each camera using cross-correlation. For this data set, we have used the cross-correlation algorithm we refer to as IDM-BL48-SincLP1.5-GD9. Here BL48 means Blackman weighted 48×48 pixel interrogation regions, SincLP1.5 is a 20×20 grid point Blackman weighted sinc kernel with low-pass factor 1.5 applied to the vector field after each iteration of the algorithm, and GD9 refers to a 9×9 pixel (0.9×0.9mm) grid spacing (81.25% overlap between adjacent interrogation regions). The algorithm uses the iterative deformation method (IDM, Astarita & Cardone, 2005) and satisfactory convergence is reached after 8 iterations. Turbulence wavelengths greater than 3mm are resolved by the measurement system while smaller scales are attenuated. This measurement resolution is sufficient to identify and quantify the LSMs and the VLSMs that are of primary interest in this study. However, second-order bulk statistics are likely under resolved in the near-bed region. Three-component vector fields are re-constructed from the 2-component vector fields obtained for each camera using the local view angles obtained from a camera calibration procedure. The four camera PIV system used here permits two independent estimates of each velocity component which we use when calculating bulk statistics, correlation functions, and spectra to reduce the contribution of measurement noise.

 

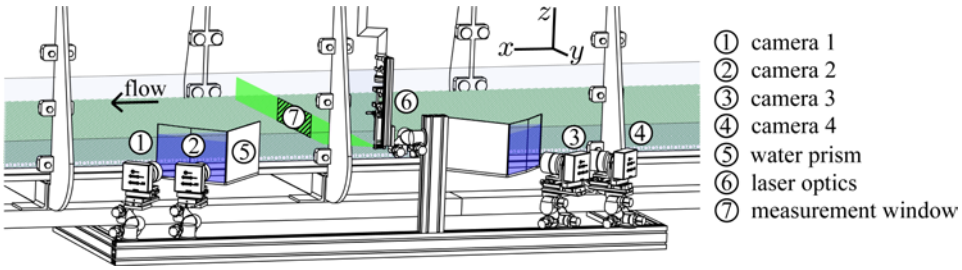


**Figure 1**. Measurement section of the Aberdeen Open-Channel Facility and stereoscopic particle image velocimetry setup.

## 3 RESULTS

### 3.1 Bulk statistics

In this section, the 2-dimensionality of the studied flows in the measurement area are confirmed, the potential existence of a logarithmic scaling region in the mean velocity profile are examined, and potential effects of flow relative submergence on bulk statistics are observed. These statistics provide background information on the studied flows as bulk characteristics are likely to be associated with features of large and very large scale motions identified in the following sections.

The experiments were conducted with large flow aspect ratios (*B/H*>≈10) which according to traditional wisdom (e.g. Nezu & Nakagawa, 1993) should be sufficient to establish 2-dimensional flow conditions at the flume centre, i.e., $\frac{\partial \overline{\cdot}}{\partial y} = \overline{v} = \overline{w} = 0$, where the overbar represents time averaging. With the long record length and small sampling error in this study, however, small amplitude transverse fluctuations with period 2*H* in all time averaged velocity statistics are able to be detected consistent with the presence of secondary currents (e.g. Nezu & Nakagawa, 1993). In order to reduce the dataset and suppress weak transverse fluctuations, spatial averaging are incorporated over a transverse domain of width *n*2*H* (*n*=3,2,1,1,1 for H030,...,H120 respectively). With this averaging, denoted here with angle brackets, it is reasonably expected that far from the side wall the relation $\frac{\partial \langle \overline{\cdot} \rangle}{\partial y} \approx \langle \overline{v} \rangle \approx \langle \overline{w} \rangle \approx 0$ to hold. In this case, the double averaged momentum conservation equation (e.g. Nikora et al., 2007) in the streamwise direction for the flow region above the roughness tops reduces to:

$$-\rho g S_0 = \frac{\partial}{\partial z}\left\{-\rho\left\langle \widetilde{\overline{u}}\widetilde{\overline{w}} \right\rangle - \rho\left\langle \overline{u'w'} \right\rangle + \mu \frac{\partial \langle \overline{u} \rangle}{\partial z}\right\} \qquad [1]$$

where $\rho$ is fluid density, $\mu$ is fluid dynamic viscosity and we decompose the $i^{th}$ instantaneous velocity component as $u_i = \langle \overline{u}_i \rangle + \widetilde{\overline{u}}_i + u_i'$ where tilde and prime symbols represent space and time fluctuations, respectively. Away from the bed, the form-induced stress $-\rho\left\langle \widetilde{\overline{u}}\widetilde{\overline{w}} \right\rangle$ can be used as a measure of the contribution of secondary currents to the total momentum flux. Figure 2c indicates that for these experiments $\left\langle \widetilde{\overline{u}}\widetilde{\overline{w}} \right\rangle / u_*^2$ is quite small (≈-0.006 at *z/H*=0.5) and $\left\langle \overline{u'w'} \right\rangle / u_*^2$ approaches the linear trend expected for 2-dimensional OCF. It is therefore concluded that secondary currents make only a minimal (essentially negligible) contribution to the total momentum flux and thus the studied flow region can safely be treated as 2-dimensional.

The overlap region of wall bounded flows where the mean velocity is expected to scale with the log of wall normal distance remains the subject of intensive theoretical and experimental research (e.g. Adrian & Marusic, 2012). Debate has largely centred on the limits of the log region and appropriate value of the von Kármán coefficient ($\kappa$) and its potential variation between different flow types. The data suggest that the von Kármán coefficient is likely not universal and for smooth walls has a value of around 0.41 for pipe flow, 0.38 for boundary layers, 0.37 for closed-channels (Nagib & Chauhan, 2008), and 0.41 for open-channels (Nezu & Nakagawa, 1993). For rough-bed flows with low relative submergence (small *H/D*) the log layer may be disrupted by the roughness elements and appear with modified $\kappa$ (e.g. Dittrich & Koll, 1997); for sufficiently small *H/D* the log layer is not expected to exist at all (e.g. Jiménez, 2004). Due to a lack of quality experimental data for low submergence OCF, the flow conditions required for a logarithmic layer to develop have not yet been established and thus our data my help with clarifying this matter.

 

The differential form of the log law can be written as $\left(\partial\overline{u}/\partial z\right)^{-1}=\kappa\left(z+d\right)/u_*$, where $z$=0 corresponds to the level of the roughness tops, and $d$ is zero plane displacement which sets the 'virtual' bed level. This 'diagnostic' form of the log law is preferable for analysing experimental data as small deviations from logarithmic behaviour are easy to detect. It is somewhat surprising, given the low submergence of the studied flows, to find that the present data support a logarithmic range with $\kappa$ =0.38 extending to $z/H$≈0.5 (figure 2a), well beyond the $z/H$≈0.15 upper bound expected in other flow types. The extended range of the log scaling observed here suggests that the low submergence log law may develop due to different physical mechanisms and require different theoretical justification compared to its high submergence and smooth bed counterparts. These differences may be further explored as new accurate data at other flow conditions and different roughness types become available.

Second order statistics $\left\langle\overline{u'u'}\right\rangle$, $\left\langle\overline{v'v'}\right\rangle$, and $\left\langle\overline{w'w'}\right\rangle$ (figure 2b) indicate a trend of increasing variance in the near-bed region with growing submergence. Such an effect has been noted before (e.g. Bayazit, 1976; Dittrich & Koll, 1997) although the physical mechanisms behind this trend remain unclear.

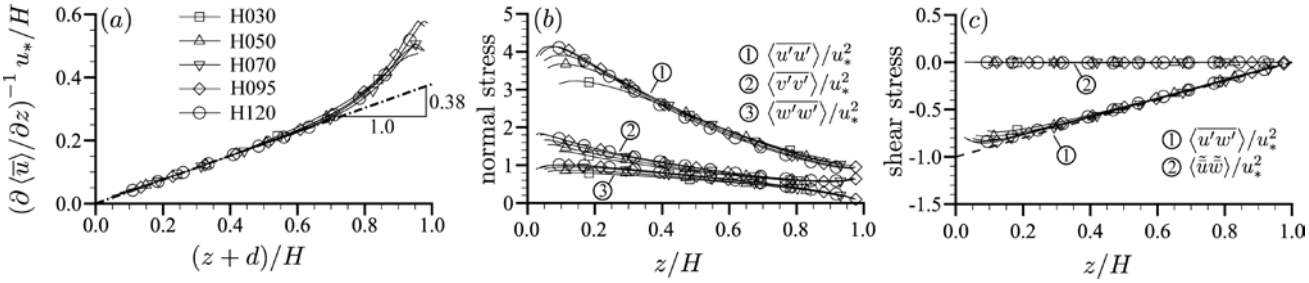


**Figure 2**. Mean velocity distribution (a), Reynolds normal stresses (b), and Reynolds shear stress and form-induced stress (c). Symbols are shown every tenth measurement point for clarity.

3.2 Large scale streaks

The pseudo-instantaneous velocity field (figure 3) reconstructed from time series records using Taylor's frozen turbulence hypothesis is composed of alternating in the transverse direction and elongated in the streamwise direction regions of high and low momentum fluid visually very similar to the superstructures identified by Hutchins & Marusic (2007) in their boundary layer studies. It is not easy to directly identify length scales of the large streaks from the 'instantaneous' flow fields as they tend to meander, fade, and merge with other features without providing discernible start and end points. The next section uses correlation functions and spectra to extract characteristic scales and examine the potential influence of relative submergence.

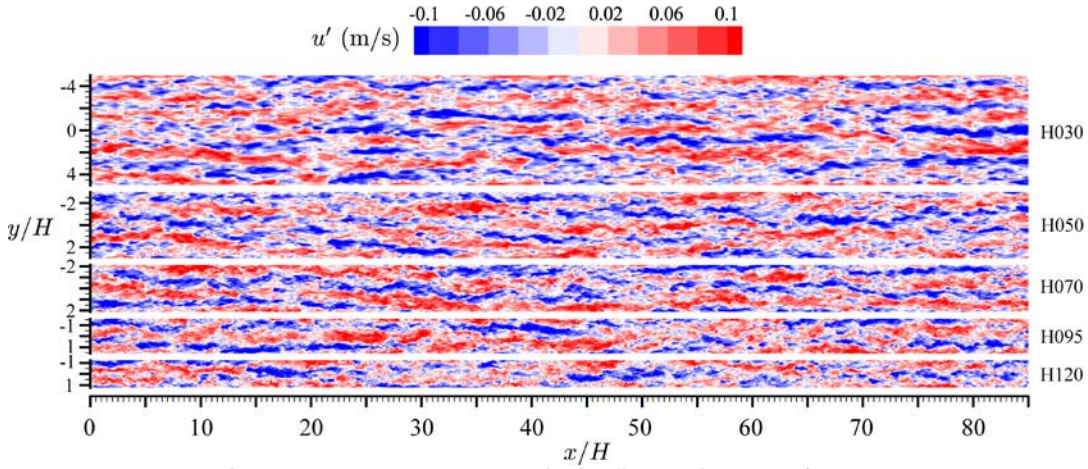


**Figure 3**. 'Instantaneous' velocity fluctuations at $z/H$=0.5.

3.3 Correlation functions and spectra

Selected components of the two-point correlation tensor:

$$Cu_iu_j\left(\Delta y,\Delta z,z_0\right)=\frac{\sum^{y}\sum^{t}u_i'(y,z_0,t)u_j'(y+\Delta y,z_0+\Delta z,t)}{\left(\sum^{y}\sum^{t}[u_i'(y,z_0,t)]^2\right)^{0.5}\left(\sum^{y}\sum^{t}[u_j'(y+\Delta y,z_0+\Delta z,t)]^2\right)^{0.5}} \quad [2]$$

 

calculated assuming homogeneity in the transverse direction are plotted in figure 4 for $z_0$=*0.5H*; where *t* is a time index, $z_0$ is a reference elevation, and Δ*y* and Δ*z* are displacement increments. The -$C_{uw}$ and -$C_{uv}$ components when plotted as vectors (as in Marusic & Hutchins, 2008) indicate that fluctuations in the streamwise velocity component are correlated with a pattern of repeating counter-rotating depth-scale cells which may be associated with the large scale streaks identified in figure 3. Figure 4 shows that with increasing submergence, the transverse separation of the cells becomes progressively smaller and the central lobe of the $C_{uu}$ correlation shrinks. The counter rotating depth-scale cells are reminiscent of secondary current flow patterns which appear near side walls in open channels (e.g. Nezu & Nakagawa, 1993). The origin, dynamics, and energetics of secondary currents in OCF are still the subject of ongoing research and it is possible that they form due to a preferential alignment of meandering VLSMs caused by the channel sidewalls (see also Adrian & Marusic, 2012 for discussion of potential links between VLSMs and secondary currents).

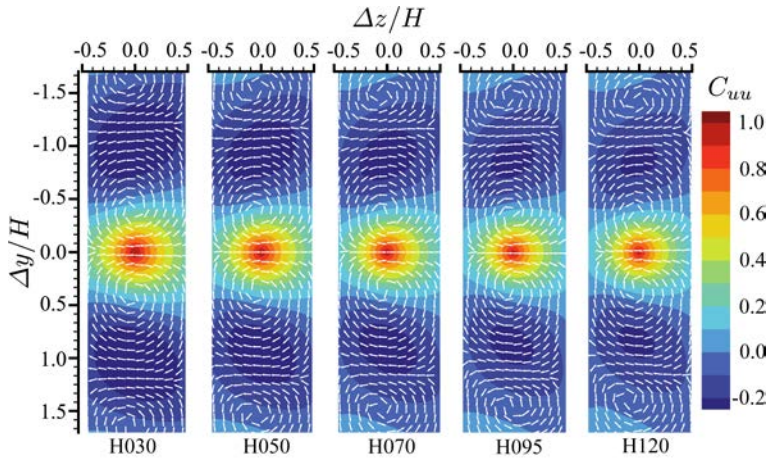


**Figure 4**. Two-point correlation functions $C_{uu}$, $C_{uw}$, *and* $C_{uv}$ for $z_0/H$=0.5. Note that $C_{uw}$ and $C_{uv}$ are shown as vectors (-$C_{uw}$,-$C_{uv}$) with unit magnitude.

To identify the prevailing scales in the flow field, pre-multiplied wave-number spectra was used as in other LSM and VLSM studies (e.g. Kim & Adrian, 1999; Hutchins & Marusic, 2007; Monty et al., 2009). The pre-multiplied spectra for the streamwise velocity component ($k_xF_{uu}(k_x)/u_*^2$, where $k_x=2\pi/\lambda_x$ and $\lambda_x$ is streamwise wavelength) were calculated in the frequency domain and averaged over 225×32 second windows with, assuming homogeneity, additional averaging over the transverse extent of the measurement domain. Taylor's frozen turbulence hypothesis was used to transform the frequency spectra to the wavenumber domain using a convection velocity equal to the local mean velocity $\langle\overline{u}\rangle$. The spectra (figure 5) reveal two characteristic length scales in the outer flow and resemble spectra measured in pipe and closed-channels with smooth wall conditions (e.g. Monty et al., 2009). Following the terminology of Kim & Adrian (1999), the flow structures associated with the shorter of these length scales are referred as large scale motions (LSMs) and structures associated with the larger length scale as very large scale motions (VLSMs). The length scales determined from spectral peaks may not directly relate to the physical length of turbulent structures due to their transverse meandering (Hutchins & Marusic, 2007) but, nevertheless, the spectral length scale provides a convenient and consistent reference to compare with other studies. Near the bed (*z/H*<0.1) the spectral maps are dominated by a single length scale and experiments with larger *H* suggest a bifurcation point where the distinct LSM and VLSM scales emerge. Peak amplitudes of the pre-multiplied spectra at the LSM and VLSM wavelengths ($\lambda_{x\_LSM}$ and $\lambda_{x\_VLSM}$ respectively) are approximately the same (figure 5f and 5g). Amplitude dependence on flow submergence is observed near the bed consistent with the trend noted earlier for the bulk variance. Combining the normalised LSM and VLSM length scales for all experiments (figure 5h), it is surprising to find that although estimates of the LSM length scale collapse onto a single curve, the estimates of VLSM length scale are stratified according to flow submergence (or equivalently to flow aspect ratio).

Plotting the maximum of each $\lambda_{x\_VLSM}/H$ distribution (figure 5i), the VLSMs appear to scale according to $MAX[\lambda_{x\_VLSM}/H]=5.7[B/H]^{0.60}=75[H/D]^{-0.60}=3500[H^+]^{-0.60}$ where given that the ratios *B/D* and $Du_*/v$ are constant for all experiments, all three depth normalisations (*B/H*, *H/D*, $H^+$) have equivalent empirical fit. Although further data are required to identify the most appropriate scaling for the VLSMs, it can speculated that *H/D* scaling does not seem likely given that the smaller LSMs scale independently of the relative submergence (figure 5h). Reynolds number ($H^+$) effects have been assessed in other flow types and found to have minimal influence on VLSM length scale (e.g. Balakumar & Adrian, 2007) though the amplitudes of the pre-multiplied spectra have been found to exhibit Reynolds number dependence (Hutchins & Marusic, 2007). Flow aspect ratio (*B/H*) is perhaps the most plausible scaling given that *B* and $\lambda_{x\_VLSM}$ are of the same order of magnitude and keeping in mind the potential constraining effect of the flow width.

 

Data presented here indicate that in rough-bed open-channel flow, VLSMs scale differently to LSMs in terms of their streamwise length scales. This scaling difference suggests that VLSMs may form independently of LSMs rather than as a streamwise alignment of the smaller structures. Further experimental data is required to resolve scaling and formation mechanisms of large and very-large scale motions in rough-bed open-channel flows.

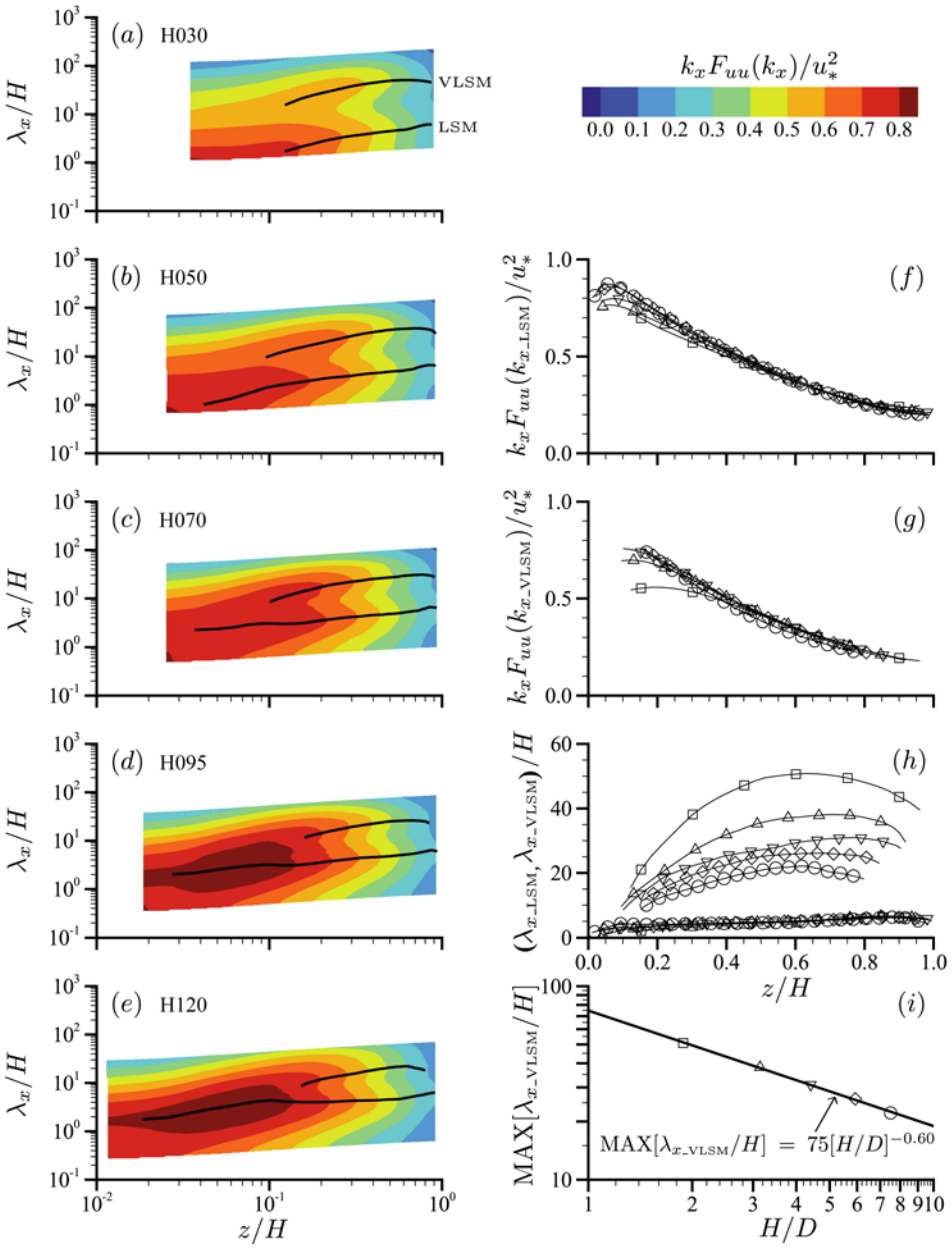


**Figure 5**. Pre-multiplied spectra (a-e); amplitude of the LSM (f) and VLSM (g) spectral peaks; wavelengths of the LSM and VLSM peaks (h); maximum wavelength of the VLSM versus flow relative submergence (i) Symbols defined in figure 2.

## 4 CONCLUSIONS

The obtained pre-multiplied spectra in rough-bed open-channel flow exhibit a bimodal shape in the outer flow corresponding to the presence of large and very large scale motions. The latter motions are also evident as large scale streaks in 'instantaneous' streamwise velocity fields. Two-point correlations suggest that VLSMs may be associated with repeating depth scale counter-rotating cells reminiscent of and potentially related to secondary currents in the mean (time-averaged) flow. The energy content of the two motion scales is approximately the same although some dependence of the spectral shape and amplitudes on relative submergence is found in the near-bed region. The streamwise length scale of the LSM collapses across experiments when normalised with the flow depth. However, the depth-normalised VLSM length scale does not collapse. Instead, it exhibits a power-type dependence on either Reynolds number $H^+$, relative

 

submergence *H/D*, or flow aspect ratio *B/H*. Since in these experiments, the channel width, particle size, and shear velocity were kept constant, it is difficult to unambiguously identify which particular factor (*H/D*, *B/H*, or $H^+$) is responsible for the variation of the depth-normalised VLSM length scale. Further data are required to establish which of them is most appropriate and physically justifiable. At this stage, it can only be speculated that the true scaling is associated with the aspect ratio *B/H*. Differences in the scaling of LSMs and VLSMs suggest that these two motions may form independently of each other. Additionally, the obtained data support the existence of a logarithmic scaling region with $\kappa$=0.38 extending to $z/H \approx 0.5$ despite the low relative submergence of the studied flows.

**ACKNOWLEDGEMENTS**

The study has been supported by two EPSRC/UK grants, “High-resolution numerical and experimental studies of turbulence-induced sediment erosion and near-bed transport” (EP/G056404/1) and “Bed friction in rough-bed free-surface flows: a theoretical framework, roughness regimes, and quantification” (EP/K041169/1).

**REFERENCES**

Adrian, R.J. & Marusic, I. (2012). Coherent Structures in Flow over Hydraulic Engineering Surfaces. *Journal of Hydraulic Research*, 50(5), 451-464.

Astarita, T. & Cardone, G. (2005). Analysis of Interpolation Schemes for Image Deformation Methods in PIV. *Experiments in Fluids,* 38(2), 233-243.

Balakumar, B.J. & Adrian, R.J. (2007). Large- and Very-Large-Scale Motions in Channel and Boundary-Layer Flows. *Philosophical Transaction of the Royal Society A*, 365(1852), 665-681.

Bayazit, M. (1976). Free Surface Flow in a Channel of Large Relative Roughness. *Journal of Hydraulic Research,* 14(2), 115-126.

Dittrich, A. & Koll, K. (1997) Velocity Field and Resistance of Flow over Rough Surfaces with Large and Small Relative Submergence. *International Journal of Sediment Research*, 12(3), 21-33.

Hutchins, N. & Marusic, I. (2007). Evidence of Very Long Meandering Features in the Logarithmic Region of Turbulent Boundary Layers. *Journal of Fluid Mechanics,* 579, 1-28.

Hwang, Y. & Cossu, C. (2010). Self-Sustained Process at Large Scales in Turbulent Channel Flow. *Physical Review Letter,* 105(4), 044505.

Jiménez, J. (2004). Turbulent Flows Over Rough Walls. *Annual Review of Fluid Mechanics,* 36, 173-196.

Kim, K.C. & Adrian, R.J. (1999). Very Large-Scale Motion in the Outer Layer. *Physics of Fluids,* 11(2), 417-422.

Marusic, I. & Hutchins, N. (2008). Study of the Log-Layer Structure in Wall Turbulence over a Very Large Range of Reynolds Number. *Flow Turbulence and Combustion,* 81(1-2), 115-130.

Monty, J.P., Hutchins, N., Ng, H.C.H., Marusic, I. & Chong, M.S. (2009). A Comparison of Turbulent Pipe, Channel and Boundary Layer Flows. *Journal of Fluid Mechanics,* 632, 431-442.

Nagib, H.M. & Chauhan, K.A. (2008). Variations of Von Kármán Coefficient in Canonical Flows. *Physics of Fluids,* 20(10), 1518.

Nezu, I. & Nakagawa, H. (1993). Turbulence in Open Channel Flows. *Balkema*, 269, 286

Nikora, V., Mcewan, I., Mclean, S., Coleman, S., Pokrajac, D., & Walters, R. (2007). Double-Averaging Concept for Rough-Bed Open-Channel and Overland Flows: Theoretical Background. *Journal of Hydraulic Engineering,* 133(8), 873-883.

Stewart, M.T. (2014). Turbulence Structure of Rough-Bed Open-Channel Flow. Phd Thesis, University of Aberdeen.

 

Proceedings of the 37th IAHR World Congress
August 13 – 18, 2017, Kuala Lumpur, Malaysia

# EXPERIMENTAL STUDY OF SEDIMENT TRANSPORT OVER A NON-ERODIBLE ROUGH BED

DAVID RAUS[(1)], FREDERIC MOULIN[(2)] & OLIVIER EIFF[(3)]

[(1,2)] Institut de Mécanique des fluides de Toulouse, Toulouse, France,
david.raus@imft.fr; frederic.moulin@imft.fr

[(3)] Karlsruhe Institute of Technology, Karlsruhe, Germany,
olivier.eiff@kit.edu

## ABSTRACT

Transport of sediment over a non-erodible bed of hemispheres was experimentally studied in two complementary flume experiments. Firstly, a morphological study at the flume scale showed the importance of bedforms on sediment transport and on the sediment elevation between the hemispheres: the protrusion of the hemispheres, $P$ (defined as $P=k/R$ where $k$ is the protrusion height and $R$ the hemisphere radius) was never greater than 30% in the lee of dunes, and reached high levels of around *40%* only after the erosion front has crossed the measurement region. In a second experiment, the local hydrodynamics study of the turbulent flow over patches of spherical caps and glued sediment confirms that an analysis of only the total shear stress or the turbulence intensity near the bed is misleading for the question of sediment mobility and transport. Quadrant analysis of the instantaneous flow at $z=d_{50}$ between the eroded hemispheres gives far more relevant information, showing in particular an enhancement of sweep and ejection events when hemispheres begin to protrude (at *P=20%*). This is followed by a gradual disappearance of these events as the level of protrusion increases. From *P=60%*, the sediment bed is dominated by intense but small turbulent eddies which have limited capacity to transport the sediment.

**Keywords:** Sediment transport; turbulent boundary layer; river hydraulics; rough bed; shear stress partitioning.

## 1 INTRODUCTION

Prediction and management of sediment transport in rivers is a key issue to try to limit erosion or to maintain aquatic ecosystems. Many studies have studied analytically or experimentally, the transport of sediment for the case of a uniform distribution of sediment size, or for bimodal movable sediments. In rivers, the amount of fine mobile sediment is often limited, leading to the apparition of a sublayer of coarser sediments, rarely moved by the river flow. This coarser sediment protrudes through the mobile grains, and the classical sediment transport laws cannot be directly applied.

A shear-stress partitioning model (Raupach et al., 1993; Yager et al., 2007) has been proposed to predict the sediment transport rate with the presence of immobile boulders. This is done by taking into account the armoring effect of the protruded roughness elements. Part of the flow momentum is dissipated in the wake of the immobile elements, thus reducing the shear stress available to move the finer sediment, and decreasing the erosion rate. However, some processes are not taken into account in this armoring effect approach. For instance, if a horseshoe vortex is created by the turbulent boundary layer impacting the roughness element, local high velocities and turbulence intensities can lead to scouring around the immobile element, associated with a local increase of the erosion rate (Manes and Brocchini, 2015). Interestingly, it has been shown that when the main source of turbulence is not the shear by the sediment bed itself, but an external source (for example grid generated turbulence), the transport rate does not depend on the Shields number alone, but also on the turbulence intensity near the bed, as found by Sumer et al. (2003). The presence of protruded elements may thus increase the turbulence intensity of the flow near the bed, and might enhance bed load transport even when the bed shear stress is reduced by the armoring effect. It was also shown that the use of the Reynolds stress and mean flow conditions to predict sediment motion leads to an underestimation of the sediment transport rate (Nelson et al., 1995; Keylock et al., 2014). It is therefore more relevant to take into account the instantaneous interaction between the turbulent coherent structures in the flow and the sediment bed, in particular the turbulent sweeps that remain hidden in the statistics when time-averaging is performed (Nelson et al., 1995; Keylock et al., 2014). Indeed, the presence of protruding elements may enhance the rate of sweeping events (Hardy et al., 2010).

In the present study, sediment transport over non-erodible rough beds are investigated by combining two complementary experimental approaches: (a) a morphodynamical study at a larger-than-the-roughness-scale over hemispherical immobile roughness elements and (b) a study at smaller scale of the local hydrodynamics inside a patch of hemispherical roughness elements protruding through a sediment bed. In the second

 

experiment, the shear stress and turbulent intensity fields are analyzed in the context of sediment transport. Quadrant analysis is also performed to investigate how the protruding rate impacts the generation of coherent structures in this system, yielding information on the protrusion levels for which the sediment is completely sheltered from these sweeping events (initially enhanced by the protrusions themselves).

## 2 EXPERIMENTAL SETUP

### 2.1 Morphodynamics of the bed

A first series of experiments was performed in a 26-m long, 1.1-m wide, 0,5-m deep open channel flume with a 0,3% slope covered by immobile artificial cobble-like roughness elements modeled by 0,0195 m radius hemispheres arranged in a staggered geometry, as illustrated in figure 1 (a). The frontal density was $\lambda_f$=0.45 (where $\lambda_f=A_f/A_{pattern}$ with $A_f$ the frontal area and $A_{pattern}$ the periodic pattern planar area) and the planar density was $\lambda_p$=0.91 (where $\lambda_p=A_p/A_{pattern}$ with $A_p$ the planar area). The hemispheres were attached to glass plates. Before the beginning of the experiments, light-weight wet plastic sediment (median diameter $d_{50}$ = *0,0022m,* specific gravity $G$ = 1.25, dimensionless particle diameter $d^*=d_{50}((G-1)g/\nu^2)^{1/3}$=29) was uniformly distributed manually in the flume in a layer of thickness $h_{sed}$, so that the hemispheres were completely covered at the beginning of the experiments. The flow velocity and water depth were initially selected to be just below the incipient motion of sediment. Then, the water depth was slowly decreased until a Shields parameter value greater than the critical Shields parameter of the sediment is reached. The investigated flow and sediment regimes are given in Table 1. In order to obtain a condition of supply-limited sediment and thus allow erosion, no sediment was supplied from the inlet during the experiments.

During the experiments, images of the bed were recorded from above by three high resolution cameras (PCO 2000) located at three longitudinal positions of the flume (see Figure 1.a). Using image analysis, the protruding hemispheres caps were detected and analyzed to estimate the sediment level around the hemispheres given the hemispheric shape.

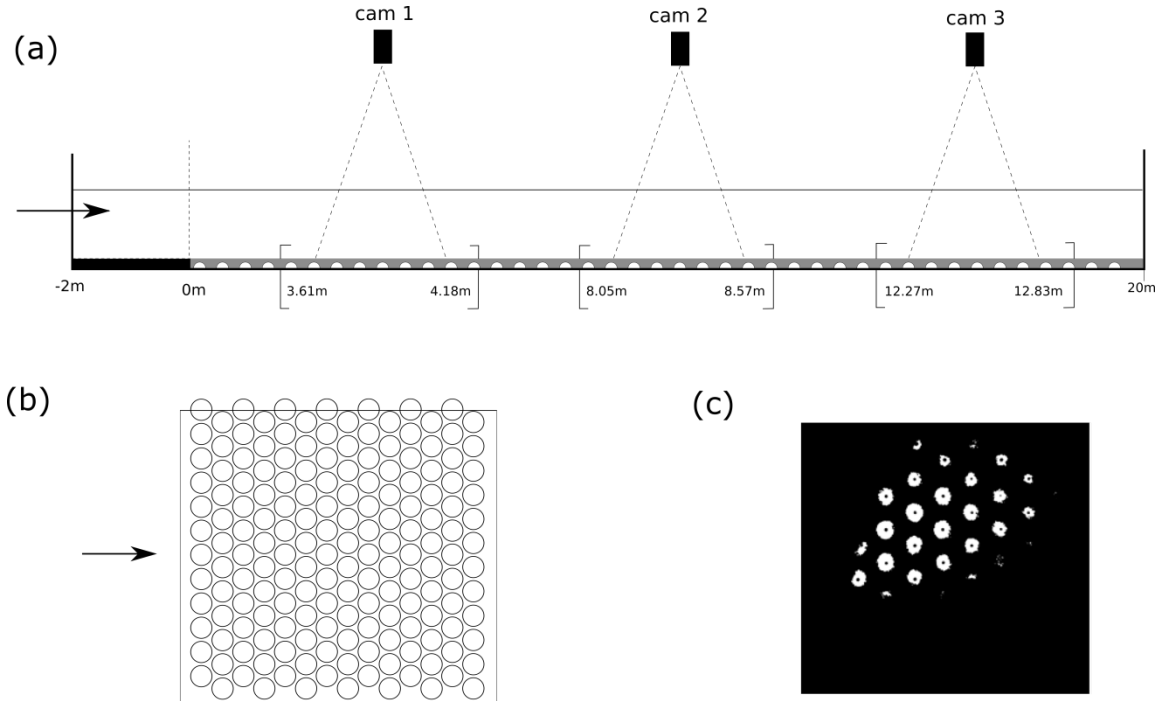


**Figure 1.** (a) Side view of the flume and position of the three cameras which are attached 2.1 m above the flume bed. (b) Camera view from half of the flume bed, showing the hemisphere positions (a staggered distribution). (c) A typical image recorded during the experiment and analyzed to estimate the sediment level around the protruding hemispheres.

 

**Table 1**. Flow and sediment regimes. The 'up' and 'down' indices represent the inlet and the outlet conditions of the flume, respectively (given downstream distances), given that the flow is slightly non-uniform. The friction velocity $u_*$ is estimated assuming a logarithmic velocity profile over a rough bed with a hydraulic roughness $k_s=d_{50}$. Values of the Shield parameter $\theta$ are calculated using this friction velocity values. T is the transport parameter defined by Van Rijn (1984) as $T=(\theta-\theta_c)/\theta_c$ where $\theta_c$ is the critical shields parameter value for incipient motion.

| | Q ($m^3s^{-1}$) | $h_{sed}$ (m) | $H_{up}$ (m) | $H_{down}$ (m) | $u_{*up}$ ($ms^{-1}$) | $u_{*down}$ ($ms^{-1}$) | $\theta_{up}$ | $\theta_{down}$ | $T_{up}$ | $T_{down}$ |
|---|---|---|---|---|---|---|---|---|---|---|
| **expQ60Hs30** | 60 | 0.03 | 0.207 | 0.243 | 0.0184 | 0.0148 | 0.086 | 0.056 | 0.78 | 0.16 |
| **expQ30Hs30** | 30 | 0.03 | 0.110 | 0.140 | 0.0234 | 0.0160 | 0.128 | 0.06 | 1.60 | 0.20 |
| **expQ30Hs25** | 30 | 0.025 | 0.117 | 0.159 | 0.0199 | 0.0129 | 0.09 | 0.039 | 0.84 | -0.20 |
| **expQ20Hs30** | 20 | 0.03 | 0.064 | 0.096 | 0.036 | 0.018 | 0.31 | 0.07 | 5.2 | 0.6 |

2.2 Local hydrodynamic measurements

The second set of experiments were conducted in a 11-m long, 0,5-m wide, 0,2-m deep horizontal flume covered by immobile glued sediments along 2,3m before the measurement section. Three patches of 3D-printed spherical caps were used to represent three states of the erosion (*P = 20%*, *40%* and *60%*) of a square distribution of hemispheres (with a frontal density $\lambda_f$=*0.39* and a planar density $\lambda_p$=*0.79*).

The protrusion *P* of a spherical cap is defined here as a percentage equal to:

$$P = 100\frac{h_{cap}}{h_{hem}} \qquad [1]$$

with $h_{cap}$ and $h_{hem}$ respectively the height of the spherical cap and the height of complete hemisphere. A 100% protrusion corresponds to a completely uncovered (eroded) hemisphere.

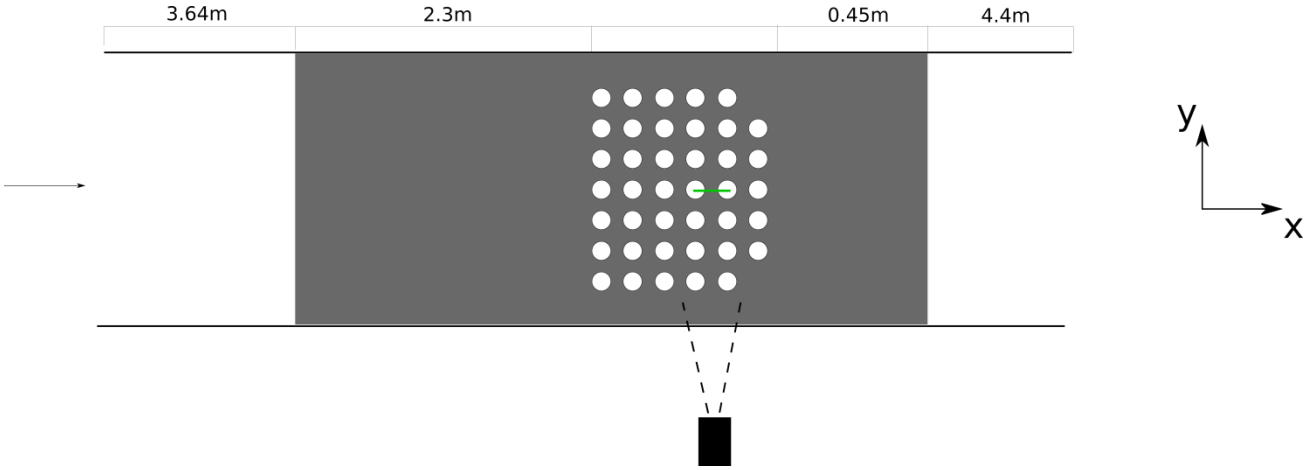


**Figure 2.** Top view of the flume with the array of spherical caps attached to the rough plate. The grey color indicates where the flume bed is covered with glued sediments.

A square distribution for the hemispheres was chosen instead of a staggered one to facilitate the optical access to the flow near the sediment bed. 2D Particle Image Velocimetry (PIV) measurements with a 16bit high resolution PCO Edge camera were performed over the patches of spherical caps, with a vertical longitudinal laser sheet crossing the plane of symmetry of the spherical cap at the middle of the fourth row of the patch (see figure 2). The laser sheet (2x 30mJ Nd: Yag Quantel Twins Ultra) was generated above the flume and penetrates into the water through a very slender glass window skimming the water surface which does not disturb the flow. All the experiments were performed with a water depth *H = 0.12m* above the basis of the spherical caps and a bulk velocity of $U_{bulk}$= *0.24* $ms^{-1}$. The PIV images were analyzed via the in-house software IMFT-CPIV.

## 3 MORPHODYNAMICS AND EROSION PATTERNS AT FLUME SCALE

In Table 1, the Shields parameter values near the entrance of the flume are all above the critical Shields parameter, and consequently bedload and bedform growth are observed in all experiments. The estimated values of the transport-stage parameter *T* to predict the formation of dunes, according to Van Rijn (1984), are also observed to correspond in the flume. However, the amount of available sediment being limited, the bed forms are not able to fully develop: as described by Tuijnder et al. (2009), patches of erosion appear on the bed between the dunes (in the present study, erosion patterns are only appearing in the middle of the flume

 

and not on all the width). A typical example of an erosion pattern is given in Figure 1 (c). The non-erodible hemispheres are visible but not totally eroded, and a layer of sediment remains sheltered between the hemispheres. Such erosion patterns propagate in the streamwise flow direction, along with the dunes.

In addition to the erosion patterns than form between successive dunes in the flume, an erosion front forms and propagates from the flume entrance. Secondary currents that develop in the flume due to the walls lead to the formation of longitudinal erosion ripples that develop gradually and invade first the camera 1 field of view, then camera 2 and camera 3 fields of view. These erosion patterns are very different from the erosion patterns that form in the lee of the dunes.

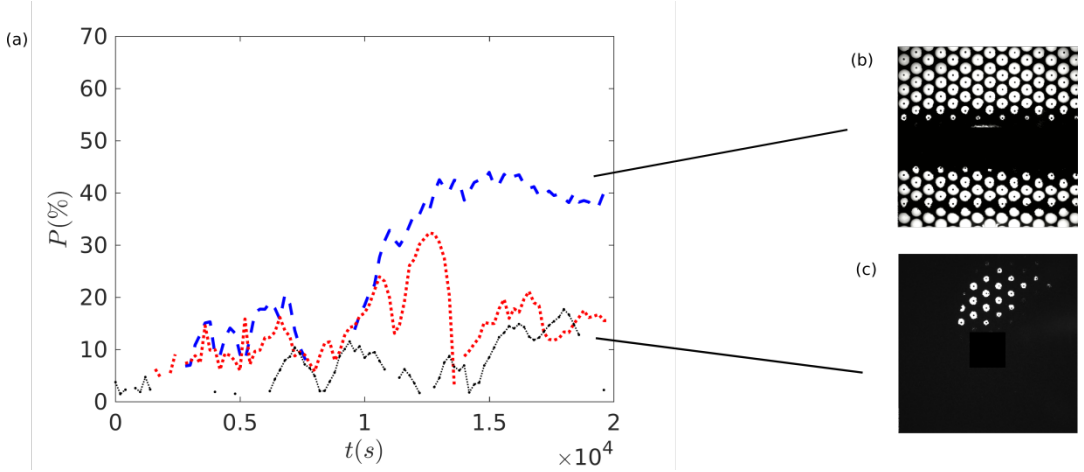


**Figure 3.** (a) Average protrusion level for protruding hemispheres in the erosion patterns seen in the cameras' field of views. Blue dash line: Camera 1. Red dot line: Camera 2. Black dash-dotted line: Camera 3. (b) Typical erosion pattern associated with the erosion front and (c) typical erosion pattern formed in the lee of a growing dune.

In figure 3, the average level of protrusion for protruding hemispheres is plotted as a function of time for experiment expQ60Hs30 for the three cameras. The tendency is the same for the other experiments. For erosion patterns crossing the camera field of view in this experiment and associated to patterns formed in the lee of dunes, the average level of protrusion is in the range 10 to 30%, in agreement with Grams and Wilcock (2007) who investigated the sediment transport over an immobile rough bed and observed that it was only possible to obtain a mean protrusion of less than 50% in the presence of large bedforms. In this experiment, longitudinal erosion ripples associated with the developing erosion front invades camera 1's field of view around t=10 000s, almost 3 hours after the start of the experiment. The average level of protrusion in these erosion longitudinal ripples is larger, around 40%, sediment between hemispheres being exposed to the flow and not sheltered anymore by the upcoming dune.

In the experiments presented here, uniform flow conditions could not be attained due to the fixed slope, and the water depth increasing in the streamwise direction. Consequently, erosion and transport rates were higher near the flume entrance (camera 1) and decreased when approaching the flume end (camera 3) as shown in Table 1. The sediment eroded near the flume entrance tended to accumulate at the end of the flume. As a consequence, it was not possible to obtain equilibrium states as in the work of Grams and Wilcock (2014).

In Grams and Wilcock (2007) equilibrium states with protrusion smaller than 50% were not observed, which the authors explained by a competition triggered by the protrusions between turbulence intensity enhancement on one hand and a sheltering effect on the other. Here, only the patterns associated with the erosion front appear to be in agreement with this interpretation. It is worth mentioning that Grams and Wilcock (2007) observed such levels of protrusion in the final equilibrium states obtained after all bed forms were evacuated and the erosion front crossed the whole flume. In this case, such levels are obtained when the erosion front has crossed the camera field of view.

Here, lower levels of protrusion are observed, for erosion patterns formed in the lee of dunes. If the competition invoked by Grams and Wilcock (2007) applies, why are lower levels observed? Probably because the flow structure in the lee of the dune must be taken into account. Following Tuijnder et al. (2009), erosion patterns begin to appear in the through between two successive dunes if the dune height is large enough to reach the non-erodible rough elements. As the dunes grow in amplitudes, the recirculation region in the dune's lee corresponds to the through where the roughness elements protrude. These are then sheltered by the dune itself, and the competition invoked by Grams and Wilcock (2007) should also include this sheltering effect induced by bed forms.

 

## 4 HYDRODYNAMICS AT THE NON ERODABLE ROUGHNESS SCALE

### 4. 1 Time-average flow velocity field

Mean longitudinal and vertical velocity fields $\bar{u}(x,z)$ and $\bar{w}(x,z)$ are plotted in Figure 4 for three levels of protrusion. Flow recirculations occur in the lee side of the spherical caps for the three protrusion levels. However, the recirculation reaches the next cap only for *P = 40%* and *P = 60%* experiments. For the patch with *P = 20%* spherical caps, the recirculation bubble is not limited by the distance between the caps and the magnitude of the mean vertical velocity remains weak.

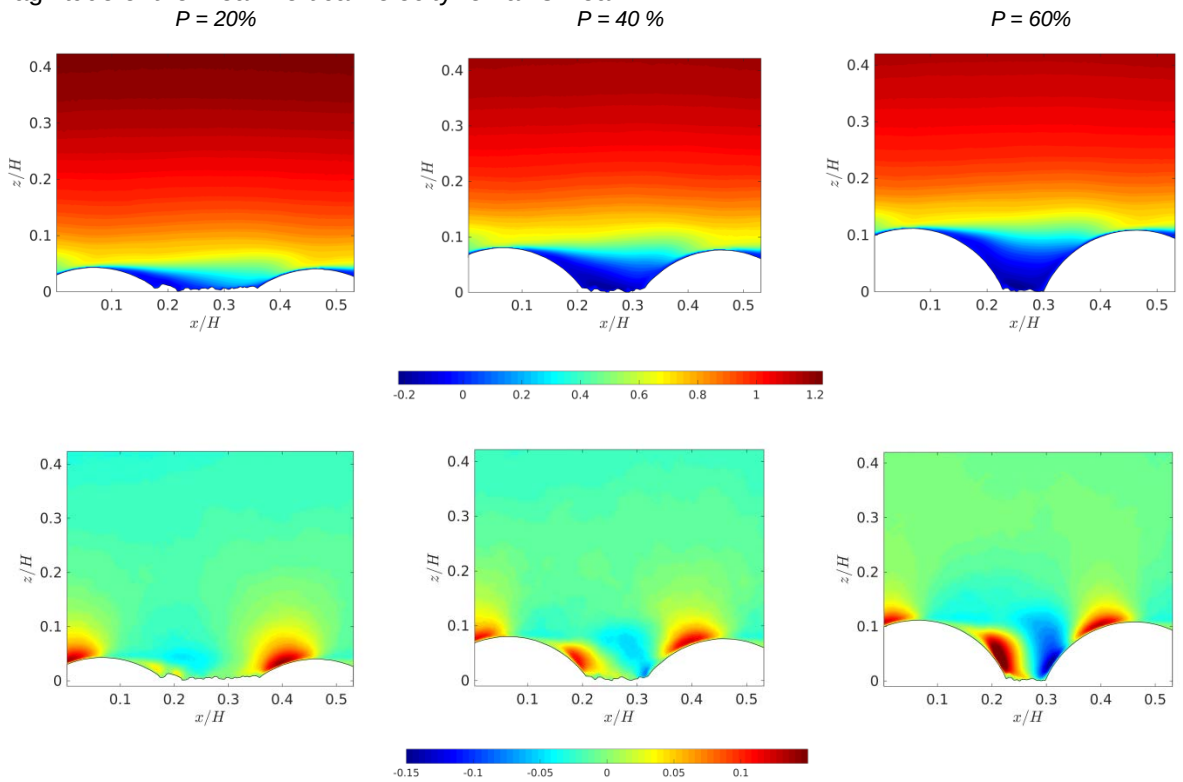


**Figure 4.** Mean longitudinal (top) and vertical (bottom) velocity fields $\bar{u}(x,z)$ and $\bar{w}(x,z)$for the three protrusions, normalized by the bulk velocity $U_{bulk}$.

### 4.2 Double-averaged vertical profiles of the turbulent quantities

In order to help predict if sediment transport occurs between the protruded elements, the first step is to evaluate the shear stress near the bed for the three regimes, following the approach of Raupach et al. (1993) and Yager et al. (2007). It was shown by Nikora et al. (2007) that for canopy flows, it is relevant to describe the flow in terms of double-averaged quantities (i.e., both time and spatial averaging in the horizontal directions). Here, the spatial averaging is made only in the *x* direction, and is noted as $< >_x$.

The total shear stress $\langle\tau\rangle_x$ includes the viscous stress $\nu\ (\partial\langle\bar{u}\rangle_x)/\partial z$, the Reynolds stress $-\langle\overline{u'w'}\rangle_x$ and the dispersive stress $-\langle\tilde{u}\tilde{w}\rangle_x$. Double-averaged profiles of these quantities estimated with only one plane measurement have been plotted in Figure 5 for P ranging from 0% (bed of sediment without protrusion) to 60%. Stresses are normalized by the friction velocity $u_*$ which is estimated here by extrapolating linearly the total shear stress to the top of the spherical cap (or sediment bed for P=0%) and applying $u_* = \sqrt{\tau(z \to h)/\rho}$ (following Florens et al., 2013 & Eiff et al., 2014). Values of the friction velocity $u_*$ were found to be equal to *0,0150 ms$^{-1}$, 0,0214 ms$^{-1}$, 0,0245 ms$^{-1}$* and *0,0230 ms$^{-1}$* for respectively the P=0%, 20%, 40% and 60% experiments. The linear extrapolation relies on the fact that $\langle\tau\rangle$ is linear for fully developed boundary layers, as found in Florens et al. (2013). The fact that the total shear stress approaches zero around *z/H=0.4* reflects the fact that the external turbulent boundary layer is not completely developed and the non-linearity is likely due the one-plane limitation.

For all patches, the double-averaged total shear stress values decrease dramatically when approaching the bed at z=0. This reflects that the measurements were performed in plane along the crests and not in the alley between caps. In all cases, the viscous shear stress is negligible. The dispersive stress contribution to the total shear stress evolves during the different states of erosion. When the spherical caps are not present, the dispersive stress is of course zero. At *P = 20%*, the contribution of the dispersive stress to the total shear stress is only negative, with a peak at the spherical cap crest, decreasing to zero near the bed. For *P = 40%* and *P = 60%,* the negative peak of the dispersive stress at the spherical cap crest is maintained, but a positive peak appears closer to bed, leading to an increase of the total shear stress. The main contribution to the total

 

shear stress is the Reynolds stress. For all the protrusions, it shows a peak at the crest of the spherical cap (due to the presence of the wake of the previous roughness element), and then decreases closer to the bed.

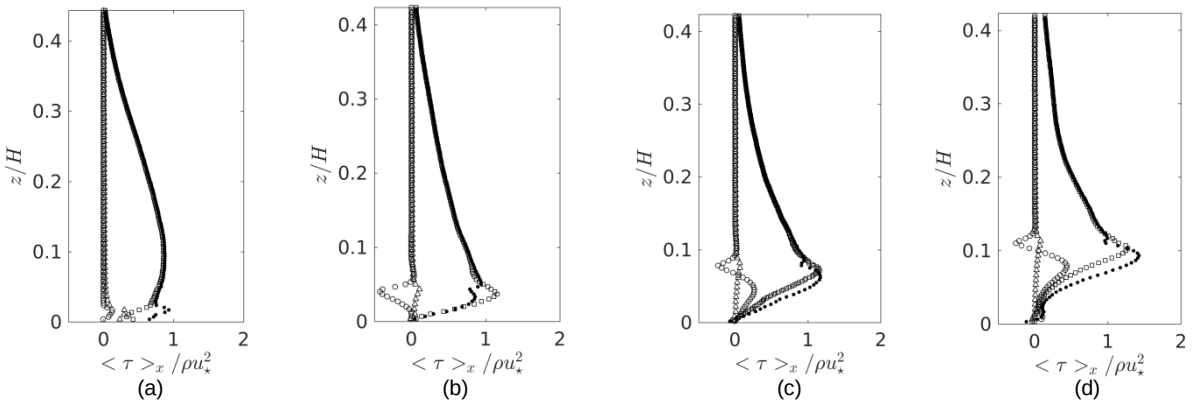


**Figure 5**. Vertical profiles of double-averaged shear stresses $\langle\tau\rangle_x$ (●), along with contributions from the Reynolds shear stress $-\langle\overline{u'w'}\rangle_x$ (□), the viscous shear stress $\nu\langle\partial\bar{u}/\partial z\rangle_x$ (Δ) and the dispersive shear stress $-\langle\tilde{u}\tilde{w}\rangle_x$ (○) for (a) *P = 0%* (b) *P = 20 %*, (c) *P = 40%* and (d) *P = 60%*. The friction velocity $u_*$ is equal to (a) *0,0150 ms$^{-1}$,* (b) *0,0214 ms$^{-1}$,* (c) *0,0245 ms$^{-1}$* and (d) *0,0230 ms$^{-1}$*

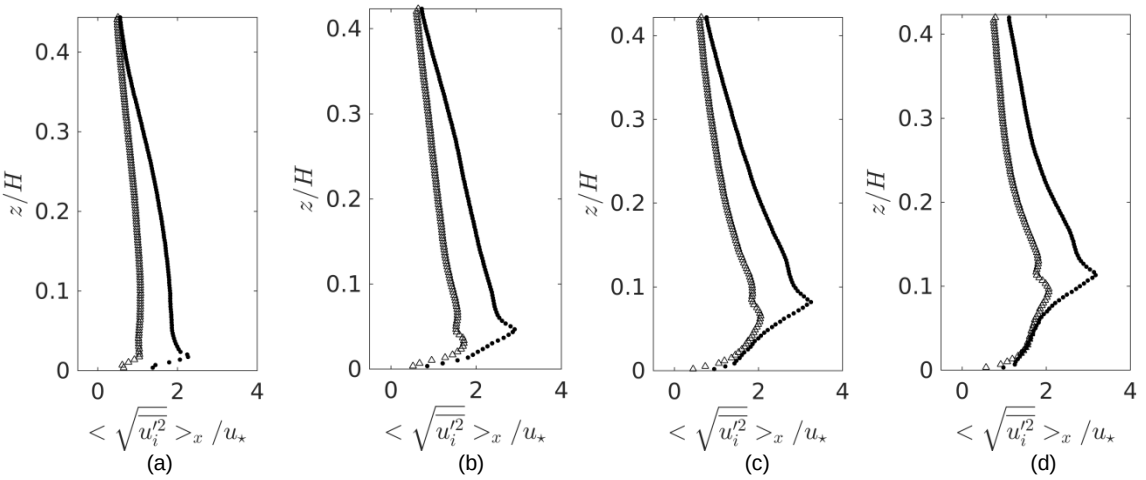


**Figure 6.** (●) Double-averaged downstream turbulence intensity profile $\sqrt{\overline{\boldsymbol{u'^2}}}$ and (Δ) Double-averaged vertical turbulence intensity profile $\sqrt{\overline{\boldsymbol{w'^2}}}$ for (a) *P = 0%* (b) *P = 20 %*, (c) *P = 40%* and (d) *P = 60%*

In Figure 6, vertical profiles of the normalized r.m.s value of the fluctuating components $u'$ and $w'$ of the velocity have been plotted for different erosion levels. Both the normalized $\sqrt{\overline{u'^2}}$ and $\sqrt{\overline{w'^2}}$ peaks increase between *P =0%* and *P=20%,* and then stop increasing when the hemisphere become more eroded. The value of $\sqrt{\overline{u'^2}}$ and $\sqrt{\overline{w'^2}}$ approach each other near the bed for *P = 60%*, revealing a quasi-isotropic turbulence.

It can be observed by comparing Figures 5 and 6 that using only the value of $\langle\tau\rangle$ or $\langle\tau\rangle_x$ to estimate a transport rate is inconclusive here since the stresses are uncorrelated with the turbulence intensity and the eddy size. As shown by Sumer et al. (2003) in experiments where turbulence intensity could be controlled independently of the bed friction, for a same Shields number determined by using the bed velocity friction, sediment transport rate could be as large as ten times greater when the factor $\sqrt{\overline{u'^2}}/u^*_{bed}$ was two times larger than for a simple flow over a sediment bed. In the presence of protruding spherical caps, sediment particles are submitted to the turbulent wake of obstacles. The protruding hemispheres act as independent turbulence sources, eddies generated in their wakes reaching the sediment bed and locally increasing the turbulence intensity.

In these experiments performed at constant bulk velocity, $U_{bulk}$=0,23 ms$^{-1}$, the friction velocity $u_*$ is initially low when only sediment appears (P=0%). As soon as hemispheres begin to protrude (P=20%), $u_*$ increases, and the level of turbulence intensity near the bed is enhanced (see Figure 6(b)) even if the bed total shear stress $\langle\tau\rangle(z \to 0)$ is reduced by the sheltering effect. The turbulence intensity near the sediment bed remains relatively high even for P=60%. However, this quantity does not give information on the size of involved

 

eddies or on the kind of events responsible for these high levels of turbulence intensity. This is the aim of the following subsection.

4.3 Quadrant analysis and coherent structures

Only considering time-averaged turbulent quantities is not always effective to predict the sediment transport rate, since the sediment can be set into motion by intermittent powerful eddies in the flow, these eddies being washed out by their non-Gaussian nature in the time averaging process. For example, it has been shown that it is possible to correlate the apparition of turbulent sweeps (and outward interactions) with the beginning of a grain motion (Nelson et al., 1995; Sechet & Le Guennec, 1999; Wu & Shih, 2012). Following these studies, quadrant analysis for the flow near our glued sediment bed could give relevant information whether or not mobile sediment would be set into motion.

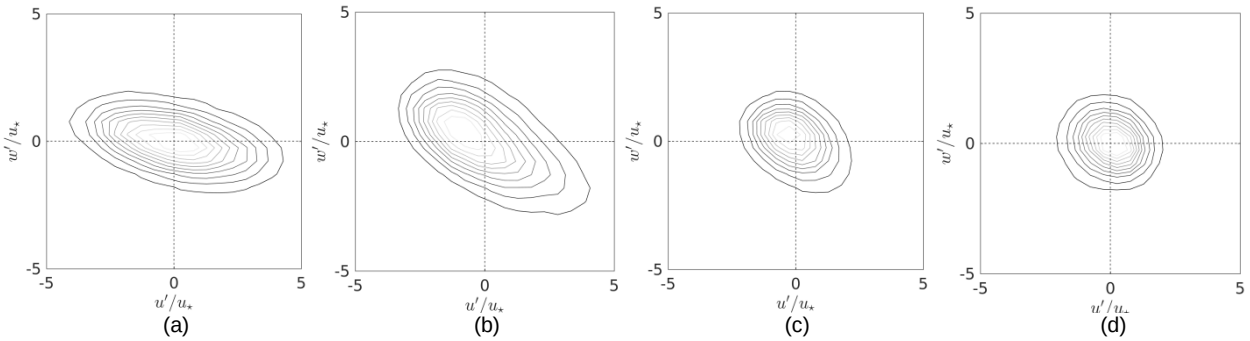


**Figure 7.** Joint PDF of the velocity fluctuations at $z=d_{50}$ between the protruded spherical caps. Contours correspond to 10% steps

To understand how the coherent structures, behave during the erosion of the hemispheres, a quadrant analysis was performed at $z = d_{50}$ between the protruded elements. The results are shown on Figure 7. For the bed without any spherical caps, the classical quadrant shape appears, with majority of quadrant Q2 and Q4, being the signature of hairpins like structures, sediment motion and transport being driven by these structures over pure sediment beds. For a protrusion level of *P = 20%*, the angle of the ellipse is modified, leading to an enhancement of both Q2 and Q4 quadrants (in particular greater fluctuating negative vertical velocity $w'$ in the Q4 quadrant). With mobile sediment, the motion and transport rate would be enhanced by this modification. However, at a protrusion level of *P = 40%*, both contributions of Q2 and Q4 quadrant begin to drop, leading the fluctuation's magnitude to be reduced near the bed. This phenomenon is enhanced for the *P = 60%* patch, the joint PDF of the velocity fluctuations becoming a circle, the occurrence of ejections and sweeps becoming notably rare near the sediment bed.

These modifications of the joint PDF of the velocity fluctuations near the bed reflect something that could not be inferred directly from the analysis of vertical profiles of velocity fluctuations. When spherical caps first protrude, turbulence is introduced by the interaction between the flow and the immobile obstacles, and eddies (especially turbulent sweeps) are enhanced and can reach the sediment bed to set grains into motion. As the obstacles protrudes more and more, a deep canopy of roughness elements builds up. Turbulent eddies near the bed remain powerful but are smaller in size, and sweeping / ejection events become rarer. These cannot reach deep into the canopy to attain the sediment bed. This phenomenon leads to a sheltering of the sediment between the protruded elements.

This result is in agreement with the studies of Grams and Wilcock (2007). They observed that for a staggered geometry, when the immobile roughness elements start protruding from the sediments, bed load can be enhanced due to the turbulence generated near the bed. These studies also showed that when the protrusion reaches *50%,* the erosion rate drops, and a layer of sediment can be sheltered in between the protruding elements. With the measurements in this study, we show that it coincides with the disappearance of sweep / injection strong events.

## 5 CONCLUSION AND PERSPECTIVES

This study investigates experimentally the transport of fine sediment over a layer of coarse immobile staggered hemispheres, and the local hydrodynamics during the apparition of a patch of spherical caps. The first set of large-scale experiments has shown the importance of the bedforms on sediment entrainment and on the amount of sediment being sheltered between the hemispheres. The hemispheres did not protruded more than *30%* in the lee side of a dune. With the second set of experiments with artificially set protrusions of caps, we have shown that an analysis of the total shear stress and the turbulence intensity profiles leads to apparently contradictory conclusions in terms of sediment mobility and transport. A study of the coherent structures generated in the flow by quadrant analysis as a function of the protrusion rate P shows how the sweeps and ejections are first enhanced when the roughness elements begin to appear (low P at 20%),

 

followed by a drop of such events for P between 40% and 60%, in agreement with observations of such erosion levels in large scale experiments reaching equilibrium states.

In the near future, PIV measurements performed in other vertical planes will be processed and analyzed in order to obtain a more complete picture of flow conditions near the sediment bed when the hemispheres protrude. On the basis of quadrant analysis, the gradual disappearance of the sweep and injection events with increasing *P* will be investigated. Experiments with mobile sediments could be also performed to validate the link between the sediment levels for the equilibrium states and the sheltering of the sediment bed from sweep and ejection events.

**ACKNOWLEDGMENTS**

This work and the PhD of David Raus are funded by the AFB (French Agency for Biodiversity).

**REFERENCES**

Eiff, O., Florens, E. & Moulin, F.Y. (2014). Roughness Parameters in Shallow Open-Channel Flows. *River Flow 2014, 7th International Conference on Fluvial Hydraulics*, Lausanne, Switzerland.

Florens, E., Eiff, O. & Moulin, F.Y. (2013). Defining the Roughness Sublayer and Its Turbulent Statistics. *Experiments in Fluids,* 54 (5000), 1-15.

Grams, P.E. & Wilcock, P.R. (2007). Equilibrium Entrainment of Fine Sediment over a Coarse Immobile Bed. *Water Resources Research,* 43(10), 1-14.

Grams, P.E. & Wilcock, P.R. (2014). Transport of Fine Sediment Over a Coarse, Immobile Riverbed. *Journal of Geophysical Research: Earth Surface,* 119, 188-211.

Hardy, R.J., Best, J.L., Lane, S.N. & Carbonneau, P.E. (2010). Coherent Flow Structures in a Depth-Limited Flow Over a Gravel Surface: The Influence of Surface Roughness. *Journal of Geophysical Research*, 115(3), F03006.

Keylock, C.J., Lane, S.N. & Richards, K.S. (2014). Quadrant/Octant Sequencing and the Role of Coherent Structures in Bed Load Sediment Entrainment. *Journal of Geophysical Research: Earth Surface,* 119(2), 264-286.

Manes, C. & Brocchini, M. (2015). Local Scour Around Structures and the Phenomenology of Turbulence. *Journal of Fluid Mechanics*, 779, 309–324.

Nelson, J.L., Shreve, R.L., Mclean, S.R. & Drake, T.G. (1995). Role of Near-Bed Turbulence Structure in Bed Load Transport and Bed Form Mechanics. *Water Resources Research*, 31(8), 2071-2086.

Nikora, V., Mcewan, I., Mclean, S., Coleman, S., Pokrajak, D. & Walters, R. (2007). Double-Averaging Concept for Rough-Bed Open-Channel and Overland Flows: Theoretical Background. *Journal of Hydraulic Engineering,* 133(8), 873–883.

Raupach, M.R., Gilette, D.A. & Leys, J.F. (1993). The Effect of Roughness Elements on Wind Erosion Threshold. *Journal of Geophysical Research*, 98 (2), 3023-3029.

Sechet, P. & Le Guennec, B. (1999). Bursting Phenomenon and Incipient Motion of Solid Particles in Bed-Load Transport. *Journal of Hydraulic Research*, 37(5), 683-696.

Sumer, B.M., Chua, L., Cheng, N.S. & Fredsøe, J. (2003). Influence of Turbulence on Bed Load Sediment Transport. *Journal of Hydraulic Engineering*, 129(8), 585-596.

Tuijnder, A.P., Ribberink, J.S. & Hulscher, S.J.M. (2009). An Experimental Study into the Geometry of Supply-Limited Dunes. *Sedimentology*, 56(6), 1713-1727.

Van Rijn, L.C. (1984). Sediment Transport, Part III: Bedforms And Alluvial Roughness. *Journal of Hydraulic Engineering,* 110(12), 1733-54.

Yager, E.M., Kirchner, J.W. & Dietrich, W.E. (2007). Calculating Bed Load Transport in Steep Boulder Bed Channels*. Water Resources. Research*, 43(7), 1-24.

 

Proceedings of the 37th IAHR World Congress
August 13 – 18, 2017, Kuala Lumpur, Malaysia

# A 1D NUMERICAL MODEL FOR AGGRADING CHANNEL OF NONUNIFORM SEDIMENT BED

BHOOMI R. ANDHARIA[(1)], PREM LAL PATEL[(2)], VIVEK L. MANEKAR[(3)], PRAKASH D. POREY[(4)]

[(1)] PhD Research Scholar, *Department of Civil Engineering, S.V. National Institute of Technology, Surat, 395007, India, andharia.bhoomi@gmail.com*

[(2)] Professor, Member IAHR, Department of Civil Engineering, SVNIT, Surat, India, *premlalpatel1966@gmail.com*

[(3)] *Associate Professor, Department of Civil Engineering, SVNIT, Surat, India, vivek_manekar@yahoo.co.in*

[(4)] *Ex-Director,* SVNIT, Surat, India, prakash.porey@gmail.com

## ABSTRACT

In present study, a semi-coupled numerical model, based on one dimensional de Saint-Venant equations along with sediment continuity equation, is developed for prediction of bed levels in case of graded noncohesive sediments in aggrading alluvial channels. One dimensional, unsteady flow equations and sediment continuity equations are solved using 'shock-capturing', second order accurate, explicit MacCormack finite difference scheme while considering upstream and downstream boundary conditions in the channel. Series of experimental investigations have been undertaken for measurements of bed and water levels in an aggrading channel due to overloading of nonuniform sediments, extracted from the bed of Tapi River at Surat City, at sediment transport flume installed in Advanced Hydraulics Laboratory of SVNIT, Surat, India. A strong coupling between the water flow and sediment variables has been achieved. The sediment continuity equation is used for the each size class to compute the volume of each size class after each time step at any computational node in the computational grid. The fractional bed and suspended load transport capacities for different size fractions have been computed using fractional transport laws for nonuniform sediments using active bed layer concept to consider the interaction and exchange of sediment and water flow near the mixing layer. The developed numerical model for bed level variation of nonuniform sediment bed has been compared with numerical model for uniform sediment bed while using the 7 test runs having total 26 sets of data collected in the laboratory. The performance of the model have been found better while considering the sediment nonuniformity in the model. The performance of developed numerical model has been satisfactorily verified with other independent experimental data on non-uniform sediment bed.

**Keywords:** Numerical model, aggradation, noncohesive sediment mixture, active bed layer, fractional sediment transport

## 1 INTRODUCTION

The natural rivers are overloaded from sediments due to extensive catchment erosion, landslides and releases in the form of mining wastes. Due to rapid industrialization and human interferences along the river, such natural and/or artificial overloading of sediments are responsible for bed level rise and the reduction in the capacity of alluvial rivers. Under such circumstances, prediction of river morphology, and maintenance of their ecological balance have become challenging problems for the hydraulic and environmental engineering fraternity. A delicate balance between water discharge, sediment discharge, river slope and sediment size is, often, disturbed by human and natural inferences which may result aggradation and degradation in alluvial streams. Aggradation occurs under variety of situations in alluvial streams like excessive sediment supply from badly eroding catchments during heavy rainfall or landslides; reduction of clear water in the river by withdrawing the same for irrigation and domestic usage; formation of delta or alluvial fans in upstream of lakes or reservoirs due to reduction of bed shear stresses, and dumping of large quantity of mining wastes in the natural streams etc. In general, aggradation in a stream takes place as and when the stream carrying capacity decreases in the direction of flow; or sediment inflow is more than its carrying capacity. Proper quantification of aggradation and/or degradation and changes in channel form of such alluvial rivers still has been a subject of active research. The development of numerical model for prediction of bed levels due to overloading of sediments could be useful to the river engineers in monitoring and controlling the behavior of alluvial streams, particularly the sediments with nonuniform characteristics, studies on migration of natural channels and precise prediction of flood and their control along the river (Garde and Ranga Raju, 2000).

Starting from the pioneering work of Adachi and Nakato (1969) on the evolution of river beds due to silting of reservoir, numerous analytical aggradation models were proposed and supported with overloading experiments in the laboratory flumes (Soni et al., 1980; Seal et al.,1997, SAFL runs). The analytical models

 

developed in previous studies were based on gross assumptions, and their applicability is limited to actual conditions in the field. In the modern era, due to the advent of high end computational facilities, numerical modeling is the most preferred approach in solving the governing equations for the computation of bed and water level changes in alluvial rivers. The numerical models are classified as uncoupled models (Thomas and Prasuhn, 1977; Wu et al., 2004); semi-coupled models (Rahuel et al., 1989, Capart and Young, 2002; Termini, 2014), and fully-coupled models (Correia et al., 1992; Singh et al., 2004). In uncoupled models, hydraulic characteristics are, first, estimated at a particular time step; and, then, estimated hydraulic information are used for prediction of sediment bed levels at the same time step. The major limitations of uncoupled models are that they consider "fixed bed" channel boundary during solution of flow equations, and exclude sediment parameters in determining the flow resistance. Under such circumstances, applications of coupled models become necessary due to strong coupling between water and sediment continuity equations (Saiedi, 1997). The physical interaction and interchange between water and sediment phase become possible in coupled approach for accurate prediction of bed levels in alluvial rivers, and getting the solutions of water and sediment parameters simultaneously. The leading studies on modeling bed level variations using coupled modeling approach include, Correia et al. (1992), Saiedi (1997) and Wu (2004). The nonlinearity in flow problems reduces the efficiency of sediment transport simulations, and coupled models may not be cost effective wherein time scales of flow and channel morphodynamic processes may be different (Wu, 2004). Hence, semi coupled models are the desired option wherein flow calculations are decoupled from sediment calculations, however, three components of sediment module, viz. sediment transport, bed change and material sorting, are solved in a coupled manner. The leading studies on semi-coupled models are Rahuel et al. (1989), Bhallamudi and Chaudhry (1991), Saiedi (1997), Capart and Young (2002), Ferguson and Church (2009), Tayfur and Singh (2011) and Termini (2014).

Previous investigations also emphasized the need for consideration of sediment nonuniformity in prediction of bed level of alluvial streams (Borah et al., 1982; Rahuel et al., 1989). The need for fractional bed load transport model vis-a-vis uniform sediment transport model is required to be demonstrated in numerical model for prediction of bed levels in aggrading channels.

In present study (Andharia, 2017), a one dimensional numerical model, based on de Saint-Venant equations and Exner's sediment continuity equation, is developed for prediction of bed and water levels in aggrading alluvial channels with noncohesive nonuniform sediment bed. Series of experimental investigations have been undertaken for measurements of bed and water levels in an aggrading channel due to overloading of noncohesive sediment mixture. The fractional bed and suspended load transport capacities for different size fractions have been computed using fractional sediment transport laws for nonuniform sediments channel bed. The performance of developed numerical model has been satisfactorily verified with 26 sets of independent experimental data of total 7 test runs of nonuniform sediment bed with different flow conditions and sediment characteristics.

## 2 EXPERIMENTAL SETUP AND PROCEDURE

The detailed description of experimental set up, detailed procedure of data collection; and salient features of data being used in the present study can be referred in Andharia et al. (2014, 2017). The flume setup and other flow conditions and sediment characteristics are presented here.

### 2.1 Experimental flume setup

The series of experimental runs were undertaken in a straight, recirculating tilting flume having 15m length, 0.89m width and 0.6m height (see Figure 1) at Advanced Hydraulics Laboratory of Civil Engineering Department at SVNIT, Surat, India. The measuring test section starts at 5.0 m distance from inlet to the flume, and consists of steel frame with side glass wall of 6m length. The complete experimental set up for measurement of bed and water surface profiles including different components of tilting flume, viz., centrifugal pumps, recirculating pipe, digital flow meter, control panel board, screw jack drive with DC motor, flow regulating valve, inlet, flow straightener, test section, sediment feeder with conveyor belt, pointer gauge with point and flat bottom mounted on carrier trolley, sliding and lifting arrangement for sediment trap, water level sensor, tail gate operated by lever arm at downstream end, volumetric tank, and downstream reservoir. The discharge into the channel is supplied from downstream reservoir. Flow rate is measured by a digital flow meter having capacity of 24 LPS to 240 LPS, with accuracy of $\pm 1\%$. Water levels and bed levels were measured using pointer gauge and a gauge having circular flat bottom respectively with least count of 0.1mm throughout length of the test section. Five numbers of water level sensors were also installed to record the water levels covering the entire working section of the flume. Such observations were recorded from a digital panel board, installed at upstream end of the channel.

The turbulent flow was fully developed by laying coarse gravel bed of 16 mm to 32 mm, over initial 3m length at upstream end of test section. The sediment feeder, having a hopper and a conveyor belt, was used for continuous feeding of sediment at the upstream end of the test section over the entire width of the channel. The sediment trap section, containing two box type sediment samplers, with sliding and lifting arrangement, were used for continuous sampling of bed load without disturbing the flow. An electronic weighing machine

 

with 0.01 gram least count and an automatic sieve shaker with series of 0.0625 to 45.0 mm sieves at 0.5 unit interval were used for sieve size analysis of bed material.


**Figure 1.** Sediment transport flume at Advanced Hydraulic Laboratory, SVNIT, Surat, India

2.2 Preparation of fluvial channel bed

The sediments, obtained from the river source, having sediment sizes up to 64 mm, were sieved into different size ranges of six fractions. The uniform sediment fractions, obtained after sieving, were mixed into the required proportions to get the sediment mixtures of designed gradation and nonuniformity. The sediment used for experimental work, was filled up in the test section of the flume carefully to avoid segregation of the bed material. The prepared bed of sediment layer (0.07 m thick) was leveled carefully to achieve uniform longitudinal slope throughout the test section.

2.3 Development and measurement of aggrading bed profiles

For each experimental run, initially, a small discharge was allowed to enter into the flume, and uniform flow condition was established by operating the tail gate. The discharge was increased in small increments by operating the inlet valve, and uniform flow conditions were maintained for each discharge in the channel. The increase in discharges was continued till adequate measurements of sediments were observed in the channel bed. The transported bed material were sampled at regular intervals (15 to 30 minutes depending upon flow conditions) using sediment sampler. The transported materials were brought back to upstream to feed the same through sediment feeder to maintain the equilibrium sediment transport conditions in the system. The equilibrium sediment transport condition was said to be achieved as and when the weights of three consecutive samples, collected for fixed duration, were of the same magnitude. The sediment supply rate to the system was increased to a predetermined value varied from 1.50 to 6.50 times of equilibrium sediment discharge, by continuously feeding excess sediment at the upstream end using sediment feeder. Due to excess feeding of sediment, the sediments started depositing in upstream end, and aggrading profiles were formed. The bed and water surface profiles were measured simultaneously at 1m interval in the working section using a gauge with flat bottom and a pointer gauge respectively, at 15 minutes intervals just after the commencement of aggrading profile. The measurement of transient profiles continued till the aggrading bed front likely to reach at the end of working section. At the end of the test run, bed was allowed to drain and become dry. The complete experimental data collected in the present investigation on nonuniform sediments; and bed and water surface profiles are included in Table 1. In Table 1, M-series mean (4 test runs, M1-1, M1-2, M1-3, M1-4 of Mixture 1 and 3 test runs, M2-1, M2-2, M2-3 of Mixture 2) data collected for nonuniform sediments.

**Table 1** Hydraulic characteristics of experimental runs for bed level variation of nonuniform sediments bed (Andharia, 2017)

 

| Run No. | Flow Discharge ($m^3$/sec) | Unit Flow Discharge $q_o$ ($m_2$/s) | Flow Depth (ho) (m) | Particle geometric mean size (mm) | Flow Width $B_o$ (m) | Velocity of Flow $U_o$ (m/s) | Water Surface Slope (%) | Bed Load Transport Rate (kg/15 min) | Bed Load Transport Rate $q_{s0}$ ($m^2$/s) | $\Delta q_s/q_{s0}$ | Transient profiles recorded during run (min) |
|---|---|---|---|---|---|---|---|---|---|---|---|
| **$M_1$-2** | 0.0519 | 0.0584 | 0.125 | 1.38 | 0.89 | 0.467 | 0.3125 | 6.16 | 2.9E-06 | 3 | 15,30,45,60,75,90,110,120 |
| **$M_1$-3** | 0.0532 | 0.0597 | 0.125 | 1.38 | 0.89 | 0.478 | 0.3125 | 6.28 | 3E-06 | 4 | 15,30,45,60 |
| **$M_1$-4** | 0.0519 | 0.0583 | 0.125 | 1.38 | 0.89 | 0.467 | 0.3125 | 6.00 | 2.8E-06 | 2 | 15,30,45,90,120, 150,180,210,240 |
| **$M_2$-1** | 0.0549 | 0.0617 | 0.125 | 1.14 | 0.89 | 0.494 | 0.3125 | 3.365 | 1.6E-06 | 6 | 15,30,45,60,75 |
| **$M_2$-2** | 0.0571 | 0.0641 | 0.12 | 1.14 | 0.89 | 0.534 | 0.375 | 10.43 | 4.9E-06 | 3 | 15,30,45,60 |
| **$M_2$-3** | 0.0571 | 0.0641 | 0.125 | 1.14 | 0.89 | 0.513 | 0.375 | 7.175 | 3.4E-06 | 4 | 15,30,45,60 |

## 3 MATHEMATICAL FORMULATIONS

### 3.1 Basic equations

The basic one-dimensional partial differential equations describing unsteady free surface flow in wide rectangular alluvial channels, also known as Saint Venant equations, are expressed as:

Continuity equation for water $$\frac{\partial q}{\partial x}+\frac{\partial h}{\partial t}=0 \quad [1]$$

Momentum equation for water $$\frac{\partial q}{\partial t}+\frac{\partial}{\partial x}\left(\frac{q^2}{h}+\frac{1}{2}gh^2\right)+gh\frac{\partial z}{\partial x}+ghS_f=0 \quad [2]$$

Continuity equation for sediment $$\frac{\partial}{\partial t}\left[(1-p)z+\frac{q_s h}{q}\right]+\frac{\partial q_s}{\partial x}=0 \quad [3]$$

Here, q = water discharge per unit width of the channel, h = flow depth, z = bed elevation, qs = equilibrium sediment discharge per unit width of channel, g = acceleration due to gravity, Sf = friction slope, x = distance along the channel, t = time and p= porosity of bed layer. The system of above equations along with resistance law such as Manning's equation for wide rectangular channel), and suitable sediment transport formulae, to be used in estimation of sediment discharge in sediment continuity equation can be used for prediction of bed and water levels along the flow of the channel.

### 3.2 Numerical scheme

In present study, Eq. [1-3], linking unknown dependent variables, viz., *h, q* and z with independent variables x and t, have been solved using explicit finite difference numerical scheme (MacCormack scheme) with appropriate boundary conditions described in following section . The MacCormack, predictor –corrector scheme, is second order accurate in space and time, and able to capture the 'shock', i.e., it is able to describe discontinuities due to steep moving slopes, and, thus, very stable and suitable for aggradation processes (MacCormack, 1976). The MacCormack scheme also allows the strong coupling between the flow hydraulic and sediment variables. The two step predictor-corrector approach enables the simultaneous solution of the de Saint Venant-Exner equations (Eqs. 1-3). The finite difference grid being used in foregoing numerical scheme is shown in Figure 2. In Figure 2, *i* denotes the space node; while *k* denotes the time node; L=length of the channel; $\Delta t$ = temporal step(s); $\Delta x$ = spatial step (m) /distance increment.

### 3.3 Fractional sediment transport laws for nonuniform sediments

Invariably, natural stream beds consist of nonuniform sediments. The sediment transport rates for such stream are estimated by summing up sediment transport rates of individual size fraction for known hydraulic and sediment characteristics. In numerical scheme, proposed in present study, fractional rates of bed load and suspended load transport for each size class were estimated using Patel and Ranga Raju (1996) and Samaga et al. (1986) respectively. The total sediment transport rates were, then, estimated by summing up the fractional bed load and suspended load for all size fractions computed above. The variation in particle size composition with time and space for each computational node were computed using the procedure described in following paragraphs.

 

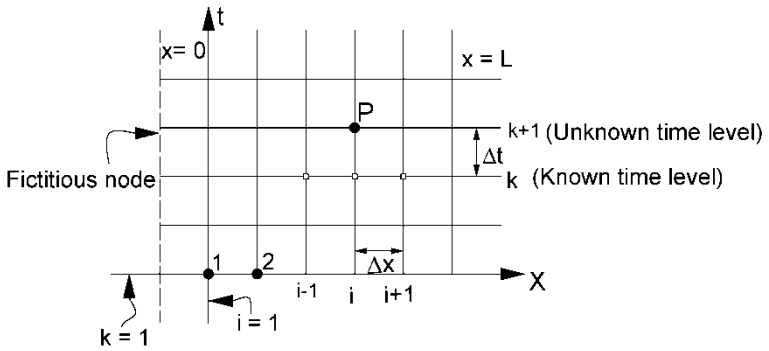


**Figure 2.** Finite difference grid for MacCormack scheme (P represents the unknown variables $h_i^{k+1}$, $q_i^{k+1}$ and $z_i^{k+1}$)

3.4 Thickness of active bed layer

The mixing zone of sediment remaining in contact with the flow is referred as active layer (ABL). The thickness and particle size distribution of ABL can vary throughout the computation, however, the layer is assumed to be homogeneous within itself at any given point of time. The bed material below the active layer is termed as substrate. In the past studies, the thickness of active layer was considered as function of depth of flow and particle size. Here, both the approaches has been combined for computation of thickness of active layer as (Borah et al., 1982),

$$T_b = d_{90} + 0.3h\left(1 - \frac{\tau_{0c}}{\tau_0}\right) \quad [4]$$

Here, $d_{90}$ is representative size in the bed material such that 90% fractions, by weight, are finer than this size, $\tau_{oc}$ = critical shear stress; and $\tau_o$ = mean shear stress. In dune regime, the flow depth has predominant effect on ABL thickness while particle size plays important role under plane bed condition. Initially, the mixing zone was assumed to be homogeneous in composition. The thickness of ABL ($T_b$) at each computational node for a given time line can be estimated using Eq. [4].

Total volume of any particle size, $d_j$, present in the ABL in $\Delta x$ length of the channel, at $i^{th}$ space node and $k^{th}$ time line, can be expressed as

$$V_{i,j}^k = T_{bi}^k B_0 \Delta x(1-p)(\Delta p_{i,j}^k / 100) \quad [5]$$

In Eq. [5], $\Delta p_j$ is the percentage of sediment size fraction, $d_j$, in the ABL. The percentage of the sediment of the $j^{th}$ size fraction in the ABL at the $k^{th}$ time step for each computational node, $\Delta p_{i,j}^k$, is calculated using Eq. (6). Here, $r$ represents total number of size fractions in sediment mixture.

$$\Delta p_{i,j}^k = \frac{V_{i,j}^k}{\sum_{j=r+1}^{j=1} V_{i,j}^k} \quad [6]$$

3.5 Input parameters of proposed scheme

The required space interval in computational grid ($\Delta x$), porosity of bed material (p), length (L) and width ($B_0$) of channel, initial uniform flow discharge ($q_0$), flow depth ($h_0$), bed slope ($S_0$), initial bed level at upstream boundary ($z_0$), ratio of increased rate of sediment discharge to rate of equilibrium sediment discharge ($\Delta q_T/q_{T0}$), grain size distribution of bed material (% finer, $p_j$, of each sizes, $d_j$,), total number of size fractions, and total computational duration, in seconds, are the input parameters of present scheme.

3.6 Initial conditions

Initially (for k=1 time line), flow depth, discharge and bed slope at all computational node (i=1 to N+1) over the length of channel were considered uniform. Also, it is assumed that initial bed material composition is

 

constant along the depth, width and length of channel. Thus, parameters $d_{90}$, $h$ and $\tau_{0c}/\tau_0$ are known, initially, along the length of the channel.

Initially, thickness of active bed layer and volume of individual size fractions in active bed layer (ABL) are computed as

Computation of $T_{bi}^{1}$ for i = 1 to N+1 for k=1: $$T_{bi}^{1} = \left(d_{90}\right)_i^1 + 0.3h_i^1\left(1-\frac{\tau_{0c}}{\tau_0}\right)_i^1 \quad [7]$$

Computation of $V_{i,j}^{1}$ for i = 1 to N+1 for k=1: $$V_{i,j}^{1} = T_{bi}^{1} B_0 \Delta x(1-p)(\Delta p_{i,j}^{1}/100) \quad [8]$$

The $\Delta p_{i,j}^{1}$ values of individual size fraction are computed using Eq. [6] for $k$=1.

3.7 Computation of time interval for the stability of the scheme

The minimum value of $\Delta t$ along current time line (k+1) is computed for entire length (i=1 to N+1) using Courant-Friedrichs-Lewy (CFL) condition as given in Bhallamudi and Chaudhry (1991), while using computed flow parameters ($h_i^k$, $q_i^k$) along previous time line (initially, k=1 time line, Eq. 9) as

$$C_n = \frac{(q/h+\sqrt{gh})\Delta t}{\Delta x} \le 1 \quad [9]$$

3.8 Boundary conditions

The water discharge ($q_0$) is considered constant at upstream node ($i$ =1). The flow depth at upstream node was estimated from continuity equation of water using explicit forward difference scheme (Eq. 1) as

$$h_1^{k+1} = h_1^{\,k} - \frac{\Delta t}{\Delta x}\left[q_2^{\,k} - q_1^{\,k}\right] \quad [10]$$

Total volume of sediment particle of $j^{th}$ size fraction at upstream node ($i$=1) were computed using Eq.[11] at different time lines as

$$V_{1,j}^{k+1} = V_{1,j}^{k} + \Delta t B_0\left[q_{Tin,j} - (q_{T1,j}^{k})\right] + \Delta x B_0\left[\left(\frac{q_{T1,j}^{k} h_1^{k}}{q_1^{k}}\right) - \left(\frac{q_{T1,j}^{k+1} h_1^{k+1}}{q_1^{k+1}}\right)\right] \quad [11]$$

Eq. [11] is valid for second time line (k=2) onwards till it reaches the last time step; $q_{Tin} = \left(q_{T0} + \Delta q_T\right)$; $q_{T0} = \sum q_{T_{i,j}}^{1}$; $q_{Ti,j}^{1} = q_{Bi,j}^{1} + q_{Si,j}^{1}$; $q_{Bi,j}^{1}$ and $q_{Si,j}^{1}$ represent fractional rates of bed and suspended load transport for $j^{th}$ size fraction along k=1, i.e., initial condition. As stated earlier, the fractional bed load and suspended loads were computed using Patel and Ranga Raju (1996) and Samaga et al. (1986) methods respectively. The solution of Eq. [11] requires trial and error procedure. In present study, standard Newton-Raphson method was used to reduce the number of trials. The values of $V_{1,j}^{k+1}$, is taken as the final, as and when the residual error (ε) was reached to 0.0001. After getting the refined value of $V_{1,j}^{k+1}$ and $\Delta p_{i,j}^{k+1}$, the thickness of ABL, $T_{b1}^{k+1}$, was computed using Eq. [5].

Subsequently, the bed levels at i=1 at different time levels were calculated as

$$z_1^{\,k+1} = z_1^{k} + \frac{1}{(1-p)}\left[\left(\frac{q_T h}{q}\right)_1^{k} - \left(\frac{q_T h}{q}\right)_1^{k+1}\right] + \frac{1}{(1-p)}\frac{\Delta t}{\Delta x}\left[\left(q_{T0}+\Delta q_T\right) - \left(q_T\right)_1^{\,k}\right] \quad [12]$$

Using downstream boundary conditions, the discharge ($q_{N+1}^{k+1}$) and bed levels ($z_{N+1}^{k+1}$) are estimated by extrapolating the values from interior nodes.

3.9 Computation at interior nodes

The flow depth and flow discharge ($h_{i+1}^{k+1}, q_{i+1}^{k+1}$) at node i=2 to N (for k=2 to N) were computed using the predictor-corrector approach described in Bhallamudi and Chaudhry (1991). The composition of the active bed

 

layer is altered due to varying transport rates of the individual size classes with time in the channel bed. The estimation of varying composition of active bed layer is dealt as per Borah *et al.* (1982) approach. The *grain sorting equation* for different size classes which has derived from Exner's sediment continuity equation, is applied at each computational node to compute the total volume of each size class ($d_j$) present in active layer as,

$$V_{i+1,j}^{k+1} = V_{i+1,j}^{k} + \Delta t B_0 \left[ q_{Bi,j}^{k} + q_{si,j}^{k} - q_{Bi+1,j}^{k} - q_{si+1,j}^{k} \right] + \Delta x B_0 \left[ \left( \frac{q_{Ti+1,j}^{k} h_{i+1}^{k}}{q_{i+1}^{k}} \right) - \left( \frac{q_{Ti+1,j}^{k+1} h_{i+1}^{k+1}}{q_{i+1}^{k+1}} \right) \right] \quad [13]$$

Eq. [13] is valid for second time line onwards till it reaches the last time step; In Eq. [13], $q_{Ti+1,j}^{k} = q_{Bi+1,j}^{k} + q_{Si+1,j}^{k}$; $q_{Ti+1,j}^{k+1} = q_{Bi+1,j}^{k+1} + q_{Si+1,j}^{k+1}$; $q_{Bi+1}^{k+1} = \sum_{j=1}^{r+1} q_{Bi+1,j}^{k+1}$; $q_{Si+1}^{k+1} = \sum_{j=1}^{r+1} q_{Si+1,j}^{k+1}$; $q_{Bi,j}^{k} = \sum_{j=1}^{r+1} q_{Bi,j}^{k}$; $q_{Si,j}^{k} = \sum_{j=1}^{r+1} q_{Si,j}^{k}$; $q_{Bi,j}^{k}, q_{Si,j}^{k}$ and $q_{Bi+1,j}^{k+1}, q_{Ti+1,j}^{k+1}$ represent fractional rates of bed and suspended load transport $j^{th}$ size fraction at $i^{th}$ and $(i+1)^{th}$ nodes and $k$ and $(k+1)$ time lines respectively. $V_{i+1,j}^{k}, h_{i+1}^{k}, q_{i+1}^{k}$ and $V_{i+1,j}^{k+1}, h_{i+1}^{k+1}, q_{i+1}^{k+1}$ represent total volume for each size class ($d_j$) present in active layer, depth of flow and flow discharge at $(i+1)^{th}$ nodes and $k$ and $(k+1)$ time lines respectively. The solution of Eq. [13] requires trial and error procedure. The standard Newton-Raphson method was applied in present study, to reduce the number of trials. The values of $V_{i+1,j}^{k+1}$ were taken as the final, as and when the residual error (ϵ) was reached to 0.0001. After getting the refined value of $V_{i+1,j}^{k+1}$, the thickness of active bed layer, $T_{bi+1}^{k+1}$, was computed using Eq. [5]. Subsequently, the bed levels at interior nodes at any time step were calculated using predictor-corrector approach for already computed values of $h_{i+1}^{*}, q_{i+1}^{*}$, $h_{i+1}^{**}, q_{i+1}^{**}$ at k+1 time step and final values of $q_{Ti+1}^{k+1}$, where, superscripts $*$ and $**$ refer to the values of the dependent variables after the predictor and corrector steps respectively at unknown time *k+1* level.

## 4 APPLICATION OF THE MODEL

The active bed layer concept has been implemented to consider the interaction and exchange of sediment and water flow near the mixing layer.

### 4.1 Performance of Numerical Model for Nonuniform Sediment Bed

The developed numerical model has been used to simulate the transient bed and water levels corresponding to 15, 60, 90, 110 and 120 minutes timings from the beginning of overloading in nonuniform sediment beds ($M_1$ and $M_2$). The performance of the model with corresponding observed bed and water levels using statistical analysis and graphical representation are included in Table 2 and Figures 3-5 respectively. From Table 2 and Figures 3-5, it is apparent that root mean square error (rmse) between observed and simulated bed levels are within 0.87. On other hand, root mean square error (rmse) in computation of water levels for the reported experimental runs are within 0.45. Thus, performance of numerical model for nonuniform sediment bed is satisfactory for the whole range of data.

The model simulation of the transient profiles after 15, 60, 90, 110, 120 minutes from the beginning of the overloading are shown in Table 2 and Figure 3(a) for the Run $M_1$-2 of the channel bed having Mixture-1 as bed material. The model simulation of the transient profiles after 15, 30, 45 and 60 minutes from the beginning of the overloading are shown in Table 2 for the Run $M_1$-3 of the channel bed having Mixture-1 as bed material. Figure 5(a) and Figure 3 (b) is showing the comparisons of observed and computed levels for the transient profiles recorded after 3 hours,4 hours having RMSE of 0.15 cm and 0.87 cm for $M_1$-4.

Similarly, Table 2 also shows the performance for the Run $M_2$-1,2,3 of the channel bed having Mixture-2 as bed material for transient profile time of having RMSE = 0.11cm, 0.22 cm, 0.15 cm and 0.27 cm respectively for bed levels for Run $M_2$-2. Figure 4(b) shows the bed profile predictions for 1 hour transient time having RMSE = 0.24 cm and 0.19 cm respectively for Run $M_2$-3 (see Table 2).

The different overloading may also affect the maximum rise in the bed level. Comparing, Run $M_2$-2 and $M_2$-3 with 3 and 4 times overloading respectively (see Figures 4 a-b), it confirms that the higher sediment overloading may cause greater depth of deposition and incensed rise in bed level.

### 4.2 Performance of numerical models for uniform vis-a-vis nonuniform sediments

The developed numerical model for bed level variation of uniform and nonuniform sediments beds have been compared with available data of M1 sediment mixture (run 4). Here, bed level variation model for uniform sediment was used while considering the average size as the representative size for estimation of sediment-transport using Karim and Kennedy (1983) formula (Andharia et al., 2014) as sediment transport function. The performance of both the models is included in Table 3 and also shown in Figure 5(a)-(b).

 

**Table 2.** Performance of numerical model developed for nonuniform sediments used in present study

| Experimental Runs | Parameters | Time (Minutes)→ rmse (cm) | | | | | | | | | |
|---|---|---|---|---|---|---|---|---|---|---|---|
| | | 15 | 30 | 45 | 60 | 75 | 90 | 110 | 120 | 180 | 240 |
| $M_1$-2 | BL[b] | 0.15 | - | - | 0.23 | - | 0.20 | 0.20 | 0.50 | - | - |
| | WL | 0.22 | - | - | 0.27 | - | 0.18 | 0.25 | 0.34 | - | - |
| $M_1$-3 | BL | 0.07 | 0.11 | 0.14 | 0.29 | - | - | - | - | - | - |
| | WL | 0.06 | 0.23 | 0.13 | 0.18 | - | - | - | - | - | - |
| $M_1$-4 | BL | 0.23 | - | - | 0.25 | - | - | - | 0.22 | 0.15 | 0.87 |
| | WL | 0.18 | - | - | 0.16 | - | - | - | 0.2 | 0.29 | 0.20 |
| $M_2$-1 | BL | 0.27 | 0.38 | - | 0.37 | 0.50 | - | - | - | - | - |
| | WL | 0.26 | 0.27 | - | 0.4 | 0.45 | - | - | - | - | - |
| $M_2$-2 | BL | 0.11 | 0.22 | 0.15 | 0.27 | - | - | - | - | - | - |
| | WL | 0.2 | 0.3 | 0.24 | 0.25 | - | - | - | - | - | - |
| $M_2$-3 | BL | 0.19 | 0.31 | 0.30 | 0.24 | - | - | - | - | - | - |
| | WL | 0.20 | 0.22 | 0.30 | 0.19 | - | - | - | - | - | - |

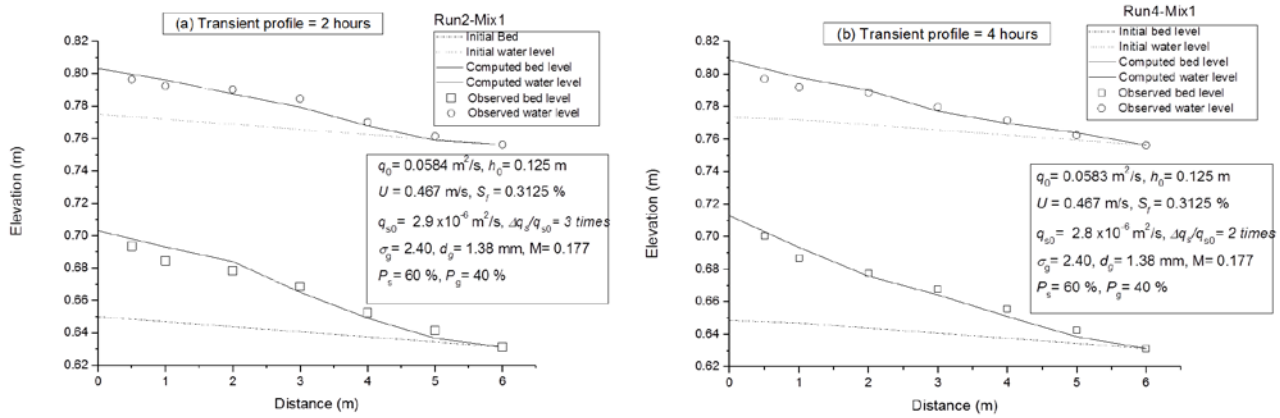


**Figure 3.** Comparison of predicted and measured bed level (BL) and water surface level (WL) transient profiles after (a) 2 hours for Run $M_1$-2 (b) 4 hours for Run $M_1$-4

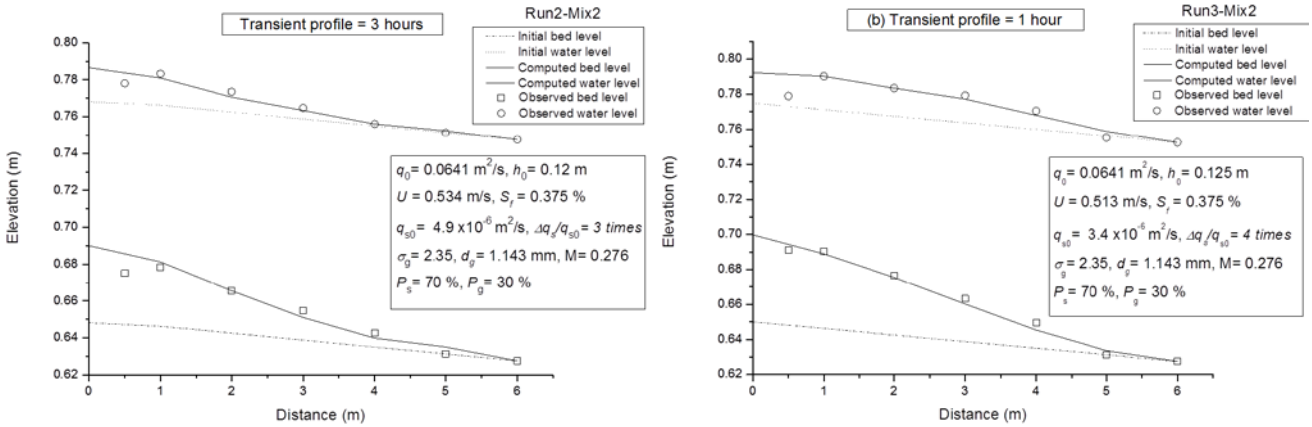


**Figure 4.** Comparison of predicted and measured bed (BL) and water surface (WL) profile for transient profiles after (a) 3 hour of Run $M_2$-2 (b) 1 hour of Run $M_2$-3

[b] BL- bed level, WL- water level, rmse (cm) = $\sum \sqrt{(M-P)^2/n}$,M=Measured value, P=Predicted value, n=number of observations.

 

From Figures 5 (a-b) and Table 3, it is apparent that numerical model based on nonuniform sediments performs significantly better than the model based on uniform sediments, particularly for higher transition time period. Thus, it is utmost important to choose suitable sediment transport functions, depending upon the nature sediment bed, in computation of bed level of aggrading channels.

**Table 3.** Statistical performance of numerical models based on uniform and nonuniform sediments using statistical performance indices

| **Run** | **Uniform Sediments** (Run $M_1$-4) | | | | **Nonuniform Sediments** (Run $M_1$-4) | | | |
|---|---|---|---|---|---|---|---|---|
| **Transient profiles** | **RMSE(cm)** $\sum \sqrt{(M-P)^2}/n$ | | **MASE (cm)** $\sum \lvert M-P \rvert/n$ | | **RMSE(cm)** | | **MASE (cm)** $\sum \lvert M-P \rvert/n$ | |
| **Time** | **BL** | **WL** | **BL** | **WL** | **BL** | **WL** | **BL** | **WL** |
| 60 min | 0.25 | 0.26 | 0.17 | 0.21 | 0.25 | 0.16 | 0.17 | 0.11 |
| 180 min | 0.38 | 0.36 | 0.29 | 0.28 | 0.15 | 0.29 | 0.10 | 0.20 |

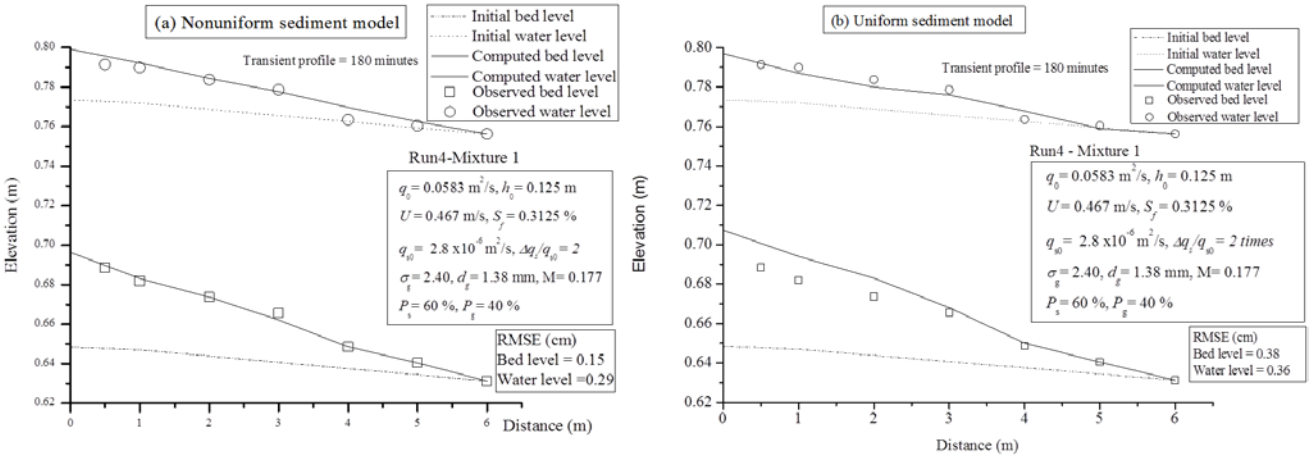


**Figure 5.** Performance assessment of numerical models developed for nonuniform and uniform sediments (run $M_1$-4)

## 5 CONCLUSIONS

The key conclusions arrived from foregoing study is summarized in following paragraphs:

i. A one-dimensional numerical model is developed for prediction of bed level variations in aggrading channel due to sediment overloading in nonuniform sediments bed.
ii. The 'Active bed layer' theory given by Borah et al. (1982) has used to derive the grain sorting equation for different size classes for channel bed made up of nonuniform sediments.
iii. Series of experimental investigations have been undertaken to measure bed and water level variations due to overloading of alluvial channel with sediment bed made up of nonuniform sediments with standard deviation of 2.40 and 2.35.
iv. The numerical model developed based on fractional bed load transport and suspended load transport rates, i.e. Patel and Ranga Raju (1996) and Samaga et al. (1986) have been validated with observed data in present study on aggrading channels. The model has been found to be satisfactory in prediction of bed and water level variations of aggrading channels.
v. The statistical performance of the numerical model developed for nonuniform sediment bed has also been compared with the numerical model based on uniform sediment transport function. The comparative performance clearly highlights the importance of numerical model based on nonuniform sediments over the model for uniform sediments.

## ACKNOWLEDGEMENTS

The authors will be ever grateful to the Department of Science and Technology (DST), New Delhi, Government of India, for the financial support for installing the flume facilities through the Research Project "Erosion of nonuniform unimodal and bimodal sediments" with project Grant No. SR/S3 /MERC/015/2009.

## REFERENCES

Adachi, S. and Nakato, T. (1969). Changes of Top-Set Bed in a Silted Reservoir. *13th Congress, IAHR*, 5-1, 269-272.

 

Andharia, B.R., Patel, P.L., Manekar, V.L., and Porey, P.D.(2014). Experimental and numerical studies on Aggradation for alluvial stream bed. *HYDRO 2014 International 19th Conference on Hydraulics, Water resources and Environmental Engineering*. Dec. 18-20, Maulana Azad National Institute of Technology, Bhopal, India.

Andharia, B.R. (2017). Prediction of flow resistance and bed level variations ion alluvial channels. *Ph.D. Thesis.* Departments of Civil Engineering, S. V. National Institute of Technology, Surat, India.

Bhallamudi, S.M. and Chaudhry, H. M. (1991). Numerical modeling of aggradation and degradation in alluvial channel. *Journal of Hydraulic Engineering, ASCE*, 117(9), 1145-1164.

Borah, D.K., Alonso, C.V. and Prasad, S.N. (1982a). Routing Graded Sediment in Stream Formulations. *J. Hydraul. Engng., ASCE*, 108(12), 1486–1503.

Capart, H. and Young, D.L. (2002). Two layer shallow water computation of torrential geomorphic flows. *Proc. Int. Conf. on Fluvial Hydraulics, River Flow 2002*. Louvain-la-Neuve, Belgium, September, 2, 1003.

Correia, L.R.P., Krishnappan, B.G. and Graf, W.H. (1992). Fully coupled unsteady mobile boundary flow model. *J. Hydraul. Engng., Proc. ASCE*, 118(3), 476–494.

Ferguson, R. and Church, M. (2009). A critical perspective on 1-D modeling of river processes: Gravel load and aggradation in lower Fraser River. *Water Resources Research*, 45(11), W11424, doi:10.1029/2009WR007740.

Garde, R.J. and Ranga Raju, K.G. (2000). *Mechanics of sediment transportation and alluvial stream problems*. New Age Publishers, New Delhi.

Karim, M.F. and Kennedy, J.F. (1983). Computer based predictors for sediment discharge and friction factor of alluvial streams. *Proc. of 2nd Int. Symposium on River Sedimentation*, Oct.-Nov. Nanjing, China.

MacCormack, R.W.(1976). An efficient numerical method for solving the time dependent compressible Navier-Stokes equations at high Reynolds number. *Computing in Applied Mechanics*; A77-46133 21-59, ASME, 49-64; *Proceedings of the Winter Annual Meeting*, New York, N.Y.

Patel, P.L. and Ranga Raju, K.G. (1996). Fraction wise Calculation of Bed Load Transport. *J. Hydraul. Res*., 34(3), 363–379.

Rahuel, J.L., Holly, F.M., Chollet, J.P., Belludy, P. and Yang, G. (1989). Modelling of river bed evolution for bed load sediment mixtures. *J. Hydraul. Engng., ASCE*, 115(11), 1521–1542.

Saiedi, S. (1997). Coupled modeling of alluvial flows. *J. of Hydraulic Engineering, ASCE*, 123 (5), 440-446.

Samaga, B.R. Ranga Raju, K.G. and Garde, R.J. (1986). Suspended load transport of sediment mixtures. *Journal of Hydraulic Engineering,* 112(11), 1019-1035.

Seal, R., Paola, C., Parker, G., Southard, J. B., and Wilcock, P. R. (1997). Experiments on downstream fining of gravel. I: Narrow-channel runs. *J. Hydraul. Eng., ASCE*, 123(10), 874–884.

Singh, A. K., Kothyari, U. C., and Ranga Raju, K. G. (2004). Rapidly varying transient flows in alluvial rivers. *Journal of Hydraulic Research, IAHR*, 42(5), 473-486.

Soni, J.P., Garde, R.J. and Ranga Raju, K.G. (1980). Aggradation in streams due to overloading. *J. Hydraul. Engng., ASCE*, 106(1), 117-131.

Tayfur, G. and Singh, V.P. (2011). Simulating transient sediment waves in aggraded alluvial channels by double-decomposition method. *J. of Hydrologic Engineering ASCE*, 16(4), 362-370.

Termini, D. (2014). Nonuniform sediment transport estimation in non-equilibrium situations: case studies. *12th International Conference on Computing and Control for the Water Industry, CCWI2013. Procedia Engineering,* 70, 1639-1648.

Thomas, W. A., and Prasuhn, A. L. (1977). Mathematical modeling of scour and deposition. *J. Hydr. Div., ASCE*, 103(8), 851-863.

Wu, W. (2004). Depth-averaged two-dimensional numerical modelling of unsteady flow and nonuniform sediment transport in open channels. *J. Hydraul. Eng. ASCE*, 130(10), 1013–1024.

Wu, W., Vieira, D. A., and Wang, S. S. Y. (2004). 1D numerical model for nonuniform sediment transport under unsteady flows in channel networks. *J. Hydraul. Eng*., 130(9), 914–923.

 

Proceedings of the 37th IAHR World Congress
August 13 – 18, 2017, Kuala Lumpur, Malaysia

# ESTIMATE OF FRICTION FACTOR FOR FLOWS SUBJECT TO LARGE-SCALE ROUGHNESS

NIAN-SHENG CHENG [(1)]

[(1)] School of Civil and Environmental Engineering,
Nanyang Technological University, Nanyang Avenue, Singapore, 639798
cnscheng@ntu.edu.sg

## ABSTRACT

The Manning-Strickler (MS) formula is only applicable for small-scale roughness conditions. This study demonstrates that with simple modifications, it can be also applied for large-scale roughness to estimate the friction factor for pipe and open channel flows. The modifications are developed simply by considering the roughness induced flow constriction. Without adjusting constants involved, the derived formulas agree well with experimental data in the range of small to large-scale roughness. Comparisons are presented with large-scale roughness data, which include three series of rough-pipe data, of which two are collected in this study and the other is reported in the literature, and 404 sets of gravel-bed data from five previous studies.

**Keywords:** Friction factor; large-scale roughness; Manning-Strickler formula; rough pipe; gravel bed.

## 1 INTRODUCTION

The Manning-Strickler (MS) formula can be used to link the friction factor f to the relative roughness height in the following power-law form (Yen, 1992),

$$f = N(k_s/r)^{1/3} \qquad [1]$$

where $k_s$ is the roughness height, r is the hydraulic radius and N is a constant. Using the empirical results summarized by Yen (1993), it can be shown that N varies from 0.049 to 0.179. It is also noted that Eq. [1] with N = 0.115 agrees well with Nikuradse's (1933) data for fully rough pipes.

To estimate the friction factor affected by large-scale roughness, various revisions of Eq. [1] have been presented in the literature. For example, Griffiths (1981) suggested Eq. [1] be changed to $f = 0.57(D_{50}/r)^{0.574}$, where $D_{50}$ is the median size of gravel bed materials. Lawrence (1997) showed that the friction factor varies linearly with the squared ratio of roughness height to flow depth, i.e. $f \sim (k_s/h)^2$. Ferguson (2007) developed an interpolation between the two different power-law relations, one being Eq. [1] with a slightly different coefficient for deep flows and the other similar to Lawrence's (1997) square relation for shallow flows. All these studies reveal that in the presence of the large-scale roughness, both laboratory and field measurements of the friction factor clearly deviate from predictions by the MS formula. On the other hand, they also demonstrate that the power-law function similar to Eq. [1] can still provide a good representation of measurements for intermediate to large-scale roughness if scale-based adjustments are made in the coefficient and exponent (Rickenmann and Recking, 2011).

In the present study, by considering the flow constricted by roughness elements, a simple modification is developed to correct the deviation of the friction factor from the prediction by Eq. [1]. To validate the modification, the friction factors calculated using the modified MS formula are compared with several series of experimental data for both pipe and open channel flows subject to large-scale roughness.

## 2 MODIFIED MANNING-STRICKLER FORMULA

To modify the MS formula for the case of large-scale roughness, flows through rough pipes are first considered. Nikuradse (1933) pioneered such experiments with sand-roughened pipes, of which the relative roughness height can be described by the ratio of the grain diameter $k_s$ to the pipe diameter D. Nikuradse's experiments were completed for $k_s/D$ in the range of 0.001 to 0.033, which was small so that cross section constriction due to the roughness was negligible. In comparison, for large-scale roughness, $k_s/D$ becomes large and the flow was obviously constricted by roughness elements. Such constrictions should be taken into account in the calculation of the friction factor.

Figure 1 shows a schematic of a pipe of diameter D being roughened with a single layer of grains of diameter $k_s$. Because of the roughness elements, the effective pipe diameter reduces from D to $D_e$. The two pipe diameters are related as follows:

 

$$D_e = D - 2k_s + 2\delta \quad [2]$$

where $\delta$ is the surface displacement from the crest of roughness elements to the virtual pipe wall.

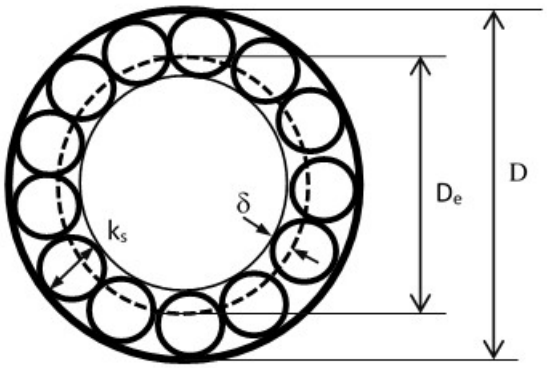


**Figure 1**. Constriction of cross section in the presence of boundary roughness elements

Since it quantifies the average depression due to the irregular surface of roughness elements, $\delta$ can be considered small in comparison to $k_s$ for closely packed sand grains. To some extent, this displacement is very similar to the zero-plane displacement, which was used to define the so-called theoretical bed level for the logarithmic velocity profile applied to rough walls. Einstein and El-Samni (1949) reported that the theoretical bed level was $0.2k_s$ below the crest of roughness elements. Other studies also showed similar displacements, which vary in the range of $0.15k_s$ to $0.35k_s$ with an average of $0.25k_s$, as summarized by Bayazit (1976). In the following analysis, this zero-plane displacement will be adopted and $\delta$ will be taken to be $mk_s$ where $m = 0.25$.

To estimate the average velocity of the flow through the effective cross section of diameter $D_e$, the mass of fluid flowing through the porous space near the wall is assumed to be relatively small. Hence, the flow rate remains when the pipe diameter reduces from D to $D_e$, which yields

$$V_e/V = (D/D_e)^2 \quad [3]$$

where $V_e$ is the average flow velocity calculated based on $D_e$. As a result, the friction factor f can be expressed as

$$f = 2gDS/V^2 = (2gD_eS/V_e^2)\,(D/D_e)^5 \quad [4]$$

where g is the gravitational acceleration. By defining an effective friction factor $f_e$ as

$$f_e = 2gD_eS/V_e^2 \quad [5]$$

f can be further expressed as

$$f = f_e\,(D/D_e)^5 \quad [6]$$

Since V is calculated according to the pipe diameter D, the corresponding friction factor f describes the resistance to the bulk flow through the pipe. In comparison, $V_e$ is evaluated based on $D_e$ and thus $f_e$ is only associated with the virtual pipe that excludes the roughness elements. If the flow boundary was reasonably adjusted according to the virtual pipe, or $D_e$ will be correctly selected, $f_e$ could be still evaluated using the formula that is already available for flows in the presence of small-scale roughness, for example, Eq. [1]. This idea will be tested in the following section.

## 3 COMPARISONS WITH EXPERIMENTAL DATA

To check if the proposed correction or the resulting formula, Eq. [6], is acceptable, comparisons of calculated flow resistance of large-scale roughness with experimental data were first made for rough pipes, and then for shallow flows over gravel beds.

### 3.1 Turbulent Flow through Rough Pipes

With the consideration presented in the foregoing section, Eq. [1] can be applied to the flow in the core zone of diameter $D_e$, yielding

 

$$f_e = N\,(k_s/r_e)^{1/3} \quad [7]$$

where $r_e = D_e/4$. Then substituting Eq. [7] into Eq. [6], one gets

$$f = N\,(4k_s/D_e)^{1/3}\,(D/D_e)^5 \quad [8]$$

Using Eq. [2] with $\delta = 0.25k$, and taking N = 0.115, Eq. [8] can be rewritten as

$$f = 0.18\,\alpha^{1/3}\,(1\text{-}1.5\alpha)^{-16/3} \quad [9]$$

where $\alpha$ (= $k_s/D$) is the relative roughness height of the pipe. Eq. [9] provides a modified version of the original MS formula, i.e. Eq. [1], to correct the large-scale roughness effect on the flow resistance. In the following, Eq. [9] will be used to calculate the friction factor and then compare with experimental data for pipe flows subject to small to large-scale roughness.

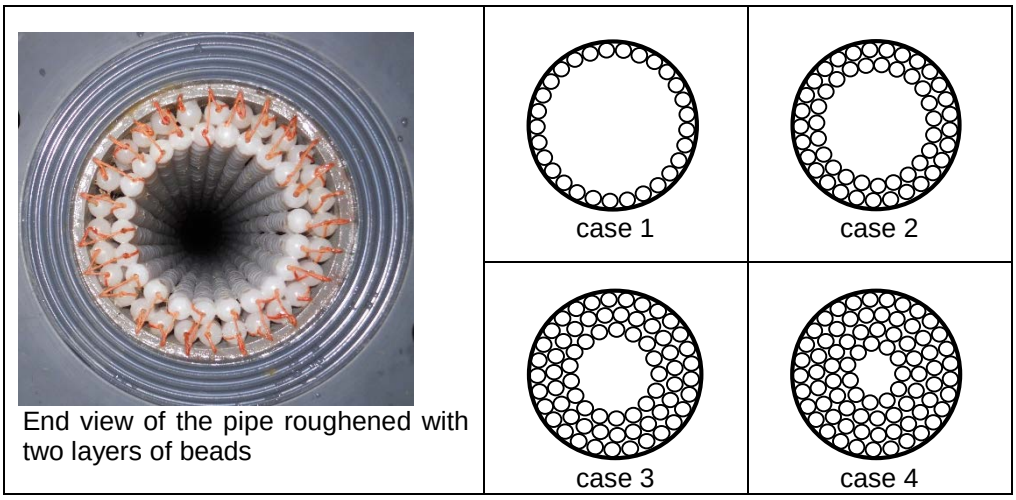


**Figure 2**. Pipes of 100 mm diameter roughened with one to four layers of 10 mm diameter plastic beads

For rough pipes, comparisons were made with three series of experimental data, of which two were collected in this study and the other were reported in the literature (Huang et al., 2013). For each case of the pipe flows, the variation of the friction factor was typically observed for a range of Reynolds numbers. However, in the following comparison, only the friction factors measured for fully rough pipes (independent of the Reynolds number) were used.

In the present study, two different series of experiments were conducted. In the first series, two Perspex pipes (diameter 12 and 24 mm) were roughened with sand grains with diameter of 0.76 mm in an approach similar to Nikuradse's study. The grain size was chosen to be relatively coarse, with $k_s/D$ = 0.032 and 0.063, to enhance wall roughness effects on the pipe flow.

The second series of experiments was different from the first in that four PVC pipes (5 m long and 100 mm in diameter) were roughened with one to four layers of plastic beads (10 mm in diameter), respectively. The cross sections of the four different pipes are shown in Figure 2.

The third series of data used for analysis were reported by Huang et al. (2013). Their data were derived from 11 experiments, of which six were conducted for pipes roughened with natural sand grains and the others for pipes roughened with acrylic spheres. Two sizes of pipes were used in their experiments, and the ratio of grain diameter to pipe diameter varied from 0.0084 to 0.417.

 

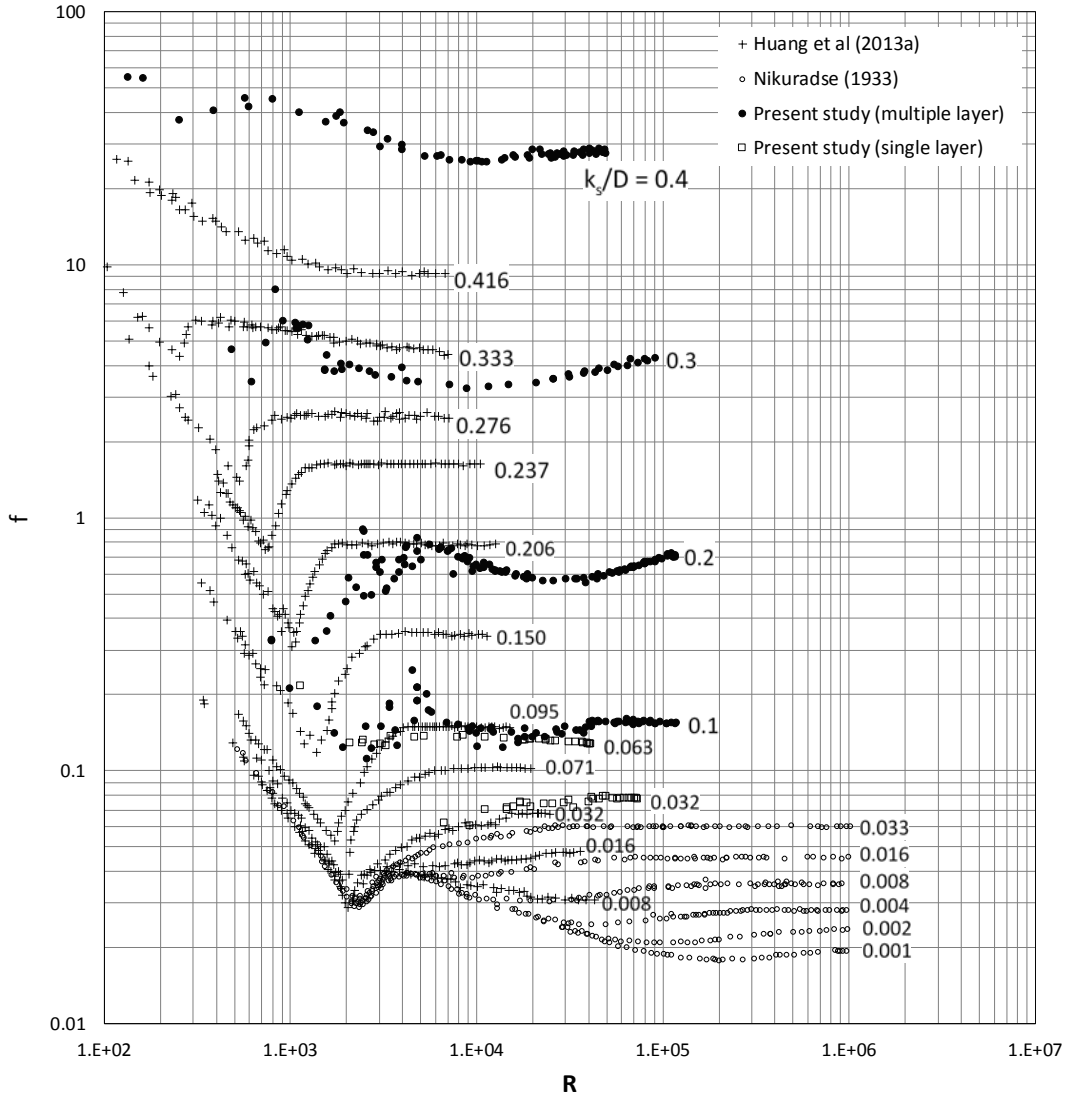


**Figure 3**. Measurements of friction factor for pipe flows subject to small to large-scale roughness

All the three series of data were plotted in Figure 3, together with the measurements by Nikuradse (1933) for small-scale roughness. From Figure 3, it can be observed that for small-scale roughness, the variation of f with **R** may exhibit three typical regimes, i.e. laminar flow, smooth-pipe turbulent flow (**R**-dependent), and rough-pipe turbulent flow (**R**-independent). For large-scale roughness, the smooth-pipe regime disappears, and only the other two regimes occur, i.e. laminar flow and **R**-independent turbulent flow (rough pipe). However, for roughness comprising multiple grain layers, the smooth-pipe regime still exists in the range of large-scale roughness.

The comparison of the calculated f using Eq. [9] with the data, which were measured in (or close to) the **R**-independent rough-pipe regime, is shown in Figure 4. To perform the relevant calculations, the following assumptions are made. First, $\delta$ is taken to be mk with m = 0.25. Second, for the experiments with the multilayer of grain roughness, $k_s$ is taken as the thickness of the boundary roughness, i.e. $k_s$ = id, where i is the number of the bead layer and d is the bead diameter. This is because the bulk flow was constricted by the entire roughness layer. Figure 4 shows that for pipes roughened with the multilayer of grains, the results calculated with $k_s$ = id vary consistently with the others for a single layer of grain roughness.

Both Eqs. [1] and [9] are plotted in Figure 4, in comparison with the data. It can be seen that Nikuradse's data agree well with the MS formula, Eq. [1], was expected for small-scale roughness. When $k_s/D > 0.05$, the measured friction factor increases markedly with increasing $k_s/D$, and deviates clearly from the MS formula. However, the trend line of all the data points, ranging from small to large-scale roughness ($k_s/D$ = 0.001-0.42), can be described satisfactorily using Eq. [9], in spite of its simple form.

 

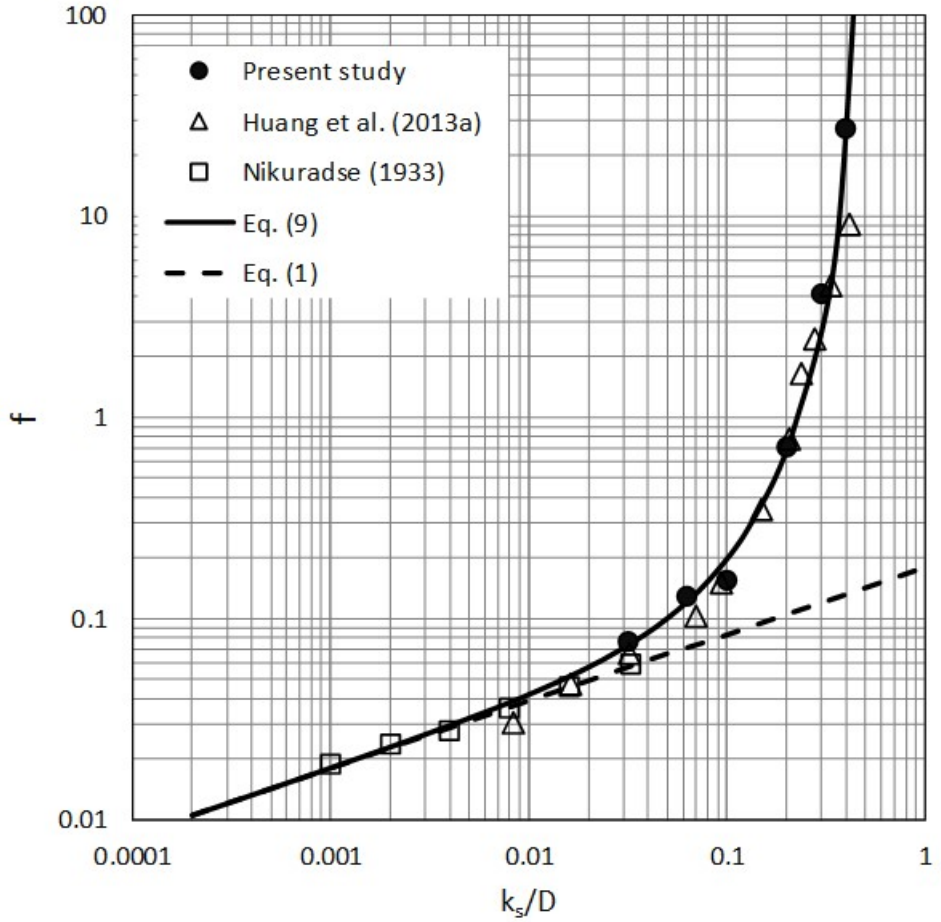


**Figure 4**. Comparison of modified Manning-Strickler formula with **R**-independent rough pipe data for small to large-scale roughness

3.2 Gravel Bed Resistance

The gravel bed resistance can be evaluated using two different methods. As sketched in Figure 5, the boundary roughness elements may comprise of different size of gravels, but their effect on the flow resistance is assumed to be solely described using roughness height $k_s$. Following what had been done for the rough pipes, two kinds of domains were identified for the gravel bed flow. The first was the effective surface domain that is quantified by the usually defined flow depth h. The second was the entire domain including the bed roughness, which is measured as

$$H = h + k_s - mk_s = h + (1 - m)k_s \quad [10]$$

where m = 0.25. Then, the friction factor for gravel beds can be calculated with Eq. [9] by replacing the hydraulic diameter D with 4H (= 4h + 3$k_s$), which yields

$$f = 0.115\beta^{1/3}(1+0.75\beta)^{5}(1+0.375\beta)^{-16/3} \quad [11]$$

where $\beta$ (= $k_s$/h) is the relative roughness height for open channel flows.

 

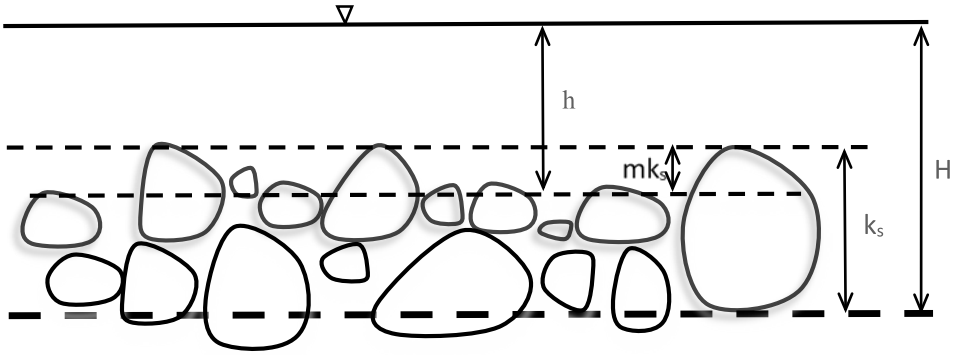


**Figure 5**. Gravel bed channel

In the processing of the experimental data, the roughness height $k_s$ is calculated as a multiple of $D_{84}$ (Cheng, 2016),

$$k_s = \sigma_g^{1.33} D_{84} = \sigma_g^{2.33} D_{50} \qquad [12]$$

where $\sigma_g$ is the geometric standard derivation of grain size distribution. Applicability of Eq. [12] had been discussed by Cheng (2016). The value of $k_s$ calculated using Eq. [12] varies from $2.5D_{84}$ to $4.3D_{84}$ for $\sigma_g$ = 2-3, which generally agrees with field observations for typical gravel beds (Hey, 1979; Whiting and Dietrich, 1990; Ferguson, 2013).

Eq. [11] was plotted in Figure 6, in comparison with 404 sets of laboratory data from five gravel bed studies, Paintal (1971), Bathurst et al. (1981), Ho (1984), Cao (1985) and Recking et al. (2008), which were compiled by Cheng (2015). The value of $k_s$ was calculated using Eq. [12], where $\sigma_g$ is assumed to 1.1 for Ho (1984), who used sieved uniform grains in his experiments but did not report the value of $\sigma_g$. From Figure 6, it can be seen that Eq. [11] is in good agreement with the measurements except for the data of $k_s/h > 1.5$.

In addition to the direct application of Eq. [9], the second approach to estimat the gravel bed resistance can be developed as described subsequently. With reference to Figure 5, the flow depth h is measured as the average distance between the water surface and the top surface of bed roughness. To compare the open channel flow with the rough pipe, it was proposed that the 'solid' channel bottom was virtually situated at H below the water surface, in spite of the fact that the real sediment bed may be much thicker than $k_s$. In a typical laboratory experiment, the flow rate was measured for the water flowing in the surface layer and also through the pores in the top layer of bed roughness, similar to a rough pipe. Therefore, it can be assumed that $VH = V_e h$, where $V_e$ is the average flow velocity defined based on the flow depth h. Here, the mass flowing through the porous bed is considered small in comparison to that in the surface layer.

With the above consideration,

$$f = 8ghS/V^2 = (8ghS/V_e^2)(V_e/V)^2 = f_e(H/h)^2 \qquad [13]$$

where $f_e$ (= $8ghS/V_e^2$) is the friction factor for the effective surface layer of thickness h. Furthermore, by applying Eq. [1] to the surface layer for the completely rough regime, one gets $f_e = N(k_s/h)^{1/3}$. Substituting this and Eq. [10] into Eq. [13],

$$f = N(k_s/h)^{1/3} [\, (h+(1-m)k_s) / h]^2 \qquad [14]$$

By taking m = 0.25 and N = 0.115,

$$f = 0.115\, \beta^{1/3} (1+0.75\beta)^2 \qquad [15]$$

Similar to Eq. [11], Eq. [15] also provides a modified version of the MS formula for open channel flows affected by large-scale roughness. As displayed in Figure 6, Eq. [15] is very close to Eq. [11] for $k_s/h < 1.5$, but provides a better representation of the experimental data for large $k_s/h$.

 

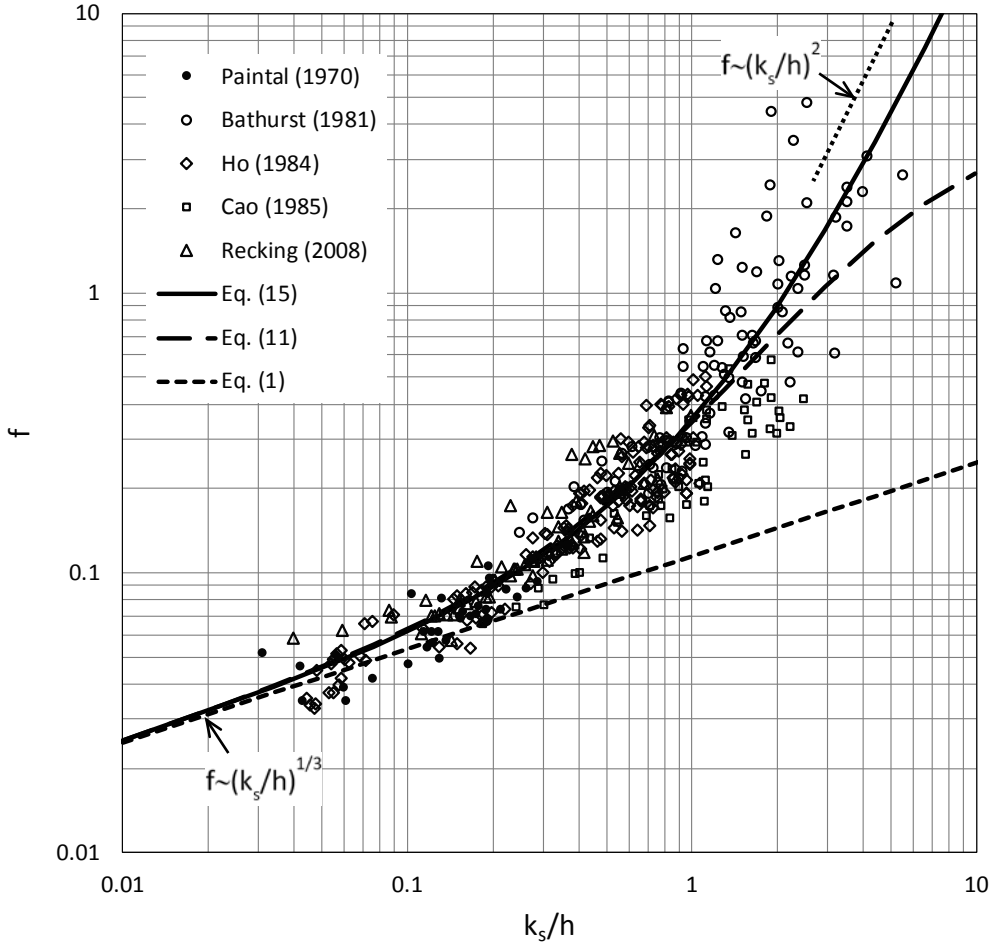


**Figure 6**. Comparison of modified Manning-Strickler formulas with gravel-bed data

Furthermore, as observed from Figure 6, the roughness height may be considered as small-scale if $k_s/h < 0.1$ (where $f \sim (k_s/h)^{1/3}$), the intermediate scale if $k_s/h = 0.1$-1, and large-scale if $k_s/h > 1$ (where $f \sim (k_s/h)^2$). This $k_s$-based categorization could be more rational than that involving particular grain sizes, e.g. $D_{84}$, as proposed by Bathurst et al. (1981).

## 4 CONCLUSIONS

Previous studies have demonstrated that the Manning-Strickler (MS) formula significantly underestimates flow resistance in the presence of large-scale roughness. In this paper, two different modified versions of the MS formula, Eq. [9] and [15], have been derived for pipe and open channel flows, respectively. It is shown that the proposed formulas, which reduce to the original MS formula for small-scale roughness conditions, agree well with the large-scale roughness data, which were either collected in this study or reported in the literature. In the theoretical derivation, two constants, m and N, are involved with pre-set values, and none of them has been tuned to fit the data used. The results imply that the increase in the friction factor in the presence of large-scale roughness can be well explained by the flow constriction due to the roughness elements. It should be mentioned that the seepage through the porous roughness layer may have certain effects on the flow resistance, which is worthy of further considerations.

## ACKNOWLEDGEMENTS

The experiments are conducted in the Hydraulic Laboratory of the School of Civil and Environmental Engineering, Nanyang Technoloical University. The data are collected with the great help of undergraduate students Stephen Franseda Wijaya, Lin Wanxi, Jeslyn Toh Jie Ying, and Richard Widjaja, and technician Lim Kok Hin.

## REFERENCES

Bathurst, J. C., Li, R. M. & Simons, D. B. (1981). Resistance Equation for Large-Scale Roughness. *Journal of the Hydraulics Division-ASCE*, 107(12), 1593-1613.

Bayazit, M. (1976). Free Surface Flow in a Channel of Large Relative Roughness. *Journal of Hydraulic Research*, 14(2), 115-126.

 

Cao, H. H. (1985). Resistance Hydraulique D'un Lit À Gravier Mobile À Pente Raide; Étude Expérimentale. *Ph. D. Thesis*, Ecole PolytechniqueFederale de Lausane.

Cheng, N.-S. (2015). Resistance Coefficients for Artificial and Natural Coarse-Bed Channels: Alternative Approach for Large-scale Roughness. *Journal of Hydraulic Engineering*, 141(2).

Cheng, N.-S. (2016). Representative Grain Size and Equivalent Roughness Height of a Sediment Bed. *Journal of Hydraulic Engineering*, 142(1).

Einstein, H. A. & El-Samni, E. A. (1949). Hydrodynamic Forces on a Rough Wall. *Reviews of Modern Physics*, 21(3), 520-524.

Ferguson, R. (2007). Flow Resistance Equations for Gravel- and Boulder-Bed Streams. *Water Resources Research*, 43(5).

Ferguson, R. (2013). Research-Scale Flow Resistance. *Treatise on geomorphology*, J. F. Shroder, ed., Academic Press, San Diego, 50-68.

Griffiths, G. A. (1981). Flow Resistance in Coarse Gravel Bed Rivers. *Journal of the Hydraulics Division-ASCE*, 107(7), 899-918.

Hey, R. D. (1979). Flow Resistance in Gravel-Bed Rivers. *Journal of the Hydraulics Division-ASCE*, 105(4), 365-379.

Ho, C. M. (1984). Study of Bedload Transport in Turbulent Open Channel Flows. *Ph. D. Thesis*, National Taiwan University, Taiwan.

Huang, K., Wan, J. W., Chen, C. X., Li, Y. Q., Mao, D. F. & Zhang, M. Y. (2013). Experimental Investigation on Friction Factor in Pipes with Large Roughness. *Experimental Thermal and Fluid Science*, 50, 147-153.

Lawrence, D. S. L. (1997). Macroscale Surface Roughness and Frictional Resistance in Overland Flow. *Earth Surface Processes and Landforms*, 22(4), 365-382.

Nikuradse, J. (1933). Stromungsgesetze in Rauhen Rohren. Forschung auf dem Gebiete des Ingenieurwesens, Forschungsheft 361. VDI Verlag, Berlin, Germany (in German). (English translation: *Laws of flow in rough pipes*, NACA TM 1292, 1950).

Paintal, A. S. (1971). Concept of Critical Shear Stress in Loose Boundary Open Channels. *Journal of Hydraulic Research*, 9(1), 91-113.

Recking, A., Frey, P., Paquier, A., Belleudy, P. & Champagne, J. Y. (2008). Bed-Load Transport Flume Experiments on Steep Slopes. *Journal of Hydraulic Engineering-ASCE*, 134(9), 1302-1310.

Rickenmann, D. & Recking, A. (2011). Evaluation of Flow Resistance in Gravel-Bed Rivers Through a Large Field Data Set. *Water Resources Research*, 47.

Whiting, P. J. & Dietrich, W. E. (1990). Boundary Shear Stress and Roughness Over Mobile Aluvial Beds. *Journal of Hydraulic Engineering-ASCE*, 116(12), 1495-1511.

Yen, B. C. (1992). Dimensionally Homogeneous Manning formula. *Journal of Hydraulic Engineering-ASCE*, 118(9), 1326-1332.

Yen, B. C. (1993). Dimensionally Homogeneous Manning formula - Closure. *Journal of Hydraulic Engineering-ASCE*, 119(12), 1443-1445.

 

# LINEAR STABILITY ANALYSIS ON BED CONFIGURATION OF SOFT ROCK PARTIALLY COVERED WITH SEDIMENT

KEIGO IMORI[(1)] & YASUHARU WATANEBE[(2)]

[(1,2)] Kitami Institute of Technology, Kitami, Japan,
m1652200021@std.kitami-it.ac.jp

## ABSTRACT

When the layer of soft rock which exists under a gravel bed is exposed at river beds, the degradation speed of bed becomes very high. In recent years, river structures have been become unstable due to erosion of soft rock bed. A linear stability analysis is conducted for understanding the bed shape of soft rock rivers. The stability analysis in this paper reproduces the bed configuration of soft rock partially covered with sediment. It is found that the wavelength of the bed configuration of soft rock partially covered with sediment becomes long compared with the wavelength of an alternate bar.

**Keywords**: Soft rock; gravel; sediment; bed configuration; stability analysis.

## 1 INTRODUCTION

In recent years, river structures have been become unstable due to erosion of soft rock bed. When the layer of soft rock which exists under a gravel bed is exposed at river beds, the degradation speed of bed becomes very high. As a result, serious problems such as the rise of river dike and insufficient rooting of bridge piers occurred.

Figure 1 is a bridge where the foundation has been exposed by the erosion of the soft rock because the sand gravel layer of the surface layer is lost.

**Figure 1**. A bridge where the foundation has been exposed by the erosion of the soft rock because the sand gravel layer of the surface layer is lost.

Soft rock has a certain hardness, but it is weak against collisions by gravel sands. It is characteristic of soft rock to be easily eroded deeply and locally when riverbed composed of soft rock is eroded by concentration of water and sediment. For this reason, further local erosion may progress at the time of flooding.

In order to take countermeasures, it is necessary to get to know the scouring characteristic of a soft rock bed. A linear stability analysis is conducted for understanding the bed shape of soft rock rivers.

In recent years, many researches on soft rock scouring have been carried out, but the shape of the riverbed appearing during soft rock scouring has not been sufficiently clarified. Based on date of the reproduction experiment of soft rock erosion using steel channel (Sumner et al., 2016), a linear stability analysis is conducted for understanding the bed shape of soft rock rivers.

As a result, this study presents that wavelength of the bed configuration of soft rock partially covered with sediment become infinite. The stability analysis reproduces the feature of the bed form which is a hydraulic experiment result.

In the area of riverbed partially covered with sediment, the erosion phenomenon is partially attenuated due to blocking that prevents collision of sediment to the soft rocks. This mechanism is different from erosion of riverbed fully exposed. Therefore, basing on previous research (Nelson and Seminara, 2012), the stability analysis in this paper reproduces the bed configuration of soft rock partially covered with sediment.

 

## 2 COVER RATIO

Basing on previous model (Nelson and Seminara, 2012), we used a ratio of sediment to examine. However, we supposed in this paper that elevation difference results from only the erosion of soft rock.

Average sediment depth is defined as the ratio of a volume of a monolayer of sediment over the area of the bed. It varies between 0.0 and a maximum $\widetilde{e_m}$ ($\widetilde{e_m}$ is defined as $\tilde{e}$ when the bed is completely covered). If we assumed the sediment to be consisted of spheres of a uniform diameter $\widetilde{d_s}$, then $\widetilde{e_m} = C\,\widetilde{d_s}\,\pi/6$ (we used ~ superscripts to denote dimensional variables). A dimensionless areal concentration is expressed by the ratio of areal concentration to maximum. Such as dimensionless areal concentration means equal cover ratio sediment on riverbed.

$$e = \tilde{e} / \tilde{e}_m = C \qquad [1]$$

Therefore, it may be distinguished; ①a fully exposed bedrock surface ($C$ = 0) ②partially exposed bedrock surface (0 <$C$< 1) ③an alluviated bed ($C$ = 1). Figure 2 shows the pattern diagram of our model.

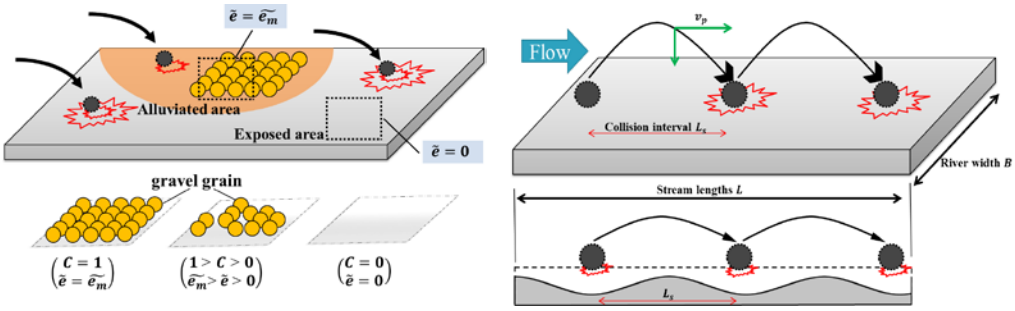


**Figure 2**. Outline of Model.

## 3 SALTATION MODEL

We used the relationship that the erosion volume of soft rock $\widetilde{W_S}$ is proportional to the collision energy (Ishibashi, 1983) for this analysis.

$$\tilde{W}_S = \tilde{\gamma}\sum\left(\tilde{W}\frac{\tilde{v}_p^2}{2\tilde{g}}\right) \qquad [2]$$

where, $\widetilde{W_S}$ is erosion volume of soft rock, $\tilde{\gamma}$ is damage modulus, $\widetilde{W}$ is total weight of sediment, $\widetilde{v_p}$ is collision velocity, $\tilde{g}$ is gravitational acceleration.

Also, $\widetilde{W_S}$ is represented as a product of $\tilde{D}$, $\tilde{L}$ and $\tilde{B}$.

$$\tilde{W}_S = \tilde{D}\tilde{L}\tilde{B} \qquad [3]$$

And, these equations can be organized as Eq. [4]:

$$\tilde{D} = \tilde{\gamma}\sum\left(\tilde{W}\frac{\tilde{v}_p^2}{2\tilde{g}}\right)\frac{1}{\tilde{L}\tilde{B}} \qquad [4]$$

A gravel sand collides $T_S$ time for each $\widetilde{L_S}$ meters, while $\tilde{L}$ in meters.

$$T_S = \frac{\tilde{L}}{\widetilde{L_S}} \qquad [5]$$

Number of sand can be represented as function of $\widetilde{q_b}$, $\tilde{T}$, $\tilde{B}$ and $\widetilde{d_S}$.

$$N = \frac{\tilde{q}_b\tilde{T}\tilde{B}}{\tilde{d}_S^3\pi/6} \qquad [6]$$

 

Total number of collision is represented in Eq. [7] from Eq. [5] and Eq. [6].

$$\sum T_S = \frac{\tilde{q}_b \tilde{T} \tilde{B}}{\tilde{d}_S^3 \pi / 6} \frac{\tilde{L}}{\tilde{L}_S} \quad [7]$$

The total weight of gravel can be obtained by using the weight $\tilde{w}$ per unit gravel.

$$\tilde{W} = \frac{\tilde{q}_b \tilde{T} \tilde{B}}{\tilde{d}_S^3 \pi / 6} \frac{\tilde{L}}{\tilde{L}_S} \tilde{w} \quad [8]$$

The erosion depth of soft rock is obtained in Eq. [9] from Eq. [4] and Eq. [8].

$$\tilde{D} = \tilde{\gamma} \sum \left( \frac{\tilde{q}_b \tilde{T} \tilde{w}}{\tilde{d}_S^3 \pi / 6 \tilde{L}_S} \frac{\tilde{v}_p^2}{2\tilde{g}} \right) \quad [9]$$

We supposed in this paper that elevation difference results from only the erosion of soft rock. Elevation difference is expressed in Eq. [10] from Eq. [9].

$$\frac{\partial \tilde{\eta}}{\partial \tilde{t}} + (1-C)\tilde{\gamma} \frac{s\tilde{\rho}}{2} \frac{\tilde{q}_b \tilde{v}_p^2}{\tilde{L}_S} = 0 \quad [10]$$

where, $\tilde{\eta}$ is elevation of river bed, $\tilde{t}$ is time, $C$ is cover ratio gravel on riverbed, $\tilde{\gamma}$ is parameter of degradation, $\tilde{s}$ is water specific gravity of gravel (=1.65), $\tilde{\rho}$ is density of gravel, $\widetilde{q_b}$ is transport rate, $\widetilde{v_p}$ is speed at which the stream of quicksand, $\widetilde{L_S}$ is collision interval of quicksand.

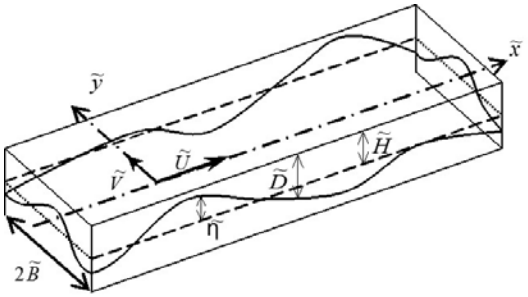


**Figure 3**. Coordinate system.

## 4 CALCULATION MODEL

Basic equations; the 2-dimensional shallow-water equations excluding diffusion term in a straight rectangular channel with constant width (Figure 4), equation of continuous flow, equation of continuous sediment, are shown in Eq. [11] ~ Eq. [14].

$$\frac{\partial \tilde{u}}{\partial \tilde{t}} + \tilde{u} \frac{\partial \tilde{u}}{\partial \tilde{x}} + \tilde{v} \frac{\partial \tilde{u}}{\partial \tilde{y}} + \tilde{g} \frac{\partial \tilde{H}}{\partial \tilde{x}} + \frac{\tilde{\tau}_x}{\tilde{\rho} \tilde{D}} = 0 \quad [11]$$

$$\frac{\partial \tilde{v}}{\partial \tilde{t}} + \tilde{u} \frac{\partial \tilde{v}}{\partial \tilde{x}} + \tilde{v} \frac{\partial \tilde{v}}{\partial \tilde{y}} + \tilde{g} \frac{\partial \tilde{H}}{\partial \tilde{y}} + \frac{\tilde{\tau}_y}{\tilde{\rho} \tilde{D}} = 0 \quad [12]$$

$$\frac{\partial \tilde{D}}{\partial \tilde{t}} + \tilde{u} \frac{\partial (\tilde{u} \tilde{D})}{\partial \tilde{x}} + \frac{\partial (\tilde{v} \tilde{D})}{\partial \tilde{y}} = 0 \quad [13]$$

$$\frac{\partial \tilde{e}}{\partial \tilde{t}} + \left( \frac{\partial \tilde{q}_{bx}}{\partial \tilde{x}} + \frac{\partial \tilde{q}_{by}}{\partial \tilde{y}} \right) = 0 \quad [14]$$

where, $\tilde{t}$ is time, $\tilde{x}$,$\tilde{y}$ are coordinates in the downstream and cross stream directions, respectively, $\tilde{u}$,$\tilde{v}$ are the components of the velocity vector in the $\tilde{x}$ and $\tilde{y}$ directions, respectively, $\tilde{H}$ is water surface elevation, $\tilde{D}$ is water depth, $\widetilde{\tau_x}$, $\widetilde{\tau_y}$ are the shear stresses, $\widetilde{q_{bx}}$,$\widetilde{q_{by}}$ are the transport rates of sediment, $\tilde{e}$ is average sediment

 

depth, $F_r$ is Froude number, $\tilde{s}$ is water specific gravity of gravel, $\tilde{\eta}$ is elevation of river bed (we used 0 subscripts to denote coefficient in uniform flow, $\tilde{x}$ and $\tilde{y}$ subscripts to denote variables in the $\tilde{x}$ and $\tilde{y}$ directions, respectively).

The dimensionless equation used in this paper is as follows:

$$\begin{gathered}(x,y)=(\tilde{x},\tilde{y})/\tilde{D}_0,(u,v)=(\tilde{u},\tilde{v})/\tilde{u}_0\\ D=\tilde{D}/\tilde{D}_0\ ,\ H=\tilde{H}/(F_{r0}^2\tilde{D}_0)\\ \eta=\tilde{\eta}/\tilde{D}_0,\gamma=\tilde{\gamma}\tilde{\alpha}_0\\ F_{r0}=\tilde{u}_0/(\tilde{g}\tilde{D}_0)^{1/2}\\ (q_{bx},q_{by})=(\tilde{q}_{bx},\tilde{q}_{by})/(s\tilde{g}\tilde{d}_S^3)^{1/2}\\ (\tau_x,\tau_y)=(\tilde{\tau}_x,\tilde{\tau}_y)/(\tilde{\rho}\tilde{u}_0^2)\ ,\ v_p=\tilde{v}_p/\tilde{u}_0\\ L_S=\tilde{L}_S/\tilde{D}_0\ ,\ t=\tilde{t}\tilde{u}_0/\tilde{B}\end{gathered} \quad [15]$$

According to above equations, Eq. [10]~Eq. [14] shows Eq. [16]~Eq. [20].

$$\frac{\partial u}{\partial t}+u\frac{\partial u}{\partial x}+v\frac{\partial u}{\partial y}+\frac{\partial H}{\partial x}+\beta\frac{\tau_x}{\tilde{D}}=0 \quad [16]$$

$$\frac{\partial v}{\partial t}+u\frac{\partial v}{\partial x}+v\frac{\partial v}{\partial y}+\frac{\partial H}{\partial y}+\beta\frac{\tau_y}{D}=0 \quad [17]$$

$$\frac{\partial D}{\partial t}+\frac{\partial(uD)}{\partial x}+\frac{\partial(vD)}{\partial y}=0 \quad [18]$$

$$\frac{\pi}{6}\frac{\partial e}{\partial t}+\frac{\beta\sqrt{sd_S}}{F_{r0}}\left(\frac{\partial q_{bx}}{\partial x}+\frac{\partial q_{by}}{\partial y}\right)=0 \quad [19]$$

$$\frac{\partial\eta}{\partial t}+(1-C)\frac{R\gamma}{F_{r0}}(sd_S)^{3/2}\frac{q_b v_p^2}{L_S}=0 \quad [20]$$

where, $\beta$ is ratio of width and water depth in uniform flow ($=\tilde{B}/\widetilde{D_0}$), $R$ is dimensionless parameter that depends on kinematic energy of flow and unconfined compression strength of soft rock ($=\tilde{\rho}\widetilde{u_0}^2/(2\widetilde{\alpha_0})$).

Expand ($\tilde{u},\tilde{v},\tilde{H},\tilde{D},\tilde{C}$) to coefficient in uniform flow and perturbation variables using perturbation parameter ε.

$$(u,v,H,D,C)=(1,0,H_0,1,C_0)+\varepsilon(u_1,v_1,h_1,d_1,C_1) \quad [21]$$

where

$$(u_1,v_1,h_1,d_1,C_1)=(S_{y1}\hat{u}_1,C_{y1}\hat{v}_1,S_{y1}\hat{h}_1,S_{y1}\hat{d}_1,S_{y1}\hat{C}_1)E_1 \quad [22]$$

where $E_1=\exp\{\mathrm{i}[\lambda_r x-\omega t]\}$、$S_{y1}=\sin(ny\pi/2)$、$C_{y1}=\cos(ny\pi/2)$.

According to that $\omega$ is complex number, real part means angular frequency, imaginary part means time amplification factor.

Event promotes when $\omega_i$ has positive value and event decreases when $\omega_i$ has negative value. $\lambda_r$ is wavelength of the bed configuration of soft rock in the downstream ($\lambda_r=2\pi\tilde{B}/\widetilde{L_S}$). According to Eq. [16]~Eq. [22], Eq. [23] is obtained about one-dimensional order.

$$\begin{pmatrix}f_{11}&f_{12}&f_{13}&f_{14}&f_{15}\\ f_{21}&f_{22}&f_{23}&f_{24}&f_{25}\\ f_{31}&f_{32}&f_{33}&f_{34}&f_{35}\\ f_{41}&f_{42}&f_{43}&f_{44}&f_{45}\\ f_{51}&f_{52}&f_{53}&f_{54}&f_{55}\end{pmatrix}\begin{pmatrix}\hat{u}_1\\ \hat{v}_1\\ \hat{h}_1\\ \hat{d}_1\\ \hat{C}_1\end{pmatrix}=0 \quad [23]$$

 

$f_{11} \sim f_{55}$ is as follows.

$$(f_{11}, f_{12}, f_{13}, f_{14}, f_{15}) = \left( i\lambda_r + \frac{2\beta C_{f0}}{1-C_T}, 0, i\lambda_r, \beta C_{f0}\left(\frac{C_H}{1-C_T} - 1\right), \beta C_{f0}\frac{C_H}{1-C_T} \right) \quad [24]$$

$$(f_{21}, f_{22}, f_{23}, f_{24}, f_{25}) = \left( 0, i\lambda_r + \beta C_{f0}, \frac{1}{2}\pi n, 0, 0 \right) \quad [25]$$

$$(f_{31}, f_{32}, f_{33}, f_{34}, f_{35}) = \left( i\lambda_r, -\frac{1}{2}\pi n, 0, i\lambda_r, 0 \right) \quad [26]$$

$$\begin{aligned}
f_{41} &= 2R_2\beta q_0 \frac{C_0(1-C_0)}{1-C_T}\left(F_T + \frac{\tau_0}{\tau_0 - \tau_{cr}}\right) \\
f_{42} &= 0 \\
f_{43} &= -i\omega F_{r0}^2 \\
f_{44} &= i\omega + R_2\beta q_0 C_0(1-C_0)\left(F_H + \frac{C_H}{1-C_T}\left(F_T + \frac{0.1\tau_0}{\tau_0 - \tau_{cr}}\right)\right) \\
f_{45} &= R_2\beta q_0(1-2C_0) + R_2\beta q_0 C_0(1-C_0)\left(\frac{C_C}{1-C_T}\left(F_T + \frac{0.1\tau_0}{\tau_0 - \tau_{cr}}\right) - \frac{1-k_r}{2k_{r0}}\right)
\end{aligned} \quad [27]$$

$$\begin{aligned}
f_{51} &= 2iF_{rs}\lambda_r q_0 C_0 \frac{F_T}{1-C_T} \\
f_{52} &= -\frac{1}{2}\pi n F_{rs} q_0 C_0 \\
f_{53} &= \frac{1}{4}\pi^2 n^2 \frac{F_{rs} r r q_0 C_0}{\beta\sqrt{\tau_0}} \\
f_{54} &= iF_{rs}\lambda_r q_0 C_0 \frac{F_T}{1-C_T}\left(F_H + \frac{C_H F_T}{1-C_T}\right) - \frac{1}{4}\pi^2 n^2 \frac{F_{rs} r r q_0 C_0}{\beta\sqrt{\tau_0}} \\
f_{55} &= \frac{\pi}{6} i\omega + iF_{rs}\lambda_r q_0\left(1 + \frac{C_H F_T}{1-C_T} C_0\right)
\end{aligned} \quad [28]$$

where

$$\begin{aligned}
C_T = 0, C_H &= \frac{1}{C_{f0}}\frac{\partial C_f}{\partial H}\bigg|_{H=H_0}, C_C = \frac{\partial C_f}{\partial C}\bigg|_{C=C_0} \\
F_T &= \frac{\tau_0}{q_0}\frac{\partial q_b}{\partial \tau_*}\bigg|_{\tau_*=\tau_0}, F_H = 0, F_C = \frac{1}{q_0}\frac{\partial q_b}{\partial C}\bigg|_{C=C_0}
\end{aligned} \quad [29]$$

Eq. [23] is needed in order to obtain ($u_1$, $v_1$, $h_1$, $d_1$, $C_1$).

$$\begin{vmatrix} f_{11} & f_{12} & f_{13} & f_{14} & f_{15} \\ f_{21} & f_{22} & f_{23} & f_{24} & f_{25} \\ f_{31} & f_{32} & f_{33} & f_{34} & f_{35} \\ f_{41} & f_{42} & f_{43} & f_{44} & f_{45} \\ f_{51} & f_{52} & f_{53} & f_{54} & f_{55} \end{vmatrix} = F(\omega_i, \lambda_r, \beta, \tau_*, d_S) = 0 \quad [30]$$

After $d_S$ and $\tau_*$ are determined, $\omega_i$ depends on ratio of width and depth $\beta$. According to observation of the trend of $\omega_i$ which depends on $\beta$ and $\lambda_r$, we can discuss the shape composed of soft rocks.

## 5 HYDRAULIC CONDITIONS

We used the experimental conditions similar to those by Sumner et al. (Sumner et al, 2016) (Table1). It reported that vertical streaky erosion forms appeared on soft rock bed simulated with mortar. Figure 4 shows the shape of soft rock bed after the experiment.

 

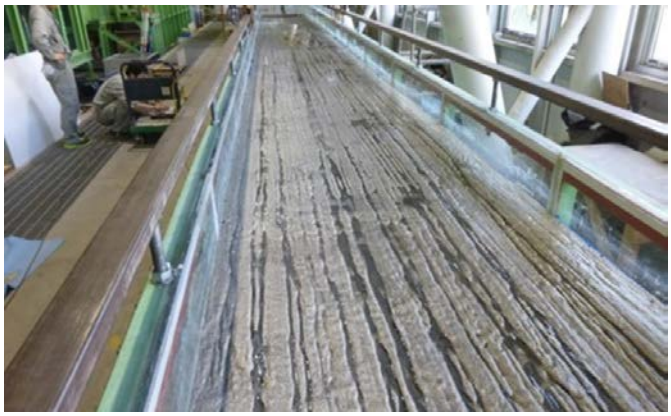

**Figure 4**. Experimental result (Sumner et al, 2016).

**Table 1**. Hydraulic condition.

| | **Condition** |
|---|---|
| **Channel width *B*** | 0.9 [m] |
| **Flow rate *Q*** | 10.0 [L/s] |
| **Depth in uniform flow $D_0$** | 3.0 [cm] |
| **Grain diameter $d_s$** | 1.18 [mm] |
| **Bed slope *I*** | 1/300 |
| **Shields parameter$\tau_*$** | 0.051 |
| **Bed configuration** | Alternate bars |

The transport rate of sediment $q_b$ is calculated as follows:

$$q_b = 8(\tau_* - \tau_{cr})^{3/2} \quad [31]$$

However, we used the component of it in $\tilde{x}$ and $\tilde{y}$ directions.

$$q_{bx} = q_0 + q_0(\frac{\tau_1}{\tau_0}F_T - F_H d_1)\varepsilon$$
$$q_{by} = q_0\left(v_1 - \frac{rr}{\beta}\sqrt{\frac{1}{\tau_0}}\frac{\partial}{\partial y}(F_{r0}^2 h_1 - d_1)\right)\varepsilon \quad [32]$$

A friction coefficient is shown (33).

$$C_f = (6 + 2.5\ln(\tilde{D}/\tilde{k}_t))^{-2} \quad [33]$$

Sklar and Dietrich (2004) assumed that $\widetilde{v_p}$、$\widetilde{L_S}$ are expressed as follow ($\alpha_1$=10, $\alpha_2$=8).

$$\tilde{v}_p \Big/ \sqrt{s\tilde{g}\tilde{d}_S} = \alpha_1\left(\tilde{d}_S/\tilde{k}_t\right)^{1/4}(\tau_* - \tau_{cr})^{0.5}$$
$$\tilde{L}_S \Big/ \tilde{d}_S = \alpha_2(\tau_* - \tau_{cr})^{0.9} \quad [34]$$

Equivalent roughness $\widetilde{k_t}$ takes apart smooth surface part $\widetilde{k_r}$ and rough surface part $\widetilde{k_s}$.

$$\tilde{k}_t = C\tilde{k}_S + (1-C)\tilde{k}_r \quad [35]$$

where $\widetilde{k_t}$= $\widetilde{k_s}$ in alluviated bed ($C$=1).
Sediment transport capacity $\widetilde{q_{bc}}$ is expressed with cover ratio sediment on riverbed, $C$.

$$\tilde{q}_b = C\tilde{q}_{bc} \quad [36]$$

Critical shear stress $\tau_{cr}$ is calculated as follow (Inoue, 2014).

$$\tau_{cr} = \frac{\alpha_1}{\frac{1}{\kappa}\ln\left(30.1\frac{\alpha_* d_s}{k_s}\right)} \quad [37]$$

where

$$\alpha_1 = \frac{2A_3}{0.4A_2}\frac{(\mu_f - \tan\theta)}{(\mu_f + (1/0.85))}\frac{\cos\theta}{0.85} \quad [38]$$

where $\theta$ is bed slope, $\mu_f$ is coefficient of static friction (=0.85), ($\kappa = 0.4, A_2 = \pi/4, A_3 = \pi/6$, $\alpha_* = 0.65$).

According to the experiment using soft rock bed simulated with mortar by Oosawa (2013), we used $\widetilde{\alpha_0}$=76[kN] and $\tilde{\gamma}$=7.256[kgf].

## 6 CALCULATION

### 6.1 Reference experiment (Sumner et al, 2016)

We performed stability analysis of riverbed fully covered with sediment under condition of Table-1, prior to discussion of the bedrock shape. Calculation result is shown as $\omega_i$ contour (Figure 5).

The wavelength of an alternate bar grows when $\omega_i$ has positive value. This suggests that the wavelength of an alternate bar does not appear under $\beta$> 8.

$\omega_i$ mostly developed around $\lambda_r$ = 1.0. Therefore, it predicted that an alternate bar had about $\widetilde{L_S}$ = 2.8m of wavelength from $\lambda_r = 2\pi\tilde{B}/\widetilde{L_S}$ appearing.

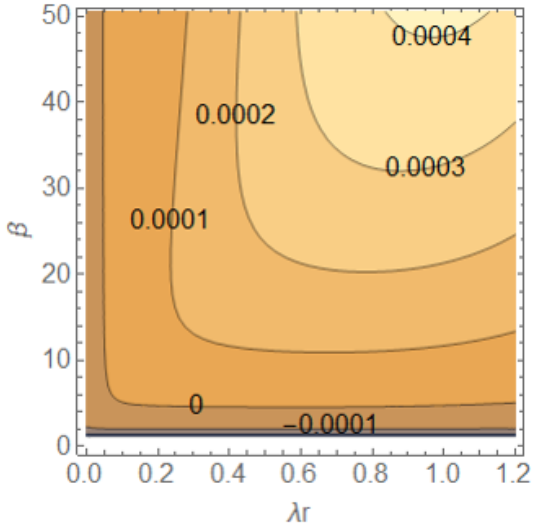


**Figure 5**. Calculation result as $\boldsymbol{\omega_i}$ contour (soft rock bed fully covered with sediment).

### 6.2 Fully exposed case

We performed a liner stability analysis in case of riverbed fully exposed under $d_S$=0.04 and $\tau_0$=0.05. Calculation result is shown as $\omega_i$ contour (Figure 6).

From this contour, $\lambda_r$ most developed placing was at 0.0. According to the wavelength of the bed configuration of soft rock in the downstream $\lambda_r$ which is defined as $\lambda_r = 2\pi\tilde{B}/\widetilde{L_S}$, wavelength of the bed configuration of soft rock fully exposed became infinite. It was found that the soft rock bed was scoured uniformly along the longitudinal direction under the condition in which sediment did not deposit on bed. We suggested that the alteration function to be included as a part of the factors.

 

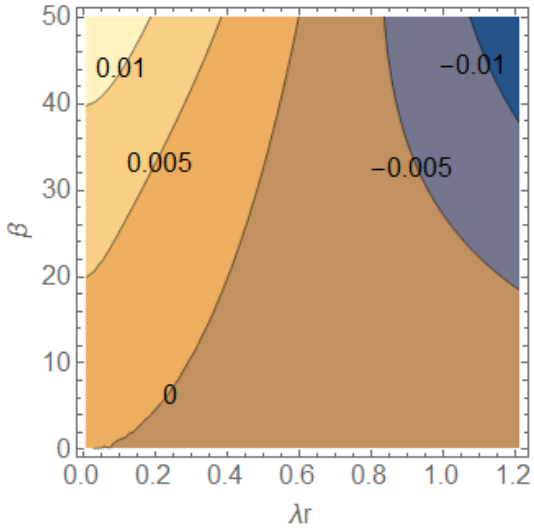


**Figure 6**. Calculation result as $\boldsymbol{\omega_i}$ contour (riverbed fully exposed).

6.3 Partially covered case

Figure 7 shows the calculation result as $\omega_i$ contour based on (23). From this contour, the position of $\lambda_r$ at which $\omega_i$ was the maximum placing was at 0.0. According to $\lambda_r$ which is defined as $\lambda_r = 2\pi\tilde{B}/\widetilde{L_S}$, an alternate bar had about $\widetilde{L_S}$ = 2.8m wavelength from $\lambda_r = 2\pi\tilde{B}/\widetilde{L_S}$ appearing.

Even when wavelength of the bed configuration of soft rock in the cross-stream changes, the position of $\lambda_r$ at which $\omega_i$ is the maximum does not change. It does not depend on wavelength of the bed configuration of soft rock in the cross stream. So, we assumed that the soft rock bed was scoured uniformly along the longitudinal direction under the condition in which sediment did not deposit on bed. It follows from Figure 6 and Figure 7 that it is necessary to have some gravel exist on the riverbed of soft rock in order for bed erosion to have a constant wave.

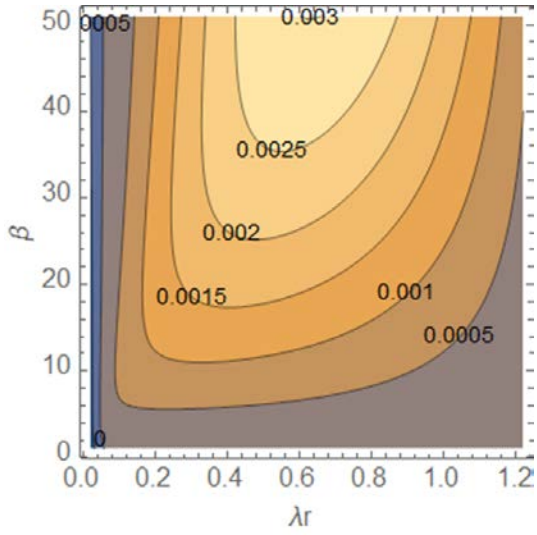


**Figure 7**. Calculation result as $\boldsymbol{\omega_i}$ contour (riverbed partially covered with sediment).

6.4 Influence of hydraulic condition

We examined the effects on the calculation results by varying the conditions used for analysis.

6.4.1 Changing $C_0$

Figure 8 shows the case of calculation result by changing cover ratio in uniform flow from 0.01 to 1.00. The position of $\lambda_r$ at which $\omega_i$ was the maximum changed to smaller when $C_0$ decreased in constant $\beta$. It is similar to the knowledge that wavelength becomes longer as cover ratio becomes smaller.

Maximum value of $\omega_i$ changed to smaller when $C_0$ decreased in constant $\beta$. This means that the transport rate decreased in this study. Therefore, growth rate of riverbed shape decreased with less sediment.

Though there was enough sediment, the results in case of $C_0$=1.0 did not correspond with those in Figure 5. It is expected because this topography does not accord with riverbed shape formed by sedimentation and erosion like sandy gravel bed layer. In this paper, it is thought that only erosion of soft rock occurs as displacement with time of elevation.

 

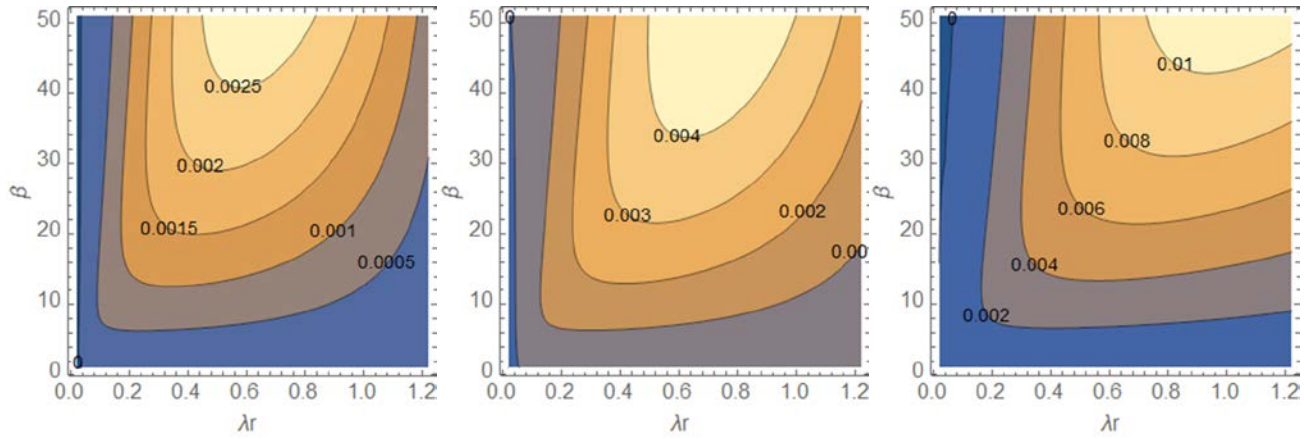


(a) $\boldsymbol{C_0}$=0.01 (b) $\boldsymbol{C_0}$=0.5 (c) $\boldsymbol{C_0}$=1.0

**Figure 8**. Calculation result as $\boldsymbol{\omega_i}$ contour (Changing$\boldsymbol{C_0}$).

6.4.2 Changing $d_S$ and $\tau_0$

Figure 9 shows the case of calculation result by changing the gravel diameter ($d_S$) from 0.02 to 0.06. And, Figure 10 shows the case of calculation result by changing the dimensionless tractive force ($\tau_0$) from 0.03 to 0.07.

When decreasing $d_S$ and $\tau_0$ in constant $\beta$, the position of $\lambda_r$ at which $\omega_i$ was the maximum changed to smaller and maximum value of $\omega_i$ amplified.

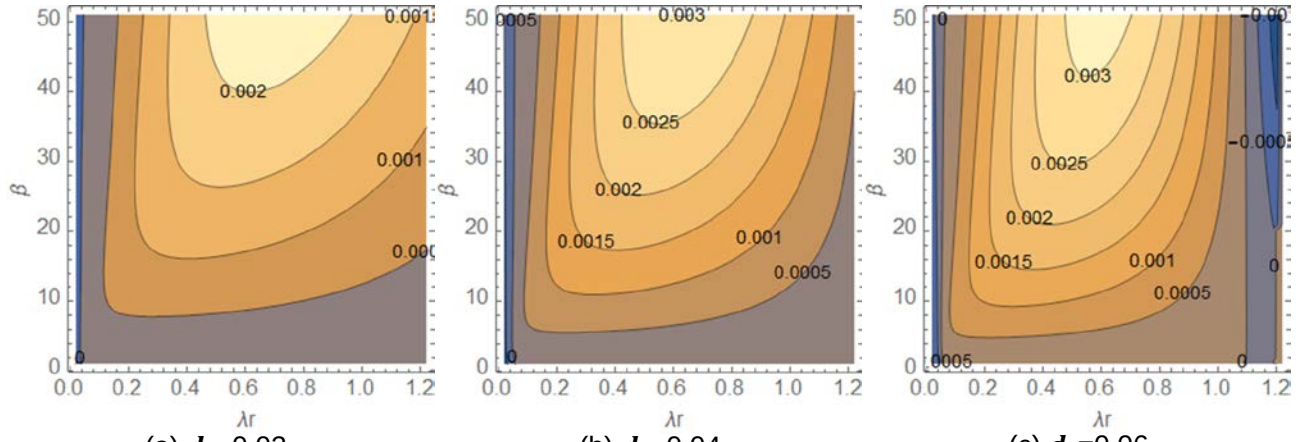


(a) $\boldsymbol{d_s}$=0.02 (b) $\boldsymbol{d_s}$=0.04 (c) $\boldsymbol{d_s}$=0.06

**Figure 9**. Calculation result as $\boldsymbol{\omega_i}$ contour (Changing $\boldsymbol{d_s}$).

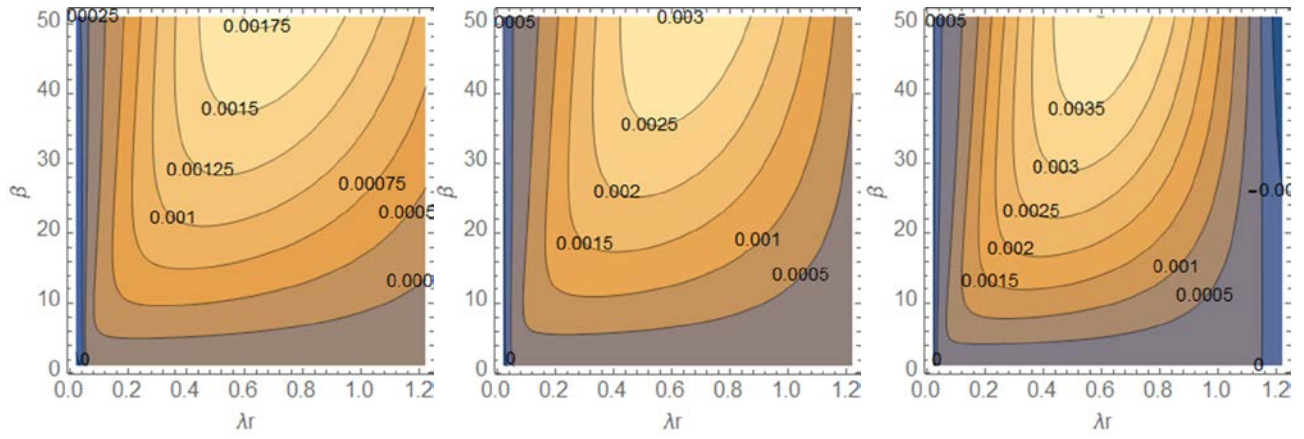


(a) $\boldsymbol{\tau_0}$=0.03 (b) $\boldsymbol{\tau_0}$=0.05 (c) $\boldsymbol{\tau_0}$=0.07

**Figure 10**. Calculation result as $\boldsymbol{\omega_i}$ contour (Changing $\boldsymbol{\tau_0}$).

 

## 7 CONCLUSIONS

We elucidate the formation factor of the riverbed shape using a model considering the distribution of the sediment covering the riverbed under the conditions in the experiment of soft rock erosion by Sumner et al. (2016). As a result, the wavelength of distraction as a factor to form mesoscale bed configurations increases when the cover ratio decreases. This tendency accords with the trend reported in experiments by Yano et al. (2015).

However, we do not consider recovery of riverbed supposing that erosion of soft rock occurs only as displacement with time of elevation.

It is necessary to consider the extent of how sedimentation and erosion affect riverbed shape.

## REFERENCES

Inoue, T., Shimizu, Y., Gray, P., Yamaguchi, S. & Itou, A. (2014). Influence of Sediment Supply on Bedrock Erosional Morphology. *Journal of Japan Society of Civil Engineers, Ser. B1 (Hydraulic Engineering)*, 70(4), I_1039-I_1044, (In Japanese)

Nelson, P.A. & Seminara, G. (2012). *A Theoretical Framework for the Morphodynamics of Bedrock Channels.* Geophysical Research Letters, 39(6).

Oosawa, R., Watanabe, Y. & Yoshikawa, Y. (2014). Scouring of Soft Rock by Collision and Rolling of Gravels. *Proceeding of Hokkaido chapter of JSCE,* 70(B-17). (In Japanese)

Sumner, T., Inoue, T. & Shimizu, Y. (2016). A Study of Sandbar Formation on Bedrock and Bedrock Erosional Morphology. *Annual Journal of Hydraulic Engineering, JSCE* 60, I_817-822. (In Japanese)

Sklar, L.S. & Dietrich, W.E. (2004). A Mechanistic Model for River Incision into Bedrock by Saltating bed Load. *Water Resources Research*, 40(6), 1-22.

Yano, M., Watanabe, Y., Inoue, T., Yamaguchi, S., Watanabe, K., Hirai, Y. (2015). The effect of bedrock cover thickness on free bar morphology in rock bed river. *Journal of Japan Society of Civil Engineers, Ser. B1 (Hydraulic Engineering*), Vol. 71 (4), I_1003-I_1008. (In Japanese).

Zhang, L., Parker, G., Stark, C.P., Inoue, T., Viparelli, E., Fu, X. & Izumi, N. (2015). Macro-Roughness Model of Bedrock-Alluvial River Morphodynamics. *Earth Surface Dynamics*, 3(1), 113.

 

Proceedings of the 37th IAHR World Congress
August 13 – 18, 2017, Kuala Lumpur, Malaysia

# A ROBUST TWO-DIMENSIONAL COUPLED FLOW-SEDIMENT TRANSPORT MODEL BASED ON AN IMPROVED UNSTRUCTURED FINITE VOLUME ALGORITHM

GANGFENG WU[(1)] & KEFENG ZHANG[(2)]

[(1,2)] School of Civil Engineering and Architecture,
Ningbo Institute of Technology, Zhejiang University, Ningbo, China
zjdxwgf@gmail.com; kfzhang@nit.net.cn

## ABSTRACT

A two-dimensional coupled flow-sediment transport model based on a triangular grid is developed to simulate flows over an erodible bed involving wet-dry fronts. In the present study, the shallow water equations that consider the effects of sediment transport and bed change on flow are adopted to calculate bed erosion and sediment transport. The model uses central upwind scheme, which is a type of Riemann-problem-solver-free method for hyperbolic conservation laws which is used to compute mass and momentum flux at interface. The non-equilibrium approach is adopted for the total-load sediment transport. The developed model is capable of being well balanced and preserving the computed water depth to be non-negative, which is important for accurate and efficient simulation of morphological problems. The effectiveness and robustness of proposed model are validated against two sets of experimental data. Results show that the model generally predicts well of the flow characteristics over movable beds, the induced sediment transport and bed changes.

**Keywords:** Central upwind method; bed erosion; sediment transport; shallow water equations; finite volume method.

## 1 INTRODUCTION

Numerical modelling of flood flow involving sediment transport and bed evolution is significant in flood risk management and disaster prevention. In the past decades, depth-averaged two-dimensional (2D) numerical models have been widely used for predicting the water surface, sediment transport and bed evolution(Canelas et al., 2013; Guan et al., 2014; Liu et al., 2016; Murillo and García-Navarro, 2010; Wu et al., 2011; Xia et al., 2010). Because sediment-laden flows are usually in mixed flow regimes and exhibit discontinuities, the numerical schemes often used in depth-averaged 2D models are shock-capturing schemes, such as approximate Riemann solvers and total variation diminishing (TVD) schemes(Toro, 2001).

Nowadays two types of sediment transport model have been presented in the literature. One is local equilibrium capacity model, representative of which is the Shallow-water Exner model(Murillo & García-Navarro, 2010). The limitation of this model is that the sediment transport rate is assumed to be equal to the transport capacity at any time, which introduce inaccuracy due to spatial and temporal lags in the sediment transport's adaptation to local flow conditions(Cao et al., 2007; Phillips and Sutherland, 1989). The other one is non-equilibrium model, which is more appropriate than the capacity model and increasingly adopted in the sediment-laden flows simulation(Canelas et al., 2013; Cao et al., 2007; Guan et al., 2014; Liu et al., 2016; Wu et al., 2011).

In this paper, coupled 2D shallow water hydrodynamic and non-equilibrium sediment transport model has been developed based on the triangular mesh. The model considers the effects of sediment concentration and bed change on the flow and adopts a non-equilibrium transport model for the total-load sediment. The novelty of the proposed model is that Riemann-problem-solver-free central upwind scheme is used to calculate mass and momentum flux at interface and the non-negative water depth reconstruction method proposed by Liang (2010) for Cartesian grids is implemented in our unstructured model to achieve second-order accuracy in space. The developed model is validated against two laboratory experiments of dam break flow over movable bed.

## 2 GOVERNING EQUATIONS

Based on the concept of non-equilibrium sediment transport, the two-dimensional coupled flow-sediment transport mathematical model consisted of the mass and momentum conservation equations for the sediment-laden flow. The mass conservation equations for total sediment load and bed change can be written in a matrix form as follows(Wu, 2008; Wu et al., 2011):

$$\frac{\partial \boldsymbol{q}}{\partial t}+\frac{\partial \boldsymbol{f}}{\partial x}+\frac{\partial \boldsymbol{g}}{\partial y}=\boldsymbol{s_1}+\boldsymbol{s_2} \qquad [1]$$

with

 

$$\boldsymbol{q}=\begin{bmatrix}\eta\\ hu\\ hv\\ hC_t\end{bmatrix},\ \boldsymbol{f}=\begin{bmatrix}hu\\ hu^2+\frac{1}{2}gh^2\\ huv\\ huC_t\end{bmatrix},\ \boldsymbol{g}=\begin{bmatrix}hv\\ huv\\ hv^2+\frac{1}{2}gh^2\\ hvC_t\end{bmatrix},\ \boldsymbol{s_1}=\begin{bmatrix}0\\ -gh\frac{\partial z_b}{\partial x}-g\frac{n^2u\sqrt{u^2+v^2}}{h^{1/3}}\\ -gh\frac{\partial z_b}{\partial y}-g\frac{n^2v\sqrt{u^2+v^2}}{h^{1/3}}\\ 0\end{bmatrix},$$

$$\boldsymbol{s_2}=\begin{bmatrix}0\\ -\frac{1}{2}gh^2\frac{1}{\rho}\frac{\partial\rho}{\partial x}+u\frac{\rho_s-\rho_w}{\rho}(1-\frac{C_t}{1-p_m})\frac{\sqrt{u^2+v^2}hC_t-q_t^*}{L}\\ -\frac{1}{2}gh^2\frac{1}{\rho}\frac{\partial\rho}{\partial y}+v\frac{\rho_s-\rho_w}{\rho}(1-\frac{C_t}{1-p_m})\frac{\sqrt{u^2+v^2}hC_t-q_t^*}{L}\\ -\frac{1}{L}\left(hC_t\sqrt{u^2+v^2}-q_t^*\right)\end{bmatrix}$$

$$\frac{\partial z_b}{\partial t}=\frac{1}{1-p_m}\frac{\sqrt{u^2+v^2}hC_t-q_t^*}{L} \qquad [2]$$

where $\boldsymbol{q}$ = vector of the conserved variables; $\boldsymbol{f}$ and $\boldsymbol{g}$ = vectors of the fluxes; $\boldsymbol{s}_1$ = vector of source term for bed slope and bed friction; $\boldsymbol{s}_2$ = vector of source term related to sediment transport and bed elevation change; $t$ = time; $x$ and $y$ = the space coordinate; $h$ = flow depth; $z_b$ = bed elevation; $\eta$ = water level, $\eta = h + z_b$; $u$ and $v$ = flow velocity in $x$ and $y$ directions; $g$ = gravity acceleration; $\rho$ = density of water and sediment mixture, $\rho = \rho_w(1 - C_t) + \rho_s C_t$; $C_t$ = the volumetric concentration of total-load sediment; $\rho_w$ and $\rho_s$ = density of sediment and water; $n$ = the manning coefficient; $p_m$= the porosity of the bed material; $q_t^*$ = total-load sediment transport capacity, $q_t^* = q_b^* + q_s^*$; $q_b^*$ and $q_s^*$ = the equilibrium bed load and suspended sediment transport rate and $L$ = the non-equilibrium adaption length.

## 3 EMPIRICAL RELATIONS

The non-equilibrium adaptation length $L$ is a characteristic distance for sediment to adjust from a non-equilibrium state to the equilibrium state, which has been investigated by many researchers. Following Wu and Wang (2007) and Wu (2008), it could be determined by

$$L=\max\left(L_b,\frac{h\sqrt{u^2+v^2}}{\alpha\omega_s}\right) \qquad [3]$$

Where $\omega_s$ = settling velocity of the sediment particles, $\omega_s = \omega_{s0}(1 - C_t)^4$; $\omega_{s0}$ = the settling velocity of single sediment particles in quiescent, distilled water, $\omega_{s0} = \sqrt{(13.95\upsilon/d)^2 + 1.09(\rho_s/\rho_w - 1)gd} - 13.95\,\upsilon/d$; d = the diameter of the sediment particles; $\upsilon$ = the kinematic viscosity of water; $L_b$ = the adaption length of bed-load, which is related to the dominant bed form or sediment transport scale; $\alpha$ = adaptation coefficient of suspended-load, which is mostly ranging from 0.25-5.0;

Wu's formula was adopted to calculate the equilibrium sediment transport rates for bed load and suspended load, which are expressed as(Wu, 2008)

$$q_b^*=0.0053\sqrt{(\rho_s/\rho_w-1)gd^3}\,[\left(\frac{d^{1/6}}{20*n}\right)^{3/2}\frac{\tau_b}{\tau_c}-1]^{2.2} \qquad [4]$$

$$q_s^*=0.0000262\sqrt{(\rho_s/\rho_w-1)gd^3}\,[(\frac{\tau_b}{\tau_c}-1)\frac{\sqrt{u^2+v^2}}{\omega_s}]^{1.74} \qquad [5]$$

Where $\tau_b$ = bed shear stress, $\tau_b = n^2(u^2 + v^2)g/h^{1/3}(\rho_s - \rho_w)gd$; $\tau_c$ = the critical bed shear stress for incipient sediment motion, $\tau_c = 0.03(\rho_s - \rho_w)gd$;

## 4 NUMERICAL METHOD

### 4.1 Finite-volume discretization

The whole computational domain is discretized using a number of triangular cells defined as control volumes, as shown in Figure 1. The primary variables$\eta$, $h$, $z_b$, $u$, $v$ and $C_t$ are defined at cell center and represent the average value over the cell.

Integrating Eq. [1] over a triangular control volume $i$ and applying the Green theorem, the following discretized equation is given:

 

$$\frac{\partial \boldsymbol{q}}{\partial t}\Omega + \oint_{\Gamma} \boldsymbol{F}(\boldsymbol{q}) \cdot \boldsymbol{n}\, d\Gamma = \boldsymbol{s_1}(\boldsymbol{q})\Omega + \boldsymbol{s_2}(\boldsymbol{q})\Omega \qquad [6]$$

Where Ω = the control volume i; Γ = the boundary of the control volume i; $\boldsymbol{n}$ = the unit outward normal vector of the boundary Γ; $n_x$ and $n_y$ = the component of $\boldsymbol{n}$ in x and y directions, respectively; $\boldsymbol{F}(\boldsymbol{q}) \cdot \boldsymbol{n}$ = the interface flux, which is expressed as

$$\boldsymbol{F}(\boldsymbol{q}) \cdot \boldsymbol{n} = \boldsymbol{f}n_x + \boldsymbol{g}n_y = \begin{bmatrix} hun_x + hvn_y \\ (hu^2 + gh^2/2)n_x + (huv)n_y \\ (huv)n_x + (hv^2 + gh^2/2)n_y \\ huC_tn_x + hvC_tn_y \end{bmatrix} \qquad [7]$$

Using Euler scheme for the time derivative and replacing the line integral term with an algebraic form, Eq. [6] can be rewritten as

$$\boldsymbol{q}_i^{o+1} = \boldsymbol{q}_i^{o} - \frac{\Delta t}{A_i}\sum_{k=1}^{3} \boldsymbol{F}_{ik}(\boldsymbol{q}) \cdot \boldsymbol{n}_{ik} l_{ik} + \Delta t \boldsymbol{s_1}(\boldsymbol{q}) + \Delta t \boldsymbol{s_2}(\boldsymbol{q}) \qquad [8]$$

Where superscript *o* = the time level; $\Delta t$ = the time step; $A_i$ = the area of the control volume *i*; $l_{ik}$ = the length of *k*th edge of the control volume *i*.

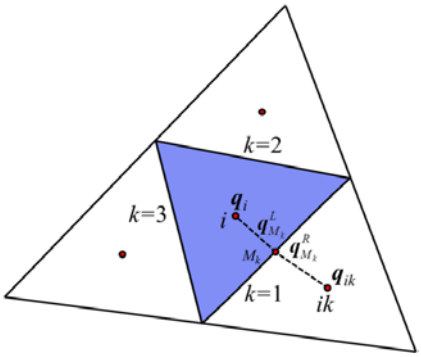


**Figure 1.** The sketch of triangle element

4.2 Non-negative water depth reconstruction

The limited central difference (LCD) scheme(Hubbard, 1999), one of the most widely used limiters, is employed to calculate the variables at the center of the edge to achieve the second-order accuracy in space. Let $M_k$ be the midpoint of the *k*th edge of the cell *i*, *k* = 1, 2, 3 (see Figure 1). Then interface value *q* that is the component of conserved variable $\boldsymbol{q}$ at $M_k$ can be calculated as

$$\bar{q}_{i,M_k} = q_i + \nabla q_i \cdot \boldsymbol{r}_{i,M_k} \qquad [9]$$

Where $q_i$ is the value at the centroid of the cell i. $\boldsymbol{r}_{i,M_k}$ is the position vector of midpoint $M_k$ related to the cell center; $\nabla q_i$ is the limited gradient of the variable q over cell i.

In the framework of Godunov-type scheme, the determination of the interface fluxes requires the values at both sides of the edge. Thus, the left states of the variables at the midpoint $M_k$ can be obtained using Eq. [9]:

$$\begin{gathered} \bar{\eta}^L_{M_k} = \eta_i + \nabla\eta_i \cdot \boldsymbol{r}_{i,M_k} \quad \bar{h}^L_{M_k} = h_i + \nabla h_i \cdot \boldsymbol{r}_{i,M_k} \quad (\bar{z}_b)^L_{M_k} = \bar{\eta}^L_{M_k} - \bar{h}^L_{M_k} \\ (\overline{hu})^L_{M_k} = (hu)_i + \nabla(hu)_i \cdot \boldsymbol{r}_{i,M_k} \quad (\overline{hv})^L_{M_k} = (hv)_i + \nabla(hv)_i \cdot \boldsymbol{r}_{i,M_k} \end{gathered} \qquad [10]$$

Similarly, the right states of the variables at the midpoint $M_k$ can be calculated by

$$\begin{gathered} \bar{\eta}^R_{M_k} = \eta_{ik} + \nabla\eta_{ik} \cdot \boldsymbol{r}_{ik,M_k} \quad \bar{h}^R_{M_k} = h_{ik} + \nabla h_{ik} \cdot \boldsymbol{r}_{ik,M_k} \quad (\bar{z}_b)^R_{M_k} = \bar{\eta}^R_{M_k} - h^R_{M_k} \\ (\overline{hu})^R_{M_k} = (hu)_{ik} + \nabla(hu)_{ik} \cdot \boldsymbol{r}_{ik,M_k} \quad (\overline{hv})^R_{M_k} = (hv)_{ik} + \nabla(hv)_{ik} \cdot \boldsymbol{r}_{ik,M_k} \end{gathered} \qquad [11]$$

In order to obtain the final states, a single value of bed elevation suggested by Audusse et al. (2004) should be defined as

 

$$(z_b)_{M_k} = \max\left\{(\overline{z_b})^L_{M_k}, (\overline{z_b})^R_{M_k}\right\} \quad [12]$$

Then, the reconstructed water depth at the midpoint $M_k$ should be redefined as

$$(h)^L_{M_k} = \max\left\{(\overline{\eta})^L_{M_k} - (z_b)_{M_k}, 0\right\} \quad (h)^R_{M_k} = \max\left\{(\overline{\eta})^R_{M_k} - (z_b)_{M_k}, 0\right\} \quad [13]$$

Obviously, Eq. [13] could ensure the reconstructed water depth to be non-negative. However, the reconstructed water depths may be very small or even zero and lead to local extremely high values of velocity, which might produce negative water depths and affect the stability of the numerical model. In order to prevent this problem, the regularization technique suggested by Kurganov and Petrova (2007) is used to calculate the corresponding velocity components at the midpoint of $M_k$

$$(u)^L_{M_k} = \frac{\sqrt{2}h^L_{M_k}(\overline{hu})^L_{M_k}}{\sqrt{(h^L_{M_k})^4 + \max\{(h^L_{M_k})^4, \varepsilon\}}} \quad (v)^L_{M_k} = \frac{\sqrt{2}h^L_{M_k}(\overline{hv})^L_{M_k}}{\sqrt{(h^L_{M_k})^4 + \max\{(h^L_{M_k})^4, \varepsilon\}}} \quad [14]$$

$$(u)^R_{M_k} = \frac{\sqrt{2}h^R_{M_k}(\overline{hu})^R_{M_k}}{\sqrt{(h^R_{M_k})^4 + \max\{(h^R_{M_k})^4, \varepsilon\}}} \quad (v)^R_{M_k} = \frac{\sqrt{2}h^R_{M_k}(\overline{hv})^R_{M_k}}{\sqrt{(h^R_{M_k})^4 + \max\{(h^R_{M_k})^4, \varepsilon\}}} \quad [15]$$

Where, $\varepsilon$ is an empirically pre-defined positive number with $\varepsilon$ being 10-6 m in all simulations in this paper. It should also be mentioned that $\varepsilon = 10^{-6}$ m is used to distinguish the dry and wet cells. When the water depth at the cell center is less than 10-6 m, the cell is defined as a dry cell and the velocity is set to be zero without solving momentum equations.

4.3 Mass and momentum flux calculation

The Godunov-type central upwind scheme is adopted in this study to calculate mass and momentum fluxes (the first, second and third component of $\boldsymbol{F}(\boldsymbol{q}) \cdot \boldsymbol{n}$) at interface since this scheme is a Riemann-problem-solver-free method with good robustness and accuracy(Kurganov and Petrova, 2007). The interface flux can be calculated as

$$\begin{aligned}\sum_{k=1}^{3} \boldsymbol{F}_{ik}(\boldsymbol{q}) \cdot \boldsymbol{n}_{ik} l_{ik} = &\sum_{k=1}^{3} \frac{l_{ik}(n_x)_{ik}}{a^{in}_{ik} + a^{out}_{ik}} \left[a^{in}_{ik} \boldsymbol{f}\left(\boldsymbol{q}^R_{M_k}\right) + a^{out}_{ik} \boldsymbol{f}\left(\boldsymbol{q}^L_{M_k}\right)\right] \\ &+ \sum_{k=1}^{3} \frac{l_{ik}(n_y)_{ik}}{a^{in}_{ik} + a^{out}_{ik}} \left[a^{in}_{ik} \boldsymbol{g}\left(\boldsymbol{q}^R_{M_k}\right) + a^{out}_{ik} \boldsymbol{g}\left(\boldsymbol{q}^L_{M_k}\right)\right] \\ &- \sum_{k=1}^{3} l_{ik} \frac{a^{in}_{ik} a^{out}_{ik}}{a^{in}_{ik} + a^{out}_{ik}} \left[\left(\boldsymbol{q}^R_{M_k}\right) - \left(\boldsymbol{q}^L_{M_k}\right)\right]\end{aligned} \quad [16]$$

Where $\boldsymbol{q}^L_{M_k}$ and $\boldsymbol{q}^R_{M_k}$ = the reconstructed variables at the left and right side of the midpoint $M_k$, respectively; $a^{in}_{ik}$ and $a^{out}_{ik}$ = the local one sided speeds of wave propagation, given by

$$a^{in}_{ik} = -\min\left\{w^L_{M_k} - \sqrt{g h^L_{M_k}}, w^R_{M_k} - \sqrt{g h^R_{M_k}}, 0\right\} \quad [17]$$

$$a^{out}_{ik} = \max\left\{w^L_{M_k} + \sqrt{g h^L_{M_k}}, w^R_{M_k} + \sqrt{g h^R_{M_k}}, 0\right\} \quad [18]$$

Where $w^L_{M_k}$ and $w^R_{M_k}$ = the normal velocities at the left and right side of the midpoint of $M_k$ is calculated by

$$w^L_{M_k} = u^L_{M_k}(n_x)_{ik} + v^L_{M_k}(n_y)_{ik} \quad [19]$$

$$w^R_{M_k} = u^R_{M_k}(n_x)_{ik} + v^R_{M_k}(n_y)_{ik} \quad [20]$$

4.4 Sediment transport flux and bed deformation calculation

 

The sediment transport flux (the fourth component of $\boldsymbol{F}(\boldsymbol{q})\cdot\boldsymbol{n}$) at cell face is determined by using the first order upwind scheme. The sediment transport flux can be evaluated as

$$\sum_{k=1}^{3}\boldsymbol{F}_{ik}(\boldsymbol{q})\cdot\boldsymbol{n}_{ik}l_{ik}=\sum_{k=1}^{3}l_{ik}\left[\max\left\{\left(hun_x+hvn_y\right)_{ik},0.0\right\}\times(C_t)_i+\min\left\{\left(hun_x+hvn_y\right)_{ik},0.0\right\}\times(C_t)_{ik}\right] \quad [21]$$

where $\left(hun_x+hvn_y\right)_{ik}$ = mass flux through the kth edge of control volume i, which is given by Eq. [16].

The bed deformation is updated at each time step using the following explicit equation:

$$(z_b)^{o+1}=(z_b)^{o}+\frac{\Delta t}{1-p_m}\frac{\sqrt{u^2+v^2}hC_t-q_t^*}{L} \quad [22]$$

4.5 Source term treatment

In order to guarantee the well-balanced property of the model, the bed slope source terms need to be specially treated to exactly balance the numerical flux. A well-balanced slope source term discretization proposed by Bryson et al. (2011) is adopted in this paper. It had been proved to be an effective way to preserve the well-balanced property. Hence, the bed slope source terms are approximated as

$$(gh\frac{\partial z_b}{\partial x})_i=\left[\frac{g}{2\Delta A_i}\sum_{k=1}^{3}l_{ik}\left(h_{M_k}^{L}\right)^2(n_x)_{ik}\right]-g(\eta_x)_i h_i \quad [23]$$

$$(gh\frac{\partial z_b}{\partial y})_i=\left[\frac{g}{2\Delta A_i}\sum_{k=1}^{3}l_{ik}\left(h_{M_k}^{L}\right)^2\left(n_y\right)_{ik}\right]-g(\eta_y)_i h_i \quad [24]$$

where $(\eta_x)_i$ and $(\eta_y)_i$ are the components of the limited gradient of the water level $\eta$ over control volume *i* in x and y direction respectively.

For the treatment of the bed friction source terms, the semi-implicit scheme was more stable than fully explicit scheme. Thus, the bed friction source terms are approximated by the following semi-implicit scheme:

$$g\frac{n^2u\sqrt{u^2+v^2}}{h^{1/3}}=g(\frac{n^2\sqrt{u^2+v^2}}{h^{4/3}})^{o}(hu)^{o+1} \quad [25]$$

$$g\frac{n^2v\sqrt{u^2+v^2}}{h^{1/3}}=g(\frac{n^2\sqrt{u^2+v^2}}{h^{4/3}})^{o}(hv)^{o+1} \quad [26]$$

and then $(hu)^{o+1}$ and $(hv)^{o+1}$ are moved to the left-hand side of Eq. [8].

4.6 Model stability

The numerical scheme is explicit, so the CFL condition should be satisfied to maintain its stability. In this study, the adaptive time step $\Delta t$ is given by

$$\Delta t=C_r\cdot\min_{\substack{i,k\\ i=1,2,\cdots,N\quad k=1,2,3}}\left[\frac{r_{ik}}{\max\{a_{ik}^{out},a_{ik}^{in}\}}\right] \quad [27]$$

Where $\Delta t$ = the time step; $C_r$ = the Courant number specified in the range $0<C_r<1/6$; $C_r=0.15$ is adopted in this paper. $r_{ik}$ = the corresponding altitude of the *k*th edge of the *i*th cell. *N* = the total number of triangle elements in the computational domain. It had been proved that the model could preserve the positivity of the water depth when the time step satisfies Eq. [27] (see Bryson et al. (2011) for mathematical proof).

## 5 NUMERICAL TESTS

In this section, two laboratory experiments were simulated to test the performance of the developed model. All the computational triangular grids were generated using an open grid generation package "Triangle" developed by Shewchuk (1996).

5.1 Dam-break flow in an erodible channel with a sudden enlargement

The experiment of dam break flow in an erodible channel with a sudden enlargement, which was conducted at the laboratory of Université Catholique de Louvain (UCL) in Belgium(Goutiere et al., 2011), is used to test the proposed model. As shown in Figure 2, the experimental flume was 6 m long with a sudden

 

enlargement of width from 0.25 m to 0.5 m at 4 m downstream of the flume inlet. The fixed bed of the flume was covered by 0.1 m thick fully saturated, uniform coarse sand with a median diameter of 1.82 mm. The density of sand was $2.68\times10^3$ kg/m$^3$ and bed porosity was 0.47. A thin gate located at 1 m upstream of the sudden expansion was removed instantaneously to generate dam break flow. The initial water depth before and after the gate, was 0.15 m and 0 m, respectively. Considering the erodible sediment layer with 0.1 m thickness, the initial upstream and downstream water levels were 0.25 m and 0.1 m, respectively.

Eight ultrasonic gauges P1-P8 were placed at downstream of channel to record the time history of the water level, as sketched in Figure 2. The gauges P1, P3, P5 and P7 were aligned along a line at 0.125 m away from the right flume wall (the bottom wall of Figure 3) and located at 0.75, 1.2, 1.45, and 1.95 m downstream of the gate, respectively. The gauges P2, P4, P6 and P8 were aligned along a line 0.125 m away from the left flume wall and located at 1.2, 1.45, 1.95, and 2.45 m downstream of the gate, respectively. At the end of the experiment, bed elevations at nine cross sections cs1-cs9 was located every 5 cm from 10 to 50 cm after the sudden expansion were measured using a laser sheet imaging technique.

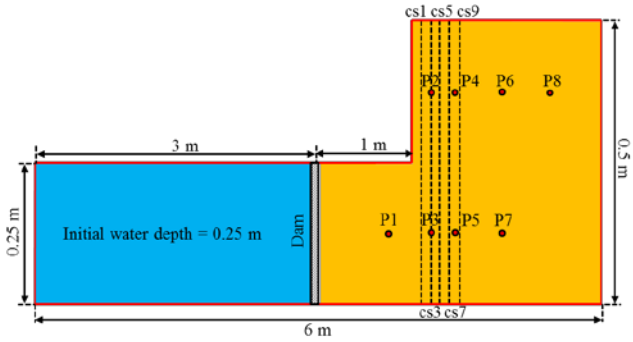


**Figure 2.** Sketch of the UCL dam-break flow experiment setup

For the simulation, the computational domain was discretized by 63397 triangle elements with approximate mean area of $5.0\times10^{-5}$ m$^2$. As suggested by the pioneering simulation work (Wu et al., 2011), the Manning coefficient *n* was set to be 0.025, the calibrated adaption length of bed-load $L_b$ was equal to 0.025 m and the adaptation coefficient of suspended-load $\alpha$ was set to be at 4.0. Figure 3 showed the comparison of the calculated and measured water level at gauges P1, P2, P3, P5, P6 and P7 in a period of 12 s. It can be found the calculated results and it agree with the measurement quite well. The calculated final bed elevation at cross sections cs1, cs2, cs3, cs4 and cs5 was shown in Figure 4. At cross sections cs5, cs7 and cs9, the simulated bed profile by the present model achieved a fairly good agreement with the measured cross section. At cross sections cs1 and cs3, the model reproduced the general trend of morphological change quite well, but slightly underestimated the maximum height of the deposited mound at the expansion zone along the left flume wall.

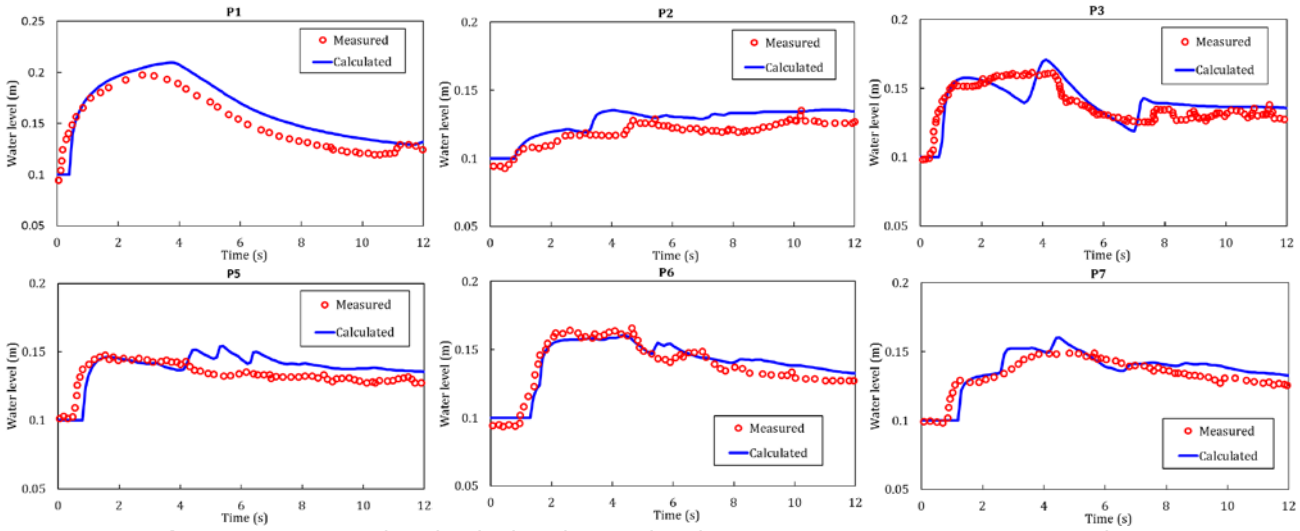


**Figure 3.** Measured and calculated water level at gauges P1, P2, P3, P5, P6 and P7

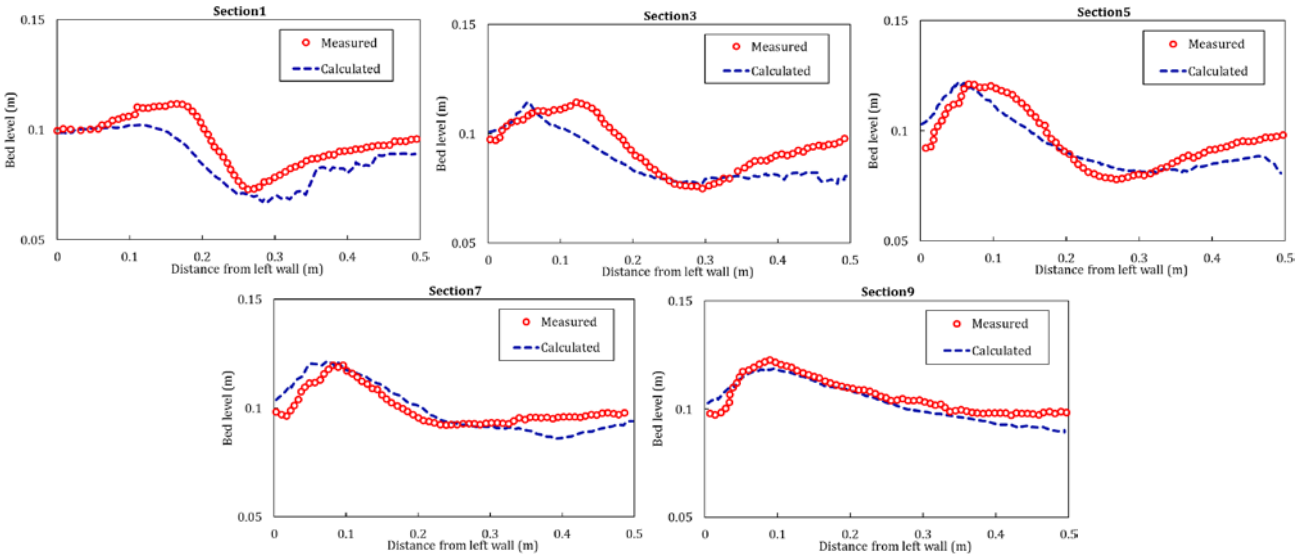


**Figure 4.** Measured and calculated final bed elevation at cs1, cs3, cs5, cs7 and cs9.

5.2 Partial dam-break flow over movable bed in a straight channel

The laboratory experiment of partial dam-break flow over movable bed in a straight channel was performed at UCL-Belgium to investigate the hydrodynamics and morphological evolution (Soares-Frazao et al., 2012). The flume was 3.6 m wide and about 36 m long, as shown in Figure 5. The 1 m wide gate between two impervious blocks was lifted quickly to generate partial dam break flow. The fixed bed of flume was covered by an 85 mm thick sand layer extending from 1.0 m upstream of the gate to 9.0 m downstream of the gate. The fully saturated sand had a medium diameter of 1.61 mm, specific gravity of 2.63, and initial bed porosity of 0.42. The experiment involved both initially wet and dry beds downstream of the gate, but only the dry bed case was simulated here, which was assumed to be more difficult to simulate. The initial water level before the gate was 0.47 m above the fixed bed of the flume. The experiment was stopped at $t$ = 20 s after the lifting of the gate to ensure the dam break wave at the front did not reach the downstream end of flume and avoid the reflection impact from downstream end. As shown in Figure 5, eight ultrasonic gauges were placed at downstream of the gate to measure temporal evolution of water level and bed elevations along three longitudinal sections of y=0.2, 0.7 and 1.45 m, and were measured at the end of experiment.

The whole computational domain was discretized by triangle elements and the meshes in the area covered by the movable sediment were refined, as shown in Figure 6. The total number of triangle elements was 75060. The Manning roughness n was set as 0.0165, which was estimated using the Manning-Strickler formula corresponding to a plain bed. The calibrated adaption length of bed-load $L_b$ was equal to 0.025 m and the adaptation coefficient of suspended-load $\alpha$ was set to be 4.0, which was the same as the previous case. The variable time step was controlled by the CFL restriction and total simulation time was 20 s.

The comparison of calculated and measured stage hydrographs at eight gauges was presented in Figure 7. Due to the symmetrical setup of the experiment, the measured and calculated stage hydrographs at gauges 1 and 4 had the same trend. Similar trends can also be observed between gauges 2 and 3, between gauges 5 and 8, and between gauges 6 and 7. The calculated water levels at gauges 1 and 4 were about 40 cm lower than the measurement, which was also reported by other researchers(Huang et al., 2015; Wu et al., 2011). One of the possible reasons for this deviation was that gauges at 1 and 4 were located at the corners of the sudden expansion of the flume width which also had strong 3D feature which cannot be accurately resolved by the two dimensional depth average hydrodynamic model. For the rest gauges, the calculated stage hydrographs agreed with the measurement quite well.

Figure 8 showed the calculated and measured bed topography at the end of the experiment (t = 20 s). It can be found that intense bed erosion led to a large scouring hole at the downstream of the gate. The eroded sediment deposited at the flume sidewalls where hydraulic jumps occurred and downstream of the scour hole. The main erosion and deposition patterns computed and measured are rather similar, although the calculated scour hole was deeper than the measurement and the measured bed topography is not as symmetric as the computed one. Considering the complexity of the problem, the present model could reproduce morphological evolution generally well. Further quantitative comparison between calculated and measured bed profile along three longitudinal sections (y=0.2, 0.7 and 1.45 m) was presented in Figure 9. The figure included two sets of experimental bed elevation data (Exp1 and Exp2), which was measured using the same experimental setup. The discrepancy between two experiments showed the difficulty of repeating such experiments and it also should be noted that the deviations between calculated and measured bed elevation were in a similar magnitude with the discrepancy of the measured bed elevation among different experiment runs. In this respect, the computed bed elevations were generally in good agreement with the measurements.

 

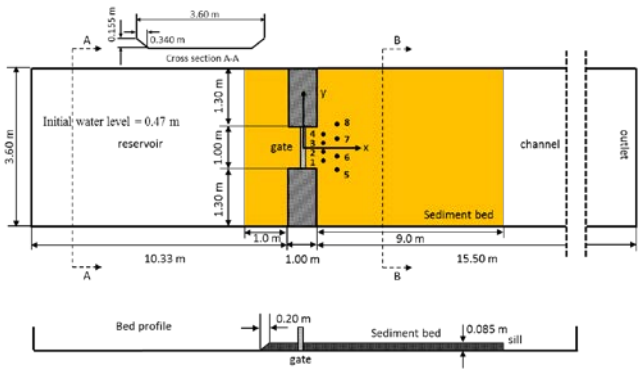


**Figure 5.** Configurations of the UCL partial dam-break experiment

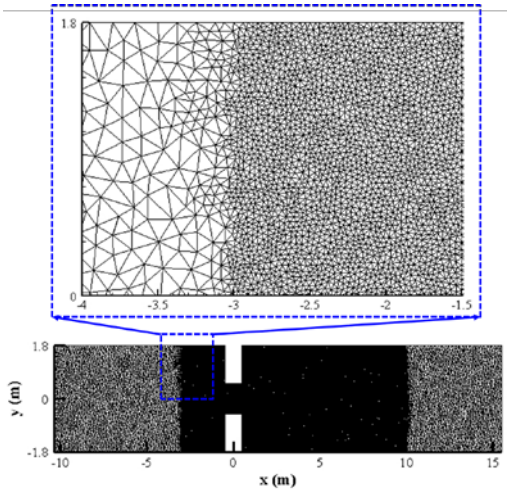


**Figure 6.** Triangle elements near the gate

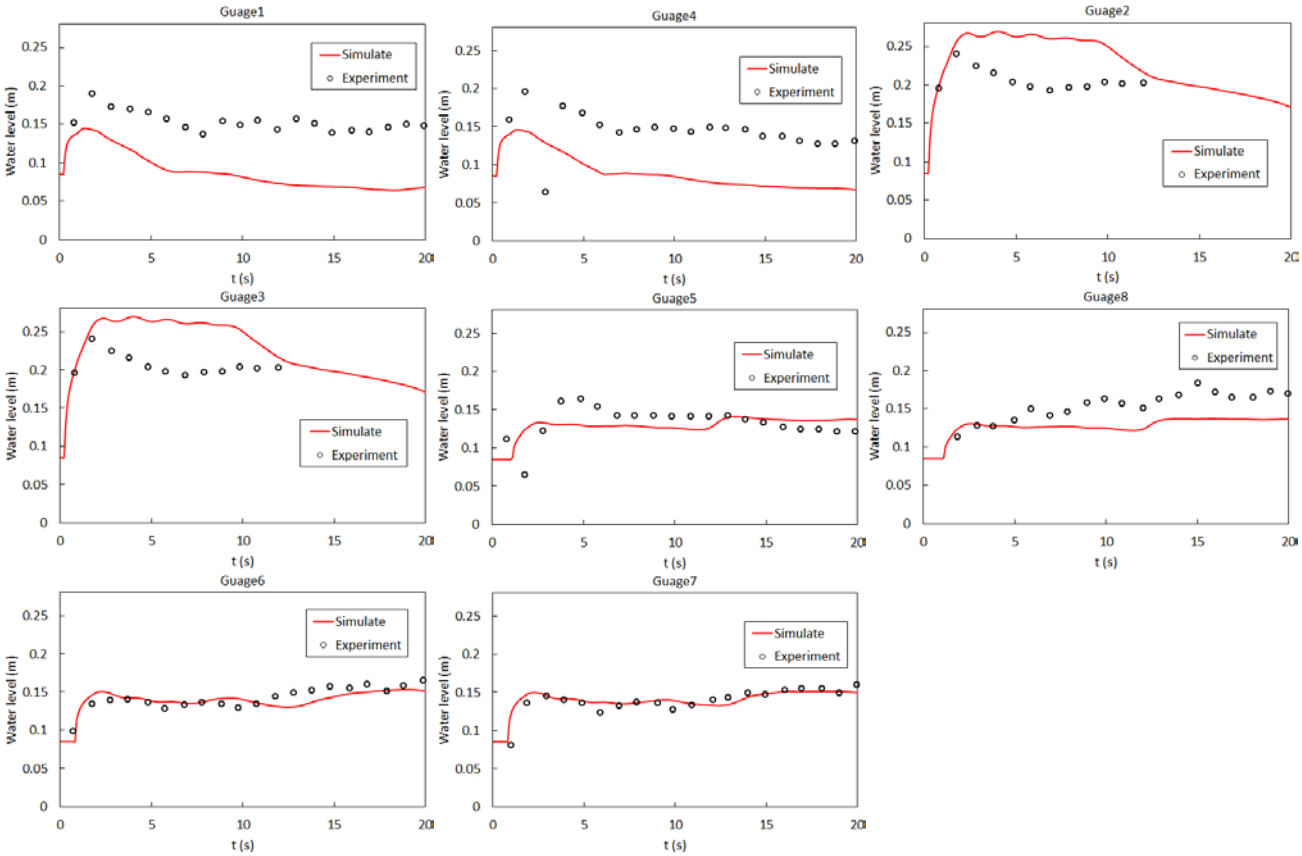


**Figure 7.** Calculated and measured water level at eight gauges

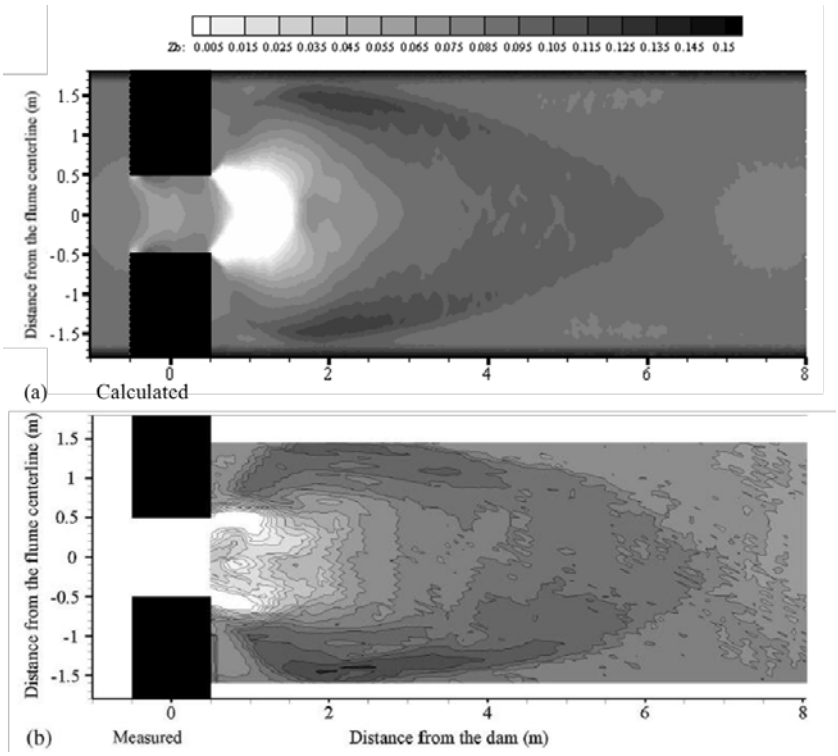


**Figure 8.** Calculated and measured bed topography at $t$ = 20 s

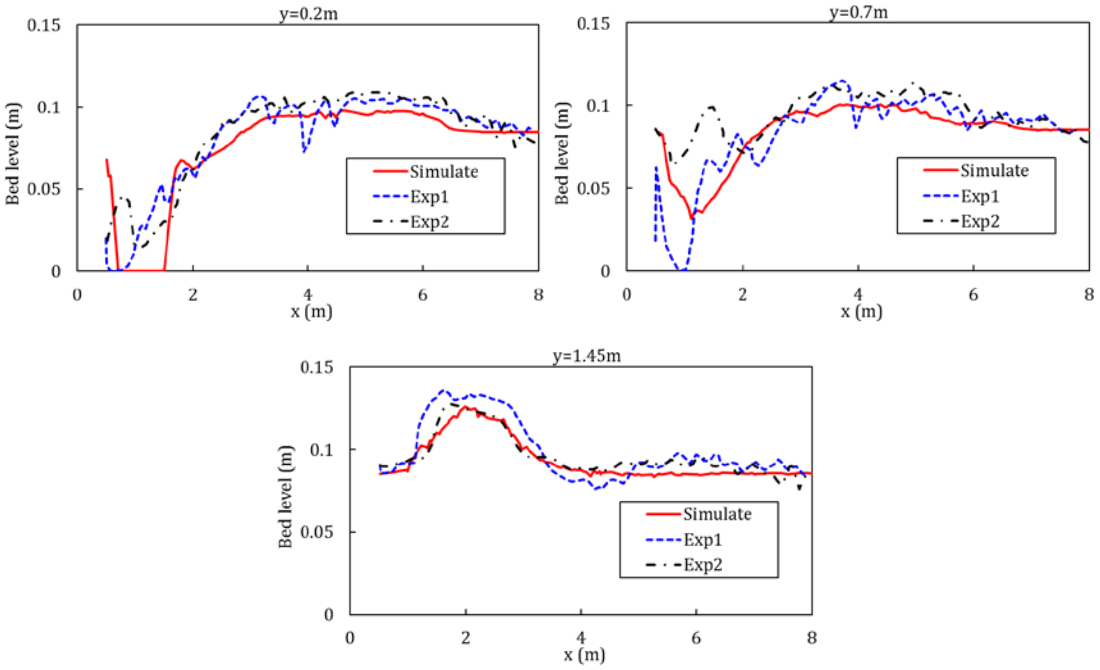


**Figure 9.** Measured and calculated final bed profiles along three longitudinal sections

## 6 CONCLUSIONS

A coupled 2D shallow water hydrodynamic and non-equilibrium sediment transport model has been developed based on the triangle mesh. The governing equations are solved using an explicit finite-volume method with the central upwind scheme to calculate mass and momentum flux at interface. No Riemann problems need to be solved at the central upwind scheme, which makes the central upwind scheme a particularly simple and universal numerical tool for general hyperbolic systems. The model has first-order accuracy in time and second-order accuracy in space. The developed model was validated using two laboratory experiments of dam-break flow over movable bed in a sudden-expanded flume and partial dam-break flow in a straight flume conducted at the UCL, Belgium. The calculated water level and final bed elevation agrees with the measurements quite well, which demonstrate the model is capable of accurately simulating flow-sediment transport events.

 

**ACKNOWLEDGEMENTS**

This work is part of the research project sponsored by the National Basic Research Program of China (973 Program) (No 2013CB035900), Natural Science Foundation of China (51009120), Zhejiang Province Ocean and Fisheries Bureau (2010210), and Zhejiang University (2012HY012B).

**REFERENCES**

Audusse, E., Bouchut, F., Bristeau, M.-O., Klein, R. & Perthame, B. t. (2004). A Fast And Stable Well-Balanced Scheme With Hydrostatic Reconstruction for Shallow Water Flows. *SIAM Journal on Scientific Computing,* 25(6), 2050-2065.

Bryson, S., Epshteyn, Y., Kurganov, A. & Petrova, G. (2011). Well-Balanced Positivity Preserving Central-Upwind Scheme On Triangular Grids For The Saint-Venant System. *ESAIM: Mathematical Modelling and Numerical Analysis*, 45(3), 423-446.

Canelas, R., Murillo, J. & Ferreira, R. M. (2013). Two-Dimensional Depth-Averaged Modelling of Dam-Break Flows Over Mobile Beds. *Journal of Hydraulic Research*, 51(4), 392-407.

Cao, Z., Li, Y., & Yue, Z. (2007). Multiple Time Scales of Alluvial Rivers Carrying Suspended Sediment and Their Implications for Mathematical Modeling. *Advances in Water Resources*, 30(4), 715-729.

Goutiere, L., Soares-Frazão, S. & Zech, Y. (2011). Dam-Break Flow on Mobile Bed in Abruptly Widening Channel: Experimental Data. *Journal of Hydraulic Research*, 49(3), 367-371.

Guan, M., Wright, N. G. & Sleigh, P. A. (2014). 2D Process-Based Morphodynamic Model for Flooding by Noncohesive Dyke Breach. *Journal of Hydraulic Engineering*, 140(7), 04014022.

Huang, W., Cao, Z., Pender, G., Liu, Q. & Carling, P. (2015). Coupled Flood and Sediment Transport Modelling With Adaptive Mesh Refinement. *Science China Technological Sciences*, 58(8), 1425-1438.

Hubbard, M. (1999). Multidimensional Slope Limiters for MUSCL-Type Finite Volume Schemes on Unstructured Grids. *Journal of Computational Physics*, 155(1), 54-74.

Kurganov, A. & Petrova, G. (2007). A Second-Order Well-Balanced Positivity Preserving Central-Upwind Scheme For The Saint-Venant System. *Communications in Mathematical Sciences*, 5(1), 133-160.

Liang, Q. (2010). Flood Simulation Using a Well-Balanced Shallow Flow Model. *Journal of Hydraulic Engineering*, 136(9), 669-675.

Liu, W., He, S. & Xu, Q. (2016). Two-Dimension Coupling Model to Simulate Water Flow, Sediment Transport And Bed Evolution. *Hydrology Research*, nh2016139.

Murillo, J. & García-Navarro, P. (2010). An Exner-Based Coupled Model for Two-Dimensional Transient Flow Over Erodible Bed. *Journal of Computational Physics*, 229(23), 8704-8732.

Phillips, B. C. & Sutherland, A. J. (1989). Spatial Lag Effects in Bed Load Sediment Transport. *Journal of Hydraulic Research*, 27(1), 115-133.

Shewchuk, J. R. (1996). Triangle: Engineering a 2D Quality Mesh Generator and Delaunay triangulator Applied Computational Geometry Towards Geometric Engineering, 203-222, Springer.

Soares-Frazao, S., Canelas, R., Cao, Z., Cea, L., Chaudhry, H.M., Die Moran, A., El Kadi, K., Ferreira, R., Cadórniga, I.F., Gonzalez-Ramirez, N. & Greco, M. (2012). Dam-Break Flows Over Mobile Beds: Experiments and Benchmark Tests for Numerical Models. *Journal of Hydraulic Research*, 50(4), 364-375.

Toro, E. F. (2001). *Shock-Capturing Methods for Free-Surface Shallow Flows*. John Wiley.

Wu, W. (2008). *Computational River Dynamics*, Taylor & Francis London, Vol. 78.

Wu, W., Marsooli, R. & He, Z. (2011). Depth-Averaged Two-Dimensional Model of Unsteady Flow and Sediment Transport due to Noncohesive Embankment Break/Breaching. *Journal of Hydraulic Engineering*, 138(6), 503-516.

Wu, W. & Wang, S. S. (2007). One-Dimensional Modeling of Dam-Break Flow over Movable Beds. *Journal of Hydraulic Engineering*, 133(1), 48-58.

Xia, J., Lin, B., Falconer, R. A. & Wang, G. (2010). Modelling Dam-Break Flows over Mobile Beds Using A 2D Coupled Approach. *Advances in Water Resources*, 33(2), 171-183.

 

Proceedings of the 37th IAHR World Congress
August 13 – 18, 2017, Kuala Lumpur, Malaysia

# EXPERIMENTAL AND NUMERICAL INVESTIGATION OF BED LOAD DUE TO TRIANGULAR FLOOD WAVE PROPAGATION

GÖKÇEN BOMBAR[(1)] & MEHMET ŞÜKRÜ GÜNEY[(2)]

[(1)] İzmir Katip Çelebi University, Civil Engineering Department, İzmir, Turkey,
gokcen.bombar@ikc.edu.tr; sukru.guney@deu.edu.tr

## ABSTRACT

An elaborate experimental system is designed and built in Hydraulics Laboratory of Dokuz Eylul University, in order to study the bed load transport under unsteady flow conditions. Two triangular shaped input hydrographs having same base and peak discharges but different rising limb durations are generated by adjusting the pump rotational speed. The bed load is collected at the downstream end of the channel by means of mobile baskets. The time-varied water depths are measured. The velocity profiles are obtained by using Ultrasonic Velocity Profiler (UVP). The governing equations are numerically solved by using the simplified finite differences technique. The variations of bed elevations, velocities, flow depths and the bed loads collected in baskets are compared with those obtained from the numerical solutions. Different time and space increments are taken into consideration and an error analysis is also performed. The obtained results are evaluated, and an acceptable accordance between experimental findings and numerical results is observed. It is revealed that, the equation given by Engelund and Fredsoe for the calculation of bed load transport is more compatible with the experimental findings.

**Keywords:** Bed load transport; unsteady flows; mobile bed; numerical solution.

## 1 INTRODUCTION

In open channels; the bed load transport under unsteady flow conditions is concerned with continuous interaction between flowing water and sediment particles The sediment transport in unsteady flow conditions has been studied by different researchers (Qu, 2002; Lee et al., 2004; Mrokowska et al., 2016; Waters and Curran, 2016). It was generally intended to correlate the flow parameters to the transported sediment amount. Neverthless, the time lag between the flow and the sediment transport is one of the main issues discussed in literature (Bombar, 2009).

Francalanci et al. (2013) conducted field measurements of bed load, suspended load, flow velocities and water depths during flood events at a monitoring station near the mouth of the Versilia River, Italy. Ferrer-Boix and Hassan (2015) studied the evolution of the surface texture under successive storm events. Spiller et al. (2015) measured the dynamic lift acting on the streambed section of a static armor layer during unsteady flow. They revealed that the magnitude of the lift depends on the initial flow depth, the ramping duration and the total discharge increases. They proposed an adjusted unsteadiness parameter and find out a correlations between the unsteadiness parameter and the measured dynamic lift. Waters and Curran (2015) conducted flume experiments to measure bed morphology adjustments in sediment mixtures during repeated hydrographs and linked these changes to sediment transport patterns over multiple time scales. Orrú et al. (2016) studied experimentally the armor breakup and reformation using a trimodal mixture without sediment supply. An armor formed under partial transport conditions led to an abrupt spatial transition in the bed slope. After an increase in flow rate the armor broke up and a new coarser armor quickly formed. Mrokowska et al. (2016) presented the initial results of laboratory experiments on bed load transport which are performed for hydrographs and revealed a clockwise hysteresis of bed load rate versus flow rate.

In this study, the experiments are carried out on an experimental system, designed and built in Hydraulics Laboratory of Civil Engineering Department of Dokuz Eylul University, in order to study bed load transport in unsteady flow conditions and without sediment feeding from the upstream. The unsteady flow experiments were conducted with two hydrographs having rising durations of 90 seconds and 120 seconds. The water depths were 4.0 cm and 10.4 cm in the case of base flow and peak flow, respectively. The bed load is collected at the downstream end of the channel. The one dimensional partial differential equations for the continuity of water and sediment and the differential momentum equation with diffusive wave assumption are numerically solved by the finite differences scheme developed by Lax. The bed elevations along the channel, the velocity and flow depth variations with time and the bed loads collected in baskets during the experiment are compared with the simplified numerical model solutions considering different time and space increments and an error analysis is also performed to determine the most appropriate one.

 

## 2 EXPERIMENTAL SETUPS

Experimental studies were carried out on an experimental system involving a rectangular flume 80 cm wide and 18.6 m long (Figure 1). The transparent sides of the flume made from acrylic were 75 cm high. The water was circulated continuously. The volume of the water supply reservoir (main tank) was 27 $m^3$. The main tank and rectangular Bazin weir which was used for flow rate measurements were located at the downstream end of the channel. The pump having a maximum capacity of 100 L/s was connected to the pump rotational speed control unit which can control the flow rate by adjusting the settings in order to generate the hydrographs. The experiments were conducted in the flume with a bottom slope of 0.005. The thickness of the mobile bed was 8 cm along the flume. Bed material used in the flume was composed of material with median diameter $D_{50}$ =4.8 mm. The geometric standard deviation was $\sigma_g$ =1.4 mm which implies that the sediment may be assumed as uniform. The porosity, $p$ of the bed layer was 0.5. The velocities were measured by using Ultrasonic Velocity Profiler (UVP) which is manufactured by Met-Flow SA. The velocity profile along the ultrasonic beam axis was measured by detecting the doppler shift frequency. The hydrolysis was used for the generation of the hydrogen bubbles since UVP needs seeding particles for the velocity measurements, like all other ultrasonic instruments. The experimental results of flow depth and velocity were measured at $x$=11m (Bombar, 2009).

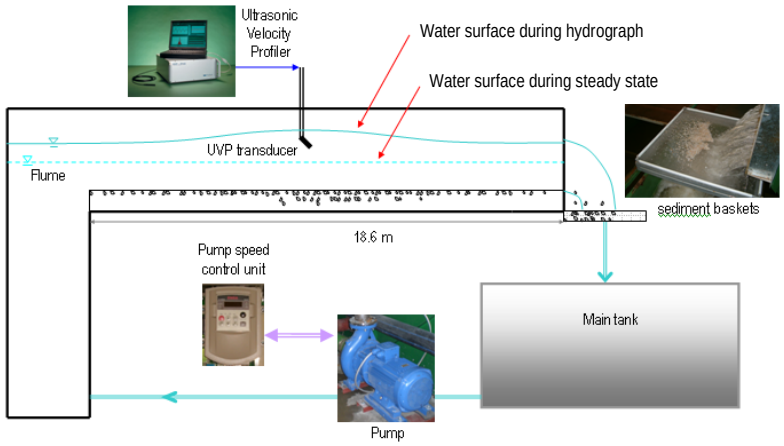


**Figure 1**. The scheme of the experimental system. (Bombar, 2009)

## 3 GOVERNING EQUATIONS OF SEDIMENT TRANSPORT

### 3.1 Differential Equations of One Dimensional Bed Load Transport

The differential equation for the continuity of water is given in equation (1) (Tayfur and Singh, 2006).

$$\frac{\partial h}{\partial t}+\frac{\partial hu}{\partial x}+p\frac{\partial z}{\partial t}=0 \qquad [1]$$

where, $x$ =independent variable representing the coordinate in the longitudinal direction (L), $t$ =independent variable of time (T), $u$ = flow velocity (L/T), $h$ = flow depth (L), $z$ = mobile bed layer elevation (L) and $p$ = porosity of the bed layer ($L^3$ / $L^3$).

The continuity equation for sediment may be expressed as follows (Tayfur and Singh, 2006; Bor, 2008; Mrokowska and Rowiński, 2016):

$$(1-p)\frac{\partial z}{\partial t}+\frac{\partial q_b}{\partial x}=0 \qquad [2]$$

where, $q_b$ =the sediment flux in the movable bed layer ($L^2$ / T) .

The one dimensional partial differential momentum equation of unsteady flow with dynamic wave assumption is (Mrokowska et al., 2015a; 2015b; Bombar, 2016);

$$\frac{\partial u}{\partial t}+u\frac{\partial u}{\partial x}+g\frac{\partial h}{\partial x}+g\frac{\partial z}{\partial x}=-gS_f \qquad [3]$$

where, $S_f$ =the energy slope (L / L), $g$ is the gravitational acceleration (L / $T^2$).

 

If the diffusion wave model which neglects the local acceleration, $\partial u/\partial t$ and convective acceleration, $\partial u/\partial x$ was neglected, then the momentum equation for flow in a rectangular channel may be simulated as:

$$\frac{\partial h}{\partial x}+\frac{\partial z}{\partial x}=-S_f \quad [4]$$

In the scope of this study only one dimensional transport with diffusion wave model was studied numerically. In equations (1), (2) and (4), the unknown parameters are $h$, $u$, $z$, $q_b$ and $S_f$. Therefore, two additional equations needed to be introduced.

The equation (2) requires a relation for the sediment flux in the movable bed layer. The $q_b$ in this equation can be obtained from various empirical equations given by different researchers such as Meyer, Peter and Müller (1948) as in equation (5) and Engelund and Fredsoe (1976) as given in equation (6).

$$q_b = 8\sqrt{\Delta g D_{50}^3}\left(\tau_* - \tau_{*cr}\right)^{3/2} \quad [5]$$

$$q_b = 18.74\sqrt{\Delta g D_{50}^3}\left(\tau_* - \tau_{*cr}\right)\left(\sqrt{\tau_*} - 0.7\sqrt{\tau_{*cr}}\right) \quad [6]$$

where, $\Delta = (\rho_s - \rho)/\rho$, $\rho_s$ and $\rho$ are the densities of sediment and water, $\tau_*$ is the Shields parameter $\tau_* = u_*^2/g\Delta D_{50}$ and $u_*$ is the shear velocity $u_* = \sqrt{ghS_f}$. The critical value of Shields parameter for threshold of sediment inception $\tau_{*cr}$ is taken as 0.047 and 0.05, for equations (5) and (6), respectively.

Manning-Strickler equation was used to express the velocity $u$. If $B$ denotes the channel width;

$$u = \frac{1}{n}\left(\frac{Bh}{B+2h}\right)^{2/3} S_f^{1/2} \quad [7]$$

The Manning roughness coefficient, $n$ was calculated for various steady flow experiments where h was not constant. For compound channels, the Manning roughness coefficient, $n$ may be calculated according to the equation (8) proposed by Lotter (Güney, 2006).

$$n = \frac{2h+B}{\left(\frac{2h}{n_1}+\frac{B}{n_2}\right)} \quad [8]$$

where $n_1$ is the Manning roughness coefficient of the side walls and $n_2$ is the Manning roughness coefficient of the bottom.

### 3.2 Numerical Model

In this study, a finite difference scheme developed by Lax (1954) was used. The partial derivatives and other variables were approximated as follows:

$$\frac{\partial f}{\partial t} = \frac{f_i^{j+1} - 0.5\left(f_{i+1}^{j} + f_{i-1}^{j}\right)}{\Delta t} \quad [9]$$

$$\frac{\partial f}{\partial x} = \frac{f_{i+1}^{j} - f_{i-1}^{j}}{2\Delta x} \quad [10]$$

where, $f$ represents any arbitrary function, $i$=the node number (index) in space, $j$=the node number (index) in time, $\Delta x$ and $\Delta t$ = the distance and time steps, respectively.

The statements so obtained for $h_i^{j+1}$, $u_i^{j+1}$, $S_{f_i}^{j+1}$, $z_i^{j+1}$ and $q_{b_i}^{j+1}$, by using the bed load empirical formula (5) are presented by equations (11) to (15), after neglecting variation of some terms and making some assumptions resulting in the following simple expressions:

 

$$S_{fi}^{j+1} = -\frac{\left(h_{i+1}^{j} - h_{i-1}^{j}\right)}{2\Delta x} - \frac{\left(z_{i+1}^{j} - z_{i-1}^{j}\right)}{2\Delta x} \quad [11]$$

$$z_i^{j+1} = -8\sqrt{\Delta g D_{50}^3}\,\frac{3}{2}\left(\frac{h_i^j S_{fi}^{j+1}}{\Delta D_{50}} - \tau_{cr}^*\right)^{1/2}\left(\frac{S_{fi}^{j+1}}{\Delta D_{50}}\right)\left(\frac{h_{i+1}^j - h_{i-1}^j}{2\Delta x}\right)\frac{\Delta t}{(1-p)} + \frac{\left(z_{i+1}^j - z_{i-1}^j\right)}{2} \quad [12]$$

$$h_i^{j+1} = -\frac{2}{3n}\left(\frac{b+2h_i^j}{bh_i^j}\right)^{1/3}\left[\frac{-2b\left(h_i^j\right)^2}{\left(b+2h_i^j\right)^2} + \frac{5bh_i^j}{2\left(b+2h_i^j\right)}\right]\left(S_{fi}^{j+1}\right)^{1/2}\left(\frac{h_{i+1}^j - h_{i-1}^j}{2\Delta x}\right)\Delta t - p\left[z_i^{j+1} + 0.5\left(z_{i+1}^j + z_{i-1}^j\right)\right] + 0.5\left[h_{i+1}^j + h_{i-1}^j\right] \quad [13]$$

$$u_i^{j+1} = \frac{1}{n}\left(\frac{bh_i^{j+1}}{b+2h_i^{j+1}}\right)^{2/3}\left(S_{fi}^{j+1}\right)^{1/2} \quad [14]$$

$$q_{bi}^{\,j+1} = -8\sqrt{\Delta g D_{50}^3}\left(\frac{h_i^{j+1} S_{fi}^{j+1}}{\Delta D_{50}} - \tau_{cr}^*\right)^{3/2} \quad [15]$$

If the empirical relation (6) given by Engelund and Fredsoe (1976) is used, the expressions of $z_i^{j+1}$ and $q_{bi}^{\,j+1}$ become:

$$z_i^{j+1} = -18.74\sqrt{\Delta g D_{50}^3}\left\{\frac{3}{2}\left(\frac{h_i^j S_{fi}^{j+1}}{\Delta D_{50}}\right)^{1/2} - \tau_{cr}^*\left(\frac{\Delta D_{50}}{4h_i^j S_{fi}^{j+1}}\right)^{1/2} - 0.7\sqrt{\tau_{cr}^*}\right\} * \left(\frac{S_{fi}^{j+1}}{\Delta D_{50}}\right)\left(\frac{h_{i+1}^j - h_{i-1}^j}{2\Delta x}\right)\frac{\Delta t}{(1-p)} + \frac{\left(z_{i+1}^j - z_{i-1}^j\right)}{2} \quad [16]$$

$$q_{bi}^{\,j+1} = 18.74\sqrt{\Delta g D_{50}^3}\left(\frac{h_i^{j+1} S_{fi}^{j+1}}{\Delta D_{50}} - \tau_{cr}^*\right)\left[\left(\frac{h_i^{j+1} S_{fi}^{j+1}}{\Delta D_{50}}\right)^{1/2} - 0.7\sqrt{\tau_{cr}^*}\right] \quad [17]$$

The channel length L was divided into N parts. The length reach becomes $\Delta x$ = L / N. The subscripts of nodes vary from 1 to N+1. $\Delta t$ was selected so that the following Courant condition

$$\Delta t \le \Delta x/(u+c) \quad [18]$$

was satisfied to get a stable numerical solution. In this equation $c$ denotes wave celerity whose expression for the shallow water case is $c = \sqrt{gh}$ .

One begins to calculate the unknown values at $t = \Delta t$ by using the initial values which correspond to $t$=0. As the parameters corresponding to time $t = \Delta t$ become known, the values for $t = 2\Delta t$ can be easily determined from the values corresponding to time $t = \Delta t$. The procedure continues similarly for the subsequent times until the desired time limit was attained.

First $S_{f\,i}^{\,j+1}$ and $z_i^{j+1}$ were calculated from equations (11) and (12) or equations (11) and (16), respectively. The other unknowns were found by substituting these values in related equations.

Initial conditions were specified as $h(x,0) = h_o$, $z(x,0) = z_o$, $u(x,0) = u_o$, $q_b(x,0) = q_{bo}$, $S_f(x,0) = S_{fo}$, where, the subscript (o) denotes the values at time $t$=0.

 

The upstream boundary condition was specified as input hydrograph, $h(0,t) = h(t)$ given in Figure 2. The input hydrographs used in two experiments had the same base and peak depths but different durations.

The downstream boundary condition was specified as:

$$\frac{\partial h((L,t))}{\partial x} = 0 \qquad (h_{N+1}^{j+1} = h_N^{j+1} \quad \text{for} \quad t > 0.0) \qquad [19]$$

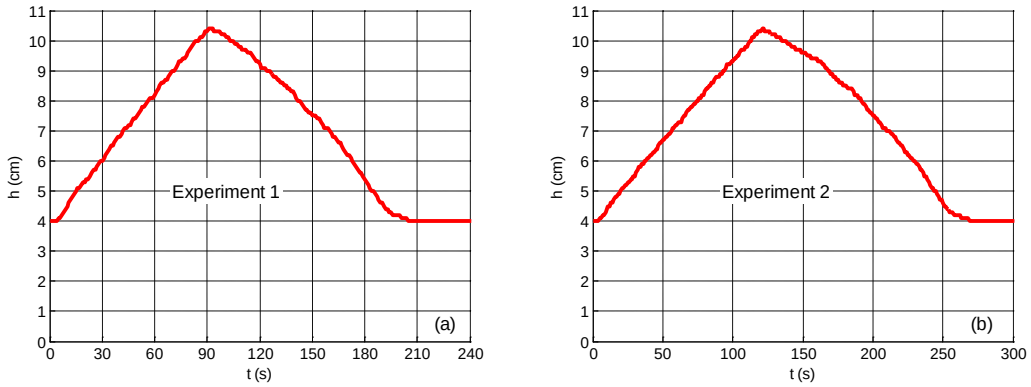


**Figure 2**. The upstream boundary condition (a) Experiment 1, (b) Experiment 2.

## 4 COMPARISON OF NUMERICAL AND EXPERIMENTAL RESULTS

Although numerous hydrographs were generated, the experiments corresponding to the triangle shaped hydrograph having rising limb durations of 90 s and 120 s were given as illustrative examples in order to compare the experimental findings with the numerical model solutions. For these hydrographs, when the water depth $h_o$ = 0.04 m, the velocity $u_o$ is equal to 0.375 m/s. Initially, there was no sediment transport which implies $q_{bo}$ =0, and since the initial water flow was uniform $S_{fo}$ = $S_o$ =0.005. $T_{max}$ was taken as 360 s. The Manning coefficient $n$ was calculated for compound channels according to the equation (8) where $n_1$ is the Manning roughness coefficient of the side walls and it was taken as 0.009, while the Manning roughness coefficient of the sediment layer at bottom, $n_2$ , was taken as equal to 0.023. A new Manning coefficient was calculated for each iteration by using new flow depth values.

The maximum water depth in the experiments was $h_{max}$ =0.104 m which corresponds to a maximum flow velocity of $u_{max}$ =82.5 cm/s. Hence, the Courant condition becomes.

$$\Delta t_{\max} \le \frac{\Delta x}{u_{\max} + \sqrt{g h_{\max}}} = \frac{\Delta x}{0.825 + \sqrt{9.81 x 0.104}} = \frac{\Delta x}{1.86} = 0.53\,\Delta x \qquad [20]$$

The numerical model parameters used for the investigation of effect of time increment $\Delta t$ and distance increment $\Delta x$ are given in Table 1, together with the number of nodes $N_{nodes.}$ In all scenarios the Courant criterion was satisfied. The empirical formulas (equations 5 and 6) related to bed load were used for each of the scenario. The effect of time increment $\Delta t$ was investigated within the scenarios A1, A2 and A3. In order to investigate the effect of distance increment, the channel was divided into 10, 19 and 38 parts giving for $\Delta x$ at 0.5m, 1m and 1.9m, respectively (Scenarios B1, A2 and B3). The effect of both $\Delta t$ and $\Delta x$ was investigated in the scope of the scenarios C1, A2 and C3.

**Table 1**. Numerical model parameters for the investigation of effect of time and space increments.

| Scenario | A1 | A2 | A3 | B1 | B3 | C1 | C3 |
|---|---|---|---|---|---|---|---|
| $\Delta t$ (s) | 0.01 | 0.1 | 0.2 | 0.1 | 0.1 | 0.01 | 0.01 |
| $\Delta x$ (m) | 1 | 1 | 1 | 0.5 | 1.9 | 0.5 | 1.9 |
| $N_{nodes}$ | 20 | 20 | 20 | 39 | 11 | 39 | 11 |
| $N_{parts}$ | 19 | 19 | 19 | 38 | 10 | 38 | 10 |
| $\Delta t_{\max}$ | 0.50 | 0.50 | 0.50 | 0.50 | 0.50 | 0.25 | 0.95 |

The bed elevations, the velocity and flow depth variations and the bed loads collected in baskets were compared with those obtained from the numerical model solution. The criteria considered for error calculation were the root mean square error (RMSE) and mean absolute error (MAE) whose expressions are as follows:

$$RMSE = \sqrt{\frac{1}{N}\sum_{i=1}^{N}\{f_M(i) - f_C(i)\}^2} \quad [21]$$

$$MAE = \frac{1}{N}\sum_{i=1}^{N}\left|f_M(i) - f_C(i)\right| \quad [22]$$

The $f_M$ is any parameter obtained from the experiments (such as $h$, $u$ and $g_b$), $f_H$ is the parameter calculated by the numerical model, $N$ is number of data. The $g_b$ is defined as the product $\rho g\, q_b$. The errors calculated by equations (21) and (22) were normalized by the peak value of the experimental data in order to make the values dimensionless. In the case of the first experiment, the normalized MAE values of r $h$, $u$ and $g_b$ for different scenarios and by using the equations (5) and (6) are given in Figure 3.a and 3.b, respectively. The normalized MAE values concerning the experiment 2 are given in Figure 4.a and 4.b. The normalized RMSE values for $h$, $u$ and $g_b$ were in similar tendency, thus they are not depicted here because of the space limitation.

The parameters studied in scenario A1 with equation (6) were likely to give the minimum error. For experiment 1, the velocity variations with time at the section $x$=11m from the entrance are given in Figure 5.a, while the flow depth variations versus time at the same section are illustrated in Figure 5.b, The numerical results related to $g_b$ (gr/m/s) are presented in Figure 5.c, together with the experimental findings. The similar results corresponding to the second experiment are given in Figure 5.d, 5.e and 5.f.

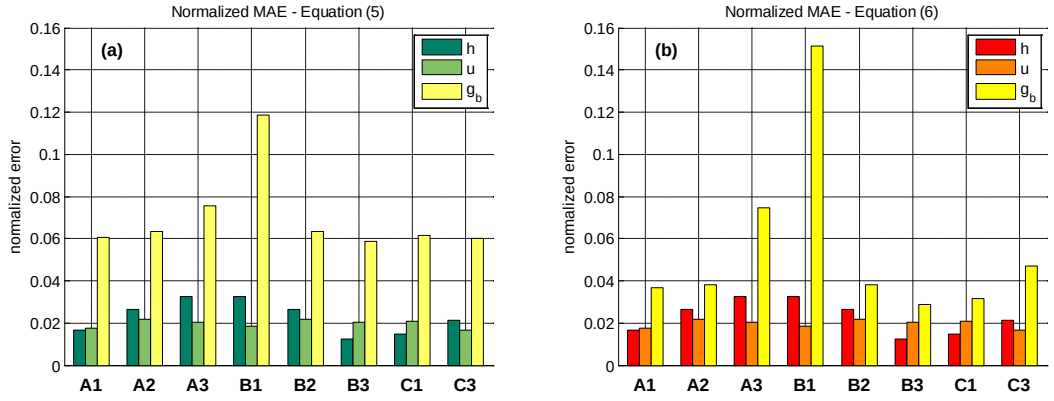


**Figure 3**. The MAE values of $h$, $u$ and $g_b$ in the case of different scenarios for experiment 1, by using (a) equation (5), (b) equation (6).

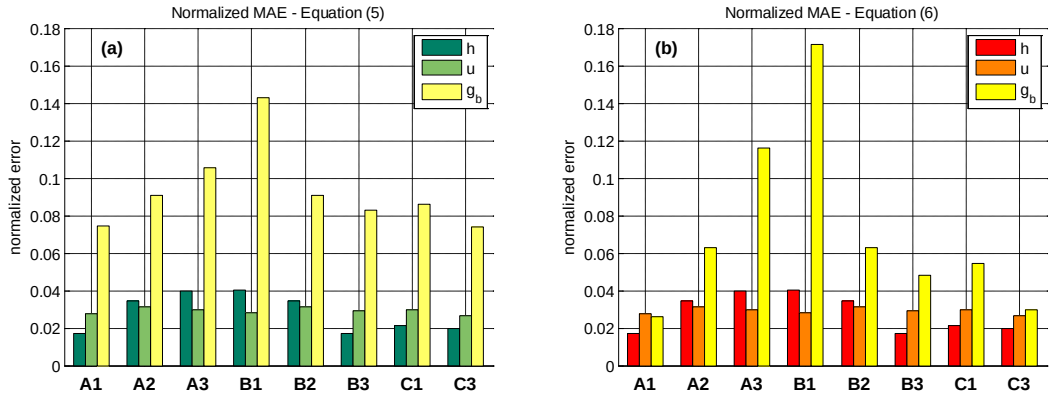


**Figure 4**. The MAE values of $h$, $u$ and $g_b$ in the case of different scenarios for experiment 2 by using (a) equation (5), (b) equation (6).

 

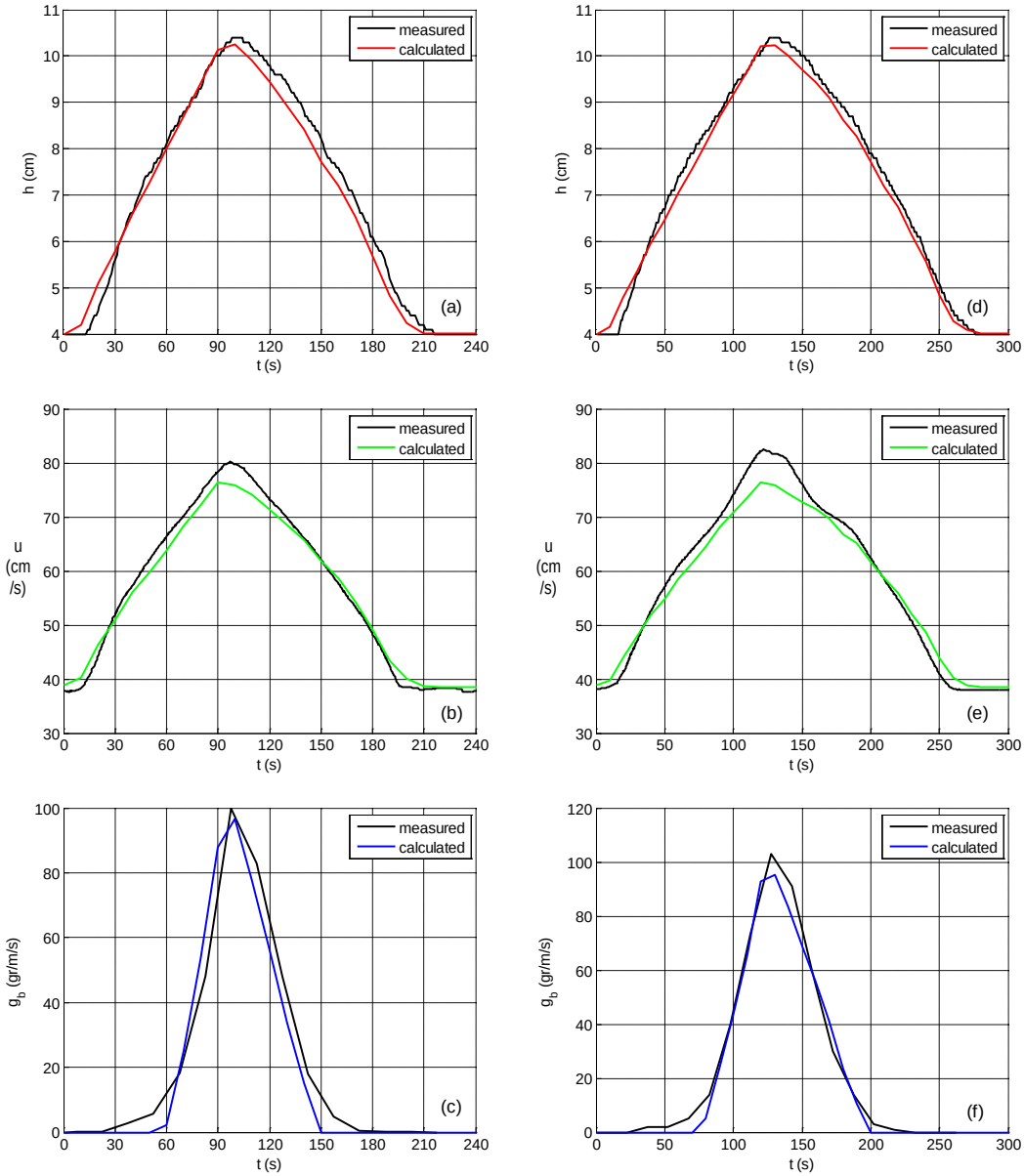


**Figure 5**. Experimental and theoretical variations of water depth, velocity and bed load with time [(a), (b), (c) correspond to the results of experiment 1; (d), (e), (f) correspond to the results of experiment 2]

Figure 6 and Figure 7 represent the initial and final experimental bed elevations along the channel, together with the theoretical ones obtained from numerical analyses. The total bed load yield was 3.95 kg and 5.25 kg in the case of experiment 1 and experiment 2, respectively. This induced approximately a decrease of 0.2 mm in bed elevations revealing that the bed was not eroded significantly.

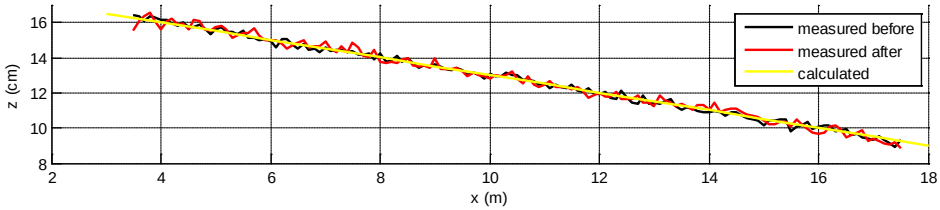


**Figure 6**. Experimental bed elevations along the channel before and after the experiments together with the theoretical ones by using Eq. (6), in the case of Experiment 1

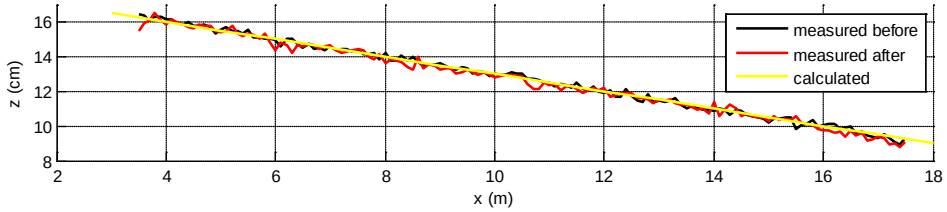


**Figure 7**. Experimental bed elevations along the channel before and after the experiments together with the theoretical ones by using Eq. (6), in the case of Experiment 2

## 5 CONCLUDING REMARKS

Partial differential equations for the continuity of water and sediment are combined with the differential momentum equation with diffusive wave assumption and they are numerically solved in one dimension by using the finite difference scheme developed by Lax (1954). The Manning coefficient, n is calculated according to the equation for compound channels, proposed by Lotter (Güney, 2006). Two experiments are considered as illustrative examples. The bed elevations along the channel, the velocity and flow depth variations with time and the bed loads collected in baskets during the experiment were compared with the numerical model solutions by selecting different time and space increments.

It was revealed that, if the above mentioned simplified approach is used, the results of the Eq. (6) of Engelund and Fredsoe (1976), related to the bed load transport, are more compatible with the experimental findings. The changes in flow depths and velocity are found to be non-significant.

In the further studies, it is intended to use more sophisticated numerical solution methods which take into account all the terms of the basic equations. Two or three dimensional equations will also be handled in order to study the variations of $h$, $u$, $g_b$ as well as the bed deformations accurately.

## ACKNOWLEDGEMENTS

The authors thanks TÜBİTAK (project number 106M274) for the financial support. This study is a part of a PhD thesis done in DEU, The Graduate School of Natural and Applied Sciences.

## REFERENCES

Bombar, G. (2009). Experimental and Numerical Investigation of Bed Load Transport in Unsteady Flows. *PhD Thesis*, Dokuz Eylül Üniversitesi Fen Bilimleri Enstitüsü, 152.

Bombar, G. (2016). The Hysteresis and Shear Velocity In Unsteady Flows. *Journal of Applied Fluid Mechanics*, 9(2), 839-853.

Bor, A. (2008). Numerical Modeling of Unsteady and Non-Equilibrium Sediment Transport in Rivers. *MSc Thesis*, The Graduate School of Engineering and Sciences of İzmir Institute of Technology. 135.

Ferrer-Boix, C. & Hassan, M.A., (2015). Channel Adjustments to a Succession of Water Pulses in Gravel Bed Rivers. *Water Resources Research*. 51, 8773–8790, DOI:10.1002/2015WR017664.

Francalanci, S., Paris, E. & Solari, L (2013). A combined field sampling-modeling approach for computing sediment transport during flash floods in a gravel-bed stream. *Water Resources Research*, 49(10), 6642–6655, DOI:10.1002/wrcr.20544.

Güney, M.Ş. (2006). *Laboratuvar Uygulamalı Hidrolik.* Dokuz Eylül Üniversitesi Mühendislik Fakültesi Basım Ünitesi, İzmir.

Lax, P. D. (1954). Weak Solutions of Nonlinear Hyperbolic Equations and Their Numerical Computation. *Communications on pure and applied mathematics*, 7(1), 159-193.

Lee, T.L, Liu, Y.L. & Cheng, K.H. (2004). Experimental Investigation of Bedload Transport Processes under Unsteady Flow Condition. *Hydrological Processes*, 18, 2439-2454.

Meyer-Peter, E., & Müller, R. (1948). Formulas for Bed-Load Transport: Report on Second Meeting of International Association for Hydraulics Research (IAHR). *IAHR: Stockholm, Sweden*.

Mrokowska, M.M. & Rowiński, P.M., (2016). Notes On Bed Load Transport Under Unsteady Flow Conditions. *12th International Conference on Hydroscience & Engineering Hydroscience & Engineering for Environmental Resilience*, Tainan, Taiwan, November 2016.

Mrokowska, M. M., Rowiński, P. M., Książek, L., Strużyński, A., Wyrębek, M., & Radecki-Pawlik, A. (2016). Flume Experiments on Gravel Bed Load Transport in Unsteady Flow—Preliminary Results. In *Hydrodynamic and Mass Transport at Freshwater Aquatic Interfaces*, 221-233, Springer International Publishing, DOI 10.1007/978-3-319-27750-9_18.

Mrokowska, M.M., Rowiński, P.M. & Kalinowska, M.B., (2015a). Evaluation of Friction Velocity in Unsteady Flow Experiments. *Journal of Hydraulic Research*, 53(5), 659-669, DOI: 10.1080/00221686.2015.1072853.

Mrokowska, M.M., Rowiński, P.M., and Kalinowska, M.B., (2015b). A Methodological Approach of Estimating Resistance To Flow Under Unsteady Flow Conditions. *Hydrol. Earth Syst. Sci.*, 19, 4041–4053, DOI:10.5194/hess-19-4041-2015.

 

Orrú, C.B., Astrid & Uijttewaal Wim S.J. (2016). Armor Breakup and Reformation in a Degradational Laboratory Experiment, *Earth Surf. Dynam.,* 4, 461–470, DOI:10.5194/esurf-4-461-2016.

Qu, Z. (2003). Unsteady Open-Channel Flow over a Mobile Bed, École Polytechnique Fédérale de Lausanne. *PhD Thesis*, no 2688, 196.

Spiller, M.S, Rüther, N. & Friedrich, H., (2015). Dynamic Lift on an Artificial Static Armor Layer During Highly Unsteady Open Channel Flow. *Water*, 7, 4951-4970, DOI:10.3390/w7094951.

Tayfur, G., Singh, V.P. (2006). Kinematic Wave Model of Bed Profiles In Alluvial Channels, *Water Resources Research*, 42, W06414.

Waters, K.A. & Curran J.C., (2015). Linking Bed Morphology Changes of Two Sediment Mixtures To Sediment Transport Predictions in Unsteady Flows. *Water Resources Research*, 51, 2724–2741, DOI:10.1002/2014WR016083.

Waters, K.A. & Crowe C.J., (2016). Effects of an Emergent Vegetation Patch on Channel Reach Bathymetry And Stability During Repeated Unsteady Flows, *Water Resources Research*, 52, DOI: 10.1002/2015WR018411.

 

# COMBINING LOCAL 3-D FLOW INFORMATION WITH UNSTEADY FRACTIONAL SEDIMENT TRANSPORT TO ASSESS POOL-RIFFLE SELF-MAINTENANCE

ESMAEEL BAYAT[(1)], ELHAM VAHIDI[(2)], JOSE F. RODRIGUEZ[(3)], PATRICIA M. SACO[(4)] & GUSTAVO A. M. DE ALMEIDA[(5)]

[(1,2,3,4)] School of Engineering, The University of Newcastle, Callaghan 2308, Australia, jose.rodriguez@newcastle.edu.au
[(5)] Civil Engineering, Engineering and the Environment, University of Southampton, UK

## ABSTRACT

Pool-riffle sequences are one of the most common geomorphological features in streams. The morphodynamics of pools and riffles has been the subject of research for over a century and has more recently attracted intense attention for their central role in providing habitat diversity conditions both in terms of flow and substrate. Initial efforts to explain the long-term stability of the pool-riffle sequences (often referred to as self-maintenance) has focused almost exclusively on cross sectional flow characteristics (either average or near bed velocity or shear stress). More recently, attention has focused on three-dimensional flow features and sediment size characteristics, but this has been done in a compartmentalised way, with studies either focusing on one or the other aspect. This paper bridges the gap between these two aspects by combining the effects of flow distribution with fractional sediment transport and sorting. Firstly, detailed 3-D flow patterns from experimental data are used on typical pool-riffle sequences to reconstruct shear stress distributions and near-bed streamlines for different flow condition. Local instantaneous bedload transport was obtained by combining these experimental results with field and simulated data from an unsteady fractional sediment transport and bed evolution model of an existing stream. Average cross sectional and 'local' sediment transport (i.e. obtained by assuming sediment transport follows the streamlines) are evaluated in this paper as indications for self-maintenance. The results demonstrate that local flow can produce near-bed self-maintenance conditions even under conditions in which average flow could not, accounting for the 3-D flow field results in more self-maintenance episodes compared to traditional methods based on cross sectional variables. These results are relevant for the design of artificial pools and riffles in stream restoration projects aiming at improving habitat conditions.

**Keywords:** Fluvial hydraulics; sediment transport; size distribution; unsteady flow; stream restoration.

## 1 INTRODUCTION

One of the common geomorphological features in gravel bed streams is pool-riffle (PR) sequences, which provide essential habitat conditions both in terms of flow and substrate. In recent river rehabilitation and naturalization projects, artificial PR sequences have frequently been used. Their long-term stability is a key factor for designing these artificial structures which can be accomplished by studying existing PR in nature (Newbury and Gaboury, 1993; Rhoads *et al.*, 2011).

Velocity reversal hypothesis is one of the first theories for explaining the dynamic stability of natural PR sequences (Gilbert and Murphy, 1914; Keller, 1971). This hypothesis discusses self-maintenance mechanism as a shifting of maximum near-bed velocities from riffles, where they occur during most flow conditions, to the pools during high flows based on geometrical differences. This velocity shift ($V_p/V_r$ >1 subindices $p$ and $r$ denote pool and riffle, respectively) allows for the removal of the sediment deposited in pools during low to medium flows which ultimately results in long term stability of PR sequences. While some research supported this theory based on averaged near-bed velocity or averaged bed shear stress (Keller, 1971; Keller and Florsheim, 1993), several other studies reported the absence or limited reversal conditions (Bhowmik and Demissie, 1982; Carling, 1991; Clifford and Richards, 1992; Clifford, 1993; Carling and Wood, 1994; Sear, 1996; Thompson *et al.*, 1996; Thompson *et al.*, 1999; Booker *et al.*, 2001; Cao *et al.*, 2003; Caamaño *et al.*, 2009). Therefore, velocity reversal hypothesis solely cannot explain self-maintenance in all PR sequences (refer to Thompson (2011) and references therein).

Inconsistent observation of velocity reversal conditions drove researchers to investigate the alternative theories including multi-dimensional (2- or 3-D) flow features (Thompson et al., 1996; Thompson et al., 1999; Booker et al., 2001; MacWilliams et al., 2006; MacVicar and Roy, 2007a, b; Caamaño et al., 2009; Thompson, 2011; Caamaño et al., 2012; MacVicar and Best, 2013; Rodríguez et al., 2013; MacVicar and Obach, 2015; Strom et al., 2016) or sediment transport characteristics (Clifford, 1993; Sear, 1996; Cui et al., 2008; De Almeida and Rodríguez, 2011; MacVicar and Roy, 2011; De Almeida and Rodríguez, 2012; Hodge et al., 2013; Milan, 2013).

 

In terms of multi-dimensional flow analysis, (Thompson et al., 1996; Thompson et al., 1999) identified a recirculating eddy produced by a forced constriction (an obstacle) at the head of the pool in laboratory experiments which generated a jet of local high velocities in the pool centre. They argued that the formation of the jet provided a mechanism for preventing deposition at the pool. Several studies using 2-D and 3-D numerical models identified other zones of flow concentration produced by lateral flow convergence and divergence in an unforced PR sequences (Booker et al., 2001; MacWilliams et al., 2006; Caamaño et al., 2012). They argued that the high velocity zones occur in a narrow region of the pool, away from the deepest part make sediment being routed around, away from the pool centre and ultimately preventing deposition. Similarly, 3-D measurements by (Rodríguez et al., 2013) in a laboratory PR sequence showed areas of flow concentration at the pool, with a different concentration pattern for different flow discharges.

An additional mechanism for complementing the velocity reversal hypothesis is sediment processes including sediment erosion, deposition and transport which are related to grain size, packing arrangements and mobility (Sear, 1996; De Almeida and Rodríguez, 2011; Vetter, 2011; De Almeida and Rodríguez, 2012; Hodge et al., 2013; Milan, 2013) Sedimentological differences between pools and riffles indicate that pool surface sediments are finer, loosely interacting and unstable particles, whereas riffle surface sediments are coarser, tightly interacting and more stable [Sear, 1996]. Both friction angle and critical shear stress are higher at riffles than at pools and, therefore, sediment transport rates in pools increase with discharge more rapidly than in riffles (Sear, 1996). Hodge et al.(2013) used field estimations of sediment characteristics and a 2-D numerical model to simulate flow conditions. They indicated that even though pools experienced lower shear stresses than riffles, their sediment was more likely to be transported than the sediment in the riffles. De Almeida and Rodríguez (2011; 2012) applied a 1-D morphodynamic model comprising fractional sediment transport, unsteady flow, bed deformation and bed sediment sorting to a real stream. They reported a number of events (typically below bankfull flow) in which sediment transport at the pools was higher than at the riffles, even though bed shear stresses were higher at the riffles which result in overall self-maintenance of the PR sequence. They used the ratio of cross sectional averaged bedload sediment transport $Qs_p/Qs_r>1$ (subindices p and r denoting pool and riffle, respectively) in the form of velocity reversal concept to identify self-maintenance conditions.

Incorporating detailed information about flow and sediment transport characteristics provides insight in understanding PR self-maintenance beyond the velocity reversal hypothesis. However, this has been done in a compartmentalised way, with studies either focusing on one or the other aspect. In this study, using a real PR sequence, we combine observed characteristic stage-dependent 3-D flow patterns with time-varying cross sectional information on bed shear stresses, sediment distribution and sediment bed changes during a one-year record of continuous discharges. Using this methodology, we are able to identify self-maintenance conditions due to the combined effect of both flow multi-dimensionality and sediment transport and track the behavior of different sediment size fractions along flow streamlines over time.

## 2 METHODS

### 2.1 Estimation of cross sectional averaged bed shear stresses and shear stress distributions

In this study, field data from a research on a reach of the Bear Creek (a gravel bed river), Arkansas, United States is used. This reach has stable PR sequences with an average slope of 0.2%, width between 30 and 40 m, bankfull depth between 5 and 7 m, and bed sediment $D_{50}$ =29.5 mm. Based on this set of field data, De Almeida and Rodríguez (2011, 2012) developed a 1-D unsteady flow-sediment-bed elevation model. This model solved the Saint-Venant 1-D unsteady flow equation coupled with the fractional sediment transport formulation of (Wilcock and Crowe, 2003), Hirano (1971) equation for grain size distribution changes in the active layer and Exner's law for bed level modifications. Their results for the period June 2001-June 2002 showed a very good agreement with measured data. Only PR1 and PR2 of the three PR units of the Bear Creek studied by (De Almeida and Rodríguez, 2011) were focused, as backwater effects from a downstream junction displays a specific condition on PR3.

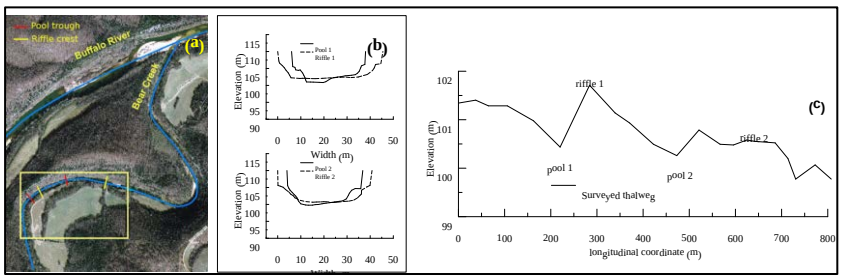


**Figure 1.** (a) Satellite image showing the reach location (35°59´37.46´´N, 92°41´53.92´´W), (b) representative pool-riffle cross sections, and (c) longitudinal bed profile with locations of pools and riffles (modified from De Almeida and Rodríguez (2011)).

 

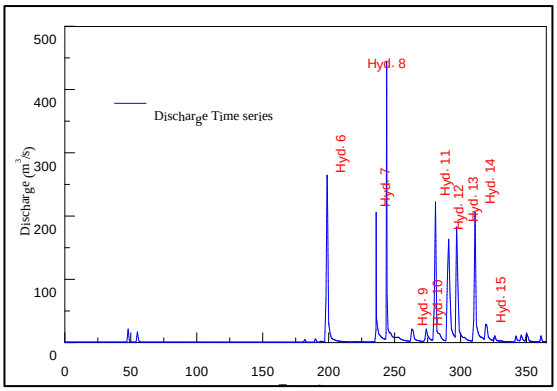


**Figure 2.** Discharge time series in Bear Creek.

The results from the simulations of De Almeida and Rodríguez (2011) were used to derive from the discharge time series of Figure 2 cross sectional averaged values of bed shear stresses, $\tau$, at the pools and the riffles of PR1 and PR2. Values of $\tau$ were determined from the cross sectional averaged values of downstream velocity U, water depth H and sediment diameter for which 90% of the particles in the sample are finer $D_{90}$, as follows:

$$\tau = \rho C_f U^2 \quad [1]$$

$$C_f^{0.5} = \frac{U}{u_*} = \frac{1}{\kappa} Ln\left(\frac{11H}{k_s}\right) \quad [2]$$

$$k_s = 2D_{90} \quad [3]$$

Where $\rho$ is the water density and $C_f$ is a friction factor that needs to be estimated from resistance relations (here Keulegan law (Chaudhry, 2008) is used), $u_*$ is the shear velocity, $\kappa$ the von Karman constant ($\kappa$ =0.41 adopted here) and $k_s$ the roughness height as a function of $D_{90}$.

2.2 Estimation of bed shear stress transverse distributions and near-bed streamlines

Based on local investigation values of the flow condition and sediment transport in our study, detailed 3-D flow data obtained in a laboratory PR sequence by Rodríguez et al. (2013) were used. The experimental setup consisted of three pools and three riffles on a 1-m wide straight channel with a slope of 0.25%. The distance between consecutive pools (or riffles) was about five times the riffle width. The bed was made out of crushed stone chips ($D_{50}$=57 mm), which provided the same fully rough bed conditions. The pool width varied between 0.6 and 0.8 of the riffle width in different discharges. The 3-D velocity data was collected for two representative discharges: low flow and high flow. In low flow, the topography affects the flow significantly. However, in high flow representing bankfull condition, the PR topography gets drowned and works more as a large roughness element. The experimental data included 3-D velocities measured using a down-looking ADV over one-half of the cross section at five locations: upstream riffle, pool entrance, pool centre, pool exit and downstream riffle were used to draw the near-bed streamlines to estimate sediment routing through pools and riffles and compute local shear stress and sediment transport. Transverse bed shear stress distribution based on law of the wall is presented in Figure 3.

 

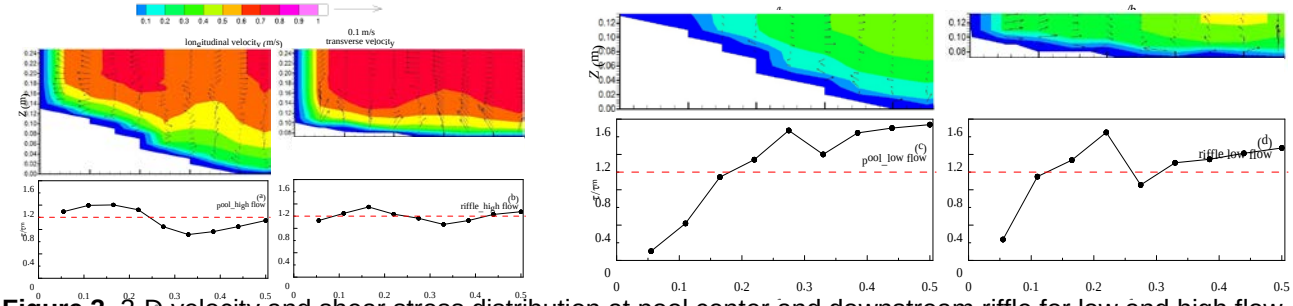

**Figure 3.** 3-D velocity and shear stress distribution at pool center and downstream riffle for low and high flow (modified from (Rodríguez *et al.*, 2013)).

Points where velocity was measured had grid spacing in the vertical and transverse directions $\Delta z$ and $\Delta y$ between 1/10 and 1/20 of depth $h$ and width $b$, respectively. From this fine grid, 18 equi-spaced near-bed streamlines at the downstream riffle are backtracked into the pool and continued all the way to the downstream riffle and local sediment transport were assumed to occur along these streamlines.

2.3 Estimation of self-maintenance indices based on sediment transport

As the grain size distribution varied from sand to cobbles, it was decided to use the fractional sediment transport formula of Wilcock and Crowe (2003) and sediment transport reversal concept, introduced by De Almeida and Rodríguez (2011), to assess self-maintenance.

Wilcock and Crowe (2003) consider the total bedload transport of a mixture $Qs$ as the integration of the bed load transport per unit width of each size fraction $q_{si}$, where $i$ is an index to denote each fraction $F_i$ of diameter $D_i$. Dimensionless parameters $W_i^*$ and $\varphi$ represent respectively the bedload transport and the relative shear stress for the size $i$ fraction and are related through:

$$W_i^* = \begin{cases} 0.002\varphi^{7.5} & \varphi < 1.35 \\ 14\left(1-\frac{0.894}{\varphi^{0.5}}\right)^{4.5} & \varphi \geq 1.35 \end{cases} \quad [4]$$

The dimensionless parameters are defined as:

$$W_i^* = \frac{(s-1)gq_{si}}{F_i u_*^3} \quad [5]$$

$$\varphi = \frac{\tau}{\tau_{ri}} \quad [6]$$

Where $s$ is the ratio of sediment to water density, $g$ is the gravitational acceleration, $u_* = (\tau/\rho)^{1/2}$ is the shear velocity and $\tau_{ri}$ is the reference shear stress for each individual size. $\tau_{ri}$ can be obtained using:

$$\tau_{ri} = \tau_{rsm}\left(\frac{D_i}{D_{sm}}\right)^c \quad [7]$$

$$c = \begin{cases} 0.12 & \frac{D_i}{D_{sm}} < 1 \\ \frac{0.67}{1+\exp\left(1.5-\frac{D_i}{D_{sm}}\right)} & \frac{D_i}{D_{sm}} \geq 1 \end{cases} \quad [8]$$

Where $\tau_{rsm}$ is the value of $\tau_{ri}$ that corresponds to the mean size of the bed $D_{sm}$ and depends on the full particles size distribution in the bed, and can be expressed as a function of the sand fraction in the mixture $F_s$:

 

$$\tau_{rsm} = (s-1)\rho)\rho_{sm}\left[0.021+0.015\exp(-20F_S)\right] \quad [9]$$

During the discharge time series, river bed experiences different conditions. The size distribution varies at different times. In order to use a reasonable size distribution in the computations, the model of De Almeida and Rodríguez (2011) was used to obtain time series of each sediment fraction at the pools and the riffles of PR1 and PR2 for the period June 2001-June 2002. The instantaneous values of $Qs$ at the pools ($Qs_p$) and the downstream riffles ($Qs_r$) based on bed shear stress and grain size information and sediment transport reversal conditions ($Qs_p/Qs_r$ >1) at PR1 and PR2 were determined.

Based on the results from 3-D velocity measurement, 18 streamlines were selected covering the whole cross sections and going from the pool to the downstream riffle. For each streamline, the instantaneous local values of $Qs_p$ and $Qs_r$ were calculated and 18 instantaneous local values of $Qs_p/Qs_r$ were determined at each PR. Reversal conditions on streamlines can then be analysed individually (i.e., $Qs_p/Qs_r$ >1 in one streamline) and be compared to cross sectional ones.

## 3 RESULTS

Estimation of the fractional sediment transport used in the methodology required the knowledge of the sediment size distribution at different locations in PR1 and PR2. Hourly values of each of the eight fractions used during the one-year simulation were extracted from the model results of de Almeida and Rodríguez (2011) and used to construct sediment size distribution curves at the pools and the riffles. Figure 4 shows the envelope (finer and coarser) of all size distributions obtained at the pool and the riffle of PR1 (labelled P1 and R1, respectively) and the pool and the riffle of PR2 (labelled P2 and R2, respectively).

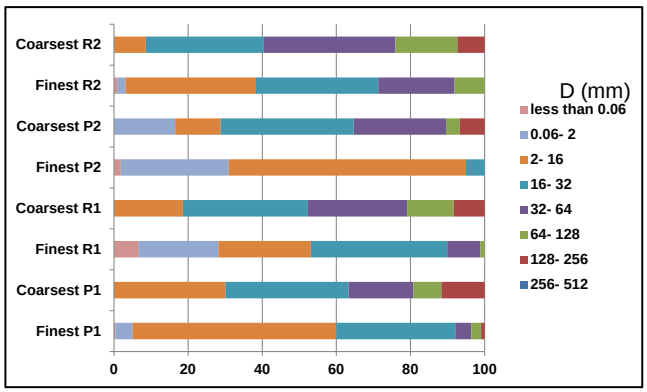


**Figure 4.** Envelope range of sediment size distributions in PR1 and PR2.

The figure shows that PR1 has in general coarser sediment than PR2, and also that the distributions in P1 and R1 are less differentiated than P2 and R2. PR2 clearly shows coarser material at the riffle than at the pool, while in PR1 the size distributions in the pool and the riffle considerably overlap. Even though the size distributions varied over the year of simulation, the pattern of Figure 4 was maintained.

The low and high flow measurements used to represent the 3-D effects not only displayed different shear stress distributions but also specific near-bed streamline patterns. Figure 5 shows the near-bed streamline patterns obtained for the two flow conditions overlaid to the bed contour lines, where a noticeable contraction at the pool induced by the narrower and deeper cross section is evident. The level of contraction of streamlines is different for the two flow conditions, with the high flow showing a more localised effect of the pool than the low flow.

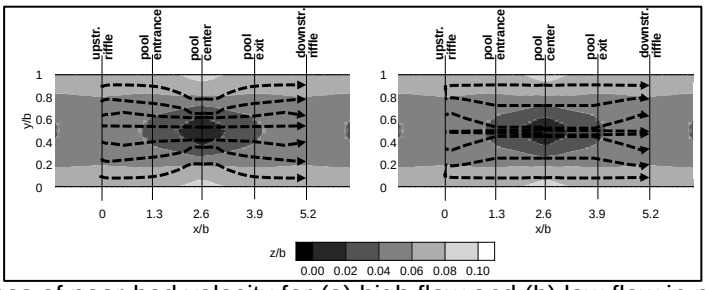


**Figure 5.** Streamlines of near-bed velocity for (a) high flow and (b) low flow in pool-riffle sequences (only some of the 18 calculated streamlines are shown for clarity with their corresponding number).

As explained in the introduction, by incorporating a 3-D flow distribution, an increase in reversal occurrences are expected compared to reversals detected using cross sectional averaged information because reversal may occur in only part of the cross section. The sediment transport reversal indices $Qs_p/Qs_r$

 

were computed for the entire year of simulations at PR1 and PR2 both using cross sectional averaged shear stresses and the local streamline values to identify reversal conditions. Figure 6 shows the results for PR1 and PR2 during all hydrographs in which sediment transport reversal was detected. PR1 displayed cross sectional averaged reversal conditions in 6 hydrographs, but the incorporation of local information helped identify one more hydrograph (number 11) with reversal conditions (Figure 6 (a) and (b)).

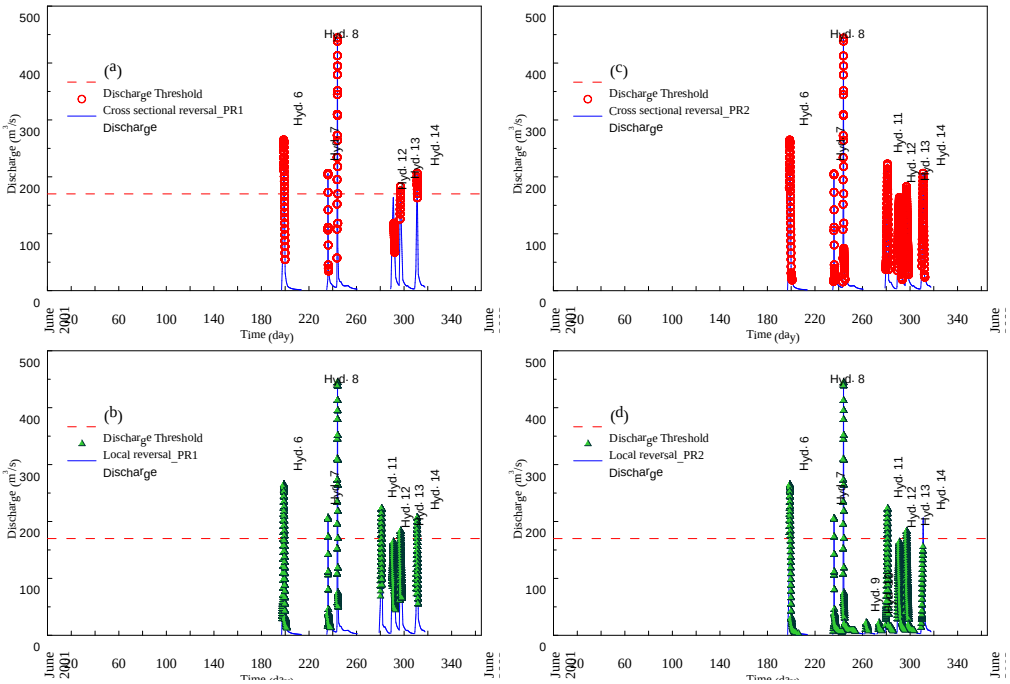


**Figure 6.** Sediment transport reversal events (a) and (b) Average cross sectional in PR1 and PR2; (c) and (d) local in PR1and PR2.

Also, in hydrographs where both cross sectional averaged and local reversal occurred, local reversal conditions started earlier on the raising limb and finished later on the receding limb. When considering all hydrographs, local reversal conditions occurred during a total of 203 hours compared to 102 hours of cross sectional averaged reversal conditions. A similar situation was observed in PR2, where the 3-D streamline methodology helped identify reversal conditions for three additional hydrographs (number 9, 10 and 15) than the cross sectional averaged calculations (Figure 6 (c) and (d)). Total time of reversal conditions increased from 344 to 525 hours when the 3-D flow effects were incorporated.

Local reversal conditions did not necessarily occur simultaneously in all streamlines, as each one of them were experiencing different bed shear stresses conditions. Figure 7 shows the total time for which each streamline experienced sediment transport reversal conditions in PR1 and PR2. This figure clearly shows that the ten central streamlines (number 5 to 14) are the ones with more frequent reversal, whereas the region close to the banks seldom experience reversal. This pattern is more evident in PR1 than in PR2. The maximum reversal time did not occur on the streamlines at the centre of the cross section but slightly to the sides (streamlines number 5-7 and 12-14).

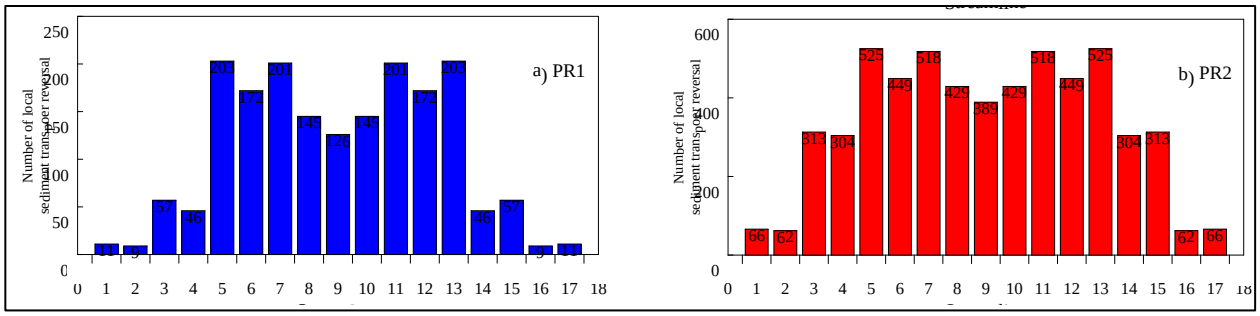


**Figure 7.** Number of local sediment transport reversal events in different streamline strips for (a) PR1 and (b) PR2.

The previous results show that PR1 and PR2 have different dynamics, with PR2 experiencing reversal much more frequently and more uniformly distributed over the cross section than PR1. This characteristic behaviour can be associated with differences in flow three-dimensionality and/or differences in sediment

 

composition, as both factors affect sediment transport. In order to further explore this aspect, the relation between the sediment transport reversal index $Qs_p/Qs_r$ and the shear stress reversal index $\tau_p/\tau_r$ in PR1 and PR2 were analysed considering both cross sectional averaged and local (streamline) reversal indices (Figure 8). The calculations were performed every one hour and each point is referred as an event.

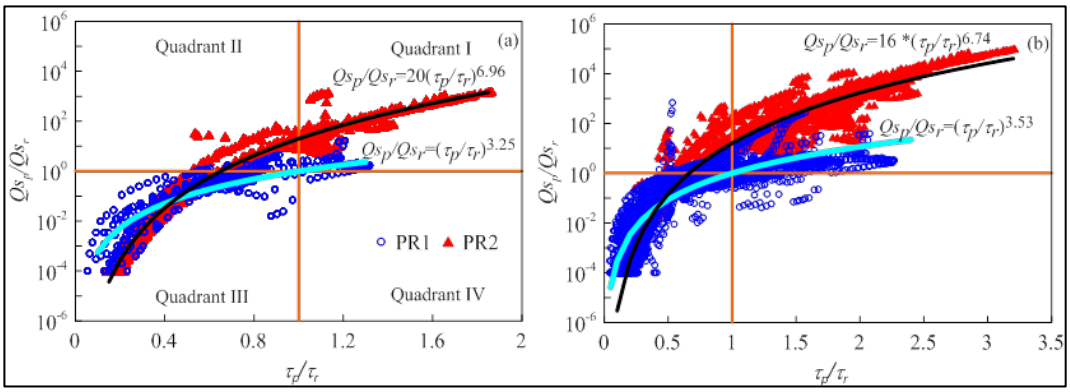


**Figure 8.** Relationship between flow reversal and sediment transport reversal indices in PR1 and PR2: a) cross sectional formulation using 1D information, b) local formulation using 3-D information.

Figures 8a and 8b are divided into four quadrants defined by the lines of $Qs_p/Qs_r$ =1and $\tau_p/\tau_r$ =1. Events in quadrants III and IV display no sediment transport reversal ($Qs_p/Qs_r$ < 1) and promote riffle erosion and pool deposition. Events in quadrants I ($Qs_p/Qs_r$ >1and $\tau_p/\tau_r$>1) and II ($Qs_p/Qs_r$ >1and $\tau_p/\tau_r$ <1) both indicate sediment transport reversal, but only in the first case the sediment transport reversal can be associated with differences in flow conditions that generate shear stress reversal. Quadrant I events can in principle be explained by the traditional velocity reversal hypothesis and the complementary theories of sediment routing based on flow information alone. Quadrant II events require finer sediment at the pools than at the riffles, as flow mechanisms alone are not enough to produce self-maintenance. When cross sectional values are considered (Figure 8a) PR1 experiences less quadrant II events than PR2, so differences in bed sediment in pool and riffle are less important for self-maintenance. The same trend is observed when local values of shear stresses and sediment transport are considered (Figure 8b), even though the spread of the data makes this behaviour less evident. In fact, curve fits to the data of Figures 8a and 8b have essentially the same mathematical formulation. For the cross sectional averaged values (Figure 8a), the lines of best fit for PR1 and PR2 are, respectively:

$$\frac{Qs_p}{Qs_r} = \left(\frac{\tau_p}{\tau_r}\right)^{3.25} \quad [9]$$

$$\frac{Qs_p}{Qs_r} = 20\left(\frac{\tau_p}{\tau_r}\right)^{6.96} \quad [10]$$

When local values are considered (Figure 9b), the best fit lines for data on PR1 and PR2 are:

$$\frac{Qs_p}{Qs_r} = \left(\frac{\tau_p}{\tau_r}\right)^{3.53} \quad [11]$$

$$\frac{Qs_p}{Qs_r} = 16\left(\frac{\tau_p}{\tau_r}\right)^{6.74} \quad [12]$$

## 4 DISCUSSION

Even though PR1 and PR2 are both stable pools and riffles that are located in close proximity within the Bear Creek, they present significant differences in geometric and sediment characteristics. Compared to PR2, PR1 has a pool that is more constricted and closer to the riffle (Figure 1), and does not have the same degree of differentiation between sediment size at the pool and the riffle (Figure 4). These differences in

 

characteristics drive two contrasting dynamics for self-maintenance that we can explain based on our new approach.

The level of flow contraction at the pools is also different for flows below and above bankfull, which has implications for self-maintenance when combined with the bed shear stress distributions of Figure 3. The streamlines of Figure 5 show that flows below bankfull are affected by contraction effects over a wider pool area than flows above bankfull. In addition, below bankfull flows display high bed shear stresses in the deepest areas of the pool, unlike above bankfull flows that have noticeable lower bed shear stress values in these areas. This highlights the importance of below bankfull 3-D flow patterns as contributors to self-maintenance, particularly since below bankfull flows are considerably more frequent. Figure 6 shows that only hydrographs 6 and 8 have maximum values well above bankfull discharge, yet most other hydrographs still provide conditions for self-maintenance.

As mentioned in the previous section, the transverse distribution of reversal events displayed in Figure 7 reveals that streamlines 5-7 and 12-14 experience reversal conditions more frequently, both in PR1 and PR2. During below bankfull flows, these streamlines are located slightly away from the deepest part of the pool (Figure 5) and over the areas of maximum bed shear stress (Figure 3). This behaviour is consistent with the flow convergence routing hypothesis (MacWilliams et al., 2006), which postulates that sediment is routed around the deepest part of the pool without actually going through it. However, our results also show that the deepest part of the pool still experience a considerable reversal frequency. The above bankfull conditions are slightly different, as streamlines 5-7 and 12-14 do not experience similar high values of bed shear stress at the pool. Therefore, the magnitude of reversals on these streamlines is likely to be less important than in the below bankfull situation.

Figure 8 also shows that PR1 and PR2 have quite a different behaviour in terms of total number of reversal events. More insight can be gained by looking at the relationship between the sediment transport reversal index $Qs_p/Qs_r$ and the shear stress reversal index $\tau_p/\tau_r$ presented in Figure 8. Assuming a typical relationship between Qs and $\tau$ of the form $Qs=a\tau^d$, it is easy to show that the best fit curves given by Eq. [9] and [11] describe a situation in which both the riffle and the pool have similar values of the coefficients a and d. Since the (Wilcock and Crowe, 2003) sediment transport equation used in this work can be considered to have values of a and d that are dependent on the sediment size distribution, the general behaviour described by Eq. [9] and (11) implies that a and d are the same at the pool and the riffle and the sediment size differences between them are not important for the self-maintenance process in PR1. The exponents d of 3.25 and 3.53 of the best fit curves are consistent with low mobility material in the Wilcock and Crowe (2003) formula corresponding to the relative shear stress coefficient $\varphi \geq 1.35$ in Eq. [4].

In contrast, the best fit curves for PR2 given by Eq. [10] and (12) include an amplification factors of 20 and 16, respectively, which can be interpreted to be associated with differences in sediment size distribution between the pool and the riffle. Exponent d of 6.96 and 6.74 correspond to the middle to upper range given by the Wilcock and Crowe (2003) methodology for $\varphi < 1.35$, and indicate a more mobile sediment than in PR1.

Consequently, Eq. [9] to [12] imply that a key reason for the distinct dynamics of PR1 and PR2 is their differences in sediment size distribution. PR2 has on average a finer sediment size distribution than PR1 and also more marked differences between sediment sizes at the pool and the riffle. This explanation is consistent with the sediment size distributions of Figure 4. Due to these differences reversal events in PR1 are located mainly in quadrant I of Figure 8, where the original velocity reversal hypothesis can be used to explain self-maintenance. Reversals events in PR2, on the other hand, are located both in quadrants I and II, a region where the effects of sediment size contributes to the explanation of self-maintenance.

When local flow patterns are used in the estimation of bed shear stresses and sediment transport, the trend line Eq. [11] and [12] are similar to the corresponding trend line Eq. [9] and [10] obtained from the cross sectional averaged results, both in the general form and in the value of the coefficients. However, the range of values of $Qs_p/Qs_r$ and $\tau_p/\tau_r$ expands considerably (Figure 8b), which means that stronger and potentially more severe events of erosion and deposition can occur locally.

The events are classified into below and above bankfull flow events, using the discharge of 170 $m^3/s$ as the transition between the two stages. In general, reversal conditions are present more frequently during below bankfull than during above bankfull flows. This occurs because the bed experiences more below bankfull flows, as explained before. Detection of events during above bankfull flows is only marginally affected by the incorporation of 3-D flow effects and unaffected by the consideration of sediment size effects. As already pointed out and based on the streamline patterns of Figure 5, these high flows experience less contraction compared to low flows and thus a more uniform velocity and bed shear stress pattern. The absence of sediment size effects is expected during high flows, as generalised sediment movement during high flows generates a very similar size distribution in pools and riffles.

## 5 CONCLUSION

The combined effect of 3-D flow and sediment mobility into the assessment of reversal conditions shows that conditions for self-maintenance can occur far more often (2 to 4 times) than previously thought based on

 

predictions of the traditional velocity reversal hypothesis. Self-maintenance conditions can occur for discharges substantially smaller than bankfull discharge, and hydrographs with discharges as low as 1/7 of the bankfull discharge can display local sediment transport reversal conditions because of finer sediment and flow concentration at the pools.

The effects of flow three-dimensionality were unable to be separated from the effects of sediment mobility by analysing local reversal on bed shear stresses. This computation was of interest since sediment differential mobility can vary widely not only between PR sequences in different reaches but also within pools and riffles in the same reach. In addition, sediment mobility information is sometimes difficult to obtain and can be substantially modified during hydrographs. Flow three dimensionality alone can explain between 70 and 100 % of the local reversal events, which supports previous findings by Booker et al. (2001), MacWilliams et al. (2006), Caamaño et al. (2012) and Strom et al. (2016) that relied on bed shear stress information to assess self-maintenance.

We also isolated sediment transport effects from flow three-dimensionality by computing reversal of cross sectional averaged values of sediment transport and comparing it with cross sectional averaged bed shear stress reversal. Our results show an increase in self-maintenance events due to sediment effects of between 40 and 100% when compared with the flow processes associated with the original velocity reversal hypothesis, in agreement with results from De Almeida and Rodríguez (2011) and Hodge et al. (2013).

The methodology has allowed the separation of the individual effects of three-dimensional and sediment transport processes, which can be important from a practical point of view in order to assess the predictive capability of simplified assessments of self-maintenance that do not consider all interacting processes. Perhaps more importantly, the results can also be used to analyse the potential different response of individual pools and riffles, like the two pools and riffles of this study.

The two pools and riffles analysed, PR1 and PR2, rely on different mechanisms for self-maintenance. Compared to PR2, PR1 has consistently a more similar sediment size distribution in the pool and the riffle and a more constricted pool, so an important mechanism for self-maintenance is the shift of the maximum bed shear stresses towards the pool during hydrographs as stated in the velocity reversal hypothesis. Incorporation of 3-D flow effects significantly increases the number of reversal events, particularly in the central half of the stream width. Sediment size and mobility effects, on the other hand, do not substantially increase the occurrence of reversal events.

In contrast, the self-maintenance of PR2 is heavily influenced by the clear difference in sizes between the pool and the riffle. Compared to predictions based on the velocity reversal hypothesis, both 3-D flow effects and differential sediment mobility mechanisms increase the number of reversal events in similar amounts.

## ACKNOWLEDEMENT

This work has been possible due to funding from the University of Newcastle PhD scholarships for E. Bayat and E. Vahidi, and a grant from the Australian Research Council awarded to P.M.Saco (FT).

## REFERENCES

Bhowmik, N.G. & Demissie, M. (1982). Bed Material Sorting in Pools and Riffles. *Journal of the Hydraulics Division,* 108, 1227-1231.

Booker, D., Sear, D. & Payne, A. (2001). Modelling Three-Dimensional Flow Structures and Patterns of Boundary Shear Stress in a Natural Pool–Riffle Sequence. *Earth Surface Processes and Landforms,* 26, 553-576.

Caamaño, D., Goodwin, P., Buffington, J.M., Liou, J.C. & Daley-Laursen, S. (2009). Unifying Criterion for the Velocity Reversal Hypothesis in Gravel-Bed Rivers. *Journal of Hydraulic Engineering,* 135, 66-70.

Caamaño, D., Goodwin P. & Buffington, J. (2012). Flow Structure through Pool-Riffle Sequences and a Conceptual Model for their Sustainability in Gravel-Bed Rivers. *River Research and Applications,* 28, 377-389.

Cao, Z., Carling, P. & Oakey, R. (2003). Flow Reversal over a Natural Pool–Riffle Sequence: A Computational Study. *Earth Surface Processes and Landforms,* 28, 689-705.

Carling, P. (1991). An Appraisal of the Velocity-Reversal Hypothesis for Stable Pool-Riffle Sequences in the River Severn, England. *Earth Surface Processes and Landforms,* 16, 19-31.

Carling, P. & Wood, N. (1994). Simulation of Flow over Pool-Riffle Topography: A Consideration of the Velocity Reversal Hypothesis. *Earth Surface Processes and Landforms,* 19, 319-332.

Chaudhry, M.H. (2008). *Open-channel flow*. Springer.

Clifford, N. (1993). Differential Bed Sedimentology and the Maintenance of Riffle-Pool Sequences. *Catena* 20, 447-468.

Clifford, N.J. & Richards, K.S. (1992). The Reversal Hypothesis and the Maintenance of Riffle-Pool Sequences: A Review and Field Appraisal. *Lowland Floodplain Rivers: Geomorphological Perspectives*, John Wiley and Sons Ltd, Chichester, UK, 43-70.

 

Cui, Y., Wooster, J.K., Venditti, J.G., Dusterhoff, S.R., Dietrich, W.E. & Sklar, L.S. (2008). Simulating Sediment Transport in a Flume with Forced Pool-Riffle Morphology: Examinations of Two One-Dimensional Numerical Models. *Journal of Hydraulic Engineering*, 134(7), 892-904.

De Almeida, G.A.M. & Rodríguez, J.F. (2011). Understanding Pool-Riffle Dynamics through Continuous Morphological Simulations. *Water Resources Research,* 47(1), 1-15.

De Almeida, G.A.M. & Rodríguez, J.F. (2012). Spontaneous Formation and Degradation of Pool-Riffle Morphology and Sediment Sorting using a Simple Fractional Transport Model. *Geophysical Research Letters,* 39(6), 1-7.

Gilbert, G.K. & Murphy, E.C. (1914). The Transportation of Debris by Running Water. *US Geological Survey Professional Paper* 86. US Government Printing Office, Washington, DC.

Hodge, R.A., Sear, D.A. & Leyland, J. (2013). Spatial Variations in Surface Sediment Structure in Riffle–Pool Sequences: A Preliminary Test of the Differential Sediment Entrainment Hypothesis (DSEH). *Earth Surface Processes and Landforms,* 38, 449-465.

Keller, E. & Florsheim, J.L. (1993). Velocity-Reversal Hypothesis: A Model Approach. *Earth Surface Processes and Landforms,* 18, 733-740.

Keller, E.A. (1971). Areal Sorting of Bed-Load Material: The Hypothesis of Velocity Reversal. *Geological Society of America Bulletin,* 82, 753-756.

MacVicar, B. & Best, J. (2013). A Flume Experiment on the Effect of Channel Width on the Perturbation and Recovery of Flow in Straight Pools and Riffles with Smooth Boundaries. *Journal of Geophysical Research: Earth Surface,* 118, 1850-1863.

MacVicar, B. & Obach, L. (2015). Shear Stress and Hydrodynamic Recovery over Bedforms of Different Lengths in a Straight Channel. *Journal of Hydraulic Engineering,* 141(11), 1-13.

MacVicar, B. & Roy, A. (2007a). Hydrodynamics of a Forced Riffle Pool in a Gravel Bed River: 1. Mean Velocity and Turbulence Intensity. *Water Resources Research,* 43(12), 1-19.

MacVicar & B., Roy, A. (2007b). Hydrodynamics of a Forced Riffle Pool in a Gravel Bed River: 2. Scale and Structure of Coherent Turbulent Events. *Water Resources Research,* 43(12), 1-17.

MacVicar, B. & Roy, A. (2011). Sediment Mobility in a Forced Riffle-Pool. *Geomorphology* 125, 445-456.

MacWilliams, M.L., Wheaton, J.M., Pasternack, G.B., Street, R.L. & Kitanidis, P.K. (2006). Flow Convergence Routing Hypothesis for Pool-Riffle Maintenance in Alluvial Rivers. *Water Resources Research,* 42(10), 1-21.

Milan, D.J. (2013). Sediment Routing Hypothesis for Pool-Riffle Maintenance. *Earth Surface Processes and Landforms,* 38, 1623-1641.

Newbury, R. & Gaboury, M. (1993). Exploration and Rehabilitation of Hydraulic Habitats in Streams using Principles of Fluvial Behaviour. *Freshwater Biology,* 29, 195-210.

Rhoads, B.L., Engel, F.L. & Abad, J.D. (2011). Pool-Riffle Design Based on Geomorphological Principles for Naturalizing Straight Channels. *Stream Restoration in Dynamic Fluvial Systems,* 194, 367-384.

Rodríguez, J.F., García, C.M. & García, M.H. (2013). Three-Dimensional Flow in Centered Pool-Riffle Sequences. *Water Resources Research,* 49, 202-215.

Sear, D. (1996). Sediment Transport Processes in Pool–Riffle Sequences. *Earth Surface Processes and Landforms,* 21, 241-262.

Strom, M.A., Pasternack, G.B. & Wyrick, J.R. (2016). Reenvisioning Velocity Reversal as a Diversity of Hydraulic Patch Behaviors. *Hydrological Processes,* 30(13), 2348-2365.

Thompson, D. M. (2011). The Velocity-Reversal Hypothesis Revisited. *Progress in Physical Geography*, 35(1), 123-132.

Thompson, D.M., Wohl, E.E. & Jarrett, R.D. (1996). A Revised Velocity-Reversal and Sediment-Sorting Model for a High-Gradient, Pool-Riffle Stream. *Physical Geography,* 17, 142-156.

Thompson, D.M., Wohl, E.E. & Jarrett, R.D. (1999). Velocity Reversals and Sediment Sorting in Pools and Riffles Controlled by Channel Constrictions. *Geomorphology,* 27, 229-241.

Vetter, T. (2011). Riffle-Pool Morphometry and Stage-Dependant Morphodynamics of a Large Floodplain River (Vereinigte Mulde, Sachsen-Anhalt, Germany). *Earth Surface Processes and Landforms,* 36, 1647-1657.

Wilcock, P.R. & Crowe, J.C. (2003). Surface-Based Transport Model for Mixed-Size Sediment. *Journal of Hydraulic Engineering,* 129, 120-128.

 

# PROBLEMS IN SEDIMENT TRANSPORT FORMULAS AND ITS IMPROVEMENT

SHU-QING YANG [(1)]

[(1)]School of Civil, Mining & Environ. Eng., Univ. of Wollongong, NSW 2522, Australia
shuqing@uow.edu.au

## ABSTRACT

For sediment transport, by far, many formulae have been developed based on different assumptions, but unfortunately, almost none of them is universally applicable. Generally, there are two methods available in the literature to express sediment transport; the shear stress approach and velocity approach. The velocity approach assumes that if the mean velocity $U$ exceeds the critical velocity, then sediment motion can be observed. The shear stress approach has been widely used by researchers as it accounts for the forces acting on a particle in horizontal plane. The earliest researcher to use the shear stress approach is Shields (1936), who related the dimensionless shear stress, or Shields number $\tau/(\rho_s-\rho)gd_{50}$. Both approaches assume that sediment transport rate is increased when $U$ or $\tau$ is higher. But by comparing with experimental data, the performance of these formulae is not very satisfactory.
In this paper, the measured bedload is analyzed against the famous equations available in the literature. It is found that the measured data do not always support the hypothesis that the higher parameters of shear stress or mean velocity always generate higher sediment transport rate. The mechanism of this high discrepancy has been examined and it is found that the disagreement can be attributed to the missing parameter in vertical direction, which has never been systematically measured and included in the existing sediment transport formulae due to its subtle characteristics, but its existence can be inferred from the vertical force induced by seepage, pressure variation over time and space. A new model has been established by including the new vertical parameter in the sediment transport formula and the agreement with experimental data has been improved significantly.

**Keywords**: Sediment transport; shear stress; mean velocity; vertical velocity; unsteady flow.

## 1 INTRODUCTION

Sediment transport is important in geomorphology and sedimentology, as well as hydrological and hydraulic engineering. Sediment is the most important agent responsible for evolution of the Earth's surface. Its actual prediction is found to be very difficult, for example, Albert Einstein concluded, after detailed study, that "As a young man, my fondest dream was to become a geographer. However, while working in the customs office I thought deeply about the matter and concluded it was far too difficult a subject. With some reluctance, I then turned to Physics as a substitute." Without giving up, he requested his son, Hanson Albert Einstein to carry out his research and finally together with others his son found the subject of sediment transport. The new subject deals with interactions between turbulence and sediment particles. Two of them are very complicated and till today, none of them has been fully understood, even for pure fluid flow without particles. In spite of many research endeavors, our knowledge of sediment transport mechanism remains remarkably meagre (Yalin, 1977), almost all models available in the literature are found to be notoriously uncertain and progress towards reliable prediction has been frustratingly slow.

Sediment transport is generally divided into two or three groups: bed-load transport, suspended load and wash load. Bedload transports intermittently moves on or near the stream bed at velocities much slower than the flow, its motion modes include rolling, sliding and hopping. Suspended load moves at the same velocity as the flow and the wash load is generally assumed to have no exchange with particles at the bed. Accordingly, different equations are available to describe these three modes. Furthermore, equations are available to express sediment transport in mountains, plain reaches, tidal and wave environments. All these equations are applicable for some location, few have been widely accepted. Thus it is important to review the basic assumptions used in sediment transport, and reveal their weakness.

Generally speaking, different researchers have selected different parameters to express the driving force like mean velocity $U$, boundary shear stress $\tau$, stream power $\tau U$, shear velocity $u_*$ or shear velocity related with grains $u_*$', energy slope $S$, and unit stream power $US$, etc. All of them assume that the higher these parameters, the higher sediment transport rate is. The balance between the driving force and resistance determines the transport, the latter is usually described by parameters like particle size $d$ (or settling velocity $\omega$), density $\rho_s$, gravitational acceleration $g$; fluid density $\rho$ and fluid viscosity $v$, sediment shape, orientation and gradation etc. The general assumption is that the higher these parameters, the less sediment transport rate will be. The objective of this paper is to examine these basic assumptions using experimental data

 

available in literature. The famous existing models of sediment transport are tested against bedload data, and only the main parameters in these equations are used, and their correlation coefficients are calculated and compared. The research will identify the underlying mechanism of sediment transport. The purpose is to develop a unified sediment transport formula with higher accuracy for its transport rate. It is expected that new formula is superior to existing models and is applicable for waterways, coastal water and local scours.

## 2 LITERATURE REVIEW AND RESEARCH BACKGROUND

In sediment transport, researchers began from sediment transport from simplest case, and then apply their equations to complicated cases, e.g., equations of sediment transport in steady-uniform flows are established first, then their application in non-uniform flows or unsteady flows is tested. At its beginning stage, pioneer researchers like Einstein (1942), Meyer-Peter and Muller (1948), Bagnold (1966), Yalin (1977), Engelund and Hansen (1972) and Ackers and White (1973) agree that sediment discharge depends on the bed shear stress or in its dimensionless form

$$g_t' = f(\tau_*) \quad \text{and } \tau_* = \tau/[(\rho_s-\rho)gd] \qquad [1]$$

Shields (1936) used $\tau_*$ to express the dimensionless shear stress $\tau$ (= $ghS$), and $g_t'$ is the dimensionless sediment discharge. All of them believed that the parameter $\tau_*$ alone could fully express the sediment transport rate. Globally, the other group of researchers mainly in Russia and China believe that velocity is more explicit for sediment transport as they noticed that more particles are transported at higher velocity $U$. Typically, Velikanov (1954) parameter has the following expression:

$$C = k\left(\frac{U^3}{gh\omega}\right)^m \qquad [2]$$

where $C$ = sediment concentration, $U^3/(gh\omega)$ is Velikanov parameter. This parameter was initially developed for suspended load, it is also to examine its extension to bed-load. As both mean velocity $U$ and the boundary shear stress $\tau$ correlate poorly with the measured sediment transport rate, another parameter, known as the stream power (= $\tau U$) was proposed by Bagnold (1966), who hypothesized that the work used to transport sediment comes from the stream power. He assumed that

$$g_t' = f(\tau U) \qquad [3]$$

Yalin (1977) commented that the stream power is actually $\rho gSq$ where the discharge per unit width $q$ = $Uh$. For a channel its slope S is constant, then he concluded that Eq. 3 tells that sediment discharge is proportional to the water discharge. This implies that other parameters like bedform roughness has no influence on sediment discharge. For a river with constant width, its slope must be very steep in mountainous reach, and S becomes smaller in its middle reach, Eq. 3 indicates that the rate of sediment transport only depends on channel's slope $S$. According to Yalin, this is unacceptable. Obviously, the parameters $U$ and $S$ alone cannot express the measured sediment transport very well, Yang (1973) empirically found that the parameter of unit stream power $US/\omega$ yields the highest correlation coefficient among the existing hydraulic parameters. This discovery has significantly advanced the knowledge of sediment transport and greatly improved the accuracy of sediment prediction. But the unit stream power cannot be extended to the coastal waters because the energy slope $S$ is not available.

$$C = f(US/\omega) \qquad [4]$$

Probably van Rijn (1984) was the first one who realized the importance of bedforms and proposed the new parameter $u_*'$, the shear velocity related grains. He believed that the driving force of sediment can be fully expressed using this parameter:

$$T = \frac{u_*'^2 - u^2{}_{*c}}{u_{*c}^2} \qquad [5]$$

and the resistance force can be fully expressed by

 

$$d_* = d\left[\frac{(\rho_s/\rho - 1)g}{\nu^2}\right]^{1/3} \quad [6]$$

and the shear velocity related to grains is

$$u_*' = \frac{U}{2.5\ln\frac{11h}{2d_{50}}} \quad [7]$$

2.1 Existing models give totally opposite predictions

As noted by Yalin, bed roughness has significant influence on sediment transport rate. It is worthwhile to analyze this influence based on different assumptions shown in Eqs. 1-7. For a channel with constant slope $S$, discharge per unit width, $q$, and constant $d_{50}$, the Manning equation gives that

$$U = \frac{q}{h} = \frac{1}{n}h^{2/3}S^{1/2} \quad [8]$$

Eq. 8 shows higher roughness has lower velocity. As the discharge per unit width is constant, thus the water depth is higher. Therefore Eq. 1 predicts that the sediment transport rate is reduced due to the higher water depth as $\tau = ghS$ and every parameter except $h$ is constant in $\tau_*$. However, other equations give totally different prediction as the velocity is reduced in higher roughness, Eq. 2 says the sediment concentration is reduced (lower $U$ and higher $h$). Eq. 4 also predicts lower sediment concentration as $S$ and $\omega$ are constant but $U$ become smaller when the bed is roughened. Similarly van Rijin's method predicts the sediment transport rate is reduced as $d_*$ is constant and $u_*'$ is smaller in a roughened channel.

Bagnold's stream power in Eq. 3 shows that sediment transport is independent of the bed roughness. In this case, the discharge per unit width is constant, thus the driving force remains unchanged. Therefore, the sediment discharge remains unchanged.

Now for the case that a channel is roughened, it is interesting to note that there are three totally different results predicted by the existing models:

i. Sediment transport rate is increased (see Eq. 1);
ii. Sediment transport rate is reduced (see Eq. 2, 4 and 5);
iii. Sediment transport rate keeps unchanged (Eq. 3).

These results are shown in Figure. 1.

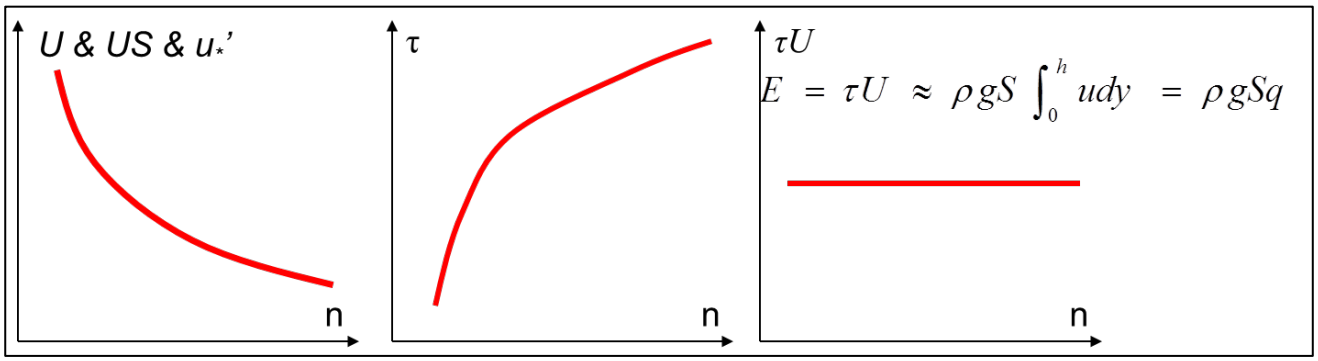


**Figure 1.** Different predications for sediment discharge or concentration by existing models in literature for a roughened channel with increasing $n$, but constant $S$, $d_{50}$, and $q$.

Figure. 2 shows the sediment transport versus various hydraulic parameters in order to check the relationship between sediment transport and these parameters shown in Eqs. 1-4. It can be seen that, based on Stein's (1965) data which covers initiation of sediment transport, ripples, dunes, and antidunes from bed-load to suspended load, none of them has the one-to-one relationship, at the same value of hydraulic parameter, the measured sediment concentration or discharge has 5-10 times difference. This implies that the equations shown above are not reliable.

 

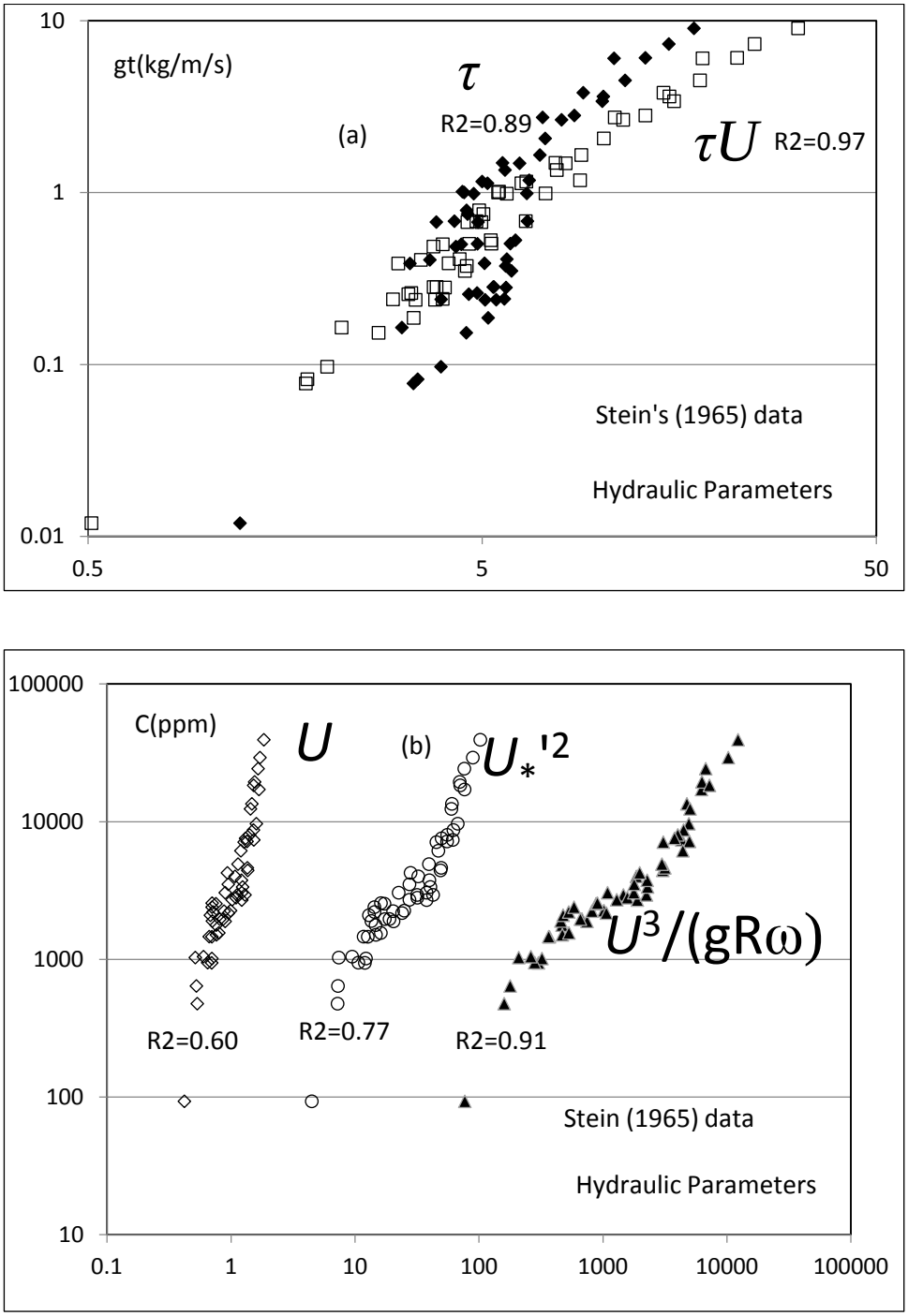


**Figure 2.** Measured sediment transport rate or concentration versus different hydraulic parameters based on Stein's (1965) data with $d_{50}$ = 1.5mm.

## 3 PROPOSED SEDIMENT TRANSPORT FORMULA

The investigations of the problem have resulted in numerous studies on calculating the sediment discharge. To date, many sophisticated equations have been proposed to calculate the total-load rate or bed material load. Most of the existing models involve factors that are summarized as:

$$C_t = f(U, g, h, S, \rho, \rho_s, \nu, \omega, d_{50}, B, \sigma_g) \qquad [9]$$

where $C_t$ = total sediment transport concentration in kg/m$^3$; $g$ = gravitational acceleration; $h$ = water depth; $S$ = energy slope; $\rho$ = water density; $\rho_s$ = sediment density; $\nu$ = fluid viscosity; $\omega$ = particle fall velocity; $d_{50}$ = particle median diameter; $B$ = width of channel; $\sigma_g$ = gradation of sediment size.

Since sediment transport is a near boundary phenomenon, Yang and Lim (2003) noticed that all parameters to describe the phenomenon should be those related with boundary, thus they chose these parameters like boundary shear stress τ, and they did not choose the mean velocity V, rather than the shear

 

velocity related with grains, i.e., $u_*'$ as defined in Eq. 7. They argued in this way to clarify van Rijn's treatment based on the physical interpretation as shown in Figure. 3. It is clearly that

$$u_*' = u_* = (gRS)^{0.5} \qquad [10]$$

is valid only when the bed is flat, and no energy is dissipated on large vortices which do not contribute to transport sediment, but just stirring up or re-suspend sediment, and $u_* \geq u_*'$

Once the bedform is present, there is a relationship:

$$\tau = \tau' + \tau'' \qquad [11]$$

Einstein is the first one who realized that the total shear stress should be divided into two parts, shear tress related with grains and shear stress related with bedforms, but he did not define τ' correctly till van Rijn (1984).

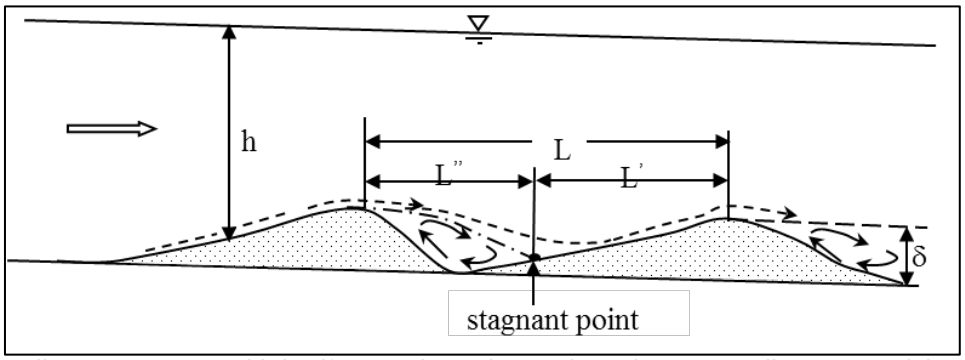


**Figure 3.** Sediment transport with bedforms where the vortices do not contribute to particle movement.

In fact, van Rijin found the importance of $u_*'$ empirically, and he did not link his discovery with Eq. 11. Yang and Lim (2003) analyzed the mechanism of energy transport and dissipation in channel flow and bridge the gap between Eqs. 7 and 11 using Figure. 3 by pointing out that not all energy dissipated on the bed contributes to sediment transport, and the average velocity of particles should not be proportional to the average velocity $V$ as assumed by Bagnold, it also should not be proportional to $u_*$ as assumed by Yalin. It should be proportional to $u_*'$. Based on these considerations, they revised Eq. 1 by introducing $E$ and $u_*'$ where $E$ is the work done per unit time on a unit area by the flow is $\tau u_p$, where $\tau$ is the bed shear stress and $u_p$ is the flow velocity near the bed, part of which is used to transport the sediment and is expressed as

$$E = \tau (u_*' - u_{*c}) \qquad [12]$$

where $u_{*c}$ is the critical velocity at incipient sediment motion. $E$ is the energy transferred from the main flow region and exerts on the boundary flow region. The kinetic energy generated enables the particles to collide with each other and saltate, the work rate of sediment transport by gravity may be expressed as

$$E_s = \lim_{a \to 0} \int_a^h (\rho_s - \rho) C_y \, \omega \, dy = (\rho_s - \rho) \omega h \overline{C} \qquad [13]$$

where a = thickness of bed–load layer, $C_y$ and $\overline{C}$ is local and mean sediment concentration, respectively. Therefore, the sediment discharge $g_t$ is

$$g_t = \int_a^h \rho_s g C_y u_y \, dy = \rho_s \alpha g h u_*' \overline{C} \qquad [14]$$

where $\alpha$ is a coefficient, $u_y$ and $u_*'$ are the local and mean velocity, respectively. Substituting 13 into 12, and assuming $E_s = k_1 \tau (u_*' - u_{*c})$, where $k_1$ is an "efficiency coefficient' of the flow yields

For the simplification. With these considerations, (14) becomes

$$g_t = k \left( \frac{\rho_s}{\rho_s - \rho} \right) \tau \left( \frac{u_*'^2 - u_{*c}^2}{\omega} \right) = k \frac{\rho_s}{\rho_s - \rho} T_T \qquad [15]$$

Where,

$T_T = \tau (u_*'^2 - u_{*c}^2) / \omega$ is called the total-load transport parameter.

The procedure of calculation is as follows:

1. Determine $u_{*c}^2$ from the Shields curve based on $d_{50}$.

2. Calculate the grain shear velocity $u_*^{'2}$ using

$$\frac{U}{u_*'} = 2.5\ln(\frac{11R}{2d_{50}}) \qquad [16]$$

3. Calculate the mean bed shear stress, $\tau = \rho gRS$

4. Use $k$ = 12.5.

Based on same data set, Figure. 4 exhibits that one-to-one and linear relationship can be provided only by the new total-load transport parameter, $T_T = \tau(u_*^{'2} - u_{*c}^2)/\omega$ which achieved the highest correlation coefficient of R = 0.987. A semi-theoretical derivation of a new sediment discharge formula based on the new total-load transport parameter, $T_T$ is given in the following section.

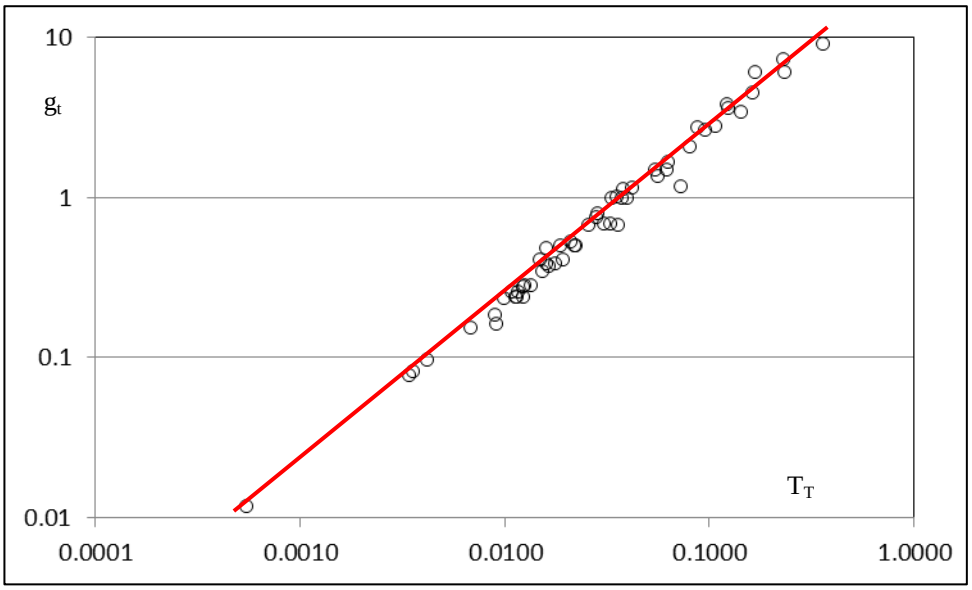


**Figure 4.** Measured sediment discharge versus the new hydraulic parameter TT based on Stein's (1965) data in Figure.2, but TT demonstrates the best one-to-one relationship.

The above conclusion is confirmed when Gilbert's dataset is used to analyse the correlation coefficients between the measured sediment concentration with TT and VS/ω. Total 780 observation sets are used and the results are shown in Table 1, it can be seen that the new parameter for sediment transport is obviously better than C. T. Yang's unit stream power. In table 1, all Gilbert's 780 observations are used in the calculation of correlation coefficients in order to avoid a prejudice. The row 1 shows the sediment size and row 2 indicates the number of experimental runs done by Gilbert. The correlation coefficients between measured sediment concentration, C and VS/ω are listed in row 3, the calculated results of parameter TT are listed in row 4 based on similar data shown in row 3. The last row exhibits the ratio of difference in row 4 and row 3 to the values in row 3. It can be seen from the last row of Table 1 that the parameter TT achieves obviously higher correlation coefficient in all cases, in other words, sediment transport is strongly related to TT. Gilbert's data confirms the conclusion drawn from Figure. 4.

**Table 1.** Correlation coefficient based on Gilbert's data in terms of $VS/\omega$ and $\tau/(u_*^{'2}-u_{*c}^{'2})/\omega$

| | | | | | | | | |
|---|---|---|---|---|---|---|---|---|
| (1) | $d_{50}$ (mm) | 0.305 | 0.37 | 0.51 | 0.79 | 1.71 | 3.08 | 4.94 |
| (2) | No. of runs | 57 | 205 | 233 | 115 | 48 | 36 | 69 |
| (3) | C versus VS/ω) | 0.863 | 0.845 | 0.781 | 0.901 | 0.903 | 0.893 | 0.926 |
| (4) | $g_t$ versus $\tau(u_*^{'2} - u_{*c}^2)/\omega$) | 0.972 | 0.921 | 0.956 | 0.988 | 0.973 | 0.972 | 0.989 |
| (5) | [(4)-(3)]/(3) (%) | 12.6 | 9.0 | 22.4 | 9.6 | 7.8 | 8.8 | 6.8 |

## 4 DATA ANALYSIS AND VERIFICATION

The 3500 data sets used for the verification of Eq. 15 were compiled by Brownlie (1981). The large

number of data sets were sub-divided and plotted in Figure. 5 in the format of predicted sediment discharge against the measured values where the solid lines represent perfect agreement and the dotted lines represent ±100 % discrepancy. The main objective is to study the influence of the various parameters in Eq. 16 on the constancy of k and also to achieve clearer presentation. Note that the authors of the data in the Figure are not quoted, it can be found in the reference section (Brownlie, 1981). On the left of Figure. 5, the field data is included for comparison based on a total of 341 data sets from 10 different researchers. The good agreement as shown in Figure. 5 testifies that k = 12.5 is indeed a constant and that sediment discharge exhibits a one-to-one linear relationship with the total-load transport parameter $T_T$. The remaining data is shown on the right of Figure. 5, and good agreement is also achieved.

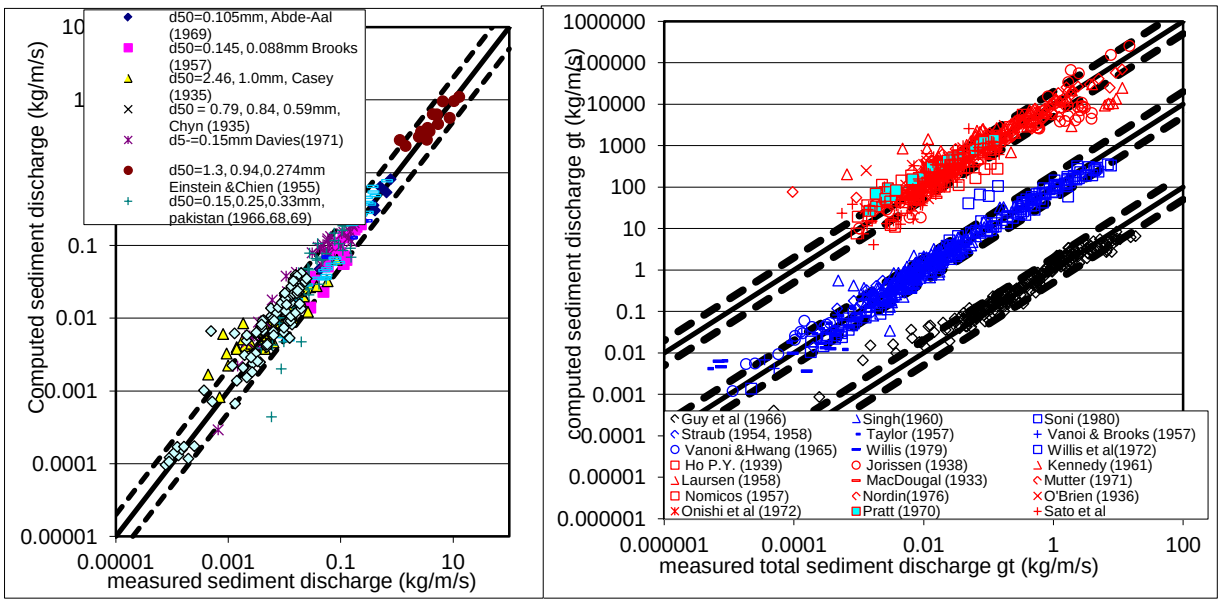


**Figure 5.** Comparison of total sediment discharge computed using (15) and measured data from different researchers.

From the above discussion, it is clear that Eq. 15 is a very practical and user-friendly predictive formula to calculate total sediment discharge in alluvial channel. The factor of proportionality, k in Eq. 15 has been checked for a wide range of hydraulic conditions and is a constant with a value of 12.5, irrespective of sediment size, sediment density, channel aspect ratio, sediment concentration.

Considering the large database used and the range of applicability of the formula, the result obtained is comparable, if not better than most of the existing total sediment discharge formulas. In particular, the writers have made specific comparisons on the accuracy of Eq. 15 with some of the better-received existing formulas in terms of their predictability for Gilbert's data, the ability to address the effect of aspect ratio, as well as silt transport. Equation 9 scores remarkably well in all these comparisons. Though no direct comparison with other formulas is presented here, it is obvious that all previous formulas would have used some of the data sets compiled by Brownlie (1981) for verification. In this respect, we can reasonably say that an indirect comparison has been achieved and our results showed, on average, that 84% of the data sets were predicted within a factor of 2 times of the measured values.

## 5 INFLUENCE OF VERTICAL VELOCITY ON SEDIMENT DISCHARGE

Sediment transport is obviously a phenomenon of particle movement driven by fluid motions in streamwise and vertical directions. Sediment discharge could be very high if vertical motion is torrent and streamwise motion is gentle. This can be seen from sediment transport caused by tidal flows, where the highest concentration always appears when the streamwise parameters ($\tau$, $U$ or $u_*$') are minimum, and all equations listed above are invalid to express sediment transport. The mechanism is discovered by Yang (2013) who claims that the vertical velocity $V$ plays an important role for the invalidity of sediment transport. Francalanci et al. (2008) also attributed the invalidity to pressure variation. Contrary to Francalanci et al. (2008) treatment, Yang (2013) re-examined the observed data and concluded that the parameters to express the vertical driving force could be pressure $P$ (Francalanci et al., 2008), vertical velocity $V$ (Yang 2013), vertical hydraulic gradient $i$ in sediment layer (Cheng and Chiew 1999) etc.

The vertical and horizontal velocities always coexist, the omission of vertical motion could be the main reason leading to the poor performance of models for sediment transport prediction because none of them are good enough to explain the formation of phase lag and dune formation. In other words, the inclusion of vertical motion could significantly improve the understanding of sediment transport in turbulence. If the inference is

 

correct, the similarities between turbulence and waves must be observable as they both have the upward velocity (or ejection) and downward velocity (sweep), this interplay is responsible in affecting the threshold of particle movement, the entrainment and transport of bedload and suspension load. To this end, the study on the similarities of sediment transport by vertical motions in waves and bursting conditions is helpful to clarify the mechanism of sediment transport. To include the vertical motions, the writer considers a simple model shown in Figure. 1 in which a permeable bed comprising sand and gravels on a bed is represented by uniform spherical particles with diameter d. The water velocity on the interface, which is represented by $V_s$, is the flow between the ground water and main flow with mean velocity $U$ and depth $h$. The introduction of vertical velocity $V_s$ is simpler and more convenient as compared to the pressure $P$ and hydraulic gradient $i$ in terms of mathematical treatment and also measurement. For the particles with diameter $d$, the settling velocity $\omega$ in still water can be determined by:

$$C_d \pi \frac{d^2}{4} \frac{\rho \omega^2}{2} = \pi \frac{d^3}{6} g(\rho_s - \rho) \qquad [17]$$

where $C_d$ is the drag coefficient and depends on the Reynolds number Re ( = ωd/v).

In the environment that the ambient fluid moves upward with velocity $V_s$, the settling velocity reduces to $\omega - V_s$. The same settling velocity in still water could be achieved if the particle's size remains unchanged but its density is changed to $\rho_s'$, and the force balance equation is similar to Eq. 17 with the following form:

$$C_d' \pi \frac{d^2}{4} \frac{\rho(\omega - V_s)^2}{2} = \pi \frac{d^3}{6} g(\rho_s' - \rho) \qquad [18]$$

From Eqs. 17 and 18, one can derive the following relationship:

$$\frac{\rho_s' - \rho}{\rho_s - \rho} = \alpha \left(1 - \frac{V_s}{\omega}\right)^2 \qquad [19]$$

where $\alpha = C_d'/C_d \approx 1$. Contrary to Francalanci et al. (2008) treatment in which they modified the fluid density in order to express the influence of upward motion. Eq. 19 introduces the "apparent" particle density of ρs' and Eq. 19 implies that the effects of non-hydrostatic pressure can be equivalently expressed by the variation of sediment density. If an upward seepage across the porous boundary ($V_s > 0$) is present, Eq. 7 gives $\rho_s' < \rho_s$, which suggests that sediment transport in such case is similar to the lightweight material transport without seepage. Therefore, Eq. 19 simplifies the very complex sediment transport into a relatively simple transport model, it demonstrates that the upward velocity Vs promotes particles' mobility and the downward velocity $V_s$ has the effect to increase sediment density or stability as it becomes heavier.

The brief review reveals that currently all researchers believe that sediment transport can be fully expressed by horizontal parameters like $U$, $u_*'$, $\tau$, $E$ or $US$ etc. All equations including Eq. 15 predict that higher the horizontal parameters are, the more particles are transported. However, this prediction is wrong under wave conditions where the highest rate of sediment transport never occurs when the streamwise parameters listed above are the highest. Instead, the peak sediment concentration or transport rate always occurs after the peak driving force in the streamwise direction. This phase lag has been widely documented in the literature. The equation of sediment discharge subject to the vertical velocity can be obtained by modifying the sediment density in Eq. 15 with the following form:

$$g_t(Y) = k\left[\frac{\rho}{\rho_s - \rho}\left(\frac{1}{1-Y}\right)^2 + 1\right]\tau_o \frac{u_*'^2 - u_{*c}'^2}{\omega(1-Y)} \quad \text{and} \quad Y = V_s/\omega \qquad [20]$$

$$\frac{g_t(Y)}{g_t(0)} = \frac{\rho}{\rho_s (1-Y)^3} + \frac{\rho_s - \rho}{\rho_s (1-Y)} \qquad [21]$$

## 6 VERIFICATION BY OBSERVATIONS

The research group in Nanyang Technological University, Singapore led by Prof. Chiew has been carrying out a series of research works to measure the influence of vertical velocity on sediment transport. The tests in this study were conducted in a rectangular perspex flume that was 4.8m long, 0.25m wide and 0.25m deep supported on a steel frame. Figure. 4 shows the measured data (from personal communication with Prof. Chiew). It can be seen from Figure. 4 that the sediment transport rate can be significantly promoted by an upward velocity. If the upward velocity is 80% of settling velocity (Y = 0.8), then the predicted sediment transport rate can be increased to 50 times of $g_t(0)$. This explains why the scour holes are formed. Figure. 4

 

also shows that the sediment transport rate is reduced if a downward flow exists in a river. If the downward velocity = settling velocity, i.e., $Y$ = -1, then the sediment transport rate will be reduced to 1/3 of $g_t(0)$. This transport rate is achieved as the particles becomes “heavier”.

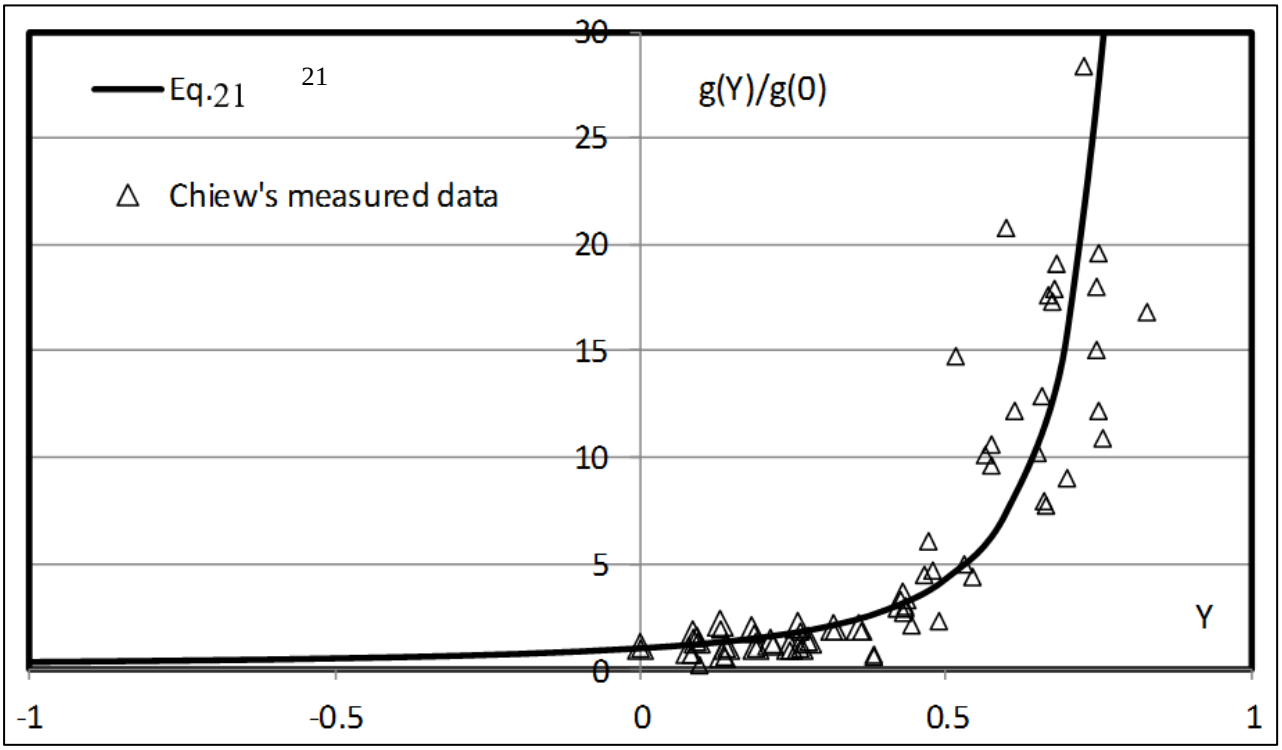


**Figure 6.** Comparison of predicted and measured sediment discharge versus the vertical motion, in which Y = 0 means no vertical velocity; Y < 0 stands for accelerating flow where the sediment discharge is reduced and Y > 0 for decelerating flow where sediment discharge is increased significantly.

## 7 CONCLUSIONS

A sediment discharge formula, Eq. 21 has been developed. The main advantages of the formula are its accuracy, ease of computation and the wide range of applicability. The total sediment discharge, $g_t$ is computed directly and is linearly proportional to the total-load transport parameter. The constant of proportionality, k has been tested and verified against a wide range of hydraulic conditions. The k-value is 12.5, irrespective of sediment size, channel aspect ratio and sediment concentration. The verification exercise for the proposed equation used over 3500 published total-load data from both field and flume studies. The results showed that, on average, 84% of the data were predicted within a factor of 2, i.e. 0.5 and 2 times of the measured values. This study investigates why models of sediment transport are invalid in prediction, why the bedforms are ubiquitous in natural and laboratorial flows, and why the maximum sediment concentration always lags behind the maximum of discharge. It has been clarified that all are caused by the omission of vertical motions. The upward velocity enhances sediment mobility and downward velocity increases its stability. Mathematically the behavior of sediment transport subject to a vertical motion can be equivalently treated by the introduction of apparent density. Particles become “heavier” when they experience the downward flows, this reduces the sediment transport rate. But particles become “lighter” in flows with upward velocity where the sediment discharge is increased significantly. This conclusion can well explain the formation of scour hole. The vertical velocity can be induced by channel’s geometry, non-uniformity, unsteadiness, burst, density stratification, surface waves etc. Generally speaking, accelerating flows produce downward velocity, decelerating flows generates upward velocity. Severe scour is always associated with the upward flows or decelerating flows. This is why severe erosion always occurs in decelerating flows that generates the upward velocity. Its influence on turbulence structures and sediment transport should not be underestimated. More theoretical and experimental studies are required in the future.

## REFERENCES

Ackers, P. & White, W. R. (1973). Sediment Transport: New Approach and Analysis. *Journal of the Hydraulics Division*, 99(11), 2041-2060.

Bagnold, R. A. (1966). *An Approach to the Sediment Transport Problem from General Physics*. Geol. Survey Professional Paper No. 422-I, US government printing office.

 

Brownlie, W. R. (1981). *Compilation of Alluvial Channel Data: Laboratory and Field*. California Institute of Technology, California. Report No. KH-R-43B.

Cheng, N. S. & Chiew, Y. M. (1999). Incipient Sediment Motion with Upward Seepage. *Journal of Hydraulic Research*, 37(5), 665-681.

Einstein, H. A. (1942). Formulas for the Transport of Bed Load. *Trans. American Society of Civil Engineers*, 107, 561-597.

Engelund, F. & Hansen, E. (1967). *A Monograph on Sediment Transport in Alluvial Streams*. TEKNISKFORLAG Skelbrekgade 4 Copenhagen V, Denmark.

Francalanci, S., Parker, G., & Solari, L. (2008). Effect of Seepage-Induced Nonhydrostatic Pressure Distribution on Bed-Load Transport and Bed Morphodynamics. *Journal of Hydraulic Engineering*, 134(4), 378-389.

Meyer-Peter, E. & Muller, R. (1948). Formula for Bed Load Transport. *IAHR*.

Shields, A. (1936). *Anwendung der Aehnlichkeitsmechanik und der Turbulenzforschung auf die Geschiebebewegung*. Preussischen Versuchsanstalt für Wasserbau.（English translation by W.P. Ott and J.C. van Uchelen, 36pp. US Dept. of Agric. Soil Conser. Serv. Coop. Lab., California Institute of Technology. Pasadena, 1936）

Stein, R. A. (1965). Laboratory Studies of Total Load and Apparent Bed Load. *Journal of Geophysical Research*, 70(8), 1831-1842.

Van Rijn, L. C. (1984). Sediment Transport, Part I: Bed Load Transport. *Journal of hydraulic engineering*, 110(10), 1431-1456.

Velikanov, M. A. (1954). Gravitational theory for sediment transport. Journal of Science of the Soviet Union, Geophysics, 4, 349–359. (In Russian).

Yalin, M.S. (1977). *Mechanics of Sediment Transport*. 2nd Edition, Pergamon Press, Sydney.

Yang, S. Q. & Lim, S. Y. (1997). Mechanism of Energy Transportation and Turbulent Flow in a 3D Channel. *Journal of Hydraulic Engineering*, 130(9), 163-173.

Yang, S. Q. & Lim, S. Y. (2003). Total Load Transport Formula for Flow in Alluvial Channels. *Journal of hydraulic engineering*, 129(1), 68-72.

Yang, C. T. (1973). Incipient Motion and Sediment Transport. *Journal of the hydraulics division*, 99(10), 1679-1704.

Yang S.Q. (2013). Why cannot Sediment Transport be Accurately Predicted, *Proceeding of 35th IAHR World congress, Chengdu, China.*

 

# TEMPORAL CHANGE STUDY ON TAPI RIVER MEANDER USING REMOTE SENSING AND GIS

KEYUR J. PRAJAPATI[(1)] , SAHITA I. WAIKHOM[(2)] & SANJAY M. YADAV[(3)]

[(1)]Shri Swami Atmanand Saraswati Institute of Technology, Varachha, Surat, Gujarat, India.
keyurprajapati34@gmail.com
[(2)] Dr. S. & S. S. Ghandhy Government engineering college, Majuragate, Surat, Gujarat, India.
siwgecs@gmail.com
[(3)]Sardar Vallabhbhai National Institute of Technology, Surat, Gujarat, India.
smy@ced.svnit.ac.in

## ABSTRACT

A meander forms when moving water in a stream erodes the outer banks and widens its valley, and the inner part of the river has less energy and deposits silt. Meander characteristics play an important role in location, design and maintenance of hydraulic structures such as bridge, barrage, flood embankment and guide bank. Tapi river is known for occurrence of large floods due to influence of depressions originating from bay of Bengal traveling East to West causing rainfall, first in the upper catchments and then in lower catchments resulting of flood along its course. The present paper deals with the study of meander of Tapi River around Surat city. Temporal change study is done for Tapi River from Kamrej to Adajan using LANDSAT images from 1973, 1990, 2003 & 2015 i.e. a time span of approximately 13 years and toposheet of year 1950. Morphometric parameters such as Sinuosity Index and Island Area were measured to detect the periodical change. From the observation and analysis of temporal changes, it is deduced that the channel shifting is more at the ends of meander curvature to the apex of the meander portion of Tapi River. The study also indicates that the flood events and construction of Singanpore weir as major factor which causes erosion and sedimentation that ultimately leads to the shift of river banks and changes in the width of the river.

**Keywords:** Tapi river; river meandering; morphometric parameters; satellite images; temporal change.

## 1 INTRODUCTION

A meander, in general, is a bend in a sinuous watercourse or river. A meander forms when moving water in a stream erodes the outer banks and widens its valley, and the inner part of the river has less energy and deposits silt. A stream of any volume may assume a meandering course, alternately eroding sediments from the outside of a bend and depositing them on the inside. Over time, meanders migrate downstream, sometimes in such a short time as to create civil engineering problems for local municipalities attempting to maintain stable roads and bridges.

It is very rare to find straight alluvial channels, because most streams tend to meander unless they are confined in a narrow valley or gully. A curve along the channel introduces an additional form of energy dissipation not present in a comparable straight reach, an energy loss due to change of flow direction (Leopold et al., 1960). Meandering nature are common in alluvial river mainly of low gradient. On flat ground a river tends to form a relatively broad channel that slowly wanders back and forth.

The evolution of a meandering planform is characterized by three basic processes: (1) the continuous elongation of the river axis, with single or compound lobe formation, (2) the downstream (sometimes upstream) migration of the meander loops, and (3) the occurrence of cutoff events. Through time, the configuration and position of rivers changes as part of meander evolution, development, and migration processes. The process of migration does not occur simultaneously along the entire length of a channel but, at discrete location at any one time, leading to the alteration of individual meanders. Channel migration or meander migration is a combination of translation and extension of river channels (Brice, 1984). Bank erosion and accretion leads to bank retreat and advance respectively. Changes in the configuration of a single bend may include rotation, elongation, and a shift in meander axis .When meanders change their shape and shift in their position, the associated erosion and deposition that enables these changes to occur can cause loss or damage to private properties and structures.

Channel migration through time and space is critical for many geo-morphological and river management problems (Petts, 1995; Milton et al., 1995; Hickin, 1983). The Lateral migration refers to the positional change of a river channel as a response to variations in fluid flow and sediment discharges which is associated with bank erosion of the stream bed or channel wall under turbulent flow conditions (Yang et al., 1999). Pati et al. (2008) carried out the river bank erosion study on Majuli, the world's largest river island, situated in the middle of river Brahmaputra in Assam. They studied that the trends of erosion in a small part of Majuli island, near Kaniajan village in south Majuli—a 11 km stretch, using satellite data of 1991, 1997, and 1998. Erosion

 

and deposition maps of the area were prepared and at various sections at 1-km interval the erosion of island is measured. Satellite remote sensing and geographic information system (GIS)-based monitoring of dynamic environmental change of the active Yellow River Delta, China was done by Yang(1996) and Yang et al.(1999). The main data source in this study was a series of time-sequential Landsat images spanning a period of approximately 19 years. A GIS was used to support modernized channel position mapping and measurement. The study demonstrated the utility of satellite remote sensing in investigating channel migration, integrated with a GIS. Milton et al. (1995) investigated change in fluvial systems using remotely sensed data. A GIS-based approach has been used by Winterbottom and Gilvear (2000) for mapping probabilities of river bank erosion in regulated River Tummel, Scotland. Mani et al. (2003) used remote sensing data for erosion study of a part of Majuli River Island. The nature of bank erosion has been studied by Kotoky et al.(2005) along the Brahmaputra river channel, Assam, India. Kummu et al. (2008) studied and detected the riverbank changes using remote sensing data along the Mekong River in the Vientiane–Nong Khai area. Thakur et al. (2012) analyzed the river bank erosion hazard due to morphometric change of Ganga River in the upstream of Farakka barrage up to Rajmahal where they used the LANDSAT and IRS(Indian remote sensing) satellite images. Temporal shift measurements for the river reach has been done with the help of 22 cross-section in the reach. In the context of the present study, the above cited studies proves that remote sensing along with GIS plays an important role in river morphological and river bank change detection.

Tapi river is known for occurrence of large floods due to influence of depressions originating from bay of Bengal traveling East to West causing rainfall, first in the upper catchments and then in lower catchments resulting of flood along its course. At the time of floods in river Tapi, Surat city and surrounding regions are most affected. The city has faced many floods since long back. The Surat city and surrounding villages are part of flood drainage of Tapi river. Present study on river Tapi is undertaken to quantify the temporal change in the Tapi river from Kamrej to Adajan from 1950 to 2015 using satellite images and GIS.

## 2 STUDY AREA

### 2.1 Tapi river basin

The Tapi basin is situated in the northern part of the Deccan Plateau and extends over an area of 65,145 km which is nearly 2% of the total geographical area of the country. The catchment area up to Ukai dam is 62,225 sq. km. Nearly 80% of the basin lies in State of Maharashtra. The basin lies between east longitudes 78° 17′ E to 72° 33′ E and north latitudes of 20° 9′ N to 21o 50’ N. It is bound on the north by the Satpura range, on the east by the Mahadev hills, on the south by the Ajanta range and by the Satmala hills and on the west by the Arabian Sea. Bounded on the three sides by the hill ranges, the Tapi River along with its tributaries flows over the plains of Vidarbha, Khandesh, and Gujarat and covers large areas in the state of Maharashtra and small areas in Madhya Pradesh and Gujarat. The basin has an elongated shape with a maximum length of 534 km from east to west and the maximum width of 196 km from north to south. Perimeter of the basin is about 1,840 km. Figure 1 shows map of the Tapi river basin.

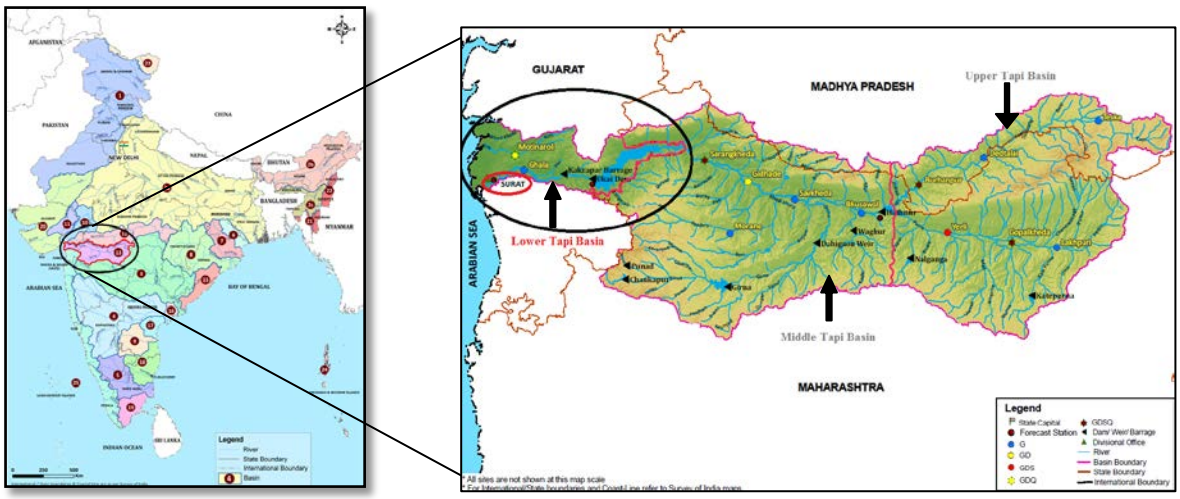


**Figure 1**. Tapi River Basin (India –WRIS)

### 2.2 Description of river system

The Tapi River originates near Multai in Betul district of Madhya Pradesh in the Satpura range at an elevation of 752 m above MSL. Apart from the Narmada river, Tapi is the only river which flows in the westward direction and merges into the Arabian Sea. The total length of this west flowing river from its origin

 

to its out fall into the sea is 724 Km. For the first 282 km the river flows in Madhya Pradesh, out of which 54 km forms the common boundary with Maharashtra State. It flows for 228 km in Maharashtra before entering Gujarat. Traversing a length of 214 km in Gujarat, the Tapi River joins Arabian Sea in the Gulf of Cambay after flowing past the Surat city. The river receives tidal influence for a length of about 25 Km upstream from the mouth. (Up to Singanpore weir causeway). Tapi River receives several tributaries on both the banks and there are 14 major tributaries having length more than 50 km. On the right bank, 4 tributaries namely Vaki, Gomai, Arunavati and Aner join the Tapi River. On the left bank, 10 important tributaries namely the Nesu, Amaravati, Buray, Panjhra, Bori, Girna, Waghur, Purna, Mona and Sipna drain into the main river channel. The drainage system on the left bank of the Tapi river is, therefore, more extensive as compared to the right bank area. The Purna and Girna, the two important left bank tributaries, together account for nearly 45 % of the total catchment area of the Tapi River. The city of Surat and the flat fertile lands in this area are severely affected by floods in the river which is shown in Table 1.

**Table 1**. Flood history at Surat

| Sr. No. | Flood Event (Year) | Discharge (Lakh Cusecs) |
|---|---|---|
| **1** | 1883 | 10.05 |
| **2** | 1884 | 8.46 |
| **3** | 1942 | 8.60 |
| **4** | 1944 | 11.84 |
| **5** | 1945 | 10.24 |
| **6** | 1949 | 8.42 |
| **7** | 1959 | 12.94 |
| **8** | 1968 | 15.5 |
| **9** | 1994 | 5.25 |
| **10** | 1998 | 7.00 |
| **11** | 2006 | 9.09 |
| **12** | 2012 | 10.0 |

The area in the lower Tapi basin, located between latitudes 21° 11′ and 21° 18′ N and longitudes 72° 48′ and 72°56′ E extending for about 18 km, which is the portion from Kamrej to near about Adajan, is chosen as a case study characterized by active river processes as shown in Figure 2. As there are number of flood events occurred in the past causing large sediment discharge and velocity during the flood, the change detection near the city area is important for the infrastructure developments nearby them.


**Figure 2.** Study area location from Kamrej to Adajan indicated by rectangle for temporal change detection.

## 3 DATA COLLECTION

For the temporal shift of the Tapi river from 1950 to 2015, Toposheet of year 1950 (U.S. Army Map Service, scale 1:250,000) and Landsat images of the year 1973, 1990, 2003, 2015 were used. The time span between two satellite images is taken as 13 years which include the occurrence of two flood events. Summary of images and toposheet collected for detection of temporal change is given in Table 2.

 

**Table 2.** Summary of Images used for change detection of Tapi River Meander

| Sr.No. | Data Type | Satellite Sensor | Date (dd.mm.yyyy) | Spatial Resolution (m) Or Scale | Source |
|---|---|---|---|---|---|
| 1 | Topographical map | NF 43-09 | 1950 | 1:2,50,000 | Series U502,US Army Map Service |
| 2 | Remote sensing images | Landsat-MSS | 04.03.1973 | 57 | USGS |
| 3 | | Landsat-TM | 25.03.1990 | 30 | USGS |
| 4 | | Landsat-ETM+ | 05.03.2003 | 30 | USGS |
| 5 | | Landsat-OLI,TIRS | 09.11.2015 | 30 | USGS |

*MSS–multispectral scanner system, TM-thematic mapper, ETM+– enhanced thematic mapper plus, OLI–operational land imager, TIRS–thermal infrared sensor*

## 4 METHODOLOGY

For the temporal change detection of Tapi River meander, ortho-rectified image of satellites such as LANDSAT multi-spectral scanner (MSS), thematic mapper (TM), enhanced TM, operational land imager (OLI) and thermal infrared sensor (TIRS) along with topographical sheets are used for river change analysis using ArcGIS 10.1. All the LANDSAT images and the toposheet were georeferenced with the universal transverse mercator (UTM) projection with zone 43N with datum of World geodetic system (WGS) 84 are used in all the geospatial data. Image classification was done for making land use land cover (LULC) maps with 4 classes. The unsupervised LULC classification has been carried out for 1973 and 1990 images as shown in Figure 3, and supervised LULC classification has been carried out for 2003 and 2015 images as shown in Figure 4.

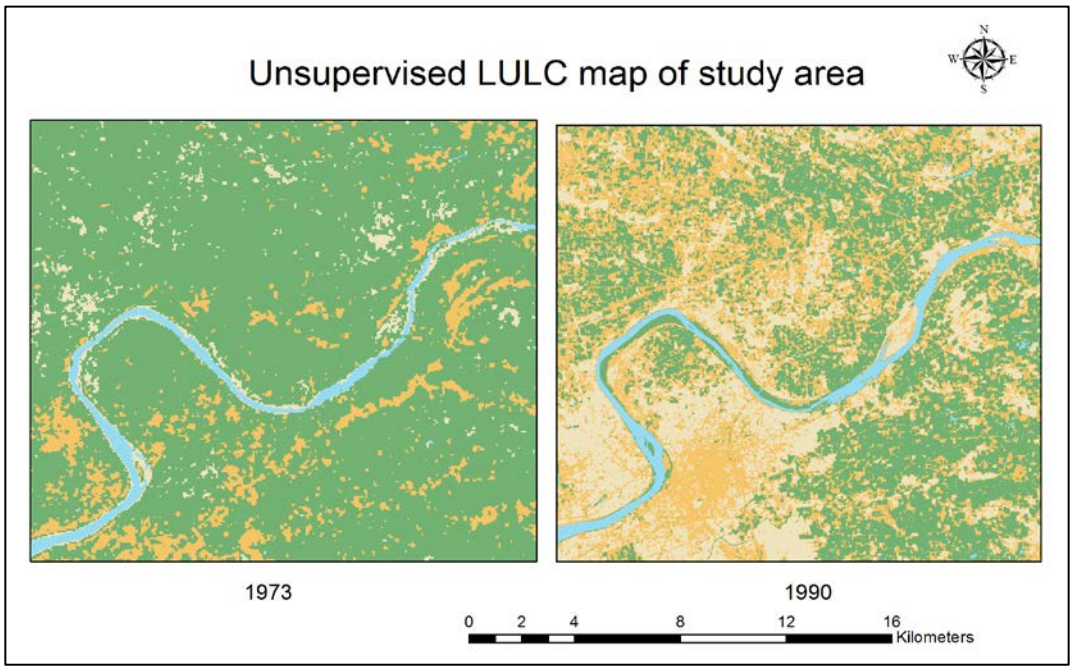


**Figure 3.** Unsupervised LULC classified image of 1973 and 1990

The 26 fixed cross-section were made in study area with references to 1950 map and 2015 image, considering base and latest position of Tapi River as shown in the Figure 5. The cross-section were created at unequal distance from east to west, giving more consideration to morphometric changes of river. The location of the cross-section is decided on the basis of visual analysis of temporal remote sensing images and major morphometric changes in river, with more dense cross-sections at locations where large changes in river bank. The cross-sections were extended on both the sides to ensure the river shifting measurement in both sides of the river. The red cross-section indicate the location of Singanpore weir in Figure 5.

Along those cross-sections, the distance between the left bank of two consecutive years has been calculated by measuring the distance between two points of the left bank of the respective year at each cross-sections as shown in the following Figure 6.

 

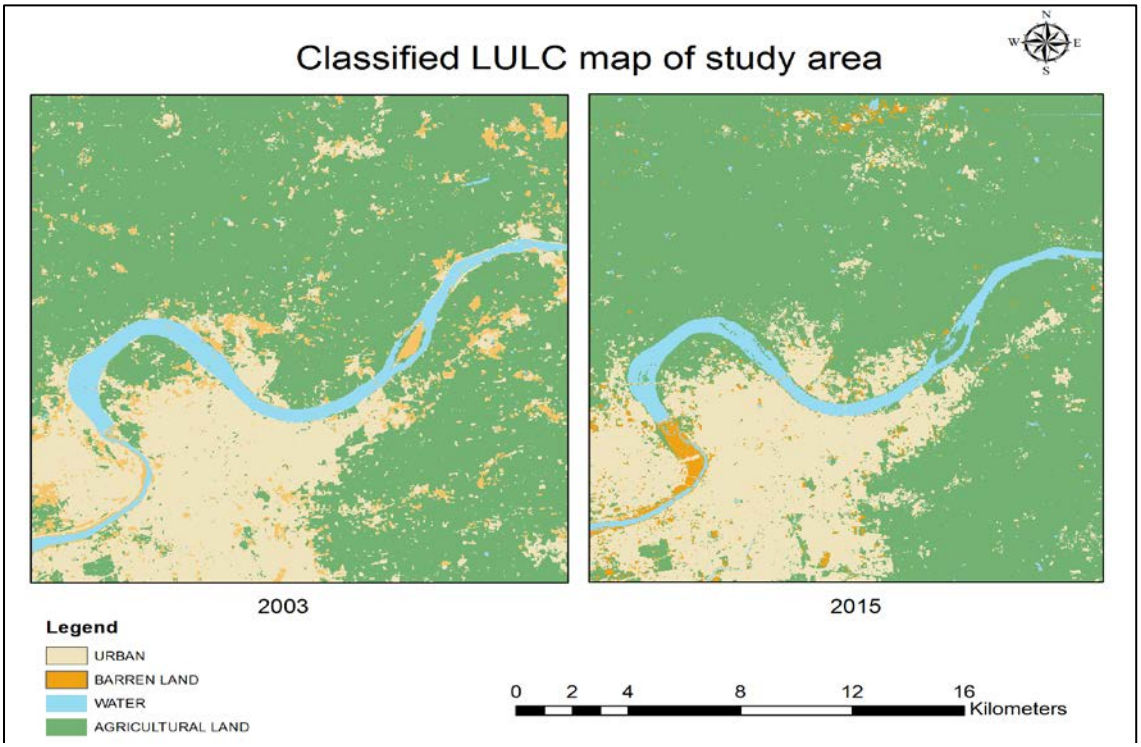


**Figure 4.** Supervised LULC classified image of 2003 and 2015

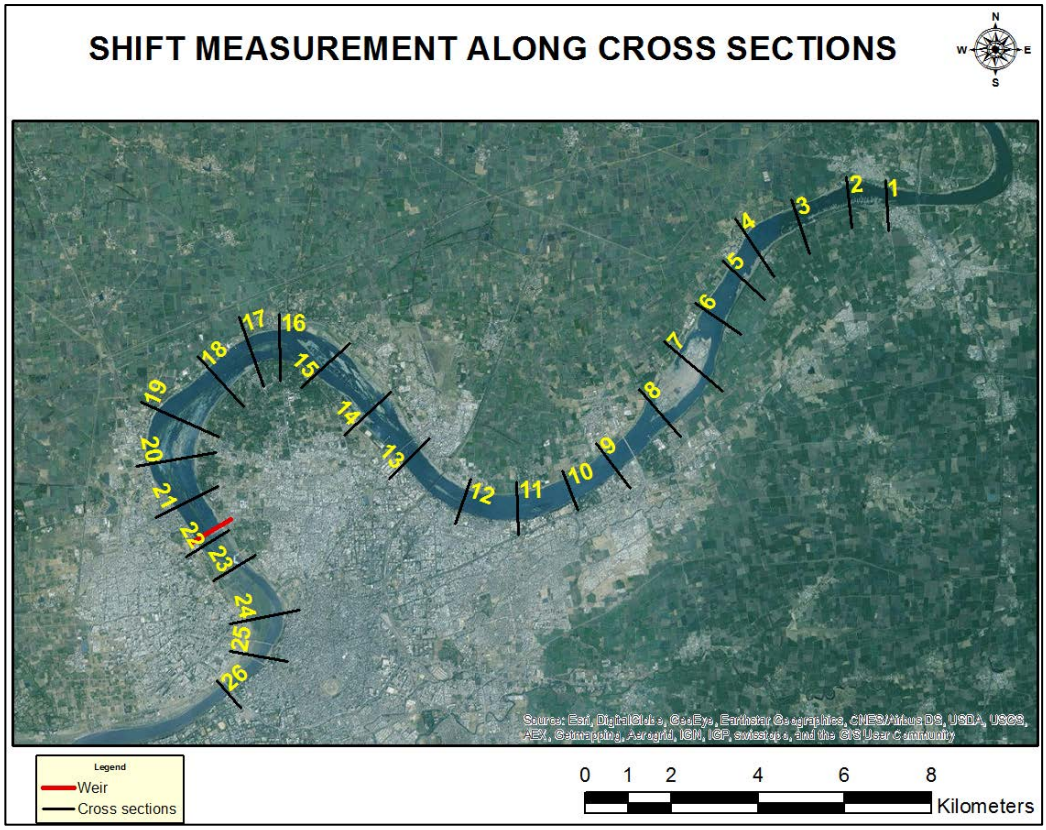


**Figure 5.** Cross-sections across Tapi River for measuring temporal shift

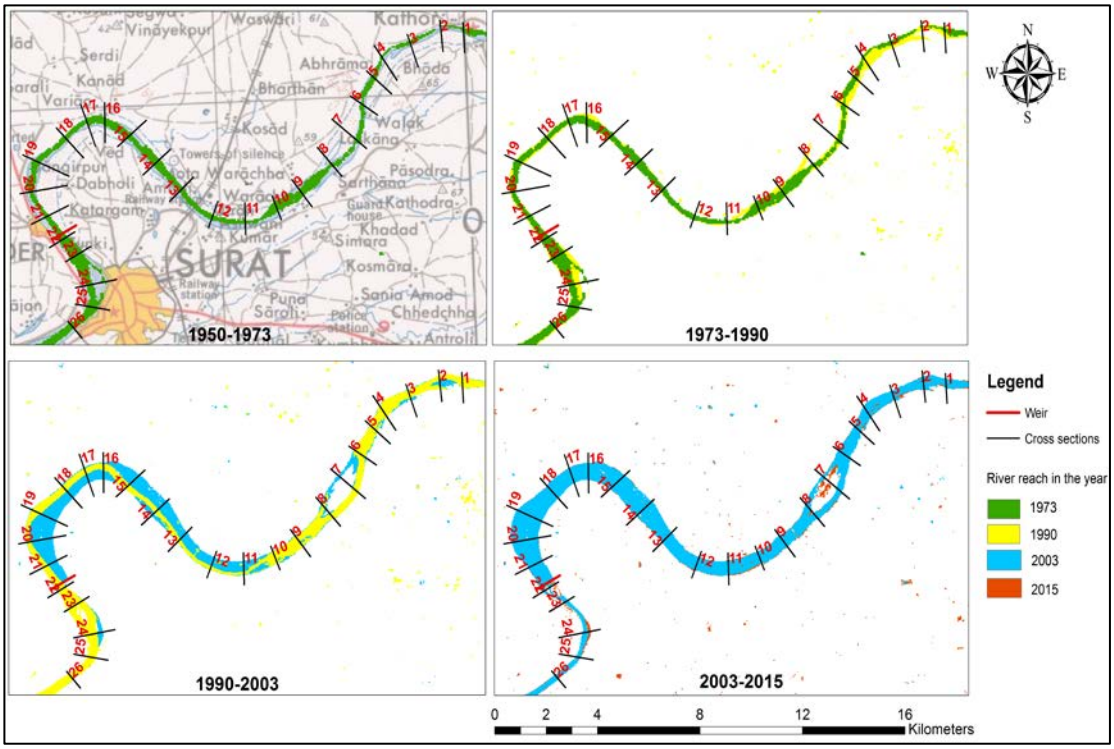


**Figure 6.** Temporal river shift over the years

Sinuosity index and Island area are used as morphometric indices in this study. Meandering rives have sinuous channels. The sinuosity (*P*) is the ratio of the channel length (*lc*) to the length of the meander belt axis (k) (Leopold et al. 1964). So, the higher the sinuosity value of the river, the higher the meandering character will be.

## 5 RESULTS AND ANALYSIS

Temporal variation refers to changes accrued with elapsing time and horizon to geographical/horizontal variations which are also denoted as vertical and horizontal variation. In our study, the Tapi river reach is taken for the analysis from 1950 to 2015 with the time span of 13 years between two consecutive satellite images.

### 5.1 Change detection in morphometry of Tapi river with time

#### 5.1.1 1950 Tapi river reach

The river course has been taken from the 1950 US army map service (Series U502) with scale 1:2,50,000. The sinuosity index for the entire river reach from Kamrej to Adajan was 1.595 as shown in Figure 7. There was no island during this time in the river reach.

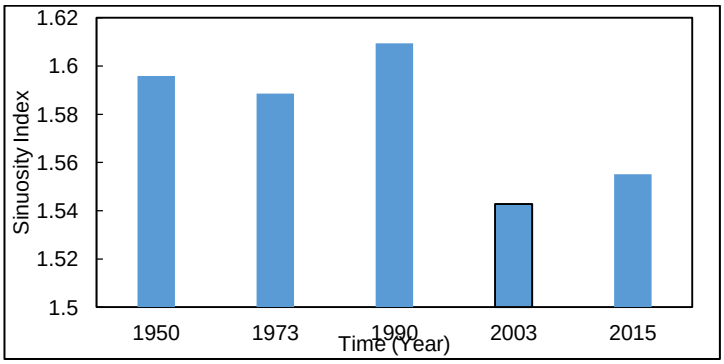


**Figure 7.** Sinuosity index variation with time (year)

 

5.1.2 1972 Tapi river reach

The river has been digitized from the orthorectified LandSAT MSS data of 4 March 1972. During this period a two major flood of magnitude 15.5 lakh cusecs in 1968 and of 12.0 lakh cusecs in 1970 hit the Surat city. The sinuosity index became slightly lower from 1950. It was 1.588. The island area is 0.28 $km^2$ between the cross-sections 23-25 in the study area.

5.1.3 1990 Tapi river reach

The river course has been digitized from orthorectified LandSAT TM imagery of 25 March 1990. The sinuosity index was increased to 1.609 Table 3. In this year, the bend became wider up to the cross-section 1-10. The island area was 0.0923 $km^2$ between the cross-sections 23-24 which is decreased by 6.77% from the year 1972 as shown in Table 3.

**Table 3.** River morphometric parameters

| Year | Sinuosity | Island area ($km^2$) |
|---|---|---|
| **1950** | 1.595 | 0 |
| **1972** | 1.588 | 0.286 |
| **1990** | 1.609 | 0.0923 |
| **2003** | 1.542 | 0.811 |
| **2015** | 1.555 | 0.818 |

5.1.4 2003 Tapi river reach

The river reach has been digitized from the orthirectified LandSAT ETM+ imagery of 5 March 2003. The sinuosity index was decreased drastically to 1.542 as during the period two floods of magnitude of 5.25 lakh cusecs in 1994 and of 7.00 lakh cusecs in 1998. Also the Singanpore weir was constructed in 1995 just before the cross-section no. 22. This cause the pounding of water on the upstream side of the cross-section and also increased the width of the river, while on the downstream side the river width is decreased and the path is also shifted towards the south – west direction. The island area was 0.811 km2 between the cross-sections 6-8 due to the pounding of water on the upstream side of the weir (Figure 8).

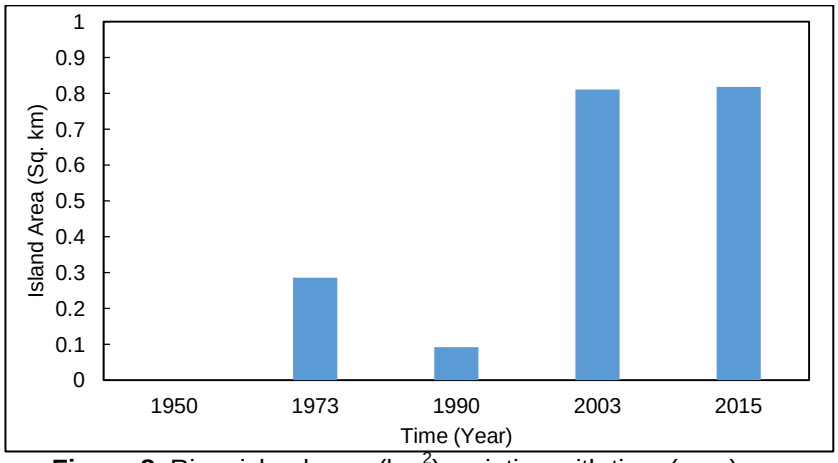


**Figure 8.** River island area ($km^2$) variation with time (year)

5.1.5 2015 Tapi river reach

The river reach was identified and analyzed from LansSAT (OLI,TIRS) data of 9th November 2015. Sinuosity calculated higher than the previous year as 1.55, also during this period two floods of magnitude of 9.09 lakh cusecs in 2006 and of 10 lakh cusecs occurred. The island area is slightly increased to 0.818 $km^2$ between the cross-sections 6-8. The river on the downstream side of weir shifts more in the south-east direction with decreased with than 2003.

5.2 Temporal shift of the left bank of river

The shift in each of the cross-section in 1950-1972 time span shows that the maximum shift was at cross-section no. 21,which was about 266.65 meter with respect to left bank site of the year 1950. Also there is high shift in cross-section 10 and 12 which was about 257.09 and 224.89, respectively. From 1972 to 1990, the highest channel shift was observed at cross-section no. 6, which was about 201.5 m. Also, at section 9 and 16, there is significant shift which was about 176.99 m and 104.83 m. The highest shift in 1990-2003 at

 

section 7 is mainly due to the pounding of water on the upstream side of the weir. There is also significant shift in the river on the upstream side at section 11-15 due to standing water on the upstream side of weir. On the downstream side, the river shift is significant at section 23-24 of about 486.16m and 457.57m, respectively in the south west direction.

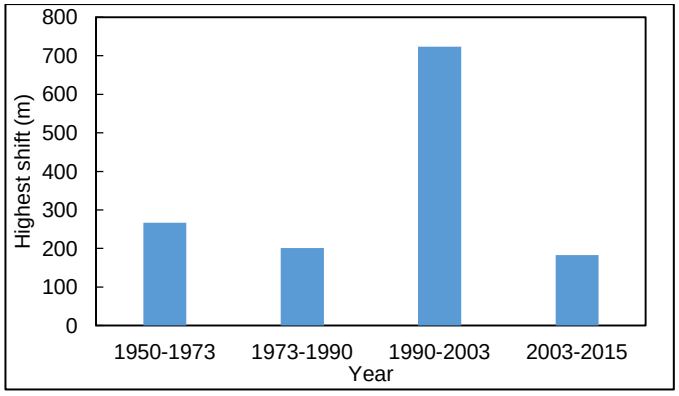


**Figure 9.** Highest river shift (m) along cross- section with time (years)

Between 2003 and 2015, the highest shift in left bank of river is at section 24, located on the downstream side of the weir which is about 182.92m (Table 4, Figure 9) in the south west direction. The significant shift on the upstream side is at section no. 14 at about 81.33m. With respect to the left bank of the 2003.

**Table 4.** Temporal river changes along each cross-section

| Cross-section | Shift in meters | | | |
|---|---|---|---|---|
| | **1950-1973** | **1973-1990** | **1990-2003** | **2003-2015** |
| **1** | 155 | -14 | -30 | 0 |
| **2** | 121 | -14 | 29 | -30 |
| **3** | 80 | 16 | 0 | 0 |
| **4** | 42 | 3 | 0 | 0 |
| **5** | 22 | 20 | 0 | 0 |
| **6** | -42 | 202 | 31 | -31 |
| **7** | 21 | 23 | 724 | -79 |
| **8** | -1 | -4 | 467 | 0 |
| **9** | -133 | 177 | 1 | 1 |
| **10** | 240 | -16 | 32 | 0 |
| **11** | 197 | -105 | 420 | -30 |
| **12** | 257 | -79 | 352 | 0 |
| **13** | 70 | -71 | 350 | -43 |
| **14** | 225 | -65 | 478 | -81 |
| **15** | -15 | -68 | 498 | 22 |
| **16** | 191 | 105 | 60 | -30 |
| **17** | 95 | 16 | 32 | -1 |
| **18** | 120 | 21 | 2 | -2 |
| **19** | 10 | -20 | 0 | 0 |
| **20** | -99 | -15 | 0 | 0 |
| **21** | -267 | 50 | -10 | -23 |
| **22** | -144 | -28 | 51 | -1 |
| **23** | 44 | 3 | -486 | 69 |
| **24** | -53 | -46 | -458 | -183 |
| **25** | -27 | -85 | -85 | -31 |
| **26** | 120 | -58 | -39 | 0 |

5.3 River width measurement

Due to the high river discharge, velocity during heavy floods and river morphometry, there were significant increase in channel shifting over time. To account for this shift of river bank, the river width measurement along the fixed cross-section is important. Channel width is observed for each section for particular year as show in Table 5. Graphical representation of the river width at each cross-section for each year is shown in Figure 10.

**Table 5.** Temporal river width along each cross section

| Cross-section | Width in meters | | | | |
|---|---|---|---|---|---|
| | **1950** | **1972** | **1990** | **2003** | **2015** |
| **1** | 183 | 180 | 361 | 300 | 330 |
| **2** | 208 | 59 | 483 | 512 | 419 |
| **3** | 193 | 127 | 252 | 347 | 350 |
| **4** | 257 | 136 | 441 | 450 | 450 |
| **5** | 226 | 214 | 327 | 345 | 368 |
| **6** | 257 | 147 | 440 | 513 | 491 |
| **7** | 282 | 221 | 264 | 948 | 829 |
| **8** | 385 | 157 | 212 | 717 | 718 |
| **9** | 340 | 287 | 483 | 484 | 483 |
| **10** | 319 | 385 | 418 | 477 | 449 |
| **11** | 232 | 180 | 91 | 540 | 540 |
| **12** | 205 | 237 | 130 | 482 | 482 |
| **13** | 295 | 175 | 125 | 475 | 431 |
| **14** | 342 | 404 | 182 | 806 | 725 |
| **15** | 416 | 273 | 229 | 698 | 720 |
| **16** | 311 | 361 | 210 | 630 | 600 |
| **17** | 314 | 253 | 221 | 603 | 539 |
| **18** | 148 | 179 | 265 | 606 | 583 |
| **19** | 484 | 285 | 298 | 994 | 994 |
| **20** | 408 | 182 | 122 | 911 | 914 |
| **21** | 299 | 201 | 217 | 619 | 567 |
| **22** | 341 | 352 | 297 | 349 | 313 |
| **23** | 452 | 536 | 659 | 174 | 139 |
| **24** | 832 | 671 | 427 | 213 | 91 |
| **25** | 495 | 366 | 266 | 183 | 152 |
| **26** | 262 | 232 | 232 | 157 | 157 |

From Figure 10. It is observed that the channel width is changing in higher magnitudes over time. It is to be noted that the channel width at different sections were changed significantly even after the construction of Singanpore Weir. One cause may be due to sedimentation and higher discharge, where erosion has increased. And that higher channel width matches well with higher island area, showing the correlation between the two parameters.

## 6 DISCUSSIONS AND CONCLUSIONS

Most of the images analyzed in this study refers to dry season (November to March) only, during which water level or discharge in Tapi river and also in Singanpore pond remains relatively stable. Therefore, the errors in comparisons of the island area and river banks during different dates of satellite images are reduced. As the spatial resolution of images is limited up to 24–30 m only, which can cause mixed land-water pixels at land water boundaries, there can be small error in calculation of island area, LULC maps, and river bank locations. Within the limitations of these small errors, morphometric change analysis has been done and it was found that the sinuosity has changed drastically over the time period of 65 years (1950–2015). In 1950, it was 1.595 whereas, in 2015, it has decreased to 1.555.

 

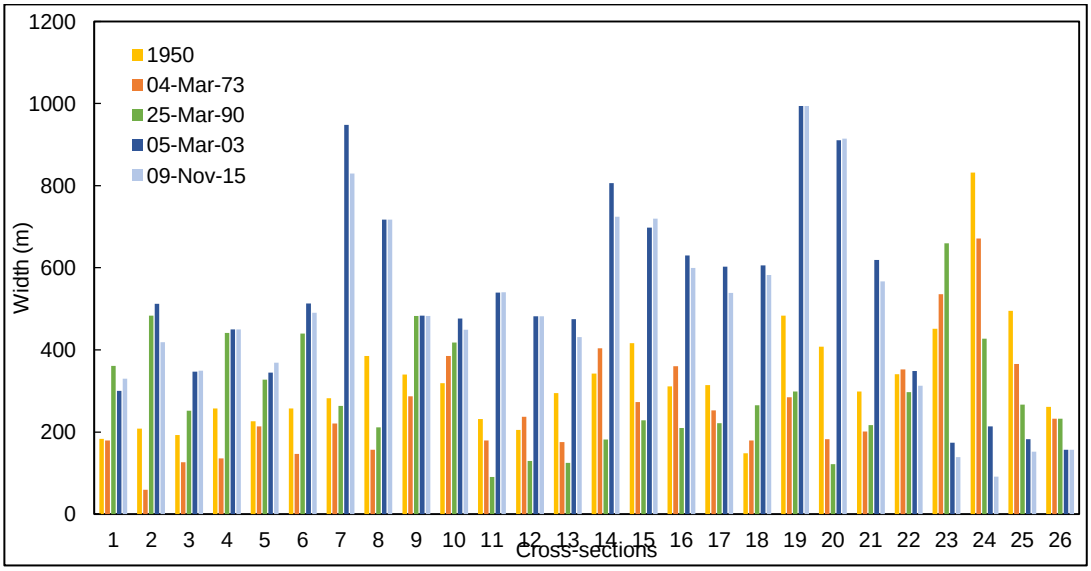


**Figure 10.** Temporal changes of river width at various cross-sections

The change in the island area before 1996 is mainly due to the flood events. Whereas the formation and change in the island area after 1996 is due to the flood events and the construction of the Singanpore weir (Pond level 10.25 m). Changes are observed in river width around the meander portion of the Tapi River, which may be the effect of sedimentation and erosion process at different cross-sections. Width of the Tapi River on the upstream of weir is increased significantly in 2003 and 2015 mainly due to the construction of the weir in 1996.Temporal shift of the bank of Tapi River meander is observed at many locations just around the meander curvature but channel shifting is significant at the ends of meander curvature to the apex of the meander portion of Tapi River.

## REFERENCES

Brice, J. C. (1984). Planform Properties of Meandering Rivers*. River Meandering Proceedings of the Conference Rivers*. 1-15.

Hickin, E. J. (1983). River Channel Changes: Retrospect and Prospect. *Modern and Ancient Fluvial Systems. Special Publication*, 6, 61-83.

Kotoky, P., Bezbaruah, D., Baruah, J. & Sarma, J. N. (2005). Assam, India. *Current science*, 88(4), 634-640.

Kummu, M., Lu, X. X., Rasphone, A., Sarkkula, J. & Koponen, J. (2008). Riverbank Changes along the Mekong River: Remote Sensing Detection in the Vientiane–Nong Khai Area. *Quaternary International*, 186(1), 100-112.

Leopold, L. B. & Wolman, M. G. (1960). River Meanders. *Geological Society of America Bulletin*, 71(6), 769-794.

Leopold L.B., Wolman M.G. & Miller J.P. (1964) *Fluvial Processes in Geomorphology*, Freemand and Co., San Francisco, U.S.A.

Mani, P., Kumar, R. & Chatterjee, C. (2003). Erosion Study of a Part of Majuli River-Island using Remote Sensing Data. *Journal of the Indian Society of Remote Sensing*, 31(1), 12-18.

Milton, E. J., Gilvear, D. J. & Hooper, I. D. (1995). Investigating change in Fluvial Systems using Remotely Sensed Data. *Changing river channels*, 276-301.

Pati, J. K., Lal, J., Prakash, K. & Bhusan, R. (2008). Spatio-Temporal Shift of Western Bank of the Ganga River, Allahabad City and ITS Implications. *Journal of the Indian Society of Remote Sensing*, 36(3), 289-297.

Petts G.E. (1995). *Changing River Channels.* The Geographical Tradition. Wiley, 1–23 pp.

Thakur, P. K., Laha, C. & Aggarwal, S. P. (2012). River Bank Erosion Hazard Study of River Ganga, Upstream of Farakka Barrage using Remote Sensing and GIS. *Natural Hazards*, 61(3), 967-987.

Winterbottom, S. J. & Gilvear, D. J. (2000). A GIS-Based Approach to Mapping Probabilities of River Bank Erosion: Regulated River Tummel, Scotland. *Regulated Rivers: Research & Management*, 16(2), 127-140.

Yang, X. (1996). Satellite Monitoring of the Dynamic Environmental Change of the Active Yellow River Delta, China. *International archives of photogrammetry and remote sensing*, 20(7), 801-806.

Yang, X., Damen, M. C. & Van Zuidam, R. A. (1999). Satellite Remote Sensing And GIS For The Analysis Of Channel Migration Changes in the Active Yellow River Delta, China. *International Journal of Applied Earth Observation and Geoinformation*, 1(2), 146-157.

 

# COMPUTATION OF MORPHOLOGICAL CHANGE IN A CHANNEL BEND WITH NON-UNIFORM CURVATURE USING THE 2D SHALLOW WATER EQUATIONS

SEONMIN LEE [(1)], CHAEWOONG BAN [(2)] & SUNG-UK CHOI [(3)]

[(1, 2, 3)]School of Civil and Environmental Engineering, Yonsei University, Republic of Korea
lee.sm@yonsei.ac.kr; blue8803@yonsei.ac.kr; schoi@yonsei.ac.kr

## ABSTRACT

This study presents a 2D numerical model for predicting the flow and morphological change in a curved channel. For the flow, the shallow water equations are solved by the finite volume method. Engelund-Hansen's formula is used to account for the total sediment load. To update the bed elevation changed by sediment transport, Exner's equation is solved. Since the conventional 2D models predict the morphological change poorly when applied to a curved channel with a low sinuosity, a method to slow down the inertia adaptation is proposed. Flow and morphological change are simulated for curved channels with non-constant curvatures, and results are discussed.

**Keywords:** Curved channel; non-uniform curvature; shallow water equations; Exner's equation; inertia adaptation.

## 1 INTRODUCTION

Most natural streams are meandering. Predicting the flow and resulting morphological change in the meandering stream is important but still challenging. The prediction is critical in the assessment of stream stability, maintaining the navigable depth, determining the location of instream installations, and etc. Recent 3D modelings have reported successful applications to various engineering problems. However, the 3D models require elaborate efforts and computations are very expensive. As an alternative choice, 2D models can be used and they are cost-effective, but have certain limitations.

Based on the 2D shallow water equations, various numerical models that are capable of predicting both flow and morphological change have been presented. Their predictions seem to be successful when compared with measurements. Examples include Kassem and Chaudhry (2002), Choi et al. (2005), and Vasquez et al. (2008). However, their applications were mainly limited to curved channels with a constant curvature unlike the natural streams. In fact, natural meandering streams are of non-uniform curvature, as indicated by Leopold and Langbein (1966). Moreover, previous studies by Shimizu and Itakura (1989) and Shimizu et al. (1990) indicated that 2D numerical models predict the morphological change poorly when they were applied to a curved channel with a low sinuosity.

For the 2D flow model, the depth-averaged velocity is, in general, different from the velocity near the bed specially in the meandering channel. The difference is the major source of errors in predicting the bed elevation change. That is, the secondary flows alter the velocity near the bed or the direction of the bed shear stress in the meandering channel. Normally, the direction is adjusted using the curvature of the streamlines of computed depth-averaged flows. Rozovskii (1957) proposed the so called inertia adaptation equation to consider both the secondary flows and inertia adaptation. However, still unknown is a parameter, which is related with the adaptation length of the secondary flows and is thought to be function of the local curvature. Previous researchers such as de Vriend (1981) and Struiksma (1985) suggested a constant value of this parameter, which is found to be invalid for channels with low sinousity.

This study presents a numerical model for computing the flow and morphological change in a curved channel. A special emphasis is made on the computation of morphological change in a bend with non-uniform curvatures. The 2D shallow water equations in the curvilinear coordinates are solved. The dispersion stress terms are added to the momentum equations due to the helical flows or secondary flows in the channel bend. The zero equation model is solved for the turbulence closure. The finite volume method is used with the projection method for velocity-pressure coupling. Engelund-Hansen formula is used to predict the total sediment load. To update the morphological change due to sediment transport, Exner's equation is solved. For the correct assessment of the morphological change in a channel bend, the direction of bedload transport is adjusted due to secondary flows and the lateral slope effect on the sediment transport is considered. In order to improve the predictive ability of the model, a method to strengthen the inertia effect is proposed. The model is applied to a 180° channel bend and a sine-generated channel. Both flow and morphological change are presented and discussed.

 

## 2 GOVERNING EQUATIONS

### 2.1 Flow and morphological change

For flow computations, the 2D shallow water equations were solved. The continuity and *x*- and *y*-momentum equations are, respectively, given by

$$\frac{\partial h}{\partial t}+\frac{\partial (hu)}{\partial x}+\frac{\partial (hv)}{\partial y}=0 \quad [1]$$

$$\frac{\partial hu}{\partial t}+\frac{\partial (huu)}{\partial x}+\frac{\partial (hvu)}{\partial y}=\frac{1}{\rho}\frac{\partial (hT_{xx})}{\partial x}+\frac{1}{\rho}\frac{\partial (hT_{xy})}{\partial y}-gh\frac{\partial (h+Z_b)}{\partial x}-\frac{\tau_{bx}}{\rho}+\frac{\partial D_{xx}}{\partial x}+\frac{\partial D_{xy}}{\partial y} \quad [2]$$

$$\frac{\partial hv}{\partial t}+\frac{\partial (huv)}{\partial x}+\frac{\partial (hvv)}{\partial y}=\frac{1}{\rho}\frac{\partial (hT_{yx})}{\partial x}+\frac{1}{\rho}\frac{\partial (hT_{yy})}{\partial y}-gh\frac{\partial (h+Z_b)}{\partial y}-\frac{\tau_{by}}{\rho}+\frac{\partial D_{yx}}{\partial x}+\frac{\partial D_{yy}}{\partial y} \quad [3]$$

where $t$ is the time, $x$ and $y$ denote the horizontal coordinates, $h$ is the water depth, $u$ and $v$ are depth-averaged $x$- and $y$-velocities, respectively, $z_b$ is bed elevation from a datum, $g$ is the gravitational acceleration, ρ is the water density, $T_{ij}$ is the depth-averaged turbulent shear stress tensor, $D_{ij}$ is the dispersion stress tensor due to the effect of the secondary flows, and $\tau_{bi}$ is the $i$-component bed shear stress. In the present study, the following parabolic model for the depth-averaged eddy viscosity is used:

$$\nu_t=\frac{\kappa}{6}U_*h \quad [4]$$

where $\kappa$ is von Karman constant and $U_*$ is the shear velocity.

In order to compute the morphological change due to sediment transport, Exner's equation or bed sediment conservation equation needs to be solved together with flow equations, Eqs.[1]-[3]. Exner's equation takes the form such as

$$(1-\lambda)\frac{\partial z_b}{\partial t}+\frac{\partial q_{tx}}{\partial x}+\frac{\partial q_{ty}}{\partial y}=0 \quad [5]$$

where $\lambda$ is the porosity of bed sediment, and $q_{tx}$ and $q_{ty}$ are the $x$- and $y$-component of the total sediment load, respectively. In the present study, the relationship by Engelund and Hansen (1972) is used for the total sediment load.

In computing the morphological change with the 2D model, two adjustments were made herein. First, since the 2D model did not take into account the flow in a plane normal to the streamwise direction, the change in the direction of the bed shear stress due to the secondary flows should be considered. For this, using the relationship by Struiksma et al. (1985), the direction of bed shear stress was adjusted. Second, for a particle located on a laterally-sloped surface, the particle was pulled not only in the longitudinal direction but also in the lateral direction. This lateral slope adjustment was made with the help of the relationship by Struiksma et al. (1985).

### 2.2 Inertia effect

Previous studies revealed that the 2D model computes successfully the flow and morphological change in a curved open channel with a constant curvature. However, when the 2D model is applied to a sine-generated channel, the model computes the morphological change poorly. The problem becomes serious especially when the deflection angle is small, namely less than 40°. This is due to the inertia effect from the upstream reach. For the sine-generated channel, the curvature is not uniform and the sinuosity of the channel is determined by the deflection angle. In the present study, a method was presented to strengthen the inertia effect on the downstream curved channel.

In order to adjust the direction of bed shear stress due to secondary flows, the curvature of streamline $R$ used is given by

$$\frac{1}{R}=\frac{\left|\overline{u}\times\overline{a_c}\right|}{\left|\overline{u}\right|^3} \quad [6]$$

 

where $a_c$ is the centripetal acceleration. Assuming a steady flow, Eq. [6] can be approximated as (Abad et al. 2008; Vasquez et al. 2008)

$$\frac{1}{R}=\frac{1}{V^3}\left[\left(u^2\frac{\partial v}{\partial x}+uv\frac{\partial v}{\partial y}\right)-\left(uv\frac{\partial u}{\partial x}+v^2\frac{\partial u}{\partial y}\right)\right] \quad [7]$$

The curvature by Eq. [7] assumes that the flow field adapts to the change in curvature instantaneously, ignoring the inertia effect. In the present study, for inertia adaptation, the following semi-heuristic relationship proposed by Rozovskii (1957) is used:

$$\beta\frac{h^{1/6}}{n\sqrt{g}}\frac{h}{\sqrt{u^2+v^2}}\left[u\frac{\partial(1/R_s)}{\partial x}+v\frac{\partial(1/R_s)}{\partial y}\right]+\frac{1}{R_s}=\frac{1}{R} \quad [8]$$

where $R_s$ is the adjusted radius of curvature and $\beta$ is a calibration parameter of order 1.

## 3 FLOW VALIDATION

The numerical model was applied to flows in curved-channels with non-uniform curvatures experimented by da Silva (1995). Experimental conditions are listed in Table 1. In the table, σ is the sinuosity of a meandering channel, B is the channel width, Q is the discharge, $h_{av}$ is the flow depth, $S_c$ is the bed slope along centerline of meandering channel, $v_*$ is shear velocity, $c_{av}$ is the dimensionless Chezy resistance factor, Re is Reynolds number, Fr is Froude number, and $R_*$ is the roughness Reynolds number ($=v_*d/\nu$). Figures 1(a) and 1(b) show the plan views of channels with deflection angle of 30° and 110°, respectively. The straight channels at the beginning and end of meandering parts were the same as ones employed in the laboratory experiments. The grid sizes were 0.03 m and 0.02 m in the longitudinal and lateral directions, respectively. The total numbers of grids were 4,520 (= 226x20) and 13,340 (= 667x20) for Figures 1(a) and 1(b), respectively.

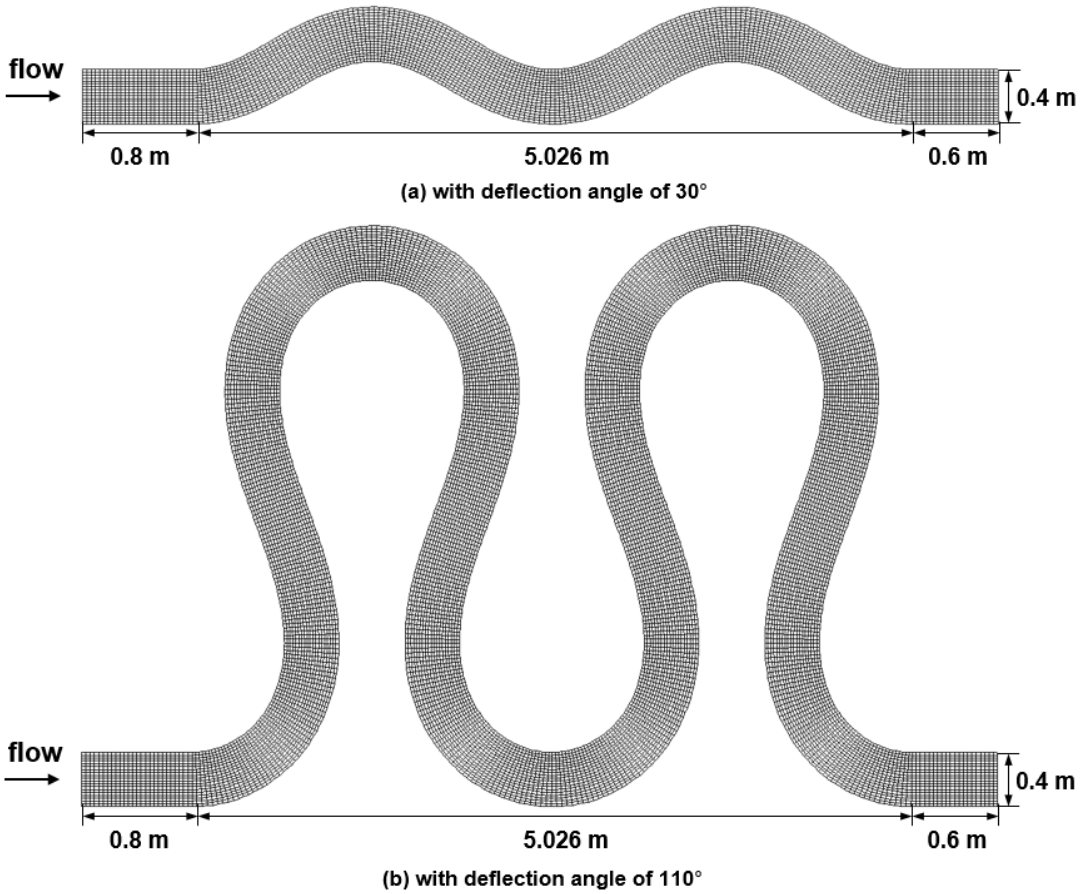


**Figure 1.** Computational domain.

**Table 1.** Experimental conditions (da Silva, 1995).

| Deflection angle | σ | $B/R_a$ | Q ($m^3/s$) | $h_{av}$ (m) | $S_c$ | $u_{av}$ (m/s) | $v_*$ (m/s) | $c_{av}$ | $B/h_{av}$ | Re | Fr | $R_*$ |
|---|---|---|---|---|---|---|---|---|---|---|---|---|
| 30° | 1.07 | 0.49 | 0.0021 | 0.032 | 1/1,000 | 0.164 | 0.0177 | 9.3 | 12.5 | 5,250 | 0.293 | 78 |
| 110° | 3.70 | 0.52 | 0.0020 | 0.030 | 1/1,120 | 0.167 | 0.0162 | 10.3 | 13.3 | 5,025 | 0.309 | 71 |

Figures 2 and 3 show both measured and computed velocity vectors in curved channels with deflection angles of 30° and 110°, respectively. It can be said that overall velocity field computed by the numerical model corresponded well with the measured data. Specifically, the velocity maximum occurred at the inner part of the apex for the curved channel with a deflection angle of 30°. However, for the channel with a deflection angle of 110°, the velocity maximum occurred at the outer part at a location near the inflection point. This conformed to previous findings by da Silva et al. (2006) and was seen in both computed results and measured data.

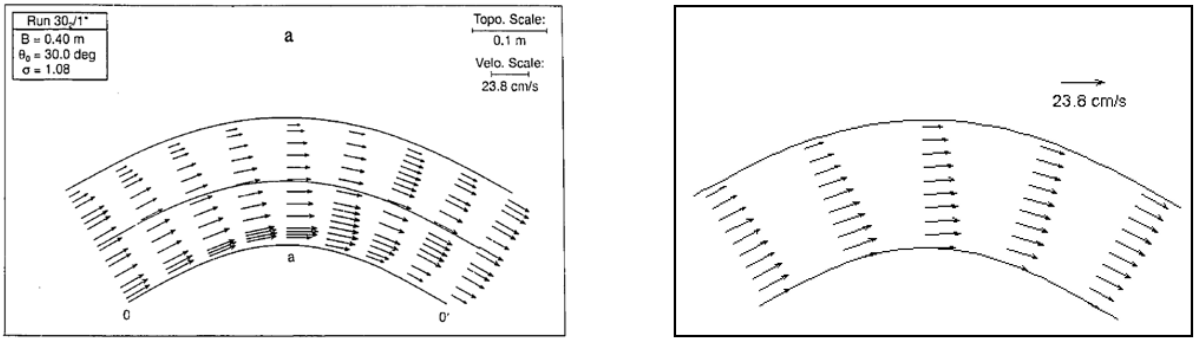


**(a) measured data (da Silva, 1995)** **(b) our study**

**Figure 2.** Velocity vectors in a channel with deflection angle of 30°.

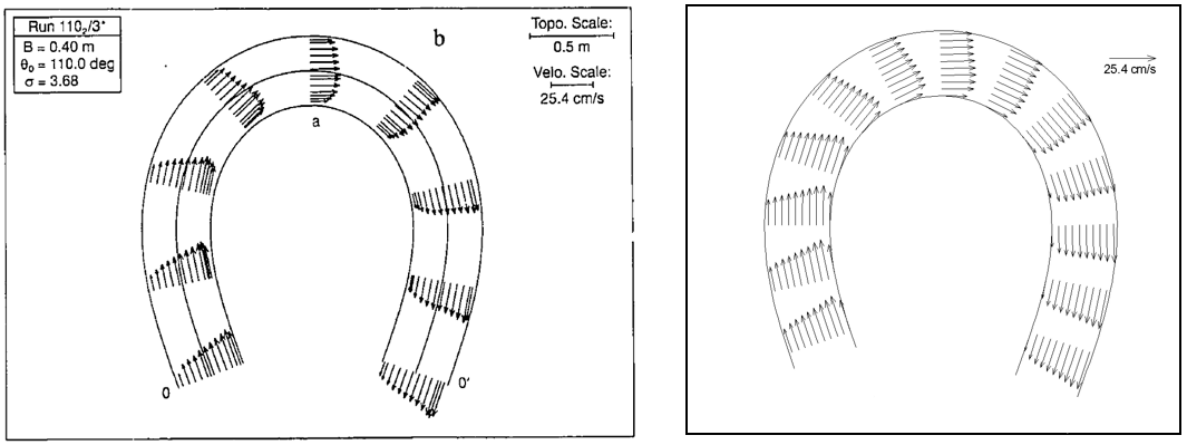


**(a) measured data (da Silva,1995)** **(b) our study**

**Figure 3.** Velocity vectors in a channel with deflection angle of 110°.

## 4 APPLICATIONS

Now, the numerical model was used to compute the morphological change in the curved channel, experimented by Hasegawa (1983). The curved channel had a deflection angle of 30°. The discharge was 0.00187 $m^3/s$ with a flow depth of 0.026 m and a channel width of 0.3 m. The median size of bed sediment particles was 0.43 mm. Detailed experimental conditions are given in Table 2. Figure 4 shows the plan view of channel for application of the numerical model. The straight channels at the beginning and end of the meandering channel were the same as ones used in the experiments. The grid sizes were 0.03 m and 0.015 m in the longitudinal and lateral directions, respectively, resulting in the total number of grids of 4,140 (= 207x20).

**Table 2.** Experimental conditions (Hasegawa, 1983).

| Deflection angle | σ | Q ($m^3/s$) | $h_{av}$ (m) | $S_c$ | $u_{av}$ (m/s) | $c_{av}$ | $B/h_{av}$ | Re | Fr | $R_*$ |
|---|---|---|---|---|---|---|---|---|---|---|
| 30° | 1.07 | 0.00187 | 0.026 | 1/300 | 0.24 | 15.3 | 11.6 | 6,233 | 0.47 | 25.1 |

 

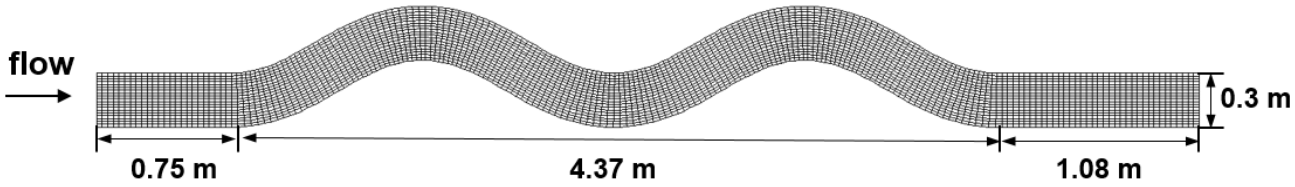


**Figure 4.** Computational domain for computing the morphological change.

Figure 5 shows the morphological changes in the curved channel. Measured data are given together with morphological changes computed with and without inertia adaptation. The bed elevations given in the figure were obtained after equilibrium. Both computed results showed that sediment deposition and erosion occurred alternatively in the curved channel. However, it is clear that the zone of deposition and erosion is shifted slightly downstream with the use of inertia adaptation. This makes resulting prediction of morphological change closer to measured data in Figure 5(a).

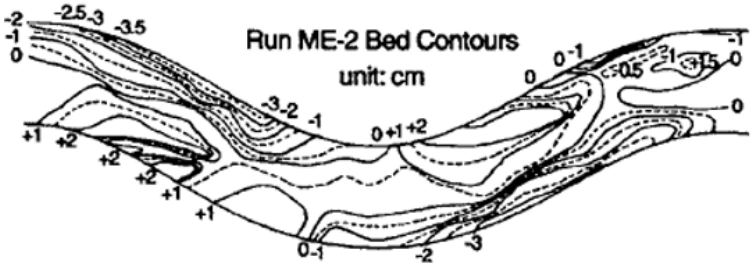


(a) measured data (Hasegawa, 1983)

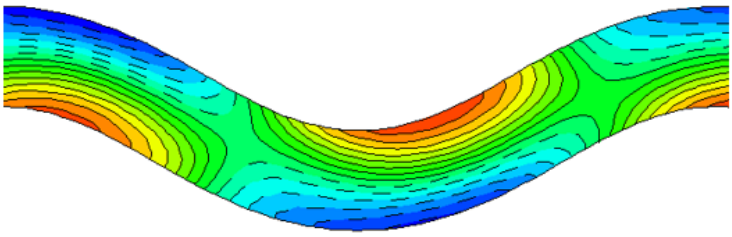

(b) our study (w/o inertia effect)

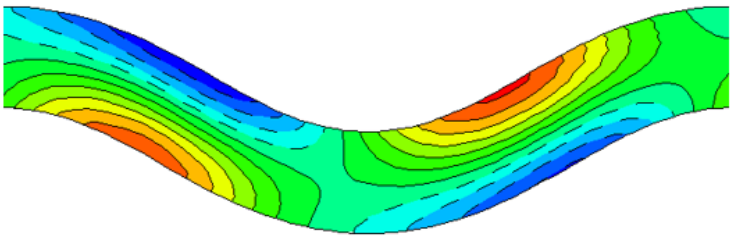

(c) our study (w/ inertia effect; β = 2.0)

**Figure 5.** Morphological change in a curved channel with non-constant curvature.

## 4 CONCLUSIONS

This study presents a 2D numerical model that is capable of computing flow and morphological change in a curved channel. The shallow water equations and Exner's equation are solved for the flow and morphological change, respectively. Elgelund-Hansen's formula is used for the total sediment load. A special emphasis is made on computing the morphological change in a curved channel with a low deflection angle.

First, the model is applied to flows in curved channels with non-constant curvatures. It is found that the computed flow field is in good agreement with measured data. Interestingly, the location of the velocity maximum is observed to change depending upon the deflection angle.

Next, the morphological change in a curved channel with a low deflection angle is reproduced by the numerical model. It is shown that the reduction of inertia adaptation contributes to correct prediction of the morphological change in such meandering channels.

## ACKNOWLEDGEMENTS

This work is supported by the National Research Foundation of Korea (NRF) grant funded by the Korean Government [NRF-2014R1A2A1A11054236].

 

**REFERENCES**

Abad, J.D., Buscaglia, G.C. & Garcia, M.H. (2008). 2D Stream Hydrodynamic, Sediment Transport and Bed Morphology Model for Engineering Applications. *Hydrological Processes*, 22(10), 1443-1459.

Choi, S.-U., Kim, T.B. & Min, K.D. (2005). *2D Finite Element Modeling of Bed Elevation Change in a Curved Channel.* River, Coastal and Estuarine Morphodynamics, 1280.

Engelund, F. & Hansen, E. (1967). *A Monograph on Sediment Transport in Alluvial Streams*. TEKNISKFORLAG Skelbrekgade 4 Copenhagen V, Denmark.

Hasegawa, K. (1983). Hydraulic Research on Planimetric Forms, Bed Topographies and Flow in Alluvial Rivers, *Ph.D. Thesis.* Hokkaido University, Sapporo, Japan. (In Japanese)

Kassem, A.A. & Chaudhry, M.H. (2002). Numerical Modeling of Bed Evolution in Channel Bends. *Journal of Hydraulic Engineering*, ASCE, 128(5), 507-514.

Leopold, L.B. & Langbein, W.B. (1966). River Meanders. *Scientific American,* 214(6), 60–70.

Rozovskii, I.L. (1957). *Flow of Water in Bends of Open Channels,* Academy of Science of Ukrainian SSR, Russia.

Shimizu, Y. & Itakura, T. (1989). Calculation of Bed Variation in Alluvial Channels. *Journal of Hydraulic Engineering*, 115(3), 367-384.

Shimizu, Y., Yamaguchi, H. & Itakura, T. (1990). Three-Dimensional Computation of Flow and Bed Deformation. *Journal of Hydraulic Engineering*, 116(9), 1090-1108.

da Silva, A. (1995). Turbulent Flow in Sine-Generated Meandering Channel, *Ph.D. Thesis*. Queen's University, Kingston, Ontario, Canada.

da Silva, A., El-Tahawy, T. & Tape, W.D. (2006). Variation of Flow Pattern with Sinuosity in Sine-Generated Meandering Streams. *Journal of Hydraulic Engineering*, 132(10), 1003-1014.

Struiksma, N., Olsen, K.W., Flokstra, C. & De Vriend, H.J. (1985). Bed Deformation in Curved Alluvial Channels. *Journal of Hydraulic Research*, IAHR, 23(1), 57-79.

Vasquez, J.A., Steffler, P.M. & Millar, R.G. (2008). Modeling Bed changes in Meandering Rivers using Triangular Finite Elements. *Journal of Hydraulic Engineering*, ASCE, 134(9), 1348-1352.

 

# RESEARCH ON THE METHOD OF RECOGNITION AND EXTRACTION FOR AUDIO SIGNAL OF THE GRAVEL MOVEMENT IN NATURAL RIVERS

MI TIAN [(1)], SHENG FA YANG [(2)] & QI GUO [(3)]

[(1,3)] School of River & Ocean Engineering, Chongqing Jiaotong University(CQJTU), Chongqing, China
tm0519@163.com; 1670852080@qq.com

[(2)] National Inland Waterway Regulation Engineering Research Center (NIWRERC), Chongqing Jiaotong University, Chongqing, China
ysf777@163.com

## ABSTRACT

In the background of the obstruction problem caused by gravel transport in fluctuating backwater area of the Three Gorges Reservoir, the field data is collected by using underwater high-fidelity audio recorder. The data collected are the peak frequency, pitch frequency and energy distribution characteristics after wavelet transforms the initial data which are extracted as characteristic parameters for gravel movements. The recognition result of gravel transport from the synthesis audio signals with the three parameters is in good agreement with the artificial judgment. It indicates that this method has the accuracy and feasibility for recognizing gravel transport.

**Keywords:** Gravel transport; signal recognition; characteristic parameters; audio signal processing.

## 1 INTRODUCTION

The channel conditions in fluctuating backwater area have been greatly improved with the impoundment of the Three Gorges Reservoir up to 175 m. However, there is still some local erosion and deposition of bed material in different degrees in local area. In order to solve the problem of obstruction caused by scouring and silting of gravel, the channel management and maintenance department and scientific research units have adopted various measures to observe the bed-load. Yet, unfortunately, dissatisfactory results were obtained. In general, the monitor of bed-load transport has been concentrated in two methods: direct measurement with samplers and indirect method by collecting some relative physical parameters. Examples of direct method consist of bed-load baskets, bedload samplers, scales or traps in a confined area (Bunte et al., 2004). Portable bedload samplers are the most commonly used direct measurement device. These may disturb the hydraulic parameters around the apparatus. It is difficult to sample effectively with high flow conditions in the steep mountain streams because of the instability of a suspended device, at the same time it is dangerous for sampler operators. The direct-measuring devices have been employed in a very limited range of hydraulic conditions. Examples of indirect method include transport relations, radioactive marking, and measurement of sediment result from surrogate apparatus. Each of bedload physical relations has the limitation in estimating the bedload discharge. Sediment traps allow only a summarized investigation of the sediment transport with a low temporal resolution. The radioactive tracer technique is a good way to capture the pathway of bedload particles in natural streams and their movement distances with less intrusivity, but it is not without drawback (Papanicolaou et al., 2010). The limitation of recovery rate due to coexistence of particles results the method not-applicable for the river with complicated flow conditions. The application of optical systems for identifying the bedload in movement through cameras cannot be used to a large scale due to the high concentrations of suspended matter and high turbidity. As a result, no single apparatus or procedure, whether theoretical or empirical, has been shown general applicability in the definition of bedload discharge (Rigby et al., 2016).

Acoustic techniques express some merits for monitoring bedload transport in real time, both in high and low discharge under undisturbed conditions (Barton et al., 2010; Graff, 2010). These methods provide continuous data, and because acoustic signals travel great distances in water, they integrate over a large area of the bed. Based on the existing bed-load prototype observation technology, Sheng-fa Yang etc (2014) have been concentrating on the development of new observation equipment. And in March to June of 2015, they completed filed observation of gravel transport using underwater high-fidelity audio recorder in delta moraine of Chongqing reach. In this study, based on the field observation data, the sound signal processing method is used to analyze and process three kind of main original audio signals, such as gravel movement, ship, and water. Finally, an advanced method of audio signal is proposed to recognize and extract the characteristic parameters of gravel movement in natural rivers.

 

## 2 DATA ACQUISTION

### 2.1 Acoustic System Design

The basis of the acoustic instrumentation in this study is the Song Meter SM2M+ Marine Recorder,which features flexible scheduling, extremely low power consumption, 16-bit digital recording and ease of use in a cost effective and easy to use package. The sensitivity of the hydrophone was calibrated to a .1 dB resolution by the hydrophone manufacture. The device allows sample rates from 4kHz to 96kHz and up to 384kHz with the Ultrasonic Upgrade. Up to four SDHC or SDXC cards can be installed in the recorder. The hydrophone was placed within a 79.4 cm long, 16.5 cm PVC pipe, and in a Submersible case, PVC housing was conservatively rated to 150m.The operator can store cell batteries according to specific case for a long-time observation.

### 2.2 Study Site Description

Triangular moraine is located in the upper reaches of the Chongqing reach in the Yangtze River. The minimum width of the channel is about 60 m, the water depth is about 3.0 m in the period of low level, and the bend radius of the main channel is only about 600 m in the dry season. It is extremely difficult to ship during the falling period, and it is prone to dangerous situation such as stranding. It had been accepted as one of the most sinister waterway in Chongqing with the characteristics of bend, narrow, shallow and dangerous.

### 2.3 Study Site Description

The apparatus used in the experiments is fixed in a stainless steel frame which was suspended from a buoy boat. Taking into account the flow resistance, the equipment was completely immersed in 1 meter below the water surface. Based on the result of Barton (2006), and according to the Nyquist sampling theorem, the sampling frequency was selected as 32kHz. In order to ensure long-term observation, it was necessary to replace the battery and memory card after a couple of days due to a mass of voice data from continuous sampling.

**Figure 1.** One end of the stainless steel frame is fixed on the buoy boat and one end is deep underwater.

## 3 AUDIO SIGNAL PRETREATMENT

### 3.1 Target signal detection and extraction

The original sound signal usually contains the target signal that we need to analyze, and also contains the background sound that we don't need. If the target signal can be detected and extracted from the initial signal, then it can greatly reduce the workload and improve the accuracy of the result.

Pebble collision or other mutations in the sound (such as a ship sound) that occurs in the original signal will cause a change in energy. According to the change, we can judge that the time of the target signal occurs. For example, Figure 2a contains the spectrum of recording of three collisions, Figure 2b is the change of energy, with three corresponding mutations.

If the maximum energy of the background sound was the threshold value, then the time period of which energy was greater than the threshold value is regarded as the objective signal segments. After that, each target signal segments can individually be extracted and marked in $S_1$, $S_2$, $S_3$ of Figure 2C. Eventually the original signal is classified as short clips to analyze.

 

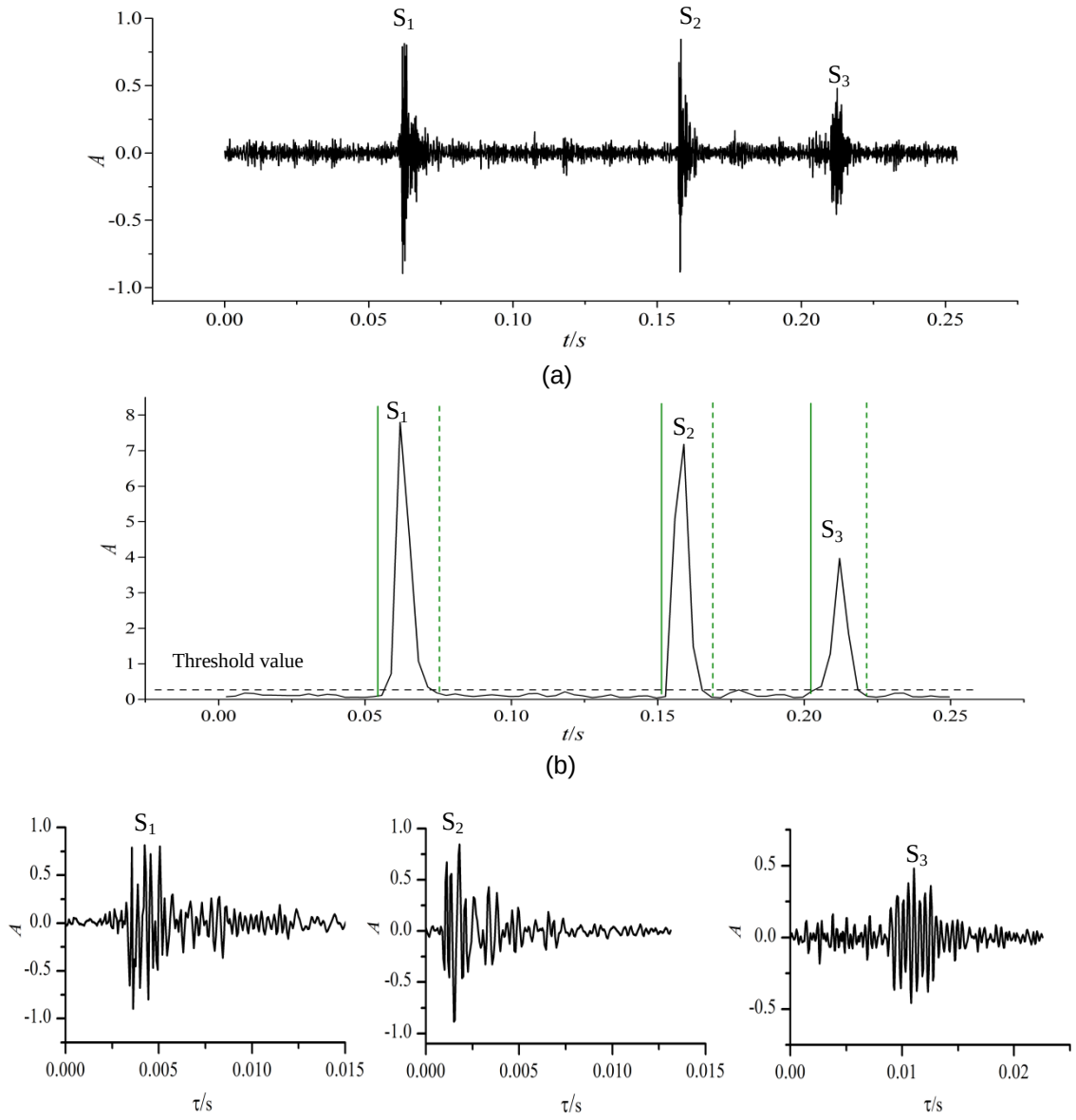


**Figure 2.** Extraction of target signal

3.2 Reduction of environmental background noise in pretreatment

Background sound is the sound that always exists in the whole audio signal, such as the water sound of the water. Its presence may cause serious interference to the analysis result. In order to remove the background sound, and compress the amount of data, it was necessary to reduce and eliminate the noise before analyzing the background sound. In this paper, spectral subtraction method was used to reduce the background noise of the experimental signal in the flume (Song, 2013; Boll, 1979). Spectral subtraction was the most common method of speech de-noising. The method consists of subtracting the spectrum of the noise signal from a spectrum of the original signal. Herein the time sequence of speech signal was set to be $x(n)$, the speech signal at the i-th frame after framing windowing is set to be $x_i(m)$ and the frame length is N, the basic spectral subtraction algorithm is:

$$\left|\hat{X}_i(k)\right|^2 = \begin{cases} \left|X_i(k)\right|^2 - a \times D(k) & \left|X_i(k)\right|^2 \geq a \times D(k) \\ b \times D(k) & \left|X_i(k)\right|^2 < a \times D(k) \end{cases} \quad k = 0,1,\ldots,N-1 \quad [1]$$

Where $\left|X_i(k)\right|^2$ is the energy of each frequency after Fourier transformation of original signal, and $D(k)$ is the average energy of each frequency for precursor without signal, moreover $|\hat{X}_i(k)|^2$ is the energy of each frequency after spectrum subtraction. Wherein a and b are two constants which are referred to as over-subtraction factor and gain compensation factor.

After spectral subtraction, the amplitude is $|\hat{X}_i(k)|$. We may then obtain the sound signal sequence via inverse Fourier transform. In the process, we select the time for precursor without signal as 0.5s before the pebble movement, as shown in Figure 3a, in addition, the audio signal of the flume experiment was reduced by the spectral subtraction and the waveform is shown in Figure 3b.

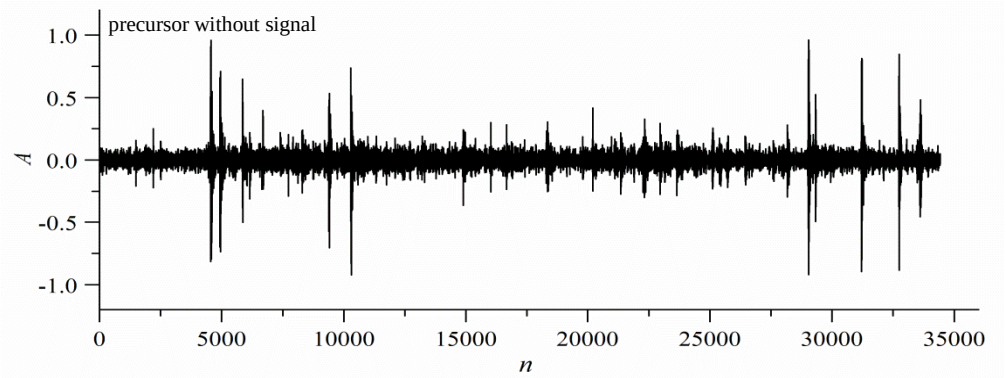


(a) The original waveform

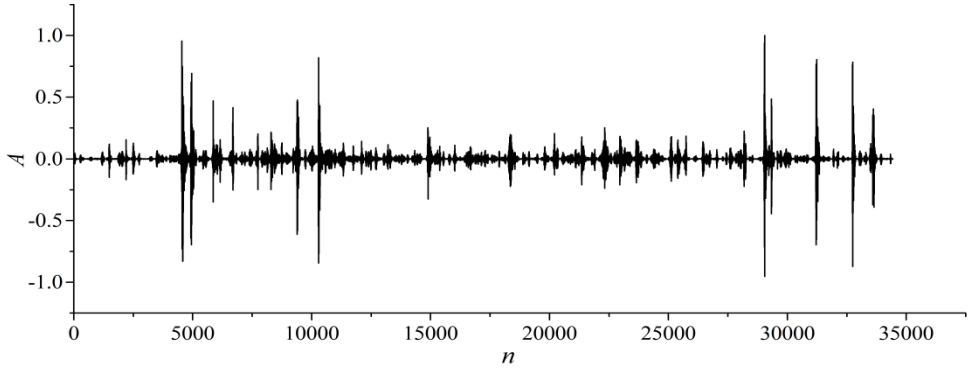


(b) The waveform after spectral subtraction

**Figure 3.** Comparison of waveform before and after noise reduction

## 4 SOUND CHARACTERISTICS ANALYSIS

### 4.1 Peak frequency

The transform spectrum, which can reflect the characteristics of the signal in frequency domain, will be obtained after Fourier transformation. There are 3 schematic diagrams of sound signal frequency spectrum respectively for pebble, ships and water (where f is the frequency, and En is the energy)

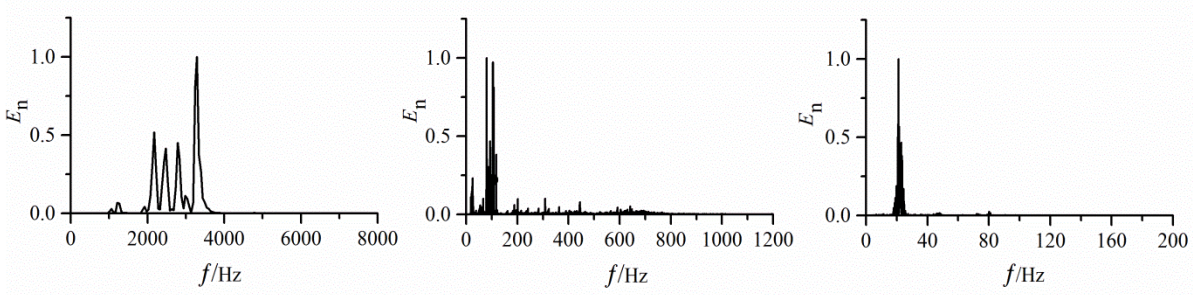


(1) The pebble （2）The ship （3）The water

**Figure 4.** The frequency spectrum for three kinds of signals

The position of maximum energy in the spectrum is different in the three kinds of signals. For a more detailed description of it, the peak frequency of the pebble is around 3200 Hz, the peak frequency of the ship is 100Hz or so, and the water is at about 25 Hz (Fig.4).This difference may be related to the material and the internal structure of the signal itself, so we can put the spectrum diagram energy corresponding to the maximum frequency as a feature of the signal, and it is called the peak frequency. In this paper, the sample size of collected sound, such as pebble, ship and water, are 300, 100 and 200, respectively. The peak frequency of these sound was statistically analyzed, and the probability density distribution curve of the peak frequency is obtained (Fig.5).

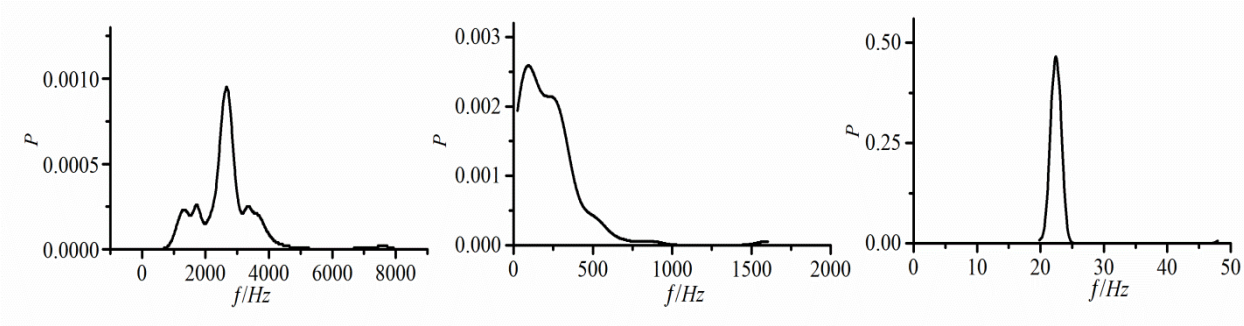


(1) The pebble （2）The ship （3）The water

**Figure 5.** The probability density distribution curve of peak frequency for three kinds of signals

There is an difference of peak frequency distribution among Pebble, ship and water. For a more detailed description of it, the peak frequency of pebbles, which was influenced by the particle size and material, is around1000~5000Hz. The ship's peak frequency mainly ranges between 25 to 500 Hz, and it was affected by ship type. The peak frequency of water is between 20 to 30 Hz. Therefore, the peak frequency can be used as an indicatior for the pebble identification.

4.2 Pitch frequency analysis

Audio signal is produced by the vibration of the object, and the reciprocal of the vibration period was called the pitch frequency, which is an important parameter in audio signal recognition. There were abundant of methods to extract pitch, such as average magnitude difference function method (AMDF), center clipping (auto-correlation function, ACF), Cepstrum method (CEP), Linear prediction method (Atal), and so on. The auto-correlation method was widely employed, as it is one of the most practical and reliable method. This method compares two signals and attributes a correlation factor that tends to 0 the more the signals are different. On the contrary, if the two signals waveform is the same, a peak will appear in the lead and lag spikes.

Signal is set as $x(n)$ , then the auto-correlation is defined as

$$\phi(\mathrm{k}) = \sum_{m=-\infty}^{\infty} x(m)\,x(m+k) \qquad [2]$$

Where k is the retardation.

If the sound signal has a period, p, then it will obtain the maximum value at k=0，$\pm p$，$\pm 2p$，... As the pebble collision signal is not purely cyclical, a peak will appear instead of the maximum value in the pitch. The auto-correlation functions for the sound of pebbles, ship and water are given in Figure 6.

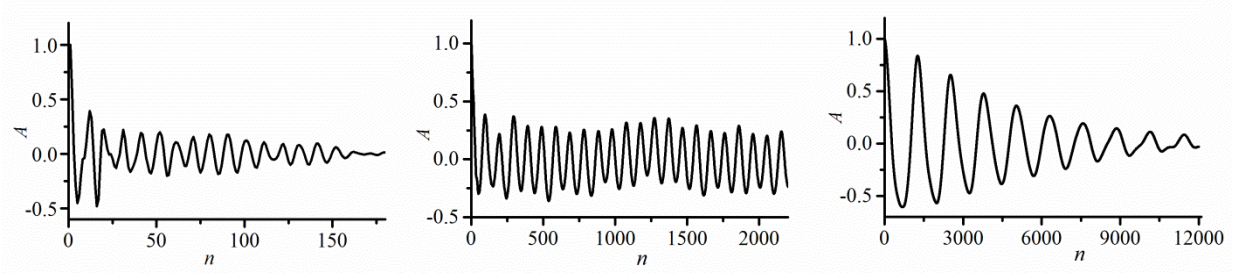


(1)The pebble （2）The ship （3）The water

**Fig.6** Self correlation of the three signals

Given is statistical analysis to the pitch frequency of three kinds of signals, and it displays the probability density distribution:

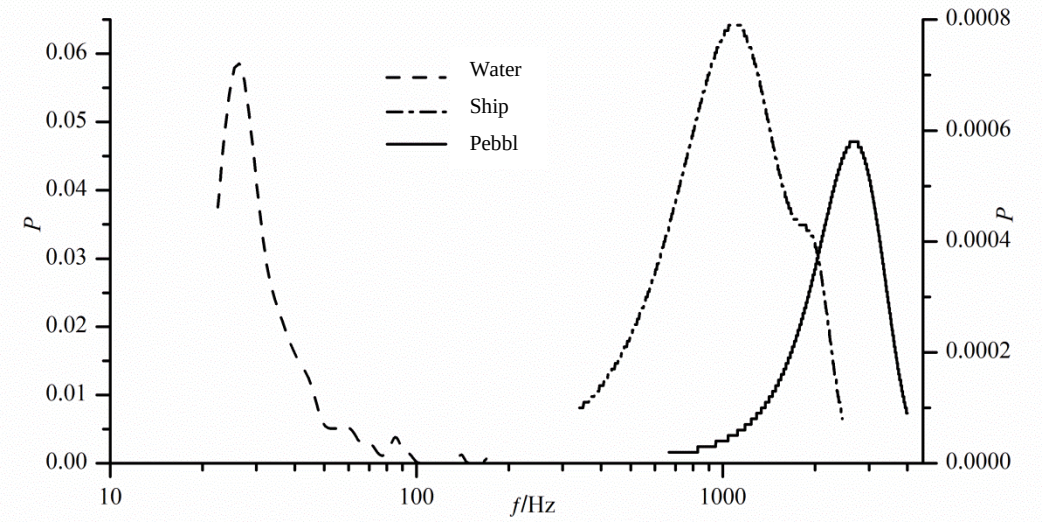


**Fig.7** The probability density distribution of the three kinds of signals for fundamental frequency

The pebble pitch frequency is between 2000 ~ 4000 Hz. The pitch frequency of ship, which was affected by the type of the vessel, concentrates between 100 ~ 1500 Hz. The Water pitch frequency was in about 25 Hz, which was very close to its dominant frequency (Fig.7). It follows that the pitch frequency characteristics of Pebbles was significantly different from other two kinds of sound, and so pitch frequency can be used to identify the pebble's signal.

4.3 Energy distribution characteristics after wavelet transform

Wavelet transform can decompose the signal at multiple scales, and provide the coefficient collection of subspace in various scales. The wavelet coefficients reflect the energy information that can provide the time-frequency local features of the original signal, especially in different frequency bands. Since the amount of information of the wavelet coefficients when they are directly being, the characteristic value is too large, so we need to focus the solution of signal energy on various scale, and to appoint them as identification parameters. This is the basic principle of energy characteristic value based on wavelet transform (Zhang et al., 2000).

The order of wavelet transform is J. The detail information of each scale (high frequency coefficient) and the approximate information of the last layer (low frequency coefficient) are combined into the calculation of the energy formula:

$$E_j^d = \frac{1}{E}\sum_{k=1}^{l/2^j} cD_{j,k}^2, \quad j = 1, \ldots, J \qquad [3]$$

$$E_J^a = \frac{1}{E}\sum_{k=1}^{l/2^J} cA_{J,k}^2 \qquad [4]$$

Where $E = \sum_{k}^{l} f_k^{\,2} = E_j^a + \sum_{j=1}^{J} E_j^d$ , j is the corresponding scale.

Subsequently, the energy characteristic vector of J scale can be obtained:

$$\mathrm{T} = \left[E_j^a, E_1^d, E_2^d \ldots E_J^d\right] \qquad [5]$$

Herein "db5" was selected as the wavelet basis function and take order for wavelet transform as 6, by representativeness of the data. The sample size of collected sound, such as pebble, ship and water, are 300, 100 and 200, respectively. The energy eigenvector and the average feature vectors of all signals were obtained. (Fig.8).

 

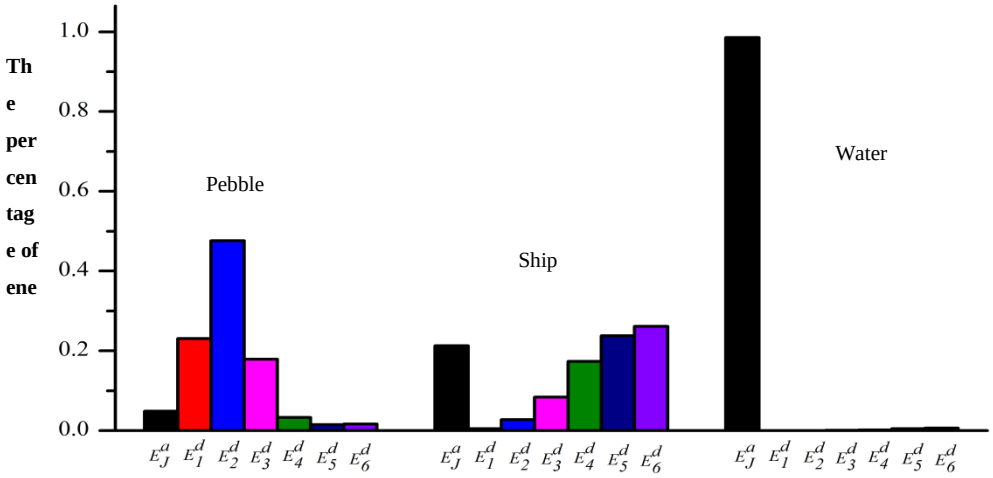


**Figure 8.** The energy distribution of the three signals

The three types of energy distribution differ in three main ways:

i. The energy of pebble sound was centered on the high-frequency coefficients in the order of 1 to 3,, which exceeds 80% of the total energy, and the energy of the low frequency coefficient does not exceed 10%;
ii. The Ship's sound energy was mainly concentrated in the low frequency coefficients and high frequency coefficient in the order of 4 to 6;
iii. More than 90% of the water sound energy was concentrated on the low frequency coefficients.

Above all, the distribution range of characteristic parameter of the pebble movement can be obtained by comparing the differences among the pebble and the other two kinds of sound signal. The confidence interval was determined as 0.8, and then the pebble peak frequency were in the range of 1400 ~ 4000 Hz. The pitch frequency range was from 2000 to 3800Hz. For pebbles, the total energy of the high frequency coefficients in order of 1~3 order, can be used to characterize the energy distribution of wavelet transform. The total energy is denoted by $T$ and should satisfy $0.8 < T < 1$ .

## 5 IDENTIFICATION EFFECT ANALYSIS

In order to verify whether the characteristic parameters can describe the pebble movement sound, in this paper, synthetic analysis of the complex audio signal plays a role in identifying the recognition effect. The synthetic signal contains a series of complex sound signals, such as the sound of water, ship's navigation, pebble movement, thunder and etc. Figure 9 is the time-domain waveform of the synthetic signal.

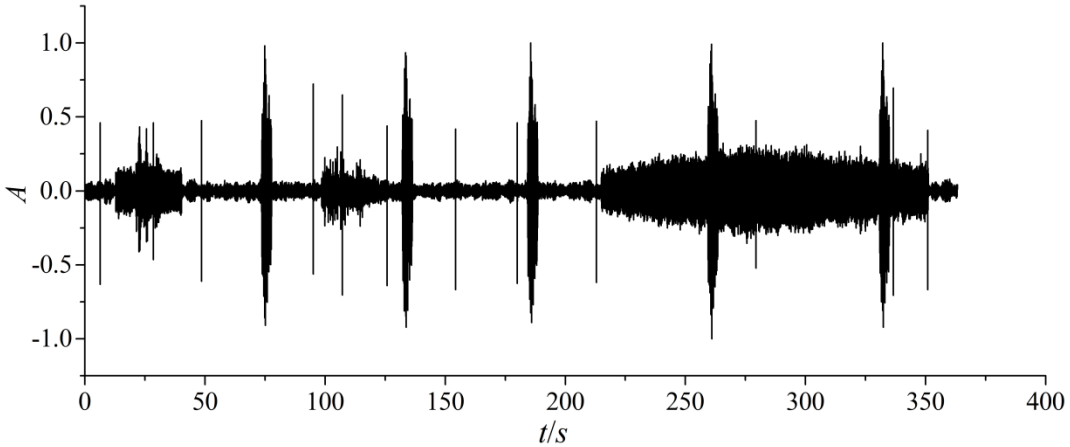


**Fig. 9** The time- domain waveform of the synthetic signal

There are 677 pieces of sound clips obtained after completing the detection and extraction for the target signal. And then the distribution characteristic of each sound segment will be represented by a vector ( $f1$, $f2$, $T$ ), where $f1$ is the peak frequency, $f2$ is the fundamental frequency and $T$ is the energy

distribution through wavelet transform. Figure 10 is a representation of the distribution characteristic of each sound segment.

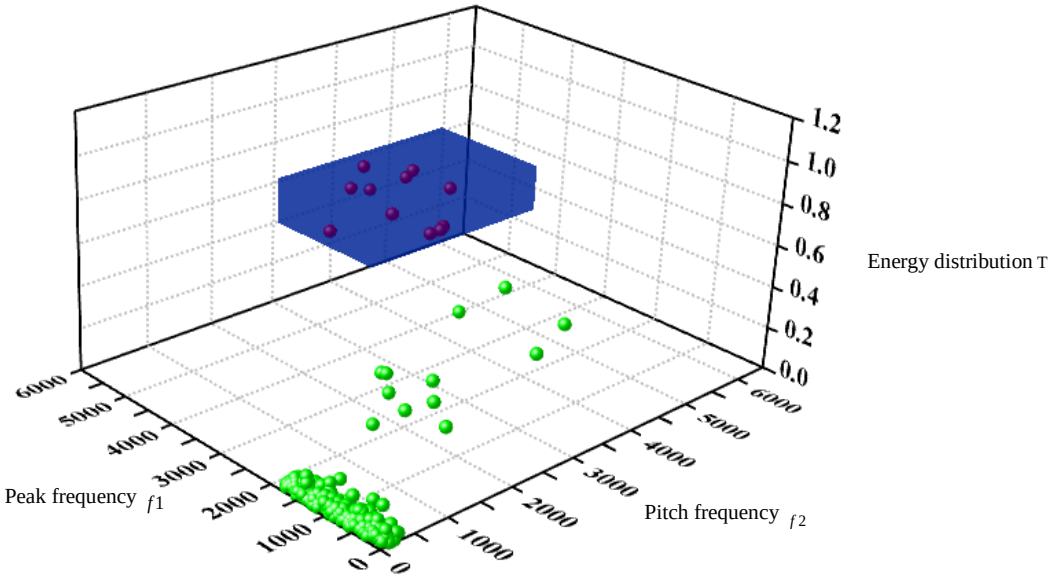


**Figure 10.** The distribution characteristic of each sound segment

The blue rectangle in the figure is the characteristic distribution region of the pebble moving. From the 677 pieces there were 11 pieces of sound segment falling in the region. It indicates that the synthesis signal features 11 occurrences of pebble collision. Comparing the recognition result with 12 times of recognition, the recognition result gap was only one.

## 6 CONCLUSIONS

Part of the rivers in China, especially in mountainous rivers, the gravel movement often causes navigation obstruction. It is today difficult to measure the space-time characteristics (time, quantity.) of the pebble movement. That restricts the development of the key mechanism of the navigation obstructing and other relevant research. Therefore, this research focuses on the acoustic method, and expects to obtain the real and reliable pebble motion data through more convenient methods.

The research starts from the identification of pebble movement and then draws lessons from the voice signal processing methods to analyze the common audio signal of field measurement such as pebble, ship and water. Meanwhile, the peak frequency, fundamental frequency and energy distribution characteristics of wavelet transform are extracted as the characteristic parameters for pebble movement. Finally, the analysis of the synthesis signals is completed on the basis of the characteristic parameters for identifying pebble movement. The main conclusions are as follows:

i. For the background noise in the field measurement, it can be reduced and eliminated by using spectral subtraction method. At the same time, in order to reduce the workload, the time period of energy mutation is extracted and analyzed according to the energy change.
ii. The characteristic parameters of the pebble movement can be expressed in terms of the fundamental peak frequency and its location and the energy distribution after wavelet transform. Those parameters are different when signals providing from the ship are compared to the signals coming from the water. The pebble peak frequency is in the range of 1400 ~ 4000 Hz, and pitch frequency ranges from 2000 to 3800Hz. The energy of pebble sound is centered on the high-frequency coefficients in the order of 1 to 3, which exceeds 80% of the total energy.
iii. On the basis of the characteristic parameters for identifying pebble movement, the analysis of the synthesis signals is completed, and 11 pebble collisions are extracted from 677 pieces of sound bite. Comparing the recognition result with 12 times of ear recognition, the gap of recognition result is only one. It shows that the method has high recognition accuracy.

In summary, the acoustic method is simple and easy to operate, and reliable on measurement results. For observing the gravel movement, this method is feasible.

## ACKNOWLEDGEMENTS

This study is supported by the National Key Technology R&D Program, grant2011BAB09B01 and Chongqing Municipal Education Commission Technology Research Project, grant KJ1500539. The authors thank numerous students for their support with fieldwork in the Yangtze River.

 

**REFERENCES**

Bunte, K., Abt, S. R., Potyondy, J. P. & Ryan, S. E. (2004). Measurement of Coarse Gravel and Cobble Transport Using Portable Bedload Traps. *Journal of Hydraulic Engineering*,130(9), 879-893.

Rigby, J.R, Wren,D. G. & Kuhnle, R.A. (2016). Passive Acoustic Monitoring of Bed Load For Fluvial Applications. *Journal of Hydraulic Engineering*, 142(9), 02516003.

Papanicolaou, A.N & Knapp D. (2010). A Particle Tracking Technique for Bedload Motion[J]. *Geological Survey Scientific Investigations Report*，352-367.

Barton, J.S., Slingerland, R.L., Pittman, S. & Gabrielson, T.B. (2010). Monitoring Coarse Bedload Transport with Passive Acoustic Instrumentation: A Field Study. 38-51.

Graff, B. (2010). Monitoring of Bedload in River Beds with an Hydrophone: First Trials Of Signal Analyses[C]. *Proceedings of the International Conference on Fluvial Hydraulics River Flow*.

Barton, J.S. (2006). Passive Acoustic Monitoring of Coarse Bedload in Mountain Streams. *Doctoral dissertation*, The Pennsylvania State University.

Song Zh.Y. (2013). Application of MATLAB in Speech Signal Analysis and Synthesis*. Beijing University of Aeronautics and Astronautics Press.*

Boll, S. (1979). Suppression of Acoustic Noise in Speech Using Spectral Subtraction. *IEEE Transactions on Acoustics Speech & Signal Processing*, 27(2), 113-120.

Zhang, J. Y., Zhang, B. & Jiang, X. Z. (2000). Analyses of Feature Extraction Methods Based on Wavelet Transform. *Signal Processing*, 16(2), 156-162. (in Chinese)

 